ANL-7710
Reactor Technology

Argonne National Laboratory

9700 South Cass Avenue
Argonne, Illinois 60439

APPLIED PHYSICS DIVISION ANNUAL REPORT

July 1, 1969, to June 30, 1970

Robert Avery, Division Director
Fred W. Thalgott, Deputy Division Director
Harry H. Hummel, Associate Division Director
W. C. Redman, Associate Division Director
William J. Sturm, Assistant Division Director
Lyman J. Templin, Assistant Division Director

January 1971

DISCLAIMER

FOREWORD

It was noted in the last Reactor Physics Division Annual Report, ANL-7610, that the name of the Division was changed to Applied Physics at a date subsequent to the period reported in ANL-7610. Thus, this becomes the first issue of the Applied Physics Division Annual Report. However, the material presented is totally concerned with reactor physics, as was true of all preceding issues. As in previous annual reports, this report emphasizes work performed by members of the Division, rather than integrated programmatic accomplishments. When reasonable and possible, papers related to a given subject are grouped together within a Section.

In order to assist those who may wish to pursue a given subject more extensively, a list of pertinent references is included in each article. A catalog of open literature and report publications and of abstracts prepared by staff of the Applied Physics Division during the reporting period is appended in Section V to further aid those who may be interested in having additional information concerning work done in this Division.

In February 1970, the Laboratory combined all reactor safety work within one organization—the Reactor Analysis and Safety Division—, thus removing from several Divisions reactor safety work for which each had been previously responsible. Thus this issue of the Annual Report—unlike those of past years—includes no work on reactor safety.

Table of Contents

SECTION I
FISSION PROPERTIES AND CROSS SECTION DATA

I-1. Fast Neutron Total and Scattering Cross Sections of Bismuth 3
A. B. Smith, J. F. Whalen, E. Barnard, J. A. M. de Villiers and D. Reitmann

I-2. Fast Neutron Total and Scattering Cross Sections of Ho-165 4
J. Meadows, A. B. Smith, J. Whalen and T. D. Beynon

I-3. Fast Neutron Total and Scattering Cross Sections of the Even Molybdenum Isotopes 5
P. Lambropoulos, J. Whalen and A. B. Smith

I-4. Fast Neutron Total and Scattering Cross Sections of Elemental Titanium 7
E. Barnard, J. A. M. de Villiers, D. Reitmann, P. Moldauer, A. B. Smith and J. Whalen

I-5. Fast Neutron Total and Scattering Cross Sections of U-238 9
P. Lambropoulos

I-6. Fast Neutron Total and Scattering Cross Sections of Pu-240 from 0.1 to 1.5 MeV 11
P. Lambropoulos, J. Whalen and A. B. Smith

I-7. Fast Neutron Total Cross Sections 12
J. Whalen and J. Meadows

I-8. The Fission Cross Section of U-233 Relative to U-235 from 500 to 1500 keV 13
J. W. Meadows

I-9. Fast Neutron Inelastic Gamma Ray Studies of Arsenic and Sodium 15
D. L. Smith

I-10. The Level Scheme of U-238 24
W. P. Poenitz

I-11. Some Remarks on Prompt Fission Neutron Spectra 26
A. B. Smith

I-12. Analysis of Intermediate Structure in the Fission Cross Section of Pu-239 28
Yasuyuki Kikuchi

I-13. Analysis of Intermediate Structure in the Fission Cross Section of Pu-241 31
Yasuyuki Kikuchi

I-14. Recent Experimental Data for Heavy Nuclei 33
W. P. Poenitz

I-15. Spin Determination of Resonances in Ho^{165} (n, γ) from Low Level Occupation Probability Ratios 44
W. P. Poenitz and J. R. Tatarczuk

I-16. Statistical Distribution of Nuclear Shell Model Matrix Elements 48
K. Takeuchi and P. A. Moldauer

I-17. R-Matrix Shell-Model Calculations of Scattering and Reaction Cross Sections 49
K. Takeuchi and P. A. Moldauer

I-18. Developments Relating to the ENDF/B Project 50
E. M. Pennington and J. P. Regis

SECTION II
FAST REACTOR PHYSICS

II-1. The FTR-2 Program on the Zero Power Plutonium Reactor (ZPPR) 55
W. P. Keeney, J. C. Young and A. Travelli

II-2. ZPR-9 Assembly 26, FTR-3 58
J. W. Daughtry, R. B. Pond, C. D. Swanson and R. M. Fleischman

II-3. Central Reaction Ratios in ZPR-9 Assembly 26, FTR-3 63
A. B. Long and C. D. Swanson

II-4. Measured Reaction Rate Distributions in ZPR-9 Assembly 26, FTR-3 65
A. B. Long and C. D. Swanson

II-5. Small Sample Reactivity Worth Measurements in ZPR-9 Assembly 26, FTR-3 70
J. W. Daughtry and R. M. Fleischman

II-6. Plutonium and U-238 Doppler Measurements in ZPR-9 Assembly 26, FTR-3 73
R. B. Pond, J. W. Daughtry, C. E. Till, E. F. Groh, C. D. Swanson and P. H. Kier

II-7. Analytical Studies in Support of the Fast Flux Test Facility (FFTF) Critical Experiments on ZPPR and ZPR-9 77
A. Travelli, A. J. Ulrich and J. C. Beitel
II-8. Doppler-Effect, Heterogeneity, and Sodium-Voiding Experiments in ZPR-3 Assemblies 48 and 48B 97
J. M. Gasidlo, A. M. Broomfield, R. L. McVean and W. P. Keeney
II-9. Neutron Spectra and Spectra Indices in ZPR-3 Assemblies 53 and 54 100
R. O. Vosburgh, R. E. Kaiser, J. M. Gasidlo, J. E. Powell and N. A. Hill
II-10. Analysis of Reactivity Doppler Experiments for ZPR-3 Assembly 53 109
R. E. Kaiser and J. M. Gasidlo
II-11. Pu-239, U-235 and U-238 Capture-to-Fission Ratios in ZPR-3 Assembly 57 Measured by the Reactivity-Reaction Rate Method 112
M. M. Bretscher, J. M. Gasidlo and W. C. Redman
II-12. An Integral Measurement of Pu-239 and U-233 Alpha 122
W. Y. Kato, R. J. Armani, R. P. Larsen, P. E. Moreland, L. A. Mountford, J. M. Gasidlo, R. J. Popek and C. D. Swanson
II-13. Experimental Results for ZPR-3 Assemblies 58 and 59 128
J. M. Stevenson, J. M. Gasidlo and R. O. Vosburgh
II-14. The EBR-II Critical Assemblies—ZPR-3 Assemblies 60, 61, and 62 137
W. P. Keeney, R. O. Vosburgh, J. M. Gasidlo and D. Meneghetti
II-15. Critical Mass Evaluation in ZPPR Assembly 2, a Demonstration Reactor Benchmark Assembly 140
R. E. Kaiser and R. J. Norris
II-16. Heterogeneity and Criticality Studies on the Zero Power Plutonium Reactor (ZPPR) Assembly 2, a Demonstration Reactor Benchmark Critical 146
Arne P. Olson and Nam Chin Paik
II-17. Zero Power Plutonium Reactor (ZPPR) Assembly 2 Noise Studies 155
W. K. Lehto
II-18. Fast Neutron Spectrum Measurements in the Zero Power Plutonium Reactor (ZPPR) and ZPR-3 Critical Assemblies 157
G. G. Simons
II-19. ZPR-9 Assembly 25: Description and Experimental Results 165
L. G. Lesage and W. R. Robinson
II-20. Gamma Spectrum in ZPR-6 Assembly 6 173
R. Gold
II-21. ZPR-6 Assembly 6A, A 4000-Liter UO_2 Fast Core 175
R. A. Karam, W. R. Robinson, G. S. Stanford and G. K. Rusch
II-22. Measured Neutron Spectra in ZPR-6 Assembly 6A, ZPR-9 Assembly 25, and ZPR-9 Assembly 26, FTR-3 183
T. J. Yule, E. F. Bennett and I. K. Olson
II-23. The Variable Temperature Rodded Zone (VTRZ) Project 189
R. A. Lewis, K. D. Dance, J. F. Meyer and E. F. Groh
II-24. Analysis of Time-of-Flight Measurements 197
Burt A. Zolotar
II-25. Conditional Variances Pertinent to Doppler Effect Studies 200
R. N. Hwang and L. B. Miller
II-26. Typical Absolute Activation Measurements in Zero Power Reactor (ZPR) Cores ... 201
D. W. Maddison and L. S. Beller
II-27. β_{eff} Measurements in Two Fast Reactor Critical Assemblies 202
S. G. Carpenter, J. M. Gasidlo and J. M. Stevenson
II-28. Rod Drop Measurements of Subcriticality 206
S. G. Carpenter and R. W. Goin
II-29. Experimental Determination of the Perturbation Denominator in Fast Critical Assemblies 209
W. C. Redman and M. M. Bretscher
II-30. The Effects of Gaps and Foils on the Measured Fission and Capture Rates in Depleted and 16.4% Enriched UO_2 Fuel Rods 214
A. B. Long, W. R. Robinson and G. S. Stanford
II-31. Measurement of the Fission Yields of Mo-99 and Ba-140 from Pu-239 in Fast Neutron Spectra 219
R. J. Armani, Raymond Gold, R. P. Larsen and J. H. Roberts
II-32. Reactivity Effects in Critical Facilities Due to Fissile Isotope Decay 222
R. G. Matlock, R. E. Kaiser and J. M. Gasidlo
II-33. A Postanalytical Study of Eight ZPR-3 Benchmark Criticals Using ENDF/B Data. 224
A. L. Hess, R. G. Palmer and J. M. Stevenson

II-34. A Study of Methods of Cross Section Error Identification Utilizing Integral Data from Fast Critical Assemblies 227
K. O. Ott, R. B. Pond and J. M. Kallfelz
II-35. Fuel Management Design With the REBUS System 230
J. Hoover and D. A. Meneley
II-36. Alternative Neutron Energy Group Collapsing Schemes Applied to Fuel Cycle Calculations 235
J. Hoover and D. A. Meneley
II-37. Neutronics of Advanced Liquid Metal Fast Breeder Reactors With Refractory-Clad Fuel 238
D. A. Meneley, E. L. Fuller and A. E. McArthy
II-38. Parametric Study of Neutronic Characteristics of LMFBR Types 242
J. T. Madell and R. Abington
II-39. Effect of Subassembly Clearances on Some Performance Characteristics of 1000 MWe LMFBR Designs 252
J. T. Madell and H. H. Hummel
II-40. A Dual Spectrum Concept for Liquid Metal Fast Breeder Reactor (LMFBR) Fuel Assay 259
C. N. Kelber
II-41. Calculated Gamma-Ray Heating in an Assembly for Irradiating Fast Reactor Fuel Elements in the Center of the Engineering Test Reactor (ETR) Core 260
A. E. McArthy

SECTION III

EXPERIMENTAL TECHNIQUES AND FACILITIES

III-1. The Fast Neutron Generator (FNG) Facility 265
S. A. Cox
III-2. Klystron Buncher for Pulsed FNG Single-Ended Operation 266
D. L. Smith
III-3. Time-of-Flight Errors in Pulsed Neutron Measurements 269
J. W. Meadows
III-4. Time Resolution of a Ge(Li) Detector in (n, n'γ)Experiments 269
W. P. Poenitz
III-5. Variation of Efficiency of a Ge(Li) Detector as a Function of Source Distance 271
D. L. Smith
III-6. On-Line and Interactive Computer System 273
J. Whalen, P. Guenther and W. P. Poenitz
III-7. Critical Reactivity Measurement Techniques at the Zero Power Plutonium Reactor (ZPPR) 274
R. W. Goin and C. L. Beck
III-8. Zero Power Plutonium Reactor (ZPPR) Computer Interfaces 277
J. E. Hutton, R. J. Forrester and D. L. Hall
III-9. Precision Efficiency Calibration Procedures for Ge(LI) Detectors 283
D. W. Maddison and L. S. Beller
III-10. Contamination Determination with Lithium-Drifted-Germanium [Ge(Li)] Detectors 285
L. S. Beller and D. W. Maddison
III-11. Detector for B^{10}(n, α)-to-Fission Ratio Measurements 288
L. S. Beller
III-12. Thermoluminescent Dosimetry Applied to Gamma Ray Dose Measurements in Critical Assemblies 289
G. G. Simons
III-13. Non-Perturbing Fission Counter for Use in Plate-Type Critical Assemblies 294
A. B. Long and E. M. Bohn
III-14. Development of an Improved Tritium Counting Facility 296
A. De Volpi and M. Bretscher
III-15. Pulse Selector 297
J. M. Larson
III-16. High Energy Limitation of Proton-Recoil Proportional Counters for Neutron Spectroscopy 300
T. J. Yule
III-17. Electronics for Proton-Recoil Systems Using Proportional Counters 304
J. M. Larson

III-18. Developments in the Electronic System for Neutron Spectroscopy with Proton-Recoil Proportional Counters 308
T. J. Yule and E. F. Bennett
III-19. Comparison of Neutron Spectra from Proton-Recoil Counters Measured with the Idaho and Illinois Configurations 314
T. J. Yule and G. G. Simons
III-20. A Precision dc Baseline Restorer for Proton Recoil Proportional Counting 316
J. M. Larson
III-21. Spectrum Analysis for a Silicon Fission-Fragment Detector 318
E. M. Bohn and A. B. Long
III-22. He-3 Gas Scintillator for Time-of-Flight Neutron Measurements 321
Raymond Gold and Dale M. Smith
III-23. Statistical Fluctuations and the False Alarm Frequency of Safety Channels 323
K. G. A. Porges
III-24. Fluctuations of Count Rate Meter Signals 325
K. G. A. Porges and W. Corwin
III-25. Neutron Source Self-Absorption and Cavity-Wall Absorption 327
A. De Volpi
III 26. Neutron Escape from Water-Moderated Tanks 328
A. De Volpi
III-27. Digital Delay with Substantially Reduced Deadtime 331
A. De Volpi, G. E. Caya, C. J. Rush and S. J. Rudnick
III-28. Deadtime Correction in Counting Rapidly Decaying Sources 332
K. G. A. Porges and A. De Volpi
III-29. Speed Tests on Some Small-to Medium Computers 334
Charles Erwin Cohn
III 30. The Optimum Evaluation of Series of Measurements by Maximum Likelihood, as Applied to Nuclear Source Counting 338
K. G. A. Porges and A. De Volpi
III-31. Estimates of Variance from Measured Quantities of Fluctuating Origin and Inherent Correlation 340
A. De Volpi
III-32. Random Numbers from Electronic Noise 342
Charles Erwin Cohn
III-33. Gamma-Ray Spectral Measurements at JANUS 344
Raymond Gold and K. E. Freese
III-34. A Neutron Spectrum Map of the JANUS Irradiation Facility Using Proton-Recoil Proportional Counters 350
E. F. Bennett and T. J. Yule
III-35. A Code for Calculating the Temperatures of Effluent Air from the ZPR-6 and -9 Sand Filters 358
G. K. Rusch
III-36. A Sodium Vapor Monitor 359
J. F. Meyer, T. W. Johnson and J. E. Sustman
III-37. Fast Neutron Hodoscope Progress 362
A. De Volpi

SECTION IV
REACTOR COMPUTATION METHODS AND THEORY

IV-1. MC² Capability in the Argonne Reactor Computation (ARC) System 367
C. G. Stenberg and H. Henryson, II
IV-2. Plans for the New Mc² Code, MC²-2 371
B. J. Toppel
IV-3. Heterogeneous Formulation of the Resolved Resonance Broad-Group Reaction Cross Section 373
W. M. Stacey, Jr. and B. A. Zolotar
IV-4. Inelastic Matrices in Multigroup Calculations 374
M. Segev
IV-5. Higher-Order Transport Approximations for MC²-2 381
C. N. Kelber, H. Henryson, II, E. M. Pennington and W. M. Stacey, Jr.
IV-6. Preliminary Investigations of the Resolved Resonance Algorithms for the New Mc² Code 387
R. N. Hwang

IV-7. Heterogeneity Algorithms for MC² 2 393
R. G. Palmer and B. A. Zolotar
IV-8. Calculation of Elastic Scattering Matrices 395
H. Henryson, II, C. G. Stenberg and B. J. Toppel
IV-9. Calculation of Heterogeneous Fluxes and Reactivity Worths . 403
W. M. Stacey, Jr.
IV-10. Continuous Slowing-Down Theory for the Elastic Moderation of Neutrons 404
W. M. Stacey, Jr.
IV-11. An Integral-Attenuation Factor Treatment of Resolved Narrow Resonance Absorption ... 407
W. M. Stacey, Jr.
IV-12. General Multigroup and Spectral Synthesis Equations 408
W. M. Stacey, Jr.
IV-13. Applications of Spectral Synthesis to Fast Reactor Dynamics 409
W. M. Stacey, Jr.
IV-14. Some Variational Models for Flux Synthesis in Space-Time 410
W. L. Woodruff and V. Luco
IV-15. Formulation of Space-Energy-Time Iterative Synthesis . 417
E. L. Fuller
IV-16. Further Studies on the Use of the Method of Undetermined Parameters to Integrate the Multimode Kinetics Equations 426
E. L. Fuller
IV-17. Spurious Eigenvalues in Flux Synthesis 428
V. Luco and W. Woodruff
IV-18. Modification of the Multiregion Resonance Absorption Code RABBLE 433
P. H. Kier
IV-19. Further Developments in Integral Transport Methods for Resonance Region Calculations in Plate-Type-Lattices Using the RABID Code 434
Arne P. Olson
IV-20. Testing of the Perturbation Modules in the Argonne Reactor Computation (ARC) System 437
P. H. Kier
IV-21. Modifications to the Integral Transport Heterogeneity Code CALHET-2 440
Arne P. Olson and P. H. Kier
IV-22. The Improved Spatial Cross Section Homogenization Capability of the Double S_n Transport Theory Code TESS . 441
J. P. Plummer and R. W. Goin
IV-23. Self Shielding of Annular and Solid Cylinders 443
R. B. Nicholson
IV-24. An Extended Equivalence Relation 445
C. N. Kelber
IV-25. A Fast Exponential Subroutine for Calculating Collision Probabilities on the IBM/360 . 446
Arne P. Olson
IV-26. Improved Subroutine Efficiency Through Calling-Sequence Modification . 447
Charles Erwin Cohn and Mark H. Elfield
IV-27. Software Methods of Data Acquisition on a Small Computer 449
D. W. Maddison and C. L. Beck
IV-28. New Features in the NURF Foil-Data Program 450
G. S. Stanford
IV-29. The Effects of S/N Ratio on the Results of Polarity Correlation Experiments 451
W. K. Lehto and R. W. Goin
IV-30. MATDIAG, A Program for Computing Multilevel S-Matrix Resonance Parameters 453
P. A. Moldauer, R. N. Hwang and B. S. Garbow
IV-31. Shielding Study for the University of Chicago Experiment in Pioneer F/G 456
C. N. Kelber and A. E. McArthy

SECTION V

PUBLICATIONS

June 1, 1969 to June 30, 1970

Open Literature 465
Reports 466
Abstracts 466

Section I

Fission Properties and Cross Section Data

In close support of the reactor program, experimental and theoretical studies of neutron interactions with those nuclei found in the structural and fuel components of reactor systems continue to be carried out. This work is performed principally to provide information necessary for optimal reactor physics design. The major portion of the effort is devoted to studies of fast neutron induced processes, especially those which are important in fast reactors. The studies are directed toward neutron elastic and inelastic scattering, neutron induced reactions including capture, and to characteristics of the fission process.

I-1. Fast Neutron Total and Scattering Cross Sections of Bismuth[1]

A. B. Smith, J. F. Whalen, E. Barnard,* J. A. M. de Villiers* and D. Reitmann*

Total neutron cross sections of bismuth were measured with resolutions $\gtrsim 1$ keV over the energy range 0.2 to 1.4 MeV. Differential elastic scattering cross sections were determined at intervals <50 keV from 0.3 to 1.5 MeV with resolutions of approximately 20 keV. The inelastic neutron excitation of a state at 896 $\pm$ 1 keV was observed and the respective differential excitation cross sections determined with incident resolutions $\gtrsim 10$ keV. Partially resolved resonance structure was evident in all the measured values as illustrated in Fig. I-1-1. The experimental results were assayed for possible intermediate structure and were compared with the results of optical model and statistical calculations. The model calculations were cognizant of the fluctuation and correlation of compound-nucleus resonance widths and of the shell closure at $N = 126$.

The experiments reasonably achieved the objective of providing well-defined total, elastic, and inelastic neutron scattering cross sections of bismuth up to incident neutron energies of approximately 1.5 MeV. The energy-averaged total and elastic scattering cross sections were well described by a surface absorption optical potential and statistical theory. Best agreement between experiment and calculation was achieved with a surface absorption smaller than that found widely applicable in other mass regions. This reduced absorption was attributed to the effects of the shell closure at $Z = 82$ and $N = 126$ and is consistent with similar effects reported elsewhere. The optical potential and statistical theory led to calculated inelastic scattering cross sections approximately 15% larger than observed experimentally. Fluctuation corrections to the calculated inelastic scattering led to only marginally improved agreement with experiment. The optical potential derived from the present measurements was extended to a wider energy range and found qualitatively descriptive of reported experimental values. However, the potential was not unique. Considerable energy-dependent structure was observed in the measured cross sections. A quantitative assay of the structure observed in the total cross sections led to results consistent with well-known compound nucleus resonance structure and the experimental resolution.

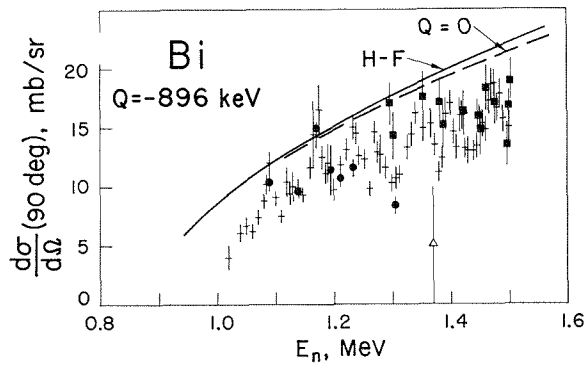

Fig. I-1-1. Differential Cross Sections for the Excitation of the 896 keV State in Bismuth at a Scattering Angle of 90 deg. Crosses Indicate the Results of the Present Fine Resolution Measurements. Solid Circles Are the Result of the Angle Integral of Fine Resolution Differential-Angular Distributions Divided by 4π. Solid Squares Denote the Results of Broad Resolution Measurements. Vertical Bars Indicate Cross Section Uncertainties. The Triangular Datum Point Indicates the Value Given in Ref 2. The Solid Curve Indicates the Result of Hauser-Feshbach Calculations[3] and the Dashed Curve Indicates Calculated Values Inclusive of Correction Factors as Described in Ref 4 *ANL Neg. No. 113-2547 Rev. 1.*

* Atomic Energy Board, Pelindaba, Transvaal, Republic of South Africa.

References

1. A. B. Smith, J. F. Whalen, E. Barnard, J. A. M. de Villiers and D. Reitmann, *Fast Neutron Total and Scattering Cross Sections of Bismuth*, Nucl. Sci. Eng. **41**, 63–69 (1970).
2. J. Beyster et al., *Inelastic Collision Cross Sections at 1.0-, 4.0- and 4.5-MeV Neutron Energies*, Phys. Rev. **98**, 1216 (1955).
3. W. Hauser and H. Feshbach, *The Inelastic Scattering of Neutrons*, Phys. Rev. **87**, 366 (1952).
4. P. A. Moldauer, *Average Compound-Nucleus Cross Sections*, Rev. Mod. Phys. **36**, 1079 (1964).

I-2. Fast Neutron Total and Scattering Cross Sections of Ho-165[1]

J. Meadows, A. B. Smith, J. Whalen and T. D. Beynon*

Total neutron cross sections of Ho-165 were measured from 0.1 to 1.5 MeV with resolutions of $\lesssim$2.5 keV. The observed total cross sections varied slowly with energy and displayed no significant structure. Differential neutron elastic and inealistic scattering cross sections were determined at intervals $\lesssim$50 keV

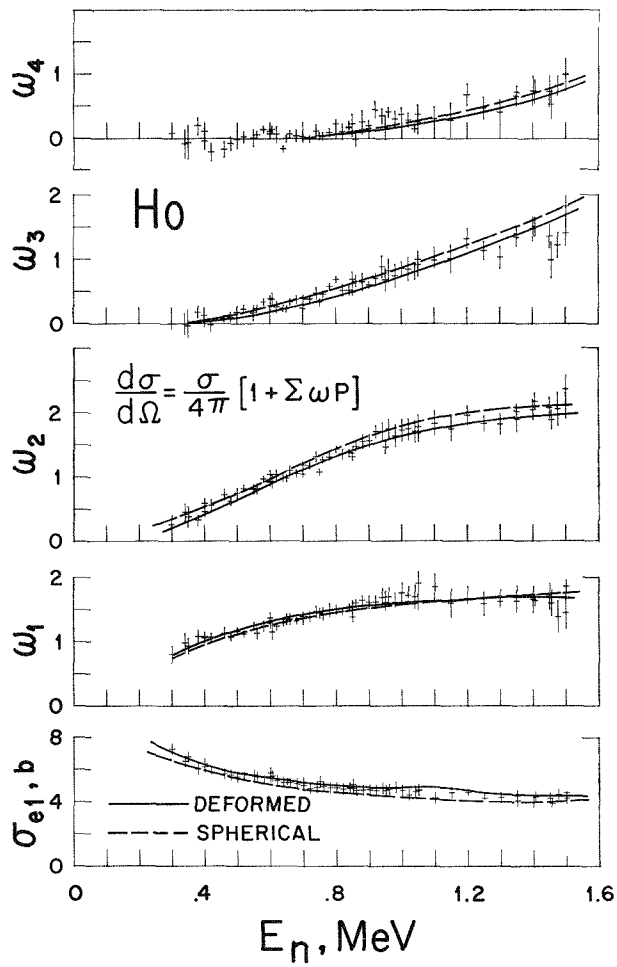

Fig. I-2-1. Summary of Measured Differential Elastic Scattering Cross Sections of Ho-165 Expressed in Format of the Illustrated Legendre Expansion. Curves Indicate the Results of Spherical and of Deformed Potential. *ANL Neg. No. 116-173.*

from 0.3 to 1.5 MeV with results illustrated in Fig. I-2-1. The inelastic excitation of states in Ho-165 at 98, 214, 371, 460, 517, 586, 712, 824, 995, 1104 and 1143 keV was positively observed with probable identification of several additional states. (See Fig. I-2-2.) The prominent excitation cross sections were correlated

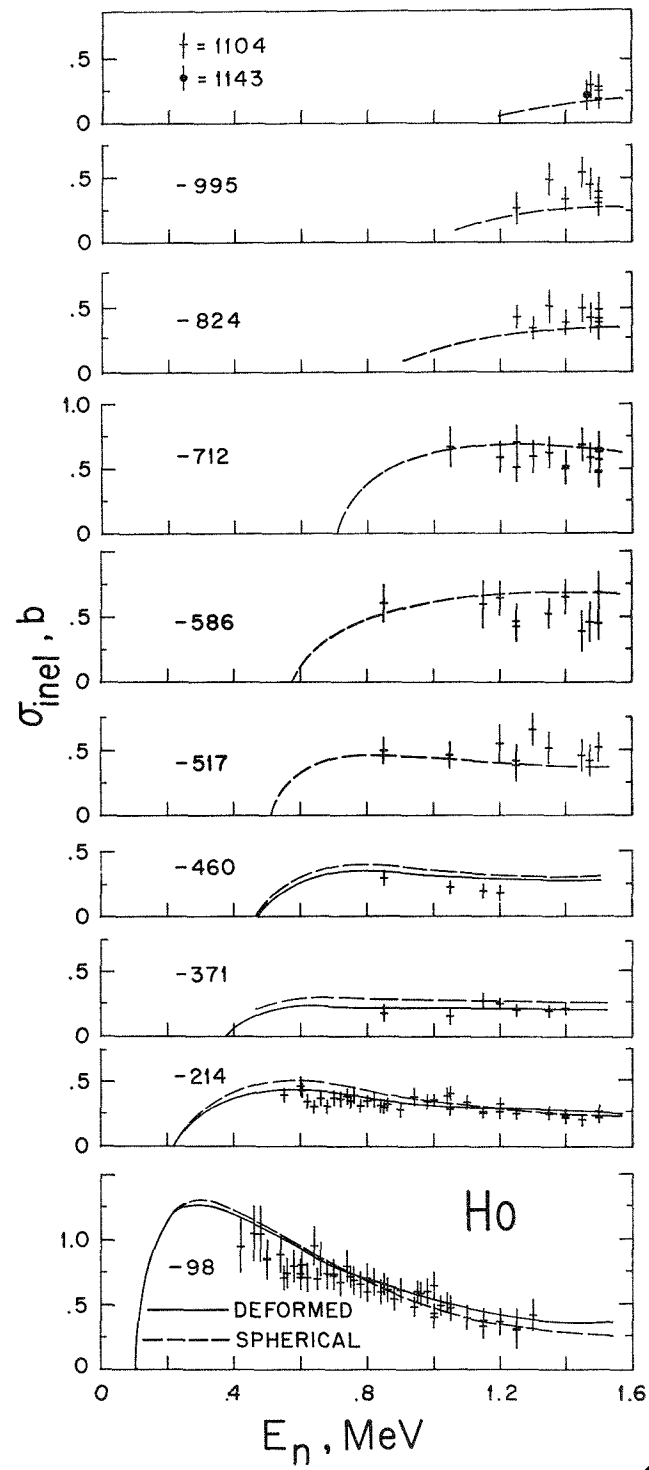

Fig. I-2-2. Measured Inelastic Cross Sections of Ho-16 Crosses Show the Results of the Present Experiments wit the Vertical Bars Indicating Uncertainty. Dashed and Solid Curves Indicate the Results of Calculations Using Spherical and Deformed Optical Potentials and Statistical Formalism. *ANL Neg. No. 116-177.*

* University of Birmingham, Birmingham, England

with known single-particle and collective states and with excited structure postulated from systematics.

The experimental values extended over an appreciable energy range and included consistent total and partial cross sections. Calculations based upon a simple-spherical optical-potential and statistical concepts[2] were reasonably descriptive of the experimental results. Interpretation based upon a more physically acceptable deformed-potential and coupled-channel formalism[3] led to a good agreement with measured total neutron cross sections and gave a better description of elastic scattering processes than obtained with the spherical model. The potential parameters of the spherical and the deformed potential models were independently selected and not particularly similar, indicating a lack of uniqueness. Inelastic neutron scattering cross sections calculated from the Hauser-Feshbach formalism[1] and spherical potential qualitatively agreed with experimental observation but quantitatively deviated from measurement. Use of the deformed-potential and the introduction of channel-coupling did not appreciably improve the agreement between measured and calculated inelastic excitation cross sections. Generally, at the energies of the present experiments direct-inelastic processes were calculated to be $\lesssim 10\%$ of the observed inelastic cross sections.

The effects of resonance-width fluctuations and correlations were examined and found to be small.[4] The experimental results indicated that the structure of Ho-165 at excitations >700 keV was considerably more complex than previously reported. A speculative structure was suggested consistent with the present experimental observation and with a logical extension of established systematics.

REFERENCES

1. J. Meadows, A Smith, J. Whalen and T. D. Beynon, *Ho-165 Fast Neutron Cross Sections*, Zeits fur Physik (submitted for publication)
2. P. Hodgson, "The Optical Model of Elastic Scattering," (Oxford Press, London, 1963)
3. H. Feshbach et al., *Model for Nuclear Reactions with Neutrons*, Phys. Rev. **96**, 448 (1954).
4. T. Tamura, *Analysis of the Scattering of Nuclear Particles by Collective Nuclei in Terms of the Coupled Channel Calculations*, Rev. Mod. Phys **37**, 679 (1965).
5. P. A. Moldauer, *Average Compound Nucleus Cross Sections*, Rev. Mod. Phys **36**, 1079 (1964).

I-3. Fast Neutron Total and Scattering Cross Sections of the Even Molybdenum Isotopes

P. LAMBROPOULOS, J. WHALEN and A. B. SMITH

Molybdenum is a structural material used in reactors and critical assemblies. Macroscopic molybdenum displacement experiments in fast critical assemblies have led to anomalous results. Thus from both the applied and physical points of view the interaction of fast neutrons with molybdenum is of interest. For this reason the elastic and inelastic scattering cross sections and the total cross sections of the isotopes Mo-92, 94, 96, 98 and 100 were determined for incident neutron energies from 0.1 to 1.6 MeV.* Typical results are the total and elastic scattering cross sections of Mo-98 shown in Fig. I-3-1 and the inelastic excitation cross sections of Mo-98 illustrated in Fig. I-3-2.

The even isotopes of molybdenum belong to a large class of even-even nuclei in the mass region $66 < A < 150$ whose low lying excited states are of a collective nature but cannot be rigorously assigned to either pure rotation or vibration configurations. This was pointed out by Scharff-Goldhaber and Weneser,[1] and a theoretical interpretation based on the collective model was given by Davydov and Filippov.[2] These authors considered the Bohr collective Hamiltonian for axially-symmetric even-even nuclei. By solving directly the Schroedinger equation, they showed that the low lying collective excitations of such nuclei can be classified into two types: excitations which do not involve an appreciable change in the nuclear quadrupole moment, and excitations in which the quadrupole moment changes considerably. As a result, the first excited state tends to be a 2^+, although in some cases it can be a 0^+.

A detailed analysis of these experimental results has been undertaken. The present analysis has shown that Mo-98 is one of these few cases where the first excited state is at 0.75 MeV with spin 0^+. The second excited state of this type of nucleus can have spins 0^-, 2^+ or 4^+. The ratio of the energy of the second excited state to that of the first fluctuates about 2.0, and it can be as low as 1.07 as is the case for Mo-98.

The fast neutron scattering cross sections for Mo-94, Mo-96, Mo-98 and Mo-100 have been interpreted on

* The experimental measurements are complete and the numerical data are available on request from the authors

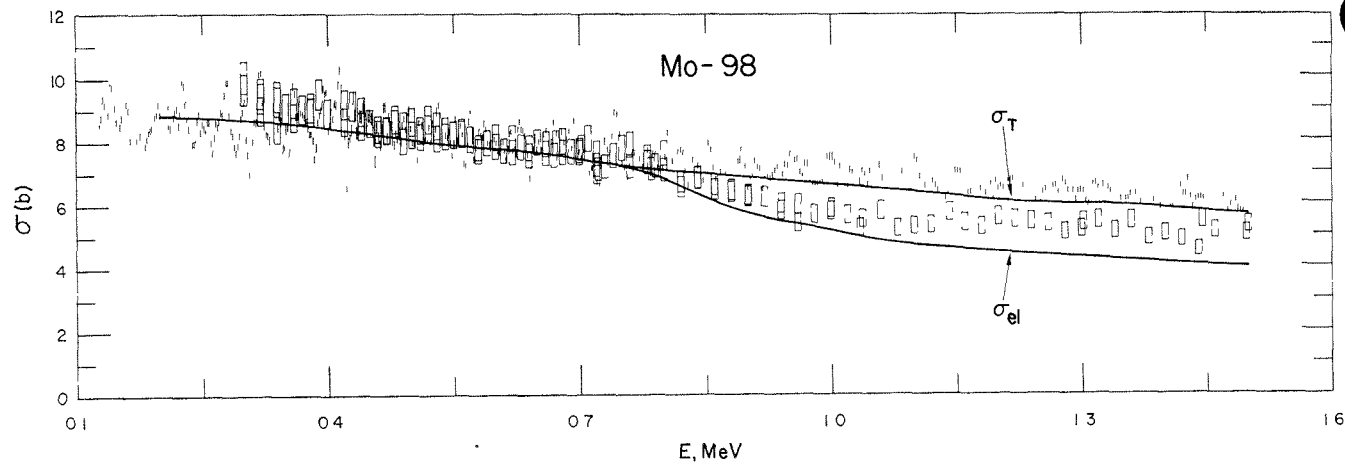

FIG. I-3-1. Total and Elastic Scattering Cross Sections of Mo-98. Vertical Lines are the Experimental Total Cross Section Values Taken with 1–2 keV Resolution. The Boxes Denote the Elastic Scattering Results. The Curves Indicate the Results of Optical Model Calculations. *ANL Neg. No. 116-447.*

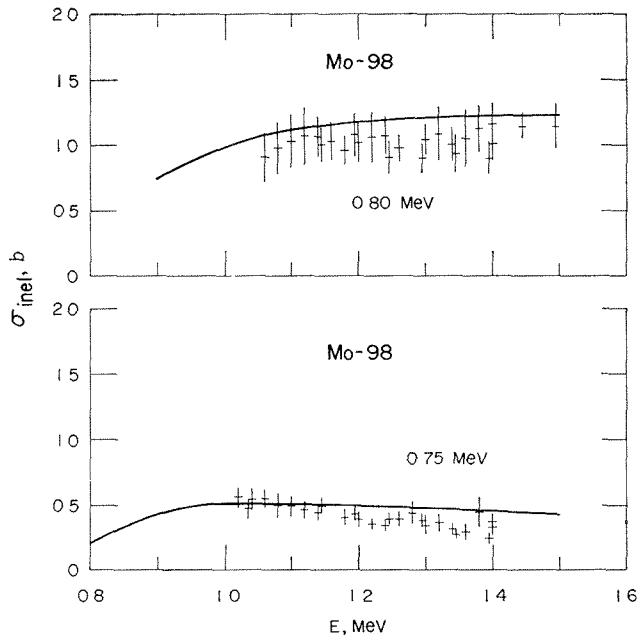

FIG. I-3-2. Inelastic Excitation Cross Sections of Mo-98. Curves Indicate the Results of Optical Model Calculations. *ANL Neg. No. 116-448*

the basis of the Davydov-Filippov model. The cross sections have been calculated using the optical model computer code ABACUS-2. Typical preliminary results are indicated by Figs. I-3-1 and I-3-2. Spins have been assigned to the experimentally observed excited states. The results are consistent with the theoretical model as well as with γ-ray experimental results and analyses recently reported by other authors. Several new levels have been found. Some of these levels have also been identified in Refs. 3 and 4, while others have apparently been identified for the first time in the present experiment. Further analysis of the experimental results is in progress.

REFERENCES

1. G. Scharff-Goldhaber and J. Weneser, *System of Even-Even Nuclei*, Phys. Rev. **98,** 212 (1955).
2. A. S. Davydov and G. F. Filippov, *Collective Excitations of Even-Even Nuclei*, Soviet Physics JETP **6,** 555 (1958).
3. G. Lamoureux et al., *A Study of the Levels of Mo-96 by Means of Coulomb Excitation with O-16 and Ge(Li)-Ge(Li) Directional Correlations of γ-Rays in the Decays of Tc-96 and Nb-96*, Bull. Am. Phys. Soc. **15,** 805 (1970).
4. Karl Swartz et al., *Mo-98 Levels and Their Decays,* Bull. Am. Phys. Soc. **15,** 807 (1970) and private communication with the authors.

I-4. Fast Neutron Total and Scattering Cross Sections of Elemental Titanium

E. BARNARD,* J. A. M. DE VILLIERS,* D. REITMANN,* P. MOLDAUER, A. SMITH and J. WHALEN

Fast neutron cross sections of titanium have long been of reactor interest. Furthermore, the element is of considerable physical interest due to its complex resonance structure and known deformation. Studies of fast neutron interactions with this element provide a good test of the statistical theories or resonance structure and of the effect of nuclear deformation in an intermediate nucleus near the peak of the *s*-wave strength function. In order to provide information of both applied and structure interest these studies of fast neutron interactions with titanium were undertaken.

Total, elastic scattering, and broad resolution inelastic scattering neutron cross sections were measured at ANL and fine resolution inelastic neutron cross section measurements were made at Pelindaba. The methods employed at both laboratories have been extensively described elsewhere.[1-3] The total cross section values were deduced from transmission measurements. Monoenergetic source techniques were employed to determine total cross sections over the incident neutron energy ranges 0.1 to 0.45 MeV and 1.025 to 1.475 MeV, with incident energy resolutions of $\lesssim$2.0 keV. From 0.45 to 1.025 MeV time-of-flight techniques were utilized with a velocity resolution of ~0.01 nsec/m. The experimental results were consistent with previously reported values but displayed a great deal more structure due to improved experimental resolution. Resonances were evidently interfering when from a single isotope, overlapping when from various isotopes, and merged when averaged to give the appearance of an intermediate resonance structure.

Differential elastic scattering cross sections were measured at incident neutron energies from 0.3 to 1.5 MeV and at eight scattering angles distributed between 25 and 155 degrees. The incident neutron energy resolution was $\approx$20 keV. The elastic scattering results are relatively consistent with the measured total neutron cross sections when the different resolutions and small variations in absolute energy scale are considered. Representative angular distributions are shown in Fig. I-4-1.

The inelastic neutron excitation of states at 889 ± 4 and 987 ± 0.7 keV was clearly observed and attributed to known 2+ states in Ti-46 and Ti-48 respectively. In addition, the excitation of a 150 ± 10 keV state was tentatively observed and associated with known 160 keV ($\frac{7}{2}$ −) state of Ti-47. The corresponding excitation cross sections were small ($\lesssim$3 mb/sr) and only marginally observable. The excitation energies were determined from the observed velocities of the inelastically scattered neutrons and, in the case of the 987.5 keV state, from the energies of the subsequent gamma-ray emission as determined in an auxillary experiment using a calibrated Ge(Li) detector.

The angular distributions of inelastically scattered neutrons were determined with incident neutron resolutions of ~20 keV. Generally these distributions were isotropic to within the experimental uncertainties as illustrated in Fig. I-4-1. Differential inelastic cross sections were determined with "fine" incident resolutions (5 to 10 keV) at a scattering angle of ninety degrees. In view of the observed isotropy the inelastic excitation cross sections were obtained from the averaged angular distribution measurements or fine resolution ninety degree values by multiplying by 4π. The results are summarized in Fig. I-4-2. The *broad* and the *fine* resolution results are relatively consistent.

The experimental values were compared with those calculated from optical model and statistical theories.[4] The majority of the calculations employed a spherical

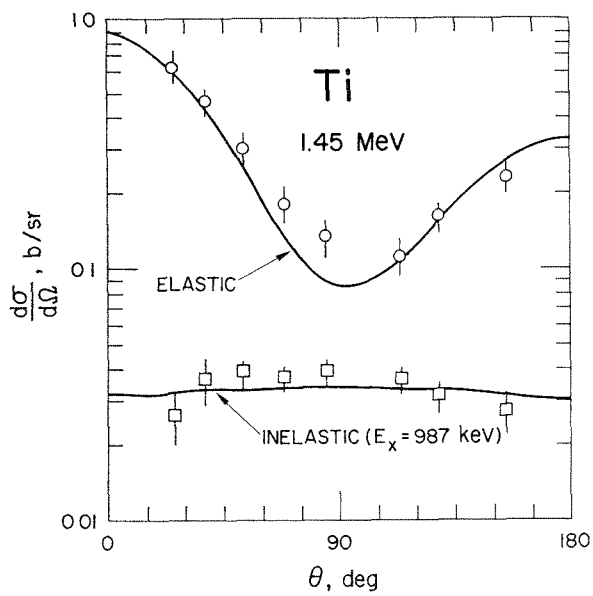

FIG. I-4-1. Angular Distribution of 1.45 MeV Neutrons Scattered from Titanium. Elastic and Inelastic Scattering Results are Indicated Together with the Results of Calculations *ANL Neg No. 116-544.*

* Atomic Energy Board, Pelindaba, Transvaal, Republic of South Africa.

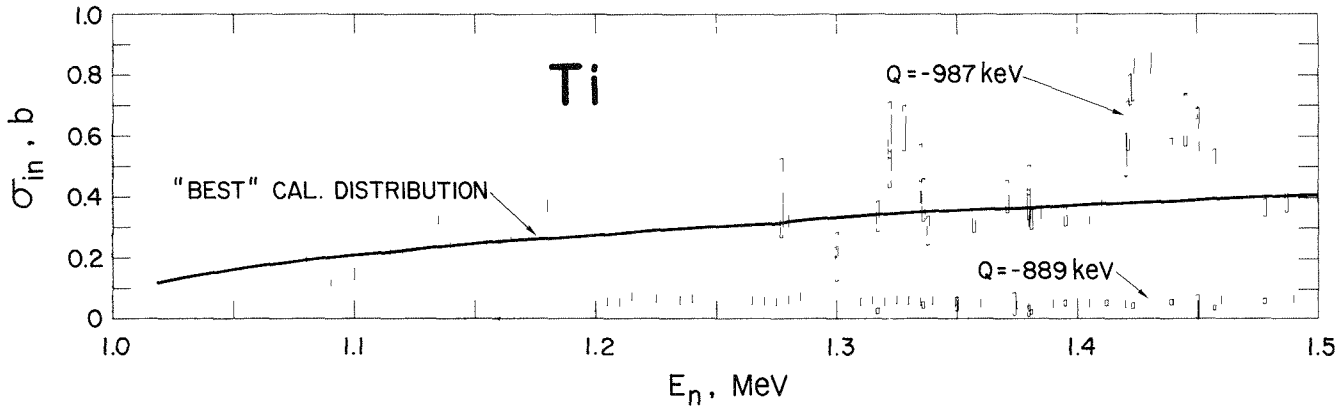

FIG. I-4-2. Cross Sections for the Inelastic Neutron Excitation of the 987 and the 889 keV States in Titanium. "Fine" Resolution (Bars) and the Coarse Resolution (Boxes) Results are Shown. The Vertical Extent of the Respective Symbols is Indicative of the Total Experimental Uncertainty. The Curves Indicate the Results of Calculations as Discussed in the Text. *ANL Neg. No. 116-545.*

potential consisting of a Saxon-Woods real form, a Gaussian surface-imaginary form, and a Thomas spin-orbit term. Non-locality was approximated with energy dependent parameters. The effects of deformation and direct reactions were assayed using a non-spherical optical potential inclusive of two-channel coupling to the first excited state. The calculated total neutron cross sections were descriptive of energy-averaged experimental values. The agreement between calculated and measured elastic angular distributions varied as the structure of the measured results changed with energy. For example, calculated and measured values were similar at 1.0 MeV, but differed appreciably at 1.45 MeV, as indicated in Fig. I-4-1. Over the full measured energy range the calculated elastic scattering generally followed the measured elastic cross sections.

Inelastic neutron excitation cross sections were calculated using the above "selected" potential and the Hauser-Feshbach formalism.[5] The calculations explicitly considered the excitation of the 987 (Ti-48), 889 (Ti-46), and 160 (Ti-47) keV states, assuming the former two are 2+ configurations and the latter is a 7/2 state. These states made the only observed contribution to the measured inelastic scattering cross sections. The calculated cross sections for the excitation of the 2+ states tended to be slightly smaller than the experimental values as shown in Fig. I-4-2. The calculated excitation of the 7/2− state, corrected for isotopic abundance, was ~3 mb/sr, consistent with the marginal experimental observation. Calculated inelastic angular distributions were nearly isotropic and qualitatively consistent with the measured values as illustrated in Fig. I-4-1.

The even isotopes of titanium are deformed with two-phonon (2+) vibrational first-excited states.[6] Of these the 987 keV state in Ti-48 was the major contributor. The excitation of these vibrational states and the effect of deformation was examined using a non-spherical optical-model with two-channel coupling. The form factors and the parameters of the non-spherical potential were identical to those employed in the numerical calculations above. The nuclear deformation was varied between 0.0 and 0.3, with 0.2 being selected as consistent with the present experiments and with values reported in the literature. Elastic angular distributions obtained from the deformed potential differed from those from the spherical potential and tended to be in better agreement with experiment as indicated in Fig. I-4-1. The calculated inelastic angular distributions showed a small asymmetry about ninety degrees (a few mb/sr). Throughout the energy range of the present measurements the calculated direct excitation of the 2+ vibrational states was less than 15 mb and could not be detected experimentally as it was less than the uncertainties in the measured values.

The Evaluated Nuclear Data File-B (ENDF/B)[7] contains titanium (material 1016). This evaluation was prepared by Pennington and was largely based upon prior evaluated data sets.[7] In order to make available the results of the present work and other recent experimental values in a readily usable form the titanium ENDF file was modified and updated. Modifications were confined to incident energies above 0.1 MeV and values at all lower incident energies were retained in the original form. The modification emphasized experimental values and used model-calculations to extrapolate the measured values where necessary. Internal consistency was sought. However, measured partial cross sections were not always available with equivalent resolutions. Thus, while energy-averaged consistency was relatively good, the consistency at specific isolated energies was less satisfactory.

Following the above precepts a modified evaluation was constructed in ENDF format.[6] The results have been communicated to the National Neutron Cross

Section Center (NNCSC). The housekeeping of this evaluation has been verified using CHECKER[7] and the physical content examined using several ad-hoc graphical procedures. It is hoped that the present modification has resulted in a significant improvement in the titanium-ENDF evaluated file at energies above 0.1 MeV. It is inclusive of the most recent and accurate experimental results.

REFERENCES

1. A. Smith, *Nuclear Research with Low Energy Accelerators*, Ed. J. Marion and D. Van Patter (Academic Press, New York, 1967).
2. E. Barnard et al., *High Resolution Fast Neutron Cross Sections of Iron*, Nucl. Phys. **A118**, 321 (1968).
3. A. Smith, P. Guenther, R. Larson, C. Nelson, P. Walker and J. F. Whalen, *Multi-Angle Fast Neutron Time-of-Flight System*, Nucl. Inst. Methods **50**, 277 (1967).
4. P. Hodgson, *Optical Model of Elastic Scattering*, (Oxford Press, London, 1963).
5. W. Hauser and H. Feshbach, *The Inelastic Scattering of Neutrons*, Phys. Rev. **87**, 366 (1952).
6. Nuclear Data Sheets, National Academy of Science, National Research Council, U.S. Government Printing Office, Washington D.C.
7. Evaluated Neutron Data File-B, National Neutron Cross Section Center, Brookhaven National Laboratory (1970).

I-5. Fast Neutron Total and Scattering Cross Sections of U-238

P. LAMBROPOULOS

Neutron total and scattering cross sections of U-238 have been interpreted from 0.1 to 10.00 MeV in terms of a local energy-dependent, spherical optical potential with spin-orbit coupling. The analysis was based upon experimental data to energies of 10.0 MeV selected from the literature. Where possible, numerical data were obtained from the files of the NNCSC.(1) The selection was subjective, employing judgements of the reported quality of the result, the appropriateness of the method, and the consistency of the results both internally and with respect to related physical values. Where necessary, measured values were evaluated to provide readily comparable cross section values. In addition, new experimental results were explicitly obtained for this work including a precision determination of total neutron cross sections to 1.5 MeV,(2) an extension of elastic and inelastic scattering measurements,[3] and level structure information from the observation of the gamma-ray emission following the inelastic scattering process.[4] Calculated results were compared with measured total neutron cross sections to 10.00 MeV, with measured scattering cross sections to 1.5 MeV, at 2.0 MeV and at 7.0 MeV. Particular attention was given to cross sections at energies of less than 1.3 MeV where detailed comparisons between measured and calculated inelastic excitation cross sections were possible.

The theoretical calculations were primarily based on the spherical optical model with spin-orbit coupling.[5] Reaction cross sections were calculated using the Hauser-Feshbach formalism.[6] Most of the computation procedures employed the computer program ABACUS-2.(7) The effect of fission and capture processes, and of resonance interference effects was computed using the program NEARREX.(8) The contributions of deformation and direct reactions were estimated using the non-spherical optical model computer program 2-PLUS.(9) Uranium is known to be deformed and a spherical optical potential would not be expected, a priori, to suitably describe the experimental results. However, it was found that a simple spherical model could give a satisfactory representation of the experimental results and was very useful in the parameterization of the neutron cross sections. The use of more complex formulations, such as coupled channel calculations, was generally not required by the available experimental information.

Satisfactory agreement was obtained between the calculated and experimental total and total elastic cross sections (Figs. I-5-1 and I-5-2). The calculated total inelastic cross section (Fig. I-5-3) also agrees well with the experimental data above 0.6 and below 1.4 MeV. The disagreement below 0.6 MeV can be reasonably attributed to width fluctuation and correlation effects which tend to lower the cross section. Calculations with NEARREX tend to support this explanation. There is also the possibility that the experimental values are somewhat too low, this being an experimentally difficult energy range. The disagreement above 1.4 MeV is due to the unobserved excitations which are not included in the calculated curve. With the above qualifications, the Parker (see Fig. I-5-3) total inelastic cross section may also be considered to be in general agreement with the present calculation. There is, however, rather substantial disagreement with the ENDF/B curve before revision (Fig.

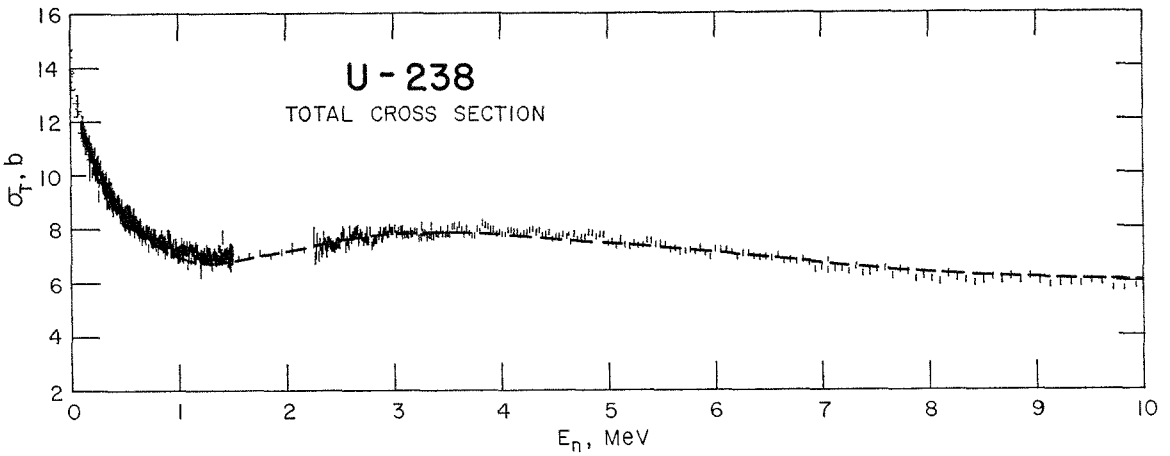

FIG. I-5-1. Comparison of Measured and Calculated Total Neutron Cross Sections of U-238. Vertical Bars Indicate Measured Values and Associated Errors Selected from the Literature and Recent Measurements as Discussed in the Text Calculated Results are Indicated by the Dashed Curve *ANL Neg No 116-34*

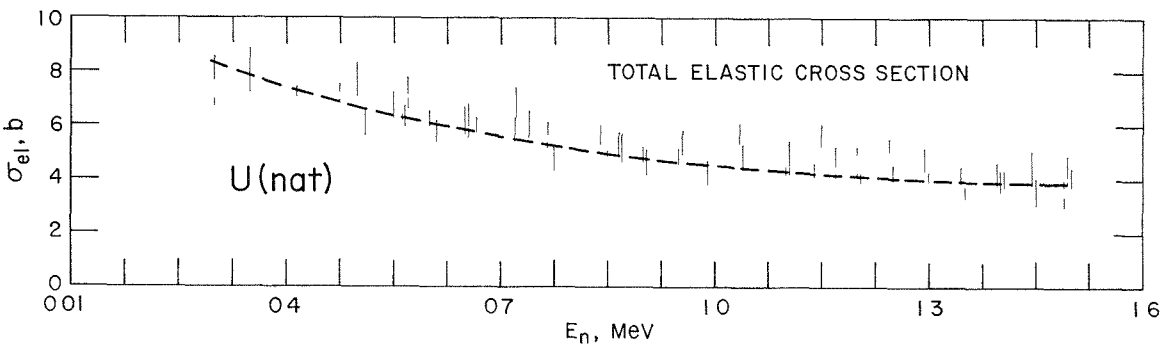

FIG. I-5-2. Comparison of Measured (Vertical Lines) and Calculated (Curve) Elastic Scattering Cross Section of U-238. *ANL Neg No 116-33*

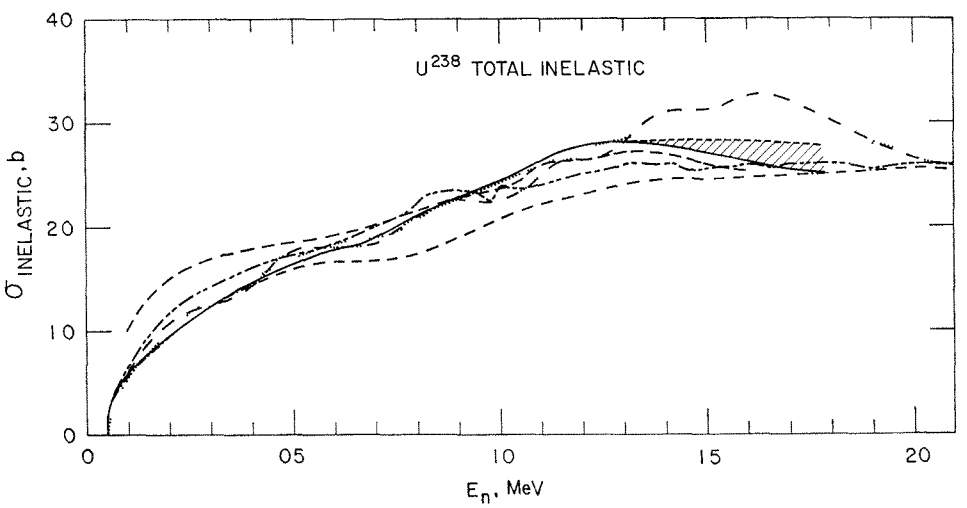

FIG. I-5-3. Total Inelastic Cross Sections of U-238. The Cross-Hatched Area Indicates an Estimate of Excitation not Observed in the Experimental Measurements. —— Experimental Curve of Ref 3; — — Curve Previously Recommended in Ref 11, — — — — Curve Taken from Ref 12; ··· Curve Based on ENDF/B Version II, — ·— Curve Recommended for ENDF/B in Ref 11, — — — — ABACUS Calculation Corrected for Fission and Capture *ANL Neg No 116-183 Rev 1*

I-5-3). This curve gives cross section values considerably larger than the calculated as well as the experimental results of this paper above 1.3 MeV. The present analysis does not justify such large values nor does it seem probable that deformed model calculations would do so. The analysis of reactivity, central reaction ratio and other macroscopic parameters in various fast critical assemblies[10] has also indicated that the ENDF/B inelastic cross section values before the recent revision were too large.

The ENDF/B-revised curve gives total inelastic values closer to the results of the present analysis (see Fig. I-5-3). It does seem, however, that even these values may be somewhat too large. Further details on the present analysis can be found in Ref. 13.

References

1. National Neutron Cross Section Center (NNCSC), Brookhaven National Laboratory. (Throughout this reference, values measured for natural uranium are assumed equivalent to U-238 values.)
2. J. F. Whalen and A. B. Smith, Argonne National Laboratory (private communication).
3. A. B. Smith, Argonne National Laboratory (private communication).
4. W. P. Poenitz, Argonne National Laboratory (private communication).
5. H. Feshbach, *The Optical Model and its Justification*, Annual Review of Nuclear Science, E. Ségré, Ed. (Annual Rev., Inc., Palo Alto, California, 1958) pp. 49-104.
6. W. Hauser and H. Feshbach, *The Inelastic Scattering of Neutrons*, Phys. Rev. **87**, 366 (1952).
7. E. H. Auerbach, *ABACUS-2*, BNL-6562 (1962).
8. P. A. Moldauer, C. A. Engelbrecht and G. J. Duffy, *NEAR-REX, A Computer Code for Nuclear Reaction Calculations*, ANL-6978 (1964).
9. C. L. Dunford, *2-PLUS, A Nonspherical Optical Model for Fast Neutron Cross Sections*, NAA-SR-11706 (1966).
10. B. A. Zolotar, B. R. Sehgal and J. M. Kallfelz, *Fast Reactor Integral Studies of Modifications to ENDF/B U-238 Inelastic Scattering*, Trans. Am. Nucl. Soc. **12**, 743 (1969).
11. J. J. Schmidt, *Neutron Cross Sections for Fast Reactor Materials. Part I: Evaluation*, KFK-120 (EANDC-E-35U), (February 1966).
12. K. Parker, *Best Cross Sections for U-238*, AWRE O-79/63 (1964).
13. P. Lambropoulos, *Fast Neutron Total and Scattering Cross Sections of U-238*, Nucl. Sci. Eng. (to be published).

I-6. Fast Neutron Total and Scattering Cross Sections of Pu-240 from 0.1 to 1.5 MeV

P. Lambropoulos, J. Whalen and A. B. Smith

Experimental determination of the total cross sections and of the elastic and inelastic scattering cross sections of Pu-240 has been completed for neutron energies from 0.1 to 1.5 MeV. Theoretical interpretation of the experimental results is in progress.

Mono-energetic neutron source techniques were employed to determine the total neutron cross sections at approximately 1 keV intervals with resolutions of about 2 keV.[1] Nano-second time-of-flight techniques were used to measure elastic and inelastic scattering cross sections.[2] Scattered neutron resolutions were approximately 1.5 nsec/m and measurements were made at incident neutron energy intervals of 50 keV or less. All measurements utilized a unique sample of high-purity Pu-240, made available by the Los Alamos Scientific Laboratory. The material was compressed foil

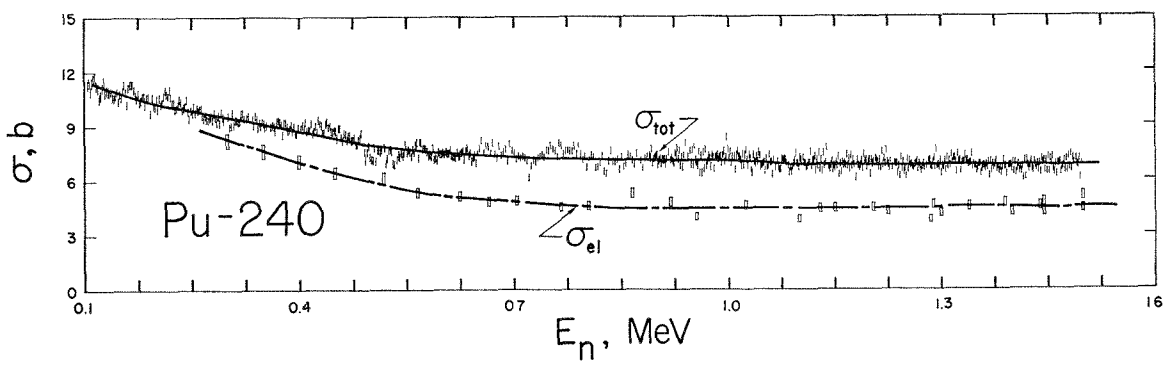

Fig. I-6-1. Total and Elastic Scattering Cross Sections of Pu-240. The Dashed Curves Indicate "Eye Guides" Through the Experimental Points. The Solid Curve Is the Result of Preliminary Optical-Model Analysis. *ANL Neg. No. 116-293.*

of plutonium-aluminum alloy. Corrections were made for aluminum content (about 10 a/o).

Representative experimental results are shown in Fig. I-6-1. The total cross section displays appreciable structure. This effect is believed anomalous, arising from the contribution of aluminum resonances. Corrections were applied but small differences in energy resolution and/or incident energy calibration can easily lead to the structured behavior. Averages over energy intervals large compared with that of the structure should result in reliable average cross section values. The figure also indicates the measured elastic scattering cross sections. These, combined with the measured inelastic scattering cross sections, are consistent with the observed total cross sections. A preliminary result of theoretical interpretation based on the optical-model is indicated on the figure.[3] Further analysis now in progress is based upon the compound nucleus processes,[4] channel coupling effects,[5] and resonance interference properties.[6] The measurements and the interpretation constitute the only known detailed study of fast neutron processes in Pu-240, a major constituent of many fast reactor systems.

References

1. D. Miller, *Fast Nuclear Physics*, Eds., J. Marion and J. Fowler (Interscience Publishers, Inc., New York, 1963) Vol. 2, p. 985.
2. A. B. Smith, *Nuclear Research with Low Energy Accelerators*, Eds., J. Marion and D. Van Patter (Academic Press, New York, 1967).
3. P. Hodgson, *The Optical Model of Elastic Scattering*, (Oxford Press, London, 1963).
4. H. Feshbach et al., *Model for Nuclear Reactions with Neutrons*, Phys. Rev. **96,** 448 (1954).
5. T. Tamura, *Analysis of the Scattering of Nuclear Particles by Collective Nuclei in Terms of the Coupled Channel Calculations*, Rev. Mod. Phys. **37,** 679 (1965).
6. P. A. Moldauer, *Average Compound Nucleus Cross Sections*, Rev. Mod. Phys. **36,** 1079 (1964).

I-7. Fast Neutron Total Cross Sections

J. Whalen and J. Meadows

Neutron total cross section measurements made with monoenergetic neutrons have been extended to include the elements of paladium, thorium, copper and the separated isotope Li-6. These measurements were made as part of a continuing experimental program previously reported,[1] using the automated on-line computer system. The resulting total cross sections are shown in Fig. I-7-1.

The Li-6 data shown in the figure were measured with a sample fabricated at Los Alamos Scientific Laboratory. Another similar set of measurements was made with a sample fabricated in England and made available by Dr. E. Rae, AERE, Harwell; the values agree within 1% at the peak of the resonance. The location of the resonance indicated by each of two data sets agree within 2 keV.

References

1. J. F. Whalen and J. W. Meadows, *Extension of Automated Neutron Cross Section Measurements to Higher Energies*, Reactor Physics Division Annual Report, July 1, 1967 to June 30, 1968, ANL-7410, p. 21.

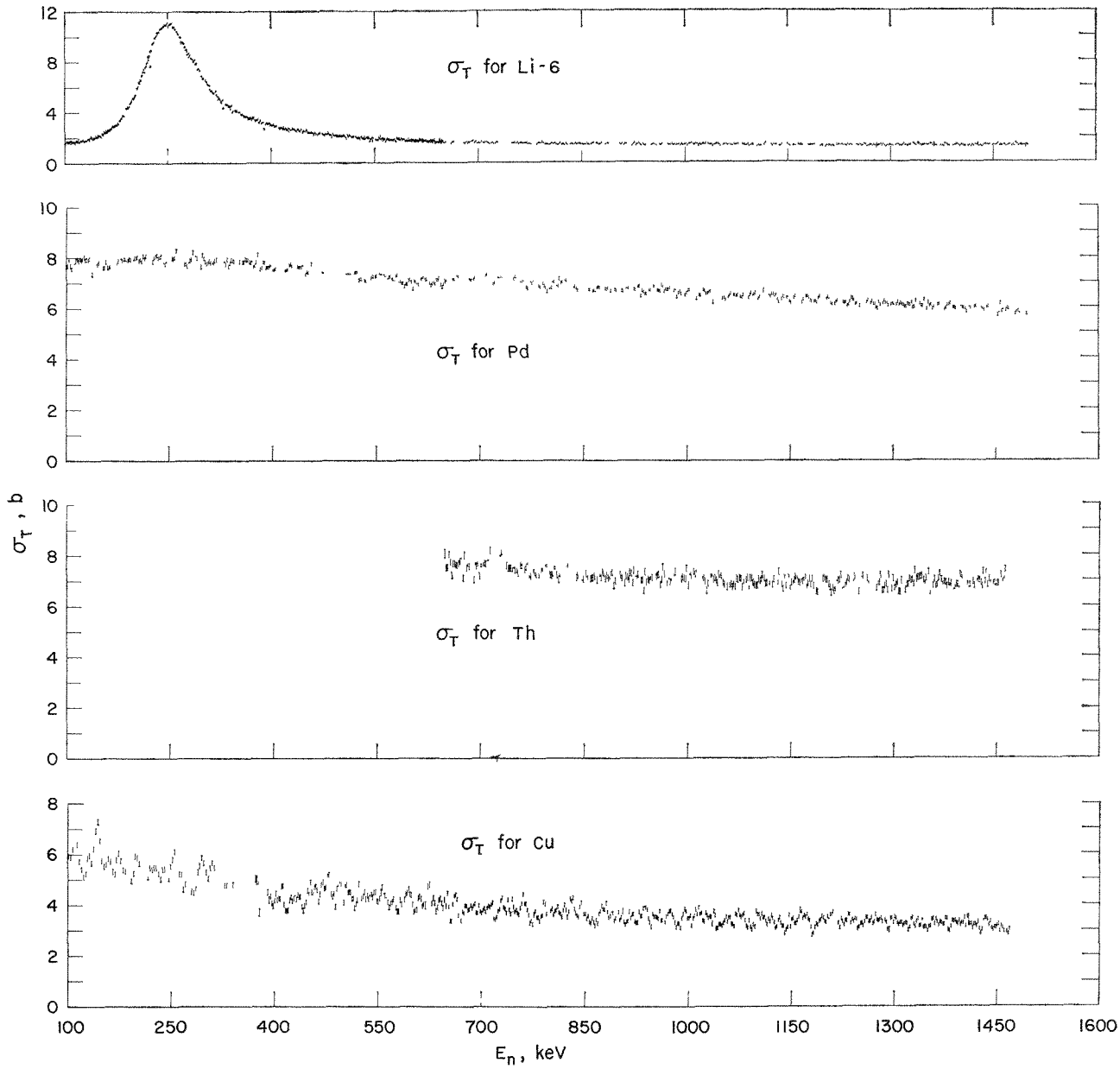

FIG. I-7-1. Total Cross Sections for Li-6, Palladium, Thorium and Copper. *ANL Neg. No. 116-543.*

I-8. The Fission Cross Section of U-233 Relative to U-235 from 500 to 1500 keV

J. W. MEADOWS

INTRODUCTION

The available data on the ratio σ_f(U-233)/σ_f(U-235) show differences far larger than the errors claimed for the individual measurements. The results of Lamphere,[1] Allen and Ferguson[2] and Pfletschinger and Kaeppeler[3] disagree by as much as 10% near 1 MeV neutron energy. This is far too large if the ratio is to be useful in reactor calculations or in providing a check on the reliability of absolute cross section measurements. Therefore a new effort was made to get ad-

ditional measurements. The following paper reports the initial results of a series of measurements between 0.5 and 1.5 MeV.

Experimental Method and Procedure

Known amounts of fissile materials were deposited on thin plates, placed back-to-back in a fission detector, and irradiated with pulses of monoenergetic neutrons. The neutron bursts were approximately 30 nsec wide and were obtained from a Van de Graaff accelerator and the $Li^7(p,n)Be^7$ reaction. The data were stored in two arrays (32 time channels by 128 energy channels) for later examination and processing.

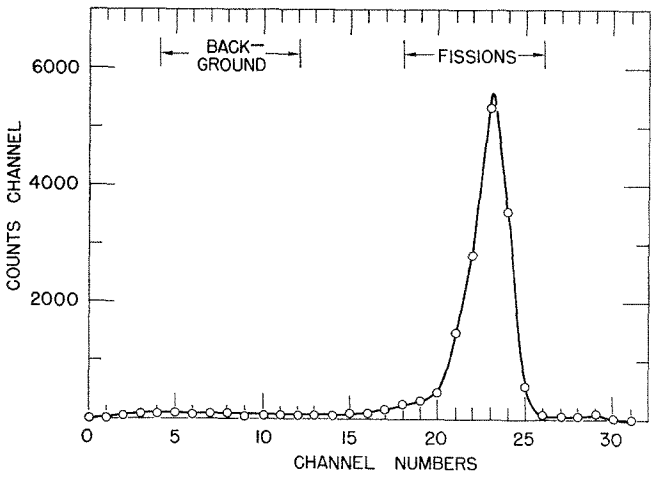

Fig. I-8-1. A Time Spectrum. *ANL Neg. No. 116-467.*

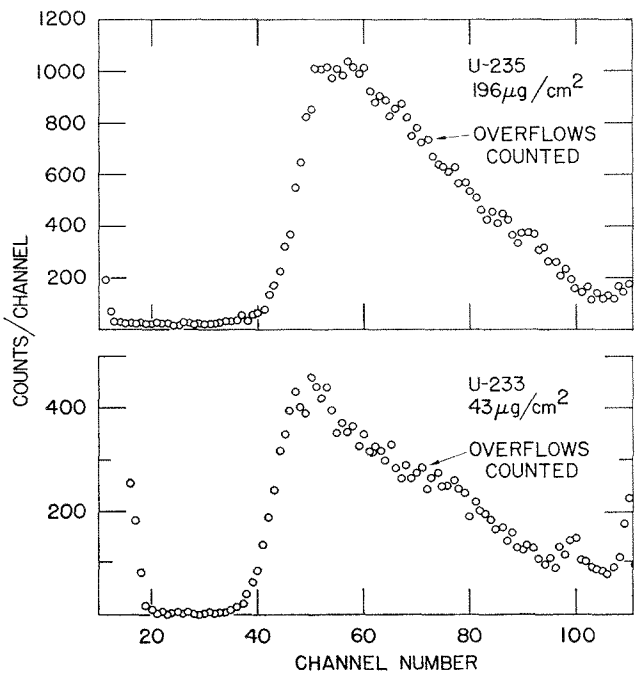

Fig. I-8-2. Fission Fragment Pulse Height Spectra for U-235 and U-233. *ANL Neg. No. 116-472.*

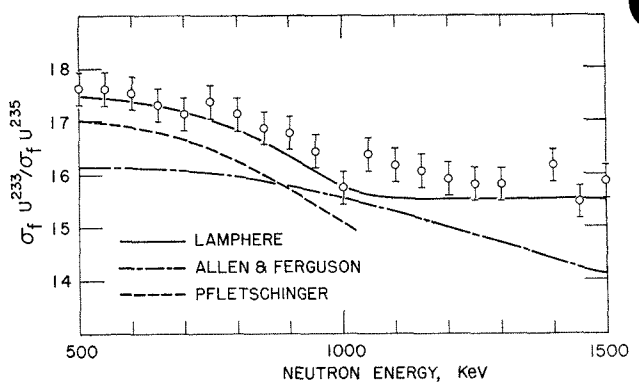

Fig. I-8-3. The Fission Cross Section Ratio U-233/U-235. *ANL Neg. No. 116-456.*

TABLE I-8-I. Isotopic Composition of the Samples in Atom %

Isotope	U-233 Sample	U-235 Sample
U-232	0.8 ppm	
U-233	99.54	
U-234	0.184	0 856
U-235	0.062	93.25
U-236	0.013	0.332
U-238	0 203	5.562

The fission fragments were detected by an ion chamber of low mass construction and a plate separation of 0.6 cm. It was flushed continuously with methane gas at 1 atm. With a bias of 300 V the pulse rise time was ~20 nsec. The pulse was clipped after 5 nsec to obtain an acceptable time spread and to reduce alpha pile-up. A time spectrum is shown in Fig. I-8-1. The energy spectra are shown in Fig. I-8-2.

The U-235 deposits were prepared by vacuum evaporating UF_4 on to 0.025 cm stainless steel plates. Deposits covered an area 2.54 cm in diam and had thicknesses of ~70 to ~350 $\mu g/cm^2$. The one used for most of the measurements had a thickness of 196 $\mu g/cm^2$. The U-233 deposits were similar but were prepared by electrolytic deposition. The mass analysis of the samples is given in Table I-8-I.

The mass determination of the U-235 plates was based on low geometry alpha counting and chemical analysis. The final value for the specific activity was based on data from 10 plates. The U-233 sample masses were determined solely by alpha counting and isotopic analysis.

Corrections and Errors

All the data were subjected to the following corrections:

1. *Background.* The time intervals used for the data and the background are shown in Fig. I-8-1. Alpha

particles made up the greater part of the background. The correction to the fission yield was ~0.5%.

2. *Extrapolation under the alpha peak.* A linear extrapolation was made from the alpha cut-off to zero. The correction was typically 1.0% for U-235 and 0.3% for U-233. The larger correction for U-235 was due to the thicker deposit.

3. *Deposit thickness.* This correction was determined experimentally by measuring the specific fission rates of U-235 deposits of several thicknesses. The correction was 2.1 ± 0.1%.

4. *Detector geometry.* The U-235 deposit was slightly closer to the neutron source due to the thickness of the backing plates. The correction is 1.6 ± 0.3%.

5. *Transmission.* The relative fission rate of the U-233 foil was reduced by scattering in the backing plates. The fission rate was increased by 1.2 ± 0.3% to correct for this.

6. *Second neutron group and other isotopes.* The contribution of the second group from the $Li^7(p,n)Be^7$ reaction was based on the data of Bevington et al.[8] This correction was combined with the one due to the isotopic composition of the samples.[9] The maximum correction was 0.8 ± 0.1%.

The errors indicated in the above corrections were generally small and of minor importance. The principal uncertainties were counting statistics (~1.0%) and the masses of the fission deposits. The error for the U-235 mass was small, only 0.3%, but the corresponding error for U-233 was 1.4%. The U-233 mass was strongly dependent on its half life. There are several measurements available but they differ by as much as 6%. The value used here was (1.591 ± 0.021) × 10^5 years. It is a simple average of five independent measurements.[5-8]

Discussion

The results are shown in Fig. I-8-3. The energy spread is 25 to 30 keV for all points. The error bars include both systematic and random errors.

The results of three other measurements would have several points in the energy range we indicated in Fig. I-8-3 for comparison. The results of Allen and Ferguson[2] differ by 6 to 10% and that of Pfletschinger and Kaeppeler[3] differ by about 4%. The agreement with the Lamphere[1] data is reasonably good.

References

1. R. W. Lamphere, *Fission Cross Sections of the Uranium Isotopes 233, 234, 236, and 238 for Fast Neutrons*, Phys. Rev. **104**, 1654 (1956).
2. W. D. Allen and A. T. G. Ferguson, *The Fission Cross Sections of U-233, U-235, U-238, and Pu-239 for Neutrons in the Energy Range 0.030 MeV to 3.0 MeV*, Proc. Phys. Soc. (London), **A70**, 573 (1959).
3. C. Pfletschinger and F. Kaeppeler, *A Measurement of the Fission Cross Sections of Pu-239 and U-233 Relative to U-235*. Nucl. Sci. Eng. **40**, 375 (1970).
4. IA. P. Dokuchaev and I. S. Dsipov, *The Specific Alpha-Activity and Half-Life of U-233*, J. Nucl. Energy **11**, 194 (1959).
5. D. S. Popplewell, *The Specific Alpha-Activity and Half-Life of U-233*, J. Nucl. Energy **14**, 50 (1961).
6. H. R. Ihle, E. Langenscheidt and A. P. Murrenhoff, *Determination of the Specific Alpha Activity of U-233 with the Help of a Liquid Scintillation Counter*, JUL-491-PC (1967).
7. F. L. Oetting, *Recent Calorimetric Determination of the Specific Powers and Half-Lives for Certain Long Lived Alpha-Emitting Radionuclides*, Thermodynamics of Nuclear Materials, (International Atomic Energy Agency, Vienna, 1968) p. 55.
8. P. R. Bevington, W. W. Rolland and H. W. Lewis, *Relative Yields of Neutron Groups from $Li^7(p,n)Be^7$, Be^{7*} Reactions*, Phys. Rev. **121**, 871 (1961).
9. John R. Stehn et al., *Neutron Cross Sections*, Vol. III, Z = 88 to 98, BNL-325 (1965)

I-9. Fast Neutron Inelastic Gamma Ray Studies of Arsenic and Sodium

D. L. Smith

Introduction

Measurement of the energies and intensities of gamma rays produced by the inelastic scattering of fast neutrons provides data which is complementary to that resulting from direct measurement of the energies and intensities of the inelastically scattered neutrons. Lithium drifted germanium detectors can be used to determine the gamma ray energies—and thus, by deduction, the nuclear level energies—to within a few kilovolts. In principle, the neutron inelastic scattering cross sections can be deduced from the gamma-ray production cross sections if all the gamma rays resulting from transitions to or from the various levels are accounted for, and the internal conversion coefficients are known. In practice, this is quite difficult for all but the simplest level schemes. Nevertheless, the inelastic gamma ray measurements provide important information about nuclear level structures and the neutron

inelastic scattering process which may be very difficult or impossible to deduce from direct inelastic neutron measurements. The usefulness of this technique has been reviewed in an article by McEllistrem.[1]

The production of gamma rays by inelastic scattering of fast neutrons from samples of arsenic (As-75) and metallic sodium (Na-23) has been the object of a recent study in the Applied Nuclear Physics Group. A knowledge of pertinent cross sections for sodium is of critical importance because of the role played by this element in the LMFBR program. Both the $Na^{23}(n,n')$ and $Na^{23}(n,n'\gamma)$ cross sections have been measured previously and the data have been compiled.[2] A survey of these data reveals considerable disparity among the different cross section measurements. Consequently, an additional measurement was felt to be entirely justified. Much of the available data on the level scheme of As-75 comes from radioactivity and coulomb excitation studies (e.g., see Refs. 3–5). No recent studies of neutron inelastic scattering from As-75 were found in the literature at the time the present work was undertaken.

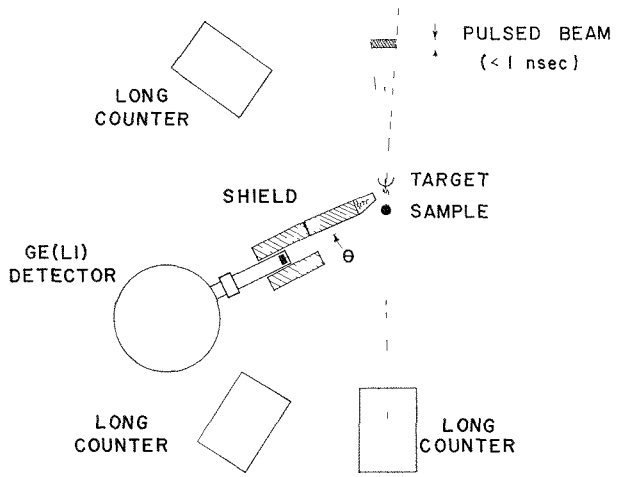

FIG. I-9-1. Schematic Diagram of the Apparatus Employed in Inelastic Gamma-Ray Measurements. *ANL Neg. No. 116-150.*

EXPERIMENTAL PROCEDURE

Short (~1 nsec) bursts of monoenergetic neutrons with energies in the range 300 keV $< E_N <$ 1600 keV were generated by bombardment of approximately 25 keV thick lithium targets with pulsed and bunched proton beams from the Applied Physics Division 3-MeV Van de Graaff accelerator.[6] Small (~1 in. diam × 1 in. height) cylindrical samples of metallic arsenic and sodium (sealed in thin-walled stainless steel containers) were irradiated with neutrons and in turn viewed by a Ge(Li) detector which was shielded from the direct flux of neutrons by lead bricks and hydrogenous material. The detector and shielding were supported on a cart which rotated about the sample position permitting gamma-ray angular distribution measurements over the angular range 50–110 deg in the laboratory system (see Fig. I-9-1). A 7.2 cm^3 planar Ge(Li) detector and a 30 cm^3 modified coaxial Ge(Li) detector were used in the measurements.

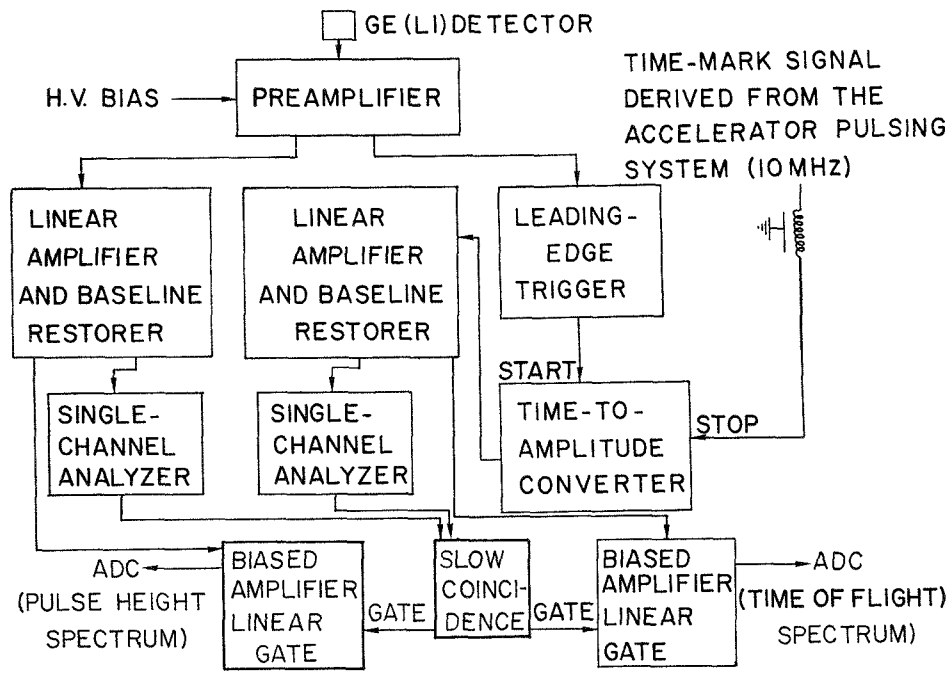

FIG. I-9-2. Schematic Diagram of Electronics Utilized in Inelastic Neutron Gamma-Ray Studies. *ANL Neg. No. 116-145.*

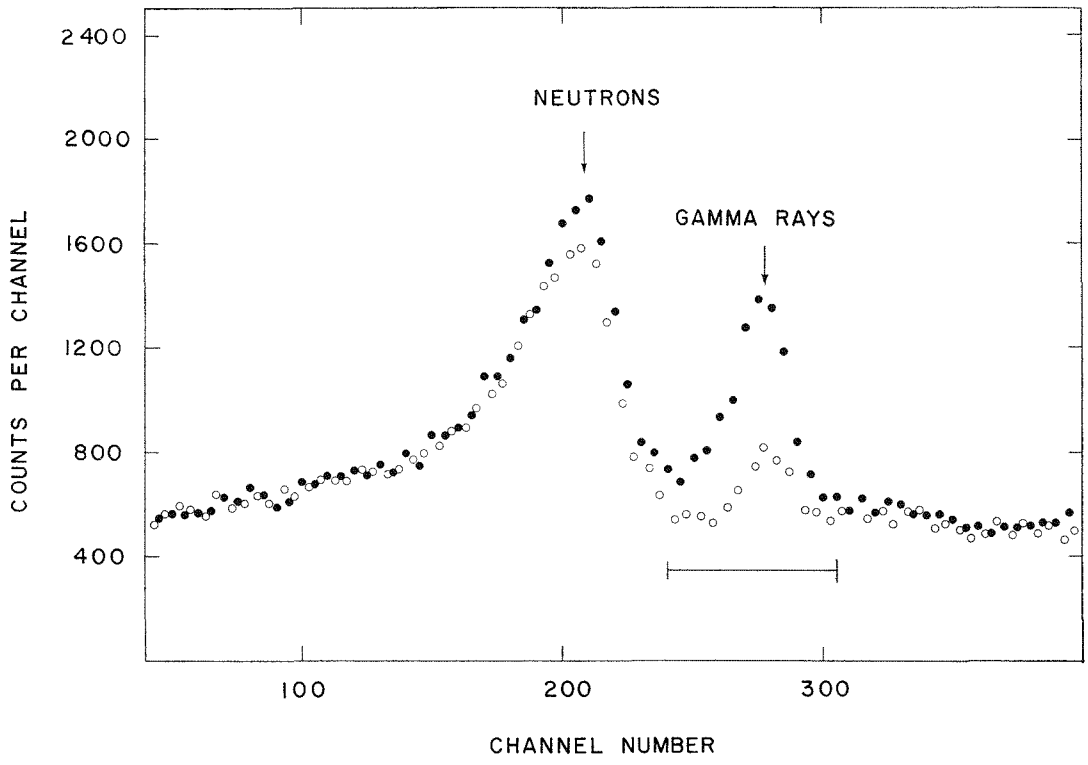

FIG. I-9-3. Typical Time-of-Flight Spectrum Observed in Inelastic Neutron Gamma-Ray Measurements. The Solid Circles Correspond to Data Taken with a Copper Sample and the Open Circles to Data Taken with a Carbon Sample which Produces No Inelastic Gamma Rays for Neutrons with Energies in the Range of Investigation. *ANL Neg. No. 116-148.*

Standard fast-slow electronics were employed in data acquisition. Background neutron and gamma ray interference was partially eliminated by employing time-of-flight techniques.[1] Fig. I-9-2 is a block diagram of the electronics. Some of the data were accumulated by a 512-channel analyzer and the remainder in 512-channels with the Applied Nuclear Physics Group on-line computer facility.[7] The separation of prompt gamma-rays from neutrons is illustrated by the sample time-of-flight spectrum in Fig. I-9-3.

The current study consisted entirely of relative measurements. The intensities of the As-75 transitions were normalized relative to either the 198.8 keV transition or the 820.1 keV transition. The yield of the 440 keV gamma ray from Na-23 was measured relative to the yield of the 670 keV gamma ray from Cu-63 in a sample of natural copper. Copper was chosen to normalize the sodium measurements for four reasons:

1. There are several reasonably consistent sets of cross section data available for Cu-63[(2)].

2. The total and inelastic neutron scattering cross sections for Cu-63 are relatively smooth and free of sharp resonances.

3. The experimental environment was relatively free of copper which would contribute background problems. The same could not be said of iron, which is the most commonly used standard for measurements of this sort.[1]

4. The 670 keV level of Cu-63 has spin ½ so that

TABLE I-9-I. ASSUMED CROSS SECTIONS FOR PRODUCTION OF THE 670 keV GAMMA-RAY FROM Cu-63

Neutron Energy, keV	σ, mb	Neutron Energy, keV	σ, mb
700	51	1150	140
725	68	1175	141
750	82	1200	141
775	93	1225	142
800	102	1250	142
825	108	1275	143
850	114	1300	143
875	118	1325	143
900	122	1350	143
925	125	1375	143
950	128	1400	143
975	130	1425	143
1000	133	1450	143
1025	135	1475	144
1050	136	1500	144
1075	137	1525	144
1100	138	1550	144
1125	139		

the inelastic neutron gamma ray production is isotropic.

Table I-9-I is a tabulation of the assumed gamma-ray production cross section versus neutron energy as deduced from an "eye guide" to the ENDF-B data compilation.[2] The available data for Cu-63 (670 keV) is generally consistent with this table to within ±15% for E_N < 800 keV and ±10% for 800 keV < E_N < 1500 keV. Additional spectra were accumulated at certain energies using a carbon sample. Carbon isotopes have no low lying excited states which can be excited by inelastic neutron scattering in the energy range in-

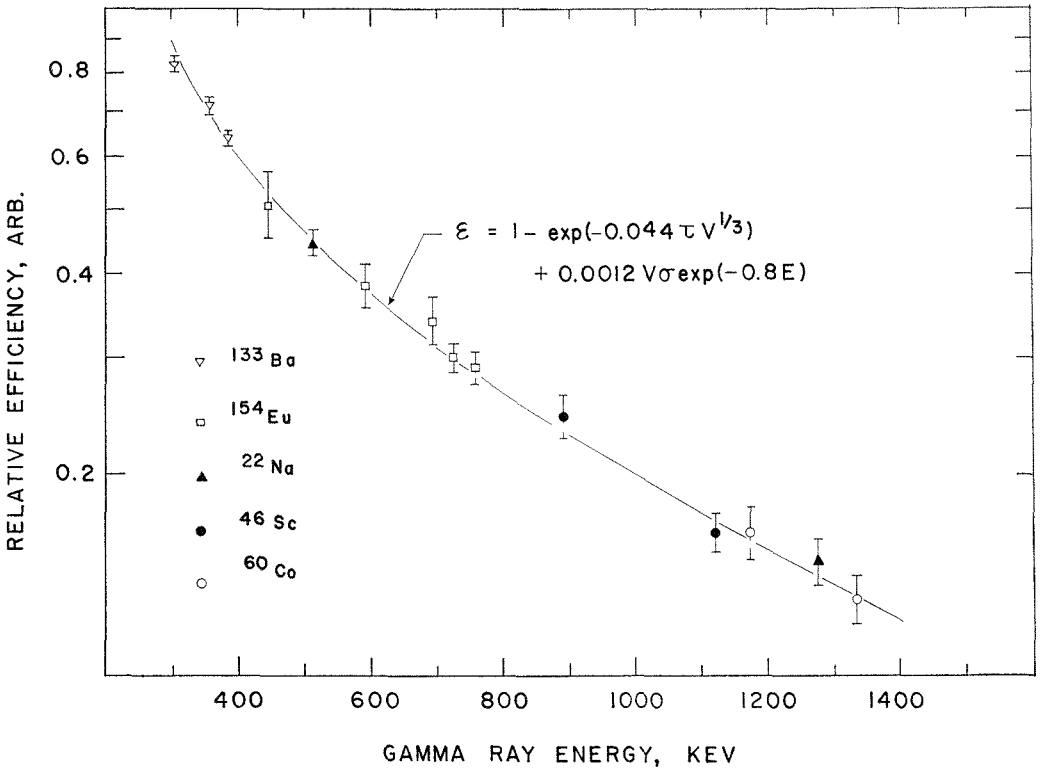

FIG. I-9-4. Relative Full-Energy Peak Detection Efficiency for Gamma Rays of a 30 cm³ Detector. The Parameters of the For mula for the Smooth Curve are: $\tau \equiv$ Photoelectric Cross Section (b), $\sigma \equiv$ Compton Cross Section (b), $V \equiv$ Detector Volume cm³), and $E \equiv$ Gamma Ray Energy (MeV). *ANL Neg. No. 116-149.*

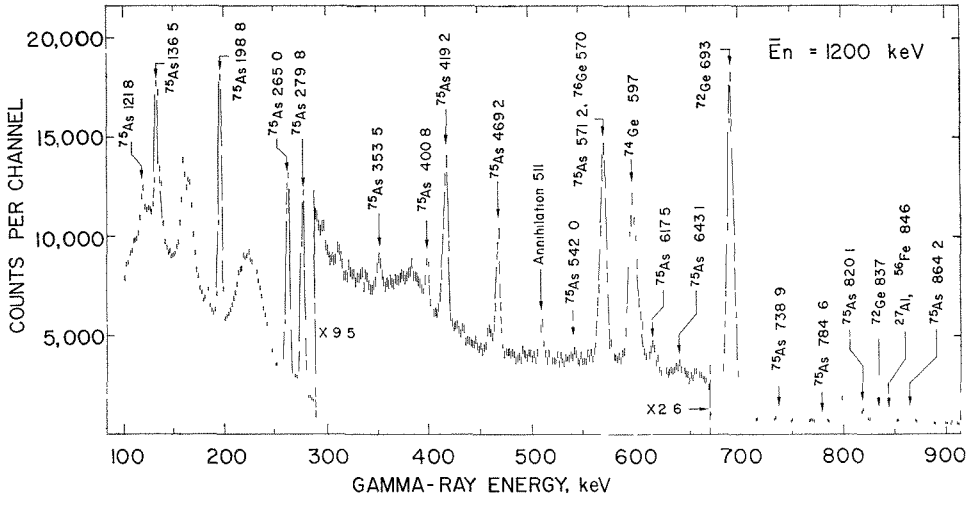

FIG. I-9-5. Ge(Li) Detector Spectrum Measured at 90 deg to the Incident Neutron Flux with E_N = 1200 keV. *ANL Neg. No 113-3174.*

vestigated. Consequently, these measurements served to monitor the background under conditions closely resembling those for sodium, arsenic and copper runs.

Corrections to the data were made for gamma attenuation in the samples and for Ge(Li) detector efficiency. The attenuation correction factors were computed from tabulated photon cross section information.[8] The relative efficiency curves for the Ge(Li) detectors were measured using radioactive sources of Ba-133, Na-22, Sc-46, Co-60 and Eu-154 placed at the sample position.[9] These data were fitted by a smooth semi-empirical curve according to a method described by Paradellis and Hontzeas.[10] The relative efficiency curve for the 30 cm³ detector appears in Fig. I-9-4.

The relative measurements were normalized against

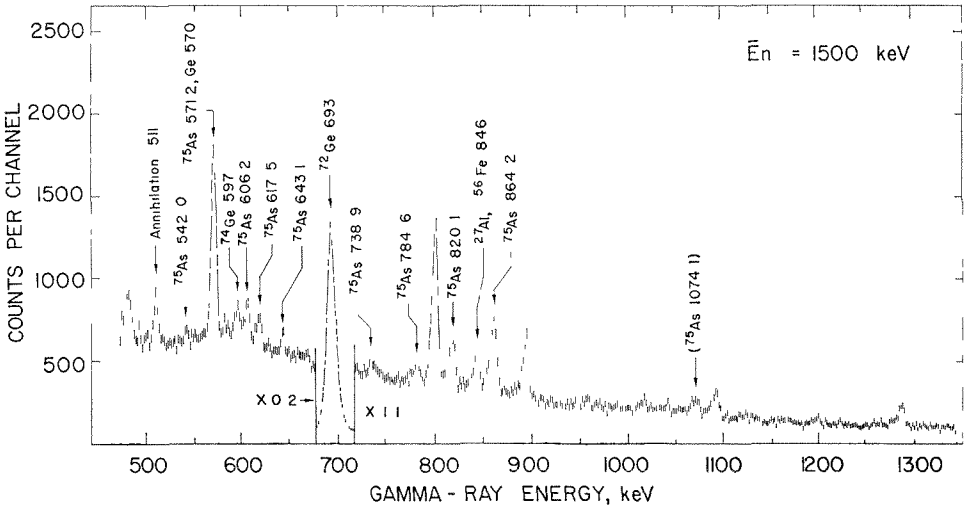

FIG. I-9-6. Ge(Li) Detector Spectrum Measured at 90 deg to the Incident Neutron Flux with E_N = 1500 keV. *ANL Neg. No. 113-3173.*

UNASSIGNED GAMMA RAYS:

606.2 ± 0.3 (1000)
643.1 ± 0.9 (1200)
738.9 ± 1.0 (1200)
784.6 ± 2.3 (1100)
1074.1 ± 0.5 (1400)

ALL ENERGIES IN keV

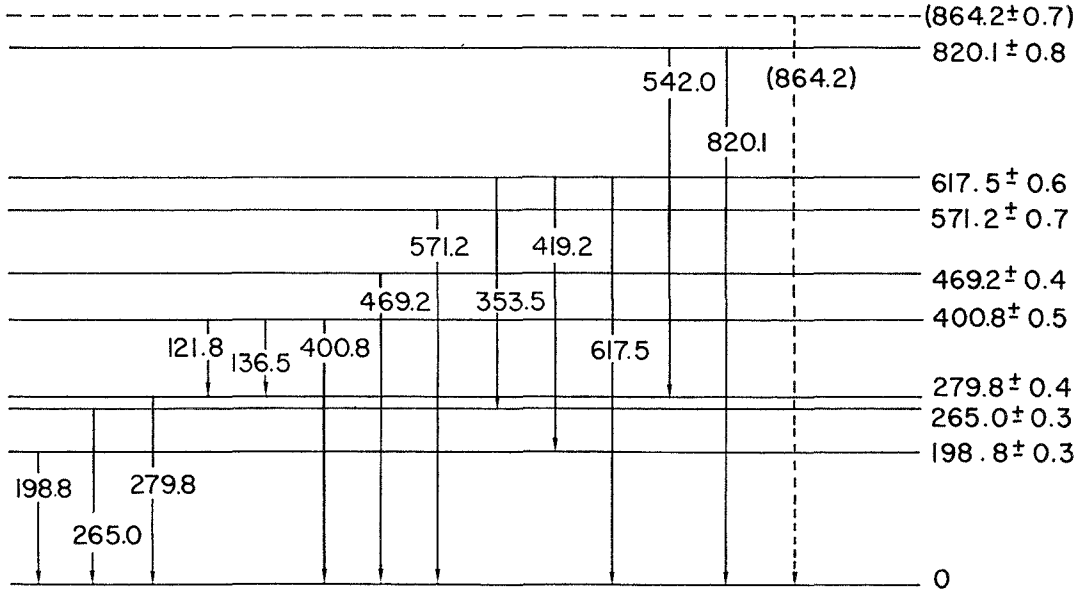

FIG. I-9-7. As$^{75}(n,n'\gamma)$ Transitions and the Assumed Low-Lying Level Scheme for As-75. *ANL Neg. No. 113-3177.*

TABLE I-9-II. YIELDS OF $As^{75}(n,n'\gamma)$ GAMMA RAYS

E_γ, keV / E_N, keV	Relative to 198.8 keV								Relative to 820.1 keV			
	300	400	500	600	700	800	1000	1200	1100	1300	1400	1500
121.8	Yield data invalidated by electronic losses								x	x	x	x
136.5									x	x	x	x
198.8	100	100	100	100	100	100	100	100	x	x	x	x
265.0	43 ± 9	145 ± 19	174 ± 19	181 ± 20	165 ± 19	155 ± 17	149 ± 15	137 ± 14	x	x	x	x
279.8	28 ± 7	105 ± 14	143 ± 15	164 ± 18	141 ± 17	145 ± 17	139 ± 14	140 ± 14	x	x	x	x
353.5	—	—	—	—	—	4 ± 1	5 ± 1	7 ± 1	x	x	x	x
400.8	—	—	7 ± 2	8 ± 3	11 ± 4	9 ± 1	9 ± 2	9 ± 2	x	x	x	x
419.2	—	—	—	—	20 ± 4	28 ± 5	34 ± 4	35 ± 5	x	x	x	x
469.2	—	—	11 ± 3	17 ± 3	34 ± 6	36 ± 6	34 ± 4	35 ± 4	x	x	x	x
542.0	—	—	—	—	—	—	—	5 ± 2	—	38 ± 10	17 ± 6	17 ± 6
571.2	—	—	—	13 ± 4	28 ± 5	48 ± 8	50 ± 13	78 ± 11	303 ± 50	238 ± 45	183 ± 26	176 ± 31
606.2[a]	—	—	—	—	—	—	—	—	49 ± 11	30 ± 8	45 ± 8	70 ± 14
617.5	—	—	—	—	—	6 ± 1	10 ± 2	11 ± 3	41 ± 12	53 ± 12	54 ± 9	56 ± 14
643.1[a]	—	—	—	—	—	—	—	8 ± 2	—	26 ± 9	49 ± 8	31 ± 10
738.9[a]	—	—	—	—	—	—	—	11 ± 3	—	24 ± 7	35 ± 8	42 ± 8
784.6	—	—	—	—	—	—	—	5 ± 2	16 ± 10	27 ± 9	36 ± 8	45 ± 13
820.1	—	—	—	—	—	—	12 ± 2	19 ± 3	100	100	100	100
864.2	—	—	—	—	—	—	15 ± 3	23 ± 3	114 ± 20	132 ± 20	145 ± 16	177 ± 24
1074.1[a]	—	—	—	—	—	—	—	—	—	—	38 ± 7	49 ± 13

[a] Transitions which have not been assigned positions in the level schemes.

a long counter at each chosen neutron energy. The counts in the gamma-ray full energy peaks were determined by subtracting assumed linear backgrounds from beneath the peaks. Although no detailed corrections were made for neutron attenuation and multiple scattering by the samples, an estimate was made of the error which might be incurred by neglect of neutron attentuation. Compiled total and elastic scattering data were employed in this evaluation.[2] It was concluded that in the worst set of circumstances, the difference in the effective primary fluxes for sodium and copper, averaged over the sample volumes, was about 12%. This number was arrived at by assuming that the neutrons which interact elastically as well as inelastically are effectively lost from the primary neutron beam. In reality, small angle elastic scattering tends to diminish the deficit in primary neutron flux on the shadowed sides of the samples. This effect has been the object of some study and it has been concluded that the elastic scattering portion of the total neutron cross section can be disregarded in making sample attenuation corrections in $(n,n'\gamma)$ work.[11] Inelastic processes account for a small portion of the total cross sections in the energy region in question (certainly less than 30% in all instances). Consequently, it appears that the neglect of the sample attenuation correction cannot induce an error of more than ~5% in the measured cross sections. The effect of the second group of neutrons from the $Li^7(p,n)Be^7$ reaction was also considered. This correction was computed to be ~1.6% for a worst case and, in fact, is negligible over most of the range. The effect of the corrections which have been discussed are minimized considerably by the fact that the measurements are relative rather than absolute so that there is a tendency toward cancellation.

The energies of the gamma rays were determined from a quadratic polynomial calibration curve fitted to calibration data acquired with the aid of radioactive gamma-ray sources.[12]

Results

ARSENIC

Inelastic neutron scattering gamma-ray production measurements for As-75 were made at several neutron energies between 300 and 1500 keV with the Ge(Li) detector at 90 deg to the incident neutron flux. Figs. I-9-5 and I-9-6 are examples of the measured spectra with the most prominent transitions appropriately labeled.

Fig. I-9-7 shows the $As^{75}(n,n'\gamma)$ transitions identified and the As-75 level scheme deduced from the data. This scheme is in good agreement with those deduced by other methods.[3-5] The transition energies also agree with reported values to within the assigned uncertainties. The existence of a level at 864.2 ± 0.7 keV is still in question. More extensive measurements will be required at higher neutron energies to resolve this uncertainty and to unravel the level scheme at higher excitation energies. This region is not accessible in radioactivity studies because of energy limitations.

The relative intensities of the $As^{75}(n,n'\gamma)$ transitions are presented in Table I-9-II. These data have not been reduced to absolute cross sections. One of the valuable features of $(n,n'\gamma)$ reactions is the rapid increase of the intensity of a transition with increase of neutron energy above threshold. This generally permits unambiguous assignment of transitions within the level scheme.

TABLE I-9-III. Measured Relative Intensities for Production of the 440 keV Gamma Ray from Na-23 and the 670 kev Gamma Ray from Cu-63 via the $(n\,n'\gamma)$ Reaction

E_N, keV	$(d\sigma/d\Omega)^{90°}_{Na}/(d\sigma/d\Omega)^{90°}_{Cu}$	$4\pi(d\sigma/d\Omega)^{90}_{Na}$, mb
750	5.13 ± 0.59	420 ± 48
775	4.68 ± 0.55	436 ± 51
780	4.70 ± 0.76	442 ± 72
800	3.94 ± 0.46, 5.20 ± 0.74	402 ± 47, 531 ± 76
825	3.28 ± 0.52	355 ± 56
850	3.14 ± 0.46	358 ± 53
875	2.30 ± 0.32, 2.06 ± 0.25	276 ± 38, 243 ± 30
900	2.80 ± 0.32, 2.18 ± 0.28	341 ± 39, 265 ± 34
910	2.50 ± 0.30	307 ± 37
925	2.39 ± 0.28, 2.79 ± 0.40	295 ± 34, 348 ± 50
950	2.46 ± 0.29, 1.69 ± 0.22	315 ± 37, 216 ± 28
975	1.68 ± 0.20, 1.64 ± 0.19	218 ± 26, 213 ± 25
1000	2.81 ± 0.35, 3.30 ± 0.38	373 ± 46, 440 ± 51
1025	3.19 ± 0.43	430 ± 58
1050	3.48 ± 0.41, 3.39 ± 0.44	473 ± 56, 461 ± 60
1070	3.25 ± 0.36	445 ± 49
1075	3.27 ± 0.37, 3.20 ± 0.37	448 ± 51, 439 ± 51
1100	3.05 ± 0.33, 3.09 ± 0.33	420 ± 45, 426 ± 46
1125	2.83 ± 0.36, 2.92 ± 0.33	394 ± 50, 406 ± 46
1150	2.79 ± 0.32, 2.94 ± 0.33	390 ± 45, 411 ± 46
1175	3.42 ± 0.40	482 ± 56
1230	3.19 ± 0.40	454 ± 57
1250	3.38 ± 0.45	480 ± 63
1275	3.82 ± 0.47	546 ± 68
1300	2.89 ± 0.42	414 ± 60
1325	1.85 ± 0.27	264 ± 38
1350	2.12 ± 0.34, 1.70 ± 0.19	304 ± 49, 243 ± 27
1375	1.23 ± 0.17	175 ± 24
1400	1.53 ± 0.22	218 ± 32
1425	1.89 ± 0.27, 1.98 ± 0.24	271 ± 39, 283 ± 34
1450	1.75 ± 0.28	250 ± 40
1475	2.30 ± 0.38, 1.73 ± 0.26	332 ± 55, 247 ± 37
1500	1.57 ± 0.25	225 ± 36
1525	1.77 ± 0.24	255 ± 34
1550	2.22 ± 0.36	320 ± 53

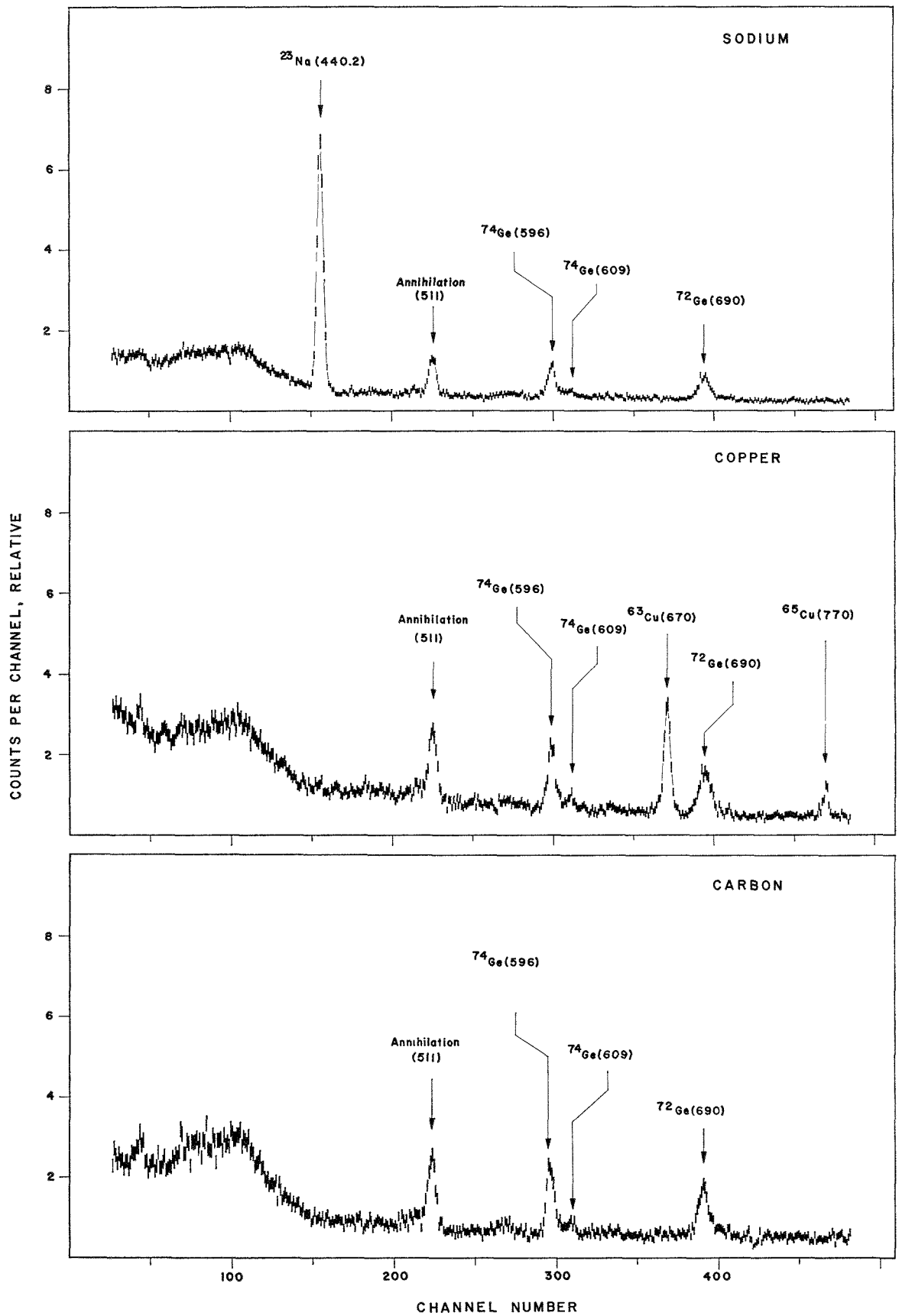

FIG. I-9-8. Sample Ge(Li) Detector Spectra Measured at 90 deg to the Incident Neutron Flux for Samples of Sodium, Copper and Carbon. *ANL Neg. No. 116-146.*

SODIUM

The average of a number of independent measurements of the energy of the first excited state of Na-23 is 440.2 ± 0.6 keV. The measured relative cross sections for the production of the 440 keV gamma ray by the $Na^{23}(n,n'\gamma)$ reaction and the 670 keV gamma ray by the $Cu^{63}(n,n'\gamma)$ reaction are presented in Table I-9-III. Duplicate measurements were made at several neutron energies. The assumed gamma production cross sections in Table I-9-I were then used to arrive at a set of cross sections for sodium. Table I-9-III contains these computed values of $4\pi(d\sigma/d\Omega)^{90°}_{Na}$. The cross sections measured in the present work agree well with the $Na^{23}(n,n')$ time-of-flight measurements reported by Chien and Smith[13] in the energy ranges 800–1050 keV and 1300–1500 keV, but are systematically lower by as much as 30% in the range 1100–1250 keV.[13] Tabulated ring geometry measurements on the reaction $Na^{23}(n,n'\gamma)$ tend to support the values of Chien and Smith in this region, but are systematically high in the two regions where the values of Chien and Smith are in agreement with those from the present work.[14-16] Measurements of the $Na^{23}(n,n'\gamma)$ reaction at the Texas Nuclear Corporation facility[17] agree with the present results; however, no data are available from this source for the energy range 1100–1250 keV.[(17)] Fig. I-9-8 shows typical spectra required during exposures with sodium, copper and carbon samples. The lines used in computing cross sections were clearly resolved from background peaks.

Angular distribution measurements were made for the 440 keV gamma ray from the $Na^{23}(n,n'\gamma)$ reaction at neutron energies of 780, 910, 1070, 1150 and 1230 keV. These data were then fit by even-order Legendre polynomial expansions by the method of least squares. The results of this fitting procedure are shown in Fig. I-9-9. No significant improvement in the fit was achieved by inclusion of the second- and fourth-order polynomials. It was therefore concluded that the distributions were essentially isotropic, although additional data at larger and smaller angles would have been very helpful in establishing this point. The essential isotropy of the angular distributions, as deduced from the present work, is supported by angular distribution measurements made at a neutron energy of 1000 keV by the group at Texas Nuclear Corporation.[17] However, Towle and Gilboy measured the angular distribution of the 440 keV gamma ray at 1500 keV neutron energy and observed a measurable $P_2(\cos\theta)$ contribution (i.e., $A_2/A_0 \approx 0.14$).[(15)] Furthermore, anisotropy measurements $[W(137°)/W(90°)]$ at other neutron energies exhibit considerable fluctuations in magnitude and sign.[15] These angular

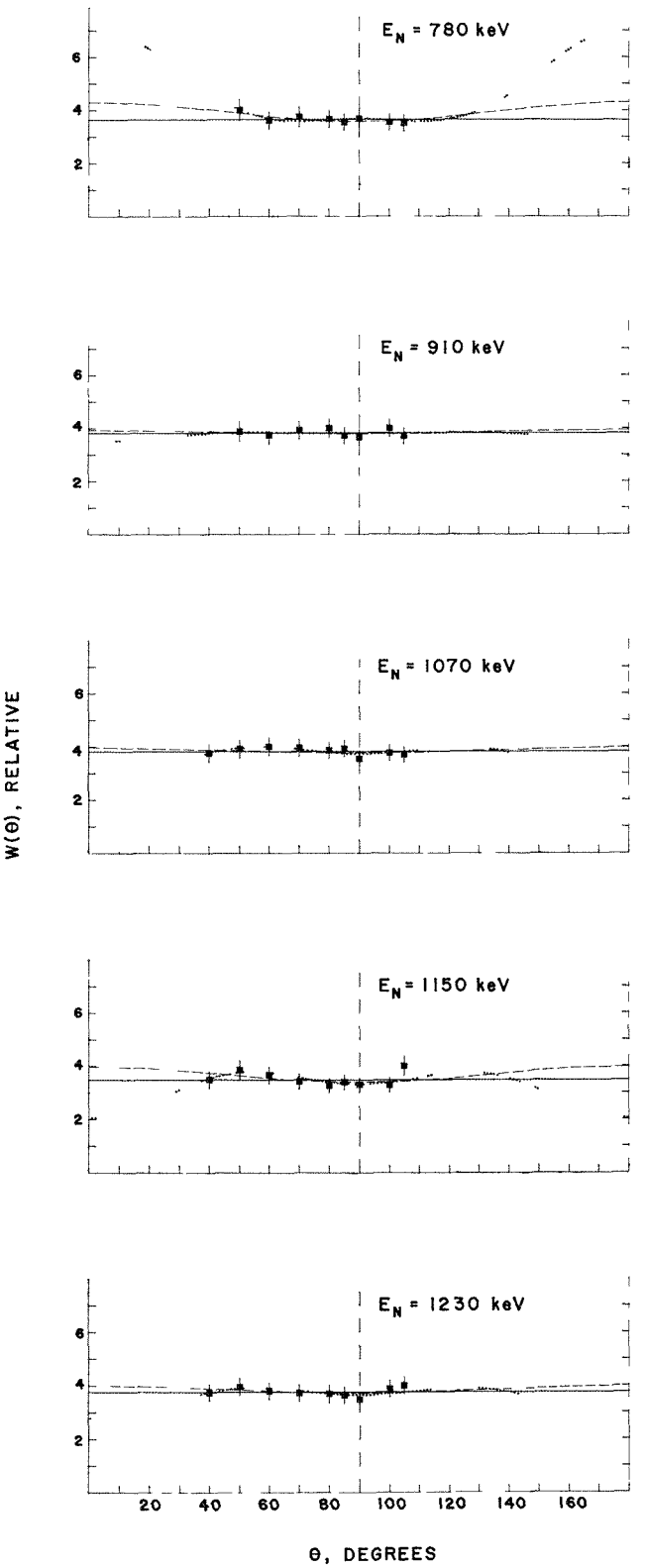

FIG. I-9-9. Angular Distributions of the 440 keV Gamma Ray from the $Na^{23}(n,n'\gamma)$ Reaction. *ANL Neg. No 116-147*

distribution effects are still not sufficient to resolve the discrepancies in the various data.

It is not clear at this point what effects may be responsible for the discrepancies between the various sets of data on the production of the 440 keV gamma ray by the reaction $Na^{23}(n,n'\gamma)$. The various assumptions and corrections employed in reducing the data reported in the present paper are being re-examined for possible systematic errors. Furthermore, a new series of measurements on sodium are planned and will be carried out with improved apparatus at the FNG facility.

References

1. M. T. McEllistrem, *Nuclear Research with Low Energy Accelerators*, J. B. Marion and D. M. Van Patter, Ed. (Academic Press, New York and London, 1967) pp. 167–194.
2. *Evaluated Nuclear Data File-B (ENDF-B)*, National Neutron Cross Section Center, Brookhaven National Laboratory (1970).
3. Anne Ng, R. E. Wood, J. M. Palms, P. Venugopala Rao and R. W. Fink, *Gamma Rays from the Decay of ^{75}Ge and ^{77}Ge*, Phys. Rev. **176,** 1329 (1968).
4. D. E. Raeside, M. A. Ludington, J. J. Reidy and M. L. Wiedenbeck, *The Decay of ^{75}Se*, Nucl. Phys. **A130,** 677 (1969).
5. R. L. Robinson, F. K. McGowan, P. H. Stelson and M. T. Milner, *Coulomb Excitation of ^{75}As*, Nucl. Phys. **A104,** 401 (1967).
6. A. B. Smith, P. Guenther, R. Larson, C. Nelson, P. Walker and J. F. Whalen, *Multi-Angle Fast Neutron Time-of-Flight System*, Nucl. Instr. Meth. **50,** 277 (1967).
7. J. F. Whalen, R. Roge and A. B. Smith, *A Digital Computer System for the Executive Control of a Fast Neutron Laboratory*, Nucl. Instr. Meth. **39,** 185 (1966).
8. Ellery Storm and Harvey I. Israel, *Photon Cross Sections from 0.001 to 100 MeV for Elements 1 through 100*, LA-3753 (June 1967).
9. J. M. Freeman and J. G. Jenkin, *The Accurate Measurement of the Relative Efficiency of Ge(Li) Gamma-Ray Detectors in the Energy Range 500 to 1500 keV*, Nucl. Instr. Meth. **43,** 269 (1966).
10. T. Paradellis and S. Hontzeas, *A Semi-Emperical Efficiency Equation for Ge(Li) Detectors*, Nucl. Instr. Meth. **73,** 210 (1969).
11. A. W. Burrows, R. C. Lamb, D. Velkley and M. T. McEllistrem, *Levels of ^{51}V and ^{55}Mn via $(n,n'\gamma)$ Reactions*, Nucl. Phys. **A107,** 153 (1968).
12. J. B. Marion, *Gamma-Ray Calibration Energies*, Nucl. Data **A4,** 301 (1968).
13. J. P. Chien and A. B. Smith, *Fast Neutron Scattering from Beryllium, Sodium, and Aluminum*, Nucl. Sci. Eng. **26,** 500 (1966).
14. D. A. Lind and R. B. Day, *Studies of Gamma Rays from Neutron Inelastic Scattering*, Annals of Physics **12,** 485 (1961).
15. J. H. Towle and W. B. Gilboy, *The Interaction of Neutrons with Sodium in the Energy Range 0.5 to 4 MeV*, Nucl. Phys. **32,** 610 (1962).
16. J. M. Freeman and J. H. Montague, *Gamma Rays from Inelastic Neutron Scattering in Sodium*, Nucl. Phys. **9,** 181 (1958/59).
17. W. E. Tucker, *Reports to the AEC Nuclear Cross Section Advisory Committee, October 17–18, 1967*, WASH-1079, Compiled by M. S. Moore, Secretary. Also, see *Annual Report*, Texas Nuclear Corporation 1967, Austin, Texas.

I-10. The Level Scheme of U-238

W. P. Poenitz

The level scheme of U-238 is of practical importance due to the application of uranium in fast reactors. A knowledge of the level scheme allows the theoretical evaluation of the inelastic scattering cross sections which are needed to supplement experimental values. Different techniques are in use to investigate the level schemes of heavy nuclei. Measurements of α- and γ-spectra associated with the α-decay of radioactive isotopes has contributed largely to the determination of level schemes of heavy nuclei. For U-238 this technique is difficult to apply because of the long half life of the parent isotope Pu-242. Coulomb excitation with heavy ions has been used instead;[1,2] however, not all levels which contribute to the inelastic neutron scattering process were excited by this method. In neutron time-of-flight measurements[3,4] new levels were revealed. However, the resolution was insufficient to resolve the levels existing in the higher energy range.

In the present investigations the γ-rays emitted in the $(n,n'\gamma)$ process have been detected using a Ge(Li)-detector. The $Li^7(p,n)Be^7$ reaction has been utilized as a neutron source. The sample (2 mm thick, 5 cm diam) has been positioned 10–15 cm from the target with the Ge(Li) detector at a 45 degree angle and 40–50 cm from the sample. The time-of-flight method has been used to suppress the background. Background has been further reduced by storing the γ-spectra from an equal range in the time spectrum adjacent to the

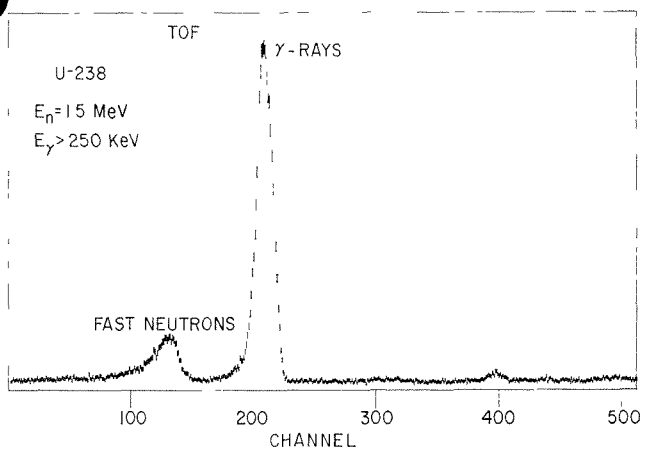

FIG. I-10-1. Time of Flight Spectrum for Gamma Rays of U-238. *ANL Neg. No. 116-107.*

prompt γ-peak for later subtraction. A time-of-flight spectrum is shown in Fig. I-10-1. A γ-spectrum with the background subtracted is shown in Fig. I-10-2.

Measurements of the intensity at different neutron energies yielded additional information as to the approximate origin of an observed γ-ray. This is illustrated in Fig. I-10-3 where the intensity of the 885 keV γ-ray is related to the sum of the intensities of the 679

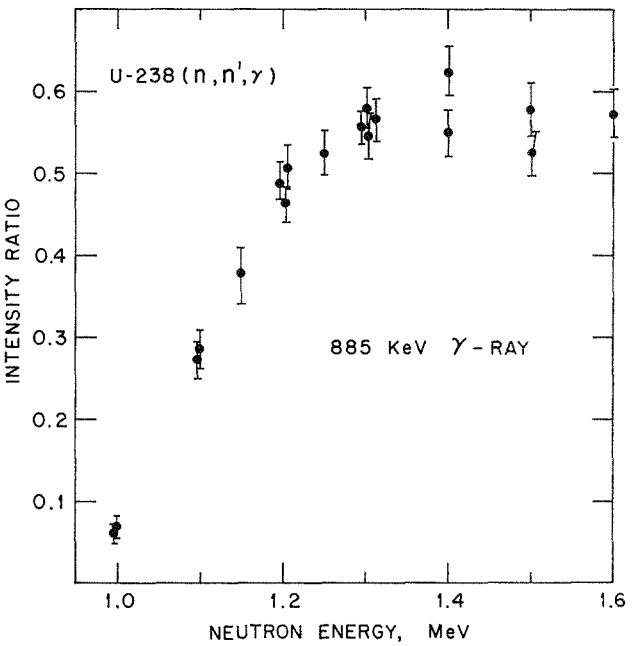

FIG. I-10-3. Intensity Variation of the 885 keV Gamma Ray. *ANL Neg. No. 116-514.*

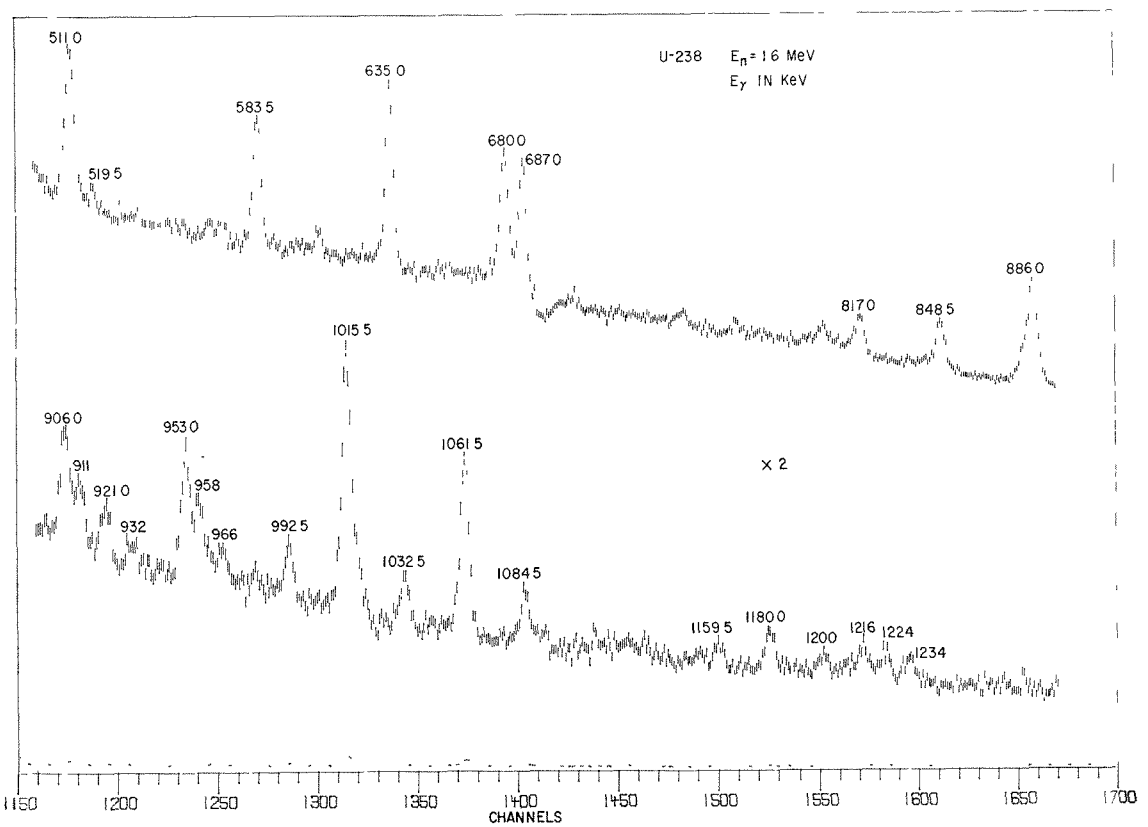

FIG. I-10-2. Gamma Ray Energy Spectrum of U-238. *ANL Neg. No. 116-105.*

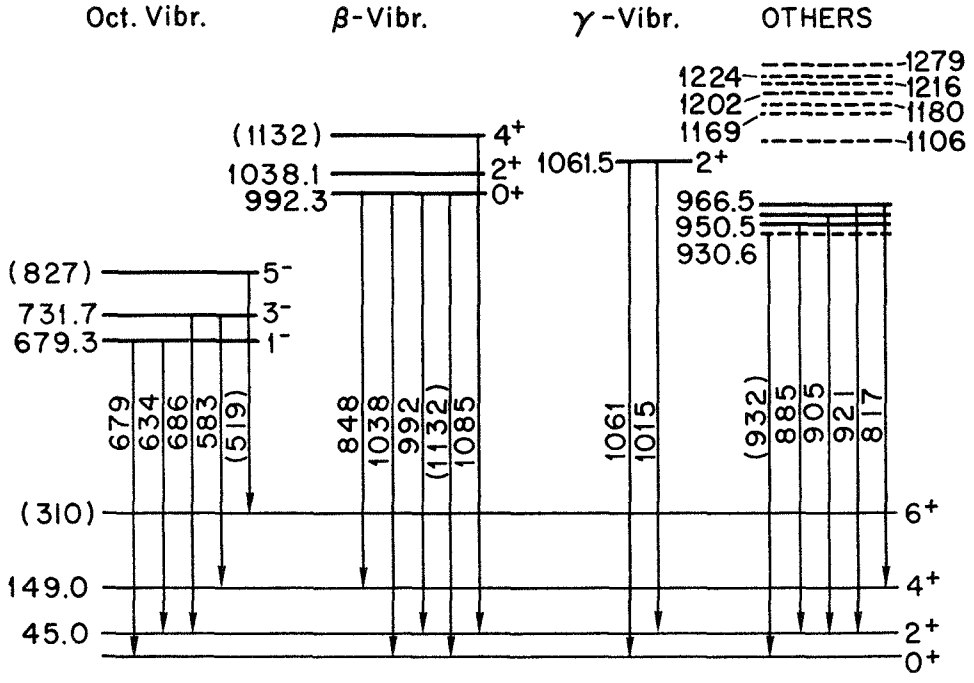

FIG. I-10-4. Level Scheme of U-238. *ANL Neg. No. 116-515.*

and 634 keV γ-rays. The main γ-lines observed in the present experiment are shown in the level scheme in Fig. I-10-4. The basic scheme consisting of ground state rotational band, octupole, and β- and γ-vibrational bands had been suggested by F. S. Stephens et al.[1,2] Three, possibly even four, levels were observed between 930 and 970 keV where only one had been reported before.[4] More important is the observation of a strong 848 keV γ-ray which can be attributed to the de-excitation of the 997 keV level. This casts strong doubts on the validity of the assumption of this level as the base of the vibrational band. Several additional levels remain which cannot be assigned to any of the suggested bands.[5]

REFERENCES

1. F. S. Stephens, Jr., R. M. Diamond and I. Perlman, *Multiple Coulomb Excitation in Th-232 and U-238*, Phys. Rev. Letters **9**, 435 (1959).
2. F. S. Stephens, B. Elbek and R. M. Diamond, *Heavy Ion Coulomb Excitation of Deformed Nuclei*, Proc. Third Conference on Reactions Between Complex Nuclei, University of California Press, 303 (1963).
3. A. B. Smith, *Scattering of Fast Neutrons from Natural Uranium*, Nucl. Phys. **47**, 633 (1963).
4. E. Barnard, E. T. G. Ferguson, W. R. McMurray and I. Y. VanHurten, *Scattering of Fast Neutrons by U-238*, Nucl. Phys. **80**, 46 (1966).
5. A. Faessler, W. Greiner and R. K. Sheline, *Rotation Vibration Interaction in Deformed Nuclei*, Nucl. Phys. **70**, 33 (1965).

I-11. Some Remarks on Prompt Fission Neutron Spectra

A. B. SMITH

Recent macroscopic and spectrum-averaged measurements[1-3] and the analysis of fast critical experiments[4] suggest an uncertain knowledge of the prompt fission-neutron spectrum. This uncertainty is of concern in reactor design.*

In view of the above situation an experimental determination of the prompt fission neutron spectra of U-235 and Pu-239 was undertaken. The primary goal was to test the validity of U-235 and Pu-239 spectra as determined by microscopic measurement and as deduced from macroscopic experiments. The secondary objective was to determine the relative average spectral energies of U-235 and Pu-239. It was not the intent to

* Expressed by European-American Committee on Reactor Physics, for example.

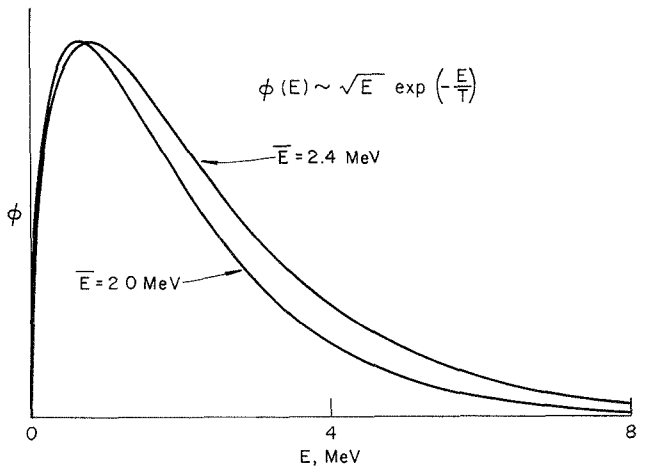

FIG. I-11-1. Maxwellian Fission Spectra Corresponding to Average Energies of 2.4 MeV (Macroscopic Results) and 2.0 MeV (Microscopic Results). *ANL Neg. No. 116-487.*

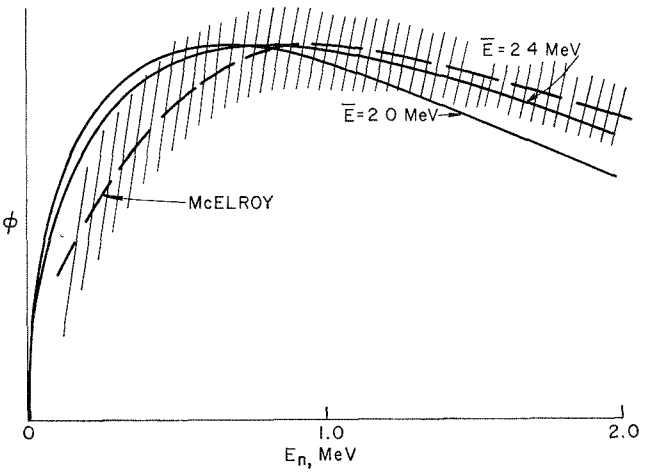

FIG. I-11-2. Comparison of Maxwellian Fission Neutron Spectra Over a Lower Neutron Energy Range. *ANL Neg. No. 116-486.*

undertake a comprehensive spectral measurement for neutron energies from 0 to ∞.

With this objective in mind, one seeks sensitive indexes commensurate with experimental capability and precision. Figure I-11-1 shows two spectral distributions generated assuming a Maxwellian shape. The distribution with an average energy of 2.4 MeV is consistent with macroscopic results; that with an average energy of 2.0 MeV is descriptive of the results of a number of microscopic measurements. The two distributions do not differ by large amounts, perhaps 25% near 4.0 MeV. Such differences are very difficult to determine when dealing with continuum spectra in the interval 3–5 MeV. A more suitable area for investigation occurs at energies below 2.0 MeV. As shown in Fig. I-11-2, there are differences at low energies and these become considerable when compared with the results of macroscopic interpretation carried out by McElroy.[5] Further, at these low energies good relative spectral measurements are possible. Thus this work primarily emphasized a careful determination at neutron energies below 2.0 MeV.

Pulsed beam time-of-flight techniques were employed throughout the work. Spectra were observed concurrently at eight scattering angles between ~25 and ~155 deg and at incident neutron energies of between 100 and 450 keV. Sixteen detector energy biases were employed with selection such as to void scattered neutrons. Effective time resolutions were 1.5 to 2.0 nsec/m. Samples were U-235 (enriched to ~95%) and Pu-239 (enriched to ~97%). Detector sensitivity was carefully determined to energies of ~1.6 MeV using scattering from a carbon standard corrected for multiple scattering, flux attentuation, etc.

Approximately fifty spectral determinations were made. The initial measurements were qualitative, made

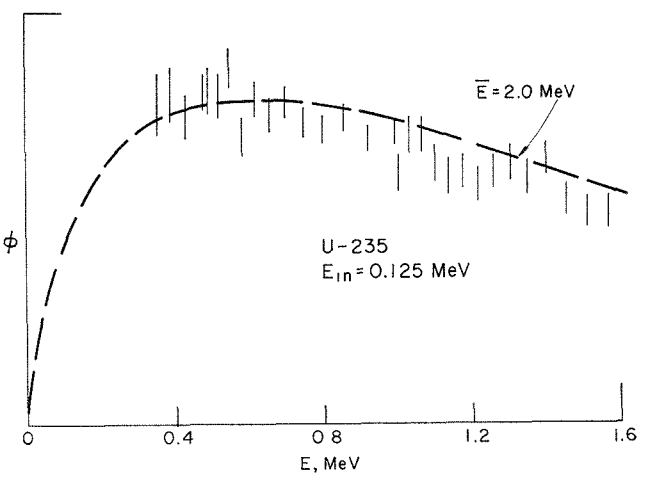

FIG. I-11-3. Relative Spectrum of Neutrons from the Fission of U-235 Induced by 125 keV Neutrons. No Sensitivity Corrections Have Been Made to the Data. *ANL Neg. No. 116-485.*

in an effort to establish a best set of experimental conditions. Only these initial measurements have been reasonably reduced to energy spectra at this time. A typical result is shown in Fig. I-11-3 where relative counting rate is given as a function of energy. The sample was U-235 and the incident neutron energy 125 keV. No detector sensitivity correction has been applied to these results. More complete data, now being processed, have an uncertainty ~⅕ that of this illustration.

Generally, at this point, the results are entirely consistent with the previous microscopic results.

REFERENCES

1. A. Fabry, *Test of U-235 Thermal Fission Spectrum Representations by Means of Activation Detectors*, Nukleonik **10**, 280 (1967).

2. J. Grundl, *A Study of Fission-Neutron Spectra with High-Energy Activation Detectors—Part I: Detector Development and Excitation Measurements*, Nucl. Sci. Eng. **30**, 39 (1967).
3. J. Grundl, *A Study of Fission-Neutron Spectra with High-Energy Activation Detectors—Part II: Fission Spectra*, Nucl. Sci. Eng. **31**, 191 (1968).
4. D. Okrent, J. M. Kallfelz, W. B. Loewenstein, A. D. Rossin, A. B. Smith and B. Zolotar, *Neutron Energy Spectra for Fast Reactor Irradiation Effects*, Trans. Am. Nucl. Soc. **12**, 701 (1969).
5. W. N. McElroy, *Implications of Recent Fission-Averaged Cross-Section Measurements*, Nucl. Sci. Eng. **36**, 109 (1969).

I-12. Analysis of Intermediate Structure in the Fission Cross Section of Pu-239

YASUYUKI KIKUCHI

The intermediate structure observed in recent Pu-239 fission cross section data is considered to be caused by structure in the fission width of the 1^+ state because of the existence of a quasi-stable state at the second minimum point of a double-humped fission potential.

The formulation of the fission width with a double-humped potential has been developeed by Lynn[1] and Weigmann.[2] According to these authors, the mean value of the fission width at energy E is expressed as

$$\langle \Gamma_{f(E)} \rangle = \sum_i \frac{\bar{W}_i^2 \Gamma_i^{\uparrow}}{(E - E_i)^2 + \frac{1}{4}(\Gamma_i^{\uparrow})^2},$$

and the statistical distribution is a χ^2-distribution with one degree of freedom.[3] E_i, $\Gamma_i^{\uparrow}$ and $\bar{W}_i^2$ are the energy, the decaying width into fission, and a measure of the coupling with Class I states of the ith Class II state respectively, and these are defined as the intermediate resonance parameters of the ith Class II state.

In the present analysis, the Petrel data[4] for the fission cross section were used. The actual procedure was as follows.

First, the Petrel data were averaged over several energy intervals. After a trial and error procedure, averaging over intervals between 50 and 100 eV was found most appropriate. In the actual calculation, 100 eV intervals which overlap each other (0–100, 50–150, 100–200, ··· eV) were mainly used but some 50 eV intervals were also used.

Secondly, the contributions from the states other than the 1^+ state were calculated with resonance parameters from the ENDF/B version II compilation. These contributions were then subtracted from the

TABLE I-12-I. INTERMEDIATE RESONANCE PARAMETERS

E_i, eV	Γ_i, eV	$\bar{W}_i^2$, (eV)^2	Peak Value, eV
83	22	5.0	0.909
264	32	1.3	0.163
490	33	6.2	0.752
791	25	1.2	0.192
995	40	4.2	0.420
1145	10	1.0	0.400
1335	52	2.7	0.208
1608	17	0.12	0.028
1801	16	0.65	0.163
2301	36	0.5	0.056
2450	16	0.7	0.181
2677	19	0.5	0.105
2788	55	1.5	0.109
2953	70	0.3	0.017
3160	30	2.6	0.347
3256	10	1.4	0.560
3683	110	1.8	0.065
3800	40	1.1	0.110
3930	54	1.0	0.074
4192	60	1.0	0.067
4444	43	0.8	0.074
4563	91	2.9	0.127
4695	21	0.3	0.057
4900	200	0.3	0.006
5098	15	0.2	0.053
5236	52	4.5	0.346
5517	76	3.3	0.174
5610	57	1.6	0.112
5815	63	6.6	0.419
6200	23	3.2	0.056
6546	55	0.6	0.044
6699	28	3.7	0.529
6799	17	0.8	0.184
7042	23	1.0	0.174
7394	132	8.4	0.255
7543	51	4.3	0.337
Mean	53	2.15	0.163

TABLE I-12-II. THE ESTIMATED PARAMETERS FOR THE FISSION BARRIER OF Pu-240, MeV

E_B (neutron binding energy)	6.5
V_A (the first barrier height)	6.6 (for $\hbar\omega$ = 0.3 MeV)
V_{II} (the second minimum point)	2.9–2.9
V_B (the second barrier height)	6.2

average cross section deduced from the Petrel data to obtain the cross section of the 1^+ state. The statistical uncertainty due to the small sampling was also considered.[5]

Finally, an initial guess of the intermediate resonance parameters was made, based on an inspection of the structure in the fission cross section of the 1^+ state. A least squares fitting method was then employed to obtain the final values of the intermediate resonance parameters. (Further discussion of the overall procedure is presented in Refs. 6 and 7.)

The intermediate resonance parameters thus obtained are tabulated in Table I-12-I. From these values the barrier height of the double-humped potential can be estimated. The results are shown in Table I-12-II. The fission widths obtained from the intermediate resonance parameters are compared with ENDF/B values in Fig. I-12-1. With these fission widths, the fission cross sections were calculated and compared with the Petrel data in Fig. I-12-2.

The intermediate structure in the fission cross section can be described very accurately with 36 sets of intermediate resonance parameters. Hence, this intermediate resonance parameter representation will reduce the computer memory requirement for input data for reactor calculations.

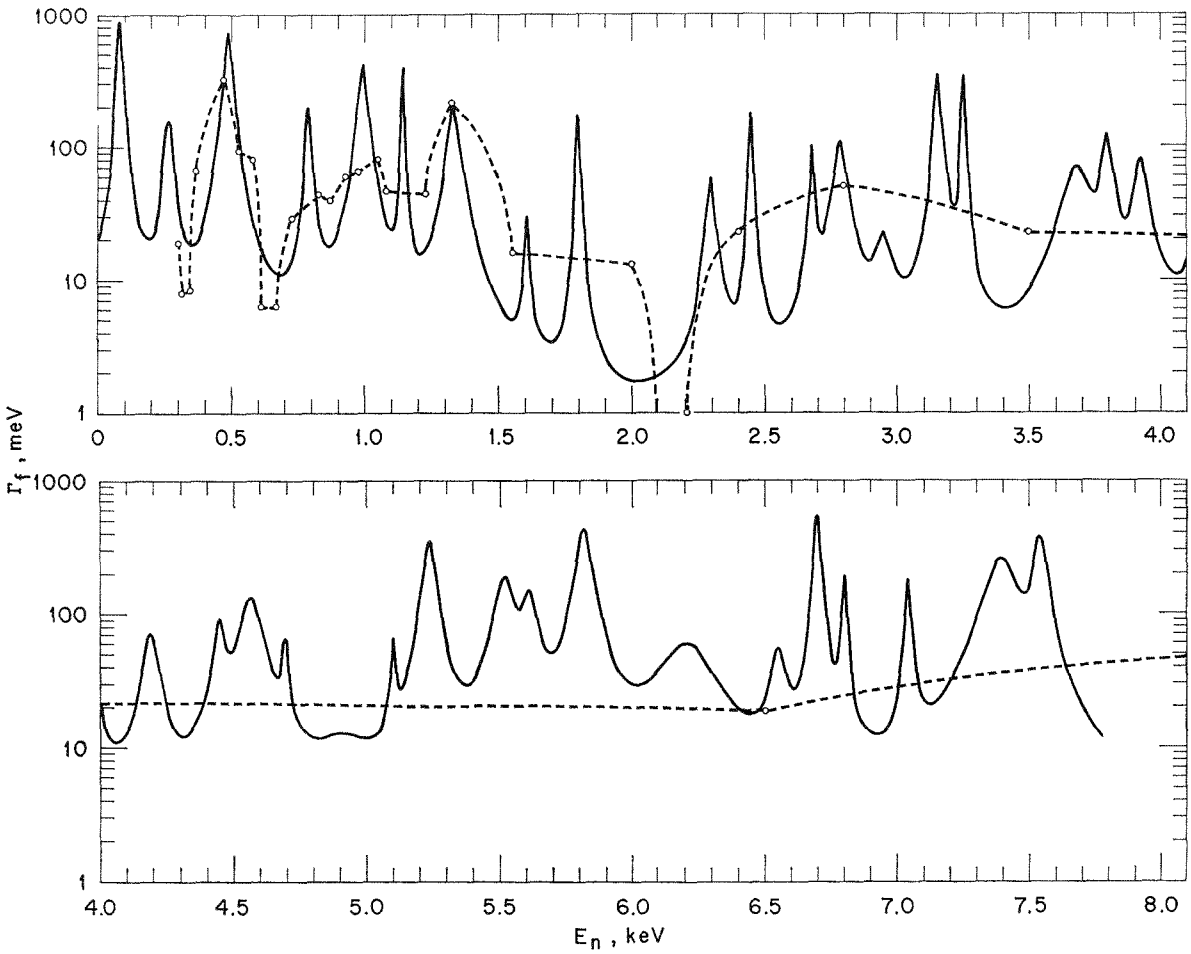

FIG. I-12-1. Fission Width of the 1^+ State. The Solid Line is Calculated from the Intermediate Resonance Parameters. The Point and the Dashed Line Indicate the Evaluated Values in the ENDF/B File and the Recommended Interpolation (Linear-Linear). *ANL Neg. No. 116-209.*

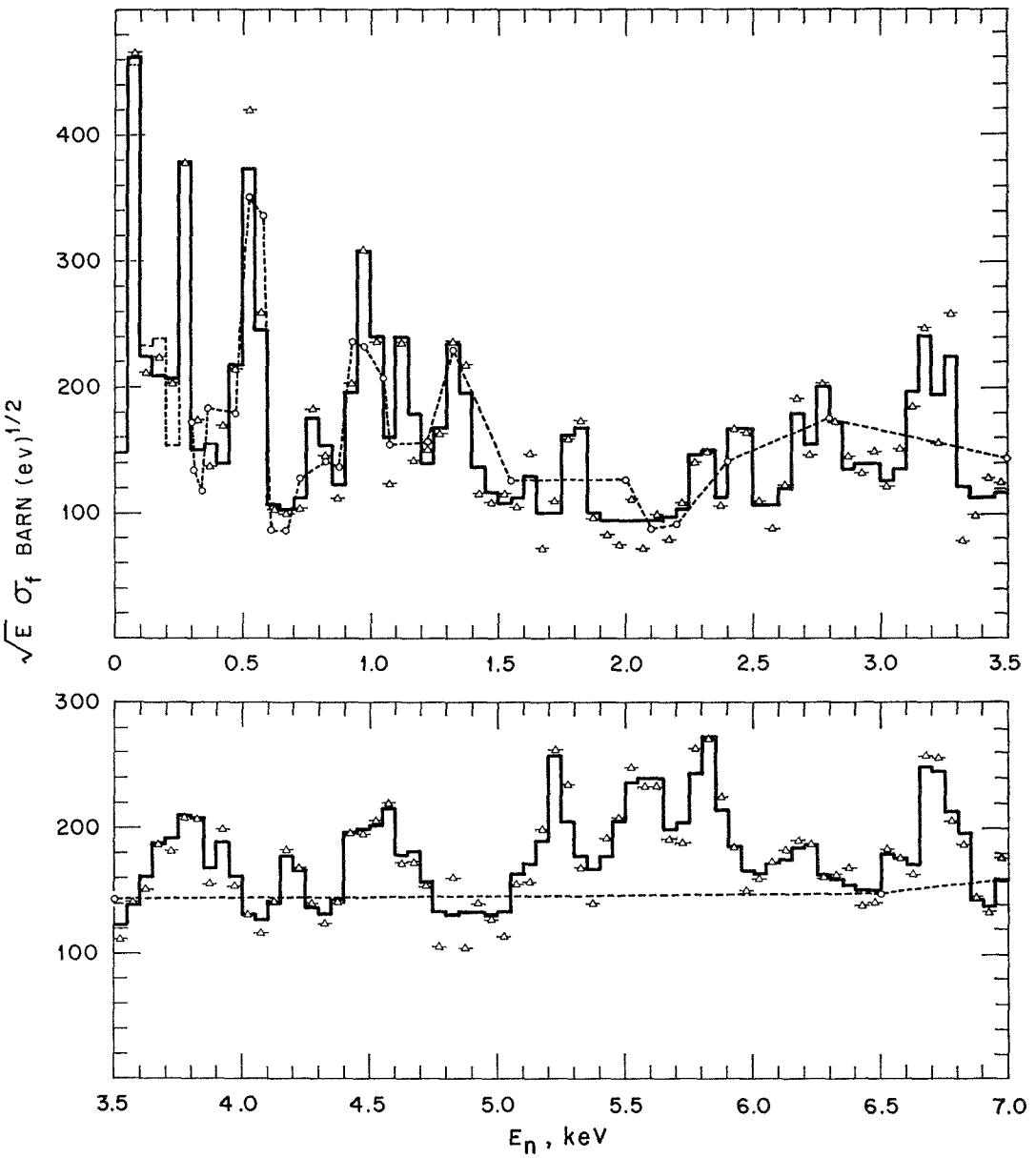

FIG. I-12-2. Fission Cross Section. The Points Designated by Triangles with Horizontal Lines are the Petrel Data Averaged over 50 eV Intervals. The Histogram with a Solid Line is Calculated from the Intermediate Resonance Parameters. The Data Points Designated by Open Circles Connected with a Dashed Line are Obtained from the ENDF/B Compilation. The Histogram with a Dashed Line below 300 eV is Obtained from the Resolved Resonance Parameters in the ENDF/B File. *ANL Neg. No. 116-205.*

REFERENCES

1. J. E. Lynn, *Structure in Subthreshold Fission Modes*, AERE-R 5891 (1968).
2. H. Weigmann, *An Interpretation of the Structure of Subthreshold Fission Cross Section of* ^{240}Pu, Z. Physik **214**, 7 (1968).
3. J. E. Lynn, Atomic Energy Research Establishment, Harwell (private communication).
4. P-3 and W-8 Staff, *Fission Cross Sections from Petrel*, LA-3586, 45 (September 1966).
5. R. N. Hwang, Argonne National Laboratory (private communication).
6. Y. Kikuchi, *The Intermediate Structure of the Fission Width of* ^{239}Pu, Trans. Am. Nucl. Soc. **13**, 312 (1970).
7. Y. Kikuchi, *Analysis of Intermediate Structure in Fission Cross Section of* ^{239}Pu, Nucl. Sci. Eng. (submitted for publication).

I-13. Analysis of Intermediate Structure in the Fission Cross Section of Pu-241

YASUYUKI KIKUCHI

Recent Pu-241 fission cross section data show an intermediate structure similar to that of Pu-239. This structure is expected because of the effect of the double-humped fission potential, since the structure of Pu-239 can be explained very well by assuming a double-humped fission potential[1] (see Paper I-12). Hence the same procedure was employed to analyze Pu-241 as was used to analyze the structure of Pu-239.

The following two points are, however, considered differently in the two cases. First, it is not clear for Pu-241 which state, the 2^+ or the 3^+ state, has the intermediate structure. According to the analysis by Kikuchi and An from channel theory,[2] the 2^+ state has one completely open channel. The second channel of the 2^+ state and the first channel of the 3^+ state belong to the same vibration band (a gamma-vibration) and can be considered to be subthreshold channels. Therefore we assume that the 3^+ state has the structure because the intermediate structure is predominant in a subthreshold channel. Expressions for $\Gamma_f^{(2+)}$ and $\Gamma_f^{(3+)}$ averaged over many intermediate states are

$$\bar{\Gamma}_f^{(2^+)} = \frac{D^{(2^+)}}{2\pi}(1 + P)$$

$$\bar{\Gamma}_f^{(3^+)} = \frac{D^{(3^+)}}{2\pi} P,$$

where D is the mean level spacing and P is the penetrability of the gamma vibration channel.

Secondly, the s-wave strength function evaluated by Yiftah et al.[3] ($s_0 = 1.3 \times 10^{-4}$) upon which the ENDF/B value depends, was found to be too small to obtain the peak values of the structure. Hence we used the larger value from the total cross section measurement by Craig and Westcott[4] ($s_0 = 1.9 \times 10^{-4}$).

The intermediate resonance parameters thus obtained and the parameters of the fission potential shape estimated from these intermediate resonance parameters are tabulated in Tables I-13-I and I-13-II, respectively. The fission widths obtained from these intermediate resonance parameters are compared with ENDF/B values in Fig. I-13-1. The present calculated value is smaller because of the assumed large strength function. The calculated fission cross sections are compared with the Petrel data in Fig. I-13-2. The intermediate structure is very well described with the intermediate resonance parameters. (A more detailed discussion of the procedures employed is presented in Ref. 5.)

TABLE I-13-I. INTERMEDIATE RESONANCE PARAMETERS

E_i, eV	$\Gamma_i^{\uparrow}$, eV	$\bar{W}_i^2$, $(\text{eV})^2$	Peak Value, eV
246	33	5.5	0.667
404	30	2.9	0.387
534	25	1.3	0.208
1050	109	1.8	0.066
1540	170	2.5	0.059
1707	11	0.3	0.109
1921	173	0.6	0.014
2280	95	0.62	0.026
2491	80	1.2	0.060
2806	10	2.1	0.840
3031	110	9.0	0.327
3247	22	3.1	0.564
3401	10	0.6	0.240
3771	182	4.5	0.099
3900	27	0.64	0.095
4164	32	1.3	0.163
4298	20	1.9	0.380
4641	102	2.1	0.082
4947	72	3.2	0.178
5260	18	1.1	0.244
5471	107	1.5	0.056
5903	106	2.1	0.079
Mean	70	2.3	0.129

TABLE I-13-II. THE ESTIMATED PARAMETERS FOR THE FISSION BARRIER OF Pu-240, MeV

E_B (neutron binding energy)	5.52
V_A (first barrier height)	5.6
V_{II} (second minimum point)	2.6–3.0
V_B (second barrier height)	4.5–5.0

REFERENCES

1. Y. Kikuchi, *The Intermediate Structure of the Fission Width of ^{239}Pu*, Trans. Am. Nucl. Soc. **13**, 312 (1970).
2. P-3 and W-8 Staff, *Fission Cross Sections from Petrel*, LA-3586, 45 (September 1966).
3. S. Yiftah et al., *Nuclear Data for Plutonium-240, Plutonium-241 and Plutonium-242*, IA-1152, Soreq Nuclear Research Center, (1967).
4. D. S. Craig and C. H. Westcott, *The Total Neutron Cross Section of ^{241}Pu below 1000 eV*, Can. J. Phys. **42**, 2384 (1964).
5. Y. Kikuchi, *Analysis of Intermediate Structure in the Fission Cross Section of ^{241}Pu*, Nucl. Sci. Eng. (submitted for publication).

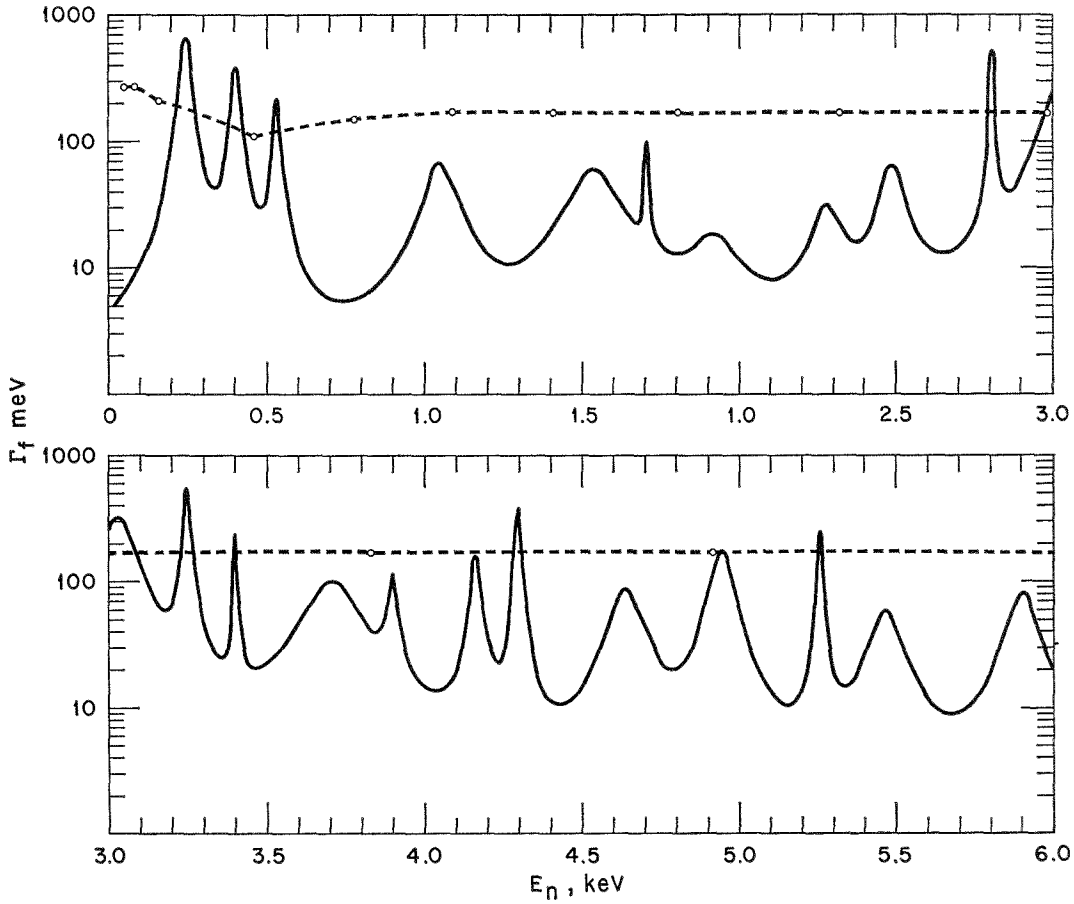

FIG. I-13-1. Fission Width of the 3^+ State. The Solid Line is Calculated from the Intermediate Resonance Parameters. The Points and the Dashed Line Indicate the Evaluated Values in the ENDF/B File and the Recommended Interpolation (Linear-Linear). *ANL Neg. No. 116-203.*

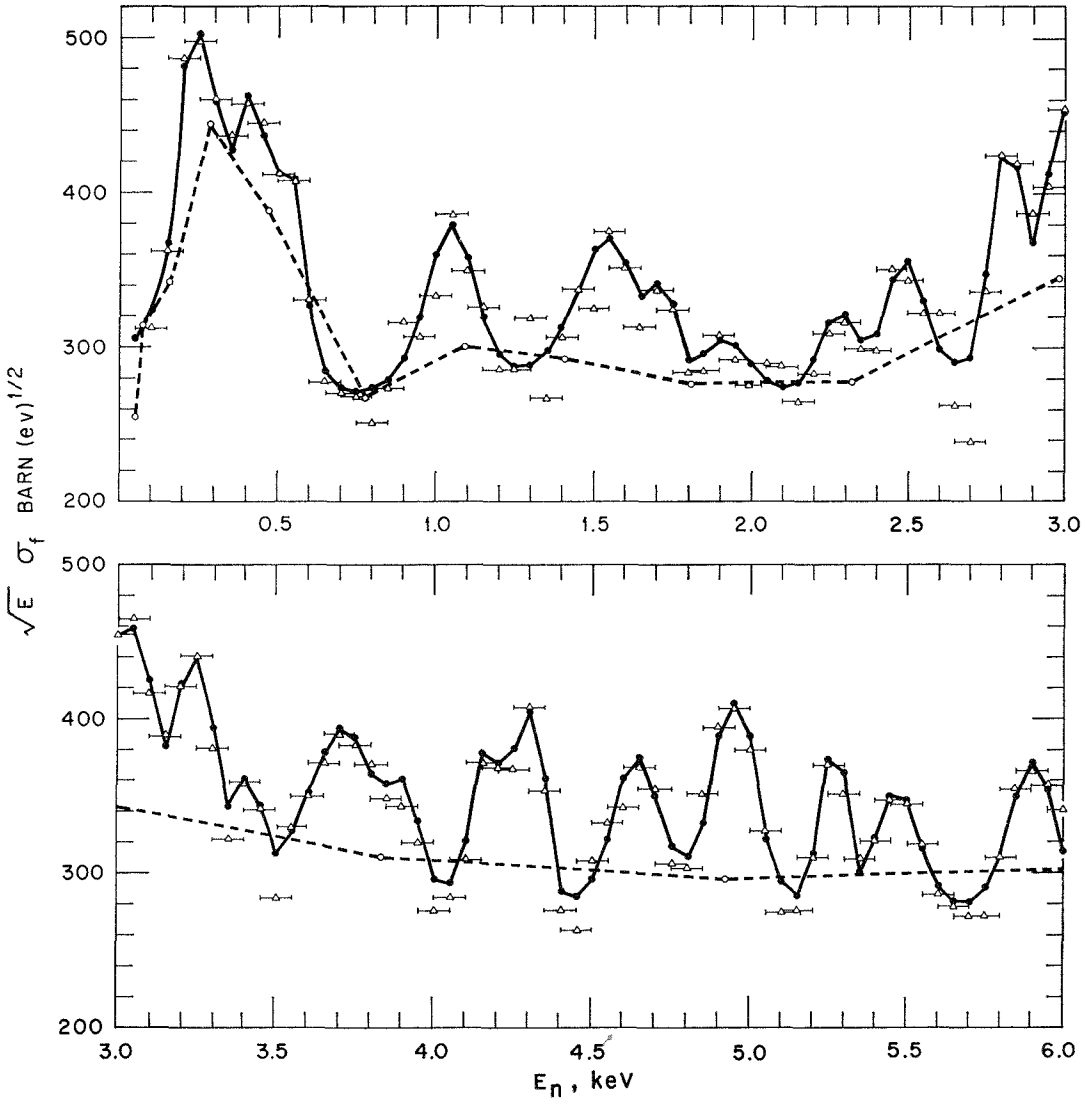

FIG. I-13-2. Fission Cross Section. The Points Designated by Triangles with Horizontal Lines are the Petrel Data Averaged over 100 eV Intervals. The Points Designated with Closed Circles Connected with a Solid Line are Calculated from the Intermediate Resonance Parameters. The Data Points Designated by Open Circles Connected with a Dashed Line are Obtained from the ENDF/B Compilation. *ANL Neg. No. 116-207.*

I-14. Recent Experimental Data for Heavy Nuclei

W. P. POENITZ

The present knowledge of experimental nuclear data for fertile and fissile nuclei above the resonance energy region has been reviewed for presentation at the Second IAEA Conference on Nuclear Data for Reactors. Because of the large amounts of data involved the review has been restricted to those heavy nuclei and their properties which have the strongest influence on the neutronics of fast reactors. Therefore, the consideration for nuclear data of *U-235*, *U-238* and *Pu-239* has been emphasized. The capture and fission cross sections as well as $\bar{\nu}$, of these nuclei represent the negative and positive sources of neutrons in a reactor and

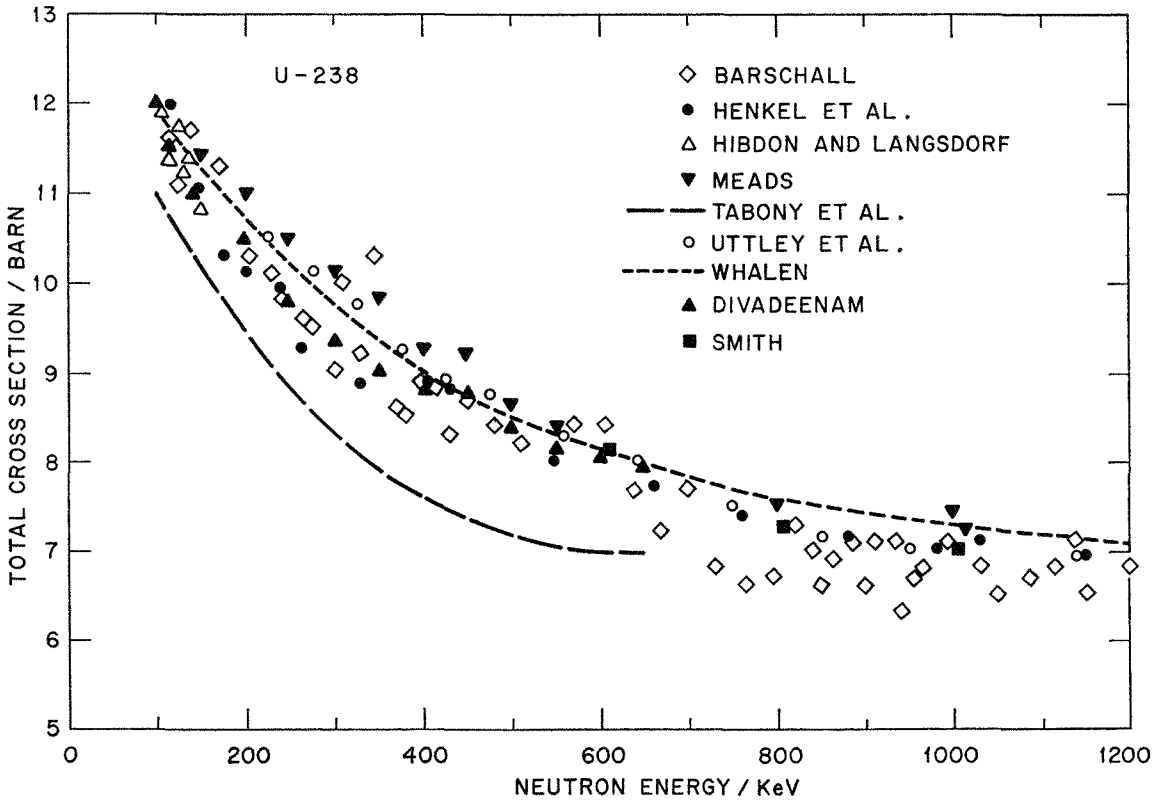

FIG. I-14-1. The Total Cross Section of U-238. *ANL Neg. No. 116-100.*

are thus of predominant importance. The importance of the inelastic scattering cross sections lies in their influence on the neutron energy spectrum in a reactor.

FAST NEUTRON TOTAL AND SCATTERING CROSS SECTIONS

THE TOTAL CROSS SECTION OF URANIUM

Measurements of absolute total cross sections have always been considered to be relatively easy because no determination of the absolute neutron flux or the detector efficiency has to be carried out. However, even with this consideration, discrepancies up to 15 percent exist between different measurements. Particularly notable were the low total cross section data reported for uranium and thorium in Ref. 1 and some new high resolution data for several elements in Ref. 2 which are discrepant up to 15 percent compared to previous measurements which had been considered to be reliable.

Data of the total cross section of U-238 are shown in Fig. I-14-1 for the energy range 100–1200 keV. The data of Divadeenam[3] are about 10–15% higher and replace the previous results given in Ref. 1. They agree very well with measurements by Henkel[4] and by Adair.[5] Measurements by Meads,[6] Uttley et al.[7] and Whalen[8] yield values which are up to 6% higher in the energy range from 200–400 keV. The data from both groups agree at 100 keV, the energy at which values were also measured by Hibdon and Langsdorf.[9] Above 500 keV both groups are also in agreement. Recent measurements by Smith[10] in the higher energy range confirm both the measurements by Henkel[4] and by Uttley et al.[7] which are, however, discrepant at lower energies. On the basis of the data shown in Fig. I-14-1 it seems feasible to suggest values for the total cross section for uranium with an approximate uncertainty of 3%.

INELASTIC SCATTERING CROSS SECTION OF U-238

The inelastic scattering cross section of U-238 appears to be the best measured of any nuclei with $A > 220$. Extensive measurements have been reported by Barnard et al.[11] These measurements have been carried out with sufficient resolution to resolve most of the important levels up to about 1.1 MeV. An appreciable contribution to the inelastic scattering process has been observed from two levels, 930 and 960 keV,—levels unknown from Coulomb-excitation experiments. Recent Ge(Li)-detector measurements confirmed the existence of these levels (930.5 and 966.5 keV) and showed the presence of a third level at 950.5 keV.[12] For energies above 1.1 MeV Barnard et al.[11] reported several levels which contribute about 1.2 *b* to the total inelastic cross section at 1.6 MeV.

The measurements by Barnard et al.[11] have been

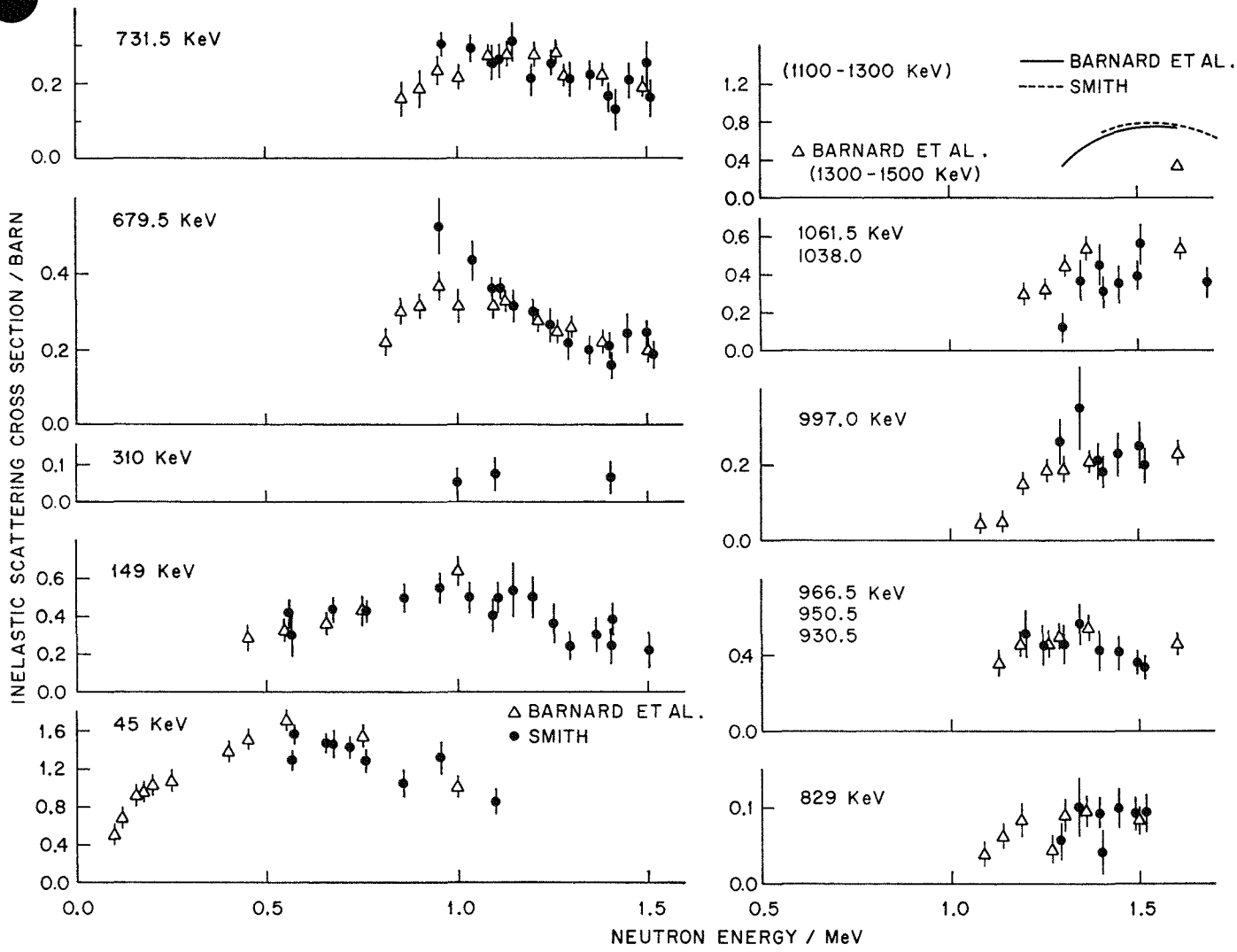

FIG. I-14-2. Inelastic Scattering Cross Sections of U-238. *ANL Neg. No. 116-93.*

carried out at 90 deg only. The cross sections reported at that angle have been multiplied by 4π, and are shown in Fig. I-14-2. The energies given in Fig. I-14-2 are from Ge(Li)-detector γ-ray measurements.[12] Recent measurements by Smith[13] at 8 angles showed that the anisotropy does not exceed 10%. These new measurements by Smith are also shown in Fig. I-14-2. In addition, Smith measured cross sections for the sum of several levels which indicate that the values obtained by Barnard et al.[11] at 1.6 MeV for several cross sections might be too high. The agreement between the two sets of measurements shown in Fig. I-14-2 is good. This may, however, be deceptive because the sum of the elastic and inelastic scattering cross section as measured by Barnard et al.[11] exceeds the total cross section by 10–30%. A comparison for the total inelastic cross section at 1.6 MeV has been given in Table I-14-I. The values given by Barnard et al.[11] are based upon an analysis by Schmidt.[14] The values measured by Smith[13] have been corrected for missing levels above 1.3 MeV as indicated in Table I-14-I. The sum of the total inelastic scattering cross section and the elastic scattering cross section as measured by Smith is 6.57 *b*, which compares very well with 6.60 *b* for the total scattering cross section as measured by Lane et al.[15] and Langsdorf et al.[16] Adding 0.40 *b* for the fission cross section and 0.08 *b* for the capture cross section, one obtains 7.05 *b* which compares well with the total cross section of 7.10 *b* as measured by Henkel et al.[4] and Leroy et al.[17] The values obtained from Barnard et al.[11] do not fit the total cross section data quite as well, though they agree within the error bars.

Capture Cross Section Ratios

Next to α of Pu-239 the ratio of the capture cross section of U-238 to the fission cross section of U-235

TABLE I-14-I. Inelastic Scattering Cross Sections of U-238 AT 1.6 MeV

Q, keV	Barnard et al.[a] (see Ref. 11)	Smith (see Ref. 10)
45	[b]	[b]
149	0.16	0.18
310	0.06	0.05
680	0.17	0.17
731	0.17	0.15
829	0.09	0.08
930–966	0.45	0.34
977	0.21	0.22
1038–1061	0.55	0.41
1100–1300	0.84	0.81
1300–1500	0.44	0.36[c]
1500–1600	0.10[d]	0.10[d]
	3.24	2.87

[a] Analysis by Schmidt.[14]

[b] Values cannot be obtained from measurements. 0.0 *b* is an extrapolated value (Ref. 14).

[c] Value has not been measured. The value given by Barnard et al. has been used and it was corrected for an assumed error in the detector efficiency.

[d] Value is from analysis of other available data given in Ref. 14.

is the most important capture cross section ratio for fast reactor applications. Direct measurements of σ_γ(U-238)/σ_f(U-235) were carried out in 1944 by Linenberger et al.[18] using the activation method. Additional values for this ratio can be obtained from measurements of the U-238 capture cross section relative to the capture and fission cross section of U-235 by De Saussure et al.[19] and by Diven et al.,[20] if one corrects for the contribution of the capture in U-235 using α-measurements. Measurements reported by Barry et al.[21] as relative to the hydrogen scattering cross section should be considered as ratio measurements relative to the fission cross section of U-235 if one uses the fission cross section reported by White,[22] since Barry et al. sandwiched U-238 foils between two of White's fission counters and did not measure recoil protons. They measured the Np-239 activity of the U-238 sample after chemical separation, using a $4\pi\beta$-counter.

The chemical separation was avoided in a recent measurement of the ratios σ_γ(U-238)/σ_f(U-235) and σ_γ(U-238)/σ_f(Pu-239) by Poenitz[23] using a high resolution Ge(Li)-detector to measure the 228 keV and 278

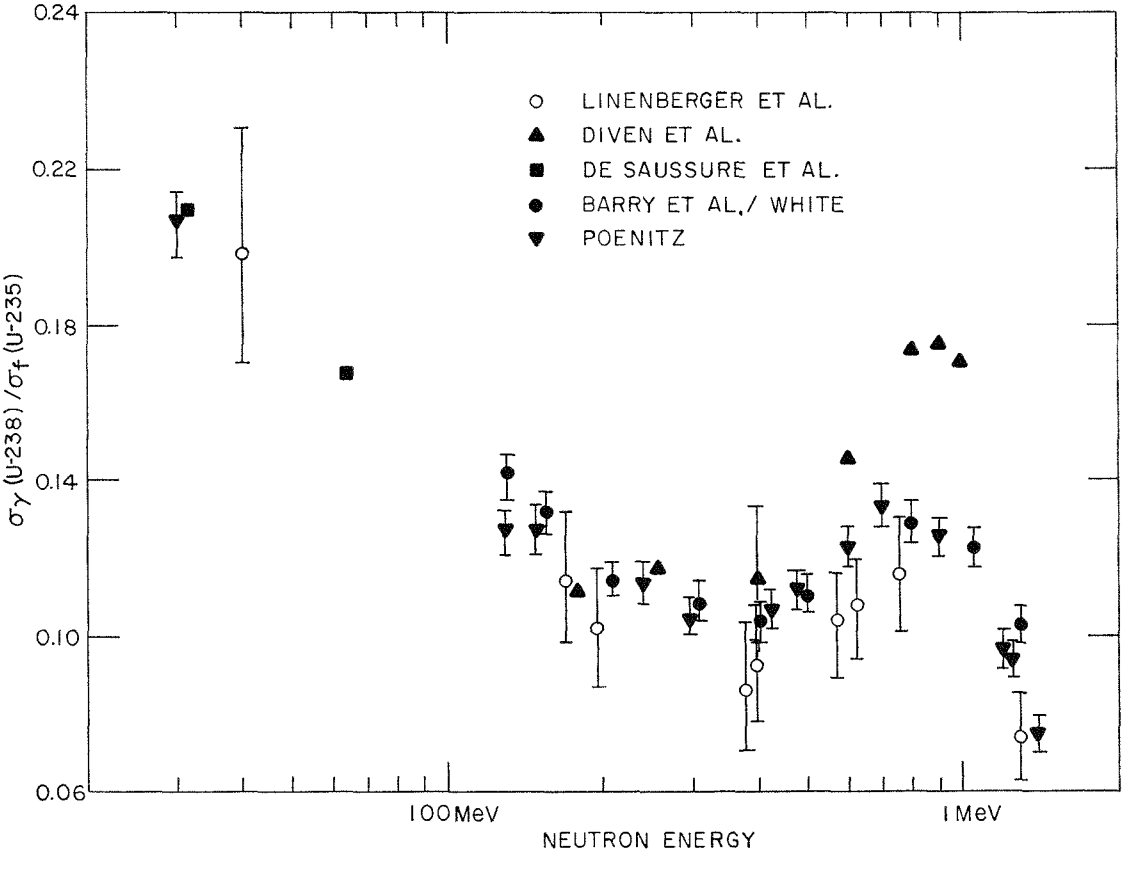

Fig. I-14-3. The Ratio σ_γ(U-238)/σ_f(U-235). *ANL Neg. No. 116-97.*

keV γ-rays which occur in the decay of Np-239. Values for the ratio σ_γ(U-238)/σ_f(U-235) are shown in Fig. I-14-3. The available values below 100 keV are too few to draw a conclusion about the shape as well as the amplitude. Above 130 keV the ratios measured by Barry et al.[21] and Poenitz[23] are in good agreement; the values measured in 1944 by Linenberger et al.[18] agree within error bars or at least overlap the former two with their error bars. Therefore, there is no justification to renormalize these data as had been done recently. Above 1 MeV the values measured by Barry et al. are somewhat higher than those measured by Poenitz. The latter still overlap the results by Linenberger et al.[18] The figure indicates a clear need for additional data in the lower keV energy range where data are most important for fast power reactors. Such measurements should be carried out with a prompt capture γ-ray detector as the activation method may not supply accurate data in a region where background from scattered neutrons is usually high.

One of the most exciting nuclear data problems of recent times was the measurement of the capture-to-fission ratio of Pu-239 in the energy range 0.1 to 30 keV. There have been many direct and indirect measurements made after Schomberg et al.[24] presented, in 1967, preliminary results which indicated much higher values than had been previously assumed. In Fig. I-14-4 some recent measurements of α(Pu-239) are shown. The difference between the values measured by Gwin et al.[25] using a large liquid scintillator, and by Schomberg et al.[26] using a low efficiency counter in the energy range above 10 keV is obvious. It had been suggested that this difference might be due to a different normalization of the two data sets. Because of the good agreement of the data measured by Hopkins and Diven[27] and by De Saussure[28] in the higher keV energy range it would be reasonable to renormalize in the 20–30 keV energy range to these data. The advantage of such renormalization would be that the data measured by Schomberg et al.[26] would then agree for energies above 0.5 keV with the new data measured by Ryabov et al.[29], as well as with the measurements by Czirr.[30] The data measured by Gwin et al.[25] would be exceedingly large compared to these other renormalized values.

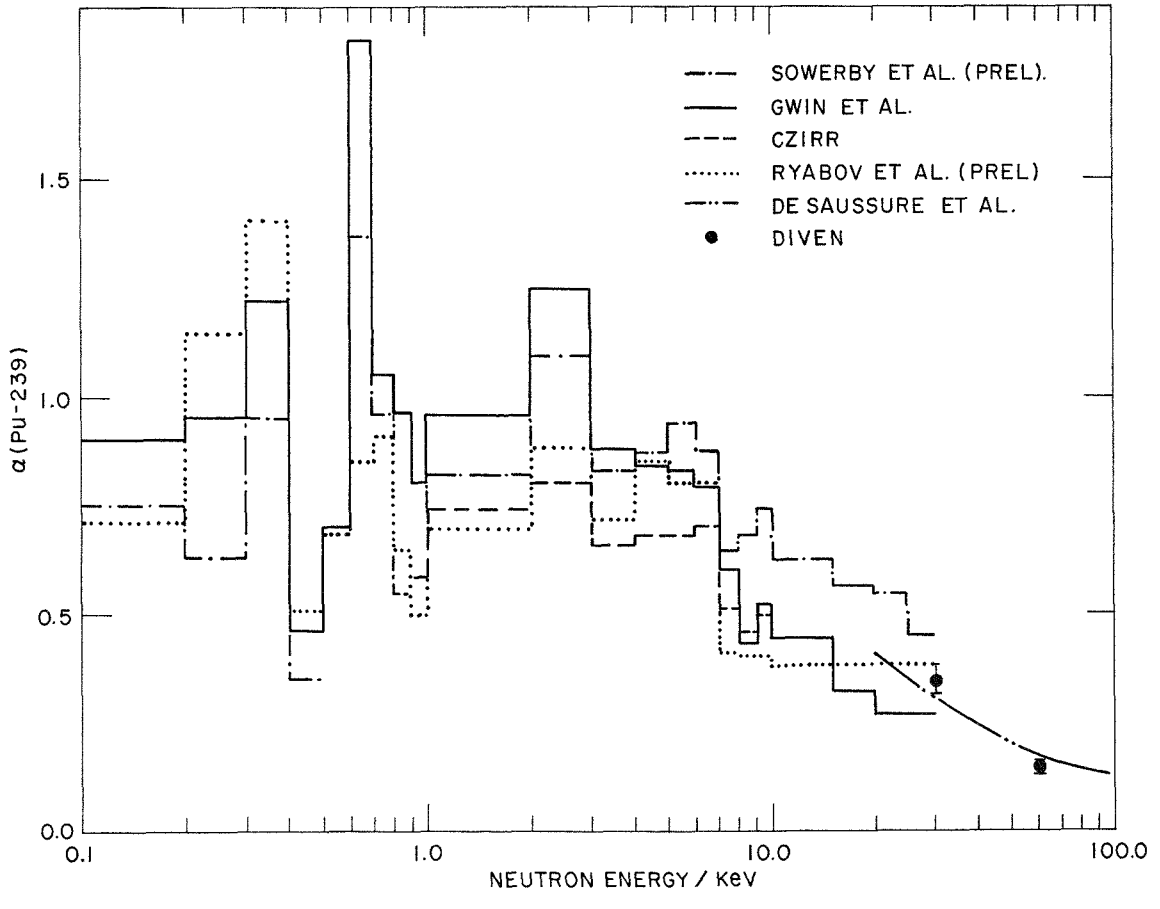

FIG. I-14-4. The Capture-to-Fission Ratio of Pu-239. *ANL Neg. No. 116-99.*

Fission Cross Section Ratios

The overwhelming majority of the fission cross sections have been measured relative to the U-235 fission cross section. Of major importance are the ratios of U-233, U-238, and Pu-239 to U-235.

In Fig. I-14-5 some data for the ratio σ_f(U-233)/σ_f(U-235) are shown. A comparison shows differences which exceed by far the given error bars. The values reported by White et al.,[31] which are in good agreement with the results by Allen and Ferguson,[32] had been generally accepted and were the basis of suggested cross sections. Such selected cross section ratios have been revised in the energy range above 1 MeV after the measurements by White and Warner[33] were reported. The measurements by White et al.[31,33] have been considered as very reliable because the same fission counters have been used in the U-235 fission cross section measurement relative to the $H(n,n)$ cross section of White.[22] However, the new measurements by Nesterov and Smirenkin[34] support the data of Lamphere[35] with the exception of one low value at 500 keV, which is outside error bars. Time-of-flight measurements by Pfletschinger and Kaeppeler[36] are, with the exception of the 100–250 keV range, about 3 per cent lower than the results from Lamphere.[35] A similar discrepancy of the Karlsruhe data can be noted for the Pu-239 to U-235 ratio. A good agreement with the Lamphere data at the low energy side is obtained in measurements by Lehto,[37] and in the energy range 500–1500 keV in measurements by Meadows.[38] The latter are time-of-flight measurements using monoenergetic neutrons and a two-dimensional recording of fission fragment energy versus neutron time-of-flight. Special care has been taken to obtain an accurate mass assignment. In the energy range considered in Fig. I-14-5 the values measured by Lamphere[35] seem to be strongly supported by the newest results. A possible reason for the low value derived from the absolute measurements by Perkin et al.[39] using an Sb-Be source might be fluctuations in the fission cross sections of U-233 and U-235; however, it is hard to suggest a reason for the discrepancy of the values reported by White et al.[31,33] by up to 5 times their error bars and the similarly low values for data reported by Allen and Ferguson.[32]

The ratio of the Pu-239 to the U-235 fission cross section in the energy region 100 keV–10 MeV is shown in Fig. I-14-6. A recent time-of-flight measurement by Poenitz[23] using back-to-back scintillation counters con-

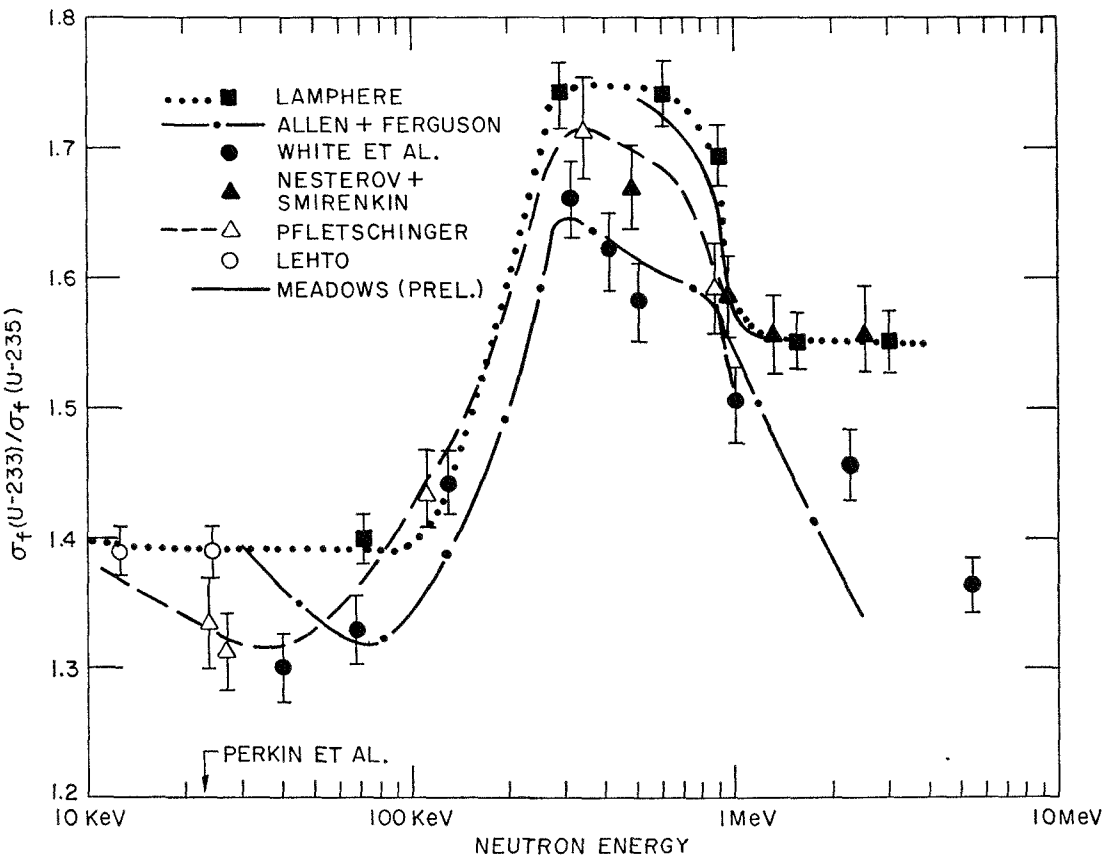

Fig. I-14-5. The Fission Cross Section Ratio σ_f(U-233)/σ_f(U-235). *ANL Neg. No. 116-95.*

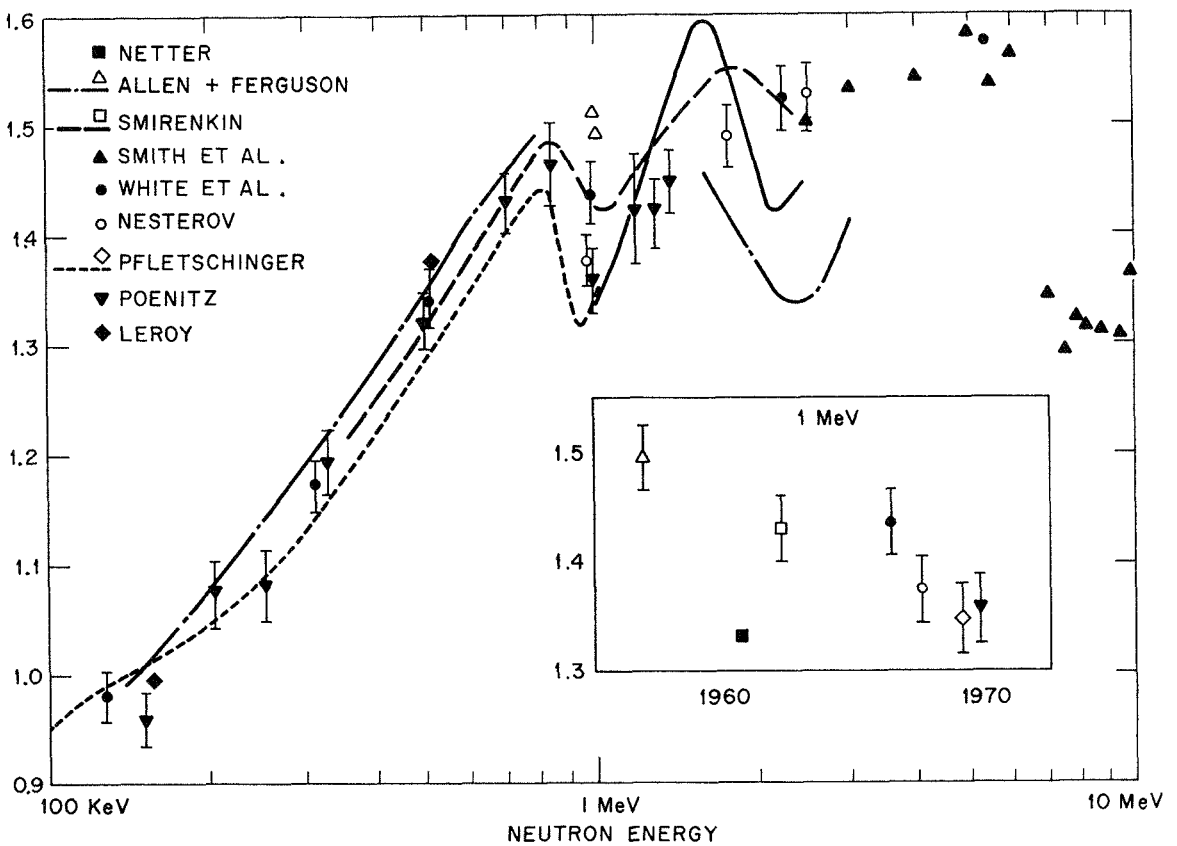

FIG. I-14-6. The Fission Cross Section Ratio σ_f(Pu-239)/σ_f(U-235). *ANL Neg. No. 116-101.*

firmed previous dc measurements by Allen and Ferguson,[32] Smirenkin et al.,[40] and White et al.[31] in the energy range below 1 MeV. In the energy range from 1 to 2 MeV these measurements are in good agreement with the new results reported by Nesterov and Smirenkin.[34] The new Karlsruhe measurements by Pfletschinger and Kaeppeler[36] are lower by about 3–4%. The step in the cross section ratio at 900 keV is due to a 10% step of the U-235 fission cross section at that energy.

The agreement in measured ratios is not as good in the lower as in the higher keV energy range. A value reported by White et al.[31] at 40 keV is lower than the results of measurements by Allen and Ferguson[32] by 4 to 5 times the associated error. The latter measurements are better supported by the new measurements from Pfletschinger and Kaeppeler[36] and Szabo et al.[41] than those from White et al.[31]

An interesting question in connection with the results for U-233 arises if one considers the ratio for σ_f(U-238)/σ_f(U-235). This ratio has also been measured by Lamphere.[35] Measurements by Stein et al.[42] using a time-of-flight method and monoenergetic neutrons are about 8% lower than Lamphere's measurements. A measurement by Smirenkin et al.[40] strongly supports the results of Lamphere; however, less accurate data by Kalinin and Ponkratov,[43] as well as revised data by Hanson et al.,[44] agree better with the results reported by Stein et al.[42] Measurements by White and Warner[33] agree with Stein et al.,[42] and have led to the values reported by Lamphere being multiplied by 0.94 in some cross section compilations. This procedure may be questionable in view of the situation for U-233.

Absolute Capture and Fission Cross Sections

Only very few absolute measurements of the capture cross section of U-238 are available. Other data based on reliable features of certain reference cross sections supplement these data. Results of this type are presented in Fig. I-14-7.

Measurements by Macklin et al.[45] and Lyon and Macklin[46] are based on calibrated photo neutron sources. Hanna and Rose[47] used the $H(n,n)$ cross section as a reference cross section. The measurements by Barry et al.[21] are based on the calibration of a fission detector by White[22] and therefore must be considered a cross section ratio. Menlove and Poenitz[48] measured the shape of the capture cross section using a large liquid scintillator tank and a beam catcher-flux integration type neutron-detector. Tolstikov et al.[49] used the activation technique for measurements in the energy

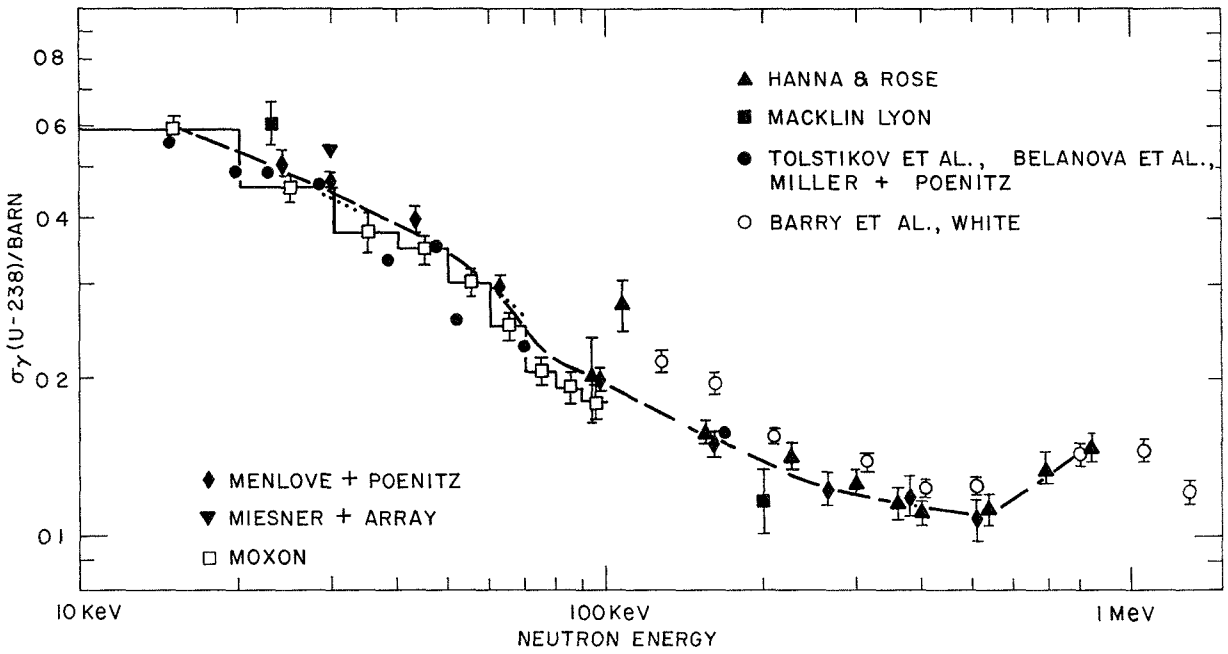

FIG. I-14-7. The Capture Cross Section of U-238. *ANL Neg. No. 116-98.*

range 5–200 keV. They utilized the shape of the $B^{10}(n,\alpha)$ reaction and normalized to the result from a shell transmission experiment by Belanova et al.[50] for which a new Monte Carlo evaluation had been carried out recently by Miller and Poenitz.[51] Measurements by Moxon[52] essentially confirmed the absolute values of their older results. The values shown in Fig. I-14-7 allow the suggestion of a cross section which satisfies essentially all sets of measurements with the exception of the values reported by Barry et al.[21] which are systematically higher below 700 keV. It should be noted that the shapes measured by Moxon,[52] Tolstikov et al.,[49] and by Menlove and Poenitz,[48] adjusted to the values measured by Barry et al.,[21] lead to higher values for U-238 at low energies than those determined in an absolute cross section experiment.

Fig. I-14-8 shows the fission cross section of U-235 in the energy range from 10–100 keV. Recent measurements by Bowman et al.[53] showed strong fluctuations of this cross section in the low keV energy range.

Measurements using absolutely calibrated Sb-Be sources by Perkin et al.[39] and by Doroffeev and Dobrynin[54] are in very good agreement with the value obtained by Knoll and Poenitz[55] using the associated activity method. The latter measurement has been extended by Poenitz[56] to the higher energy range using a shape measurement based on a beam catcher neutron flux integration detector. A very good confirmation of these measurements in the lower keV energy range is given by recent absolute measurements by Szabo et al.[41] Barry[57] measured the ratio of the $Li(n,\alpha)$ cross section relative to the U-235 fission cross section in the energy range 25–100 keV. His results are in good agreement with older measurement by Bame and Cubitt.[58] In the energy range up to 100 keV independent and absolute measurements of the $Li(n,\alpha)$ cross section are available from measurements by Schwarz et al.[59] and from total cross section measurements by Uttley.[60] These values are in good agreement with a single point at 100 keV measured by Condé.[61] σ_f(U-235) values obtained from the measured ratios and the absolute $Li(n,\alpha)$ cross sections are shown in Fig. I-14-8. Values obtained relative to the $H(n,n)$ cross section suffer from the disagreement between different measurements of the ratio $\sigma_f(\text{U-235})/\sigma_n(H)$.

Figure I-14-9 shows the higher energy part of the U-235 fission cross section. At 100 keV the value relative to the $Li(n,\alpha)$ cross section has been indicated. Measurements relative to the hydrogen scattering cross section are also inconsistent in this energy range. Measurements by Diven[62] essentially confirm the results from Allen and Ferguson;[32] however, the results reported by White[22] agree better with the absolute measurements by Gorlov et al.[63] and Leroy.[17] Preliminary measurements by Poenitz[56] resulted in still lower values which are, however, in agreement with the results by Gorlov et al.[63] and compatible with the absolute values for U-238(n,γ) and the Au(n,γ) standard cross section. It is noticeable that the cross sections for U-238 capture and gold capture which have been

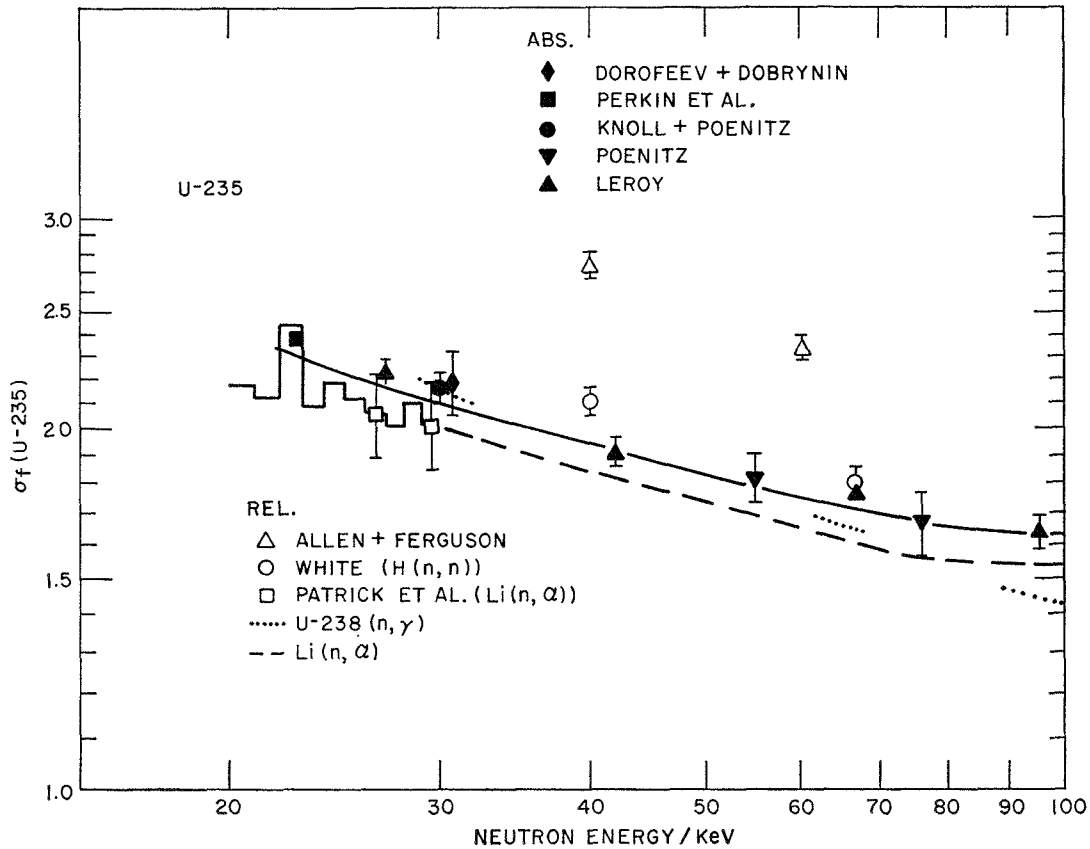

FIG. I-14-8. The Fission Cross Section of U-235 below 100 keV. *ANL Neg. No. 116-103.*

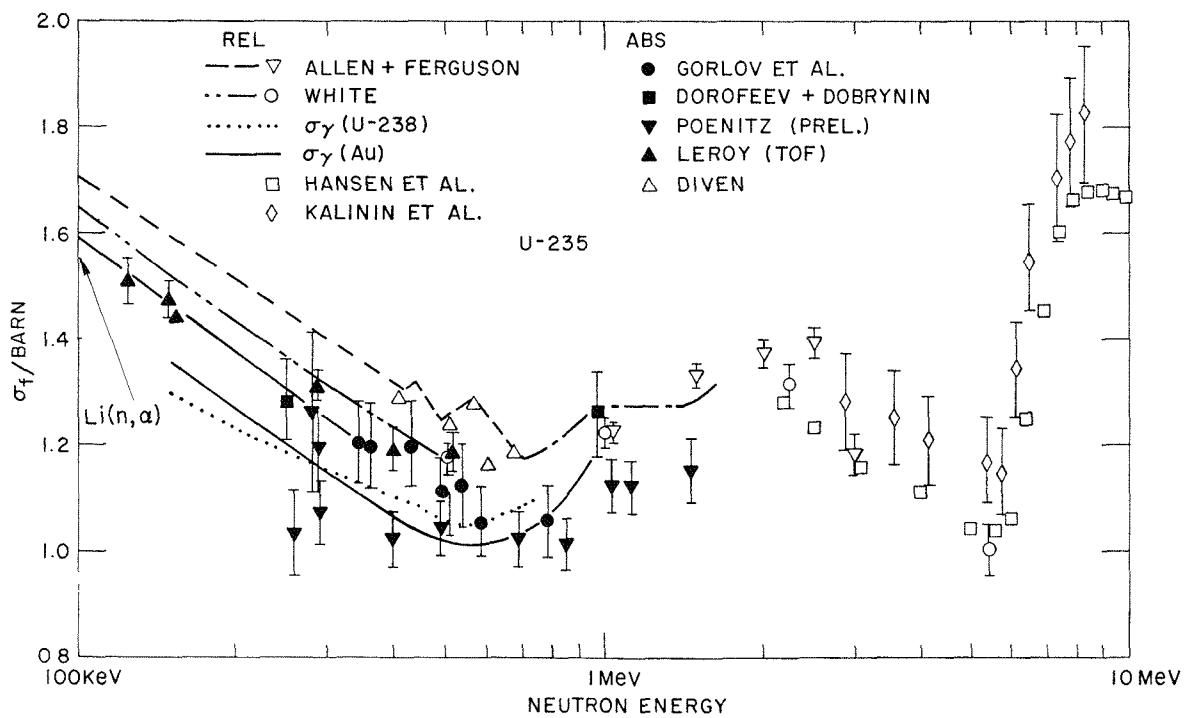

FIG. I-14-9. The Fission Cross Section of U-235 above 100 keV. *ANL Neg. No. 116-102.*

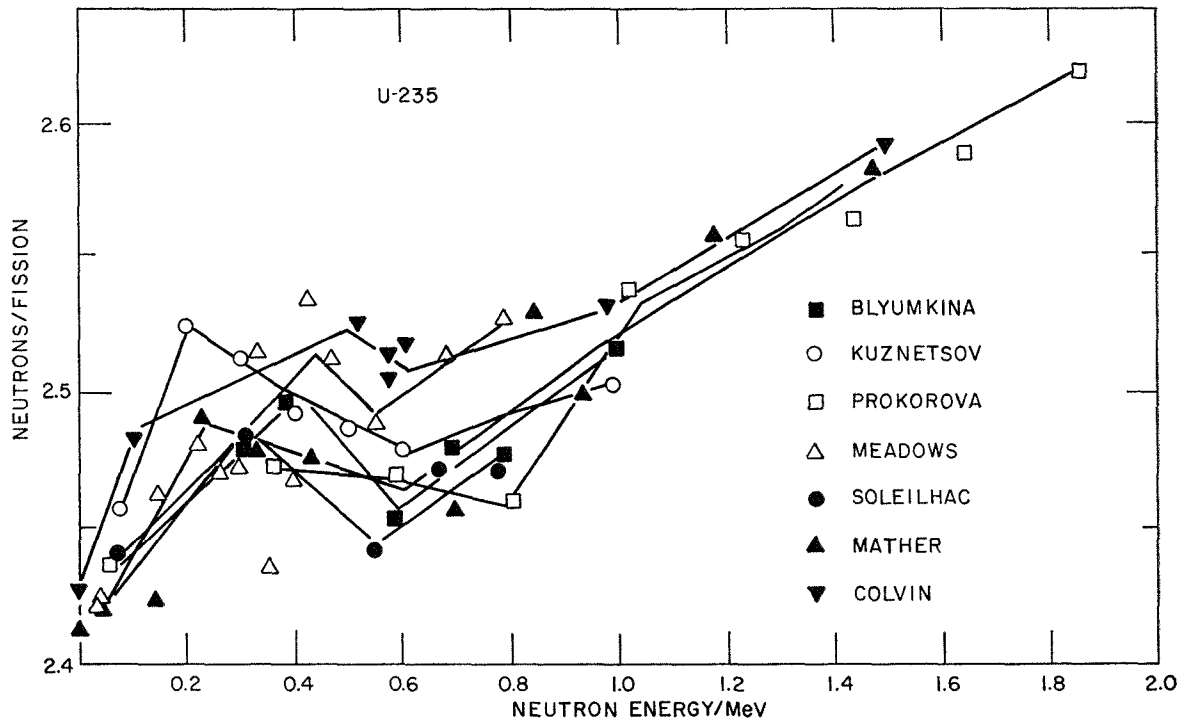

FIG. I-14-10. The Energy Dependence of $\bar{\nu}$(U-235). *ANL Neg. No. 116-104.*

used to derive the U-235 fission cross sections in Fig. I-14-9 are well supported or are based on measurements relative to the $H(n,n)$ cross section.

Fission Properties

In previous compilations the energy dependence of $\bar{\nu}(E)$ has usually been considered linear. In Fig. I-14-10 $\bar{\nu}(E)$ measurements by a number of experimenters are shown. These are normalized values discussed by Fillmore[64] in a recent review. Straight lines have been drawn between several points of each experimenter. This procedure may be very rough, but it clearly demonstrates the need for a very different approach to the energy dependence of $\bar{\nu}$. It is remarkable that the deviation from a linear dependence of $\bar{\nu}$, as established by measurements at higher energy, is about 2–3% in the region around 400 keV. It is surprising that the observed nonlinearity has apparently never been taken into account in data compilations, although the effect is well known and has been discussed in the field of fission physics for nearly 10 years. Values of $\bar{\nu}(E)$ in nuclear data sets like the ENDF(B) data file are clearly underestimated in this region which contributes appreciably to the neutronics of fast reactors. This underevaluation of $\bar{\nu}$ in the energy region around 400 keV is independent of the problem of absolute $\bar{\nu}$ values of Cf-252 for which two different groups of values are available and which disagree by more than their error bars.

Conclusions

In consideration of discrepancies up to a factor of two in some nuclear data, tremendous improvements have been achieved in the last ten years. This was essentially possible because of the introduction of new experimental methods and techniques. Unfortunately, discrepancies still exist for different magnitudes of uncertainties.

References

1. R. H. Tabony, Dissertation, Duke University (1966).
2. S. Cierjacks, P. Forti, D. Kopsch, L. Kropp, J. Nebe and H. Unseld, *High Resolution Total Neutron Cross Sections between 0.5–30 MeV*, KFK-1000 (1968).
3. M. Divadeenam, *Strength Functions and the Optical Model*, Dissertation, Duke University (1969).
4. R. L. Henkel, L. Cranberg, G. A. Jarvis, R. Nobles and J. E. Perry, Jr., *Total Neutron Cross Section for Uranium from 20 keV to 20 MeV*, Phys. Rev. **94**, 141 (1954).
5. H. H. Barshall, *The Total Neutron Cross Section of Normal Uranium in the Energy Range 20–1600 keV*, LA-1060 (1950).
6. R. E. Meads, AERE-NP/R-1643 (1955).
7. C. A. Uttley, C. M. Newstead and K. M. Diment, *Neutron Strength Function Measurements in the Medium and Heavy Nuclei*, Proc. IAEA Conference on Nuclear Data, Paris, 1966, CN-23/36.
8. J. F. Whalen, Argonne National Laboratory (private communication).
9. C. T. Hibdon and A. S. Langsdorf, Argonne National Laboratory (private communication to Brookhaven Sigma Center, 1953).

10. A. B. Smith, Argonne National Laboratory (private communication).
11. E. Barnard, A. T. G. Ferguson, W. R. McMurray and I. J. Van Heerden, *Scattering of Fast Neutrons by U-238*, Nucl. Phys. **80,** 46 (1966).
12. W. P. Poenitz, Argonne National Laboratory (to be published).
13. A. B. Smith, Argonne National Laboratory (private communication).
14. J. J. Schmidt, *Neutron Cross Sections for Fast Reactor Materials*, KFK-120 (1966).
15. R. O. Lane, A. S. Langsdorf, Jr., J. E. Monahan and A. J. Elwyn, *The Angular Distributions of Neutrons Scattered from Various Nuclei*, Ann. Phys. **12,** 135 (1961).
16. A. Langsdorf, Jr., R. O. Lane and J. E. Monahan, *Angular Distribution of Scattered Neutrons*, Phys. Rev. **107,** 1077 (1957).
17. J. L. Leroy, F. C. Berthelot and E. Pomelas, *Determination of the Total Cross Sections of Sodium, Thorium, and Uranium for Neutrons with Energies of 2–10 MeV*, J. de Physique **24,** 826 (1963).
18. G. A. Linenberger, J. Miskel and E. Segre, *Capture Cross Section of U-238 for Neutrons of Various Energies*, LA-179 (1944).
19. G. de Saussure and L. W. Weston, *The Measurement of α as a Function of Energy*, ORNL-3360, 51 (1963).
20. B. C. Diven, Y. Terrell and A. Hemmendinger, *Radiative Capture Cross Section for Fast Neutrons*, Phys. Rev. **120,** 556 (1960).
21. Y. F. Barry, Y. Brunce and P. H. White, *Cross Section for the Reaction $U^{238}(n,\gamma)U^{239}$ in the Energy Range 0.12–7.6 MeV*, J. Nucl. Energy A/B **18,** 481 (1964).
22. P. H. White, *Measurements of the U-235 Neutron Fission Cross Section in the Energy Range 0.04–14 MeV*, J. Nucl. Energy A/B **19,** 325 (1965).
23. W. P. Poenitz, *Measurements of the Ratios of Capture and Fission Neutron Cross Sections of U-235, U-238 and Pu-239 at 130 to 1400 keV*, Nucl. Sci. Eng. **40,** 383 (1970).
24. M. G. Schomberg, M. G. Sowerby and F. W. Evans, *A New Method of Measuring Alpha(E) for Pu-239*, Proc. IAEA Conference on Fast Reactor Physics, Karlsruhe, 1967, SM-101/41.
25. R. Gwin et al., *Measurements of the Neutron Fission and Absorption Cross Sections of Pu-239 over the Energy Region 0.02 eV to 30 keV*, Nucl. Sci. Eng. **40,** 306 (1970).
26. M. G. Schomberg, M. G. Sowerby, D. A. Boyce, K. J. Murray and Miss D. L. Sutton, *The Ratio of the Capture and Fission Cross Sections of Pu-239 in the Energy Range 100 eV to 30 keV*, Proc. IAEA Conference on Nuclear Data for Reactors, Helsinki, 1970, CN-26/33.
27. J. C. Hopkins and B. C. Diven, *Neutron Capture to Fission Ratios in U-233, U-235, Pu-239*, Nucl. Sci. Eng. **12,** 169 (1962).
28. G. de Saussure, L. W. Weston, R. Gwin, R. W. Ingle and J. H. Todd, *Measurement of the Neutron Capture and Fission Cross Sections and of Their Ratio Alpha for U-233, U-235 and Pu-239*, Proc. IAEA Conference on Nuclear Data for Reactors, Paris, 1966.
29. Yu. B. Ryabov et al., *Measurement of the Ratio of the Radioactive Capture to Fission Cross Sections (α) for Plutonium-239 in the Neutron Energy Region 0.1–30 keV*, Proc. IAEA Conference on Nuclear Data for Reactors, Helsinki, 1970, CN-26/89.
30. J. B. Czirr, *A Measurement of Pu-239 Capture and Fission Cross Sections*, Trans. Am. Nucl. Soc. **12,** 261 (1969).
31. P. H. White, Y. G. Hodgkinson and G. Y. Wall, *Measurements of Fission Cross Sections for Neutrons of Energies in the Range 40–500 keV*, Proc. IAEA Symposium on the Physics and Chemistry of Fission, Salzburg, March 22–26, 1965, Vol. I, 219 (1965), SM-60/14.
32. W. D. Allen and A. T. G. Ferguson, *The Fission Cross Sections of U-233, U-235, U-238 and Pu-239 for Neutrons in the Energy Range 0.030–3.0 MeV*, Proc. Phys. Soc. **A70,** 573 (1957).
33. P. H. White and G. P. Warner, *The Fission Cross Sections of U-233, U-235, U-238, Np-237, Pu-239, Pu-240 and Pu-241 Relative to that of U-235 for Neutrons in the Energy Range 1–14 keV*, J. Nucl. Energy **21,** 671 (1967).
34. V. G. Nesterov and G. N. Smirenkin, *Ratios of Fast Neutron Fission Cross Sections of ^{233}U, ^{235}U and ^{239}Pu*, Atomnaya Energiya **24,** 185 (1968).
35. R. W. Lamphere, *Fission Cross Sections of Uranium Isotopes 233, 235, 236, and 238 for Fast Neutrons*, Phys. Rev. **104,** 1654 (1956).
36. L. Pfletschinger and F. Kaeppeler, *A Measurement of the Fission Cross Sections of Pu-239 and U-233 Relative to U-235*, Nucl. Sci. Eng. **40,** 375 (1970).
37. W. K. Lehto, *Fission Cross Section Ratio Measurements of Pu-239 and U-233 to U-235 from 0.24 to 24 keV*, Nucl. Sci. Eng. **39,** 361 (1970).
38. J. W. Meadows, Argonne National Laboratory (private communication).
39. J. L. Perkin, P. H. White, P. Fieldhouse, E. J. Axton, P. Cross and J. C. Robertson, *The Fission Cross Sections of U-233, U-234, U-235, U-236, Np-237, Pu-239, Pu-240 and Pu-241 for 24 keV Neutrons*, J. Nucl. Energy **18,** 423 (1965).
40. G. N. Smirenkin, V. G. Nesterov and I. I. Bondarenko, *U-233, U-235 and Pu-239 Fission Cross Sections for 0.3–2.5 MeV Neutrons*, Atomnaya Energiya **13,** 366 (1962).
41. I. Szabo, J. P. Marquette, E. Fort and J. L. Leroy, *Mesure Absolue de la Section Efficace de Fission*, Proc. IAEA Conference on Nuclear Data for Reactors, Helsinki, 1970, CN-26/69.
42. W. E. Stein, R. K. Smith and H. L. Smith, *Relative Fission Cross Section of U-236, U-238, Np-237 and U-235*, Second Conference on Neutron Cross Sections and Technology, Washington, D. C., 1968, NBS Special Publication **299,** 627 (1968).
43. S. P. Kalinin and V. N. Ponkratov, *Neutron Induced Fission Cross Sections of Th-232 and U-238 in the Energy Range 3–11 MeV*, Proc. 1958 Geneva Conference **16,** Paper No. 2149, p. 136.
44. G. Hansen, S. McGuire and R. K. Smith, *U-235 and U-238(n,f) Cross Sections*, Nucl. Sci. Eng. (to be published).
45. R. L. Macklin, N. H. Lazar and W. S. Lyon, *Neutron Activation Cross Sections with Sb-Be Neutrons*, Phys. Rev. **107,** 504 (1957).
46. W. S. Lyon and R. L. Macklin, *Neutron Activation at 195 keV*, Phys. Rev. **114,** 1619 (1959).
47. R. C. Hanna and B. Rose, *Fast Neutron Capture in U-238 and Th-232*, J. Nucl. Energy **8,** 197 (1959).
48. H. O. Menlove and W. P. Poenitz, *Absolute Radiative Capture Cross Section for Fast Neutrons in U-238*, Nucl. Sci. Eng. **33,** 24 (1968).
49. V. A. Tolstikov, L. E. Sherman and Yu. Ya. Stavisskii, *A Measurement of the Capture Cross Section of U-238 and Th-232 for 5–100 keV Neutrons*, J. Nucl. Energy **18,** 599 (1964).

50. T. S. Belanova, A. A. Vankov, F. F. Mikhailus and Yu. Ya. Stavisskii, *Absolute Measurements of the Absorption Cross Sections of 24 keV Neutrons*, J. Nucl. Energy **20**, 411 (1966).
51. L. B. Miller and W. P. Poenitz, *Monte Carlo Interpretation of a U-238 Spherical Shell Transmission Experiment of 23 keV*, Nucl. Sci. Eng. **35**, 295 (1969).
52. M. C. Moxon, Atomic Energy Research Establishment (private communication).
53. C. D. Bowman, M. L. Stelts and R. T. Baglan, *The keV Fission Cross Section of U-235 measured with High Resolution*, Proc. IAEA Conference on Nuclear Data for Reactors, Helsinki, 1970, CN-26/41.
54. G. A. Dorofeev and Y. P. Dobrynin, *Effective Fission Cross Sections of U-233, U-235, Pu-239 and Pu-240 in the Neutron Energy Range 30 keV–5 MeV*, J. Nucl. Energy **5**, 217 (1957).
55. G. F. Knoll and W. P. Poenitz, *A Measurement of the U-235 Fission Cross Section at 30 keV and 64 keV*, J. Nucl. Energy **1**, 643 (1967).
56. W. P. Poenitz, *Measurement of the U-235 Fission Cross Section in the keV Energy Range*, Proc. Second Conference on Neutron Cross Sections and Technology, Washington, D. C., 1968, NBS Special Publication **299**, Vol. I, p. 503, Conf. 680307.
57. J. F. Barry, *Cross Section for the Reaction Li-6$(n,\alpha)T$*, Proc. Conference on Neutron Cross Sections and Technology, Washington, D. C., March 22–24, 1966, Conf. 660303.
58. S. J. Bame and R. L. Cubitt, *$Li^6(n,t)He^4$ Reaction at Intermediate Energies*, Phys. Rev. **114**, 1580 (1959).
59. S. Schwarz, L. G. Stroemberg and A. Bergstroem, *A Relative Measurement of the $Li^6(n,\alpha)$ Reaction Cross Section in the Range $1 < E_n < 600$ keV*, Nucl. Phys. **63**, 593 (1955).
60. M. C. Sowerby et al., *A Measurement of the Ratio of the $Li^6(n,\alpha)$ and $B^{10}(n,\alpha)$ Cross Sections from 10 eV to 80 keV and Recommended Values of the Cross Sections Up to 200 keV*, Proc. IAEA Conference on Nuclear Data for Reactors, Helsinki, 1970, CN-26/26. (Data of C. A. Uttley).
61. H. Condé, S. Schwartz and N. Starfelt, *A Method for the Absolute Measurement of Fast Neutron Flux with a Large Liquid Scintillator*, Arkiv Fysik **29**, 45 (1965).
62. B. C. Diven, *Fission Cross Section of U-235 for Fast Neutrons*, Phys. Rev. 105, 1350 (1957).
63. G. V. Gorlov, B. M. Goshberg, V. M. Morozov, G. A. Ostroshehenko and V. A. Shigin, *The Fission Cross-Sections of U-233 and U-235 for Neutrons Having Energies between 3 and 800 keV*, J. Nucl. Energy **12**, 79 (1960).
64. F. L. Fillmore, *Recommended Values for the Number of Neutrons per Fission*, J. Nucl. Energy **22**, 79 (1967).

I-15. Spin Determination of Resonances in $Ho^{165}(n,\gamma)$ from Low Level Occupation Probability Ratios

W. P. Poenitz and J. R. Tatarczuk*

The determination of spins, J, of neutron resonances is of considerable interest in the field of neutron spectroscopy. The knowledge of J is necessary for the determination of the spin dependence of the nuclear level density, of the neutron strength functions, and for the paramaterization of the observed resonances. Considerable effort has been devoted to the investigation of techniques based on certain features of the γ-rays emitted in the de-excitation of the resonance state. Two methods based on the statistical behavior of γ-cascades which occur in the de-excitation of a compound state have been discussed recently.[1-4] The method of interest here makes use of the compound state spin sensitivity to the occupation probabilities of low lying levels known from the investigation of isomeric cross section ratios.[1,2,5-7] The dependence of such ratios on the spin of the initial compound states has beeen quantitatively analyzed by Vandenbosch and Huizenga[1] and by Poenitz.[2] Draper et al.[8] have related the differences of the intensities of the low energy γ-spectra observed in different resonances of indium to the same mechanism which determines the formation of the isomeric cross section ratios. Later Keisch[9] attempted to assign spins of negative energy resonances by observing the isomeric cross section ratio in the thermal and subthermal energy range. The measurement of prompt γ-transitions from low lying levels, as done by Draper et al.[8] and with a high resolution spectrometer by Schult et al.,[10] extends this method for determining spins of resonances in the (n,γ) processes to the majority of medium and heavy weight nuclei. In connection with the present experiment a Ge(Li)-detector was used in time-of-flight measurements at the Rensselaer electron-linear accelerator to determine spins of resonances in the reaction $Ho^{165}(n,\gamma)Ho^{166}$.

* Rensselaer Polytechnic Institute, Troy, New York.

Cascade Statistics and Low Level Occupation Probability Ratios

A γ-cascade model has been described previously[2] which combines and extends the different approach of Huizenga and Vandenbosch[1] and of Troubetzkoy. In this model the level scheme of a nucleus is presented in a "continuum" range described by the level density $\rho(J_i, \pi_i, E_i)$, $i = 1, 2 \cdots$, where J is the spin of a level,

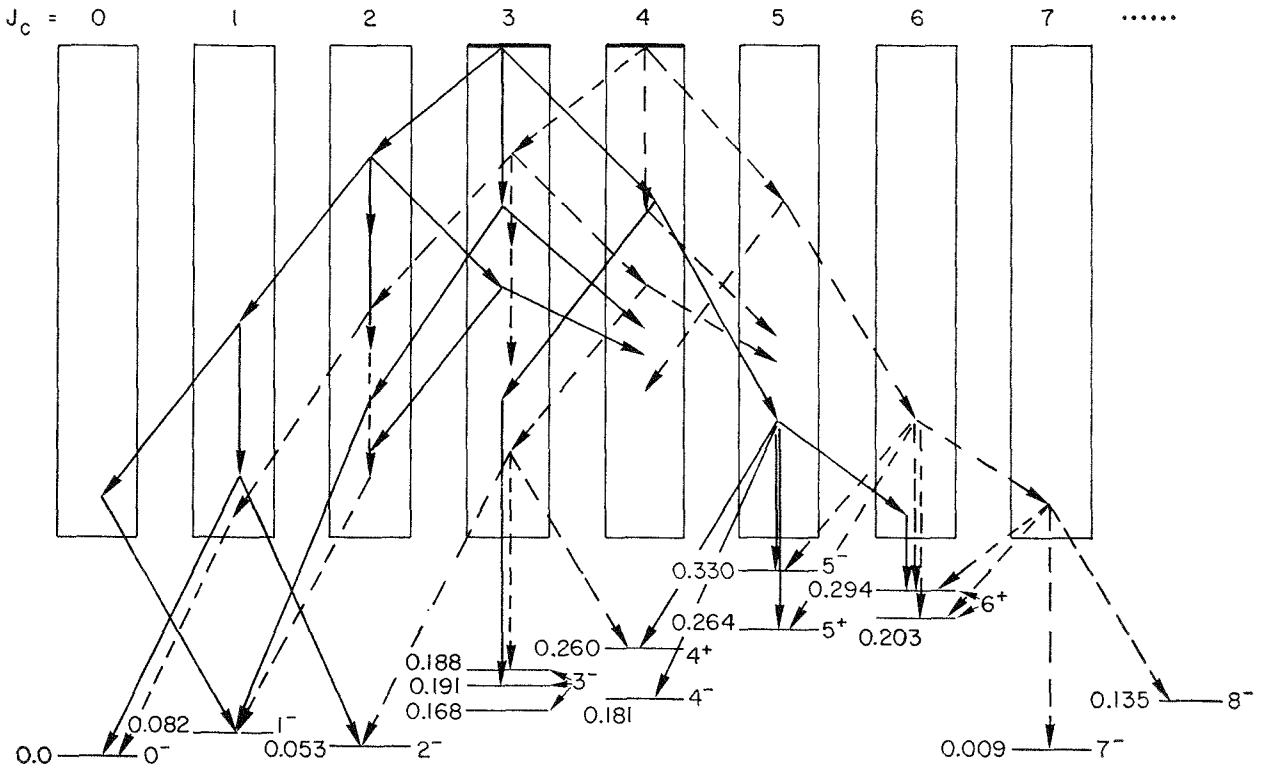

FIG. I-15-1. Schematic of the Level Scheme and Behavior of γ-Cascades for Ho-166. *ANL Neg. No. 113-3179.*

π the parity of this state, and E is the energy. The de-excitation of the compound states are assumed to take place by dipole or quadrupole transitions to the low lying levels or, more probably, to states in the "continuum" range. In the first step, levels with spins differing by zero, one, or two from the spin of the initial compound state can be occupied. Subsequent de-excitations spread out these transition cascades in the E-J-π space. Toward the lower energy part of the level-scheme transitions take place most probably with the smallest difference in spins to the low lying levels.

Figure I-15-1 shows the level scheme of Ho-166 in terms of the above described model. Parts of two cascades are shown starting from initial compound states with spins 3 and 4. This figure qualitatively shows that a higher occupation probability of low lying levels with spins larger than 4 is expected for an initial compound state with spin 4 than for 3. The occupation probability for levels with spins smaller than 3 is expected to be larger for the initial spin value 3 than for 4.

Many data are available for the level scheme of Ho-166 and have been collected by Groshev et al.[12] The 14 lowest levels have been used in calculations using the computer program CASCADE.[2] Table I-15-I shows the occupation probabilities T_i of these levels for the two spins, $J = 3$ and 4 of the initial state (which can be reached by s-wave capture), for the γ-cascade multiplicities $\nu = 1$, and $\nu = \infty$. In the same table the γ-intensities, I_γ^{12}, are given for high energy transitions to these states for thermal neutron capture. The latter values are comparable to the occupation probabilities

TABLE I-15-I. RESULTS FOR THE LOW LEVEL OCCUPATION PROBABILITIES USING CASCADE
(a = 18.4 MeV^{-1}, σ = 6.5, q = 0.05)

E_i, MeV	J_i	π_i	$I_\gamma/10^{-4}$[a]	$T_i/10^{-4}$	$T_i/10^{-4}$	T_i	T_i
			$\nu = 1$, therm.	$J = 3$, $\nu = 1$	$J = 4$, $\nu = 1$	$J = 3$, $\nu = \infty$	$J = 4$, $\nu = \infty$
0.000	0	−		—	—	0.039	0.016
0.009	7	−		—	—	0.028	0.074
0.053	2	−		1.5	0.1	0.153	0.099
0.082	1	−		0.1	—	0.079	0.041
0.135	8	−	2	—	—	0.004	0.013
0.168	3	−	5.1	1.5	1.3	0.109	0.092
0.181	4	−		1.4	1.3	0.121	0.134
0.191	3	−	25.	1.4	1.3	0.096	0.081
0.198	3	−	4.1	1.4	1.3	0.092	0.068
0.260	4	+		2.4	2.1	0.116	0.121
0.264	5	+	11.	2.3	2.1	0.072	0.095
0.283	6	+	3.	—	2.0	0.028	0.054
0.294	6	+	1.	—	2.0	0.026	0.050
0.330	5	−	1.5	0.1	1.2	0.037	0.054

[a] Gamma intensity per capture event.

with the multiplicity $\nu = 1$. The ratio of the occupation probabilities with $\nu = \infty$ of the 0.330 MeV-5^- and the 0.168 MeV-3^- levels is 0.34 for the resonance spin 3 and 0.58 for the resonance spin 4. All parameters of the model have been used as described previously,[2] the level density parameters a and σ having been adjusted to obtain the level density in the eV energy range as observed in total cross section measurements and compiled in BNL-325.[13] The expected behavior of the low level occupation probability ratio as a function of energy has been discussed in Ref. 14. In the present experiment, the measured data have been integrated over single resonances to improve counting statistics.

Measurements and Results

The low level occupation probability was measured by observing γ-rays de-exciting the considered levels. This was done by detecting the low energy part of the capture γ-ray spectra using a Ge(Li)-detector in a time-of-flight experiment with a pulsed neutron source. The time-of-flight spectra of the 115 and 149 keV photopeaks and three appropriate background regions were recorded instead of setting windows on neutron resonances and recording the γ-spectra. This approach had the advantage of better background subtraction for small resonances occurring between large resonances. In addition, the background due to the isomeric state was properly subtracted.

The 116 keV γ-ray de-excites the 3^- level at 168 keV and the 149 keV γ-ray de-excites the 5^- level at 330 keV.[12] Their branching ratios are 98.5 percent and 98.0 percent, respectively.[12]

The Linac was operated at 540 pulses per second with a pulse width of 100 nsec producing an average current of 100 μamp at a beam energy of 60 MeV. The experimental arrangement is shown in Fig. I-15-2. Neutrons were produced in a water cooled tantalum target that was shielded so as to be out of the line-of-sight of the detector stations. A 2.5 cm thick polyethylene moderator scattered the neutrons in the direction of the sample. A cadmium overlap filter was used before the large shielding wall to remove thermal neutrons. The detector was a 25 cm^3 lithium drifted germanium crystal positioned at 90 deg relative to the neutron beam at a flight path of 12.65 m. The holmium sample was positioned in front of the crystal at an angle of 45 deg relative to the neutron beam direction. A 10 cm thick lead shield lined with 4 cm of lithium carbonate enclosed the detector and sample. The crystal was also shielded by 2.5 cm of lithium loaded polyethylene to reduce background in the crystal due to neutrons scattered from the sample.

The measured intensity of a γ-photopeak is given by

$$C_{\gamma i} = \eta_{\gamma i} T_i a_i \alpha_i \int_0^d \exp(-\mu_i x) \cdot \int_{E_1}^{E_2} Q_\gamma(x, E)\, dE dx, \tag{1}$$

where η_γ is the photopeak efficiency for the observed γ-ray, T_i the occupation probability of the level from which this γ-ray is originated, a_i the branching ratio, α_i the conversion coefficient, μ_i the γ-ray attenuation coefficient, d the effective thickness of the sample, and E_1 and E_2 the integration limits for the neutron reso-

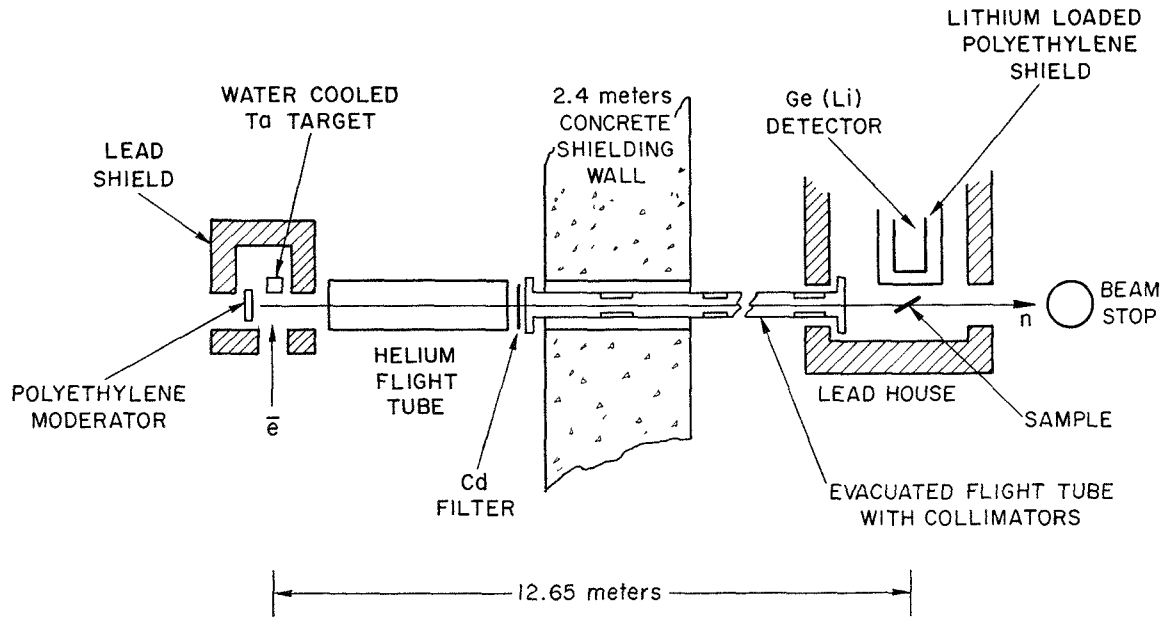

Fig. I-15-2. Schematic of the Experimental Arrangement. *ANL Neg. No. 116-10.*

nance. The capture rate at a neutron energy E and at the sample thickness x is given by

$$Q_\gamma(x, E) = \phi'(x)N\sigma_\gamma(E) + \frac{1}{2}\int_0^{\pi/2}\int_0^d \phi'(y)N\sigma_s(E)\exp\left[\frac{|x-y|N\sigma_t(E)}{\cos\theta}\right]dy \cdot\sigma_\gamma(E)N\frac{dx}{\cos\theta}d(\cos\theta).$$

The first term represents the contributions from the primary neutron flux $\phi(0)$ which, at a thickness z, is attenuated to

$$\phi'(z) = \phi(0)\exp(-zN\sigma_t(E)).$$

The second term represents contributions from scattered neutrons. The integration over the scattering angle θ leads to the exponential integral E_1. The neutron cross sections are given by

$$\sigma_\gamma(E) = \sigma_0\frac{\Gamma_\gamma}{\Gamma}\psi(\theta,\chi)$$

$$\sigma_s(E) = \sigma_0\frac{\Gamma_n}{\Gamma}\psi(\theta,\chi) + \sqrt{\sigma_0\sigma_p g_J\frac{\Gamma_n}{\Gamma}}X(\theta,\chi) + \sigma_p$$

$$\sigma_t(E) = \sigma_0\psi(\theta,\chi) + \sqrt{\sigma_0\sigma_p g_J\frac{\Gamma_n}{\Gamma}}X(\theta,\chi) + \sigma_p$$

where $\psi(\theta,\chi)$ and $X(\theta,\chi)$ are the Doppler broadened line shapes for absorption and scattering.

The ratio of the photopeak intensities integrated over a resonance is

$$\left[\frac{C_\gamma(149\text{ keV})}{C_\gamma(116\text{ keV})}\right]_{E_R} = \frac{\eta_\gamma(149\text{ keV})}{\eta_\gamma(116\text{ keV})}\cdot\frac{a(149\text{ keV})}{a(116\text{ keV})}\cdot\frac{\alpha(149\text{ keV})}{\alpha(116\text{ keV})}\cdot kR(J; 168\text{ keV}, 3^-; 330\text{ keV}, 5^-).$$

R is the occupation probability ratio of the levels at 168 and 330 keV. The correction k for γ-ray attenuation is given by the appropriate ratio of the integrals given in Eq. (1). Values for k have been evaluated using appropriate parameters as given in BNL-325.[13] Values for the branching ratio as given by Groshev et al.[12] have been used. The photopeak efficiencies of the present system have been determined using recent calculations and measurements by Aubin et al.[15] Values for the internal electron conversion coefficients have been obtained from the tables given by Sliv and Band.[16] The corrections for the branching ratios, the internal conversion, and the detector efficiencies influence only the absolute values of the ratios for the different resonances, but they do not change the relative ratios from resonance to resonance. Therefore, the determination of values for the compound state spins is not influenced by errors in these corrections but only the comparison with values calculated with CASCADE.

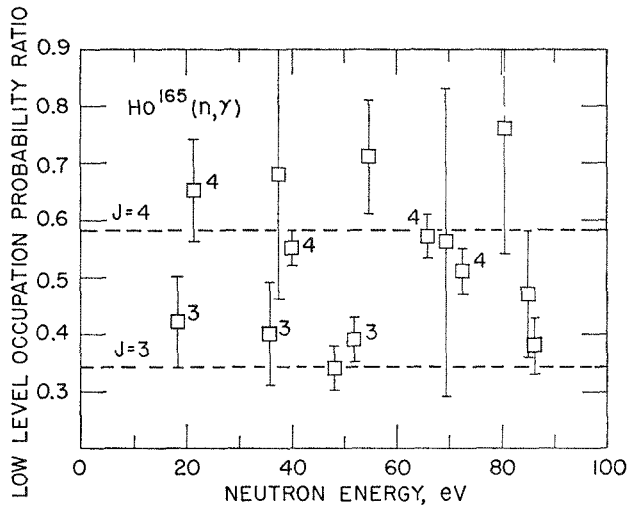

FIG. I-15-3. Comparison of Experimental Results of the Low Level Occupation Probability Ratio with Theoretical Values. The Spin Values Shown in the Figure are Recommended in BNL-325.[19] *ANL Neg. No. 113-3178.*

The final results are shown in Fig. I-15-3. The theoretical ratios for the two different spins evaluated from Table I-15-I are shown in the figures as dashed lines. The error bars represent the statistical uncertainties only and do not include the errors of the corrections discussed above. The spin values shown in the figure are recommended values from BNL-325.[13] The spins assigned according to Fig. I-15-3 are listed in Table

TABLE I-15-II. EXPERIMENTAL RESULTS FOR THE LOW LEVEL OCCUPATION PROBABILITY RATIOS AND ASSIGNED SPIN VALUES

E_R, eV	R	ΔR	Spin				
			Present	Alfimenkov[17]	Asghar[18]	Brunhart[19]	BNL-325[13] recom.
18.3	0.42	0.08	3	3	(3, 4)	3	3
21.2	0.65	0.09	4	4	(3, 4)	3	4
35.6	0.40	0.09	3	3	3		3
37.4	0.68	0.27	4	3	(3, 4)		
39.8	0.55	0.03	4	4	4		4
48.0	0.34	0.04	3	3	4		
51.7	0.39	0.04	3	3	3		3
54.5	0.71	0.10	4	3	(3, 4)		
65.5	0.57	0.04	4		4		4
69.1	0.56	0.27	(4)		(3, 4)		
72.2	0.51	0.04	4		(3, 4)		
80.3	0.76	0.22	4		(3, 4)		
84.3[a]	0.47	0.11	(3)		(4)		
84.7[a]			—		(3, 4)		
86.0	0.38	0.05	3				

[a] See Ref. 13.

I-15-II. The value for the resonance at 84.3 eV contains a contribution from a smaller resonance at 84.7 eV[13], which has not been resolved in the present measurements.

References

1. J. R. Huizenga and R. Vandenbosch, *Interpretation of Isomeric Cross Section Ratios for (n,γ) and (γ,n) Reactions*, Phys. Rev. **120**, 1305 (1960).
2. W. P. Poenitz, *A Gamma-Ray Cascade Model for the Calculation of Average γ-Ray Multiplicities and Isomeric Cross Section Ratios*, Z. Physik **197**, 275 (1966).
3. C. Coceva, F. Corvi, P. Giacoble and G. Carraro, *A Method of Spin Assignment of Neutron Resonances Based on Capture Gamma-Ray Detection*, Nucl. Phys. **A117**, 586 (1968).
4. W. P. Poenitz, *Low Level Occupation Probability Ratios in the (n,γ) Processes*, Bull. Am. Phys. Soc. II, **13** BG2, 1389 (1968).
5. L. Katz, L. Pease and H. Moody, *The Photoneutron Cross Sections for the Reactions $Br^{81}(\gamma,n)$ Br^{80} and $Br^{81}(\gamma,n)$ Br^{80m} and an Analysis of the Ratios Between these Cross Sections*, Can. J. Phys. **30**, 476 (1952).
6. J. W. Meadows, R. M. Diamond and R. A. Sharp, *Excitation Functions and Yield Ratios for the Isomeric Pairs $Br^{80,80m}$, $Co^{58,58m}$ and $Sc^{44,44m}$ Formed in (p,p,n) Reactions*, Phys. Rev. **102**, 190 (1956).
7. R. Vandenbosch and J. R. Huizenga, *Isomeric Cross Section Ratios for Producing the Isomeric Pair Hg-197,197m*, Phys. Rev. **120**, 1313 (1960).
8. J. E. Draper, C. A. Fenstermacher and H. L. Schultz, *Variation in Spectra of Resonance Neutron Capture Gamma Rays in Indium*, Phys. Rev. **111**, 906 (1958).
9. B. Keisch, *Yield Ratios of Isomers Produced by Neutron Activation*, Phys. Rev. **129**, 769 (1963); also, see cited references.
10. O. W. B. Schult, P. B. K. Maier and U. Gruber, *Gammaübergänge und Energieniveaus in Dy-165*, Z. Physik **182**, 171 (1964).
11. E. S. Troubetzkoy, *Statistical Theory of Gamma-Ray Spectra Following Nuclear Reactions*, Phys. Rev. **122**, 212 (1961).
12. L. V. Groshev, A. M. Demidov, V. L. Pelekov, L. L. Sokolovskii, G. A. Bartholomew, A. Doveika, K. M. Eastwood and S. Monaro, *Compendium of Thermal-Neutron-Capture γ-Ray Measurements*, Nucl. Data, Sec. A, 5, No. 1–2, 217 (1968).
13. J. Stehn et al., *Neutron Cross Sections*, BNL-325, 2nd Ed., Suppl. 2 (1956).
14. W. P. Poenitz, *Statistical Behavior of Gamma Ray Cascades*, Reactor Physics Division Annual Report, July 1, 1968 to June 30, 1969, ANL-7610, pp. 58–59.
15. G. Aubin, J. Barrette, G. Lamoureux and S. Monaro, *Calculated Relative Efficiency for Coaxial and Planar Ge(Li) Detectors*, Nucl. Instr. Methods **76**, 85 (1969).
16. L. A. Sliv and I. M. Band, *Tables of Internal Conversion Coefficients*, K. Siegbahn, Ed., (North-Holland Publishing Company 1965), p. 1639.
17. J. Stehn et al., *Neutron Cross Sections*, BNL-325, 2nd Ed., Suppl. 2 (1956).
18. M. Asghar, M. C. Moxon and C. M. Chaffey, *The Low Energy Neutron Resonance Parameters of $^{107,109}Ag$, ^{169}Tm, ^{197}Au, ^{159}Tb and ^{165}Ho*, Proc. of the Conference on the Study of Nuclear Structure with Neutrons, Amsterdam, 1965, (North Holland Publishing Company, Amsterdam), Paper 65.
19. G. Brunhart, H. Postma and V. L. Sailor, *Determination of Spins of Neutron Resonances and the Hyperfine Coupling Constant in Ho^{165}*, Phys. Rev. **137**, B1484 (1965).

I-16. Statistical Distribution of Nuclear Shell Model Matrix Elements

K. Takeuchi and P. A. Moldauer

The statistical theory of spectra assumes that the distribution of off-diagonal shell model matrix elements is symmetric about zero. Furthermore, discussions of the distributions of partial reaction widths are based on arguments which imply that the distribution of off-diagonal shell model matrix elements is Gaussian.

In the course of carrying out R-matrix shell model calculations, some 20 shell model submatrices with different sets of spin, parity, and isospin quantum numbers were evaluated for a system of two particles and a core. The numbers of independent off-diagonal elements in these matrices ranged from 45 to 1128, with the majority exceeeding 500.

The distributions of these matrix elements were analyzed. It was found that symmetry about zero is very well satisfied in all cases. However in most cases the Gaussian distribution could be excluded.

I-17. *R*-Matrix Shell-Model Calculations of Scattering and Reaction Cross Sections[1]

K. Takeuchi and P. A. Moldauer

The Wigner-Eisenbud R-matrix theory has been applied to the calculation of neutron total and inelastic scattering cross sections for a system consisting of two neutrons interacting with an inert O-16 core through a spherically symmetric Wood-Saxon potential and interacting with each other through a δ-function force. The calculational method employed has the advantages that it includes the effects of shell model configurations in which both neutrons are unbound, that it presents no obstacles to inelastic or reaction calculations, that it permits antisymmetrization of the compound space wave functions, and that it requires only one shell model diagonalization for the computation of cross sections up to 5 MeV neutron energy.

Particular emphasis was placed upon the development and critical evaluation of the calculational method. Thus it was shown that the use of antisymmetrized wave functions reduced substantially the number of compound nucleus resonances and also the magnitude of the inelastic cross section. These effects are demonstrated in Figs I-17-1 and I-17-2. The frequently mentioned difficulty of a channel radius dependence of R-matrix cross sections was removed by a simple and practical scheme for the evaluation of the distant resonance contribution to the R-matrix. Generalizations of the method to more complex systems and to the inclusion of direct reaction effects were also included in this study.

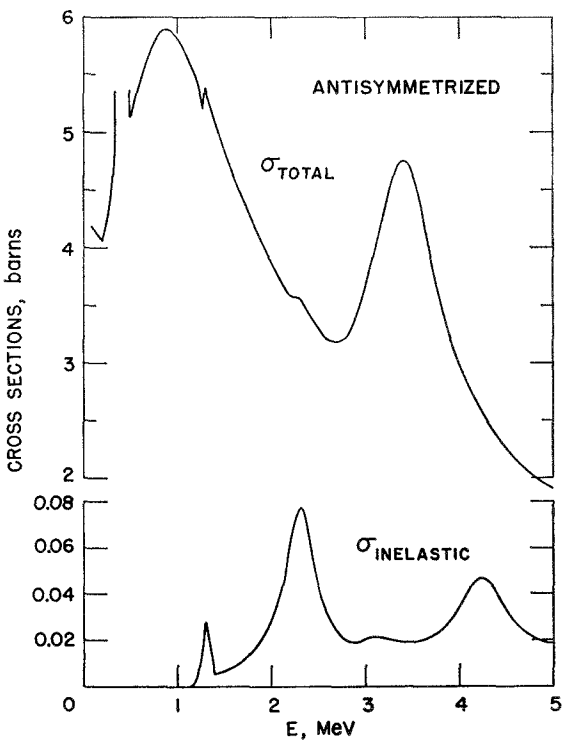

Fig. I-17-1. Total and Inelastic Scattering Cross Sections for Neutrons Scattered by O-17, Calculated with Antisymmetrized Wave Functions. *ANL Neg. No. 116-17.*

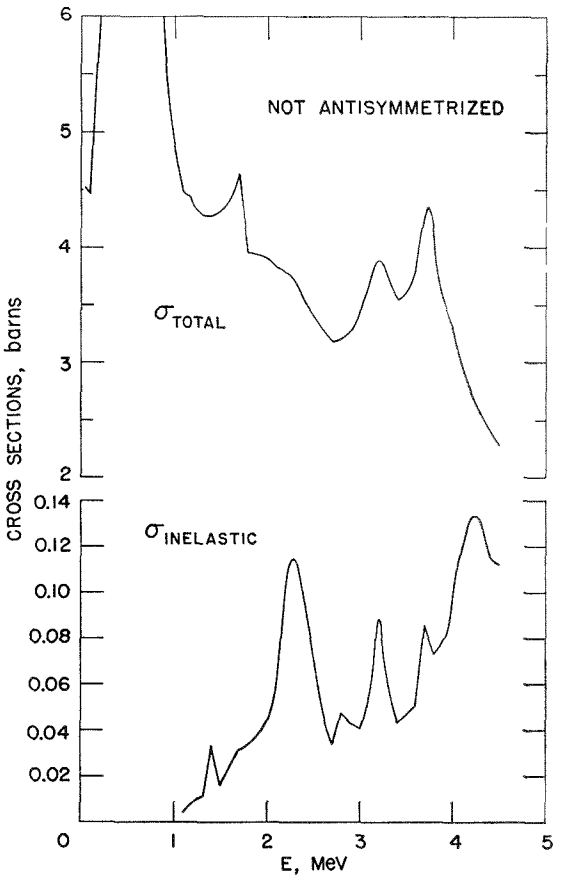

Fig. I-17-2. Total and Inelastic Scattering Cross Sections for Neutrons Scattered by O-17, Calculated without Antisymmetrization. *ANL Neg. No. 116-16.*

Reference

1. K. Takeuchi and P. A. Moldauer, *R-Matrix Shell-Model Calculations of Scattering and Reaction Cross Sections*, Phys. Rev. **C2**, 925 (1970).

I-18. Developments Relating to the ENDF/B Project

E. M. Pennington and J. P. Regis

The ENDF/B system of neutron cross section data and associated processing codes is used at Argonne to produce library data for both the CDC-3600 and IBM 360 ARC system versions of the multigroup cross section code MC² [1]. Summaries of earlier work on codes, data processing, and cross section compilation have been presented in previous annual reports.[2-6] More recent work is described here.

ENDF/B Data Compilations

Preparation of a revised version of ENDF/B data, to be referenced as Version II, was started in the summer of 1969 and released in the spring and summer of 1970. The preparation of this version involved many people at various laboratories throughout the country. The Argonne contribution consisted of a revision of the earlier ENDF/B molybdenum cross sections[2,7] and the preparation of unresolved resonance parameters for U-235 and Pu-241.

MOLYBDENUM

The original ENDF/B molybdenum has a capture cross section which is too high, especially in the range from about 1 to 20 keV. This leads to high values of calculated central worths for fast assemblies. Thus recent experimental capture cross section data were examined in detail. New resolved parameters were provided for the energy range below one keV, based on measurements of several experimenters. Unresolved parameters with some smooth background were supplied for the range from 1 to 100 keV to replace the original data, which were entirely smooth. Thus self-shielding and Doppler calculations can be carried out over the resonance range. The unresolved parameters were based on Ref. 8. The background capture cross section, which is to be combined with that calculated from unresolved resonance parameters, was chosen to produce recommended cross sections in the 1–100 keV range. These recommended cross sections were based on a large selection of experimental data summarized in Refs. 9–11, and evaluated curves by Schmidt[9,12] and Poenitz.[10] Above 100 keV, the capture cross section was based on Refs. 9, 10 and 12.

U-235 UNRESOLVED RESONANCE PARAMETERS

Unresolved resonance parameters for U-235 were derived by fitting capture and fission cross sections, generally averaged over quarter-lethargy intervals, over the energy range from 64.504 eV to 24.788 keV. FORTRAN program UR[5,6] was used for this purpose, with both neutron and fission widths for s-wave states being varied to fit the data. The trial parameters used in the fitting were chosen as described in Ref. 5. The data to be fitted were chosen by other members of the Cross Section Evaluation Working Group, and are based on the data of G. deSaussure et al[13] below 3 keV, an evaluation by Schmidt[14] from 3 to 15 keV, and an evaluation by Alter and Dunford[15] above 15 keV.

PU-241 UNRESOLVED RESONANCE PARAMETERS

Unresolved resonance parameters for Pu-241 were determined over the range from 49.5 eV to 52.4 keV. Petrel fission data,[16] averaged over half- or quarter-lethargy intervals by E. O. Ottewitte,[17] were fitted using program UR. The capture cross sections to be fitted were determined below 1 keV with some guidance from measured total cross sections[18] and considerations of plausible statistical variations. Above 1 keV the capture cross sections to be fitted were α times the corresponding fission cross sections, where α, the ratio of neutron capture-to-fission cross sections, was calculated from the trial resonance parameters without iteration. The trial resonance parameters were based on those in Ref. 19, except that two degrees of freedom rather than one were used for the fission width distributions and a capture width of 0.030 eV was used instead of 0.040 eV. This capture width was suggested by fitting the resolved resonance data below 49.5 eV.[20] The neutron and fission widths for the s-wave states were varied in program UR to fit the capture and fission data.

Since there are no capture cross section data available above the resolved resonance region, the capture cross sections calculated from the unresolved resonance parameters are highly uncertain. The fission cross sections should be much more reliable than the capture cross sections.

FORTRAN Codes

Version II ENDF/B data involves several changes of formats from those used with Version I. Thus all processing codes had to be modified to accept the new formats. New versions of the codes CHECKER[3] and DAMMET[3] were received from Brookhaven a made operational on both the CDC-3600 and IBM-3 computers. Since the new formats necessitated changes

the format of the MC^2 library in the unresolved resonance region, the code MERMC2[3] was revised to accommodate these changes. Extensive changes in ETOE[3] were required to handle the new formats. These changes are outlined in the section below.

The MAGIC code,[6] which plots selected data from an MC^2 library, was converted from the CDC-3600 to the IBM-360 system. Some differences in the versions for the two computers were necessitated by the differences in the binary plotting packages for the two systems. An Argonne topical report[22] was written which describes the CDC-3600 versions of both MAGIC and MERMC2.

REVISIONS IN ETØE FOR VERSION II ENDF/B DATA

Format changes[21] made for ENDF/B Version II data pertain to inelastic scattering, unresolved resonance parameters, minimum ENDF/B File 2 data for materials without resonance parameters, and fission spectra.

In the case of inelastic scattering, cross sections for scattering to various resolved levels and the continuum may now be given in File 3, with only the nuclear temperature for continuum scattering being given in File 5. Formerly the total inelastic cross section was given in File 3, and probabilities for scattering to individual levels and the continuum were given in File 5. Also new reaction type (MT) numbers for individual level and continuum scattering were introduced. ETØE can now treat inelastic scattering data presented in either the old or new formats.

Unresolved resonance parameters may now be given in a format in which all widths and level spacings are functions of energy. Originally only the fission widths could be energy-dependent. Changes were made in ETØE to handle this format, which necessitated changes in the format of the MC^2 library. Changes were also made to allow 50 energies per isotope in the unresolved region, 7 isotopes per material, and the treatment of unresolved parameters for $\ell = 2$.

For materials which have no ENDF/B resolved or unresolved resonance parameters, a scattering length, a, has been introduced into ENDF/B File 2. ETØE will now calculate the potential scattering cross section, σ_p, as $\sigma_p = 4\pi a^2$ rather than using an input value.

The MC^2 code can use only ENDF/B fission spectra with laws[21] $LF = 6$ or 8 in which nuclear temperatures are constant. New ENDF/B data contain spectra with laws $LF = 7$ and 9, which correspond to $LF = 6$ and 8 except that the nuclear temperatures are energy-dependent. For such materials ETØE treats the nuclear temperature as being constant and having the value at the lowest energy of the tabulation.

The new ETØE code was made operational only on the IBM-360 system because it would have been very difficult to prepare a version which would fit into the core of the CDC-3600. This space difficulty arises from the changes in the unresolved resonance region. Thus a Version II MC^2 library will be prepared only for the IBM-360 ARC system version of MC^2.

Version II ENDF/B tape 201, which contains data for ten fissionable materials, was received from Brookhaven. These data were processed through DAMMET and the new ETØE to produce a 10-material MC^2 library. A test MC^2 problem was run using these data. This problem was the Godiva assembly, which contains only U-235, U-238 and U-234, and is one of the ten assemblies specified for ENDF/B data testing. The MC^2 output cross sections were then used in an ARC system S_{16} sphere transport theory calculation. The resultant k_{eff} was 1.0012.

REFERENCES

1. B. J. Toppel, A. L. Rago and D. M. O'Shea, *MC²*, *A Code to Calculate Multigroup Cross Sections*, ANL-7318 (1967).
2. E. M. Pennington, *Compilation of ENDF/B Cross Sections for Magnesium, Titanium, Vanadium, Molybdenum and Gadolinium*, Reactor Physics Division Annual Report, July 1, 1966 to June 30, 1967, ANL-7310, pp. 22–30.
3. E. M. Pennington, J. C. Gajniak and W. Bohl, *Fortran Codes for Processing Neutron Cross Section Data*, Reactor Physics Division Annual Report, July 1, 1966 to June 30, 1967, ANL-7310, pp. 442–444.
4. E. M. Pennington, *Compilation of Neutron Cross Section Data for Natural Helium*, Reactor Physics Division Annual Report, July 1, 1967 to June 30, 1968, ANL-7410, pp. 40–41.
5. E. M. Pennington and J. C. Gajniak, *Developments Relating to the Evaluated Nuclear Data File/B (ENDF/B) Project*, Reactor Physics Division Annual Report, July 1, 1967 to June 30, 1968, ANL-7410, pp. 41–46.
6. E. M. Pennington, J. C. Gajniak and A. B. Cohen, *Developments Relating to the ENDF/B Project*, Reactor Physics Division Annual Report, July 1, 1968 to June 30, 1969, ANL-7610, pp. 40–43.
7. E. M. Pennington and J. C. Gajniak, *Compilation of ENDF/B Data for Magnesium, Titanium, Vanadium, Molybdenum and Gadolinium*, ANL-7387 (1968).
8. A. R. de L. Musgrove, *Resonance Parameters for Measured keV Neutron Capture Cross Sections*, AAEC/E198 (1969).
9. J. J. Schmidt, *Neutron Cross Sections for Fast Reactor Materials, Part I: Evaluation*, KFK-120 (1966).
10. W. Poenitz, Argonne National Laboratory (private communication).
11. M. Drake, Brookhaven National Laboratory (private communication).
12. L. Langner, J. J. Schmidt and D. Woll, *Tables of Evaluated Neutron Cross Sections for Fast Reactor Materials*, KFK-750 (1968).
13. G. deSaussure et al., *Simultaneous Measurements of the Neutron Fission and Capture Cross Sections for ^{235}U for Incident Neutron Energies from 0.4 eV to 3 keV*, ORNL-TM-1804 (1967).

14. J. J. Schmidt, *Neutron Cross Sections for Fast Reactor Materials*, KFK-120, Part II (1962).
15. H. Alter and C. L. Dunford, *An Evaluation of Uranium-235 Neutron Cross Section Data for Energies Above 15 keV*, AI-AEC-MEMO-12916 (1970).
16. *Fission Cross Sections from Petrel*, LA-3586 (1966).
17. E. Ottewitte, Atomics International (private communication).
18. D. G. Craig and C. H. Westcott, *The Total Neutron Cross Section of ^{241}Pu Below 1000 eV*, Can. Jour. Phys. **42**, 2384 (1964).
19. S. Yiftah et al., *Nuclear Data for Plutonium-240, Plutonium-241 and Plutonium-242*, IA-1152 (1967).
20. J. R. Smith, Idaho Nuclear Corporation (private communication).
21. M. K. Drake, Ed., *Data Formats and Procedures for the ENDF Neutron Cross Section Library*, BNL—(to be published).
22. E. M. Pennington, J. C. Gajniak, A. B. Cohen and W. Bohl, *Service Routines for the Multigroup Cross Section Code, MC^2*, ANL-7654 (1970).

Section II

Fast Reactor Physics

The section on Fast Reactor Physics is concerned with the analyses and measurements of liquid metal fast breeder reactor characteristics and parameters. The measurements are generally made on the critical facilities ZPPR (Zero Power Plutonium Reactor), ZPR-3, ZPR-6 and ZPR-9, and are often performed to check calculated results and hence to evaluate the analytical methods and the nuclear constants used in the calculations. Again, the critical assemblies may be constructed to permit measurements on mockups of liquid metal fast breeder power reactors. The results may possibly be extrapolated to aid in the design of the originally conceived reactor. The work reported in this section is of value in understanding the fundamentals of the liquid metal fast breeder and in developing analytic methods for predicting with accuracy the performance of such reactors.

II-1. The FTR-2 Program on the Zero Power Plutonium Reactor (ZPPR)

W. P. Keeney, J. C. Young and A. Travelli

Introduction

In the period of June to December 1969, the entire effort on the Reactor Physics Division's Zero Power Plutonium Reactor (ZPPR) was directed toward experiments in support of the Fast Flux Test Facility (FFTF). These experiments had begun at ZPPR in March of 1969 with the construction of the FTR-1, which had previously been constructed on ZPR-3 as Assembly 56B[1,2]. The FTR-1 was then modified on ZPPR by the addition of a two-drawer-thick simulated boron control ring at the core/radial reflector interface, thus constructing the ZPPR Assembly 1 which is referred to as Assembly 2 of the Fast Test Reactor Resumed Phase B Critical Experiments Program, or FTR-2[1,2].

The experimental program of the FTR-2 was designed to supply data for the evaluation of calculational models used for the design of the Fast Test Reactor (FTR). These experiments, which were designed as a result of discussions among Pacific Northwest Laboratories (PNL), Westinghouse Electric Corporation, and Argonne National Laboratory, were primarily directed toward investigations of critical mass, peripheral control worth studies, power density distributions, shielding requirements, in-vessel fuel storage, neutron spectra, and neutron and gamma flux distributions.

The reference critical configuration, assembly composition, and drawer loadings are given in Refs. 1 and 2. The detailed experimental results are described in Refs. 3, 4, 7–9.

Experiments in Reference Core

The primary experiments conducted in the reference core were an extensive set of "edge worth" measurements in which the worths of core composition, control ring composition, and radial reflector composition were measured at the boundaries of these zones with exchanges of materials of adjacent zones, and a set of radial reaction rate traverses with U-238, Pu-239 and B-10 counters.[3]

FTR Shielding Experiment

Starting with the reference core, the boron-containing control ring was removed from the assembly in steps and the resulting reactivity effects compensated for by alternately substituting depleted uranium for the plutonium fuel plates in the central region of the core. The worths of these alternate steps were measured to provide for analytical methods and reactor counter evaluations.[4-6] With the removal of the boron-containing control ring completed, the sodium-stainless steel shield was added to the assembly as shown in Fig. II-1-1.[4] Proton recoil neutron spectrum measurements were made close to the axial midplane of the assembly at radial positions near the center of the reflector and shield annuli.[7] A simulated fuel storage zone was then installed in the shield as shown in Fig. II-1-2 and the effect upon the reactivity of the system and test reactor counters was measured.[4] A series of radial traverses at three different axial elevations with Pu-239, U-238, and B-10 counters were made with and without the simulated fuel zone, and activation profiles of sodium and manganese were made throughout the system.[8,9] These data, in conjunction with thermoluminescent gamma detectors irradiated for PNL, were obtained to supply information for the shield design of the FTR.

Following the fuel storage portion of the shielding experiment, the boron-containing control ring was replaced in the assembly and plutonium fuel plates reloaded in place of the depleted uranium plates previously installed, bringing the reactor to critical again, while the effect of the approach to critical upon the test reactor counters was recorded.[8] In this configuration, with the boron-containing control ring and the shield in place, central fission ratios were measured.[8]

The assembly was then unloaded in order to permit the program to continue at ZPR-9.

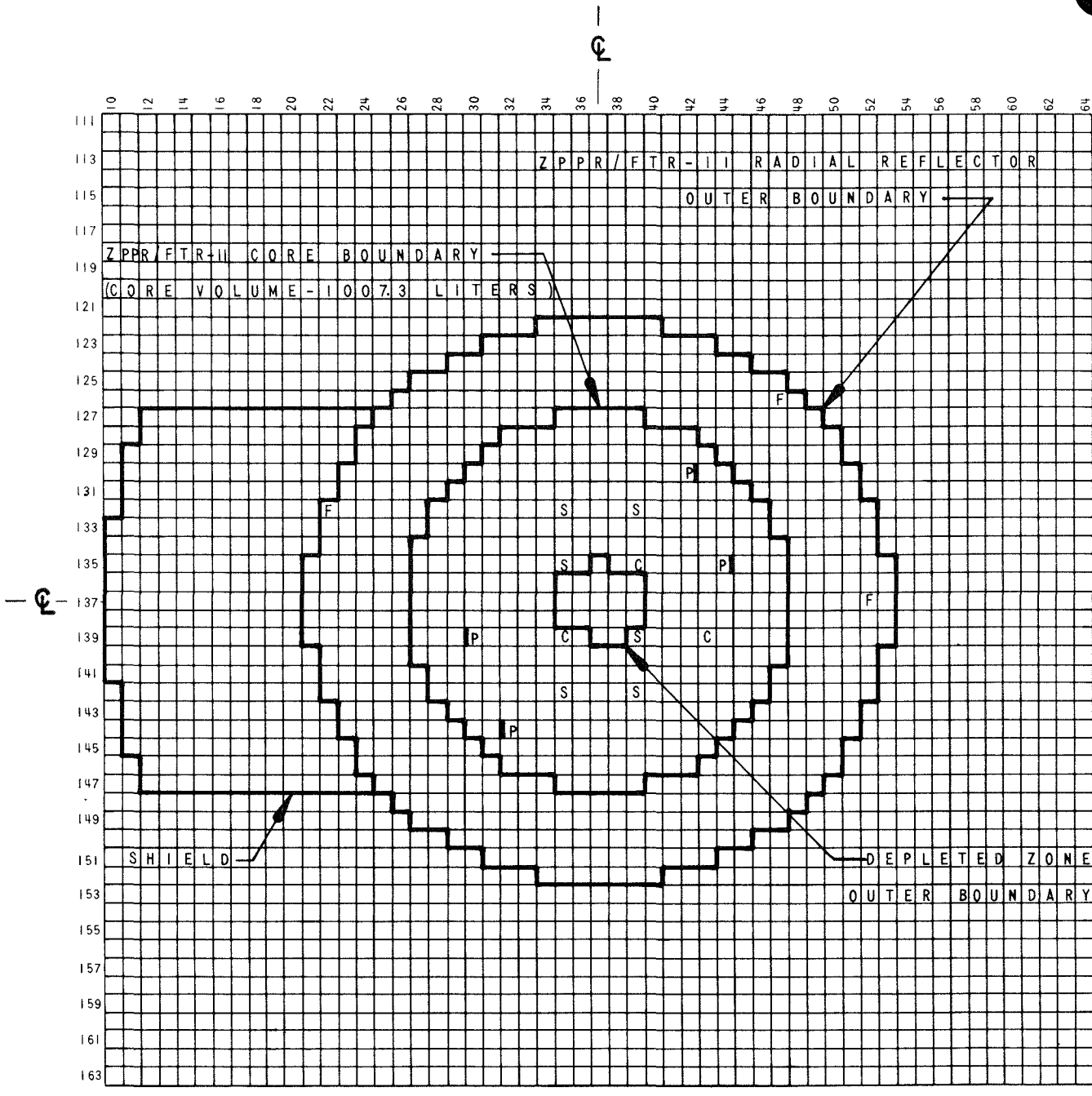

ZPPR HALF 1

(HALF 2 IS A MIRROR IMAGE OF HALF 1)

S - SAFETY ROD C - CONTROL ROD P - DRAWER ADJACENT TO POISON SAFETY ROD

| - POISON SAFETY ROD (WITHDRAWN DURING OPERATION)

F - U-235 FISSION CHAMBER (FRONT OF CHAMBER AT REACTOR MIDPLANE. NO F's IN HALF 2)

FIG. II-1-1. ZPPR/FTR-2 Shield Configuration. *ANL-ID-103-A11167.*

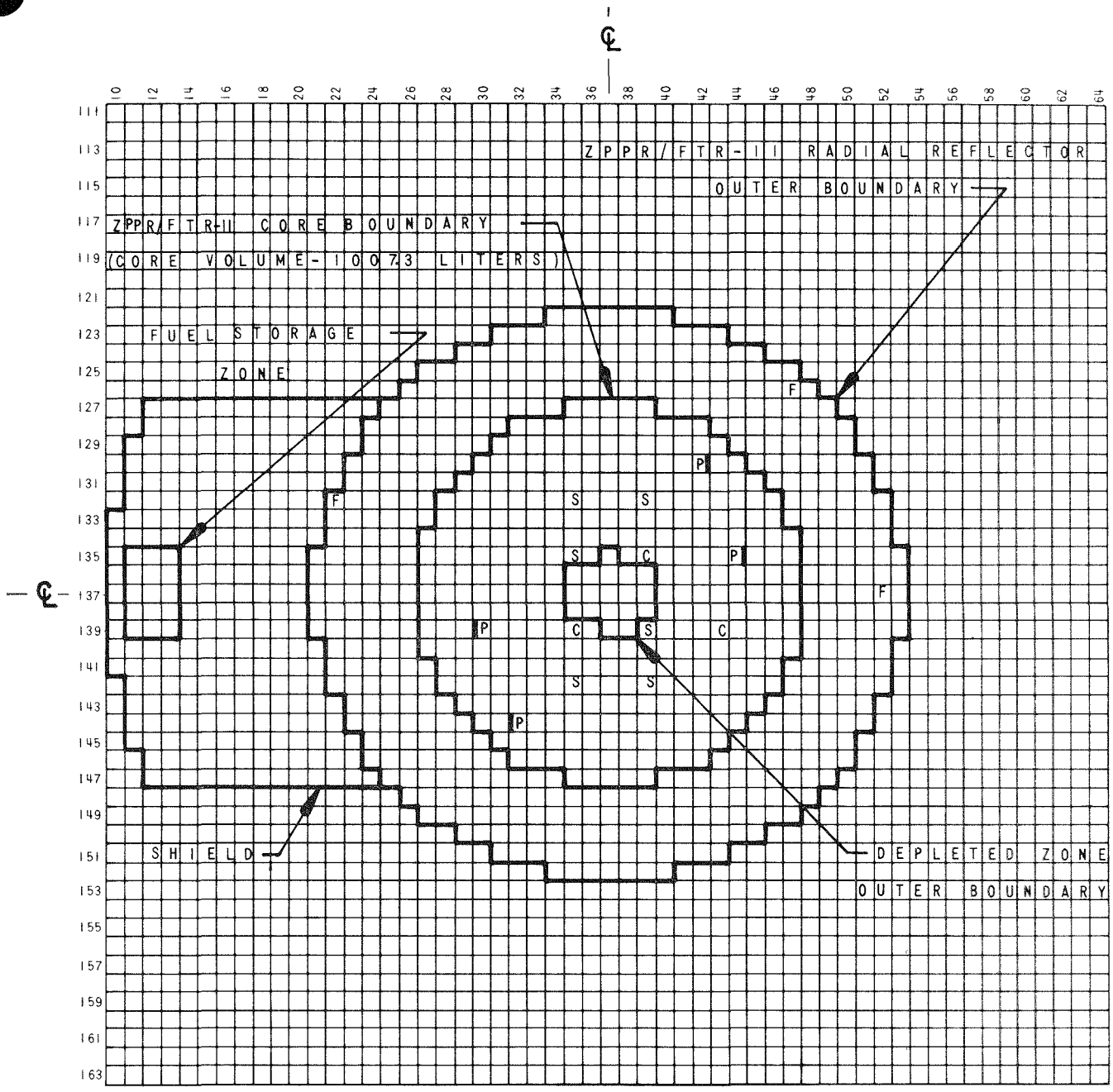

ZPPR HALF 1

(HALF 2 IS A MIRROR IMAGE OF HALF 1)

S - SAFETY ROD C - CONTROL ROD P - DRAWER ADJACENT TO POISON SAFETY ROD

| - POISON SAFETY ROD (WITHDRAWN DURING OPERATION)

F - U-235 FISSION CHAMBER (FRONT OF CHAMBER AT REACTOR MIDPLANE. NO F's IN HALF 2)

FIG. II-1-2. ZPPR/FTR-2 Shield with Fuel Storage Configuration. *ANL-ID-103-A11166.*

References

1. A. Travelli, A. J. Ulrich, D. Meneghetti and J. C. Beitel, *Calculational Studies in Support of the Fast Flux Test Facility (FFTF) Critical Experiments on ZPR-3 and ZPPR*, Reactor Physics Division Annual Report, July 1, 1968 to June 30, 1969, ANL-7610, pp. 115–137.
2. P. I. Amundson, R. G. Matlock, R. O. Vosburgh and J. C. Young, *Start-up and Initial Operation of the Zero Power Plutonium Reactor (ZPPR)*, Reactor Physics Division Annual Report, July 1, 1968 to June 30, 1969, ANL-7610, pp. 63–69.
3. Reactor Development Program Progress Report, *ZPR-3 and ZPPR Operations and Analysis, Mockup Critical Experments*, ANL-7606, 25–30 (1969).
4. Reactor Development Program Progress Report, *ZPR-3 and ZPPR Operations and Analysis, Mockup Critical Experiments*, ANL-7632, 14–22 (1969).
5. A. Travelli, A. J. Ulrich, J. C. Beitel, *Analysis of Reactivity Changes Associated with Large Perturbations in ZPPR/FTR-2*, Trans. Am. Nucl. Soc. **13**, 321 (1970).
6. R. A. Bennett and J. V. Nelson, *Central Fuel and Peripheral Control Ring Reactivity Worths in the FTR-2 Critical*, Trans. Am. Nucl. Soc. **13**, 322 (1970).
7. Reactor Development Program Progress Report, *Experimental Reactor Physics, Fast Critical Experiments—Experimental Support—Idaho*, ANL-7640, 10–12 (1969).
8. Reactor Development Program Progress Report, *ZPR-3 and ZPPR Operations and Analysis, Mockup Critical Experiments*, ANL-7655, 18–42 (1969).
9. Reactor Development Program Progress Report, *Experimental Reactor Physics, Fast Critical Experiments—Experimental Support—Idaho*, ANL-7661, 4–8 (1970).

II-2. ZPR-9 Assembly 26, FTR-3

J. W. Daughtry, R. B. Pond, C. D. Swanson and R. M. Fleischman*

Introduction

FTR-3 is the third of a series of three assemblies built for the purpose of obtaining data to evaluate neutronics models being used to design the Fast Test Reactor (FTR) which is to be a part of the Fast Flux Test Facility (FFTF). The FTR-1 core geometry was a simple reflected right circular cylinder.[1] FTR-2 was similar to FTR-1 but had a continuous ring of boron control material surrounding the core.[2] FTR-3 is slightly more complex, having a two zone PuO_2-UO_2 core and a ring of sixteen simulated control rods in place of the continuous ring of control material. The experiments currently underway in ZPR-9 in the FTR-3 core are designed to yield data for the assessment of the uncertainties in the preliminary design parameters of the FTR related to critical mass, neutron spectrum, Doppler effects, absolute flux level, power density distribution, in-core and peripheral control worth, test loop worth, sodium-void effects, and neutron lifetime. In addition, the FTR-3 will serve as a reference for the Engineering Mockup Critical (EMC) that will be assembled upon completion of the FTR-3 experiments.

Approximately half of the experiments scheduled for FTR-3 have been completed in this reporting period with the remainder scheduled to be completed before the end of 1970. The experiments that have been completed include measurements of neutron spectrum, Doppler effect, small sample central worths, radial worth traverses, radial and axial reaction rate traverses and central reaction rate ratios. All of these experiments are being reported in other papers (referenced below) in this annual report.

The purpose of this paper is to provide a detailed description of the assembly including the worths of the ZPR-9 control and safety rods, the temperature coefficient of reactivity, the critical mass, and worths of core boundary adjustments.

Description of the Assembly

Figures II-2-1 and II-2-2 show the matrix loading pattern for the assembly. Table II-2-I lists the major dimensions and core volumes. The radii given are the radii of area-equivalent circles. The peripheral control zones have the same axial height as the inner and outer cores. Each control zone is made up of four drawers in each half of the assembly. The atom densities for each region of the assembly are listed in Table II-2-II. Drawer loading patterns are shown in Figs. II-2-3 through II-2-10. Some minor deviations from the piece-size distributions shown were required because of inventory limitations. The inner core zone has a two drawer cell; each of the other regions has a one drawer cell. The inner core Type A drawers are in the even-numbered matrix columns, the Type B drawers are in the odd-numbered columns. The radial shield consists of 224 tubes of material. As used here, a tube of material is 2 x 2 x 60 in., i.e., the contents of a matrix

* WADCO Corporation, a Subsidiary of Westinghouse Electric Corporation, Richland, Washington.

tube extending through both halves of the reactor. The inner ring of the radial shield, consisting of 128 tubes, is loaded as shown in Fig. II-2-9. The outer ring of the radial shield, consisting of 96 tubes, is loaded as shown in Fig. II-2-10. The spring gaps indicated in Figs. II-2-7 and II-2-8 are 0.79 cm. In the radial shield the gap is 0.47 cm.

Control and Safety Rods

Five fuel-bearing dual-purpose control/safety rods were installed in each half of the reactor. The locations of these rods could be changed to meet the requirements of the experimental program. When located in the inner core region they were always assigned a Type B location and loading. When partially or fully withdrawn a void was left in the core region. The stroke of this type rod from full-in to full-out is approximately 61 cm. Table II-2-III gives the measured worth for full travel of the fuel bearing rods as a function of the radial location of the rod in the core.

In addition to the fuel rods there were five or six poison rods in each half of the reactor. The flexibility for locating the poison rods is somewhat limited. With a core the size of FTR-3 there are only twelve locations for poison rods within the boundaries of the fueled zones. Four of these locations are at a radius of 38.7 cm and the other eight are at 42.9 cm from the core axis which is at the center of tube 23-23. The poison rods contain boron powder, and the loading varies significantly from rod to rod. The average is about 160 g of B-10 in each rod. The active length of the rods is

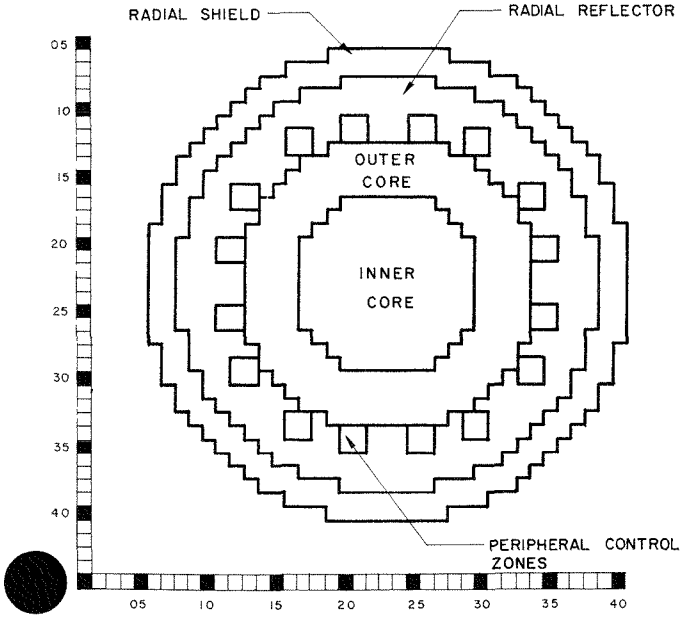

Fig. II-2-1. FTR-3 Reference Configuration. *ANL Neg. No. 116-526.*

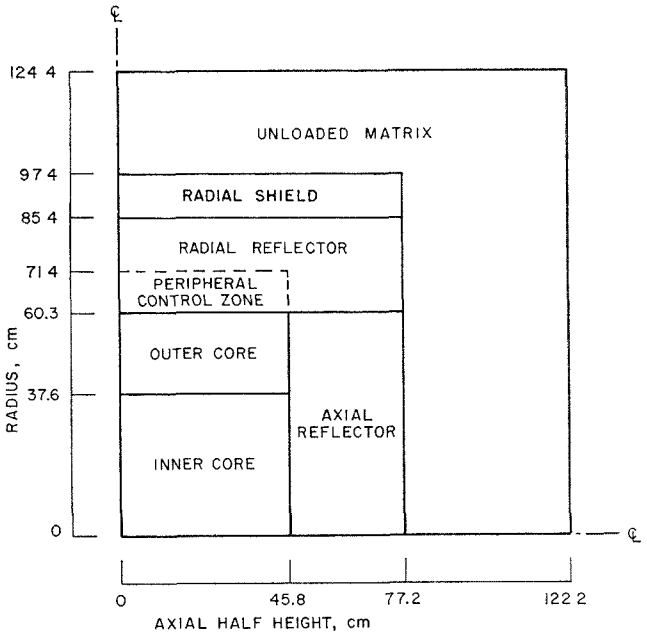

Fig. II-2-2. Side View of FTR-3 in ZPR-9. *ANL Neg. No. 116-525.*

TABLE II-2-I. Dimensions and Core Volume of FTR-3

Inner zone radius, cm	37.6
Outer zone radius, cm	60.3
Radial reflector outer radius, cm	85.4
Radial shield outer radius, cm	97.4
Core height (excluding axial reflector), cm	91.6
Axial reflector thickness, cm	31.4
Core volume, liters	
Inner core	406.3
Outer core	638.9
Total	1045.2

61 cm and they have a stroke of 76 cm. The average worths of the rods were determined to be about 140 Ih at the 38.7 cm radius and 120 Ih at the 42.9 cm radius.

Temperature Coefficient

The temperature coefficient of reactivity for FTR-3 was determined by making repeated observations of the critical control rod configuration in the reference core to determine the excess reactivity at different core temperatures.

The data consisted of the average position of a previously calibrated control rod required to maintain a specified power level and the readings from 21 thermocouples distributed throughout the reactor core. Although the average of the thermocouple readings did not truly represent the core average temperature, it did give a consistent sampling of the temperature distribution and provided a relative gauge of changes of core temperature.

TABLE II-2-II. FTR-3 ATOM DENSITIES, 10^{21} ATOMS/CM^3

Isotope or Element	Inner Core Type A Drawer	Inner Core Type B Drawer	Inner Core Avg[a]	Outer Core	Outer Core Drawer Next to B-10 Rods	Peripheral Control Zones	Radial Reflector	Axial Reflector	Radial Shield
Pu-238	0.0006	—	0.0003	0.0006	0.0006	—	—	—	—
Pu-239	0.8814	1.0690	0.9784	1.4669	1.4466	—	—	—	—
Pu-240	0.1167	0.0510	0.0827	0.1723	0.1704	—	—	—	—
Pu-241	0.0181	0.0049	0.0113	0.0227	0.0225	—	—	—	—
Pu-242	0.0019	0.0001	0.0010	0.0022	0.0022	—	—	—	—
Pu-239 + Pu-241	0.8995	1.0739	0.9897	1.4896	1.4691	—	—	—	—
Pu-240 + Pu-242	0.1186	0.0511	0.0837	0.1745	0.1726	—	—	—	—
Pu	1.0187	1.1250	1.0737	1.6647	1.6423	—	—	—	—
U-235	0.0125	0.0069	0.0096	0.0125	0.0114	—	—	—	—
U-238	5.7811	3.2769	4.4864	5.9000	4.9970	—	—	—	—
U	5.7936	3.2838	4.4960	5.9125	5.0084	—	—	—	—
Mo	0.2340	0.0123	0.1194	0.4412	0.4338	0.0105	0.0078	0.0079	0.036
Na	9.1731	11.208	10.225	8.7013	6.2784	4.1257	6.7544	9.2102	6.754
C	0.0257	0.0356	0.0308	1.0686	1.0684	14.043	0.1646	0.0231	0.105
O	14.454	8.7577	11.509	12.717	8.0809	—	—	—	—
Fe	13.363	13.234	13.296	15.906	14.124	11.320	8.4575	8.5898	39.022
Cr	2.7593	3.8193	3.3073	3.1571	3.1204	3.2536	2.432	2.4614	11.258
Ni	1.3166	1.8224	1.5781	1.5064	1.4889	1.5525	48.072	38.1013	5.372
Mn	0.2026	0.2804	0.2428	0.2318	0.2291	0.2389	0.2864	0.2789	0.827
Al	—	0.1109	0.0574	—	—	—	—	—	—
B-10	—	—	—	—	—	10.698	—	—	—
B-11	—	—	—	—	—	43.387	—	—	—
B	—	—	—	—	—	54.085	—	—	—

[a] 140 Type A drawers and 150 Type B drawers.

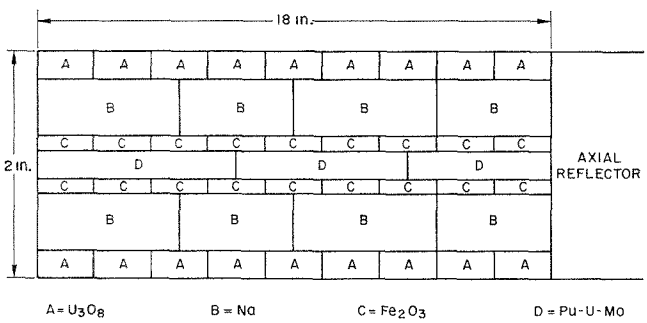

FIG. II-2-3. Inner Core Drawer-Type A Loading Pattern. *ANL Neg. No. 116-442.*

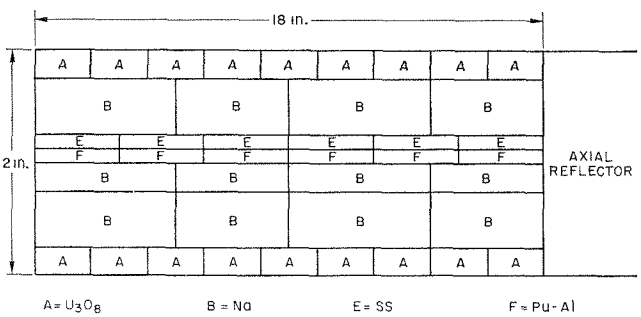

FIG. II-2-4. Inner Core Drawer-Type B Loading Pattern. *ANL Neg. No. 116-523.*

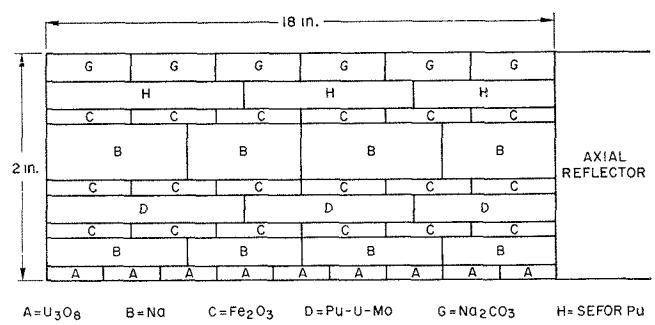

FIG. II-2-5. Outer Core Drawer Loading Pattern. *ANL Neg. No. 116-438.*

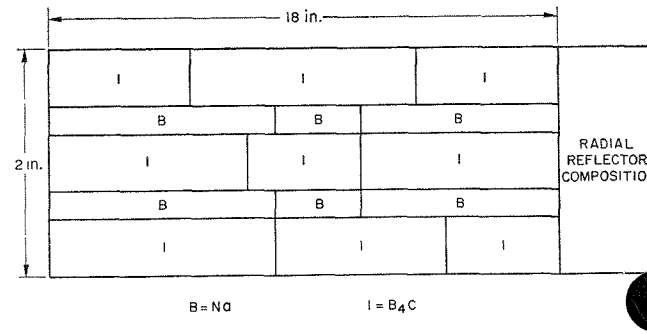

FIG. II-2-6. Peripheral Control Zone Drawer Loading Pattern. *ANL Neg. No. 116-439.*

The core excess reactivity appeared to be a linear function of temperature over the range of the measurements. A least squares analysis gave a value of 3.39 ± 0.04 Ih/°C for the temperature coefficient of reactivity for the reference core.

Edge Worth Measurements and Critical Mass Adjustment

The worths of outer-core drawers relative to radial reflector material and the worths of inner core drawers relative to outer core material were measured at selected locations along the outer core- -reflector and inner core- -outer core boundaries of FTR-3. Each

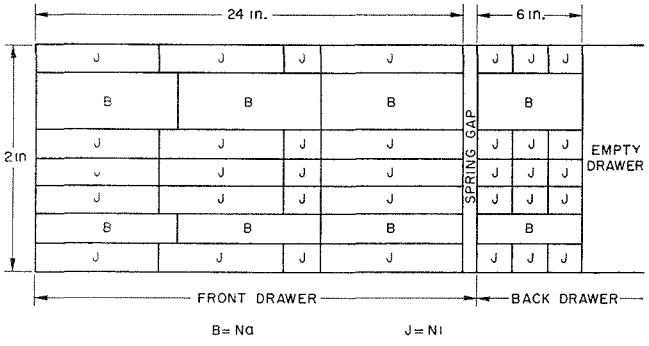

Fig. II-2-7. Radial Reflector Drawer Loading Pattern. *ANL Neg. No. 116-440.*

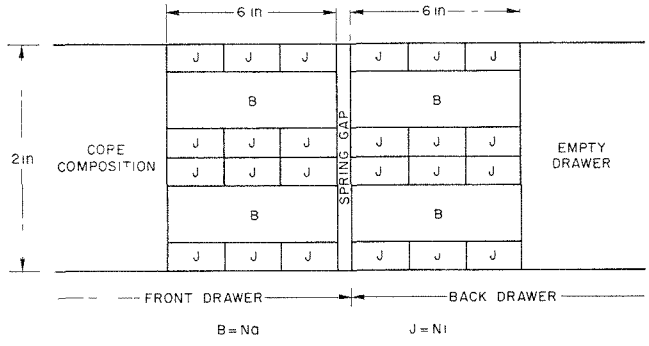

Fig. II-2-8. Axial Reflector Drawer Loading Pattern. *ANL Neg. No. 116-441.*

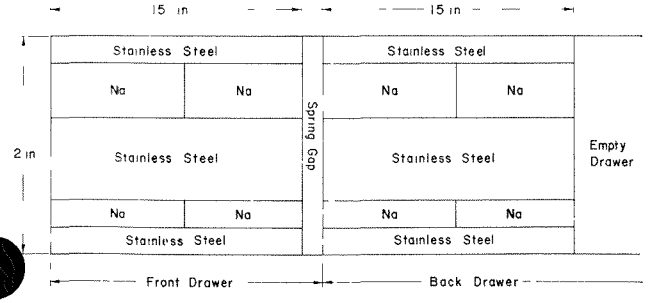

Fig. II-2-9. Radial Shield Drawer Loading Pattern—Inner Ring. *ANL Neg. No. 116-522.*

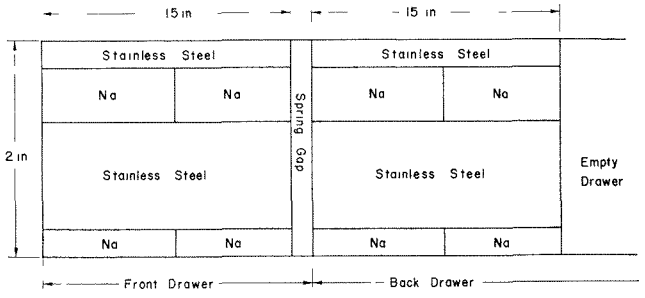

Fig. II-2-10. Radial Shield Drawer Loading Pattern—Outer Ring. *ANL Neg. No. 116-521.*

TABLE II-2-III. Fuel-Bearing Rod Worth

Radius, cm	Worth, Ih	Type
5.53	95.0	Inner Core, Type B
15.64	93.6	Inner Core, Type B
22.80	87.4	Inner Core, Type B
42.12	81.7	Outer Core
44.59	76.5	Outer Core

worth was measured by determining the position of a previously calibrated control rod necessary to maintain a specified power level. Corrections were made for temperature differences and for the reactivity effect of the decay of Pu-241. The measured worths of the drawer exchanges are listed in Table II-2-IV. The last column of the table gives the worth of the exchange divided by the net gain or loss of fissile mass (Pu-239 + Pu-241 + U-235). The estimated uncertainty in the worth does not include uncertainties due to inaccuracy in the calibration of the control rods used in making the measurements.

All outer core drawers were loaded the same except for different sizes of plutonium plates used to make up the fuel columns in the drawers. The type of outer core drawer used in these exchanges was designated Outer Core C. The atom densities for this type drawer are given in Table II-2-V. The atom densities for the inner core and radial reflector drawers are given in Table II-2-II.

The specific worths of drawer exchanges were analyzed as a function of radius (core center to drawer center) using a linear least-squares analysis. Each point was weighted by the inverse of its uncertainty. At the outer core- -radial reflector boundary the specific worth can be represented by:

$$\rho \pm 3.54(\text{Ih/kg}) = -2.05(\text{Ih/kg-cm})\ r\ (\text{cm}) + 144.88(\text{Ih/kg})$$

for the range 55 cm $< r <$ 63 cm. Evaluating this at the average outer core radius (60.27 cm) gave 21.33 ±

TABLE II-2-IV. SUMMARY OF MEASUREMENTS OF DRAWER EXCHANGE WORTH IN FTR-3

Type of Drawer Removed	Type of Drawer Added	Matrix Position	Radius, cm	Worth of Exchange,[a] Ih	Specific Worth,[b] Ih/kg
Inner Core A	Outer Core C	M-19-28	35.41	39.24	124.38
Inner Core A	Outer Core C	M-17-26	37.1	37.41	118.58
Outer Core C	Inner Core A	M-18-28	39.11	−38.27	121.30
Outer Core C	Inner Core A	M-16-26	42.12	−33.69 ± 0.96	106.79 ± 3.04
Inner Core B	Outer Core C	M-17-23	33.19	21.33	96.25
Inner Core B	Outer Core C	M-18-27	35.41	20.10	90.70
Inner Core B	Outer Core C	M-20-29	37.1	19.78	89.26
Outer Core C	Inner Core B	M-18-28	39.11	−20.52	92.60
Outer Core C	Radial Reflector	M-23-33	55.31	−26.19	31.84
Outer Core C	Radial Reflector	M-16-31	58.79	−21.74	26.43
Radial Reflector	Outer Core C	M-23-34	60.84	14.47	17.59
Radial Reflector	Outer Core C	M-23-34	60.84	13.66	16.60
Radial Reflector	Outer Core C	M-15-31	62.51	16.82	20.45
Boron Control 0–10 in.	Radial Reflector 0–10 in.	S 20-11 S 20-12 S 21-11 S 21-12	—	90.41	—

[a] The estimated error equals ±0.68 Ih unless otherwise stated.

[b] The estimated error equals ±2.16 Ih/kg, ±3.07 Ih/kg, and ±0.83 Ih/kg for ICA-OC, ICB-OC, and OC-RR types of exchange, respectively, unless otherwise stated.

TABLE II-2-V. ATOM DENSITIES FOR OUTER CORE DRAWER—TYPE C

Isotope or Element	Atom Densities, 10^{21} atoms/cm^3
Pu-238	0.0006
Pu-239	1.4445
Pu-240	0.1702
Pu-241	0.0225
Pu-242	0.0022
U-235	0.0122
U-238	5.8008
Mo	0.4332
Na	8.7013
C	1.0686
O	12.7174
Fe	15.9273
Cr	3.1633
Ni	1.5094
Mn	0.2325

3.54 Ih/kg for the conversion factor from outer-edge fissile mass to reactivity. (The average radius is the radius of a cylinder having the cross-sectional area of the core.)

At the inner core- -outer core boundary the fissile-mass normalization did not completely account for the difference between A- and B-type drawers. It was assumed, however, that the slopes of the curves of specific worth versus radius were the same for both sets of data. A fit to the data was made by carrying an additive normalization constant through the weighted least-squares analysis. The root-mean-square deviation of the normalized specific worths about the fitted line was minimized with respect to the normalization constant. The fitted slope and weighted average specific worth and radius were then used to determine fitted lines for both sets of data. An average of these two lines weighted by the total number of A or B drawers in the inner core is the best representation of the average specific worth function across the boundary:

$$\rho \pm 4.05\,(\text{Ih/kg}) = -1.624\,(\text{Ih/kg-cm})\ r\ (\text{cm}) + 165.27\,(\text{Ih/kg})$$

for the range 33 cm $< r <$ 43 cm. Evaluating this at the average inner core radius (37.58 cm) gave 104.24 ± 4.05 Ih/kg for the conversion factor from inner-boundary fissile mass to reactivity.

The final entry at the bottom of Table II-2-IV gives the results of a substitution of radial-reflector material for peripheral boron control material. This substitution was made in a cluster of four drawers of one peripheral control zone. The volume in which the substitution was made extended 10 in. into the stationary half from the midplane of the assembly.

The FTR-3 critical mass is summarized in Table II-2-VI. The average specific worth of fissile-mass exchange at the two boundaries was used to determine the fissile-mass adjustment for fully inserting control rod No. 9 and correcting for the fact that the core was subcritical at the reference power level. Adjustment at the inner core-outer core boundary effectively increases the inner core radius. Adjustment at the outer core-radial reflector boundary effectively decreases the outer core radius. It should be noted that the corrected criti-

TABLE II-2-VI. CRITICAL MASS OF ZPR-9 ASSEMBLY 26 (FTR-3)

Reference Conditions of FTR-3 As Built

1) Temperature 30°C
2) No. 9 Control rod withdrawn 57.18 cm (all others fully inserted)
3) All B-10 blades fully withdrawn
4) Subcritical by 0.99 Ih
5) 541.948 (kg of Pu-239, Pu-241, U-235)

Adjustment for:	Reactivity effect of adjustment,[a] Ih	Fissile-mass adjustment at outer core-inner core boundary (kg of Pu-239 + Pu-241 + U-235)	Fissile-mass adjustment at outer core-radial reflector boundary (kg of Pu-239, Pu-241, U-235)
Control rod No. 9 partially withdrawn	−80.27 ± 0.48	−0.771 ± 0.031	−3.768 ± 0.626
Reference core subcritical at reference power level	+0.99 ± 0.08	+0.010 ± 0.001	+0.046 ± 0.009
Adjusted critical mass of unsmoothed, heterogeneous cylinder		541.19	538.23

[a] 1% $\Delta k/k$ = 1064 Ih.

cal mass includes no corrections for smoothing of the boundaries, for the reactivity effect of the interface gap between assembly halves, or for the effect of core heterogeneity. It should be noted that the core-average thermocouple reading (30°C) is not a true representation of the core-average temperature.

FTR-3 PROGRAM OF EXPERIMENTS

The material covered in the previous sections of this paper represents Step No. 1 of the Detailed Plans for FTR-3 Experiments. Steps 1 through 7 were completed in this reporting period. Steps 2 through 7 are reported in other papers in this annual report as follows:

Step No.	Paper No.
2	Paper II-22
3	Paper II-6
4 and 5	Paper II-5
6	Paper II-5
7	Paper II-3

REFERENCES

1. Reactor Development Program Progress Report, *ANL-7553, pp. 12-13 (1969)*.
2. Reactor Development Program Progress Report, *ANL-7595, pp. 21-26 (1969)*.

II-3. Central Reaction Ratios in ZPR-9 Assembly 26, FTR-3

A. B. LONG AND C. D. SWANSON

The seventh step of the FTR-3 Phase B Critical Experiments Program consisted of measuring fission and capture ratios at the center of ZPR-9 Assembly 26. The fission ratios of Pu-239/U-235, U-238/U-235, and Pu-240/U-235, as well as the U-238 capture to U-235 fission ratios were measured and are reported here.

The fission ratio measurements were made with gas flow fission counters of the Kirn design.[1] The U-238 capture to U-235 fission ratio was determined by radiochemical means.[2]

EXPERIMENTAL METHOD

The reaction ratio measurements were performed in loading No. 69 of Assembly 26. This loading was a slightly modified version of the reference core configuration. (See Paper II-2). The modifications included the fine autorod in matrix position 24-16 and two Kirn counters. One Kirn counter was used as a monitor to normalize different reactor runs to the same power level and it was located in position M 28-19. The second Kirn counter was used for the actual fission rate measurements and it was located in a 2 x 2 x 2 in. void at the front of matrix position M 23-23. A diagram of the detector position, drawer loading, and cable void is shown in Fig. II-3-1.

All of the different fission rates were measured by placing the proper source foil in the central Kirn counter and counting the fissions while the reactor was

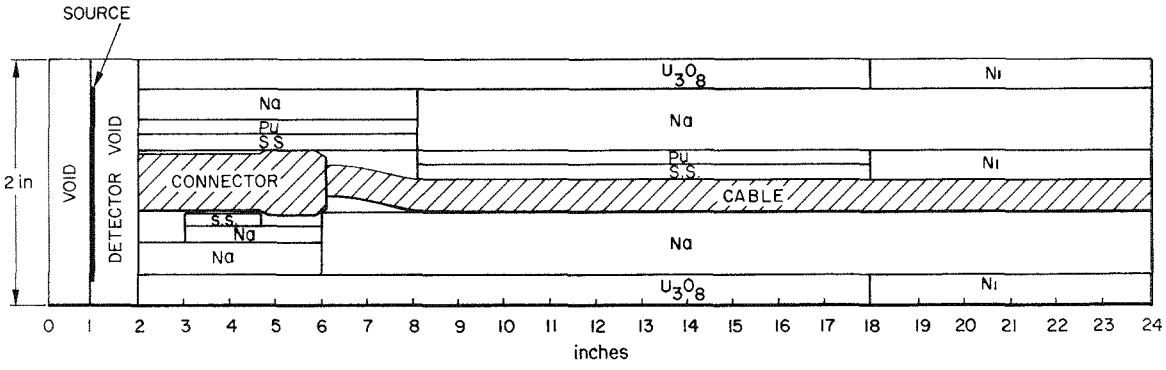

FIG. II-3-1. Load Diagram of Drawer Containing a Kirn Fission Counter. *ANL Neg. No. 116-379.*

TABLE II-3-I. COMPOSITION AND MASS OF FISSION DETECTOR SOURCES AND FISSION FOILS

Source or Foil	Total Mass	Weight Percent						
		U-234	U-235	U-236	U-238	Pu-239	Pu-240	Pu-241
U-235 detector source	79.43 μg	0.03	99.86	0.06	0.05	—	—	—
U-238 detector source	98.72 μg	—	0.01	—	99.99	—	—	—
Pu-239 detector source	82.29 μg	—	—	—	—	98.94	1.01	0.05
Pu-240 detector source	60.78 μg	—	—	—	—	0.77	98.58	0.54
U-235 foils	0.1093 g	1.03	93.06	0.26	5.63	—	—	—
U-238 foils	0.5123 g	—	0.22	—	99.78	—	—	—

TABLE II-3-II. MEASURED FISSION AND CAPTURE RATIOS

Ratio and Measurement Technique	Value
$^{239}Pu_f/^{235}U_f$ by detector	0.984 ± 0.022
$^{240}Pu_f/^{235}U_f$ by detector	0.256 ± 0.006
$^{238}U_f/^{235}U_f$ by detector	0 0250 ± 0.0006
$^{238}U_f/^{235}U_f$ by radiochemistry	0.0234 ± 0.0013
$^{238}U_c/^{235}U_f$ by radiochemistry	0.161 ± 0.009

at a predetermined power. The following six reactor runs were performed:

1. U-235 fission
2. U-235 fission—test of reproducibility
3. Pu-239 fission
4. U-238 fission
5. Pu-240 fission
6. U-235 fission + foil irradiation to determine U-235 fission and U-238 capture rates.

During each run several scaler counts were taken of both the central detector and the monitor detector. In addition a fission or alpha spectrum was recorded for both detectors in coincidence with the discriminator output that was counted by the scalers.

The fission rates were determined by correcting the scaler counts for deadtime and then for background using the recorded spectra. Because of small long-term drifts in the reactor instrumentation it was necessary to normalize the fission rates measured in different reactor runs with the corrected monitor count rate.

During the sixth reactor run, two U-238 foils (⅝ in. diam by 0.0055 in. thick) and two U-235 foils (5/16 in. diam by 0.0044 in. thick) were attached to the front face of the central counter. Following the irradiation the total number of fissions which occurred in each foil was determined by radiochemical separation and counting of Mo-99.[2] In addition, the total number of captures which occurred in the U-238 foils was determined by radiochemical separation and counting of Np-239.[2]

RESULTS

The isotopic compositions of the various fission sources and fission foils are given in Table II-3-I. The thickness of each of the fission sources was about 20 μg/cm². For this reason any error in the absolute fission rate which was produced by finite source thickness, cancels when the ratio of two fission rates is determined. The fission in the U-235 counter and foils which were due to the U-238 impurities, and the fissions in the U-238 counters and foils which were due to the U-235 impurities were corrected for by solving the simultaneous equations using the corrected data and the isotopic concentrations. The same type of correction was made for the Pu-240 impurities in the Pu-239 counter and the Pu-239 impurities in the Pu-240 counter.

The values for the fission ratios of Pu-239/U-235,

-238/U-235 and Pu-240/U-235 and for the U-238 capture to U-235 fission ratio are given in Table II-3-II. In the case of the detector measurements, the errors can be attributed mostly to the uncertainty in the mass of the fission foils. The errors due to counting statistics and background correction were always less than 1%. The standard deviations in the three detector measurements of the U-235 fission rate which were made on different days, was less than 0.2%. The errors associated with the radiochemical analysis were somewhat larger (6%). This larger error and the possible effect of foil thickness on fission rate probably account for the difference between the radiochemical and the detector values for the fission ratio of U-238/U-235.

References

1. F. S. Kirn, *Neutron Detection with an Absolute Fission Counter*, Proc. Symposium on Neutron Detection, Dosimetry and Standardization, International Atomic Energy Agency, Harwell, England, December 1962, Vol. 2, pp. 497–512.
2. R. J. Armani, *Absolute Determination of Fission Rates in U-235 and U-238 and Capture Rates in U-238 by Radiochemical Techniques*, Proc. Symposium on the Standardization of Radionuclides, International Atomic Energy Agency, Vienna, 1966, pp. 613–620.

II-4. Measured Reaction Rate Distributions in ZPR-9 Assembly 26, FTR-3

A. B. Long and C. D. Swanson

The sixth step of the FTR-3 Phase B Critical Experiments Program consisted of measuring the $Pu^{239}(n,f)$, $U^{238}(n,f)$ and $B^{10}(n,\alpha)$ reaction rate distributions in ZPR-9 Assembly 26. Two sets of radial distributions were measured, the first near the center plane of the reactor and the second close to the core-reflector interface; and two sets of axial distributions were measured, the first along the axis of the inner core and the second along the middle of the outer core. The perturbation produced by the traverse void and detector was investigated by comparing the $U^{238}(n,f)$ detector measurements with foil activation data taken before the traverse void was installed. The effect of neutron streaming in the void was studied by placing stainless steel plugs in front of the detectors.

Experimental Procedure

For each of the four sets of traverse measurements, modifications were made to the reference core configuration. (See Paper II-2). In addition to the void intro-

TABLE II-4-I. Radial Traverse near Midplane

Radial Distance From Center, in.	Relative Reaction Rate				
	$Pu^{239}(n,f)$	$Pu^{239}(n,f)$ With SS Plug	$U^{238}(n,f)$	$U^{238}(n,f)$ with SS Plug	$B^{10}(n,\alpha)$
0.000	17062 ± 144	17565 ± 142	2686 ± 29	2610 ± 28	19032 ± 73
2.177	17282 ± 187	17473 ± 188	2645 ± 44	2539 ± 43	19009 ± 146
4.534	17048 ± 186	17211 ± 186	2651 ± 44	2576 ± 44	18907 ± 146
6.531	16795 ± 184	16843 ± 184	2582 ± 43	2508 ± 43	18115 ± 142
8.708	15908 ± 178	15955 ± 137	2480 ± 28	2392 ± 30	17238 ± 69
10.885	15092 ± 166	14990 ± 168	2423 ± 42	2304 ± 41	16302 ± 135
13.062	14004 ± 154	14036 ± 159	2348 ± 42	2243 ± 40	14435 ± 127
15.239	12940 ± 142	12700 ± 147	2227 ± 41	2181 ± 39	13068 ± 121
17.416	11128 ± 125	10984 ± 109	1979 ± 38	1948 ± 36	11259 ± 113
19.593	9731 ± 113	9418 ± 77	1686 ± 24	1597 ± 21	9784 ± 37
20.681					9276 ± 72
21.770	8300 ± 61	8166 ± 85	1212 ± 30	1213 ± 21	9192 ± 71
22.858	8205 ± 81	8125 ± 84			9666 ± 72
23.947	8215 ± 82	8144 ± 83	698 ± 23	665 ± 14	10720 ± 75
26.124	8032 ± 82	8022 ± 81	368 ± 15	347 ± 7	12269 ± 79
28.301	7656 ± 81	7721 ± 77	248 ± 12	172 ± 4	12942 ± 81
30.478	7037 ± 77	7026 ± 49	100 ± 5	93 ± 2	12410 ± 39
32.655	5493 ± 65	5425 ± 60	57 ± 3	54 ± 2	9794 ± 70
34.832	3862 ± 44	3721 ± 41	30 ± 2	28 ± 1	6706 ± 58
37.009	2520 ± 30	2387 ± 27	47 ± 3	13 ± 1	4193 ± 46

TABLE II-4-II. Radial Traverse near Core-Reflector Interface

Radial Distance From Center, in.	Relative Reaction Rate			
	$Pu^{239}(n,f)$	$U^{238}(n,f)$	$U^{238}(n,f)$ With Hole Mat. in Refl.	$B^{10}(n,\alpha)$
0.000	13505 ± 171	1715 ± 26	1716 ± 26	21350 ± 56
2.177	13073 ± 197	1711 ± 36		21229 ± 160
4.354	13037 ± 198	1665 ± 35		20686 ± 158
6.531	12261 ± 190	1640 ± 35		20214 ± 156
8.708	11961 ± 163	1586 ± 24	1596 ± 24	18991 ± 76
10.885	11118 ± 174	1554 ± 35		17737 ± 147
13.062	10339 ± 162	1514 ± 34		15991 ± 140
15.239	9011 ± 144	1413 ± 33		13638 ± 131
17.416	7703 ± 111	1240 ± 31		11316 ± 120
19.593	6640 ± 85	1031 ± 20	1025 ± 21	10096 ± 56
20.682				9513 ± 108
21.770	5894 ± 89	787 ± 20		9581 ± 107
22.858				9643 ± 106
23.947	5719 ± 88	456 ± 14	460 ± 12	10663 ± 77
26.124	5691 ± 89	231 ± 6	237 ± 6	11772 ± 79
28.301	5522 ± 89	127 ± 4	120 ± 4	12265 ± 79
30.478	5041 ± 74	70 ± 2	69 ± 1	11765 ± 38
32.655	3975 ± 64	42 ± 1	39 ± 1	9512 ± 69
34.832	2956 ± 50	23 ± 1	22 ± 1	6743 ± 58
37.009	2148 ± 36	15 ± 1		4463 ± 47

TABLE II-4-III. Axial Traverse, Inner Core

Axial Distance From Midplane, in.	Relative Reaction Rate			
	$Pu^{239}(n,f)$	$U^{238}(n,f)$	$U^{238}(n,f)$ with SS Plug	$B^{10}(n,\alpha)$
0.0	17152 ± 200	2849 ± 33	2832 ± 32	19614 ± 48
2.0	17071 ± 209	2836 ± 49	2819 ± 46	19725 ± 145
4.0	16967 ± 215	2774 ± 48	2769 ± 46	19301 ± 143
6.0	16296 ± 197	2733 ± 35	2703 ± 32	18631 ± 140
8.0	15585 ± 221	2576 ± 47	2475 ± 36	18152 ± 98
10.0	15173 ± 219	2369 ± 45	2439 ± 44	17397 ± 135
12.0	14124 ± 210	2213 ± 44	2161 ± 41	17103 ± 67
14.0	13413 ± 204	1987 ± 42	1952 ± 39	17423 ± 135
16.0	13572 ± 183	1690 ± 28	1670 ± 25	18951 ± 140
17.0	14109 ± 212			
18.0	15405 ± 225	1256 ± 31	1233 ± 28	24471 ± 158
19.0	17343 ± 245	994 ± 32	1000 ± 30	28980 ± 171
19.5	18836 ± 260			
20.0	20496 ± 258	752 ± 24	778 ± 21	34348 ± 186
21.0	21042 ± 278	607 ± 21	641 ± 21	
22.0	21630 ± 259	464 ± 16	488 ± 16	39430 ± 199
24.0	20543 ± 223	309 ± 12	292 ± 11	39161 ± 99
26.0	17714 ± 227	213 ± 8	245 ± 9	35226 ± 187
28.0	13908 ± 186	134 ± 5	139 ± 5	27930 ± 167
30.0	9966 ± 143	83 ± 3		19011 ± 138

duced for the detectors to move through, the autorod remained in matrix position 24-16 and a Kirn[1] counter was installed in position M 28-19. The Kirn counter was to have been used as a flux monitor, although this was later found to be unnecessary. The reactivity changes caused by these modifications were compensated by adjusting the inner-outer core boundary.

The central radial traverses were made by moving the various detectors through a 2.8 cm diam hole approximately 4.4 cm from the reactor midplane using the radial sample changer. The radial traverses near the core-reflector interface were made in the same manner except that the cross section of the traverse hole was 3.8 x 5.1 cm and it was located 38.1 cm from the reactor midplane. Both voids extended from the edge of the reflector to 14 cm past the core center.

TABLE II-4-IV. Axial Traverse, Outer Core

Axial Distance From Midplane, in.	Relative Reaction Rate		
	$Pu^{239}(n,f)$	$U^{238}(n,f)$	$B^{10}(n,\alpha)$
0.0	10226 ± 147	1999 ± 24	28751 ± 63
2.0	10411 ± 161	2009 ± 37	28291 ± 176
4.0	9923 ± 176	2013 ± 31	27429 ± 174
6.0	9794 ± 176	1924 ± 37	27423 ± 174
8.0	9274 ± 157	1882 ± 30	25681 ± 168
10.0	9343 ± 160	1765 ± 29	24770 ± 165
12.0	8111 ± 135	1626 ± 24	23672 ± 80
14.0	7581 ± 144	1444 ± 35	23155 ± 159
16.0	7354 ± 138	1227 ± 36	25470 ± 164
17.0	7577 ± 140		
18.0	8327 ± 135	890 ± 31	34458 ± 189
19.0	9847 ± 170		43468 ± 210
20.0	10974 ± 184	489 ± 17	52853 ± 231
21.0	12036 ± 196		
22.0	13118 ± 187	308 ± 14	63071 ± 251
23.0	12383 ± 196		65099 ± 255
24.0	12087 ± 165	181 ± 8	63751 ± 126
26.0	10686 ± 171	117 ± 6	57776 ± 240
28.0	8190 ± 138	80 ± 4	45781 ± 214
30.0	5870 ± 107	71 ± 3	32922 ± 181

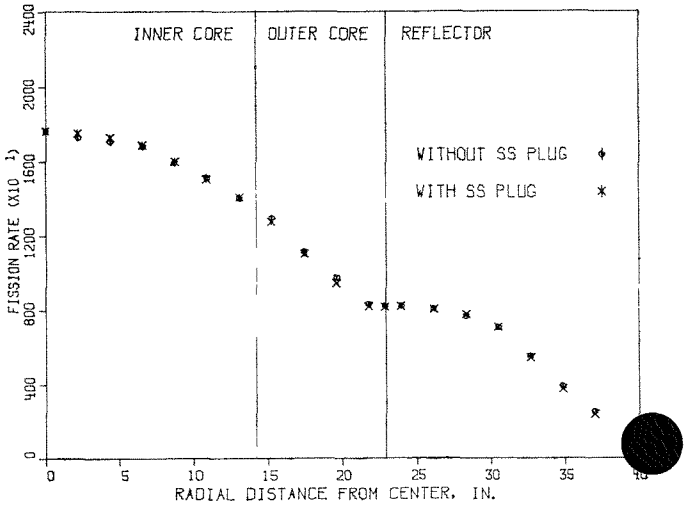

FIG. II-4-1. $Pu^{239}(n,f)$ Reaction Rate, Radial Traverse Near Reactor Midplane. *ANL Neg. No. 116-401.*

The axial traverses were made using a special "L" shaped drawer which provided a 2.7 x 2.7 cm void extending the entire length of the core. The different detectors were placed in a 2.6 x 2.6 cm drawer which was then traversed through the void using the Doppler oscillator equipment. The inner core axial traverse was done in the central matrix position S/M 23–23. The axial traverse in the outer core was done in matrix position S/M 15–24. In both cases the "L" drawer was loaded to provide atom density ratios as close as possible to those of the surrounding drawers.

The $Pu^{239}(n,f)$ and $U^{238}(n,f)$ measurements were made with a 2.54 cm diam gas flow counter similar in design to F. S. Kirn's design.[1] The fissionable material with electrolytically deposited to a thickness of 20 $\mu g/cm^2$ on a polished stainless steel disk. The disk served as one end of the detector and was positioned perpendicularly to the direction of traverse. The composition of the Pu-239 foil was 98.94% Pu-239, 1.01% Pu-240 and 0.05% Pu-241. The composition of the U-238 foil was 99.99% U-238 and 0.014% U-235. Because of the high purity of the foils no corrections were made for isotopic composition. The counting results were corrected for background as a function of detector position. This was accomplished by recording fission spectra at different points along the traverse and determining the background correction from these spectra.

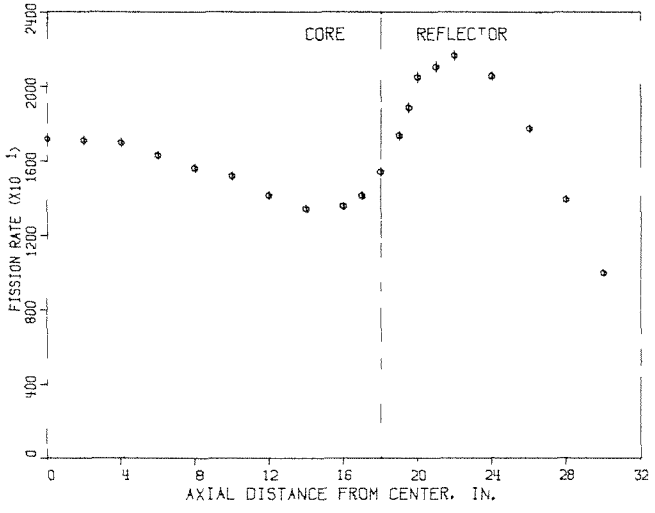

FIG. II-4-2 $Pu^{239}(n,f)$ Reaction Rate, Axial Traverse, Inner Core. *ANL Neg No. 116-399.*

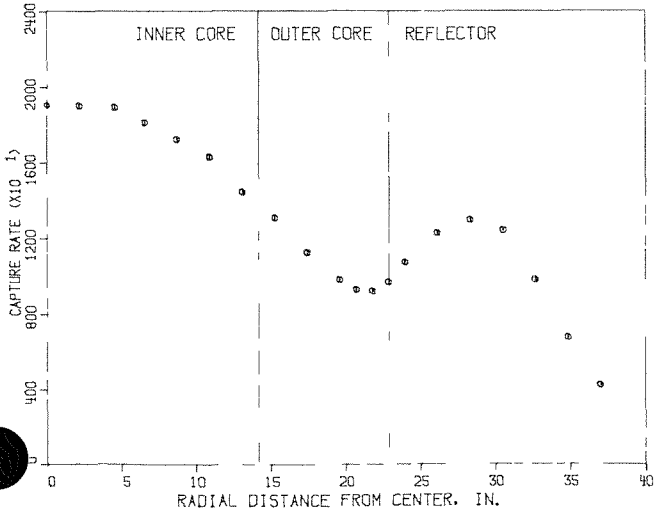

FIG. II-4-3. $B^{10}(n,\alpha)$ Reaction Rate, Radial Traverse Near Reactor Midplane. *ANL Neg No. 116-402.*

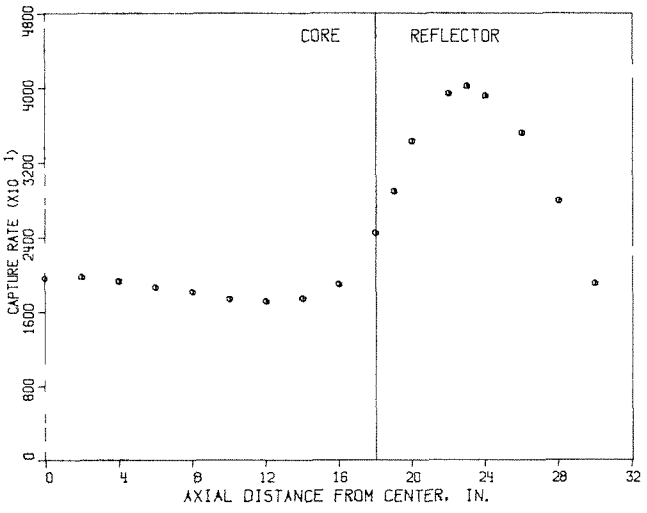

FIG. II-4-4. $B^{10}(n,\alpha)$ Reaction Rate, Axial Traverse, Inner Core. *ANL Neg. No. 116-398.*

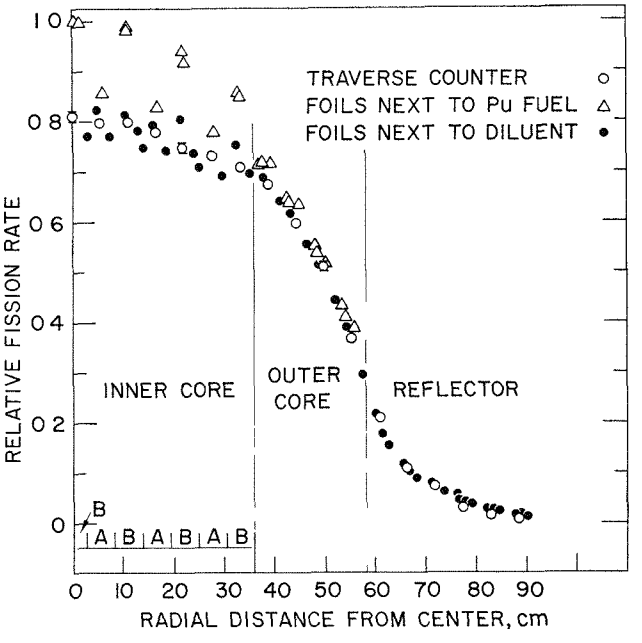

FIG. II-4-5. Comparison of Foil and Counter Data for U^{238} (n,f) Radial Traverse Near Reactor Midplane. *ANL Neg. No. 116-140 Rev. 1.*

TABLE II-4-V. U-238 RADIAL FISSION DISTRIBUTION NEAR MIDPLANE MEASURED WITH FOILS

Distance from Core Centerline, cm	Relative Fission Activity, Counting Error <1%	Foil Location			Distance from Core Centerline, cm	Relative Fission Activity, Counting Error <1%	Foil Location		
		Drawer Type	Intra Cell Plate Components				Drawer Type	Intra Cell Plate Components	
			Left Plate	Right Plate				Left Plate	Right Plate
3.0	0.772	Inner Core Type A	SS Drawer	Na	37.4	0.717		Pu-SEFOR	Fe_2O_3
14.0	0.750				42.9	0.638			
25.1	0.708				48.4	0.538			
					53.9	0.410			
4.9	0.824		Na	Fe_2O_3					
15.9	0.794				37.7	0.689		Fe_2O_3	Na
27.0	0.734				43.2	0.618			
					48.7	0.514			
5.8	0.858		Pu-U-Mo	Fe_2O_3	54.2	0.389			
16.9	0.828								
27.9	0.779				39.3	0.716		Fe_2O_3	Pu-U-Mo
					44.8	0.635			
7.4	0.771		Na	U_3O_8	50.3	0.516			
18.5	0.741				55.8	0.389			
29.5	0.690								
					40.9	0.641		Na	U_3O_8
10.4	0.864	Inner Core Type B	Na	SS	46.4	0.556			
21.4	0.805				51.9	0.445			
32.5	0.753				57.4	0.296			
0.3	1.000		SS	Pu-Al	60.1	0.219	Radial Reflector	Na	Ni or SS
10.7	0.981				65.6	0.118			
21.8	0.940				71.1	0.0706			
32.8	0.858				76.6	0.0471			
					82.2	0.0309			
11.0	0.987		Pu-Al	Na	87.7	0.0180			
22.1	0.918				95.7	0.0105			
33.1	0.852								
					61.3	0.177		Ni or SS	Ni or SS
12.9	0.783		Na	U_3O_8	66.9	0.101			
24.0	0.736				72.4	0.0624			
35.0	0.697				77.9	0.0417			
					83.4	0.0262			
36.7	0 712	Outer Core	$NaCO_3$	Pu-SEFOR	90.2	0.0154			
42.3	0.645								
47.8	0.552				62.6	0.155		Na	Ni or SS
53.3	0.432				68.1	0.0894			
					73.7	0.0575			
					79.2	0.0378			
					84.7	0.0231			
					90.2	0.0137			
					95.7	0.0066			

The $B^{10}(n,\alpha)$ measurements were made with a back-to-back cylindrical gas flow proportional counter designed by L. S. Beller.[2] The detector was divided along its length to form two half cylinders, one containing the B-10 source and the other a blank. The source covered an area 5.5 x 0.95 cm^2 and was positioned parallel to the direction of traverse. The B-10 data were corrected for background, using the counts from the blank half of the detector.

A detailed U-238 foil irradition was performed to measure the perturbation of the counters and the traverse void. The irradiation consisted of a radial traverse near the reactor midplane in which the foils were placed between a number of different plates in each drawer, and a central axial traverse which consisted of placing foils between three different types of plates along the full length of the core and reflector. The depleted foils which were used were 0.012 cm thick and 1.59 cm in diam. After irradiation the foils were counted for fissions and the data analyzed according to

standard techniques.[3] The foil irradiations were carried out in the reference core configuration without any traverse void and without the autorod.

Results

The results of the $Pu^{239}(n,f,)$ $U^{238}(n,f)$ and $B^{10}(n,\alpha)$ counter reaction rate traverses for the central radial traverse, the core-reflector interface traverse, the inner core axial traverse, and the outer core axial traverse are given in Tables II-4-I through II-4-IV, respectively. In addition, the data for the central radial and axial inner core traverses are plotted in Figs. II-4-1 through II-4-6. The traverse data have not been corrected for the efficiency of the detectors or for the mass of the foils; therefore, the results of traverses with different foils cannot be compared directly.

In order to check the effects of neutrons streaming down the void a 1 in. long by 1 in. diam stainless steel plug was placed in front of the fission detector. Stainless steel of this thickness has an attenuation of approximately 0.6 for the mean energy neutron in the core. With this plug in place the $Pu^{239}(n,f)$ and $U^{238}(n,f)$ central radial traverses and the $U^{238}(n,f)$ inner core axial traverse were remeasured. The results are included in the appropriate tables and it is apparent that any difference is less than the statistical uncertainty of the data. A comparison of the $Pu^{239}(n,f)$ data with and without the plug is shown in Fig. II-4-1.

Because of the misalignment of the reactor matrix it was necessary to make the void used for the radial traverse near the core-reflector interface larger than the size required by the detector. The effect of this increased void on neutron streaming was measured by using plates having the proper size traverse hole in the reflector region. The $U^{238}(n,f)$ counter traverse was then rerun in the modified region and the count rate decreased by approximately 6% as indicated in Table II-4-II.

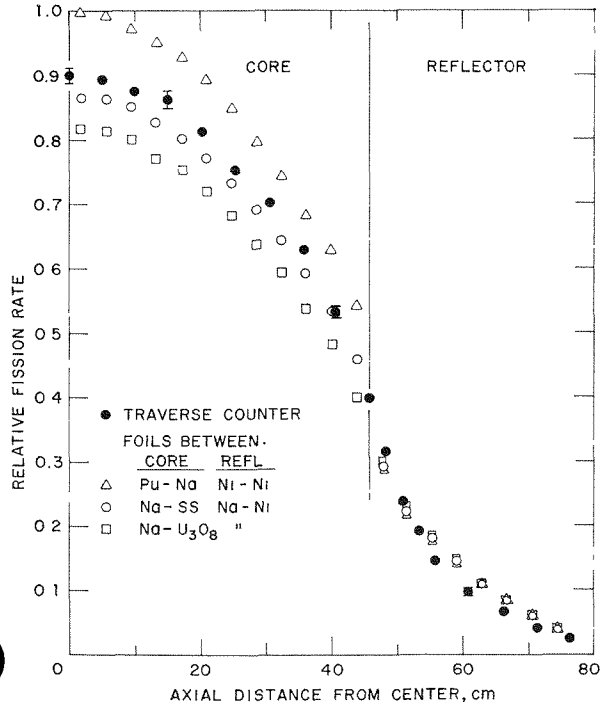

FIG. II-4-6. Comparison of Foil and Counter Data for $U^{238}(n,f)$ Axial Traverse, Inner Core. *ANL Neg. No. 116-400.*

TABLE II-4-VI. U-238 AXIAL FISSION DISTRIBUTION, INNER CORE, MEASURED WITH FOILS

Distance from Core Centerline, cm	Relative Fission Activity, Counting Error < 1%; Inner Core Type B Drawer—Intra Cell Foil Locations		
	Left Plate—Na Right Plate—SS	Left Plate—Pu-Al Right Plate—Na	Left Plate—Na Right Plate—U_3O_8
1.9	0.865	0.998	0.816
5.7	0.864	0.992	0.814
9.5	0.852	0.972	0.799
13.3	0.827	0.952	0.770
17.2	0.802	0.927	0.752
21.0	0.773	0.891	0.720
24.8	0.734	0.848	0.681
28.6	0.690	0.796	0.636
32.4	0.643	0.744	0.594
36.2	0.592	0.684	0.536
40.0	0.534	0.628	0.482
43.8	0.460	0.543	0.399
	Axial Reflector—Intra Cell Foil Locations (continuation of above traverses)		
	Left Plate—Na Right Plate—Ni	Left Plate—Ni Right Plate—Ni	Left Plate—Na Right Plate—Ni
47.6	0.292	0.290	0.304
51.4	0.221	0.218	0.230
55.3	0.179	0.175	0.189
59.1	0.143	0.141	0.150
62.9	0.112	0.106	0.109
66.7	0.085	0.081	0.083
70.5	0.060	0.058	0.060
74.3	0.039	0.039	0.039

The results of the central radial and axial $U^{238}(n,f)$ foil traverses are presented in Tables II-4-V and II-4-VI respectively. A comparison between these two foil traverses and the similar counter traverses, is presented in Figs. II-4-5 and II-4-6. From a traverse with a fission counter across the center drawer it was found that the counters were insensitive to the intra-cell flux distribution. The foils, on the other hand, do not produce significant flux perturbations and they are very sensitive to the changes in the intra-cell flux distribution produced by the surrounding plates. This fact should be remembered when measured counter distribu-

tions are interpreted in terms of the actual distribution in a heterogeneous assembly.

References

1. F. S. Kirn, *Neutron Detectors With an Absolute Fission Counter,* Symposium on Neutron Detection, Dosimetry and Standardization, Harwell, England (1962), IAEA 2[illegible] p. 497.
2. L. S. Beller, Argonne National Laboratory (private communication).
3. G. S. Stanford, *The Codes Nurf, Combo, and Twosource for Processing Foil Counting Data,* ANL-7356 (1967).

II-5. Small Sample Reactivity Worth Measurements in ZPR-9 Assembly 26, FTR-3

J. W. Daughtry and R. M. Fleischman*

Introduction

The central reactivity worths of Pu, U, B-10 and an assortment of other materials of interest were measured in ZPR-9 Assembly 26. In addition, radial reactivity worth traverses were made with samples of Pu, U-238, and B-10. These measurements were done as part of the FTR-3 critical experiments program. The plutonium and boron data are of particular interest due to problems that exist in calculating the worths of these materials. The traverse data should prove useful in investigating computational difficulties encountered at core-reflector boundaries and zoned core interfaces.

Reactor Configuration

For these experiments a number of modifications were made to the FTR-3 reference configuration described in Paper II-2. The modifications were: 1) the insertion hole for the radial sample changer, 2) the installation of the autorod, and 3) adjustment at the inner core-outer core boundary to compensate for the reactivity losses due to 1 and 2. The insertion hole was approximately 2.86 cm in diameter located 4.45 cm axially from the core midplane and extended radially along matrix row 23 from the center of the core to the outer edge of the radial shield.

Experimental Method and Equipment

The measurements reported here were made by monitoring the position of the calibrated autorod while pneumatically oscillating the sample in and out of the core. A diagram illustrating the sample oscillation and autorod control systems is shown in Fig. II-5-1. Two boron ion chambers connected in parallel and located above the stationary half of the reactor continuously monitored the neutron population at that location and the servo-control system positioned the autorod to maintain a constant current from these chambers.

The sample changer can hold up to eight samples which can be selected remotely from the reactor control room. The sample transfer tube is of double wall stainless steel construction. A two inch long stainless steel plug at the end of the tube was provided to minimize neutron streaming effects for the off-center measurements. Neutron streaming with this equipment is discussed in Ref. 1. The transfer tube is attached to the sample changer which in turn is mounted on a carriage that can be moved horizontally to position the samples at any point along the radius of the core.

The samples used in these measurements are described in detail in Tables II-5-I and II-5-II. All samples were contained in stainless steel capsules. The reactivity worths of empty capsules were measured in order to make the necessary stainless steel subtractions.

Experimental Results

The integral worth of the autorod was determined by two calibration methods. Both methods utilized computer acquisition of reactor flux data from an ion chamber located on top of the ZPR-9 matrix. The first method was a computer code based on the Hurliman-Schmidt[2] period evaluation. This method gave a value of 5.83 ± 0.12 Ih for the total autorod worth. The second method used inverse kinetics and gave a result of 5.848 ± 0.009 Ih for the worth. This is the average and standard deviation obtained from thirteen measurements. The results obtained by the two methods were in agreement within the accuracy of the measurements. The second result was used in analyzing the data since it was more accurate and because the inverse kinetics method was considered more reliable for the conditions of these calibrations.

The linearity of the autorod was checked by oscillating a sample, worth about 2.4% of the total autorod worth, with the autorod at different positions along its total travel. The results of 34 observations of the sam-

* WADCO Corporation, a Subsidiary of Westinghouse Electric Corporation, Richland, Washington.

ple worth indicated no significant deviation from linearity.

The gross reactivity effect of each sample was determined from the difference in the average position of the calibrated autorod with sample-in and sample-out as the autorod maintained a constant power level during oscillations. The autorod position, $\rho(t)$, was electronically integrated over a 180 or 300 sec interval to give an average position ρ_i. The difference in autorod position corresponding to the sample worth was obtained by grouping the ρ_i's in the form:

$$D_{i-1} = (-1)^{i-1}[\rho_i - \tfrac{1}{2}(\rho_{i+1} + \rho_{i-1})], \qquad (i = 2, \cdots, M-1),$$

where M is the number of ρ_i. There are $N = M - 2$ values of D_k. Treating the data in this manner results in the cancellation of errors caused by linear and second order drift in $\rho(t)$, when one obtains the average:

$$\bar{D} = \frac{1}{N}\sum_{k=1}^{N} D_k .$$

Several position integrations were made with the autorod at its most reactive position, A, and at its least reactive position, B. The gross worth, W, of a sample as a fraction of the total autorod worth, is

$$W = \frac{\bar{D}}{B - A}$$

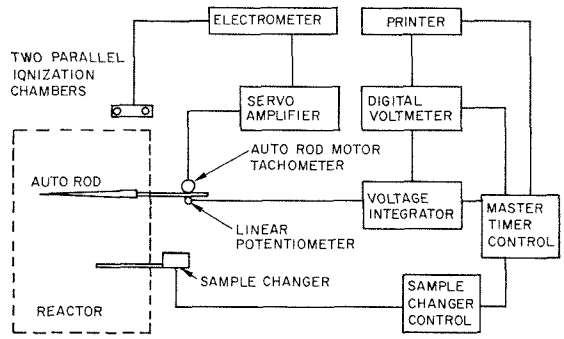

FIG. II-5-1. Radial Sample Changer and Autorod Control Diagram. *ANL Neg. No. 116-437.*

TABLE II-5-I. PERTURBATION SAMPLE DESCRIPTIONS

Sample Identification	Material Element or Isotope	State	Geometry	Dimensions, in.			Sample Wt, g	Sample Composition
				OD	Thickness	Length		
Ta-4	Tantalum	Solid	Annulus	0.378	0.021	2.174	13.859	Natural
Ta-5	Tantalum	Solid	Annulus	0.378	0.011	2.175	5.893	Natural
Fe-1	Iron	Solid	Cylinder	0.389	—	2.172	33.277	Natural
Fe_2O_3-2	Iron Oxide	Powder	Cylinder	0.401	—	2.169	5.265	Natural
Al-1	Aluminum	Solid	Cylinder	0.390	—	2.173	11.437	Natural
Al_2O_3-3	Aluminum Oxide	Solid	Cylinder	0.376	—	2.174	15.061	Natural
B-7	B-10	Powder	Annulus	0.400	0.0094	2.1733	0.4968	Enriched[a]
Poly-1	Polyethylene	Solid	Cylinder	0.390	—	2.173	4.024	Natural
Pu-7	Plutonium	Solid	Annulus	0.390	0.005	2.175	2.7059	R-524[b]
Pu-9	Plutonium	Solid	Annulus	0.390	0.015	2.173	8.8533	R-524
Pu-11	Plutonium	Solid	Annulus	0.390	0.025	2.173	15.1219	R-524
Pu-13	Plutonium	Solid	Annulus	0.390	0.005	2.172	3.0306	R-528
Pu-15	Plutonium	Solid	Annulus	0.390	0.015	2.173	8.5102	R-528
Pu-17	Plutonium	Solid	Annulus	0.390	0.025	2.1725	13.9392	R-528
Pu-19	Plutonium	Solid	Annulus	0.390	0.005	2.173	3.4424	R-529
Pu-21	Plutonium	Solid	Annulus	0.390	0.015	2.173	8.5079	R-529
Pu-23	Plutonium	Solid	Annulus	0.390	0.025	2.172	13.9231	R-529
MB-20	U-235	Solid	Annulus	0.835	0.005	1.6875	5.23061	Enriched[c]
MB-21	U-235	Solid	Annulus	0.835	0.015	1.6875	15.77801	Enriched[c]
MB-23	U-238	Solid	Annulus	0.835	0.005	1.6875	6.31491	Depleted[d]
MB-24	U-238	Solid	Annulus	0.835	0.015	1.6875	19.07423	Depleted[d]
MB-25	U-238	Solid	Annulus	0.835	0.030	1.6875	38.16314	Depleted[d]
D-1	304 SS	Dummy						
D-29	304 SS	Dummy						
D-33	304 SS	Dummy						
D-37	304 SS	Dummy						
MB-19	304 SS	Dummy						

[a] 92.88 w/o B-10.
[b] Melt No.; see Table II-5-II.
[c] 0.661759 w/o U-234, 93.17648 w/o U-235, 0.317281 w/o U-236, 5.844484 w/o U-238.
[d] 0.232774 w/o U-235, 99.767225 w/o U-238.

and

$$S_W = \frac{S_{\bar{D}}}{B - A}$$

where S_W is the uncertainty in W and $S_{\bar{D}}$ is obtained by the method of Bennett and Long.[3]

An independent method for obtaining the difference in the autorod position with sample-in and with sample-out of the core was developed. This method consists of a least squares analysis of the ρ_i's versus time with the sample-out ρ_i's carrying on additive normalization constant that is determined from the fitting process. This normalization constant is the difference in autorod position that gives the sample worth.

The results of the two independent methods of analysis did not differ significantly; however, the calculated uncertainty using the least squares technique was generally slightly less. The results that are given in the accompanying tables are based on the method of Bennett and Long since this method was used in reporting results obtained in past FTR cores.

The gross sample worths were converted to inhours by multiplying W by the worth of the autorod. The worth of the sample material was obtained by subtracting the worth of the stainless steel. The specific worth was then obtained by dividing the sample worth by the weight of the sample material. The empty capsule worth measurements were used to give a specific worth for stainless steel which in turn was multiplied by the weight of stainless steel in each of the other capsules to give the appropriate stainless steel worth to be subtracted from the measured gross worth. A radial worth traverse was made with sample MB-19 to provide a stainless steel subtraction for the U-238 traverse made with sample MB-25. The traverse data obtained with sample D-29 was used to obtain the stainless steel subtractions for both the B-10 and Pu traverses since these capsules were of similar design.

The results of the radial worth traverses are shown in Fig. II-5-2. The results of the central worth measurements are given in Table II-5-III.

TABLE II-5-II. Plutonium Sample Compositions

Melt No. R-	Major Elements, w/o		Gas Analysis,[a] ppm		
	Pu[b]	Al[c]	H_2	O_2	N_2
524	98.96	1.10	1	72	84
528	98.39	1.27	4	224	54
529	97.67	1.20	2	340	35

	Isotopic Composition,[d] w/o					
	Pu-238	Pu-239	Pu-240	Pu-241	Pu-242	Am-241
524	0.005	86.273	11.461	2.084	0.178	0.134
528	0.002	73.502	22.033	3.841	0.625	0.624
529	0.191	40.964	42.258	12.090	4.688	0.946

	Minor Elements,[e] ppm				
	Fe	Ni	Cr	Y	C
524	150	50	10	400	380
528	100	10	10	200	230
529	100	50	5	1000	230

[a] ±5.00%.
[b] ±0.30%.
[c] ±5.00%.
[d] Within 0.01%.
[e] Factor of two.

TABLE II-5-III. Results of Small Sample Central Worth Measurements

Sample Identification	Stainless Steel Weight, g	Sample Worth	Standard Deviation	Specific Worth	Standard Deviation
		Ih		Ih/kg	
Ta-4	20.579	−1.1604	0.0032	−83.73	0.23
Ta-5	20.302	−0.5617	0.0045	−95.33	0.78
Fe-1	20.740	−0.1809	0.0044	−5.44	0.13
Fe_2O_3-2	20.878	−0.0302	0.0061	−5.7	1.1
Al-1	20.668	−0.0925	0.0089	−8.09	0.78
Al_2O_3-3	20.391	−0.1354	0.0089	−8.99	0.59
B-7	31.033	−2.2521	0.0094	−4533	19
B-7	31.033	−2.2468	0.0074	−4523	15
Poly-1	20.824	1.7746	0.0042	441.0	1.0
Pu-7	21.107	0.600	0.010	221.7	3.7
Pu-9	20.983	1.9734	0.0099	223.0	1.1
Pu-11	31.370	3.3925	0.0079	224.34	0.53
Pu-11	31.370	3.4364	0.0080	227.24	0.53
Pu-11	31.370	3.435	0.011	227.13	0.75
Pu-13	20.814	0.5915	0.0072	195.2	2.4
Pu-15	21.561	1.6845	0.0065	197.93	0.77
Pu-17	21.174	2.8145	0.0057	201.91	0.42
Pu-19	21.159	0.5226	0.0050	151.8	1.5
Pu-21	21.069	1.3149	0.0058	154.56	0.69
Pu-23	21.214	2.1709	0.0089	155.92	0.64
MB-20	48.404	0.955	0.017	182.5	3.2
Mb-21	48.240	2.876	0.011	182.30	0.71
MB-23	48.370	−0.1112	0.0095	−17.6	1.5
MB-24	48.345	−0.307	0.010	−16.11	0.52
MB-25	48.185	−0.583	0.015	−15.27	0.39
MB-25	48.185	−0.5715	0.0096	−14.98	0.25
MB-25	48.185	−0.574	0.012	−15.03	0.32
D-1	21.069	−0.1433	0.0052	−6.80	0.25
D-1	21.069	−0.1433	0.0017	−6.800	0.083
D-29	30.809	−0.2240	0.0041	−7.27	0.13
D-29	30.809	−0.2143	0.0081	−6.96	0.27
D-33	28.258	−0.2035	0 0046	−7.20	0.16
D-37	27.522	−0.1842	0.0070	−6.69	0.26
MB-19	48.295	−0.3234	0.0070	−6.70	0.15

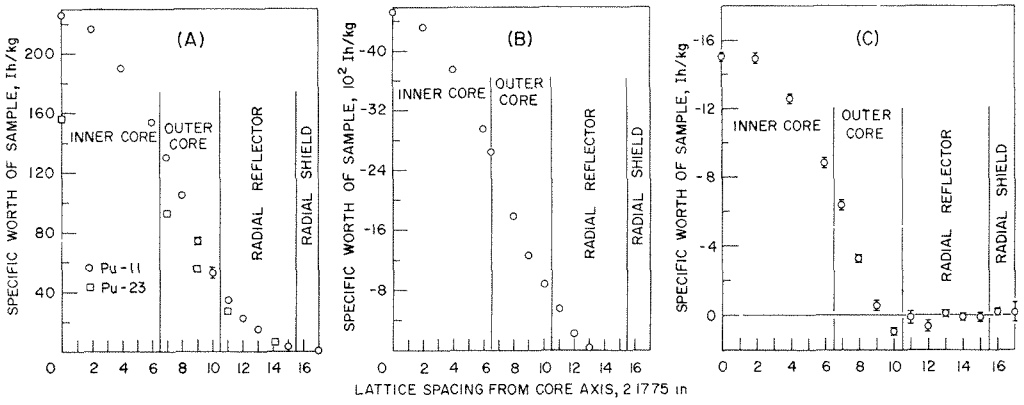

FIG. II-5-2. Radial Worth Traverses, ZPR-9 Assembly 26, FTR-3: (A) Pu; (B) B-7; (C) MB-25. *ANL Neg. No. 116-520.*

REFERENCES

1. L. G. LeSage, E. F. Groh and W. R. Robinson, *An Investigation of the Properties of Zoned Cores,* Reactor Physics Division Annual Report, July 1, 1967 to June 30, 1968, ANL-7410, pp. 145–151.
2. T. Hurliman and P. Schmid, *Determination of the Stable Reactor Period in the Presence of a Neutron Source,* Nucleonik **5,** No. 6, 236–239 (1963).
3. E. F. Bennett and R. L. Long, *Precision Limitations in the Measurement of Small Reactivity Changes,* Nucl. Sci. Eng. **17,** 425–432 (1963).

II-6. Plutonium and U-238 Doppler Measurements in ZPR-9 Assembly 26, FTR-3

R. B. POND, J. W. DAUGHTRY, C. E. TILL, E. F. GROH, C. D. SWANSON and P. H. KIER

INTRODUCTION

The Doppler effects of plutonium and U-238 have been measured in the plutonium-fueled Assembly 26 of ZPR-9. This assembly was one of a series specifically planned to provide physics information needed in the design of the Fast Test Reactor (FTR). A complete description of this assembly (also designated FTR-3 in the series of FTR criticals) is given in Paper II-2.

DOPPLER MEASUREMENT TECHNIQUE

The Doppler measurement method used at ANL is the sample oscillation-reactivity difference technique. In this technique, a Doppler sample and a reference sample are periodically exchanged at the point in the reactor where the Doppler effect is to be measured. A calibrated servo-controlled autorod is used to maintain the reactor critical with either sample in place in the reactor. The difference in these autorod positions gives the reactivity worth of the sample relative to the reference. This oscillation procedure is repeated for various Doppler sample temperatures to obtain the reactivity change as a function of Doppler sample temperature.

EXPERIMENTAL EQUIPMENT

DOPPLER-OSCILLATOR DRAWER

A Doppler-oscillator drawer, running through both reactor halves, was substituted for the normal central matrix drawers of the reactor. This drawer was attached to a train arrangement which periodically oscillated the Doppler and reference samples to a position at the reactor midplane. The drawer construction was such that when either sample was at the midplane, the other sample was entirely outside the critical reactor. The remainder of the drawer in line with the sample positions was loaded to be as nearly identical to the normal core drawer loading as was consistent with the requirement of maintaining a maximum of a few inhours reactivity swing as the Doppler and reference samples were oscillated. The oscillator platform also held the associated equipment for heating the sample and monitoring its temperature, and the vacuum and cooling systems used to thermally isolate the heated sample from the cool reactor.

AUTOROD DRAWER

An autorod drawer, also running through both reactor halves, was substituted for the usual matrix

drawers 15.4 in. from the center of the reactor. This drawer contained a servo-controlled, wedge shaped polyethylene blade, the length of which exceeded the active core length of the reactor. Over the total travel of the blade, the amount of polyethylene in the core at any time was a linear function of the relative rod position. On either side of the blade, the drawer was loaded with the reactor constituent materials of the region in which the drawer was located.

The autorod position was indicated by electronically integrating the voltage across a linear helipot attached directly to the rod. Figure II-6-1 is a block diagram of the Doppler oscillator and autorod systems.

DOPPLER SAMPLES

Three Doppler samples were used in these measurements: (1) a freely expandable (FE) $^{238}UO_2$ sample; (2) a freely expandable PuO_2 sample; and (3) a constrained expansion (NNE) PuO_2 sample. The samples were of a reduced density ceramic form, nominally 1 kg in weight, 12 in. long and 1 in. in diam.

The expansion reactivity effect has been found to be negligible for the $^{238}UO_2$ sample; however, for fissile materials the expansion effect cannot be ignored. The two PuO_2 samples were designed with different expansion characteristics in order to investigate this effect. The sample's radial expansion characteristics are determined by the jacket material used to can the various samples and the axial characteristics by the end

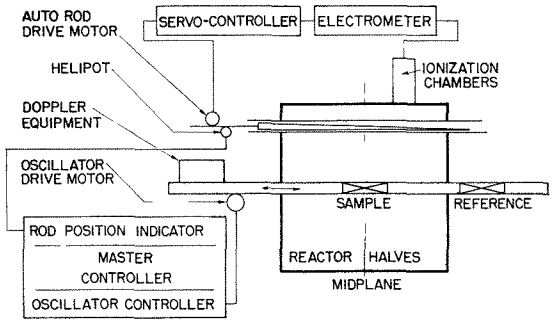

FIG. II-6-1. Doppler Oscillator and Autorod Systems. *ANL Neg. No. 116-416.*

TABLE II-6-I. DOPPLER SAMPLE MATERIAL SPECIFICATIONS

Sample Identification	Expansion Type	Sample Material	Form	Total Sample Weight, kg	Heavy Metal Weight,[a] kg	Active Sample Length, in.
N-1	FE	UO_2	Pellets	1.26629	1.11687	12.0000
INC-5	FE	PuO_2	Powder	1.04122	0.92351	12.7500
INV-3	NNE	PuO_2	Powder	1.05928	0.92822	12.1875

[a] N-1: 99.28 w/o U-238; 0.72 w/o U-235; 0.01 w/o U-234. INC-5 and INV-3: 85.92 w/o Pu-239; 11.46 w/o Pu-240; 2.43 w/o Pu-241; 0.18 w/o Pu-242.

TABLE II-6-II. DOPPLER CAPSULE DIMENSION SPECIFICATIONS

	Dimensions, in.		Material
	O.D.	Wall Thickness	
Thermocouple probe			
Wires			Chromel-Alumel
Sheath	0.075		Inconel
Thermocouple well	0.125	0.020	Inconel
Sample material	1.010[a]		UO_2 or PuO_2
	1.050[b]		
Inner jacket[c]	1.150	0.050	Inconel
	1.150	0.070	Invar
Heater coil[d]	1.200		Inconel
Outer tube			
Silver lining	1.474	0.005	Polished silver
Stainless steel	1.566	0.046	Stainless steel
Capsule cover		0.050	Stainless steel
Oscillator drawer	2.000	0.050	Stainless steel
Matrix tube	2.173	0.040	Stainless steel

[a] Outside diameter of sample material in Invar jacket.
[b] Outside diameter of sample material in Inconel jacket.
[c] Jacket threaded on outer surface to a depth of 0.030 in. to accommodate a 0.055 in. o.d. co-axial heater coil.
[d] Heater is an Inconel wire inside an Inconel sheath with Al_2O_3 insulation.

supports. The FE samples were canned in Inconel which has a thermal expansion coefficient larger than that of the sample material. The NNE sample was canned in Invar which has a thermal expansion coefficient smaller than that of the sample material over a temperature range of 300–500°K. Above 500°K the expansion of Invar parallels that of Inconel. The FE samples had spring loaded end supports and the NNE sample had rigidly fixed end supports in order to prevent any axial expansion. A complete description of the PuO_2 samples and the expansion characteristics of these types of samples are given in Refs. 1 and 2.

Tables II-6-I and II-6-II give the Doppler capsule specifications and Fig. II-6-2 shows a cross section of the capsule as loaded in the oscillator drawer in a reactor matrix tube.

REACTOR ENVIRONMENT

The Doppler measurements were made in a reactor environment slightly different from the usual core drawers surrounding the Doppler oscillator drawer. Figure II-6-3 shows the reactor materials in the core drawer loadings of the drawers immediately surrounding the oscillator drawer.

The contents of the drawers immediately above and below the oscillator were rotated 90 deg, and in all drawers the ¼ in. of U_3O_8 nearest the oscillator was replaced with stainless steel. In effect, a ¼ in. stain-

less steel ring or filter, extending the entire active axial length of the core, was inserted between the sample and the reactor core. The purpose of this filter was to reduce the hot sample-cold reactor resonance interaction effect. A previous detailed study[3] of this effect indicated that this additional amount of stainless steel should reduce the interaction effect to insignificant proportions.

Experimental Results

A probe containing 5 thermocouples was used to measure the axial temperature profile of the Doppler samples during the reactivity measurements. The thermocouples were located approximately 0.5, 2.5, 6.0, 9.5 and 11.5 in. into the nominally 12 in. long samples.

During each oscillation in which the Doppler sample was in the reactor, the temperature profile was recorded. An effective average sample temperature was then calculated from the function of a 5 coefficient polynomial fitted to the profile. These effective average temperatures were then averaged over the period of data taking in which the reactivity difference measurements between the Doppler and reference samples were also being made. The reactivity data analysis was done by the method of Ref. 4 which allows elimination of both first- and second-order reactor reactivity drifts.

DOPPLER-EFFECT MEASUREMENTS

Table II-6-III lists the results of the Doppler measurements. The listed reactivity changes are per kilogram of heavy metal in each sample from the reference temperature to the indicated temperature. For the uranium sample, the reference temperature was 293°K; for the plutonium samples, due to self-heating of the sample, the reference was approximately 305°K.

Figure II-6-4 shows a plot of the tabulated data.

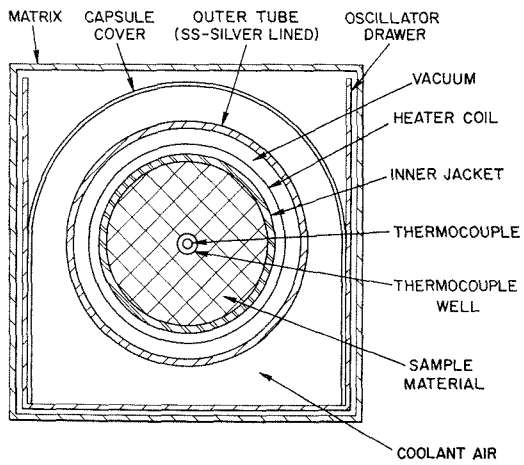

Fig. II-6-2. Cross Sectional View of Doppler Capsule. *ANL Neg. No. 116-417.*

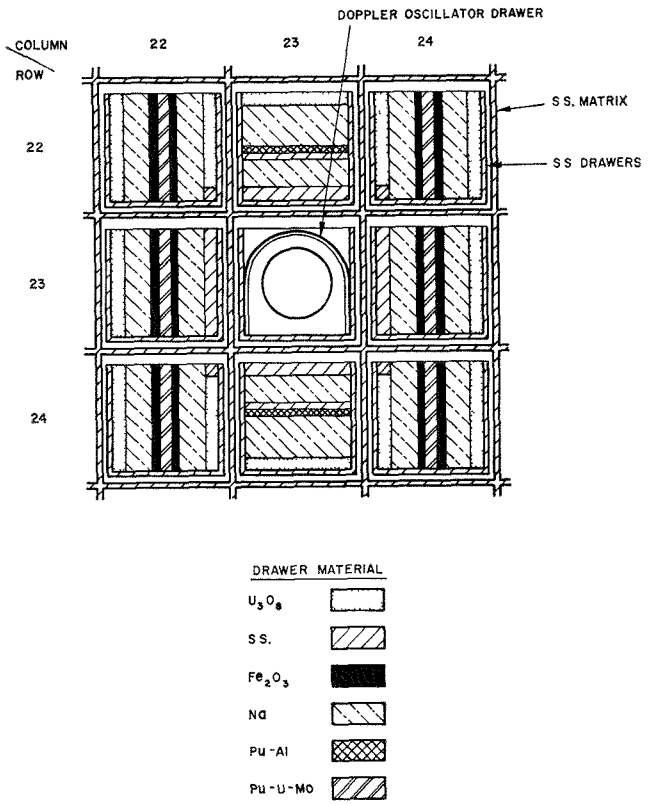

Fig. II-6-3. Modified Core Surrounding Doppler-Oscillator Drawer. *ANL Neg. No. 116-418.*

The curves are a result of a least squares fit of the data to the function $\delta\rho/\delta T \alpha T^{-\gamma}$, where γ is a constant. For N-1, the U-238 sample, γ was 0.8, a result similar to previous work on uranium cores.

The plutonium data, INC-5 and INV-3, have also been fitted to this form, although the resultant value of γ is not expected to have the same physical significance it has for the U-238 data, because of the presence of expansion effects. The value of γ was found to be 0.0 for INC-5 and 0.5 for INV-3, but the latter data could be fitted almost as well with a straight line. In the fit of the INV-3 data shown in the figure, the 359°K point was deleted and the dotted curve from 800–1100°K is an extrapolation of the data with γ equal to 0.5. In case of a linear fit, the extrapolated value at 1100°K is approximately 10% larger than the value shown.

Discussion of Results

The freely expanding PuO_2 sample indicates that the plutonium Doppler effect is negative and is approximately linear over the temperature range of these investigations. The constrained expansion PuO_2 sample indicates that the expansion reactivity effect is relatively small and negative.

TABLE II-6-III. FTR-3 Experimental Doppler Results

Sample	Average Temperature, °K	Standard Deviation in Average Temperature, ±°K	Average Reactivity Worth,[a] Ih/kg	Standard Deviation in Average Reactivity Worth, ±Ih/kg
N-1	293.2	0.0	0.000	0.010
	782.8	0.6	−1.006	0.004
	1071.0	0.2	−1.371	0.002
	783.4	1.0	−1.002	0.006
INC-5	303.0	0.0	0.000	0.007
	792.1	0.4	−0.527	0.003
	1064.3	0.3	−0.837	0.007
INV-3	307.7	0.0	0.000	0.009
	359.0	0.4	−0.013	0.004
	392.8	1.9	−0.071	0.008
	382.7	0.7	−0.073	0.004
	413.1	0.4	−0.097	0.005
	438.6	0.6	−0.108	0.006
	473.9	0.9	−0.144	0.004
	521.5	0.7	−0.199	0.004
	572.1	0.7	−0.253	0.006
	615.1	1.5	−0.295	0.005
	599.5	1.8	−0.270	0.008
	634.7	1.5	−0.314	0.003
	653.3	0.8	−0.311	0.013
	679.5	1.9	−0.322	0.007
	694.4	2.2	−0.345	0.004
	718.3	0.9	−0.359	0.006
	785.1	3.0	−0.411	0.003

[a] 1% $\Delta k/k$ = 1064 Ih.

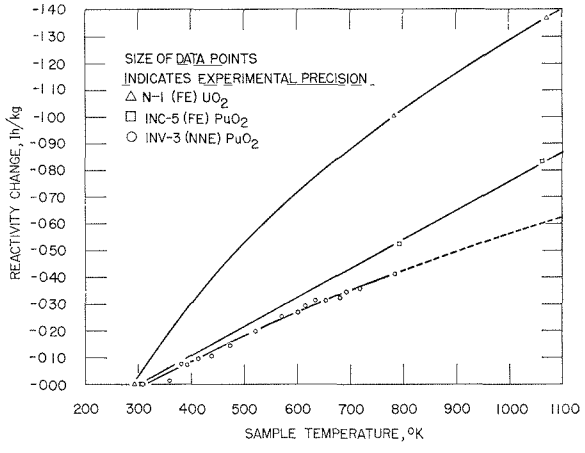

Fig. II-6-4. FTR-3 Experimental Doppler Results. *ANL Neg. No. 116-410.*

The two major Doppler-effect contributions in the PuO_2 samples come from Pu-239 (85.9 w/o) and Pu-240 (11.5 w/o). The separate contributions from these two isotopes have not been assessed. Previous Pu-239 measurements[5,6] have indicated a near-zero Doppler effect over the same temperature range as these measurements. However, the previous Pu-239 measurements relied heavily upon the calculated expansion reactivity effect in $^{239}PuO_2$ samples and the prorating of the U-238 component in $^{238}U^{239}PuO_2$ samples. The present measurements could also be interpreted as showing a small plutonium Doppler effect for the constrained PuO_2 sample over the first fifty degree change in temperature, but the remainder of the data up to 500°K, where the expansion is expected to be minimal, appears to be inconsistent with this one data point.

For the uranium data, the curve shown in the figure is essentially the U-238 Doppler effect since expansion effects have previously been shown to be negligible and since the Doppler effect due to the small percentage of U-235 in natural uranium is not expected to be of any significant consequence.

A Doppler effect calculation for this sample was made and the results, shown in Table II-6-IV, underestimated the two experimental measurements by approximately 3%. This agreement is better than the 25% underestimate, for similar calculations in uranium fueled reactors, using the same set of prescriptions for both Doppler effect calculations. Briefly, the prescription used to calculate these Doppler effects is the following. Homogeneous cross sections for each regional composition of the reactor are generated with MC²,[7] using ENDF/B, version 1, data, and then corrected for spatial resonance self-shielding using equivalence theory. These cross sections are then flux- and volume-weighted using unit-cell S_n calculated fluxes to generate effective homogenized unit-cell cross sections. The UO_2 sample cross sections are generated with MC² using a fine-group weighting spectrum characteristic of the reactor core. For the U-238 resolved resonance region, RABBLE[8]-generated U-238 capture cross sections are substituted for the corresponding MC² cross sections. The cross sections for the reactor are then used with two-dimensional diffusion theory to generate real and adjoint fluxes for the reactor when it is unperturbed by the Doppler sample and its surrounding

TABLE II-6-IV. Comparison of Calculated and Measured Reactivity Change for UO_2 Doppler Sample

Data Point	Temperature, °K	Reactivity Change, Ih/kg	
		Measured	Calculated
1	293.2 ± 0.0	0.0 ± 0.010	—
2	782.8 ± 0.6	−1.006 ± 0.004	—
3	783.4 ± 1.0	−1.002 ± 0.006	—
4[a]	783.1 ± 0.5	−1.004 ± 0.003	−0.979
5	1071.0 ± 0.2	−1.371 ± 0.002	−1.320

[a] Data point 4 is the average of the data for points 2 and 3.

ructure. The reactivity effect due to the change in sample temperature is obtained from two-dimensional perturbation theory using effective U-238 broad-group capture cross sections which include sample flux perturbation and resonance interaction effects, which are obtained by the procedure described by Lewis and Johnson.[3]

References

1. J. E. Ayer, C. F. Konicek, F. E. Soppet and E. J. Petkus, *The Manufacture of Vibratorily Compacted Fuel Elements for Doppler-Coefficient Measurements*, ANL-7647 (1970).
2. C. E. Till, R. A. Lewis and E. F. Groh, *U-235 Doppler Effect Measurement Data and Techniques*, Reactor Physics Division Annual Report, July 1, 1966 to June 30, 1967, ANL-7310, pp. 151–158.
3. R. A. Lewis and T. W. Johnson, *Sensitivity of Small-Sample Doppler-Effect Measurements to Environment*, Reactor Physics Division Annual Report, July, 1, 1967 to June 30, 1968, ANL-7410, pp. 96–103.
4. E. F. Bennett and R. L. Long, *Precision Limitations in the Measurement of Small Reactivity Changes*, Nucl. Sci. Eng. **17**, 425 (1963).
5. G. J. Fischer, D. A. Meneley, R. N. Hwang, E. F. Groh and C. E. Till, *Doppler Effect Measurements in Plutonium-Fueled Fast Power Breeder Reactor Spectra*, Reactor Physics Division Annual Report, July 1, 1964 to June 30, 1965, ANL-7110, pp. 120–124.
6. J. M. Gasidlo, *Results of Recent Doppler Experiments in ZPR-3*, Proc. Conference on Fast Critical Experiments and Their Analysis, October 10–13, 1966, ANL-7320, pp. 345–349.
7. B. J. Toppel, A. L. Rago and D. M. O'Shea, *MC²*, *A Code to Calculate Multigroup Cross Sections*, ANL-7318 (1967).
8. P. H. Kier and A. A. Robba, *RABBLE, A Program for Computation of Resonance Absorption in Multiregion Reactor Cells*, ANL-7326 (1967).

II-7. Analytical Studies in Support of the Fast Flux Test Facility (FFTF) Critical Experiments on ZPPR and ZPR-9

A. Travelli, A. J. Ulrich and J. C. Beitel

Introduction

The Applied Physics Division is involved in a continuing effort to provide basic physics information needed for the design of the Fast Test Reactor (FTR), which is an integral part of the Fast Flux Test Facility (FFTF). The overall responsibility for managing the FFTF project, previously vested with the Pacific Northwest Laboratories (PNL), is now vested with the WADCO Corporation, a subsidiary of the Westinghouse Electric Corporation in Richland, Washington. The Advanced Reactors Division of the Westinghouse Corporation (WARD) in Pittsburgh, Pennsylvania, is the core designer.

One activity of the Applied Physics Division in this connection consists of planning and evaluating a series of critical experiments to be performed on ANL facilities according to the needs of the FTR manager (WADCO) and designer (WARD), and in performing computational studies to evaluate the results of the experiments. Long range planning, as well as detailed and operational planning, are carried out by personnel of Argonne's Applied Physics Division in close cooperation with WADCO and WARD personnel.

The experiments planned and evaluated in the current reporting period were performed in the FTR-2 and FTR-3 assemblies. These experiments are part of the resumed Phase B of the FFTF critical experiments program, and they are a continuation of other studies previously reported (Ref. 1).

FTR-2 on ZPPR

The FTR-2 assembly was built on ZPPR. It comprised a cylindrical core with an axial length of 36.08 in. and a volume of about 1000 liters, surrounded by a B_4C-Na-SS control annulus and by radial and axial reflectors. Figure II-7-1 shows the critical configuration on ZPPR and Fig. II-7-2 gives the dimensions of the volume-equivalent cylindrical loading. The assembly had the same core and reflector compositions as FTR-1, which are given in Table II-7-I. The control ring compositions are given in Table II-7-II.

Calculation of reaction rate traverses in ZPPR/FTR-2

The radial variations of Pu-239 and U-238 fission and B-10 capture detector responses in ZPPR/FTR-2 have been calculated and compared with the experimental results.

The flux distribution was obtained using the 29-group cross-section set 29004.2[(1)] in one-dimensional cylindrical-transport theory in the S-4 approximation. The SNARG-1D[(2)] code was used in the calculations with the transport approximation for the anisotropic scattering.

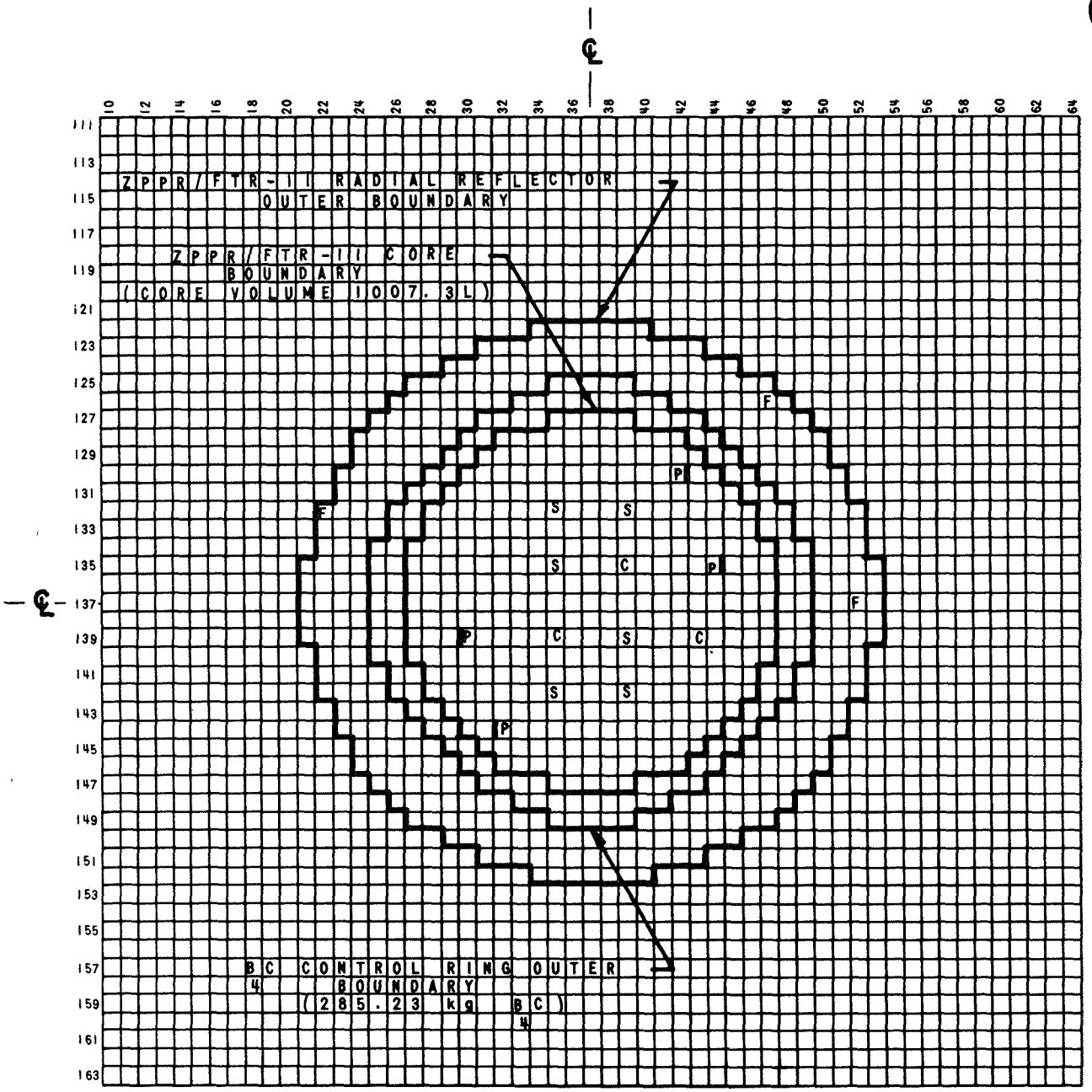

ZPPR HALF 1

(HALF 2 IS A MIRROR IMAGE OF HALF 1)

S = SAFETY ROD C = CONTROL ROD P = DRAWER ADJACENT TO POISON SAFETY ROD

I = POISON SAFETY ROD (WITHDRAWN DURING OPERATION)

F = U-235 FISSION CHAMBER (FRONT OF CHAMBER AT REACTOR MIDPLANE. NO F's IN HALF 2)

FIG. II-7-1. ZPPR/FTR-2 Reference Critical Configuration (Loading 1–70). *ANL-ID-103-A11073.*

The axial leakage was simulated by a DB^2 absorber. The transverse buckling ($6.077 \times 10^{-4}/cm^2$) was obtained through a series of cylindrical and slab calculations converging by iteration to a pair of calculations corresponding to the same k and to transverse bucklings adding up to the material buckling ($1.778 \times 10^{-3}/cm^2$). The value of k obtained through this procedure was 0.9935.

Two reaction rate traverses were computed for each of the three detector types from the neutron flux distribution. The calculation of the first reaction rate traverse used the 29-group cross sections obtained from a 2,100-group fundamental mode $MC^{2(3)}$ flux averaging for the core composition at criticality. The flux was normalized so that the reaction rate obtained in this calculation was unity at the core center. Calculation of the second reaction rate traverse used the 29-group cross sections obtained from a 2,100 fundamental mode MC^2 flux averaging for the reflector composition with zero buckling. The same flux, with the same normalization, was used as in the calculation of the first reaction rate traverse.

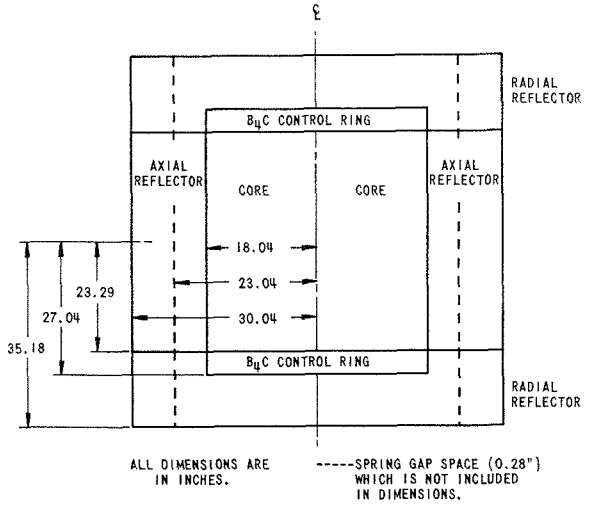

FIG. II-7-2. Equivalent Cylindrical Loading for ZPPR/FTR-2 Reference Loading (Loading 1-70). *ANL-ID-103-A11074.*

The computed responses for the three types of detectors are compared in Fig. II-7-3 with the experimental values.[4] The experimental data are indicated by crosses, the reaction rates obtained in the first calculation (core spectrum averaging) are indicated by the dotted curves labeled "1", and the reaction rates obtained in the second calculation (reflector spectrum averaging) are indicated by the dotted curves labeled "2". Thus, type-1 curves are valid close to the core center, and type-2 curves are valid in the regions well inside the reflector.

Comparison of the Pu-239 and B-10 radial detector response curves with the analogous curves for Assembly 56B[1] shows clearly that the B_4C control ring depresses the Pu-239 and B-10 reaction rates in the reflector and in the outer 20–30 cm of the core. Agreement between calculated and measured responses is

TABLE II-7-I. AS-BUILT COMPOSITION—FTR-1 ON ZPPR, LOADING 17, atoms/b-cm

	Core						
Nuclide	1-Column Pu Drawer[a]	2-Column Pu Drawer[b]	Cell Average	Movable Fuel Rod[c]	Drawer Adjacent to Poison Safety Rod[d]	Axial Reflector	Radial Reflector
Pu-239	0.0008491	0.0016983	0.0012737	0.0016983	0.0008491		
Pu-240	0.0001125	0.0002251	0.0001688	0.0002251	0.0001125		
Pu-241	0.0000168	0.0000337	0.0000252	0.0000337	0.0000168		
Pu-242	0.0000017	0.0000035	0.0000026	0.0000035	0.0000017		
U-238	0.0055684	0.0063849	0.0059766	0.0063849	0.0055684		
U-235	0.0000122	0.0000139	0.0000131	0.0000139	0.0000122		
O	0.0150075	0.0154338	0.0152206	0.0137617	0.0150075		
Na	0.107196	0.0063408	0.0085302	0.0063610	0.0062787	0.0133588	0.0065078
C	0.0021888		0.0010944	0.0032025	0.0021888	0.0000284	0.0001547
Fe	0.0087888	0.0162589	0.0125238	0.0180022	0.0097185	0.0079227	0.0068787
Ni	0.0011626	0.0011636	0.0011631	0.0023373	0.0012671	0.0189744	0.0460037
Cr	0.0025337	0.0025358	0.0025348	0.0051353	0.0027964	0.0022823	0.0019747
Mn	0.0002025	0.0002027	0.0002026	0.0004248	0.0002204	0.0002295	0.0002639
Mo	0.0002322	0.0004475	0.0003398	0.0004567	0.0002355	0.0000161	0.0000154

[a] Occupies even-numbered matrix columns.
[b] Occupies odd-numbered matrix columns (center column is odd-numbered).
[c] Both fuel safety and control rods of this composition.
[d] Poison rod withdrawn during operation.

TABLE II-7-II. As-Built Composition of Control Ring for ZPPR/FTR-2 Reference Configuration (*Loading 1–70*)

Nuclide	Composition, atoms/b-cm
Na	0.0082408
C	0.0089729
Fe	0.0094642
Ni	0.0012605
Cr	0.0027303
Mn	0.0002167
Mo	0.0000174
B-10	0.0069348
B-11	0.0281204

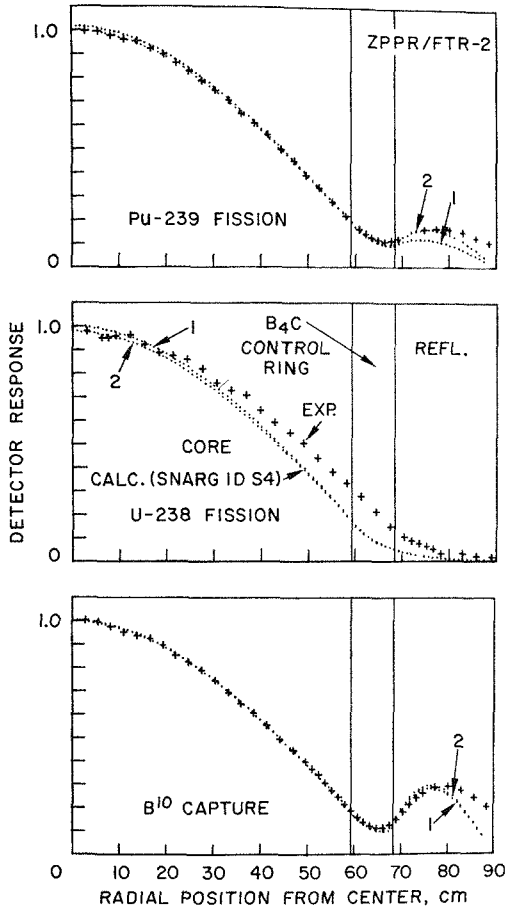

Fig. II-7-3. Radial Reaction Rate Traverses in ZPPR/FTR-2. *ANL Neg. No. 116-560.*

within 10% for Pu-239 and B-10, except near the outer edge of the radial reflector of ZPPR/FTR-2.

The calculated curves are based on the approximation that the outer edge of the radial reflector is bare, which causes the calculated detector responses to rapidly approach zero at that boundary. Actually, a considerable amount of neutron back-scattering was caused by the stainless steel matrix structure outside the reflector. This effect explains why the calculated detector responses for Pu-239 fission and B-10 capture, both of which are more sensitive than the U-238 fission detector responses to the relatively slow back-scattered neutrons, are especially low near the outer edge of the reflector. The contribution of back-scattering by the matrix is almost negligible in the radial detector responses for Assembly 56B, where there was no B_4C control ring.

The calculated U-238 fission response in ZPPR/FTR-2 shows a depression in the B_4C control ring and in the outer 20–30 cm of the core, which is not reflected in the results of experiments; the measured U-238 fission response shows little change in shape from that found in Assembly 56B[1].

Calculation of the U-235/B-10 Reaction Rate Ratio in ZPPR/FTR-2

The value of the reaction rate ratio $[^{235}U(n,f)/^{10}B(n,\alpha)]$ described in Ref. 5 was calculated for comparison with the experimental result. The neutron spectrum was derived through a DS_4 calculation by means of the SNARG-1D Code with the cross sections of set 29004.2. The calculation corresponded to $k = 0.9935$. The cross sections of B-10 were also taken from set 29004.2, while the U-235 cross sections were taken from an equivalent set in which no heterogeneity correction was applied to the U-235 cross sections. The calculation yielded a value of 0.772 for the $[^{235}U(n,f)/^{10}B(n,\alpha)]$ reaction rate ratio at the center of the core. When compared with the experimental result (0.893 ± 0.037), this result corresponds to a C/E (calculated/experimental) value of 0.865.

FTR-2 Shield Configuration

A sector of radial shield was added to FTR-2 on ZPPR outside the radial reflector in order to perform shielding experiments. Its axial length was equal to that of the radial reflector, and the transverse configuration of the assembly is shown in Fig. II-7-4. A cylindrical zone surrounding the axis of the core was depleted of plutonium in steps to reduce reactivity so that the B_4C-Na-SS control annulus could be gradually replaced by radial reflector. The removal of the control annulus made it possible to perform shielding experiments in the shield sector in the presence of a greater neutron flux. The composition of the shield zone and depleted matrix locations are given in Table II-7-III. The shielding experiments included the evaluation of the effect of storing fuel in a zone in the reflector on the reaction rate profiles of a number of isotopes within the core, the radial reflector, and the shield. The position of the stored fuel, when used, is

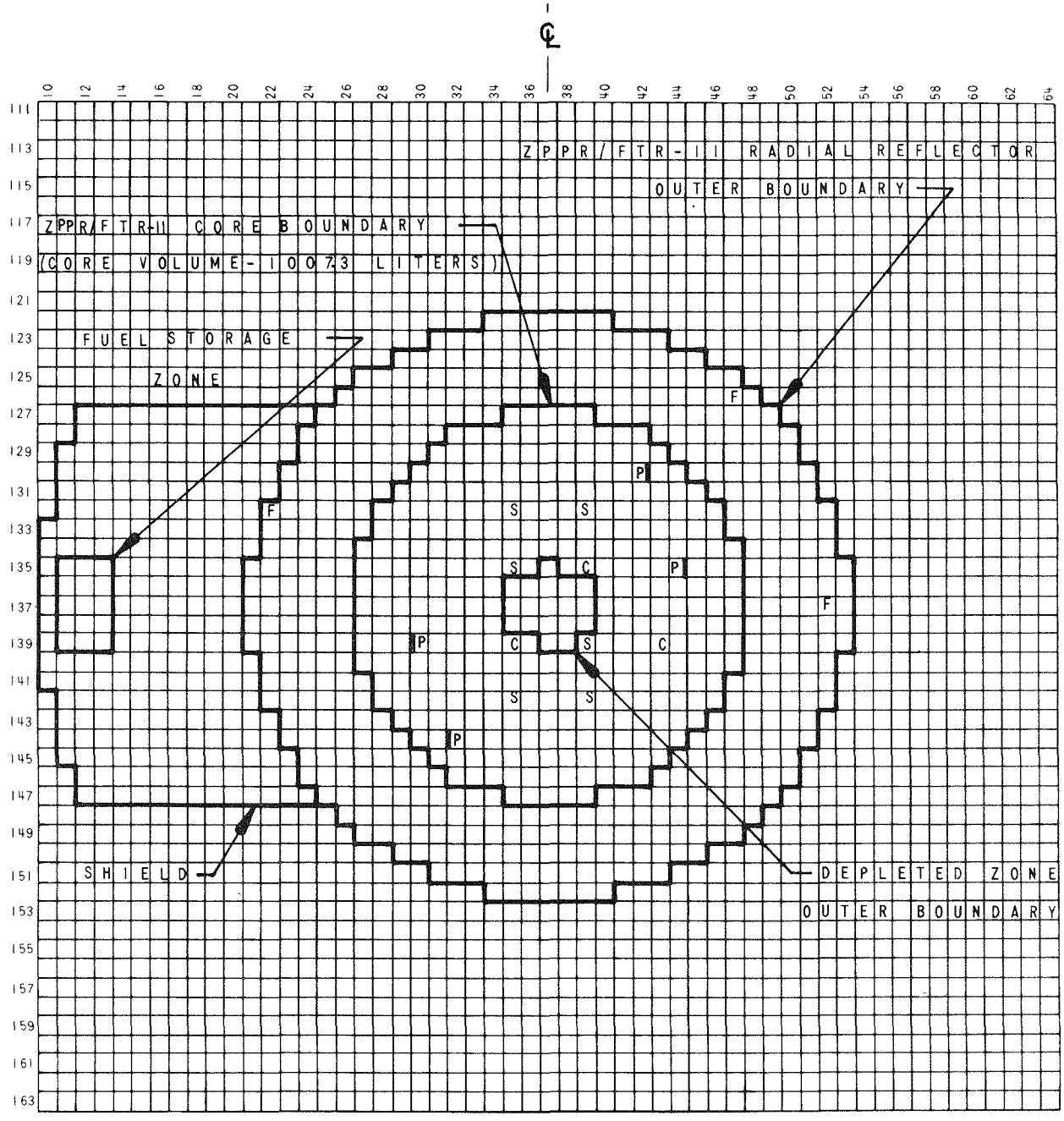

ZPPR HALF 1

(HALF 2 IS A MIRROR IMAGE OF HALF 1)

S - SAFETY ROD C - CONTROL ROD P - DRAWER ADJACENT TO POISON SAFETY ROD

| - POISON SAFETY ROD (WITHDRAWN DURING OPERATION)

F - U-235 FISSION CHAMBER (FRONT OF CHAMBER AT REACTOR MIDPLANE. NO F's IN HALF 2)

FIG. II-7-4. ZPPR/FTR-2 Shield with Fuel-Storage Configuration (Loading 1–130). *ANL-ID-103-A11166.*

TABLE II-7-III. As-Built Composition of Shield and Depleted Core Zones for the ZPPR/FTR-2 Shield Configuration, atoms/b-cm

Nuclide	Shield Zone	Depleted Core Zone	
		Drawer with One ¼-in.-column U-238[a]	Drawer with Two ¼-in.-columns U-238[b]
U-238		0.0078084	0.0108669
U-235		0.0000164	0.0000223
O		0.0150075	0.0154338
Na	0.0059617	0.0107196	0.0063408
C	0.0000264	0.0021888	
Fe	0.0371696	0.0078562	0.0143938
Ni	0.0045539	0.0010273	0.0008931
Cr	0.0102972	0.0022623	0.0019930
Mn	0.0005741	0.0001829	0.0001635
Mo	0.0000269	0.0000161	0.0000154

[a] Located in even-numbered matrix columns.
[b] Located in odd-numbered matrix columns.

shown in Fig. II-7-4. The matrix locations containing fuel and corresponding to odd-numbered columns contained two plates of plutonium, while those corresponding to even-numbered columns contained one plate of plutonium. The compositions of the 1- and 2-plutonium plate loadings are given in Table II-7-I. The fuel-storage zone had the same height as the core, and therefore extended 18.04 in. from the assembly axial midplane in both axial directions.

EVALUATION OF FISSILE DEPLETION AND BORON REMOVAL EXPERIMENTS IN ZPPR/FTR-2

The FTR-2 experiments in which the B_4C ring was gradually removed from the periphery of the core while a central region was depleted of fissile material have been analyzed. Figure II-7-5 shows the assembly configurations that were built on ZPPR in all the main steps of the experiments. Every region in the figure is labeled with the number of the loading which was obtained from the previous loading by depleting that region (if the region belongs to the central zone of the core) or by replacing its control composition with reflector composition (if the region belongs to the control ring). Thus, the depleted zone of any loading includes all the central regions labeled with numbers smaller than or equal to the loading number, while the control zone includes all the control ring regions labeled with numbers larger than the loading number.

In general, the progressive removal of boron from the ring corresponded to removing ring sectors with areas equal to the area of four matrix drawers from a control ring which was virtually complete at the beginning while it was devoid of boron at the end. Thus, the ring looked like a complete ring with two-drawer gaps at the beginning of the experiments and like an empty ring with two-drawer fillings at the end. The computational model was chosen according to these considerations and is depicted in Fig. II-7-6. The symbols R and D are defined, respectively, as the fraction of the initial complete ring and of the final depleted zone present in any loading. The reactor is represented in (R,θ) geometry, with the outer radii of the core and of the reflector chosen so that their areas correspond to the effective midplane areas of the experimental assembly. The central depleted zone is represented by a circle of radius r, whose area also corresponds to the effective experimental value. The intermittent control ring is represented by a series of sectors (half of one sector is shown shaded in Fig. II-7-6) whose thickness equals the effective thickness of the complete experimental ring. When less than half of the ring is present ($R < 0.5$) the half-thickness of each control section (θ_1) is chosen so that the area of the sector is equal to the area of four matrix drawers; the half-thickness of the reflector sector that separates two control sectors (θ_2) is chosen so that the total ring area occupied by control regions equals the experimental value. When more than half of the ring is present, θ_2 is chosen so that the area of each reflector sector between control sectors is equal to the area of four matrix drawers, while θ_1 is chosen so that the desired amount of boron is represented in the reactor. Obviously, both methods yield the same values for both angles when half of the ring is present ($R = 0.5$). For the number of control sectors present in the ring, this approach yields a value close to the number that was actually used in all of the loadings built during the experiments in question. The computational model that has been described does not take into account the jagged outlines of the core and

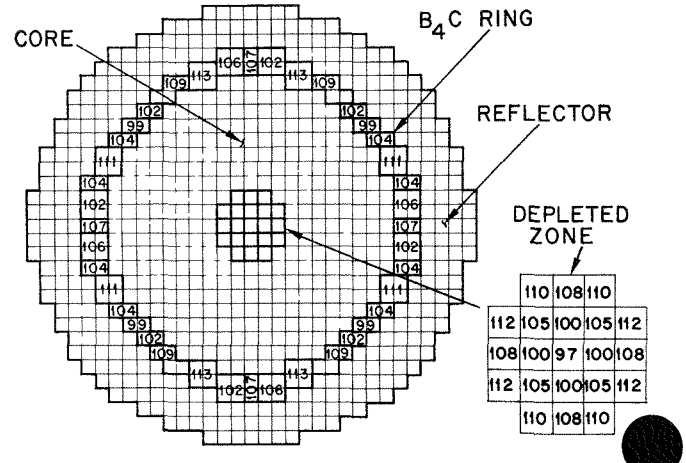

Fig. II-7-5. The Various Assembly Configurations of ZPPR Corresponding to the Core Loadings of the Fissile and Boron Removal Experiments in ZPPR/FTR-2. *ANL Neg. No. 116-559.*

of the control regions. Only a two-dimensional (X,Y) calculation could do this adequately. However, the fact that only a very small fraction of the core volume needs to be considered in the (R,θ) geometry makes it possible to use a large number of energy groups and a large number of mesh points. Since the change of the energy spectrum of the neutron flux in the reflector and in the boron regions is very important in establishing the worth of the boron region, and since a large number of energy groups and of mesh points was deemed more important than a rigorous geometric representation in achieving the correct spectrum, the (R,θ) geometry was chosen over the (X,Y) geometry.

The cross sections used in the calculations were taken from the 29-group Argonne cross section set 29004.2. The calculation was run in diffusion theory by means of the DIF2D code.[6]

The value of the axial buckling was assumed to be independent of radius, energy, and azimuthal angle, and it was calculated for four cases (no ring, no depletion; no ring, full depletion; full ring, no depletion; full ring, full depletion) so that it would yield the same value of the effective multiplication constant in a one-dimensional (R) calculation as obtained in a two-dimensional $(R\text{-}Z)$ calculation. The values of the buckling for all other intermediate values of R and D were calculated by interpolation.

The interference effects between boron ring and depleted zone were calculated by expanding the effective multiplication constant of the reactor in power series of the fraction (R) of the control ring and of the fraction (D) of the depleted zone:

$$
\begin{aligned}
k(R,D) &= \sum_{m=0}^{\infty}\sum_{n=0}^{\infty}\left[\frac{\partial^{m+n}k}{\partial R^m \partial D^n}\right]_{\substack{R=0\\D=0}}\frac{R^m D^n}{m!n!} \\
&= \sum_{m=0}^{\infty}\left[\frac{\partial^m k}{\partial R^m}_{\substack{R=0\\D=0}}\right]\frac{R^m}{m!} \\
&\quad + \sum_{n=0}^{\infty}\left[\frac{\partial^n k}{\partial D^n}\right]_{\substack{R=0\\D=0}}\frac{D^n}{n!} - k(0,0) \qquad (1)\\
&\quad + \sum_{m=1}^{\infty}\sum_{n=1}^{\infty}\left[\frac{\partial^{m+n}k}{\partial R^m \partial D^n}\right]_{\substack{R=0\\D=0}}\frac{R^m D^n}{m!n!} \\
&= k(R,0) + k(0,D) - k(0,0) \\
&\qquad + RD\cdot C(R,D),
\end{aligned}
$$

$$
C(R,D) \equiv \sum_{m=0}^{\infty}\sum_{n=0}^{\infty}\frac{\partial^{m+n+2}k}{\partial R^{m+1}\partial D^{n+1}}\,\frac{R^m D^n}{(m+1)!(n+1)!}. \qquad (2)
$$

As shown in Eq. (1), the function $C(R,D)$ makes it possible to infer exactly any value of the effective multiplication constant of any loading from the knowledge of the effective multiplication constants of two loadings which have, respectively, the same ring and no depleted zone or the same depleted zone and no ring. The $C(R,D)$ function corresponds to the interference effects between the ring and the depletion.

Table II-7-IV shows the results obtained from a series of calculations run for five different values of R and D. In particular, the values obtained for $C(R,D)$ show that the function has generally a small value (i.e., the interference effects between ring and depletion are small), smoothly varying, and separable in the two variables. The values of C shown in Table II-7-IV were then used to obtain by interpolation the values of C for any other (R,D) combination.

Figure II-7-7 shows the values of $(k_{eff} - 1)$ in % as a function of R for every configuration having no de-

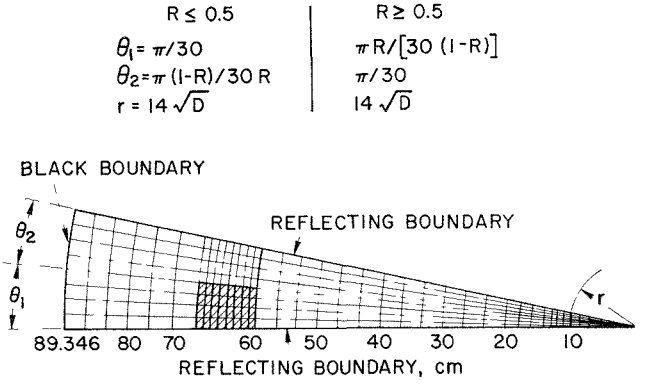

FIG. II-7-6. The Model Used in the Computations. *ANL Neg. No. 116-558.*

TABLE II-7-IV. VALUES OF THE AXIAL BUCKLING, OF THE EFFECTIVE MULTIPLICATION CONSTANT, AND OF THE INTERFERENCE FUNCTION AS CALCULATED FOR VARIOUS VALUES OF R AND D

D	R = 0.0	0.25	0.50	0.75	1.0	
1.0	5.920	5.946	5.972	5.998	6.024	$B_z^2 \times 10^4$ cm^{-2}
	0.987	0.959	0.937	0.925	0.914	k
	—	−0.018	−0.017	−0.014	−0.012	c
0.75	5.922	5.949	5.976	6.002	6.028	
	1.001	0.974	0.953	0.941	0.930	
	—	−0.019	−0.017	−0.014	−0.013	
0.50	5.924	5.952	5.980	6.006	6.033	
	1.015	0.990	0.969	0.958	0.948	
	—	−0.020	−0.018	−0.015	−0.013	
0.25	5.926	5.955	5.984	6.010	6.037	
	1.031	1.007	0.987	0.976	0.967	
	—	−0.021	−0.019	−0.016	−0.014	
0.0	5.928	5.958	5.988	6.014	6.042	
	1.048	1.025	1.007	0.997	0.988	
	—	—	—	—	—	

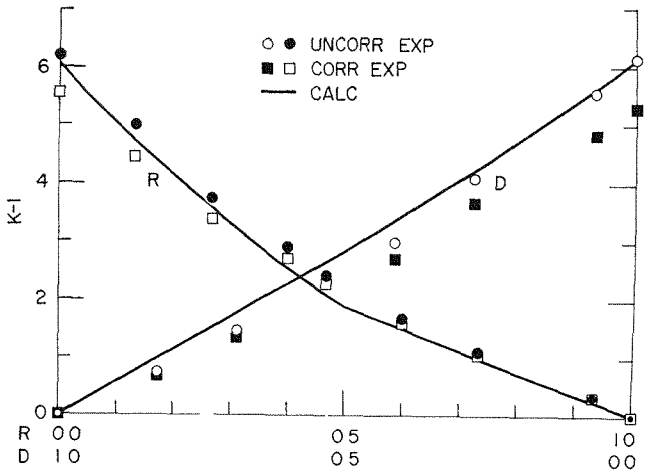

FIG. II-7-7. Comparison of Calculations with Experimental Values (Corrected and Uncorrected) of the Effective Multiplication Constant of a Reactor with No Depletion and a Fraction (R) of the Control Ring, and of a Reactor with No Control Ring and a Fraction (D) of the Depleted Zone. *ANL Neg. No. 116-557*

pleted zone and a fraction R of the control ring, and the values of $(k_{eff} - 1)$ in % as a function of D for every configuration having no ring and a fraction D of the depleted zone. The uncorrected experimental points are obtained by adding all the measured reactivity changes corresponding, respectively, to ring (or depleted zone) changes in a series of experiments leading to the reactor in question from a reactor with full ring (or full depletion). However, the experiments were usually performed with both depletion and ring present in the reactor; the corrected experimental points were obtained from the uncorrected points by using the calculated values of C to correct for this difference. Every reactivity change observed in the experiments was modified so that it would correspond to what would have been found had there been no depletion (or ring) in the reactor. The solid curves show the results of direct calculations.

The comparison shown in Fig. II-7-7 indicates that experiments and calculations are in good qualitative agreement with each other. The B-10 and Pu-239 worths are overestimated in the calculations by approximately 8% and 12%, in this order; these values are almost exactly the same as those found in previous comparisons between experimental worths of B-10 and Pu-239 in FTR-1 and calculations using the same cross section set.[7] The correction of the experimental data is always rather small, and never exceeds 12% of their value; even though the correction is based exclusively on calculations, the fact that it is small and little dependent on the reactor details makes it possible to place reasonable confidence on the values of the corrected experimental data plotted in Fig. II-7-7. The data indicate that the total worth of the control ring in FTR-2 is close to 5.5% of the effective multiplication constant.

Reducing the measured reactivity changes to the corresponding values that would be obtained in the absence of different types of perturbations (as in Fig. II-7-7) offers the advantages of a clear physical meaning and of a more regular behavior of the curves. However, it is also interesting to investigate how accurately the calculations matched the results of the experiments that were actually performed. This procedure does not offer a clear physical interpretation, but it removes the uncertainty inherent in the application of a calculated correction to the experimental data.

The results of this comparison are shown in Fig. II-7-8 and in Table II-7-V. The curve calculated for k_{eff} in Fig. II-7-8 has been shifted upwards by 0.017. This value was chosen so that the best agreement between calculations and experiments could be found, but is also very close to the amount by which the calculations may be expected to underestimate k_{eff} because of the combined effects of using diffusion theory and of neglecting high-energy heterogeneity effects.

Table II-7-V shows in condensed form the main properties of the various loadings and the calculated and experimental values of k_{eff}. In addition, the table lists both for fissile and for control exchanges the experimental k-changes, the calculated k-changes, and their ratios. The results are consistent with those shown graphically in Fig. II-7-7 and previously discussed.

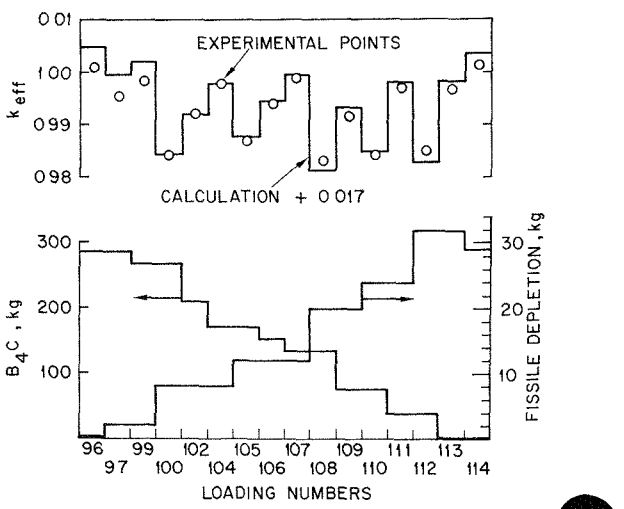

FIG. II-7-8. Comparison of Calculations with the Experimental Values of k_{eff} as Measured for the Various Loadings. *ANL Neg. No. 116-550.*

TABLE II-7-V. DESCRIPTION OF THE MAIN PROPERTIES OF THE VARIOUS LOADINGS AND COMPARISON OF CALCULATIONS WITH EXPERIMENTS

Loading Number	Fissile Mass, kg	B_4C Drawers	$k(E)$	$k(C)$	$k(E)$-$k(C)$ %	Fissile Exchanges			Control Exchanges		
						$\%\Delta k(E)$	$\%\Delta k(C)$	C/E	$\%\Delta k(E)$	$\%\Delta k(C)$	C/E
96	527.041	240	1.00086	0.98776	1.310						
97	525.043	240	0.99522	0.98255	1.267	−0.564	−0.521	0.924			
99	525.043	224	0.99841	0.98493	1.348				0.319	0.238	0.747
100	519.050	224	0.98408	0.96727	1.681	−1.433	−1.766	1.233			
102	519.050	176	0.99206	0.97513	1.693				0.798	0.786	0.985
104	519.050	144	0.99774	0.98062	1.712				0.568	0.549	0.966
105	515.054	144	0.98658	0.97052	1.606	−1.116	−1.010	0.905			
106	515.054	112	0.99397	0.97743	1.654				0.739	0.691	0.935
107	515.054	96	0.99880	0.98254	1.626				0.483	0.511	1.058
108	507.064	96	0.98338	0.96433	1.905	−1.542	−1.821	1.181			
109	507.064	64	0.99158	0.97615	1.543				0.820	1.182	1.442
110	503.068	64	0.98425	0.96780	1.645	−0.733	−0.835	1.140			
111	503.068	32	0.99700	0.98134	1.566				1.275	1.354	1.062
112	495.077	32	0.98503	0.96597	1.906	−1.197	−1.536	1.284			
113	495.077	0	0.99695	0.98154	1.541				1.192	1.556	1.306
114	498.073	0	1.00167	0.98697	1.470	+0.472	+0.544	1.152			

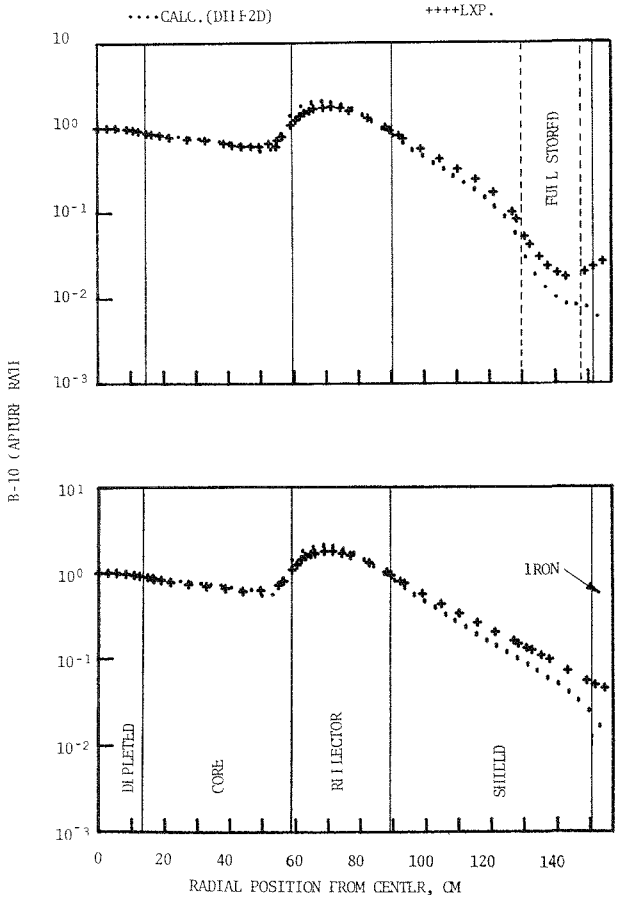

FIG. II-7-9. B-10 Capture Rate versus Radial Position in ZPPR/FTR-2 Shield Configuration at Axial Position 7.62 cm from Center. *ANL Neg. No. 116-554.*

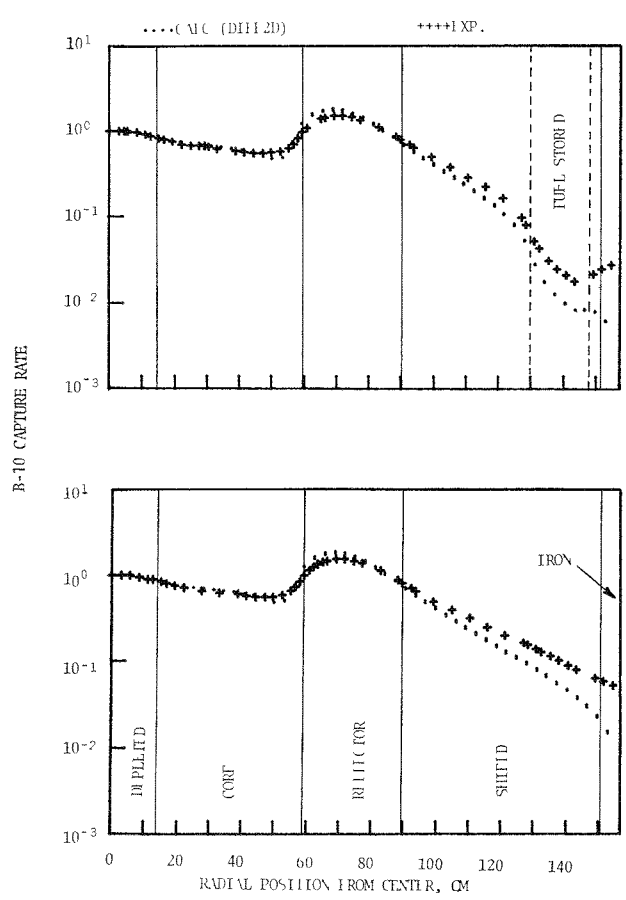

FIG. II-7-10. B-10 Capture Rate versus Radial Position in ZPPR/FTR-2 Shield Configuration at Axial Position 35.56 cm from Center. *ANL Neg. No. 116-562.*

CALCULATION OF REACTION RATE TRAVERSES IN ZPPR/FTR-2 SHIELDING CONFIGURATION

The radial variation of B-10 capture, U-238 fission, Pu-239 fission, and Na-23 capture rates have been computed for axial positions at 7.62, 35.56 and 55.88 cm from the dividing plane in ZPPR/FTR-2 in the shield configuration (loading 130). The neutron fluxes used in the computations were obtained from a DIF2D diffusion solution in R, Z geometry. In order to simulate the leakage in the direction perpendicular to the plane in which the three radial traverse measurements were made, fictitious DB_θ^2 absorbers were added at each radial mesh point for all axial values closer to the midplane than the core half-height. The B_θ^2 values were group-dependent and R-dependent. They were derived from the flux solutions of an R, θ representation of the reactor and shield sector with stored fuel. Thus, the solution of the R, Z problem has meaning only in the plane of the measurements, but includes the effect of the azimuthal finiteness of the fuel stored

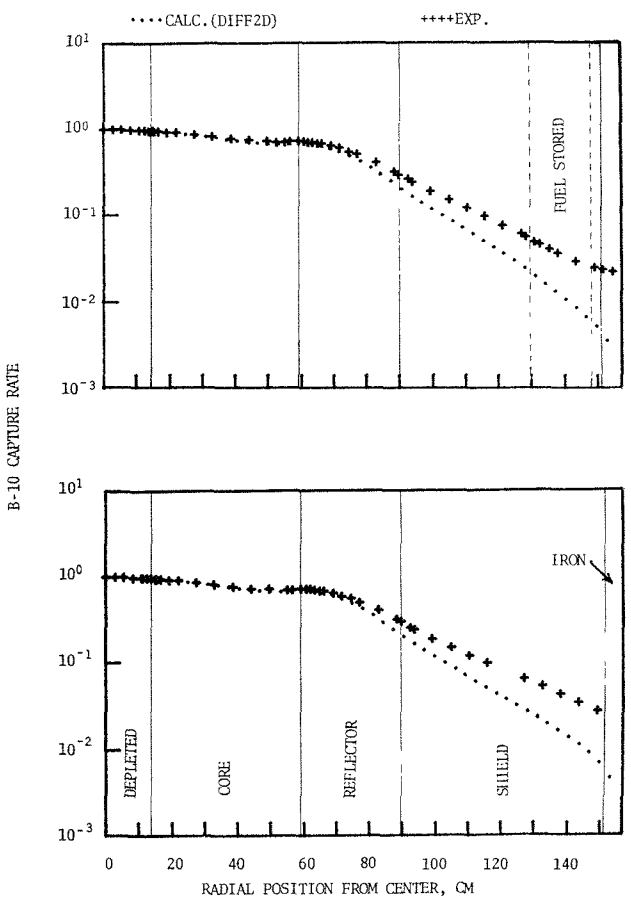

FIG. II-7-11. B-10 Capture Rate versus Radial Position in ZPPR/FTR-2 Shield Configuration at Axial Position 55.88 cm from Center. *ANL Neg. No. 116-556.*

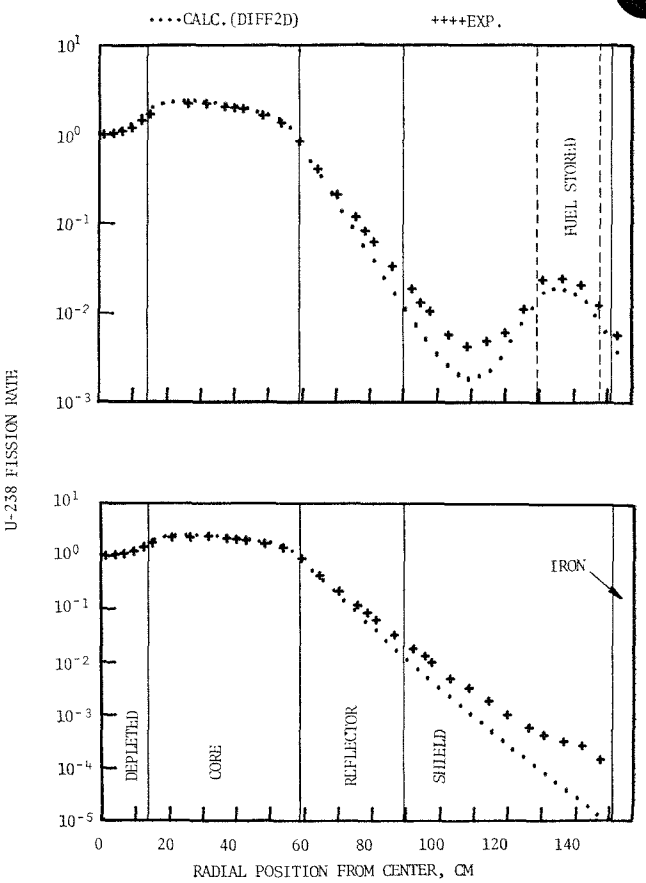

FIG. II-7-12. U-238 Fission Rate versus Radial Position in ZPPR/FTR-2 Shield Configuration at Axial Position 7.62 cm from Center. *ANL Neg. No. 116-551.*

in the shield and of the shield itself. The 29 energy group cross section set 29004.2 was used, giving $k_{eff} = 0.9946$.

The reaction rates were also calculated for the case of no stored fuel using R, Z flux solutions obtained by the same technique, where the B_θ^2 were derived from the solutions of an R, θ representation of the reactor and shield sector without stored fuel. These reaction rates agreed with other simpler calculations assuming zero θ-leakage, with a relative discrepancy of 7% or less.

The traverses at 7.62 and 35.56 cm passed through the depleted zone, core, radial reflector, shield, and 5.53 cm of iron which simulated the heavy clamp that held the matrix tubes in position. The core-axial reflector interface was at 45.811 cm from the midplane and the axial reflector ended at 76.302 cm. Thus, the traverse at 55.88 cm passed through the axial reflector for radii smaller than the core radius, then through the radial reflector, shield, and iron clamp.

Two reaction rate curves were computed for each

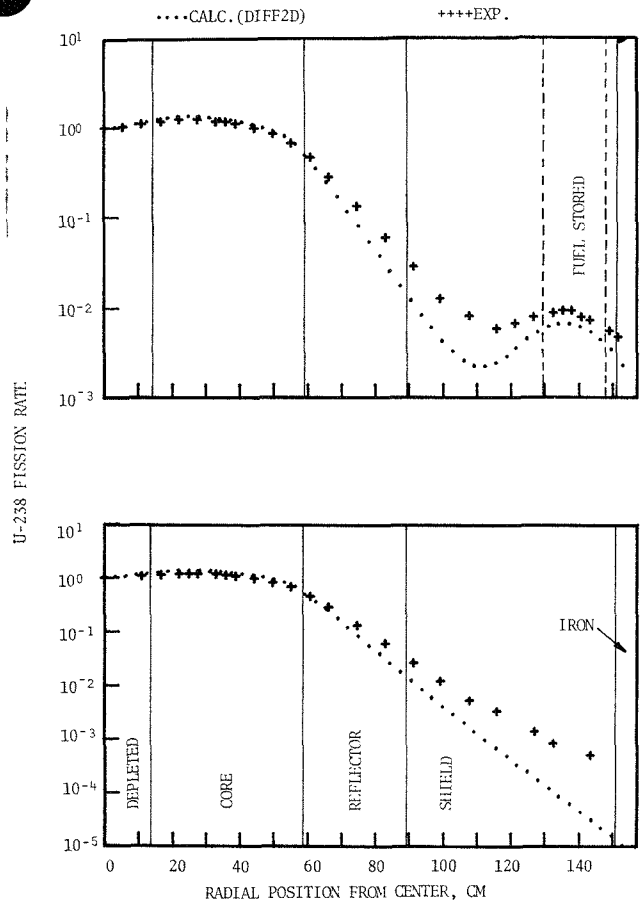

FIG. II-7-13. U-238 Fission Rate versus Radial Position in ZPPR/FTR-2 Shield Configuration at Axial Position 35.56 cm from Center. *ANL Neg. No. 116-565.*

traverse at 7.62 and 35.56 cm. The calculation of the first reaction rate used the 29-group cross sections obtained from a 2100-group fundamental mode MC^2 flux averaging for the core composition at criticality. Calculation of the second reaction rate traverse used the 29-group cross sections obtained from a 2100-group fundamental mode MC^2 flux averaging for the radial reflector composition with zero buckling. The flux was normalized so that the B-10 capture and U-238 fission rates for the first calculation and the Pu-239 fission rate from the second calculation were unity at zero radius.

Two reaction rate curves were also computed for each traverse at 55.88 cm. The calculation of the first reaction rate used cross sections averaged for the axial reflector composition with zero buckling. The flux normalization was chosen so that the reaction rates of B-10 capture, U-238 fission, and Pu-239 fission were unity at zero radius for the first calculation. The calculation of the second reaction rate traverse used cross sections averaged for the radial reflector composition. The same flux, with the same normalization, was used as in the calculation of the first reaction rate traverse.

In the case of Na-23 capture the flux to be used for all traverses was normalized so that the Na-23 capture rate for the first calculation was unity at zero radius in the 7.62 cm traverse.

In Figs. II-7-9 through II-7-20 computed reaction rates are compared on a logarithmic scale with measured values[8,9] with stored fuel in the upper graph (radial position indicated by dotted lines) and without it in the lower graph.

In Figs. II-7-15 and II-7-16 (Pu-239 fission) and Figs. II-7-18 and II-7-19 (Na-23 capture) reaction rates computed with core-averaged cross sections (1) differ enough from the rates computed with the radial reflector-averaged cross sections (2) so that labels are provided. In all other traverses through the core the difference is almost indistinguishable. The reaction rates computed with the axial reflector-averaged cross

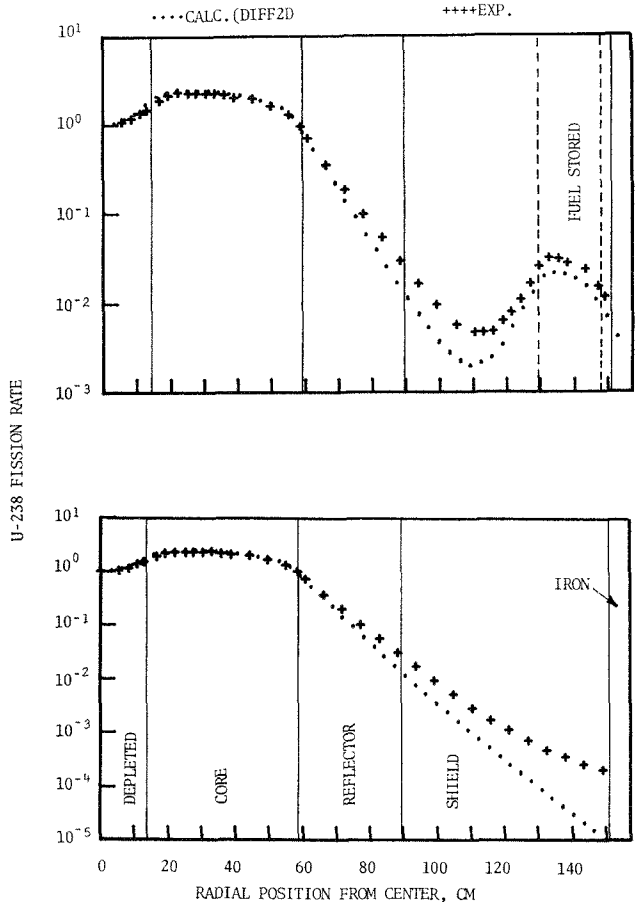

FIG. II-7-14. U-238 Fission Rate versus Radial Position in ZPPR/FTR-2 Shield Configuration at Axial Position 55.88 cm from Center. *ANL Neg. No. 116-552.*

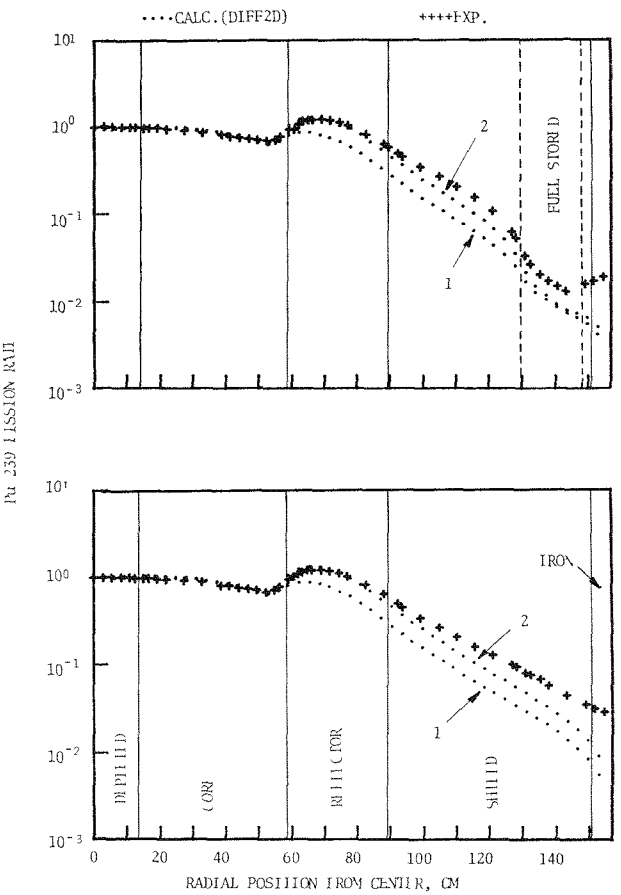

FIG. II-7-15. Pu-239 Fission Rate versus Radial Position in ZPPR/FTR-2 Shield Configuration at Axial Position 7.62 cm from Center. *ANL Neg. No. 116-564.*

sections at an axial position 55.88 cm from the center are also almost identical with their radial counterpart.

In the radial reflector the calculated B-10 capture reaches a peak which is too great by about 20% for the traverses at 7.62 and 35.56 cm (see Figs. II-7-9 and II-7-10). The calculated B-10 capture rate along a radial traverse near the dividing plane in ZPR-3 Assembly 56B was found by S_4 transport theory to be about 12% higher than the measured value in the radial reflector.[1] In the case of Assembly 56B the boundary of the problem was at the outer edge of the reflector rather than at the outer edge of the matrix tube clamp. The calculated peak of the Pu-239 fission rate using reflector averaged cross sections is higher than the measured one by about 8% in the radial reflector for the 7.62 and 35.56 cm traverses (see Figs. II-7-15 and II-7-16). This compares to a value of about 6% for the case of Assembly 56B, mentioned previously.

The relatively soft flux components which activate B-10 and Pu-239 are depressed by the presence of stored fuel in the shield (see Figs. II-7-9, II-7-10, II-7-15 and II-7-16). These depressions do not extend far enough to be seen in the 55.88 cm traverse. Notice that a soft flux component appears to be present (possibly due to room backscatter) which increases the experimental reaction rate near the outer radius of the shield, but which is not present in the computation.

On the other hand, the relatively hard flux which activates U-238 shows a maximum in the stored fuel which extends far enough to be seen in the 55.88 cm traverse (see Figs. II-7-12 through II-7-14). Stored fuel has only a small net depressing effect on the flux components which activate Na-23 (see Figs. II-7-18 and II-7-19).

In general, the qualitative agreement between calculated and experimental data is satisfactory when one considers the approximate nature of the computations. In particular, the method used to take into account the azimuthal finiteness of the shield and of the stored fuel appears to be quite satisfactory. The main discrepancy is found in the negative gradient of the computed reaction rate curves, which is usually more negative than the slope of the corresponding experi-

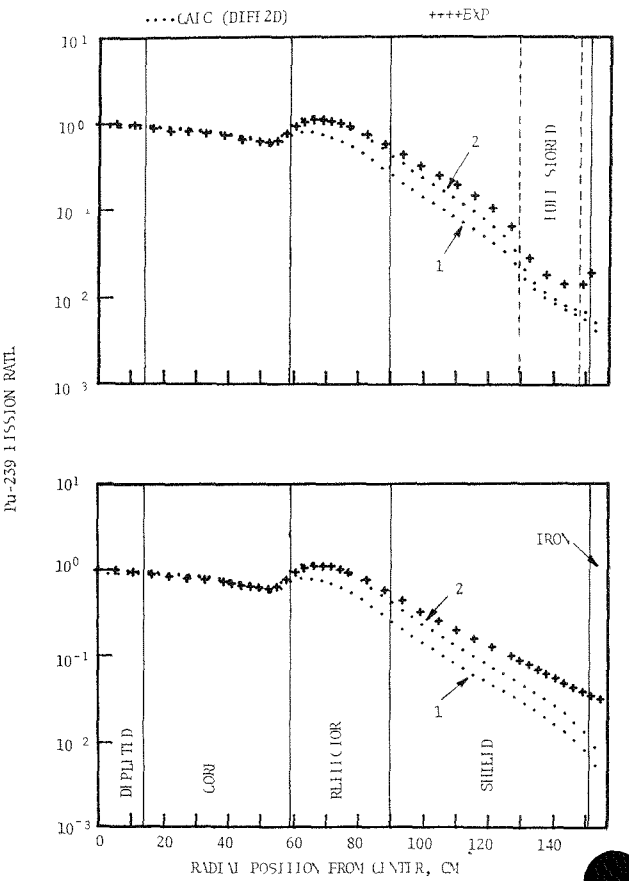

FIG. II-7-16. Pu-239 Fission Rate versus Radial Position in ZPPR/FTR-2 Shield Configuration at Axial Position 35.56 cm from Center. *ANL Neg. No. 116-547.*

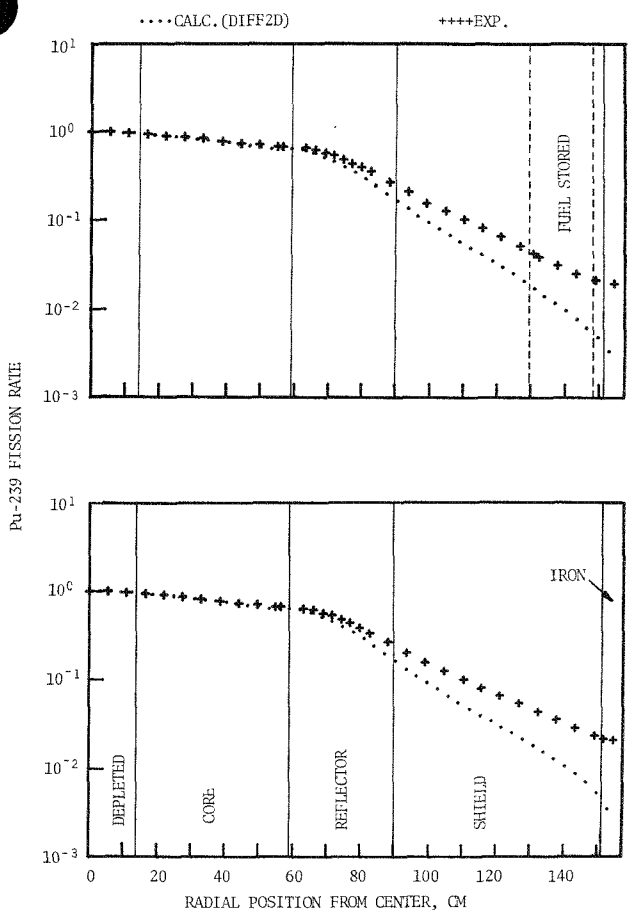

FIG. II-7-17. Pu-239 Fission Rate versus Radial Position in ZPPR/FTR-2 Shield Configuration at Axial Position 55.88 cm from Center. *ANL Neg. No. 116-563.*

mental curves in the shield region. This difference depends on the particular reaction and on the axial position and may be attributed to the deficiencies of diffusion theory, to angular dependence of the scattering matrices, or to the cross sections used. The effect could also be due to flux streaming down the channel through the assembly in which the traverse tube was placed; however, the Na-23 curves for no fuel stored in Figs. II-7-18 through II-7-20 seem to contradict this explanation, because there was no channel for streaming in these cases and the effect is still present.

The method of normalizing the radial variations of the B-10 capture, U-238 fission, and Pu-239 fission rates does not give a comparison of computed and measured reaction rates as a function of axial position. In order to evaluate this effect, the fluxes from the DIF2D solution were also used to calculate each of the three reaction rates at zero radius and axial distances of 35.56 and 55.88 cm from the dividing plane when the reaction rate at an axial distance of 7.62 cm was unity. These rates are compared with measured values[8] in Table II-7-VI.

FTR-3 ON ZPR-9

The next assembly in phase B of the FFTF critical experiments program was FTR-3, built on ZPR-9. This assembly was similar to FTR-2, but its core had two zones of different enrichment and the control annulus was replaced by a ring of sixteen control clusters surrounding the core and located in the radial reflector. The volume of each control cluster was very close to the volume of an FTR control rod, so that the sixteen control clusters corresponded closely to the fifteen-rod peripheral control system of the FTR even though maintaining 45 deg symmetry.

The matrix loading pattern for the first FTR-3 critical assembly is shown in Fig. II-7-21. The dimensions of the assembly when all zones are transformed into cylinders or cylindrical annulii preserving volume are given in Fig. II-7-22. The atom densities for the zones are given in Table II-7-VII. Type A drawers

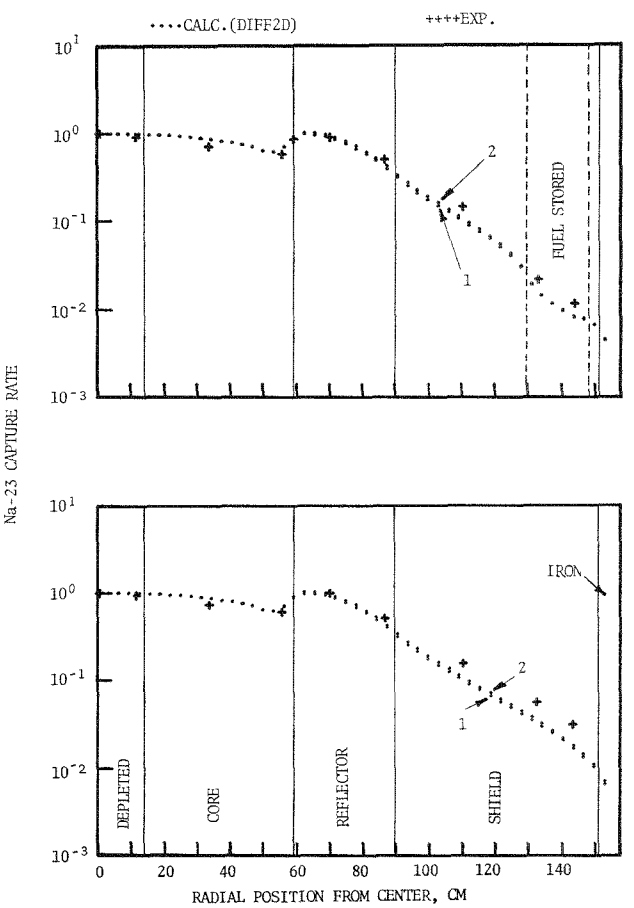

FIG. II-7-18. Na-23 Capture Rate versus Radial Position in ZPPR/FTR-2 Shield Configuration at Axial Position 7.62 cm from Center. *ANL Neg. No. 116-548.*

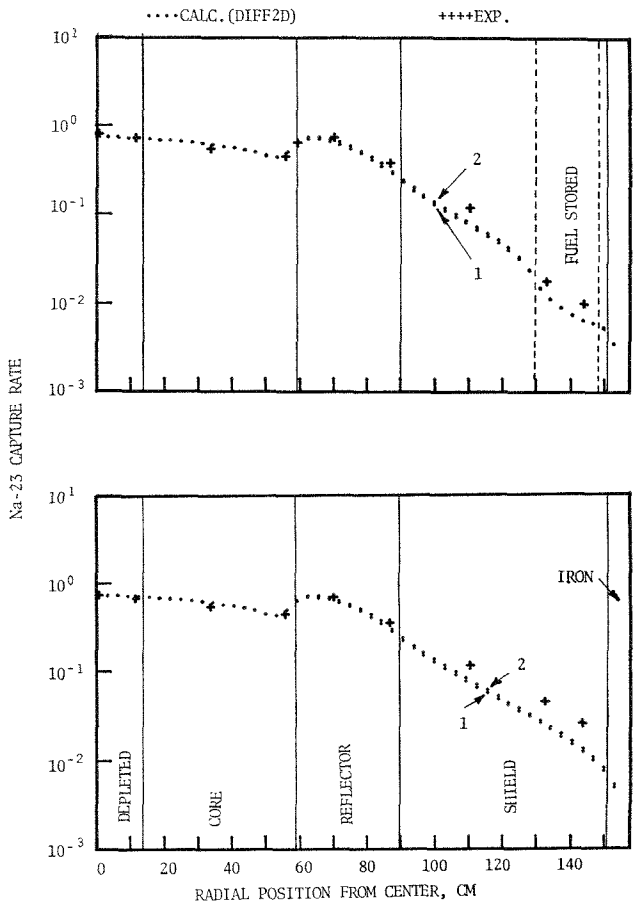

FIG. II-7-19. Na-23 Capture Rate versus Radial Position in ZPPR/FTR-2 Shield Configuration at Axial Position 35.56 cm from Center. *ANL Neg. No. 116-549.*

were loaded into matrix positions corresponding to even numbered columns and type B drawers were loaded into matrix positions corresponding to odd numbered columns.

In order to supply nickel for another program the reactor underwent a slight modification after achieving first criticality, so that some nickel could be made available for the EBR-II mockup studies which were simultaneously under way in ZPR-3. The reflector was made thinner while a radial shield with a large volume fraction of stainless steel was added around the reflector. The atom densities in the radial shield are given in Table II-7-VIII. The resulting FTR-3 Reference configuration is shown in Fig. II-7-23.

The critical mass of the FTR-3 assembly was precalculated for a large number of core compositions which were considered during the planning phase of the assembly. The large number of calculations needed made it necessary to develop an approximate and economical procedure to evaluate the critical mass of the assembly by means of a series of one- and two-dimensional configurations using the DIF1D, DIF2[illegible] and MACH-1 diffusion codes.[6,10]

A first simplification of the basic problem was the replacement of the sixteen peripheral control rods with a fictitious annular region of control composition located between the core and the radial reflector with the same worth as the control rods. The FTR-3 reference configuration was defined in Rθ geometry in a problem in which the sixteen control rods were present, using the cross section set 29004.2. The control annulus was represented in a similar problem in one-

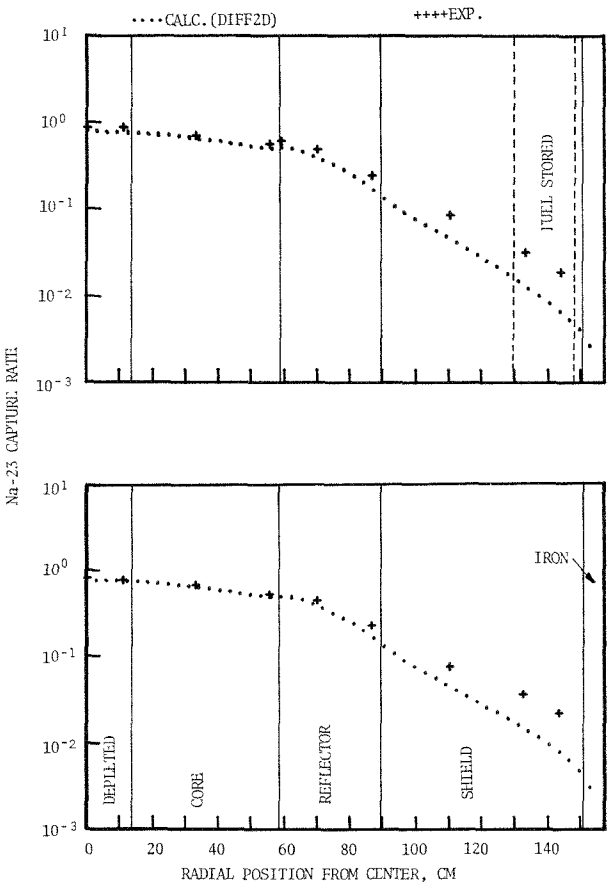

FIG. II-7-20. Na-23 Capture Rate versus Radial Position in ZPPR/FTR-2 Shield Configuration at Axial Position 55.88 cm from Center. *ANL Neg. No. 116-561.*

TABLE II-7-VI. RELATIVE REACTION RATES AT ZERO RADIUS

Axial Position	7.62 cm		35.56 cm		55.88 cm	
	Calc.	Meas.	Calc.	Meas.	Calc.	Meas.
B-10 capture	1.00	1.00	0.821	0.847	1.599	1.37[illegible]
U-238 fission	1.00	1.00	0.639	0.619	0.221	0.2[illegible]
Pu-239 fission	1.00	1.00	0.767	0.808	1.064	1.093

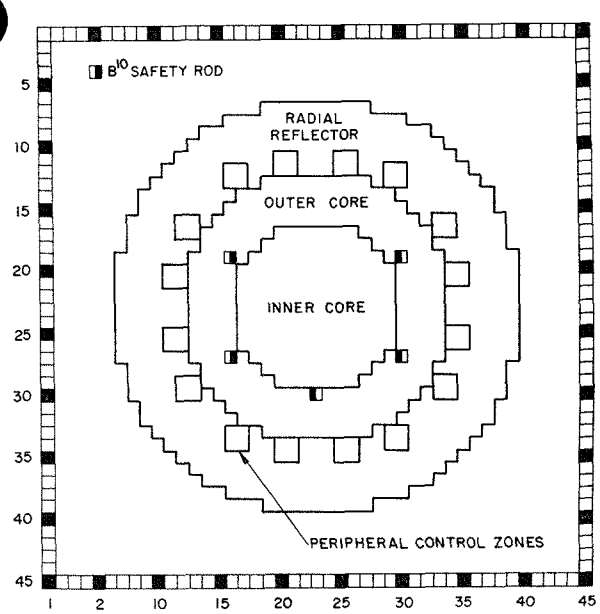

FIG. II-7-21. Stationary Half of FTR-3 Initial Matrix-Loading Pattern. *ANL Neg No. 116-567.*

dimensional cylindrical geometry. The same axial buckling, selected on the basis of experience with FTR-2 computations,[1] was used for both the Rθ and cylindrical problems. The thickness of the one-dimensional ring was then adjusted to give the same multiplication constant as that of the *R*θ problem. This thickness was found to be rather insensitive to the choice of the axial buckling.

A value of the axial buckling that could be used in a one-dimensional cylindrical model of the FTR-3 was taken to be the weighted average of the axial bucklings associated with the inner and outer core compositions. The axial buckling for each core composition was determined from a radial buckling search in a slab problem in which the core composition was reflected by axial reflector slabs. The axial buckling was taken to be the core material buckling minus the radial buckling obtained in the search.

The weighting factors were determined by a comparison of a series of FTR-3 problems solved with set 29601,[(11)] a collapsed six energy group cross section set. Axial bucklings to be associated with each core composition were obtained in six groups by the method described above. A six-group FTR-3 problem in *RZ* geometry using the control annulus yielded a value for the multiplication constant. Next, one-dimensional calculations with the same multiplication constant and with the same cross sections yielded the value of axial buckling required for a cylindrical representation of FTR-3. The cylindrical representation contained a control annulus with the thickness found previously. Weighting factors for the six-group bucklings for each of the core compositions were then chosen so that the weighted average was equal to the six-group buckling required in the one-dimensional cylindrical representation of FTR-3.

These weighting factors were then used to obtain a weighted average 29-group axial buckling for use in the 29-group one-dimensional cylindrical representation of FTR-3 which contained the control annulus. In this final problem the outer boundary of the outer core was varied until the multiplication constant equaled that of the FTR-2 assembly. The thicknesses of the control annulus, radial reflector, and radial shield were held constant. The multiplication constant of FTR-2 was chosen because that assembly was the one of the phase B series which was most similar to FTR-3.

On the basis of the above computational procedure the critical mass of FTR-3 with the core compositions that were eventually chosen was calculated to be 539.6 kg of fissile materials (Pu-239, Pu-241. U-235). The experimental fissile critical mass was 538.23 kg (see Paper II-2).

CALCULATION OF EDGE WORTHS IN THE ZPR-9/FTR-3 CORE

The worth of modifying slightly the boundary between the inner core and the outer core of FTR-3 was calculated and compared with the results of experimental edge worth measurements (see Paper II-2).

The calculations were performed in cylindrical geometry by means of the diffusion program MACH-1 with the aid of the Argonne cross section set 29004.2.

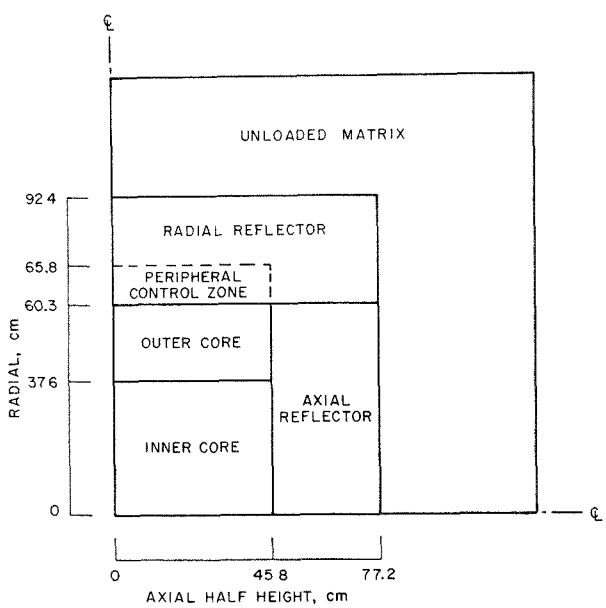

FIG. II-7-22. Side View of FTR-3 in ZPR-9. *ANL Neg. No. 116-553.*

TABLE II-7-VII. FTR-3 ATOM DENSITIES

Isotope or Element	Atom Densities, 10^{21} atoms/cm^3							
	Inner Core Type A Drawer	Inner Core Type B Drawer	Inner Core Avg.[a]	Outer Core	Outer Core Drawer Next to B-10 Rods	Peripheral Control Zones	Radial Reflector	Axial Reflector
Pu-238	0.0006	—	0.0003	0.0006	0.0006	—	—	—
Pu-239	0.8814	1.0690	0.9784	1.4669	1.4466	—	—	—
Pu-240	0.1167	0.0510	0.0827	0.1723	0.1704	—	—	—
Pu-241	0.0181	0 0049	0.0113	0.0227	0.0225	—	—	—
Pu-242	0.0019	0.0001	0.0010	0 0022	0.0022	—	—	—
Pu-239 + Pu-241	0.8995	1.0739	0.9897	1.4896	1.4691	—	—	—
Pu-240 + Pu-242	0.1186	0.0511	0.0837	0.1745	0.1726			
Pu	1.0187	1.1250	1.0737	1.6647	1.6423	—	—	—
U-235	0.0125	0.0069	0.0096	0.0125	0.0114	—	—	—
U-238	5.7811	3.2769	4.4858	5.9000	4.9970	—	—	—
U	5.7936	3.2838	4.4960	5.9125	5.0084	—	—	—
Mo	0.2340	0.0123	0.1194	0.4412	0.4338	0.0105	0.0078	0.0079
Na	9.1731	11.208	10.225	8.7013	6.2784	4.1257	6.7544	9.2102
C	0.0257	0.0356	0.0308	1.0686	1.0684	14.043	0.1646	0.0231
O	14.454	8.7577	11.5076	12.717	8.0809	—	—	—
Fe	13.363	13.234	13.296	15.906	14.124	11.320	8.4575	8.5898
Cr	2.7593	3.8193	3.3076	3.1571	3.1204	3.2536	2.432	2.4614
Ni	1.3166	1.8224	1.5781	1.5064	1.4889	1.5525	48.072	38.1013
Mn	0.2026	0.2804	0.2428	0.2318	0.2291	0.2389	0.2864	0.2789
Al	—	0.1109	0.0574	—	—	—	—	—
B-10	—	—	—	—	—	10.698	—	—
B-11	—	—	—	—	—	43.387	—	—
B	—	—	—	—	—	54.085	—	—

[a] 140 Type A drawers and 150 Type B drawers.

TABLE II-7-VIII. ATOM DENSITIES IN THE RADIAL SHIELD, 10^{21} atoms/cm^3

Element	Atom Density
Na	6.754
Fe	39.022
Cr	11.258
Ni	5.372
Mn	0.827
C	0.105
Mo	0.036

The compositions and radial sizes of the reactor considered in the calculations corresponded exactly to the values given in Figs. II-7-22 and II-7-23 and Tables II-7-VII and II-7-VIII, with the exception of the radius of the inner core/outer core interface. The axial buckling was chosen to be $B_z^2 = 5.435 \times 10^{-4}/\text{cm}^2$ in all regions and for all energy groups; this corresponded to $k = 0.9841$.

The radius of the inner-core/outer-core interface was chosen to equal the average radius of the region where the change in composition had occurred in the experiments. Then, according to the procedure described in Ref. 1, the calculated worth of the substitution was inferred from perturbation calculations as the limit of the perturbation worth of the substitution at the location of the interface.

The same computational method was used to determine edge worths at the outer-core/reflector interface.

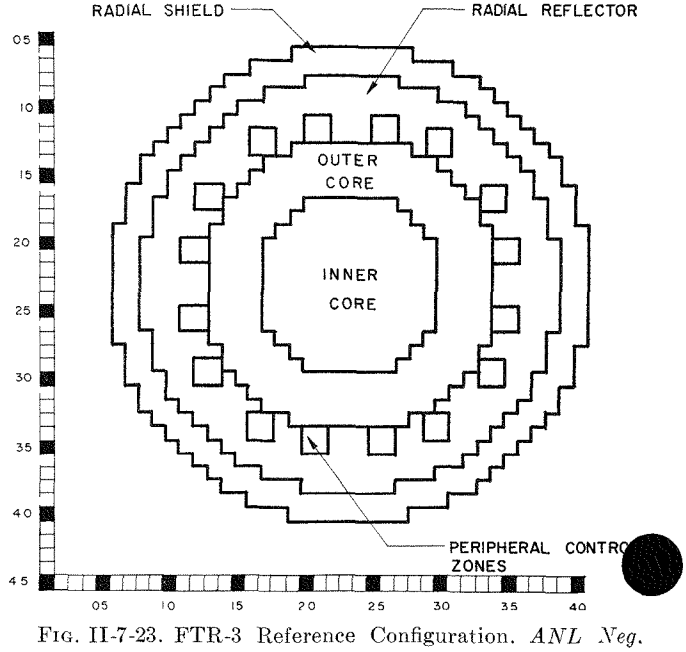

FIG. II-7-23. FTR-3 Reference Configuration. *ANL Neg. No. 116-397 T-1.*

The experiments involved the interchange of an outer core drawer near the inner-core/outer-core interface either with an inner core type A drawer or with an inner core type B drawer (see Paper II-2). The outer core drawer used in the interchanges was of type C and its composition differed slightly from the average composition of the outer core. The compositions of the three drawers used in the interchanges are listed in Table II-7-IX.

The results of the calculations are compared with the experimental data in Tables II-7-X and II-7-XI. The calculations tend to overestimate the worth of the fuel additions that result from the substitutions. The excess of the calculations as compared with the experiments ranged from 10 to 18%, with an average close to 14%. The excess is probably enhanced by (a) the use of perturbation theory as described, and (b) the fact that cross section set 29004.2 does not take properly into account low-energy heterogeneity effects in the various zones of FTR-3.

The overall results are consistent with previous experience with the cross sections of set 29004.2, which have been found to lead to over-estimate by approximately 10% of the fuel worth in various assemblies of the FTR critical experiments program.

TABLE II-7-IX. Compositions of Various Drawers Used in Edge Worth Measurements, 10^{21} atoms/cm^3

	Inner Core Type A	Inner Core Type B	Outer Core Type C
Pu-238	0.0006	—	0.0006
Pu-239	0.8814	1.0690	1.4445
Pu-240	0.1167	0.0510	0.1702
Pu-241	0.0181	0.0049	0.0225
Pu-242	0.0019	0.0001	0.0022
U-235	0.0125	0.0069	0.0122
U-238	5.7811	3.2769	5.8008
Mo	0.2340	0.0123	0.4332
Na	9.1731	11.2080	8.7013
C	0.0257	0.0356	1.0686
O	14.4570	8.7577	12.7174
Fe	13.3630	13.2340	15.9273
Cr	2.7593	3.8193	3.1633
Ni	1.3166	1.8224	1.5094
Mn	0.2026	0.2804	0.2323
Al	—	0.1109	—

TABLE II-7-X. Worths of Substituting an Inner Core Type B Drawer with an Outer Core Type C Drawer at Various Radii

Radius, cm	Calculated, Ih	Experimental, Ih	C/E
33.19	23.99	21.33	1.12
35.41	23.62	20.10	1.17
37.10	23.29	19.78	1.17
39.11	22.80	20.52	1.11

TABLE II-7-XI. Worths of Substituting an Inner Core Type A Drawer with an Outer Core Type C Drawer at Various Radii

Radius, cm	Calculated, Ih	Experimental, Ih	C/E
35.41	45.88	39.04	1.16
37.10	44.36	37.41	1.18
39.11	42.36	38.27	1.10
42.12	28.69	33.69	1.15

Calculation of the Neutron Spectrum at the Center of ZPR-9/FTR-3

A preliminary calculation of the neutron spectrum as measured at a location near the center of ZPR-9/FTR-3 was obtained by means of the MC^2 code. The experimental results and the details of the experiment appear in another section of this report (see Paper II-22).

The calculation used the ENDF/B-I nuclear data and an ultrafine group structure which included the use of 1980 groups of equal lethargy width and spanning over the energy range from 10 MeV to 0.68 eV.

The calculation of the spectrum was based on a fundamental-mode model in the P_1 approximation. This simple model may be applied with some confidence to the analysis of the experiment in question because (1) the neutron spectrum was measured at a location very close to the center of the inner zone of the core; (2) the size of the inner-core zone is such that it may be safely assumed that the spectral perturbations arising from the inner-core/outer-core interface do not extend to the center of the core; (3) the material buckling of the inner-core zone is relatively small (1.06×10^{-3}/cm^2); (4) the measurement was performed in an assembly that was very close to critical ($k = 0.979$), so that the excitation of higher-order modes could be neglected.

The homogeneous composition used in the calculation was the composition of the inner core of FTR-3. The effect of the heterogeneous structure surrounding the counter was partially considered by using the heterogeneous MC^2 option that corresponded to a modified Bell approximation for a structure resembling, to some extent, the plate arrangement around the counter. The calculation did not account in any way for the effect on the neutron spectrum measured by the counter due to the presence of the counter itself.

The results of the direct MC^2 calculation are compared with the experimental results in Fig. II-7-24. The continuous curve that corresponds to the calculation is normalized so that its integral over the energy

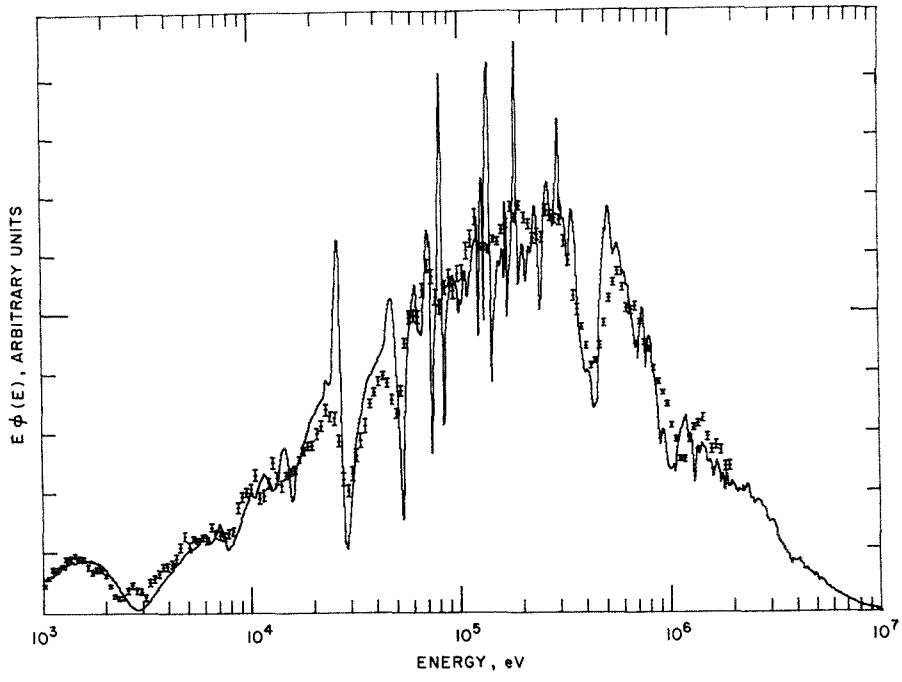

FIG. II-7-24. Comparison of the Neutron Spectrum Measured at the Center of ZPR-9/FTR-3 with the Result of a 1980-Group MC² Calculation. *ANL Neg. No. 116-116.*

range considered in the experiments is equal to the corresponding integral of the experimental data, which are indicated by vertical bars. The average energy of the measured spectrum is in good agreement with the calculation, and so is the location of the main oscillations of the spectrum. These oscillations, which correspond to resonances in the cross sections, have much wider amplitudes in the calculation than in the experiments. The effect is due to the finite energy resolution of the counter.

If the counter is tentatively assumed to have a lethargy resolution corresponding to a gaussian window with a standard lethargy deviation of 0.15, the energy response $f(u)$ of the counter can be calculated easily on the basis of the following expression:[12]

$$f(u) = \frac{\sqrt{2}}{0.15\sqrt{\pi}} \int_0^\infty \phi(u') \exp\left[-2\left(\frac{u-u'}{0.15}\right)^2\right] du',$$

where $\phi(u')$ is the MC² spectrum. Figure II-7-25 shows a comparison of the measured spectrum with the calculated MC² spectrum smoothed by the gaussian window mentioned above. The calculated curve is normalized according to the same method used for the normalization in Fig. II-7-24.

The agreement between measured and calculated counter responses, as depicted in Fig. II-7-25, is very good. Every measurable oscillation in the calculated curve is found to correspond closely in energy, width, and amplitude to a similar oscillation of the experimental data. Minor discrepancies are found in the energy ranges from 15 to 50 keV and from 1.5 to 2 MeV, where the calculation is respectively higher and lower than the experimental data.

A more accurate analysis of the experiment, taking into account the energy-dependence of the counter-resolution is reported in Paper II-22.

PREPARATION OF A CROSS-SECTION SET FOR ANALYSIS OF THE FTR-3 EXPERIMENT

A 29-group cross section set, designated 29006, was prepared from ENDF/B nuclear data, version I revised Category 1, for computational analysis of the FTR-3 critical experiment. The energy-group structure of set 29006 is the same as that of set 29004.2. Inner and outer core 29-group cross sections were obtained by averaging in a 2100-group fundamental mode MC² flux spectrum at criticality for the inner and outer core compositions, respectively. The two-region heterogeneous treatment of MC² was used to obtain cross sections for the isotopes present in the fertile and fissile plates (see Paper II-2) in the inner and outer core. Cross sections for the other isotopes in the inner and outer core were obtained through the homogeneous treatment. Axial reflector cross sections were averaged in the 2100-group flux spectrum for the axial reflector composition with zero buckling and using the homogeneous treatment. Radial reflector cross sections were taken from set 29004.2 because of the almost identical

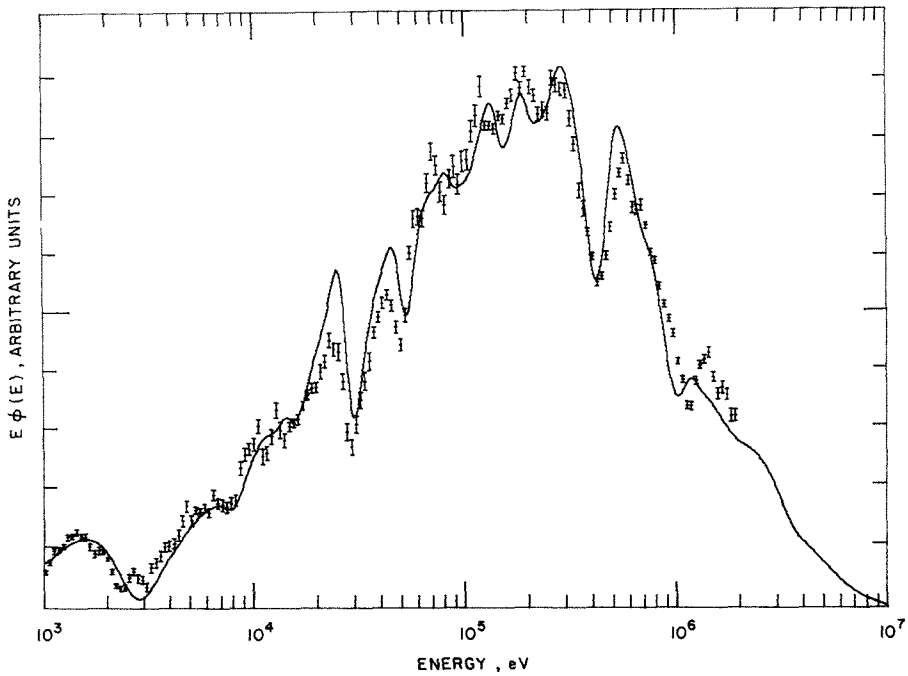

FIG. II-7-25. Comparison of the Neutron Spectrum Measured at the Center of ZPR-9/FTR-3 with the Result of a 1980-Group MC² Calculation Smoothed by a Guassian Lethargy Window with a 0.15 Standard Deviation. *ANL Neg. No. 116-115.*

composition of the radial reflector used in the generation of that set.

CALCULATED RADIAL AND AXIAL REACTION RATES IN FTR-3

Using the 29006 cross-section set the variations of Pu-239 fission, U-238 fission, and B-10 capture have been computed along the central axis of the inner core of FTR-3 and in the midplane of FTR-3 along a radius which passes halfway between two of the 16 peripheral B_4C control clusters. The 29-group flux distribution for the computation of the radial variations were obtained from the DIF2D diffusion theory solution of a representation of FTR in $R\theta$ geometry. For this solution a Z-buckling of $5.39 \times 10^{-4}/cm^2$ was used in a DB² absorber simulation of the axial leakage giving a k of 0.977. An auxiliary to the $R\theta$ problem was the computation by DIF1D, in a one-dimensional radial problem with the same axial buckling, of the thickness of an annular control zone which gave the same k as that of the $R\theta$ problem. The annular control zone therefore had the same control worth as that of the sixteen peripheral control zones of the problem in $R\theta$ geometry. The 29-group flux distribution used for calculation of the axial variations were obtained from the DIF2D solution of a model of FTR-3 in RZ geometry, also giving a k of 0.977. In this model the 16 peripheral iron control clusters were replaced by the control annulus whose thickness has previously been computed. An auxiliary to the RZ problem was the search for that Z-buckling which was required in the 1D cylindrical problem with the control annulus to give the same k as that of the problem in RZ geometry. This buckling was then entered into the problem in $R\theta$ geometry. The $R\theta$ solution and the RZ solution were made self-consistent by iterating in this manner through the two auxiliary calculations.

The radial reaction rate traverses were calculated for each of the detector types. The calculation of the first traverse used cross sections averaged by MC² with the homogeneous treatment in the 2100-group fundamental mode flux spectrum of the inner core composition at criticality for Pu-239 fission and U-238 fission, and of the outer core composition at criticality for B-10 capture. These cross sections do not depend much on whether the averaging has been done in the inner or outer core composition. The flux was normalized to give a reaction rate of unity at the center. The calculation of the second traverse used cross sections averaged by MC² with the homogeneous treatment in the 2100-group flux spectrum of the radial reflector composition with zero buckling. The same flux with the same normalization was used as in the calculation of the first reaction rate.

Two axial reaction rate traverses were also computed for each of the detector types using the same method. In Figs. II-7-26 and II-7-27 the computed reaction rates for each of the detectors in the radial and

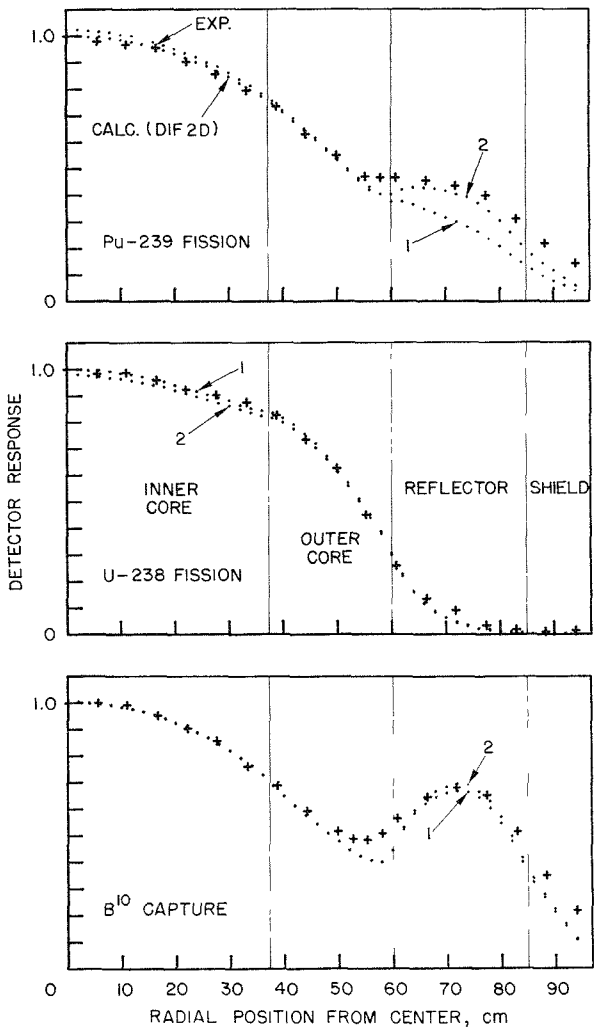

FIG. II-7-26. Radial Variation of Detector Responses near the Midplane of FTR-3 (ZPR-9 Assembly 26) and Halfway between Two of the Control Clusters. *ANL Neg. No. 116-555.*

axial directions, respectively, are compared with the experimental values (see Paper II-4). The computed curves are dotted while the experimental data are represented by crosses. The reaction rates from the first calculation with reflector averaged cross sections, are labeled "1". The reaction rates from the second calculation, with reflector averaged cross sections, are labeled "2" or "3" to designate the radial or axial reflector, respectively. The type-1 curves are valid in the inner core and outer core far from the reflector boundary. The type-2 and type-3 curves are valid well within the radial and axial reflector regions, respectively.

The radial variations of the Pu-239 fission and B-10 capture rates near the midplane of FTR-3 represent a transition between those of ZPPR/FTR-2 which has a continuous peripheral B_4C control ring, and ZPR-3 Assembly 56B[1] which has no peripheral B_4C control ring. The reaction rates for ZPPR/FTR-2 and ZPR-3 Assembly 56B were computed using neutron fluxes obtained from solutions of the 1D-cylindrical transport equation in the S_4 approximation. However, the reaction rates calculated in this way for ZPPR/FTR-2 and ZPR-3 Assembly 56B were found to differ very little from other calculations using diffusion theory fluxes.

In FTR-3, the Pu-239 fission rate and B-10 capture rate are both under-calculated near the outer edge of the shield. This effect has been observed also in connection with FTR-2 and ZPR-3 Assembly 56B, and has been discussed previously.[1] The separation of calculated curves 1 and 2 for the Pu-239 fission rate has also been discussed previously.

Comparison of the radial variation of the U-238 fission rate with that of ZPPR/FTR-2 and ZPR-3 Assembly 56B shows most clearly the effect of flux flattening in the two zone core of FTR-3.

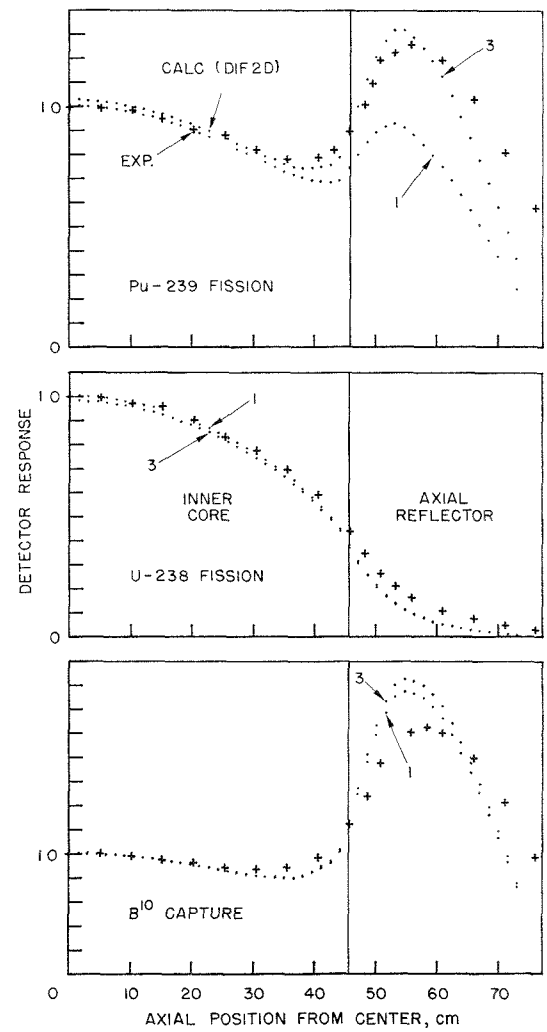

FIG. II-7-27. Axial Variation of Detector Responses Along the Central Axis of the Inner Core of FTR-3 (ZPR-9 Assembly 26). *ANL Neg. No. 116-556.*

The behaviour of the axial variations of the Pu-239 fission, U-238 fission, and B-10 capture in FTR-3 are very similar to those of ZPR-3 Assembly 56B. However, the computation of reaction rates in FTR-3 used fluxes from an *RZ* problem instead of fluxes from a slab problem. Over-calculation of the Pu-239 fission and B-10 capture rates in the axial reflector in FTR-3 are the most prominent dissimilarities between the two sets of calculations. Again, the effects at the edge of the reflector have been previously discussed.

References

1. A. Travelli, A. J. Ulrich, D. Meneghetti and J. C. Beitel, *Calculational Studies in Support of the Fast Flux Test Facility (FFTF) Critical Experiments on ZPR-3 and ZPPR*, Reactor Physics Division Annual Report, July 1, 1968 to June 30, 1969, ANL-7610, pp. 115–137.
2. G. J. Duffy, H. Greenspan, S. D. Sparck, J. V. Zapatka and M. K. Butler, *SNARG-1D, A One-dimensional Discrete-ordinate, Transport-theory Program of the CDC-3600*, ANL-7221 (1966).
3. B. J. Toppel, A. L. Rago and D. M. O'Shea, *MC²*, *A Code to Calculate Multigroup Cross Sections*, ANL-7318 (1967).
4. Reactor Development Program Progress Report, *ZPR-3 and ZPPR Operations and Analysis, Mockup Critical Experiments*, ANL-7606, 24–30 (1969).
5. Reactor Development Program Progress Report, *Experimental Reactor Physics, Development of Experimental Techniques*, ANL-7688, 9 (1970).
6. B. J. Toppel, *The Argonne Reactor Computation (ARC) System*, ANL-7332 (1967).
7. Reactor Development Program Progress Report, *ZPR-3 Operations and Analysis, Mockup Studies*, ANL-7577, 33 (1969).
8. Reactor Development Program Progress Report, *ZPR-3 and ZPPR Operations and Analysis, Mockup Critical Experiments*, ANL-7655, 29–37 (1969).
9. Reactor Development Program Progress Report, *Experimental Reactor Physics, Development of Experimental Techniques*, ANL-7661, 6–7 (1970).
10. D. A. Meneley, L. C. Kvitek and D. M. O'Shea, *Mach-1, A One-Dimensional Theory Package*, ANL-7223 (1966).
11. D. Meneghetti, A. J. Ulrich, P. J. Persiani and J. C. Beitel, *Calculational Studies in Support of the Fast Flux Test Facility (FFTF) Critical Experiments on ZPR-3*, Reactor Physics Division Annual Report, July 1, 1967 to June 30, 1968, ANL-7410, pp. 221–227.
12. A. Travelli, *A Comment on the Comparison of Theoretical with Experimental Neutron Spectra in Fast Critical Assemblies*, Proc. International Conference on Fast Critical Experiments and Their Analysis, ANL-7320, 481 (1966).

II-8. Doppler-Effect, Heterogeneity, and Sodium-Voiding Experiments in ZPR-3 Assemblies 48 and 48B

J. M. Gasidlo, A. M. Broomfield,* R. L. McVean and W. P. Keeney

Introduction

ZPR-3 Assembly 48 was a small, dilute plutonium-fueled fast critical assembly which in neutron-spectral character simulated the large fast reactors envisaged for power production. Assembly 48B was a modification of Assembly 48 in which the isotopic fraction of Pu-240 in the plutonium fuel was increased from 6.01 to 17.2% in a small zone at the center of the core. Among the measurements conducted in these two systems which relate importantly to the design of fast power reactors and to the understanding of the critical experiments were the Doppler effects in plutonium and uranium, the worth of sodium voiding, and the effects of fuel-cell plate rearrangements (heterogeneity effects).

Doppler Effect Measurements in Assemblies 48 and 48B

The uranium-oxide and plutonium-oxide materials used consisted of 70%-theoretical-density glass-bonded pellets, 1.27-cm diam by 1.27-cm long, stacked into stainless steel capsules. Sample elements for each material contained 12 pellets for a total stack length of 15.24 cm. Additional details on the design and compositions of the samples can be found in Ref. 1.

The Doppler samples used in Assembly 48 consisted of two elements separated axially by 12 cm located with the core midplane at the center of the gap. The Doppler sample used in the Assembly 48B measurements consisted of a single element centered at the midplane because of the limited length of the high Pu-240 core zone. The core drawers surrounding the Doppler sample were loaded to simulate an "average"

TABLE II-8-I. Reactivity Change due to Heating Oxide Samples in Assemblies 48 and 48B

Assembly	Sample	Δt, °K	Ih/kg of Metal Component
48	Nat U	300 to 1100	−2.03 ± 0.03
48	Pu	355 to 1100	−0.50 ± 0.03
48B	Nat U	300 to 1100	−2.57 ± 0.17

* UKAEA, Winfrith, Dorchester, Dorset, England.

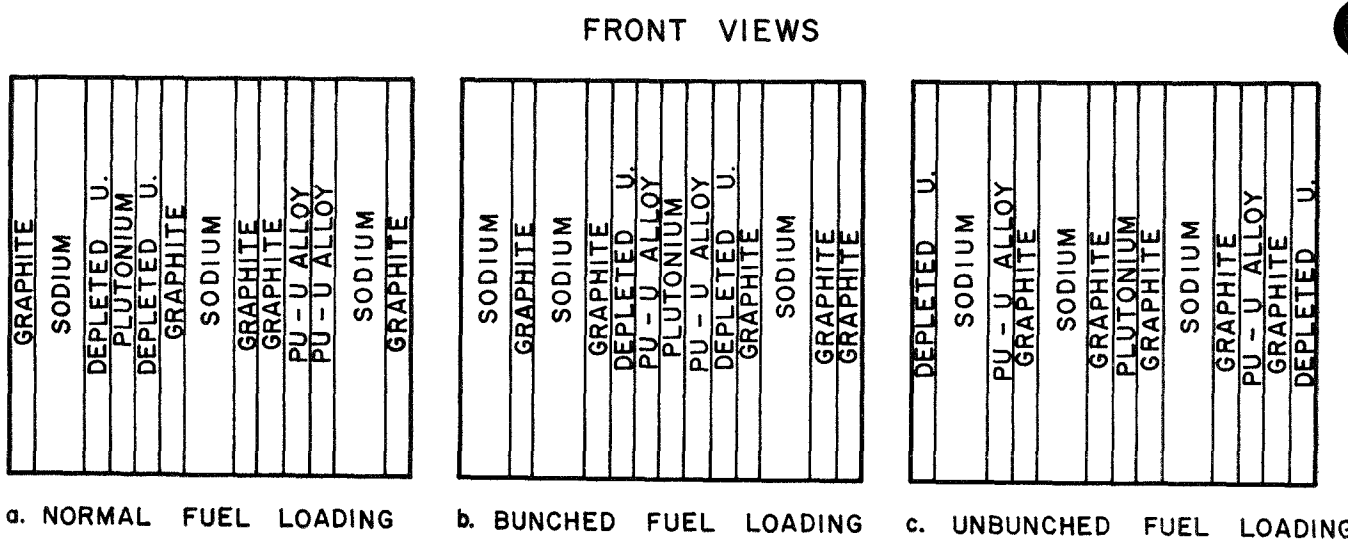

FIG. II-8-1. Plate Arrangements for the Heterogeneity and Sodium Void Measurements in Assembly 48. *ANL-ID-103-2681.*

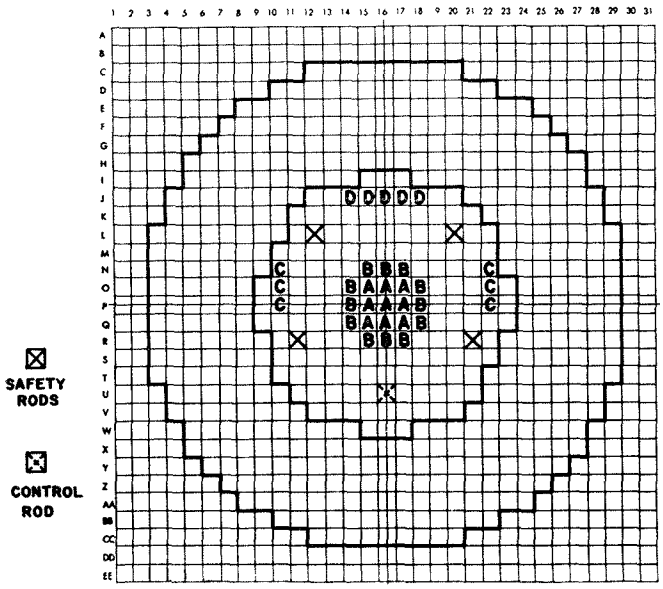

FIG. II-8-2. Core Drawer Locations for the Heterogeneity and Sodium Void Measurements in Assembly 48 in Half 1. *ANL-ID-103-2656.*

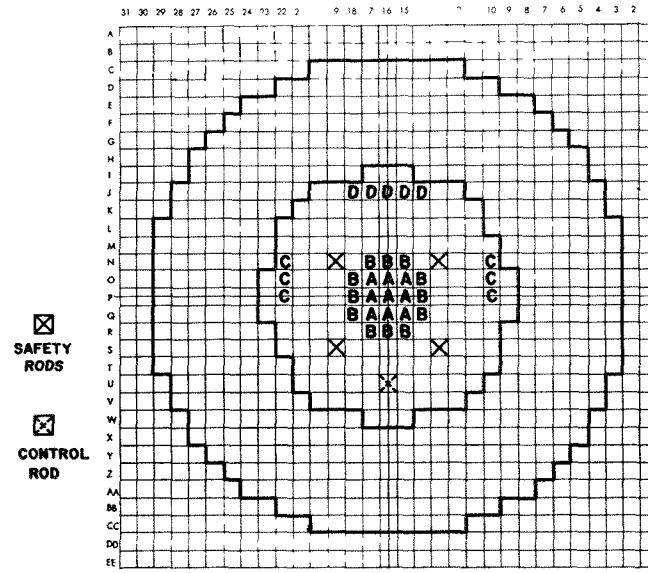

FIG. II-8-3. Core Drawer Locations for the Heterogeneity and Sodium Void Measurements in Assembly 48 in Half 2. *ANL-ID-103-2656.*

core environment. The only change between the two assemblies was the change in the core fuel composition. Additional details on the experimental technique can be found in Ref. 2.

The experimental results uncorrected for expansion effects are given in Table II-8-I. Expansion effects for the natural uranium samples are very small while the expansion and Doppler effects for the plutonium sample are similar in magnitude. The larger measured natural uranium Doppler effect in Assembly 48B is due in large part to the sample being located in a

TABLE II-8-II. WORTH OF FUEL HETEROGENEITY CHANGES IN ASSEMBLY 48

Core Location	Effective Radii, cm	Ih/Liter of Core	
		Unbunched	Bunched
Midplane[a]	0–9.37	−1.48 ± 0.18	5.92 ± 0.26
Midplane	0–14 31	−1.53 ± 0.08	5.75 ± 0.08
Axial Edge[b]	0–14.31	—	1.28 ± 0.08

[a] Region extended axially from 0.08 to 10.24 cm on both sides of the core midplane (midplane = 0.0).

[b] Region extended from 28.02 to 38.18 cm, where 38.18 the core-axial blanket interface.

TABLE II-8-III. Sodium Void Coefficients Measured in Assemblies 48 and 48B

Core Location	Effective Radii, cm	Sodium Void Coefficient, Ih/kg of Sodium Removed				
		Assembly 48				Assembly 48B Standard
		Unbunched[a]	Normal[b]	Bunched[a]	Standard	
Midplane[c]	0–9.37	—	7.9 ± 0 8	—	—	8.4 ± 1.1
Midplane	0–14.31	5.7 ± 0.3	5.2 ± 0.3	3.1 ± 0.3	5.6 ± 0.3	7.8 ± 0.5
Axial Edge[d]	0–14.31	—	−20.7 ± 0.3	−23.6 ± 0.3[e]	−20.5 ± 0.3	—
Radial Edge[e]	31.2–36.8	—	—	—	−18.5 ± 0.6	—

[a] Fuel heterogeneity loaded in sodium voiding region only.
[b] This is the standard cell composition with the ¼ in. fuel alloy plate replaced with two ⅛ in. plates.
[c] Region extended axially from 0.08 to 10.24 on both sides of the midplane.
[d] Region extended from 28.02 to 38.18 cm, where 38.18 cm is the core-axial blanket interface.
[e] A similar experiment with the remaining fuel in the sodium-voided drawers bunched to provide streaming paths gave a result of −23.5 ± 0.3.

position of higher average worth than the sample in Assembly 48.

Heterogeneity Experiments in Assembly 48

Four variations of the core basic cell—the pattern of material columns loaded across the 2-in. wide drawers—were involved in the Assembly 48 heterogeneity and sodium-worth experiments. The column arrangement called "Normal Fuel Loading" in Fig. II-8-1 differed from the standard core drawer only by having two ⅛ in. thick columns of Pu-U alloy in place of a single ¼-in. column of fuel alloy. These loadings extended only for the first 4 in. of core for the midplane measurements, or the last 4 in. of core for the axial edge measurements. The remainder of the drawer contained the standard loading.

The drawer patterns used to establish the radial geometry are shown in Figs. II-8-2 and II-8-3. The regions of radii 0 to 9.37 cm and 0 to 14.31 cm correspond to the drawers marked A, and A plus B, respectively. At the start of the core-center experiments, the front 4 in. only of all the A and B drawers were reloaded from the standard to the normal cell pattern. Then, the measurements were performed by changing first the A and then the B drawers. Then for the measurements at the axial edge of the core, the 4 in. normal cell sections of the A and B drawers were moved to the rear.

The results of the fuel heterogeneity changes are given in Table II-8-II.

Sodium Voiding Experiments

Sodium voiding experiments were performed with the same drawer loadings in the same drawer patterns as the fuel heterogeneity experiments at the core centerline. An additional measurement was made near the radial edge of the core (drawers marked C and D in Fig. II-8-2). Sodium-filled cans were replaced with stainless steel picture frames with negligibly small differences in steel mass. The results are given in Table II-8-III for both assemblies.

The comparison between the sodium void coefficients in the two assemblies should be viewed with caution since the high Pu-240 zone was not sufficiently large to obtain an equilibrium spectrum throughout.

Except for an additional experiment performed at the axial edge of Assembly 48 to determine the effects of streaming, all other sodium voiding experiments were performed with fuel heterogeneity changes in the sodium voided region only. In this case, the entire core drawer fuel columns were bunched before the sodium was voided. The result of −23.5 ± 0.3 Ih/kg agrees well with the value of −23.6 ± 0.3 obtained when the fuel was bunched in the sodium voided region only.

References

1. G. J. Fischer, D. A. Meneley, R. N. Hwang, E. F. Groh and C. E. Till, *Doppler Effect Measurements in Plutonium-Fueled Fast Power Breeder Reactor Spectra*, Nucl. Sci. Eng. **25**, 37–46 (1966).
2. J. M. Gasidlo, *Results of Recent Doppler Experiments in ZPR-3*, Proc. International Conference on Fast Critical Experiments and Their Analysis, October 1–3, 1966, ANL-7320, pp. 345–349.

II-9. Neutron Spectra and Spectral Indices in ZPR-3 Assemblies 53 and 54

R. O. Vosburgh, R. E. Kaiser, J. M. Gasidlo, J. E. Powell* and N. A. Hill†

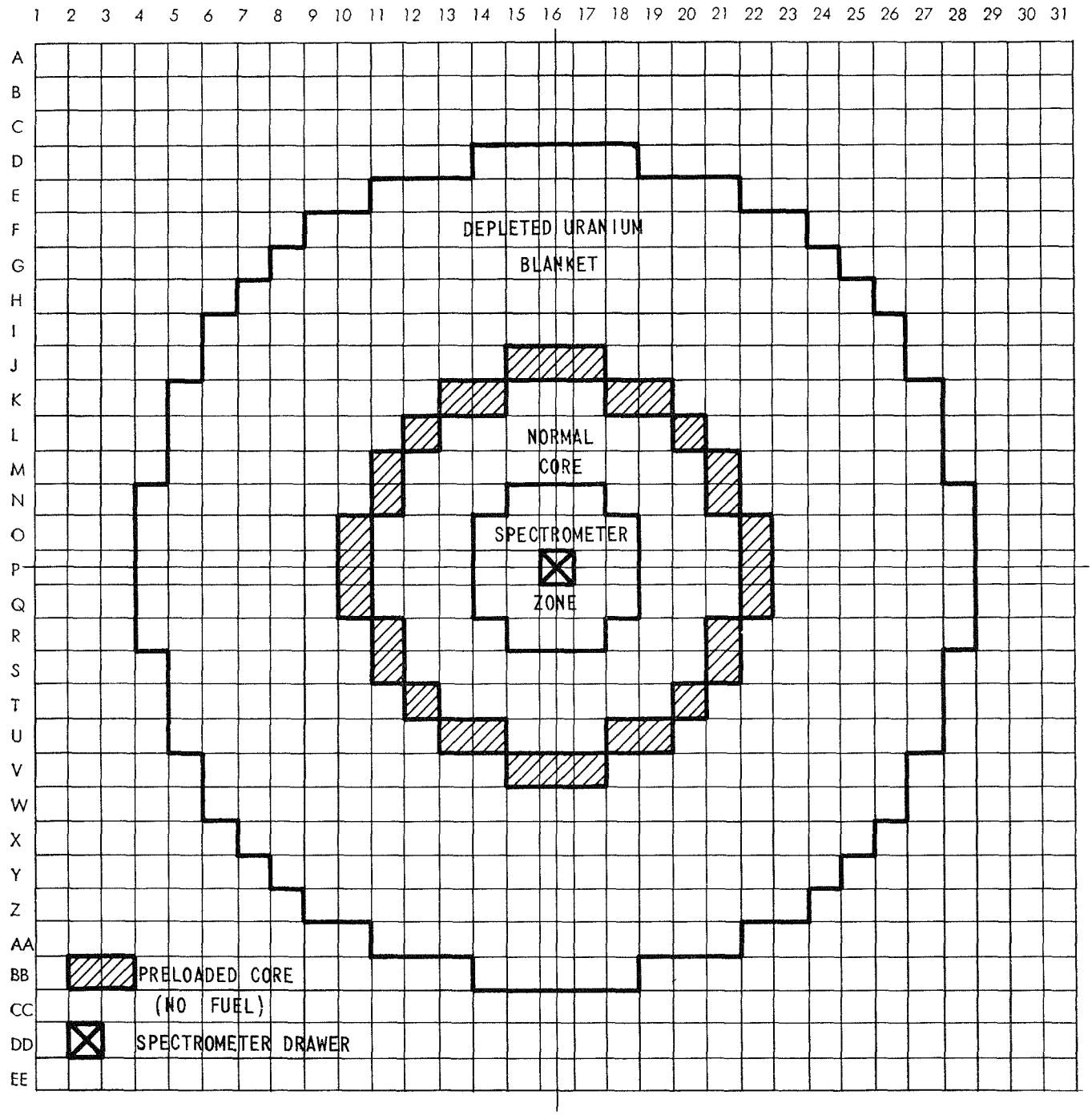

Fig. II-9-1. Interface Diagram of Assembly 53 During Proton-Recoil Spectrum Measurements. *ANL-ID-103-2954.*

Introduction

ZPR-3 Assemblies 53 and 54 were depleted uranium and iron reflected versions, respectively, of the fourth in a series of basic physics cores beginning with Assemblies 48, 49 and 50. This report includes a description of the measurements of the central neutron spectrum in Assembly 53 and central fission ratios and reaction rate traverses from both Assemblies 53 and 54.

* Sandia Corporation, Albuquerque, New Mexico.
† Student, University of Washington, Seattle, Washington.

TABLE II 9 I ATOM DENSITIES IN THE SPECTROMETER ZONE OF ZPR 3 ASSEMBLY 53[a]

Element	10^{24} atoms/cm^3
Pu 239	0 001658
Pu 240	0 000107
Pu 241	0 0000114
U 235	0 0000061
U 238	0 002610
Fe	0 009582
Ni	0 001137
Cr	0 002383
Si	0 000116
Al	0 000103
C	0 055822
Mo	0 000208

[a] Low gamma background zone at core center

PROTON-RECOIL SPECTRUM MEASUREMENTS IN ZPR-3 ASSEMBLY 53

Several count rate checks were made during the approach-to-critical in order to determine the lowest degree of subcriticality at which the measurement could be made Since these checks indicated a relatively high gamma ray background from the fuel, a special zone was built into the center of the reactor using nickel-clad fuel plates which had not been exposed to a significant neutron flux for an appreciable length of time This low gamma-ray zone extended 9 in in depth in the half containing the counter and 6 in in depth in the half opposite the counter The configuration is shown in Fig II-9-1 The atom densities, which differ only slightly from the standard core, are

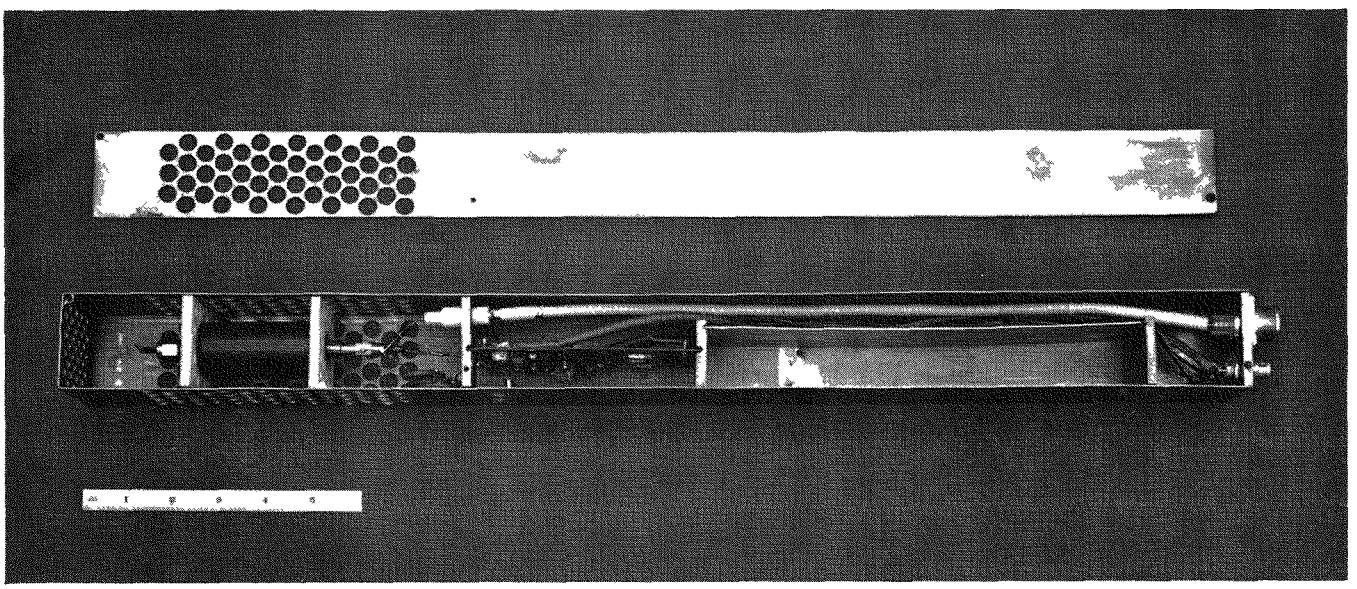

FIG II 9 2 Typical Proton Recoil Counter Arrangement in a ZPR 3 Drawer *ANL ID 103 A11292*

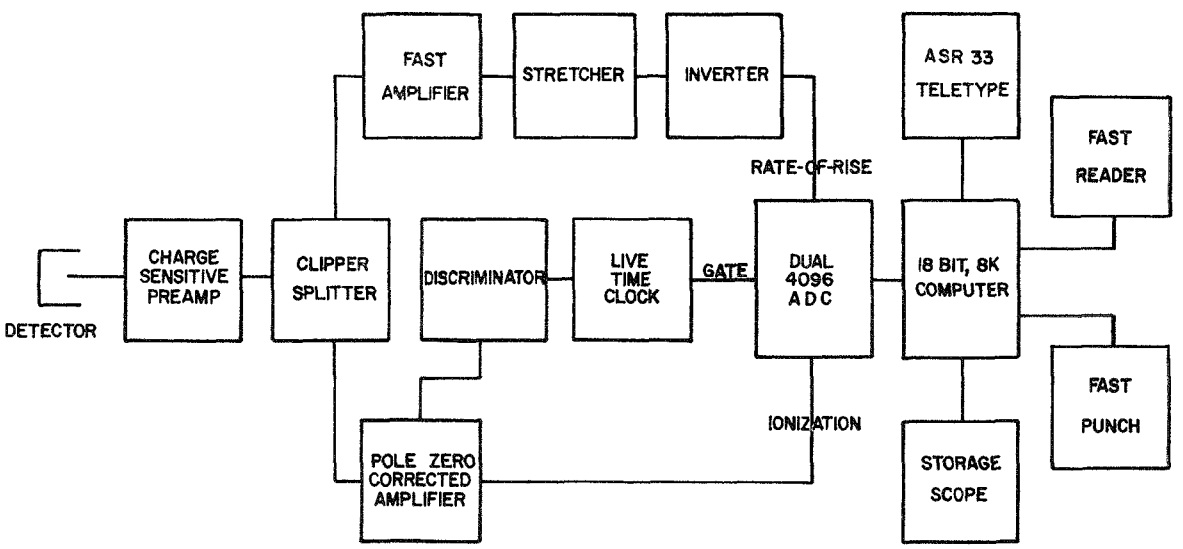

FIG II 9 3 Block Diagram of Proton Recoil Electronics System *ANL ID 103 11991*

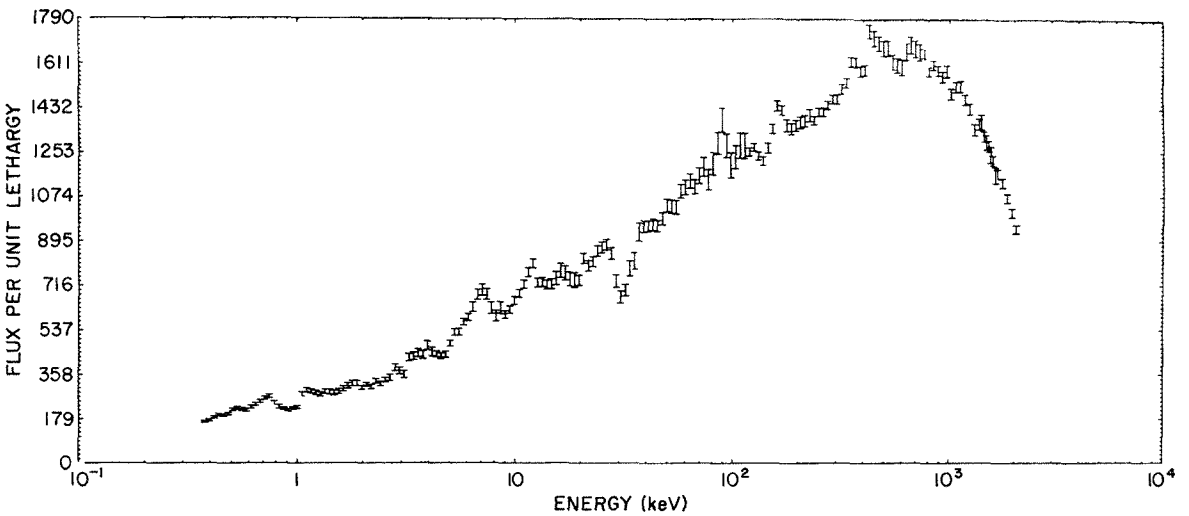

FIG. II-9-4. Measured Neutron Spectrum in ZPR-3 Assembly 53. *ANL-ID-103-A2061 Rev. 1.*

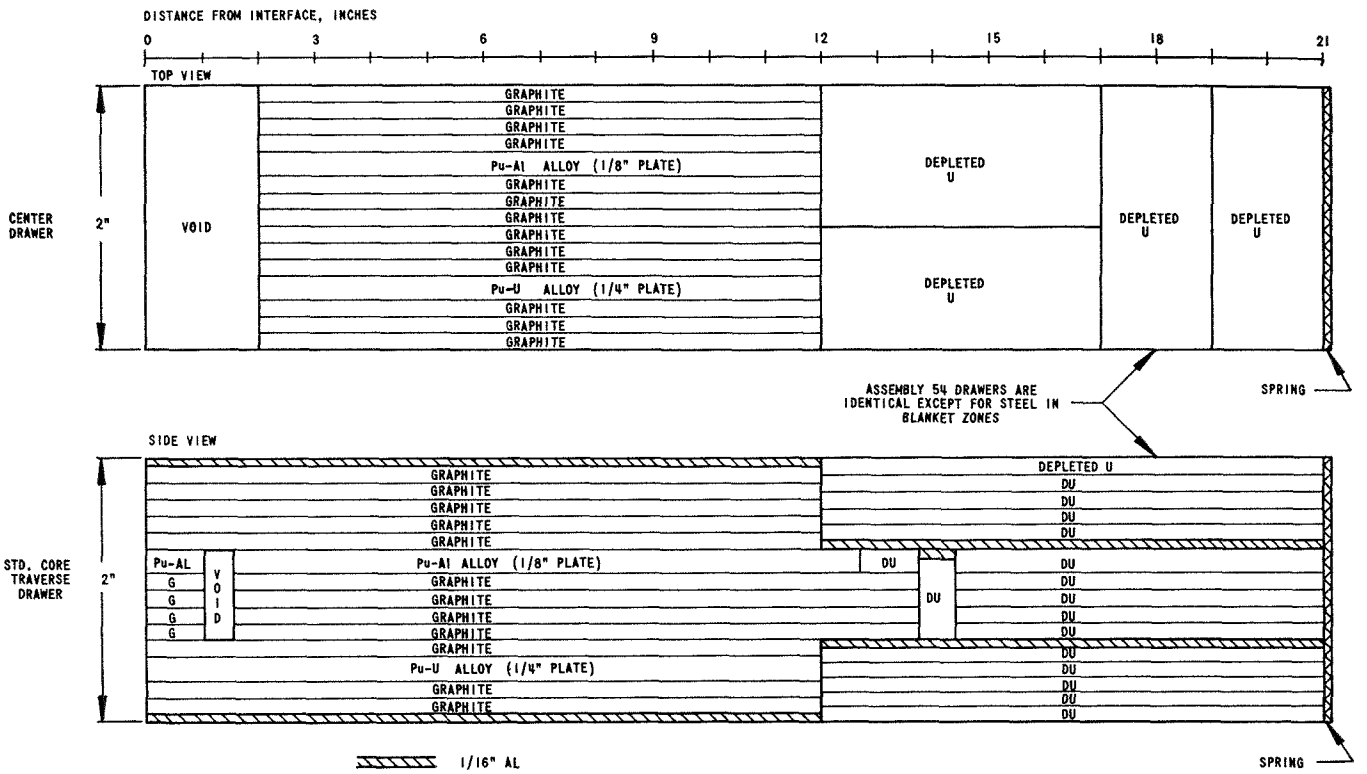

FIG. II-9-5. Traverse Drawer Configurations for ZPR-3 Assemblies 53 and 54. *ANL-ID-103-2053.*

given in Table II-9-I. After completion of the spectrum measurement, the original fuel was replaced so that the nickel-clad fuel was not present in the reference core.

The measurement was made over the energy range 308 eV to 1.5 MeV with the reactor approximately 6.6% Δk subcritical. Two cylindrical proportional counters were used to obtain the proton-recoil data. One counter had a predominantly hydrogen gas filling at 5 atm total pressure and was used below 130 keV. The gas filling also included methane as a quenching gas and a small amount of nitrogen for calibration. A 6 mm thick lead sleeve surrounded the effective counting length and provided a decrease in gamma sensitivity (approximately a factor of 2) with no significant effect upon the neutron spectrum, as demonstrated by Bennett.[1]

The second counter was filled with methane to a

TABLE II-9-II. PROTON RECOIL SPECTRUM DATA FOR 0.05 LETHARGY SPACING

Energy	Flux, (per unit lethargy)	Flux Error	Energy	Flux, (per unit lethargy)	Flux Error	Energy	Flux, (per unit lethargy)	Flux Error	Energy	Flux, (per unit lethargy)	Flux Error
2026. keV	946.8	17.0	225.5 keV	1410.	24.7	26.4 keV	885.2	21.8	3.08 keV	360.0	14.5
1929.	1013.	18.2	214.7	1388.	22.7	25.1	874.6	22.3	2.93	374.4	13.7
1837.	1073.	17.8	204.5	1382.	23.5	23.9	860.0	21.5	2.79	388.0	13.7
1750.	1135.	19.0	194.8	1369.	21.6	22.8	817.3	20.4	2.66	347.2	12.5
1667.	1172.	19.8	185.5	1356.	22.7	21.7	800.6	21.4	2.53	337.5	9 5
1587.	1226.	20.8	176.7	1370.	24.1	20.6	830.0	20.6	2.41	321.6	8.8
1512.	1284.	21.9	168.2	1430.	19.3	19.7	742.4	20.8	2.30	333.1	9.5
1440.	1325.	20.9	160.2	1448.	20.6	18.7	743.8	30.2	2.19	309.4	8.9
1371.	1376.	22.1	152.6	1355.	18.9	17.8	745.6	27.9	2.08	318.4	8.4
1306.	1352.	23.2	145.3	1277.	20.2	17.0	769.9	28.5	1.98	306.3	8.3
1244.	1437.	22.2	138.4	1225.	17.6	16.2	780.9	29.0	1.89	322.1	11.8
1184.	1475.	20.8	131.8	1245.	16.4	15.4	749.1	26.7	1.80	322.3	11.6
1128.	1528.	22.0	125.5	1280.	15.2	14.7	727.2	20.6	1.72	313.5	11.4
1074.	1526.	20.6	119.6	1262.	16.6	14.0	723.9	18.2	1.63	301.4	11.0
1023.	1498.	21.6	113.9	1287.	51.7	13.3	733.5	18.1	1.56	290.5	10.1
974.5	1590.	23.5	108.5	1288.	51.5	12.7	731.4	17.5	1.48	285.2	9.8
928.1	1567.	21.6	103.3	1241.	47.3	12.1	809.9	18.0	1.41	289.5	9.6
883.9	1592.	20.4	98.4	1208.	51.9	11.5	774.4	18.3	1.34	290.0	9.6
841.8	1614.	18.6	93.7	1288.	48.2	10.9	725.5	16.8	1.28	279.1	9.4
801.7	1588.	17.6	89.2	1392.	48.6	10.4	688.1	16.1	1.22	285.3	9.3
763.5	1659.	18.4	85.0	1299.	44.6	9.93	659.5	16.6	1.16	291.2	8.5
727.2	1664.	33.1	80.9	1214.	45.5	9.46	622.1	15.4	1.10	296.2	8.4
692.5	1678.	33.3	77.1	1148.	42.2	9.01	603.0	16.0	1.05	279.6	8.4
659.5	1694.	33.7	73.4	1201.	38.8	8.58	629.9	23.5	1.00	226.7	5.7
628.1	1666.	34.2	69.9	1165.	32.7	8.17	596.8	21.7	954 eV	222.4	5.4
598.2	1604.	31.7	66.6	1120.	28.8	7.78	629.3	23.9	909	215.7	5.3
569.7	1612.	29.4	63.4	1143.	29.4	7.41	685.1	22.2	866	220.7	5.3
542.6	1625.	29.8	60.4	1117.	29.9	7.06	702.3	22.7	825	228.6	7.3
516.8	1681.	30.5	57.5	1102.	27.4	6.72	683.8	20.9	786	244.5	7.3
492.2	1681.	31.5	54.8	1037.	28.5	6.40	633.6	19.3	748	271.5	7.0
468.7	1701.	29.1	52.2	1039.	27.0	6.10	591.8	14.6	712	264.0	6.7
446.4	1722.	30.5	49.7	1044.	25.7	5.81	573.0	13.8	678	250.8	6.4
425.2	1751.	28.2	47.3	990.2	24.5	5.53	532.5	13.8	646	239.1	6.2
404.9	1593.	21.2	45.0	960.3	23.3	5.27	531.7	13.4	615	228.1	6.2
385.6	1588.	20.3	42.9	965.8	23.8	5.02	485.7	12.3	586	215.2	5.8
367.3	1625.	19.8	40.9	959.8	22.0	4.78	441.6	12.4	558	218.5	5.7
349.8	1625.	19.1	38.9	957.2	23.4	4.55	435.1	11.8	532	223.4	5.5
331.1	1540.	18.9	37.1	934.9	36.4	4.33	442.7	12.0	506	217.7	5.3
317.3	1516.	19.9	35.3	818.2	33.3	4.13	451.9	18.0	482	199.7	5.1
302.1	1475.	18.3	33.6	788.7	30.6	3.93	476.5	17.7	459	193.9	4.7
287.8	1475.	17.5	32.0	701.2	24.1	3.74	439.1	16.2	437	197.0	4.6
274.1	1451.	16.7	30.5	673.7	24.3	3.56	447.2	16.2	416	185.6	4.4
261.0	1424.	17.1	29.0	738.3	24.9	3.40	433.9	16.0	397	174.3	4.3
248.6	1423.	16.5	27.7	850.2	23.6	3.23	428.7	14.8	378	168.1	4.0
236.7	1390.	16.9									

TABLE II-9-III. Reaction Rate Data for Pu-239 and U-235 in Assembly 53

Pu-239			U-235		
Transverse Position,[a] in.	Total Counts[b]	Count Time, sec	Transverse Position,[a] in.	Total Counts[b]	Count Time, sec
29	47437	30	29	44409	60
31	54194	↓	31	50262(2)	↓
32	56074		32	51162(2)	
33	58078		33	53972	
34	59052		34	54417	
34.5	60011		34.5	55659	
35	60122		35	56684	
35.5	61005		35.5	57156	
36	60820(5)		36	56595(5)	
36.5	61579		36.5	56664	
37	60267		37	56929	
37.5	60184		37.5	57519	
38	59380(2)		38	56440	
39	59653(2)		39	55625	
40	57398(2)		40	56112(3)	
41	55314		41	53936	
43	49992		43	48471	
45	42280		45	44310	
47	33736		47	37768	
48	30026		48	31622(2)	
49	24256		49	29428	
50	18721	↓	50	21957	
51	28737	60	51	16520	
52	22107	↓	52	12462	↓
53	17050		53	19066	120
54	12482		55	11060	↓
55	9469		57	6698	
57	5494	↓			

[a] Center line is at 36 in.

[b] (N) indicates that the listed number is the average of N measurements.

pressure of 5 atm and was used over the energy range of 100 keV to 1.5 MeV. As in the hydrogen counters, some nitrogen was included to aid in calibration and the sensitive volume was covered with a 0.6 mm thick lead cylinder. A typical counter arrangement in a ZPR-3 drawer is shown in Fig. II-9-2.

A block diagram of the electronics system is shown in Fig. II-9-3. It is similar to one that has been previously reported[2], except that the preamplifier[3] is a charge-sensitive device and the linear amplifier[4] is pole-zero corrected and matched to the preamplifier.

Results of the measurements are shown in Fig. II-9-4. The spectrum is relatively soft, reflecting the high carbon content of the core. Except for the depressions at 9, 30 and 100 keV, which are attributed to iron resonances, there is little structure in the spectrum. Tabulated results of the measurement are included in Table II-9-II.

Reaction Rate Traverses

Reaction rate traverses along the radial center line were made with small chambers using Pu-239, U-238, U-235, and B-10 as the sensitive materials. Similar experiments were performed in the previous assemblies of this series. The experiment was performed in both Assemblies 53 and 54 and include data in the reflector as well as in the core.

Reaction rate traverses were made by positioning the small traverse counters in a stainless steel guide tube. The tube was located in the fixed half with its

TABLE II-9-IV. Reaction Rate Data for U-238 and B-10 in Assembly 53

U-238			$B^{10}F_3$		
Transverse Position,[a] in.	Total Counts[b]	Count Time, sec	Transverse Position,[a] in.	Total Counts[b]	Count Time, sec
29	36586	30	29	66470	30
31	41321	↓	31	74360	↓
32	43063		32	77022	
33	43917		33	80192	
34	45502		33.5	80638	
34.5	45326		34	81001	
35	44390		34.5	82195	
35.5	44357		35	82673	
36	44834(5)		35.5	83179	
36.5	44420		36	83326(9)	
37	45220		36.5	83229	
37.5	45901		37	83173	
38	46533(3)		37.5	82637(2)	
39	44762(2)		38	81450	
40	44383(2)		38.5	81060	
41	41456		39	80795	
43	37629		40	79521	
45	32038		41	76551	
47	25655		43	68922	
48	21253		45	59580	
49	17227		47	47230	
50	12304	↓	48	40717	
51	16412	60	49	33018	
52	12050		50	25332	
53	7427		51	36740	
54	4914		52	27424	
55	3457		53	20224	
57	1680		54	14966	
			55	11330	
			57	6490	
		↓	59	3629	↓

[a] Center line is at 36 in.

[b] (N) indicates that the listed number is the average of N measurements.

TABLE II-9-V. REACTION RATE DATA FOR Pu-239 AND U-235 IN ASSEMBLY 54

Pu-239			U-235		
Transverse Position,[a] in.	Total Count[b]	Count Time, sec	Transverse Position,[a] in.	Total Count[b]	Count Time, sec
29	59186	30	29	73315	30
30	62260		30	77553	
31	65329		31	81123	
32	68820		32	83718	
33	70407		33	87044	
34	71624		34	88116	
35	73226		35	88962	
36	72488(7)		36	89559(7)	
38	71063		38	87851	
40	68512		40	83555	
42	63658		42	77518	
44	57061		44	69198	
45	52121		45	64098	
46	50465		46	60019	
47	47269(2)		47	56050(2)	
47.5	46053		47.5	54750	
48	47701		48	53731(2)	
48.5	49022		48.5	53253	
49	48284(2)		49	52555	
49.5	47662		49 5	51337	
50	47060		50	50083	
51	44538		50.5	48332	
52	41197		51	46171	
53	37601		52	42293	
54	34370		53	38279	
56	28030		54	33662	
58	21626		56	25419	
60	15767	↓	60	10989	↓

[a] Center line is at 36 in.

[b] (N) indicates that the listed number is the average of N measurements.

axis 1 in. back from the interface. The drawer configuration was the same as for the perturbation measurements, Fig. II-9-5, and included the 2 x 2 x 2 in. cavity at the front of the fixed half central drawer. After every few measurements, the measurement at the core center was repeated to check for counter or electronic drift.

The chambers used included a stainless-steel clad BF_3 proportional counter and three brass, gas-filled fission counters employing Pu-239, U-238 or U-235 as the sensitive material.

During the measurements, the autorod was used to maintain constant reactor power, so that no reference was required to correct for counter variations. All count rates were corrected for dead time effects, which were small (0.5% or less). The errors in the measurements are thus primarily due to count rate statistics, with the exception of U-235 and U-238, where an additional error of slightly less than 1% is caused by the relative constituent ratios in the uranium platings and the small fission ratio of U-238 to U-235. The fission profiles obtained with the plutonium counter are roughly those for the average plutonium isotopic mixture of the core.

The results of the four traverses, in terms of total counts over a stated interval, are given in Tables II-9-III through II-9-VI, for Assemblies 53 and 54. Count rate data normalized to 1.0 at the reactor centerline are shown graphically in Figs. II-9-6 through II-9-13 for each traverse made in the two assemblies. A slight dip can be seen at core center on some of these

TABLE II-9-VI. REACTION RATE DATA FOR U-238 AND B-10 IN ASSEMBLY 54

U-238			$^{10}BF_3$		
Transverse Position,[a] in.	Total Counts[b]	Count Time, sec	Transverse Position,[a] in.	Total Counts[b]	Count Time, sec
29	23132	30	29	55660	30
31	26123		30	59040	
32	27061		31	61733	
33	27912		32	63775	
34	28933		33	65178	
34.5	28248		34	67143	
35	28187		35	68327	
35.5	28160		36	67917(6)	
36	28387(8)		38	66843	
36.5	28247		40	64002	
37	28342		42	59306	
37.5	28718		44	53453(2)	
38	28760		45	50167	
39	27880(2)		46	48845	
40	27334		47	48234(2)	
41	25737		47.5	48269	
43	23234		48	49961	
45	19125	↓	48.5	50831	
47	27458	60	49	51450	
48	20110		49.5	51876	
49	13949		50	52296	
50	10078		50.5	51901	
51	7066		51	51842	
53	3493	↓	51.5	50202	
57	1838	120	52	48304	
			53	44000	
			54	40051	
			55	34552	
			56	29831	
			57	25373	
			58	20419	
			60	11730	↓

[a] Center line is at 36 in.

[b] (N) indicates that the listed number is the average of N measurements.

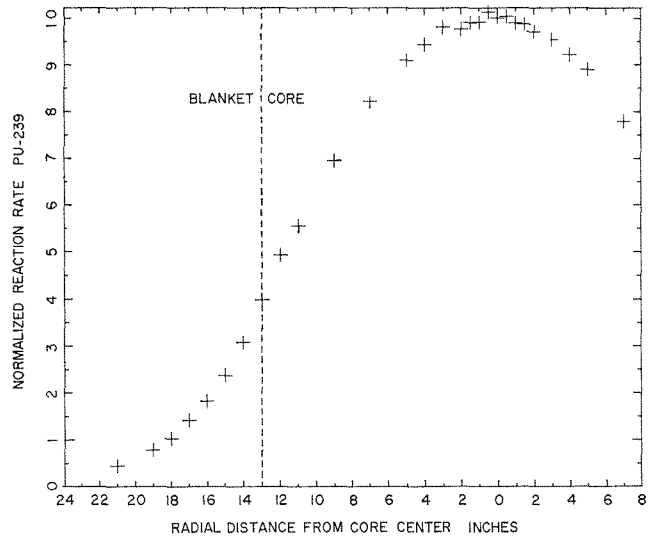

FIG. II-9-6. Normalized Radial Reaction Rate Traverses for Pu-239 in Assembly 53. *ANL-ID-103-2945.*

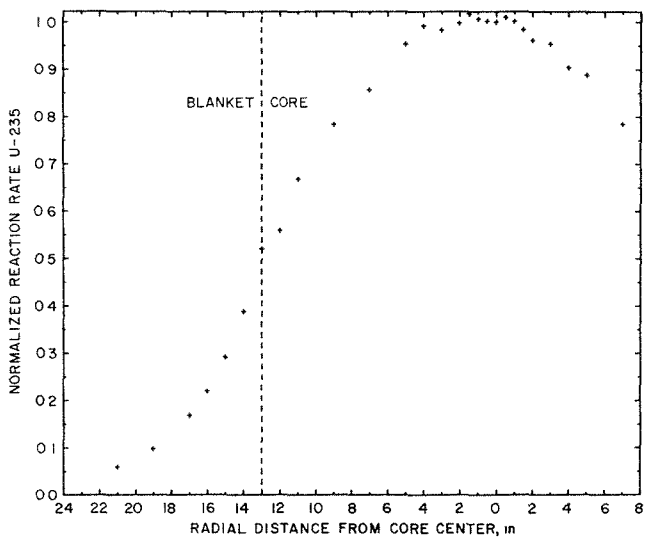

FIG. II-9-7. Normalized Radial Reaction Rate Traverses for U-235 in Assembly 53. *ANL-ID-103-2946 Rev. 1.*

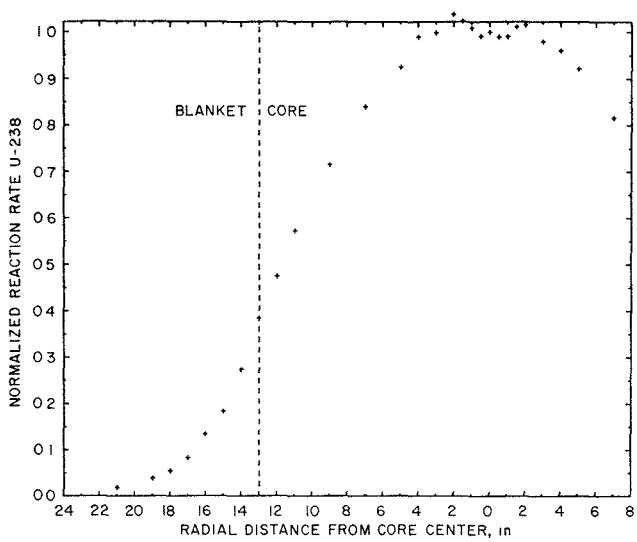

FIG. II-9-8. Normalized Radial Reaction Rate Traverses for U-238 in Assembly 53. *ANL-ID-103-2950 Rev. 1.*

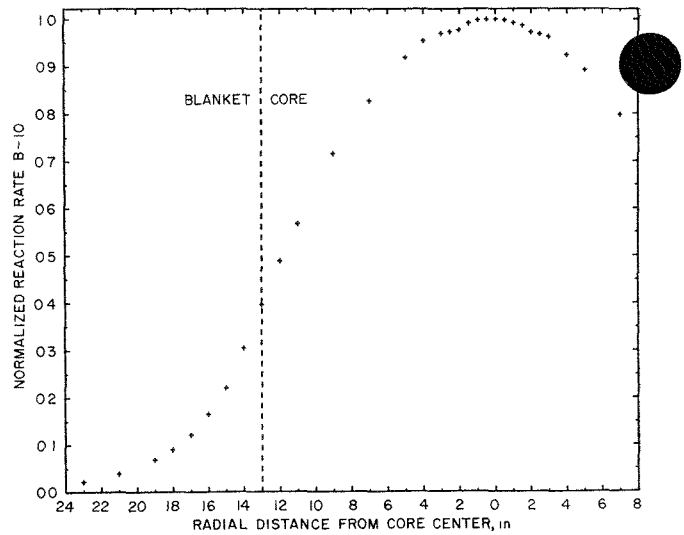

FIG. II-9-9. Normalized Radial Reaction Rate Traverses for B-10 in Assembly 53. *ANL-ID-103-2947 Rev. 1.*

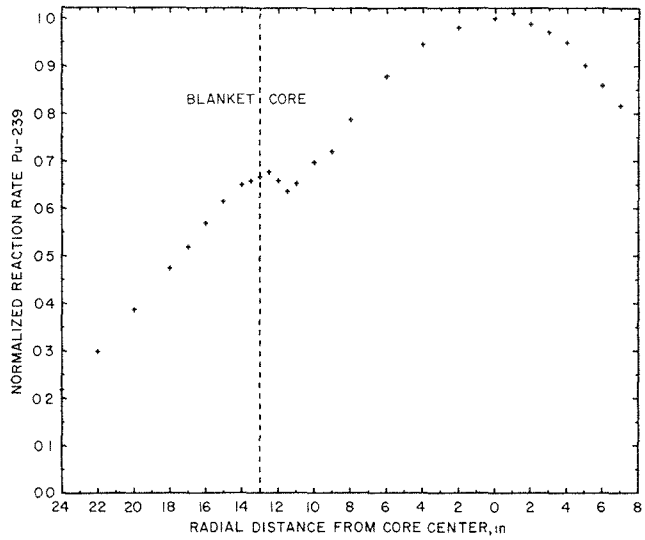

FIG. II-9-10. Normalized Radial Reaction Rate Traverses for Pu-239 in Assembly 54. *ANL-ID-103-2948 Rev. 1.*

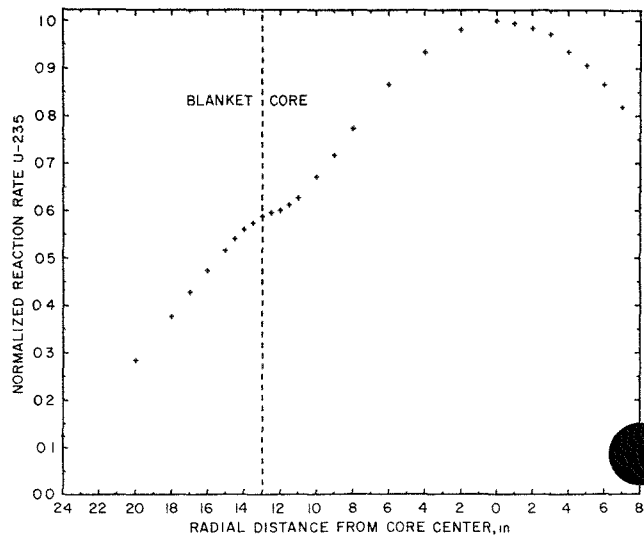

FIG. II-9-11. Normalized Radial Reaction Rate Traverses for U-235 in Assembly 54. *ANL-ID-103-2949 Rev. 1.*

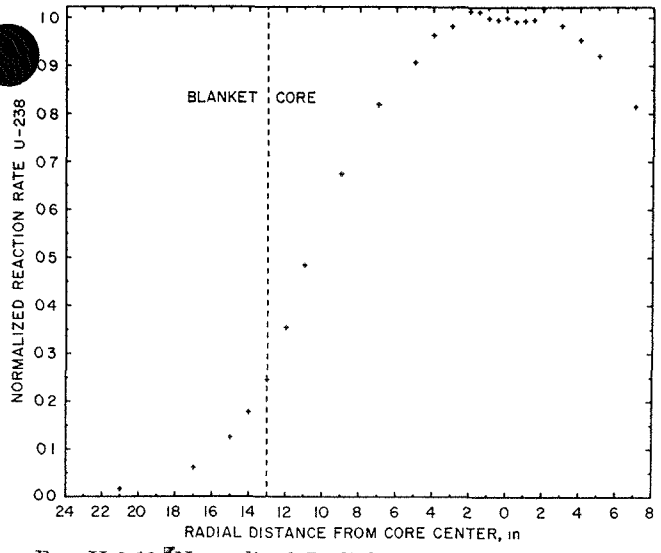

FIG. II-9-12. Normalized Radial Reaction Rate Traverses for U-238 in Assembly 54. *ANL-ID-103-2951 Rev. 1.*

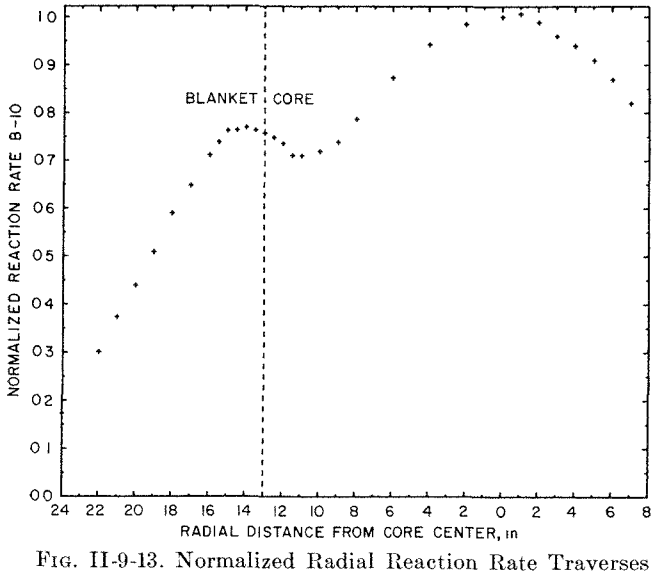

FIG. II-9-13. Normalized Radial Reaction Rate Traverses for B-10 in Assembly 54. *ANL-ID-103-2952 Rev. 1.*

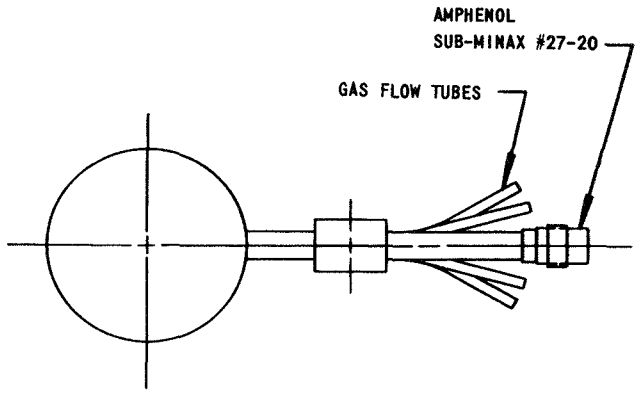

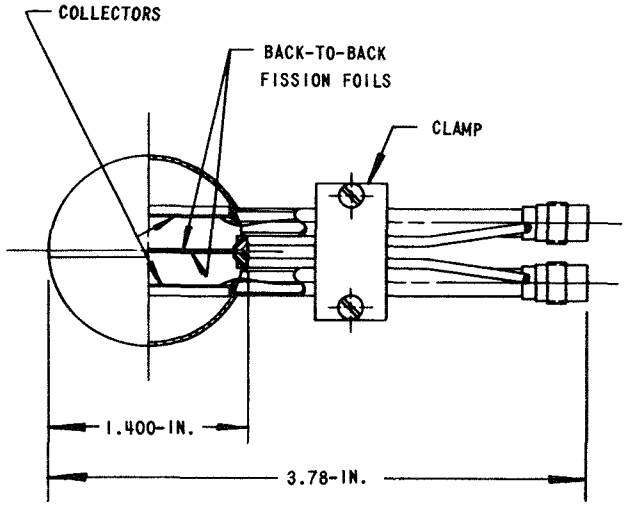

FIG. II-9-14. Back-to-Back Fission Chamber Configuration. *ANL-ID-103-A2080.*

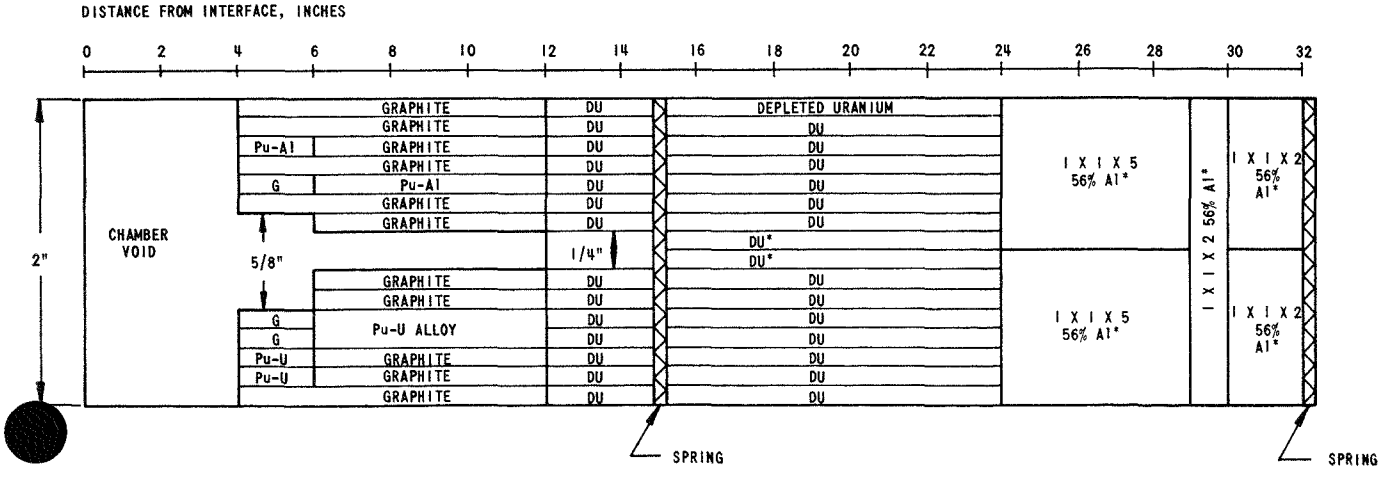

* DENOTES ONE-INCH HIGH PLATES

FIG. II-9-15. Drawer Configuration for Central Fission Ratio Measurements in Assembly 53. *ANL-ID-103-A2079.*

curves, which is attributed to the presence of the 2 x 2 x 2 in. void in the center drawer.

Differences in spectral effects between the two assemblies are particularly apparent in the graphs of Pu-239 and B-10 reaction rates. In both cases, the greater slowing down in the iron blanket is demonstrated by the marked increase in reaction rate as the detector enters the reflector, a phenomenon that does not occur with the uranium blanket. The curve for U-235 shows the same property, though to a lesser degree, since it is not as sensitive to a softening of the spectrum as are Pu-239 and B-10.

TABLE II-9-VII. Fission Ratio Foil Compositions and Masses

Foil Number	Primary Isotope	Total Mass, μg	Composition	
			Isotope	w/o
11	U-238	124.86	U-234	0.005
			U-235	0.713
			U-238	99.282
8, 9, 22, 23, 25, 27	U-235	see below	U-235	93.28
			U-234	1.045
			U-236	0.287
			U-238	5.38
29	U-236	101.22	U-236	93.21
			U-234	0.047
			U-235	4.57
			U-238	2.17
28	U-234	98.93	U-234	79.58
			U-235	15.08
			U-236	—
			U-238	5.34
30	U-233	104.03	U-233	95.597
			U-234	0.063
			U-235	4.042
			U-236	0.012
			U-238	0.286
72	Pu-240	116.44	Pu-240	95.505
			Pu-239	4.290
			Pu-241	0.186
			Pu-242	0.019
65	Pu-239	108.88	Pu-239	94.414
			Pu-240	5.264
			Pu-241	0.307
			Pu-242	0.016

U-235 Foil Weights		Atomic Masses	
No.	Wt, μg		
		U-233	233.0395
		U-234	234.0409
8	88.12	U-235	235.0439
19	112.45	U-236	236.0457
22	109.81	U-238	238.0508
23	108.65	Pu-239	239.0522
25	113.06	Pu-240	240.0540
27	111.61	Pu-241	241.0564
		Pu-242	242.0587

TABLE II-9-VIII. Central Fission Ratios in ZPR Assemblies 50 and 53

Ratio	Assembly 50	Assembly 53
U-233/U-235	1.412 ± 0.014	1.454 ± 0.014
U-234/U-235	0.158 ± 0.002	0.146 ± 0.002
U-236/U-235	0.054 ± 0.0005	0.053 ± 0.0005
U-238/U-235	0.0251 ± 0.0003	0.0254 ± 0.0002
Pu-239/U-235	0.903 ± 0.009	0.928 ± 0.009
Pu-240/U-235	0.159 ± 0.002	0.174 ± 0.002

Central Fission Ratios

Central fission ratios were measured in Assembly 53 for U-233/U-235, U-234/U-235, U-236/U-235, U-238/U-235, Pu-239/U-235, and Pu-240/U-235. Spherical gas-flow chambers, containing plated foils of the different isotopes, were used as in the previous assemblies of this series (see Fig. II-9-14).

Spherical gas-flow counters, containing back-to-back fission foils, were placed in a 2 x 2 x 4 in. voided section in the front of a standard core drawer as shown in Fig. II-9-15. Two ratios were measured during a single reactor run, each at a position one drawer diagonally away from the core center which is at matrix position P-16. No changes were made in the orientation of plates in the neighboring drawers. Descriptive data on the foils used is included in Table II-9-VII.

Count rates for each isotope were obtained separately for a given ratio; two counts were obtained for each foil for a given ratio. Four counter-rate ratios were then determined using different combinations of individual count rates, and the average given as the count-rate ratio for that particular pair of isotopes. Reactor power was held constant during the measurement by the autorod. Each of the count-rate ratios was then normalized to the same U-235 foil mass, and the resulting values were fed into a computer code which corrected for isotopic impurities.

The fully corrected, pure-isotope fission ratios which were obtained in Assembly 53 are listed in Table II-9-VIII along with corresponding values from Assembly 50, which was very similar in design. Although no rigorous conclusions can be drawn without a detailed analysis, the comparison does appear to accurately reflect the reduction in inelastic scattering due to the reduction in the U/Pu ratio (4.1/1.6), and the in-

reased scattering at low energies due to the addition of extra carbon, which constitutes the principle difference between the two assemblies.

References

1. E. F. Bennett, *Fast Neutron Spectroscopy by Proton-Recoil Proportional Counting*, Nucl. Sci. Eng. **27**, 16 (1967).
2. J. E. Powell, *Fast Neutron Spectrum Measurements in the Core and Reflector of ZPR-3 Assembly 51*, Trans. Am. Nucl. Soc. **11**, 217 (1968).
3. J. M. Larson, *A Wide Band Charge Sensitive Preamplifier for Proton Recoil Proportional Counting*, ANL-7517 (1969).
4. J. M. Larson and J. E. Powell, *Spectrum Distortion from Amplifier Overloads in Proton Recoil Proportional Counting*, Nucl. Instr. Methods **71**, 157 (1969).

II-10. Analysis of Reactivity Doppler Experiments for ZPR-3 Assembly 53

R. E. Kaiser and J. M. Gasidlo

Introduction

Reactivity Doppler experiments were performed in ZPR-3 Assembly 53[1], using PuO_2 and UO_2 samples ½-in. in diameter by 6 in. in length. This type of experiment is performed by oscillating the heated sample in and out of a cold reactor and measuring the reactivity change as a function of sample temperature as described by Gasidlo[2]. The analysis of these experiments involved the use of the RABBLE[3] code to generate group cross-sections and 2-D diffusion-perturbation calculations[4] to determine the reactivity effects.

Resonance Data

Resonance parameters in the resolved region were taken from Schmidt[5] for U-238 and for Pu-239. In the natural UO_2 sample, the U-235 was assumed to be of essentially infinite dilution ($\sigma_P > 10^3$), so that only the U-238 resonances were treated. Similar assumptions were made regarding the higher isotopes of plutonium in the PuO_2 sample, as this was almost pure Pu-239. Each broad group was calculated in separate runs on RABBLE so as to avoid any possible accumulation of round-off errors in the computer calculation. Resonances were used extending to energies slightly below and above the broad group limits, so that the broadened tails would be included where significant. The energy width of the fine groups in each broad group was determined such that the Doppler broadened width,

$$\Delta = \frac{2(kTE_0m)^{1/2}}{M},$$

t room temperature was equivalent to at least five ne groups.

The unresolved resonance region was treated by generating a statistical ladder of resonances based on given average parameters. The average parameters for U-238 were obtained from Schmidt,[5] and those for Pu-239 from Durston and Katsuragi.[6] Each ladder was selected according to the given averages in such a way that the original average value was reproduced exactly, and resonance spacings were assigned according to a Wigner distribution.

Each broad group in the unresolved region was subdivided into three to five sub-groups about 400 eV in width and equally spaced. A resonance ladder was then obtained and separate RABBLE problems run for each sub-group.

Group Cross-Section Calculations

The calculation of broad group sample cross sections was performed with the RABBLE code for each in-

TABLE II-10-I. Energy Group Structure used in Assembly 53 Doppler Analysis

Group		E_L	ΔU
1		1.35 MeV	2.0
2		302 keV	1.5
3		67.4	1.5
4		24.8	1.0
5		15.0	0.5
6		9.12	0.5
7	b	5.53	0.5
8	b	3.35	0.5
9	b	2.03	0.5
10	a, b	961 eV	0.75
11	b	454	0.75
12	b	275	0.5
13	b	61.4	1.5
14	b	13.7	1.5
15		0.682	3.0

NOTE:
a—Groups used in PuO_2 RABBLE calculations
b—Groups used in UO_2 RABBLE calculations

dividual group at temperatures of 300, 500, 800 and 1100°K. The calculations followed the group structure shown in Table II-10-I, with the groups involved in the RABBLE calculation indicated. The lower limit of the RABBLE calculations was dictated in part by the resonance data and in part by the relative contribution to the total effect of the resonances in that group. The relative contribution from a given group was assumed proportional to $\phi\phi^*(\sigma_T - \sigma_{300})$, where σ_T is the cross-section at some higher temperature and ϕ and ϕ^* are real and adjoint fluxes at the core center as obtained from a one-dimensional diffusion problem. If the product $\phi\phi^*\Delta\sigma$ for any one broad group were less than one percent of the sum over all groups, that group was not included in the calculation.

The p-wave resonances were included for both the PuO_2 and UO_2 samples, and parameters were obtained as described above. The s-wave RABBLE calculations were programmed first, assuming no constant background cross section for the resonance material. The average cross-section obtained from the s-wave calculation was then used as the constant background cross-section in the p-wave calculation. The two Pu-239 p-wave sequences were run together, thus allowing for interference between the sequences.

In the resolved region the values of σ_a, (and σ_f for Pu-239) obtained from the RABBLE runs were used as the broad group sample cross sections. In the unresolved region, the average of the sub-group values, assuming constant flux across the broad group, was used. The complete set of sample cross sections was obtained from the MC² code[6], with the oxide sample treated as the fuel pin surrounded by a diluent region of stainless steel, and using fluxes calculated with the homogeneous core composition. The purpose of the steel diluent was to represent the structural material in the capsule, heater, vacuum can, Doppler rod, and Doppler rod guide tube. The values of σ_a and σ_f obtained from the RABBLE problems at 300° were then inserted into the MC² cross-section set for each sample. Appropriate adjustments were made to the transport cross sections in the modified groups in order to maintain a consistent set. Thus sets of cross sections were obtained which were characteristic of U-238 and Pu-239 at 300°, and consistent with the RABBLE calculations at higher temperatures. A homogeneous MC²

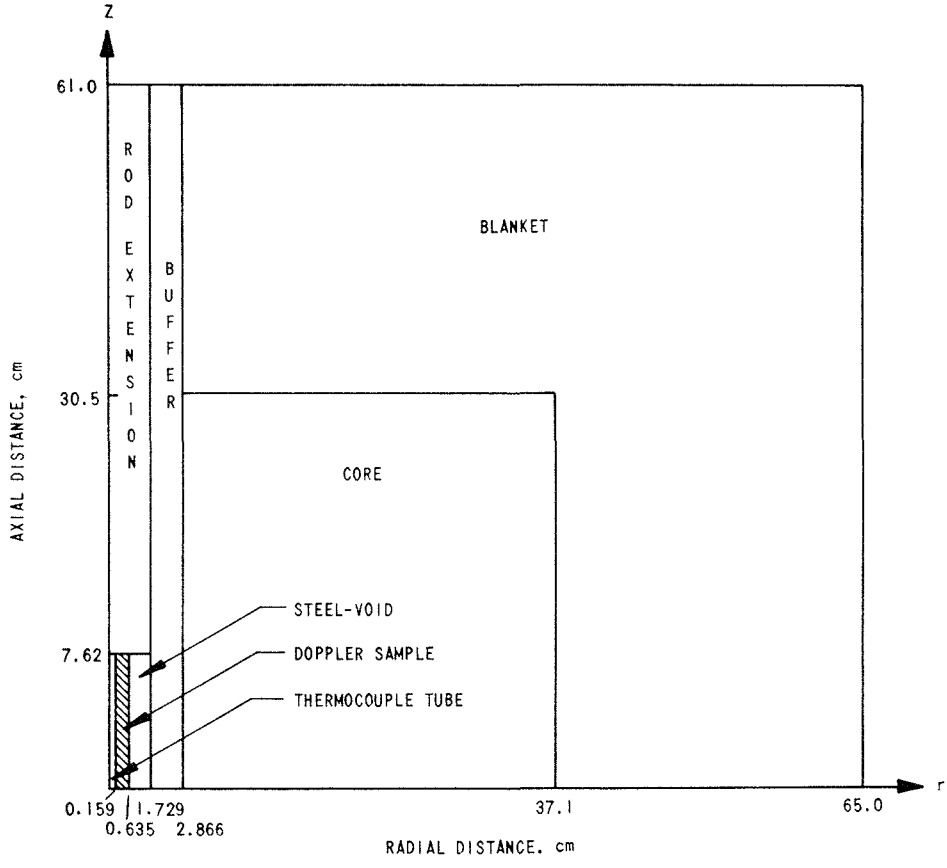

FIG. II-10-1. 2-D Geometry for Assembly 53 Doppler Calculations. *ANL-ID-103-A2143.*

lculation was run to produce core cross sections for use in the final calculation, and a zero-buckling MC^2 calculation provided the blanket cross sections. All MC^2 cases used the ENDF/B-68 cross sections as input.

Reactivity Calculations

The final calculations of the reactivity worth of the samples as a function of temperature were performed using the 2-D diffusion module of the ARC system to generate real and adjoint fluxes for the configuration shown in Fig. II-10-1. These fluxes were than used in the perturbation module to determine the reactivity effect of the substitution of the higher temperature cross sections for the sample material. The values obtained were then reduced to Ih/kg based on the amount of material in the computer representation, and an Ih/percent $\Delta k/k$ conversion of 1038.7. The total worths of the capsules were calculated by reducing the atom densities by 10 percent and multiplying the value of that perturbation by 10. The rod extension section shown in Fig. II-10-1 consisted of stainless steel plus some depleted uranium (or plutonium for the PuO_2 sample) used in balancing the reactivity swing of the rod. The buffer region was a graphite zone about ½ in. thick around the Doppler rod, which served as an anti-Dancoff region. Cross sections for carbon from the homogeneous core MC^2 case were used in the buffer region.

Comparison of Results

The results of the UO_2 calculations, shown in Table II-10-II, were quite close to the experimental values, including the total sample worth. In all cases, the calculation predicted a higher result than was actually measured, a phenomenon that is consistent with most calculations of material worths. No corrections were made to the UO_2 results to account for thermal expansion, as this has been found to be negligible for non-fissile oxide samples.

TABLE II-10-II. Comparison of Experimental and Calculational Results for the UO_2 Doppler Experiment in ZPR-3 Assembly 53

ΔT, °K	$\Delta\rho$, Ih/kg of U-238		C/E
	Experiment	Calculation	
300–500	−4.43 ± 0.04	−4.76	1.047
300–800	−9.54 ± 0.04	−9.72	1.019
300–1100	−13.62 ± 0.04	−14.56	1.069
otal sample at 300°K	−59.1 ± 1.2	−67.6	1.144

Tabli II-10-III. Comparison of Experimental and Calculational Results for the PuO_2 Doppler Experiment in ZPR-3 Assembly 53

ΔT, °K	$\Delta\rho$, Ih/kg of Pu-239			
	Experiment	Calc. (No. Expansion)	Calc. (Cyl. Exp)[a]	Calc. (Rat. Approx)[b]
300–500	−2.47 ± 0.05	+1.30	−6.82	−5.04
300–800	−6.03 ± 0.05	+2.76	−17.55	−13.08
300–1100	−8.52 ± 0.05	+3.54	−29.11	−21.93
Total sample at 300°K	+661.8 ± 1.7	998.1	—	—

[a] Expansion calculation based on Case, de Hoffmann and Placzek.

[b] Expansion calculation based on the rational approximation.

The analysis of the PuO_2 experiment was complicated by the fact that thermal expansion does contribute significantly to the result. The technique used to determine an expansion correction is described by Till,[8] and is based on a collison probability analysis. Two approaches were used, one using flat-source collison probabilities given by Case, de Hoffmann and Placzek,[9] and the other employing the rational approximation. The results for both cases, including the measurement results, are presented in Table II-10-III.

The PuO_2 Doppler calculations indicate a small, positive Doppler effect which is more than balanced by a large, negative expansion effect. Although the comparison with experiment is poor, the relative contributions of Doppler and expansion effects appear reasonable. The known inaccuracies in the ENDF/B cross sections, and the somewhat approximate nature of the expansion calculation are likely contributors to the discrepancy, as is the lack of precise data on the expansion properties of 70% theoretical density, sintered PuO_2 pellets.

References

1. R. E. Kaiser et al., *ZPR-3 Assemblies 53 and 54—Continuation of Studies of Basic Physics Cores—Depleted Uranium Blanket and Iron Reflected Versions*, Reactor Physics Division Annual Report, July 1, 1968 to June 30, 1969, ANL-7610, pp. 84–94.
2. J. M. Gasidlo, *Results of Recent Doppler Experiments in ZPR-3*, Proc. International Conference on Fast Critical Experiments and Their Analysis, ANL-7320, 345 (1966).
3. P. H. Kier and A. A. Robba, *RABBLE, A Program for Computation of Resonance Absorption in Multiregion Reactor Cells*, ANL-7326 (1967).

4. B. J. Toppel, Ed., *The Argonne Reactor Computation (ARC) System*, ANL-7332 (1967).
5. J. J. Schmidt, *Neutron Cross Sections for Fast Reactor Materials, Part 1: Evaluation*, KFK-120 (1966).
6. C. Durston and S. Katsuragi, *On the Evaluation of Pu-239 Data in the keV and Resolved Resonance Region*, JAERI-1162 (1968).
7. B. J. Toppel, A. L. Rago and D. M. O'Shea, *MC²*, *A Code Calculate Multigroup Cross Sections*, ANL-7318 (1967).
8. C. E. Till, *Fissile Doppler Effect Measurement and the Effects of Thermal Expansion*, ANL-7310, 143 (1968).
9. K. M. Case, F. de Hoffmann, and G. Placzek, *Introduction to the Theory of Neutron Diffusion (U. S. Government Printing Office, 1953)*, Vol. I.

II-11. Pu-239, U-235 and U-238 Capture-to-Fission Ratios in ZPR-3 Assembly 57 Measured by the Reactivity-Reaction Rate Method

M. M. Bretscher, J. M. Gasidlo and W. C. Redman

Introduction

In spectra characteristic of large dilute fast reactors, the effective Pu-239 capture-to-fission ratio (alpha), on which the breeding ratio depends, is largely determined by the differential alpha values in the 0.1–30 keV range. The initial data of Schomberg[1] suggested that the plutonium alpha values in this range should be increased by an average of about 30%. Recently, a number of new differential measurements of the Pu-239 capture and fission cross sections, and their ratio, covering this energy interval have been reported.[2-8]

To test the differential data, integral Pu-239 alpha values were measured in two different reactor cores, both designed to emphasize the 0.1–30 keV range. For ZPR-9 Assembly 24, the results for the null-zone measurement[9] and those obtained by the reactivity-reaction rate technique[10] have been reported. In ZPR-3 Assembly 57, Kato et al.[11] made a direct integral measurement of the Pu-239 capture-to-fission ratio using a combination of mass spectrometer techniques and fission track recorders.

This report is concerned with an independent, but less direct, determination of Pu-239, U-235 and U-238 capture-to-fission ratios measured in ZPR-3 Assembly 57. These integral alpha values, obtained by a combination of relative reactivity and absolute reaction rate measurements, are compared with those determined by other experimental techniques and with values calculated from differential cross section data using both measured and calculated neutron spectra. The values given here supersede the preliminary results reported earlier.[12]

Method

The reactivity-reaction rate technique provides an integral measurement of capture-to-fission ratios ($\bar{\alpha}$) in low flux reactors. Since the method has been described elsewhere,[10] only the final equation, which forms the basis of the measurements, will be repeated here:

$$(1 + \bar{\alpha}) = \frac{R_a(A)[(\rho/R_f)(1 - \rho_s/\rho) - (\bar{\nu}/S)\rho'(\mathrm{Cf})\bar{\phi}_f^*/\bar{\phi}_f^*(\mathrm{Cf})]\bar{\phi}_a^*(A)/\bar{\phi}_a^*}{\rho(A)[1 - \rho_s(A)/\rho(A)]}. \quad (1)$$

The measured quantities are the relative reactivities of the fissile material (ρ) and the Li-6 absorber [$\rho(A)$]; the relative apparent reactivity of a californium source $\rho'(\mathrm{Cf})$; the absolute fission and absorption rates R_f and $R_a(A)$; and the neutron emission rate S from the californium source. The remaining factors in this equation must be calculated from fundamental nuclear data. $\bar{\nu}$ is the average number of neutrons emitted per fission in the sample. Note that $(1 - \rho_s/\rho)$ corrects for the scattering contribution to the total reactivity, $\bar{\phi}_a^*(A)/\bar{\phi}_a^*$ accounts for the small difference in neutron importance between neutrons absorbed in the Li-6 sample and those absorbed in the fissile material, while $\bar{\phi}_f^*/\bar{\phi}_f^*(\mathrm{Cf})$ corrects for the difference in importance between neutrons from induced fission in the sample and from spontaneous fission in the source. These correction factors are generally small, but do depend somewhat on the neutron spectrum used in the calculation.

Equation (1) was derived from first-order perturbation theory and applies to measurements made at the center of a reactor where flux gradients are essentially zero. For the equation to be valid, the measured values of R_f, $R_a(A)$ and $\rho'(\mathrm{Cf})$ must be normalized to a common power level. R_f and ρ [and similarly $R_a(A)$ and $\rho(A)$] refer to samples of identical dimensions so that self-shielding effects will be the same.

The reactivity-reaction rate method for determining integral alpha values is somewhat indirect in that the results depend on a calculated value of $\bar{\nu}$. However, the measurements can be made at power levels of the order of 50 W or less, which are at least two orders of magnitude lower than those required by the mass spectrometer technique. This is an important consideration for ZPR

TABLE II-11-I. ZPR-3 ASSEMBLY 57

Region	Outer Radius, cm	Atom Density, 10^{22} atoms/cm^3								
		U-235	U-238	Be	O	Al	Fe	Cr	Ni	Mn
Core	20.60	0.4081	0.6347	3.901	3.901	0.5546				
Core[a]		0.4130	0.6408	3.934	3.941	0.570				
Inner reflector	61.92						7.554	0.1129	0.0494	0.0047
Outer reflector	81.51	0.0083	3.989				0.4540	0.1129	0.0494	0.0047

[a] Core composition for Gulf General Atomic Subcritical Time-of-Flight Spectrum Facility, Assembly 1A.

installations where shielding is limited and fuel changes frequent.

CRITICAL ASSEMBLY

Assembly 57 of ZPR-3 was a cylindrical three region reactor. The compact 54 liter core contained plates of enriched and depleted uranium and beryllium oxide. Surrounding the core was an inner reflector of stainless steel and an outer reflector of depleted uranium. Regional radii and average homogeneous atom concentrations are shown in Table II-11-I. Table II-11-II gives the drawer loading pattern for the core. Excluding the axial reflectors, the core height was 40.8 cm with a 20.5 cm radius. A more complete description of Assembly 57 is given elsewhere.[13] This core was designed to give a rather soft spectrum so that integral Pu-239 alpha measurements would be sensitive to capture events in the 1–30 keV range.

SAMPLES AND MEASUREMENTS

All of the samples used in these measurements were contained in thin-walled stainless steel cans 2 in. long and 7/8 in. in diameter. Table II-11-III gives a description of the physical dimensions of the samples and Table II-11-IV lists their isotopic composition. The plutonium was alloyed with 1.2 w/o aluminum and rolled into foil thicknesses of 5, 15, and 30 mils.

Samples of identical dimensions were used for both reactivity and reaction rate measurements so that self-shielding effects would be the same. A pneumatic device[14] was used to transfer the samples to and from the center of the reactor core along a radius of the cylindrical assembly.

TABLE II-11-II. DRAWER LOADING CONFIGURATION FOR CORE OF ZPR-3 ASSEMBLY 57[a]

1/8 BeO, 1/16 D, 2(1/8)BeO, 1/16 D, 1/8 E, 2(1/8)BeO, 1/16 D, 2(1/8)-BeO, 1/16 D, 2(1/8)BeO, 1/8 E, 1/16 D, 2(1/8)BeO

Drawer Loading Configuration for GGA-STSF Assembly 1A

BeO, 1/16 D, 2(1/8)BeO, 1/8 E, 2(1/8)BeO, 1/16 D, 1/8 BeO, 1/16 D, 1/8 BeO, 1/16 D, 2(1/8)BeO, 1/8 E, 1/8 BeO, 1/16 D, 1/8 BeO

[a] Plate thicknesses in inches; D ≡ depleted uranium, E ≡ enriched uranium, BeO ≡ beryllium oxide.

TABLE II-11-III. PERTURBATION SAMPLE DESCRIPTIONS

Material[a]	Geometry	Dimensions, in.			Mass, g
		O.D.	Wall Thickness	Length	
Pu(Al)	Annulus	0.835	0 005	1.250	3.524
Pu(Al)	Annulus	0.835	0.015	1.250	9.956
Pu(Al)	Annulus	0.835	0.030	1.250	21.409
U(E)	Annulus	0.835	0.005	1.688	5.2306
U(E)	Annulus	0.835	0.015	1.688	15.7780
U(E)	Annulus	0.835	0.030	1.688	30.8380
U(D)	Annulus	0.835	0.031	1.688	38.1631
Li(E)	Cylinder	0.300	—	1 360	0.6047
Li(E)	Cylinder	0.623	–	0.850	1.8300
Li(D)	Cylinder	0.623	—	1.700	4.2532
304-SS	Annulus	0.865	0.015	2.000	13.8070
Al	Cylinder	0.865		2.000	53.0630

[a] E ≡ enriched, D ≡ depleted, Al ≡ aluminum alloy.

Relative reactivities were measured with an autorod which held the flux level constant as the sample was periodically driven into and out of the reactor core. The integral worth of the autorod, as well as that of the 0.623 in. diam Li-6 sample, was determined by the inverse kinetics method. Photoneutrons, primarily from the beryllium in the core, affect the kinetic behavior of the reactor and make the absolute calibration of the autorod somewhat uncertain. Fortunately, reactivities appear only as ratios in Eq. (1) and so the measured integral alpha values are independent of the absolute calibration of the integral worth of the autorod. For the case of the californium source, measurements were made at several different power levels in order to separate the apparent reactivity of the extraneous source neutrons from the true reactivity of the container.

Figure II-11-1 shows a typical set of measurements made with the californium source plotted as a function of a quantity inversely proportional to the reactor power level. Three such sets of measurements were taken and adjusted to a common date to account for the decay of the californium source. The reactor power was monitored by a fission counter and with gold foils located in the reflector region. $N = 1.00$ corresponds to

TABLE II-11-IV. Isotopic Composition of Samples

Sample	Isotope—Weight Percent			
Pu	^{239}Pu-98.9315	^{240}Pu-1.0123	^{241}Pu-0.0528	^{242}Pu-0.0034
U(E)	^{234}U-0.6632	^{235}U-93.1075	^{236}U-0.3186	^{238}U-5.9107
U(D)		^{235}U-0.2106		^{238}U-99.7894
Li(E), 0.300 in.		^{6}Li-99.2077	^{7}Li-0.7923	
Li(E), 0.623 in.		^{6}Li-94.9397	^{7}Li-5.0603	
Li(D)		^{6}Li-0.0060	^{7}Li-99.9940	

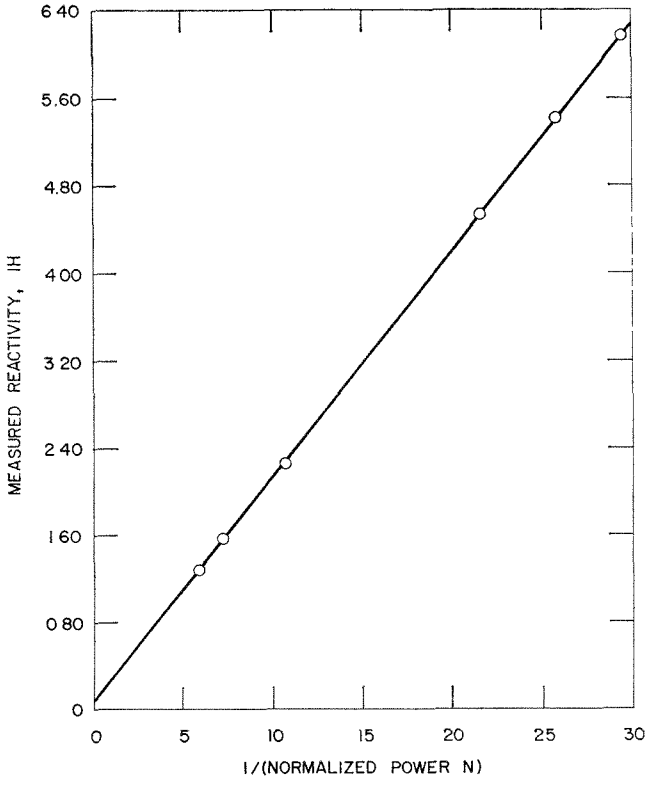

Fig. II-11-1. Apparent Reactivity of Cf-252 Spontaneous Fission Source. *ANL Neg. No. 116-404.*

the power level (about 50 W) to which all the reaction rate data have been normalized. The intercept of the graph is the reactivity of the source container while the slope divided by N is the apparent reactivity, $\rho'(\mathrm{Cf})$. The californium source was calibrated by the manganese bath technique.[15] To correct for decay, a Cf-252 half life of (2.621 ± 0.006) yr[(16)] was used. The source strength, together with its apparent reactivity at a power level corresponding to $N = 1.00$, is given at the bottom of Table II-11-V.

Samples for reaction rate measurements were irradiated at the same location used for the reactivity determinations. Fission rates were measured radiochemically[17] by determining the absolute activity of the Mo-99 fission product in the irradiated sample. Thus, the accuracy of the fission rates is limited by imprecise knowledge of the yield of Mo-99 in fast fission. Recently, Armani[18] reported a precise measurement (±0.9%) of the Mo-99 yield in the fast fission of Pu-239. This measurement was made in ZPR-3 Assembly 57, using a combination of solid state track recorders (SSTR) and radiochemistry techniques. So as not to ignore other, but less precise, measurements of this fast fission yield, we have used the weighted mean of the values given in Ref. 18 in the analysis of the Pu-239 fission rates. However, this mean value (5.82 ± 0.05)% is strongly dominated by the SSTR measurement.

Unfortunately, an accurate value for the Mo-99 yield in U-235 fast fission is not available at this time. Larsen[19] has determined a value of (5.80 ± 0.20)% for this yield in EBR-II. His value was obtained from measured Tc-99/Cs-137 yield ratios of 0.930 (EBR-I) and 0.940 (EBR-II) and the Cs-137 yield of (6.20 ± 0.16)% determined by Idaho Nuclear Corporation.[20]

From measurements made in ZPR-3 Assembly 57, one can obtain a value for the ratio of Mo-99 yields for U-235 and Pu-239 fast fission. The Pu-239 to U-235 fission ratio was measured with a back-to-back fission counter.[21] Using the CALHET code[22] (see Paper IV-21) to obtain the detailed flux distribution in the unit cell, a small correction (~1%) was applied to this fission ratio to account for the fact that the fission chamber viewed a different portion of the unit cell than that

TABLE II-11-V. Measured Isotopic Specific Reactivities and Normalized Reaction Rates[a]

Isotope	O.D. or Wall Thickness, in.	ρ, Ih/g	R_f or R_a, 10^7/g-sec
Pu-239	0.005	0.6124 ± 0.0012	2.093 ± 0.022
Pu-239	0.015	0.6272 ± 0.0009	2.068 ± 0.020
Pu-239	0.030	0.6397 ± 0.0030	2.000 ± 0.020
U-235	0.005	0.4291 ± 0.0012	2.151 ± 0.049
U-235	0.015	0.4302 ± 0.0005	2.116 ± 0.042
U-235	0.030	0.4313 ± 0.0020	1.970 ± 0.038
U-238	0.031	−(0.03322 ± 0.00015)	0.0690 ± 0.0018
Li-6	0.300	−(11.592 ± 0.030)	41.94 ± 0.32
Li-6	0.623	−(11.100 ± 0.030)	40.49 ± 0.3

[a] $\rho(\mathrm{Cf}) = (0.21000 \pm 0.00063)$ Ih
$S(\mathrm{Cf}) = (9.205 \pm 0.027)10^6$ n/sec
$\bar{\alpha}^{238}_{\text{radiochemical}} = 3.715 \pm 0.129$

seen" by the irradiated foils. Combining this adjusted fission ratio with the measured Mo-99 activities from thin (0.005 in.) foils of plutonium and enriched uranium gives a yield ratio of

$$^{235}Y(\text{Mo-99})/^{239}Y(\text{Mo-99}) = 1.005 \pm 0.017.$$

From this ratio and the above value for the yield in Pu-239 fission one obtains (5.85 ± 0.11) % for the yield in U-235 fission, in excellent agreement with Larsen's value.

The yields used in the evaluation of the various fission rates are summarized in Table II-11-VI. For U-238 fission we have used the same yield as before.[10]

U-238 capture rates were also measured radiochemically[17] by determining the absolute activity of Np-239 resulting from the decay of U-239. Combining this with the corresponding fission rate gives the radiochemical value for the U-238 capture-to-fission ratio shown at the bottom of Table II-11-V.

The Li-6 absorption rate was measured by determining the amount of tritium induced in irradiated samples.[23] Tritium was removed from the lithium samples by an isotopic dilution method using normal hydrogen as the carrier gas. After converting the hydrogen to water, liquid scintillation counting methods were used to determine the tritium activity. The counting system was calibrated in terms of a tritiated water standard obtained from the National Bureau of Standards.

The results of the reactivity and reaction rate measurements (normalized to a power level corresponding to $N = 1.00$), together with the californium data, are summarized in Table II-11-V. Since the capture-to-fission ratio depends on reactivity quotients, the errors quoted for the reactivity measurement do not include uncertainties associated with the integral worth of the autorod. Errors in the reaction rate measurements correspond to the standard deviation in the mean of several measurements and include estimates of the uncertainties in power normalizations, fission yields, and the calibration of the NBS tritiated water standard.

Neutron Spectra

Central flux and adjoint distributions are needed to calculate $\bar{\nu}$ and the various correction factors appearing in the reactivity-reaction rate expression (Eq. 1) for alpha. Multigroup cross sections were generated from

TABLE II-11-VI. Mo-99 Fast Fission Yields

Isotope	Yield, %
U-235	5.85 ± 0.11
U-238	6.29 ± 0.15
Pu-239	5.82 ± 0.05

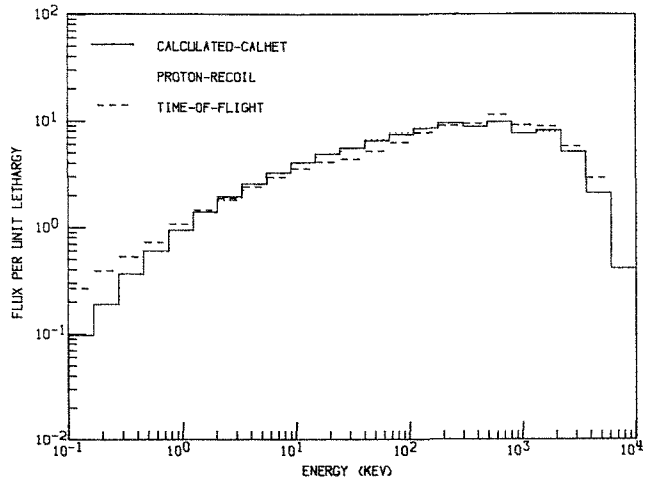

Fig. II-11-2. Central Neutron Spectra Calculated from the CALHET Code and Measured by Proton-Recoil and Time-of-Flight Techniques. *ANL Neg. No. 116-347.*

ENDF/B data using the MC² code.[24] Slab geometry equivalence theory was used in this calculation to correct the U-238 cross sections for spatial self-shielding. To account for the heterogeneous plate structure of the core, the perturbation code CALHET,[22] (also, see Paper IV-21) which is based on a collision probability approach, was used to calculate the detailed flux variations across the plates of the unit cell. Flux and volume-weighted cell-averaged cross sections were also evaluated by CALHET. These cross sections, together with the atom densities given in Table II-11-I, were used in a diffusion-theory calculation to determine the central adjoint distribution.

To account for the small perturbation in the flux distribution resulting from the double-walled stainless steel oscillator tube and sample holder, an S_n transport calculation[25] in cylindrical geometry was made using the CALHET flux distribution, integrated over the axial extent of the sample, as the input shell source. This slightly softened flux distribution together with the central adjoints was used to calculate $\bar{\nu}$ and the importance-dependent correction terms.

Figure II-11-2 shows a comparison of the calculated neutron flux distribution with spectra measured by proton-recoil (P-R) and time-of-flight (T-O-F) techniques. The P-R measurements[26] were made in ZPR-3 Assembly 57, whereas the T-O-F data[27,28] were taken on the Subcritical Time-of-Flight Spectrum Facility (STSF) at Gulf General Atomic for Assembly 1A whose composition[29] nearly duplicated that of Assembly 57. A comparison of the atom densities and drawer loading configurations for the cores of Assemblies 57 and 1A is provided in Tables II-11-I and II-11-II. The flux distributions shown in Fig. II-11-2 were normalized by equating the integrals, evaluated over the energy range

of the measurement, for the measured and calculated spectra. Note that the time-of-flight spectrum rises above the calculated spectrum for neutron energies above 0.3 MeV and below 2 keV. The proton-recoil and CALHET spectra are in reasonable agreement.

For the T-O-F measurements the re-entrant tube of the STSF "viewed" a BeO plate near the center of the drawer. Thus, the T-O-F spectrum is expected to be somewhat softer than the CALHET distribution which refers to the extended sample position which spanned most of the plate widths of the unit cell. The CALHET spectrum for the same BeO region viewed by the STSF is compared with the T-O-F spectrum in Fig. II-11-3. Also included in this figure is the calculated spectrum integrated over the 1.25 in. length of the plutonium samples. No attempt has been made to modify the T-O-F spectrum for the small differences in atom densities for the cores of Assemblies 1A and 57 and for spectral differences between the BeO region and the regions covered by the samples used for the reactivity-reaction rate measurements.

To characterize the spectrum, the fraction of the total number of Pu-239 capture and fission events for several energy intervals is shown in Table II-11-VII. These calculations refer to the CALHET distribution using

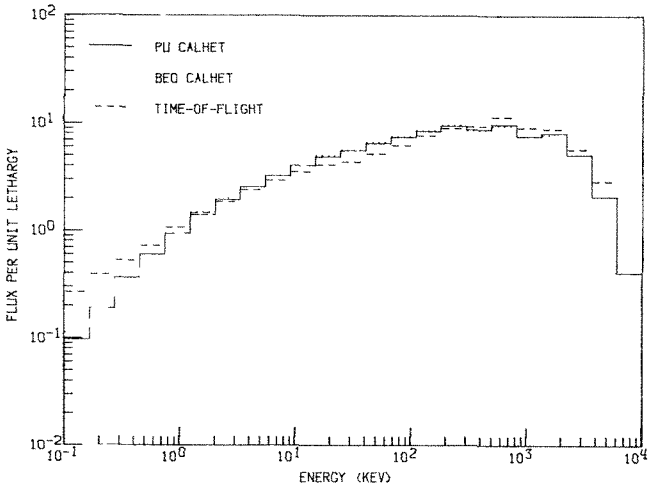

FIG. II-11-3. CALHET—Calculated Neutron Spectra for BeO Region and Regions Spanned by Pu Samples Compared with Time-of-Flight Distribution. *ANL Neg. No. 116-403.*

TABLE II-11-VII. Pu-239 SPECTRAL DEPENDENCE

Energy Interval, keV	Fraction of Total Captures	Fraction of Total Fissions
>25	0.187	0.667
1–25	0.507	0.215
0.1–1	0.277	0.100
<0.1	0.029	0.018

TABLE II-11-VIII. CALCULATED QUANTITIES FOR CALHET FLUX DISTRIBUTION

Isotope	Thickness, in.	$1-\rho_s/\rho$	$\frac{\bar{\phi}^*_f}{\bar{\phi}^*_f(\mathrm{Cf})}$	$\frac{\bar{\phi}_a^*(\mathrm{Li\text{-}6})}{\bar{\phi}_a^*}$	$\bar{\nu}$
Pu-239	0.000	0.9960	0.9955	1.0011	2.9503
Pu-239	0.005	0.9962	0.9955	1.0042	2.9539
Pu-239	0.015	0.9963	0.9956	1.0086	2.9592
Pu-239	0.030	0.9966	0.9956	1.0140	2.9658
U-235	0.000	0.9932	0.9925	0.9891	2.4709
U-235	0.005	0.9934	0.9925	0.9919	2.4732
U-235	0.015	0.9936	0.9925	0.9959	2.4766
U-235	0.030	0.9939	0.9925	1.0008	2.4809
U-238	0.031	1.2079	0.9940	1.0245	2.7963
Li-6	0 300	1.0084			

TABLE II-11-IX. CALCULATED QUANTITIES FOR CALHET, P-R AND T-O-F SPECTRA

Isotope	Thickness, in.	Spectrum	$1-\rho_s/\rho$	$\frac{\bar{\phi}_f^*}{\bar{\phi}_f^*(\mathrm{Cf})}$	$\frac{\bar{\phi}_a^*(\mathrm{Li\text{-}6})}{\bar{\phi}_a^*}$	$\bar{\nu}$
Pu-239	0.000	CALHET	0.9960	0.9955	1.0011	2.9503
Pu-239	0.000	P-R	0.9960	0.9955	1.0036	2.9516
Pu-239	0.000	T-O-F	0.9963	0.9956	1.0004	2.9561
U-235	0.000	CALHET	0.9932	0.9925	0.9891	2.4709
U-235	0.000	P-R	0.9930	0.9925	0.9902	2.4712
U-235	0.000	T-O-F	0.9934	0.9925	0.9883	2.4745
U-238	0.031	CALHET	1.2079	0.9940	1.0245	2.7956
U-238	0.031	P-R	1.2149	0.9940	1.0258	2.7962
U-238	0.031	T-O-F	1.2617	0.9940	1.0361	2.8032
Li-6	0.300	CALHET	1.0084			
Li-6	0.300	P-R	1.0084			
Li-6	0.300	T-O-F	1.0071			

ENDF/B (Version I) cross sections modified by the ORNL data[3] in the 0.1–30 keV range.

CALCULATED QUANTITIES

Following the procedures described in Ref. 10, $\bar{\nu}$ and the correction factors for scattering reactivity effects and differences in neutron importance were evaluated on the basis of the calculated and measured neutron spectra using the central adjoint distribution obtained from the CALHET cell-averaged cross sections. These cross sections were generated from ENDF/B (Version I) but for the case of Pu-239 were modified in the 0.1 to 30 keV range to incorporate the ORNL[3] differential data.* A typical set of calculated parameters is given in Tables II-11-VIII and II-11-IX. Table II-11-VIII refers to the CALHET spectrum and shows how these parameters vary as a function of sample thickness; per-

* The ORNL cross sections were measured by both a fission chamber and with metal foils. To obtain the modified ENDF/B cross sections, the weighted mean of these two measurements was used.

rbed fluxes were obtained from a self-shielding calculation.[30] This self-shielding calculation was not applied to the U-238 sample since its thickness was chosen to be approximately equivalent to the thickness of the depleted uranium plates in the unit cell. Therefore, the U-238 cell-averaged cross sections account for self-shielding effects in this sample. The quantities shown in Table II-11-IX have been evaluated using the calculated, proton-recoil, and time-of-flight neutron spectra.

In general, these numerical quantities are not very sensitive to the neutron spectrum used in the calculation, as can be seen from Table II-11-IX. For Pu-239 and U-235, corrections for differences in neutron importance and scattering contributions to the total reactivity are very small, amounting to about 1 % or less. In the case of U-238, however, the corrections are larger, particularly that for scattering which amounts to 21 %. Since the magnitude of the calculated ratio ρ_s/ρ is very sensitive to the adjoint distribution, the reactivity-reaction rate value of $\bar{\alpha}^{238}$ is much more sensitive to errors in the adjoint fluxes and elastic and inelastic transfer cross sections than is the case for either $\bar{\alpha}^{235}$ or $\bar{\alpha}^{239}$.

Integral Alpha Values

The reactivity-reaction rate integral alpha values for Pu-239 and U-235 are listed in Table II-11-X as a function of sample thickness. It will be recalled that fission rates and reactivities were measured for hollow-cylindrical samples having wall thicknesses of 5, 15 and 30 mils. These results were extrapolated to zero thickness and then substituted into Eq. (1) to obtain the infinitely dilute alpha values. The correction factors (Table II-11-VIII), as well as the calculated capture-to-fission ratios, were evaluated on the basis of the theoretical (CALHET) neutron spectrum using ENDF/B cross sections. For Pu-239, however, the absorption and fission cross sections were modified in the 0.1 to 30 keV range to incorporate the ORNL data.[3] The quoted errors are the standard deviations in the measurements. They include estimates of the uncertainties in $\bar{\nu}$, the Mo-99 fast fission yields, and the calibration of the NBS tritiated water standard. However, no error has been assigned to the calculated correction factors.

TABLE II-11-X. Pu-239 and U-235 Capture-to-Fission Ratios

Thickness, in.	$\bar{\alpha}^{239}$		$\bar{\alpha}^{235}$	
	Calc.	Measured	Calc.	Measured
0.000	0.351	(0.380 ± 0.030)[a]	0.294	(0.289 ± 0.029)[a]
0.005	0.343	0.367 ± 0.030	0.291	0.289 ± 0.029
0.015	0.331	0.339 ± 0.030	0.285	0.283 ± 0.028
0.030	0.316	0.291 ± 0.031	0.278	0.237 ± 0.029

[a] By extrapolation of R_f and ρ to zero thickness.

Except for the 30 mil sample the U-235 results agree with the calculated quantities. The low alpha value for the 30 mil sample results from an abnormally small value for R_f-235 (see Table II-11-V), suggesting an error in the radiochemistry determination of this particular fission rate. For the thin Pu-239 samples the measured capture-to-fission ratios are somewhat larger than the calculated ones. Also, the measured Pu-239 alpha values decrease with sample thickness more rapidly than theory predicts. This may be due to a deficiency in the code[30] used to evaluate the perturbed fluxes. However, the code adequately predicted the thickness variation in $\bar{\alpha}^{239}$ in the somewhat softer spectrum of ZPR-9 Assembly 24.[10]

Table II-11-XI shows the results of the plutonium zero-thickness data evaluated on the basis of the calculated, proton-recoil, and time-of-flight spectra using ORNL,[3] UK[4], and ENDF/B (Version I) cross sections. The small variation in the measured alpha values reflects the weak dependence of the calculated quantities on the spectrum and cross sections used in the calculation.

Using a combination of mass spectrometer techniques and fission track recorders, Kato et al.[11] made a direct

TABLE II-11-XI. Dilute Pu-239 Integral Alphas

Spectrum	ORNL σ's		UK σ's		ENDF/B σ's	
	Calc.	Measured	Calc.	Measured	Calc.	Measured
CALHET	0.351	0.380 ± 0.030	0.293	0.388 ± 0.030	0.257	0.390 ± 0.030
P-R	0.344	0.385 ± 0.030	0.288	0.391 ± 0.031	0.253	0.393 ± 0.031
T-O-F	0.365	0.386 ± 0.030	0.308	0.391 ± 0.030	0.266	0.393 ± 0.031

s spectrometer measurement:[a] $\bar{\alpha}^{239} = 0.363 \pm 0.024$.
ified result to account for spectral differences:[b] $\bar{\alpha}^{239} = 0.350 \pm 0.023$.

[a] See Ref. 11.
[b] See text.

TABLE II-11-XII. DILUTE U-235 AND U-238 (0.031 in.) INTEGRAL ALPHAS
(*Radiochemical* $\bar{\alpha}^{238} = 3.715 \pm 0.129$)

Neutron Spectrum	Adjoint Distrib.	$\bar{\alpha}^{235}$		$\bar{\alpha}^{238}$	
		Calc.	Measured	Calc.	Measured
Calculated	FW[a]	0.294	0.289 ± 0.029	3.805	3.499 ± 0.071
	UW[b]	0.294	0.293 ± 0.029	3.805	3.644 ± 0.074
Proton-Recoil	FW[a]	0.294	0.291 ± 0.029	3.830	3.518 ± 0.071
	UW[b]	0.294	0.295 ± 0.029	3.830	3.665 ± 0.075
Time-of-Flight	FW[a]	0.300	0.292 ± 0.029	3.254	3.654 ± 0.074
	UW[b]	0.300	0.296 ± 0.029	3.254	3.866 ± 0.079

[a] FW ≡ flux-weighted cross sections used in evaluation of $\phi^*(E)$.
[b] UW ≡ unweighted cross sections used in evaluation of $\phi^*(E)$.

measurement of the Pu-239 capture-to-fission ratio for an ultra thin sample irradiated in a BeO region at the center of ZPR-3 Assembly 57. This result is shown at the bottom of Table II-11-XI. To compare the mass spectrometer value with the reactivity-reaction rate result one must account for the fact that the two measurements were made in different regions of the unit cell. Using the region-dependent CALHET spectrum together with ENDF/B cross sections modified by the ORNL data,[3] the calculated alpha ratio for the cell regions covered by the reactivity-reaction rate samples to the BeO region in which the mass spectrometer sample was exposed is 0.965. For purposes of comparison, the mass spectrometer alpha value should be reduced by this factor. This modified value is also given in Table II-11-XI. Although the reactivity-reaction rate result is somewhat larger than the modified mass spectrometer value, the errors do overlap. Integral alpha values calculated from the Oak Ridge data[3] are in best agreement with the experimental ones.

The sensitivity of the U-235 and U-238 capture-to-fission ratios to spectrum-dependent correction factors is illustrated in Table II-11-XII where the results have been evaluated on the basis of the theoretical, proton-recoil and time-of-flight spectra. The U-235 values are for a sample of zero thickness whereas the U-238 results correspond to a thickness approximately equivalent to the width of the depleted uranium plates in the unit cell. For purposes of comparison, the radiochemical value for U-238 alpha is given at the top of the table. To illustrate the sensitivity of the results to the adjoint distribution used to evaluate the importance-dependent correction terms, the alpha values were calculated for adjoint distributions obtained from CALHET flux-weighted (FW) cell-averaged cross sections and from unweighted (UW) cross sections.

For U-235 the reactivity-reaction rate alpha value is quite insensitive to the neutron spectrum and adjoint distribution used in the evaluation of the various correction terms and is in good agreement with the calculated value. The situation is quite reversed, however, for the U-238 sample, as Table II-11-XII shows. Because the calculated ratio ρ_s/ρ is very sensitive to the adjoint distribution and is quite large for U-238, $\bar{\alpha}^{238}$ changes by about 5% in going from one adjoint spectrum to the next. From a theoretical point of view, it is not clear what adjoint distribution should be used for evaluating neutron importances. Perhaps, for example, adjoint-weighted rather than flux-weighted cross sections should be used for this purpose. Fortunately, the U-235 and Pu-239 measured alphas are very insensitive to the detailed nature of the adjoint distribution. The U-238 values quoted in Table II-11-XII clearly favor the adjoint spectrum calculated from un-weighted cross sections. Because of the high fission threshold for U-238(~0.5 MeV), the calculated value of alpha is very sensitive to the shape of the neutron spectrum above 1 MeV. In this region the T-O-F spectrum rises above the CALHET and P-R distributions, as Fig. II-11-2 shows, and is the reason why the calculated value of $\bar{\alpha}^{238}$ for the T-O-F spectrum is so much lower than the others. The radiochemistry result favors the CALHET flux distribution.

It was mentioned earlier that a transport correction was applied to account for the stainless steel tube and holder surrounding the sample. The effect of the stainless steel is to soften the spectrum somewhat, which tends to increase the Pu-239 and U-235 alpha values by about 0.5%. For U-238, however, the effect is larger. The calculated value of $\bar{\alpha}^{238}$ is increased by nearly 5% while the measured value decreases by less than 0.5%.

ALPHA SENSITIVITIES AND ERRORS

The sensitivity of the reactivity-reaction rate integral alpha values to errors in both measured and calculated quantities is illustrated in Table II-11-XIII. For ex-

ample, a 1% increase in the Li-6 absorption rate results in increases of 3.6, 4.5 and 1.3% in the alpha values for Pu-239, U-235 and U-238, respectively. A 1% increase in the fission rate will increase $\bar{\alpha}^{239}$ by 2.7%. Note that the results are very sensitive to the value used for $\bar{\nu}$. If $\bar{\nu}$ is increased by 1%, $\bar{\alpha}^{239}$ increases by 6.3% and $\bar{\alpha}^{235}$ by 6.9%. The importance term for fission neutrons depends on the Maxwellian temperature parameter T used to characterize the primary fission neutron distribution. Only small changes in $\bar{\alpha}$ result from 1% variations in T.

The errors assigned to the various quantities and the corresponding uncertainties in $\bar{\alpha}$ are shown in Table II-11-XIV. These values apply to the 5 mil Pu-239 and U-235 samples, but are typical of the errors for the other thicknesses. The error in the Li-6 absorption rate includes an estimate of 0.5% in the calibration of the NBS tritiated water standard.[31] Uncertainties of 0.9, 1.9 and 2.4% in the Mo-99 yields for Pu-239, U-235 and U-238 fast fission respectively, contribute most of the errors in R_f and contribute a large fraction of the total uncertainty in $\bar{\alpha}$. Reactivities appear only as ratios in the basic equation [Eq. (1)] for alpha. Therefore, the errors quoted in Table II-11-XIV are the uncertainties associated with the relative reactivity values and do not include the error in the absolute calibration of the autorod.

Table II-11-XIII shows that the Pu-239 and U-235 alphas are very sensitive to the values used for $\bar{\nu}$. For the purpose of estimating the error in $\bar{\nu}$, it was assumed that $\nu(E)$ varies linearly with energy: $\nu(E) = a + bE$. Then,

$$\bar{\nu} = \frac{\int \nu(E)\sigma_f(E)\phi(E)\,dE}{\int \sigma_f(E)\phi(E)\,dE} = a + b\bar{E}.$$

Since $b\bar{E}$ contributes only about 2% to the total value of $\bar{\nu}$, almost all the uncertainties in $\bar{\nu}$ result from the energy-independent term a. Estimates of the uncertainties associated with a and b are given in Ref. 32, but they do not include the error in $\bar{\nu}$(Cf-252) to which the data have been normalized. In view of the uncertainty in $\bar{\nu}$(Cf-252), an error of 1% has been assigned to the $\bar{\nu}$ values used in the alpha evaluations. Most of the error in the Pu-239 and U-235 capture-to-fission ratios results from the uncertainties in $\bar{\nu}$, as Table II-11-XIV indicates.

It has already been pointed out that the calculated correction factors for differences in neutron importance and for the component in the total reactivity due to scattering depend on the neutron flux and adjoint distributions. Except for the scattering correction in U-238, these calculated corrections are very small and no error has been assigned to them.

TABLE II-11-XIII. Alpha Sensitivities

A 1.0% Increase In	Causes Per Cent Increase In		
	$\bar{\alpha}^{239}$	$\bar{\alpha}^{235}$	$\bar{\alpha}^{238}$
$\frac{R_a(\text{Li-6})\bar{\phi}_a^*(\text{Li-6})/\bar{\phi}_a^*}{\rho(\text{Li-6})[1 - \rho_s(\text{Li-6})/\rho(\text{Li-6})]}$	3.63	4.46	1.28
$(\bar{\nu}/S)\rho'(\text{Cf-252})\bar{\phi}_f^*/\bar{\phi}_f^*(\text{Cf-252})$	6.33	6.88	0.67
$(1 - \rho_s/\rho)/R_f$	−2.70	−2.41	0.61
T-252	−0.48	−0.52	−0.05
T-239, T-235, T-238	0.41	0.39	0.04

TABLE II-11-XIV. Errors

Quantity	% Error	% Error In		
		$\bar{\alpha}^{239}$	$\bar{\alpha}^{235}$	$\bar{\alpha}^{238}$
R_a(Li-6)	0.76	2.77	3.40	0.98
R_f : 239, 235, 238	1.04, 2.27, 2.57	2.81	5.46	1.57
S(Cf-252)	0.29	1.83	1.99	0.19
ρ(Li-6)	0.26	0.94	1.15	0.33
ρ: 239, 235, 238	0.2, 0.3, 0.4	0.51	0.65	0.27
ρ'(Cf-252)	0.30	1.90	2.06	0.20
$\bar{\nu}$: 239, 235, 238	1.0, 1.0, 1.0	6.33	6.88	0.67
T(Cf-252)	2.0	0.96	1.04	0.10
T: 239, 235, 238	2.0, 1.0, 3.0	0.82	0.39	0.12
Combined Error		8.08	10.0	2.04

Possible Systematic Errors in $\bar{\nu}$

Integral alpha values measured by the reactivity-reaction rate technique depend, in a very sensitive way, on the calculated value of $\bar{\nu}$, the average number of neutrons per fission. For the Pu-239 and U-235 measurements reported here a 1.0% change in $\bar{\nu}$ results in changes of 6.3 and 6.9% in $\bar{\alpha}^{239}$ and $\bar{\alpha}^{235}$ respectively (Table II-11-XIII). It is therefore appropriate to examine the possibilities for systematic errors in the evaluation of $\bar{\nu}$ for the fast reactor spectrum.

The best measured values of $\nu(E)$ and ν_{th} are made relative to ν(Cf-252) or are normalized to this value. Thus, the $\bar{\nu}$ values used in these capture-to-fission ratio measurements are related to $\bar{\nu}$ for Cf-252. Unfortunately, the experimental values for $\bar{\nu}$(Cf-252) tend to lie in two groups differing by about 2%.[33] Generally speaking, measurements using a large liquid scintillation detector lie close to 3.8 while those using a manganese bath give values close to 3.7. An accurate measurement has been reported recently by De Volpi and Porges[35] and their value (3.725 ± 0.015) supports the lower data. The value adopted for ENDF/B (Version

I) is 3.772 ± 0.015.[35] Thus, $\bar{\nu}$ values calculated from ENDF/B may be somewhat large (~1%).

In fast reactor calculations one commonly assumes a linear energy dependence for $\nu(E)$ in the lower energy range and a similar dependence, but with different slope, at higher energies where the $(n,n'f)$ reaction is possible.[32] In effect, this assumes a ν-value in the fission resonance region equal to the thermal value. The measurements of Weinstein et al.[36] indicate that this may not be a good approximation for Pu-239. They found that the ν-values for Pu-239 in the energy range 0.01 to 100 eV fall into two groups, differing by about 3%, depending on the spin states (J = 0,1) of the individual resonances. For example, at 0.198 eV they found ν to be 1% lower than the thermal value. Similar, but less pronounced, effects exist for U-235. At 0.3 eV they found ν^{235} to be 0.6% higher than the thermal value. Preliminary data reported by Condé[37] suggest that the actual value of $\bar{\nu}$ for Pu-239 in a fast reactor spectrum is somewhat less than what one calculates assuming $\nu(E)$ varies linearly with energy with the intercept corresponding to ν_{th}. In view of these considerations, it seems likely that too large a value of $\bar{\nu}$ was used in the analysis of α^{239} and that this is the most important reason for the difference between the reactivity-reaction rate and mass spectrometer determinations of α^{239}.

The experiments of Meadows and Whalen[38] show that for U-235 $\nu(E)$ has structure and varies non-linearly in the several hundred keV region, where a significant part of the neutron spectrum lies in a fast reactor. Davey[39] points out that at 300 keV this structure effect results in a value of $\nu(E)$ which is 2% larger than one would calculate assuming a linear energy dependence. All things considered, it is not clear whether the spectrum-weighted value of ν^{235} calculated from ENDF/B is too large or too small.

Summary

Integral capture-to-fission ratios for Pu-239, U-235 and U-238 have been measured by the reactivity-reaction rate method in a fast reactor spectrum tailored to emphasize Pu-239 capture events in the 0.1–30 keV range. For Pu-239 and U-235 uncertainties in $\bar{\nu}$ contribute most of the error to the measured capture-to-fission ratios. The measured Pu-239 alpha values are somewhat larger than those calculated from fundamental nuclear data, but are best described by ENDF/B cross sections modified in the 0.1–30 keV range by the recent ORNL-data.[3] This conclusion applies whether one uses the theoretical neutron flux distribution or spectra measured by proton-recoil and time-of-flight techniques.

Although the errors overlap, the infinitely dilute value of $\bar{\alpha}^{239}$ is about 8% larger than an independent value measured in a direct way using a combination of mass spectrometer techniques and fission track recorders.[11] The reactivity-reaction rate value of $\bar{\alpha}^{239}$ depends very sensitively on the calculated value for $\bar{\nu}$. For reasons discussed in the previous section, it seems likely that the value of $\bar{\nu}$ calculated from ENDF/B is too large by 1–2%. This would account for the difference between the two independent measurements of $\bar{\alpha}^{239}$ and would also provide good agreement between the measured and calculated values. By combining the mass spectrometer result with the measurements reported here one can derive a value for $\bar{\nu}$ corresponding to a zero-thickness sample of Pu-239 in the fast reactor spectrum. This evaluation gives $\bar{\nu}^{239}$ = 2.913 ± 0.036 which is 1.3% lower than the calculated value of 2.950.

The measured Pu-239 alpha values decrease as a function of sample thickness much more rapidly than theory predicts. This may be due to a deficiency in the code used to calculate the perturbed fluxes. However, this code adequately accounts for the thickness effect in U-235 and for the earlier Pu-239 measurements made in another core.[10]

For U-235 the measured alpha values are in excellent agreement with those calculated from ENDF/B. However, the results are dependent on a rather tentative value for the Mo-99 yield in the fast fission of U-235.

Unlike Pu-239 and U-235 the U-238 alpha values vary significantly depending on the flux and adjoint distributions used. The calculated value of $\bar{\alpha}^{238}$ is very sensitive to that portion of the neutron spectrum above the fast fission threshold (~0.6 MeV). The high energy portion of the time-of-flight spectrum rises above the theoretical CALHET distribution and this is the primary reason why the calculated value of $\bar{\alpha}^{238}$ based on CALHET is 17% larger than the result evaluated from the T-O-F data. A large scattering correction must be applied to obtain the reactivity-reaction rate value of $\bar{\alpha}^{238}$. The magnitude of this correction depends rather sensitively on the adjoint distribution. The use of the CALHET fluxes and adjoints calculated from MC² cross sections, without cell-averaging, leads to good agreement among the calculated, radiochemical and reactivity-reaction rate U-238 alpha values.

References

1. M. G. Schomberg, M. G. Sowerby and F. W. Evans, *New Methods of Measuring Alpha(E) for Pu-239*, Proc. IAEA Symposium on Fast Reactor Physics and Related Safety Problems, Vienna, 1968, Vol. 1, p. 289.
2. R. Gwin et al., *Simultaneous Measurements of the Neutron Fission and Absorption Cross Sections of ^{239}Pu Over the Energy Region 0.02 to 30 keV*, Nucl. Sci. Eng. **40**, 306 (1970).
3. R. Gwin et al., *Measurement of the Neutron Fission and Ab-*

sorption Cross Sections of ^{239}Pu Over the Energy Region 0.02 eV to 30 keV, Nucl. Sci. Eng. (to be published).
4. M. G. Schomberg et al., *The Ratio of the Capture and Fission Cross Sections of ^{239}Pu in the Energy Range 100 eV to 30 keV*, IAEA International Conference on Nuclear Data for Reactors, Helsinki, June 1970, CN-26/33.
5. J. A. Farrell et al., *A Simultaneous Measurement of the Fission, Capture, Scattering and Total Cross Sections of ^{239}Pu*, IAEA International Conference on Nuclear Data for Reactors, Helsinki, June 1970, CN-26/46.
6. J. B. Czirr and J. S. Lindsey, *A Measurement of the Capture-to-Fission Ratio for ^{239}Pu*, Nucl. Sci. Eng. **41,** 56 (1970).
7. J. B. Czirr and J. S. Lindsey, *^{235}U and ^{239}Pu Capture-to-Fission Ratio*, IAEA International Conference on Nuclear Data for Reactors, Helsinski, June 1970, CN-26/47.
8. F. N. Belyaev et al., *Measurement of the Ratio of the ^{235}U and ^{239}Pu Capture and Fission Cross Sections*, IAEA International Conference on Nuclear Data for Reactors, Helsinki, June 1970, CN-26/89.
9. C. E. Till, J. M. Gasidlo, E. F. Groh, L. G. LeSage, W. R. Robinson and G. S. Stanford, *Null-Reactivity Measurements of Capture/Fission Ratio in ^{235}U and ^{239}Pu*, Nucl. Sci. Eng. **40,** 132 (1970).
10. M. M. Bretscher and W. C. Redman, *Low Flux Measurements of ^{239}Pu and ^{235}U Capture-to-Fission Ratios in a Fast Reactor Spectrum*, Nucl. Sci. Eng. **39,** 368 (1970).
11. W. Y. Kato, R. J. Armani, R. P. Larsen, P. E. Moreland, L. A. Mountford, J. M. Gasidlo, R. J. Popek and C. D. Swanson, *An Integral Measurement of ^{239}Pu Alpha*, Trans. Am. Nucl. Soc. **13,** 88 (1970).
12. M. M. Bretscher, J. M. Gasidlo and W. C. Redman, *Comparison of Measured and Calculated Capture-to-Fission Ratios in a Soft Spectrum Fast Critical Assembly*, Trans. Am. Nucl. Soc. **13,** 89 (1970).
13. Reactor Development Program Progress Report, ANL-7581, p. 8 (June 1969).
14. L. G. LeSage, E. F. Groh and W. R. Robinson, *An Investigation of the Properties of Zoned Systems*, Reactor Physics Division Annual Report, July 1, 1967 to June 30, 1968, ANL-7410, pp. 145–151.
15. A. De Volpi and K. G. Porges, *Absolute Calibration of Neutron Sources Having a Wide Range of Emission Spectra*, Metrologia **5,** 128 (1969).
16. A. De Volpi and K. G. Porges, *^{252}Cf Half-Life by Neutron Counting*, Inorg. Nucl. Chem. Letters **5,** 111 (1969); **5,** 669 (1969).
17. R. J. Armani, *Absolute Determination of Fission Rates in U-235 and U-238 and Capture Rates in U-238 by Radiochemical Techniques*, Reactor Physics Division Annual Report, July 1, 1965 to June 30, 1966, ANL-7210, p. 304.
18. R. J. Armani, R. Gold, R. P. Larsen and J. H. Roberts, *Measured Fission Yields of ^{99}Mo and ^{140}Ba in Fast-Neutron-Induced Fission of ^{239}Pu*, Trans. Am. Nucl. Soc. **13,** 90 (1970).
19. R. P. Larsen, Argonne National Laboratory (private communication).
20. F. L. Lisman et al., *Fission Yields of over 40 Stable and Long-Lived Fission Products for Thermal Neutron Fissioned ^{233}U, ^{235}U, ^{239}Pu, and ^{241}Pu and Fast Reactor Fissioned ^{235}U and ^{239}Pu*, Nucl. Sci. Eng. **42,** 191 (1970).
21. Reactor Development Program Progress Report, ANL-7595, 19 (July 1969).
22. F. L. Fillmore, *The CALHET-2 Heterogeneous Perturbation Theory Code and Application to ZPR-3-48*, AI-69-13 (March 1969).
23. M. M. Bretscher, *Li-6 as a Reference Absorber for Capture-to-Fission Ratio Measurements in Zero Power Fast Critical Assemblies*, Reactor Physics Division Annual Report, July 1, 1967 to June 30, 1968, ANL-7410, pp. 178–182.
24. B. J. Toppel, A. L. Rago and D. M. O'Shea, *MC², A Code to Calculate Multigroup Cross Sections*, ANL-7318 (1967).
25. B. J. Toppel, *The Argonne Reactor Computation (ARC) System*, ANL-7332 (1967).
26. J. W. Powell, *Comparison of Proton-Recoil Proportional Counter and Time-of-Flight Neutron Spectrum Measurements in a ^{235}U-Fueled Fast Reactor*, Trans. Am. Nucl. Soc. **12,** 712 (1969).
27. P. d'Oultremont, J. C. Young, J. M. Neill and C. A. Preskitt, *Neutron Spectrum Measurements and Analysis in the Fast Assemblies STSF-5, STSF-6 and STSF-1A*, Trans. Am. Nucl. Soc. **13,** 267 (1970).
28. P. d'Oultremont, Gulf General Atomic Incorporated (private communication).
29. C. A. Preskitt et al., *Fast Reactor Spectrum Measurements*, GA-9259 (March 1969).
30. C. E. Till, *Fissile Doppler Effect Measurement and the Effects of Thermal Expansion*, Reactor Physics Division Annual Report, July 1, 1966 to June 30, 1967, ANL-7310, pp. 143–151.
31. W. B. Mann and A. Spernol, *The National Bureau of Standards Tritiated Water Standards*, Intern. J. Appl. Rad. Isotopes **15,** 628 (1964).
32. F. L. Fillmore, *Recommended Values for the Number of Neutrons Per Fission*, J. Nucl. Energy **22,** 79 (1968).
33. C. G. Hanna et al., *Revision of Values for the 2200 m/s Neutron Constants for Four Fissile Nuclides*, Atomic Energy Rev. **7**(4), 3 (1969).
34. A. De Volpi and K. G. Porges, *Neutron Yield of ^{252}Cf Based on Absolute Measurements of the Neutron Rate and Fission Rate*, Phys. Rev. C **1,** 683 (1970).
35. C. H. Westcott et al., *A Survey of Values of the 2200 m/s Constants for Four Fissile Nuclides*, Atomic Energy Rev. **3**(2), 3 (1965).
36. S. Weinstein, R. Reed and R. C. Block, *Neutron Multiplicity Measurements for ^{233}U, ^{235}U, and ^{239}Pu Resonance Fission*, Proc. IAEA Symposium on the Physics and Chemistry of Fission, Vienna, July 28–August 1, 1969, p. 477.
37. H. Condé and L. Widen, *$\bar{\nu}$ of ^{235}U and ^{239}Pu in a Fast Reactor Spectrum*, IAEA International Conference on Nuclear Data for Reactors, Helsinki, June 1970, CN-26/59.
38. J. W. Meadows and J. F. Whalen, *Energy Dependence of $\bar{\nu}_p$ for Neutron-Induced Fission of ^{235}U Below 1.0 MeV*, J. Nucl. Energy **21,** 157 (1967).
39. W. G. Davey, *Status of Important Heavy Element Nuclear Data Above the Resonance Region*, IAEA International Conference on Nuclear Data for Reactors, Helsinki, June 1970, CN-26/112.

II-12. An Integral Measurement of Pu-239 and U-233 Alpha

W. Y. Kato, R. J. Armani, R. P. Larsen*, P. E. Moreland**, L. A. Mountford,†
J. M. Gasidlo, R. J. Popek* and C. D. Swanson

Introduction

A number of differential capture and fission cross sections for Pu-239 have been reported.[1-3] Because of the discrepancy between the reported values, an experiment has been performed on ZPR-3 to measure directly the integral value of the Pu-239 capture-to-fission ratio (alpha) in a fast spectrum to attempt to determine the correct differential values. In addition, an attempt was made to measure the U-233 and U-235 alphas. The experiment basically consisted of irradiating highly purified samples of Pu-239, U-233, and U-235 near the center of a special uranium-fueled assembly whose spectrum was tailored to enhance the 1–50 keV neutron energy region and measure the number of fissions and captures which had occurred in the sample during the irradiation. The experimentally determined values of the integral alpha were then compared with theoretically calculated values using various differential cross sections and measured and calculated spectra.

Description of Assembly

Since the ZPR-3 facility was limited to a maximum power level of 5 kW, it was necessary to design a core which was as small as possible to maximize the neutron flux and whose fast spectrum enhanced the 1–50 keV region to as high a degree as possible. It was also desirable to minimize the number of neutrons below about 100 eV. An additional limitation was imposed by the available inventory of materials.

ZPR-3 Assembly 57 was designed to meet these criteria. It is a three-region assembly, with a central core of U-235, U-238, beryllium oxide, and aluminum surrounded by an inner reflector of iron and an outer reflector of depleted uranium. The core composition of this assembly was the same as that of the Gulf General Atomic STSF-1A[4] whose central spectrum had been measured by time-of-flight techniques. Furthermore, Assembly 57 had a depleted uranium reflector to provide additional radiation shielding. The core drawers contained two ⅛-in. columns of enriched uranium, five 1/16-in. columns of depleted uranium, and eleven ⅛-in. columns of beryllium oxide as shown in Fig. II-12-1. Instead of the standard ANL-ZPR enriched uranium fuel plates, enriched uranium fuel from the former CANEL project was used. This was done so that the fuel could be stored for an indefinite period after the high-power irradiation without affecting the normal ZPR fuel inventory. In addition, the 1.75-in. height of the CANEL plates, which is less than the standard ZPR fuel plates, provided a ¼-in. channel above the fuel columns which was used as a cooling channel. In order to take maximum advantage of this as a cooling channel during the high-power run, the axial reflector columns behind the fuel were also made shorter. The central 13 drawers in each half had this composition. The remaining axial reflector and the radial reflector consisted of solid blocks of iron and depleted uranium. The core control and safety drawers had the same loading as shown in Fig. II-12-1, except for the removal of one column of beryllium oxide, iron, and depleted uranium required by the thicker drawer walls.

The vertical cross-section geometry of Assembly 57 is shown in Figs. II-12-2 and II-12-3. Figure II-12-4 shows the geometry of the equivalent cylindrical loading for this assembly. The atom densities corresponding to the regions shown in Fig. II-12-4 are listed in Table II-12-I. The breakdown of the assembly into regions is complicated by four characteristics of the assembly which were brought about because of the desire to reproduce the atom densities of STSF-1A as closely as possible:

(1) Each half of the reactor in the central region

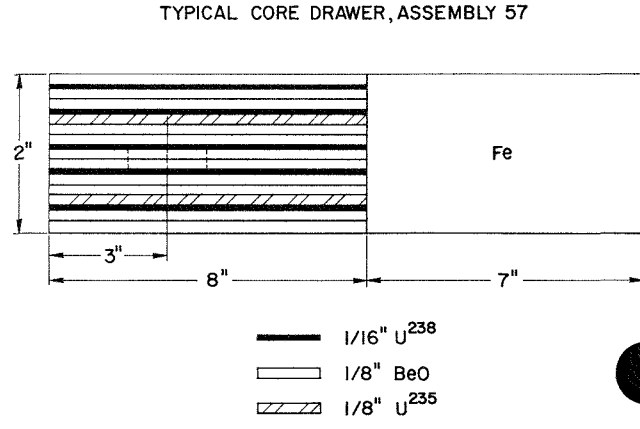

Fig. II-12-1. Typical Core Drawer, Assembly 57. *ANL Neg. No. 116-356T-1.*

* Chemical Engineering Divison, Argonne National Laboratory.

** Chemistry Division, Argonne National Laboratory.

† Atomics International, a Division of North American Rockwell Corporation, Canoga Park, California.

contains a 7 x 7 array of aluminum tubes which were placed in the normal matrix assembly of stainless steel tubes. The reactor core and the axial reflector are loaded in aluminum matrix tubes, while the radial reflector is, in general, loaded in stainless steel matrix tubes.

(2) The core drawers, containing some axial reflector, are aluminum. The drawers containing the remainder of the axial reflector, which consists of solid blocks of iron and uranium, are stainless steel.

(3) The central axial reflector has cooling channels, which gives them lower atom densities than the solid reflector regions.

(4) The radial reflector in the aluminum matrix is in drawers. In the stainless steel matrix the pieces are loaded directly into the matrix.

The critical loading of Assembly 57 is shown in Figs. II-12-2 and II-12-3. The assembly was built off center in the matrix to provide additional matrix locations on the control room side for shielding materials. This loading contained 85.59 kg U-235, and was critical with one control rod withdrawn 4.35 in. and all other rods fully inserted. The integral worth of the control rod at this position was 152 Ih, which is equivalent to 1.12 kg of U-235. The critical mass is then 84 5 kg of U-235. When corrected for core differences, this compares well with the extrapolated critical mass of 89 kg U-235 for the STSF-1A, and a calculated value of 88 kg U-235 using ENDF/B microscopic cross sections, MC²,[5] and a one-dimensional diffusion code DIFID.[6]

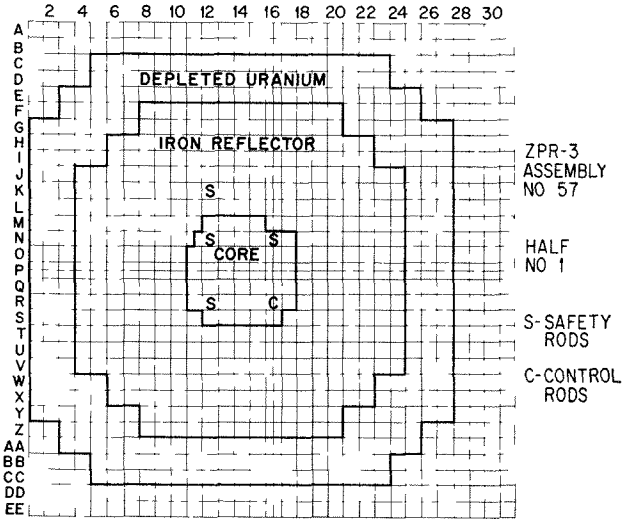

FIG. II-12-2 Vertical Cross Section of Half No 1 *ANL Neg. No. 116-345.*

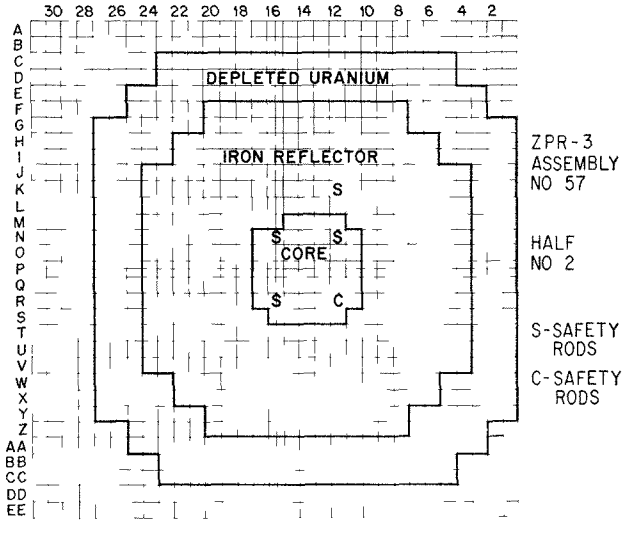

FIG II 12-3. Vertical Cross Section of Half No 2 *ANL Neg. No 116-346*

MEASUREMENTS

In order to calculate the integral values of alpha for Pu-239, U-233, or U-235 for comparison with a measured value it is necessary to know the neutron spectrum at the point where the samples are irradiated in addition to having the differential capture and fission cross sections as a function of energy for these isotopes. To verify the theoretically calculated spectrum, measurements of the neutron spectrum were made at the location where foils were to be irradiated using a proton-recoil spectrometer.[7] Neutron spectra obtained using time-of-flight techniques[8,9] on the Gulf General Atomic STSF-1A assembly were also available for comparison.

As an additional check on the calculated spectrum of Assembly 57, a series of central fission ratios were measured relative to U-235 using "back-to-back" gas-flow spherical counters.[10] The counters were placed in a 2 x 2 x 2-in. cavity in the front of the central drawer in Half No. 1 (1-P-14). The cavity extended further toward the rear of the drawer in the central section to accommodate the connectors and cables. The drawer-loading diagram is shown in Fig. II-12-5. The foil orientation was perpendicular to the horizontal plane of the reactor material plates. The fission rates of materials in which one of seven fissionable materials (U-233, U-234, U-235, U-236, U-238, Pu-239, and Pu-240) was dominant, were measured by placing pairs of foils in counters. These four counters were placed in the cavity in succession in four reactor runs. The fission rates were normalized for power variations among the runs using the counting rates of a gas-flow fission counter positioned in the radial blanket.

The data for all of the detectors were taken with a pulse-height analyzer. The differential spectra were converted to fission rates with a computer code using

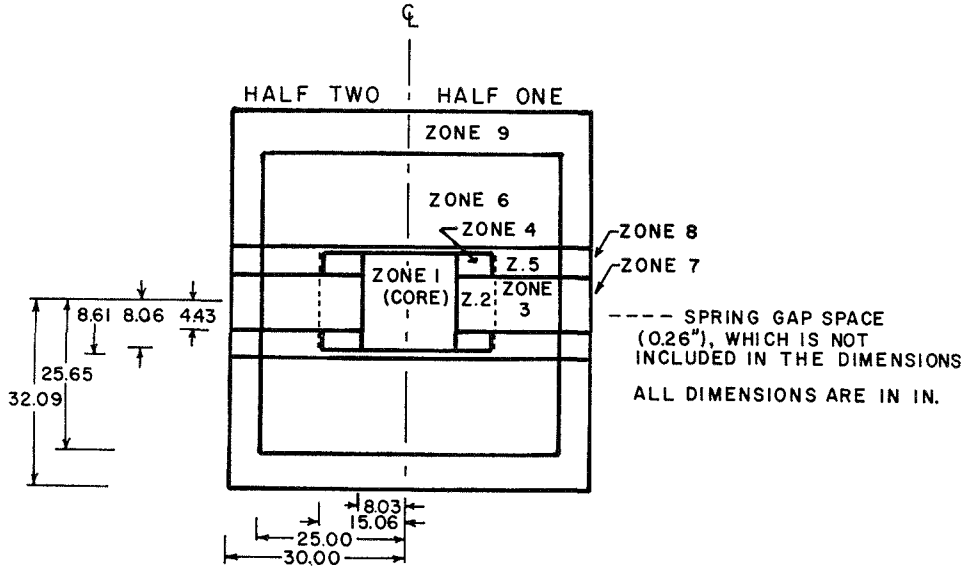

FIG. II-12-4. Geometry of Equivalent Cylindical Loading. *ANL-ID-103-2920 T-1.*

TABLE II-12-I. COMPOSITION OF ZPR-3 ASSEMBLY 57, 10^{22} atoms/cm^3

Zone	U-235	U-238	Be	O	Al	Fe	Cr	Ni	Mn	Si
Core										
Zone 1	0.4081	0.6347	3.901	3.901	0.5546	—	—	—	—	—
Safety (control rods)	0.4065	0.6322	3.533	3.533	0.4339	0.5281	0.1314	0.0575	0.0055	0.0064
Inner reflector										
Zone 2	—	—	—	—	0.5472	6.555	0.0506	0.0221	0.0021	0.0025
Zone 3	—	—	—	—	0.4339	5.000	1.243	0.5443	0.0519	0.0609
Zone 4	—	—	—	—	0.5472	7.093	—	—	—	—
Zone 5	—	—	—	—	0.4339	7.205	0.0262	0.0115	0.0011	0.0013
Zone 6	—	—	—	—	—	7.554	0.1129	0.0494	0.0047	0.0055
Safety rod—core	—	—	—	—	0.4339	5.226	1.300	0.5689	0.0543	0.0637
Safety rod—reflector	—	—	—	—	—	4.521	1.125	0.4921	0.0469	0.0551
Outer reflector										
Zone 7	0.0078	3.741	—	—	0.4339	0.1053	0.0262	0.0115	0.0011	0.0013
Zone 8	0.0083	4.000	—	—	0.4339	0.1053	0.0262	0.0115	0.0011	0.0013
Zone 9	0.0083	3.989	—	—	—	0.4540	0.1129	0.0494	0.0047	0.0055
Safety rod—core	0.0076	3.619	—	—	0.4339	0.4926	0.1225	0.0536	0.0051	0.0060
Safety rod—reflector	0.0077	3.674	—	—	—	0.9487	0.2360	0.1033	0.0099	0.0116

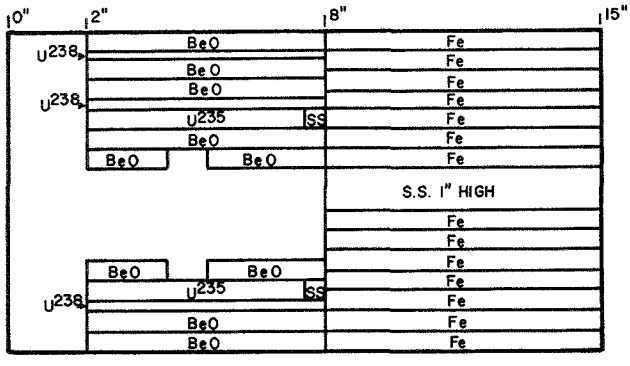

FIG. II-12-5. Core Drawer Location of Fission Counter. *ANL-ID-103-A11075.*

an identical integration technique for all of the detectors. The detector fission rates were then reduced to isotopic fission rates using the masses and isotopic concentrations of the foils. The reduced isotopic fission ratios are given in Table II-12-II. Calculated values are also given in Table II-12-II for comparison.

In order to measure the change in the Pu-240 content in a Pu-239 sample or U-234 content in a U-233 sample or U-236 content in a U-235 sample after an irradiation in a critical facility where neutron flux levels are relatively limited, it is necessary to irradiate samples of Pu-239, U-233, or U-235 which have exceptionally low Pu-240, U-234, and U-236 contents, re-

spectively. The original intent in this irradiation experiment was to measure the integral capture-to-fission ratio for Pu-239, U-233, and U-235. With starting materials of 10 mg of Pu-239 and 10 mg of U-233 containing 8 ppm of Pu-240 and 1 ppm of U-234, respectively, approximately 500 μg of Pu-239 containing 25 ppb of Pu-240 and 500 μg of U-233 containing 64 ppb of U-234 were prepared by J. L. Lerner* using the Argonne Chemistry Division's mass separator. The attempt to obtain U-235 having exceptionally low U-236 content was not successful, probably because of cross contamination during the chemical processing stage. Although U-235 containing about 1 ppm U-236 was irradiated, meaningful capture rate determination was not possible because of the high U-236 content. The highly purified samples of Pu-239 and U-233 were used only for capture rate determinations. Conventional plutonium with 4% Pu-240 and 93% enriched U-235 were used for the fission rate determinations. Since appropriate metallic U-233 foil material was not available at the time of the experiment, the U-233 fission rate in the long irradiation was established, in part, by means of the U-235 and Pu-239 foils.

The total number of fissions occurring in the Pu-239 and U-235 foils during the long-term irradiation were determined by measuring the fission product Ba-140 gamma activity. Because of the uncertainty in the fission yield for Ba-140 in a fast spectrum, a short-term irradiation (80 min) for an integrated power of about 4 kWh was carried out to establish a calibration factor (Ba-140 counts/min-fission) for the long-term irradiation.

This calibration factor was established in the short-term irradiation by simultaneously irradiating nanogram amounts of Pu-239, U-233, and U-235 in contact with mica fission track recorders and Pu-239 and U-235 foils. The total number of Pu-239, U-233, and U-235 fissions occurring during the short irradiation was determined by counting the fission tracks in mica track recorders using the technique developed by Gold et al.[11] The amounts of Pu-239, U-233, and U-235 in contact with the track recorders were determined by alpha counting in a calibrated alpha counter. (The specific activity of the U-235 was enhanced by a factor of 10^4 by the addition of U-232.) The Ba-140-La-140 fission product activity was measured by gamma-ray spectrometry using a lithium-drifted germanium diode multichannel analyzer system. The 1.59-MeV gamma ray emitted by the La-140 was used for the assay. That this gamma ray was due entirely to La-140 and that the La-140 was in equilibrium with the Ba-140 at the time of analysis was demonstrated by the fact that this gamma ray decayed with a half-life of 12.8 days, the half-life of Ba-140. The plutonium and uranium foils were analyzed for their fissile nuclide content by weighing coupled with chemical analysis and mass spectrometry.

* Chemistry Division, Argonne National Laboratory.

TABLE II-12-II. Comparison of Measured and Calculated Fission Ratios $\bar{\sigma}_f(i)/\bar{\sigma}_f$ (U-235) in ZPR-3 Assembly 57

	Measured[a]		Calculated[b]		
			Spectra		
	Counter	Foils	Homog.	Hetero.	Time-of-Flight
U-233	1.447	1.39	1.410	1.399	1.391
U-234	0.201	—	0.211	0.193	0.229
U-236	0.0741	—	0.082	0.075	0.091
U-238	0.0351	0.0323	0.040	0.036	0.044
Pu-239	0.973	0.998	0.919	0.907	0.939
Pu-240	0.228	—	0.247	0.227	0.264

[a] The experimental uncertainty is approximately ±1% for the fission counter measurements.

[b] Calculations were based on using infinitely dilute cross sections from ENDF/B Version 1 and spectra obtained from a homogeneous and a heterogeneous (CALHET) calculation and time-of-flight measurement.

Two capsules were used in the long-term irradiation. Each of these capsules contained four plutonium foils, four enriched uranium foils, and four 50-μg samples each of the high isotopic purities U-233, U-235, and Pu-239. The fissile samples were evaporated from a nitrate solution onto thin stainless steel disks. Each disk was then placed inside thin aluminum double-walled containers to prevent cross contamination. The aluminum containers, each of which contained the various samples, were then placed inside a 2-in. diam ¼-in. thick thin-walled (approximately 13-mil) stainless steel capsules. The capsules were irradiated in the center column of drawers 1P14 and 2P14 which were located in the center of the core. The centerlines of the two capsules were located approximately 3 in. from the front face of the drawer as shown by dotted lines in Fig. II-12-1. The long-term irradiation was carried out continuously from 1340 MDT, August 25, 1969, to 0004 MDT, August 29, 1969, on ZPR-3 at a power level of about 5 kW.

The relative fluences in the short- and long-term irradiations as determined by the Ba-140-La-140 measurements on the plutonium foils from two samples in the same capsule were 86.7 ± 1.2 and 90.0 ± 1.3. The relative fluence in the short- and long-term irradiations obtained from the U-235 foils was 89.4 ± 1.3.

These numbers were calculated by dividing the

average Ba-140-La-140 activity/mg ratio obtained in the long irradiation by that obtained in the short irradiation. The Ba-140-La-140 activities were corrected for in-pile and out-pile decay of the Ba-140. The relative standard deviation of the activity-to-weight ratio for a single foil in a set of four was ±2.0% and for the average ±1.0%. The relative standard deviation of the relative fluence measurements is, therefore, ±1.4%. The use of this technique for the total fission determination has two major advantages: it is unnecessary to know the fission yield of Ba-140 and it is unnecessary to make an absolute efficiency-geometry calibration of the detector. (Both the short-term and long-term foils were counted at the same geometry.)

With the short-term irradiation sample giving a value of $(9.63 \pm 0.06) \times 10^{12}$ fissions/g of Pu-239, the number of fissions per 10^9 Pu-239 atoms in the long-term samples were 331 ± 5 (Sample No. 133) and 344 ± 5 (Sample No. 134).

The U-233 sample in the short-term irradiation gave a value of 1.375×10^{13} fissions/g U-233. Assuming an average value of 89.7 for the ratio of fluence of the long-to-short-term irradiations from the Pu-239 and U-235 samples irradiated in the two irradiations, a value of 477 fissions per 10^9 U-233 atoms was obtained.

Mass spectrometric analyses of the highly purified Pu-239 and U-233 samples were carried out using the Argonne Chemistry Division tandem mass spectrometer. Two irradiated and two control (unirradiated) Pu-239 samples were analyzed using the mass spectrometer. These samples gave the following results:

	Pu-240/Pu-239
Irradiated Sample No. 9-2	142 ± 7 ppb (8 measurements)
Irradiated Sample No. 9-3	153 ± 8 ppb (3 measurements)
Control Sample No. 2	25 ± 3 ppb (4 measurements)
Control Sample No. 1	24 ± 5 ppb (1 measurement).

The irradiated plutonium isotopic ratios were obtained by measuring ion currents with an electron multiplier and introducing a calibrated gain of 10^7 to measure the Pu-240 ion current. Voltage-to-frequency conversion and integration of multiple scans with a multiscaler were used to improve the signal-to-noise ratio. The isotopic ratio for the control samples was obtained by monitoring the Pu-239 ion current with a Faraday cup-slit plate while pulse counting the Pu-240 ions reaching the electron multiplier. Integration of multiple scans was again used. In both cases, instrumental discrimination effects were determined and corrected by alternating measurements of a standardized isotopic mixture of uranium with the plutonium measurements. The uranium mixture used for this internal calibration consisted of U-233 + (120 ± 2 ppm) U-234 + (220 ± 3 ppm) U-236. An acid solution of this mixture was used to dissolve the plutonium from the irradiation sample plates and transferred to the mass spectrometer sample filament, insuring that the analysis of the two elements took place under identical conditions. Precautions were taken throughout to insure that no $^{239}PuH^+$ would be observed.

The tandem mass spectrometer gave the following results for the U-233 samples:

	U-234/U-233
Irradiated U-233 No. 3-1	99 ± 7 ppb
Unirradiated Control Samples	64 ± 7 ppb

This results in a value of 35 ± 10 atoms of U-234 per 10^9 U-233 atoms.

Results and Analysis

Fission sample No. 133 was located next to capture sample No. 9-2 and sample No. 134 next to sample No. 9-3 within the stainless steel capsule. Because of the axial neutron flux distribution, it appeared appropriate to take the ratio of sample No. 9-2 to sample No. 133 and sample No. 9-3 to sample No. 134 and average the two results. This gave a value of 0.363 ± 0.024 for the Pu-239 capture-to-fission ratio in this spectrum.

The ratio of the capture and fission measurements for the U-233 samples gave a value of 0.10 ± 0.04 for the capture-to-fission ratio for U-233. The large uncertainty in this value results from the fact that it was not possible to obtain a lower U-234 content U-233 sample than the 64 ppb of U-234.

Theoretical calculations of the Pu-239 capture-to-fission ratio have been made using the ENDF/B (Version 1), Gwin,[3] preliminary revised Gwin,[12] Schomberg[1] and revised Schomberg[13] cross-section data in the 0.1 to 25-keV energy range and the ENDF/B cross-section data above 25 keV. The calculations were carried out using these cross sections and spectra obtained from theoretical calculations, proton-recoil spectrometer, and time-of-flight technique.[8,9] Two types of theoretical calculations of the neutron spectrum were made. The first involved the use of the ENDF/B cross-section set, MC²,[5] and DIF1D, the one-dimensional diffusion code of the ARC[6] system. Since the reactor core had plate-type geometry, a calculation using slab geometry with the CALHET code[14] was carried out in order to determine the effects of heterogeneity on the spectrum. The calculation of alpha was carried out on a 31-group basis with the region below 25 keV divided into groups which matched the experimental differential cross-section measurement energy grouping. The values of the flux from the homogenized calculation and the heterogenous cal-

ration, proton-recoil, and time-of-flight measurements are tabulated in units of flux per unit lethargy in Table II-12-III after being normalized to the total number of neutrons between 100 eV and 10 MeV. The calculated values of the Pu-239 alpha based on the various spectra and the five different cross-section sets are tabulated in Table II-12-IV. Although there is some discrepancy between the time-of-flight spectrum and the calculated spectrum there is good agreement of the alpha values calculated using the five different cross-section sets and the CALHET proton-recoil and time-of-flight spectra. The best agreement between the experimental value of alpha of 0.363 results from using the revised Gwin capture and fission cross sections. Table II-12-V lists the fraction of fissions occurring in the various energy regions for this assembly. Since a large fraction of the captures occurs below 25 keV the alpha calculations given in Table II-12-V are particularly sensitive to the uncertainties in this region.

Using the ENDF/B microscopic cross sections for U-233 and the three spectra listed in Table II-12-III,

TABLE II-12-III. Flux Per Unit Lethargy

E_L, keV	Theoretical		Proton-Recoil	T-O-F
	DIFID	CALHET		
3670	16.850	15.88	15.44	23.27
2230	69.24	66.32	64.46	77.45
1350	109.9	106.4	108.00	120.4
825	103.1	98.59	123.9	122.5
500	133.4	130.3	134.0	153.2
300	119.1	117.5	114.9	126.5
180	130.8	130.7	122.1	122.9
110	115.3	115.9	155.9	104.8
67	101.4	102.1	104.9	84.84
41	89.59	90.97	88.95	69.81
25	75.89	76.42	71.60	59.33
15	66.89	68.40	62.04	55.46
10	55.30	57.06	55.05	47.67
9	54.30	55.74	53.26	42.69
8	46.90	45.97	51.78	39.92
7	46.25	45.97	49.74	38.12
6	40.48	45.97	44.39	51.19
5	38.62	40.93	36.11	35.23
4	35.35	36.46	30.85	33.51
3	33.55	33.32	28.11	29.45
2	24.64	27.35	23.47	24.39
1	16.66	18.66	19.13	19.07
0.9	11.15	13.70	13.32	17.53
0.8	10.12	13.70	13.32	8.96
0.7	8.957	11.45	11.13	12.00
0.6	7.752	8.90	8.65	10.77
0.5	6.085	8.90	8.65	9.16
0.4	5.010	7.04	7.00	7.97
0.3	3.723	5.45	5.30	7.03
0.2	2.199	3.55	3.45	5.76
0.1	0.927	1.97	1.92	4.04

TABLE II-12-IV Pu-239 Alpha Comparison between Experiment and Theory

(*Integral Experiment* = 0.363 ± 0.024)

Cross Sections		Spectra			
<25 keV	>25 keV	Homogeneous (DIFID)	Heterogeneous (CALHET)	Proton-Recoil	T-O-F
ENDF/B	ENDF/B	0.243	0.266	0.257	0.266
Gwin[3]	ENDF/B	0.296	0.330	0.318	0.335
Gwin (Rev.)[12]	ENDF/B	0.317	0.348	0.335	0.349
Schomberg[1]	ENDF/B	0.373	0 406	0.389	0.401
Schomberg (Rev.)[13]	ENDF/B	0.275	0 302	0.291	0.307

TABLE II-12-V. Fraction of Captures and Fissions with Gwin Revised Data

Reaction	Spectra	0.1–1 keV	1–25 keV	>25 keV
Capture	THEO-CALHET	0.28	0.54	0.18
	T-O-F	0.37	0.48	0.15
Fission	THEO-CALHET	0.11	0.24	0.65
	T-O-F	0.14	0.21	0.65

values of 0.12, 0.12, and 0.12 were obtained for the capture-to-fission ratio for U-233. The experimental value of 0.10 ± 0.04 is within experimental error and in reasonable agreement with the theoretical values.

Conclusions

On the basis of the experimental value of alpha, the following conclusions may be drawn:

(1) The values of the capture-to-fission ratios as deduced from the capture and fission cross sections for Pu-239 in the ENDF/B Version 1 files are too low.

(2) The revised Gwin[12] data give the best agreement with the integral value. It does appear that the revised Schomberg[13] data are now also low.

References

1. M. G. Schomberg, M. G. Sowerby and F. W. Evans, *A New Method of Measuring Alpha (E) for ^{239}Pu*, Fast Reactor Physics (International Atomic Energy Agency, Vienna, 1968), Vol. 1, p. 289.
2. B. H. Patrick, UKAEA (private communication).
3. R. Gwin et al., *Measurements of the Neutron Fission and Absorption Cross Sections of ^{239}Pu Over the Energy Region 0.02 eV to 30 eV*, Nucl. Sci. Eng. **40**, 306 (1970); also, ORNL-TM-2598 (October 7, 1969).
4. W. Y. Kato, C. A. Preskitt, J. C. Young, J. M. Neill, C. D. Swanson, R. J. Armani and J. H. Roberts, *Measurement of Reaction Ratios and Neutron Spectra in a Soft-Spectrum Fast Reactor*, Trans. Am. Nucl. Soc. **11**, 599 (1968); also, *Measurement of Reaction Ratios and Neutron Spectra in a*

Soft-Spectrum Fast Reactor, Reactor Physics Division Annual Report, June 30, 1968 to July 1, 1969, ANL-7610, pp. 184–187.
5. B. J. Toppel, A. L. Rago and D. M. O'Shea, *MC²—A Code to Calculate Multigroup Cross Sections*, ANL-7318 (1967).
6. B. J. Toppel, *The Argonne Reactor Computation (ARC) System*, ANL-7332 (1967).
7. J. E. Powell, *Comparison of Proton-Recoil Proportional Counter and Time-of-Flight Neutron Spectrum Measurements in a ^{235}U-Fueled Fast Reactor*, Trans. Am. Nucl. Soc. **12**, 712 (1969).
8. P. d'Oultremont et al., *Neutron Spectrum Measurements and Analyses in the Fast Assemblies STSF-5, STSF-6 and STSF-1A*, Trans. Am. Nucl. Soc. **13**, 267 (1970).
9. J. C. Young et al., *Fast Spectrum Measurements*, GA-10280 (1970).
10. W. G. Davey and P. J. Amundson, *Inelastic Scatter Measurements in a Fast Reactor by the Spherical Shell Method*, Nucl. Sci. Eng. **24**, 111 (1968).
11. R. Gold, R. J. Armani and J. H. Roberts, *Absolute Fission Rate Measurements with Solid-State Track Recorders*, Nucl. Sci. Eng. **34**, 13 (1968).
12. R. Gwin et al., *Nuclear Physics Division Annual Report Ending May 1970*, ORNL-4592 (to be published).
13. M. G. Schomberg et al., *The Ratio of the Capture and Fission Cross Sections of Pu^{239} in the Energy Range 100 eV to 30 keV*, Proc. IAEA Second International Conference on Nuclear Data for Reactors, Helsinki, June 1970, Paper No. CN-26/33 (to be published).
14. F. L. Fillmore, *The CALHET-2 Heterogeneous Perturbation Theory Code and Application to ZPR-3-48*, AI-69-13 (March 1, 1969).

II-13. Experimental Results for ZPR-3 Assemblies 58 and 59

J. M. Stevenson,* J. M. Gasidlo and R. O. Vosburgh

Introduction

The essential purpose of these two assemblies was to study the discrepancy between calculated and measured central reactivity worths, and nearly all of the experiments had some bearing on this discrepancy. The assemblies were constructed with a single drawer cell containing two plutonium-aluminum fuel columns and fourteen graphite columns, thus forming a natural continuation of the series of benchmark physics assemblies (ZPR-3 Assemblies 48, 49, 50, 53 and 54). The core contained no uranium. Assembly 58 had a depleted uranium blanket while Assembly 59 had a lead reflector. The depleted uranium preserved the continuity of the series, and lead was chosen because of its small capture cross section and its lower moderating effect compared with possible alternatives, such as steel or graphite which would modify the spectrum in the core to a greater extent than lead.

Brief descriptions of the experiments carried out in these two assemblies—except the measurement of the central neutron spectrum using proton recoil counters (see Paper II-18)—are given here. Further details can be found in Ref. 1.

Description of the Assemblies

The standard core drawer loadings for Assembly 58 are shown in Fig. II-13-1. A back drawer contained the remaining 8 in. of axial reflector in Half 1. The drawers for control and safety rods had an inside width of 1.875 in. and differed from the standard drawer in that one graphite column in the core was omitted, leaving a symmetrical loading. The asymmetric loading on the reactor matrix was used because the lead blocks for the reflector in Assembly 59 were available only in 4-in. lengths. The critical loadings are given in Figs. II-13-2 and II-13-3. The half drawer in Assembly 59 was used to keep the excess reactivity below the maximum allowed. The numbers in the matrix positions refer to slightly different drawer loadings, but here only the

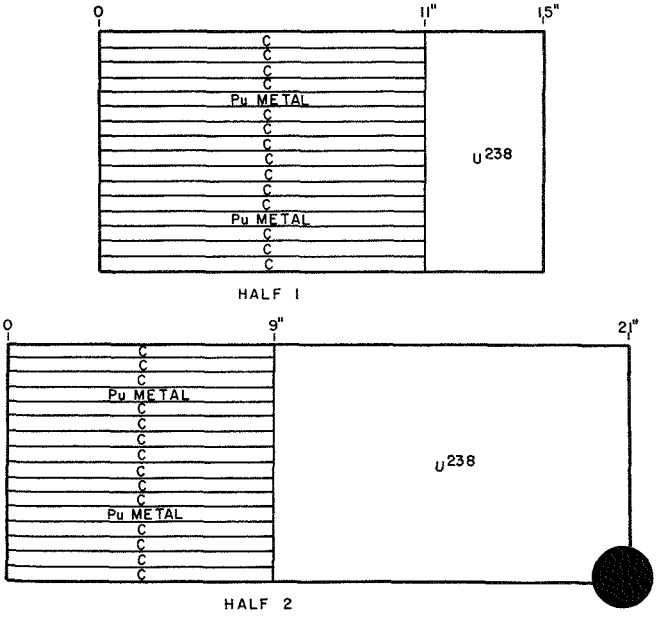

Fig. II-13-1. Core Drawer Loading for Assembly 58. *ANL-ID-103-2990.*

* UKAEA, Winfrith, England.

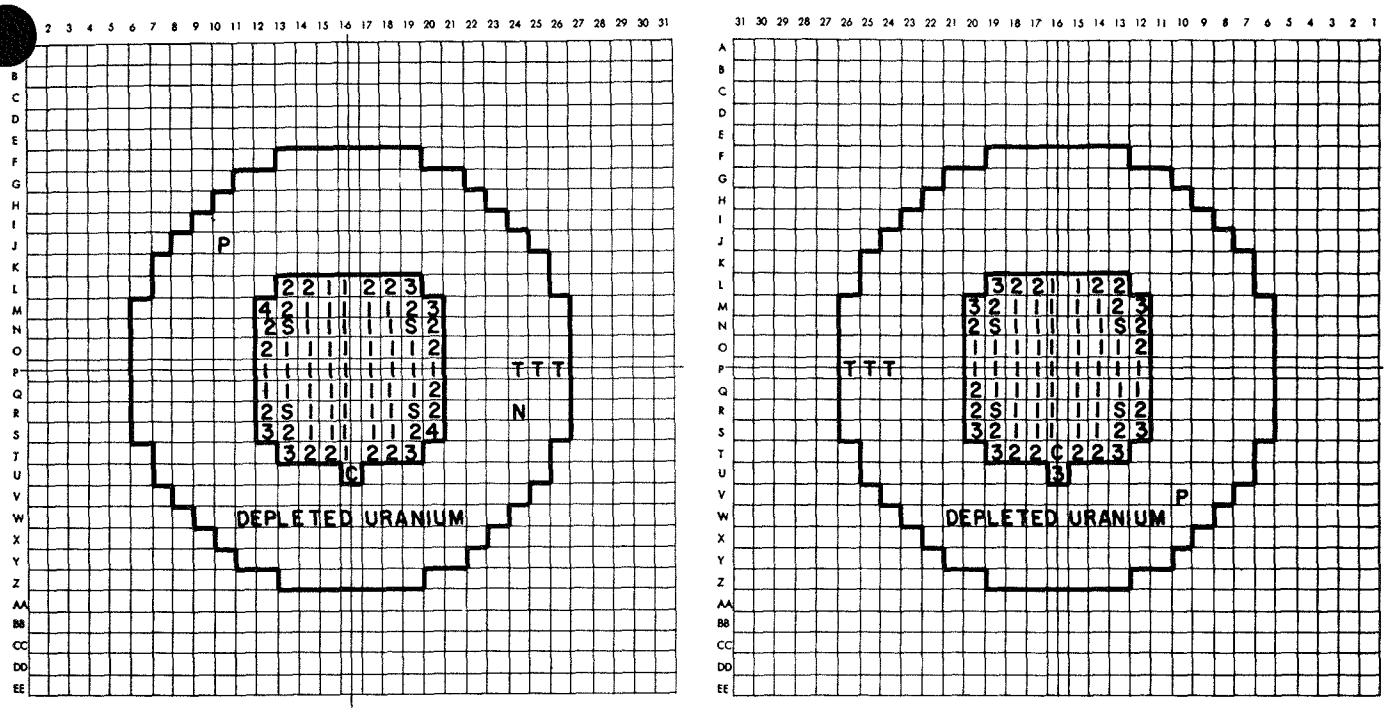

FIG. II-13-2. Reference Core Loading for Assembly 58. *ANL-ID-103-2988.*

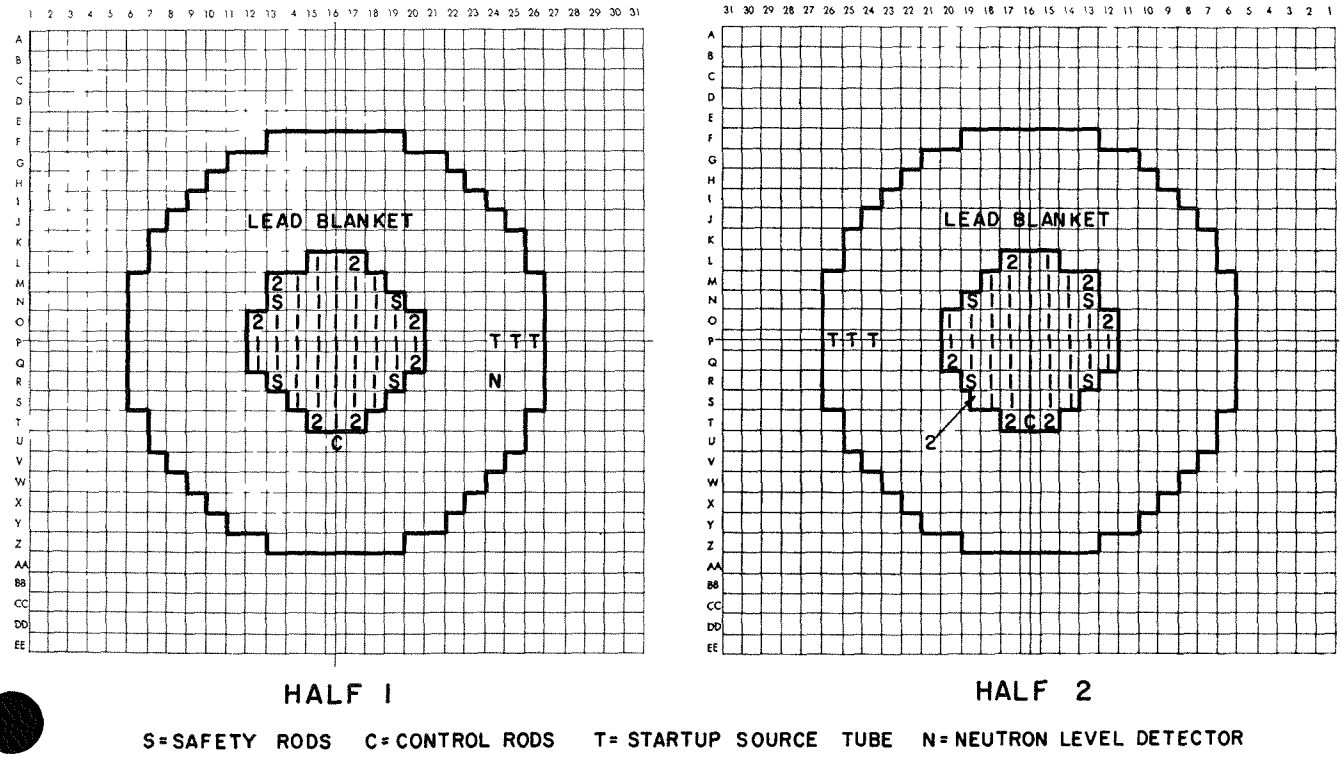

FIG. II-13-3. Reference Core Loading for Assembly 59. *ANL-ID-103-A2026.*

TABLE II-13-I. Average Core and Reflector Compositions of ZPR-3 Assembly 58

Isotope	Region Composition, 10^{21} atoms/cm^3		
	Core	Axial Reflector	Radial Reflector
Pu-239	2 1024	—	—
Pu-240	0.1001	—	—
Pu-241	0.0058	—	—
Al	0.213	—	—
C	59.07	—	—
Fe	7.689	5.593	4.540
Cr	1.912	1.391	1.129
Ni	0.928	0.609	0.494
Mn	0.0798	0.0581	0.0471
Si	0.0937	0.0682	0.0553
U-238	—	39.05	38.71
U-235	—	0.086	0.086

TABLE II-13-II. Average Core and Reflector Compositions of ZPR-3 Assembly 59

Isotope	Region Composition, 10^{21} atoms/cm^3		
	Core	Axial Reflector	Radial Reflector
Pu-239	2.1030	—	—
Pu-240	0.1003	—	—
Pu-241	0.0056	—	—
Al	0.217	—	—
C	59.02	—	—
Fe	7.717	5.593	4.540
Cr	1.919	1.391	1.129
Ni	0.875	0.609	0.494
Mn	0.0801	0.0581	0.0471
Si	0.0941	0.0682	0.0553
Pb	—	28.16	28.24

core average compositions together with the reflector average compositions are given (Tables II-13-I and II-13-II).

An equivalent cylindrical loading for Assembly 58 is shown in Fig. II-13-4. The equivalent cylindrical loading for Assembly 59 differed only in the core radius which was 23.83 cm. The fissile contents were 101.9 kg (Pu-239 + Pu-241) in Assembly 58 and 76.1 kg (Pu-239 + Pu-241) in Assembly 59. The control rod calibration curves showed that the excess reactivities of the loadings in Figs. II-13-2 and II-13-3 were 0.020% $\Delta k/k$ and 0.080% $\Delta k/k$, respectively. Examination of the final stages of the approaches to critical and use of the rod worth curves enabled these reactivities to be converted to equivalents of 0.07 kg and 0.22 kg of edge fuel respectively.

Fission Rate Distributions

Fission rate distributions were measured radially in Assembly 58 and both radially and axially in Assembly 59. Cylindrical counters containing Pu-239 (5% Pu-240) and U-238 (20 ppm U-235) with a coated length of 0.8125 in. were used. The axial traverse tube was inserted through drawers where the plates had been rotated and special small graphite pieces used to leave a 0.5 in. square hole as shown in Fig. II-13-5. For the radial traverses, the front two inches of all the Half 1 core drawers in row P were rotated and arranged in the same way. The results of the six traverses are seen in Figs. II-13-6 through II-13-11. Two points are worth noting:

a. The radial traverses in both assemblies show a marked fine structure. The Pu-239 fission rate was higher when the counter straddled two drawers, whereas the U-238 count rate was higher when the counter was centered on a drawer.

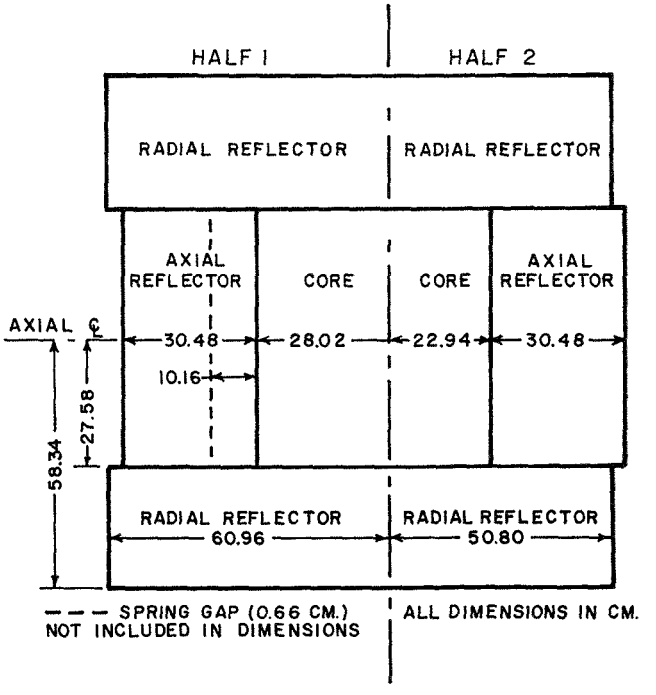

Fig. II-13-4. Equivalent Cylindrical Dimensions for Assembly 58. *ANL-ID-103-2989.*

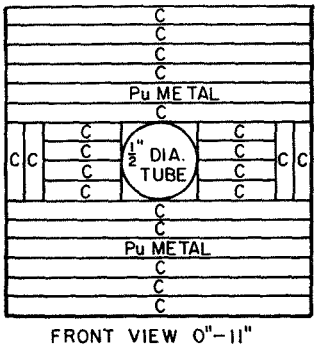

Fig. II-13-5. Axial Traverse Drawer Loading in Half 1 of Assembly 59. *ANL-ID-103-A2014.*

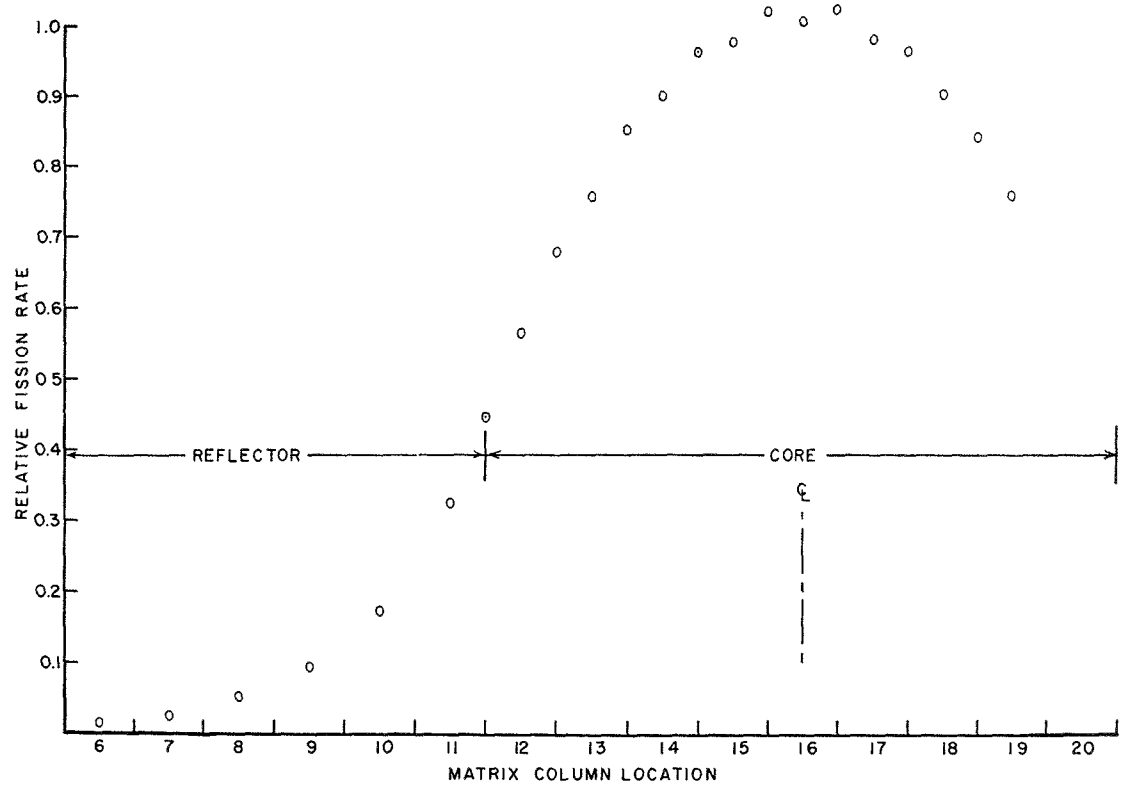

FIG. II-13-6. Pu-239 Fission-Rate Radial Traverse in Assembly 58. *ANL-ID-103-2994.*

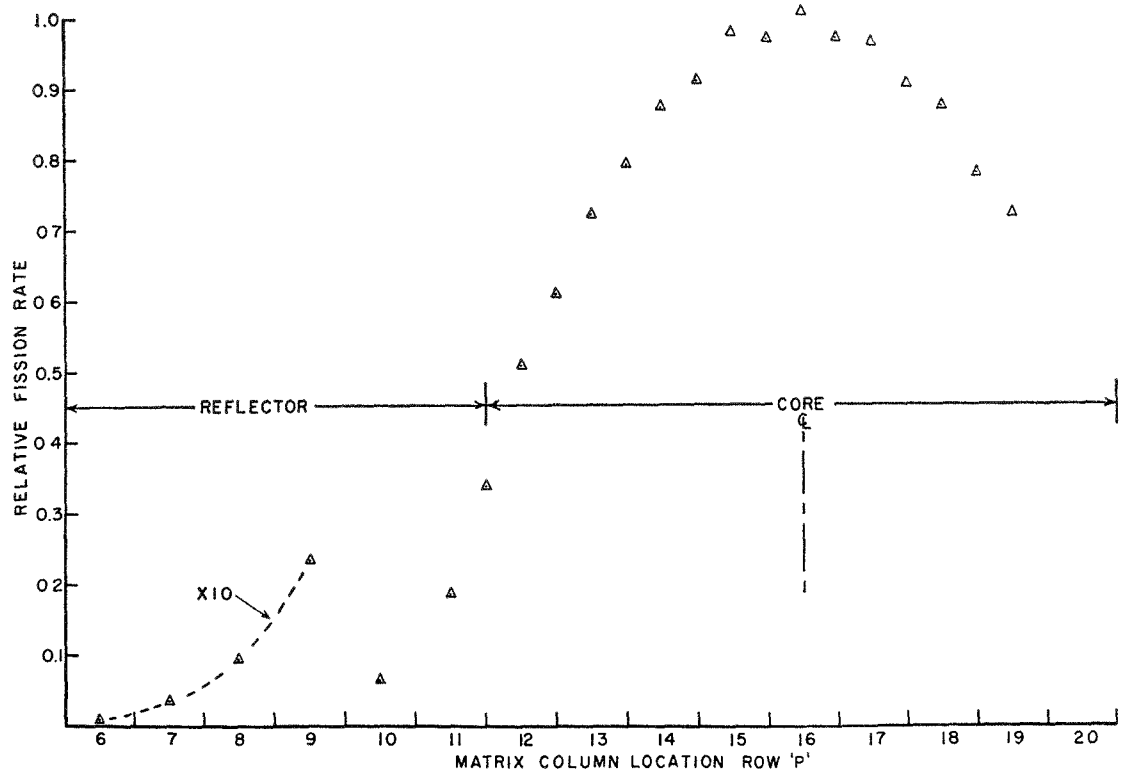

FIG. II-13-7. U-238 Fission-Rate Radial Traverse in Assembly 58. *ANL-ID-103-2993.*

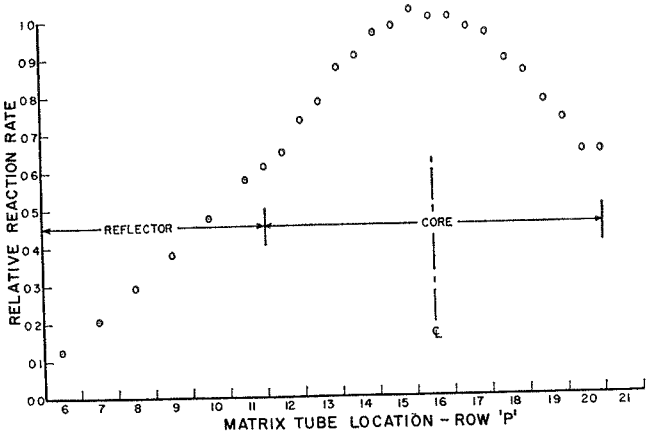

FIG. II-13-8. Pu-239 Fission-Rate Radial Traverse in Assembly 59. *ANL-ID-103-A2013*.

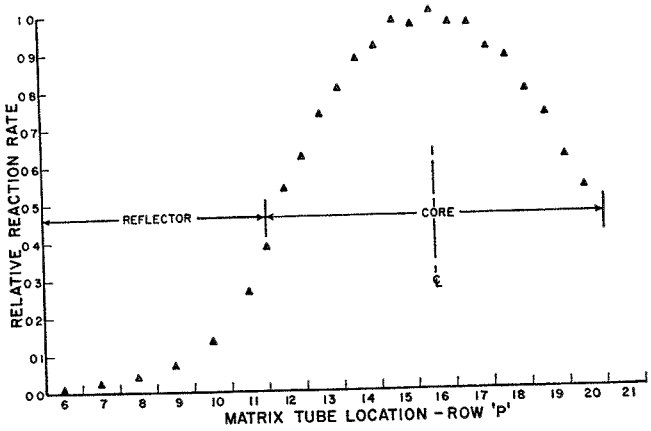

FIG. II-13-9. U-238 Fission-Rate Radial Traverse in Assembly 59. *ANL-ID-103-A2011*.

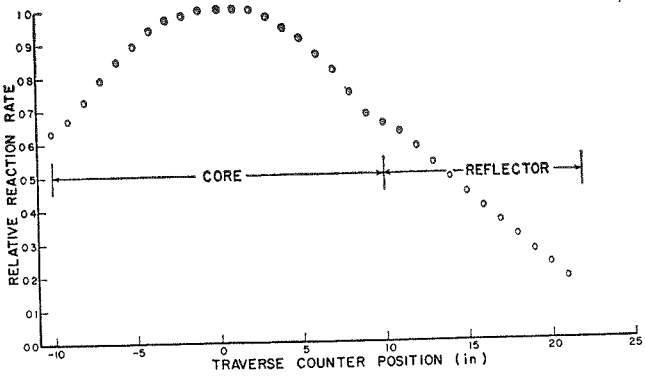

FIG. II-13-10. Pu-239 Fission-Rate Axial Traverse in Assembly 59. *ANL-ID-103-A2012*.

b. In Assembly 59, the Pu-239 radial traverse extended further than in Assembly 58. It extended to the core-radial reflector interface (P-20/21) where the count rate differed significantly from that at the equivalent position (P-11/12). This trend continued into the reflector and it was found that the results in positions P-21 and P-22 were a function of the autorod position. The count rate was several percent higher when the autorod polyethylene blade was almost fully inserted compared with the almost withdrawn position. Thus the discrepancy in the Pu-239 fission rate at

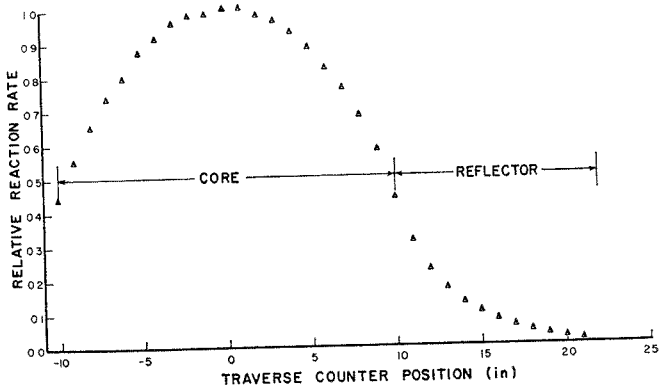

FIG. II-13-11. U-238 Fission-Rate Axial Traverse in Assembly 59. *ANL-ID-103-A2010*.

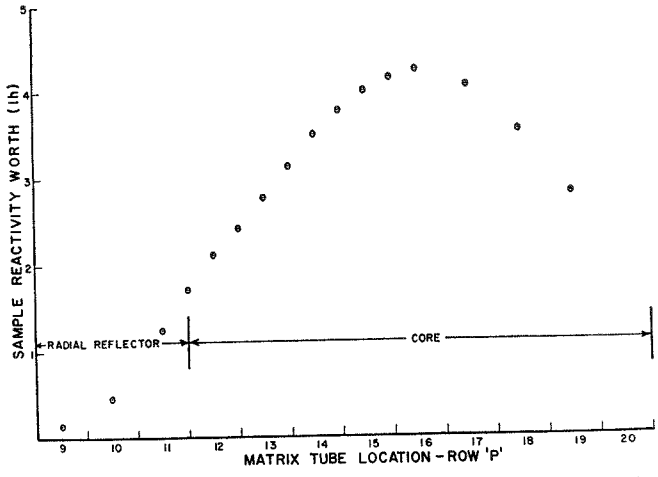

FIG. II-13-12. Pu-239 Perturbation Radial Traverse in Assembly 58. *ANL-ID-103-A2009*.

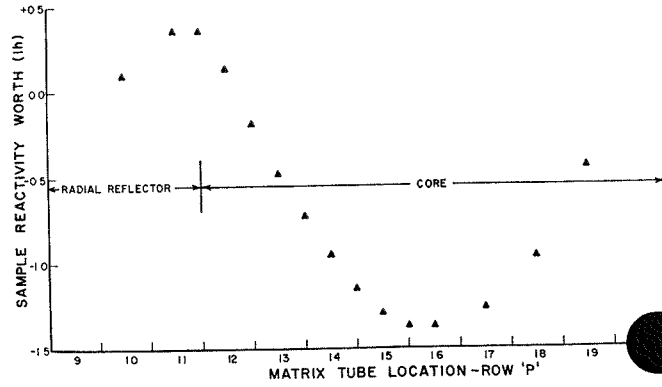

FIG. II-13-13. U-238 Perturbation Radial Traverse in Assembly 58. *ANL-ID-103-A2008*.

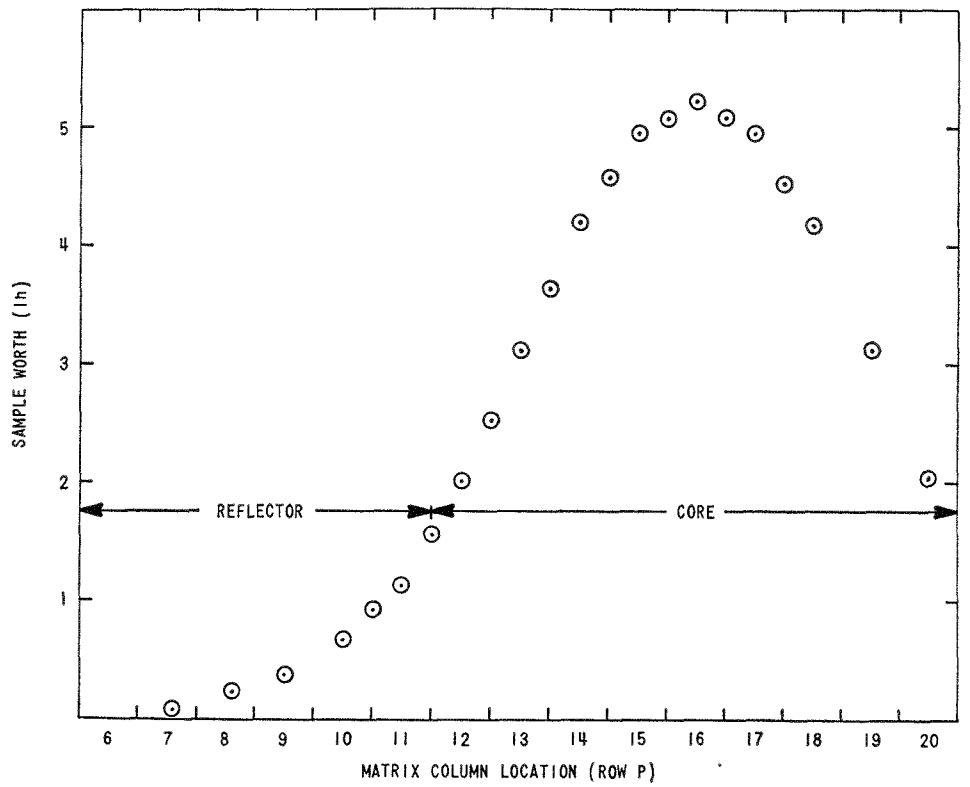

FIG. II-13-14. Pu-239 Perturbation Radial Traverse in Assembly 59. *ANL-ID-103-A2018.*

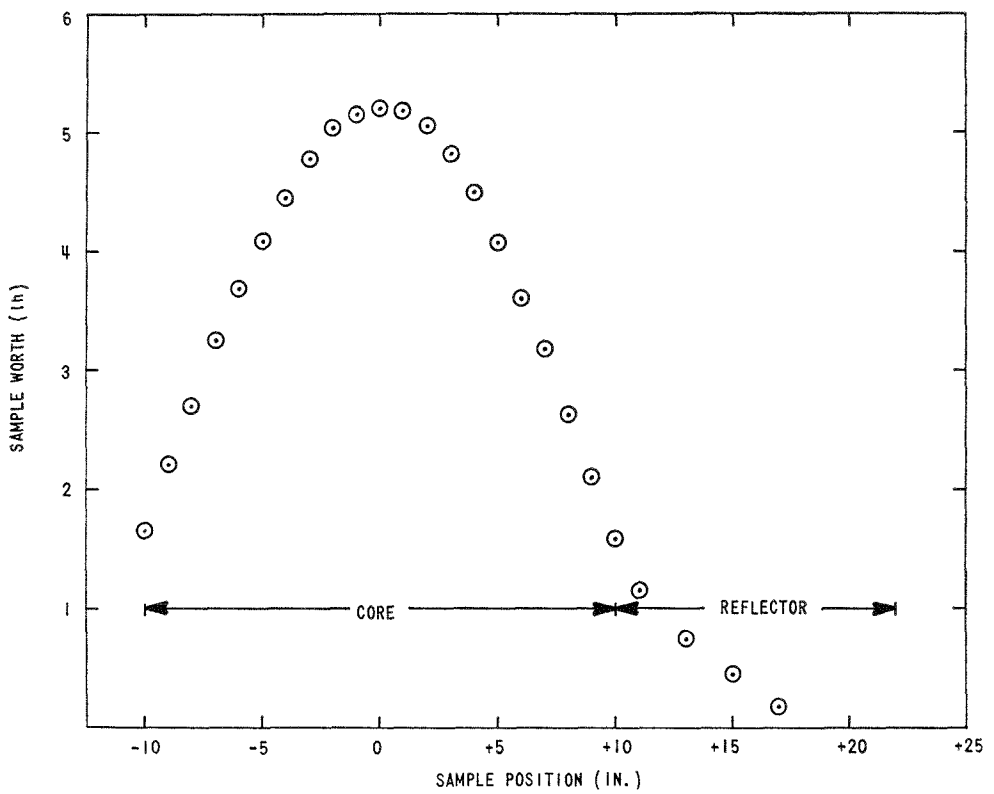

FIG. II-13-15. Pu-239 Perturbation Axial Traverse in Assembly 59. *ANL-ID-103-A2017.*

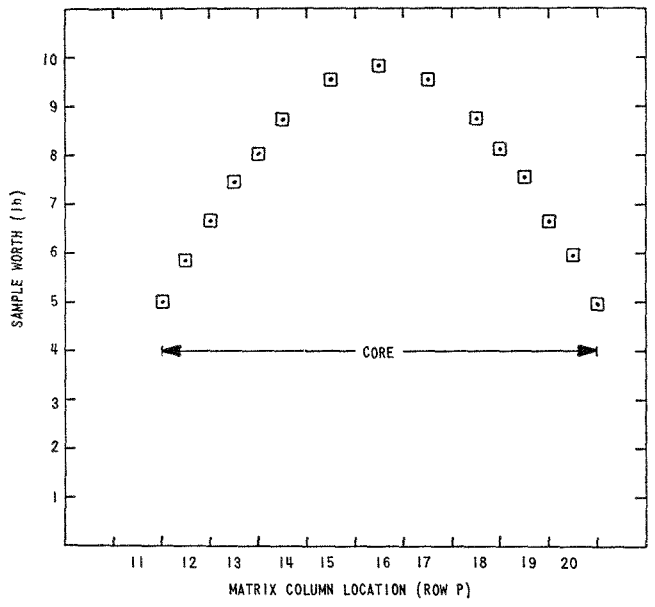

FIG. II-13-16. Cf-252 Source-Perturbation Radial Traverse in Asembly 59. *ANL-ID-103-A2020.*

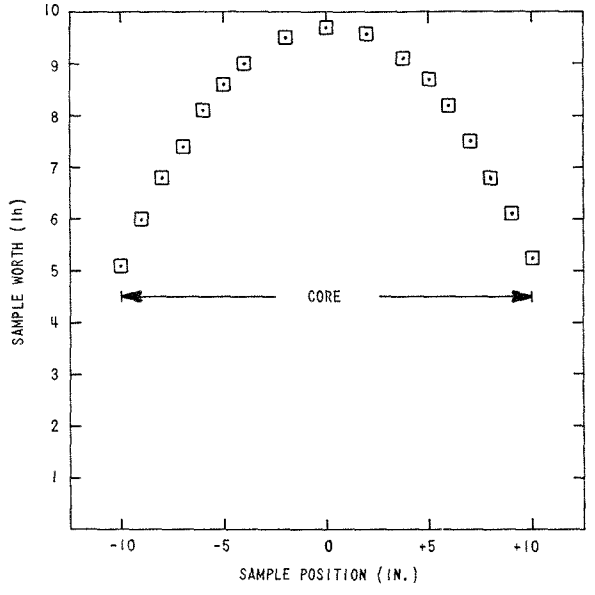

FIG. II-13-17. Cf-252 Source-Perturbation Axial Traverse in Assembly 59. *ANL-ID-103-A2019.*

position P-20/21 appears to be associated with the autorod in position O-22.

PERTURBATION DISTRIBUTIONS

The radial perturbation distributions of a Pu-239 annulus and a U-238 cylinder in Assembly 58 and the radial and axial perturbation distributions of the Pu-239 annulus in Assembly 59 were measured, all at a power level of about 10 W. The environments were the same as for the fission rate traverses. The results of the sample perturbation traverses are shown in Figs. II-13-12 through II-13-15. Because the samples are 2 in. long, almost the length of the horizontal unit cell, no significant fine structure is seen in the radial traverses.

In Assembly 59, radial and axial perturbation distributions with a Cf-252 source were measured as part of the determination of β_{eff} (see Paper II-27). The environment was the same as that for the sample perturbation traverses. Measurements were made at two power levels (50 and 8 W approximately) to separate the neutron source and material reactivity contributions. All the source worths in Figs. II-13-16 and II-13-17 correspond to a fission rate of 632.1 fissions/sec in a 108.9 μg foil (94.4 w/o Pu-239, 5.3 w/o Pu-240 and 0.3 w/o Pu-241) positioned 2 in. back from the interface in matrix position 2-P-16.

CENTRAL FISSION RATIOS

Thin walled aluminum, spherical back-to-back fission counters[2] were used in Assembly 59. The counters were positioned at the center of the cavity shown in Fig. II-13-18, in matrix position 1-P-16. Thus the foils (which were in a horizontal orientation) were extremely close to the core center. Each foil was paired

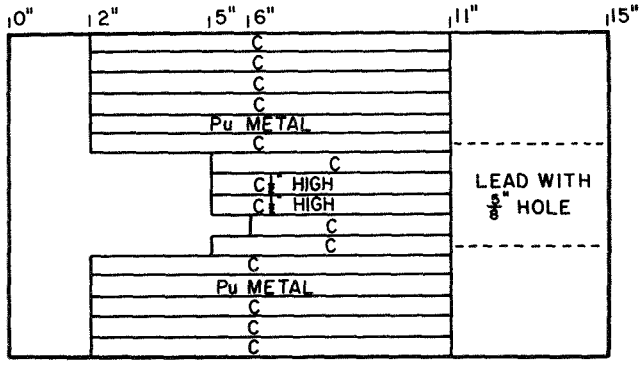

FIG. II-13-18. Core Drawer for Back-to-Back Fission Counter. *ANL-ID-103-A2006.*

TABLE II-13-III. CENTRAL FISSION RATIOS IN ZPR-3 ASSEMBLY 59

Ratio to U-235	Result	Error,[a] %
U-233	1.466	1.0
U-234	0.183	2.0
U-236	0.068	1.7
U-238	0.0325	1.8
Pu-239	0.942	1.0
Pu-240	0.207	1.0

[a] Error arises mostly from uncertainty in the calibration of foils. (Assumed error was ~1% for all foils except U-238 where error was ~1.5%.) The errors in some of the fission ratios are higher to allow for the significant fraction of fission in the U-235 present in the foils.

with a U-235 foil. The results are shown in Table II-13-III.

Central Perturbations

The small-cylinder sample changer (described in detail in Ref. 3) was used to measure the worth of series of samples against dummy cans or matched holders. A reactor power of about 10 W was used. The standard environment, used in both assemblies, was the same as that used for the radial traverses. A voided environment, seen in top view in Fig. II-13-19, was also used in Assembly 59. The three sets of results are given in Table II-13-IV. Ratios of results from Table II-13-IV are found in Table II-13-V. The ratio of perturbations

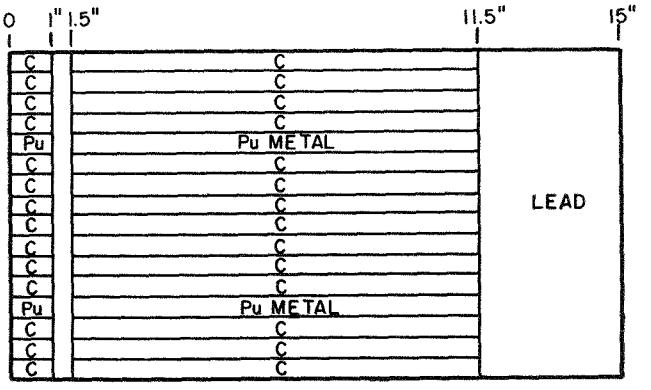

Fig. II-13-19. Half-Inch Voided Drawer for Central Perturbations. *ANL-ID-103-A2007.*

in the standard environment in the two assemblies (59/58) is a constant for the Pu-239, U-235, and B-10 samples. The ratios for the U-238 cylinders are somewhat less. The differences in Assembly 59 between the results for the standard environment, where the samples were in a graphite modified spectrum, and the

TABLE II-13-V. Central Perturbation Ratios in ZPR-3 Assemblies 58 and 59[a]

Sample	Assembly 59 Standard Environment / Assembly 58 Standard Environment	Assembly 59 Voided Environment / Assembly 59 Standard Environment
Pu-239 annulus 0.010 in	1.256 ± 0.004	0.932 ± 0.005
Pu-239 annulus 0.007 in.	1.248 ± 0.010	0.936 ± 0.009
U-235 annulus 0.010 in.	1.252 ± 0.006	0 938 ± 0.005
U-235 annulus 0.005 in.	1.251 ± 0.006	0.945 ± 0.009
U-235 annulus 0.003 in.	1.257 ± 0 012	—
U-238 cylinder 0.42 in. diam	1.118 ± 0.004	1 060 ± 0.004
U-238 cylinder 0.2 in. diam	1.139 ± 0.018	1.041 ± 0.017
U-238 cylinder 0.1 in. diam	1.180 ± 0.044	1.043 ± 0.049
B-10 cylinder 0.06 in. diam	1.240 ± 0.005	0.989 ± 0.005
C cylinder 0.4 in. diam	—	0.957 ± 0.012
Ta annulus 0.003 in.	—	0.985 ± 0.011

[a] The errors quoted are standard errors calculated from the spread of the perturbation measurements. In comparing the standard environments in the two assemblies, systematic uncertainties of 1% from the autorod calibration in each assembly must be added.

TABLE II-13-IV. Central Perturbation Results in ZPR-3 Assemblies 58 and 59

Sample[b,c]	Mass, g	Sample Worth, Ih/kg[a]		
		Assembly 58 Standard Environment	Assembly 59 Standard Environment	Assembly 59 Voided Environment
Pu-239 annulus 0.010 in.	4.801	875.7 ± 1.7	1100 ± 3	1025 ± 4
Pu-239 annulus 0.007 in.	2.761	862.0 ± 2.9	1076 ± 7	1007 ± 5
U-235 annulus 0.010 in.	7.128	566.4 ± 1.6	709.0 ± 2.8	665.0 ± 2.2
U-235 annulus 0.005 in.	3.638	552.4 ± 1.1	691.0 ± 3.6	653.1 ± 5.5
U-235 annulus 0.003 in.	2.327	554.0 ± 3.4	696.6 ± 4.6	—
U-238 cylinder 0.42 in. diam	85.76	−54.8 ± 0.1	−61.3 ± 0.2	−65.0 ± 0.2
U-238 cylinder 0.20 in. diam	19.63	−72.0 ± 0.5	−82.0 ± 1.3	−85.4 ± 0.7
U-238 cylinder 0.10 in. diam	4.908	−88.3 ± 2.0	−104.1 ± 2.9	−108.6 ± 4.3
B-10 cylinder 0.06 in. diam	0.0988	−39710 ± 110	−49230 ± 180	−48710 ± 190
C cylinder 0.4 in. diam	6.910	—	333.4 ± 3.2	319.2 ± 1.9
Pb cylinder 0.4 in. diam	51.36	—	—	6.9 ± 0.3
SS cylinder 0.4 in. diam	35.90	—	—	4.9 ± 0.6
Ta annulus 0.005 in.	3.300	—	—	−1205 ± 5
Ta annulus 0.003 in.	1.888	—	−1322 ± 13	−1302 ± 6
Ta annulus 0.002 in.	1.317	—	—	−1374 ± 8

[a] Errors quoted are standard errors calculated from spread of inhour determinations. Not included are errors in sample masses.
[b] All samples are 2 in. long. The annuli have outside diameters of approximately 0.40 in.
[c] Sample compositions—Pu-239: 98.78 w/o Pu; 95.05 w/o Pu-239; 4.50 w/o Pu-240; 0.45 w/o Pu-241—U-235: 0.010 in. annulus 93.20 w/o U-235; others 93.10 w/o U-235—U-238: 0.21 w/o U-235—B-10: 92.8 w/o boron; 92.1 w/o B-10 in boron—others: no significant contaminants.

TABLE II-13-VI. CENTRAL SUBSTITUTION EXPERIMENTS IN ASSEMBLY 59

Substitution (in 1-P-16)	Changes in Mass, g	Reactivity, Ih
Remove one 2 × 1 × 1/8 Pu plate and seven 2 × 1 × 1/8 in. C plates (i.e., front one inch of half a drawer)	Pu-239 −30.64 Pu-240 −1.43 Pu-241 −0.08 Al −0.37 Steel −9.37 Ni −1.2 C −40.406	−46.3 ± 2.0
Replace front 2 inches of central column of graphite by 2 × 2 × 1/8 in. B-10 plate (i.e., midway between fuel plates)	B-10 +3.1 B-11 (+impurities) +0.5 Steel +33.3 C −13.1	−144.7 ± 2.0
Replace front 2 inches of central column of graphite by four 1 × 1 × 1/8 in. U-235 plates	U-235 +133.77 U-238 +9.67 C −13.1	103.4 ± 2.0
Replace front 2 inches of central column of graphite by 2 × 2 × 1/8 in. Pu plates	Pu-239 +65.72 Pu-240 +3.18 Pu-241 +0.18 Al +0.76 Steel +16.77 C −13.1	77.7 ± 2.0
Replace two front 2 × 2 × 1/8 in. Pu-239 plates by four 2 × 1 × 1/8 in. Pu-239 plates (using boxes)	Pu-239 −9.05 Pu-240 −0.44 Pu-241 −0.01 Al −0.07 Steel +1.54 C +0.08	−10.0 ± 0.2

Note: For discussion of errors see text.

voided environment, where the samples were in an approximate cell average spectrum, demonstrate the perturbation uncertainties associated with the sample environment chosen.

CENTRAL SUBSTITUTION MEASUREMENTS

A series of alterations to the front of the core drawer in position 1-P-16 in Assembly 59 were made. The reactor was shut down for each alteration. The changes in reactivity were determined from the balance positions of control rod 5. Temperature readings on ten thermocouples attached to the reactor matrix were taken at each balance. Reference loadings (with the plate arrangement in the core drawer chosen to make the substitution simple) were repeated before and after each substitution experiment, and the change in the average temperature allowed a temperature coefficient to be obtained to correct all the results for drifts. The actual substitutions and the reactivity changes are detailed in Table II-13-VI. For the last substitution experiment, (the replacement of two 2-in. fuel plates by four 1-in. fuel plates), the front 2 in. of each set of core material was loaded into small 2-in. cube boxes to prevent movement of the rest of the contents of matrix position 1-P-16, (loaded in a standard 21-in. drawer). The two boxes were interchanged for the measurement. The small differences in the graphite plate and steel box masses, as well as the fuel plate mass changes, are included in the table.

The errors quoted in Table II-13-VI arise from estimates of the uncertainties in the temperature corrections, the effect of opening and closing the reactor halves, and in the repositioning of the drawers. Whereas the other perturbed measurements were made only once, the boxes were interchanged several times (and only the front 2 in. were moved), hence the significantly reduced error for the last measurement. The uncertainty in the autorod calibration (~1%) is not included.

DOPPLER REACTIVITY EFFECT— NATURAL URANIUM OXIDE

The temperature coefficient of reactivity for a single 6 in. natural UO_2 sample was measured at the center of Assembly 59. The rod traverse mechanism has been described elsewhere.[4] The annular sample has an inner radius of 0.16 cm and an outer radius of 0.63 cm. The mass of UO_2 is 137.2 g. The drawer through which the traverse mechanism passed is shown in Fig. II-13-20.

The total worth of the single sample was −9.34 ± 0.09 Ih at cell temperature. Measurements were made at a power of about 10 W with the sample at 300, 500, 800 and 1100°K approximately. The results (without corrections for expansion effects) are given in Table II-13-VII.

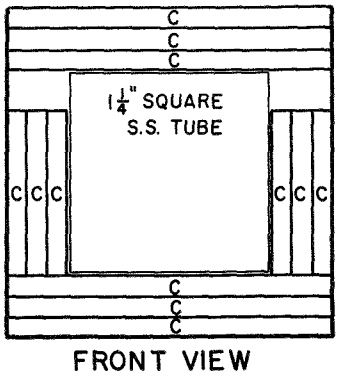

FIG. II-13-20. Core Drawer for Doppler Sample in Assembly 59. *ANL-ID-103-A2016.*

[redacted]LE II-13-VII. Reactivity Changes of Natural UO_2 Sample

Temperature, °K	Reactivity Change,[a] Ih
295	0
500	−0.994 ± 0.014
800	−1.980 ± 0.010
1099	−2.765 ± 0.007

[a] Errors quoted are standard errors calculated from the spread of the perturbation measurements only.

Summary

Measurements of several parameters have been made in the last two of the series of the benchmark physics assemblies in ZPR-3. Most of these have relevance to the central perturbation worth discrepancy. Only a comparison between the experimental results and a detailed calculational analysis will show whether the study has proved successful in isolating any reasons for this discrepancy.

References

1. J. M. Stevenson, J. M. Gasidlo, G. G. Simons and R. O. Vosburgh, *Experimental Results for ZPR-3 Assemblies 58 and 59*, ANL-7695 (1970).
2. W. G. Davey and P. I. Amundson, *Inelastic Scattering Measurements in a Fast Reactor by the Spherical Shell Method*, Nucl. Sci. Eng. **28**, 111 (April 1967).
3. A. L. Hess, Q. L. Baird and A. M. Broomfield, *Material Worth Measurements in ZPR-3 Assemblies 48, 48A and 48B*, ZPR-TM-7 (1969).
4. J. M. Gasidlo, A. M. Broomfield, R. L. McVean, W. P. Keeney and A. L. Hess, *Doppler Effect, Heterogeneity and Sodium-Voiding Experiments in ZPR-3 Assemblies 48 and 48B*, ZPR-TM-8 (1969).

II-14. The EBR-II Critical Assemblies—ZPR-3 Assemblies 60, 61, and 62

W. P. Keeney, R. O. Vosburgh, J. M. Gasidlo and D. Meneghetti*

Introduction

ZPR-3 Assemblies 60, 61, and 62 were a set of critical assemblies having cores whose compositions approximate an homogenization of representative subassembly types encountered in the EBR-II core loadings. Assembly 60 had a radial blanket, approximating in composition the current EBR-II blanket which is rich in depleted-uranium. Assemblies 61 and 62 had the internal half of this blanket replaced by a nickel-rich and by a steel-rich reflector, respectively.

Using the three types of reflectors, these homogeneous-core assemblies were constructed to obtain intercomparison experimental data on the critical masses, spatial-dependence of spectra, activation of dosimetry foils, and fission rate variations. These data, coupled with calculational analyses, will enable a more confident prediction of the effects of a nickel or a steel reflector contemplated for use in the EBR-II system.

Description of Assemblies

All three assemblies were constructed with a single ZPR-3 matrix element comprising a unit cell. The initial composition of Assembly 60, Table II-14-I, was designed to simulate a typical homogenized 91 element [redacted]R-II loading with U-235 replacing the Pu-239 in [redacted]e critical assembly. The Assembly 60 core-radial blanket boundary was quasi-hexagonal with a radial depleted uranium blanket similar to that of EBR-II. The top and bottom axial reflectors were asymmetric, each consisting of two regions representing a sodium-rich gap and a stainless steel-rich reflector. These axial regions were retained in all three assemblies. The compositions of the reflector and blanket regions are listed in Table II-14-II.

Assembly 61 consisted of three loadings. In the first

TABLE II-14-I. Average Core Compositions of ZPR-3 Assemblies 60, 61, and 62, atoms/cm³[a]

Element	Assembly 60 and 61[b]	Assembly 61 Final Step and Assembly 62	Control/Safety Rods
U-235	0.005594	0.005080	[c]
U-238	0.004570	0.005053	[c]
Na	0.01033	0.01033	0.01033
Fe	0.01337	0.01337	0.01462
Cr	0.00343	0.00343	0.00364
Ni	0.00149	0.00149	0.00159
Mn	0.000172	0.000172	0.000152
Si	0.00013	0.00013	0.00017
O	0.002135	0.002135	0.002135

[a] Represents weighted core average not including control and safety rods.

[b] Assembly 61, first and second step.

[c] The weighted average of the U-235 and U-238 content is identical to that of the average for each assembly.

* EBR-II Project, Argonne National Laboratory.

TABLE II-14-II. Reflector and Blanket Compositions of ZPR-3 Assemblies 60, 61, and 62, 10^{24} atoms/cm^3

Element	(R1) Upper Gap	(R2) Upper Reflector[a]	(R3) Lower Gap	(R4) Lower Reflector[a]	(R5) Ni Reflector	(R6) SS Reflector	(R7) Radial Blanket, Half 1[a]	(R7) Radial Blanket, Half 2[a]
U-235	—	—	—	—	—	—	0.000055	0.000054
U-238	—	—	—	—	—	—	0.026505	0.026548
Na	0.01480	0.01029	0.01199	0.00898	0.00205	0.00203	0.00457	0.00455
Fe	0.01844	0.02802	0.02332	0.03175	0.00662	0.04982	0.00964	0.00963
Cr	0.00480	0.00762	0.00622	0.00881	0.00164	0.01337	0.00254	0.00253
Ni	0.00209	0.00331	0.00271	0.00382	0.06615	0.00581	0.00111	0.00110
Mn	0.000260	0.000501	0.000379	0.000626	0.000216	0.000835	0.000146	0.000145
Si	0.00015	0.00012	0.00014	0.00007	0.000135	0.000265	0.00007	0.00007
Mo	0.00001	0.00003	0.00002	0.00004	—	—	—	—
C	—	—	—	—	0.000225	—	—	—

[a] Spring gap (0.66 cm wide) is located 21.03 in. from the interface in Half 1 and the core region of Half 2 and is 15.03 in. from the interface in the radial blanket of Half 2. Its composition is (10^{24} atoms/cm^3): Fe 0.01685, Cr 0.00419, Ni 0.00184, Mn 0.000175, Si 0.00020. This composition includes the spring, the back of the front drawer, and the front of the back drawer.

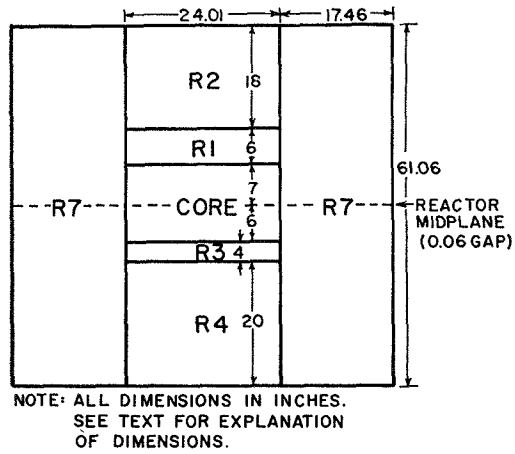

Fig. II-14-1. Assembly 60, Horizontal Section. *ANL-ID-103-A2023.*

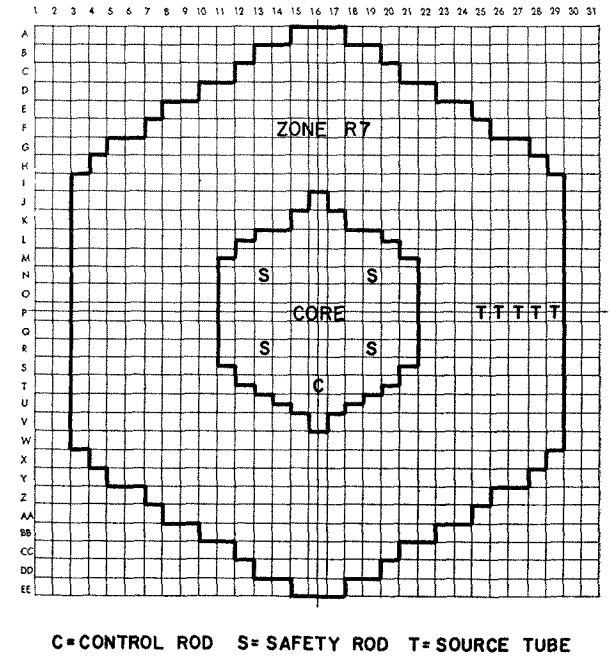

Fig. II-14-2. Reference Loading, Assembly 60. *ANL-ID-103-A2022.*

step a nickel-rich reflector region, nominally two matrix elements thick, replaced the depleted uranium radial blanket adjacent to the core of Assembly 60. The nickel-rich reflector, R5 of Table II-14-II, was the height of the core, and a stainless steel-rich region, R6 of Table II-14-II, was loaded axially above and below the nickel region to complete the full assembly height. In the second step of Assembly 61, the nickel-rich region was expanded to a radial thickness of four matrix elements. The final loading of Assembly 61 (Table II-14-I) was an adjustment of the U-235 concentration of the core to produce an assembly closer to that of EBR-II.

In Assembly 62 the modified core composition was retained and a full-height stainless steel-rich inner radial reflector, R6, was added to a fully depleted uranium blanketed core in two steps.

Figure II-14-1 is a horizontal section of Assembly 60 showing the zone dimensions. All radial dimensions are in inches across the flats of the quasi-hexagon. The interface views of the critical loadings for the reference cores of each assembly are shown in Figs. II-14-2 through II-14-7 and the physical data for each assembly is listed in Table II-14-III.

Experimental Program

The experimental program for Assembly 60 inclu an extensive set of radial and axial reaction rate traverses with counters. The axial traverses, in addition

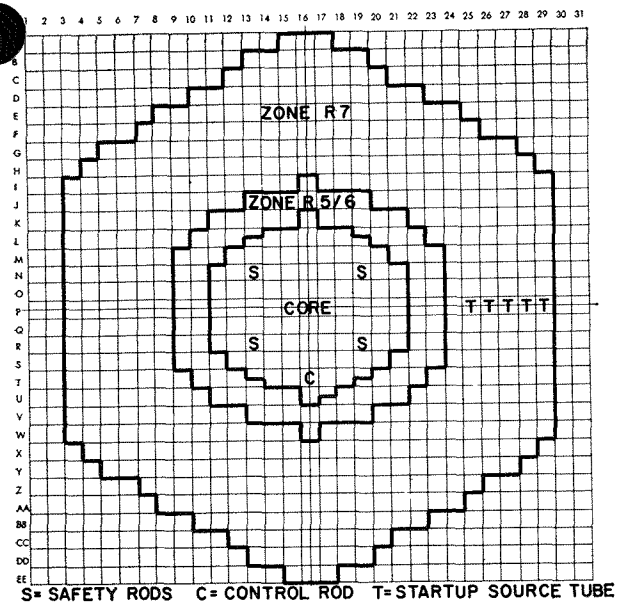

FIG. II-14-3. Reference Loading, Assembly 61, First Step. *ANL-ID-103-A2039.*

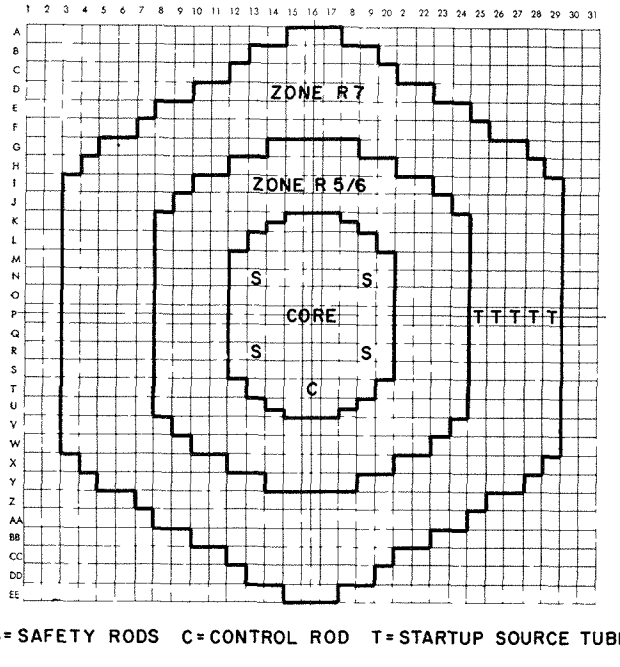

FIG II-14-4 Reference Loading, Assembly 61, Second Step. *ANL-ID-103-A2062.*

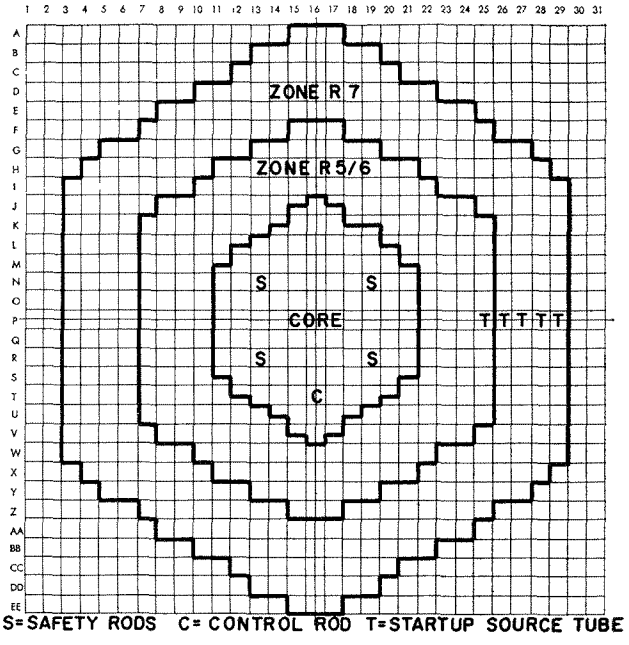

FIG. II-14-5. Reference Loading, Assembly 61, Final Step. *ANL-ID-103-A11400.*

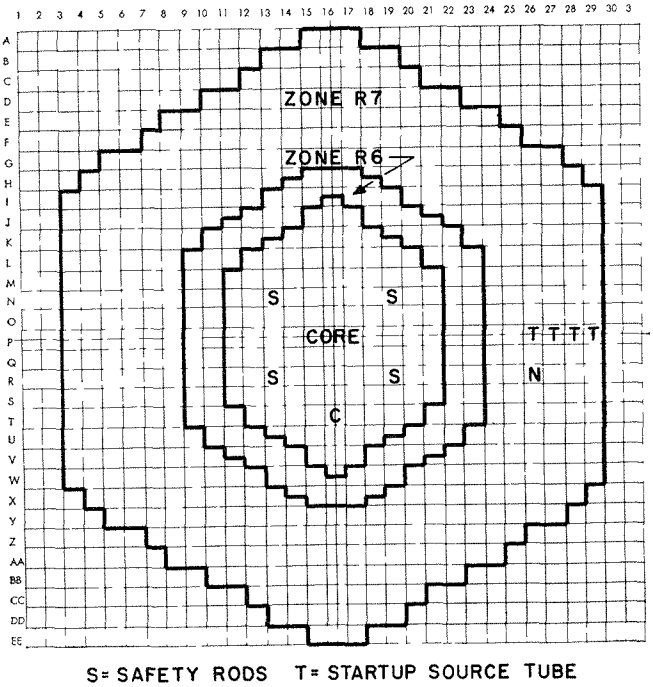

FIG. II-14-6. Reference Loading, Assembly 62, First Step. *ANL-ID-103-A2108 Modified.*

to being done along the flat of the core, included the effect on the central traverses of modifications of the composition of the top central axial reflector from R2 to R1 composition. Irradiations of thermoluminescent gamma detectors and foils throughout the core and blanket were done to determine the gamma energy deposition and reaction rates. The foil reaction rates, in addition to proton recoil neutron spectrum measurements at the core center, core edge, and in the axial blanket, were measured to verify neutron distribution calculations of the EBR-II Project. The experiments of Assembly 61 included these experiments as well as

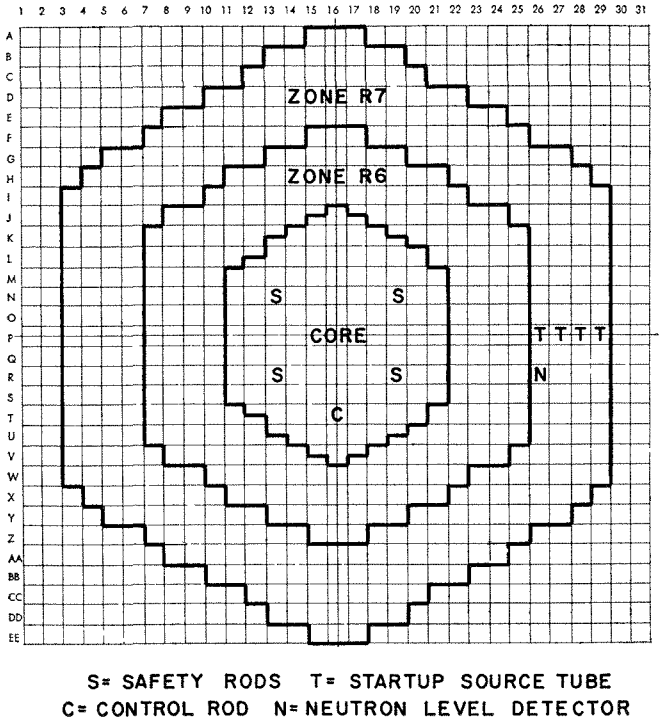

FIG. II-14-7. Reference Loading, Assembly 62, Final Step. *ANL-ID-103-A2109 Modified.*

TABLE II-14-III. PHYSICAL DATA FOR ZPR-3 ASSEMBLIES 60, 61 AND 62

Assembly	Critical Data		Neutronic Parameters	
	U-235 Loading, kg	Available k_{ex}, $\%\Delta k/k$	β_{eff}, 10^{-3}	Ih/$\%\Delta k/k$
60	221.93	+0.187	7.04	434.0
61 first step	194.29	+0.259	6.89	433.5
61 second step	188.63	+0.258	6.89	433.5
61 final step	208.58	+0.110	6.94	433.5
62 first step	229.63	+0.142	6.96	433.0
62 final step	221.61	+0.146	6.96	433.0

radial traverses in the intermediate transition steps between assemblies. Assembly 62 will repeat the experiments of Assembly 61 plus a set of core edge and central simulated boron control rod studies. This assembly program also includes tantalum core edge worth measurements as a function of axial position and sample size to assist in the analysis of design calculations for an EBR-II drop rod.

The detailed experimental measurement for Assemblies 60 and 61 have been reported in the Reactor Development Program Progress Reports, January through June, 1970.

II-15. Critical Mass Evaluation in ZPPR Assembly 2, a Demonstration Reactor Benchmark Assembly

R. E. KAISER and R. J. NORRIS

INTRODUCTION

ZPPR Assembly 2 is a benchmark core which reproduces many of the essentials of current demonstration reactor concepts. The reactor configuration and experimental program are based on the current needs of industry for information applicable to the design of 300–500 MW demonstration plants. The central zone of the two-zone system matches in composition both the standard rodded zone experiments and the Variable Temperature Rodded Zone (VTRZ) experiments designed for Argonne reactors.

Assembly 2 was conceived as a two-zone core with an enrichment ratio (outer zone/inner zone) of 1.5 and equal zone volumes. Since the preliminary calculations of critical mass, on which the initial loadings were based, were not exact, the initial critical configuration did not have equal zone volumes but instead had a volume ratio of 52/48 (inner zone/outer zone). Reactivity calibrations and edge worth measurements were performed, in sufficient number to allow evaluation of the critical mass of this configuration, and the zone volumes were then adjusted to a 50/50 proportion, and the full experimental program was begun. Both the initial critical (52/48) and the equal-zone (50/50) configurations are described in this report.

ASSEMBLY DESCRIPTION

ZPPR Assembly 2 was designed to have an approximate core composition of 32% oxide fuel equivalent, 40% sodium, 19% steel, and 9% void. The inner core was built with a one-drawer cell and the outer core with a two-drawer cell, as shown in Fig. II-15-1, where the Type A drawer contains two fuel columns and the Type B drawer contains one fuel column. Loading pat

for the radial and axial blanket drawers are also shown.

INITIAL CRITICAL CORE

The actual configuration of the initial critical 52/48 version of the assembly is shown in the interface diagram for half one, Fig. II-15-2. Locations of B_4C poison safety blades and fueled control rods are shown along with the general reactor configuration. The radial reflector consisted of AISI C1018 mild steel (99.25% Fe) block placed directly into the matrix tubes. The axial reflectors are different, primarily due to material considerations. Half one, where the counter traverses and reactivity traverses will be performed, has an 8-in. reflector that is half sodium and half steel. The reflector behind half two is 5 in. thick and is all mild steel. Atom densities for the 52/48 configuration are given in Table II-15-I, and cylindrical dimensions of the as-built core are shown in Figs. II-15-3 and II-15-4.

EQUAL-ZONE CORE

The equal zone (50/50) version of the assembly was identical to the 52/48 version except that some inner core drawers were exchanged for outer core drawers to equalize the volumes. This resulted in a significant reduction of the critical mass, since the outer zone was more highly enriched. The interface diagram for the 50/50 core is shown in Fig. II-15-5, and the cylindrical dimensions of the as-built core in Figs. II-15-6 and II-15-7. Both versions had two spiked control rods to insure sufficient control margin, and these are included in the table of atom densities, Table II-15-II.

The calculations of atom densities included the stainless steel drawer fronts, making the core half-height 18.035 in., the extra 35 mils representing the thickness of the drawer fronts. The axial dimensions given in the figures reflect this consideration.

Three different references were obtained for the 50/50 core: (1) the original 50/50 version, (2) a modified 50/50 version with a slightly higher sodium atom density in the inner core, and (3) a 50/50 version without spiked control rods which was built after installation of a shim-control rod system in August 1970.

The increase in sodium atom densities between the first and second references was accomplished by replacing pairs of quarter-inch plates with single half-inch plates, which was necessary to provide a better match with the pin-calandria compositions. The switch also caused a slight reduction in steel density, which was compensated for by adding a 304 SS shim at the bottom of each drawer. The extra 1/2 in. sodium was obtained from the radial reflector, which then had two

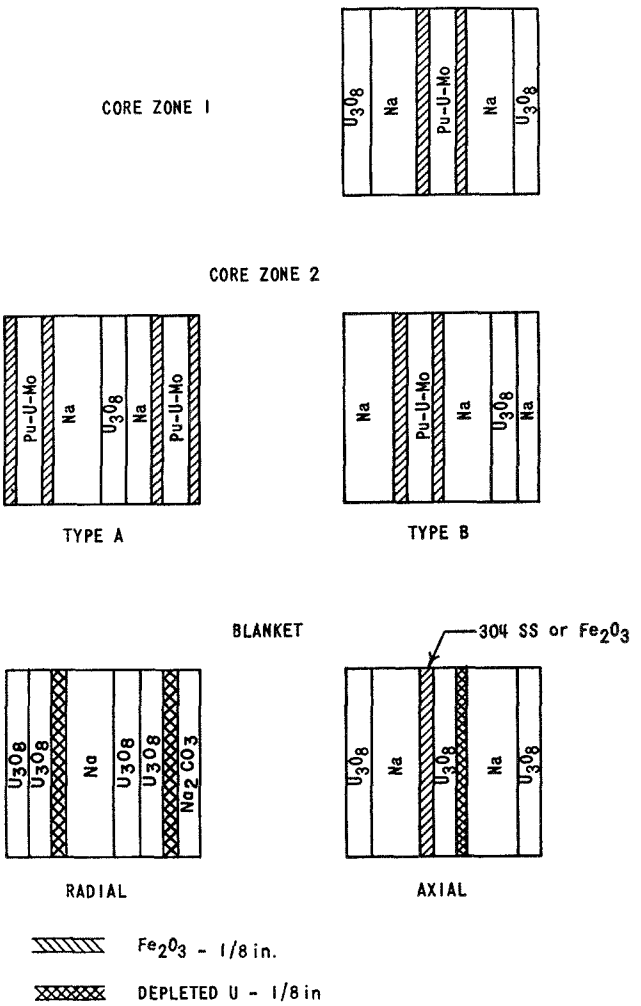

FIG. II-15-1. ZPPR Assembly 2 Drawer Configurations. *ANL-ID-103-A11278 Rev. 1.*

zones, with small differences in steel and sodium content between them. The atom densities of the two zones and the average over the whole reflector are given in Table II-15-II.

The third reference configuration for the 50/50 core differed from the second only in the absence of the spiked control drawers. Three of the B_4C blades which had previously been designated as poison safety rods now served as shim-control rods, which has no effect on the critical mass. The as-built number densities given in Table II-15-II are not applicable to the third 50/50 reference. Instead, the values without spiked rods should be used.

CRITICAL MASS CORRECTIONS

In order to state a critical mass for a smooth cylindrical core of uniform (though not necessarily homogeneous) composition, certain corrections must be made

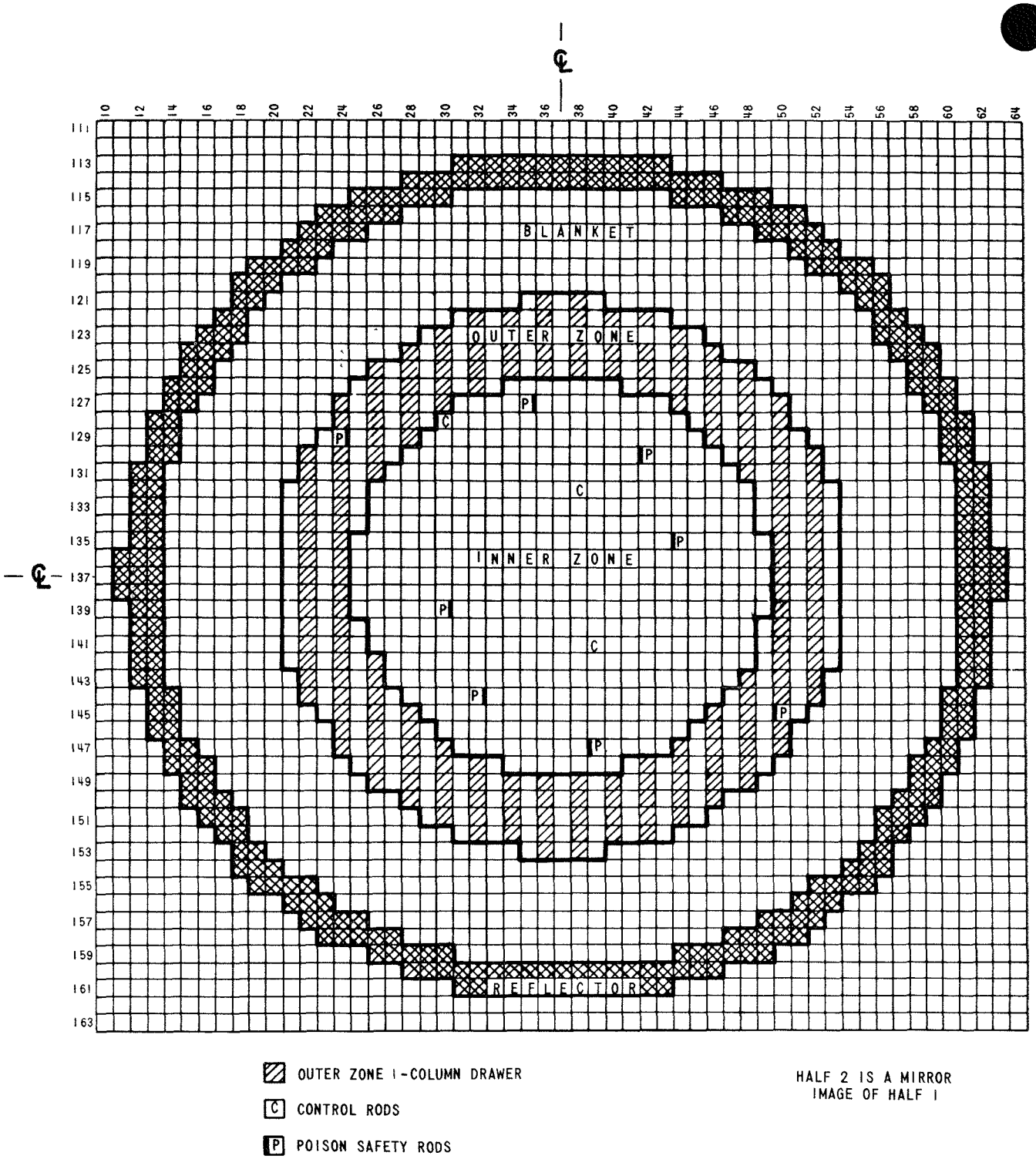

FIG. II-15-2. ZPPR Assembly 2—Reference Loading for Initial Critical Configuration. *ANL-ID-103-A11548.*

to the as-built critical mass. These corrections include allowances for temperature, interface gap, excess reactivity, spiked control rods and smoothing of the core outline.

EDGE SMOOTHING CORRECTIONS

Edge smoothing corrections were determined using calculated values of Pu-239 worth versus radius normalized to the edge drawer worths at the outer radial

TABLE II-15-I. AS-BUILT ATOM DENSITIES FOR THE INITIAL-CRITICAL CORE OF ZPPR ASSEMBLY 2, 10^{24} atoms/cm^3

Isotope	Inner Core	Outer Core	Axial Blanket	Radial Blanket	Na-Steel Axial Reflector	Steel Axial Reflector	Radial Reflector
Pu-239	0.0008456	0.0012768					
Pu-240	0.0001120	0.0001691					
Pu-241	0.0000174	0.0000261					
U-235	0.0000123	0.0000115	0.0000156	0.0000245			
U-238	0.0055591	0.0052063	0.0070447	0.0110903			
Na	0.0081095	0.0093980	0.0087263	0.0063669	0.0089848		
C	0.0000235	0.0000233	0.0000297	0.0010134	0.0001914	0.0005386	0.0005398
O	0.0131172	0.0117802	0.0139529	0.0201416			
Mo	0.0002318	0.0003420	0.0000144	0.0000143	0.0000014		
Fe	0.0120898	0.0144059	0.0094453	0.0069781	0.0332218	0.0727580	0.0717099
Ni	0.0011777	0.0012387	0.0011108	0.0009057	0.0019245	0.0007971	0.0005904
Cr	0.0025604	0.0026808	0.0024500	0.0020075	0.0044841	0.0016304	0.0012001
Mn	0.0002043	0.0002133	0.0002078	0.0001605	0.0005167	0.0006247	0.0005934
Si	0.0001145	0.0001206	0.0001131	0.0000893	0.0002365	0.0000888	0.0000636

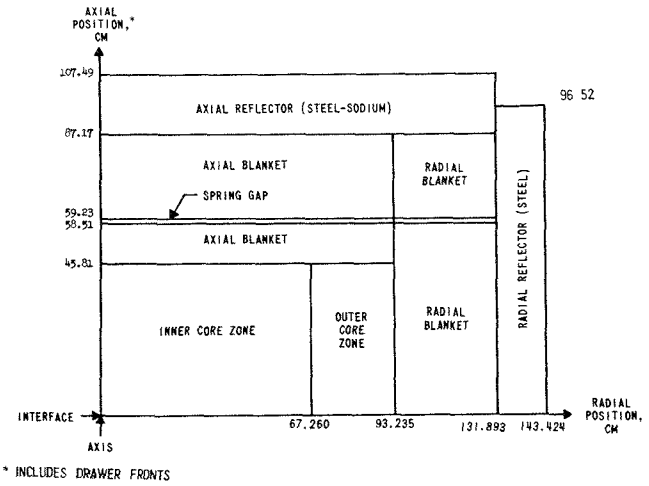

FIG. II-15-3. ZPPR Assembly 2 Initial Critical Configuration—Half 1. *ANL-ID-103-A11549.*

boundaries of the inner and outer core zones. This information was then used to calculate the reactivity effect of replacing the stepped outline by a circle of equal area.

EXCESS REACTIVITY AND SPIKED RODS

The amount of excess reactivity in a reference core, defined as $\Delta k/k$ with all control rods in, was easily determined from the control rod calibration curves. The additional worth of a spiked rod was determined as the difference in calibrated rod worth before and after spiking, which was 38.7 Ih/rod for the 50/50 cores. This number was then multiplied by the ratio of the total rod worth in the 52/48 core to that in the 50/50 core, which gave a value of 37.6 Ih/rod for the 52/48 configuration.

INTERFACE GAP

The interface gap has been measured (with a preloaded core) around the edges with feeler gauges and found to be reasonably uniform at 5 mils. If it is assumed that a slight bulging of the matrix toward the center was preventing closure to less than 5 mils at the edge, an average gap of 2.5 mils is a reasonable assumption. The worth per mil of half-closure was measured during a table scram (no rod motion) using inverse kinetics techniques, and was found to be linear for the first inch of separation at 0.78 Ih/mil and 0.73 Ih/mil for the 52/48 and the 50/50 cores, respectively. No additional correction was determined for the effect of homogenizing the stainless steel drawer fronts, as this may be considered part of the overall heterogeneity problem.

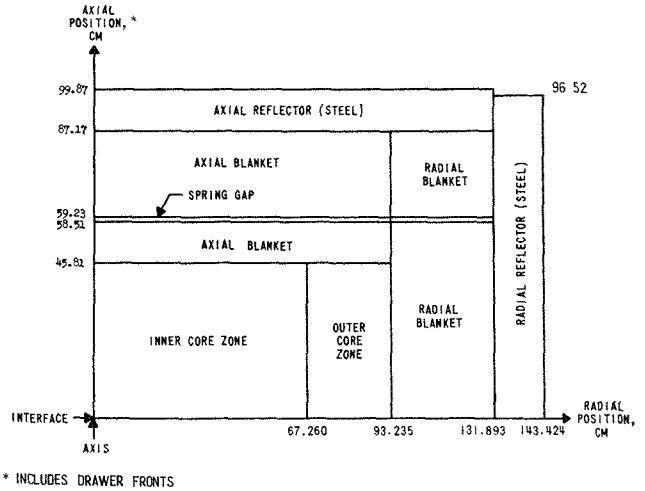

FIG. II-15-4. ZPPR Assembly 2 Initial Critical Configuration—Half 2. *ANL-ID-103-A11550.*

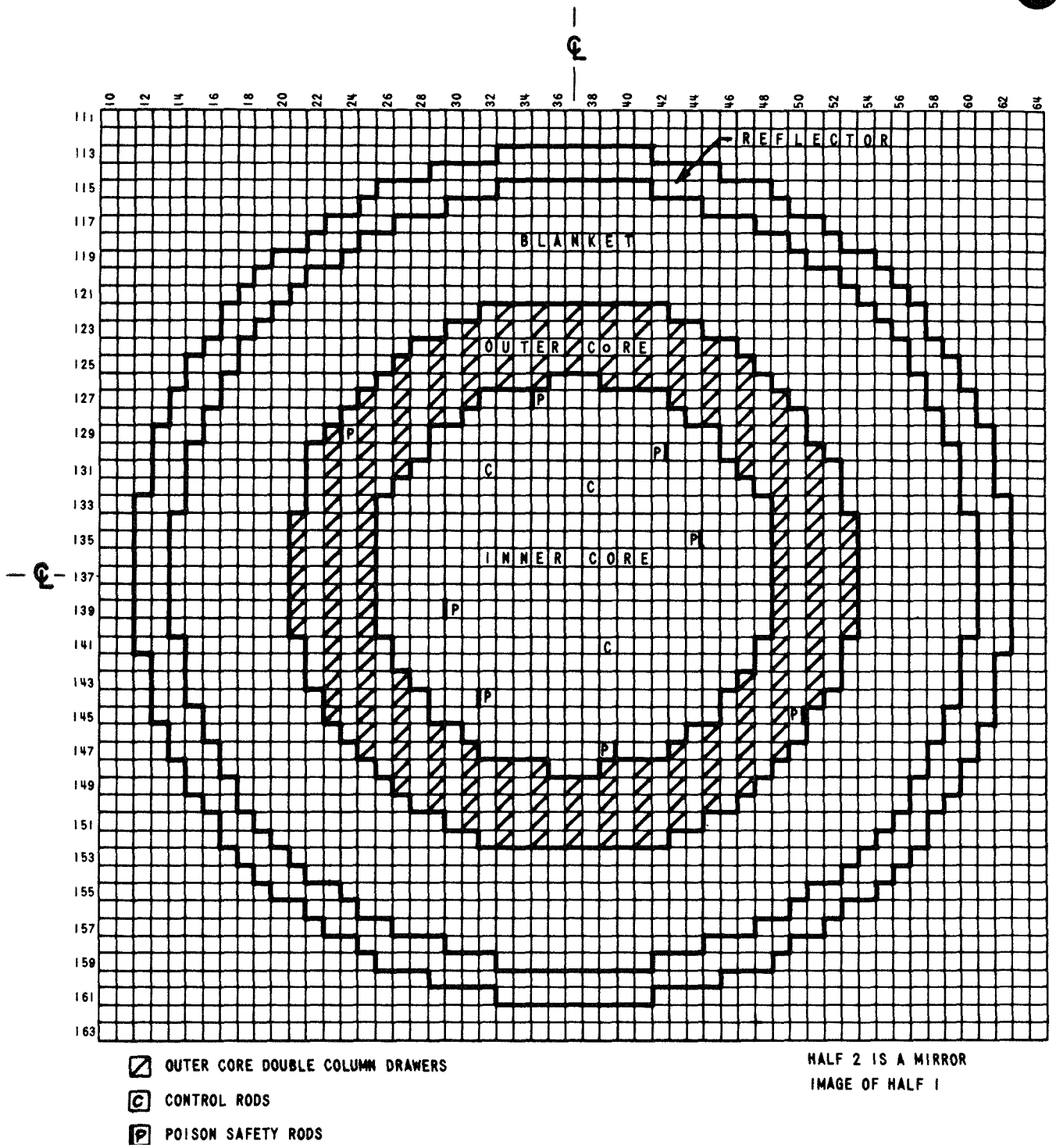

FIG. II-15-5. ZPPR Assembly 2—Reference Loading with Equal Zone Volumes. *ANL-ID-103-A11312.*

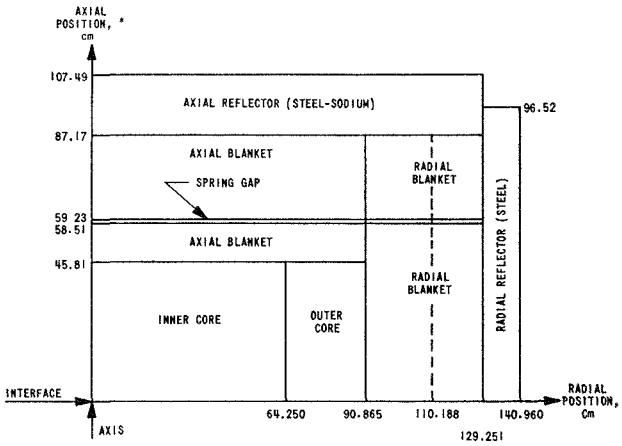

* INCLUDES DRAWER FRONTS

FIG. II-15-6. As-Built ZPPR Assembly 2 Equal Zone Configuration—Half 1. *ANL-ID-103-A11441.*

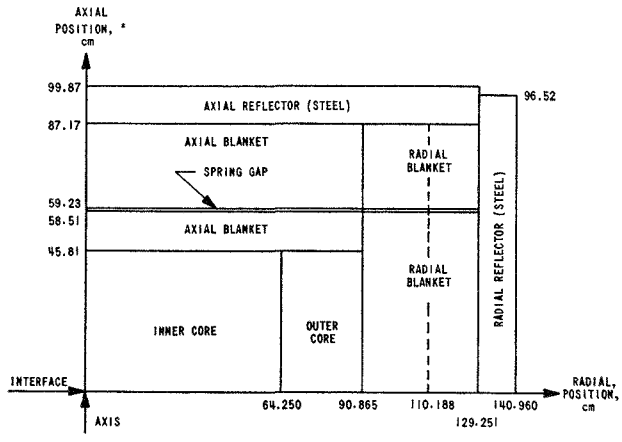

* INCLUDES DRAWER FRONTS

FIG. II-15-7. As-Built ZPPR Assembly 2 Equal Zone Configuration—Half 2. *ANL-ID-103-A11442.*

TABLE II-15-II. ATOM DENSITIES FOR THE MODIFIED EQUAL-ZONE CONFIGURATION OF ZPPR ASSEMBLY 2, 10^{24} atoms/cm³

Isotope	Inner Core		Outer Core	Radial Blanket			Axial Blanket	Radial Reflector	Axial Reflector	
	As-Built	w/o Spiked Rods		Inner	Outer	Average			Steel (5 in.)	Na-Steel (8 in.)
Pu-239	.0008477	.0008456	.0012757	—	—	—	—	—	—	—
Pu-240	.0001123	.0001120	.0001689	—	—	—	—	—	—	—
Pu-241	.0000174	.0000173	.0000260	—	—	—	—	—	—	—
U-235	.0000123	.0000123	.0000116	.0000243	.0000243	.0000243	.0000153	—	—	—
U-238	.0055723	.0055702	.0052068	.0110242	.0110242	.0110242	.0069369	—	—	—
Na	.0088143	.0088203	.0085986	.0063641	.0059302	.0061297	.0086369	—	—	.0089848
O	.0131489	.0131476	.0117808	.0200210	.0200220	.0200216	.0137264	—	—	—
Mo	.0002188	.0002182	.0003285	.0000014	.0000018	.0000016	.0000014	—	—	.0000014
Fe	.0125475	.0125377	.0138252	.0070048	.0076214	.0073379	.0101762	.0717099	.0727580	.0332218
Ni	.0013158	.0013156	.0012556	.0009984	.0010878	.0010467	.0012837	.0005904	.0007971	.0019245
Cr	.0027001	.0026995	.0025239	.0020113	.0021910	.0021084	.0026491	.0012001	.0016304	.0044841
Mn	.0002083	.0002082	.0002008	.0001573	.0001743	.0001665	.0002174	.0005934	.0006247	.0005167
Si	.0001472	.0001472	.0001296	.0001061	.0001139	.0001103	.0001435	.0000636	.0000888	.0002365
C	.0000061	.0000061	—	.0009860	.0009864	.0009862	.0000133	.0005398	.0005386	.0001914

TEMPERATURE CORRECTIONS

The temperature coefficients of the reference cores were determined by shutting off the cooling air flow and allowing the temperature to rise slowly. The reactivity as a function of time was followed with inverse kinetics during this period, and the temperature coefficients were thus found to be constant at a value of -2.9 ± 0.2 Ih/°C. These values were then used to correct the loaded masses to a temperature of 22°C.

CORRECTED CRITICAL MASS

The corrected critical masses for the two versions of Assembly 2 were obtained from the corrections described above by expressing the reactivity effect of each in terms of edge fuel worths. The resulting values give the expected critical mass for a heterogeneous, smooth, cylindrical reactor at 22°C and with no interface gap. The individual corrections for each version are listed in Tables II-15-III and II-15-IV. The corrections for edge smoothing and interface gap can be seen to be quite small, primarily due to the large core volume (2372 liters for the 50/50 version) and the fact that a loading pattern was used whereby the best approximation to a circle, based on rectangles 2.173 in. wide and 2.273 in. high, could be obtained.

The three different reference cores for the 50/50 ver-

TABLE II-15-III. Critical Mass and Mass Correcions in ZPPR Assembly 2, Initial Critical Configuration (52/48)

Correction	ρ, Ih	Δm (equiv.), kg
Excess reactivity	87.4	−5.1
Control-rod spiking		
Amount of fuel	—	−1.0
Worth of spike	75.2	+4.4
Edge smoothing		
IC/OC	−0.74	+0.044
OC/RB	+0.23	−0.014
Interface gap worth	+2	−0.1
Temperature correction to 22°C	+4.88	−0.3

Loaded Pu-239 + 241 mass = 1067.3 ± 1.1 kg
Total correction = −2.07 ± 0.1 kg
Correction critical mass = 1065.2 ± 1.1 kg of Pu-239 + 241 (heterogeneous cylindrical reactor at 22°C)

TABLE II-15-IV. Critical Mass and Mass Corrections in ZPPR Assembly 2, Equal-Zone Configuration (50/50)

Correction	ρ, Ih	Δm (equiv.), kg
Excess reactivity	79.62	−4.75
Control-rod spiking		
Amount of fuel	—	−1.0
Worth of spike	77.42	+4.62
Edge smoothing		
IC/OC	−0.03	+0.002
OC/RB	+0.04	−0.002
Interface gap worth		−0.11
Temperature correction to 22°C	+1.74	−0.1

Loaded Pu-239 + 241 mass = 1019.7 ± 1.0 kg
Total correction = −1.34 ± 0.1 kg
Corrected critical mass = 1018.4 ± 1.0 kg Pu-239 + 241 (heterogeneous cylindrical reactor at 22°C)

TABLE II-15-V. Corrected Inventory of Fissile Isotope in Core Zones of ZPPR Assembly 2, Initial Critical Configuration, kg

Isotope	Plate	Inner Zone	Outer Zone	Total
Pu-239	Fuel	437.34	606.56	1043.90
Pu-241	Fuel	8.86	12.45	21.31
U-235	Fuel	2.73	3.78	6.51
U-235	U_3O_8	3.52	1.63	5.15
Total Pu-239 + 241		446.20	619.01	1065.21
Total fissile		452.45	624.42	1076.87

TABLE II-15-VI. Corrected Inventory of Fissile Isotopes in Core Zones of ZPPR Assembly 2, Equal-Zone Configuration, kg

Isotopes	Plate	Inner Zone	Outer Zone	Total
Pu-239	Fuel	398.33	599.70	998.03
Pu-241	Fuel	8.07	12.31	20.38
U-235	Fuel	2.47	3.75	6.22
U-235	U_3O_8	3.21	1.61	4.82
Total Pu-239 + 241		406.40	612.01	1018.41
Total fissile		412.08	617.37	1029.45

sion all gave consistent results to within a small fraction of the uncertainty in the total loaded mass. This uncertainty was based on the manufacturer's specifications for the isotopic content of the fuel plates (±0.1% in Pu-239 and ±1.0% in Pu-241), and the error in the correction term is based upon typical errors for each component. The value of the loaded mass was not based on average plate weights, but was calculated from individual plate weights as a result of computerized fuel inventory procedures.

The total masses of all fissile isotopes in the two versions are presented in Tables II-15-V and II-15-VI, where the values have been adjusted to correspond to the corrected critical mass. Calculations of heterogeneity effects in Assembly 2 may be found in Paper II-16.

II-16. Heterogeneity and Criticality Studies on the Zero Power Plutonium Reactor (ZPPR) Assembly 2, a Demonstration Reactor Benchmark Critical

Arne P. Olson and Nam Chin Paik*

Introduction

ZPPR Assembly 2 is a large, zoned critical assembly designed to simulate the compositions and configurations of the LMFBR demonstration plants. The initial critical configuration had a volume ratio of 52/[illegible] (inner core/outer core). Some postanalysis results have been obtained for this configuration. These will be described together with a description of the methods and approximations used in the preanalysis.

* Westinghouse Electric Corporation, Pittsburgh, Pennsylvania.

Cross Section Data and Data Processing

The ENDF/B (1968) nuclear data set was used in the criticality determination of the ZPPR-2 core.

Since it was felt that a fast and simple calculational method other than the "ARC" System[1] would be useful during the interim period while the ARC System was being made operational at ANL-Idaho, the calculational method using the 1DX-PERT 5 combination[2] was introduced. The main effort on data generation and processing was done by the MC² code with the ENDF/B (1968) data. For each reactor region of ZPPR-2, 27-energy-group cross sections ($\Delta u = 0.5$ for groups 1 through 21, $\Delta u = 1.0$ for groups 21 through 25, $\Delta u = 2.0$ for 26 and a thermal group—see Table II-16-I for the energy group structure) were generated using the MC² code. The options used were: consistent B_1, ultrafine groups, isotropic scattering, homogeneous resonance self-shielding, the critical buckling search for the two core regions, and essentially zero bucklings for axial and radial blanket regions. For each core zone (the inner and the outer zones), three heterogeneous resonance self-shielding MC² treatments were made in order to correctly self-shield the plutonium and the U-238 in the oxide plates and the molybdenum and U-238 in the Pu-U-Mo plates in the resonance region.

TABLE II-16-I. Effect of Heterogeneity on the Central Real Flux Spectra

Energy Group	Lower Energy Limit, eV	Flux-Weighted, Heterogeneous Resonance Self-Shielding	No Flux-Weighting, Homogeneous Resonance Self-Shielding
1	6.065×10^{6}	2.87677×10^{-3}	2.94917×10^{-3}
2	3.679	1.16148×10^{-2}	1.188204×10^{-2}
3	2.23	2.81316×10^{-2}	2.88251×10^{-2}
4	1.35	3.93748×10^{-2}	4.02043×10^{-2}
5	0.821	4.92492×10^{-2}	4.97773×10^{-2}
6	0.498	9.61827×10^{-2}	9.69462×10^{-2}
7	0.320	9.09784×10^{-2}	9.14794×10^{-2}
8	0.183	1.18963×10^{-1}	1.19876×10^{-1}
9	0.111	1.12613×10^{-1}	1.13474×10^{-1}
10	6.738×10^{4}	1.02244×10^{-1}	1.03176×10^{-1}
11	4.087	8.46264×10^{-2}	8.53785×10^{-2}
12	2.48	6.85659×10^{-2}	6.89643×10^{-2}
13	1.503	6.00180×10^{-2}	6.01540×10^{-2}
14	9.12×10^{3}	4.36250×10^{-2}	4.35478×10^{-2}
15	5.53	2.62165×10^{-2}	2.59631×10^{-2}
16	3.355	1.64634×10^{-2}	1.59138×10^{-2}
17	2.035	5.60875×10^{-3}	5.49253×10^{-3}
18	1.234	1.67233×10^{-2}	1.54943×10^{-2}
19	7.485×10^{2}	1.15109×10^{-2}	1.01522×10^{-2}
20	4.54	7.35031×10^{-3}	5.92782×10^{-3}
21	2.754	$3\ 384017 \times 10^{-3}$	2.43762×10^{-3}
22	1.013	3.18741×10^{-3}	1.77372×10^{-3}
23	0.3727	4.66664×10^{-4}	2.03935×10^{-4}
24	0.1371	2.47740×10^{-5}	7.5747×10^{-6}
25	5.04×10^{0}	6.15×10^{-7}	1.885×10^{-7}
26	0.683	3.51×10^{-8}	1.03×10^{-8}
27	Thermal	1.75702×10^{-12}	1.7137×10^{-12}

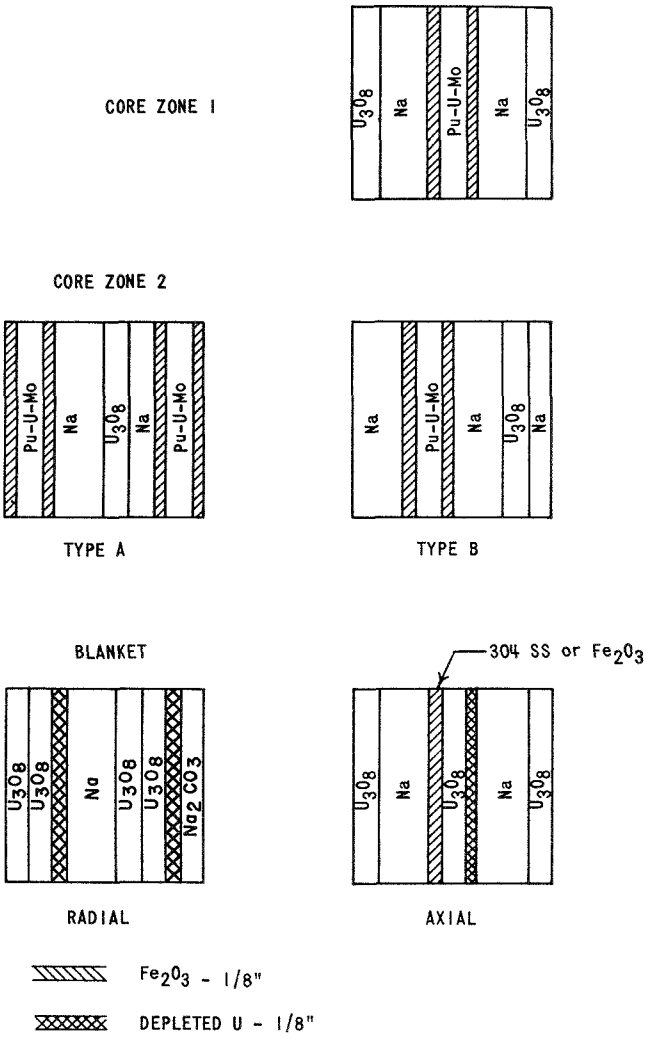

Fig. II-16-1. ZPPR Assembly 2 Drawer Configurations. *ANL-ID-103-A11278.*

The heterogeneous perturbation theory code CAL-HET,[3] based on the collision probability approach, was used to obtain flux- and volume-averaged cross sections over each core cell. The isotopic cross sections generated for the axial blanket and the radial blanket were used for the isotopes in the axial and radial reflectors (sodium, carbon, iron, chromium, nickel, and manganese), respectively.

The generalized configurations intended for ZPPR Assembly 2 are given in Fig. II-16-1. As it turned out, a large number of the inner core drawers were loaded with two ¼-in. pieces of canned sodium replacing the ½-in. pieces shown in Fig. II-16-1. The inner core zone, the axial blanket, and the radial blanket have

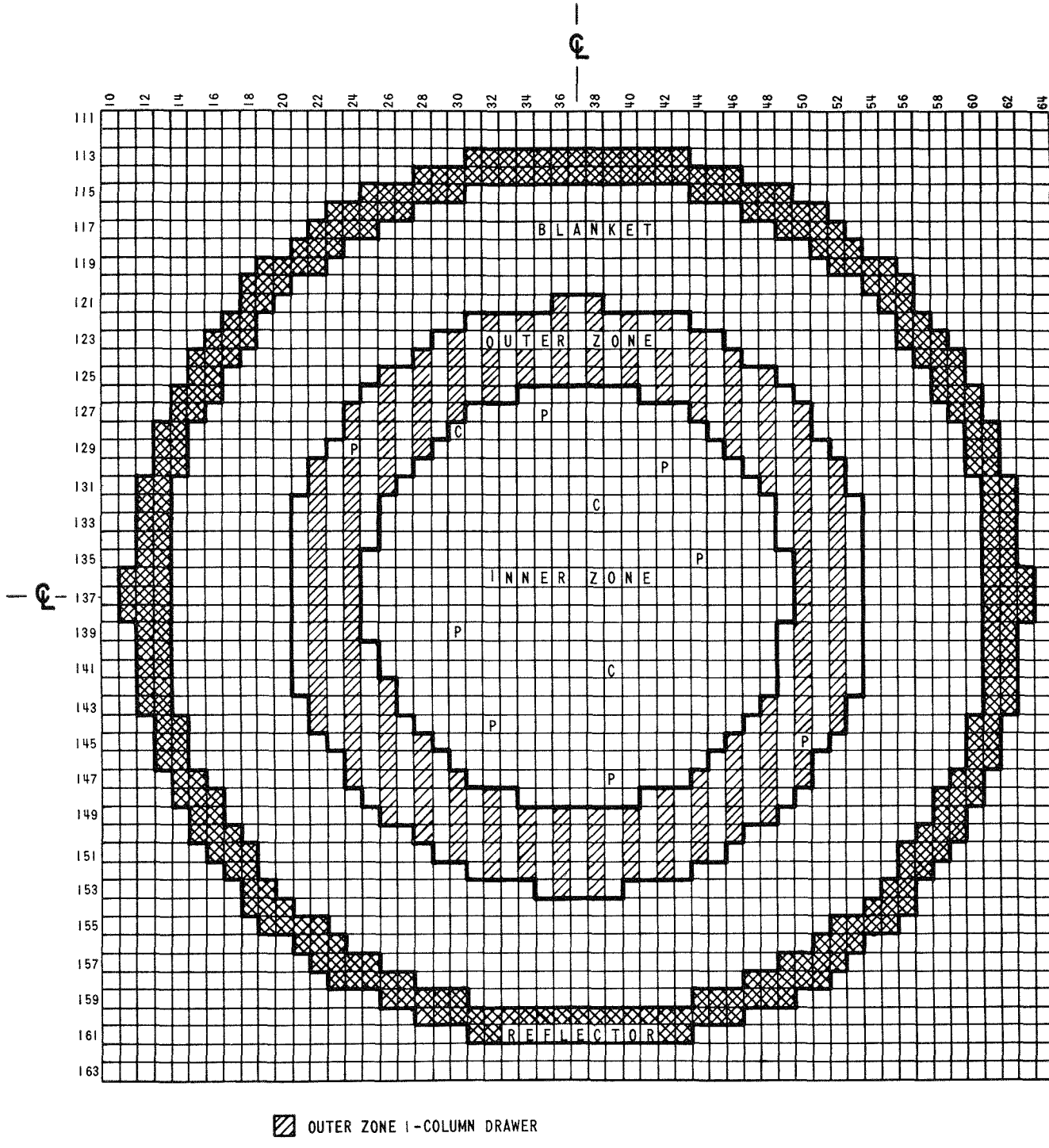

FIG. II-16-2. Interface Diagram, ZPPR Assembly 2, Initial Critical Configuration. *ANL-ID-103-A11298.*

single-drawer cells. The outer core zone has a two-drawer cell with Types A and B drawers shown in Figs. II-16-1 and II-16-2. Further descriptions of typical drawer plates are given in Table II-16-II. The 0.015 and 0.019 in. stainless steel claddings on t nominally ¼ in. ZPPR fuel plate and ¼ in. sodium plate, respectively, were smeared with the diluent in the heterogeneity effect study. Typical isotopic compo-

TABLE II-16-II. Descriptions of ZPPR Assembly 2 Cell Plates

Plate Type	Thickness, cm	Isotope	Composition Within Plate, 10^{24} atoms/cm^3
¼ in. Pu-U-Mo	0.558810	Pu-239	0.0102358
		Pu-240	0.001356
		Pu-241	0.0002034
		U-235	0.00006255
		U-238	0.0289379
		Mo	0.002596
⅛ in. Fe_2O_3[a]	0.403860	Fe	0.0366
		O	0.03774
		Cr	0.00331
		Ni	0.00165
½ in. Na[b]	1.221750	Na	0.02334
		Fe	0.00228
		Cr	0.00066
		Ni	0.00033
¼ in. Na[b]	0.586740	Na	0.02003
		Fe	0.00568
		Cr	0.00165
		Ni	0.000825
¼ in. U_3O_8	0.635000	U-238	0.015687
		U-235	0.00003442
		O	0.041779
Standard Drawer Plus Matrix	0.434340	Fe	0.03622
		Cr	0.01041
		Ni	0.0455
		Mo	0.0000975

[a] Includes a Pu-U-Mo plate cladding (0.015 in.) and a sodium plate cladding (0.019 in.).

[b] Includes a 0.019 in. sodium plate cladding (one side only).

sitions within each plate and the actual plate thicknesses are given in Table II-16-II.

Accuracy of the Two-Region Equivalence Principle

The present MC² code uses an equivalence principle to compute resonance self-shielding for a repetitive two-region cell. The cells in the inner and and the outer core zones of ZPPR-2 are in fact a multi-region type as shown in Fig. II-16-1. For example, consider the inner core zone cell in Fig. II-16-1. The single drawer cell basically consists of four regions: the fuel region A (two ¼-in. U_3O_8 plates with the standard drawer and matrix lumped together), the moderator region (½-in. sodium and ⅛-in. or 1/9-in. Fe_2O_3 plates homogenized, including the two 0.019 in. stainless steel claddings on the sodium plate and one 0.015 in. stainless steel cladding on the Pu-U-Mo ZPPR plate), the fuel region B (the Pu-U-Mo plate without the claddings), and a repetition of the moderator region.

Because of the U-238 in the two different fuel regions, the Dancoff correction factor appropriate for the four-region cell heterogeneous resonance self-shielding may not be the same as that for the two-region cell. The question is therefore raised as to the adequacy and accuracy in the use of the MC² code for heterogeneous resonance self-shielding (for U-238, in particular). The heterogeneous resonance self-shielding treatment of plutonium isotopes is rather straightforward, because the simple two-region equivalence principle is directly applicable in this case.

A general investigation[4] of the limitations and accuracy of the simple two-region equivalence principle has shown that a complicated four-region equivalence principle is not necessary, and that subdivision of the four-region cell into several two-region subcells is sufficient. First-order corrections for the finite plate size are also found to be mostly small. This correction is negligible except for the case of heterogeneous resonance self-shielding of U-238 (in two adjoining ¼-in. U_3O_8 plates) in the inner core zone.

Heterogeneous and homogeneous resonance self-shielded capture and fission cross sections of Pu-239 in each core region are given in Tables II-16-III and II-16-IV. The resonance self-shielding heterogeneity effect of three plutonium isotopes on the eigenvalue of the system is −0.2% k. In Table II-16-V, capture cross sections of U-238 in the resonance energy region

TABLE II-16-III. Comparison of Heterogeneous and Homogeneous Resonance Self-Shielding of Pu-239 in the Inner Core Zone

Group	Heterogeneous Self-Shielding		Homogeneous Self-Shielding	
	σ_c	σ_f	σ_c	σ_f
10	0.2206	1.506	0.2189	1.513
11	0.2952	1.464	0.2937	1.476
12	0.5017	1.606	0.4992	1.623
13	0.7233	1.809	0.7197	1.832
14	0.9620	2.060	0.9576	2.094
15	1.211	2.372	1.210	2.425
16	1.492	2.690	1.507	2.781
17	2.077	3.443	2.167	3.644
18	2.590	4.145	2.763	4.449
19	3.227	5.118	3.558	5.591
20	4.720	7.418	5.352	8.179
21	3.865	6.831	5.095	8.114
22	6.418	13.79	8.391	16.00
23	4.960	23.04	7.103	27.30
24	7.875	9.414	11.16	13.33
25	19.11	30.36	28.11	42.69
26	2.603	11.46	2.663	11.61
27	265.7	742.40	265.7	742.4

TABLE II-16-IV. Comparison of Heterogeneous and Homogeneous Resonance Self-Shielding of Pu-239 in the Outer Core Zone

Group	Heterogeneous Self-Shielding		Homogeneous Self-Shielding	
	σ_c	σ_f	σ_c	σ_f
10	0.2192	1.515	0.2190	1.513
11	0.2919	1.477	0.293	1.476
12	0.4975	1.622	0.4989	1.622
13	0.7164	1.827	0.7180	1.830
14	0.9527	2.083	0.9561	2.091
15	1.198	2.402	1.208	2.422
16	1.473	2.727	1.502	2.773
17	2.052	3.499	2.152	3.626
18	2.524	4.172	2.714	4.392
19	3.104	5.113	3.461	5.493
20	4.402	7.187	5.022	7.793
21	3.569	6.667	4.708	7.741
22	6.105	13.55	7.755	15.43
23	4.237	22.11	5.758	25.44
24	7.212	8.381	9.756	11.34
25	17.78	27.97	24.63	37.13
26	2.903	12.14	2.963	12.30
27	265.7	742.40	265.7	742.40

TABLE II-16-V. U-238 Self-Shielded Capture Cross Section in the Inner Core Zone

Group	Heterogeneous σ_c-238 (Oxide Plate)	Heterogeneous σ_c-238 (Pu-U-Mo Plate)	Homogeneous Self-Shielding
11	0.3317	0.3314	0.3338
12	0.4372	0.4359	0.4431
13	0.5493	0.5466	0.5611
14	0.6592	0.6545	0.6818
15	0.7563	0.7508	0.8008
16	0.8234	0.8194	0.8817
17	0.9658	0.9854	1.162
18	0.8356	0.8236	0.9804
19	1.016	0.9760	1.195
20	0.8501	0.8165	1.072
21	0.8007	0.7722	1.156
22	1.087	1.129	1.453
23	1.295	1.381	1.645
24	4.695	4.686	6.264
25	0.7224	0.7946	0.9059
26	1.468	1.547	1.512
27	2.720	2.720	2.720

are given for the inner core zone. The first and second columns list the capture cross sections for U-238 in the U_3O_8 plate and in the Pu-U-Mo plate, respectively, which are to be compared with the values in the last column of homogeneous resonance self-shielding MC² results. Similar results for the outer core zone are given in Table II-16-VI.

Capture cross section of U-238 obtained from MC² by heterogeneous resonance self-shielding are significantly lower than capture cross sections obtained using the homogeneous MC² option. These differences are responsible for the heterogeneous resonance self-shielding effect of about +0.8% k, as depicted in Table

TABLE II-16-VI. U-238 Self-Shielded Capture Cross Section in the Outer Core Zone

Group	Heterogeneous σ_c-238 (Oxide Plate)	Heterogeneous σ_c-238 (Pu-U-Mo Plate)	Homogeneous Self-Shielding
11	0.3317	0.3310	0.3335
12	0.4396	0.4359	0.4441
13	0.5544	0.5465	0.5628
14	0.6708	0.6552	0.6869
15	0.7802	0.7521	0.8113
16	0.8601	0.8197	0.8952
17	1.046	0.9797	1.178
18	0.9075	0.8261	1.018
19	1.110	0.9869	1.265
20	0.9567	0.8274	1.161
21	0.9122	0.7879	1.258
22	1.238	1.146	1.621
23	1.413	1.380	1.756
24	5.360	4.743	6.995
25	1.407	0.9852	1.444
26	1.394	1.421	1.404
27	2.720	2.720	2.720

TABLE II-16-VII. Summary of Heterogeneity Effects on the Eigenvalue k

	Heterogeneity Effects on k in %	
	ETOX-1DX Path	MC²-2D Diffusion Path
Resonance self-shielding heterogeneity effect, Δk	0.60 (Pu: −0.24; U-238: 0.84)	0.6
Spatial heterogeneity effect, Δk	ETOX-1DX-CALHET Path	MC²—CALHET Path
Inner zone	0.96	0.96
Outer zone	0.90	0.93
Core average	0.94	0.95
Total heterogeneity effect (approximate result): spatial heterogeneity effect estimate by CALHET plus resonance self-shielding heterogeneity effect	1.54	1.55
Total heterogeneity effect (best estimate)· MC²-flux weighting by CALHET-2 dimensional diffusion path	—	1.9

TABLE II-16-VIII. AS-BUILT ATOM DENSITIES FOR THE INITIAL CRITICAL CORE OF ZPPR ASSEMBLY 2

Isotope	10^{24} atoms/cm^3						
	Inner Core	Outer Core	Axial Blanket	Radial Blanket	Radial Reflector	Na-Steel Axial Reflector	Steel Axial Reflector
Pu-239	0.00084688	0.00127960					
Pu-240	0.00011450	0.00017310					
Pu-241	0.00001694	0.00002592					
U-235	0.00001244	0.00001165	0.00001506	0.00002376			
U-238	0.00556942	0.00521791	0.00693322	0.01101575			
Na	0.00809837	0.00844749	0.00859637	0.00565222		0.00898490	
C	0.00000687	0.00000699	0.00001486	0.00100286	0.00053979	0.00014497	0.00053718
O	0.01316710	0.01181889	0.01376330	0.02011209			
Mo	0.00021587	0.00032662					
Fe	0.01204720	0.01402619	0.00954698	0.00705480	0.07172669	0.03276590	0.07241600
Ni	0.00127074	0.00127927	0.00123316	0.00100584	0.00059039	0.00208898	0.00075764
Cr	0.00255229	0.00257191	0.00247898	0.00202443	0.00120005	0.00448536	0.00153349
Mn	0.00021672	0.00021839	0.00021034	0.00017158	0.00059358	0.00048507	0.00061867
Si	0.00014058	0.00014169	0.00013623	0.00011039	0.00006364	0.00024356	0.00008182

II-16-VII. However, the differences between the capture cross sections of U-238 for the oxide plate and for the Pu-U-Mo plate are about one-tenth of the differences between the average heterogeneous and homogeneous resonance self-shielded cross sections. It is clear, therefore, that the error which results from the use of the two-region equivalence principle for U-238 resonance self-shielding must be of the second order.

HETEROGENEITY EFFECTS ON EIGENVALUE AND REAL FLUX SPECTRA

Because ZPPR-2 is a large, zoned core with a different cell structure in each core zone, it is not as simple as other small, single zone critical assemblies for the spatial heterogeneity effect analysis. A reasonable method for the heterogeneity study is: (a) to generate flux-weighted isotopic cross sections over the inner core zone cell and the outer core zone cell, separately, by using either the S_n transport code TESS[5] or the heterogeneous perturbation code CALHET-3. The assumption here is that most cells in each zone have flux spectra which are not too much different from the fundamental mode spectra. (b) The resulting flux- and volume-weighted cross sections are then used in one- or two-dimensional diffusion theory calculations of the as-built core compositions and dimensions. The as-built compositions are given in Table II-16-VIII, and the dimensions are shown in Figs. II-16-2 through II-16-4.

The differences in eigenvalues and flux spectra obtained from two 2D calculations, one with flux-weighted heterogeneous resonance self-shielded cross sections, the other with unweighted homogeneous resonance self-shielded cross sections, are the total heterogeneity effects on the eigenvalue and flux spectra.

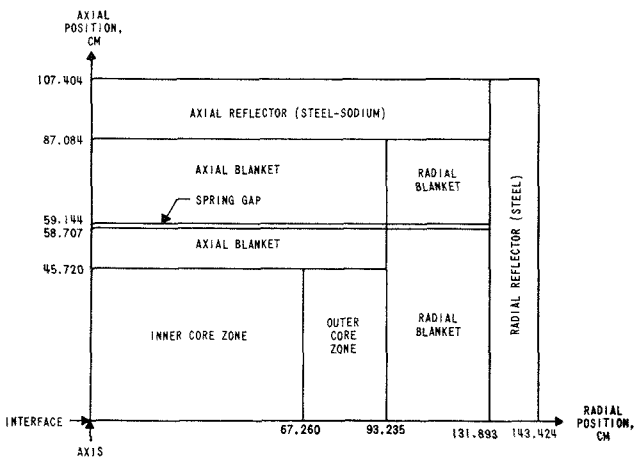

FIG. II-16-3. ZPPR Assembly 2 Initial Criticality Configuration—Half 1. *ANL-ID-103-A11299.*

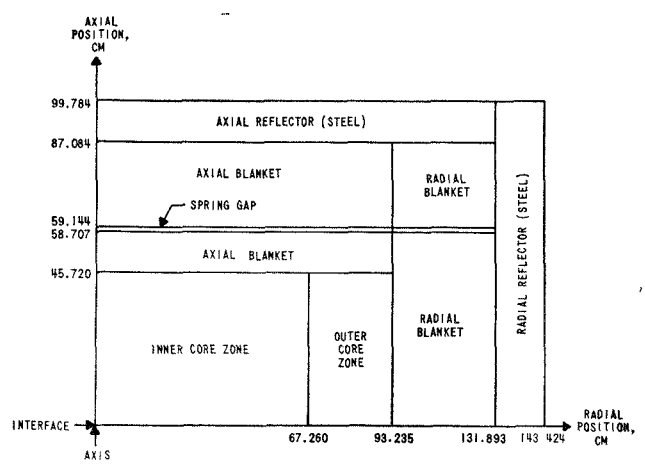

FIG. II-16-4. ZPPR Assembly 2 Initial Criticality Configuration—Half 2. *ANL-ID-103-A11300.*

TABLE II-16-IX. Energy Breakdown of Spatial Heterogeneity Effect for the Inner Core Zone CALHET-3 Study

Group	Lower Energy, eV	Heterogeneous Flux Spectra		Spatial Heterogeneity, $\Delta k(\%)$
		Pu-U-Mo Plate	Diluent Plate	
1	6.065×10^6	0.004	0.0027	0.10
2	3.679	0.014	0.0107	0.23
3	2.23	0.032	0.0268	0.31
4	1.35	0.043	0.038	0.30
5	0.821	0.053	0.047	0.26
6	0.498	0.097	0.093	0.14
7	0.320	0.091	0.088	0.10
8	0.183	0.117	0.117	0.004
9	0.111	0.110	0.112	−0.025
10	6.738×10^4	0.102	0.102	−0.025
11	4.087	0.084	0.085	−0.032
12	2.48	0.068	0.069	−0.030
13	1.503	0.060	0.062	−0.045
14	9.12×10^3	0.043	0.044	−0.042
15	5.53	0.026	0.027	−0.032
16	3.355	0.015	0.016	−0.040
17	2.035	0.005	0.006	−0.010
18	1.234	0.015	0.017	−0.046
19	7.485×10^2	0.010	0.012	−0.046
20	4.54	0.006	0.007	−0.047
21	2.754	0.0027	0.003	−0.019
22	1.013	0.0023	0.006	−0.050
23	0.3727	↓	↓	↓
24	0.1371			
26	5.04×10^0			
26	0.683			
27	Thermal			
	Total	1.00	0.99	0.955%

Two-dimensional perturbation theory calculations are required if one is interested in the detailed energy and region breakdown of the heterogeneity effect on the eigenvalue. The CALHET-3 code gives a good qualitative energy breakdown of the heterogeneity effect on the eigenvalue.

A typical CALHET-3 result for the energy breakdown of the heterogeneity effect on the eigenvalue is given in Table II-16-IX. It is evident that the total flux in diluent plates is about 1% lower than the total flux within the fuel-bearing plate. The high-energy effects are shown to be predominant compared with the negative contributions in the energy range below 183 keV. Above 183 keV, the heterogeneity effect is positive due to the peaking of both the real and adjoint fluxes in this energy range.

The flux weighting coefficients for all isotopes in inner and outer core regions are given in Tables II-16-X and II-16-XI, respectively. The values in the first column in both tables, denoted simply by Pu, are the weighting coefficients for all isotopes that exist within the Pu-U-Mo plate. The isotopes within the Pu-U-Mo plates are Pu-239, Pu-240, Pu-241, Mo, and U-238 (43% of the inner core zone U-238 and 70% of the outer core zone U-238 comes from the Pu-U-Mo plates).

A summary of the various heterogeneity effects is given in Table II-16-VII. The table shows that either data processing method, the ETOX-1DX combination or the MC² method, gives about the same resonance self-shielding and high-energy spatial heterogeneity effects. The resonance self-shielding heterogeneity effect was calculated to be 0.6% k. An approximate calculation of the spatial heterogeneity effect was obtained from the transport perturbation code CALHET-3, which considers a unit cell and not the whole reactor system. The result obtained in this way, therefore, cannot be as accurate as the difference in two eigenvalue calculations using 2D diffusion theory: one with flux-weighted (by CALHET-3) and heterogeneous resonance self-shielded cross sections, and the other with homogeneous resonance self-shielded cross sections. The best estimate of the total heterogeneity effect obtained in this way was 1.9% k.

Comparison of Calculated and Measured Critical Mass

A summary of the calculated eigenvaluve for the as-built ZPPR Assembly 2 is given in Table II-16-XII. The resonance self-shielding and spatial cell heterogeneity effects were calculated to be 0.6% k and 1.30% k, respectively, for a total heterogeneity effect of 1.9% k. The transport effect correction on the eigenvalue was found to be 0.35% k.

The calculated critical mass for this initial ZPPR-2 core was 1095 kg of Pu-239 + Pu-241, which is about 3% higher than the measured value of 1066 kg. The volume of the inner core zone was 1300 liters and the volume of the outer core zone was 1197 liters. The agreement between the measured critical mass and the calculated mass with the ENDF/B (1968) data is probably fortuitous and a result of the cancellation of errors in data, because the ENDF/B (1968) data are known to be less accurate than the present case seems to indicate.

Miscellaneous Information on the ZPPR-2 Preanalysis

Some available additional information is given here for documentation which may become useful later.

1) The axial group- and region-independent buckling (B_z^2) that gives the identical k_{eff} from 2D

TABLE II-16 X FLUX WEIGHTING COEFFICIENTS FOR ISOTOPES IN THE INNER CORE ZONE

Group	Pu (Pu-U Mo)	U-238		U 235	Na	O	Fe	Cr Ni
		Average	U_3O_8 Plate					
1	1 262	1 078	0 933	1 079	0 972	0 979	1 005	0 969
2	1 239	1 072	0 936	1 070	0 974	0 980	1 005	0 969
3	1 156	1 044	0 953	1 043	0 985	0 986	1 006	0 980
4	1 115	1 026	0 953	1 025	0 994	0 984	1 006	0 985
5	1 099	1 027	0 968	1 027	0 989	0 991	1 007	0 992
6	1 033	1 010	0 992	1 010	0 995	0 999	1 004	0 999
7	1 027	1 007	0 991	1 007	0 998	0 996	1 001	0 998
8	1 001	1 001	1 001	1 001	0 999	1 001	1 000	0 999
9	0 994	0 998	1 001	0 998	1 002	0 999	0 999	1 000
10	0 994	0 999	1 002	0 999	1 000	1 001	1 000	1 001
11	0 990	0 998	1 004	0 998	1 001	1 001	0 999	1 001
12	0 989	0 997	1 004	0 997	0 999	1 002	1 002	1 003
13	0 977	0 991	1 002	0 991	1 007	0 999	0 995	1 000
14	0 974	0 992	1 007	0 992	1 003	1 002	1 000	1 005
15	0 970	0 992	1 010	0 992	1 002	1 005	1 001	1 004
16	0 973	1 006	1 034	1 007	0 980	1 021	1 013	1 023
17	0 918	0 964	1 002	0 965	1 036	0 982	0 974	0 986
18	0 928	0 964	0 994	0 964	1 032	0 985	0 984	0 989
19	0 927	0 972	1 011	0 974	1 016	0 999	0 995	1 002
20	0 913	0 969	1 018	0 971	1 014	1 005	0 998	1 008
21	0 905	0 964	1 021	0 969	1 016	1 006	0 997	1 009
22	0 873	0 957	1 028	0 959	1 015	1 009	1 000	1 017
23	0 831	0 948	1 052	0 954	1 019	1 017	0 992	1 017
24	0 844	0 930	1 022	0 943	1 031	1 004	1 006	1 021
25	0 738	0 904	1 069	0 922	1 039	1 025	0 988	1 030
26	0 887	0 962	1 024	0 963	1 017	1 006	0 996	1 010
27	1 200	0 705	1 180	0 709	1 115	1 076	1 000	1 068

TABLE II-16-XI FLUX WEIGHTING COEFFICIENTS FOR ISOTOPES IN THE OUTER CORE ZONE

Group	Pu (Pu U Mo)	U-238		U-235	Na	O	Fe	Cr-Ni
		Average	U_3O_8 Plate					
1	1 168	1 099	0 940	1 103	0 957	0 991	0 999	0 982
2	1 152	1 092	0 942	1 091	0 960	0 991	0 999	0 982
3	1 096	1 056	0 958	1 055	0 975	0 994	1 001	0 990
4	1 063	1 032	0 956	1 032	0 985	0 992	1 004	0 998
5	1 059	1 032	0 966	1 032	0 983	0 995	1 005	1 001
6	1 021	1 012	0 990	1 012	0 993	1 000	1 003	1 001
7	1 018	1 010	0 989	1 010	0 996	0 997	1 001	1 000
8	0 999	1 000	1 002	1 000	0 999	1 001	1 000	0 999
9	0 994	0 996	1 003	0 996	1 003	1 000	0 999	0 999
10	0 995	0 997	1 004	0 997	1 001	1 001	1 000	1 000
11	0 991	0 996	1 007	0 996	1 002	1 001	0 999	0 999
12	0 990	0 994	1 003	0 994	1 000	1 002	1 002	1 003
13	0 977	0 987	1 012	0 987	1 010	1 001	1 000	0 995
14	0 977	0 985	1 007	0 986	1 006	1 000	1 001	1 004
15	0 974	0 984	1 011	0 985	1 005	1 004	1 002	1 004
16	0 989	0 995	1 012	0 996	0 984	1 016	1 019	1 020
17	0 929	0 956	1 030	0 959	1 045	0 984	0 971	0 981
18	0 931	0 952	1 013	0 955	1 040	0 986	0 982	0 991
19	0 933	0 956	1 023	0 959	1 025	0 999	0 995	1 001
20	0 923	0 949	1 028	0 954	1 024	1 003	0 999	1 007
21	0 915	0 942	1 033	0 950	1 027	1 004	0 999	1 008
22	0 898	0 930	1 035	0 938	1 030	1 007	1 003	1 013
23	0 866	0 919	1 083	0 929	1 040	1 014	0 990	1 004
24	0 936	0 930	0 973	0 947	1 027	1 003	1 012	1 022
25	0 783	0 848	1 086	0 873	1 069	1 017	0 997	1 022
26	0 906	0 939	1 029	0 942	1 027	1 004	1 002	1 012
27	0 022	0 418	1 373	0 420	1 247	1 109	1 017	1 067

diffusion theory:

$B_z^2 = 6.0095 \times 10^{-4}$ (ENDF/B 1968 Data)

2) $\frac{\Delta B_z^2}{B_z^2} = 7 \frac{\Delta k_{eff}}{k_{eff}} = \frac{7}{6} \frac{\Delta M}{M}$ (edge loading)

3) The 2D results presented here were obtained with 27 groups and 30 x 19 mesh points (R-Z). The change in eigenvalue due to doubling the number of mesh points in either direction was found to be only of the order of a few hundredths percent k.

4) The change in Pu-239 alpha (capture-to-fission cross section ratio) from the low to the high values resulted in 1.5% change in eigenvalue. The alpha change was made according to Gwin's data,[6] keeping the sum of the capture and fission cross sections constant.

5) Two-dimensional calculations of the prompt neutron lifetime ℓ_p, the effective delayed neutron fraction β_{eff}, and the conversion factor of inhours to percent reactivity are:

$\beta_{eff} = 0.003180$

$\ell_p = 5.578 \times 10^{-7}$ sec

Ih/%k = 1015.7.

TABLE II-16-XII. Two-Dimensional Diffusion Theory Criticality Calculation of ZPPR Assembly 2, the Demonstration Reactor Benchmark

ENDF/B (1968) Data	Eigenvalue of the System, k
Homogeneously self-shielded cross sections from MC²	0.9725
Heterogeneously self-shielded cross sections from MC² (Pu-239, Pu-240, Pu-241, Mo, U-238)	0.9782
Cell flux-weighted heterogeneously self-shielded cross sections from MC² (the best estimate possible)	0.9912
The best estimate including the transport effect correction	0.9947

Perturbation Calculations

Two-dimensional perturbation calculations were made to obtain reactivity worths for Pu-239, Pu-240, U-235, U-238, and sodium. The compositions and dimensions of the ZPPR-2 were the same as described elsewhere in this report. The perturbation calculations used homogeneous resonance self-shielded cross sections from MC². These results are given for the convenience of experimentalists prior to the actual measurements of reactivity traverses.

Although the assembly used in the calculation was the initial critical core (not the official ZPPR Assembly 2 with 50/50 core volume), the results given in Table II-16-XIII are not much different from those for two later cores. The calculated central reactivity worths of Pu-239, Pu-240, and U-235 given in Table II-16-XIII were found to be about 15% higher than the earlier MACH-1 calculations which used the MC²-generated cross sections for the inner core zone everywhere in the ZPPR-2 mockup regions. Considering the one-dimensional approximation and the cross sections generated for a single zone for the MACH-1 calculations, a difference of this magnitude is not surprising. In fact, the reactivity worth of U-238 at the core center (in Table II-16-XIII) is 6% higher than the MACH-1 value, but the central sodium worth was found to be 50% higher than the MACH-1 value. In

TABLE II-16-XIII. Reactivity Worths of Plutonium, Uranium, and Sodium

Region Description	Reactivity Worth of Isotope, $10^{-4}\,\Delta k/k^2$-kg[a]				
	Pu-239	Pu-240	U-235	U-238	Na
Core center	14.0	+1.356	11.75	−0.91	−0.41
Axial average near core axis	9.8	+0.93	8.3	−0.58	−0.066
Inner zone radial average near the core midplane	10.97	+1.13	9.13	−0.69	−0.30
Inner core zone average	7.74	+0.79	6.5	−0.45	−0.04
Outer core zone average	3.40	+0.71	2.4	−0.12	+0.19
Inner zone radial average near the core-axial blanket boundary	3.07	+0.20	2.82	−0.095	+0.31
Inner zone axial average near the two core zone boundary	5.5	+0.704	4.47	−0.30	+0.01
Outer zone axial average near the core radius, 80 cm	3.74	+0.545	2.82	−0.14	+0.18
Outer zone radial average near the core midplane	5.52	+0.734	3.96	−0.22	−0.17
Outer zone radial average near the core-axial blanket boundary	1.06	+0.132	1.14	−0.02	+0.22

[a] k = 0.9725.

addition to the central reactivity worth, the inner zone and outer zone average reactivity worths near the core axis and near the core radius of 80 cm are also given. The outer core zone is split into equal volumes at a core radius of about 80 cm. The reactivity worths near the core and axial blanket boundary averaged radially over the inner zone and over the outer core zone are also given in Table II-16-XIII.

Conclusions

From the foregoing discussions and the information available to date, the following conclusions are made:

1) The cells chosen for the ZPPR-2 can be adequately approximated by the simple two-region equivalence principle for heterogeneous resonance self-shielding. The resonance self-shielding heterogeneity effect was calculated to be 0.6% k.
2) The transport flux-weighting over the core cells in ZPPR-2 resulted in a spatial heterogeneity on the eigenvalue, k, of 1.3%. The total heterogeneity effect in ZPPR-2 is, therefore, 1.9% k.
3) The calculated eigenvalue of the system using ENDF/B (1968) cross sections was 0.994 which includes heterogeneity effects and 0.35% transport effect correction. The good prediction in the two-dimensional criticality calculation with the ENDF/B (1968) data for ZPPR-2 is fortuitous and must be due to the cancellation of errors, because the capture-to-fission cross section ratio alpha in Pu-239 alone can change the eigenvalue by 1.5% if the high alpha values are used instead of the low values in the ENDF/B (1968) data.
4) The measured critical mass in the initial as-built ZPPR-2 was 1066 kg (Pu-239 + Pu-241), which is to be compared with the calculated critical mass of 1095 kg using the ENDF/B (1968).

References

1. B. J. Toppel, Ed., *The Argonne Reactor Computation (ARC) System* ANL-7332 (1967).
2. R. W. Hardie and W. W. Little, Jr., *1DX, A One-Dimensional Diffusion Code for Generating Effective Nuclear Cross Sections*, BNWL-954 (1969).
3. F. L. Fillmore and L. D. Felten, *The CALHET-2 Heterogeneous Perturbation Theory Code and Application to ZPR-3-48*, AI-69-13 (1969).
4. J. P. Plummer and R. G. Palmer, *Extended Equivalence Between Homogeneous and Heterogeneous Resonance Integrals in Slabs*, Trans. Am. Nucl. Soc. **12**, 625 (1969).
5. R. W. Goin and J. P. Plummer, *A One-Dimensional S_n Transport Theory Code for the CDC-3600*, ANL-7406 (to be published).
6. R. Gwin et al., *Measurements of the Neutron Fission and Absorption Cross Sections of ^{239}Pu Over the Energy Region 0.02 eV to 30 keV*, Nucl. Sci. Eng. **40**, 306 (1970).

II-17. Zero Power Plutonium Reactor (ZPPR) Assembly 2 Noise Studies

W. K. Lehto

A polarity correlation system which utilizes the SEL-840 computer has been implemented to do noise studies on the ZPPR critical assemblies. The system samples the instantaneous sign of the analog signal from each of two detectors and calculates the polarity cross-correlation function. The system is patterned after Cohn's[1] system and is shown schematically in Fig. II-17-1. Data from each detector are used as input to trigger circuits which sense the level of the input (positive or negative) and generate a corresponding logic signal. The logic signals are time sampled by a computer-controlled shift register. After input of a set number of 24-bit words, the correlation function is calculated and displayed as a printout and on the CRT. The dual registers and exclusive-or instructions of the computer permit a considerable reduction in calculational time over that required in computers not similarly equipped. The cross-correlation function is calculated for 24 delays from 1000 input words sampled at a bit rate of up to 20 μsec/bit, with continuous updating.

Additional flexibility has been incorporated into this system by the addition of an ex-or gate and a reversing scaler which allows measurements of the polarity coherence function.[2] The positive and negative signals from the trigger circuits are compared by the ex-or gate which provides a positive logic signal whenever the inputs are in phase and a negative signal when they are out of phase. These signals instruct a reversing scaler to count external clock pulses up or down. The net result is related to the coherence function by

$$\rho = \sin \frac{\pi}{2} C(t)$$

where ρ is the coherence function and $C(t)$ is the ratio

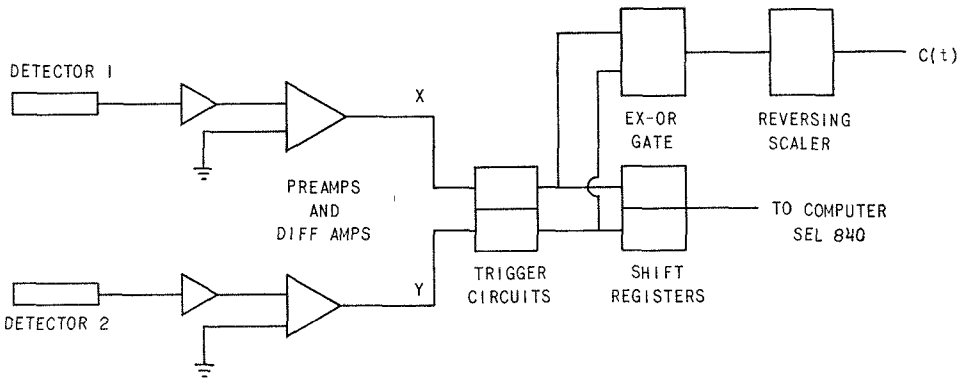

FIG. II-17-1. Schematic of the Polarity Correlation Experiment. *ANL Neg. No. 116-389.*

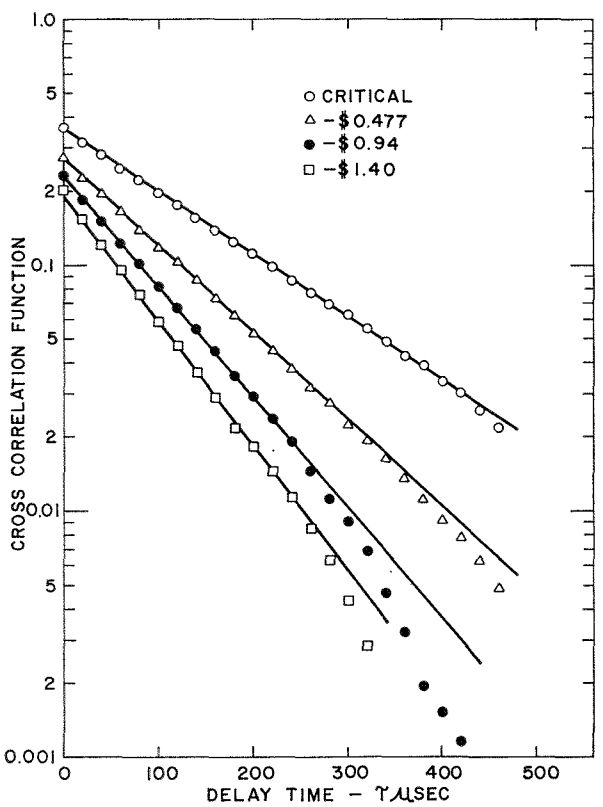

FIG. II-17-2. ZPPR Assembly 2 Polarity Correlation Functions. *ANL-ID-103-A11384.*

of the scaler counts to the total number of clock pulses. The coherence function is related to reactivity. This system is expected to be used to supplement other methods of measuring large negative reactivities.

Typical measured polarity correlation functions are shown in Fig. II-17-2 for several degrees of subcriticality. The decay constant at critical, $\alpha_c = \beta_{eff}/\ell$, was extracted from the data by a least squares fit of the function $C_{12}(\tau) = A_1 + A_2 e^{-\alpha\tau}$ to the data. The experimental critical alpha was 6003 ± 120 sec^{-1}. Calculated values of 6340 sec^{-1} and 6280 sec^{-1} were obtained from a MACH-1 spherical geometry calculation, and from a two-dimensional diffusion theory perturbation calculation, respectively. ENDF/B cross sections were used for both calculations.

The agreement between the calculation and measurement is considered adequate. It should be noted that the calculated value is higher than the experimental value, consistent with other studies.[3]

REFERENCES

1. C. E. Cohn, *Reactor Noise Studies with an On-Line Digital Computer*, Nucl. Appl. **6**, 391 (1969).
2. W. Seifritz, *The Polarity Correlation of Reactor Noise in the Frequency Domain*, Nucl. Appl. and Tech. **7**, 513 (1969).
3. W. K. Lehto, *Pulsed Neutron Experiments in ZPR-3 Assemblies 53 and 54*, Reactor Physics Division Annual Report, July 1, 1968 to June 30, 1969, ANL-7610, p. 94.

II-18. Fast Neutron Spectrum Measurements in the Zero Power Plutonium Reactor (ZPPR) and ZPR-3 Critical Assemblies

G. G. Simons

Introduction

A description of previously unreported fast-neutron spectrum measurements completed at the ZPPR and ZPR-3 reactors are presented in chronological order. Both the data acquisition system and the analysis methods were improved during this period. Each specific spectrometer configuration and analysis technique used for the critical assemblies are reported. Moreover, each counter/drawer arrangement used is shown.

Experimental Equipment

Two pairs of cylindrical proportional counters, two different electronic configurations, and four counter/drawer configurations were used to complete these spectrum measurements. Standardization of the basic associated electronics is nearing completion (see Paper III-17). However the optimum choice of counter pair and counter/drawer configurations depends on the specific reactor environment in which the neutron spectra are being studied. The various counter/drawer configurations used for each spectrum measurement are discussed under Fast Neutron Spectra Measured.

One pair of proportional counters used included a 5 atm total pressure, predominately hydrogen-filled counter, 1.59 cm in diam, and a 5 atm total pressure, predominately methane-filled, 2.54 cm diam counter. The other pair of counters consisted of a 0.953 cm diam hydrogen-filled counter containing 10 atm of total pressure and a 1.59 cm diam methane-filled counter with 8.2 atm of predominantly methane gas. All four counters had a 0.70 mil anode and a sensitive length of two diameters. Each counter also contained a small amount of nitrogen gas for calibration.

Data were generally obtained with the hydrogen-filled counters using either five or six high-voltage settings. The number of high voltages used depended upon the desired fractional overlap between data sets and on the total energy range spanned by the chamber. Typically, for six high voltages, proton recoil data of the hydrogen chambers covered the energy range from about 0.4 to 110 keV with a 30% overlap.

Three high voltage settings were used to cover the energy range from about 90 keV to 2.4 MeV with the methane-filled chambers.

The smaller pair of counters was used for the ZPPR Assembly 2 and the ZPR-3 EBR-2 series of spectra studies. Advantage was taken of the reduced counter efficiency to measure neutron spectra under more severe gamma ray background conditions and in a higher neutron field than was possible with the larger chambers. It was therefore possible to diminish the problems associated with exceeding the count-rate limitations imposed upon the electronics.

All of the reported spectra were measured with the associated electronics operating in a dual-parameter, gamma ray discrimination mode with a Data Machines 622 on-line, 18-bit, 8K computer. However, the associated electronics used to obtain the ZPPR-1/FTR-2 and ZPR-3 Assembly 58 data consisted of a basic system similar to that shown in Fig. III-17-1 without the pulse selector and two linear gates. For all measurements following ZPR-3 Assembly 58 measurements, the improved high-count-rate electronics shown in Fig. III-17-1, including pulse pile-up rejection circuitry, were used. Proper operation of this new spectrometer at count rates exceeding 30,000 cps for the methane counter and 10,000 cps for the hydrogen counter was verified in the Argonne Fast Source Reactor (AFSR). The maximum possible count rate limit has not been determined for this system. The upper limit will be set by the saturation-inducing events in the hydrogen counter.

Detector Calibration

Both the hydrogen and the methane-filled counters were calibrated in the AFSR thermal column just prior to each neutron spectrum measurement. This was a standard calibration procedure, which used the monoenergetic protons from the $N^{14}(n,p)C^{14}$ reaction induced by thermal neutrons in the nitrogen gas within the detector chambers to determine a relationship between gas multiplication (A) and voltage (V) for each counter. The calibration data were reduced on the Data Machines 622 computer using a new FORTRAN code (see Ref. 1). This code performs a least-squares fit to the straight-line relation $(\ln A)/V^x$ versus V, where x is a variable parameter chosen to minimize the sum of the squared errors associated with the fit.

During data acquisition, a precision reference pulser was used to determine recoil proton keV per channel based on settings obtained during calibration.

Data Reduction

Two codes, the original PSNS[2] and a newer code PSNS-X[1], both operational on the ZPPR SEL 840MP computer, are available for data analysis. Raw pro-

ton-recoil data for ZPPR-1/FTR-2 and ZPR-3 Assembly 58 (data accumulated with the larger pair of counters) were analyzed with PSNS since PSNS-X was not operational at that time. The PSNS-X code was used to analyze the other reported data.

The two data sets analyzed with PSNS were corrected for detector response distortions using measured response functions. They were also corrected for carbon recoils. However W (energy loss per ion pair) for hydrogen and methane was assumed constant for all proton energies.

The PSNS-X code corrected the raw proton data for distortions induced by non-uniform electric fields at the counter ends and for carbon recoils. These electric field corrections were based on calculated response functions for each detector.[1] Also, the energy-dependent variation in W for the low-energy hydrogen-filled counter data was included in the analysis according to a prescription based on data taken by Werle et al.[3]

Fast Neutron Spectra Measured

ZPPR-1/FTR-2

Neutron spectrum measurements were made over the energy range from 329 eV to 2.37 MeV in both the reflector and shield. The spectra were measured close

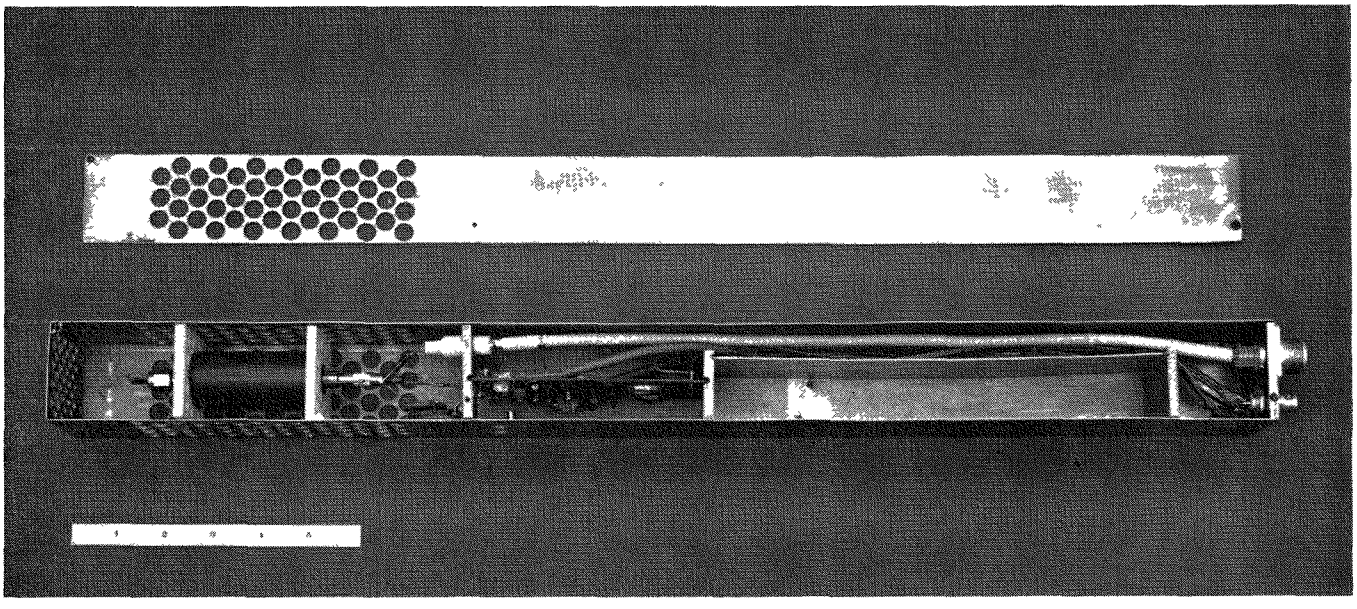

Fig. II-18-1. Matrix Drawer Containing the 1.59 cm diam Hydrogen Proportional Counter and Preamplifier. *ANL-ID-103-A11292*

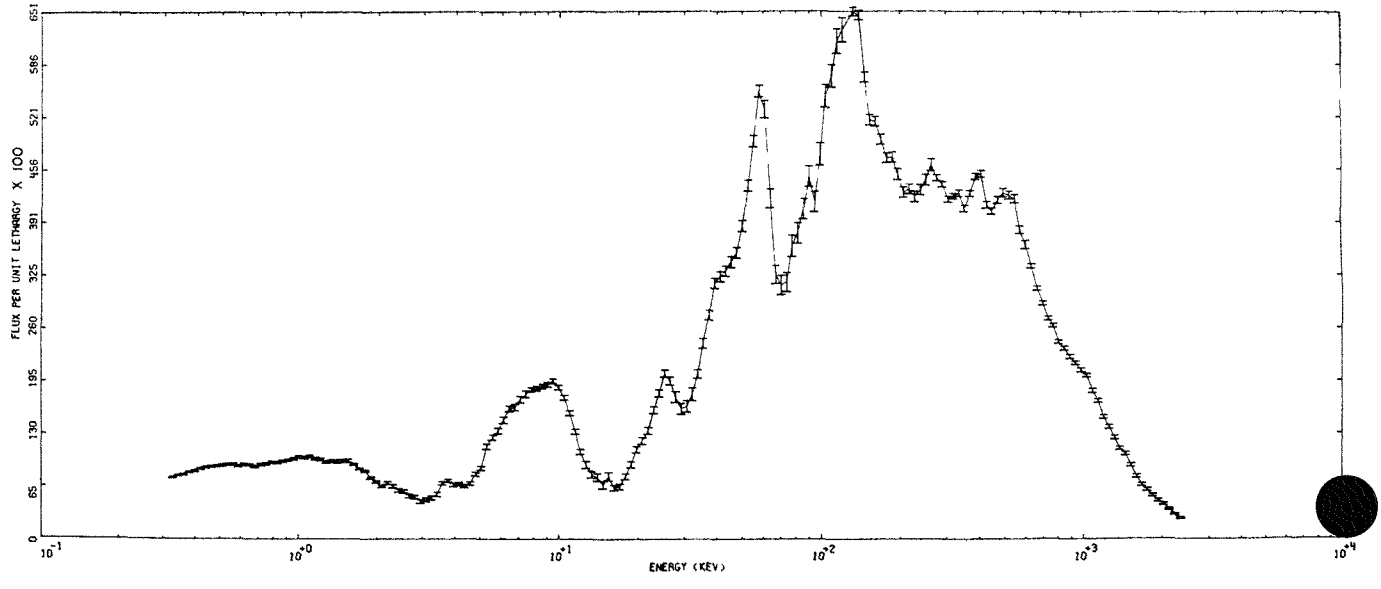

Fig. II-18-2. ZPPR-1/FTR-2 Reflector Neutron Spectrum at Matrix Position 137-23. *ANL-ID-103-A11184.*

the axial midplane in matrix positions 137-23 and 137-15. This corresponded to locations near the center of the reflector and shield annuli, respectively.

Figure II-18-1 shows the detector drawer containing the 1.59 cm diam hydrogen-filled counter and preamplifier. As shown, the counter was encased in a 0.25-in.-thick lead sleeve.

The neutron spectrum measured in the reflector is shown in Fig. II-18-2. For this measurement, the fueled safety, control, and poison safety rods were completely withdrawn. Under these conditions, the reactor was 1.67% $\Delta k/k$ subcritical.

During the shield-spectrum measurement (see Fig. II-18-3) the reactor was 0.0896% $\Delta k/k$ subcritical. All the poison rods were completely withdrawn. Also, Control Rods No. 1 at (135-39), No. 3 at (139-43), and No. 4 at (239-43) were completely withdrawn. Control Rods No. 2 at (239-35) and No. 5 at (139-35) and all fueled safety rods were completely inserted, while Control Rod No. 6 at (235-39) was withdrawn 1.704 in.

The data in the reflector spectrum clearly indicate the presence of the nickel, which has large cross-section resonances at 15.5 and 65 keV. The cross-section minima in the nickel and iron at about 30 keV and slightly above 100 keV are evident, as well as the sodium resonance at 2.8 keV.

Since the shield was composed primarily of stainless

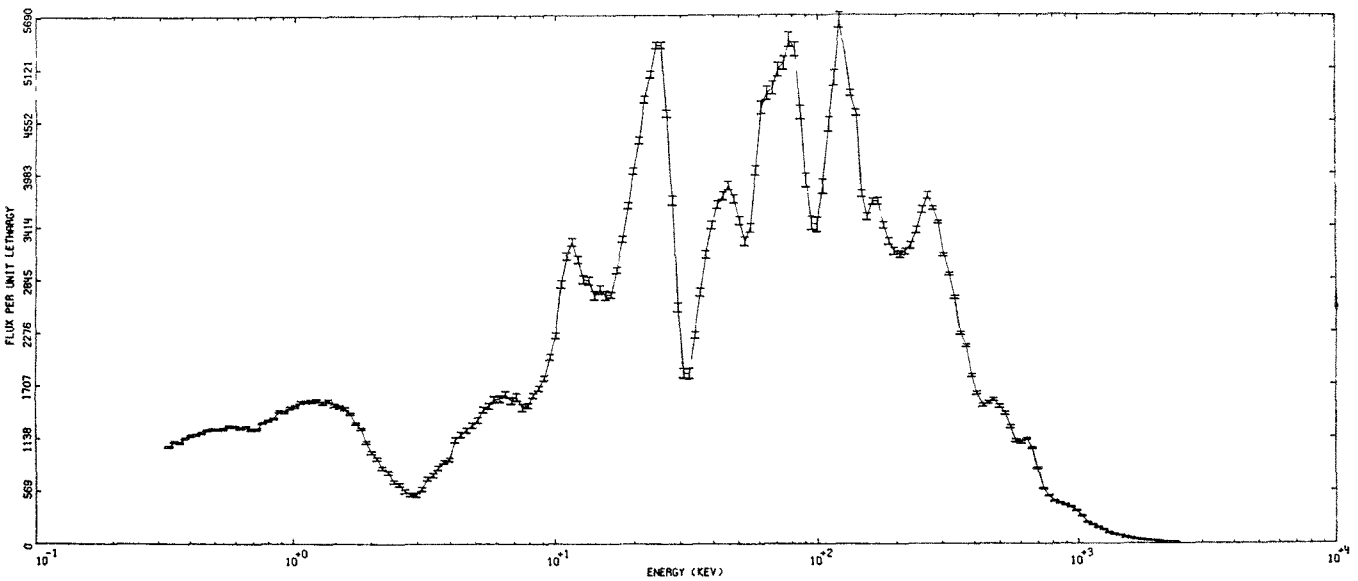

FIG. II-18-3. ZPPR-1/FTR-2 Shield Neutron Spectrum Measured at Position 137-15. *ANL-ID-103-A11183.*

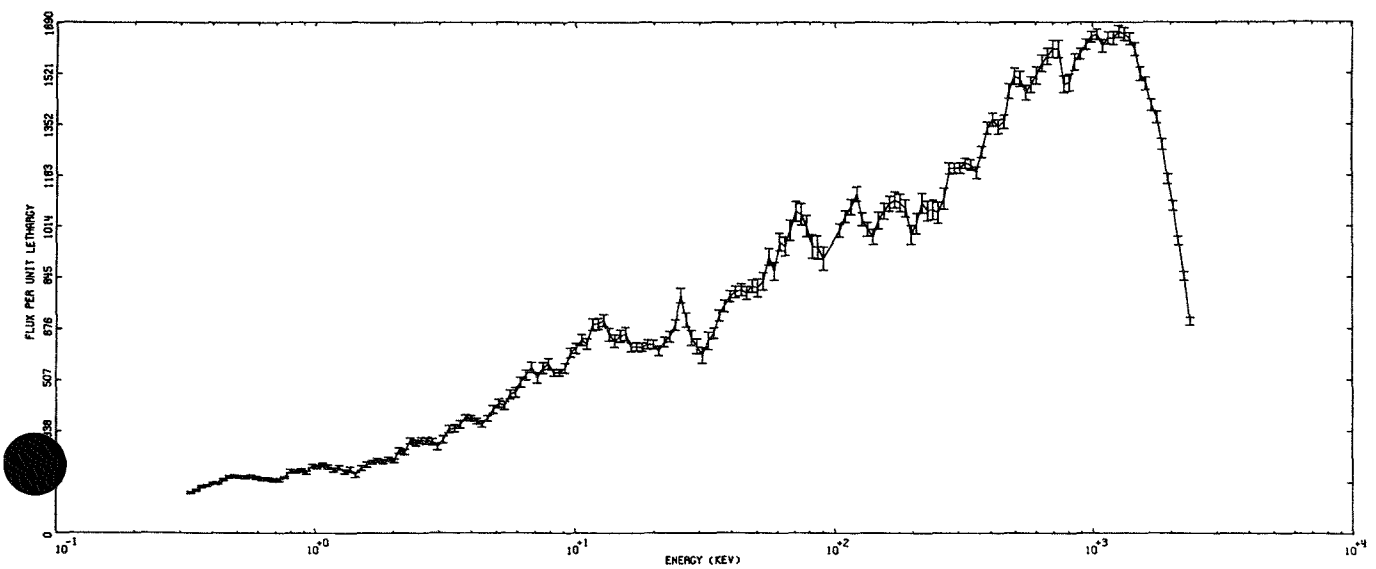

FIG. II-18-4. ZPR-3 Assembly 58 Neutron Spectrum Measured at Position 1-P-16. *ANL-ID-103-A2021.*

steel, the major spectrum shape in the shield is a result of the large iron cross-section resonances. However, the chromium resonance at 53 keV and the sodium resonance at 2.8 keV account for the flux depressions at these energies.

ZPR-3 ASSEMBLY 58

The fast neutron spectrum was measured over the energy range 0.33 keV to 2.37 MeV near the center of Assembly 58 (see Fig. II-18-4). For this measurement,

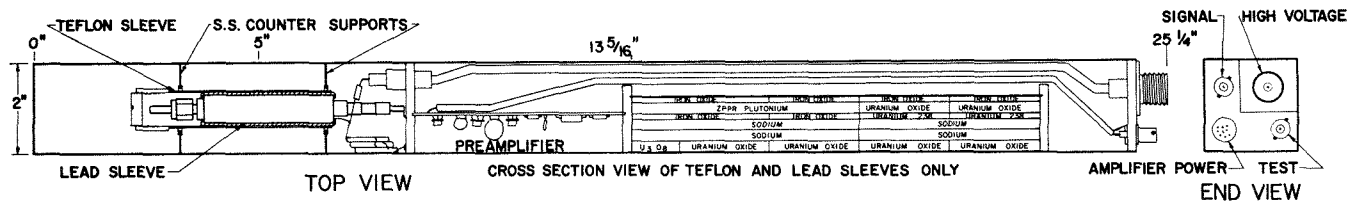

METHANE GAS FILLED PROTON RECOIL PROPORTIONAL COUNTER LOADED IN A MATRIX DRAWER

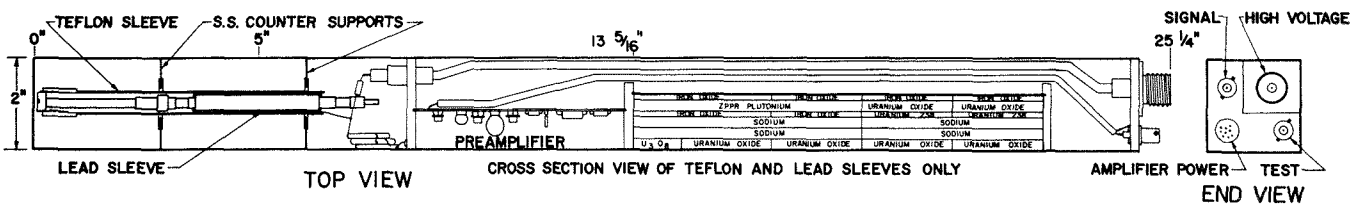

HYDROGEN GAS FILLED PROTON RECOIL PROPORTIONAL COUNTER LOADED IN A MATRIX DRAWER

FIG. II-18-5. Proportional-Counter Drawer Configurations Used in ZPPR Assembly 2. *ANL-ID-103-11317.*

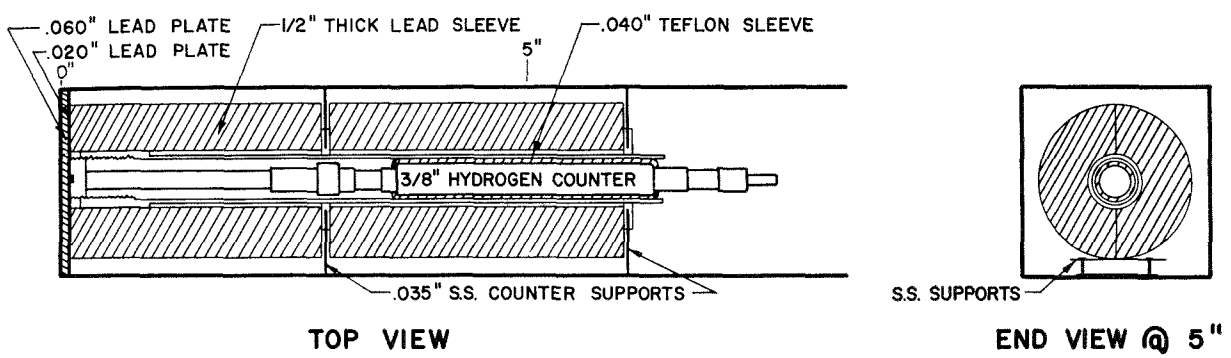

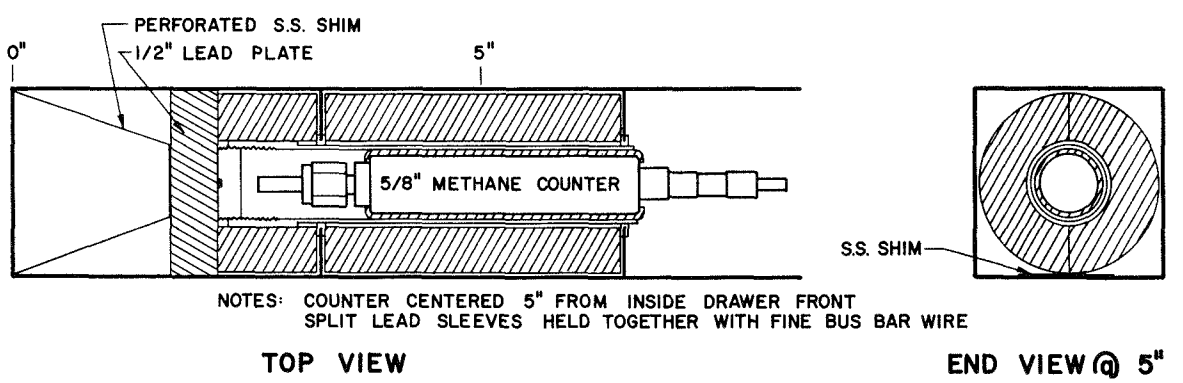

FIG. II-18-6. Proton-Recoil Proportional Counters Encased in Lead for ZPPR Assembly 2. *ANL-ID-103-A11316.*

The counter pair and matrix/drawer configuration were both the same as those used in ZPPR-1/FTR-2. The counters were positioned in matrix position 1-P-16 with their centers of active volumes four inches from the reactor interface.

The rate of ionization in the detectors from neutrons plus gamma rays in the critical configuration with all control and safety rods withdrawn was too high for proper operation of the spectrometer system. Therefore, some of the outermost core drawers were removed from the reactor and replaced by radial reflector. The core outline at the loading used contained 70 matrix positions in Half 1 and 69 matrix positions in Half 2. The measurements were made with no core material in position 1-P-16, and all the control and safety rods withdrawn, i.e., at close to 7% $\Delta k/k$ subcritical.

This relatively soft neutron spectrum clearly reflects the presence of the iron in the core, especially at approximately 30 and 85 keV which correspond to two large iron resonance regions. Similarly, other flux depressions may be attributable either to further iron resonances or to nickel, chromium and aluminum reso-

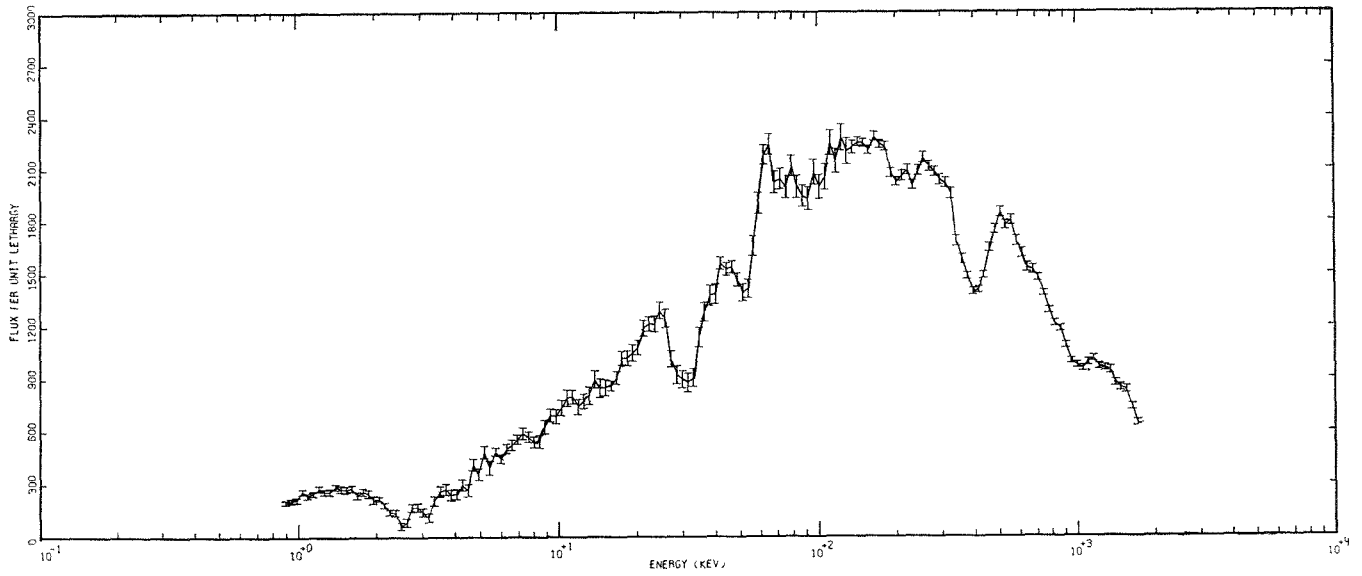

FIG. II-18-7. ZPPR Assembly 2 Neutron Spectrum from Lead-Covered Detectors in Matrix Position 137-37. *ANL-ID-103-A11410*

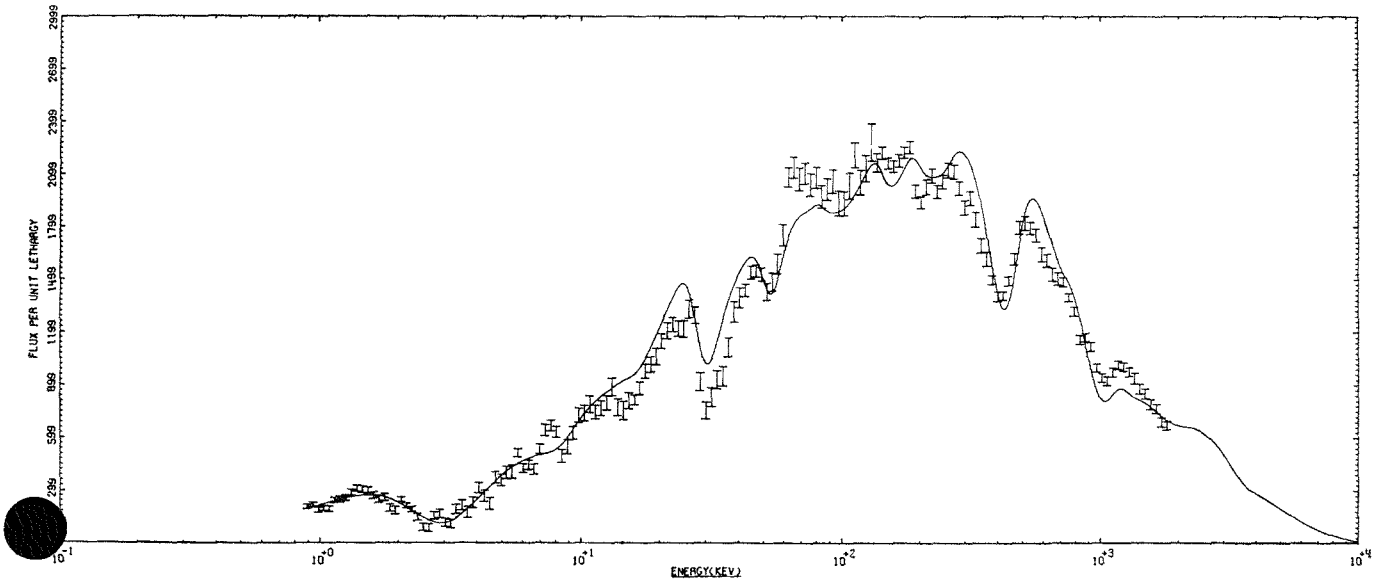

FIG. II-18-8. ZPPR Assembly 2 Experimental and Smoothed MC² Calculated Spectra at Matrix Location 137-37. *ANL-ID-103-A11412.*

nances. It is difficult to truly evaluate the causes of these flux depressions because of the basic overall lack of structure present in the spectrum.

ZPPR-2

Three fast-neutron spectrum measurements were made over the energy range 0.9 keV to 1.8 MeV at two locations in ZPPR Assembly 2. This was the first assembly in which the neutron spectra were measured with the smaller pair of proportional counters. The counters positioned with their centers of active volumes five inches from the reactor interface were contained in partially voided drawers in matrix position 137-37 and 127-47. Figure II-18-5 shows these drawer configurations containing the two counters, preamplifiers, and reactor materials.

The central measurement configuration, made at approximately 2% $\Delta k/k$ subcritical, consisted of replacing the core drawer in position 137-37 with the counter drawer and withdrawing all control and poison rods. For the outer-core measurement, poison rods Nos. 5, 7, 10, and 18 and all control rods were withdrawn. The reactor was 1.4% $\Delta k/k$ subcritical.

An auxiliary experiment was run in location 137-37,

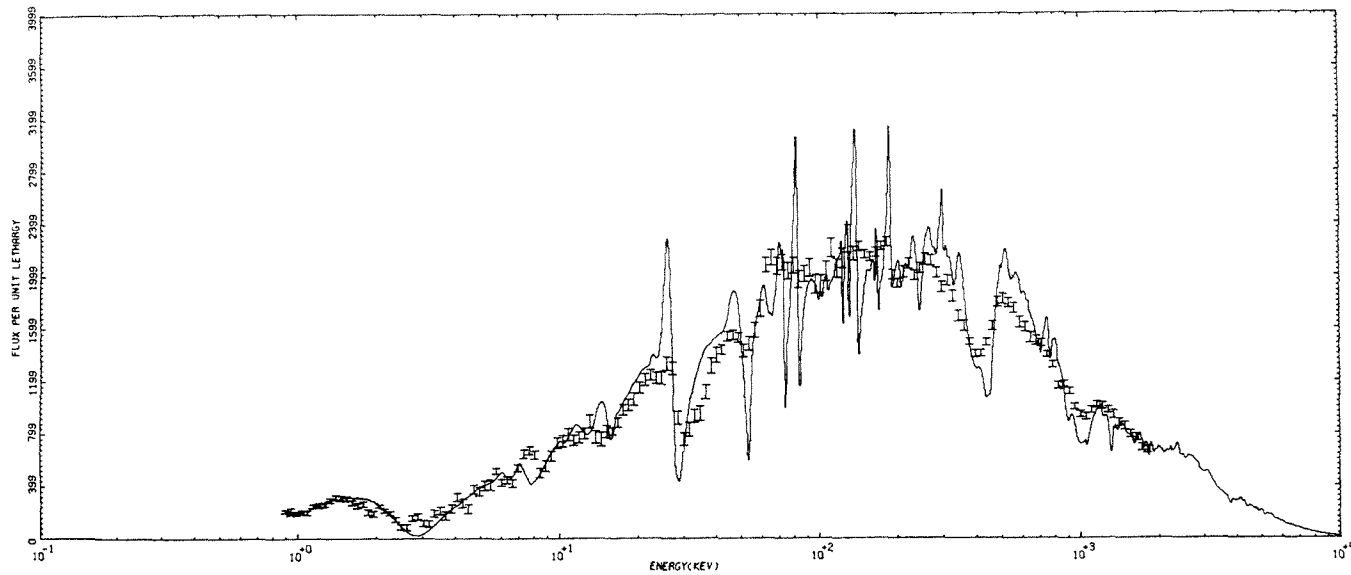

FIG. II-18-9. ZPPR Assembly 2 Experimental and Ultrafine MC² Calculated Spectra at Matrix Location 137-37. *ANL-ID-103-A11413.*

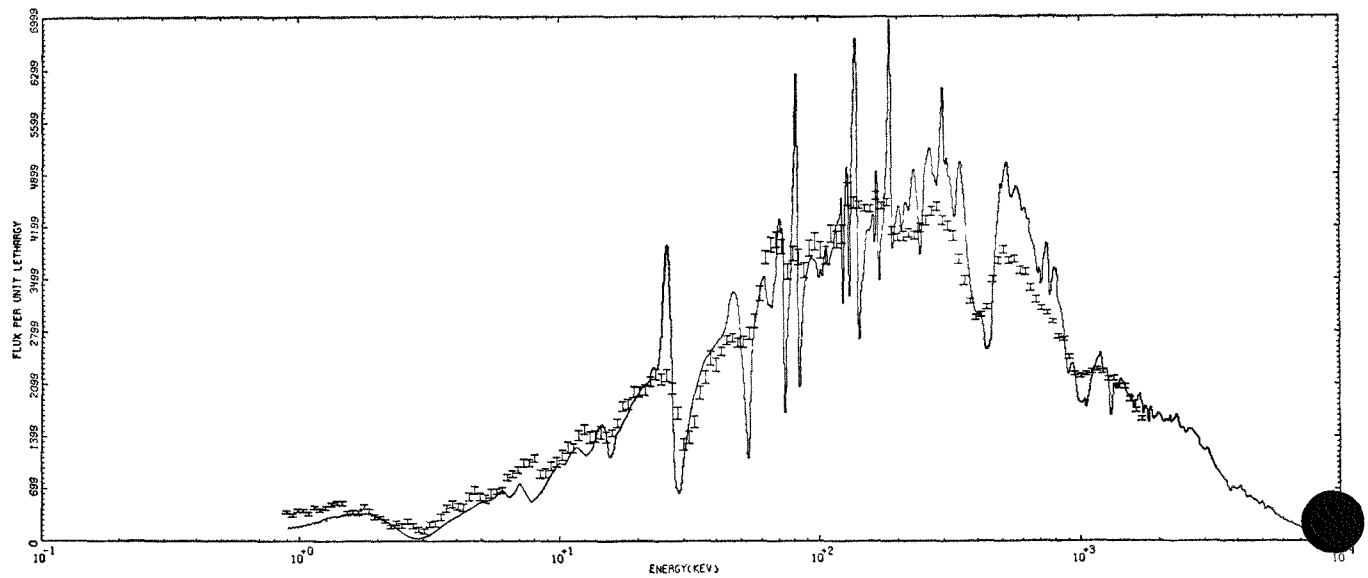

FIG. II-18-10. ZPPR Assembly 2 Experimental and Ultrafine MC² Calculated Spectra at Matrix Location 127-47. *ANL-ID-103-A11411.*

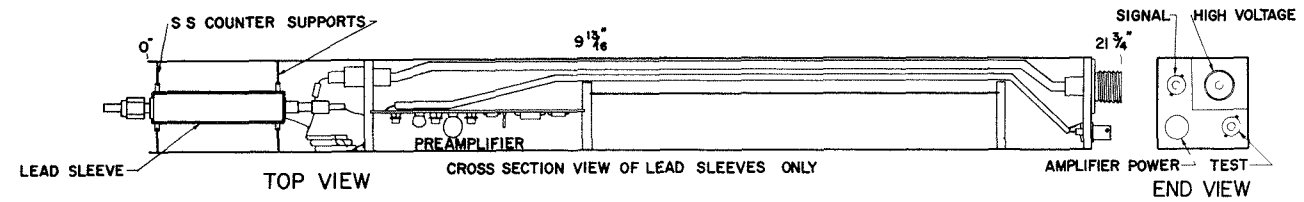

METHANE GAS FILLED PROTON RECOIL PROPORTIONAL COUNTER LOADED IN A MATRIX DRAWER

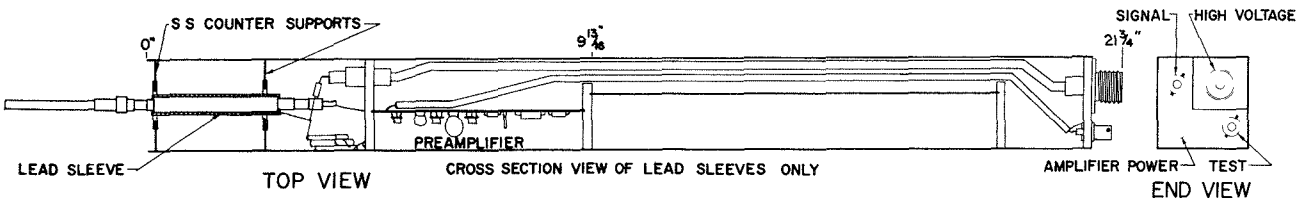

HYDROGEN GAS FILLED PROTON RECOIL PROPORTIONAL COUNTER LOADED IN A MATRIX DRAWER

FIG. II-18-11. Proportional-Counter Drawer Configurations Used in ZPR-3 Assembly 61. *ANL-ID-103-A11472.*

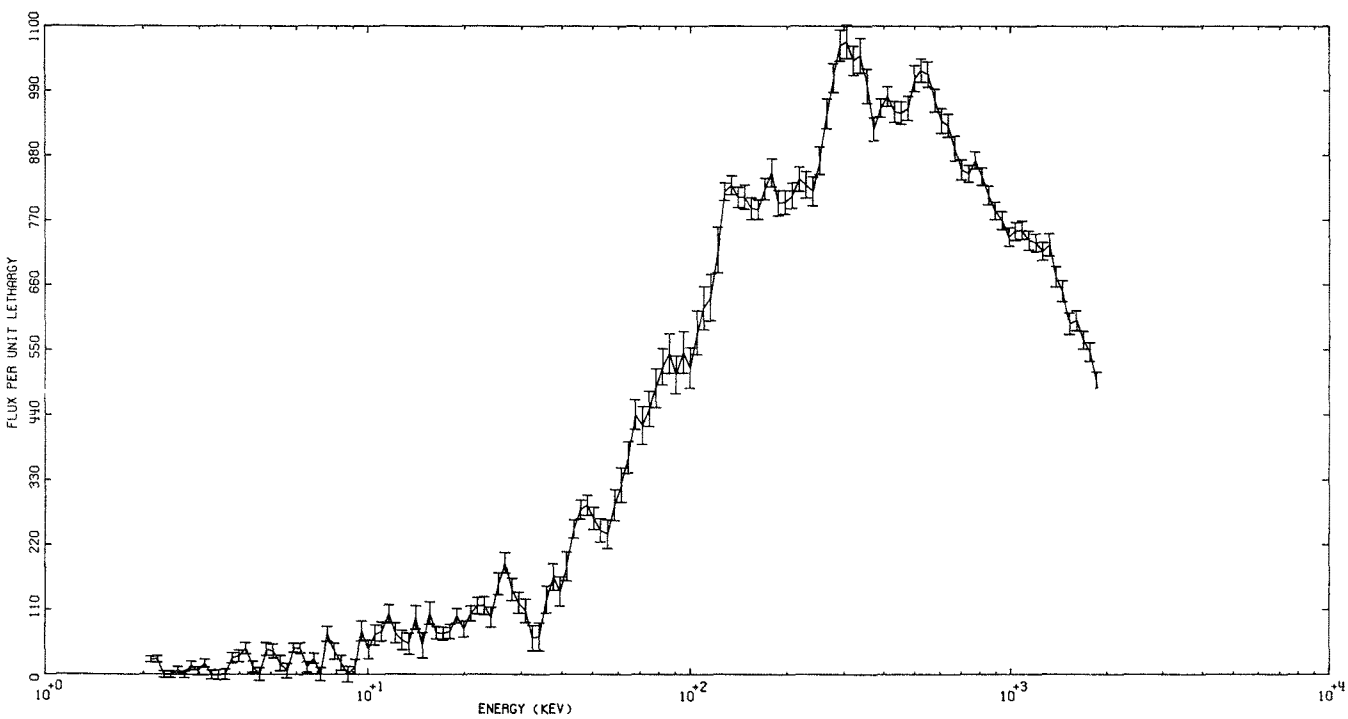

FIG. II-18-12. ZPR-3 Assembly 61 Neutron Spectrum Measured in Location 1-P-16 (Core Center) with the Proton-Recoil Proportional Counters. *ANL-ID-103-A2146.*

using the detector configurations shown in Fig. II-18-6 to ascertain the effect of encasing the detectors in ½ [illegible]f lead. Calculations were made which showed that [illegible]utron scattering in a lead sleeve would not appreciably change the neutron spectrum from 1 keV to 1 MeV.[4] The results of this experiment were required to determine if the lead would modify the neutron angular distribution such that the heterogeneity effect of the drawer loadings around the detectors would be decreased.

The two spectra measured at 137-37 are shown in Figs. II-18-7 and II-8-8. (Note that the smooth curve

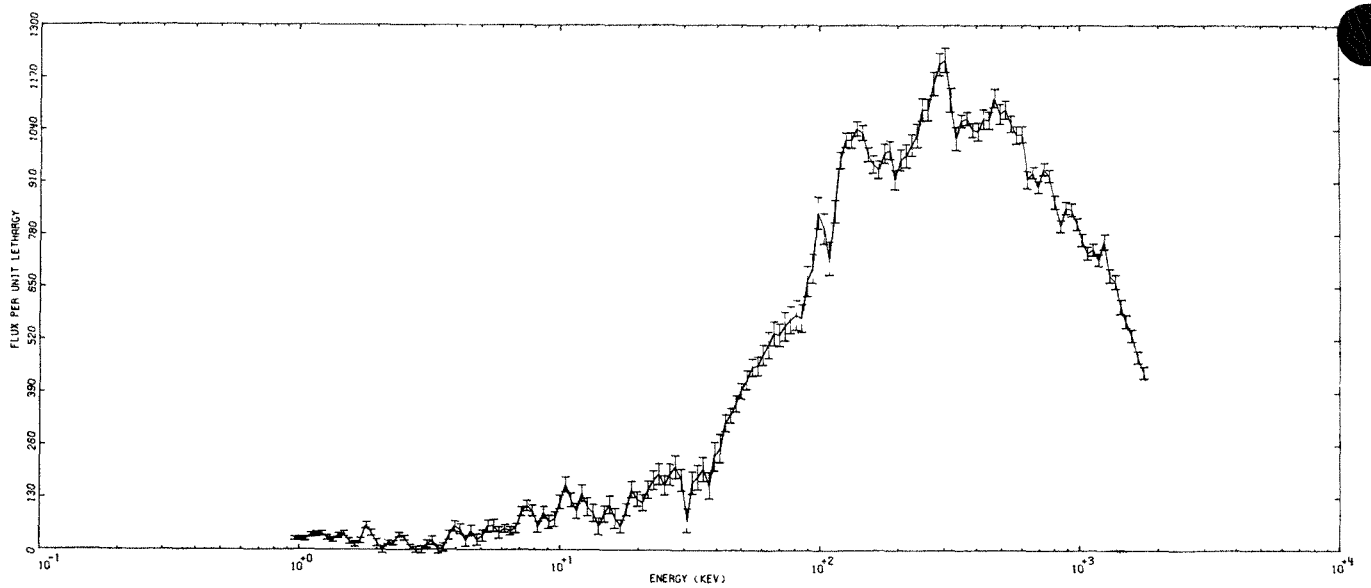

FIG. II-18-13. ZPR-3 Assembly 61 Neutron Spectrum Measured in Location 1-P-11 (Core Center) with the Proton-Recoil Proportional Counters. *ANL-ID-103-A11407.*

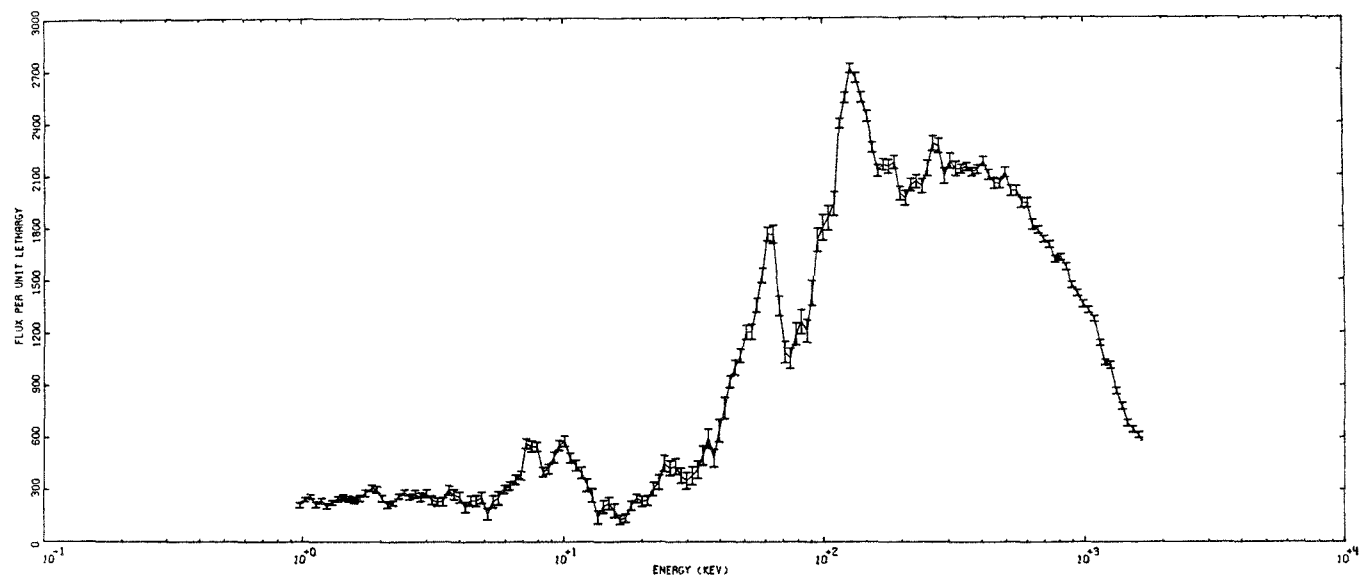

FIG. II-18-14. ZPR-3 Assembly 61 Neutron Spectrum Measured in Location 1-P-9 (Reflector) with the Proton-Recoil Proportional Counters. *ANL-ID-103-A11406.*

superimposed on the measured points in Fig. II-18-8 is the MC² calculated spectrum discussed below.) No measurable change resulted from encasing the detectors in ½ in. of lead. Thus the presence of lead did not aid in overcoming the heterogeneity of the plate-type environment in which the measurement was made. However, the lead sleeves could be used to decrease the gamma-ray background in this environment if the gamma-ray flux were too severe for otherwise proper operation of these detectors.

Figures II-18-9 and II-18-10 compare the measured spectra and a preliminary fundamental-mode, 1980-group calculation using the MC² code. The calculated flux at location 137-37, smoothed with an energy-dependent Gaussian window function, are shown in Fig. II-18-8. This fundamental-mode model should be valid near the core center. In the outer-core position (147-27), the actual neutron spectrum would be softer than the theoretical spectrum, as shown in Fig. II-18-10.

ZPR-3 ASSEMBLY 61

Neutron spectra were measured in matrix positions 1-P-16, 1-P-11 and 1-P-9. The counter/drawer configuration is shown in Fig. II-18-11, except that the voids at the back of the drawers contained reactor materials.

By removing the drawer ends, it was possible to position the center of the active detector volumes closer to the centerline of this small core. Thus the counter tips were extended into a void in matrix positions 2-P-16, 2-P-11 and 2-P-9. The three spectra are shown in Figs. II-18-12 through II-18-14. The relatively hard spectrum combined with the high residual gamma-ray background present at the core center (1-P-16) made it impossible to measure the neutron spectrum below 2.2 keV.

References

1. E. F. Bennett, Argonne National Laboratory (private communication).
2. E. F. Bennett, R. Gold and I. K. Olson, *Analysis and Reduction of Proton-Recoil Data*, ANL-7394 (1968).
3. H. Werle, G. Fieg, H. Seufert and D. Stegemann, *Investigation of the Specific Energy Loss of Protons in Hydrogen Above 1 keV with Regard to Neutron Spectrometry*, Nucl. Instr. Meth. **72,** 11 (1969).
4. A. P. Olson, Argonne National Laboratory (private communication).

II-19. ZPR-9 Assembly 25: Description axd Experimental Results

L. G. LeSage and W. R. Robinson

Introduction

Assembly 25 of ZPR-9 was a small, fast, uranium-fueled, zoned assembly with a null reactivity (i.e., $k_\infty = 1$) central test zone. The central zone, which was composed almost entirely of enriched and depleted uranium, had a relatively hard neutron energy spectrum with few resonance energy neutrons.

Assembly 25 was the third in a series of assemblies with null central zones. The other two, ZPR-9 Assembly 24 (a uranium assembly) and ZPR-3 Assembly 55 (a plutonium assembly), had relatively soft spectra due to about 50 volume percent graphite in the null zone; they were designed primarily for Pu-239 and U-235 capture-to-fission ratio measurements. The calculated broad group spectra for Assemblies 24 and 25 are shown in Fig. II-19-1 for comparison. The spectra of Assemblies 24 and 55 were similar. The results of the Assembly 24 and Assembly 55 measurements and a discussion of the null reactivity technique are included in Ref. 1.

From the measurements of the null composition and the various capture and fission ratios for U-235, U-238, and Pu-239 on Assemblies 24 and 55, it appeared that both the Pu-239 and U-238 fission rates were significantly underpredicted by the ENDF/B cross sections while the U-238 capture and the U-235 fission and capture rates were predicted correctly. Possible errors in the fission cross sections or a spectral effect resulting from an error in the U-238 inelastic scattering cross section[2] are suggested by these results. The soft spectra in Assemblies 24 and 55 made interpretation of the results difficult, however, because of the uncertainty in the resonance region heterogenity correction and the

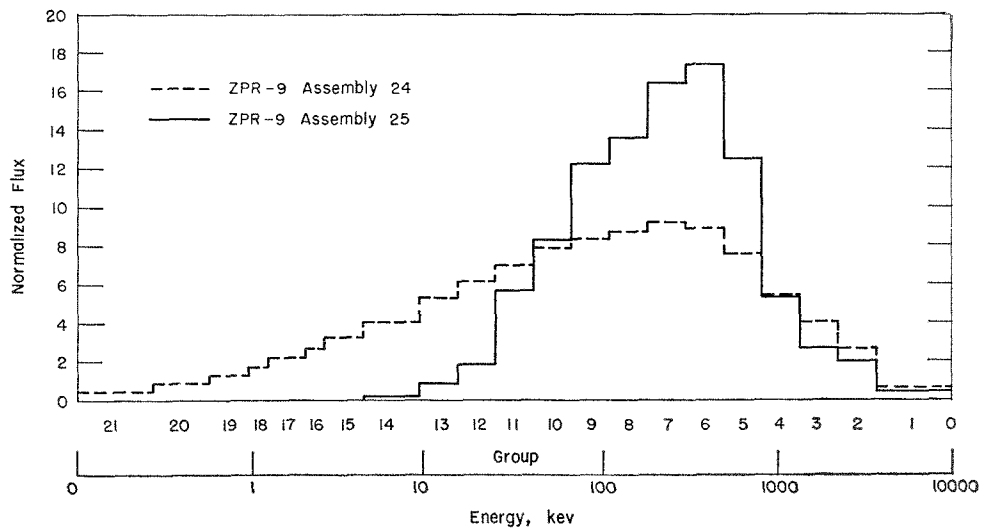

Fig. II-19-1. Calculated Central Null-Zone Spectra, Assemblies 24 and 25. *ANL Neg. No. 116-531.*

uncertainty in the alpha of Pu-239. The measurements planned for Assembly 25 were aimed at resolving some of the uncertainties in the U-238 and Pu-239 cross sections and, in addition, they were designed to complement the earlier measurements on Assemblies 24 and 55 in order to better isolate the energy regions of cross section uncertainty.

A description of Assembly 25 and the available experimental results are included in the following sections. The reaction rate measurements are currently being re-evaluated, however, so they are not included. Since these are the key measurements for evaluating the cross section uncertainties discussed above, neither a comparison of the results with analysis nor a detailed discussion of the results is included in this paper.

Description of Assembly 25

ZPR-9 Assembly 25 was a small, fast, cylindrical zoned critical assembly with a null central zone surrounded by concentric buffer, driver, and reflector regions as shown in Figs. II-19-2 and II-19-3.

Drawer plate loading arrangements are shown in Fig. II-19-4. The initial null central zone was composed primarily of enriched and depleted uranium with a small amount of 45% dense aluminum to fill out the drawers, and the stainless steel in the matrix and drawers. The calculated neutron spectrum in the central zone was relatively hard, with over 95% of the flux above 25 keV. The high energy part of the spectrum (>1 MeV) was also somewhat depleted due to the inelastic scattering in U-238.

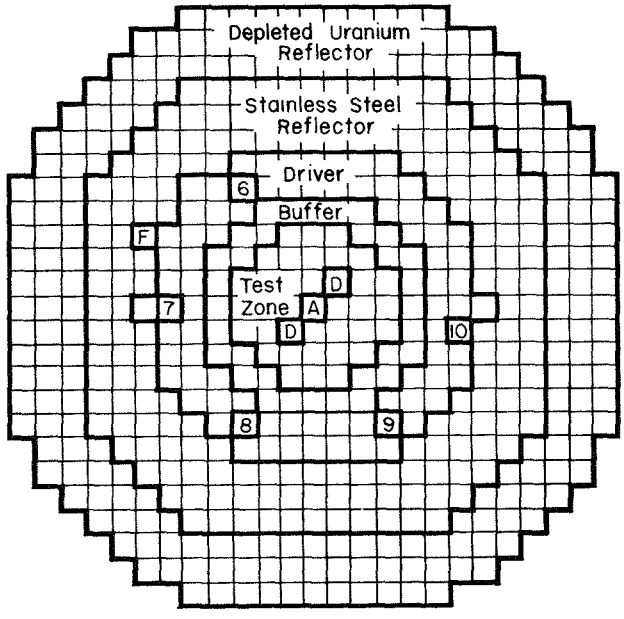

Fuel Bearing Control Rod: [6] Numbers 6 through 10
Fine Auto Rod: [F]
Axial Oscillator: [A]
Fission Detector: [D]

Fig. II-19-2. Radial Assembly Loading Pattern, ZPR-9 Assembly 25, Stationary Half. *ANL Neg. No. 116-533.*

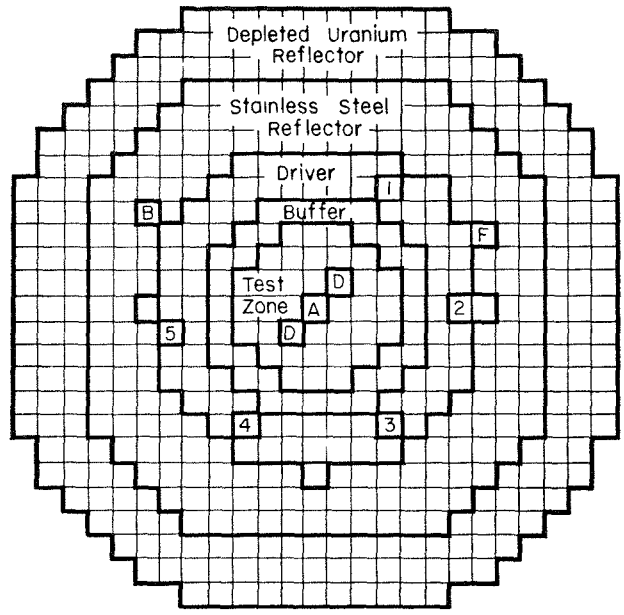

Fuel Bearing Control Rod: [1] Numbers 1 through 5
Fine Auto Rod: [F]
Axial Oscillator: [A]
Fission Detector: [D]
Boron Control Rod: [B]

Fig. II-19-3. Radial Assembly Loading Pattern, ZPR-9 Assembly 25, Movable Half. *ANL Neg. No. 116-532.*

The enriched uranium-fueled driver contained about 64 volume percent graphite to make it more reactive and to reduce the required critical loading. The buffer contained about 74 volume percent depleted uranium and 11 volume percent aluminum. Its effect was to considerably harden the relatively soft spectrum entering from the driver and better match it to the characteristic spectrum of the null zone. The ratios of enriched uranium to graphite in the driver and of depleted uranium to aluminum in the buffer were varied considerably in the design studies in order to balance the competing demands of low critical mass and optimum spectral matching in the null zone.

An elevation drawing of the assembly is shown in Fig. II-19-5. Thickness of the stainless steel drawer ends and of the spring gap are included in the axial dimension. Nickel plates in the axial reflector were included to further reduce the critical loading and to slightly flatten the axial power. The thickness of nickel

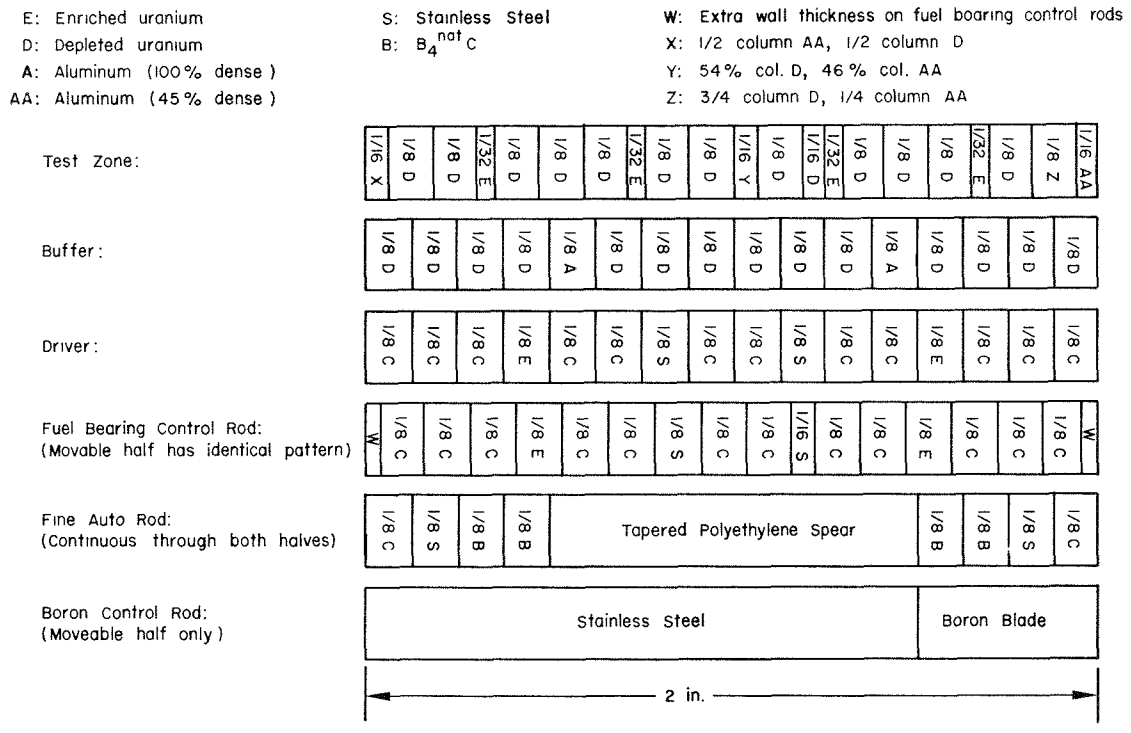

FIG. II-19-4. Drawer Loading Patterns, ZPR-9 Assembly 25. *ANL Neg. No. 116-529.*

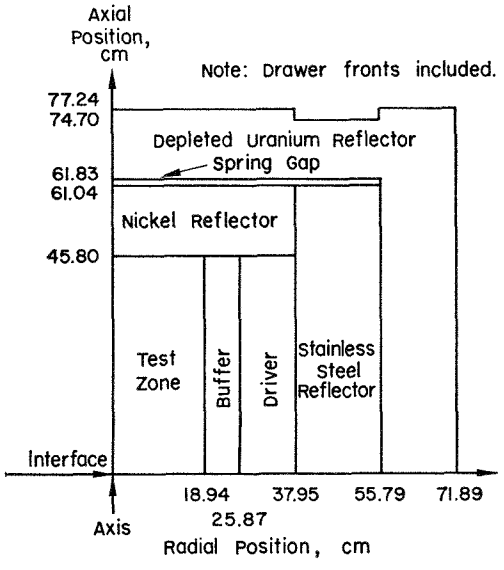

FIG. II-19-5. Elevation Drawing, ZPR-9 Assembly 25. *ANL Neg. No. 116-527.*

in the axial reflector was limited by the available supply at the time of Assembly 25.

Table II-19-I lists the regional averaged homogeneous atomic concentrations, the critical mass, measured control rod worths, and the calculated kinetic parameters for Assembly 25. The void caused by a partially inserted control rod at the critical condition has been averaged over the entire driver region, thus reducing the critical mass and the atomic concentration.

Two additional null composition zones, designated as zones 2 and 3, were constructed inside the initial null zone loaded into Assembly 25, as indicated in Fig. II-19-6. The unit-cell loading in the first null zone, designated as zone 1, contained four $\frac{1}{32}$ in. enriched uranium plates distributed uniformly in the drawer.

TABLE II-19-I. ZPR-9 ASSEMBLY 25 PARAMETERS

Atomic Concentrations, 10^{21} atoms/cm^3

Material	Null Zone 1	Buffer	Driver	Stainless Steel Reflector	Depleted Reflector
U-234	0.020	—	0.044	—	—
U-235	2.140	0.073	4.474	—	0.081
U-236	0.010	—	0.021	—	—
U-238	33.233	33.959	0.255	—	39.930
C	—	—	51.218	—	—
Al	1.649	6.255	—	—	—
Fe	6.837	6.837	12.907	56.472	4.332
Cr	1.952	1.952	3.684	16.115	1.140
Ni	0.864	0.864	1.631	7.136	0.540

Critical mass, kg U-235	475.3
Measured dual purpose fuel bearing control rod worths, % $\Delta k/k$	
control rods 1, 2, 3, 4, 6, 7, 8, 9	0.24
control rods 5, 10	0.29
Prompt neutron lifetime, sec	2.95×10^{-7}
Effective delayed neutron fraction	7.09×10^{-3}
Ih/%$\Delta k/k$	432.8

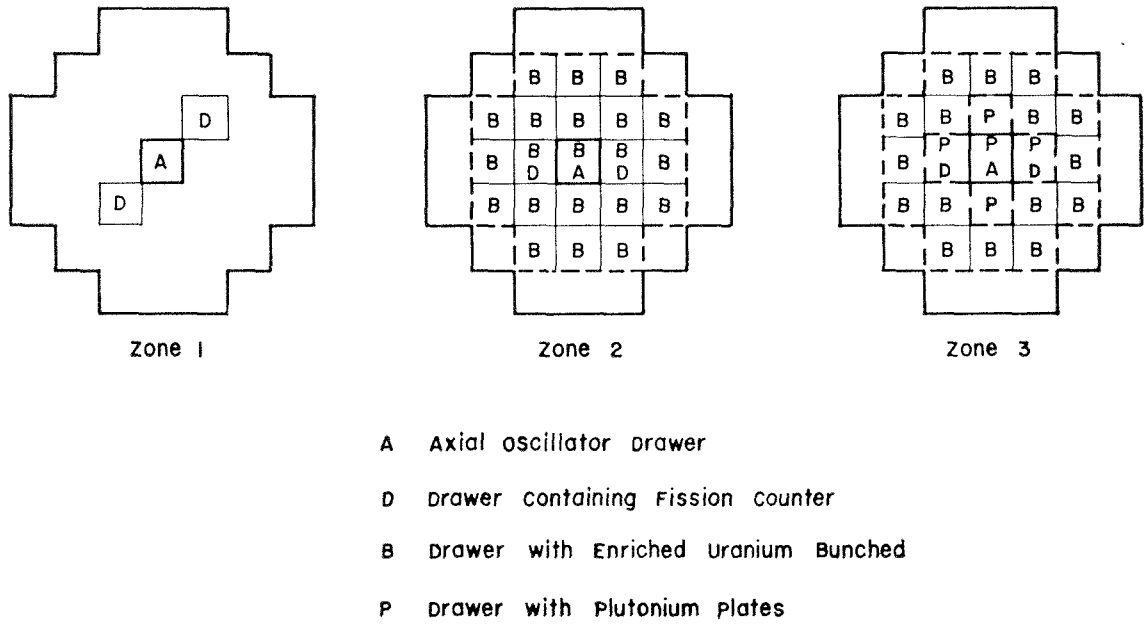

FIG. II-19-6. Loading Arrangements of Zones 1, 2, and 3, ZPR-9 Assembly 25. *ANL Neg. No. 116-530.*

The entire central region was loaded as zone 1. In zone 2 the four $\frac{1}{32}$ in. enriched plates were bunched together at the center of the unit-cell. The measured change in the null composition between zones 1 and 2 was designed as a test of the analytical techniques used to predict plate heterogeneity corrections. Zone 2 was loaded in the central 21 drawers in each half. The part of the central zone outside of the zone 2 region remained loaded as zone 1. Zone 3 consisted of a very small plutonium-aluminum alloy and depleted uranium null zone at the center of zone 2 as indicated in Fig. II-19-6. Zone 3 contained less than 1 kg of plutonium, the maximum amount of plutonium allowed in ZPR-9 at the time of Assembly 25. The exact plate loadings of the null samples for each of the three null zones are given in the following section.

Calculations indicate that the equilibrium spectrum characteristic of the null material was achieved reasonably well in both zones 1 and 2. The spectral matching in zone 3 was, of course, not as good, and this must be considered when evaluating the zone 3 results.

ASSEMBLY 25 EXPERIMENTAL RESULTS

The available experimental results for Assembly 25 are contained in this section. This includes the null composition measurements, reactivity worth measurements of the materials in the central zone unit-cell using the axial oscillator, central and radial reactivity measurements using the radial sample changer, the normalization integral measurement using a Cf-252 source, and additional special measurements to test the null reactivity technique. The reaction rate results are currently being re-evaluated and will be published at a later date.

NULL COMPOSITION

The null zone was loaded initially with the calculated null composition. Measurements were then made to experimentally determine the null composition. An axial oscillator (see Fig. III-22-2 of Ref. 3) and a calibrated autorod were used in making reactivity worth measurements of small samples of representative null zone material with respect to void at the zone center. The autorod was a thin tapered polyethylene spear which was controlled to hold the reactor power constant. $\Delta\rho/\Delta x$ for the spear was constant so that the change in reactivity associated with sample insertion was proportional to the change in the autorod position, and the average rod position was obtained by integrating over a preset time interval, the output from a potentiometer whose voltage was proportional to rod position. The constant $\Delta\rho/\Delta x$ value for the autorod spear was experimentally confirmed by making several measurements of the worth of a small sample with the autorod adjusted to several locations spanning its total travel. The results are given in Table II-19-II. The sequence of operation for the reactivity measurements was as follows: sample inserted to core center by oscillator; waiting time of 1 to 2 min for reactor to stabilize; autorod integration time of 2 to 5 min; oscillator driven out; sample removed and oscillator driven back

TABLE II-19-II. Worth of Small Sample as a Function of Autorod Position[a]

Average Autorod Insertion (% distance from in to out)	Sample Worth, Ih
12	0.232 ± 0.004
28	0.233 ± 0.002
54	0.235 ± 0.003
65	0.235 ± 0.003
78	0.232 ± 0.002

[a] The sample was worth about 6% of the autorod worth so that at 12%, for example, the autorod moved between 9 and 15% insertion when the sample was oscillated.

TABLE II-19-III. Assembly 25 Null Composition Weight Ratios[a]

Null Composition Relative Weights	Zone 1	Zone 2	Zone 3
Enriched uranium[b]	1.000	1.000	—
Plutonium[c]	—	—	1.000
Depleted uranium[d]	15.155 ± 0.04	15.354 ± 0.06	22.165 ± 0.06
304 Stainless steel	1.009	1.009	2.465
Aluminum	0.0909	0.0753	0.2192

[a] The quoted values are based on the measurement of the sample closest to null and corrected to the exact null using the measured material worths.

[b] The isotopic composition of the enriched uranium was 0.91 w/o U-234, 93.24 w/o U-235, 0.44 w/o U-236 and 5.41 w/o U-238.

[c] The isotopic composition of the plutonium was 95.06 w/o Pu-239, 4.55 w/o Pu-240, 0.44 w/o Pu-241 and 0.006 w/o Pu-242.

[d] The isotopic composition of the depleted uranium was 0.21 w/o U-235 and 99.79 w/o U-238.

into core; waiting time (as before); integration time (as before). The cycle is repeated several times to improve statistics and to cancel drift.[4]

The samples consisted of plates of enriched and depleted uranium and low-density aluminum (similar to the unit cell drawer loadings in the null zone) and they were contained in thin wall 2 × 2 × 2 in. stainless steel boxes. The ratio of depleted uranium to aluminum was varied in the samples in order to predict the exact null composition. The entire null zone was then loaded to this composition and the null composition rechecked, since the reloading may have caused a change in the spectrum which, in turn, would affect the worth of the null box. It was found in all three null zone assemblies, however, that the worth of the null sample did not change significantly after the reloading and that one reloading of the null zone was all that was necessary.

The null composition results for zones 1, 2, and 3 of Assembly 25 are given in Tables II-19-III through II-19-V. Table II-19-III gives the null composition weight ratios. Table II-19-IV gives the unit-cell plate arrangements, and Table II-19-V gives the null atomic concentrations for zones 1, 2, and 3. The data in Tables II-19-III through II-19-V are based on the measurement of the sample or samples closest to null and corrected to the exact null using the measured material worths. The uncertainty in the null measurement has been lumped into the weight ratio of depleted uranium to enriched uranium or plutonium, as indicated in Table II-19-III, while the weights of stainless steel

TABLE II-19-IV. Unit-Cell Plate Arrangements for the Null Samples[a]

Zone 1		Zone 2		Zone 3	
Material	Thickness, cm	Material	Thickness, cm	Material	Thickness, cm
SS	0.366	SS	0.366	SS	0.457
Al	0.152	Al	0.152	Void	0.850
D	0.635	D	2.222	D	1.587
E	0.0793	E	0.3175	Pu[b]	0.3175
D	0.953	D	2.222	D	1.746
E	0.0793	Al	0.152	Al	0.476
D	0.635				
Al	0.063				
D	0.565				
E	0.0793				
D	0.953				
E	0.0793				
D	0.635				
Al	0.152				

[a] The symbols used in the tables are SS—304 Stainless Steel, Al—45% dense aluminum, E—enriched uranium and D—depleted uranium.

[b] Pu is for the Pu-Al alloy plate canned in stainless steel. The plate and can includes 61.64 g of Pu, 16.19 g of SS and 0.73 g of Al. The isotopic composition of the Pu is indicated in footnote c of Table II-19-III.

TABLE II-19-V. Summary of Atomic Concentrations in the Null Samples, 10^{21} atoms/cm^3

Material	Zone 1	Zone 2	Zone 3
U-234	0.0206	0.0206	—
U-235	2.173	2.174	0.0536
U-236	0.0099	0.0099	—
U-238	33.765	34.208	25.127
Pu-239	—	—	1.075
Pu-240	—	—	0.0513
Pu-241	—	—	0.0049
Pu-242	—	—	0.00006
Fe	6.839	6.839	8.538
Ni	0.864	0.864	1.079
Cr	1.952	1.952	2.437
Al	1.785	1.477	2.197

TABLE II-19-VI. MEASURED MATERIAL WORTHS IN THE NULL SAMPLE PLATE ENVIRONMENT IN ZPR-9 ASSEMBLY 25[a,b]

Zone 1			Zone 2			Zone 3		
Material	Weight, g	Ih/kg	Material	Weight, g	Ih/kg	Material	Weight, g	Ih/kg
Enr. U	5.17	+53.5	Enr. U	5.17	54.4	Pu	7.41	86 71
Depl. U	218.6	−3.23	Enr. U	10.08	53.5	Depl. U	146.2	−3.30
304 SS	85.9	−3.46	Depl. U	147.7	−3.22	304 SS	58.6	−3.41
Al	35.7	−5.79	304 SS	27.7	−3.33	Al	8.60	−6.25
U-235	—	57.6	U-235	—	58.1	Pu-239	—	90.3
U-238	—	−3.36	U-238	—	−3.35	—	—	—

[a] The statistical uncertainty in the reactivity values quoted in this table are approximately 1–2%.
[b] The values for U-235 and U-238 are derived from the Enr. U and Depl. U values. The value for Pu-239 was calculated from the Pu value using the calculated worths of Pu-240 and Pu-241.

TABLE II-19-VII. MEASURED WORTHS OF CYLINDRICAL SAMPLES IN ZPR-9 ASSEMBLY 25 ZONE 1 USING THE RADIAL SAMPLE CHANGER[a]

Material	Weight, g	SS Plug Length, in.	Ih/kg
Enr. U	3.084	0	52.9
Depl. U	25.99	0	−3.34
Pu	3.482	2	80.4
Pu	21.152	2	82.3
B (nat.)	0.5553	2	−136.0
C	33.44	2	−22.4
Na	17.04	2	−7.48
Al	53.07	2	−5.96
304 SS	43.82	0	−3.47
U-235	—	—	56.9
U-238	—	—	−3.47
Pu-239	3.445[b]	—	81.1
Pu-239	20.926[b]	—	83.0

[a] Footnotes a and b of Table II-19-VI apply.
[b] Listed values are the weights of Pu-239 in the Pu samples.

TABLE II-19-VIII. MEASURED MATERIAL WORTHS VERSUS RADIAL POSITION FOR ZPR-9 ASSEMBLY 25[a], Ih/kg

Radial Position, cm	Material and Weight		
	Enr. U, 3.084 g	Al, 53.07 g	SS, 43.82 g
0	52.88	−5.96	−3.47
5.52	50.16	−5.74	−3.46
11.05	49.06	−5.27	−3.37
16.56	48.83	−4.69	−3.02
22.10	57.07	−3.29	−1.57
27.60	43.19	−0.88	−1.84
33.12	37.42	+6.89	+2.57
38.63	38.65	—	+4.38

[a] Footnote a of Table II-19-VI applies.

and aluminum are held constant. This is a convenient way to characterize the null composition, since it is the capture and fission in these isotopes that overwhelmingly determine the null composition.

REACTIVITY WORTH MEASUREMENTS

Two different sets of reactivity worth measurements were made on Assembly 25. The worths of the null zone constituent materials were measured at the zone center using the axial oscillator, calibrated autorod, and 2 × 2 × 2 in. plate-loaded samples. These measurements, which were made in all three zones, were used to make the small corrections from the measured null samples to the exact null composition. The procedure for these measurements was to measure the reactivity worth of a plate-loaded sample box, then remove a small part of one of the materials from the sample box and remeasure the sample worth. In this manner the worth of the material in its normal plate environment is obtained. The sample box reactivity measurements were made using the procedure described in the previous section. The results of these plate-environment worth measurements are included in Table II-19-VI.

The other set of reactivity worth measurements on Assembly 25 were made with the pneumatic radial sample changer, the calibrated autorod, and cylindrical, annular samples. The samples were 2.0 in. long, 0.87 in. in diam and had varying wall thicknesses. Both the radial sample changer and the cylindrical samples and holders are described in Ref. 5. Measurements were made, in zone 1 only, both at the center of the null zone and along a radius at the axial midplane. These results are given in Tables II-19-VII and II-19-VIII. The ratios of aluminum worth and stainless steel worth to enriched uranium worth as a function of radius are plotted in Fig. II-19-7. The ratios are both normalized to 1.0 at the core center for better comparison of the radial shapes.

The primary purpose of the radial worth measurements in Assembly 25 was to experimentally confirm that the spectrum in the null zone had converged [illegible] the center to the equilibrium spectrum characteristi[illegible] the null composition. As discussed in Ref. 5, an indication of zone spectrum convergence is obtained if the

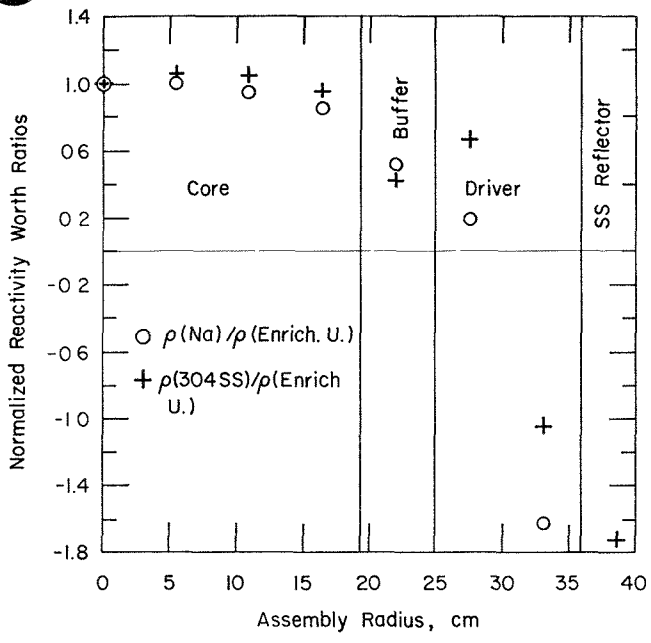

FIG. II-19-7. Radial Worth Ratios, ZPR-9 Assembly 25. *ANL Neg. No. 116-528.*

ratio of the worth of a scattering material, such as aluminum or stainless steel, to worth of an absorber like enriched uranium is relatively constant near the center of the zone. Comparison of the worth ratio curves given in Fig. II-19-7 to those shown in Figs. III-17-3, III-17-4 and III-17-5 of Ref. 5, suggests good spectral convergence in Assembly 25. Poor spectral convergence would result in a measured null that would differ slightly from the true infinite medium null composition.

Spectrum Measurement

The results of the Assembly 25 proton recoil counter central spectrum measurement are included in Paper II-22. They are compared with a spectrum calculated by the MC² code using ENDF/B data. The measured spectrum appears to be significantly greater than the calculated spectrum above approximately 1 MeV and slightly lower from 200 keV to 1 MeV. This result is consistent with the suggestion that the inelastic scattering cross section for U-238 in ENDF/B is too large.

Cf-252 Source Measurements

The apparent reactivity worth of a calibrated Cf-252 source was measured as a function of reactor power using the radial sample changer and the calibrated autorod. The source was enclosed inside an aluminum container which was placed inside one of the regular stainless steel sample holders used with the radial sample changer.[5] The source was calibrated to have a strength of (7.548 ± 0.030) × 10⁶ neutrons/sec in April 1968. Using a half life of 2.621 yr for Cf-252, this gave a source strength of (5.07 ± 0.02) × 10⁶ neutrons/sec at the time of the Assembly 25 measurements.

The results of the Cf-252 reactivity measurements are shown in Fig. II-19-8. The curve is of the form $(a + b/P)$, where a represents the power-level-independent absorption and scattering terms (due to the source container) and b is the coefficient of the source term, which is inversely proportional to the power level, P.

The Cf-252 measurements were made for two reasons: (1) to determine the Assembly 25 normalization integral (the denominator of the perturbation expression) by the method described in Ref. 6, and (2) to be used in the reactivity-reaction rate Pu-239 and U-235 capture-to-fission ratio (alpha) measurements. The preliminary value for the Assembly 25 normalization integral, using preliminary fission rate results, was (3.92 ± 0.15) × 10⁵. This value has been normalized such that both the source rate ($\sum_i (\nu\Sigma_f)_i \phi_i$) and the fission spectrum weighted adjoint ($\sum_i \chi_i \phi_i^*$) are unity at the center of Assembly 25.

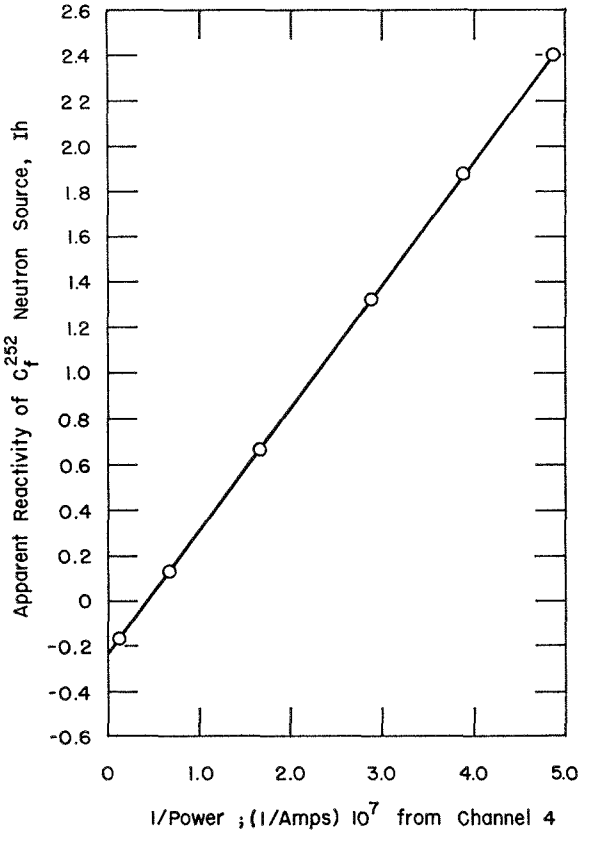

FIG. II-19-8. Apparent Reactivity of Cf-252 Source in ZPR-9 Assembly 25. *ANL Neg. No. 116-534.*

Special Measurements to Check the Null Reactivity Technique

A number of special measurements were made on Assembly 25 to evaluate some possible sources of experimental error in determining the null compositions. These measurements are described in the following paragraphs.

SAMPLE BOX SIZE

Measurements were made to determine if the measured null composition was a function of the size of the null sample. The null composition was determined using the full 2 × 2 × 2 in. samples and using 2 × 2 × 1 in. and 2 × 1 × 1 in. samples as indicated in Table II-19-IX. These measurements were made in both zone 1 and zone 2. The null composition is characterized by the depleted uranium to enriched uranium weight ratio (DU/EU) while the ratios of aluminum and stainless steel to enriched uranium are held constant. The maximum spread in the DU/EU ratio, between the full and quarter boxes on zone 2, is less than one percent and the uncertainties on the two values are overlapping. These results suggest that the null composition is not strongly affected by the sample size; however, they should not be considered conclusive since the range of sample sizes tested was not very great. The spectrum in Assembly 25 was rather hard, so that sample size effects associated with resonance region heterogeneities were expected to be less in Assembly 25 than in an assembly with a softer spectrum.

TABLE II-19-IX. Variation of the Null Enriched to Depleted Uranium Weight Ratio as a Function of Sample Box Size for ZPR-9 Assembly 25

Box Size	Box Dimension, in.			$\frac{\text{Wt Depl. U}}{\text{Wt Enr. U}}$	
	Radial, Parallel to Plates	Radial, Perpendicular to Plates	Axial	Zone 1	Zone 2
Full	2	2	2	15.15 ± 0.04	15.35 ± 0.06
Half	1	2	2	15.11 ± 0.12	15.43 ± 0.12
Half	2	1	2	15.14 ± 0.12	15.41 ± 0.12
Quarter	1	1	2	15.13 ± 0.24	15.49 ± 0.24

Table II-19-X. Worth of 304 Stainless Steel as a Function of Position in the Sample Box for ZPR-9 Assembly 25

Position of SS in Box[a]	Worth, Ih/kg
A—Distributed between plates	−3.78
B—horizontal	−3.56
C—vertical at side of box	−3.26

[a] See Fig. II-19-9.

PLATE ORIENTATION IN SAMPLE BOX

A measurement was made to determine the change in worth of the null sample box when the plates were placed in the box horizontally rather than in normal vertical position (a 90 deg rotation of the sample plates about the cylindrical axis of the assembly). The object of this measurement was to determine if the capture and fission rates in the depleted and enriched plates in the core adjacent to the sample position were affected when the sample box is removed, due to the small increase in the surface-to-volume ratio of these plates. When the plates in the box are rotated 90 deg the continuous columns of plates in the core and sample are broken and the surface-to-volume ratios for the adjacent plates are also increased. Therefore, the measurement of the sample with the plates rotated 90 deg simulates the effect which is being investigated.

The measured reactivity difference between the samples with vertical and horizontal plates was less than 0.004 Ih, which was the accuracy of the measurement. This represents a difference in the characteristic DU/EU null weight ratio of only about 0.05 percent. These measurements, therefore, tend to indicate that the measured null composition is not strongly affected by any change in capture or fission rate in the adjacent plates due to sample removal. As before, however, these results are not conclusive for all null cores, partly because the effect being investigated was not simulated exactly and partly because the effect being investigated is primarily a resonance effect which is minimized by the hard spectrum of Assembly 25.

CORRECTION FOR MATRIX STAINLESS STEEL

If the null sample boxes are loaded with exactly the same plate arrangement as the core, the weight ratios among the materials will all be approximately correct except that there will not be enough stainless steel. This is because most of the stainless steel in the core is in the matrix and drawers. Therefore, slightly undersize plates were used in the sample boxes and stainless steel shims were added to the boxes. Part of the matrix and drawer stainless steel is in horizontal columns and part in vertical columns and it was necessary to determine the relative worths of the horizontal and vertical stainless steel so that it could be properly simulated in the sample boxes. The results of these measurements are given in Table II-19-X and Fig. II-19-9. Since it was not possible in most of the sample boxes to include

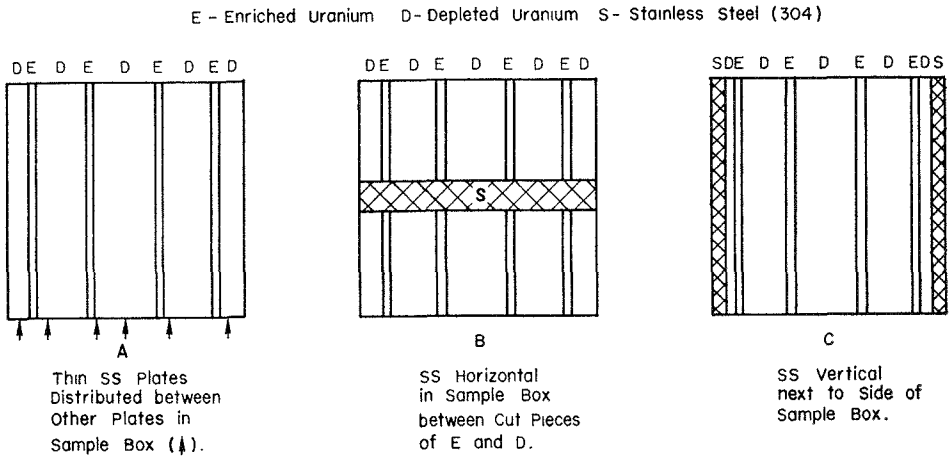

FIG. II-19-9. Stainless Steel Loadings in Special Sample Boxes (See Table II-19-X). *ANL Neg. No. 116-535.*

horizontal stainless steel, it was simulated by a combination of distributed vertical plates and side vertical plates.

REFERENCES

1. C. E. Till, J. M. Gasidlo, E. F. Groh, L. G. LeSage, W. R. Robinson and G. S. Stanford, *Null-Reactivity Measurements of Capture/Fission Ratio in U-235 and Pu-239*, Nucl. Sci. Eng. **40**, 132 (1970).
2. B. A. Zolotar, B. R. Sehgal and J. M. Kallfelz, *Fast Reactor Integral Studies of Modifications to ENDF/B U-238 Inelastic Scattering*, Trans. Am. Nucl. Soc. **12**, 743 (1969).
3. C. E. Till, L. G. LeSage, G. S. Stanford, E. F. Groh and W. R. Robinson, *Measurement of the Capture-to-Fission Ratio of U-235 and Pu-239 in the Kilovolt Region Using Critical Assembly Null Reactivity Techniques*, Reactor Physics Division Annual Report, July 1, 1967 to June 30, 1968, ANL-7410, p. 169.
4. E. F. Bennett and R. L. Long, *Precision Limitations in the Measurement of Small Reactivity Changes*, Nucl. Sci. Eng. **17**, 425 (1963).
5. L. G. LeSage, E. F. Groh and W. R. Robinson, *An Investigation of the Properties of Zoned Systems*, Reactor Physics Division Annual Report, July 1, 1967 to June 30, 1968, ANL-7410, p. 145.
6. R. A. Karam, *Measurement of Normalization Integral and Spatial Distribution of the Importance of Fission Neutrons*, Nucl. Sci. Eng. **37**, 192 (1969).

II-20. Gamma Spectrum in ZPR-6 Assembly 6

R. GOLD

Compton recoil gamma-ray spectroscopy[1,2] has been used to measure the in-core gamma spectrum in a fast critical facility. Electron measurements were carried out near the core center of ZPR-6 Assembly 6, a 4000-liter uranium oxide fast neutron critical assembly.[3] Atom density concentrations for the central core region of ZPR-6 Assembly 6 can be found in Table II-20-I.

The electron recoil spectrum observed at low reactor power is shown in Fig. II-20-1. For this irradiation, both halves of the ZPR-6 split-table facility were together and the assembly was nearly critical. The gamma continuum corresponding to this measurement is displayed in Fig. II-20-2.

The critical assembly gamma spectrum varies quite slowly below 1 MeV, with the exception of two distinct peaks, which occur at approximately 0.5 and 0.85 MeV, respectively. The peak in the neighborhood of

TABLE II-20-I. COMPOSITION OF ZPR-6 ASSEMBLY 6 (*Central Core Region*)

Element	Atom Density[a]
U-235	0.001150
U-238	0.005796
Na	0.009142
O	0.01465
Fe	0.01410
Ni	0.001365
Cr	0.002788

[a] Atoms per cm^3 $\times$ 10^{24}.

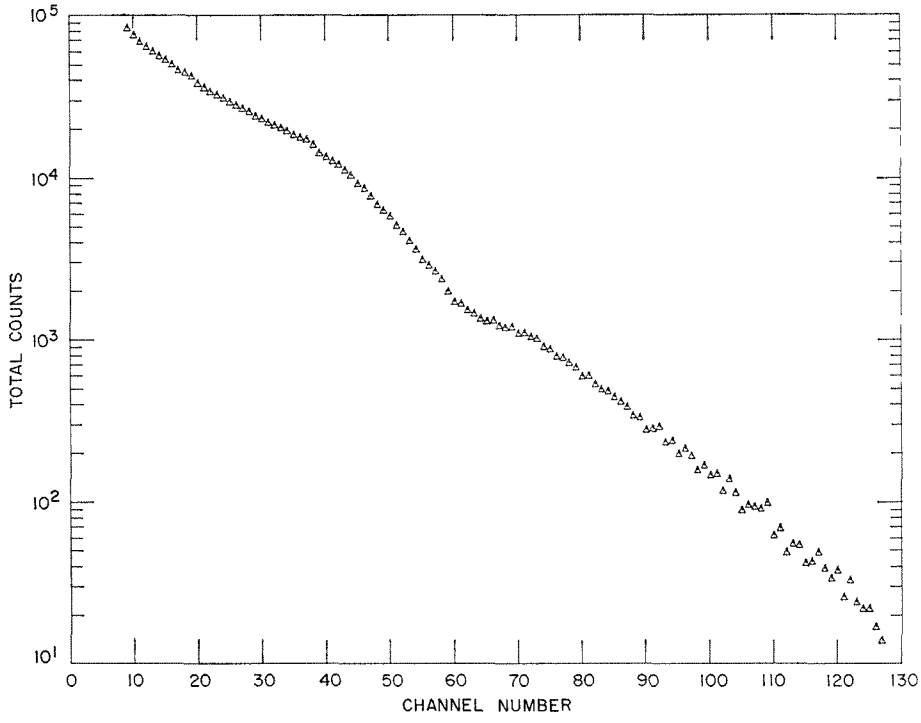

FIG. II-20-1. The Electron Recoil Spectrum Observed in ZPR-6 Assembly 6 at Low Reactor Power with a Channel Energy Width of Approximately 20 keV. *ANL Neg No 113-3031.*

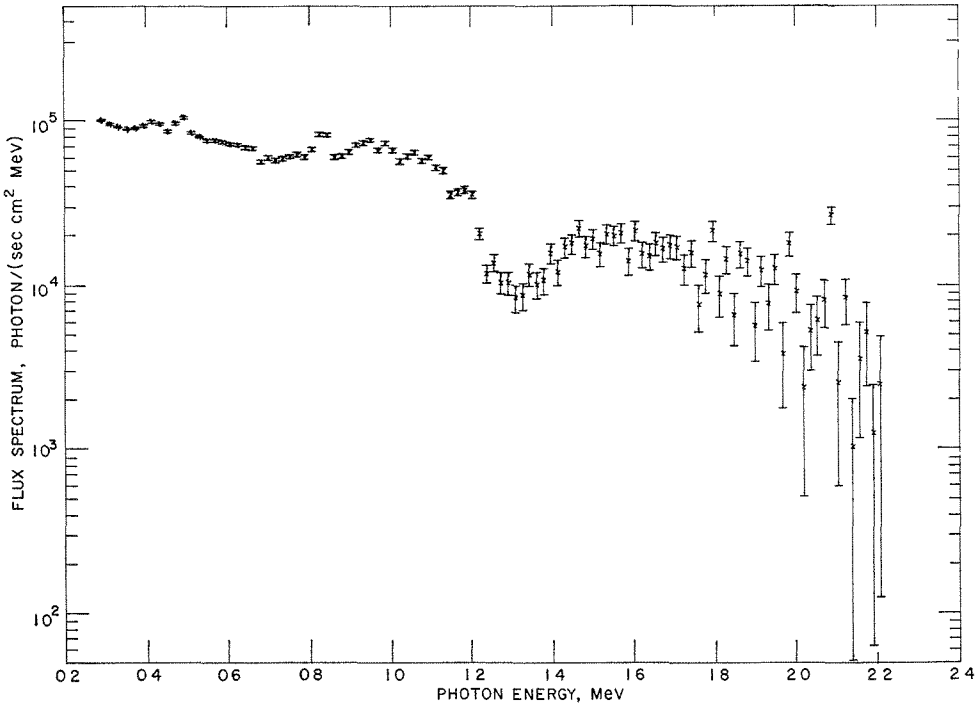

FIG. II-20-2. The Gamma-Ray Continuum Attained in the Low Power Irradiation Near the Core Center of ZPR-6 Assembly 6. *ANL Neg. No. 116-111.*

.5 MeV corresponds to a contribution from annihilation radiation. In addition to the peak near 0.85 MeV, note the existence of two other peaks in the vicinity of 1.8 and 2.1 MeV, respectively. These three peaks may correspond to gamma transitions in Fe-56, produced principally by inelastic fast neutron scattering.

The experimental error exhibited in the ZPR-6 gamma continuum becomes quite large at high energy. This high energy behavior arises directly from the process of unfolding data of poor statistical quality (i.e. low total count) and thereby emphasizes the softness of the critical assembly spectrum (see Fig. II-20-1).

REFERENCES

1. R. Gold, *Compton Recoil Gamma-Ray Spectroscopy*, Nucl. Instr. Methods **84**, 173 (1970).
2. R. Gold, *Compton Recoil Measurement of Continuous Gamma Spectra*, Trans. Am. Nucl. Soc. **13**, 421 (1970).
3. R. Karam, L. R. Dates, W. Y. Kato, J. E. Marshall, T. Nakamura and G. K. Rusch, *A 4000-Liter Uranium Oxide Fast Core, Assembly 6 of ZPR-6*, Reactor Physics Division Annual Report, July 1, 1967 to June 30, 1968, ANL-7410, pp. 75–80.

II-21. ZPR-6 Assembly 6A, A 4000-Liter UO_2 Fast Core

R. A. KARAM, W. R. ROBINSON, G. S. STANFORD and G. K. RUSCH

ZPR-6 Assembly 6A differed only slightly in material arrangement and concentrations from Assembly 6,[1-3] the 4000 liter UO_2 core, which was shutdown prior to the completion of the planned experiments so that modifications required for plutonium usage could be made on the ZPR-6 and -9 facilities. The resumed series of experiments followed largely from the previous program, but the resumed 6A program was directed at specific points in the overall program for the investigation of the effects of plates, rods and temperature.

The programmatic aims of Assembly 6A were accomplished as follows:

1. The critical size of a uniform single zone core and blanket system was experimentally established.
2. The unit-cell reaction rate fine structure was measured at various positions in the assembly so that the true plate- and cell-averaged values of the ratios of U-238 fission and capture to U-235 fission were established over the total of core and blanket. Additionally, unit-cell spectral index fine structure was measured by determining the U-238 fission rate as a function of position in the U-235 plate.
3. The 25 cm radius central region had materials chosen to match as accurately as possible calandria and rod compositions. This zone is the reference with which the comparisons of the Variable Temperature Rodded Zone (VTRZ) configurations will be made.
4. Measurements of central reactivity worths and of normalization integral were made to provide the normalization for the various VTRZ configurations.
5. Central reactivity worths of those materials that were not precisely matched between the rod and plate configurations were made in the appropriate geometry to allow corrections to be made for small differences.
6. Doppler and spectrum measurements were made to provide additional normalizations.
7. The unit-cell reaction rate fine structure, the central reactivity measurements, and the Doppler and spectrum measurements were repeated in a 40 cm, sodium-voided region.
8. Activation distributions indicative of the power distributions were made throughout the system.

The critical size, the central reactivity worths, the normalization integral, and the overall activation distributions are given in this paper. The rest of the experimental results will be reported when they become available.

DESCRIPTION OF ASSEMBLY 6A

Assembly 6A was built with as uniform a composition as was consistent with inventory and certain experimental requirements. A cross sectional view of the system is shown in Fig. II-21-1. The average material concentrations are given in Table II-21-I. The axial height of the core was 152.4 cm and the depleted uranium blanket was 30 cm thick.

Although Assembly 6A is described as a uniform, single-zone core system, it actually had four regions differing slightly in composition:

REGION I

The composition of the central substitution region was carefully selected to match the pin-calandria composition. The position and serial number of each enriched plate in every drawer were recorded so that the

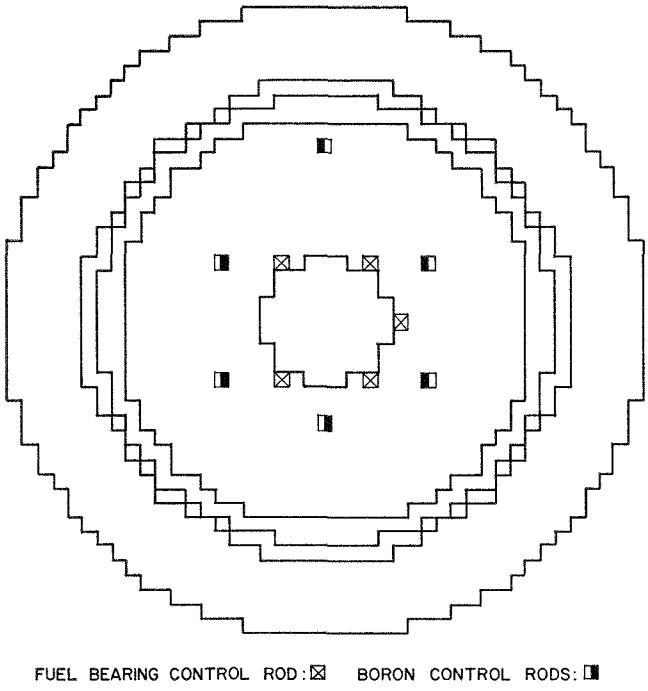

FIG. II-21-1. Cross Sectional View of ZPR-6 Assembly 6A. *ANL Neg. No. 116-490 T-1.*

TABLE II-21-I. ATOMIC DENSITIES IN ASSEMBLY 6A,[a] 10^{24} atoms/cm³

Isotopes	Region I	Region II	Region III	Region IV	Region V
Na	0.009294	0.009142	0.009376	0.009376	—
O	0.01380	0.01465	0.001465	0.01465	—
Fe	0.013535	0.01410	0.01410	0.01408	0.004224
Ni	0.001229	0.001365	0.001365	0.001364	0.0005086
Cr	0.002842	0.002796	0.002788	0.002786	0.001176
U-238	0.005796	0.005796	0.005796	0.005796	0.04008
U-235	0.001154	0.001151	0.001143	0.001115	0.0008270
Mn	0.0002174	0.0002174	0.0002174	0.0002174	0.00008997

[a] Stainless steel compositions: Fe = 71.08%, Cr = 18.43%, Ni = 9.00%, Mn = 1.49%.

spatial variation in the density of the fissile material could be obtained. Similar records were kept for the sodium cans. The weight of the other diluents, Fe_2O_3, type 304 stainless steel, depleted U_3O_8, depleted uranium, and the stainless steel in the drawer, were obtained for each drawer. The equivalent outer radius of Region I was 24.35 cm. The drawer loading pattern is shown in Fig. II-21-2.

REGION II

The drawer loading pattern in this region was identical with that in Region I. Average weights for all the materials in all the drawers were used. The equivalent outer radius of Region II was 77.30 cm.

REGION III

A top view of the drawer loading pattern is shown in Fig. II-21-3. Although this loading pattern is different from that shown in Fig. II-21-2, the material concentrations were very similar. The equivalent outer radius of this region was 85.65 cm.

REGION IV

The drawer loading pattern was very similar to that used in Region III, except that 2 × 2 × ⅛ in. enriched plates were used instead of the 2 × 3 × ⅛ in. plates used in Region III. The exact loading pattern in this region is shown in Fig. II-21-4. The experimental equivalent outer radius in this region was 90.44 cm.

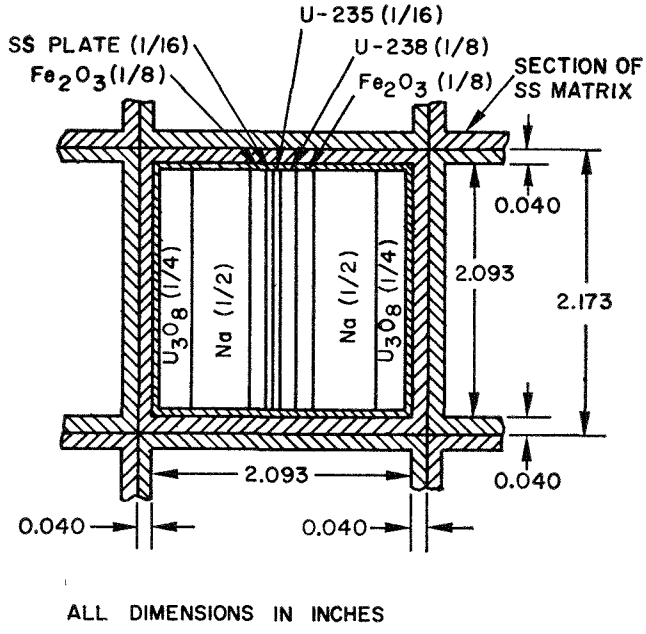

FIG. II-21-2. Unit Cell Drawer Loading Patterns in Regions I and II of Assembly 6A. *ANL Neg. No. 116-488*, Rev. 1.

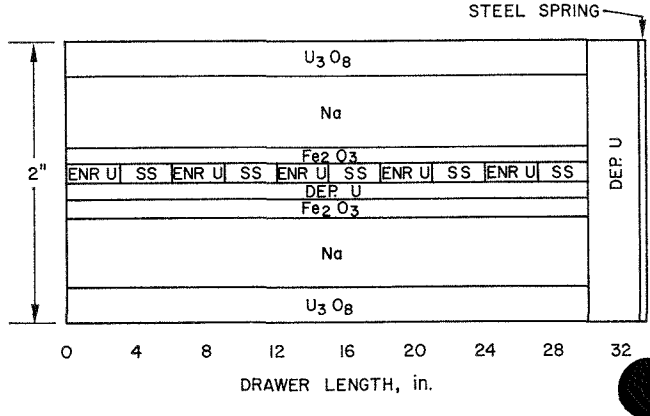

FIG. II-21-3. A Top View of the Drawer Loading Pattern in Region III, Assembly 6A. *ANL Neg. No. 116-492.*

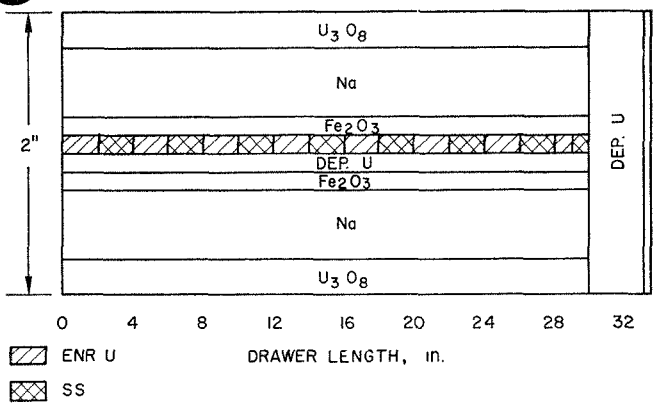

FIG. II-21-4. A Top View of the Drawer Loading Pattern in Region IV, Assembly 6A. *ANL Neg. No. 116-491.*

REGION V

This region comprises the depleted uranium blanket. Depleted uranium blocks were placed in the matrix to form the 30 cm thick blanket.

CRITICAL MASS

The critical mass of the as-built system (Fig. II-21-1) was 1760 kg of U-235. To establish the correction to a fully uniform system with the drawer loading pattern of Regions I and II, sufficient $\frac{1}{16}$ in. enriched plates were held aside to load a complete quadrant.

The reactivity difference between the loading patterns in Regions III and IV and that in Regions I and II was measured in 15-deg sector steps up to the full quadrant. These data were then used to obtain the critical mass of the clean, fully uniform core. The critical mass determined in this manner was 1798 kg of U-235. The uncertainty associated with the extrapolation is considered to be less than one kilogram.

SODIUM-VOID

Three types of sodium-void measurements were made:

1. The sodium in a central region, 39.36 cm equivalent radius, was voided primarily to provide the asymptotic spectrum of the sodium-free core.

2. The sodium void coefficient was mapped as a function of position along the axial height to provide the reference data for the VTRZ measurements.

3. The avoid coefficient was mapped as a function of radius to complement those measurements performed on ZPR-6 Assembly 6. All the sodium in a drawer was voided as a function of radius in Assembly 6, whereas the first 7 inch sections about the midplane were voided in each half of Assembly 6A.

The reactivity worth of the sodium in the 39.36 cm radius central region was -239.81 ± 0.50 Ih (458.0 Ih $= 1\%\ \Delta k/k$). A summary of the experimental results is given in Table II-21-II.

The sodium cans in the first 122 drawers in Region I were 6 in. long with the average sodium weight per can of 82.51 ± 0.38 g. The maximum deviation from this average was 0.65 g. The rest of the drawers were loaded with cans 7 and 8 in. long. In all cases sodium removal was achieved by replacing sodium-filled cans with identical empty cans. The uncertainties in the sodium weight and reactivity worths were incorporated in the standard deviations.

The void coefficient in the central 18 drawers in Assembly 6A (Table II-21-II) was -0.882 ± 0.005 Ih; the comparable coefficient in Assembly 6[2] was -0.861 ± 0.014. The average void coefficient in Region I (same size as VTRZ) was -0.934 ± 0.005 Ih.

The results of the void coefficient measurements as a function of position along the axial height are given in Table II-21-III. The measurements were performed in the central 3×3 drawers in sections 6 in. long (12 in. total) in each half of the reactor. The values obtained confirm the values obtained on Assembly 6.[2]

The void coefficient as a function of radius was measured in rings involving several drawers about the center of the core in the uniform quadrant. The axial length of the voided section was 14 in. in both halves of the ZPR-6 machine. The results are shown in Table

TABLE II-21-II. SODIUM-VOID COEFFICIENT IN CENTRAL REGION[a]

No. of Drawers Voided (Full Length)	$R_i - R_0$	kg of Na	Na Worth, Ih	Void Coefficient, Ih/kg Na
18	0.0–9.35	14.85 ± 0.07	-13.08 ± 0.20	-0.882 ± 0.005
104	9.35–24.35	85.31 ± 0.39	-80.95 ± 0.20	-0.943 ± 0.005
64	24.35–30.05	51.96 ± 0.52	-47.60 ± 0.02	-0.916 ± 0.010
64	30.05–34.85	51.96 ± 0.52	-47.72 ± 0.20	-0.918 ± 0.010
69	34.85–39.36	56.02 ± 0.56	-50.51 ± 0.20	-0.902 ± 0.010
Total 319		260.60	−239.86	−0.920

[a] The size of the void region was increased in the sequence indicated.

TABLE II-21-III. Sodium-Void Coefficient as a Function of Axial Height in the Central 3 × 3 Drawers in Assembly 6A

Section Voided[a]	Coordinate $(Z_i - Z_{i+1})$	Weight of Sodium, kg	Reactivity Change in System,[b] Ih	Void Coefficient, Ih/kg Na
1st 6 in.	0.0–15.24	2.966	−0.051 ± 0.141	−0.017 ± 0.048
2nd 6 in.	15.24–30.48	2.966	−0.846 ± 0.141	−0.285 ± 0.048
3rd 6 in.	30.48–45.72	2.966	−2.137 ± 0.141	−0.720 ± 0.048
4th 6 in.	45.72–60.96	2.966	−4.052 ± 0.141	−1.366 ± 0.048
5th 6 in.	60.96–76.20	2.966	−4.909 ± 0.151	−1.655 ± 0.048

[a] Only section indicated was voided in each half of the reactor.
[b] 1% $\Delta k/k$ = 458 Ih; uncertainties are based on reproducibility of reference runs.

TABLE II-21-IV. Sodium-Void Coefficient as a Function of Radius in ZPR-6 Assembly 6A

Average Radius, cm	Weight of Sodium Removed, kg	Reactivity Change in System,[a] Ih	Radial Void Coefficient, Ih/kg Na
4.68	2.966	−0.051 ± 0.141	−0.017 ± 0.048
25.50	4.164	−0.857 ± 0.140	−0.206 ± 0.034
40.90	3.058	−1.158 ± 0.140	−0.379 ± 0.046
48.60	3.058	−2.186 ± 0.140	−0.713 ± 0.046
58.06	3.058	−2.544 ± 0.140	−0.832 ± 0.046
68.43	3.058	−2.763 ± 0.140	−0.904 ± 0.046
79.04	3.095	−2.954 ± 0.140	−0.954 ± 0.046
89.14	3.095	−2.540 ± 0.140	−0.821 ± 0.046

[a] 1% $\Delta k/k$ = 458 Ih; uncertainties are based on reproducibility of reference runs.

II-21-IV and plotted in Fig. II-21-5. The measured value at r = 41 cm appears to be abnormally high.

Central Reactivity Worths

The central reactivity measurements were made to provide information about: (1) reactivity normalizations for the rodded zones, (2) accuracy of the calculated adjoint function and, (3) reactivity adjustments due to small differences in material concentrations between rodded and plate zones. The worths of B-10, tantalum, wolfram, rhenium, U-238, U-235, plutonium, carbon, beryllium, sodium and stainless steel (304) were measured in a 2 × 2 × 1 in. cavity at the center of the core. Absorbers such as B-10 and tantalum are not very sensitive to small spectral differences. On the other hand, scatterers such as carbon, beryllium, and sodium are very sensitive to small spectral differences and therefore provide good checks on the adjoint function. The worths of most of these samples were also measured in the 39.36 cm radius central, sodium-free region. All measurements were performed in the manner described in Ref. 4. The results are given in Table II-21-V.

The reactivity worths of the core materials were measured in the environment of the core-loading pattern. This measurement consisted of oscillating two 2 × 2 × 2 in. stainless steel cans, relative to each other, each loaded in the same manner as the core and containing the same materials except for the plate whose worth was being determined; that plate was present in

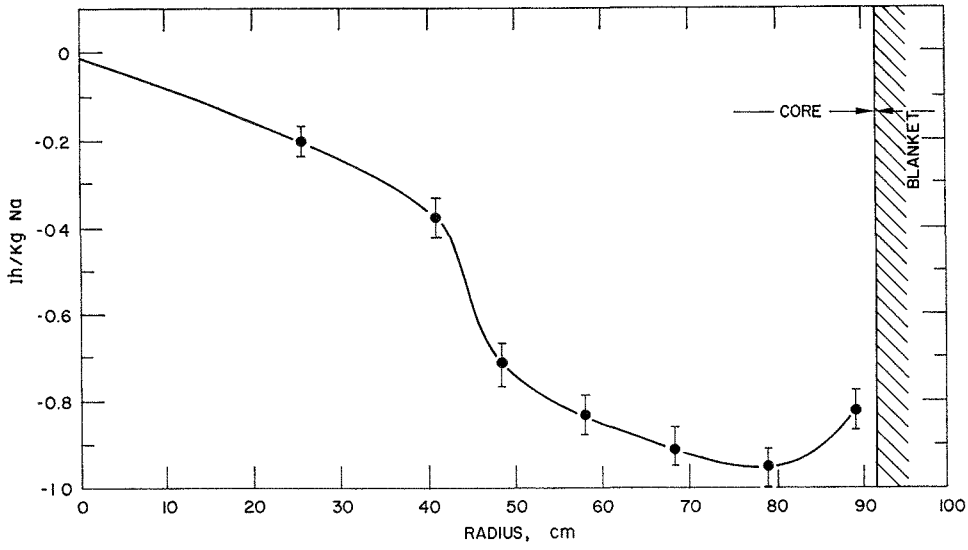

Fig. II-21-5. Sodium Void Coefficient as a Function of Radius, Assembly 6A. *ANL Neg. No. 116-489.*

TABLE II-21-V. CENTRAL REACTIVITY WORTHS, ZPR-6 ASSEMBLY 6A

Sample	Samples Measured in 2 × 2 × 1 in. Cavity							
	Sample Weight, g	Can Type and Weight, g	Central Worth With Sodium			Central Worth Without Sodium		
			Ih		Ih/kg	Ih		Ih/kg
			Gross	Net		Gross	Net	
B-10	29.29	SS, 55.73	−24.10 ± 0.01	−24.03 ± 0 01	−820.41 ± 0.34	−17.95 ± 0.01	−17.96 ± 0.01	−613.18 ± 0.34
Ta	833.69	SS, 49.47	−10.48 ± 0.01	−10.42 ± 0.01	−12.50 ± 0.01	—	—	—
W	1108.00	Bare	−5.27 ± 0.01	−5.27 ± 0.01	−4.76 ± 0.01	−4.18 ± 0.01	−4.18 ± 0.01	−3.77 ± 0.01
Re	1266.90	Bare	−20.15 ± 0.01	−20.15 ± 0.01	−15.90 ± 0.01	−15.78 ± 0.01	−15.78 ± 0.01	−12.46 ± 0.01
U-238	1151.49	Bare	−3.68 ± 0.01	−3.79 ± 0.01	−3.29 ± 0.01	−2.85 ± 0.01	−2.86 ± 0.01	−2.48 ± 0.01
Pu[a]	57.77	SS, 18.36	+2.69 ± 0.01	+2.75 ± 0.01	+47.60 ± 0.20	—	—	—
U-235	4.20	SS, 52.63	+0.1125 ± 0.0020	+0.1756 ± 0.0021	+41.80 ± 0.48	−0.0872 ± 0.0017	+0.1504 ± 0.0023	+36.00 ± 0.55
U-235	51.34	SS, 52.63	+2.12 ± 0.01	+2.19 ± 0.01	+42.65 ± 0.20	+1.82 ± 0.01	+1.86 ± 0.01	+36.23 ± 0.20
C	101.98	Bare	+0.394 ± 0.002	+0.394 ± 0.002	+3.863 ± 0.020	+0.253 ± 0.001	+0.253 ± 0.001	+2.481 ± 0.010
Be	114.31	Bare	+1.27 ± 0.01	+1.27 ± 0.01	+11.10 ± 0.10	+1.070 ± 0.0	+1.070 ± 0.01	+9.36 ± 0.10
Na	51.38	SS, 56.42	−0.0583 ± 0.0014	+0.008 ± 0.002	+0.160 ± 0.040	−0.0396 ± 0.0026	+0.0316 ± 0.0030	+0.615 ± 0.058
SS	30.08	Bare	−0.355 ± 0.001	−0.355 ± 0.001	−1.180 ± 0 330	−0 0361 ± 0.0015	−0.0361 ± 0.0015	−1.200 ± 0.050

[a] Composition of this sample 98.78 w/o Pu and 1.22 w/o Al. Isotopic composition of Pu is 0.037% Pu-238, 72.24% Pu-239, 22.28% Pu-240, 4.63% Pu-241, and 0.79% Pu-242.

TABLE II-21-VI. SAMPLES MEASURED IN CORE ENVIRONMENT

Sample	Sample Weight, g	Central Worth With Sodium		
		Ih		Ih/kg
		Gross	Net	
U-235	4.336	+0.2087 ± 0.0013	+0.2067 ± 0.002	+47.90 ± 0.69
U-235	8.636	−0.4232 ± 0.0015	+0.4043 ± 0.0033	+46.81 ± 0.35
U-235	21.435	+1.010 ± 0.010	+1.017 ± 0.010	+47.64 ± 0.93
U-235	56.830	+2.459 ± 0.010	+2.4914 ± 0.010	+43.84 ± 0.35
SS	11.586	−0.0540 ± 0.0023	−0.0165 ± 0.0025	−1.424 ± 0.216
Fe_2O_3	23.52	+0.0103 ± 0.0013	−0.0094 ± 0.0013	−0.400 ± 0.055
U_3O_8	95.755	−0.3026 ± 0.0003	−0.2762 ± 0.0010	−2.884 ± 0.011
Dep. U	50.377	−0.2006 ± 0.0003	−0.1705 ± 0.0001	−3.384 ± 0.022
Na	42.912	−0.0049 ± 0.0007	+0.0059 ± 0.0008	+0.137 ± 0.019

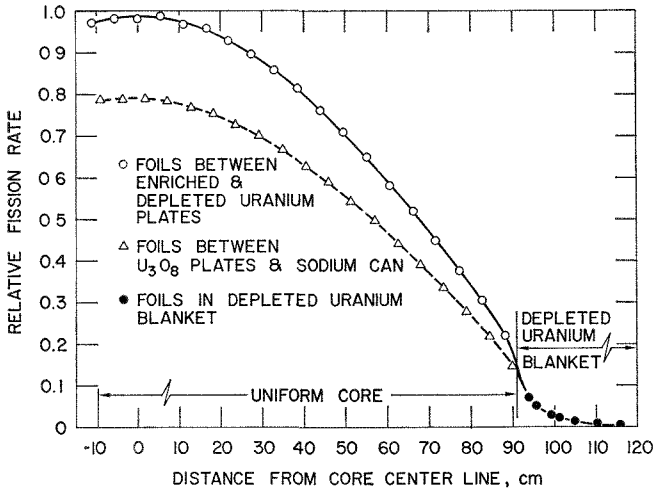

FIG. II-21-6. Radial Depleted Uranium (0.21%) Fission Rate Distribution—Sodium in Central Zone. *ANL Neg. No. 116-493.*

one can only. In some cases, when plates were thicker than 1/16 in., only a fraction was removed, i.e., a 2 × 2 × 1/8 in. plate was replaced by a 2 × 1 × 1/8 in. plate. In this manner, the relative positions of the various plates were kept intact. The results are given in Table II-21-VI.

NORMALIZATION INTEGRAL

The normalization integral in Assembly 6A was measured by the technique described elsewhere.[5] The measured value was (7.13 ± 0.10) × 10^5 with the flux and adjoint function normalized such that

$$\sum_i^N (\nu\Sigma_f)_i\phi_i = 1$$

and

$$\sum_i^N \chi_i\phi_i^* = 1$$

at the center of the reactor.

The normalization integral was also measured in the 39.36 cm radius central, sodium-free region. The value was (9.09 ± 0.10) × 10^5 with the fluxes and adjoint function normalized in the same manner as for the sodium "in" case. The normalization integral for the sodium-free case should not be used to normalize the reactivity worths in Table II-21-V to those in Table

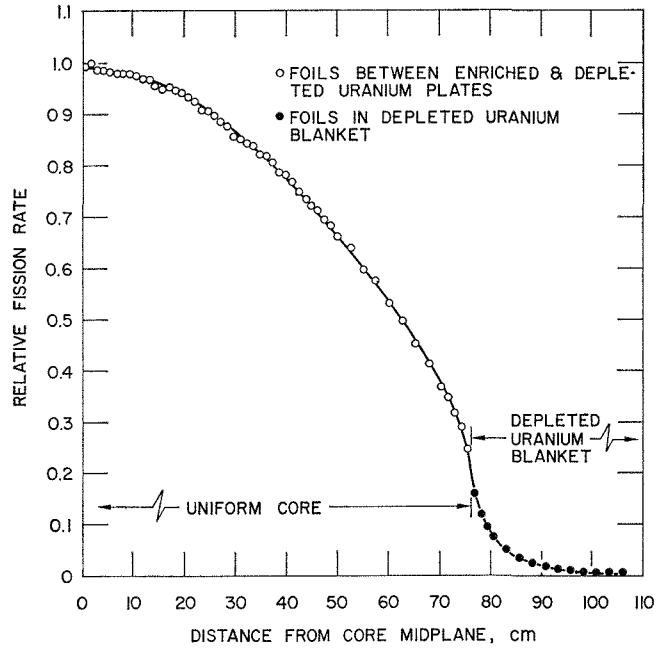

FIG. II-21-7. Axial Depleted Uranium (0.21%) Fission Rate Distribution—Sodium in Central Zone. *ANL Neg. No. 116-503.*

II-21-VI because the neutron spectrum in the two cases is significantly different.

Activation Distribution

The power distribution is quite relevant to fuel management and burnup problems in power reactors. Activation distributions such as fission rates in U-235 and U-238 and capture rates in U-238 provide important checks of the calculational methods.

Radial and axial activation distributions were measured with foils of enriched and depleted uranium. The measurements were made both in the uniform loading with the sodium "in" and in the core with the sodium-

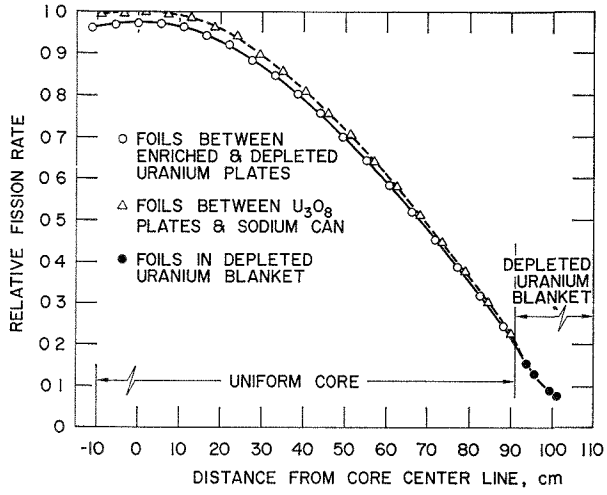

Fig. II-21-8. Radial Enriched Uranium (93%) Fission Rate Distribution—Sodium in Central Zone. *ANL Neg. No. 116-495.*

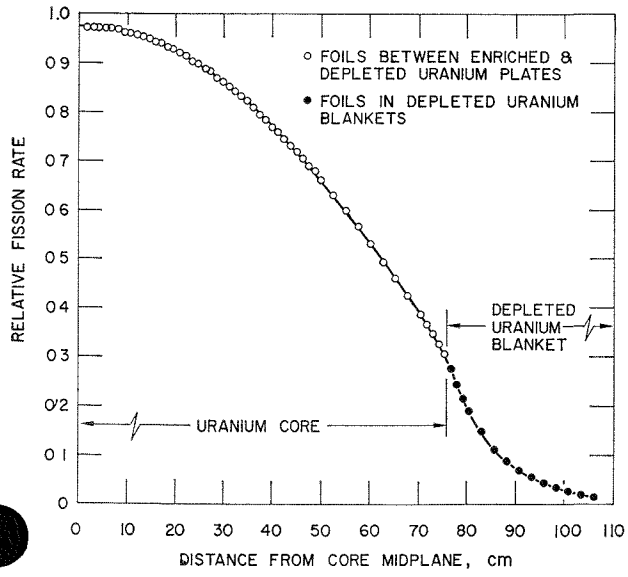

Fig. II-21-9. Axial Enriched Uranium (93%) Fission Rate Distribution—Sodium in Central Zone. *ANL Neg. No. 116-501.*

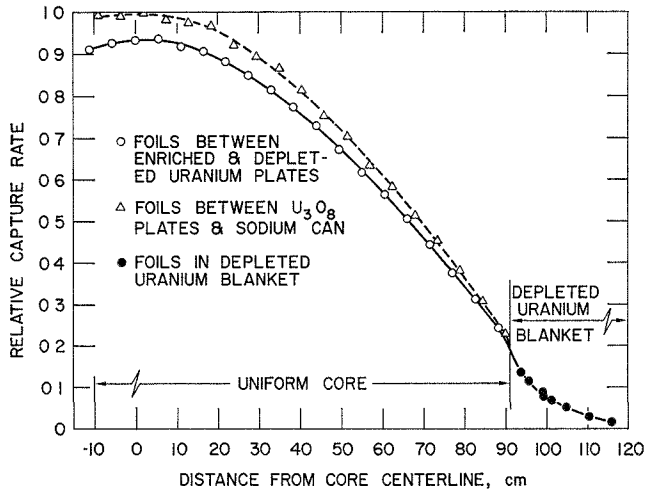

Fig. II-21-10. Radial Depleted Uranium (9.21%) Capture Rate Distribution—Sodium in Central Zone. *ANL Neg. No. 116-494.*

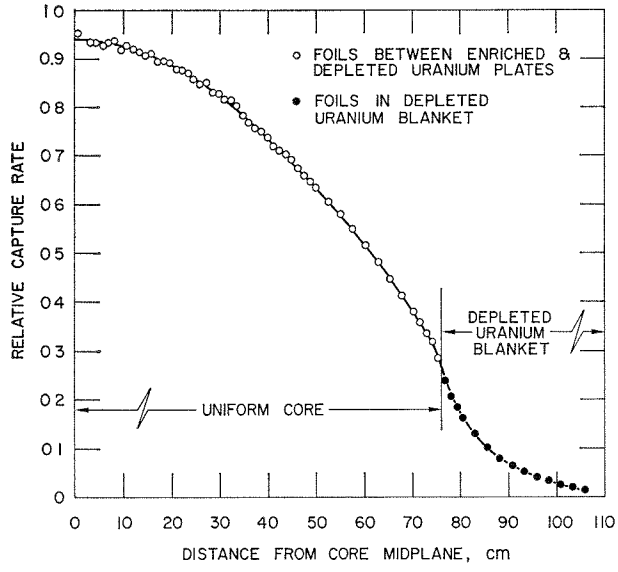

Fig. II-21-11. Axial Depleted Uranium (0.21%) Capture Rate Distribution—Sodium in Central Zone. *ANL Neg. No. 116-502.*

free central zone. The results are plotted in Figs. II-21-6 through II-21-17. For the radial traverses, foils were placed between the depleted and enriched uranium plates, and also between the U_3O_8 plate and the sodium can closest to the enriched plate. This was done in every drawer along the radius in the uniform quadrant with the foils about 1 in. from the axial midplane. For the axial traverses, the foils were between the enriched and depleted uranium plates.

The accuracy of the relative activity measurements is approximately ±0.5−1%, with some exceptions near

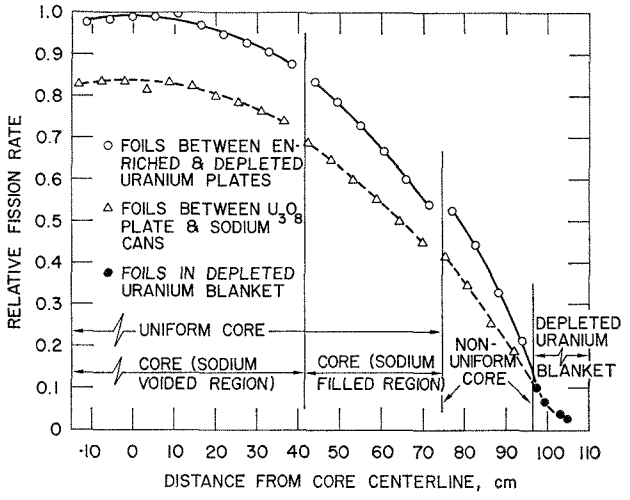

FIG. II-21-12. Radial Depleted Uranium (0.21%) Fission Rate Distribution—Sodium-Free Central Zone. *ANL Neg. No. 116-496.*

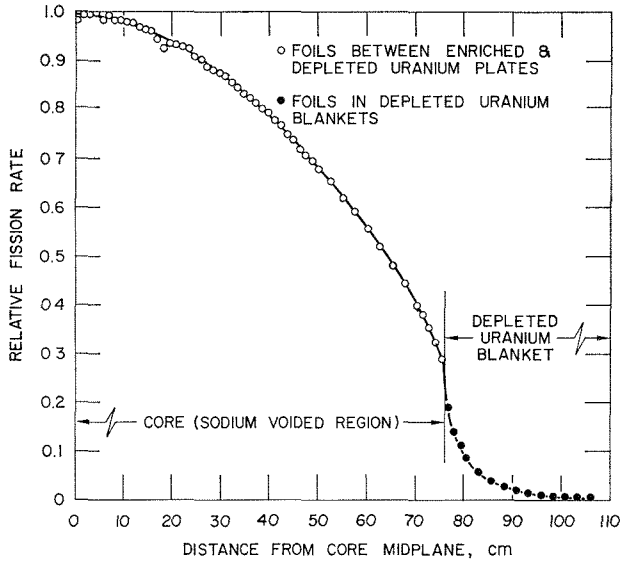

FIG. II-21-13. Axial Depleted Uranium (0.21%) Fission Rate Distribution—Sodium-Free Central Zone. *ANL Neg. No. 116-504.*

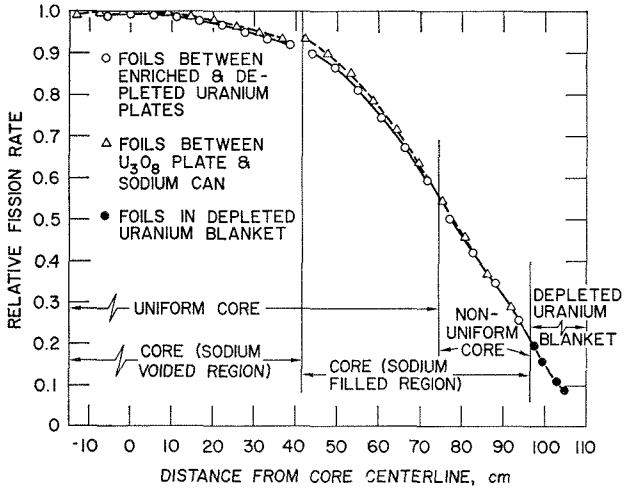

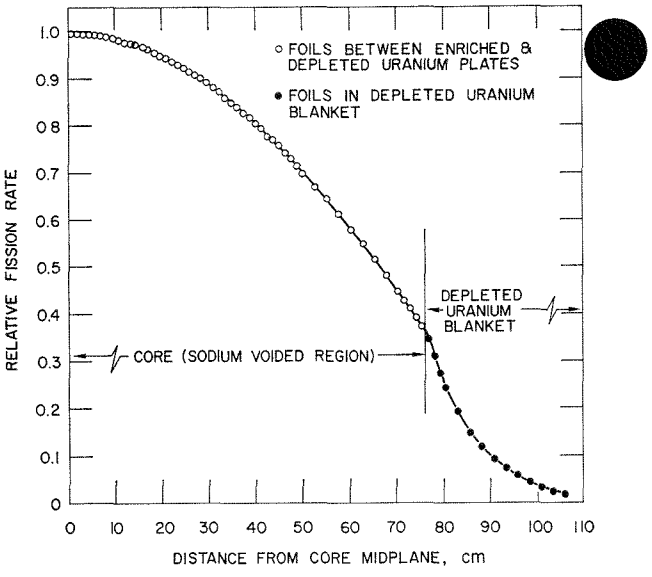

FIG. II-21-15. Axial Enriched Uranium (93%) Fission Rate Distribution—Sodium-Free Central Zone. *ANL Neg. No. 116-500.*

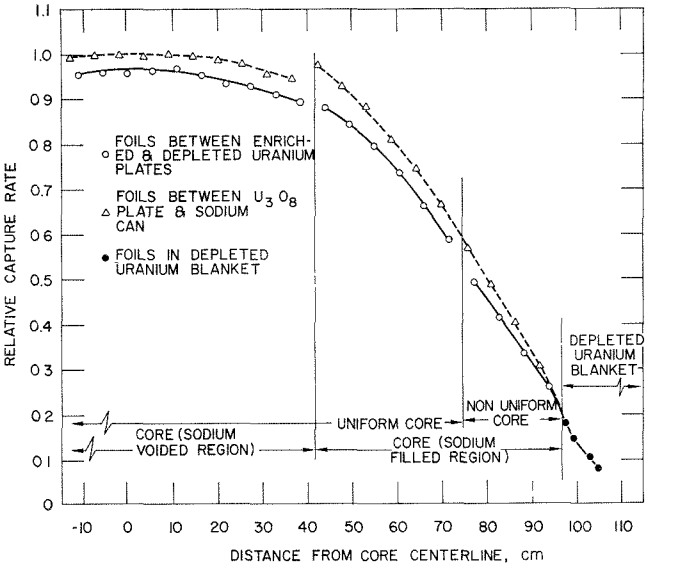

FIG. II-21-16. Radial Depleted Uranium (0.21%) Capture Rate Distribution—Sodium-Free Central Zone. *ANL Neg. No. 116-497.*

FIG. II-21-14. Radial Enriched Uranium (93%) Fission Rate Distribution—Sodium-Free Central Zone. *ANL Neg. No. 116-498.*

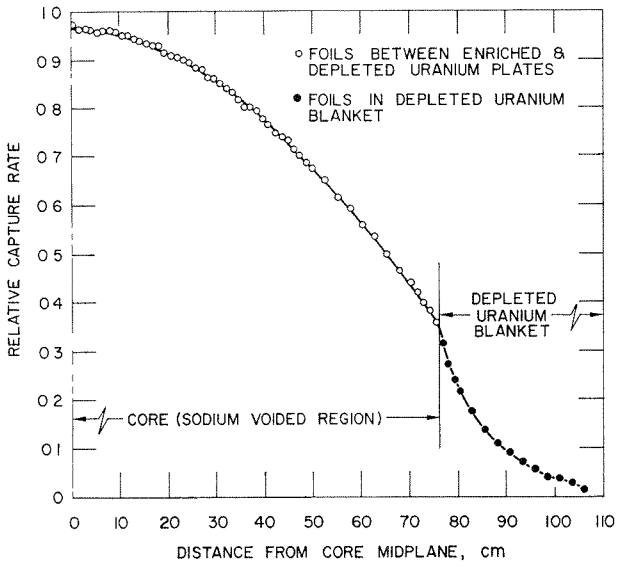

FIG. II-21-17. Axial Depleted Uranium (0.21%) Capture Rate Distribution—Sodium-Free Central Zone. *ANL Neg. No. 116-499.*

the outer ends of traverses where the activities are low and the accuracy is limited by counting statistics.

REFERENCES

1. R. A. Karam, L. R. Dates, W. Y. Kato, J. E. Marshall, T. Nakamura and G. K. Busch, *A 4000-Liter Uranium Oxide Fast Core, Assembly 6 of ZPR-6*, Reactor Physics Division Annual Report, July 1, 1967 to June 30, 1968, ANL-7410, pp. 75–80.
2. R. A. Karam, J. E. Marshall, L. R. Dates and G. K. Rusch, *Sodium-Void Effects in a Large UO_2 Core, ZPR-6 Assembly 6*, Reactor Physics Division Annual Report, July 1, 1967 to June 30, 1968, ANL-7410, pp. 125–128.
3. R. A. Karam, K. D. Dance, L. R. Dates W. Y. Kato, J. E. Marshall, T. Nakamura, and G. K. Rusch, *Heterogeneity Effects in a Large UO_2 Core, ZPR-6 Assembly 6*, Reatcor Physics Division Annual Report, July 1, 1967 to June 30, 1968, ANL-7410, pp. 133–140.
4. R. A Karam, K. Dance, T. Nakamura and J Marshall, *Analysis of Central Reactivity Worths in Fast Critical Assemblies*, Nucl. Sci. Eng. **40**, pp. 414–423 (1970).
5. R. A. Karam, *Measurements of the Normalization Integral and the Spatial Distribution of the Importance of Fission Neutrons*, Nucl. Sci. Eng **37**, pp. 192–197 (1969).

II-22. Measured Neutron Spectra in ZPR-6 Assembly 6A, ZPR-9 Assembly 25, and ZPR-9 Assembly 26, FTR-3

T. J. YULE, E. F. BENNETT and I. K. OLSON

INTRODUCTION

Spectrum measurements using proton-recoil proportional counters have been undertaken in the ZPR facilities to confirm the accuracy of calculational techniques, as well as to provide a test of basic nuclear data. Measurements of central spectra in large cores are especially valuable since such spectra may be meaningfully compared with fundamental mode calculations. As the quality of basic nuclear data improves and as the calculational techniques become more sophisticated, it is important that various sources of systematic errors in the measurements be uncovered if the comparisons are to have merit. Substantial improvements in the instrumentation and a better understanding of sources of error have occurred during the last few years (see Paper III-18). It is believed that degraded fission spectra can now be measured with good accuracy in the energy range from 1 keV to 2 MeV.

Several central spectrum measurements in recently constructed ZPR assemblies are reported herein, together with a comparison with calculated fundamental mode spectra. A grouping of several measurements permits one to easily identify systematic variations and discrepancies.

PROTON-RECOIL TECHNIQUE AND ANALYSES

The technique employed in measuring neutron spectra with proton-recoil proportional counters and the analyses of proton-recoil data necessary for the derivation of neutron spectra free from systematic errors have been discussed previously.[1, 2] A short description of the various corrections for recognized sources of error is provided here; a more comprehensive report of the technique as it is now used at ANL will be provided elsewhere.[3]

TECHNIUQE

The detectors used in the measurements are shown in Fig. II-22-1. Detector bodies are of thin-walled stainless steel and the anodes are fine stainless steel wire. Field tubes are used to define the sensitive volume of the detector. These detectors are considerably smaller than the detectors used in the earlier spectrum measurements which were made in uranium fueled cores.[4] The smaller detectors are, however, necessary for compatibility with the requirements of counting inside large plutonium-fueled fast reactors. Spontaneous fission neutrons from Pu-240 in the fuel provide a high neutron flux environment inside the cores, even

for far subcritical operation. In order to approach near-critical (less than 2% subcritical) and still maintain the total event rate within acceptable limits imposed by the electronics system, it is necessary to use small chambers. The larger detector in Fig. II-22-1 is filled with about 8 atm of predominately methane gas.

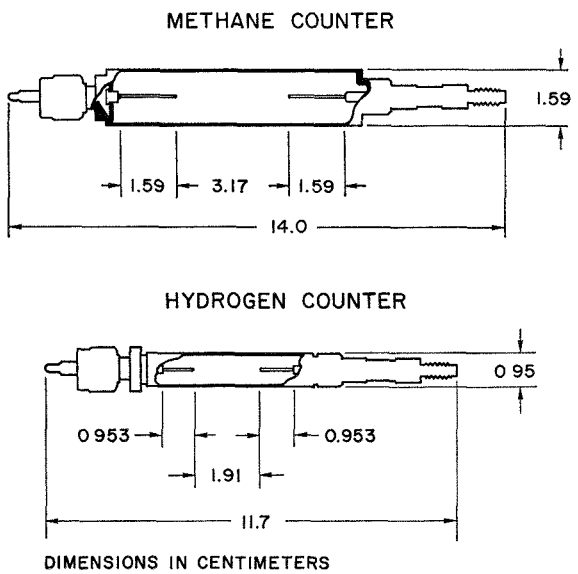

FIG. II-22-1. Proton-Recoil Proportional Counters for Use in Fast Reactors. The Anodes are 0.0254 mm in Diameter and the Field Tubes are 0 254 mm in Diameter *ANL Neg. No. 116-28 T-1.*

The methane detector is used to measure the region of the proton-recoil spectrum with energies greater than 100 keV. The smaller detector is filled with about 10 atm of predominately hydrogen gas. The hydrogen detector is used to measure the region of the proton-recoil spectrum with energies below 100 keV.

The detectors are enclosed in a lead sleeve 0.020 in. thick. This amount of high-Z material will significantly reduce the sensitivity of the detector to soft photons. The lead sleeve and detector are enclosed in a thin Teflon sleeve which electrically isolates the counter body from the drawer.

For the various measurements reported here, detectors were placed near the core axis in the movable half. Figure II-22-2 illustrates the fuel box and detector probe arrangement which was inserted in the 2 by 2 in. matrix of the ZPR cores. Plate material identical to that of which the reactor is constructed was placed around the probe and in that portion of the box not used by the preamplifier and cabling to simulate a loaded reactor drawer. The cavity occupied by the probe was ¾ in. in diam and an effort was made to homogenize the material around the cavity. This requirement cannot easily be met with the plate loading material without specially constructed sodium and plutonium cans. Figure II-22-2 shows the compromise configuration which was used for the spectrum measurement in ZPR-9 Assembly 25. Table II-22-I lists the simulated loadings that were used for the various

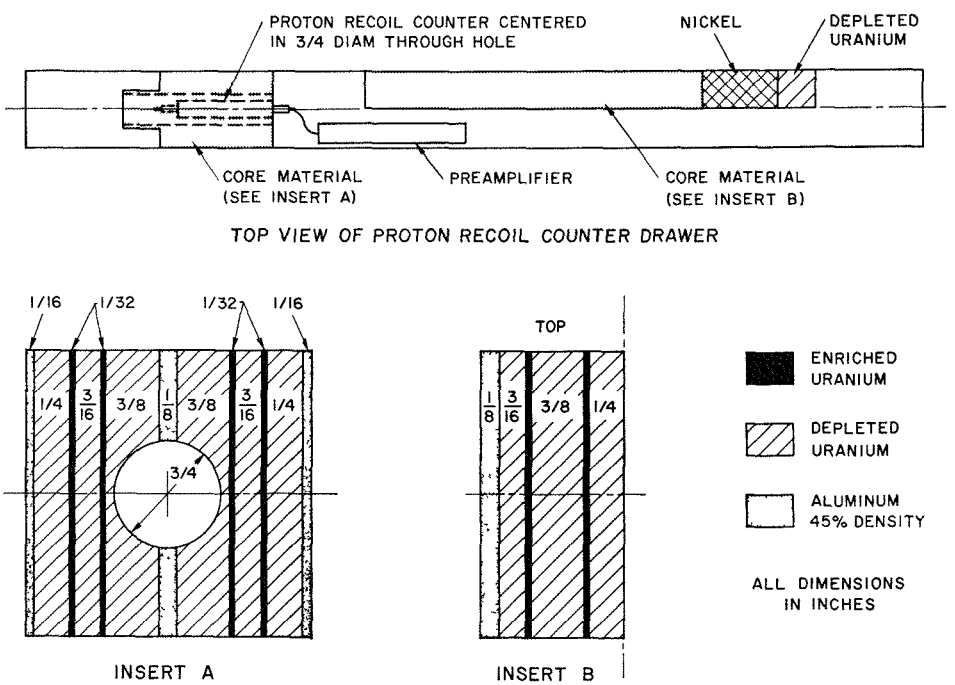

FIG. II-22-2. In-Core Detector Probe Showing Preamplifier and Material Placement for Measurement in ZPR-9 Assembly 25. *ANL Neg. No. 116-27.*

easurements. The question of the perturbation to the pectrum due to the cavity-detector arrangement is discussed later.

The detectors were calibrated by observing protons from the $N^{14}(n,p)C^{14}$ reaction when the counters were exposed to thermal neutrons. Each counter contains a small amount of nitrogen. A relative calibration was also made for the hydrogen detector by observing the electrons from the decay of A-37. The ability of these methods to provide relative and absolute calibrations is indicated in Ref. 3. A systematic bias may be introduced into the calibration if amplifiers are optimized for fast counting and low dead-time. Long track length and slow electron collection, especially in hydrogen-filled counters, may bias the calibration as measured with the $N^{14}(n,p)C^{14}$ reaction by as much as 10%. Measurements made in fast reactors containing a large amount of structural material and diluents exhibit strong resonance effects and one is justified in determining the absolute calibration by requiring agreement of the location of measured and calculated resonance detail. This procedure is quite satisfactory for the data taken with the hydrogen detector, but leads to some ambiguity for data taken with the methane detector, as is discussed in the next section.

CORRECTION FOR SYSTEMATIC ERRORS

Proton-recoil spectra taken with proportional counters must be corrected for various effects before the ideal proton-recoil spectra, i.e. the spectra which when differentiated lead to the correct neutron spectra, can be obtained. The types of corrections which were applied to the present set of measurements are described below.

Correction for Electric Field Distortion

The proton-recoil data were first corrected for electric field distortion. The simple approach used to desensitize counters near the ends by employing field tubes is not completely satisfactory, since a distortion of internal field lines occurs. The effect may be calculated, however, and with a detailed knowledge of the internal field a correction for the effect can be made.[5] The electric field distortion produces significant effects at low energies, especially when the flux is relatively low at these energies. The electric field distortion introduces a systematically higher neutron flux than actually exists.

Correction for W Variation

The proton-recoil data were then corrected for the n-linear variation of energy with ionization. The easured proton-recoil spectrum is per unit ionization and must be transformed to the proton-recoil spectrum per unit energy by dividing by the keV per ion pair, W. Above 10 keV, W has been found to be energy-independent up to the MeV region for protons stopping in hydrogen.[6] Below 10 keV W is known to vary with energy[7, 8] and a prescription for W was used which has been shown to give consistent results with previous experimental data.

TABLE II-22-I. SIMULATED LOADINGS IN COUNTER DRAWER

Assembly	Simulated Loading Starting from Edge of Drawer[a]
ZPR-6 Assembly 6A[b]	(1/16) U-235, (1/16) Stainless Steel, (1/2) Na, (1/4) U_3O_8, (1/8) Fe_2O_3, (1/4) U_3O_8, (1/8) Fe_2O_3 (1/4) Na, (1/4) U_3O_8, (1/8) U-238
ZPR-9 Assembly 25	(1/16) Al-45%, (1/4) U-238, (1/32) U-235, (3/16) U-238, (1/32) U-235, (3/8) U-238, (1/8) Al-45%, (3/8) U-238, (1/32) U-235, (3/16) U-238, (1/32) U-235, (1/4) U-238, (1/16) Al-45%
ZPR-9 Assembly 26	(1/8) U_3O_8, (1/2) Na, (3/8) U_3O_8, (1/8) Stainless Steel, (1/4) U_3O_8, (1/2) Na, (1/8) Pu-Al
ZPR-6 Assembly 7	(1/8) Fe_2O_3, (1/4) Pu-U-Mo, (1/4) Na, (3/4) U_3O_8, (1/2) Na, (1/8) Fe_2O_3

[a] Dimensions in parentheses are in inches. See Fig. II-22-2.
[b] For the sodium void measurements sodium cans in a region within 10 in. from the counter were replaced with cans from which the sodium had been removed.

Correction for Carbon Recoils

The carbon component in methane-filled counters undergoes scattering by fast neutrons and the ionization produced cannot be distinguished from that induced by recoil protons. Corrections for this effect were made.[1]

Correction for Wall-and-End Effects

Distortions are introduced by the truncation of proton-recoil tracks by the counter walls or by the extension of tracks into the end region. It is possible to calculate the response function for a particular counter and correct the data accordingly.[9] For the methane counter the maximum energy a proton-recoil can deposit in the counter is about 3 MeV—the proton-recoil spectrum is cut-off at that energy. The correction for wall-and-end distortion proceeded in two parts. The first part corrected for proton-recoils arising from neutrons above the measurement limit; the second part corrected for distortion of proton-recoils produced by neutrons below the measurement limit. In the first part, it is assumed that the neutron spectrum above 2.5 MeV is that predicted by a fundamental-mode calculation. The distorted proton-recoil spectrum was calculated for those neutrons above 2.5 MeV. The calcu-

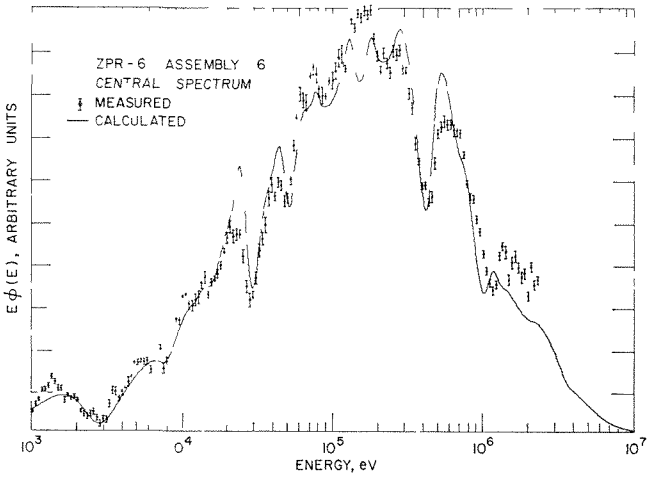

FIG. II-22-3. Central Neutron Spectrum in ZPR-6 Assembly 6A Together with a Smoothed MC² Calculation. *ANL Neg. No. 116-466*

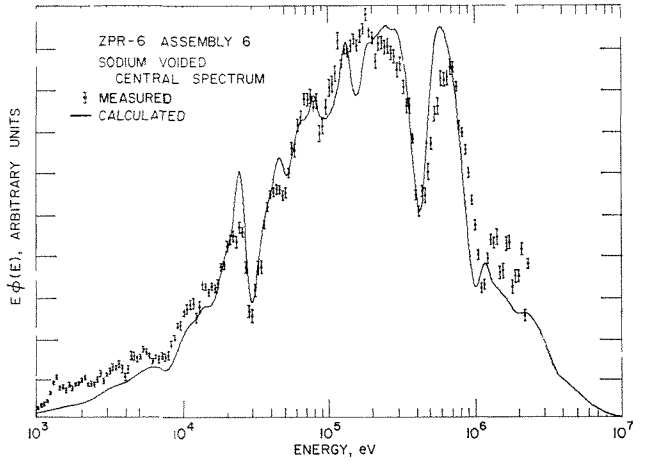

FIG. II-22-4 Central Neutron Spectrum in a Sodium-Voided Region of ZPR-6 Assembly 6A Together with a Smoothed MC² Calculation *ANL Neg No. 116-453*

lated proton-recoil distribution was normalized to the measured distribution between 2.5 and 3 MeV. The normalized calculated spectrum was then subtracted from the measured spectrum. Thus, the influence of proton-recoils from neutrons above the measurement limit was eliminated.

The second part of the correction took into account distortion of proton-recoils from neutrons below the cut-off. The measured proton-recoil spectrum was corrected with the counter response function from high energy to low energy using integral unfolding techniques. Experience has indicated that it is not necessary to make wall-and-end corrections for data taken with the hydrogen counter.

The effects of the two parts of the wall-and-end corrections, as well as of the carbon-recoil correctio[illegible] are considered in detail in Paper III-16.

Measured and Calculated Spectra

MEASUREMENTS

Spectrum measurements were made in ZPR-6 Assembly 6A, ZPR-9 Assembly 25, and ZPR-9 Assembly 26. These assemblies are representative of types of cores constructed during the last few years at the ZPR facilities.

ZPR-6 Assembly 6A

Assembly 6A of ZPR-6 was a 4000-liter UO_2 fast core which was almost identical to Assembly 6 of ZPR-6 and is reported in Paper II-21. A central spectrum measurement was made with the normal loading, as well as with the core voided of sodium. Similar neutron spectrum measurements[10] had been made in Assembly 6 of ZPR-6. Figures II-22-3 and II-22-4 show the measured spectra along with calculated spectra which will be discussed later. For the sodium-voided case a region approximately 10 in. in radius around the counter was voided of sodium. If these measurements are compared with the earlier measurements, a number of significant differences appear. At low energies the present measurements indicate a considerably lower flux. This arises from the correction for electric field distortion and W variation—corrections which were not included in the analysis of the earlier data. The previous measurements also indicate more pronounced structure near the scattering resonances, especially the iron resonance, which appears at about 30 keV. The differences may be due to the different counters used for the two measurements. Rather thick walled (0.100 in.) counters were used in the earlier measurements and the counters also had somewhat better resolution. A greater amount of scattering material in a measurement will accentuate the resonance structure.

ZPR-9 Assembly 25

Assembly 25 of ZPR-9 was a small, uranium-loaded, zoned assembly with a central test zone having k_∞ equal to unity. The test zone was composed primarily of enriched and depleted uranium. The fission spectrum was degraded by U-238 inelastic scattering and U-238 capture was effective in reducing the low energy flux. The assembly was constructed primarily to try to resolve some of the cross section uncertainties in the fertile and fissile isotopes with special emphasis on U-238. The details of the assembly are reported [illegible] Paper II-19. The measured central neutron spectru[illegible]

ogether with the calculated spectrum is shown in Fig. -22-5. It is to be noted that the large oxygen resonance which appears at about 400 keV in the ZPR-6 Assembly 6 measurement no longer appears, and that the resonance structure associated with iron is significantly reduced. The flux is virtually zero below 5 keV. The low measured flux is produced only after the corrections for electric field distortion and W variation have been made.

ZPR-9 Assembly 26

Assembly 26 of ZPR-9 was constructed as part of the Fast Flux Test Facility (FFTF) program. The FFTF is to be a plutonium oxide-fueled, sodium-cooled fast reactor with a high-intensity fast flux. Assembly 26 had a two-zone core, which smoothed out engineering details by homogenizing the material in the two zones. The details of the assembly are reported in Paper II-2. The measured central spectrum together with a calculated spectrum is shown in Fig. II-22-6. The spectrum is seen to be quite similar to that of Assembly 6A of ZPR-6 with the sodium, iron and oxygen resonances clearly visible. For some reason the oxygen resonance structure seems to be better defined in this assembly than in Assembly 6A.

COMPARISON WITH CALCULATED SPECTRA

The predicted spectra—indicated by the continuous lines in Figs. II-22-3 through II-22-6, were calculated using ENDF/B Version I nuclear data by means of the MC² code.[11] The calculation assumes a fundamental mode model in the P-1 approximation. The plate loading of the fuel was taken into account in an approximate way by using the heterogeneous MC² option which uses the modified Bell approximation to account for self-shielding in the fuel. In each figure the calculation was normalized so that the integral over the energy range of the experimental points equaled the corresponding integral for the experimental data. The continuous curve is the result of smoothing the MC² points, which are calculated for 1/120 lethargy intervals, with a Gaussian window whose width corresponds to the experimental resolution. The experimental energy resolution varied from about 12% over most of the energy range to almost 30% in the vicinity of 1 keV, where statistics in ionization become poor.

In general, the agreement between the measured spectra and calculated spectra is good. However, there are some regions of notable exception. There is some systematic disagreement in the energy calibration for the methane data, i.e. for the data above 100 keV. It is t possible to obtain agreement between the measured d calculated oxygen resonance dips at both 400 keV

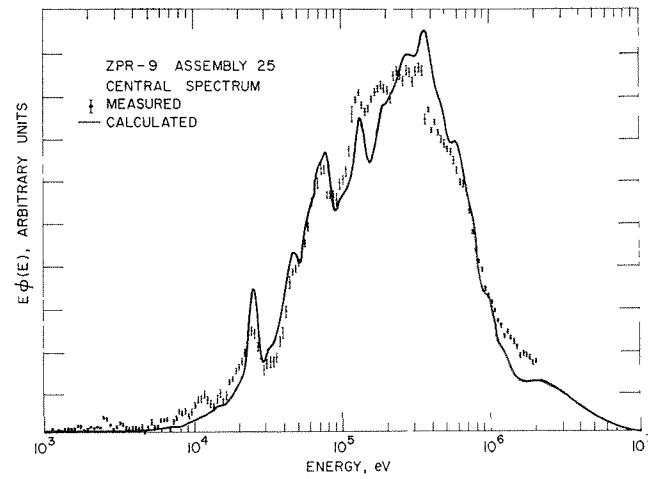

FIG. II-22-5. Central Neutron Spectrum in ZPR-9 Assembly 25 Together with a Smoothed MC² Calculation. *ANL Neg. No. 116-464.*

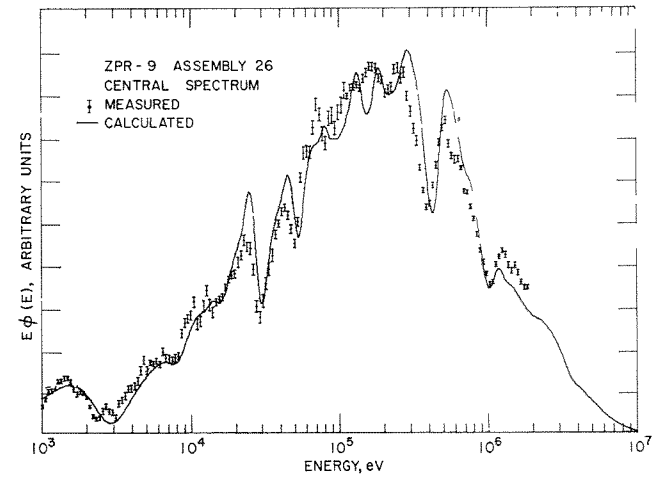

FIG. II-22-6. Central Neutron Spectrum in ZPR-9 Assembly 26 (FTR-3) Together with a Smoothed MC² Calculation. *ANL Neg. No. 900-308 Rev 1.*

and at 1 MeV. The reason for the discrepancy is being investigated.

There are also significant differences in the neighborhood of the resonances, especially the iron resonances. It is not easy to explain the discrepancies in terms of experimental resolution or instrumental distortion. As is shown below, heterogeneity effects cannot account for such large differences. There is some indication from time-of-flight work in iron blocks that the iron cross sections in ENDF/B Version I may be in error by substantial amounts.[12]

The agreement between measured and calculated spectra at high energies is not very good, especially in the ZPR-9 Assembly 25 comparison. This is not so surprising since for uranium and plutonium the region

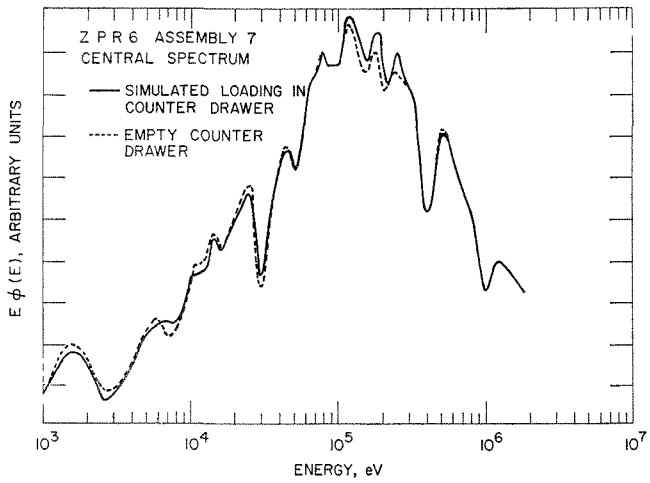

FIG. II-22-7. Central Neutron Spectrum in ZPR-6 Assembly 7 With and Without a Simulated Loading in the Counter Drawer. *ANL Neg. No. 116-319 Rev. 1.*

between reasonably known discrete excitation cross sections—up to about 1 MeV, and that at which a clear indication of the statistical distribution becomes apparent—above 3 MeV is an area of large cross section uncertainty. The fact that the comparison is especially poor for the assembly with a large amount of U-238, brings the cross sections for this isotope into question. There have been indications that its inelastic cross section in ENDF/B Version I should be lowered by approximately 6% (see Paper II-19). There is also some question concerning the accuracy of the calculations in the high energy region, since the MC² code does not use the Legendre treatment of elastic scattering on heavy elements.

The MC² calculation of the sodium-voided spectrum in ZPR-6 Assembly 6 (Fig. II-22-4) predicts substantially less low energy flux than is observed. The reason for this is unclear since a reasonably good agreement is found in the comparison of calculation with measurement for the normal (with sodium) core shown in Fig. II-22-3. This is another area deserving of additional investigation. The magnitude of the Doppler effect, for instance, will be significantly altered by a change in the low energy flux by the amount indicated.

HETEROGENEITY EFFECTS

In any detailed comparison between measured and calculated spectra, the question usually arises as to the influence of heterogeneity effects. If one examines the variation of group fluxes from one dimensional transport calculations as a function of position in a cell, large differences are noted. It is known that the counter will do some averaging, but exactly how much is not known. In these measurements an attempt was made to homogenize the material in the vicinity of the detector. In an attempt to examine the extent of local heterogeneity effects a measurement was made in Assembly 7 of ZPR-6 with and without a simulated loading of reactor material in the counter drawer. The details of the assembly and measurement will be reported later. The arrangement of material for the simulated loading is included in Table II-22-I. In the simulated loading an attempt was made to keep iron away from the counter. A comparison of the results of the two measurements are shown in Fig. II-22-7. Error bars are not shown, but are of the same size as those for the measurement in Assembly 26 of ZPR-9 (see Fig. II-22-6). For the most part, the differences are slight. There is some difference near iron resonances. When the simulated loading is not present, the counter can look directly at the stainless steel matrix structure and the counter drawer. As one might expect, one sees more resonance structure. There is also some indication that having sodium next to the counter changes the flux near the sodium resonance. All in all, the effects are insufficient to explain some of the discrepancies that have been noted between measured spectra and calculated spectra.

CONCLUSIONS

The intercomparison with theory of a series of spectrum measurements in large dilute fast reactors has revealed systematic discrepancies which are believed to be outside of experimental error, and probably not entirely associated with local heterogeneity effects. The ability to predict the detailed flux variation in the vicinity of some large resonances is not very good. Persistent disagreement at the higher energies has been observed and in some cases agreement at low energy is rather poor.

The proton-recoil technique can be improved in both the high and low energy limits and measurements with better statistical accuracy and resolution are feasible. If, as it now appears, heterogeneity effects in the measurements are not a limiting uncertainty, additional effort may clarify observed disagreement and provide a rather strong criticism of the methods for calculation and the quality of cross section sets.

No use has been made of the ability of the proton-recoil method to provide accurate absolute fluxes. Suitable reaction rate measurements made in conjunction with experimental observations of the spectrum should prove to be of considerable interest.

REFERENCES

1. E. F. Bennett, *Neutron Spectroscopy by Proton-Recoil Proportional Counting*, Nucl. Sci. Eng. **27**, 16 (1967).

2. E. F. Bennett and T. J. Yule, *Neutron Spectroscopy with Proton-Recoil Proportional Counters*, Proc. EANDC Symposium on Neutron Standards and Flux Normalization, October 21–23, 1970, Argonne National Laboratory, DTIE Symposium Series (to be published).
3. E. F. Bennett and T. J. Yule, *Techniques and Analyses for Fast Reactor Neutron Spectroscopy with Proton-Recoil Proportional Counters*, ANL-7763 (to be published).
4. E. F. Bennett, *Neutron Spectrum Measurement in a Fast Critical Assembly*, Nucl. Sci. Eng. **27,** 28 (1967).
5. E. F. Bennett, *Electrical Field Effects in Proportional Counters and Their Influence on Spectroscopy*, Reactor Physics Division Annual Report, July 1, 1968 to June 30, 1969, ANL-7610, pp. 399–403.
6. J. W. Rogers, *An Investigation of the Energy Dependence of the Specific Average Energy Loss Per Ion Pair in Methane and Hydrogen with a Proton-Recoil Spectrometer*, Trans. Am. Nucl. Soc. **12,** 936 (1969).
7. H. Werle, G. Fiege, H. Seufert and D. Stegemann, *Investigation of the Specific Energy Loss of Protons in Hydrogen above 1 keV with Regard to Neutron Spectrometry*, Nucl. Instr. Methods **72,** 111 (1969).
8. E. F. Bennett, *Low-Energy Limitations on Proton-Recoil Spectroscopy Through the Energy Dependence of W*, Trans. Am. Nucl. Soc. **13,** 269 (1970).
9. T. J. Yule, *Predictions of Geometrical Distortions in Proton-Recoil Counters and Application to Neutron Spectroscopy*, Reactor Physics Division Annual Report, July 1, 1968 to June 30, 1969, ANL-7610, pp. 404–410.
10. E. F. Bennett and R. A. Karam, *Neutron Spectroscopy in ZPR-6 Assembly 6 Using Proton-Recoil Counters*, Reactor Physics Division Annual Report, July 1, 1967 to June 30, 1968, ANL-7410, pp. 151–155.
11. B. J. Toppel, A. L. Rago and D. M. O'Shea, *MC²*, *A Code to Calculate Multigroup Cross Sections*, ANL-7318 (1967).
12. B. Malaviya, *Experimental and Analytical Studies of Fast Neutron Spectra in Iron*, pp. 259–260; R. J. Cerbone, *Neutron Transport Measurements in Iron*, p. 260; F. R. Mynatt, *Neutron Transport in Iron*, p. 260; Walter Meyer, D. H. Timmons and P. K. Shen, *One-Dimensional S_N Calculations of Neutron Spectra Reflected from Thick Slabs of Concrete and Iron, Comparison with Measurements*, pp. 261–262; Herbert Goldstein, *Survey of Theoretical Studies at Columbia University on Fast Neutron Transport in Iron*, p. 262; Trans. Am. Nucl. Soc. **13,** (1970).

II-23. The Variable Temperature Rodded Zone (VTRZ) Project

R. A. Lewis, K. D. Dance, J. F. Meyer and E. F. Groh

The VTRZ Project was initiated in 1967 for the purpose of designing, developing, and fabricating equipment for a heated zone experiment in the ZPR critical facilities. The purpose was to permit integral physics measurements to be made in environments which closely simulate the temperature conditions and fuel configuration of fast breeder power reactors. The principal intent of the measurements is to provide needed confirmation of the adequacy of current analytical techniques used to extrapolate from measurements made in cold plate-type assemblies, typical of fast critical assemblies like the Argonne ZPR facilities, to hot rodded configurations typical of power reactors. The resulting facility designated the Variable Temperature Rodded Zone (VTRZ), is to be approximately 360 liters in heatable volume (6 ft long and 20 in. in diam split axially into two 3 ft zones, one in each reactor half), capable of operation from room temperature to 500°C, and insulated from the surrounding reactor assembly.

A description of the conceptual design of the VTRZ and of the basic VTRZ experimental program is contained in Ref. 1. Reference 2 contains a description of the progress of the project during 1968–1969 including the development of a preliminary design and the fabrication and testing of a prototype of the VTRZ. This article is a progress report for the VTRZ Project in the period July 1969 to June 1970.

Progress of the VTRZ Project From July 1, 1969 to June 30, 1970

The principal accomplishments of the VTRZ Project during this period may be summarized as follows:

1. Completion of testing the VTRZ prototype
2. Preparation and AEC approval of a VTRZ Project Quality Assurance Program
3. Completion of final VTRZ design (Title II), issuance of final engineering drawings and procurement specifications, and publication of the VTRZ Design Summary Report
4. Initiation of VTRZ Heatable Zone Facility equipment procurement, completion of procurement of all VTRZ calandria cans, and continued procurement of fuel rods
5. Preparation of the VTRZ Final Safety Analysis Report and the related VTRZ-ZPR-6 Operating Limits document and submission of these documents for AEC review.

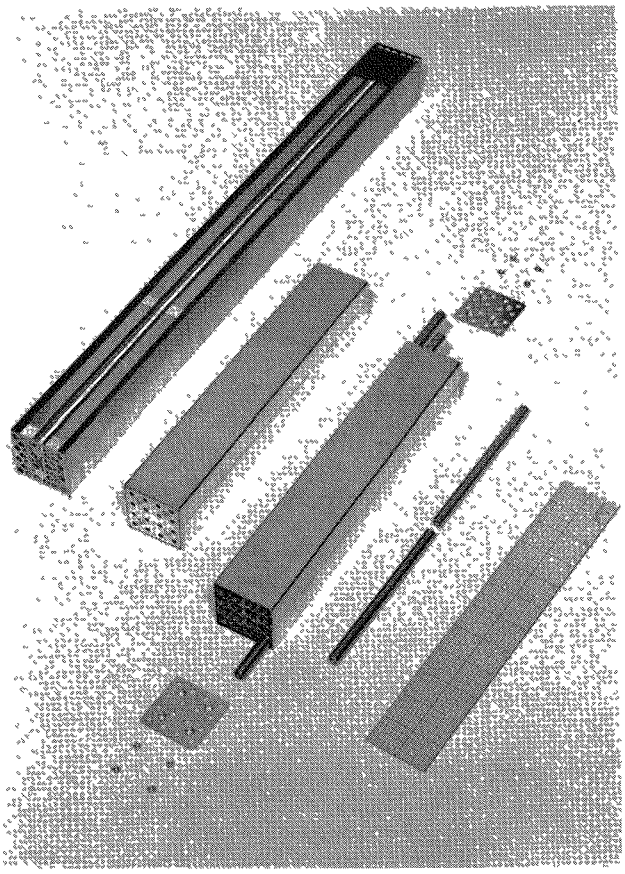

FIG. II-23-1. Typical Plate-Type Fuel Drawer, Calandria Cans, and Oxide Fuel Rods *ANL Neg. No 116-3.*

PROTOTYPE TESTING

The bulk of the performance tests on the VTRZ prototype was completed in August of 1969, although a low level of refinement and optimization tests continued throughout the reporting period. The principal tests were:

1. Structural (load-deflection) performance of the outer matrix assembly
2. Thermal performance of the insulation and cooling guard-ring
3. Temperature distribution in the heated zone
4. Structural performance of the ball mounts
5. Heat leakage across the insulation annulus
6. Performance of the electrical heating system, the thermocouple system, and the argon loop system
7. Exposure tests of the heated zone front cover
8. Thermal cycling and over-temperature tests of sodium-filled calandria cans.

Several significant design improvements were made on the basis of these tests. The most significant improvements were in the insulation type and arrangement, the cooling guard-ring ducting, and in the ball-mount design.

A notable result of the extensive prototype testing of the argon loop system has been the successful development of a sodium-vapor monitor for use in the detection of the effects of a leaking sodium-filled calandria can within the heated zone argon cover gas. (See Paper III-36).

VTRZ PROJECT QUALITY ASSURANCE PROGRAM

The VTRZ Project was the first project of ANL to be required to conform in detail to the provisions of the ANL Quality Assurance Management Policies and Procedures Manual issued May 8, 1969. In addition, the AEC-RDT Quality Assurance staff in Washington specifically required that the Quality Assurance Program for the VTRZ Project be approved by them prior to the beginning of the VTRZ Heatable Zone Facility fabrication. The VTRZ Quality Assurance Program document[3] was prepared in June and July of 1969 and, after extensive discussion with ANL QA management staff members and with AEC-RDT QA staff members in Washington, an extensively revised version of the document was approved by the AEC in October 1969.

VTRZ FINAL DESIGN

The VTRZ final design consists of an inventory of oxide fuel rods; an inventory of fuel-rod mounting assemblies, called calandria cans because of their through-tube design; and a heatable zone facility. The oxide fuel rods are designed to be used at any temperature from room temperature to a maximum of 600°C. The inventory of fuel rods includes depleted UO_2 rods, 16% and 46% enriched UO_2 rods, and 15% and 30% plutonium mixed PuO_2-UO_2 rods. The calandria can inventory includes cans filled with sodium at room temperature (which are designed for use only at room temperature), cans approximately 85% filled at room temperature which are designed for heating to a maximum of 600°C, empty cans designed for use in sodium-void measurements, and several types of special-purpose cans. The VTRZ Heatable Zone Facility is a complex assembly which is designed to replace the central portion of the ZPR-6 or -9 matrix with a special insulated and heatable matrix unit.

The oxide fuel rods and the calandria can units are designed so that they may be used in the regular ZPR matrix, at room temperature, as well as in the Heatable Zone Facility. It is, in fact, intended that many of the plate versus rod heterogeneity comparison experiments will be carried out in the regular ZPR matrix at room temperature completely independent of the Heatable Zone Facility. The regular ZPR plate fuel drawers may be used in the Heatable Zone Facility, as part of comparison measurements, but they will not be heated.

The oxide rods and rod-mounting calandria can as-

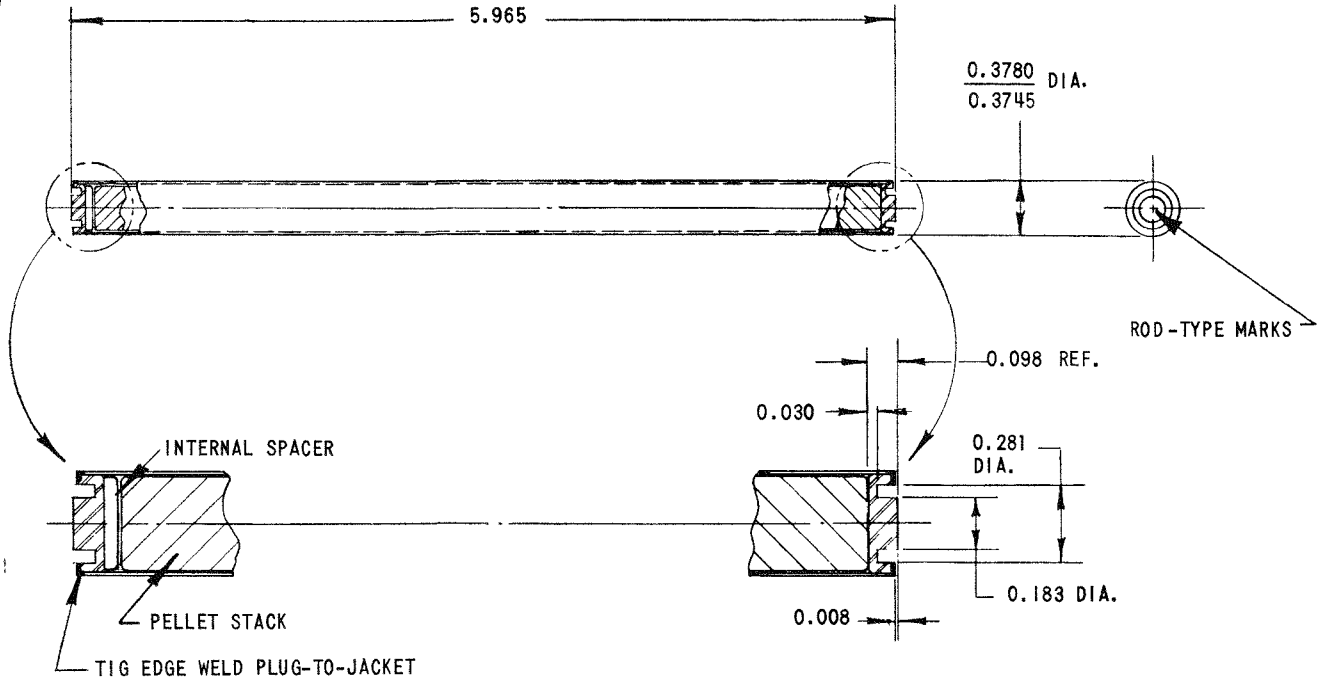

FIG. II-23-2. Fuel Rod. *ANL Neg. No. 116-431.*

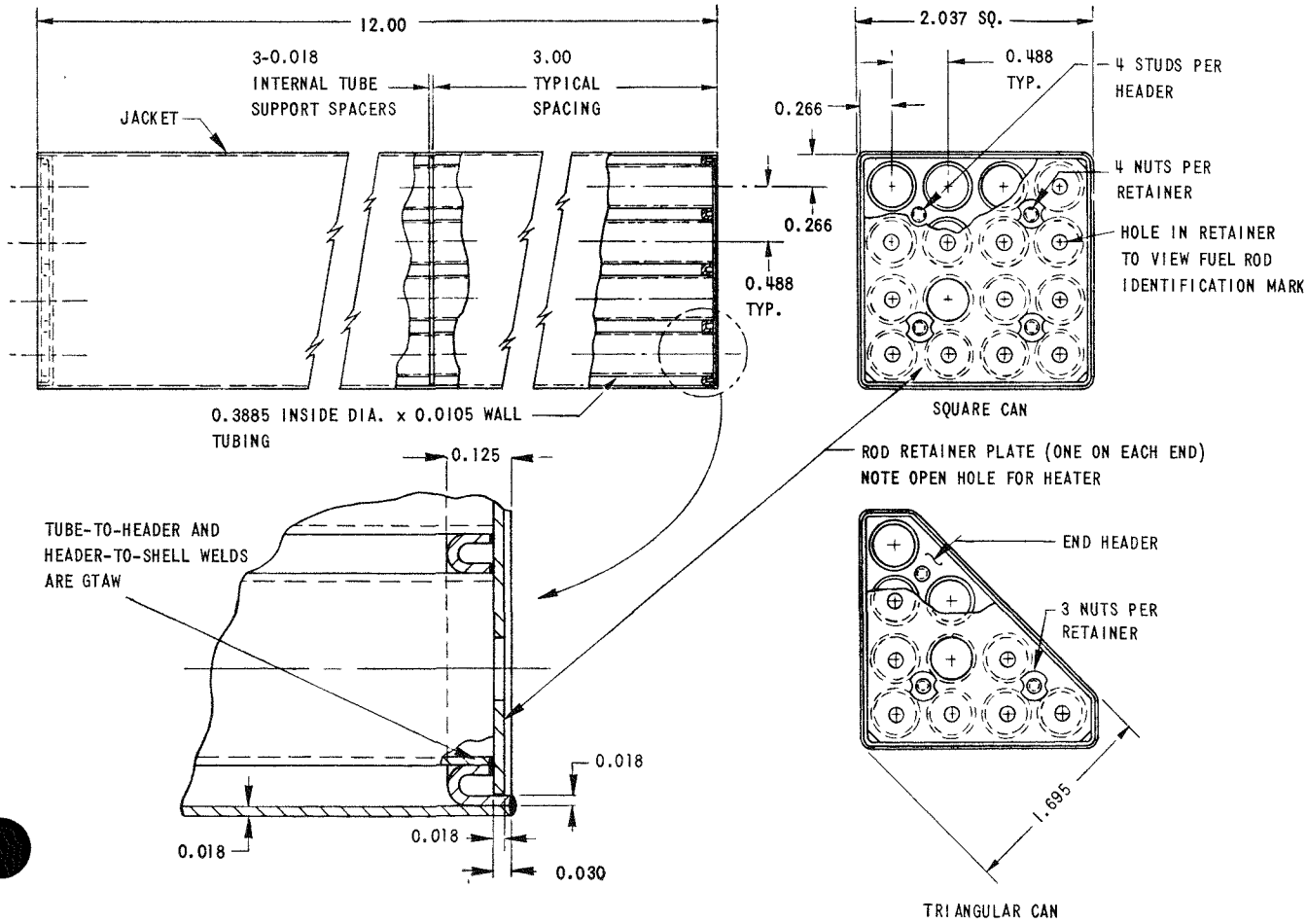

FIG. II-23-3. Square and Triangular Calandria Cans. *ANL Neg. No. 116-430.*

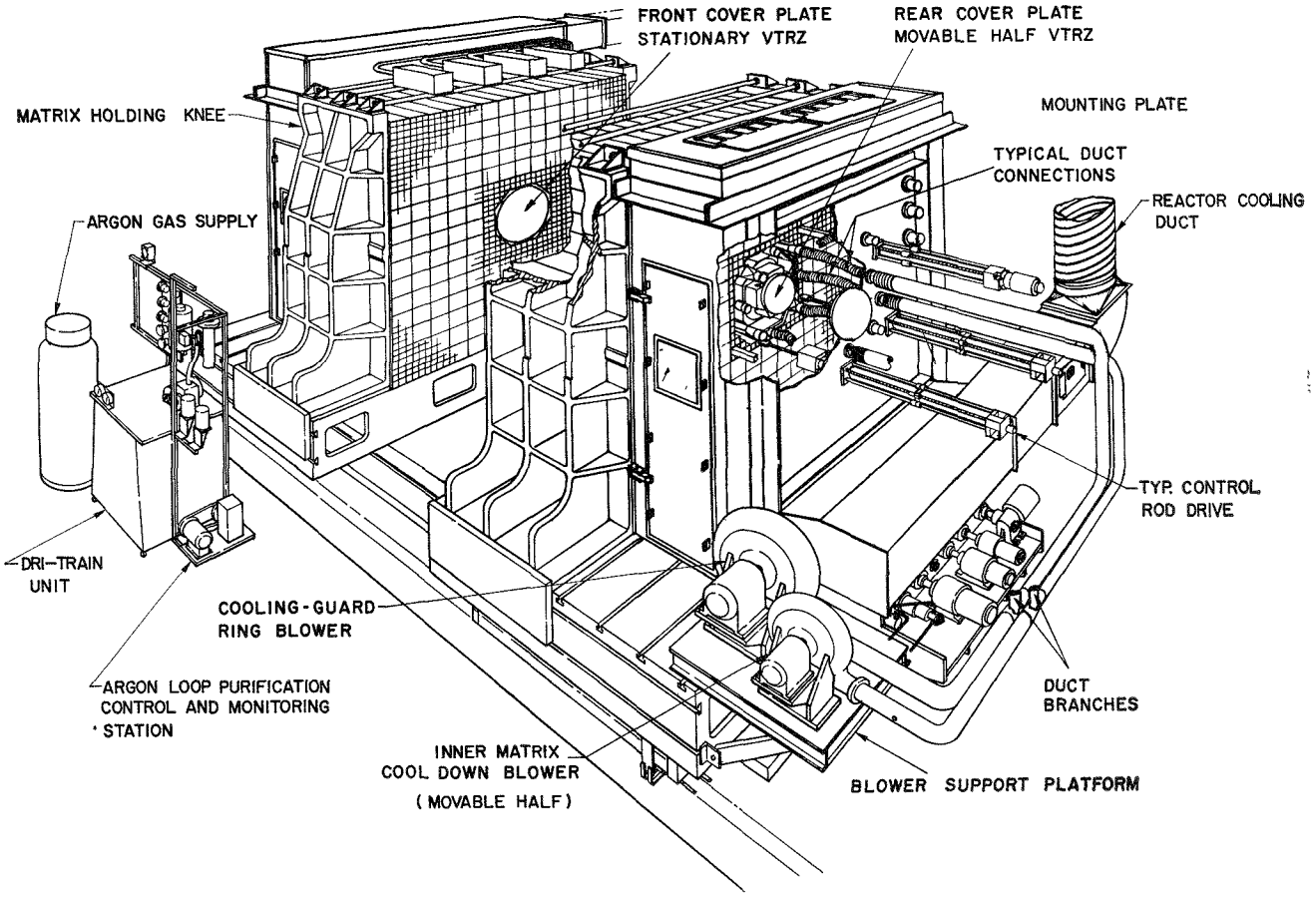

FIG. II-23-4. VTRZ in ZPR-6. *ANL Neg. No. 116-420.*

semblies are shown in Fig. II-23-1 where they are compared with the regular ZPR plate-type fuel drawers. The oxide rods are all of one size; viz., nominally ⅜ in. o.d. by 6 in. long with 12 mil 304L SS cladding as shown in Fig. II-23-2. The calandria cans, Fig. II-23-3, are 304L SS, square or triangular in cross section, and 12 in. long with 10.5 mil wall through-tubes sized to contain the clad fuel rods.

The Heatable Zone Facility consists basically of an insulated heatable zone, called the inner matrix assembly; an outer bridge unit, called the outer matrix assembly; and several auxiliary systems for air cooling, inert gas, electrical power, and instrumentation. Figure II-23-4 shows the Heatable Zone Facility installed in ZPR-6. Figure II-23-5 is a section view, normal to the horizontal axis, of the inner and outer matrix assemblies. Figure II-23-6 shows a perspective cut-away view of a single VTRZ half-zone.

The inner (heatable) matrix assembly consists of a region in the shape of a right cylinder with an octagonal cross section, approximately 20 in. inside across the flats of the octagon and 6 ft long, split normal to its long axis into two 3 ft "half-zone" sections; one is mounted in the center of each reactor half and mates at the reactor midplane when the halves come together. Each half-zone contains a matrix structure which consists of regular ZPR (2.093 in. sq. inside by 40 mil wall) 304 SS matrix tubes welded together and mounted horizontally. The matrix structure is supported and enclosed by an octagonal barrel. When operating at room temperature, with either plate or rodded fuel, the inside of the zone may be cooled, if necessary, by circulating air through the zone in exactly the same manner, and using the same equipment, as is described in Ref. 4. In the heatable configuration, the heatable zone is isolated from the reactor cell by gas-tight front and rear covers on each half-zone and a high-purity argon atmosphere, at a slightly negative pressure with respect to the cell, is provided within each half-zone. These precautions are taken to minimize the consequences if a leak occurred in a plutonium fuel rod or in a sodium-filled calandria can.

Each heatable half-zone of the VTRZ is supported radially by ten brackets arranged, five on each side, along the horizontal midplane of the half-zone and attached to the outside of the barrel enclosing the heatable matrix. The brackets are shown in Figs. II-23-3 and II-23-4. The weight of the heatable zone is transmitted through the brackets to a special welded bridge assembly, composed mainly of regular ZPR ma-

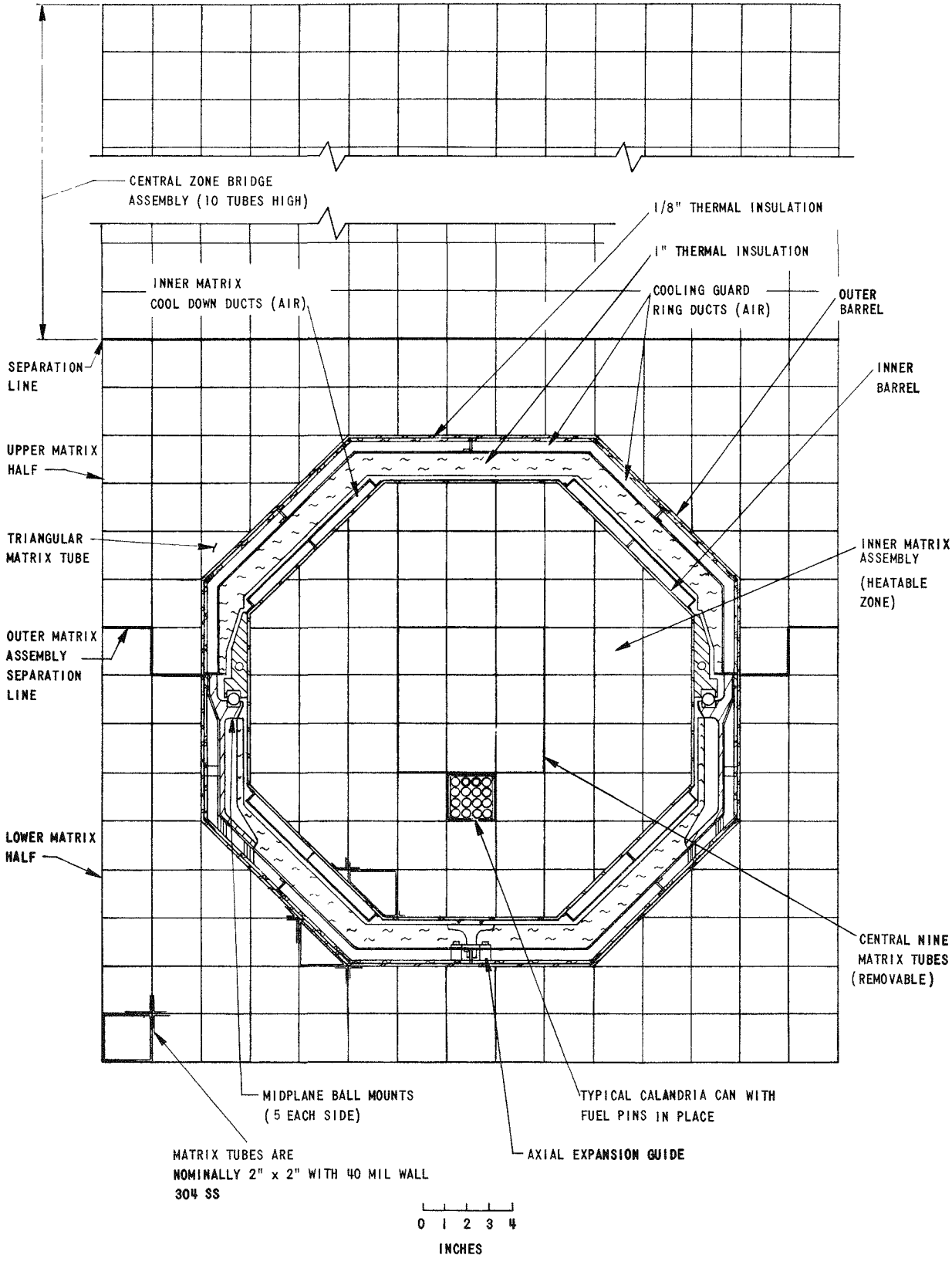

FIG. II-23-5. Section View of VTRZ. *ANL Neg. No. 116-429.*

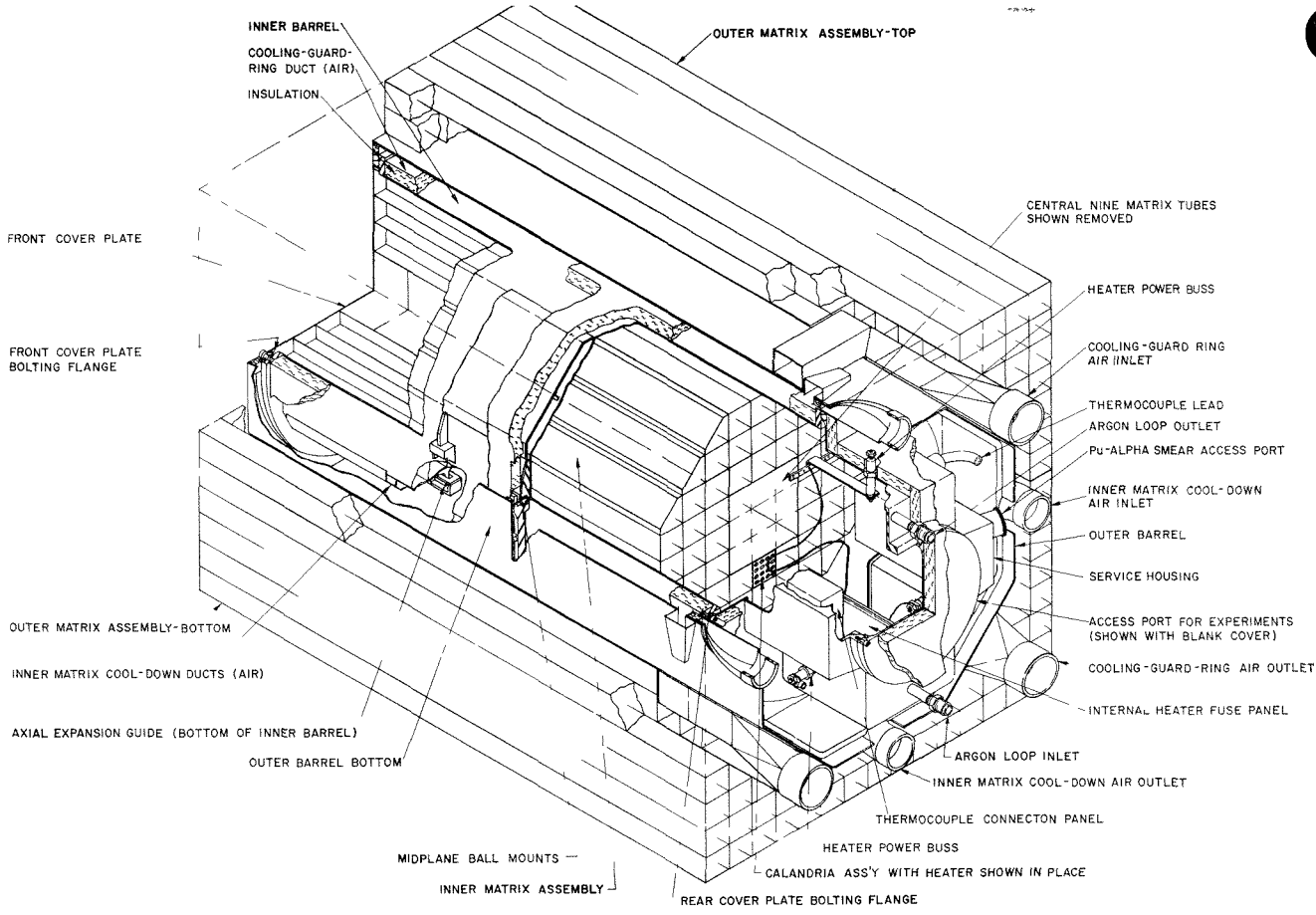

FIG. II-23-6. Perspective Cut-Away View of Single VTRZ Half-Zone. *ANL Neg. No. 116-419.*

trix tubes, which operates at room temperature and is designed to carry the load of the reactor core above the heatable zone as well as the weight of the heatable zone itself. Expansion of the heatable zone radially and axially is permitted by ball mounts in the support brackets and is controlled by radial and axial restraints and guides attached to the front and along the bottom of the heatable zone. A 2 in. thick radial insulation and air cooling guard-ring annulus separates the heatable zone from the outer bridge assembly.

The inner matrix assembly will be heated by ⅜ in. diam Inconel-clad electrical cartridge heaters of various lengths up to 36 in. The heaters will replace fuel rods in selected calandria can fuel tubes. The number of heaters will be selected on the basis of the requirements of the particular experiment being performed.

The final design of the VTRZ fuel rods was completed in October of 1968; final drawings and procurement specifications were issued at that time. Calandria can design was completed in final form with the publication of production drawings and procurement specifications in July of 1969.

The final design of the VTRZ Heatable Zone was progressively frozen over the period September–November of 1969. Final mechanical and electrical drawings and procurement specifications for all portions of the Heatable Zone equipment were issued in February of 1970. These documents were followed by the publication of the VTRZ Design Summary Report[5] (DSR) in March of 1970 which contains a description of the details of the final design together with summaries of the results of all of the prototype testing and of the structural (stress), heat transfer, and other calculations upon which the design is based.

PROCUREMENT OF VTRZ EQUIPMENT

After a period of four months (October 1968 to February 1969) in which vendor selection and contract negotiation for the fuel rod procurement was carried out, the procurement contract for the VTRZ fuel rods (UO_2 and PuO_2-UO_2) was signed in February of 1969. Actual delivery of UO_2 fuel rods began in October of 1969 and all contracted for UO_2 fuel rods were delivered by June 30, 1970. Delivery of the required PuO_2-UO^2 is expected to be complete by June 30, 1971. Tables II-23-I and II-23-II summarize the VTRZ oxide rod fuel inventory.

Actual production of VTRZ calandria cans in the ANL Central Shops Department began April 1, 1970,

TABLE II-23-I. UO_2 Fuel Rod Inventory

Attribute		UO_2 Fuel Rod Type		
		Depleted	16%	46%
Rod Type Designation (End Plug Stamp)		D	A	B
Enrichment; w/o U-235 of total uranium	Nominal[a]	0.22	16.40	46.50
	Range[a]	±0.02	±0.05	±0.05
	Analysis[a]	±0.02	±0.05	±0.05
w/o uranium of pellets	Nominal[b]	87.6 min	88.14	88.14
	Range[b]	≥87.6	+0.06, −0.74	+0.06, −0.74
	Analysis[b]	≥87.6	±0.30	±0.30
O/U ratio	Nominal	2.00	2.00	2.00
	Range	±0.02	±0.02	±0.02
	Analysis	±0.01	±0.01	±0.01
w/o impurities in pellets	Maximum	0.50	0.50	0.50
	Analysis	—[e]	±0.10	±0.10
Pellet stack wt/rod, g	Nominal[b]	89.29	90.50	90.50
	Range[b]	±1.50	±1.50	±1.50
	Analysis[b]	±0.005[e]	±0.005	±0.005
304L SS cladding wt/rod, g	Nominal[c]	12.3	12.3	12.3
	Analysis[c]	±0.01	±0.01	±0.01
Uranium wt/rod, g	Nominal[d]	78.2	79.8	79.8
Oxygen wt/rod, g	Nominal[d]	10.9	10.5	10.5
U-235 wt/rod, g	Nominal[d]	0.17	13.05	37.00
Approximate total number of rods in inventory		14,600	11,500	4,500
Approximate total U-235 inventory, kg		—	150	167

[a] Value must be within "Range" of "Nominal" and be measured within "Analysis" (2σ).

[b] Pellet and pellet stack weights include impurities.

[c] Cladding weight is not directly specified. This is a calculated value. Cladding weight will be determined by difference method to ±0.01 g.

[d] These values are calculated from the nominal value assuming 0.25 w/o impurities.

[e] Total uranium in pellet stack must be known to ±0.01 g.

and was completed on June 30. The three months production run began 8 months after completion of the calandria can design. The eight months was required for procurement of materials, for completion of process development on the calandria can fabrication technique and for the preparation and approval of the Quality Assurance Plan covering the fabrication. The calandria can job was the first job to go through the Central Shops Department under the new ANL Quality Assurance Procedures manual. Table II-23-III summarizes the existing VTRZ calandria can inventory.

Fabrication of the components of the VTRZ Heata-

TABLE II-23-II. $(Pu,U)O_2$ Fuel Rod Inventory

Attribute			$(Pu,U)O_2$ Fuel Rod Type		
			15%	30%	High-240
Rod Type Designation (End Plug Stamp)			F	G	H
Uranium isotopic composition, w/o U-235 of uranium		Nominal[a]	0.22	0.22	0.22
		Range[a]	±0.02	±0.02	±0.02
		Analysis[a]	±0.02	±0.02	±0.02
Plutonium isotopic composition w/o of plutonium	239	Nominal	86.40	86.40	67.30
		Range	±0.80	±0.80	±0.60
	240	Nominal	11.50	11.50	25.93
		Range	±0.50	±0.50	−0.18, +0.35
	241	Nominal	1.70	1.70	5.26
		Range	−0.70, +0.80	−0.70, +0.80	−0.23, +0.33
	242	Nominal	0.25	0.25	1.42
		Range	0.25	0.25	−0.08, +0.10
	238	Nominal	0.05	0.05	0.09
		Range	±0.05	±0.05	±0.02
w/o Pu-239 + Pu-241 of pellets		Nominal[b]	11.67	23.38	11.67
		Range[b]	±0.17	±0.27	±0.17
		Analysis[b]	±0.08	±0.08	±0.08
w/o total (U + Pu) of pellets		Nominal	88.05	88.05	88.05
		Range	±0.40	±0.40	±0.40
w/o plutonium of pellets		Analysis	±0.07	±0.07	±0.07
w/o uranium of pellets		Analysis	±0.03	±0.03	±0.03
O/(Pu + U) ratio		Nominal	1.98	1.98	1.98
		Range	±0.02	±0.02	±0.02
		Analysis	±0.01	±0.01	±0.01
w/o impurities in pellets		Maximum	0.50	0.50	0.50
		Analysis	±0.10	±0.10	±0.10
Pellet stack wt/rod, g		Nominal[b]	89.60	89.40	89.60
		Range[b]	±1.30	±1.50	±1.30
		Analysis[b]	±0.005	±0.005	±0.005
304L SS cladding, wt/rod, g		Nominal	12.3	12.3	12.3
		Analysis	±0.01	±0.01	±0.01
Pu-239 + Pu-241 wt/rod, g		Nominal[c]	10.46	20.90	10.46
Plutonium wt/rod, g		Nominal[c]	11.87	23.68	14.42
Uranium wt/rod, g		Nominal[c]	67.02	55.04	64.47
Oxygen wt/rod, g		Nominal[c]	10.49	10.46	10.49
Approximate total number of rods in inventory			12,700	5,900	1,600
Approximate total fissile (Pu-239 + Pu-241) inventory, kg			133	116	20

[a] Value must be within "Range" of "Nominal" and must be measured to within "Analysis" (2σ). If no range is specified, the quantity is not directly specified.

[b] Pellet and pellet stack weights include impurities.

[c] These values are calculated from nominal values assuming 0.25 w/o impurities.

TABLE II-23-III. CALANDRIA CAN INVENTORY

Can Type	Type Designation	Sodium Loading,[a] g			Stainless Steel,[b] g				Actual Number in Inventory
					Assembly[c]		Single Rod Retainer[d]		
		Nominal	Range	Measurement Precision	Nominal	Measurement Precision	Nominal	Measurement Precision	
Square Cross Section									
Full-at-20°C	F	330.0	±1.0	±0.01	579.0	±0.01	8.0	±0.01	377
6 in. axial fill	SF	165.0	±1.0	±0.01	579.0	±0.01	8.0	±0.01	66
Full-at-550°C	H	300.0	±1.0	±0.01	579.0	±0.01	8.0	±0.01	377
Empty	V	—	—	—	579.0	±0.01	8.0	±0.01	382
Triangular Cross Section									
Full-at-20°C	F	206.3	±1.0	±0.01	363.0	±0.01	5.0	±0.01	80
6 in. axial fill	SF	103.2	±1.0	±0.01	363.0	±0.01	5.0	±0.01	14
Full-at-550°C	H	187.5	±1.0	±0.01	363.0	±0.01	5.0	±0.01	81
Empty	V	—	—	—	363.0	±0.01	5.0	±0.01	90

[a] Sodium loadings are specified to be within "Range" of "Nominal" and to be measured within "Measurement Precision" (2σ).
[b] Stainless steel nominal weights are only approximate; these values are not directly specified.
[c] "Assembly" includes jacket, two headers, three spacers, all tubes, plus fill plug.
[d] Loaded assemblies use two retainer plates and 8 nuts; this value is for one retainer plate plus four nuts.

ble Zone Facility began June 1, 1970, in the ANL Central Shops Department and Electronics Department. The 4 month period from February, when the final design was issued, until June was required for the procurement of materials, fabrication process planning (and some process development), and the preparation and approval of the Quality Assurance Plan for the fabrication. Delivery of all Heatable Zone components is expected by February 1, 1971.

VTRZ Final Safety Analysis Report and VTRZ-ZPR-6 Operating Limits Documents

The VTRZ Final Safety Analysis Report[6] (FSAR) and the accompanying VTRZ-ZPR-6 Operating Limits document[7] were prepared during the period December 1969 through February 1970, and (after internal ANL review and approval) was formally submitted to the AEC for approval on April 1, 1970). These documents include analyses of the new safety questions raised by the introduction of the VTRZ into ZPR-6 and new rules and operating limits to be imposed on ZPR-6 during the period of time which the VTRZ is installed.

Outlook for July 1, 1970, Through June 30, 1971

Procurement of all VTRZ fuel rods is expected to be completed within this period.

Approval of the VTRZ FSAR is expected in the fall of 1970.

Current schedules call for out-of-pile testing of the VTRZ facility in the period February through July of 1971. This is to be followed by installation in ZPR-6 and the first heated measurements in September of 1971.

Design, development, testing, and procurement of special equipment needed for the heated experiments will be carried on throughout the period.

References

1. R. A. Lewis, F. H. Martens and C. E. Till, *The Variable Temperature Rodded Zone Project*, Reactor Physics Division Annual Report, July 1, 1967 to June 30, 1968, ANL-7410, pp. 124–125.
2. R. A. Lewis, K. D. Dance, J. F. Meyer and T. W. Johnson, *The Variable Temperature Rodded Zone (VTRZ) Program*, Reactor Physics Division Annual Report, July 1, 1968 to June 30, 1969, ANL-7610, pp. 137–143.
3. R. A. Lewis, *Quality Assurance Program Variable Temperature Rodded Zone Project Heatable Zone Facility*, (1969).
4. W. Y. Kato, G. K. Rusch, L. R. Dates, C. E. Till, A. Ancarani, J. van Doorninck, C. L. Cheever and E. M. Bohn, *Final Safety Analysis Report on the Use of Plutonium in ZPR-6 and -9*, ANL-7442 (1970).
5. R. A. Lewis, K. D. Dance, J. F. Meyer and E. M. Bohn, *Variable Temperature Rodded Zone Project Design Summary Report*, ANL-7639 (1970).
6. R. A. Lewis, K. D. Dance, J. F. Meyer and E. M. Bohn, *Variable Temperature Rodded Zone Project Final Safety Analysis Report*, ANL-7638 (1970).
7. *VTRZ-ZPR Operating Limits*, (May 15, 1970).

II-24. Analysis of Time-of-Flight Measurements

BURT A. ZOLOTAR

INTRODUCTION

The time-of-flight method of measuring reactor spectra appears to be straightforward. The basic principle is to extract neutrons from the reactor at a given instant and to then measure the time distribution of these neutrons at a detector located relatively far away. The velocity or energy distribution can then be found from these arrival times. In reality however the interpretation of the measurements is complicated by the experimental conditions.

In order to obtain a burst of neutrons it is necessary to introduce a pulse of neutrons into the system. The fact that the source has a finite length and that the neutrons spend a significant period of time in the assembly before escaping toward the detector destroys the direct correlation between arrival time and neutron velocity. A resolution correction is thus necessary to determine the spectrum from the measured distribution of arrival times.

The pulsed state of the system also presents several other problems in interpreting the results. The subcriticality of the system, the presence of the source, and the presence of the source and flight tubes all cause the measured spectrum to differ from the spectrum of the unpulsed critical system. The analysis of time-of-flight experiments must include the ability to account for these differences.

The purpose of this work was to explore some of the methods which have been developed and to determine which methods should be used in analyzing the time-of-flight measurements which will be made at Argonne on ZPR-6 critical assemblies.

RESOLUTION ANALYSIS

The time dependent neutron spectrum, $\phi(\underline{x},v,\underline{\Omega},t)$, resulting from the introduction of a source, $S(\underline{x},v,\underline{\Omega},t)$, into the reactor system is given by

$$\frac{1}{v}\frac{\partial\phi(\underline{x},v,\underline{\Omega},t)}{\partial t} = H(\underline{x},v,\underline{\Omega})\phi(\underline{x},v,\underline{\Omega},t) + S\underline{x},v,\underline{\Omega},t) \quad (1a)$$

where

$$\phi(\underline{x},v,\underline{\Omega},0) = 0 \quad (1b)$$

if

$$S(\underline{x},v,\underline{\Omega},t) = 0 \quad \text{for} \quad t \leq 0, \quad (1c)$$

and where $H(\underline{x},v,\underline{\Omega})$ is the time independent Boltzman operator. A measurement at $\underline{x}_m$, $\underline{\Omega}_m$ will give a time-of-flight spectrum

$$C(t) = \int_{L/t}^{\infty} \epsilon(v)\phi(\underline{x}_m , v, \underline{\Omega}_m , t - L/v)\, dv, \quad (2)$$

where $\epsilon(v)$ is the effective efficiency resulting from the product of the detector efficiency and flight path transmission. The purpose of the resolution analysis is to obtain the steady state spectrum

$$\phi(\underline{x}_m , v, \underline{\Omega}_m) = \int_0^{\infty} \phi(\underline{x}_m , v, \underline{\Omega}_m , t)\, dt. \quad (3)$$

Since the direct solution of Eqs. 2 and 3 does not appear to be possible, several approximations have been used to solve for the flux.

The first method is the mean emission time correction wherein the mean time that a neutron of velocity v spends in the system,

$$\bar{t}(v) = \int_0^{\infty} t\phi(\underline{x}_m , v, \underline{\Omega}_m , t)\, dt/\phi(\underline{x}_m , v, \underline{\Omega}_m) \quad (4)$$

is subtracted from the detector time, t^*, yielding

$$\phi(\underline{x}_m,v,\underline{\Omega}_m) = \frac{C(t^*)}{\epsilon(v)}\frac{L}{v^2}, \quad (5a)$$

where

$$t^* = L/v + \bar{t}(v). \quad (5b)$$

Unfortunately this method does not take into account the substantial spread in times that a neutron of velocity v can reach the detector. It does not improve the resolution of the experiment and thus is not sufficient at high energies.

The second method has been used at Aldermaston,[1] Harwell,[2] Winfrith[3] and at Karlsruhe.[4] It is based on the assumption of time separability of the flux:

$$\phi(\underline{x}_m , v, \underline{\Omega}_m , t) = \phi(\underline{x}_m , v, \underline{\Omega}_m)T(t) \quad (6a)$$

with

$$\int_0^{\infty} T(t)\, dt = 1. \quad (6b)$$

In this case Eq. (3) becomes

$$C(t) = \int_{L/t}^{\infty} \epsilon(v)\phi(\underline{x}_m , v, \underline{\Omega}_m)T(t - L/v)\, dv. \quad (7)$$

The basic procedure is to measure $T(t)$ with an in-core detector and then to solve Eq. (7) by an iterative process. The basic limitation of the method would appear to be the assumption of energy and time separability. Paterson and Shutler[1] have looked at the problem

for the VERA assemblies and have concluded that there is no significant error as long as the time shape, $T(t)$, is measured with a high energy (e.g. U-238) detector.

Gulf General Atomics has recently taken a very different approach to the problem.[5,6] They have made calculations for their STSF assemblies and have concluded that the flux (especially at short times) is not separable, and thus that large errors may be introduced by the unfolding approach outlined above. The long British pulse width of approximately 3 μsec while decreasing the resolution apparently eliminates the need for considering the short time effects which occur in the first μsec. Gulf General Atomics uses a much shorter pulse width and thus they have based their resolution analysis on a calculated correction procedure. Using a few-group time-dependent code they find two quantities,

1. $C^*(t)$, the calculated time-of-flight spectra corresponding to the experimental flight path and detector, and
2. $D^*(t)$, the calculated time-of-flight spectra for the theoretical case where all the neutrons left the system at time zero and were detected by a flat response detector. Both $C^*(t)$ and $D^*(t)$ are smoothed using the detailed spectra from a many group GAM calculation. Using these quantities they calculate

$$CF^*(t) = D^*(t)/C^*(t) \tag{8}$$

which they use as a correction factor giving the distortion of the actual spectrum caused by the time behavior of the system and the energy dependence of the detector response. This method is not an unfolding procedure. Its main limitation would appear to be the possibility of introducing calculated information into the measured spectra.

A somewhat different method, proposed here, will be applied to the future Argonne time-of-flight measurements. It does not depend on time-energy separability and it should not introduce calculated structure. We can write

$$\phi(\underline{x}_m, v, \underline{\Omega}_m, t) = \phi(\underline{x}_m, v, \underline{\Omega}_m)T(\underline{x}_m, v, \underline{\Omega}_m, t), \tag{9}$$

where

$$\int_0^\infty T(\underline{x}_m, v, \underline{\Omega}_m, t)\, dt = 1 \tag{10}$$

for all v. Using Eq. (9) gives

$$C(t) = \int_{L/t}^\infty \epsilon(v)\phi(\underline{x}_m, v, \Omega_m) T(\underline{x}_m, v, \Omega_m, t - L/v)\, dv. \tag{11}$$

$T(\underline{x}_m, v, \underline{\Omega}_m, t)$ will be found from a combination of calculation and experiment. The time response of the system can be measured with one or more detectors of varying energy response and used to verify or make corrections to a time-dependent calculation. As can be seen from the normalization of Eq. (10) no details of the calculated energy spectra are used. A few-group calculation is all that is necessary. In the case where the flux is separable Eq. (11) will reduce to Eq. (7). It should also be possible to solve Eq. (11) iteratively in the same manner that has been used to solve the separable form. It is expected that the time-dependent calculations can be made with a version of Time-Dependent ANISN[7] which is now being tested on the Argonne 360/75. This code has been modified to accept the Argonne Reactor Computation (ARC) system input formats so that the same input specifications and cross sections can be used here as are used in the standard static analysis.

The British experience has been that some smoothing of the data is necessary. This should also be the case here and will be a major factor in determining the ultimate time resolution achieved. Because of the difficulties of theoretically predicting the resolution it is hoped that at least in the initial experiments the resolution can be measured. This might be possible by placing resonance materials in the flight path and by comparing the unfolded spectra with and without the resonances. The energy locations and the broadening of the resonances should give a good measurement of the resolution achieved.

Equation (11) does not include the time response of the detector which may be on the order of 0.3 to 0.5 μsec[8] for a B-10 loaded liquid scintillator. If the detector has a resolution function $D(v,t)$ where

$$\int_0^\infty D(v,t)\, dt = 1 \tag{12}$$

for all v, then the effective total resolution function is given by

$$T'(\underline{x}_m, v, \underline{\Omega}_m, t) = \int_0^t d\tau D(v, \tau)T(\underline{x}_m, v, \underline{\Omega}_m, t - \tau). \tag{13}$$

$T'(\underline{x}_m, v, \underline{\Omega}_m, t)$ can then be used in Eq. (11) in place of $T(\underline{x}_m, v, \underline{\Omega}_m, t)$ and should not produce any further complications. It is proposed that, in addition to measurements of $D(v,t)$, calculations of the detector response also be used to aid in the analysis. Time-Dependent ANISN may also be useful in this work.

Spectrum Analysis

The goal of time-of-flight measurements will be to measure the spectrum of the critical reactor system.

In fact, however, after resolution corrections the measurement will yield the flux specified by Eq. (3). As mentioned previously this spectrum will correspond to a subcritical pulsed system. A combination of calculations and experiments will be necessary to determine the spectral effects of these changes to the system.

As an example one can look at the spectral effects of the source itself. While Eq. (1) gives the time dependent flux following the source one can show that the time integral of the flux, $\phi(\underline{x},v,\underline{\Omega})$, is given by

$$0 = H(\underline{x},v,\underline{\Omega})\phi(\underline{x},v,\underline{\Omega}) + S(\underline{x},v,\underline{\Omega}), \quad (14a)$$

where

$$\phi(\underline{x},v,\underline{\Omega}) = \int_0^\infty \phi(\underline{x},v,\underline{\Omega},t)\, dt \quad (14b)$$

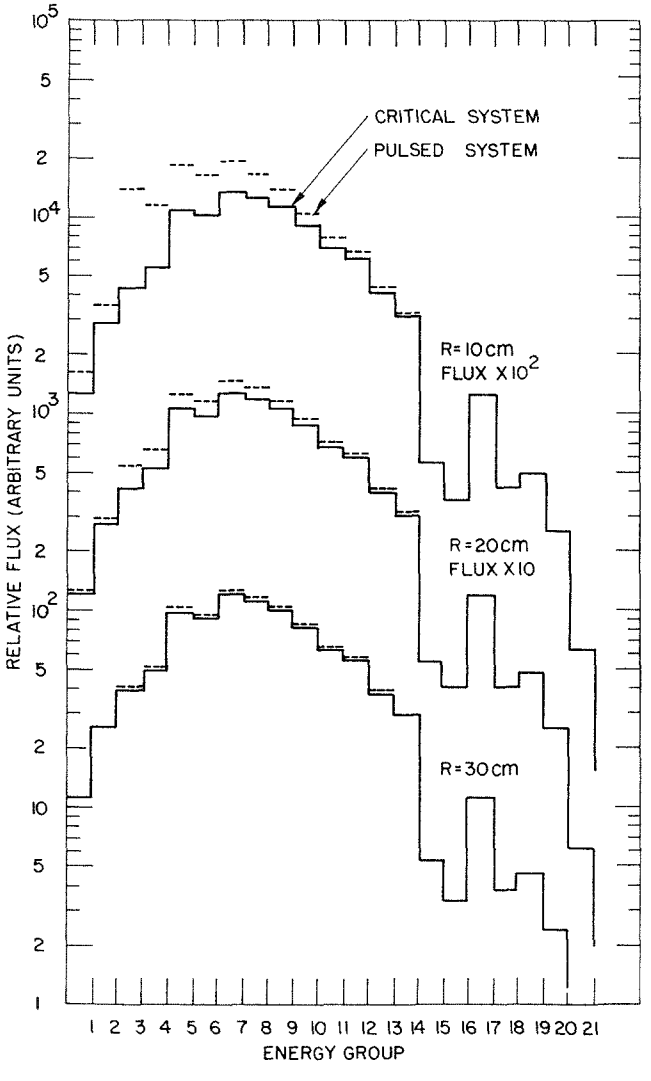

FIG. II-24-1. Fluxes at Varying Distances from a Point Source. The Calculation is for a Spherical Model of ZPR-6 Assembly 6A. The Source is Introduced at the Center of the Sphere in Group 3. *ANL Neg. No. 116-445.*

TABLE II-24-I. ENERGY GROUP STRUCTURE USED IN CALCULATION

Group	Lower Energy, eV
1	3.68×10^6
2	2.23×10^6
3	1.35×10^6
4	8.21×10^5
5	4.98×10^5
6	3.02×10^5
7	1.83×10^5
8	1.11×10^5
9	6.74×10^4
10	4.09×10^4
11	2.48×10^4
12	1.50×10^4
13	9.12×10^3
14	4.31×10^3
15	2.61×10^3
16	2.03×10^3
17	1.23×10^3
18	9.61×10^2
19	5.83×10^2
20	2.75×10^2
21	1.01×10^2
22	2.90×10^1
	1.37×10^1
24	3.05
25	0.00

and

$$S(\underline{x},v,\underline{\Omega}) = \int_0^\infty S(\underline{x},v,\underline{\Omega},t)\, dt. \quad (14c)$$

Most static reactor codes can then be used to solve Eq. 14a and to calculate the flux resulting from the source. Figure II-24-1 shows for a spherical model of ZPR 6 Assembly 6 a comparison with the flux of the critical system. A one dimensional transport calculation was used for the energy group structure shown in Table II-24-I. The source was introduced at the center of the core in energy group 3 (2.23 MeV $\leq E \leq$ 1.35 MeV). The subcritical system had a k_{eff} of 0.96. As can be seen, for a system of this size the time-of-flight measurements should be made at least 30 cm from the source location in order to minimize source contamination of the spectra. It will probably be worthwhile to verify these predictions with measurements by varying source locations. Studies of other spectral effects can be made using similar methods.

REFERENCES

1. W. J. Paterson and K. L. Shutler, *Resolution Corrections to Neutron Spectrometry by the Pulsed Source Time-of-Flight Technique*, AWRE O-8/67 (1967).
2. D. B. Gayther, P. D. Goode and D. J. Tripp, *Time-of-Flight Measurements of the Neutron Spectrum in a Sub-Critical*

Fast Reactor Assembly, J. Nucl. Energy **22**, No. 9, pp. 547–568 (September 1968).
3 J. Marshall, *WINTOF—A Program to Produce Neutron Spectra From ZEBRA Time-of-Flight Experiments*, AEEW-M 897 (1969).
4. K. Bohnel, *Methods and Programs for Evaluating Neutron Spectrum Measurements by the Time-of-Flight Method and for Correcting the Time Resolution*, EURFNR 265L (1966).
5. P. d'Oultremont and D. Houston, *Resolution Analysis of Time-of-Flight Spectra in Sub-Critical Systems*, Trans. Am. Nucl. Soc. **12**, 219 (1969).
6. P. d'Oultremont, *A Method for Correcting the Time-of-Flight Spectra for the Neutron Emission Time and the Detector Efficiency*, GA-9269 (1969).
7. W. Engle, Oak Ridge National Laboratory (private communication).
8. C. D. Bowman et al., *Threshold Photoneutron Cross Section for Fe^{56}*, Phys. Rev. **163**, 162 (1967).

II-25. Conditional Variances Pertinent to Doppler Effect Studies

R. N. Hwang and L. B. Miller*

Because of the important role that the Doppler effect plays in large fast reactors there have been a number of studies concerning the statistical uncertainties of calculated Doppler coefficients in the unresolved region.[1,2] One way of estimating the uncertainties is to construct discrete resonance sequences according to some prescribed distribution functions and average resonance parameters, and subsequently to perform Doppler coefficient calculations for each "ladder" generated.[1] From a practical point of view, some bias to the selected resonances is obviously needed in order to reproduce the observed behavior of the nuclear cross sections as a function of energy.

In the integral method, this criterion has been widely used on the averaged resonance parameters so that the average values of the infinitely dilute cross sections are in good agreement with the observed values. For this reason, Dyos[3] has suggested the use of a modified Monte Carlo technique in which the selections of the discrete resonances are biased. In this technique the resonances are selected according to two criteria. First of all, the means and variances of the nuclear parameters must match the theoretical values as closely as possible. This ensures that the resonance parameters satisfy the uniform statistics described by the theoretical distribution functions. Secondly, the calculated infinitely dilute cross sections of a given energy interval must be equal to the observed value. In a recent paper, Adkins and Dyos[4] have investigated the statistical uncertainties of the Doppler coefficient for a particular system using this technique. The point under question is whether this technique will, in fact, reduce the uncertainties of the calculated Doppler coefficient. Since the Doppler coefficient is related to the unresolved cross sections and their temperature derivatives in a rather complicated way, studies of this kind are not only time-consuming but also of dubious value if the results cannot be interpreted on theoretical grounds and generalized to all systems of interest. Hence, a complete theoretical study in addition to numerical results is needed in this area.

A study has been made of the statistical uncertainties of the self-shielded group cross section and its temperature derivative associated with the use of the biased selection technique where resonances are chosen to match the observed value of the unshielded cross section. Since the self-shielded group cross section can always be pictured as a superposition of an infinitely dilute term and a self-shielding term, the problem amounts to the estimation of the conditional variances of the self-shielding term and its temperature derivative for any given value of the infinitely dilute cross section. A semi-analytical method based on the narrow resonance (NR) approximation has been developed to estimate these conditional variances. Both qualitative and quantitative results were obtained for cases of Pu-239 and U-238 under various physical conditions. It was found that the technique of the biased selection of resonances is potentially useful, but one must apply it with caution. This method will, in general, significantly reduce the statistical uncertainty in estimating the magnitude of the self-shielding terms, but it is less effective in reducing the uncertainty in the temperature derivative of the self-shielding term. There is an obvious drawback of this technique in estimating the Doppler coefficient. The conditional variance of the Doppler change in the self-shielding term is sensitive to the presence of a statistically independent overlapping sequence. In particular, in the presence of a strongly overlapping sequence, the conditional variance of the Doppler change in the self-shielding term for the fission process of Pu-239 becomes practically the same as the corresponding variances. Consequently, this

* EBR-II Project, Argonne National Laboratory.

hnique becomes ineffective. Results of the study of statistical uncertainties and the temperature derivative are discussed in detail in Ref. 5.

REFERENCES

1. C. N. Kelber and P. H. Kier, *The Effect of Randomness on Group Cross Sections, II*, Nucl. Sci. Eng. **26,** 67 (1966).
2. L. B. Miller and R. N. Hwang, *Variance in the Dopperl Coefficient Due to Statistical Selection of Resonance Parameters*, Nucl. Sci. Eng. **34,** 181 (1968).
3. M. W. Dyos, *The Construction of Statistical Neutron Resonances*, Nucl. Sci. Eng. **34,** 181 (1970).
4. C. R. Adkins and M. W. Dyos, *The Statistical Uncertainty in Doppler Coefficient Calculations for Fast Reactors*, Nucl. Sci. Eng. **40,** 159 (1970).
5. R. N. Hwang and L. B. Miller, *Conditional Variances Pertinent to Doppler Effect Studies*, Nucl. Sci. Eng. **42,** 179–190 (1970).

II-26. Typical Absolute Activation Measurements in Zero Power Reactor (ZPR) Cores

D. W. MADDISON and L. S. BELLER*

Several measurements of absolute activity in particular materials have been performed in ZPR-3 assemblies. These activities, in turn, lead to absolute reaction rates occurring within the reactor. Materials were selected to provide information on the neutron flux in various energy ranges and also to provide reaction rate information in some reactor component materials. All of these activated materials were evaluated by using the Zero Power Plutonium Reactor (ZPPR) counting room facilities.[1] The materials used were restricted because of the activation products and the cross sections involved in their production. Very short half-life products, less than a few tens of minutes, cannot be retrieved from the critical assembly before they decay; and long half-life activities, and/or those that have small production cross sections, are not produced in sufficient quantity to evaluate them accurately.

Some materials used are essentially resonance detectors while others are threshold detectors. Our present investigations have included those materials and reactions presented in Table II-26-I. Also included in Table II-26-I are some typical reaction rates resulting from exposure of these materials in or near the core region of ZPR-3 assemblies, and their absolute accuracies as determined with the ZPPR counting facilities[1] and analyzed with our data analysis codes.[2] These values assume that the nuclear decay data and fission yield data used are accurate, which in some cases is a poor assumption. Some values may have quoted errors as large as 20% because of poorly known gamma transition intensities. Several other reactions are not included in the list that could easily be evaluated but were not investigated at this time.

TABLE II-26-I. REACTIONS AND REACTION RATES FOR VARIOUS MATERIALS IN ZPR-3

Material	Reaction	Typical Reaction Rate[a]	Absolute Error,[b] %
NaCl	$Na^{23}(n,\gamma)Na^{24}$	$1.0\text{–}4.0 \times 10^{9}$	2.9
NaCl	$Cl^{35}(n,\alpha)P^{32}$	$0.1\text{–}5.0 \times 10^{9}$	8.0[c]
Al	$Al^{27}(n,\alpha)Na^{24}$	$0.2\text{–}4.5 \times 10^{8}$	4.3
S	$S^{32}(n,p)P^{32}$	$0.04\text{–}1.5 \times 10^{11}$	8.0[c]
Sc	$Sc^{45}(n,\gamma)Sc^{46}$	$2.5\text{–}5.5 \times 10^{10}$	3.0
Ti	$Ti^{46}(n,p)Sc^{46}$	$0.5\text{–}4.5 \times 10^{9}$	6.0
Ti	$Ti^{47}(n,p)Sc^{47}$	$0.2\text{–}4.5 \times 10^{9}$	3.3
Ti	$Ti^{48}(n,p)Sc^{48}$	$0.4\text{–}8.0 \times 10^{7}$	4.0
Fe	$Fe^{54}(n,p)Mn^{54}$	$0.1\text{–}3.0 \times 10^{10}$	4.0
Fe	$Fe^{56}(n,p)Mn^{56}$	$0.08\text{–}3.0 \times 10^{8}$	3.0
Mn	$Mn^{55}(n,\gamma)Mn^{56}$	$1.0\text{–}9.0 \times 10^{10}$	2.8
Ni	$Ni^{58}(n,p)Co^{58}$	$0.1\text{–}3.5 \times 10^{10}$	3.1
Cu	$Cu^{63}(n,\gamma)Cu^{64}$	$1.0\text{–}4.0 \times 10^{10}$	2.8
Cr	$Cr^{50}(n,\gamma)Cr^{51}$	$1.0\text{–}4.3 \times 10^{10}$	6–20
Zr	$Zr^{94}(n,\gamma)Zr^{95}$	$1.5\text{–}3.0 \times 10^{9}$	7.0
Zr	$Zr^{96}(n,\gamma)Zr^{97}$	$1.5\text{–}6.0 \times 10^{9}$	4.0
In	$In^{115}(n,n')In^{115m}$	$0.3\text{–}4.5 \times 10^{10}$	2.8
In	$In^{115}(n,\gamma)In^{116}$	$0.8\text{–}7.0 \times 10^{11}$	2.8
C_6I_6	$I^{127}(n,2n)I^{126}$	$0.04\text{–}1.4 \times 10^{8}$	3–15
La	$La^{139}(n,\gamma)La^{140}$	$1.0\text{–}6.0 \times 10^{9}$	3.2
Ta	$Ta^{181}(n,\gamma)Ta^{182}$	$0.2\text{–}5.3 \times 10^{13}$	2.8
W	$W^{186}(n,\gamma)W^{187}$	$0.3\text{–}5.5 \times 10^{11}$	2.8
Au	$Au^{197}(n,\gamma)Au^{198}$	$0.8\text{–}6.8 \times 10^{11}$	2.8
Th	$Th^{232}(n,f)Nb^{97}$	$0\ 8\text{–}4.0 \times 10^{9}$	30.0
Th	$Th^{232}(n,\gamma\beta)Pa^{233}$	$0.5\text{–}2.5 \times 10^{11}$	3.0
U-238	$U^{238}(n,f)Nb^{97}$	$1.0\text{–}6.0 \times 10^{10}$	3.2
U-238	$U^{238}(n,\gamma\beta)Np^{239}$	$0.2\text{–}2.0 \times 10^{11}$	2.8
U-235	$U^{235}(n,f)Nb^{97}$	$0.9\text{–}7.0 \times 10^{11}$	2.8
Pu	$Pu^{239}(n,f)Nb^{97}$	$1.0\text{–}8.0 \times 10^{11}$	3.5

[a] Reactions/h-g at a nominal power level of 600 W.
[b] Absolute error for counting system calibration is 2.7%.
[c] Absolute calibration error for Si(Li) beta detector.

REFERENCES

1. D. W. Maddison and L. S. Beller, *Characteristics and Capabilities of Automated Counting Facilities for the Zero Power Plutonium Reactor (ZPPR)*, Reactor Physics Division Annual Report, July 1, 1968 to June 30, 1969, ANL-7610, pp. 379-381.
2. L. S. Beller and D. W. Maddison, *Automated Spectrum Analysis Methods for Ge(Li) Detectors*, Reactor Physics Division Annual Report, July 1, 1968 to June 30, 1969, ANL-7610, pp. 416-417.

* Atomics International, a Division of North American Rockwell Corporation, Canoga Park, California.

II-27. β_{eff} Measurements in Two Fast Reactor Critical Assemblies

S. G. Carpenter, J. M. Gasidlo and J. M. Stevenson*

Introduction

As part of a continuing effort to study the experimental accuracy of small sample reactivity measurements we have measured β_{eff} in two cores. One core had primarily U-235 fissions and the other primarily Pu-239 fissions. A previous paper[1] concluded that the error in the calculated value of β_{eff} in any one isotope relative to another is not large and does not affect reactivity calibrations to an important extent. The reactivity reported in cents or inhours should therefore not be in error more than 1 or 2% and nowhere near the 30% difference found in certain cores when compared with calculations.

Since the experimental results for the small sample reactivities are in cents or inhours and the calculated value is in $\Delta k_e/k$, an incorrect value of β_{eff} will produce a difference in the comparison of the same percentage as the error in β_{eff}. The purpose of these experiments was to measure β_{eff} in two cores which were particularly simple in that most of the fissions occured in only one isotope. Insofar that β_{eff} is not greatly different from β it is expected that any major uncertainty is not particularly sensitive to the core but only to the isotope. The loadings for the two cores, ZPR-57 and -59, are given in Papers II-12 and II-13. Core 57 is predominantly U-235 and BeO with an iron reflector, and Core 59 is predominantly Pu-239 and carbon with a lead reflector.

The general equation from which the experimental small sample reactivity results are obtained is [Ref. 1, Eq. (1)]

$$\frac{\Delta k_e}{k_e\beta_{eff}} + \frac{\ell S_e}{k_e\beta_{eff}n(t)} = 1 + \frac{1}{n(t)k_e}\left[\frac{\ell}{\beta_{eff}}\frac{dn(t)}{dt} - \sum a_i e^{-\lambda_i t}\left(n_0k_0 + \lambda_i\int_0^t k_e n(t)e^{\lambda_i t}\,dt\right)\right], \quad (1)$$

where $n(t)$ is proportional to reactor power. The application of Eq. (1) takes several forms some of which require $n(t)$ to behave in certain ways. In each case, the right hand side of the equation is very insensitive to β_{eff}, k_e, and ℓ and depends only on power ratios, a_i's, and λ_i's. Results noted in Ref. 1 indicated that the a_i's and λ_i's of Keepin[2] predict the delayed neutron decay rate quite well over the power ratios used in the small sample measurements.

The left hand side of the equation is then obtained correctly and provides a time history of the sum of the two terms:

$$A(t) = \$(t) + \frac{\ell S_e}{k_e\beta_{eff}n(t)}.$$

Since the neutron production rate $\nu F(t) = (n/\ell)k_e$,

$$A(t) = \$(t) + \frac{S_e}{\beta_{eff}\nu F(t)},$$

where $F(t)$ is the fission rate in the core and ν is the average number of neutrons produced per fission. If the reactor with a source S_e is leveled in power and a small change in reactivity is made then $F(t)$ will change while $\$(t)$ remains constant so that the two terms can be separated and the value of $\frac{S_e}{\beta_{eff}\nu F(t)}$ determined.

The neutron production rate relative to any instrument reading used to measure the power level is determined experimentally. This is done with absolute fission counters for each isotope in the core producing significant fissions. ν is assumed known.

Since the value of S_e is not known for the as-built core, a preliminary run is made to measure it and a second experiment is done by inserting a source of known strength into the center of the core and again determining $\frac{S_e}{\beta_{eff}\nu F(t)}$ (apparent reactivity effect) for the inserted source at this value of F. The only undetermined value other than β_{eff} is S_e:

$$S_e = S\phi^+/\overline{\phi_f^+},$$

where ϕ^+ is the average importance of a source neutron at the source position (center), $\overline{\phi_f^+}$ is the average importance of a fission neutron in the reactor, and S is the absolute source strength. S is measured outside of the reactor while the ratio of importances is determined from the measured fission distribution, a measured ϕ^+ distribution using the same source but now at all positions, and a calculated correction since the energy distribution of source (Cf-252) neutrons is not exactly the same as those from U-235 or Pu-239.

The results are then used to find

$$\beta_{eff} = \frac{S\phi^+}{V\nu F\overline{\phi_f^+}},$$

where V is the apparent reactivity of the neutron source S when the reactor fission rate is F. This method is essentially the same as the thermal reactor experiment in which the fuel is replaced point by point with a $1/v$

* UKAEA, Winfrith, Dorchester, Dorset, England.

sorber of the same strength and the reactivity effect is found and integrated over all the fissionable material in order to find the reactivity effect of turning off all the fissions. In this experiment the same type of result is found by adding fissions in the proper distribution instead of subtracting them.

The relative fission rates and importance distributions need not be measured at all points if the core is a simple shape and the fluxes are separable in space. Distributions along the axis and midplane are used with a combination of two-dimensional calculations to correct for non-separability and non-circular boundaries.

We have used the following particular form of the simple expression in which the measured numbers and corrections were taken in this combination:

$$\beta_{eff} = \frac{S}{V\nu N F_{mc}} (R_F)(R_I) \frac{F_{mc}}{F_c} \left[\frac{F_c}{F_p} \frac{\phi_s^+}{\phi_F^+} \frac{\phi_{FS}^+}{\phi_{FP}^+} R_{FC} R_{IC} \right],$$

where

S is the absolute source strength
V is the apparent reactivity effect of the source neutrons
ν is the average number of neutrons/fission
N is the number of U-235 or Pu-239 atoms in the reactor
F_{mc} is the fission rate/atom of U-235 or Pu-239 at the core center in the counter geometry
F_c is the total fission rate/atom of U-235 or Pu-239 at the core center (includes all isotopes) in the counter geometry
R_f is the peak-to-average fission rate assuming circular core, space separability, and radial and axial data
R_I is the peak-to-average importance of a source neutron assuming a circular core, space separation, and radial and axial data
F_p is the total fission rate/atom of U-235 or Pu-239 at the core center in the cell geometry
ϕ_S^+ is the average importance of a source neutron
ϕ_F^+ is the average importance of a fission neutron
ϕ_{FS}^+ is the average importance of a fission neutron at the source position
ϕ_{FP}^+ is the average importance of a fission neutron in the cell
R_{FC} is the calculated correction to account for the fact that the fission distribution was measured along the axis and a diameter, and R_F is calculated assuming a cylindrical core and R-Z fission rate separability
$_{IC}$ is a quantity similar to R_{FC} for the importance distribution.

The five ratios in the brackets are reasonably small corrections, three of which can be measured with some accuracy if necessary to reduce the overall error. The other values are measured, except ν which must be calculated from assumed ν values and relative fission rates.

Experimental Measurements

The absolute source strength, S, for the smaller source (used in Core 57) was measured using the method of the manganese-sulfate bath solution as described in Ref. 3; the value was measured by the authors of Ref. 3. The larger source strength was compared to the smaller by both a manganese sulfate bath and neutron counter using a liquid proton recoil detector. The sources, Cf-252, were contained in containers of aluminum and stainless steel so that the outer dimensions ($\approx 2 \times 0.5$ in.) were of a size handled by available sample changers and drive mechanisms.

The apparent reactivity, V, of the neutrons was determined using an autorod which had previously been calibrated in dollars using Eq. (1). As noted above this type of calibration is insensitive to β_{eff}. In order to remove the real reactivity effect of the container the measurement was made at two powers so that the terms on the left of the expression, $\left(\frac{\Delta k_e}{k_e \beta_{eff}} + \frac{\ell S_e}{k_e \beta_{eff} n(t)} \right)$, could be separated for the source and container. The central apparent worth for Core 57 was measured for another experiment by M. M. Bretscher (see Paper II-11) and his result was used for V. In a like manner an axial and a radial traverse were made to find the relative magnitude (see Fig. II-27-1) as a function of position in the core. The peak-to-average importance ratio, R_I, was found from these data and the measured fission distributions and assumed values of ν. This value contains the assumption of a cylindrical core and flux-space separation:

$$R_I = \frac{\phi^+(0,0)}{\overline{\phi^+}} = \frac{\phi^+(0,0) \iiint \sum_i \nu_i F_i(r) F_i(z) dV}{\iiint \sum_i \nu_i F_i(r) F_i(z) \phi^+(r) \phi^+(z) dV},$$

The value is independent of any normalization of F or ϕ^+.

In a like manner the value R_F was determined from fission counter traverses (see Fig. II-27-2). It is noted that in the radial traverse an oscillation of the measured points can be seen. This occurs because the measurements were made at two positions in the cell. Both curves have the same shape, so either gives the correct average. An average of the two was used.

$$R_F = \frac{\sum_i F_i(0) F_i(0) \iiint dV}{\iiint \sum_i F_i(r) F_i(z)\, dV}.$$

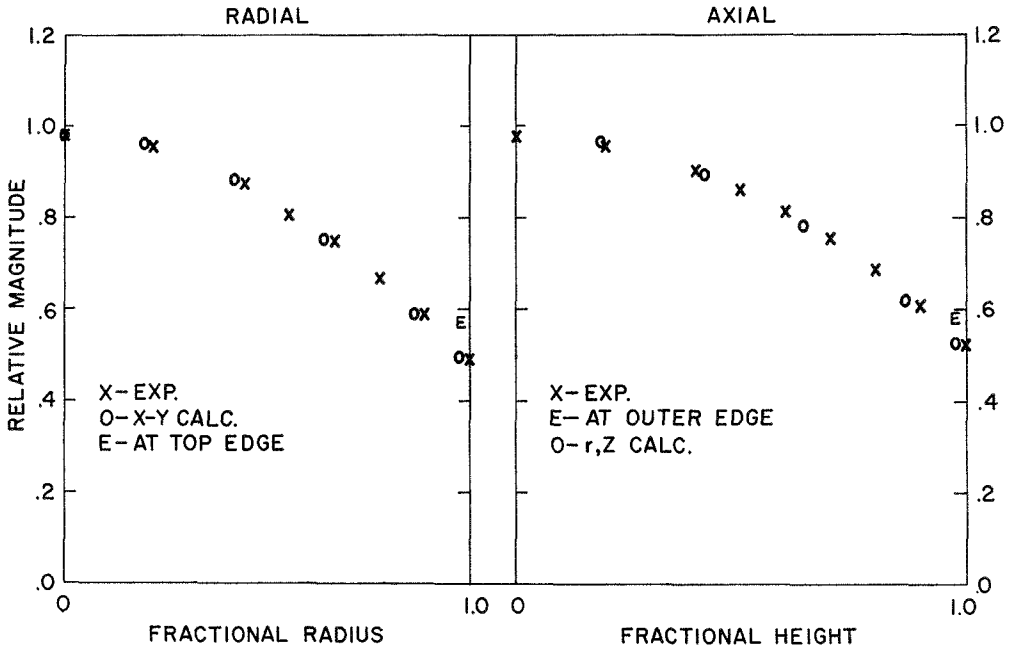

FIG. II-27-1. ϕ^*, Core 59. *ANL-ID-103-A11373.*

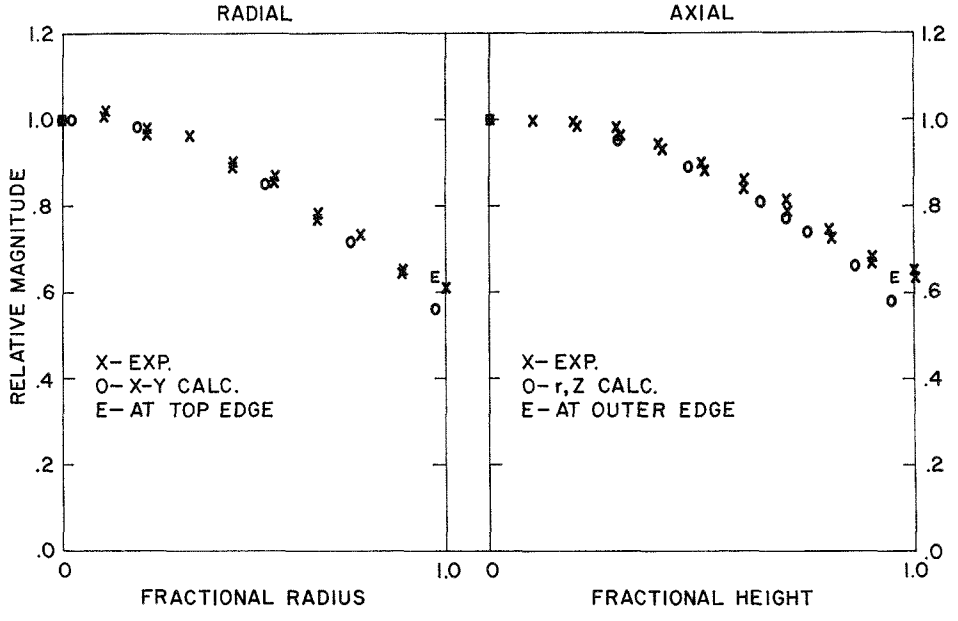

FIG. II-27-2. Fissions, Core 59. *ANL-ID-103-A11372*

Figures II-27-1 and II-27-2 also give selected calculational points which show little shape deviation from the experiments. This would indicate that the denominator of the perturbation expression is calculated correctly relative to the center or to any other point. This point is not particularly important in measuring β_{eff} but it is an additional requirement in order to expect to correctly calculate a small sample reactivity.

The factors F_{mc} and F_c were determined from the same measurements using the points at the center of the core. The value of N was taken directly from the loading records for the isotopes U-235 and Pu-239. The value of ν was determined from a core calculation of the total number of fissions as well as the total neutron production rate.

Calculated Corrections

The correction factors R_{FC} and R_{IC} were determined from two-dimensional diffusion theory calculations using the ARC System. X-Y geometry was used to

correct for the non-circular boundary. The fluxes and adjoint fluxes from the calculations were used in the same way and along the same diameter that the experimental data were used to calculate R_F and R_I, and then the full calculation was made point by point. The ratio of the latter to the former gave a partial correction. The R-Z calculation was then used in a similar way to find the correction for assumed separability in space (see Fig. II-27-3). The smaller ($\sim$1%) correction came from the R-Z calculation.

The correction factor ϕ_S^+/ϕ_F^+ was estimated assuming a Maxwellian distribution for the fission neutrons, calculating the contribution to each of the multigroup sets of the core calculation, and weighting the values for each isotope over the central calculated importances. The values used for the temperatures were 1.3 for U-235, 1.5 for Cf-252, and 1.4 for Pu-239. This correction is very small and the uncertainties were taken to be about as large as the correction.

The two correction factors, ϕ_{FS}^+/ϕ_{FP}^+ and F_c/F_p, which correct for the fact that the measurements were made with a source or counter not at the plate location where the fissions occur, were estimated from a transport theory cell calculation for Core 57[4] and a CALHET[5] calculation for Core 59. The error estimates were crude. They were estimated by observing the total swings (see Fig. II-27-4) through the cell and taking about one-third of that as the uncertainty. Foil measurements could reduce one of the uncertainties considerably but not the total uncertainty unless other errors can be reduced.

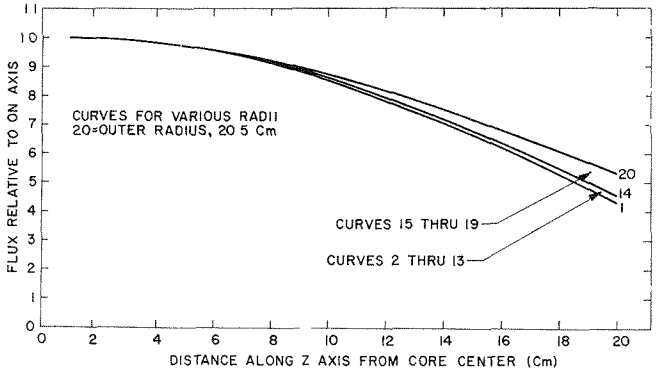

FIG. II-27-3. Core 57 R-Z Calculation. *ANL-ID-103-A11374.*

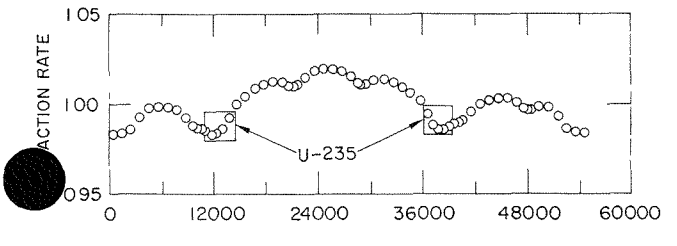

FIG. II-27-4. Core 57 Relative Fission Rate Across Cell. *ANL Neg. No. 116-469.*

TABLE II-27-I. β_{eff} RESULTS

	Core 59 (Pu-239)	Core 57 (U-235)	Error Est., %
S	5.94×10^7	9.197×10^6	±1.0
V	0.03938 $	0.06997 $	±1.0
ν	2.950	2.490	±1.0
N	1.913×10^{26}	2.165×10^{26}	±0.5
F_{mc}	2.483×10^{-15}	7.850×10^{-15}	±2.0
R_F	1.477	1.564	±2.0
R_I	1.523	1.667	±1.5
F_{mc}/F_c	0.986	0.948	±0.2
F_c/F_p	1.059	1.013	±1.5
ϕ_S^+/ϕ_F^+	0.997	1.005	±0.3
ϕ_{FS}^+/ϕ_{FP}^+	0.971	0.949	±1.0
R_{FC}	0.987	1.022	±1.0
R_{IC}	0.972	1.026	±1.0
β_{eff} (Exp.)	0.00233 ± 0.00010	0.0078 ± 0.0003	
β_{eff} (Calc.)	0.00230	0.0072	

RESULTS

Table II-27-I gives the values of the quantities along with an estimate of the uncertainties. The values between the dotted lines are all calculated ratios. The value for β_{eff} (experimentally determined) and its error are a straightforward combination of the values in the table. The largest errors came from the absolute fission rate estimates and are in F_{mc}, R_F, F_c/F_p and R_{FC}. With a much larger effort a significant improvement could be made. In the present search for a 30% difference it was not considered necessary.

The calculated β_{eff} values were obtained from spherical diffusion theory calculations[4,6] and Keepin data were used for delayed neutron parameters. These calculations could be refined but are representative of the way in which they are usually made and from which the reactivity values to be compared with experiments are usually calculated. Several other methods (2D and 1D cylindrical) were also used and these produced little change in β_{eff}. Various cross section sets were not tried. Differences of several percent could be expected from changes in input data.

CONCLUSIONS

We have not found an experimental uncertainty which can cause a 30% error in the measurement of a reactivity change. On the contrary we believe that small sample reactivity results, essentially independent of any calculated input, can be measured in the core center to about 1% in units of cents and to about 5% in units of Δk_e. If the calculated value of β_{eff} is more

accurate than the experimental value, the results will be better than 5%. The measured β_{eff} is only a few percent higher than that normally used with an uncertainty of a few percent. It is also expected that these results are not unique to these cores but are typical of the errors to be found in β_{eff} calculations.

References

1. S. G. Carpenter and S. Ramchandran, *β_{eff} Ratio Measurements*, Reactor Physics Division Annual Report, July 1, 1968 to June 30, 1969, ANL-7610, pp. 212-215 (1970).
2. G. R. Keepin, *Physics of Nuclear Kinetics*, (Addison-Wesley Publishing Company, Inc., Reading, Massachusetts, 1965).
3. A DeVolpi and K. G. Porges, *Absolute Calibration of Neutron Sources Having a Wide Range of Emission Spectra*, Metrologia **5**, 128 (1969).
4. C. D. Swanson, Argonne National Laboratory (private communication).
5. F. L. Fillmore and L. D. Felten, *The CALHET Heterogeneous Perturbation Theory Code and Application to ZPR 3-48*, AI-67-91 (1967).
6. V. C. Rogers, Argonne National Laboratory (private communication).

II-28. Rod Drop Measurements of Subcriticality

S. G. Carpenter and R. W. Goin

Introduction

Most of the usual methods of measuring the subcriticality of a system require that a reference measurement be made in the critical condition and the assumption is then made that the efficiency of a detector (or worth of a rod) remains the same for the subcritical measurement. However, in order to reproduce in a critical experiment the conditions that may occur in a power reactor, it is sometimes necessary to measure the degree of subcriticality of an experimental configuration which is never restored to criticality by compensating changes. For example, this occurs in the measurement of the worth of insertion of all control and safety rods. It is possible to use a rod drop technique to make these measurements if certain precautions are taken and if the system is less than about 10 dollars subcritical. No critical calibration is needed and in many cases the normal operating instrumentation can be used. Two descriptions of this technique are given here: a simplified method which illustrates the basic features and in which the counting rates are measured at only three points in time, and a more general method in which the entire count-rate history is utilized.

Simplified Method

Assume that the reactor is initially subcritical by an amount Δk_{e_1} and an equilibrium counting rate, R_1, from a detector is obtained under this condition. An absorbing rod is then inserted instantaneously. Immediately after the insertion (rod drop) the counting rate is R_2. At a long time after the drop a new equilibrium count rate, R_3, is obtained.

The method of performing the experiment should be chosen to assure that the detector efficiency and effective source strength are the same before and after the drop. We can then write

$$\epsilon R_1 = P_1 = \frac{S_e}{-\Delta k_{e_1}} \equiv \frac{S_e + \sum \lambda_i C_i}{-\Delta k_{e_1} + \beta_{eff}}, \qquad (1)$$

where P_1 is the neutron production rate, ϵ is the reciprocal of the counter efficiency for counting neutron production, Δk_{e_1} is the degree of subcriticality before the rod drop, so that $1/-\Delta k_{e_1}$ is the delayed multiplication and $1/(-\Delta k_{e_1} + \beta_{eff})$ is the prompt multiplication, S_e is the effective source strength, and finally $\sum \lambda_i C_i$ is the delayed neutron source at the time of the reactivity insertion. Furthermore, since the sources $(S_e + \sum \lambda_i C_i)$ are the same immediately after the drop as before the drop, we have,

$$\epsilon R_2 = P_2 = \frac{S_e + \sum \lambda_i C_i}{-\Delta k_{e_2} + \beta_{eff}};$$

and finally after a long time when the delayed neutrons are again at equilibrium,

$$\epsilon R_3 = P_3 = \frac{S_e}{-\Delta k_{e_2}}, \qquad (3)$$

where Δk_{e_2} is the subcriticality after the drop (that is, $\Delta k_{e_2} - \Delta k_{e_1}$ is the reactivity worth of the dropped rods).

From Eqs. (1) and (2) we have

$$\frac{R_1}{R_2} = \frac{-\Delta k_{e_2} + \beta_{eff}}{-\Delta k_{e_1} + \beta_{eff}},$$

and from Eqs. (1) and (3) we have

$$\frac{R_1}{R_3} = \frac{\Delta k_{e_2}}{\Delta k_{e_1}}.$$

olving these expressions for $\Delta k_{e_1}/\beta_{eff}$ and $\Delta k_{e_2}/\beta_{eff}$,

$$\frac{\Delta k_{e_1}}{\beta_{eff}} = \frac{\frac{R_2}{R_1} - 1}{\frac{R_2}{R_3} - 1}$$

and

$$\frac{\Delta k_{e_2}}{\beta_{eff}} = \frac{\frac{R_2}{R_3} - \frac{R_1}{R_3}}{\frac{R_2}{R_3} - 1}.$$

For systems in which the reactor is initially far-subcritical R_2/R_3 is close to unity, whereas R_1/R_2 may be made appreciably greater than unity by ensuring that the worth of the dropped rods is comparable to the initial subcriticality. Hence to determine the initial subcriticality, Δk_{e_1}, the most critical measurement is of the ratio (R_2/R_3). Experimentally R_3 may be determined accurately by simply increasing the counting time in the final equilibrium condition whereas R_2 is, in principle, an instantaneous measurement so that the principal source of error lies in the measurement of R_2.

General Method

The use of the instantaneous value, R_2, for the count rate after the drop is not an efficient use of all of the data. The simplified method is based upon the fact that the delayed neutron source rate is known because it is the same before and after the drop. In fact, the delayed neutron source rate is known at all times and the whole time history can be used by calculating the delayed neutron source as a function of time. It should be noted, however, that the important time regime remains that immediately after the rod drop.

Assuming point kinetics during the measurement the reactivity of the system may be written,

$$\frac{\Delta k_e}{k_e\beta_{eff}} = \frac{R(t) - S_e\ell/k_e\epsilon\beta_{eff} - (1/\epsilon k_e)\sum a_i e^{-\lambda_i t}\left(\epsilon_0 R_0 k_{e0} + \lambda_i \int_0^t k_e\epsilon R e^{\lambda_i t}\, dt\right)}{R(t)} + \frac{dR(t)}{dt}\frac{\ell}{k_e\beta_{eff}R(t)}. \tag{4}$$

(See Ref. 1 for the derivation of this equation; ϵR has been substituted for n, the number of neutrons in the system; ϵ is redefined here and the subscript 0 refers to time 0; and ℓ is neutron lifetime.) If one rearranges to solve for $R(t)$ and ignores the last term which is $\ll \Delta k_e/k_e\beta_{eff}$ (it may be retained with no change in result),

$$R(t) = \frac{S_e\ell/k_e\epsilon + (1/\epsilon k_e)\sum a_i e^{-\lambda_i t}\left(\epsilon_0 R_0 k_{e0} + \lambda_i \int_0^t k_e\epsilon R e^{\lambda_i t}\, dt\right)}{1 - (\Delta k_e/k_e\beta_{eff})}.$$

In the numerator the first term is the contribution to the instantaneous $R(t)$ from prompt multiplication of the constant source and the second term is that due to delayed neutrons. The latter can be calculated by knowing the previous count rate history, the former is a constant if S_e, ℓ, and A remain constant. If the history after a rod movement is observed (not necessarily instantaneously, but as fast as practical since the most significant information is obtained at small times), we can calculate $\Delta k_e/k_e\beta_{eff}$.

Equation (4) may be written

$$R(t) = a + b\,X(t)$$

where

$$X(t) = \sum a_i e^{-\lambda_i t}\left(\epsilon_0 R_0 k_{e0} + \lambda_i \int_0^t k_e\epsilon R e^{\lambda_i t}\, dt\right)\Big/\,\epsilon$$

and $X(t)$ can be calculated for each time, t, at which a measurement is made if it is assumed that $\epsilon = \epsilon_0$ (that is, the efficiency is not a function of time), and k_{e0} is estimated;

$$a = \frac{\frac{S_e\ell}{k_e\epsilon\beta_{eff}}}{\left(1 - \frac{\Delta k_e}{k_e\beta_{eff}}\right)}$$

which is constant after the rod movement if ϵ is constant;

$$b = \frac{1}{k_e\left(1 - \frac{\Delta k_e}{k_e\beta_{eff}}\right)}$$

and hence

$$\frac{\Delta k_e}{\beta_{eff}} = \frac{1 - \frac{1}{b}}{1 - \beta_{eff}}. \tag{5}$$

Also $X(t)$ before the drop ($t = 0$) is equal to R_0k_{e0} so that from Eq. (4)

$$R_0 = \frac{\frac{a}{bk_{e0}} + R_0}{1 - \frac{\Delta k_{e0}}{k_{e0}\beta_{eff}}}$$

and

$$\frac{\Delta k_{e0}}{\beta_{eff}} = \frac{-a}{bR_0}.$$

If ϵ is not a constant a calculational correction may

TABLE II-28-I. Reactivity Change per kg of Plutonium Removed at Core Center

Step	Total kg Pu Removed	kg Removed in This Step	% $\Delta k/k$/kg
1	2	2	0.283
2	8	6	0.243
3	12	4	0.283
4	20	8	0.196
5	24	4	0.187
6	32	8	0.152
7	35	3	0.158
8	32	−3	0.158

be made, although the position of the dropped rod should be chosen so that its insertion does not affect the detector efficiency. The solution for a and b is not sensitive to the choice of k_{e0} and no iteration is necessary even if k_{e0} is assumed to be unity.

The solution for a and b is done by least-squares fitting. The time-channel widths for accumulating the power history are selected to be short compared to the major delayed neutron half-lives so that $X(t)$ is well defined. The statistical error in $R(t)$ is then also not correlated strongly with that in $X(t)$ since the latter is a weighted average of many R's. The statistical error in $R(t)$ is large compared with that in $bX(t)$. A weighting function proportional to $R(t)$ may be used on $R(t)$ but the weights do not vary appreciably for far-subcritical systems.

An error in b can be calculated so that an error in $\Delta k_e/\beta_{eff}$ is also determined from Eq. (5)

$$d(\Delta k_e/\beta_{eff}) = \frac{db}{b^2(1-\beta_{eff})}.$$

Experimental Considerations

The usual requirement that the counting chamber and electronics should produce a count rate which is proportional to power should be carefully reviewed when setting up a data channel for subcritical measurements. This is true since the reactor operation covers power ranges not normally used when measuring power histories. The background from neutron sources and from any gamma sensitivity of the chamber must be small; this must also be true of the effects of noise sources from chamber power supplies, cables, amplifiers, microphonics, etc. The time response of the system should be short compared with the rates of power changes and the delayed neutron half lives. Finally, the necessary efficiency of the chamber (in order to follow the power fluctuations in the reactor rather than chamber counting statistics) is much higher than when the reactor is in the near-critical condition since the prompt fission chain lengths are much shorter. Poor efficiency can only be compensated by longer runs.

Assuming these points are satisfactorily met, it has been noted earlier that certain other conditions are necessary to apply the method in this straightforward form. With good statistics and modifications in data handling or theoretical corrections, some of these conditions can be relaxed. The initial power should be constant for sufficiently long ($\approx$10 min.) to allow the delayed neutron precursors to attain equilibrium. During the measurements the value of ϵ, S_e and ℓ should not change significantly, especially after the drop, and the time channels used should be short enough so that the integral may be obtained accurately and the error in it is poorly correlated to that in $R(t)$.

If these requirements are met, then one wishes to obtain the most data in a certain amount of time. Several points are worth noting. A large S_e increases the counts, and sources can be added beneficially to the system if they can be distributed reasonably. The best data are obtained immediately after the rod movement so that the movement should be done as fast as possible ($<$0.1 sec) without "bouncing" and in such a manner that it is known when its movement stops. There is an optimum size of change to be made which is dependent on the subcriticality and is of the same order as the subcriticality. The interesting data for measuring subcriticalities of the order of a few dollars occurs in tens of seconds after the drop so that repeated rod drops (which can be done in the same time history to avoid the ten minute wait which is still necessary at a run start) should be made every minute or so. It is of advantage if the reactor is as reactive as possible, and it is thus preferable to start above the reactivity which one wishes to measure and then subtract reactivity to achieve the condition to be studied. An appropriate waiting time may be chosen (depending on the measurement) and the reactivity may be re-inserted and the cycle repeated until the required accuracy is obtained. It is not essential to add reactivity rapidly if safety considerations prohibit it but loss of data results if reactivity is not added rapidly.

Sample Results

A series of measurements has been made on ZPPR Assembly 1 using an early modification of the technique of the rod drop measurement. In the measurements a B_4C control ring was removed step by step while fuel was removed at the core center to keep the system subcritical. The counting chamber was outside a B_4C ring so that its efficiency changed. The purpose of the experiments was to determine the amount of subcriticality at each step. Safety rods were used to make step reactivity change for each measurement. The consistency of the measurements can be seen by noting the Δk_e/kg obtained each time fuel was removed (see

ble II-28-I). The value of Δk_e/kg becomes smaller as the unfueled area at the core center becomes larger.

These results were obtained from single measurements of about 50 sec each, the reactivity of interest being the higher of the two in the individual experiment rather than the lower.

A second series of measurements was done on ZPR-3, the purpose being to determine the worth of massive control rods. It was of interest to note the measured worth of Control Rod 6 which was used for the step change in each measurement. This worth should remain approximately constant. An additional variable in certain experiments was that in which a neutron source was used which increased the power level by about a factor of four. Table II-28-II presents the results of these measurements. A comparison of these results shows that the worth was quite insensitive to the particular condition in which the measurements were made. The accuracy of the results is dependent upon the number of measurements; in these examples, the number of experiments was one, two, or three rod drops. Typical errors for this type of single measurement range from 2% at one dollar to 15% at 10 dollars subcritical.

TABLE II-28-II. Worth of Control Rod 6 as a Function of Subcriticality

Approx. Δk_e	Rod 6 Worth, Δk_e	Source Inserted?
0.0042	0.00208	Yes
0.0042	0.00213	No
0.0056	0.00206	No
0.0056	0.00206	Yes
0.0090	0.00180	No
0.0100	0.00212	Yes
0.0100	0.00204	No

Reference

1. S. G. Carpenter, *Reactivity Measurements in the Advanced Epithermal Thorium (AETR) Critical Experiments*, Nucl. Sci. Eng. **21**, 429 (1965).

II-29. Experimental Determination of the Perturbation Denominator in Fast Critical Assemblies

W. C. Redman and M. M. Bretscher

Introduction

A recent note[1] has focussed attention on the persistent discrepancy between measured and calculated reactivity coefficients in fast critical assemblies. An extensive intercomparison of calculated and measured central reactivity worths in a wide variety of fast reactors has shown[2] an average overestimate by the calculations of 17% for strongly reactive materials. Recent measurements[3] in uranium- and plutonium-fueled fast critical assemblies have shown that the effective delayed neutron fraction is approximately 5% larger than calculated, thereby providing a partial explanation for the observed discrepancy between calculated and measured reactivities. The likely explanation for the residual discrepancy appears to be faulty cross-section data used in the calculational models, with differences in experimental and calculated conditions a lesser contributing factor.

A by-product of the measurement of capture-to-fission ratio by the reactivity-reaction rate method[4] is data necessary to provide several experimental determinations of the denominator of the expression for the reactivity of a sample given by first-order perturbation theory. Such experimental determinations of the perturbation denominator are useful for guidance in the selection of consistent combinations of cross-section sets and computational models. Heretofore, the apparent reactivity of a calibrated Cf-252 spontaneous fission source has been used to provide[5] an experimentally based value of this quantity. In the measurements reported here absorbing and fissile samples were also used to provide independent determinations of the perturbation denominator for three fast criticals: ZPR-9 Assemblies 24 and 25 and ZPR-3 Assembly 57.

Basic Equations

First order perturbation theory gives the reactivity for a sample inserted in a reactor in terms of the ratio of the effective change in neutron population due to absorption, production and scattering of neutrons by the sample relative to the importance-weighted neutron production rate in the entire reactor, termed the perturbation denominator, D. As shown previously,[6] the perturbation denominator is related to the apparent reactivity of a spontaneous fission source as follows:

$$D_S = \frac{S\overline{\phi_f^*(S)}}{\rho'(S)} . \qquad (1)$$

TABLE II-29-I. Atom Densities of Central Regions in ZPR-9 Assemblies 24 and 25 and ZPR-3 Assembly 57, 10^{21} atoms/cm^3

	A-24	A-25	A-57
U-235	1.1347	2.1401	4.081
U-238	12.2363	33.2329	6.347
C	43.3814		
Be			39.01
O			39.01
Al		1.6494	5.546
Fe	6.7549	6.8368	
Cr	1.9280	1.9518	
Ni	0.854	0.8643	

Similarly, for a nonfissionable absorber

$$D_A = \frac{-R_a(A)\overline{\phi_a^*}(A)}{\rho(A)[1 - \rho_s(A)/\rho(A)]}, \tag{2}$$

and for a fissile material

$$D_F = \frac{R_f[\overline{\phi_f^*}\bar{\nu} - \overline{\phi_a^*}(1 + \bar{\alpha})]}{\rho(1 - \rho_s/\rho)}. \tag{3}$$

Here $\overline{\phi^*}$ is the calculated average neutron importance weighted according to the sample's neutron emission (S,F) or absorption (A) rate, and ρ_s/ρ is the calculated fraction of the total reactivity resulting from scattering. The measurable quantities are the neutron source strength S, the reaction rates (R) for fission (f), absorption (a) and capture (c), and the real (ρ) and apparent (ρ') reactivities. $\bar{\nu}$ is the average number of neutrons emitted per fission, and $\bar{\alpha} = R_c/R_f$.

The perturbation denominator is the total importance-weighted neutron production rate in the reactor and hence is proportional to the square of the power level. By normalizing the measured reaction rates and apparent source reactivity to the same power level in the reactivity-reaction rate ($\rho - R$) method for $\bar{\alpha}$, the quantities combine to yield an expression for capture-to-fission ratio which does not involve the perturbation denominator explicitly; specifically,

$$1 + \bar{\alpha} = \frac{R_a(A)\overline{\phi_a^*}(A)/\overline{\phi_a^*}}{\rho(A)[1 - \rho_s(A)/\rho(A)]} \cdot \left[\frac{\rho(1 - \rho_s/\rho)}{R_f} - \frac{\bar{\nu}\rho'(S)\overline{\phi_f^*}/\overline{\phi_f^*}(S)}{S}\right]. \tag{4}$$

Consequently, previous descriptions of such measurements have not reported values for the perturbation denominator. Here the measurements made in Assemblies 24 and 25 of ZPR-9 and Assembly 57 of ZPR-3 are used to derive values for this quantity based on measurements with a source (Cf-252), a nonfissionable absorber (Li-6), and a fissile material (U-238) in each assembly.

Calculation of a value for D based on U-238 m[illegible] appear circuitous, since the combination of measured quantities is used to obtain a value for $\bar{\alpha}$, assuming that $D_S = D_A = D_F$. However, its validity becomes apparent when one recalls that a value of $\bar{\alpha}$ for U-238 results directly from the radiochemical procedures.[7]

Description of Assemblies

Assemblies 24 and 25 in ZPR-9 were zoned fast critical experiments constructed to investigate reaction rates and cross-sections and derive information on the capture-to-fission ratio by the null-reactivity technique. The composition of a central test zone, surrounded by buffer, driver and reflector zones was adjusted in each to obtain a k_∞ of unity. The compositions of these adjusted central zones, of 25.9 and 18.9 cm radius, respectively, and 91.4 cm height, are given in Table II-29-I. Assembly 24 had a soft neutron spectrum, with about 50% of the fissions in the test zone caused by neutrons below 25 keV, while Assembly 25 had a hard spectrum, with more than 90% of the fissions occurring above 25 keV.

Assembly 57 in ZPR-3 was a uranium-fueled assembly (see Paper II-12) whose spectrum was tailored to enhance the neutron population in the 1 to 50 keV energy range. The core, approximating a cylinder of 41 cm diameter and height, was deliberately made small in order to make feasible a direct determination of the capture-to-fission ratio by the mass spectrographic-radiochemical technique. The composition of the core, which was surrounded by concentric reflector zones of iron and depleted uranium, is also given in Table II-29-I.

Experimental Values

The measured values on which the experimental determinations of the perturbation denominator for each of the three assemblies are based are collected in Table II-29-II. Values for ZPR-9 Assembly 24 are identical with those reported previously,[6] except for the apparent reactivity of the Cf-252 spontaneous fission neutron source at the reference power level. An oscillator method had been used for its determination prior to the measurements in Assembly 24 and so inadvertently the usual correction for the subcritical transfer function[8] had been applied. Such a correction is inappropriate for reactivities determined by compensating control rod motion (auto-rod) as used in the Assembly 24 measurements. Values from measurements in the other two assemblies are taken from descriptions of those experiments included in this report (see Papers I[illegible] and II-19).

The pertinent calculated quantities are presented in Table II-29-III. Since these values depend upon the

TABLE II-29-II. Measured Quantities for Experimental Determination of the Perturbation Denominator

Quantity	Units	Assembly		
		ZPR-9 No. 24	ZPR-9 No. 25	ZPR-3 No. 57
S(Cf)	neutrons/sec	$(1.251 \times 10^{7}) \pm 0.30\%$	$(5.125 \times 10^{6}) \pm 0.50\%$	$(9.205 \times 10^{6}) \pm 0.29\%$
ρ'(Cf)	Ih	$(1.690 \times 10^{-1}) \pm 0.55\%$	$(5.452 \times 10^{-2}) \pm 0.50\%$	$(2.100 \times 10^{-1}) \pm 0.30\%$
ρ(0.30 in. Li-6)	Ih/g			$(-1.159 \times 10^{1}) \pm 0.26\%$
ρ(0.623 in. Li-6)	Ih/g	$(-8.859 \times 10^{-1}) \pm 0.12\%$	$(-7.025 \times 10^{-1}) \pm 0.75\%$	$(-1.110 \times 10^{1}) \pm 0.27\%$
ρ(U-238)	Ih/g	$(-5.039 \times 10^{-3}) \pm 0.70\%$	$(-3.369 \times 10^{-3}) \pm 0.75\%$	$(-3.322 \times 10^{-2}) \pm 0.44\%$
R_A(0.30 in. Li-6)	abs/g-sec			$(4.194 \times 10^{8}) \pm 0.76\%$
R_A(0.623 in. Li-6)	abs/g-sec	$(7.251 \times 10^{7}) \pm 0.61\%$	$(8.908 \times 10^{7}) \pm 1.00\%$	$(4.049 \times 10^{8}) \pm 0.89\%$
R_c(U-238)	capt/g-sec	$(4.922 \times 10^{5}) \pm 1.20\%$	$(4.270 \times 10^{5}) \pm 1.66\%$	$(2.564 \times 10^{6}) \pm 2.32\%$
R_f(U-238)	fiss/g-sec	$(6.137 \times 10^{4}) \pm 2.61\%$	$(8.278 \times 10^{4}) \pm 2.50\%$	$(6.902 \times 10^{5}) \pm 2.57\%$

TABLE II-29-III. Calculated Quantities for Experimental Determination of the Perturbation Denominator

Quantity	Units	Assembly		
		ZPR-9 No. 24	ZPR-9 No. 25	ZPR-3 No. 57
$\overline{\Phi_f^*}$(Cf)		3.6546	4.2633	2.9378
$\overline{\Phi_A^*}$(0.30 in. Li-6)				3.3777
$\overline{\Phi_A^*}$(0.623 in. Li-6)		3.1624	2.9724	3.3692
$\overline{\Phi_f^*}$(U-238)		3.6021	4.1960	2.9201
$\overline{\Phi_A^*}$(U-238)		3.1621	3.0595	3.2971
$\bar{\nu}_{28}$	n/fiss	2.805 $\pm$ 1.0%	2.830 $\pm$ 1.0%	2.796 $\pm$ 1.0%
$1 - \frac{\rho_s(0.30 \text{ in. Li-6})}{\rho(0.30 \text{ in. Li-6})}$				1.0084
$1 - \frac{\rho_s(0.623 \text{ in. Li-6})}{\rho(0.623 \text{ in. Li-6})}$		0.9891	0.9400	1.0086
$1 - \frac{\rho_s(\text{U-238})}{\rho(\text{U-238})}$		0.8099	0.5319	1.2079

code[9] using ENDF/B (1968) data. Resonance region cross sections for U-238 were corrected for self-shielding using slab geometry equivalence theory and unit cell homogenization. These multigroup cross section sets provided the required input data for the MACH-1 code[10] which evaluated the central flux and adjoint distributions. The effects of sample thickness were evaluated using a self-shielding perturbation code with dilute cross-sections and the MACH-1 central flux and adjoint distributions as input data. Essentially the same procedure was followed for Assembly 57, except that the transport code CALHET[11] was used to account for the heterogeneous nature of the core. The resulting flux variations across the plates of the unit cell, integrated over the extent of the samples, and MACH-1 adjoints calculated from the cell-averaged cross sections obtained by a flux-weighting procedure with CALHET were used to calculate the various parameters.

The resulting values of the perturbation denominator, for the reference power level to which the reaction rates and the apparent reactivity of the Cf-252 source were related, are given in Table II-29-IV. The indicated

TABLE II-29-IV. Experimental Values of the Perturbation Denominator, 10^8

Method	Assembly		
	ZPR-9 No. 24	ZPR-9 No. 25	ZPR-3 No. 57
Cf-252 source	2.704 $\pm$ 0.63%	4.027 $\pm$ 0.71%	1.288 $\pm$ 0.42%
Li-6 absorption			
0.30 in. diam			1.212 $\pm$ 0.81%
0.623 in. diam	2.617 $\pm$ 0.62%	4.010 $\pm$ 1.25%	1.218 $\pm$ 0.93%
U-238 capt + fiss	2.665 $\pm$ 4.86%	3.191 $\pm$ 7.72%	1.251 $\pm$ 6.49%
Weighted mean	2.659 $\pm$ 1.16%	4.015 $\pm$ 1.46%	1.270 $\pm$ 1.78%[a]

[a] Excludes value for 0.623 in. Li-6.

calculational methods used and the choice of input [illegible], a description of the specific basis for these numbers is appropriate. For Assemblies 24 and 25, multigroup cross section sets were generated by the MC[2] standard deviations are only those resulting from the standard deviations for the measured quantities and $\bar{\nu}_{28}$, as given in Tables II-29-II and II-29-III. They do not include uncertainties in the calculated neutron

importances and scattering reactivities. The large error in the value for $D_{U\text{-}238}$ is a direct consequence of relatively large errors of about 2½ and 2%, respectively, in the values for the U-238 fission and capture rates and the 1% uncertainty in $\bar{\nu}_{28}$. Additional limitations in the value based on U-238 are the 20 to 50% corrections for the scattering reactivity, in contrast with $\leq 6\%$ for $D_{Li\text{-}6}$ and none for $D_{Cf\text{-}252}$, and the relatively larger uncertainty in the U-238 fission spectrum.

The weighted mean of the values based on the three types of samples used in the determination of the perturbation denominator is also given for each assembly in Table II-29-IV. Only the value for the smaller diameter Li-6 sample is included in the weighted mean for ZPR-3 Assembly 57, since the reactivity for the larger sample exceeded the worth of the auto-rod, thus requiring its measurement by reactor period rather than the reactivity compensation technique used for all other samples.

Comparison with Calculations

The one-dimensional diffusion code MACH-1 output is such that a normalization of the perturbation denominator to $\sum_i (\nu\Sigma_f)_i\phi_i = 1$ and $\sum_j \chi_j\phi_j^* = 1$ at the core center is convenient, and this is normally done. On the other hand, in the reactivity-reaction rate method for determining capture-to-fission ratios the measured reaction rates and apparent reactivity of the Cf-252 source are related to a reference power level, so an intercomparison of calculated and experimentally-based values for the perturbation denominator requires a renormalization. In addition, the latter are calculated from experimental reactivities expressed in inhours while the theoretical values are in units of $(\Delta k/k)$. Furthermore, the importance terms reported in Table II-29-III are normalized to $\sum_{i=1}^{n} \phi_i^* = 100$. Thus the normalization of the experimentally-based values requires division by a normalization factor (NF) given by

$$NF = \frac{S(r=0)S^*(r=0)}{\mathrm{Ih}\Big/\dfrac{\Delta k}{k}}.$$

Here

$$S(r=0) = \sum_i (\nu\Sigma_f)_i\phi_i(0) = \bar{\nu}^{25}R_f^{25}\frac{N^{25}}{N_0/A_{25}} + \bar{\nu}^{28}R_f^{28}\frac{N^{28}}{N_0/A_{28}},$$

where $R_f \equiv$ fissions/g-sec, $N \equiv$ atom density, $N_0 \equiv$ Avagardo's number (6.023×10^{23}), $A \equiv$ atomic weight, and

$$S^*(r=0) = \sum_j \chi_j\phi_j^*(0) = \frac{\sum_{i=1}^{n}\phi_i^*(0) = 100}{\sum_{i=1}^{n}\phi_i^*(0,\ \text{unnormalized})} S^*(r=0,\ \text{unnormalized}).$$

Only for ZPR-9 Assembly 25 were the central fission rates measured for the actual plates of which the core was constructed, so a small approximation occurs in using the central fission rates for the annular samples which most closely match the dimensions of the core plates. In addition, because of an unexplained anomaly in the measured fission rate for the annular sample of 0.030 in. wall thickness in the ZPR-3 Assembly 57 experiment, the value measured for the 0.015 in. sample has been scaled by the calculated ratio of the fission rates in 0.030 and 0.015 in. samples. Values used in computing the normalization factors are given in Table II-29-V, together with identification of the samples to which the fission rates apply.

The calculated and measured values for the perturbation denominator are compared in Table II-29-VI. Note that the error in the normalization factor in all cases exceeds that of the weighted mean of the results from measurements with the three types of samples, and thus contributes significantly to the total error in the normalized experimental mean. Major sources of the resulting error are the error of 2.38% in the value of 6.29% used for the Mo-99 yield in U-238 fission and 1.88% in that of 5.85% for U-235 fast fission.

Comments

The differences between calculated and measured values for the perturbation denominator far exceed the errors in the latter and in fact display differences in directions. Heretofore the tendency has been for the calculated reactivity values to exceed the measured ones. Since reactivity and the perturbation denominator are inversely related, the situation found for ZPR-3 Assembly 57 is not unexpected. The discrepancy has been larger for plutonium-fueled systems than for U-235-fueled ones, and larger for smaller cores, suggesting that the more significant role of the reflector for small cores is a contributing factor in the discrepancy.

The explanation for the reversal observed for the two assemblies having central zones with $k_\infty = 1$ is not clear, although the complexity of the calculations is increased because of the many regions (test zone, buffer, driver, and reflectors) involved. The discrepancy observed is larger for ZPR-9 Assembly 25 which had b[illegible] a higher average neutron energy and a smaller re[illegible] inside the reflector (driver outer radius of 37.7 cm compared with 50.9 cm for ZPR-9 Assembly 25).

TABLE II-29-V. DATA FOR NORMALIZATION OF EXPERIMENTAL TO CALCULATED PERTURBATION DENOMINATORS

Quantity	Assembly		
	ZPR-9 No. 24	ZPR-9 No. 25	ZPR-3 No. 57
U-235			
Sample, in.	0.040 annular	1/32 plate	0.030 annular
$\bar{\nu}$, n/fission	2.460 ± 1.0%	2.468 ± 1.0%	2.481 ± 1.0%
R_f, 10^6 fission/g-sec	3.707 ± 1.92%	3.621 ± 2.50%	21.049 ± 1.98%
N, 10^{21} atoms/cm^3	1.135	2.140	4.081
U-238			
Sample, in.	0.035 annular	3/16 plate	0.031 annular
$\bar{\nu}$, n/fission	2.805 ± 1.0%	2.830 ± 1.0%	2.796 ± 1.0%
R_f, 10^4 fission/g-sec	6.137 ± 2.61%	8.278 ± 2.50%	69.02 ± 2.57%
N, 10^{21} atoms/cm^3	12.236	33.233	6.347
$S(r = 0)$, 10^7	0.487 ± 1.87%	1.054 ± 3.10%	8.801 ± 2.10%
$S^*(r = 0)$	3.480	4.141	2.916
Ih $/ \frac{\Delta k}{k}$, 10^4	4.224	4.408	4.201
Norm. factor, 10^3	0.4013 ± 1.87%	0.9904 ± 3.10%	6.1089 ± 2.10%

TABLE II-29-VI. COMPARISON OF MEASURED AND CALCULATED VALUES OF THE PERTURBATION DENOMINATOR

Quantity	Assembly		
	ZPR-9 No. 24	ZPR-9 No. 25	ZPR-3 No. 57
Exptl. wtd. mean, 10^3	2.659 ± 1.16%	4.015 ± 1.46%	1.270 ± 1.78%
Normalization factor, 10^2	4.013 ± 1.87%	9.904 ± 3.10%	61.089 ± 2.10%
Normalized mean (M), 10^5	6.626 ± 2.19%	4.054 ± 3.43%	0.208 ± 2.75%
Calculated (C), 10^5	7.816	5.176	0.182
C/M	1.180 ± 2.19%	1.277 ± 3.43%	0.877 ± 2.75%

It is obvious that, until the causes of such discrepancies are both understood and eliminated, more reliance should be placed on a measured value for the perturbation denominator, particularly since values obtained with different types of samples are in good agreement. Heretofore, when measurements had been made only with a Cf-252 source, the possibility of a systematic error existed. The probability that this exists is significantly reduced by the agreement in the values with Cf-252 and Li-6, as indicated by the results given in Table II-29-IV. This is not contradicted by the results with U-238 samples, although the larger error in these values and the large magnitude of the calculated scattering correction for U-238 reduces the weight which should be given to their agreement.

Because of the absence of a correction for scattering reactivity, it is recommended that Cf-252 be used for future measurements of the perturbation denominator, if limited to a determination with only one type of sample. Li-6 is only slightly less valuable, as its scattering correction is very small except for hard neutron spectrum systems. U-238 is decidedly less useful because of its very large scattering correction, the need to account for both captures and fissions, and the comparatively large error introduced by the present uncertainty in the Mo-99 fission yield.

REFERENCES

1. W. W. Little, Jr. and R. W. Hardie, *Discrepancy Between Measured and Calculated Reactivity Coefficients in Dilute Plutonium Fueled Fast Criticals*, Nucl. Sci. Eng. **36**, 115–116 (1969).
2. H. Morewitz et al., *Annual Technical Progress Report, LMFBR Physics Programs, GFY1970*, AI-AEC-12969, 24 (August 1970).
3. S. G. Carpenter, J. M. Gasidlo and J. M. Stevenson, β_{eff} *Measurements in Two Fast Reactor Critical Assemblies*, Trans. Am. Nucl. Soc. **13**, 92–93 (1970).
4. W. C. Redman, *Pile Oscillator Determination of Capture-to-Fission Ratio*, TID-17738 (1962).
5. R. A. Karam, *Measurements of the Normalization Integral and the Spatial Distribution of the Importance of Fission Neutrons*, Nucl. Sci. Eng. **37**, 192–197 (1969).
6. M. M. Bretscher and W. C. Redman, *Low-Flux Measurements of ^{239}Pu and ^{235}U Capture-to-Fission Ratios in a Fast Reactor Spectrum*, Nucl. Sci. Eng. **39**, 368–378 (1970).
7. R. J. Armani, *Absolute Determination of Fission Rates in U-235 and U-238 and Capture Rates in U-238 by Radiochemical Techniques*, Reactor Physics Division Annual Report, July 1, 1965 to June 30, 1966, ANL-7210, p. 304.

8. W. C. Redman, *Reactor Response to an Oscillating Neutron Source*, Reactor Physics Division Annual Report, July 1, 1965 to June 30, 1966, ANL-7210, pp. 319–321.
9. B. J. Toppel, A. L. Rago and D. M. O'Shea, *MC²*, *A Code to Calculate Multigroup Cross Sections*, ANL-7318 (1967).
10. D. A. Meneley, L. C. Kvitek and D. M. O'Shea, *MACH-1 A One-Dimensional Diffusion-Theory Package*, ANL-7[illegible] (1966).
11. F. L. Fillmore, *The CALHET-2 Heterogeneous Perturbation Theory Code and Application to ZPR-3-48*, AI-69-13 (1969).

II-30. The Effects of Gaps and Foils on the Measured Fission and Capture Rates in Depleted and 16.4% Enriched UO_2 Fuel Rods

A. B. Long, W. R. Robinson and G. S. Stanford

I. Introduction

Some of the future measurements on the zero power critical assemblies at Argonne will include the use of PuO_2/UO_2 fuel pins placed in sodium calandria. In order to measure the fission and capture rates in these pins, special plutonium and uranium metal foils with thin stainless steel cladding have been developed. These foils will be placed between the ends of special fuel pins during an irradiation and then will be removed for counting. The foils cannot be used unclad or be put inside the fuel pins because of radiological hazards associated with bare plutonium. Because of the brittleness of oxide wafers, metallic foils were chosen for the measurements.

A series of experiments was performed to determine the effect that the use of metallic foils and the presence of stainless steel gaps would have on the measured fission and capture rates in depleted and 16.4% enriched UO_2 fuel pins. The actual fission and capture rates within the fuel pins were found by placing 0.010 in. thick UO_2 wafers between specially machined UO_2 pellets. The specific activities of these wafers were then compared with metallic foils which were placed between similar UO_2 pellets and irradiated under identical conditions. To minimize the effects of self-shielding, an effort was made to ensure that only the edges of the foils and wafers were exposed. The effect of foil cladding was simulated by inserting stainless steel disks between the foil and the pellets.

The depleted and 16.4% enriched UO_2 pellets used in these measurements were faced off at one end and turned to a diameter of 0.322 in. The oxide wafers were cut from similar pellets and ground to an approximate thickness of 0.010 in. The uranium and stainless steel foils were punched to the same diameter. The depleted and enriched foils had thicknesses of 5.5 and 4.4 mils, respectively.

The first set of measurements was performed using the Argonne Thermal Source Reactor (ATSR). In the irradiation each foil or wafer was pressed between two oxide pellets and then up to ten of these units were mounted around the circumference of a wheel. The entire wheel, including everything mounted on it, was covered with cadmium and placed close to the front face of the ATSR thermal reactor. Thus the foils were in a spectrum that was approximately $1/E$. During the irradiation the wheel was revolved to ensure uniform exposure. The 1 mil gold cadmium ratio at this position was about 9.

The low energy of the neutron spectrum in the ATSR reactor served to amplify the changes in self-shielding produced by introducing stainless steel gaps. The results of the measurement indicate that in the epicadmium spectrum of a thermal reactor, the gaps and foils produce a significant change in the measured capture and fission rates. A second set of measurements was then performed in ZPR-6 Assembly 6A. This 4000 liter UO_2 fueled critical assembly had a neutron spectrum with a mean energy of 90 keV and a distribution (see Paper II-22 for the measured neutron energy spectrum) similar to the assemblies in which the fuel pin calandria measurements will be performed.

In the ZPR-6 irradiation, four sets of two oxide pellets were loaded into a stainless steel tube. Sandwiched between each pair of pellets were a depleted foil or wafer and different thicknesses of stainless steel. Four tubes were loaded in this manner and substituted for a 4 in. sodium can located 8 in. from the front face of the stationary half in Drawers 27–23. The data from this irradiation were corrected for the spatial variation in the flux along the length of the tubes by using previously measured axial distributions of U-238 fission and capture rates in the core.

Following all irradiations, the enriched and depleted foils were counted for fission by recording the number of gamma-rays above 600 keV which were emitted by the fission products. The captures in the depleted foils were also determined by counting the coincident

emission of 100 keV gammas and X-rays in the decay of Np-239. Corrections had to be made for the self-absorption of these low energy photons by the foil itself. Detailed descriptions of counting techniques used can be found in Refs. 1 and 2.

II. Measurements in the ATSR Thermal Column

A. Consistency Check (ATSR)—Captures in Depleted U-238 Foils Between Depleted UO_2 Pellets

A measurement was performed to determine the consistency of the system with respect to misalignment and pellet irregularities. The results of this measurement are presented in Table II-30-I. The foils were grouped into three categories depending upon the condition of the pellet edges (good, fair, bad). The activity due to captures was corrected for the self-absorption in the foils and wafers of the 100 keV gammas and X-rays.

The counting statistics for each foil were better than 0.5% but the dispersion in the results of all the foils was about 2%. This increased dispersion can be attributed in part to the pellet irregularities. It can be seen that as the condition of the pellets became worse the activity increased due to the larger exposed surface area. In addition, the dispersion in the data also reflected the pellet irregularities by increasing from 0.7% for the good pellets to 2.1% for the bad ones.

In order to minimize the effects of pellet irregularities, all measurements were made with at least two sets of foils and pellets. The quality of the pellets was chosen to give an average number of irregularities for each measurement.

TABLE II-30-I. Consistency Check (ATSR)—Captures in Depleted U-238 Foils between Depleted UO_2 Pellets

Foil	Pellet Condition	Foil Weight, g	Rel. Act. Per Gram U-238	Rel. Act. Corrected for Self-Absorption, R.A./(1−1.851 W)	Percent Difference from Good Pellets
104	Good	0.1362	1.830	2.447	
108	Good	0.1370	1.806	2.420 } 2.428	—
105	Good	0.1369	1.805	2.418 } ± 0.7%	
107	Fair	0.1280	1.912	2.506	
109	Fair	0.1365	1.835	2.479 } 2.492	+2.6%
103	Bad	0.1361	1.914	2.558	
106	Bad	0.1369	1.834	2.456 } 2.516	+3.6%
110	Bad	0.1340	1.906	2.535 } ± 2.1%	
				Av. 2.477 ± 2.1% (STD)	

TABLE II-30-II. Consistency Check (ATSR)—Fissions in 93.3% Enriched U-235 Foils between 16.4% Enriched UO_2 Pellets

Foil	Pellet Condition	Relative Activation Per Gram U-235	Percent Difference from Good Pellets
202	Good	0.997	
207	Good	0.992 } 0.994	—
206	Fair	0.990	
211	Fair	0.991 } 0.990	−0.4%
203	Bad	0.996	
204	Bad	0.997	
205	Bad	0.996	
208	Bad	0.998 } 0.995	+0.1%
212	Bad	0.990	
213	Bad	0.995	
		Av. 0.994 ± 0.32% (STD)	

B. Consistency Check (ATSR)—Fissions in 93.3% Enriched U-235 Foils Between 16.4% Enriched UO_2 Pellets

In this experiment 93.3% enriched metal foils were irradiated between 16.4% enriched UO_2 pellets and then counted for fissions. The purpose of the experiment was the same as that discussed above. The results, which are presented in Table II-30-II, indicate that the U-235 fission activity is much less sensitive to self-shielding and therefore the pellet irregularities. Within the statistical reliability of the data (0.3%) no effect can be observed for the different pellet conditions.

C. Gap Effects (ATSR)—Captures in Depleted U-238 Foils with Different Thickness Stainless Steel Gaps Between Depleted UO_2 Pellets

To determine the effect that cladding would have on measured capture rates in depleted U-238 foils, stainless steel disks were placed on either side of the U-238 foil and the package was sandwiched between UO_2 pellets. Stainless steel thicknesses of 0, 5, 10, and 30 mils on either side of the foil were investigated. To permit averaging of the effects of pellet condition, a good set and a bad set of pellets were selected for each gap thickness. After irradiation the activity due to captures was corrected for self-absorption. The results are presented in Table II-30-III.

It is evident that there is a sizeable increase in activity with increasing gap thickness. This arises from the effective increase in the surface area of the foil visible to neutrons outside the pellets as the gap between foil and pellet is enlarged. (The mean free path of a neutron

TABLE II-30-III. GAP EFFECT (ATSR)—CAPTURES IN DEPLETED U-238 FOILS WITH DIFFERENT THICKNESS STAINLESS STEEL GAPS BETWEEN DEPLETED UO_2 PELLETS

SS Gap, mils	Foil	Pellet Condition	Foil Weight, g	Rel. Act. Per Gram U-238	Rel. Act. Corrected for Self-Absorption, R.A./(1–1.851W)	Percent Difference from Zero Gap
0	111	Good	0.1350	1.976	2.634 } 2.764	—
0	122	Fair	0.1357	2.033	2.715 }	
5	120	Good	0.1361	2.264	3.026 } 3.086	15.4%
5	126	Bad	0.1350	2.360	3.146 }	
10	113	Good	0.1356	2.534	3.383 } 3.443	28.7%
10	114	Bad	0.1358	2.623	3.503 }	
30	119	Fair	0.1354	3.353	4.474 } 4.502	68.3%
30	123	Bad	0.1345	3.403	4.531 }	

TABLE II-30-IV. GAP EFFECT (ATSR)—FISSIONS IN 93.3% ENRICHED U-235 FOILS WITH DIFFERENT THICKNESS STAINLESS STEEL GAPS BETWEEN 16.4% ENRICHED UO_2 PELLETS

SS Gap, mils	Foil	Pellet Condition	Rel. Act. Per Gram U-235	Percent Difference from Zero Gap
0	214	Good	0.945 } 0.942	—
0	220	Bad	0.939 }	
2	219	Good	0.935 } 0.939	−0.3%
2	215	Bad	0.943 }	
5	218	Fair	0.947 } 0.948	+0.6%
5	222	Bad	0.948 }	
10	221	Fair	0.959 } 0.962	+2.1%
10	217	Bad	0.964 }	
30	216	Bad	1.000 } 0.996	+5.7%
30	223	Bad	0.991 }	

in stainless steel is approximately 5 cm so that the stainless steel gaps appear essentially as a void.)

D. GAP EFFECT (ATSR)—FISSIONS IN 93.3% ENRICHED U-235 FOILS WITH DIFFERENT THICKNESS STAINLESS STEEL GAPS BETWEEN 16.4% ENRICHED UO_2 PELLETS

A measurement similar to the one discussed in the previous section was made to determine the effect of stainless steel cladding on the fission rate in 93.3% enriched U-235 foils. In this case, 16.4% enriched UO_2 pellets were used and the gap thicknesses introduced on either side of the foils were 0, 2, 5, 10 and 30 mils. The measured activities are given in Table II-30-IV.

The gap effect on the fission rate in U-235 is much smaller than it is on the capture rate in U-238. This is to be expected on the basis of the greater number of resonances in the U-238 cross section and therefore the more severe self-shielding problem. However, the introduction of a stainless steel gap between foil and pellet also affects the transfer of fission fragments from foil to pellet. Without any gap the fission fragments which are lost from the outside 0.2 mils of the foil are to some extent balanced by the influx of fragments from the 16.4% enriched UO_2 pellets. When a stainless steel gap is introduced, the fragments from the pellet can no longer reach the foil. The net result is a small decrease in foil activity which cancels some of the positive gap effect due to less self-shielding. Linear extrapolation of the 10, 5 and 2 mil points indicates that about 0.7% of the activity of the foil in contact with the pellets was due to fission fragments from the pellets.

E. FOIL EFFECT (ATSR)—CAPTURES IN DEPLETED U-238 FOILS AND WAFERS BETWEEN DEPLETED UO_2 PELLETS

The difference between the measured capture rate in a depleted uranium metal foil irradiated between two depleted UO_2 pellets and the actual capture rate in the UO_2 pellets was investigated in this experiment. To determine the capture rate in the UO_2 pellets, 10 mil thick UO_2 wafers were cut from a pellet and then during the irradiation each wafer was sandwiched between two depleted UO_2 pellets. Four wafers and four foils were measured.

The capture data had to be corrected for the self-absorption of the 100 keV gammas and X-rays within

TABLE II-30-V. FOIL EFFECT (ATSR)—CAPTURES IN DEPLETED U-238 FOILS AND WAFERS BETWEEN DEPLETED UO_2 PELLETS

Foil or Wafer	Pellet Condition	Foil or Wafer Weight, g	Rel. Act. Per Gram U-238	Rel. Act. Corrected for Self-Absorption Foil: R.A./(1–1.851 W_F) Wafer: R.A./(1–1.659 W_W)	Percent Difference from Foil with No Gap
F-112	Good	0.1366	8.69	11.63	
F-116	Good	0.1370	8.71	11.67 } 11.96 ± 4.5%	—
F-127	Fair	0.1268	9.77	12.77	
F-130	Bad	0.1372	8.77	11.76 }	
W-D	Good	0.1234	11.95	15.03	
W-E	Fair	0.1337	10.90	14.00 } 14.45 ± 3.0%	+20.8%
W-C	Bad	0.1233	12.03	14.68	
W-F	Bad	0.1305	11.33	14.46 }	

e foil or the wafer. To minimize the difference between the foils and the wafers, the wafers were cut twice as thick as the foils so that each would have approximately the same mass of U-238 per foil or wafer. The self-absorption correction was then performed with the assumption that the capture activity has the same distribution as a function of g/cm² for both foils and wafers. The uncertainty introduced by this assumption into the 20% self-absorption correction is felt to be small.

The results, which are presented in Table II-30-V, indicate a significant difference between the capture rates measured in the metal foils and the UO_2 wafers, for an epithermal spectrum. This is mostly a result of the different self-shielding of the two materials, although to some extent it may contain an error due to improper correction for self-absorption.

F. FOIL EFFECT (ATSR)—FISSIONS IN 93.3% ENRICHED U-235 FOILS AND 16.4% ENRICHED UO_2 WAFERS BETWEEN 16.4% ENRICHED UO_2 PELLETS

The difference between the measured fission rate in an enriched uranium metal foil irradiated between two 16.4% enriched UO_2 pellets and the actual fission rate in the UO_2 pellets was investigated in this experiment. The procedure used was similar to that discussed in the previous section. Four wafers, three foils without stainless steel gaps, and three foils with 2 mil stainless steel gaps were measured, and the results are given in Table II-30-VI.

The difference between the fission rate in the foils and the wafers is very small, which again points out that the problem of self-shielding is much smaller for the U-235 than for the U-238. In this case the results in Table II-30-VI are not corrected for fission fragment transfer. When comparing foil and wafer data it must be remembered that a 93.3% enriched foil will lose more fragments than it gains from the 16.4% enriched UO_2 pellets between which it was sandwiched. On the other hand, the net transfer of fragments between a 16.4% enriched wafer and 16.4% enriched UO_2 pellets should be zero. The magnitude of this transfer was discussed in Section II-D.

III. Measurements in ZPR-6 Assembly 6A

It was necessary to determine if the large gap and foil effects measured for U-238 in the epicadmium neutron spectrum of ATSR would also be present in the fast spectrum of ZPR-6 Assembly 6A. None of the U-235 measurements were repeated, nor were any consistency checks made. The discussion that follows will concern only effects which are different from those observed in the ATSR measurements.

TABLE II-30-VI. FOIL EFFECT (ATSR)—FISSIONS IN 93.3% ENRICHED U-235 FOILS AND 16.4% ENRICHED UO_2 WAFERS BETWEEN 16.4% ENRICHED UO_2 PELLETS

SS Gap, mils	Foil or Wafer	Pellet Condition	Rel. Act. Per Gram U-235		Percent Difference from Foil with No Gap
0	F-603	Good	3.723		
0	F-601	Bad	3.721	3.719 ± 0.1%	—
0	F-605	Bad	3.714		
2	F-602	Fair	3.731		
2	F-604	Bad	3.730	3.760 ± 1.3%	+1.1%
2	F-600	Bad	3.818		
0	W-Y	Good	3.683		
0	W-R	Bad	3.690		
0	W-T	Bad	3.700	3.691 ± 0.2%	−0.8%
0	W-U	Bad	3.692		

A. GAP EFFECT (ZPR-6)—CAPTURES IN DEPLETED U-238 FOILS WITH DIFFERENT THICKNESS STAINLESS STEEL GAPS BETWEEN DEPLETED UO_2 PELLETS

This measurement is similar to the one described in Section II-C. The results presented in Table II-30-VII indicate that the capture rate in U-238 increases with increasing stainless steel gap thickness. However, the effect is considerably smaller in the fast neutron spectrum of ZPR-6 than it was in the epicadmium spectrum of ATSR.

B. GAP EFFECT (ZPR-6)—FISSIONS IN DEPLETED U-238 FOILS WITH DIFFERENT THICKNESS STAINLESS STEEL GAPS BETWEEN DEPLETED UO_2 PELLETS

In this measurement depleted U-238 foils were counted for fissions, whereas in the measurement described in Section II-D, 93.3% enriched U-235 foils were counted for fissions. Otherwise, the two experiments were similar, but the results presented in Table II-30-VIII indicate that the self-shielding in the fast neutron spectrum is a smaller effect than the fission fragment transfer problem. As was mentioned in Section II-D, the introduction of a stainless steel gap prevents fission fragments from being transferred to the foil from the adjacent pellets. The result is a decrease in the fission activity of the foil which is only slightly offset by the decrease in self-shielding with the increase in gap thickness.

C. FOIL EFFECT (ZPR-6)—CAPTURES IN DEPLETED U-238 FOILS AND WAFERS BETWEEN 16.4% ENRICHED UO_2 PELLETS

The captures per gram of U-238 measured in depleted U-238 foils and depleted UO_2 wafers appear to be the

TABLE II-30-VII. GAP EFFECT (ZPR-6)—CAPTURES IN DEPLETED U-238 FOILS WITH DIFFERENT THICKNESS STAINLESS STEEL GAPS BETWEEN DEPLETED UO_2 PELLETS

SS Gap, mils	Foil	Pellet Condition	Foil Weight, g	Rel. Act. Per Gram U-238	Rel. Act. Corrected for Self-Absorption R.A./(1–1.851 W) and Position	Percent Difference from Zero Gap
0	56	Good	0.1350	1.501	3.098 } 3.100	-
0	60	Fair	0.1366	1.518	3 102 }	
5	125	Bad	0.1365	1.509	3.101 3.101	+0.0%
10	65	Good	0.1356	1.579	3.204	
10	58	Fair	0.1348	1.543	3.158 } 3.148	+1.6%
10	118	Bad	0.1367	1.487	3.082	
30	63	Fair	0.1356	1.584	3.229 } 3.234	+4.3%
30	64	Bad	0.1361	1.594	3.238 }	

TABLE II-30-VIII GAP EFFECT (ZPR-6)—FISSIONS IN DEPLETED U-238 FOILS WITH DIFFERENT THICKNESS STAINLESS STEEL GAPS BETWEEN DEPLETED UO_2 PELLETS

SS Gap, mils	Foil	Pellet Condition	Rel. Act. Per Gram U-238 Corrected for Position	Percent Difference from Zero Gap
0	56	Good	2.987 } 3.019	—
0	60	Fair	3.050 }	
5	125	Bad	2.985 2.985	−1.14%
10	65	Good	3.020	
10	58	Fair	2.964 } 2.981	−1.27%
10	118	Bad	2.958	
30	63	Fair	2.977 } 2.994	−0.83%
30	64	Bad	3.011 }	

same within the statistical uncertainty of the data (Table II-30-IX). The measurements were performed in ZPR-6 in a similar manner to the ATSR experiments described in Section II-E. Again it should be mentioned that the self-absorption correction introduces uncertainties which indicate that the close agreement between foil and wafer data is probably fortuitous. However, it is reasonable to expect the results for foils and wafers to agree within a couple of percent. This is based upon the assumption that the difference in the neutron spectrum between ATSR and ZPR-6 will affect the gap and foil measurements to the same extent: The effect of a 30 mil stainless steel gap was sixteen times greater on ATSR than on ZPR-6. If this same ratio were to hold for the difference between foil and wafer activity measured in the ATSR experiment, then the magnitude of the effect in ZPR-6 would be about 1%.

D. FOIL EFFECT (ZPR-6)—FISSIONS IN DEPLETED U-238 FOILS AND WAFERS BETWEEN 16.4% ENRICHED UO_2 PELLETS

The fissions per gram of U-238 measured in depleted U-238 foils and depleted UO_2 wafers also appear to be the same within the statistical uncertainty of the data (Table II-30-X). The experiment was performed in a similar manner to the ATSR measurement described in Section II-F. The one significant difference between the two experiments was that depleted foils were counted for fissions in the ZPR-6 measurement and enriched foils were counted in the ATSR measurement.

TABLE II-30-IX. FOIL EFFECT (ZPR-6)—CAPTURES IN DEPLETED U-238 FOILS AND WAFERS BETWEEN 16.4% ENRICHED UO_2 PELLETS

SS Gap, mils	Foil or Wafer	Pellet Condition	Foil or Wafer Weight, g	Rel. Act. Per Gram U-238	Rel. Act. Corrected for Self-Absorption Foil: R.A./(1–1.851 W_F) Wafer: R.A./(1–1.659 W_W) and Position	Percent Difference from Foil with No Gap
0	F-62	Good	0.1324	1.559	3.139 } 3.124	-
0	F-128	Fair	0.1319	1.539	3.109 }	
2	F-55	Fair	0.1317	1.507	3.061 } 3.075	−1.6%
2	F-117	Fair	0.1323	1.507	3.089 }	
0	W-A	Good	0.1377	1.546	3.102	
0	W-B	Fair	0.1357	1.586	3.125 } 3.125	+0.0%
0	W-G	Fair	0.1342	1.573	3.108 } ± 1.0%	
0	W-H	Fair	0.1358	1.614	3.166 }	

TABLE II-30-X. FOIL EFFECT (ZPR-6)—FISSIONS IN DEPLETED U-238 FOILS AND WAFERS BETWEEN 16.4% ENRICHED UO_2 PELLETS

SS Gap, mils	Foil or Wafer	Pellet Condition	Rel. Act. Per Gram U-238 Corrected for Position	Percent Difference from Foil with No Gap
0	F-62	Good	3.356 } 3.339	—
0	F-128	Fair	3.322 }	
2	F-55	Fair	3.096 } 3.070	−8.1%
2	F-117	Fair	3.043 }	
0	W-A	Good	3.379	
0	W-B	Fair	3.443	
0	W-G	Fair	3.357 } 3.389 ± 1.0%	+1.5%
0	W-H	Fair	3.377	

In the case of the ZPR-6 experiment this had the effect of amplifying the fission fragment transfer problem. This is observed when the fission count in the foil irradiated without a gap is compared to that of the foil irradiated with a 2 mil stainless steel gap. The large decrease in measured fission when the stainless steel is inserted results from the prevention of fragment transfer from the 16.4% enriched pellets. Because the fission rate in the U-235 was about thirty-five times greater than that in the U-238 it is to be expected that the transfer rate would be about eight times greater for the 16.4% enriched pellets than for the depleted pellets. This is the magnitude that is observed when the results of this measurement are compared with those discussed in Section III-B.

IV. Conclusions

Although the effects of stainless steel gaps and metal foils on the measured activities were in some cases appreciable in the epithermal spectrum of ATSR, in the harder spectrum of ZPR-6 Assembly 6A the effects were much smaller. It is concluded that in large oxide critical assemblies having the approximate neutron energy spectrum of ZPR-6 Assembly 6A, the effect of stainless steel gaps between foil and fuel in the oxide rods can be corrected by using the results in Tables II-30-VII and II-30-VIII. It is also concluded that metallic foils can be used to determine the reaction rates in oxide fuel elements. The uncertainty associated with the measured values for these effects in neutron energy spectra typical of ZPR-6 Assembly 6A is about 2% of the total activity in the case of captures and less in the case of fissions.

For these reasons, future measurements in oxide fuel pin-sodium calandria zones will be done with metallic foils. In addition the measurements will be carried out with clad plutonium foils between the ends of special fuel pins, for radiological safety reasons. The results of these measurements will be corrected for the small stainless steel gap effect.

References

1. K. E. Plumlee and M. T. Wiggins, *Automatic Foil Activity Counting Facility and Data Reduction Program*, ANL-6628 (1962).
2. G. S. Stanford, *The Codes NURF, COMBO and TWO-SOURCE*, ANL-7356 (1967).

II-31. Measurement of the Fission Yields of Mo-99 and Ba-140 from Pu-239 in Fast Neutron Spectra

R. J. Armani, Raymond Gold, R. P. Larsen* and J. H. Roberts†

Introduction

Precise fission product yields are important in many applied and basic nuclear fields. They are used in reactor physics to determine burn-up of nuclear fuels and in reactor physics calculations. Fission product yields produced in the fission of U-235 and Pu-239 by thermal neutrons are accurately known.[1] More recently, there has been a particular need in fast reactor physics for accurate fission yield data. Accurate data are scarce because of the difficulties in obtaining information on fission produced by fast neutrons. With the development of the solid state track recorder (SSTR) method for precise fission rate measurements,[2] a simple direct method for measuring fast fission yields is possible.

In this experiment[3] mica SSTRs are used to measure absolute fission rates per gram of Pu-239. The activity of Mo-99 and Ba-140 fission products produced during the experiments was determined by the radiochemical separation of Mo-99 from a plutonium target followed by beta counting, and by the direct counting of the La-140 gamma ray peak in order to determine the Ba-140 activity.

The SSTR method is particularly useful to determine the absolute yield of specific fission products without requiring high neutron fluences. Once the absolute yield of these standard fission product isotopes (for a given neutron induced fission reaction and given neutron spectrum) have been determined with high precision, other fission product yields can be measured relative to these. Other methods of measuring fission product yields are discussed in the literature.[4]

Exposure Conditions

The fission yields of Mo-99 and Ba-140 from $Pu^{239}(n,f)$ have been measured in the fast neutron spectrum of ZPR-3[5] Assembly 57.[6] Assembly 57 has

* Chemical Engineering Division, Argonne National Laboratory.
† Macalester College, St. Paul, Minnesota

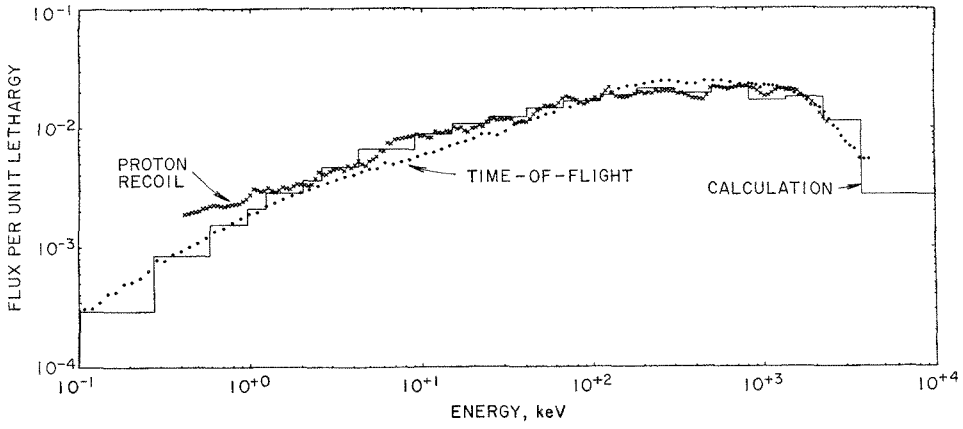

FIG. II-31-1. Comparison of Results of Proton-Recoil, Time-of-Flight, and Calculated Spectra. *ANL-ID-103-2922 Rev. 1.*

TABLE II-31-I. Pu-239 MASSES

Sample No.	C/min-Bkgd	Disint. per min	Mass in ng [a]
1	241.84 ± 0.62	467.24 ± 1.52	3.427 ± 0.013
2	167.22 ± 0.33	323.07 ± 0.91	2.370 ± 0.008
3	166.84 ± 0.33	322.34 ± 0.90	2.364 ± 0.008
4	167.021 ± 0.52	322.68 ± 1.19	2.367 ± 0.010
5	165.55 ± 0.51	319.84 ± 1.18	2.346 ± 0.010
6	165.43 ± 0.54	319.61 ± 1.22	2.344 ± 0.010
7	79.20 ± 0.23	153.01 ± 0.54	1.122 ± 0.005

[a] Counter efficiency = 0.5176 ± 0.0015. Specific activity = 136.33 ± 0.27 disintegrations per min per ng.

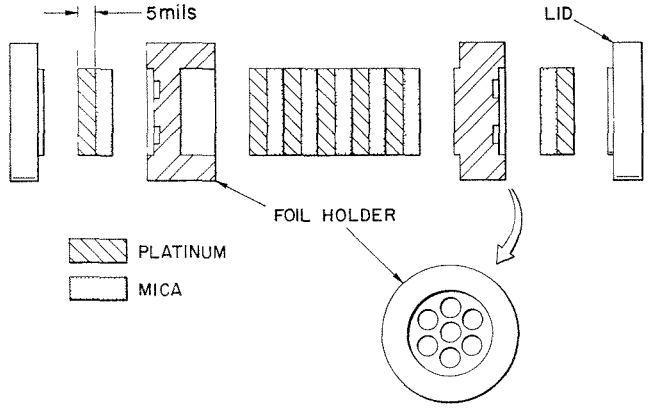

FIG. II-31-2. Irradiation Capsule. *ANL Neg. No. 116-473.*

the same core composition and configuration as the Gulf General Atomics STSF-1A.[7] The neutron energy spectrum of this core has been measured by the recoil proportional counter method at Argonne and by the time-of-flight method at Gulf General Atomic.[8] Figure II-31-1 shows a comparison of proton-recoil and time-of-flight measurements with the calculated spectrum. The irradiation to determine the fission yields was made near the center of the core.

IRRADIATION PACKAGE

The SSTRs used in this experiment were selected samples of muscovite mica ranging in thickness from 50 to 100 μm. The mica was pre-etched in 49% hydrofluoric acid for six hours to develop the "fossil" fission tracks; samples were selected on the basis of clarity and low "fossil" count. Discs $^{15}/_{16}$ in. in diam were punched to determine the fission rate. After exposure to fission fragments the mica was re-etched in 49% hydrofluoric acid for 90 min and counted as described by Gold et al.[2]

The plutonium sources used in this experiment were prepared from Pu-239 of very high isotopic purity. The isotopic analysis indicated a purity of 99.99% Pu-239 with total impurities 8 ppm. Sources prepared on platinum planchets $^{15}/_{16}$ in. in diam and 0.005 in. thick had masses ranging from 1 to about 3.5 ng of plutonium (see Table II-31-I). The masses were determined by absolute alpha counting with a 2π flow counter having an efficiency of 0.5176 ± 0.0015 for a thin source. A half life of (2.445 ± 0.005) × 10^4 years[9] for Pu-239 was used in the mass determination.

For the measurements of the Mo-99 and Ba-140 production thin metallic plutonium target samples were used. In order to machine and roll the metal readily, an alloy consisting of about 98% plutonium—the balance consisting of aluminum, oxygen and other minor impurities—was used. The alloy was rolled to a thickness of 0.005 in. and discs 0.125 in. in diam were punched from this. This produced samples of the order of 10 mg of Pu-239.

The fission sources, mica SSTR, and target samples were assembled into a package suited for this experiment. Figure II-31-2 gives an exploded view of the irradiation assembly. Five fission sources in good contact with mica are placed in the central cavity. Seven fission product target foils are placed on each side of

he cavity, making a total of 14 foils. Finally, a fission ource with mica SSTR is placed over the target samples on either side of the package. This arrangement will account for any neutron flux perturbation within the irradiation assembly. The entire assembly is held together with aluminum screws and presents a package 1.50 in. in diam and 0.25 in. thick.

The reactor was operated for about 80 min for an integrated exposure of 4 kWh. The exposure was adjusted to give about 20,000 tracks on each mica SSTR.

Experimental Results

The results of the track counting in the mica are shown in Table II-31-II. The data of sample No. 2 were rejected; apparently the Pu-239 did not make good contact with the mica in this sample. The tracks on each mica disc were counted three times by three different scanners. The result from the six samples used is 9131.67 ± 34.00 tracks per ng of Pu-239. Using the optical efficiency of mica (0.948 ± 0.0053) tracks per fission[2] yields (9.63 ± 0.06) × 10^{12} fissions per g of Pu-239.

The activity of the Mo-99 separated from the plutonium targets was measured to be (1.140 ± 0.007) × 10^8 disintegrations per sec per g of Pu-239 corrected to saturation. Similarly, the Ba-140 activity was determined to be (9.817 ± 0.113) × 10^7 per sec per g of Pu-239. The effective irradiation time for the exposure was determined to be 4900 sec. The number of atoms of Mo-99 formed per gram of irradiated Pu-239 is thus $A_s t$, where A_s is the saturated activity per sec per g of Pu-239 and t is the effective irradiation time. If we divide $A_s t$ by the number of fissions per gram of irradiated Pu-239 we have the fission yield. The result for Mo-99 is (5.80 ± 0.05)%, and for Ba-140 is (5.00 ± 0.06)%.

TABLE II-31-II. Mica SSTR Fission Track Data

Sample	Observer	Total Tracks	Source Mass, ng	Average Tracks per ng
1	A	31,386	3.247 ± 0.013	9163.31 ± 45.94
	B	31,544		
	C	31,278		
2	A	19,258	2.370 ± 0.008	8146.41 ± 44.00
	B	19,204		
	C	19,458		
3	A	21,597	2.364 ± 0.008	9145.09 ± 47.68
	B	21,263		
	C	21,997		
4	A	21,626	2.367 ± 0.010	9162.09 ± 52.57
	B	21,664		
	C	21,770		
5	A	21,550	2.346 ± 0.010	9237.43 ± 52.88
	B	21,867		
	C	21,596		
6	A	21,088	2.344 ± 0.010	9022.18 ± 52.87
	B	21,129		
	C	21,227		
7	A	10,153	1.122 ± 0.005	9008.62 ± 63.46
	B	10,038		
	C	10,132		

TABLE II-31-III. Mo-99 and Ba-140 Fast Fission Yield Measurements

Investigators	Year	Mo-99 Yield	Ba-140 Yield
Steinberg and Freedman[10]	1951	5.94 ± 0.12[a]	5.04 ± 0.07[a]
Petrzhak et al.[11]	1960	5.5 ± 0.4	4.9 ± 0.4
Bonyushkin et al.[12]	1961	5.9 ± 0.6	5.4 ± 0.5
Schwartz[13]	1967	6.11 ± 0.37	
Present work	1969	5.80 ± 0.05	5.00 ± 0.08

[a] Quoted error is standard error resulting from three measurements.

Conclusions

A new low-fluence method for the precision measurement of fission product has been established. It has been used to measure the yields of Mo-99 and Ba-140 from $Pu^{239}(n,f)$ induced by fast neutrons with an absolute accuracy of 0.9 and 1.3%, respectively.

Earlier fast fission yield measurements have been carried out with "fission spectrum" neutrons. The present results are compared with these earlier measurements in Table II-31-III.

References

1. M. E. Meek and B. F. Rider, *Summary of Fission Product Yields for U-235, U-238, Pu-239, and Pu-241*, APED-5398 (1968).
2. R. Gold, R. J. Armani and J. H. Roberts, *Absolute Fission Rate Measurements with Solid State Track Recorders*, Nucl. Sci. Eng. **34**, 13–32 (1968).
3. R. J. Armani, R. Gold, R. P. Larsen and J. H. Roberts, *Measured Fission Yields of Mo-99 and Ba-140 in Fast Neutron-Induced Fission of Pu-239*, Trans. Am. Nucl. Soc. **13**(1), 90 (1970).
4. F. L. Lisman et al., *Burnup Determination of Nuclear Fuels*, IN-1277 (1969).
5. B. C. Cerutti, H. V. Lichtenberger, D. Okrent, R. E. Rice and F. W. Thalgott, *ZPR-3, Argonne's Fast Critical Facility*, Nucl. Sci. Eng. **1**, 126 (1956).
6. Reactor Development Program Progress Report, ANL-7581, 8 (1969).

7. C. A. Preskitt et al., *Fast Reactor Spectrum Measurement*, Gulf General Atomics Quarterly Progress Report, GA-9027 (October 7, 1968).
8. J. W. Powell, *Comparison of Proton-recoil Proportional Counter and Time-of-Flight Neutron Spectrum Measurements in a U-235 Fueled Fast Reactor*, Trans. Am. Nucl. Soc. **12**(2), 712 (1969).
9. Ia. P. Dokuchev, *The Specific α-Activity of Pu-239 and Pu-240*, J. Nucl. Energy A **11**, 195 (1960).
10. E. P. Steinberg and M. S. Freedman, *Summary of Results of Fission-Yield Experiments, Radiochemical Studies: The Fission Products*, C. D. Coryell and N. Sugarman, Eds. (McGraw-Hill Book Company, Inc., New York, 1961) Book 3, pp. 1378–1390.
11. K. A Petrzhak et al., *Yields of a Number of Fission Products in the Fission of Uranium-235, Uranium-238, and Plutonium-239 by Neutrons*, AEC-TR-4696 (1961).
12. E. K. Bonyushkin et al., *Fragment Yield in the Fission of U-233 and Pu-239 by Fast Neutrons*, At. Energy, USSR, **10**, 13 (1961).
13. L. L. Schwartz, Data quoted from UCRL-50243, *The Fission Product Decay Chains* (^{239}*Pu With Fission Spectrum Neutrons*), Edward H. Fleming, Jr., Ed., Vol. I, pp. 1–3 (March 31, 1967).

II-32. Reactivity Effects in Critical Facilities Due to Fissile Isotope Decay

R. G. Matlock, R. E. Kaiser and J. M. Gasidlo

A figure of merit for a critical facility such as ZPPR is the inherent ability to reproduce configurations and to measure reactivity accurately.

During the period of initial startup of ZPPR, a number of experiments were performed to measure the reproducibility of system criticality upon half closure. Measurements made during a one- or two-day period proved satisfactory. However, as time progressed beyond this, it became apparent that there was a consistent reactivity loss with time. Subsequent investigations attributed the loss to radioactive decay of the fissionable isotope Pu-241 (13 year half-life), present in small quantities (~1.6 w/o) in the ZPPR fuel alloy. This effect has also been used to explain, in part, a similar reactivity loss observed over a three-month period in ZPR-3.

Subsequent examination of data obtained in recent cores on ZPR-3 and ZPPR has provided reference-core criticality measurements, spaced over an interval of several weeks each, on ZPR-3 Assemblies 51 and 56B and on FTR Cores 1 and 2 in ZPPR, all of which were part of the FTR Critical Program.

TABLE II-32-I. Total Worths of Pu-241 and Am-241 in ZPPR and ZPR-3 Assemblies

Assembly	Worth of Pu-241 $\left(\frac{\delta k}{k}\right)$, 10^{-4}		Worth of Am-241 $\left(\frac{\delta k}{k}\right)$, 10^{-6}	
	2.5×10^{17} atoms/cm^3	5.0×10^{17} atoms/cm^3	2.5×10^{17} atoms/cm^3	5.0×10^{17} atoms/cm^3
ZPR-3, 51	1.13	2.26	−3.00	−6.00
ZPR-3, 56B	1.46	2.91	−3.40	−6.80
ZPPR-FTR 1	1.54	3.08	−1.77	−3.54
Demonstration Plant	3.11	6.21	−1.55	−3.10

The analyses of the worths of Pu-241 and Am-241 in the particular cores studied were performed with one-dimensional diffusion theory. Cross sections for the Am-241 were obtained from the ENDF/B library, averaged over a typical FTR spectrum, and added to an existing cross section library set that had previously been prepared for analysis of the Phase B FTR cores. The actual worth calculations were then performed using one-dimensional diffusion and perturbation calculations as performed by the MACH-1 code.[1] The results of these calculations are provided in Table II-32-I.

The contribution of the Am-241 buildup to the total reactivity effect proved to be negative, and constituted only 1 to 3% of the total effect. The loss of Pu-241 thus contributed 97 to 99% of the total effect.

The results of the calculations for ZPR-3 Assembly 51 indicate that the downward trend in the excess reactivity of the reference core can be explained in large part by the loss of Pu-241 and the associated buildup of Am-241. Experimental errors on the measurements are based on the standard deviation of two or more reference core criticality measurements taken on the same or successive days. Figure II-32-1 compares experimental and calculated data for ZPR-3 Assembly 51.

The data for Assembly 51, obtained from mid-December through February, are much better than those obtained from Assembly 56B. The Assembly 56B data were taken between the end of January and early April, at a time when outside weather was becoming warmer. This would have an effect on ZPR-3 reactor

temperature because cell air can be heated but not cooled. Such a temperature drift was indeed observed in outer core regions and in the reflector. Additional heating of the air in the reactor cell causes an additional small reactivity loss due to the negative temperature coefficient of the reactor, thereby explaining the large discrepancy in the data obtained at about 60 days compared with the data obtained in the initial measurement. Figure II-32-2 compares experimental and calculated data for ZPR-3 Assembly 56.

The FTR-2 data from ZPPR were not susceptible to weather considerations, as described above, because the temperature of the ZPPR cell is held constant to within $\pm 1/4$°F regardless of the outside temperature. The data from FTR-2, taken over a 26-day period, show a good correlation between calculated and measured effects. The reactor was shut down for 28 days during August 1969 for cell isolation tests. Reference measurements made before and after this interval indicated a loss of 7.9 ± 0.7 Ih. The calculated loss over this period is about 6.6 Ih, which accounts for almost all of the measured loss. Figure II-32-3 compares experimental and calculated data for ZPPR Assembly 1.

The rate at which reactivity is lost depends primarily on the amount of Pu-241 present in the fuel. In the FTR cores on ZPPR, the Pu-241 was 1 to 2 w/o of the total plutonium present (Pu-240 is 11.5 w/o). The calculated rate of reactivity loss in this case was 0.234 Ih/day. While this would not normally be an important consideration, some reactivity measurements which require considerable time to perform could show the effects of a reactivity change of 0.1 to 0.15 Ih during the experiment. Sodium voiding experiments, which involve loading changes between measurements, could encounter problems due to the Pu-241 decay losses.

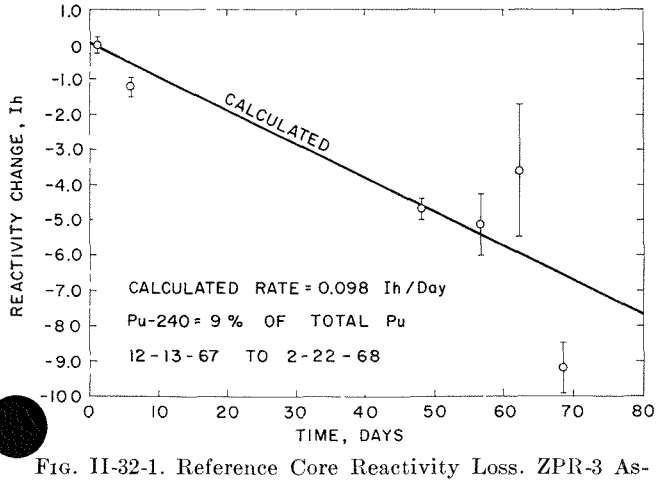

FIG. II-32-1. Reference Core Reactivity Loss. ZPR-3 Assembly 51. *ANL Neg. No. 116-225.*

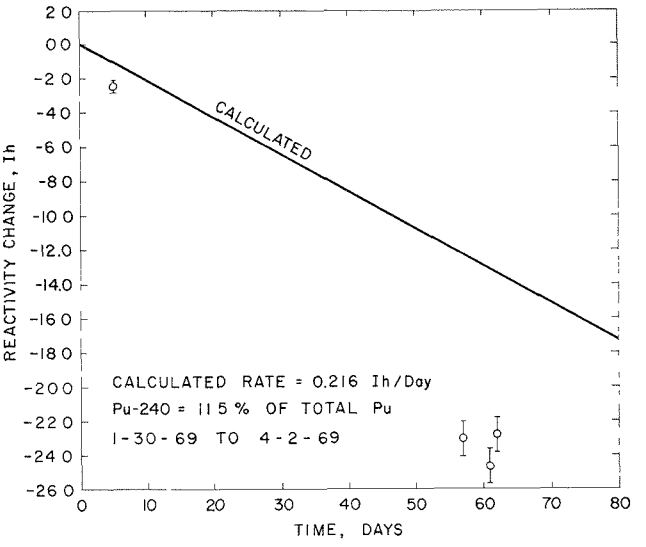

FIG. II-32-2. Reference Core Reactivity Loss, ZPR-3 Assembly 56B. *ANL Neg. No. 116-224.*

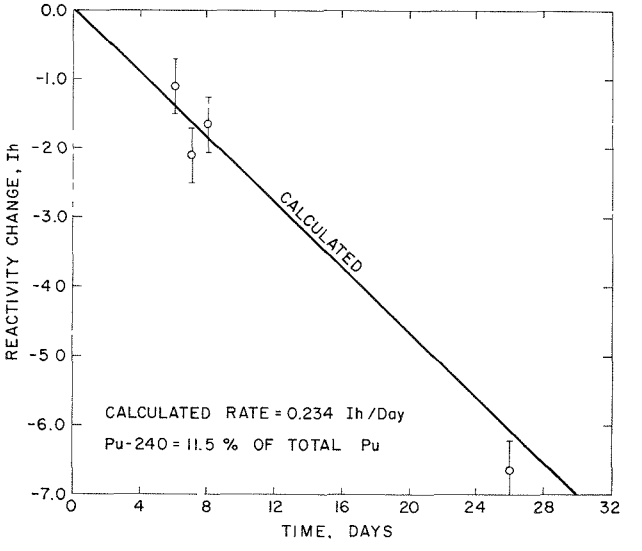

FIG. II-32-3. Reference Core Reactivity Loss, ZPPR Assembly 1. *ANL Neg. No. 116-227.*

Calculations of the effect in a power reactor indicate that for demonstration plant sizes, assumed to have a power level of at least 750 MWt, the production of Pu-241 by capture in Pu-240 balances the decay loss and essentially no loss of Pu-241 occurs. However, if there were no decay problem one would anticipate some buildup of Pu-241 in the core. This potential gain in reactivity is almost completely lost due to the Pu-241 decay.

In conclusion, the effects of decay of Pu-241 in critical facilities can be severe for experiments which require references widely spaced in time. The effect in a power reactor is simply to compensate for the buildup

of Pu-241 through capture in Pu-240. A recommended procedure for plutonium-fueled critical facilities is to repeat measurements on the reference core once or twice a week to provide sufficient data to determine an accurate experimental value of reactivity loss due to fissile isotope decay. Calculations can be performed but must be regarded as somewhat uncertain because the cross sections for such elements as Pu-241 and Am-241 are not accurately known.

Reference

1. D. A. Meneley, L. C. Kvitek and D. M. O'Shea, *MACH-1, A One-Dimensional Diffusion Theory Package*, ANL-7223 (1966).

II-33. A Postanalytical Study of Eight *ZPR-3* Benchmark Criticals Using *ENDF/B* Data

A. L. Hess, R. G. Palmer and J. M. Stevenson*

Introduction

The plutonium-fueled assemblies which have been constructed on ZPR-3 include a series of eight, simple core-blanket physics studies ranging in size from 90 to 450 liters. In order of construction, these were Assemblies No. 48, 48B, 49, 50, 53, 54, 58 and 59. A program of postanalyses has been underway on these systems using cross sections based on Version I of ENDF/B (1968 edition) and the ARC System adapted to the Idaho IBM 360/75 computer. The program includes investigation of the effect of heterogeneity on eigenvalues, on central fission ratios, and on material worths. Also, the studies include comparative calculations with 1-D and 2-D codes to establish simple models for future calculations. Although the basic data file used will be superseded by revisions in progress, these studies form the groundwork in establishing analytical techniques to be used in data testing of the 1970 edition of ENDF/B (Version II).

Models for criticality calculations were derived from the as-built, heterogeneous-structure, critical configurations. Cylindrical models for two-dimensional analysis used the actual axial lengths and average core radii of the assemblies, with only minor adjustments for smoothing the radial boundaries, for the excess reactivity of the control rods and for the interface effect. The studies of the heterogeneity effects were carried out with one-dimensional analysis, and spherical models of the assemblies for this purpose were obtained from the as-built core volumes and approximate shape factors.

Methods of Analysis

Figure II-33-1 charts the course of the analyses with the ARC System starting with the generation of multigroup cross sections using MC^2. The MC^2 problems were run in the ultrafine mode under the consistent B_1 option. Fine-group widths of ¼ lethargy units were specified, and the output broad-group structure contained 30 groups (½-lethargy widths through Group 26, then widths of 1, 1, and 2, with the 30th group representing the thermal range).

Each of the different fuel-cell arrangements used in the construction of the assemblies required several runs of MC^2 cross sections. The first MC^2 problem for each type of cell was run in the homogeneous mode: that is, the input composition was that of the average core cell and the resonance shielding of the heavy isotopes was carried out according to a homogeneous dispersion of all the materials. Then, for each of the different types of fuel or fertile plates, one additional MC^2 problem was run in the heterogeneous mode to obtain cross sections for the plate constituents with the resonance shielding according to the plate makeup and its surroundings of diluent. The combination of MC^2 problems for each case thus gave cross sections for the resonance isotopes which were both homogeneously and heterogeneously shielded.

Separate MC^2 problems were run to obtain blanket cross sections. For each uranium-blanketed core, an MC^2 problem was run which provided resonance shielding for the uranium isotopes according to the uranium concentration in the blanket, but which used an ultrafine weighting spectrum similar to the core spectrum. For Assembly 54, a zero-buckling MC^2 calculation was used to obtain cross sections for the steel reflector materials. A cross-section set for lead, to be used in the Assembly 59 calculations (reflector of lead), was adopted from the PHROG library since the ENDF/B file does not include lead.

The next phase of the procedure was to obtain a spatial weighting of the cross sections over the width

* UKAEA, Winfrith, Dorchester, Dorset, England.

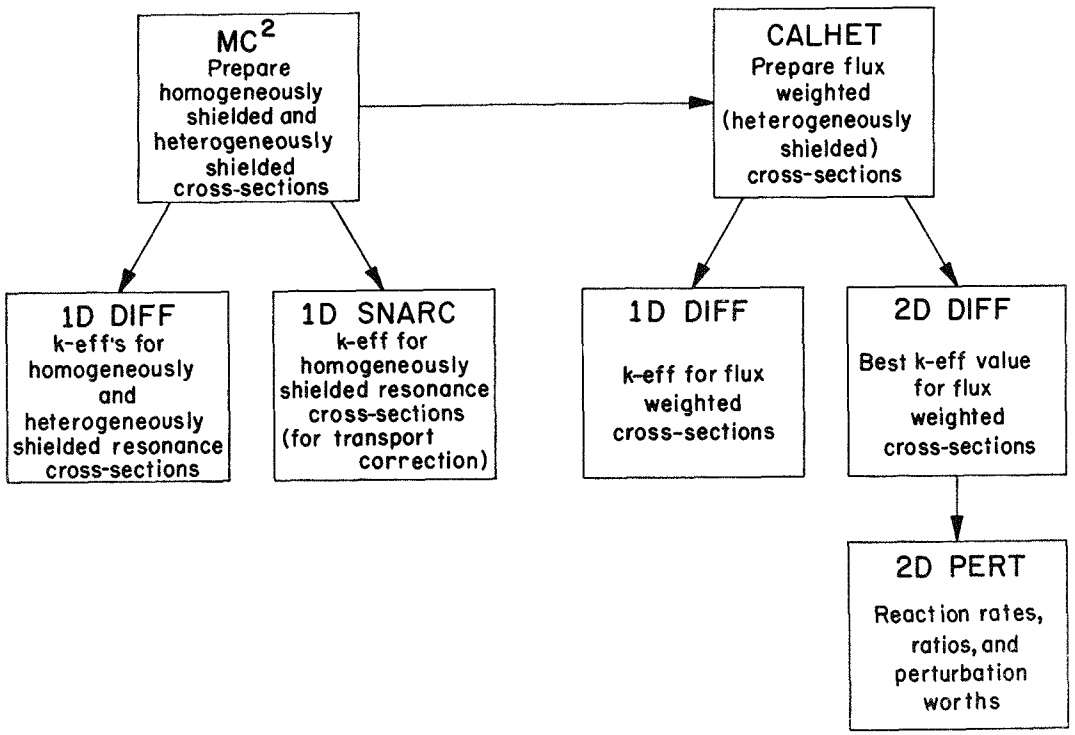

FIG. II-33-1. Calculation Flow Chart ARC System. *ANL-ID-103-A2096*

of the core cells. This is to provide reaction rates in k calculations which reflect the multiplication in the fuel plates; that is, the flux advantage/disadvantage effects. The code CALHET-2 was used for this purpose. CALHET calculates intercell, multigroup flux distributions using a collision probability formulation of the neutron-balance equations in slab geometry, a formulation based on integral transport theory. Twenty slab regions are allowed in CALHET, and each of the core cells studied was described in the inputs to the code as a 20-region representation, using two or three regions for the fuel plates. The cross section input for the fuel and fertile isotope regions were the appropriate resonance-shielded cross sections from the heterogeneous-MC^2 calculations. For the non-resonance materials, the inputs to CALHET were cross sections from the homogeneous MC^2 case. In addition to a Δk for flux advantage calculated by perturbation theory, CALHET outputs cross sections for each input cross section. The outputs have been averaged over the cell using the regionwise, real flux distributions. The next step of the analyses is the diffusion theory calculations using the spherical model and three different cross section sets: homogeneous-MC^2, heterogeneous-MC^2, and CALHET-weighted cross sections. The differences in k between cases thus gave the reactivity effects of heterogeneity. Transport corrections were obtained from SNARC calculations (S_8) for the spherical model using homogeneously shielded cross sections in the core.

Toward the end of the path in Fig. II-33-1 are the 2-D diffusion calculations which, upon adding the transport corrections, give the final k values from this study. The cross sections used in the core in these cylindrical models are the cell-averaged output from CALHET and thus account for both the resonance self-shielding and the fuel-multiplication effects of heterogeneity.

The real and adjoint fluxes from the 2-D diffusion problems also constitute the input for the final stage of analysis, namely calculations of central fission ratios, central worths of materials, and the effective delayed neutron parameters. The spectra thus more appropriately represent the environment of the cell-plate structure around the material-worth samples and the fission chambers. However, the cross sections used for the sample materials and fission-chamber platings were taken from the homogeneous MC^2 problems to provide average resonance shielding representing the sample or fissile-foil material uniformily dispersed in minute concentration across the core cell. For the non-core-constituent materials (U-233, U-234, tantalum, etc.) infinitesmal concentrations were specified in the homogeneous MC^2 input to provide infinite-dilution cross sections averaged with the homogeneous ultrafine spectrum.

The majority of the analytical program outlined above was completed during the year, and the results which have been obtained are presented below.

TABLE II-33-I. Effects of Heterogeneous Shielding of Resonances in Fuel and Fertile Plates

Assembly	k_{eff}, Calculated for Spherical Model by Diffusion Theory		Resonance Shielding Effect, % k
	With Homogeneously Shielded Resonances	With Heterogeneously Shielded Resonances	
48	0.9690	0.9746	0.56
48B	0.9694		
49	0.9631	0.9663	0 32
50	0.9707	0.9798	0.91
53	0.9884	1.0050	1.66
54	0.9517	0.9704	1.87
58	1.0027	1.0038	0.11
59	0.9712	0.9738	0.26

TABLE II-33-II. Effects of Spatial-Flux Weighting of Cross Sections and Total Heterogeneity Effect

Assembly	CALHET Cell Results (Input σ's From Het. MC²), % k	Diffusion Theory k for Sphere Using Flux-Weighted σ's (CALHET Output)	Cell-Flux Weighting Effect, % k	Combined Heterogeneity Effect, Reson. Shld. + Flux Wtg., % k
48	1.34	0.9885	1.39	1.95%
48B	1.28 (Inner Cell)	0.9891	—	1.97
49	1.07	0.9766	1.03	1 35
50	1.52	0.9949	1.51	2.42
53	1.46	1.0190	1.40	3.06
54	- -	0.9848	1.58	3.45
58	1.86	1.0191	1.53	1.64
59	—	0.9898	1.60	1.86

Effects of Heterogeneity on Calculated k_{eff}

Table II-33-I compares the k_{eff} values given by the spherical diffusion-theory calculations using core cross sections from the homogeneous and heterogeneous MC² problems. The differences obtained thus represent the low-energy heterogeneity effect due to the increased self-shielding of resonances in the cell-plate structure as compared with a homogeneous mixture. For cores containing U-238, the trend is toward increasing resonance-shielding effect with increasing spectral degradation. It was somewhat surprising to obtain a positive, yet small, effect for the Assembly 58 and 59 cores; however, the result is consistent with the change in buckling found between the homogeneous and heterogeneous MC² cases for the Assembly 58 cell. It appears that the lack of U-238 and the reduced fraction of Pu-240 in Assemblies 58 and 59 compared with the previous cores has the effect of reducing the high energy adjoint to the point where the adjoint in the fission spectrum range is less than in the energy range where resonance absorption occurs.

The effects of heterogeneity in the high-energy range are presented in Table II-33-II. The second column of the table lists the heterogeneity advantage as calculated for the cells by the CALHET Code; its inclusion here serves only as a check on the reasonableness of reactivity changes from the diffusion theory calculation using the CALHET-output cross sections. The k_{eff} values given by the CALHET cross sections (Column 3 of Table II-33-II) are not the best diffusion theory results from this study since the spherical models used were in most cases only approximately correct.

The total effect of heterogeneity, the combination of resonance shielding and fuel-plate multiplication, are given in the last column of Table II-33-II. In general, these results are about 0.4% $\Delta k/k$ higher than heterogeneity corrections which have been derived in the past, possibly due to the different effects given by CALHET as opposed to discrete-ordinate slab calculations for cell-flux distributions.

Effects of Heterogeneity on Calculated Fission Ratios

The effect of the cell heterogeneity upon the spectrum was studied by comparing fission ratios derived for the different spectra from the spherical diffusion-theory calculations using the homogeneous MC² cross sections, the heterogeneous MC² cross sections, and the CALHET-weighted cross sections. Table II-33-III gives the total heterogeneity effect on the U-238/U-235 fission ratios, the difference in ratios obtained with the homogeneous-core spectrum and the spectrum obtained with CALHET-weighted cross sections (which include heterogeneous resonance shielding and cell spa-

TABLE II-33-III. Effects of Heterogeneity on Calculated U-238/U-235 Fission Ratios

Assembly	Calculated Ratio in Homogeneous Spectrum[a]	Calculated Ratio in Heterogeneous Spectrum[b]	Effect, %
48	0.03057	0.02889	−5.5
48B	0.02909	0.02767	−4.9
49	0.03356	0.03265	−2.7
50	0.02681	0.02425	−9.5
53	0.02725	0.02458	−9.8
54	0.02629	0.02368	−9.9
58	0.03313	0.02926	−11.7
59	0.03385	0.02952	−12.8

[a] Spectrum at center of core from spherical diffusion-theory calculation using cross sections from homogeneous MC².

[b] Spectrum at center of core from spherical diffusion-theory calculation using CALHET-weighted cross sections.

tial-flux weighting). Using core cross sections from the heterogeneous MC² (with only the resonance-shielding heterogeneity effect accounted for) gave ratios approximately midway between the values in Columns 2 and 3 in Table II-33-III; this indicates that the total effect from heterogeneity in the last column is about half due to resonance shielding and half due to spatial-flux weighting.

The heterogeneity effects for the other threshold-isotope fission ratios (for U-234, U-236 and Pu-240) were almost identical to that indicated above for the U-238/U-235 ratio. Little effect was found for the Pu-239/U-235 and U-233/U-235 fission ratios; at most the differences in ratios for these isotopes using homogeneous and CALHET-weighted spectra were about 2%.

Transport Corrections and Two-Dimensional Diffusion-Theory Calculations

Table II-33-IV lists the transport corrections for the eight assemblies, in each case determined as the difference in k_{eff} between an S_8 transport-theory calculation and a diffusion-theory calculation on a spherical model. Of particular interest are the high values for the light metal-reflected systems, Assemblies 54 and 59; the small size and relatively large leakage component for each of these two systems may require that only transport-theory calculations be acceptable for benchmark-testing purposes for these cases.

Also listed in Table II-33-IV are the k_{eff} values given by the two-dimensional diffusion-theory calculations in cylindrical geometry. Adding the transport corrections gives the final k_{eff} values using ENDF/B-68-based cross sections on the assembly models used. However, a few cautionary notes are needed on these values: 1) for the uranium-blanket cores (where multigroup cross sections for the blanket were averaged with the core ultrafine spectrum), there may be up to about +0.6% k effect or uncertainty due to the blanket cross section treatment, 2) for Assembly 54, the zero-buckling-MC² cross sections are probably over-shielded and not properly representative of average cross sections for the spectrum in the vicinity of the core-reflector boundary, and therefore upwards to 4% k uncertainty may be inherent in the method, 3) the R-Z models used for Assemblies 54 and 59 had no corrections for irregular core outline. Both of these assemblies had somewhat square cross sectional loading patterns for the core, and using the equivalent-area radii probably gave models on the order of +0.5% k too reactive.

Conclusions

The results of the analyses to date on the eight ZPR-3 plutonium benchmark systems indicate a value of k too high for the softer spectrum systems —Assembly 53 and on. It is known that the α for Pu-239 is too low in the ENDF/B Version I. Correction would qualitatively improve the calculated k. The larger correction factors for core edge irregularities and transport effects, in the small assemblies, means that sophisticated analysis is required to use them as reliable benchmark tests of cross sections.

TABLE II-33-IV. Transport Theory Corrections and 2D Diffusion Calculations

Assembly	Transport Correction (1D-SNARG versus 1D-Diffusion), % $\Delta k/k$	k_{eff} from R-Z Diffusion Calculation Using CALHET-Weighted Core Cross Sections	Final k_{eff}, 2D Diffusion Result + Transport Correction
48	0 72	0.9884	0.9956
48B	0.70	0.9895	0.9965
49	0.76	0.9795	0.9871
50	0.65	0 9936	1.0001
53	0.99	1.0127	1.0226
54	3.07	1.0005	1.0312
58	1.53	1.0148	1.0301
59	4.26	1.0078	1.0504

II-34. A Study of Methods of Cross Section Error Identification Utilizing Integral Data from Fast Critical Assemblies

K. O. Ott,* R. B. Pond and J. M. Kallfelz†

As a result of inaccuracies in nuclear data, predictions of integral quantities for reactor design and performance may be significantly in error. The inaccuracies of predictions are revealed in comparisons with corresponding results of integral experiments in critical facilities. There is no doubt that the deviations between theoretical and experimental results contain "information". There is, however, considerable disagreement of how to utilize

* Purdue University, Lafayette, Indiana.
† Georgia Institute of Technology, Atlanta, Georgia.

this information. The various positions of investigators reach from a generally negative attitude about data adjustment on the one side to an optimistic attitude on the other side. Two opposing positions are:

(1) Integral experiments should be used merely for checking theoretical predictions and for finding indications of combined inaccuracies which are caused by nuclear data as well as other sources of errors.[1]

(2) Deviations between calculated and measured integral quantities should be utilized to adjust microscopic data, including their energy dependence as described, for example, by group constant sets with 16–33 groups[2-4] or 2000 groups.[5]

A number of other possibilities lying between these two opposite positions have been investigated or proposed:

(3) the use of all criticality measurements as a basis for an extensive interpolation procedure to find the criticality of other compositions[6]

(4) adjustment of group constant sets with a smaller number of groups (e.g., 4–5 groups)[7,8]

(5) adjustment of integral reaction rates in two or three typical neutron spectra.[9]

The list of intermediate positions, together with corresponding arguments and investigations, shows that the general status of the area of "utilization of results of integral experiments to improve theoretical predictions of reactor parameters" may be described as follows:

(1) there is no generally accepted philosophy or approach

(2) there is no generally accepted adjustment procedure

(3) there is no general agreement about the physical significance of specific adjustments

(4) there is no general agreement about the possibility of improving predictions of integral parameters by using sets of adjusted group constants.

The importance of this controversial problem warranted an in-depth investigation of the possibilities and limits of data adjustment.

The present investigation is carried out as a theoretical simulation of a complete adjustment procedure. The results and errors of the integral experiments are simulated as are also the errors of the microscopic data. In the theoretical simulation of experiments, the "true" values are known. The simulation procedure as used in this study consists of the following steps:

(1) Collapse of the "ABBN"[10] multigroup cross section set to a one-group constant set using a typical spectrum from the various assemblies used in the study. These one-group constants, which are considered the "true" values for the purposes of this study, are used to calculate the critical buckling for the integral experiments.

(2) Evaluation of typical errors of the one-group cross sections (standard deviations, s^σ).

(3) Construction of the "theoretical" one-group cross sections by statistical variation around the "true" values (using the standard deviations, s^σ). These "theoretical" values correspond to the cross section set which one has available in an actual situation.

(4) Calculation of the "theoretical" multiplication constants k_n for the set of assemblies (eigenvalues $\lambda_n = 1/k_n$), using the "theoretical" cross sections and the critical bucklings (for which $k_n = 1.0$ for the "true" cross sections) calculated in (1).

(5) Construction of the "experimental" results for the eigenvalues λ_n^{ex} by statistical variation around $\lambda_n = 1.0$ using an assumed standard deviation s^ρ for the experimental error of the reactivity.

(6) Calculation of the cross section variations according to the procedure for fitting theoretical and experimental reactivities, i.e., identification of the cross section changes or "errors" introduced in (3).

(7) Comparison of the identified and the known cross section errors.

A theoretical simulation has also been used in an example by Cecchini et al.[2]

A one-group, zero-dimensional model was selected in order to show comparisons of several different adjustment procedures and to show dependency upon the number and the experimental errors of integral and microscopic data.

Four fitting procedures were applied to this study. All four procedures may be formulated by the same system of equations with the only difference being that a certain parameter (γ) is to be determined in a different way.

The mean square deviation of predicted and measured results of the N integral experiments is given by

$$\frac{1}{N}\sum_n (1/s_n^\rho)^2 \left(\sum_k H_{kn}u_k + \Delta\rho_n\right)^2 = \overline{\Delta^2}, \qquad (1)$$

where

s_n^ρ is the average reactivity error of the nth integral experiment

u_k is the (unknown) change in microscopic data to be found by the fitting procedure

H_{kn} is the sensitivity of the criticality (of system n) with respect to a change in u_k

$\Delta\rho_n$ is the difference of the experimental and the theoretically predicted reactivities

s_k^σ is the assumed error (standard deviation) of σ_k.

The four adjustment procedures lead to the following system of equations for the unknowns u_k :

$$\sum_{k'} h_{kk'} u_{k'} = b_k \tag{2a}$$

with

$$b_k = -\sum_n \frac{H_{kn}}{(s_n^\sigma)^2} \Delta\rho_n \tag{2b}$$

$$h_{kk'} = \sum_n \frac{H_{kn} H_{k'n}}{(s_n^\rho)^2} + \gamma \frac{\delta_{kk'}}{(s_k^\sigma)^2}. \tag{2c}$$

Fitting Procedure No. 1—No Constraint Condition ($\gamma = 0$)

This is the standard, unconstrained, least square fit of measured and calculated results.

Fitting Procedure No. 2—Ellipsoidal Constraint Condition

The variation of the unknowns, u_k, as restricted to a domain described by a hyper-ellipsoid,

$$\sum_k \frac{u_k^2}{\omega_k^2} \leq 1. \tag{3}$$

The use of Eq. (3) leads to a two branch solution. If the relative minimum of the unconstrained problem falls within the domain of Eq. (3), then the solution is the same as that for the first procedure; if not, the minimum is to be found on the surface of the hyper-ellipsoid of Eq. (3),

$$\sum_k \frac{u_k^2(\gamma)}{\omega_k^2} = 1 \tag{4}$$

From Eqs. (2) and (4), γ and $u_k(\gamma)$ are found by iteration. This procedure is a variation of the procedure applied by Barré et al.[8] The difference is that Barré et al. used a parallelepiped as a constraint domain. The hyper-ellipsoid is, however, physically more justified since not all cross sections are in error by the maximum amount of their uncertainty and not all deviations influence the reactivity in the same direction. The fact that there is a strong compensation of errors is shown by deviations of only a few percent in [redacted]. Without any compensation, the discrepancy of experimental and theoretical results would be excessively large.

Fitting Procedure No. 3—Combined Fit of Integral and Differential Results[3]

The minimum principal of this procedure is given by

$$\sum_n \left(\frac{1}{s_n^\rho}\right)^2 \left(\sum_k H_{kn} u_k + \Delta\rho_n\right)^2 + \gamma \sum_k \frac{u_k^2}{(s_k^\sigma)^2} = \text{minimum}. \tag{5}$$

Equation (2c) follows from Eq. (5) by differentiation with respect to u_k. The value of γ in the combined fit is a controversial subject.

For the one-group case, one may assume that each cross section measurement is an integral experiment in itself. In this case $\gamma = 1$, and the contributions of all "experiments" are added in Eq. (5) with weighting factors determined from their respective accuracies. If the cross section adjustments are to be done in a multigroup representation, the number of terms in the second sum of Eq. (5) increase proportionally to the number of groups, G. The number of terms in the first sum remains the same. Hemment and Pendlebury[3] tried to account for this by dividing the second term in Eq. (5) by G, i.e. $\gamma = 1/G$. Rowlands and Macdougall[7] deemed this to be improper and they used $\gamma = 1$ also for the multigruop case. Bitelli et al.[11] called the relative weight of the two sums in Eq. (5) "optional". Pazy et al.[12] showed that theoretical considerations suggested $\gamma = 1/G$.

Fitting Procedure No. 4—Fixed Square Constraint Condition

All three procedures described above yield "some" value as a minimum value of the mean square deviation, $\overline{\Delta^2}$. This remaining square deviation may often be substantially smaller than the inaccuracy of the integral experiments. In these cases, the application of the procedure results in an "overfit" of the integral measurements. One should have in mind that the exact cross sections used in an exact computational procedure could never describe the integral experiments more accurately than their error band allows. In other words, one should expect that the integral results "verify" the errors of the integral experiments. Therefore, a new procedure is introduced by the postulate that, "the remaining square deviation be equal to the square deviation of the integral experiments." As in the combined-fit-procedure No. 3, the cross sections are allowed to deviate from the unadjusted ones in a least square sense.

The constraint condition

$$\sum_n (1/s_n^\rho)^2 \left(\sum_k H_{kn} u_k(\gamma) + \Delta\rho_n\right)^2 = 1 \tag{6}$$

is used to determine the value of γ. It should be noted, that procedures No. 2 and 4 provide a prescription to calculate γ for each case.

The general conclusions which can be drawn from this study are:

In the framework of the one-group, zero-dimensional model, it is possible to identify cross section errors from integral measurements fairly accurately.

To what extent this identification may be extended when the complexities of space and energy dependence are taken into account requires additional investigation. It appears likely, however, that cross section error identification will also be possible when such complexities are included, although the adjustment procedures may be different from the procedures presently applied. The inaccuracies in the treatment of space and energy dependence have largely the character of systematic errors rather than statistical errors, and the present study showed that systematic inaccuracies do not strongly reduce the possibility of error identification.

References

1. S. Yiftah, *Panel Discussion on Adjustments to Differential Data to Fit Integral Experiments*, Proc. British Nuclear Energy Society Conference on the Physics of Fast Reactor Operation and Design, 1969, London, pp. 277–280.
2. G. Cecchini, U. Farinelli, A. Gandini and M. Salvatores, *Analysis of Integral Data for Few-Group Parameter Evaluation of Fast Reactors*, Proc. 1964 Geneva Conference **2,** Paper No. 627, pp. 388–397.
3. Pamela C. E. Hemment and E. D. Pendlebury, *The Optimization of Neutron Cross Section Data Adjustments to Give Agreement with Experimental Critical Sizes*, Proc. International Conference on Fast Critical Experiments and Their Analysis, October 10–13, 1966, ANL-7320, pp. 88–106.
4. G. Cecchini, A. Gandini, I. Dal Bono and B. Faleschini, *Comparison Between Experimental and Theoretical Integral Data on Fast Critical Facilities. CALI, A Program for Generating 'Effective' Nuclear Group Constants by a Correlation Method*, Proc. International Conference on Fast Critical Experiments and Their Analysis, October 10–13, 1966, ANL-7320, pp. 107–115.
5. C. G. Campbell, *Panel Discussion on Adjustments to Differential Data to Fit Integral Experiments*, Proc. British Nuclear Energy Society Conference on the Physics of Fast Reactor Operation and Design, 1969, London, pp. 277–280.
6. Arthur R. Baker, *Comparative Studies of the Criticality of Fast Critical Assemblies*, Proc. International Conference on Fast Critical Experiments and Their Analysis, October 10–13, 1966, ANL-7320, pp. 116–129.
7. J. L. Rowlands and J. D. Macdougall, *The Use of Integral Measurements to Adjust Cross Sections and Predict Reactor Properties*, Proc. British Nuclear Energy Society Conference on the Physics of Fast Reactor Operation and Design, 1969, London, Paper No. 1.16, pp. 180–194.
8. J. Y. Barré, M. Heindler, T. Lacapelle and J. Ravier, *Lessons Drawn from Integral Experiments on a Set of Multigroup Cross Sections*, Proc. British Nuclear Energy Society Conference on the Physics of Fast Reactor Operation and Design, 1969, London, Paper No. 1.15, pp. 165–179.
9. K. O. Ott, Purdue University (private communication).
10. L. P. Abagyan, N. O. Bazazyants, I. I. Bondarenko and M. N. Nikolaev, *Group Constants for Nuclear Reactor Calculations*; I. I. Bondarenko, Ed., (Consultants Bureau Enterprises, Inc., New York, 1964).
11. G. Bitelli, G. Cecchini, A. Gandini and M. Salvatores, *Analysis and Correlation of Integral Experiments in Fast Reactors with Nuclear Parameters*, Proc. British Nuclear Energy Society Conference on the Physics of Fast Reactor Operation and Design, 1969, London, Paper No. 1.14, pp. 157–163.
12. A. Pazy, G. Rakavy, Y. Reiss and Y. Yeivin, *Use of Integral Measurements as Supplementary Data in Neutron Cross Section Evaluation*, Proc. International Conference on Fast Critical Experiments and Their Analysis, October 10–13, 1966, ANL-7320, pp. 270–277.

II-35. Fuel Management Design With the REBUS System

J. Hoover and D. A. Meneley

Introduction

An important phase of reactor design is the selection of a fuel management scheme. Here "fuel management" refers to both the in-reactor and ex-reactor portion of the fuel cycle. Fuel management design is significant because of the sensitivity of the energy costs, the power, and the energy output to the mode of fuel management. Fuel cycle calculations are required to determine the operating conditions of the reactor system and to evaluate the performance of the system. The objective of the design calculations is to obtain the "best" reactor performance without violating the many physical constraints.

The primary purpose of this paper is to present a proposed fuel management design procedure. The proposed procedure is preliminary in that more analysis in

particular areas mentioned herein is needed in order to establish the accuracy and the range of validity of the procedure. A secondary purpose is to illustrate the role of the REBUS System in this procedure. In addition, the utility of equilibrium fuel cycle calculations in doing design analysis is shown.

Fuel Cycle Design Analysis

In doing design analysis, an adequate fuel cycle model must be used. Specification of a reasonable fuel cycle model requires some understanding of the purpose of the design analysis. Design analyses divide quite naturally into two classes: conceptual design analysis and final design analysis. In conceptual design analysis, a large number of survey and parametric studies are done to obtain the general performance and economic characteristics of the system. The external cycle (reprocessing and refabrication) must be modeled in this analysis. In addition, conceptual design analysis involves fuel management studies to optimize burnup and power distributions, studies of various core zone enrichments to achieve uniform power distributions, and studies to minimize the impact of the control strategy. Final design analysis requires a much more detailed spatial model of the reactor to determine local power and burnup distributions and accurate mass balances. Much emphasis is placed on achieving the detailed thermal hydraulic constraints on peak fuel and clad temperatures. The detailed burnup distribution must be obtained to insure fuel and structure integrity. Note that the control strategy selection is included in fuel cycle design analysis because of the effect of control strategy on the fuel cycle results, in particular, the fissile mass balances and the power generation in individual fuel bundles.

EQUILIBRIUM FUEL CYCLE CALCULATION

Before proceeding to the discussion of the fuel management design procedure, it is necessary to understand the equilibrium calculation and its function in the procedure. The equilibrium fuel cycle calculation provides the infinite time operating conditions of a recycle system under fixed conditions. The main use of an equilibrium solution is as a first approximation to the operating conditions of the system after the first few cycles. This solution provides estimates of the burn step time, control requirements, feed enrichments, and overall system economics. As shown below the equilibrium solution can provide this for a lower cost than the direct calculation of a number of burn steps and thus can serve as a starting point for final design analysis. The projected scatter-reloading fuel management strategies for fast reactors involve up to seven or eight cycles as maximum subassembly residence time in the blankets. The direct method of solution requires explicit calculation of at least this number of cycles to establish the correct end-of-life conditions. The end-of-life conditions can only be guessed at the beginning of the calculation procedure, if the direct method is used, so a good deal of trial and error is involved in developing the solution of enrichment, burn time, and control requirements which will satisfy the thermal hydraulic, metallurgic, and nuclear constraints. The equilibrium solution on the other hand requires explicit calculation of only one burn step.

The equilibrium solution can provide the power peaking factors for use in the thermal hydraulic analysis and the flux distributions for metallurgic analysis; typically, subassembly swelling and bowing calculations. The resulting enrichments, burn step, and partially-burned fuel densities can be used as input to an explicit, step by step calculation to obtain detailed performance characteristics of the system in its normal operating (post-startup) state. Some adjustment of the design may be required at this point because of the approximations made in the equilibrium calculation. The explicit calculation can provide information for subassembly flux peaking factors in later equilibrium problems.

Computation of the optimum new-reactor startup procedure is greatly facilitated by knowing what the final operating conditions will be; an equilibrium solution can be used to supply this information. The startup strategy may involve special fuel materials, variation of burn time, recharge of partly burned fuel, or fuel shuffling. The objective is to reach the normal operating conditions at minimum incremental cost for the total number of startup cycles. The startup fuel cycle calculations must be done by direct calculation of each step; however, the results of the equilibrium problem can be used to obtain estimates of the most economical startup strategy.

Fuel Management Design Procedure

A fuel management design procedure must satisfy several requirements. First, it must be flexible enough to handle the wide class of problems to be studied. Second, the procedure must be sufficiently accurate to properly characterize the recycle systems to be studied. Third, the procedure must be reasonably economic in terms of both designer effort and computer time. The fuel management design procedure in this paper was designed to satisfy these requirements.

The fuel management design procedure is illustrated in Fig. II-35-1. The procedure is iterative as shown, as the evaluation of the reactor performance will provide

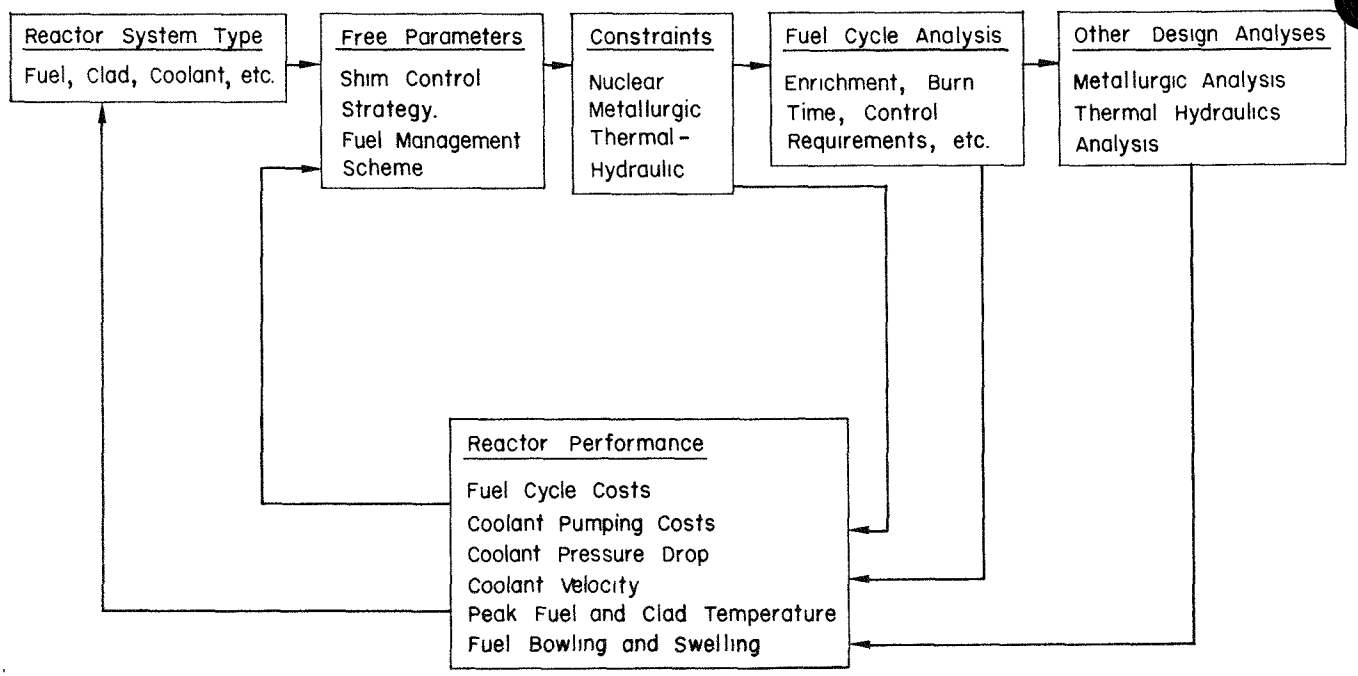

FIG. II-35-1. Fuel Management Design Procedure. *ANL Neg. No. 116-524.*

the basis for selection of alternative free parameters (shim control strategy and/or fuel management scheme) and possibly some change in the reactor system type in order to enhance reactor performance. The various terms in Fig. II-35-1 are described below.

The reactor system type includes specification of the fuel, clad and coolant. The core arrangement and structure arrangement are also specified along with the total reactor power. This phase of the procedure can itself involve design analysis; however, this paper is not concerned with this general area, but it is based on the assumption that previous experience or a preliminary design analysis is sufficient to specify the reactor system type and physical characteristics.

In selecting a fuel management scheme, the design characteristics are of two types: free parameters and constrained parameters. The free parameters are designer-specified, and the constrained parameters are determined by the design analysis. The distinction between free parameters and constrained parameters is not always clear, as is noted below. The free parameters chosen are shim control strategy and fuel management strategy. The shim control strategy includes specification of the physical location and the number of control assemblies which balance reactivity changes resulting from fuel burnup. The fuel management strategy refers to both the in-reactor and ex-reactor portion of the fuel cycle. The in-reactor fuel management scheme includes selection of the batch fraction, shuffling mode, etc. The ex-reactor portion of the fuel cycle defines the amount of bred fuel sold, the distribution of fuel discharges to reprocessing plants, and the refabrication with makeup from the reprocessing output and external feeds. Not all of the above parameters are free in the sense of being designer specified. For instance, the external feeds available depend on the type of power economy (LWR, mixed LWR and LMFBR, etc.) and the availability of fuel from other utilities and fuel owners. However, they are placed in this category because the designer or the utility can choose from the available sources.

In the design analysis, the three important types of constraints are nuclear, metallurgic, and thermal hydraulic. The nuclear constraints relate to the system reactivity and safety. In fuel cycle analysis, the limitations are criticality at the minimum reactivity operating point and continuous criticality through the use of shim control. The metallurgic constraints are concerned with swelling, bowing, corrosion, erosion, etc. This constraint usually is one of damage limitation. In fuel cycle analysis, the maximum discharge burnup is constrained. In actual calculations the metallurgic constraint is usually specified by a core averaged discharged burnup, which limit is determined by dividing the maximum permissible discharged burnup by the product of the axial maximum to average power and the radial maximum to average power. The computed fluxes are used to assess fuel and structure damage. The thermal hydraulic constraints are concerned with fuel integrity (peak fuel and clad temperature), pump-

g power (coolant pressure drop), and erosion (coolant velocity). These constraints are usually specified by a peak power density and desired average power density.

At this point the fuel cycle analysis, which is a model of the physical problem, obtains the constrained parameters which satisfy the imposed constraints for the specified free parameters. The constrained parameters are the feed fuel enrichments, the burn time, and shim control requirements. In addition the fuel cycle analysis obtains the fissile mass balance, the flux, and the power distributions which are used in further analyses to determine the reactor performance.

The Fuel Cycle Model

Figure II-35-1 depicts the fuel management design procedure; however, the adequacy of this procedure depends upon a reasonable fuel cycle model for the design analysis. The physical model, the mathematical formulation and the solution procedure for the REBUS System are presented in Ref. 1. REBUS includes models of all physical procedures which are expected in LMFBR operation with defined limits. These are: one reactor (as opposed to an interacting power system); fuel contained in discrete lumps; fully defined external conditions, that is complete specification of bred fuel disposal and refabrication make-up; fixed fuel management definition (no cycle optimization). The present version of REBUS reflects major emphasis on the first type of problem defined above, that is, the survey problem.

The time dictionary necessary for running a non-equilibrium problem is not included in REBUS. Such a dictionary would permit real-time calculation of a series of burn-shuffle-refuel steps, with changing reactor operating conditions, control rod banking, burned fuel disposal, and fresh fuel specifications. Such calculations fall into the category of detailed design work. The whole set of logic in REBUS has been designed so that the model can properly treat these problems when the extra control routines are written.

The fuel cycle model comprising REBUS describes the material motions and contains the equation set governing reactor behavior. The indexing system for describing material motions describes the following phases: fuel loading, in-reactor shuffling, discharge, reprocessing, bred fuel sale, refabrication, and storage. The indexing system can account for individual fuel bundles with completely generalized in-reactor fuel ffling. In the external cycle, fuel bundles may be ac-nted for separately or combined for reprocessing. Competition for available fuel sources (reprocessing output and external sources) is permitted at the fabrication phase with selection based on a priority distribution scheme.

The following important assumptions are made with respect to the reactor model:

1. Isotope multigroup cross sections are computed at reference compositions and temperature and therefore are time independent.
2. Reaction rates which appear in the depletion equations are computed from region- and time-averaged group fluxes.

Because of assumption 1, the fuel cycle analysis divides into two phases: computation of the multigroup cross sections and the fuel cycle calculation.

Computation of the Multigroup Cross Sections

The microscopic cross sections for use in the REBUS System are obtained from the MC² code.[2] Typically, the broad group structure used has a 0.5 lethargy width from 10 MeV to 22.6 eV (26 groups). Fuel cycle studies need fewer broad groups. A single collapse spectrum, usually obtained from MC² or from a multidimensional diffusion solution, is used to linearly weight the cross sections and collapse to a few-group description. In general, eight neutron energy groups are sufficient for reactors in which the spectrum changes between core and blanket are not severe (see Paper II-36). If a multidimensional diffusion solution is obtained for estimated mid-cycle conditions, the spectrum obtained can be used in a region-dependent collapsing scheme. With region dependent collapsing by linear flux weighting, four or fewer neutron energy groups are sufficient (see Paper II-36).

Resonance Cross Section Variations

The present REBUS System does not include the variation of group cross sections in the resonance range with the fuel temperature, background potential scattering, and atomic density of a given resonance isotope and the other resonance absorbers present in the fuel. What is required is a simplified resonance cross section generating routine, to be called from REBUS prior to each flux recalculation. This routine must be highly efficient because of the large number of calls which will be required. This is an area in which more effort is needed to assess the accuracy of the present REBUS System in which the microscopic cross sections are computed for reference conditions.

The Neutronics Solution

In doing fuel cycle calculations, the computation time should be minimized without seriously compromising the accuracy. The REBUS System consists of a burnup model and a neutronics model. The neutronics

solution requires more than 90% of the total computer time. Thus, significant economies can result by decreasing the required time for the neutronics solution and the number of neutronics solutions. Some considerable effort has been expended to do this, the results of which are discussed below.

Up to the present time, the REBUS System has been used with the one- and two-dimensional finite difference approximations to the diffusion equations in the ARC System. The results presented below are for r-z cylindrical calculations in two-dimensions. The neutronics solution time is sensitive to both the mesh point spacing and the convergence criteria used for the multiplication constant and the multigroup flux distribution. The required computer time varies nearly linearly with the total number of mesh points. A mesh point spacing (the distance between mesh points) of 3 to 5 cm in the radial direction and 4 to 6 cm in the axial direction is adequate. Near the core centerline and the core midplane, the larger mesh spacings can be used because of the fairly flat flux and power distribution. Near core-blanket interfaces, the small mesh spacings should be used because of the large flux and power variations. In doing detailed design analysis, more closely spaced mesh points would be needed as the emphasis is on detailed power distributions. In fact, some calculations would be done in hexagonal geometry to obtain the fuel pin power and burnup. This is an area in which additional effort is needed because the above results are preliminary.

The neutronics solution in the ARC System uses three convergence criteria to obtain the multiplication constant and the multigroup flux distribution. The first convergence criterion is concerned with the difference in k-effective:

$$| k^{(n)} - k^{(n-1)} | \leq \epsilon_k , \tag{1}$$

where index n refers to the nth outer iteration. The convergence criteria for the flux are

$$\sum_{ijg} \frac{|\phi_{ijg}^{(n)} - \phi_{ijg}^{(n-1)}|}{\phi_{ijg}^{(n-1)}} \leq \epsilon_p, \tag{2}$$

and

$$|\bar{\lambda}^{(n)} - \underline{\lambda}^{(n)}| \leq \epsilon_\lambda , \tag{3}$$

where

$$\bar{\lambda}^{(n)} = \max_{ijg} \left(\frac{\phi_{ijg}^{(n)}}{\phi_{ijg}^{(n-1)}} \right),$$

$$\underline{\lambda}^{(n)} = \min_{ijg} \left(\frac{\phi_{ijg}^{(n)}}{\phi_{ijg}^{(n-1)}} \right).$$

The indices i and j refer to the mesh point locations in the radial and axial direction. The index g is the neutron energy group. All three criteria must be satisfied in a converged problem. The suggested value (see Ref. 3) for the error limits is 1×10^{-3}.

In fuel cycle calculations, convergence of k-effective is needed to accurately determine the feed enrichments and control requirements. Accurate burnup and power distributions can be achieved only by convergence of the pointwise flux distribution as specified by Eqs. (2) and (3).

THE BURNUP MODEL

In using REBUS, the burn step time is divided into P subintervals; thus there are $P + 1$ time nodes at which the neutronics solution is done. Studies with different numbers of subintervals showed that for typical fast reactor designs with a six month or a year refueling period, one interval is sufficient (see Ref. 4).

The present model assumes that all materials which appear within each neutronics region are irradiated in the same flux. It is straightforward in principle to apply material, group, and time-dependent flux advantage factors during the formation of the burn matrices. These values would be obtained from prior cell calculations or from detailed plan-view fuel cycle calculations. The purpose of applying these factors would be to improve the calculational model in 2-dimensional (r-z) geometries.

FUTURE DEVELOPMENTS

1. Use of Synthesized Flux Solutions

Direct finite-difference flux solutions are relatively expensive, even in two-dimensional geometry. Flux solutions occupy over 90% of the present REBUS run time. For survey calculations, it would be useful to have a cheaper flux solution, at some expense in accuracy. It has been shown from experience with the BISYN code[5] and with the SYNBURN code[6] that even such very crude synthesis models give reasonable results if care is exercised in setting up the trial functions. The present ARC System includes an advanced spatial synthesis algorithm. The linkage between REBUS and its associated flux solution algorithm is extremely simple, so that coupling to this synthesis algorithm will require a small amount of effort.

A three-dimensional fuel cycle calculation capability will be very useful during final design of the LMFBR demonstration reactors in order to reduce uncertainties in fuel pin peaking factors, and also during operation to provide meaningful comparison of computed masses at discharge from the reactor with assays of selected fuel pins. This type of study is useful in re-

ucing predictive uncertainties, and therefore economic nalties, during design of the full scale commercial LMFBRs.

Within the next 10 or 15 years it is expected that the computation cost of direct 3-dimensional finite-difference solutions will become low enough to permit routine use of this technique in design calculations. Until that time, however, it will be necessary to use the less precise, but much more economical flux synthesis methods for 3-dimensional fuel cycle calculations. These methods are reasonably well-developed at the present time, and the main task which remains is the construction of the large computer codes to treat three dimensions. These methods always will have to be tested against more accurate methods by running a few reference problems for any given design.

The present index structure of REBUS is adequate for use in connection with 3-dimensional flux algorithms. The problems will be primarily those of maintaining adequate input error checking and output display methods so that the user does not get lost in the mass of information that makes up a realistic 3-dimensional problem.

2. Interactive Fuel Cycles in Two or More Reactors

As LMFBRs are introduced into an established thermal reactor power system, studies of fuel utilization will be required for the whole system of reactors, to provide guidance toward the most economical method of handling the large and expensive fuel inventory. The REBUS System easily can be modified to do simultaneous calculations of several reactors with interacting fuel cycles. The reason is that there are no geometric data in REBUS; when the flux solution is called, it can carry out sequential flux solutions in each of the reactors, given the atom densities in each region, then return region-averaged group fluxes in exactly the same manner as in the single-reactor computation.

3. Miscellaneous

There are several minor modifications of REBUS which will make it more useful for design. For example, the control density search routine must be modified to represent more accurately the movement of the control rod tip in the axial direction. Some improvement is required in the output displays, to make large problems easier to analyze. When fuel test reactors such as EBR-II and FFTF are reloaded, the initial criticality often is adjusted by relocation of driver fuel. This type of criticality search is satisfied on the first trial of this sequence which results in the initial criticality falling within the given satisfactory range.

References

1. J. Hoover, G. K. Leaf, D. A. Meneley and P. M. Walker, *The Fuel Cycle Analysis System, REBUS*, Nucl. Sci. Eng. (submitted for publication).
2. B. J. Toppel, A. L. Rago and D. M. O'Shea, *MC²*, *A Code to Calculate Multigroup Cross Sections*, ANL-7318, (1967).
3. J. Hoover, *Convergence Criteria for the Neutronics Solution Used by the REBUS System*, Reactor Development Program Progress Report, ANL-7758 (1970).
4. J. Hoover and D. A. Meneley, *Time Step Subinterval Length Required for REBUS*, Reactor Development Program Progress Report, ANL-7753, (1970).
5. P. Greebler et al., *BISYN—A Two Dimensional Synthesis Program*, GEAP-4922 (1965).
6. D. A. Meneley and P. A. Pizzica, *SYNBURN: A Synthesis Fuel Cycle Code*, ANL (to be published).

II-36. Alternative Neutron Energy Group Collapsing Schemes Applied to Fuel Cycle Calculations

J. Hoover and D. A. Menley

Introduction

Fuel cycle calculations are required to analyze the neutronic, thermal hydraulic, and economic performance of fast breeder reactors. Minimizing the number of neutron energy groups used in fuel cycle calculations can be beneficial, through reduced computation time, if accuracy is not seriously compromised. In the fuel e analysis system REBUS,[1] more than 90% of the computer time is required for the neutronics solution. Since the computer time required for the neutronics solution varies nearly linearly with the number of neutron energy groups, significant economies can result by reducing the number of neutron energy groups. To illustrate the effects of various group structures and collapsing methods, five different collapsed group structures were studied. Both single flux spectrum and region dependent flux spectra were used for collapsing. The results presented in this paper for collapsing with a

single flux spectrum were previously reported by L. J. Hoover.[2]

Various fuel cycle parameters were examined to determine the accuracy of the results. These are the feed enrichment, the breeding ratio, the fissile mass discharge, and the two dimensional power distribution. These parameters were chosen because of their significance in evaluating the performance of the system.

Collapsing Techniques

Two collapsing schemes were used in this study. For the first collapsing scheme, linear flux weighting with a single spectrum, the equation set used is

$$\bar{\sigma}_x^i(J) = \sum_{j \text{ in } J} \sigma_x^i(j)\phi(j) / \sum_{j \text{ in } J} \phi(j) \tag{1}$$

$$\bar{\sigma}_s^i(J \rightarrow K) = \sum_{k \text{ in } K} \sum_{j \text{ in } J} \sigma_s^i(j \rightarrow k)\phi(j) / \sum_{j \text{ in } J} \phi(j), \tag{2}$$

where

j is the jth group
J is the Jth collapsed group
$\sigma_x^i(j)$ is the microscopic cross section for isotope i of type x in group j. The transport cross section is considered in this category
$\phi(j)$ is the flux in group j
$\sigma_s^i(j \rightarrow k)$ is the microscopic scattering cross section from group j to group k for isotope i
k is the kth group
K is the Kth collapsed group
$\bar{\sigma}_x^i(J)$ is the collapsed microscopic cross section for isotope i of type x in group J
$\bar{\sigma}_s^i(J \rightarrow K)$ is the collapsed microscopic scattering cross section from group J to group K for isotope i.

The second collapsing scheme, linear flux weighting with a region-dependent flux spectrum, uses an equation set identical with the above except that region-dependent cross sections are now generated. Thus,

$$\bar{\sigma}_x^i(r, J) = \sum_{j \text{ in } J} \sigma_x^i(j)\phi(j, r) / \sum_{j \text{ in } J} \phi(j, r) \tag{3}$$

$$\bar{\sigma}_s^i(r, J \rightarrow K) = \sum_{k \text{ in } K} \sum_{j \text{ in } J} \sigma_s^i(j \rightarrow k)\phi(j, r) / \sum_{j \text{ in } J} \phi(j, r), \tag{4}$$

where

$\bar{\sigma}_x^i(r, J)$ is the collapsed microscopic cross section for isotope i in region r
$\bar{\sigma}_s^i(r, J \rightarrow K)$ is the collapsed microscopic scattering cross section for isotope i in region r.

The transport cross section is collapsed using Eq. (42) of Ref. 3.

The Fuel Cycle Calculations

The fuel cycle analysis system REBUS[1] was used to do the fuel cycle calculations. REBUS, an acronym for REactor BUrnup System, computes equilibrium fuel cycle conditions. In these calculations, the burn time or cycle time was divided into two subintervals; that is, the fluxes were computed at three time nodes: beginning of cycle, middle of cycle, and end of cycle. The burn time was adjusted to achieve 100,000 MWd/T core average discharge burnup. The feed enrichments were constrained to achieve criticality at the end of cycle. In addition, the control densities were fixed at cycle average values. The neutronics solution was done with the two-dimensional diffusion theory module in the ARC System.[4]

Two typical 1000-MWe, oxide fueled reactors,[5] the GE Advanced and Conservative designs, were analyzed. The Conservative design has a higher core-to-blanket leakage fraction than the Advanced design. Both cores have multiple enrichment zones for power flattening and fractional-batch scatter-reloading fuel management schemes.

Using the ultrafine group P_1 option in the MC^2 code,[6] the microscopic cross sections were obtained from the

TABLE II-36-I. Neutron Energy Group Structures

13 Groups, eV	8 Groups, eV	7 Groups, eV	6 Groups, eV	4 Groups, eV
10.00×10^6	10.00×10^6	10.00×10^6	10.00×10^6	10.00×10^6
36.79×10^5	22.31×10^5			
13.53×10^5		13.53×10^5	13.53×10^5	
49.79×10^4	49.79×10^4			49.79×10^4
18.32×10^4		30.20×10^4	18.32×10^4	
67.38×10^3	11.11×10^4	67.38×10^3		
24.79×10^3	24.79×10^3		24.79×10^3	24.79×10^3
91.19×10^2		15.03×10^3		
33.55×10^2	55.31×10^2	20.35×10^2	33.55×10^2	33.55×10^2
12.34×10^2	12.34×10^2			
45.40×10^1	27.54×10^1	27.54×10^1	27.54×10^1	
16.70×10^1				
61.44				
22.60	22.60	22.60	22.60	22.60

ENDF/B file for estimated mid-cycle conditions. The energy range from 10 MeV to 22.6 eV was divided into 26 groups, each having a 0.5 lethargy width.

A two-dimensional diffusion theory calculation for the estimated mid-cycle conditions gave the region-dependent flux spectrum. The centerline flux was chosen as the single flux spectrum. Problems were run using the various group structures shown in Table II-36-I.

Results

The results obtained are presented in Tables II-36-II and II-36-III. The errors obtained using the single spectrum collapse are shown in Table II-36-II. The comparisons are made relative to the 13 group results.

With these energy group structures, the feed enrichment varies less than 1.2% and the breeding ratio varies less than 0.5%. The fissile mass discharge from the reactor agrees well with the 13 group results. The core discharge fissile mass (not shown) agrees well with the 13 group results. However, the isotopes composing the fissile mass should be studied. The blanket Pu-239 discharge, the principle constituent of the blanket fissile mass, compares favorably with the 13 group results. Note the large errors in the Pu-241 blanket discharge. These errors are due to the hardness of the core spectrum used for collapsing relative to the blanket spectrum. This causes an underestimate of the Pu-239 capture rate in the blankets, which is the source of the Pu-241. Using 8 neutron energy groups, the detailed two-dimensional power distribution can be calculated within 2%.

Using the region-dependent collapse, these spectral effects can be accounted for, and the accuracy can be significantly increased. The errors for the 6 group structure and the 4 group structure are shown in Table II-36-III. Note the significantly smaller errors. In addition, with 4 neutron energy groups the two-dimensional power distribution can be obtained within 0.1%. Thus, with region dependent collapsing, fuel cycle parameters can be calculated accurately with 4 neutron energy groups.

The conclusion from this study is that region-dependent collapsing can significantly decrease the errors in fuel cycle calculations. For designs typical of those studied, in which the spectrum does not change markedly between the core and blanket, fuel cycle calculations with eight neutron energy groups and a single collapse spectrum yield good accuracy for the feed enrichment, breeding ratio, the two-dimensional power distribution and the fissile mass discharge. With region-dependent collapse, four neutron energy groups yield good accuracy. In fact, the results obtained indicate that studies should be done with fewer than four neutron energy groups.

TABLE II-36-II. Errors Obtained using Single Collapse Spectrum

Prameter	Errors, %		
	6 Groups	7 Groups	8 Groups
GE ADVANCED DESIGN			
Feed Enrichment	−0.3	−0.4	−0.7
Breeding Ratio	+0.02	−0.05	−0.1
Discharge			
fissile mass	+0.1	−0.4	−0.7
blanket Pu-239	+0.5	−0.5	−1.3
blanket Pu-241	−0.8	−6.0	−9.0
GE CONSERVATIVE DESIGN			
Feed Enrichment	−0.7	−0.7	−1.2
Breeding Ratio	+0.5	+0.2	+0.3
Discharge			
fissile mass	−0.1	−0.4	−0.9
blanket Pu-239	+0.9	+0.1	−0.5
blanket Pu-241	−3.0	−7.0	−8.0

TABLE II-36-III. Errors Obtained using Region-Dependent Collapse Spectra

Parameter	Errors, %	
	6 Groups	4 Groups
GE ADVANCED DESIGN		
Feed Enrichment	−0.01	−0.1
Breeding Ratio	+0.01	+0.05
Discharge		
fissile mass	−0.01	−0.1
blanket Pu-239	−0.01	−0.1
blanket Pu-241	−0.02	−0.2
GE CONSERVATIVE DESIGN		
Feed Enrichment	−0.02	−0.2
Breeding Ratio	+0.03	+0.2
Discharge		
fissile mass	−0.01	−0.1
blanket Pu-239	−0.01	−0.1
blanket Pu-241	−0.06	−0.8

References

1. J. Hoover, G. K. Leaf, D. A. Meneley and P. M. Walker, *The Fuel Cycle Analysis System, REBUS*, Nucl. Sci. Eng. (submitted for publication).
2. L. J. Hoover and D. A. Meneley, *The Influence of Neutron Energy Group Structure on Fuel Cycle Analysis of Fast Breeder Reactors*, Trans. Am. Nucl. Soc. **12**, pp. 441–442 (1969).
3. A. Travelli, *A New Formulation of Multigroup Microscopic Cross Sections*, Reactor Physics Division Annual Report, July 1, 1967 to June 30, 1968, pp. 413–421.
4. B. J. Toppel, Ed., *The Argonne Reactor Computation (ARC) System*, ANL-7322, (1967).
5. P. M. Murphy et al., *Comparison of Two Sodium-cooled, 1000 MWe Fast Reactor Concepts*, GEAP-5618 (1968).
6. B. J. Toppel, A. L. Rago and D. M. O'Shea, *MC²*, *A Code To Calculate Multigroup Cross Sections*, ANL-7318 (1967).

II-37. Neutronics of Advanced Liquid Metal Fast Breeder Reactors with Refractory-Clad Fuel

D. A. Meneley, E. L. Fuller and A. E. McArthy

Introduction

This work contains the results of a limited study to determine the neutronic effects of substituting certain refractory metals for stainless steel as cladding materials in advanced liquid metal fast breeder reactors (LMFBRs). Three cladding materials were considered: molybdenum, vanadium, and niobium. The analysis was carried out for rather thinly-clad oxide fuel with clad thicknesses of 5 and 10 mils. The calculations are reported in two parts. The first of these compares a series of one-dimensional calculations of idealized LMFBRs in which the various refractory metals are substituted for the stainless steel cladding of the idealized reference core. The second compares the results of two-dimensional equilibrium fuel-cycle calculations for stainless steel-clad and molybdenum-clad fuel in the core and axial blanket of the reference reactor from one of the LMFBR 1000 MWe Follow-on Studies.

One-Dimensional Analysis of Idealized LMFBRs

PHYSICAL DESCRIPTION

The dimensions of the idealized reference LMFBR are given in Table II-37-I. The core was cylindrical, with two enrichment zones of equal volume. The enrichments were chosen so that the peak power in each zone was roughly the same. The average core power density was 500 kW/liter and the total core power 2500 MWt, so that the core volume was 5000 liters.

The volume fractions of the two idealized cores appear in Table II-37-II. Note that the volume fractions for the axial blankets differ for each core, but those for the radial blankets and all reflectors remain the same. The actual core Pu/U enrichments are found from composition searches. The distribution of plutonium isotopes is 75% Pu-239 and 25% Pu-240. Fission products are assumed to have replaced 5% of the original heavy atoms in order to approximate mid-fuel-cycle conditions. Table II-37-III contains the densities of the isotopes appearing in each reactor. When these are used with the data shown in Table II-37-II, the atom densities of each reactor region can be found. These are shown in Table II-37-IV.

TABLE II-37-I. Dimensions of Idealized Reactor, cm

Inner core-zone radius	97
Outer core-zone radius	137
Core height	85
Radial blanket thickness	25
Axial blanket thickness	35
Radial reflector thickness	50
Axial reflector thickness	50

TABLE II-37-II. Volume Fractions of Idealized Reactors

	Core 1				Core 2			
	Reference	Mo Cladding	V Cladding	Nb Cladding	Reference	Mo Cladding	V Cladding	Nb Cladding
UO_2[a]	0.467	0.467	0.467	0.467	0.512	0.512	0.512	0.512
Na	0.380	0.380	0.380	0.380	0.380	0.380	0.380	0.380
SS	0.149	0.062	0.062	0.062	0.104	0.062	0.062	0.062
Ta	0.004	0.004	0.004	0.004	0.004	0.004	0.004	0.004
Mo	0.000	0.087	0.000	0.000	0.000	0.042	0.000	0.000
V	0.000	0.000	0.087	0.000	0.000	0.000	0.042	0.000
Nb	0.000	0.000	0.000	0.087	0.000	0.000	0.000	0.042

	Axial Blanket[b]				Axial Reflector[c]	Radial Blanket[d]	Radial Reflector
	Core 1		Core 2				
	Reference	Mo Cladding	Reference	Mo Cladding			
UO_2[e]	0.467	0.467	0 512	0.512	0 000	0.550	0.000
Na	0.380	0.380	0.380	0.380	0.600	0.250	0.200
SS	0.149	0.062	0.104	0.062	0.200	0.200	0 800
Ta	0.004	0.004	0.004	0.004	0.000	0.000	0.000
Mo	0.000	0.087	0.000	0 042	0.000	0.000	0.000

[a] 85% theoretical density Plutonium distribution: 75% Pu-239, 25% Pu-240, 5% of heavy atoms replaced by fission product pairs.

[b] 10 cm nearest core· 4% of uranium atoms replaced by Pu-239; 25 cm remainder: 2% of uranium atoms replaced by Pu-239.

[c] 20% void.

[d] 2% of uranium atoms replaced by Pu-239.

[e] 90% theoretical density.

TABLE II-37-III. Densities of Reactor Materials

Material	Density, g/cc	Material	Density, g/cc
UO_2	10.45	Mo	10.2
Na	0.827	V	5.96
SS[a]	7.74	Nb	8.4
Ta	15.77		

[a] 74% iron, 18% chromium, 8% nickel.

TABLE II-37-IV. Atom Densities in Idealized Reactors, atoms/b-cm

Material	Core 1 (10-mil Cladding)				Core 2 (5-mil Cladding)			
	Reference	Mo Cladding	V Cladding	Nb Cladding	Reference	Mo Cladding	V Cladding	Nb Cladding
U-238[a]	0.00765	0.00765	0.00765	0.00765	0.00839	0.00839	0.00839	0.00839
Pu-239[a]	0.00086	0.00086	0.00086	0.00086	0.00094	0.00094	0.00094	0.00094
Pu-240[a]	0.00029	0.00029	0.00029	0.00029	0.00032	0.00032	0.00032	0.00032
Fission products	0.00046	0.00046	0.00046	0.00046	0.00050	0.00050	0.00050	0.00050
O	0.01850	0.01850	0.01850	0.01850	0.02028	0.02028	0.02028	0.02028
Na	0.00823	0.00823	0.00823	0.00823	0.00823	0.00823	0.00823	0.00823
SS	0.01253	0.00521	0.00521	0.00521	0.00875	0.00522	0.00522	0.00522
Ta	0.00021	0.00021	0.00021	0.00021	0.00021	0.00021	0.00021	0.00021
Mo	0.00000	0.00557	0.00000	0.00000	0.00000	0.00269	0.00000	0.00000
V	0.00000	0.00000	0.00613	0.00000	0.00000	0.00000	0.00296	0.00000
Nb	0.00000	0.00000	0.00000	0.00474	0.00000	0.00000	0.00000	0.00228

Material	Inner Axial Blanket[b]		Outer Axial Blanket[c]		Axial Reflector	Radial Blanket	Radial Reflector
	Core 1	Core 2	Core 1	Core 2			
U-238	0.00980	0.01032	0.00960	0.01053	0.00000	0.01876	0.00000
Pu-239	0.00038	0.00042	0.00020	0.00022	0.00000	0.00038	0.00000
O	0.01960	0.02149	0.01960	0.02149	0.00000	0.03831	0.00000
Na	0.00823	0.00823	0.00823	0.00823	0.01299	0.00541	0.00433
SS	0.01253[d]	0.00875[d]	0.01253[d]	0.00875[d]	0.01682	0.01682	0.06728
	0.00521[e]	0.00522[e]	0.00521[e]	0.00522[e]			
Ta	0.00021	0.00021	0.00021	0.00021	0.00000	0.00000	0.00000
Mo	0.00000[d]	0.00000[d]	0.00000[d]	0.00000[d]			
	0.00557[e]	0.00269[e]	0.00557[e]	0.00269[e]			

[a] Initial guesses for enrichment search in inner core zone.
[b] 10 cm nearest core.
[c] 25 cm remainder of core.
[d] SS cladding in axial blanket (Reference Reactor).
[e] Mo cladding in axial blanket.

TABLE II-37-V. Neutronic Comparison of Idealized Reactors

	Core 1 (10-mil Cladding)				Core 2 (5-mil Cladding)			
	Reference	Mo Cladding	V Cladding	Nb Cladding	Reference	Mo Cladding	V Cladding	Nb Cladding
Extrapolated height, cm	124.753	124.753	124.753	124.753	124.166	124.166	124.166	124.166
Inner-zone enrichment	0.11705	0.13027	0.11603	0.13255	0.10959	0.11564	0.10911	0.11657
Outer-zone enrichment	0.14509	0.15590	0.14245	0.16011	0.14563	0.15118	0.14377	0.15329
Core-conversion ratio	0.93468	0.84215	0.94721	0.80242	0.97658	0.92692	0.98546	0.90521
Reactor breeding ratio	1.48150	1.35984	1.47185	1.34031	1.54827	1.47486	1.53957	1.46951
Critical mass, kg	2297.06	2504.56	2263.09	2561.40	2326.35	2432.92	2305.43	2460.40
Sodium-void extrapolated height, cm	129.389	129.389	129.389	129.389	129.458	129.458	129.458	129.458
Sodium void, Δk	0.01548	0.02650	0.01226	0.02629	0.01680	0.02287	0.01540	0.02261
Doppler coefficient $\left(T\frac{dk}{dT}\right)$	−0.00600	−0.00337	−0.00816	−0.00306	−0.00615	−0.00440	−0.00716	−0.00434

CROSS SECTIONS AND METHODS

A 26-group set of microscopic cross sections was generated by the MC² code from the ENDF Revised Category 1 file using ½ lethargy units and the P_1 ultrafine option. It is recognized that the molybdenum capture for 1 to 10 keV was too high in this set. Hence, more correct values for molybdenum were also used;[1] calculations were made using each set for purposes of comparison. The calculations were carried out using one-dimensional methods that have been checked

TABLE II-37-VI. COMPARISON OF MOLYBDENUM-CLAD IDEALIZED REACTORS

	Core 1 (10-mil Cladding)				Core 2 (5-mil Cladding)			
	Reference	Mo (ENDF/B)	Mo (Mod)[a]	Mo (Mod)[b]	Reference	Mo (ENDF/B)	Mo (Mod)[a]	Mo (Mod)[b]
Extrapolated height, cm	124.753	124.753	124.753	120.908	124.166	124.166	124.166	122.781
Inner-zone enrichment	0.11705	0.13476	0.13027	0.13100	0.10959	0.11793	0.11564	0.11604
Outer-zone enrichment	0.14509	0.16011	0.15590	0.15884	0.14563	0.15366	0.15118	0.15018
Core-conversion ratio	0.93468	0.80374	0.84215	0.82726	0.97658	0.90300	0.92692	0.92175
Reactor breeding ratio	1.48150	1.32485	1.34984	1.31552	1.54827	1.45870	1.47486	1.45069
Critical mass, kg	2297.06	2580.69	2504.56	2536.77	2326.35	2476.68	2432.92	2443.02
Sodium-void extrapolated height, cm	129.389	129.389	129.389	125.384	129.458	129.458	129.458	129.333
Sodium void, Δk	0.01548	0.03004	0.02650	0.02530	0.01680	0.02489	0.02287	0.02114
Doppler coefficient $\left(T\frac{dk}{dT}\right)$	−0.0060	−0.00255	−0.00337	−0.00330	−0.00615	−0.00389	−0.00440	−0.00443

[a] Incorporates the data of Kallfelz and Poenitz[1] to correct for capture which is too high in ENDF/B.
[b] Same as footnote a, but with molybdenum cladding in axial blanket as well.

TABLE II-37-VII. DIMENSIONS FOR FUEL CYCLE COMPARISONS

	Radial Dimensions	
	Ring	Radius, cm
Core zone 1	1	7.60
	2	20.10
	3	33.11
	4	46.21
	5	59.33
	6	72.46
	7	87.38
Core zone 2	8	96.98
	9	107.07
Core zone 3	10	123.70
Radial blanket	11	136.94
	12	150.21
Reflector	13	163.40
	Axial Dimensions (Axial Symmetry Assumed)[a]	
	Region	Height, cm
Core	1	38.10
Axial blanket	2	50.80
	3	63.50
	4	76.20
Reflector	5	129.54

[a] Axial regions extend radially through all radial rings. Radial blanket and reflector replace "axial blanket" designations outside outer core radius.

against two-dimensional methods in the past and found to be valid. The solution technique proceeds in the following manner. For each core, the first step is to find the enrichment of the inner core zone by running an axial enrichment search to criticality. Then, preliminary to the outer zone enrichment calculation, a bare core extrapolated height search to $k = 1.0$ is carried out using the enrichments just found. Then, the outer zone enrichment if found by running a radial enrichment search in that zone to $k = 1.0$. For this, the enrichments found for the inner zone are used, and the extrapolated height is assumed uniform across the reactor. No effort is made to obtain an outer zone extrapolated height. Furthermore, the inner zone extrapolated height is calculated only for the reference cores and used for the refractory core outer zone searches. The Doppler coefficients are calculated with full sodium, considering a change in U-238 temperature from 1100 to 1500°K. The change in k is assumed to be given by

$$\Delta k = A \int_{T_1}^{T_2} \frac{dT}{T},$$

where A is the Doppler coefficient. The sodium void Δk values are found by first carrying out a slab k-calculation with the sodium removed from the core and axial blanket, and running a bare-core extrapolated height search to the appropriate k-value. This extrapolated height (which is calculated only for the reference core and used for all of the cores) is then used in a radial calculation with the sodium removed from the core (but not from the radial blanket). The breeding ra[illegible] are calculated using an empirical method that has been found to agree quite well with two-dimensional fuel-cycle calculations.

RESULTS

Tables II-37-V and II-37-VI contain the results for both idealized cores. The results of Table II-37-V are for cases where there is no refractory material in the axial blanket. Since vanadium-clad cores have nearly the same breeding ratios, lower enrichments, and better safety characteristics than the reference cores, vanadium looks promising from a neutronic point of view.

Molybdenum and niobium cores have less desirable neutronic characteristics. (There is some evidence, however, that the ENDF/B file for niobium may require revision.) Their sodium void coefficients are quite high, and their Doppler coefficients are less negative than those of the reference cores. Their enrichments are higher and their breeding ratios are lower than those of the reference cores and the vanadium cores. Their critical masses are also larger. Furthermore, their performance characteristics deteriorate more rapidly with increasing cladding thickness than do those of stainless steel and vanadium; it should not be forgotten that even a 10 mil thickness may be too low for a practical design. The same comments are true for molybdenum, even with the corrected capture cross sections (see Table II-37-VI). When molybdenum cladding is also placed in the axial blanket, the neutronic characteristics are slightly worse, because of the increased capture cross section.

Fuel Cycle Comparisons

The reference reactor for the 1000 MWe Follow-on Study had the same volume fractions as those listed for Core 1 in Table II-37-II. The reactor dimensions differed, however; these are given in Table II-37-VII. Calculations were made for the "Reference" and "Mo Clad" cases only. Each core zone was divided into burnup regions, denoted as "Rings" in Table II-37-VII.

The calculations were carried out with the two-dimensional synthesis fuel cycle program SYNBURN which has been checked with favorable results against the direct two-dimensional fuel cycle code REBUS. The equilibrium calculation with fixed-feed isotopic distribution was performed; cycle time was adjusted to achieve a core average discharge burnup of 104,500 MWD/TONNE and charge enrichment was adjusted so that the unpoisoned k_{eff} at the end of cycle was 1.0. Fluxes were recalculated at each of five time nodes during the converged cycle time of 309.5 full-power days. Tantalum shim control (in ring 9) was adjusted

TABLE II-37-VIII. Mid-Equilibrium Cycle Loadings

Reference

Isotope, kg	Core			Axial Blanket	Radial Blanket	
	Zone 1	Zone 2	Zone 3		Row 1	Row 2
U-235	0	0	0	37	18	22
U-238	5290	2500	2500	14660	7660	8520
Pu-239	633	387	387	274	160	126
Pu-240	277	182	184	9	5	4
Pu-241	85	65	64	~0	~0	~0
Pu-242	37	25	25	~0	~0	~0

Molybdenum Cladding

U-235	0	0	0	40	20	23
U-238	5113	2402	2411	14749	7715	8565
Pu-239	703	453	457	201	117	90
Pu-240	319	215	218	4	3	2
Pu-241	103	82	83	~0	~0	~0
Pu-242	43	29	29	~0	~0	~0

TABLE II-37-IX. Charge and Discharge Masses

Reference

	Charge Masses					
	U-235	U-238	Pu-239	Pu-240	Pu-241	Pu-242
Core	0	5045	640	280	133	35
Axial blanket	20	6867	0	0	0	0
Radial blanket	14	4783	0	0	0	0
Total	34	16695	640	280	133	35
	Discharge Masses					
Core	0	4437	628	299	72	41
Axial blanket	14	6571	234	12	~0	~0
Radial blanket	10	4584	158	8	~0	~0
Total	24	15592	1020	319	72	41

Molybdenum Cladding

	Charge Masses					
	U-235	U-238	Pu-239	Pu-240	Pu-241	Pu-242
Core	0	4827	767	336	160	42
Axial blanket	20	6867	0	0	0	0
Radial blanket	14	4783	0	0	0	0
Total	34	16477	767	336	160	42
	Discharge Masses					
Core	0	4310	690	342	92	48
Axial blanket	16	6650	177	6	~0	~0
Radial blanket	11	4639	120	4	~0	~0
Total	27	15599	987	352	92	48

at each of these nodes to maintain criticality. Scatter-reload fuel management was used. In core zones 1 and 2, half of the subassemblies were refueled at each cycle. In core zone 3, one third were refueled (zone 3 differs from zone 2 only in the batch fraction). The inner radial blanket was refueled in thirds, and the outer in quarters. The time-integrated breeding ratio for the equilibrium system was 1.43 for the reference system with stainless steel clad. (The differences in geometry between this reactor and the core-1 idealized reactor account for the difference between 1.48 in that case and 1.43 in this case.) The breeding ratio for the reactor with Mo-clad fuel was 1.23.

The mid-cycle masses of the reference and molybdenum-clad alternate are given in Table II-37-VIII and the charge and discharge masses appear in Table II-37-IX. Note that the core fissile inventory is higher for the molybdenum-clad case than for the stainless steel-clad case. However, the poorer breeding characteristics of the molybdenum-clad alternate are reflected in the smaller net fissile mass gain per cycle than for the stainless steel cladding reference reactor. The breeding ratio penalty of 0.2 due to use of molybdenum is an indication of the economic effects to be expected. The main reservation to be placed on this conclusion is that the reference reactor is typical of a very advanced design using stainless steel for cladding and subassembly wrappers. The breeding ratio penalty for use of molybdenum cladding would be less if the reference design were more typical of a first-generation commercial plant, and if account were taken of the better strength properties of molybdenum in the alternate design.

Summary

In summary, it may be stated that molybdenum and niobium cores have less desirable neutronic characteristics than do stainless steel cores. This is true not only in terms of economic performance but their reactivity coefficients are such that they would be less safe than a stainless steel clad core. Vanadium, on the other hand, is nearly as good as stainless steel economically, and is even slightly better for safety. It also, like stainless steel, leads to performance characteristics that are less sensitive to volume fraction changes than those of molybdenum and niobium.

References

1. J. M. Kallfelz and W. P. Poenitz, *Fast Reactor Calculations with Consistent Sets for Some Important Neutron Cross Sections*, Reactor Physics Division Annual Report, July 1, 1967 to June 30, 1968, ANL-7410, pp. 191–197.

II-38. Parametric Study of Neutronic Characteristics of LMFBR Types

J. T. Madell and R. Abington

Introduction

A parametric study was performed to investigate the neutronic characteristics of LMFBR systems having various fuel materials, core compositions and core volumes. The investigation included oxide, carbide, nitride and metal alloy fueled systems of three fuel volume fractions and two core volumes. The range of the parameters was selected to include the values which would be of interest to the designers of LMFBR's. An attempt was also made to choose the parametric value so that comparisons of neutron characteristics could be made among systems having different fuel types or core volumes or core compositions. The purpose of the parametric study was to assist the LMFBR designer in approximating the effects of modifications to core design on the neutronic properties of the system.

Definition of the Study

The four fuel types (oxide, carbide, nitride and metal alloy) represent a rather broad group of possible fuels for an LMFBR. Two core volumes of 3500 and 5500 liters were chosen to bracket the values found in various 1000 MWe studies. The size and shape of an LMFBR is strongly influenced by the thermal hydraulic properties and, in turn, has a significant effect on the neutronic quantities of the reactor. Since no thermal hydraulic calculations were included in the study, the optimized core size and shape for the various fuel types and core compositions were not available. The parameter of reactor geometry was given a very limited range by considering only spherical reactors with 3500 and 5500 liter cores. The use of a simplified geometrical representation of the LMFBR limits the study to estimating the relative effects of the

e parameters on the neutronic properties of the pes of systems considered.

Selection of Core Composition

The volume fractions of the components (fuel, steel and sodium) were selected within the range of the volume fractions found in various 1000 MWe LMFBR studies. There was some bias, however, in favor of high performance (high fuel content, high breeding ratio) systems. For the ceramic fueled systems with 5500 liter cores, fuel volume fractions of 35, 40, and 45% were selected. The middle value of 40% yields an acceptable specific power rating of ~120 kW/kg of heavy atoms. Sodium and steel fractions of 40 and 20% for the case of a 5500 liter core with 40% ceramic fuel seemed reasonable in light of thermal hydraulic calculations for similar systems. Equal volume fractions of sodium and steel are exchanged for fuel in altering the case with 40% fuel to those having 35 and 45% fuel. There is some rationale for changing volume fractions by such a method. A decrease in the fuel fraction, for example, may result from a smaller pin size, which in turn necessitates a relatively larger fraction of steel cladding. To retain the attractiveness of a core with a smaller pin size, the linear heat rating may be increased and thereby a relatively higher sodium fraction is provided. Thus a decrease in the fuel fraction results in an increase of both the sodium and steel fractions. The above line of reasoning assumes that the fuel subassembly design was initially somewhere near an optimum. The fuel fractions for the 3500 liter core was 5% lower while the sodium was 5% higher than their counterparts for the 5500 liter core. The lower fuel (30, 35, and 40%) and corresponding higher sodium volume fractions were specified to achieve the higher power density ratings of the smaller cores.

The volume fraction of the metal alloy fuel was 5% lower than its ceramic counterparts for the 3500 and 5500 liter cores. The lower temperature limitation of the metal fuel requires smaller pins and more sodium than the ceramic fuels. The core compositions for the four fuel types and two core volumes are given in Table II-38-I. In addition to these compositions, two variations of ±5 v/o in the sodium and the steel content (+5 v/o sodium, −5 v/o steel and −5 v/o sodium, +5 v/o steel) were made for each fuel volume fraction. In total, nine calculations were performed for each of the four fuel types and two core volumes.

Description of Calculational Method

The calculations were performed with the one-di- sional diffusion theory code MACH-1,[1] and a 26 group cross section set (see Paper II-39). The reactor

TABLE II-38-I. Description of Systems for Parametric Study

	Base Case	Fuel Type (% TD)					
		Oxide, Carbide, Nitride (85%)			U, Pu-10 w/o Zr (70%)		
		Fuel	Sodium	Steel	Fuel	Sodium	Steel
Core volume = 3500 liters with 20 cm thick blanket							
Core Volume Fractions	1	30	47.5	22.5	25	50	25
	2	35	45	20	30	47.5	22.5
	3	40	42.5	17.5	35	45	20
Core volume = 5500 liters with 25 cm thick blanket							
Core Volume Fractions	4	35	42.5	22.5	30	50	20
	5	40	40	20	35	47.5	17.5
	6	45	37.5	17.5	40	45	15

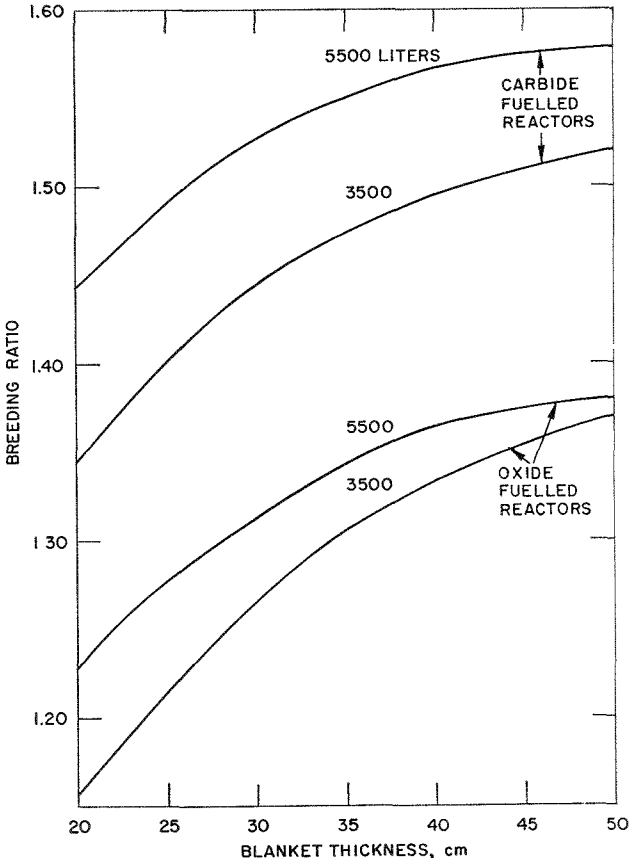

Fig. II-38-1. Breeding Ratio of Oxide and Carbide Reactors with 3500 and 5500 liter Cores as a Function of Blanket Thickness. *ANL Neg. No. 116-484.*

was represented by a four region sphere corresponding to two equal-volume core segments, a depleted-uranium blanket of the same fuel type as the core, and a steel reflector. The plutonium content in the outer core region was maintained at 50% higher level than in the inner core region. The fuel composition was adjusted to simulate that obtained at mid-cycle of a 10 a/o burnup SYNBURN[2] calculation, yielding an isotopic distribution for plutonium of 66% Pu-239, 28% Pu-240, 4% Pu-241, 2% Pu-242, and for uranium of 0.1% U-235 and 99.9% U-238. To represent mid-cycle conditions, 5% of the initial heavy atom density was replaced with fission product pairs and 0.5 v/o of tantalum in the outer core region represented the control requirements.

The blanket, whose composition was chosen to be representative of the radial blanket composition of an LMFBR, comprised 55 v/o depleted uranium fuel, 30 v/o sodium and 15 v/o steel, and the steel reflector consisted of 80 v/o steel and 20 v/o sodium.

The blanket regions of an LMFBR is very difficult to represent by a spherical model. The axial and radial blankets usually contain appreciably different amounts of fuel and coolant but only one blanket region can be adjacent to the core in a spherical representation. Also, the blanket volume in cylindrical geometry is difficult to relate to that in spherical geometry.

In the parametric study the breeding ratio was designated as one of the major figures of merit. Accordingly, the blanket volume was selected by varying the blanket thickness for both the 3500 and 5500 liter oxide-fueled cores to approximate the breeding ratio calculated by the SYNBURN code for cores of similar composition and size. The breeding ratio is plotted for various blanket thicknesses in Fig. II-38-1 for oxide and carbide-fueled reactors of 3500 and 5500 liter cores, Cases 2 and 5, respectively. Blanket thicknesses of 20 and 25 cm were selected for the 3500 and 5500 liter cores, respectively. Altering the blanket thickness between 20 and 50 cm had a small effect on such characteristics as the enrichment and the core conversion ratio. The values of ℓ_p and β also changed little with the blanket thickness.

A plutonium enrichment search to a k_{eff} of unity was performed for each reactor system described in Table II-38-I, and perturbation, β, lifetime and reaction summary calculations were carried out for the critical system. The results of the MACH-1 calculations of the four fuel types and two core volumes are presented in Tables II-38-II through II-38-IX. In the following paragraphs the trends in the breeding ratio, the Doppler effect, sodium void coefficient, and the reactivity worth of the core materials are discussed.

Breeding Ratio

The breeding ratio supplies useful information for evaluating the attractiveness of an LMFBR design, and may be estimated without a detailed fuel cycle calculation. The breeding ratios of the reactors with the four fuel types are plotted as a function of the heavy atom density for the two core volumes in Figs. II-38-2 and II-38-3, and as a function of fuel volume fraction for the two core volumes in Figs. II-38-4 and II-38-5. For all types of fuels the breeding ratio increases appreciably with increasing fuel concentration, either in terms of fuel volume fraction or heavy atom density. Upon comparing the breeding ratio of reactors with different fuels in Figs. II-38-4 and II-38-5 the influence on the light elements in the fuel is seen. For a given fuel fraction, the metal alloy fuel with no light elements has the highest breeding ratio and the oxide fuel with two atoms of oxygen for each heavy atom produces the lowest breeding ratio. Intermediate breeding ratios result from the nitride and carbide fuels with intermediate light element concentrations. The substantially different breeding ratios for the nitride and carbide-fueled systems which have identical light and heavy atom densities is due to parasitic capture in nitrogen. This subject is covered in more detail in the section "Comments on Nitride Fuels."

The breeding ratio of the oxide-fueled reactors with 5500 liter cores is plotted in Fig. II-38-6 for the three sets of sodium and steel concentrations associated with each of the three fuel fractions. Replacing 5 a/o of steel with sodium for a given colume fraction of fuel increases the value of the breeding ratio by 0.03–0.04. The effect of exchanging steel and sodium on the breeding ratio is the same for the other fuel types and the other core volume.

A larger core volume produces a larger breeding ratio, as is seen by comparing Figs. II-38-4 and II-38-5. Both the thicker blanket and the higher fertile material concentration found in the larger core contribute to the larger breeding ratio.

Doppler Effect

The Doppler effect for each core composition was obtained from the perturbation calculations in which the reactivity worth of U-238 at 1300°K was compared with that of U-238 at 2500°K. The magnitude of Doppler effect is very sensitive to the neutron spectrum. A factor which reduces the flux spectrum in the U-238 resonance region (usually by hardening the spectrum) will decrease the magnitude of the U-238 Doppler effect.

Three factors which have a significant influence the neutron spectrum and thus on the Doppler effect,

TABLE II-38-II. Results from a Parametric Study in Spherical Geometry for Oxide-Fueled Fast Reactors with a 3500 Liter Core and 20 cm Thick Blanket

Volume fractions, % Fuel	35			40			30		
Na/SS	45/20	40/25	50/15	42½/17½	37½/22½	47½/12½	47½/22½	42½/27½	52½/17½
Inner core									
% Pu	17.9	18.4	17.6	16.4	16.8	16.1	20.1	20.5	19.8
% Enrichment	12.6	13.1	12.5	11.6	11.9	11.4	14.2	14.5	14.0
Median energy flux									
Source, keV	291	280	304	318	306	334	264	255	275
Absorption, keV	50	49	51	53	52	54	46	45	47
Core conv. ratio	0.756	0.741	0.771	0.838	0.821	0.856	0.667	0.655	0.680
Breeding ratio	1.157	1.124	1.194	1.229	1.194	1.268	1.081	1.049	1.115
Core loading, kg									
Pu-239 + Pu-241	1396	1424	1367	1453	1484	1422	1335	1360	1308
U-238	6820	6779	6861	7995	7951	8040	5649	5612	5686
Reactivity worths, $\Delta k/k$									
Doppler $\times 10^3$	−4.433	−4.440	−4.274	−4.286	−4.357	−4.156	−4.423	−4.463	−4.334
Na void $\times 10^2$	2.204	1.990	2.413	2.333	2.063	2.610	1.969	1.829	2.093
1 v/o Pu fuel $\times 10$	1.001	0.998	1.024	0.965	0.954	0.978	1.061	1.048	1.074
1 v/o U fuel $\times 10^3$	−7.665	−7.800	−7.505	−7.283	−7.393	−7.154	−8.113	−8.276	−7.918
1 v/o SS $\times 10^3$	−2.969	−2.897	−3.061	−3.135	−3.033	−3.263	−2.779	−2.743	−2.830
1 v/o Na $\times 10^4$	−4.900	−4.980	−4.827	−5.490	−5.501	−5.494	−4.145	−4.304	−3.987
Kinetic parameters									
$\beta \times 10^3$	2.966	2.905	3.034	3.073	3.009	3.144	2.845	2.793	2.914
$\ell \times 10^7$, sec	4.192	4.174	4.200	3.761	3.749	3.763	4.718	4.691	4.733

TABLE II-38-III. Results from a Parametric Study in Spherical Geometry for Carbide-Fueled Fast Reactors with a 3500 Liter Core and 20 cm Thick Blanket

Volume fractions, % Fuel	35			40			30		
Na/SS	45/20	40/25	50/15	42½/17½	37½/22½	47½/12½	47½/22½	42½/27½	52½/17½
Inner core									
% Pu	15.8	16.1	15.5	14.5	14.8	14.2	17.6	18.0	17.3
% Enrichment	11.2	11.4	16.0	10.2	10.5	10.0	12.4	12.7	12.2
Median energy flux									
Source, keV	256	247	268	279	268	292	234	226	244
Absorption, keV	61	60	62	64	63	65	57	56	58
Core conv. ratio	0.903	0.886	0.920	0.993	0.973	1.013	0.805	0.791	0.820
Breeding ratio	1.343	1.306	1.384	1.418	1.379	1.460	1.263	1.227	1.302
Core loading, kg									
Pu-239 + Pu-241	1543	1573	1511	1557	1647	1579	1468	1496	1440
U-238	9593	9549	9638	11175	11128	11224	8015	7976	8056
Reactivity worths, $\Delta k/k$									
Doppler $\times 10^3$	−4.150	−4.212	−4.049	−4.008	−4.077	−3.961	−4.261	−4.316	−4.174
Na void $\times 10^2$	2.622	2.341	2.906	2.680	2.354	3.016	2.462	2.242	2.674
1 v/o Pu fuel $\times 10$	1.307	1.292	1.322	1.240	1.225	1.254	1.382	1.367	1.397
1 v/o U fuel $\times 10^3$	−7.471	−7.610	−7.313	−7.042	−7.150	−6.922	−7.990	−8.165	−7.788
1 v/o SS $\times 10^3$	−3.500	−2.919	−3.118	−3.141	−3.029	−3.277	−2.844	−2.784	−2.921
1 v/o Na $\times 10^4$	−5.826	−5.852	−5.812	−6.305	−6.276	−6.350	−5.182	−5.276	−5.094
Kinetic parameters									
$\beta \times 10^3$	3.124	3.064	3.189	3.227	3.166	3.293	3.008	2.951	3.072
$\ell \times 10^7$, sec	3.233	3.231	3.227	2.874	2.875	2.866	3.680	3.674	3.677

TABLE II-38-IV. Results from a Parametric Study in Spherical Geometry for Nitride-Fueled Fast Reactors with a 3500 Liter Core and 20 cm Thick Blanket

Volume fractions, % Fuel	35			40			30		
Na/SS	45/20	40/25	50/15	42½/17½	37½/22½	47½/12½	47½/22½	42½/27½	52½/17½
Inner core									
% Pu	16.4	16.7	16.1	15.0	15.3	14.8	18.2	18.4	17.8
% Enrichment	11.6	11.8	11.4	10.6	10.8	10.5	12.8	13.0	12.6
Median energy flux									
Source, keV	291	280	304	318	306	334	264	256	275
Absorption, keV	87	85	91	95	92	98	79	77	82
Core conv. ratio	0.834	0.822	0.847	0.913	0.899	0.928	0.749	0.739	0.760
Breeding ratio	1.252	1.221	1.284	1.314	1.283	1.348	1.183	1.154	1.215
Core loading, kg									
Pu-239 + Pu-241	1598	1624	1570	1676	1705	1646	1517	1541	1492
U-238	9514	9476	9553	11087	11045	11130	7947	7911	7982
Reactivity worths, $\Delta k/k$									
Doppler $\times 10^3$	−4.167	−4.221	−4.079	−4.041	−4.103	−3.947	−4.260	−4.305	−4.181
Na void $\times 10^2$	2.274	2.069	2.466	2.350	2.099	2.595	2.098	1.960	2.219
1 v/o Pu fuel $\times 10$	1.242	1.231	1.251	1.174	1.164	1.184	1.317	1.307	1.327
1 v/o U fuel $\times 10^3$	−7.479	−7.624	−7.313	−7.023	−7.140	−6.890	−8.035	−8.212	−7.830
1 v/o SS $\times 10^3$	−2.537	2.497	−2.590	−2.644	−2.584	−2.720	−2.402	−2.396	−2.426
1 v/o Na $\times 10^4$	−5.053	−5.173	−4.932	−5.528	−5.597	−5.462	−4.417	−4.601	−4.227
Kinetic parameters									
$\beta \times 10^3$	3.183	3.120	3.252	3.293	3.229	3.364	3.060	3.000	3.127
$\ell \times 10^7$, sec	3.151	3.152	3.143	2.800	2.803	2.791	3.589	3.587	3.583

TABLE II-38-V. Results from a Parametric Study in Spherical Geometry for Metal-Fueled Fast Reactors with a 3500 Liter Core and 20 cm Thick Blanket

Volume fractions, % Fuel	30			35			25		
Na/SS	47½/22½	42½/27½	52½/17½	45/20	40/25	50/15	50/25	45/30	55/20
Inner core									
% Pu	16.0	16.3	15.7	14.1	14.4	13.9	17.3	17.6	17.0
% Enrichment	11.3	11.5	11.1	10.0	10.2	9.8	12.2	12.4	12.0
Median energy flux									
Source, keV	310	299	323	343	330	358	267	258	277
Absorption, keV	124	121	128	137	134	142	106	102	111
Core conv. ratio	0.779	0.770	0.789	0.878	0.867	0.889	0.690	0.683	0.697
Breeding ratio	1.295	1.261	1.333	1.389	1.353	1.428	1.203	1.169	1.239
Core loading, kg									
Pu-239 + Pu-241	1354	1376	1331	1395	1420	1369	1260	1277	1241
U-238	7689	7657	7722	9233	9197	9270	6273	6247	6298
Reactivity worths, $\Delta k/k$									
Doppler $\times 10^3$	−1.990	−2.101	−1.845	−1.704	−1.814	−1.566	−2.366	−2.491	−2.202
Na void $\times 10^2$	3.622	3.343	3.878	3.870	3.514	4.211	2.463	2.372	2.520
1 v/o Pu fuel $\times 10$	1.613	1.601	1.624	1.549	1.538	1.560	1.682	1.671	1.693
1 v/o U fuel $\times 10^3$	−7.922	−8.169	−7.641	−7.268	−7.480	−7.031	−8.780	−9.097	−8.414
1 v/o SS $\times 10^3$	−2.852	−2.823	−2.901	−3.078	−3.018	−3.162	−2.265	−2.291	−2.251
1 v/o Na $\times 10^4$	−7.903	−7.866	−7.387	−8.599	−8.784	−8.421	−4.926	−5.271	−4.581
Kinetic parameters									
$\beta \times 10^3$	3.133	3.067	3.205	3.275	3.206	3.350	3.004	2.942	3.
$\ell \times 10^7$, sec	3.122	3.142	3.093	2.738	2.758	2.710	3.731	3.754	3.6

BLE II-38-VI. Results from a Parametric Study in Spherical Geometry for Oxide-Fueled Fast Reactors with 5500 Liter Core and 25 cm Thick Blanket

Volume fractions, Fuel	40			45			30		
Na/SS	40/20	35/25	45/15	37½/17½	32½/22½	42½/12½	42½/22½	37½/27½	47½/17½
Inner core									
% Pu	15.6	16.0	15.3	14.5	14.9	14.2	17.1	17.5	16.7
% Enrichment	11.1	11.3	10.8	10.3	10.5	10.1	12.1	12.4	11.8
Median energy flux									
Source, keV	206	200	215	223	215	233	190	185	197
Absorption, keV	48	49	48	51	50	52	45	44	46
Core conv. ratio	0.894	0.873	0.917	0.972	0.949	0.997	0.811	0.792	0.831
Breeding ratio	1.274	1.238	1.318	1.345	1.305	1.389	1.202	1.166	1.242
Core loading, kg									
Pu-239 + Pu-241	2170	2221	2118	2260	2314	2204	2074	2122	2026
U-238	12680	12609	12755	14523	14446	14603	10845	10778	10914
Reactivity worths, $\Delta k/k$									
Doppler $\times 10^3$	−4.876	−4.877	−4.807	−4.685	−4.712	−4.583	−5.020	−5.012	−4.983
Na void $\times 10^2$	2.680	2.325	3.041	2.642	2.255	3.048	2.650	2.344	2.957
1 v/o Pu fuel $\times 10$	1.017	1.000	1.034	0.969	0.953	0.985	1.071	1.053	1.088
1 v/o U fuel $\times 10^3$	−8.204	−8.242	−8.128	−7.747	−7.779	−7.704	−8.714	−8.780	−8.625
1 v/o SS $\times 10^3$	−3.551	−3.420	−3.709	−3.649	−3.494	−3.839	−3.440	−3.338	−3.564
1 v/o Na $\times 10^4$	−6.700	−6.644	−6.758	−7.045	−6.939	−7.172	−6.235	−6.251	−6.225
Kinetic parameters									
$\beta \times 10^3$	3.045	2.985	3.116	3.145	3.080	3.216	2.942	2.883	3.007
$\ell \times 10^7$, sec	3.945	3.915	3.961	3.547	3.527	3.558	4.423	4.385	4.451

TABLE-38-VII. Results from a Parametric Study in Spherical Geometry for Carbide-Fueled Fast Reactors with a 5500 Liter Core and 25 cm Thick Blanket

Volume fractions, % Fuel	40			45			35		
Na/SS	40/20	35/25	45/15	37½/17½	32½/22½	42½/12½	42½/22½	37½/27½	47½/17½
Inner core									
% Pu	12.8	13.1	12.5	11.9	12.1	11.6	13.9	14.2	13.6
% Enrichment	9.1	9.3	8.9	8.4	8.6	8.3	9.7	10.0	9.6
Median energy flux									
Source, keV	278	268	289	300	289	315	255	247	265
Absorption, keV	63	62	64	66	65	67	59	58	60
Core conv. ratio	1.085	1.061	1.111	1.167	1.141	1.609	0.997	0.975	1.020
Breeding ratio	1.491	1.453	1.537	1.564	1.523	1.695	1.417	1.379	1.460
Core loading, kg									
Pu-239 + Pu-241	2521	2575	2462	2639	2698	2578	2395	2446	2341
U-238	18825	18748	18908	21457	21374	21544	16203	16130	16279
Reactivity worths, $\Delta k/k$									
Doppler $\times 10^3$	−4.230	−4.245	−4.161	−4.003	−4.035	−3.942	−4.445	−4.465	−4.396
Na void $\times 10^2$	3.046	2.262	3.483	2.909	2.472	3.368	3.127	2.734	3.532
1 v/o Pu fuel $\times 10$	1.239	1.220	1.257	1.168	1.151	1.186	1.318	1.298	1.338
1 v/o U fuel $\times 10^3$	−7.487	−7.508	−7.437	−7.008	−7.020	−6.992	−8.033	−8.088	−7.966
1 v/o SS $\times 10^3$	−3.454	−3.315	−3.618	−3.488	−3.335	−3.668	−3.401	−3.280	−3.544
1 v/o Na $\times 10^4$	−7.614	−7.496	−7.741	−7.757	−7.607	−7.925	−7.358	−7.290	−7.435
Kinetic parameters									
[redacted] $\times 10^3$	3.245	3.190	3.309	3.336	3.278	3.398	3.147	3.090	3.209
[redacted] $\times 10^7$, sec	2.743	2.732	2.745	2.445	2.439	2.446	3.109	3.095	3.116

TABLE II-38-VIII. Results from a Parametric Study in Spherical Geometry for Nitride-Fueled Fast Reactors with a 5500 Liter Core and 25 cm Thick Blanket

Volume fractions, % Fuel	40			45			35		
Na/SS	40/20	35/25	45/15	37½/17½	32½/22½	42½/12½	42½/22½	37½/27½	47½/17½
Inner core									
% Pu	13.2	13.5	12.9	12.3	12.6	12.1	14.3	14.6	14.0
% Enrichment	9.4	9.5	9.2	8.7	8.9	8.6	10.1	10.3	9.9
Median energy flux									
Source, keV	315	304	329	343	330	359	287	278	298
Absorption, keV	90	88	92	97	95	99	82	80	84
Core conv. ratio	1.008	0.989	1.027	1.078	1.058	1.100	0.930	0.913	0.947
Breeding ratio	1.392	1.359	1.428	1.451	1.418	1.488	1.327	1.294	1.363
Core loading, kg									
Pu-239 + Pu-241	2602	2653	2550	2732	2785	2677	2468	2515	2419
U-238	18709	18637	18782	21325	21250	21404	16100	16033	16169
Reactivity worths, $\Delta k/k$									
Doppler $\times 10^3$	−4.283	−4.309	−4.228	−4.070	−4.104	−4.009	−4.501	−4.518	−4.455
Na void $\times 10^2$	2.830	2.467	3.197	2.712	2.330	3.102	2.897	2.563	3.228
1 v/o Pu fuel $\times 10$	1.184	1.170	1.198	1.115	1.102	1.128	1.262	1.247	1.277
1 v/o U fuel $\times 10^3$	−7.526	−7.569	−7.473	−7.042	−7.068	−7.010	−8.104	−8.167	−8.026
1 v/o SS $\times 10^3$	−3.037	−2.945	−3.146	−3.057	−2.952	−3.179	−3.002	−2.925	−3.092
1 v/o Na $\times 10^4$	−7.075	−7.049	−7.104	−7.232	−7.169	−7.300	−6.817	−6.835	−6.800
Kinetic parameters									
$\beta \times 10^3$	3.309	3.248	3.376	3.405	3.343	3.472	3.202	3.142	3.268
$\ell \times 10^7$, sec	2.690	2.683	2.692	2.399	2.395	2.398	3.053	3.042	3.058

TABLE II-38-IX. Results from a Parametric Study in Spherical Geometry for Metal-Fueled Fast Reactors with a 5500 Liter Core and 25 cm Thick Blanket

Volume fractions, % Fuel	35			40			30		
Na/SS	47½/17½	42½/22½	52½/12½	45/15	40/20	50/10	50/20	45/25	55/15
Inner core	12.9	13.2	12.6	11.6	11.9	11.4	14.6	14.9	14.3
% Enrichment	9.2	9.4	9.0	8.3	8.5	8.1	10.3	10.6	10.1
Median energy flux									
Source, keV	337	324	354	371	356	391	302	292	316
Absorption, keV	127	124	130	139	136	143	113	110	117
Core conv. ratio	0.981	0.963	0.999	1.079	1.059	1.101	0.875	0.860	0.891
Breeding ratio	1.511	1.465	1.561	1.605	1.557	1.659	1.409	1.365	1.457
Core loading, kg									
Pu-239 + Pu-241	2008	2052	1961	2063	2111	2013	1943	1984	1901
U-238	14771	14708	14837	17209	17141	17281	12345	12287	12405
Reactivity worths, $\Delta k/k$									
Doppler $\times 10^3$	−1.967	−2.079	−1.821	−1.672	−1.775	−1.540	−2.325	−2.043	−2.174
Na void $\times 10^2$	5.144	4.647	5.638	5.197	4.641	5.755	4.941	4.522	5.346
1 v/o Pu fuel $\times 10$	1.686	1.668	1.703	1.617	1.595	1.634	1.763	1.744	1.781
1 v/o U fuel $\times 10^3$	−8.346	−8.518	−8.149	−7.742	−7.884	−7.585	−9.139	−9.344	−8.898
1 v/o SS $\times 10^3$	−3.802	−3.690	−3.947	−3.981	−3.842	−4.159	−3.590	−3.512	−3.696
1 v/o Na $\times 10^4$	−1.083	−1.094	−1.074	−1.155	−1.160	−1.151	−0.988	−1.005	−0.972
Kinetic parameters									
$\beta \times 10^3$	3.319	3.245	3.401	3.451	3.375	3.534	3.175	3.104	3.253
$\ell \times 10^7$, sec	2.902	2.920	2.875	2.568	2.586	2.542	3.338	3.354	3.311

are the U-238 concentration, the fuel type, and the core size. Since the presence of U-238 depresses the flux in the resonance region, the U-238 Doppler effect is smaller for cores containing greater amounts of U-238, either on a per atom basis or on a total U-238 a basis. Cores containing a fuel type with lower he atom density and higher light element density exhibit a softer spectrum and thus a larger (more negative)

Doppler effect. The fuel types in order of decreasing Doppler effect are oxide, nitride, carbide and metal. The neutronic characteristics of a large core, such as low fuel concentration, result in a soft spectrum and thus an enhanced Doppler effect.

Worth of Sodium Voiding of the Core

The reactivity worth of total sodium voiding of the core was obtained from first order perturbation calculations in which all of the sodium was removed from the core and none was removed from either the blanket or reflector. Voiding of the core sodium produces both a positive reactivity effect due to spectrum hardening and a negative reactivity effect due to increased leakage. In the cases presented here, the effect of spectrum hardening dominates that of leakage.

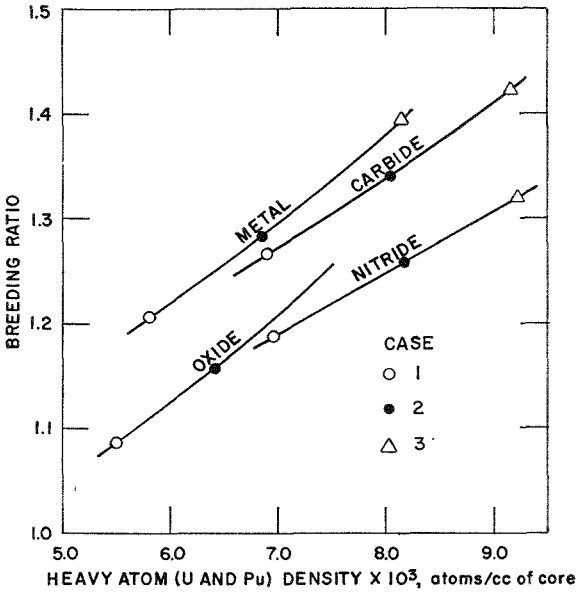

Fig. II-38-2. Breeding Ratio versus Heavy Atom Density of the Four Fuel Types in a 3500 liter Core. *ANL Neg. No. 116-481.*

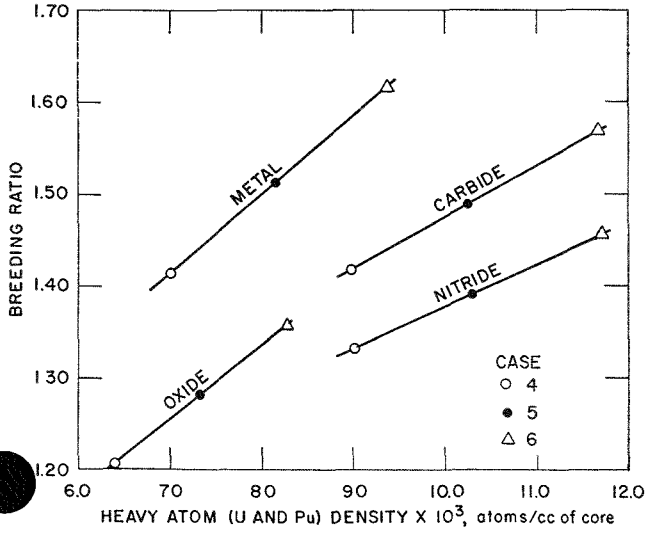

Fig. II-38-3. Breeding Ratio versus Heavy Atom Density of the Four Fuel Types in a 5500 liter Core. *ANL Neg. No. 116-478.*

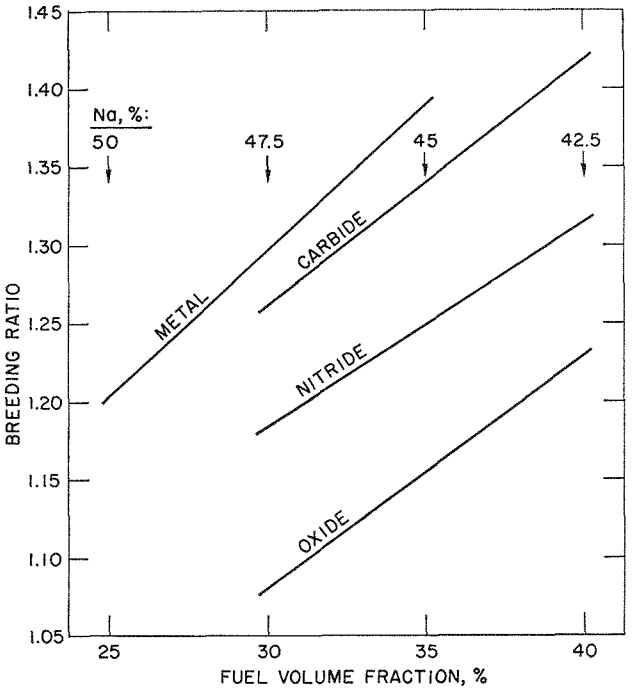

Fig. II-38-4. Breeding Ratio versus Fuel Volume Fraction for Four Fuel Types in a 3500 liter Core. *ANL Neg. No. 116-476.*

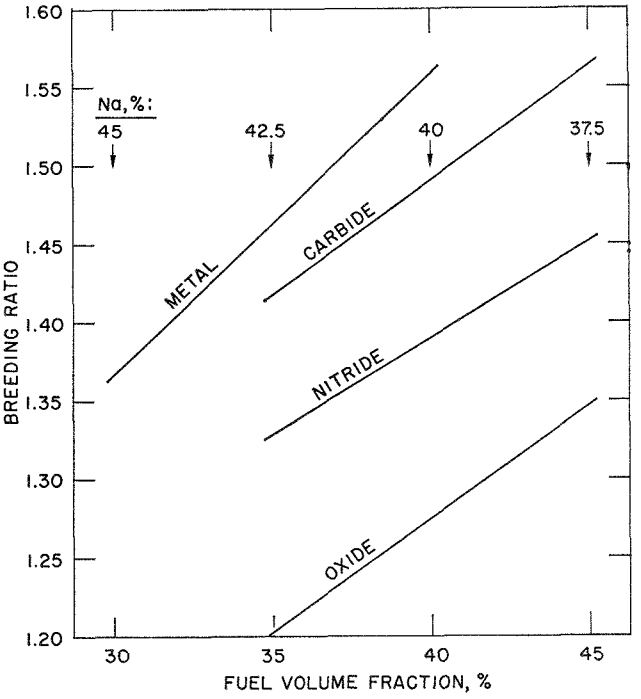

Fig. II-38-5. Breeding Ratio versus Fuel Volume Fraction for Four Types in a 5500 liter Core. *ANL Neg. No. 116-482.*

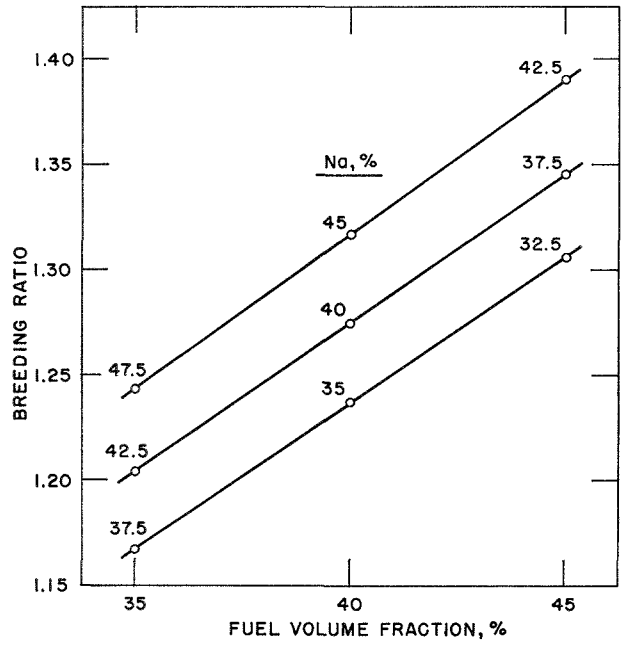

FIG. II-38-6. Breeding Ratio versus Fuel Volume Fraction for Various Core Compositions in an Oxide-Fueled 5000 liter Core *ANL Neg. No. 116-483.*

The three parameters in the study which have a significant influence on the sodium void worth are the sodium content, the core size, and the fuel concentration (also fuel type as it affects the fuel concentration).

The worth of sodium on a per atom basis is fairly insensitive to the sodium content of the core, as is seen from the results from the material worth calculation. Thus, the worth of sodium voiding of a core is almost directly proportional to the sodium content. A smaller core permits greater leakage, has a lower fuel loading for a given fuel fraction, and requires a higher ratio of fissile to fertile material. These three characteristics of a smaller core result in a smaller (less positive) sodium void worth.

Both plutonium and uranium become more reactive (that is, more fission neutrons/absorption) as the spectrum hardens in the LMFBR system considered here; in particular, U-238 is much more reactive as the portion of the flux above its fission threshold energy increases. The cores with larger loadings of U-238 possess larger (more positive) sodium void worths. The fuel material type is related to the sodium worth in the core by the concentration and enrichment of the fuel type that is required for criticality. For the systems considered in the study the sodium worth is largest for the metal-fueled reactors and smallest for the oxide-fueled reactors.

Core Material Worths

The reactivity worths of the core materials (plutonium-fuel, uranium-fuel, steel and sodium) were obtained to provide the data for estimating the reactivity effect of small changes in the core composition. In the study the composition of the core materials were specified in terms of the percentage of the core volume occupied by that material. To obtain reactivity data which is readily usable for evaluating compositional changes the first order perturbation calculations were based on the amount of material which occupies 1 v/o of the core.

There are two trends that are seen in the reactivity worths of all materials. The worth of a given material is smaller in cores which contain larger volume fractions of a given material, and secondly, is also smaller for the cores of larger volume. The relationship between the material worths and the fuel type depends upon the particular material. The fuel type influences the worth of the plutonium-fuel through the amount of plutonium that is required to achieve criticality in a reactor using that fuel type. The uranium fuel worth depends upon the critical concentration and of the fuel type, as well as the light atom concentration. The order of the fuel types which shows the effect of increasing the magnitude of the steel worth is metal, oxide, carbide and nitride fuels. The influence of various parameters on the sodium worth was presented above in the discussion of sodium void worth.

Kinetic Characteristics

The value of β_{eff} varies inversely with the percentage of plutonium in the fuel since the β_{eff} value for plutonium is smaller than that for uranium. The core size, core composition, and fuel type influence the β_{eff} values primarily through their effect on the percentage of plutonium in the fuel required for criticality. The lifetime, ℓ_p, is greater for systems having a softer spectrum. Thus a core of smaller fuel volume fraction (or heavy atom densities), larger volume, or a fuel type containing more light elements exhibit a greater value of ℓ_p. To place the above comments in proper perspective it is noted that both β and ℓ_p are not very sensitive to the changes in the parameters (fuel type, core composition, and volume). In the 72 cases considered in the study the value of β_{eff} varied between 2.79×10^{-3} and 3.54×10^{-3} and the value of ℓ_p between 2.39×10^{-7} and 4.73×10^{-7} sec.

Comments on Nitride Fuels

The results given in the section on "Breeding Ratio" showed that the concentrations of both heavy and light elements in a fuel loading have a significant influence

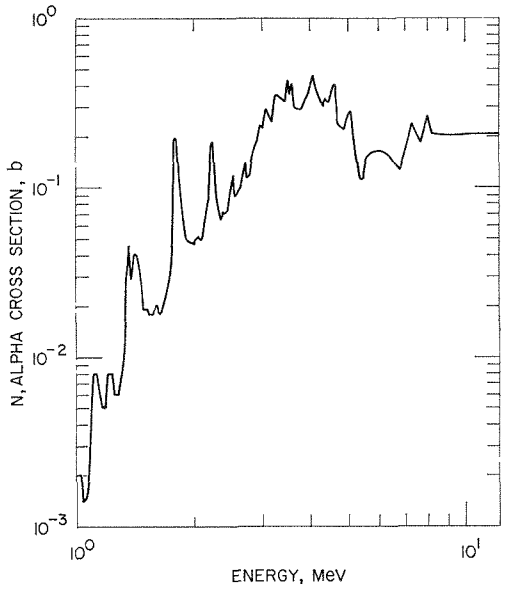

FIG. II-38-7. $N^{14}(n,\alpha)B^{11}$ Cross Section in Barns between 1 and ~10 MeV. *ANL Neg. No. 116-480.*

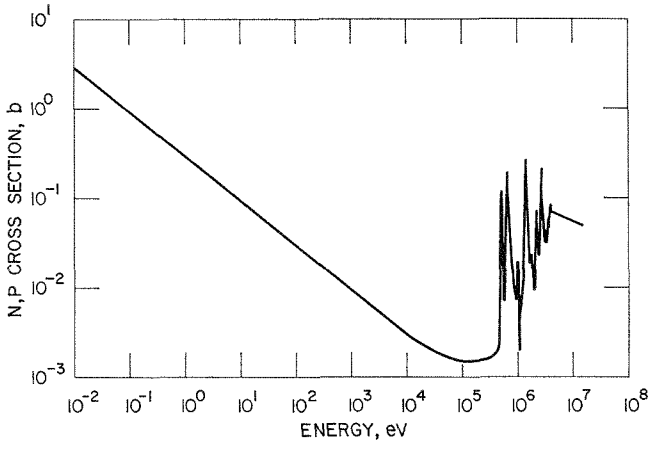

FIG. II-38-8. $N^{14}(n,p)C^{14}$ Cross Section in Barns between 0.01 eV and ~10 MeV. *ANL Neg. No. 116-477.*

on the breeding ratio. The nitride fuel appears to have an anomalous effect on the breeding ratio; although the heavy and light nuclide concentrations in the nitride fuel were specified to be identical to those in the carbide fuel, a nitride-fueled system exhibits ~7% lower breeding and core conversion ratios than those of a carbide system with the same fuel volume fraction. An investigation of the nitride-fueled reactors identified parasitic neutron capture reactions in nitrogen as the major cause of the lower breeding and core conversion ratios.

Capture cross sections for (n,α)*, (n,p) and (n,γ) reactions in N-14 are plotted as a function of energy in Figs. II-38-7 through II-38-9, respectively.[3] The total capture cross sections and reaction rates for total capture for N-14 are tabulated in Table II-38-X for the 26 energy groups. The major portion (~80%) of the

* The (n,α) reaction cross section includes some (n,D) and (n,T) reactions.

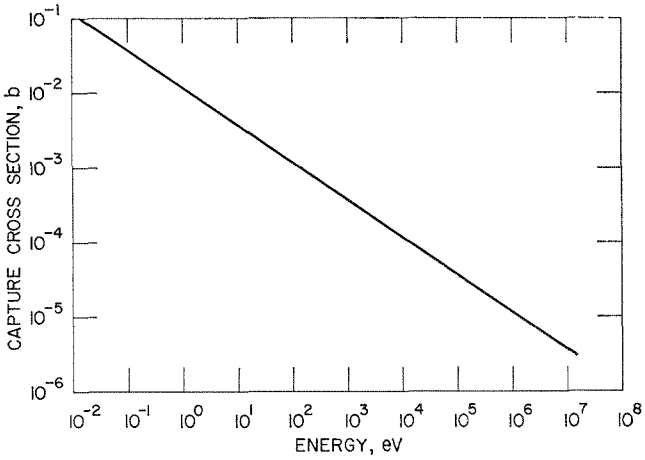

FIG. II-38-9. $N^{14}(n,\gamma)N^{15}$ Cross Section in Barns between ~0.01 eV and ~10 MeV. *ANL Neg. No. 116-479.*

TABLE II-38-X. NITROGEN CAPTURE CROSS SECTIONS, REACTION RATE AND REACTION SPECTRUM IN THE CENTER OF A NITRIDE-FUELED LMFBR BY ENERGY GROUP

Group No.	Lower Energy, eV	σ_c, b	Reaction Rate, 10^{13} captures/cm³-sec	Group Fraction
1	6.07×10^6	0.2405	0.579	0.0374
2	3.68×10^6	0.3459	3.368	0.2180
3	2.23×10^6	0.2334	4.897	0.3169
4	1.35×10^6	0.0987	3.230	0.2090
5	8.21×10^5	0.0179	1.028	0.0665
6	4.98×10^5	0.0054	0.501	0.0324
7	3.02×10^5	0.0066	0.635	0.0411
8	1.83×10^5	0.0016	0.169	0.0109
9	1.11×10^5	0.0015	0.148	0.0096
10	6.74×10^4	0.0016	0.124	0.0080
11	4.09×10^4	0.0017	0.108	0.0070
12	2.48×10^4	0.0020	0.094	0.0061
13	1.50×10^4	0.0024	0.092	0.0059
14	9.12×10^3	0.0029	0.089	0.0057
15	5.53×10^3	0.0037	0.070	0.0046
16	3.35×10^3	0.0047	0.055	0.0035
17	2.04×10^3	0.0063	0.029	0.0019
18	1.23×10^5	0.0078	0.008	0.0052
19	7.49×10^2	0.0099	0.006	0.0042
20	4.54×10^2	0.0126	0.004	0.0029
21	2.75×10^2	0.0162	0.003	0.0017
22	1.67×10^2	0.0206	0.001	0.0008
23	1.01×10^2	0.0263	0.001	0.0004
24	6.14×10^1	0.0336	—	—
25	3.73×10^1	0.0429	—	—
26	2.26×10^1	0.0569	—	—

capture in nitrogen occurs above 1 MeV. In the range from 2.23 to 10 MeV the (n,α) reaction dominates the capture process and produces 55% of the neutron captures over the total energy range. Thirty percent of the total captures occurs between 0.5 and 2.23 MeV and they are largely (n,p) reactions.

The parasitic capture in nitrogen adversely affects the economics of the nitride-fueled reactors, as the 7% lower breeding ratio suggests. The products of the parasitic reactions may also influence the performance capability of the nitride fuel. As mentioned previously, the reaction products are hydrogen, helium, deuterium and tritium. The magnitude of their presence was obtained from the reaction summary of the parametric study. In the inner region of a 5500 liter core containing 40% fuel, 40% sodium, and 20% steel, the capture rate in nitrogen is 4.58×10^{18} captures/sec compared with a fission rate of 3.98×10^{19} fissions/sec. The production rate of gaseous fission products, which is roughly 6% of the total fission products, is of the same magnitude as the gas production in nitrogen. The total gas produced from neutron capture in nitrogen at the end of 100,000 MWD/MT exposure was calculated to be ~600 gm-moles in the inner core zone. At standard temperature and pressure (20°C, 1 atm) the gas produced from parasitic capture in nitrogen occupies a volume approximately equivalent to ten times that of the fuel, and has about 1.0% of the atom density of the heavy atoms in the fuel.

The magnitude of gaseous reaction products calculated above may be useful in determining the influence of the reactions on the fuel's performance capabilities, such as fuel swelling, fission gas release, thermal conductivity, etc. The neutronic calculations presented here show that nitride-fueled systems have a lower than expected breeding ratio. Unless the nitride fuels are found to have some redeeming properties, or unless N-15 enriched fuel can be produced economically, nitride fuel does not appear to be an attractive fuel type for an LMFBR.

References

1. D. A. Meneley, L. C. Kvitek and D. M. O'Shea, *MACH1, A One-Dimensional Diffusion Theory Package*, ANL-7223 (1966).
2. P. A. Pizzica and D. A. Meneley, Argonne National Laboratory (private communication).
3. E. M. Pennington, Argonne National Laboratory (private communication).

II-39. Effect of Subassembly Clearances on Some Performance Characteristics of 1000 MWe LMFBR Designs

J. T. Madell and H. H. Hummel

Introduction

The observation of stainless steel swelling under prolonged fast neutron irradiation (nvt $\approx 10^{23}$) has raised problems in the design of fast breeder reactors. A particularly serious problem is caused by the swelling of the steel subassembly wrapper cans which, among other undesirable effects, will completely eliminate the approximately 50 mil clearance between the subassemblies, initially present, making it impossible to remove them. As further swelling occurs severe distortion of the core will result. An obvious way to deal with this problem is to increase the initial clearance between subassemblies in the core region, where the swelling is greatest. Smaller clearances are tolerable above and below the core, and the prescribed clearance of 50 mils is adequate to prevent undesirable motions of the subassemblies during operation. A study has been made of the effect of such an increase in clearance on performance characteristics of typical 1000 MWe LMFBR designs. The first part of the report discusses the neutron cross section set used in the study, while the second part describes the computational codes. The basic design features of the LMFBRs considered for the study are given in the third section and the various effects on the reactors' performance characteristics are presented in the last two sections.

Development of Neutron Cross Section Set

Modifications to Basic Cross Sections

A neutron cross section set was developed and evaluated for use in the core design study of a 1000 MWe LMFBR. The basic cross section set was produced by MC² (1) using the "77 material" version of ENDF/B(2) as the source of discrete cross section data, except that the Pu-239 cross sections given by Pitterle et al.[3] were used. Modifications to the U-238 and Pu-239 cross sections obtained from the MC² calculations were incorporated in the broad group cross section set. The most

important modification was the use of lower inelastic scattering cross sections for U-238 above about 1 MeV. Other, less significant changes were made in Pu-239 fission and capture and U-238 capture cross sections. Evaluation of the cross sections consisted of comparing neutronic quantities calculated with "regular" and modified cross sections with experimental results from appropriate critical assemblies.

The modifications, mentioned above, were based on recent experiments and analytical comparisons. Recent measurements[4] of the U-238 cross sections resulted in lower values of the inelastic scattering cross section. Also, recent work on interpretation of critical assemblies[5] indicates better agreement between theory and experiment for k and for reaction rate ratios if lower values of U-238 inelastic scattering cross sections are used for energies above about 1 MeV. Small changes from the ENDF/B values in $\sigma(n,\gamma)$ of U-238 were included between 4 and 100 keV; these are not large enough to have a very significant effect. The Pu-239 capture and fission cross sections of Pitterle were modified slightly between 2 and 183 keV, as shown in Table II-39-I, but the values of α were held constant.

The neutronic parameters obtained with the resulting cross section set, as well as a set generated from an earlier edition of ENDF/B, were compared with experimental results from ZPR-III Assembly 48 and ZEBRA 3. Both critical assemblies were loaded with Pu-239 and U-238. Assembly 48 also contained sodium and carbon which resulted in a softer spectrum than ZEBRA 3 exhibited. The atom densities for Assembly 48 and ZEBRA 3 are given in Table II-39-II. The values for a 1000 MWe core are provided for the purpose of comparison.

The neutronic calculations were carried out with the same procedure as was used in benchmark studies of the Cross Section Evaluation Working Group (CSEWG).[6] First, two 26-broad-group sets with ½ lethargy widths were generated by MC² using the current ENDF/B library tape and core compositions of Assembly 48 and of ZEBRA 3, except for the cross section modifications displayed in Table II-39-I. Below 2.23 MeV (Group 4 and greater) the modified U-238 inelastic cross sections are those of Argonne Set 224,[7] which were based on Smith's older data.[8] Between 2.23 and 6.07 MeV (Groups 2 and 3) the modified data are ~10% smaller than both that of ENDF/B and Set 224, while the ENDF/B value is used for energies above 6.07 MeV (Group 1).

A series of spherical transport ($S_n = 4$) calculations was then performed to evaluate the effect of the various cross sections on the eigen value of Assembly 48 and ZEBRA 3. The results are presented in Table II-39-III. A previously developed cross section set,[9] which was obtained from an earlier ENDF/B tape without Pitterle's data for Pu-239, served as the set for Case A. The new ENDF/B tape, with both old and new data, was used to produce the new cross section set for Cases

TABLE II-39-I. Correction Factors for Some Pu-239 and U-238 Broad Group Cross Sections used in Analyzing Assembly 48 and ZEBRA 3

Energy Group[a]	Pu-239		U-238	
	σ_c and σ_f[b]	σ_e[b]	$\sigma_{inelastic}$	
			Assembly 48	ZEBRA 3
2	—	—	0.937	0.937
3	—	—	0.881	0.881
4	—	—	0.816	0.818
5	—	1.005	0.887	0.897
6	—	0.970	0.911	0.911
7	—	0.985	0.926	0.923
8	—	0.995	0.872	0.870
9	0.98	0.985	0.748	0.743
10	0.97	1.015	0.852	0.843
11	0.96	1.040	0.866	0.796
12	0.95	1.020	—	—
13	0.90	0.982	—	—
14	1.00	0.975	—	—
15	0.93	0.960	—	—
16	1.00	0.955	—	—
17	1.10	—	—	—

[a] See Table II-39-IV for group energy limits.

[b] Same correction factors were used in analyzing Assembly 48 and ZEBRA 3.

TABLE II-39-II. Core Compositions of Assembly 48, ZEBRA 3, and a 1000 MWe LMFBR, 10^{24} atoms/cm³

Nuclide	Assembly 48	ZEBRA 3	1000 MWe AI Design[a]
Pu-239	1.645×10^{-3}	3.465×10^{-3}	8.6976×10^{-4}
Pu-240	1.070×10^{-4}	1.830×10^{-4}	3.6383×10^{-4}
Pu-241	1.100×10^{-5}	1.600×10^{-5}	4.9699×10^{-5}
Pu-242	4.000×10^{-7}	—	2.6105×10^{-5}
U-235	1.600×10^{-5}	2.280×10^{-4}	1.0387×10^{-5}
U-238	7.405×10^{-3}	3.156×10^{-2}	6.7042×10^{-3}
Fe	1.018×10^{-2}	4.559×10^{-3}	1.3250×10^{-2}
Ni	1.119×10^{-3}	3.210×10^{-4}	2.3213×10^{-3}
Cr	2.531×10^{-3}	8.180×10^{-4}	3.2884×10^{-3}
Na	6.230×10^{-3}	—	7.7833×10^{-3}
Mn	1.060×10^{-4}	—	—
Mo	2.060×10^{-4}	—	4.8360×10^{-4}
Al	2.330×10^{-4}	—	—
C	2.077×10^{-2}	—	—
Cu	—	4.794×10^{-3}	—
Ta	—	—	9.0688×10^{-5}
O	—	—	1.6681×10^{-2}

[a] Atom densities for homogenized core at mid-cycle, equilibrium conditions. Fission product density of 3.1233×10^{-4} atoms/cm³ is not given in this table.

TABLE II-39-III. EIGENVALUES OBTAINED FOR ASSEMBLY 48 AND ZEBRA 3 FROM SPHERICAL TRANSPORT CALCULATIONS USING VARIOUS CROSS SECTIONS

	"Old Set"	"New Set" Based on Present ENDF/B					
	Case A	Case B	Case C	Case D	Case E	Case F	Case G
Critical Experiment	Earlier ENDF/B	Pitterle's Pu-239	Mod. U-238	Mod. U-238, Pu-239	Case A's Pu-239	Pitterle's Mo	U-238 I
Assembly 48	0.9865	0.9882	0.9982	0.9909	0.9878	0.9895	0.9894
ZEBRA 3	0.9536	0 9752	0.9947	0.9899	0.9567	--	0.9911

B through G. Cases C through G represent variations upon the base problem, Case B.

Case B differs from Case A only in that Pitterle's data for Pu-239 was used in the generation of the weighting spectrum and in the calculation of the eigenvalues. The modified broad group cross sections for U-238 were used in Case C, while Case D was calculated with modified cross sections for both U-238 and Pu-239. Case E used the ENDF/B cross sections for Pu-239 ("non-Pitterle") from the new cross section set, and new molybdenum cross sections were substituted for the previous ones in Case F. Case G used U-238 cross sections (U-238 I) in which total inelastic data in Set 224 were substituted for the ENDF/B values.

RESULTS OBTAINED USING THE MODIFIED CROSS SECTIONS

The use of the new cross section set with its various modifications brings the eigenvalues of Assembly 48 and ZEBRA 3 closer to unity than the eigenvalue obtained with the ENDF/B data, which took into account the higher α for Pu-239 at energies below 10 keV. The eigenvalues obtained with the modified Pu-239 and U-238 cross sections are 0.991 for Assembly 48 and 0.990 for ZEBRA 3. The modification of the molybdenum cross sections (Case F) results in an additional 0.13% increase in k_{eff}. The use of Pitterle's Pu-239 data instead of the ENDF/B data yields an increase of ~0.5 and ~2.3% in the eigenvalues of Assembly 48 and ZEBRA 3, respectively (Cases B and E). A larger increase with Pitterle's data is seen in ZEBRA 3 because its harder spectrum reduces the negative effect of higher capture cross sections in the low keV region, while the positive contribution of higher ν values remained relatively unchanged. The modification of the U-238 inelastic scattering cross sections produced (Case C) an increase in the k_{eff} values of both criticals; the larger increase in the eigenvalue of ZEBRA 3 is again due to its harder spectrum. The eigenvalues of both criticals were reduced by 0.5–0.7% upon modifying Pitterle's Pu-239 cross sections (Case D).

As was mentioned previously, the weighting spectra of the new and old cross section sets were generated from different Pu-239 data; otherwise they were produced in an identical manner. The influence of the slightly different weighting spectra is seen in the slightly different results for Cases A and E. The change of U-238 inelastic cross section in Case G resulted in increasing the eigenvalue of both criticals, but not by as large an amount as was produced by the modification in Case C.

The modifications to the current ENDF/B file improve agreement between the measured and calculated values presented here and were incorporated into the cross section set for the core design study.

DESCRIPTION OF CROSS SECTION SET FOR CORE DESIGN STUDY

The 26 group cross section set used in the Core Design Study was designated CDS01. The composition used in the MC² calculations to generate CDS01 was the homogenized mid-cycle core composition of the AI 1000 MWe design given in Table II-39-II. The MC² calculations consisted of a P_1 fundamental mode problem with a B^2 search to a k_{eff} of unity. The fuel material (uranium, plutonium, oxygen and fission products) was specified to be in the form of cylindrical pins of 0.27 in. o.d., surrounded by steel and sodium. The energy structure for the 26 broad groups of ½ lethargy units each is given in Table II-39-IV, along with the list of nuclides and their identifiers on the MACHLIB and XLIBIT cross section tapes. Set CDS01 has also been converted and stored on a disk for use in the ARC system. One MC² calculation was performed with all nuclides at 1300°K and another with the fuel nuclides at 2500°K and steel and sodium at 1300°K. The cross sections produced by MC² for Pu-239 and U-238 were modified in the manner described above (MACHLIB nuclide numbers 14, 18, 34 and 42 in Table II-39-IV). The five types of fission product pairs were combined (3.58% Xe-135, 0.65% Sm-149, 0.67% FPP№1, 20.05% FPP№2, and 75.05% FPP№3 to form the sum of the fission product pairs (FP sum). Stainless steel №316 was formed from 68.5 v/o iron, 12 v/o nickel, 16.8 v/o chromium and 2.7 v/o molybdenum. The 26 group cross sections (except for

TABLE II-39-IV. Energy Group Structure and Nuclide Description for Cross Section Set CDS01

Group	Energy Structure		Name	Nuclide Description (identification on cross section tapes)			
	Lower Energy, eV	Lethargy		T = 1300° K		T = 2500°K	
				MACHLIB	XLIBIT	MACHLIB	XLIBIT
1	6.07×10^6	0.5	Mo[a]	1	MOM..L	23	MOM..H
2	3.68×10^6	1.0	Ta-181	3	TA181L	24	TA181H
3	2.23×10^6	1.5	Pu-240	3	PU240L	25	PU240H
4	1.35×10^6	2.0	Na-23	4	NA.23L	26	NA.23H
5	8.21×10^5	2.5	FPP #1[b]	5	P9FP1L	27	P9FP1H
6	4.98×10^5	3.0	FPP #2	6	P9FP2L	28	P9FP2H
7	3.02×10^5	3.5	FPP #3	7	P9FP3L	29	P9FP3H
8	1.83×10^5	4.0	U-235	8	U.235L	—	—
9	1.11×10^5	4.5	Pu-242	9	PU242L	30	PU242H
10	6.74×10^4	5.0	O-16	10	O..16L	31	O..16H
11	4.09×10^4	5.5	Fe	11	FE...L	32	FE...H
12	2.48×10^4	6.0	Xe-135	12	XE135L	33	XE135H
13	1.50×10^4	6.5	Sm-149	13	SM149L	—	—
14	9.12×10^3	7.0	U-238- mod.	14	U238ML	34	U238MH
15	5.53×10^3	7.5	Cr	15	CR...L	35	CR...H
16	3.35×10^3	8.0	Ni	16	NI...L	36	NI...H
17	2.04×10^3	8.5	Pu-241[c]	17	PU41RL	37	PU41RH
18	1.23×10^3	9.0	Pu-239- mod.	18	PU39ML	38	PU39MH
19	7.49×10^2	9.5	SS316	19	SS316L	39	SS316H
20	4.54×10^2	10.0	FPP—sum	20	P9FPTL	40	P9FPTH
21	2.75×10^2	10.5	U-238[d]	21	U238IL	41	U238IH
22	1.67×10^2	11.0	Pu-239[e]	22	PU39PL	42	PU39PH
23	1.01×10^2	11.5	U-238	—	—	43	U.238H
24	6.14×10^1	12.0	B-10	—	—	44	B..10H
25	3.73×10^1	12.5	C-12	—	—	45	C..12H
26	2.26×10^1	13.0	N-14	—	—	46	N..14H
			Zr	47	—	—	—

[a] ENDF/B modified by Pitterle.

[b] FPP #1, FPP #2, FPP #3, FPP-Sum—fission product pairs for rapidly saturating, slowly saturating, non-saturating, and total chains, respectively.

[c] ENDF/B modified to include resonance data.

[d] Inelastic data from previous MC² library tape.

[e] ENDF/B modified by Pitterle.

zirconium) were collapsed to 13 groups of one lethargy unit using the broad group flux spectra from the MC² calculations.

The AI 1000 MWe reactor[10] was used as a basis for comparing the eigenvalues obtained from Set CDS01 to those obtained from unmodified cross sections. The use of the modified cross sections of U-238 and Pu-239 resulted in about a 2% greater value of k_{eff} for the AI design than was calculated previously with unmodified cross sections. The result is consistent with the calculations performed on ZEBRA 3 and Assembly 48 with modified and unmodified cross sections.

DESCRIPTION OF COMPUTER CODES FOR FUEL CYCLE AND FUEL COST CALCULATIONS

Four codes were employed in the fuel cycle and fuel cost calculations for the core design study. The thermal hydraulics calculations using the EVALUATE Code[11] were obtained from Ref. 12 and are not reported here. A brief description of the other three codes is given in the following paragraphs of this section.

INPROC

The INPROC code was written to prepare some of the input data for the fuel cycle code. The design specifications of the various types of subassemblies in a reactor loading are used by the INPROC code to calculate the material volume fractions occurring in the various regions of the reactor. The material volume fractions and input data of the reactor loading are combined to give the material atom densities for the regions in both the radial and axial directions; the atom densities are punched on cards to serve as part of the input deck for the fuel cycle code. Since for fuel cycle calculations between 90 and 100 regions must normally be used to describe a reactor, the calculation

TABLE II-39-V. INPUT DATA FOR INPROC CODE

1. To Calculate Material Volume Fraction of Subassembly Types (20 max.)
   (a) Components: cladding, bond, fuel, pin spacer, wrapper, unit cell, 3 special components, coolant (10 max.).
   (b) Geometry of components: square, hexagonal, cylindrical.
   (c) Material of components: 8 max.
   (d) Dimension of components: o.d., i.d., thickness, % enclosed area, etc.
2. To Calculate Atom Density of Fuel Types (15 max.)
   (a) Density of chemical compound (gm/cc).
   (b) Isotopic ratios of plutonium and uranium.
   (c) Chemical weight of light element(s).
   (d) Burnup.
   (e) Ratio of light to heavy elements.
3. To Calculate Volume Fractions in Material Region Types (Compositions)
   (a) Type and number of subassembly types in Material Region Type.
4. To Calculate Atom Densities in Material Region Types
   (a) Atom densities of pure materials.
5. To Assign Material Region Types to Radial and Axial Regions
   (a) Radial and axial regions to which material region type is to be assigned.
   (b) Number of stages for radial regions.
   (c) Nuclide numbers for cross section set.

and punching of the regional atom densities data by the INPROC code represents a considerable saving of time.

The modifications to the design specifications represent minimal changes in the input to INPROC. Thus a series of core designs of various cladding thicknesses, for example, can easily be handled by the code. A list of input quantities and a flow diagram for the INPROC code are given in Table II-39-V and Fig. II-39-1, respectively.

SYNBURN

The fuel cycle calculations were carried out with SYNBURN code[13] which calculates the equilibrium concentration of the materials during the burn cycle. The neutronic portion of the code consists of a one-dimensional synthesis calculation in which the neutron balances are calculated in the radial and then axial directions until convergence is obtained. Criticality may be sustained during the burn cycle by varying the poison concentration. The fluxes are calculated at each time step and spatial interval; they are then averaged over the volume of each region to calculate the current concentration of the various materials in that region.

The SYNBURN code was slightly modified to punch out the quantities of heavy atoms at the beginning and end of the equilibrium cycle in each region and for each material stage. A small computer code than converted the heavy atom data from the SYNBURN calculation to the charge, discharge, and inventory masses required as input to the fuel cost code.

CYCOST

The CYCOST code[14] was used to calculate the equilibrium fuel cycle costs for the systems which had been investigated with the SYNBURN calculation. The code is capable of calculating fuel costs for both startup and equilibrium cycles. The major feature of the CYCOST code is its assignment of cost to the cycle in which the cost actually occurred. Since the calculations in this study are for equilibrium cycles rather than startup cycles this particular feature was not a factor in the calculations. The fabrication and reprocessing

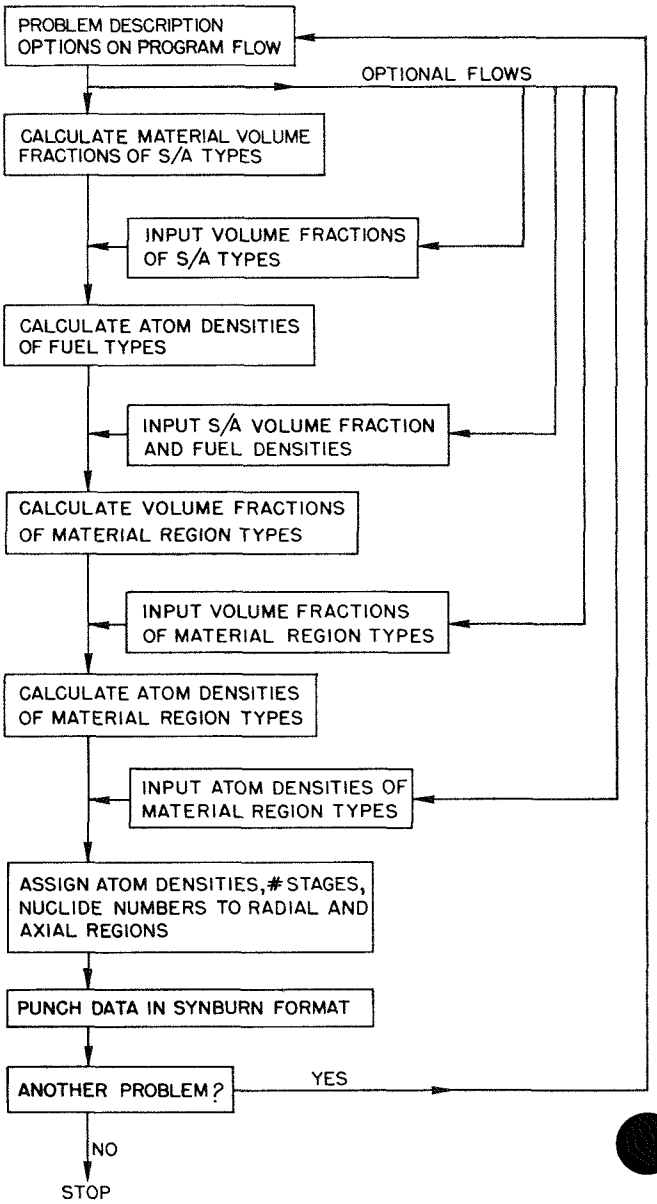

FIG. II-39-1. Flow Diagram for the INPROC Code. *ANL Neg. No. 116-454.*

rates may be either defined or calculated by the code from basic data, such as the fuel element diameter and length, etc. As mentioned in the previous paragraph the code requires the charge, discharge, and startup inventories of the heavy atoms for each cycle. A cost value for each fuel material (Pu-239, Pu-240, Pu-241, U_3O_8, etc.) may be assigned or the code may be directed to do a parametric study on the cost value of a particular heavy atom. The CYCOST output consists of the fabrication and reprocessing rates, the total interest charges and itemized and total fuel costs in mils/kWh for each cycle.

Description of Basic Designs of LMFBRs

Three oxide- and one carbide-fueled designs for a 1000 MWe reactor were selected for the fuel cycle and fuel cost studies. In addition, identical calculations were carried out for the AI 1000 MWe design[10] to provide a reference for the study. Because of the limited nature of the study an optimization of the core designs was not possible. It was decided to use pin diameter as a parameter because core size, fuel inventory, and fabrication cost are all sensitive to it. Cladding outer diameters of 0.22, 0.26, and 0.30 in. were selected. Other parameters were selected to be in a range that seemed reasonable. The 1000 MWe Follow-on Studies[15-18] have indicated that fuel cycle cost is not very sensitive to some parameters, such as core height, while in other cases the choice is constrained by conditions other than purely economic. A 50 mil clearance has been chosen between fuel pins, which are wire-wrapped. The 1000 MWe studies have indicated that it is desirable to have a small clearance to maximize core fuel volume fraction, while 50 mils is a minimum distance from the standpoint of possible flow blockage and of pin azimuthal temperature distribution. This clearance is of course related to the core sodium velocity and pressure drop. (The use of grid spacers instead of wire wrap might make a larger spacing desirable.) The sodium velocity and pressure drop have been arbitrarily selected to be about 30 ft/sec maximum and 100 psi, respectively. The 1000 MWe Follow-on Studies have indicated that economics are not very sensitive to the exact values of these parameters.[10,15] Significantly higher choices would start to pose development problems, however, while considerably lower values would start imposing considerable economic penalties. The free-standing subassembly cans are designed to accommodate pressure drops in this range.[10] Many parameters were held constant for the reactor designs to limit the scope of the study and these are given in Table II-39-VI for the oxide and carbide designs.

TABLE II-39-VI. Constant Parameters for 1000 MWe Reactors

Parameter	Oxide	Carbide
Reactor power, MWt	2400	2400
Average linear powder, kW/ft	10	22.7
Inlet temperature, °F	780	800
Temperature rise, °F	360	325
Fuel density, % TD	85	85
Fuel pins/subassembly	271	169
Pin-to-pin spacing, in.	0.050	0.060
Outer/inner core enrichment	1.5	1.5
Average core burnup, a/o	6.7	6.7
Number of stages in core	2	2
Number of control subassemblies	15 (Ta)	22 (Ta)
Axial blanket height, ft	1.13	1.25
Gas plenum height, ft	3.17	1.5
Cladding thickness, in.	0.05 × cladding o.d.	0.011

TABLE II-39-VII. Description and Performance Characteristics for the Five Reactor Designs with Two Subassembly Clearance Specifications

	Oxide-Fueled Design									
	Design #1 Cladding o.d. = 0.22 in.		Design #2 Cladding o.d. = 0.26 in.		Design #3 Cladding o.d. = 0.30 in.		AI Design		Carbide Design	
Subassembly gap, in.	0.05	0.30	0.05	0.30	0.05	0.30	0.05	0.30	0.05	0.30
Core height, ft	2.75	2.75	3.00	3.00	3.58	3.58	3.58	3.58	2.50	2.50
Core diameter, ft	7.40	7.77	8.03	8.39	8.28	8.62	8.45	8.82	8.86	9.20
Core volume, liter	3340	3690	4300	4700	5470	5920	5690	6200	4370	4710
Breeding ratio	1.22	1.17	1.27	1.23	1.30	1.25	1.26	1.22	1.49	1.47
Burn time, day	149	148	212	212	271	269	263	263	296	297
Pu fissile loading, kg	1753	1833	2175	2260	2612	2680	2528	2686	2591	2668
Enrichment—charged into inner core, a/o	13.4	14.2	11.5	12.1	10.5	11.1	11.6	12.2	9.3	9.6
Fuel cost, mills/kWh[a]	1.131	1.205	0.973	1.036	0.883	0.952	0.923	0.982	0.610	0.640

[a] The fuel costs are based on \$10/g Pu, \$8/lb. U_3O_8 and a 12.5% interest rate. CYCOST calculated the fuel fabrication costs in the range 165 to 260 dollars per kilogram.

TABLE II-39-VIII. Results of Equilibrium Fuel Cycle Calculations for 4 a/o, 6.7 a/o and 10 a/o Burnup for the Three Oxide-Fueled Designs

Design	Burnup, a/o	k_{eff} Unpoisoned	Burn Time, Days	Breeding Ratio	Fuel Cost, mills/kWh
1	4.0	1.009	87	1.23	1.873
	6.7	1.033	148	1.17	1.205
	10.0	1.054	227	1.12	0.905
2	4.0	1.006	124	1.28	1.595
	6.7	1.020	212	1.23	1.036
	10.0	1.034	324	1.18	0.795
3	4.0	1.004	157	1.29	1.438
	6.7	1.009	269	1.25	0.952
	10.0	1.021	410	1.20	0.761

Thermal-hydraulic calculations were also performed for a sodium-bonded carbide-fueled reactor. A single core design was considered in which the cladding o.d. was 0.412 in., and the pin-to-pin spacing was 0.06 in. The thermal-hydraulic calculations are based on an average linear power of 22.7 kW/ft and predict different coolant temperatures than those predicted for the oxide core designs. The design parameters which were held constant were based on the Combustion Engineering 1000 MWe design.[19] The above assumptions, together with an assumed 10 kW/ft average heat rate for oxide fuel and 227 kW/ft for carbide fuel, resulted in the core heights indicated in Table II-39-VII.

Effects of Increasing the Subassembly Clearance

Increasing the subassembly clearance affects the neutronic characteristics of a reactor and, in turn, its fuel cost. To determine the magnitude of the effects, fuel cycle and fuel cost calculations were performed for the five reactor designs described in the last section. Table II-39-VII lists the design characteristics which are influenced by the change in subassembly clearance for the five reactors. The thermal hydraulics characteristics were assumed to be unaffected by the change of subassembly clearance.

The basic core designs of the five reactors specified a 50 mil clearance over the full length of the subassemblies. In the design to accommodate steel swelling, a 300 mil clearance was allowed in the core region and a 50 mil clearance was provided in the axial and radial blanket regions. The fuel subassemblies have a wrapper thickness 125 mils greater in the axial blanket than in the core to compensate for the additional 250 mils of sodium gap in the core region.

In the fuel cycle calculations, each row of subassemblies in the reactor was represented by a radial region (13 or 14 rows or radial regions). In the axial direction, the core was represented by one region, the lower and upper blankets by two regions for each, and the lower reflector and upper gas plenum by one region for each. The smear density of the fuel for all designs was set at 85% of theoretical density and the plutonium (Pu-239, Pu-240, Pu-241, Pu-242) isotopic ratio of 67/26/5/2 was used for the feed. The core contained two enrichment zones with the enrichment in the outer zone 50% greater than that in the inner zone. The core fuel was discharged in two stages with an average burnup of 6.7 a/o. The inner radial blanket of depleted uranium was managed with five stages and the outer blanket with seven stages.

The fuel cycle and fuel cost results for the five reactor designs with 50 and 300 mil subassembly clearance are given in Table II-39-VII. The result of increasing the subassembly clearance from 50 to 300 mils in the core can be generalized for all five designs in this study. The increased clearance decreases the volume fraction of the fuel by 7–9% and increases the sodium fraction by 10 to 15%. The core volume and plutonium fissile inventory both increase by about 5% with the larger subassembly gap, while the cycle burn time is not affected. These changes in the core design specifications produce a 4% decrease in the breeding ratio. The fuel costs for the designs with 300 mil clearances are 5–8% higher than those with 50 mil clearances. The increased cost is primarily due to higher inventory costs and lower plutonium credit.

The Effect of Burnup and Other Factors on the Fuel Cost

In the last section, the clearance between subassemblies was increased without changing the allowable burnup of the fuel. In practice, an increase in the clearance between subassemblies would probably allow a greater residence time of the fuel and thus permit a larger burnup to be achieved. To investigate the influence of the burnup limitation the fuel costs of the three oxide designs (o.d. = 0.22, 0.26, 0.30 in.) were calculated for 4 a/o and 10 a/o burnup, in addition to the 6.7 a/o value of the base design. The results presented in Table II-39-VIII show that increasing the burnup from 4 a/o to 10 a/o reduces the fuel costs of all three designs by 50%. As the burnup limit for a cycle is raised, the value of the unpoisoned k_{eff} at the beginning of the cycle and the burn time of the cycle increase, while the breeding ratio decreases. A larger value of the unpoisoned k_{eff} at the beginning of cycle requires a larger amount of control to achieve criticality during the burn cycle. Difficulties may result in the scheduling of shut downs by the utilities if the burn

times are too short or too long. The primary conclusion drawn from a study of burnup is that there is an economic incentive to increase the subassembly clearance if an additional (~1.0 a/o) burnup may be achieved.

The study of the three designs of an oxide-fueled reactor also show a more desirable economic performance for those cores with a high fuel volume fraction. The improved economic performance is due to a higher breeding ratio which yields a higher plutonium credit in the fuel costs and overrides the increased cost of greater fuel inventories.

It should be emphasized that the study did not entail a complete optimization of the core designs. In particular, it should be recalled that the average linear power and pin-to-pin spacing was held constant in the oxide designs, as were the sodium temperatures in the core. The conclusions above, therefore, are only valid for the assumptions made in the study. However, it is believed that these assumptions are reasonable and probably close to optimum.

References

1. B. J. Toppel, A. L. Rago and D. M. O'Shea, *MC²*, *A Code to Calculate Multigroup Cross Sections*, ANL-7318 (1967).
2. E. M. Pennington, Argonne National Laboratory (private communication).
3. T. A. Pitterle, E. M. Page and M. Yamamoto, *Analysis of Sodium Reactivity Measurements*, APDA-216, Vol. I, *Cross Section Evaluation and Data Testing*, June 1968.
4. A. B. Smith, Argonne National Laboratory (private communication).
5. J. M. Kallfelz, B. A. Zolotar and B. R. Sehgal, *Modifications to Fissile Element Cross Sections and Their Influence on Calculated Fast Reactor Parameters*, Reactor Physics Division Annual Report, July 1, 1968 to June 30, 1969, ANL-7610, pp. 224–232.
6. W. G. Davey and A. L. Hess, *Additional Fast Reactor Benchmarks for Phase II Data Testing of ENDF/B*, CSEWG Newsletter, February 21, 1969.
7. D. M. O'Shea et al., *Twenty-Six Groups Cross Sections*, Trans. Am. Nucl. Soc. **7**, 242 (1964).
8. A. B. Smith, *Scattering of Fast Neutrons from Natural Uranium*, Nucl. Phys. **47**, 633 (1963).
9. J. M. Kallfelz, B R. Sehgal and B. A. Zolotar, Argonne National Laboratory (private communication).
10. Atomics International, *1000-MWe LMFBR Follow-on Study, Conceptual Design Report*, AI-AEC-12792, Vol. I (1968).
11. D. H. Thompson, Argonne National Laboratory (private communication).
12. W. W. Marr, Argonne National Laboratory (private communication).
13. P. A. Pizzica and D. A. Meneley, Argonne National Laboratory (private communication).
14. T. D. Wolsko, Argonne National Laboratory (private communication).
15. General Electric Company, *Methods, System Optimization, and Safety Studies for a 1000 MWe Sodium-Cooled Fast Reactor—Tasks III and V of 1000 MWe LMFBR Follow-On Work*, GEAP-5710 (February 1969).
16. Atomics International, *1000 MWe Liquid Metal Fast Breeder Reactor Follow-on Study Conceptual Design Report*, AI-AEC-12792, Vol. II (June 1969).
17. Babcock & Wilcox Company, *1000 MWe Follow-on Study Task II & III Final Report*, BAW-1328, Vol. V (January (1969).
18. Westinghouse Electric Corp., *Cost Optimization and Parametric Studies, Westinghouse 1000 MWe LMFBR Task III Topical Report*, WARD-2000-96, (March 1969).
19. Combustion Engineering, Inc., *1000 MWe LMFBR Follow-on Study, Report of Tasks II and III*, CEND-337, Vol. I (1968).

II-40. A Dual Spectrum Concept for Liquid Metal Fast Breeder Reactor (LMFBR) Fuel Assay

C. N. Kelber

The use of a reactor, usually at low power, for fuel assay is not novel. A discussion of some of the problems in such use was given in 1961 by Sandmeier,[1] and danger coefficient testing is a commonly employed technique for inspecting new fuel. The reason is obvious: a reactor is very sensitive to fissile material and small ($\sim 10^{-7}$ $\Delta k/k$) reactivity changes are readily detected. Precisely because of the sensitivity to fissile materials, however, design of a fuel assay reactor for LMFBR fuel is difficult because the response to the different fissile isotopes (Pu-239 and Pu-241) is so similar, and fast fission in U-238 and Pu-240 masks their neutron capture effect. Moreover, in a thermal spectrum assay reactor,[1] neutrons will not penetrate a typical LMFBR assembly. Recently a suggestion[2] has been made to circumvent this difficulty by assaying fuel in two different spectra—fast and slow—and unfolding the reactivity response.

If a fast reactor core had an appreciable voided fraction, additional flexibility in the use of this reactor for reactivity measurements could be achieved by provision of a system for filling the core with a liquid. By the addition of sufficient nuclear poison to the liquid, a null-reactivity effect could be achieved. Then it would

be practical to make reactivity measurements for a fuel element in both a fast and a slow spectrum, thereby providing additional data for deducing the contents. In a recent paper[3] this suggestion is developed to demonstrate how such a concept might be defined and to illustrate the problems in defining a successful concept.

The main conclusion was that a dual spectrum system can be conceived which can carry out the nondestructive assay of reactor fuel with reasonable accuracy (~ few tenths of a percent of mass) without requiring any major technological advances. The possible facility described in Ref. 3 was in no way optimized. The purpose of that study was to determine if the conclusion reached was tenable and to point out the main problems in optimizing a system. In resolving these problems one has to keep in mind the claimed advantages of the dual spectrum system:

1. The fast spectrum core is responsive to the entire radial extent of the test sample and averages over heterogeneities.

2. The slow spectrum core is responsive to the energy dependence of the cross sections of materials in the test sample.

3. The use of different types of neutron filters in the slow spectrum core affords an opportunity to determine the response in a range of incident spectra.

The problems requiring resolution are:

1. Should there be only one system?

An operational study is needed to determine if there is any validity to the assumption of easier intercalibration with just one physical system. Some of the neutron filters discussed earlier depress the reactivity by several percent. Restoration of criticality may well affect automatic reactivity compensator calibration adversely. A separate slow spectrum system would not change this problem much but it would allow the use of graphite or beryllium moderator with improved response characteristics in the low energy resonance region.

2. How can the response to the Pu-240 spontaneous fission be maximized?

This response dominates the error calculation. Increasing the response lowers the error estimate. There are two paths: selecting a loading and geometry to emphasize the importance of the source neutrons; and designing a system with very low natural source to permit operation at powers of approximately 10^{-4} W. The two paths are not necessarily contradictory. An example of experimental technique which seeks to minimize the error in the source response is given by Bretscher and Redman.[4]

3. Can extreme geometries afford an opportunity for axial scanning?

This problem has not been investigated.

4. What are the effects of photoneutrons induced by fission product gammas?

The response in, say, normal water to such photoneutrons may be an indicator of total exposure.

5. What are the effects of minor changes in the amount and kind of cladding material in the test sample?

6. What are the possible impediments to the testing of PWR and BWR fuel?

References

1. H A. Sandmeier, *On the Maximization of the Sensitivity of a Fuel Assay Reactor*, Nucl. Sc. Eng. **9**, 260 (1961).
2. W. C. Redman, Argonne National Laboratory (private communication).
3. C. N. Kelber, *A Dual Spectrum Concept for LMFBR Fuel Assay*, Nucl. Appl Tech. (to be published, January 1971).
4. M M. Bretscher and W. C. Redman, *Low Flux Measurements of Pu-239 and U-235 Capture-to-Fission Ratios in a Fast Reactor Spectrum*, Nucl. Sci. Eng. **39**, 368 (1970).

II-41. Calculated Gamma-Ray Heating in an Assembly for Irradiating Fast Reactor Fuel Elements in the Center of the Engineering Test Reactor (ETR) Core

A. E. McArthy

To assist in the design of a loop for the irradiation of fast reactor fuel, calculations were made to estimate the gamma-ray heating rate in an assembly of fast reactor fuel elements when irradiated in the center of the Engineering Test Reactor (ETR) core. The equivalent diameter of the fuel assembly containing 19 fuel rods was 4.38 cm and the water flow tube containing the assembly with its surrounding sodium, flow dividers, neutron filter, and containment vessels had an equivalent diameter of 14.3 cm. The thermal neutron filter was made of 2 w/o borated steel. The length of the assembly of highly enriched UO_2 fuel was 91.4 cm

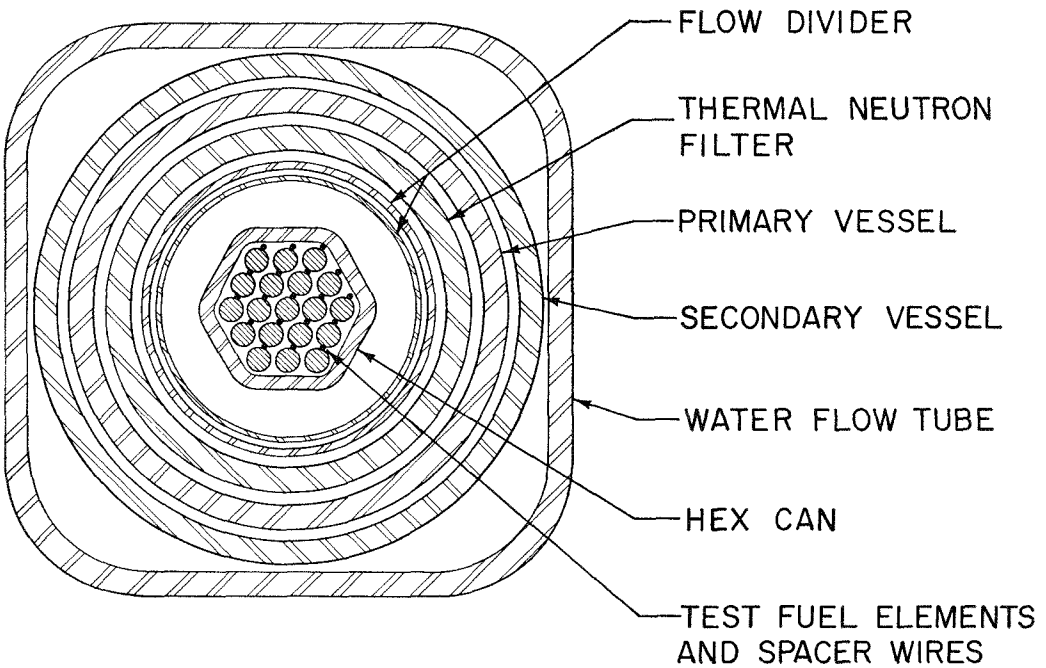

FIG. II-41-1. Cross Section of Test Loop in ETR Core *ANL Neg. No. 116-226.*

Figure II-41-1 shows a cross section of the loop and the locations of the fuel assembly, flow dividers, neutron filter, and containment vessels.

The fuel element region was homogenized for purposes of calculation. Gamma-ray source values were obtained using an average fission density of 9.3×10^{13} fissions/cm^3-sec to determine the uniformly distributed source. Gamma-ray fission source values (MeV/fission) were taken from information in Ref. 1 and include 1.15 MeV/fission of energy due to capture gamma rays. Equilibrium fission products were assumed.

Considering sources in the fuel element region, gamma ray fluxes were calculated at the horizontal midplane for the positions reported using formulas for cylindrical geometry[2] and a uniformly distributed source. Results were obtained from calculations for four photon energies (1, 2, 4 and 6 MeV). The gamma-ray flux at the center of the fuel assembly and the flux at the outside surface of the fuel were determined. The flux at the outside surface was attenuated through the other materials to find the flux contributions at the specified points from the fuel assembly sources.

The ETR core around the loop was considered to be a thick uniform gamma-ray source with a fission density of 1.53×10^{13} fissions/cm^3-sec. The gamma-ray flux at the surface of this source was determined and used as radiation incident on the loop containing the fuel elements being irradiated. This radiation was attenuated by the intervening loop material before being absorbed to contribute to the heating rates reported.

The calculated gamma-ray heating rate in the UO_2 fuel at the center of the fuel section was 47 W/g with about 85% of the heat being produced by radiation from sources in the fuel section. The gamma-ray heating rate in the UO_2 fuel located at the outside of the fuel section was 39 W/g.

The maximum heating rate in the steel of the neutron filter was calculated to be 25 W/g. The heating produced by the (n,α) reactions in the B-10 contained in the steel contributed 6 W/g to the total. A thermal neutron flux of 3.2×10^{13} neutrons/cm^2-sec incident at the outside of the loop was used to find the total number of (n,α) reactions which result in the release of 2.5 MeV of energy for each reaction.

During irradiation the gamma-ray heating rate in the steel wall of the secondary vessel in the irradiation loop was calculated to be 17 W/g. About 60% of this heating was produced by radiation from gamma-ray sources in the surrounding ETR core. The heating rate in the primary vessel was 18 W/g.

Calculations of the heating rates immediately after the loop is removed from the irradiation zone showed that the equilibrium fission products in the fuel will produce gamma-ray heating at the center of the fuel and at the outside surface of the fuel equal to 18 and 13 W/g, respectively. Immediately after removal of the loop from the irradiation zone the fission product

gamma-rays produced heating in the steel of the filter, the primary vessel, and the secondary vessel equal to about 5, 4, and 3 W/g, respectively. After the loop has cooled for one day the heating rates at the center of the fuel, the outside surface of the fuel, in the steel filter, the primary vessel, and the secondary vessel are, respectively, 1.4, 1, 0.4, 0.3, and 0.2 W/g.

Approximations in the calculations and uncertainties in the buildup factors used were sources of possible errors in the calculated heating rates. The heating rates given above were calculated to be conservative and are estimated to be no more than 50% high.

References

1. N. E. Holden, M. R. Mendelson and T. E. Dudley, *Total Gamma Energy Release Due to Thermal-Neutron Fission in* ^{235}U, Nucl. Sci. Eng. **30,** 461 (1967).
2. T. Rockwell III, Ed., Reactor Shielding Design Manual, TID-7004, 365 (1965).

Section III

Experimental Techniques and Facilities

Measured integral reactor physics parameters are necessary for either direct introduction into reactor design calculations or for comparison with values obtained analytically using basic microscopic cross section data. In the latter case the objective is to verify either the cross section data or the calculational techniques. Reactor integral parameters are obtained using special measurement techniques in exponential or critical facilities. The papers presented in this section deal largely with the development of such special techniques, facilities, and radiation detection devices. Included also are papers which describe specially developed equipment useful in obtaining microscopic nuclear data.

III-1. The Fast Neutron Generator (FNG) Facility

S. A. Cox

Introduction

During the past year the Applied Physics Division put into operation a new research facility, the Fast Neutron Generator (FNG). The FNG is designed to meet the needs for neutron cross section and neutron physics information in the fast reactor field and to be utilized as a pulsed neutron source for the study of fast reactor spectra. The FNG has the option of being operated either as a tandem accelerator or as a single-ended accelerator. In the tandem mode proton or deuteron beams of at least 8 MeV energy can be produced with beam currents of $\gtrsim 50$ μA. Beams of at least 4 MeV energy and currents $\gtrsim 1$ mA can be produced in the single-ended mode. Both pulsed or dc beams are available in either mode. Since the FNG provides both higher voltage and higher current capability than the former 3 MeV Van de Graaff facility new areas of investigation are opened. The higher voltage capability permits detailed investigation of reactions with high reaction thresholds and the high current capability permits investigation of reactions with low cross sections and those requiring unique intensities.

The basic component of the FNG is a Dynamitron, a relatively recent innovation in the accelerator field. In the past, most accelerators in the MeV range used the Van de Graaff principle in which a moving belt carried a positive charge to a high voltage terminal. The charge-current raised the terminal to a high potential. Positively charged particles were accelerated from the terminal to a target at ground potential. In the Dynamitron the charging principle is quite different and is an improvement over the Cockroft-Walton method. Cockroft-Walton accelerators attained voltages up to approximately 1 MeV by a multiplying network of rectifiers and capacitors whereby a relatively small impressed voltage was transformed into a high voltage at the accelerating terminal. The fact that the charge must be transferred in a series fashion presented an inherent limitation in the attainable voltage. As the terminal voltage was increased beyond 1 MeV the required stored energy rapidly became excessive. Both the voltage limitation and stored energy problems are greatly alleviated in the Dynamitron by changing the charging current from a series type to a parallel type configuration. This is accomplished by placing a pair of semicylindrical electrodes parallel to and enclosing the rectifier string. A 120 kHz RF voltage is applied to the electrodes. The charging current is transferred directly from the electrode to each rectifier. Since the rectifiers conduct in only one direction, the impressed charge cannot leak to ground and the induced voltage on the rectifiers adds up to form the terminal voltage. Terminal charging currents of ~ 10 mA and terminal voltages of 4 MV can be maintained in the Dynamitron.

Construction and Initial Testing

The Dynamitron was designed and constructed by Radiation Dynamics, Inc., (RDI). Following assembly in the testing vault at RDI the Dynamitron underwent a long series of inhouse tests designed to insure that it would meet performance specification when delivered to ANL. Since this was to be the first tandem Dynamitron built at RDI, the tests were comprehensive. Initial tests were carried out without beam tubes to check on high voltage performance. During these tests the Dynamitron attained terminal voltages up to 5.55 MV which were in excess of the requirement of 4 MV. After satisfactory completion of the voltage tests the beam tubes were installed and the process of beam tube conditioning was begun. This process, which consisted largely of soft electrical-discharge cleaning of the inside surface of the beam tubes, was essential to ensure stable and spark-free high voltage performance.

The Dynamitron was delivered to ANL in September 1969 and installation was begun.

Acceptance Tests at ANL

A series of accelerator acceptance tests was begun following the basic installation of the FNG. Of the many tests carried out the most important were: 1) dc tests including voltage calibration, voltage stability, energy resolution, maximum voltage and maximum beam current specs, 2) pulsed beam tests including peak pulse current specs and pulse width tests, and 3) endurance runs. The voltage calibration measurements were made to establish an energy scale for all subsequent tests. Four (p,n) reactions with well known thresholds were used for the calibration: $Li^7(p,n)$, $Cu^{65}(p,n)$, $F^{19}(p,n)$, and $Al^{27}(p,n)$ with thresholds respectively of 1.88060 $\pm$ 0.00007, 2.166 $\pm$ 0.01, 4.2343 $\pm$ 0.0008 and 5.7969 $\pm$ 0.0038 MeV. These measurements served to calibrate the 90 deg analyzing magnet with sufficient accuracy that the proton energy would

be known to better than ±10 keV over the entire operating energy range from 1.5 to 8.0 MeV. Extrapolation from the 5.7969 MeV threshold was considered reliable because the 90 deg magnet was far enough from saturation that the Hall effect and nuclear magnetic resonance probes used to measure the field should give undistorted readings. After the energy scale was established the next step was to measure the energy resolution and voltage stability. The energy resolution was determined at two points: at 1.880 MeV using the rise at threshold of the $Li^7(p,n)$ reaction, and at 6.0 MeV using a selected narrow resonance from the $Al^{27}(p,n)$ reaction. A long counter placed at 0 deg neutron emission angle was used to monitor the neutron yield from the $Li^7(p,n)$ reaction and an He-3 counter placed at 0 deg to monitor the neutron yield from the $Al^{27}(p,n)$ reaction. The energy resolution was determined to be <2 keV at 1.880 MeV and <8 keV at 6.0 MeV, within the required ±2 kV allowable voltage fluctuation on the terminal. The voltage stability was determined at the same two points, by setting the proton energy to correspond to a position half way up the threshold rise of the $Li^7(p,n)$ reaction, and half way up the resonance in the $Al^{27}(p,n)$ reaction. With the proton energy so adjusted any voltage change is directly related to a change in the neutron yield of the reaction. With the proton energy fixed, the neutron yield was measured every minute for periods up to 1½ h. A plot of the measured yields was then related to changes in proton energy which was directly related to terminal voltage. The results of the measurements were that the proton energy varied by an amount <150.0 V at 1.880 MeV and <850. V at 6.0 MeV—well within the required specs of ±2000 V. Next came a long period of beam tube conditioning to clean up the beam tubes a[illegible] the internal structure of the pressure vessel so that the maximum voltage and beam current specs could be demonstrated. These specs were actually exceeded with a proton current on target of 65. μA at 8.0 MeV and a deuteron current at target of 43 μA. The pulsed beam tests were then demonstrated. Requirements were for a pulse width of 2 nsec with a peak pulse current of 1mA. The actual measurement yielded a peak pulse current of ~1.3 mA for a 2 nsec pulse width with a minimum attainable pulse width of 1.2 nsec. One of the requirements was for an endurance run of 100 h with a maximum down time of 15 h. The accelerator passed the endurance test on the first attempt.

The FNG is to be used within the Applied Physics Division by two groups, the Applied Nuclear Physics and the Experimental Reactor Physics sections. The Applied Nuclear Physics group will utilize it primarily as a variable energy neutron source. By selecting neutron source reactions, e.g. $Li^7(p,n)$, $T^3(p,n)$, $D^2(d,n)$ and $T^3(d,n)$ the neutron energy range from keV neutrons to 11. MeV and from 16. to 25. MeV can be covered. Nuclear cross sections to be investigated include elastic and inelastic neutron scattering, neutron polarization, fission cross sections, (n,p), (n,α), $(n,2n)$, $(n,n'\gamma)$ and (n,γ) reactions. The Experimental Reactor Physics group will use the pulsed proton or deuteron beam from the FNG by directing it at a neutron-producing target in the core of a fast reactor. The purpose of the program is the investigation of neutron spectra from fast reactors. If the FNG performs as well in the future as it has to date (the pressure vessel has not been opened for more than nine months), it should prove a very efficient and productive facility.

III-2. Klystron Buncher for Pulsed FNG Single-Ended Operation

D. L. Smith

Modifications required for nanosecond-range pulsing of the Applied Physics Division Fast-Neutron Generator in single-ended operation are being made at Argonne National Laboratory. Fast pulsing is to be achieved by time compression of ion bursts from a pulsed source in the terminal through the use of a klystron bunching tube. The FNG tandem injector is already equipped with a klystron buncher which has performed well during fast-pulsing tests of the FNG in tandem operation. The results of a design study on klystron bunching for the FNG in single-ended operation are presented here. This study has shown that a time compression factor of 10:1 or better is feasible for protons ($^1H^+$), molecular hydrogen ($^1H_2^+$), deuterons ($^2H^+$), α-particles ($^4He^{++}$), and helions ($^3He^+$ and $^3He^{++}$) over the entire usable range of terminal potentials (800–4000 kV) if a small (~6 cm long) buncher tube is suitably placed in the terminal and is driven by an oscillator with peak-to-peak output voltages in t[illegible] range 0–10 kV at 15.0 MHz.

Time compression of a beam pulse width by klystron bunching is a well established technique.[1-3] The basic

TABLE III-2-I. Fixed Design Parameters for the FNG Single-Ended Buncher System

X_{G1}	= 0.5	cm
X_B	= 6.0	cm
X_{G2}	= 0.5	cm
X_{BMLG}	= 2.0	cm
X_{ML}	= 32.0	
X_{AT}	= 365.0	cm
X_{BTE}	= 1865.0	cm (not critical)
Buncher frequency	= 15.0	MHz

principle is the following: A pulse of essentially monoenergetic ions is required to traverse a region with an oscillating longitudinal electric field component prior to injection into the accelerator tube. The frequency, phase, and amplitude of the oscillation are chosen so that the ions which arrive early are slowed down somewhat in the region whereas those which arrive late are speeded up in such a way that the entire burst is compressed in time when it arrives on target. The price one pays is a loss in energy homogeneity and some deterioration in the beam focusing characteristics. Several variations of the application of this principle are possible when choosing a design for a bunching system. The design described by Tykesson and Wiedling[2] was chosen as a model for the FNG single-ended buncher because this particular design has the worthwhile feature that only slight changes in the phase of the buncher voltage are required as the accelerator energy is varied over its usable range.

For computational purposes, the source, buncher, accelerator tube and final drift tube to the target were represented mathematically by uniform longitudinal electric field regions with sharply defined boundaries. The transverse electric field components which determine the optics of the system were neglected. However, certain constraints were imposed upon the adjustable potentials in order to adhere to requisite focusing conditions. A computer program was developed to study the time schedules of ions injected under various operating conditions. The regions which the ions traverse are described below, in the order in which they are encountered by the ions during their journey from the sweep aperture to the target (all potentials except V_{EXT} are expressed relative to ground at the target):

1. First bunching gap: gap length X_{G1} between the sweep aperture at potential V_C and the buncher tube entrance at potential $V_B + V_{OS} \sin(\omega t + \phi)$.
2. Buncher tube interior: tube length X_B with potential $V_B + V_{OS} \sin(\omega t + \phi)$ and zero electric field.
3. Second bunching gap: gap length X_{G2} between the exit of the buncher tube at potential $V_B + V_{OS} \sin(\omega t + \phi)$ and another aperture at potential V_C.
4. Main lens gap: gap length X_{BMLG} between aperture at potential V_C and the main lens electrode at potential V_{ML}.
5. Main lens interior: field free region of length X_{ML} at potential V_{ML}.

TABLE III-2-II. Time Schedules for Two $^3He^+$ Ions Injected 10 nsec Apart and Accelerated by the FNG to 4000 keV at the Target

(*Values for parameters not listed in TABLE I:* V_{EXT} = 30.0 kV, V_C = 3970.0 kV, V_B = 3970.0 kV, V_{OS} = 4.673 kV, V_{ML} = 3905.0 kV, ϕ = 2.250 radians).

Element	Time In, nsec	Time Out, nsec	Transit Time, nsec	Velocity In, cm/nsec	Velocity Out, cm/nsec	Energy In, keV	Energy Out, keV
FIRST ION							
1st gap	0.000	3.717	3.717	0.138	0.131	30.000	26.941
Buncher	3.717	49.476	45.759	0.131	0.131	26.941	26.941
2nd gap	49.476	53.184	3.707	0.131	0.139	26.941	30.296
Main lens gap	53.184	63.556	10.372	0.139	0.246	30.296	95.295
Main lens	63.556	193.319	129.763	0.246	0.246	95.295	95.295
Accel. tube	193.319	589.125	395.806	0.246	1.597	95.295	4000.209
Drift tube	589.125	1756.404	1167.279	1.597	1.597	4000.209	4000.209
SECOND ION							
1st gap	10.000	13.591	3.591	0.138	0.140	30.000	31.017
Buncher	13.591	56.237	42.646	0.140	0.140	31.017	31.017
2nd gap	56.237	59.669	3.431	0.140	0.150	31.017	35.624
[illegible]in lens gap	59.669	69.566	9.896	0.150	0.253	35.624	100.623
[illegible]in lens	69.566	195.847	126.281	0.253	0.253	100.623	100.623
Accel. tube	195.847	589.973	394.126	0.253	1.598	100.623	4005.537
Drift tube	589.973	1756.475	1166.502	1.598	1.598	4005.537	4005.537

TABLE III-2-III. Values of Adjustable FNG Single-Ended Bunching Parameters Appropriate for Various Operating Conditions

Final Energy, keV	Phase, radians	$V_C - V_{ML}$, kV	Peak-to-Peak Amplitude of Buncher Voltage, kV
$^1H^+$ (protons): V_{EXT} = 15.4 kV, E_{EXT} = 15.4 keV			
800	2.696	4.6	1.584
2400	2.696	44.6	6.416
4000	2.696	84.6 (65.0)	9.112
$^2H^+$ (molecular hydrogen) and $^2H^+$ (deuterons): V_{EXT} = 30.8 kV (30.0), E_{EXT} = 30.8 keV (30.0)			
800	2.696	−10.0 (1.0)	1.800
2400	2.696	30.0	5.600
4000	2.696	70.0 (65.0)	10.000
$^4He^{++}$ (α-particles): V_{EXT} = 30.8 kV (30.0), E_{EXT} = 61.6 keV (60.0)			
1600	2.696	−10.0 (1.0)	1.800
4800	2.696	30.0	5.600
8000	2.696	70.0 (65.0)	10.000
$^3He^+$ (singly ionized helions): V_{EXT} = 46.2 kV (30.0), E_{EXT} = 46.2 keV (30.0)			
800	2.250	−10.0 (1.0)	1.800
2400	2.250	30.0	5.400
4000	2.250	70.0 (65.0)	9.346
$^3He^{++}$ (doubly ionized helions): V_{EXT} = 23.1 kV, E_{EXT} = 46.2 keV			
1600	2.696	−3.1 (1.0)	1.600
4800	2.696	36.9	6.000
8000	2.696	76.9 (65.0)	9.828

6. Accelerator tube: uniform electric field of length X_{AT} with uniform potential drop from V_{ML} to zero.
7. Drift tube: field-free region of length X_{BTE} at ground potential between the high-energy end of the accelerator tube and the target.

The values chosen for the fixed parameters of the FNG single-ended buncher system are presented in Table III-2-I. Several parameters, such as the accelerator tube length, were restricted at the outset. The 15.0 MHz buncher voltage frequency is a frequency harmonic of 1.25 MHz, the frequency of the main oscillator used to drive the pulser deflectors as well as the buncher.

In operation, ions with energies $\approx eV_{EXT}$ are swept across the sweep aperture and the buncher voltage phase is chosen so that the oscillating component $V_{OS} \sin(\omega t + \phi)$ is in the vicinity of zero-crossing when a pulse of ions to be bunched arrives at the first bunching gap. This permits usage of the most linear portion of the sinusoidal modulation voltage. The extractor voltage V_{EXT} is chosen so that the transit time of the ions in the buncher tube is approximately a half period of the buncher frequency. Tykesson and Wiedling[2] point out that satisfactory bunching can be achieved provided the relation

$$\tfrac{1}{4} \text{ period} < \text{transit time} < \tfrac{3}{4} \text{ period} \qquad (1)$$

is satisfied. The time spent by ions in the two gaps is small compared with the time spent in the buncher. The injection energy can be chosen independently over a wide range of terminal voltages provided that the equation

$$\frac{\text{final particle energy}}{\text{particle energy at injection}} \approx \frac{V_{terminal}}{V_{EXT} + (V_C - V_{ML})} \approx 40, \qquad (2)$$

which expresses the correct tube optics condition for the FNG, is satisfied.

The bunching action of the klystron tube can be understood within the framework of the model described above by studying two typical bunching schedules. The schedules in Table III-2-II show that two $^3He^+$ ions injected 10 nanoseconds apart into the accelerator arrive on target at nearly the same time with an energy difference of ≈5.5 keV after acceleration to ≈4000 keV. An interesting point is that most of the bunching occurs when the ions have low-energy (i.e., in the terminal of the FNG).

Computer calculations were made to determine values of V_{EXT}, $V_C - V_{ML}$, V_{OS} and ϕ required for bunching the different species of ions at several representative final energies. The results are presented in Table III-2-III. Values in parentheses represent those accessible in practice due to limitations in the terminal power supplies. Acceptable bunching is feasible in each instance in spite of these limitations.

Based upon these results, a buncher tube assembly has been designed and will be constructed at Argonne National Laboratory. This unit will add about 4 in. to the present length of the terminal assembly and an additional weight which probably will not exceed 10 lbs.

References

1. C. D. Moak, W. M. Good, R. F. King, J. W. Johnson, H. E. Banta, J. Judish and W. H. duPreez, *Nanosecond Pulsing for Van de Graaff Accelerators*, Rev. Sci. Instr. **35**, 672 (1964).
2. P. Tykesson and T. Wiedling, *A Klystron Bunching System for a 6 MV Van de Graaff Accelerator*, Nucl. Instr. Methods **77**, 277 (1970).
3. I. A. D. Lewis and F. H. Wells, *Millimicrosecond Pulse Techniques*, (Pergamon Press, Ltd., London, U.K., 1954).

III-3. Time-of-Flight Errors in Pulsed Neutron Measurements

J. W. Meadows

In most pulsed neutron experiments there is an appreciable distance between the detector and the source. Because of the wide range of velocities, neutrons detected at time t may have been emitted over a wide range of earlier times. Consequently, the time dependence of the detector count rate is not the same as the time dependence of the source intensity. Although the errors in the decay curves are usually small and are often ignored, the errors in capture cross sections measured by the pulsed neutron method are more serious since they depend on differences between similar numbers.

The time dependence of the detector count rate has the form

$$C(t) = \exp(-t/\tau_0)\int_{L/v_0 t}^{\infty} E(x)x^3 \exp[L/(v_0\tau_0 x) - x^2]\,dx,$$

where v_0 is the most probable neutron velocity, $x = v/v_0$, τ_0 is the true mean life, L is the neutron track length, and $E(x)$ is the detector efficiency. The apparent mean life τ' as calculated from $C(t)$ is

$$\tau'(t) = \left[\frac{d}{dt}\ln C(t)\right]^{-1}. \qquad (2)$$

Obviously $\tau'(t)$ will vary with time unless the integral in Eq. 1 approaches a constant value. Usually this does not happen since for $L \neq 0$ the exponent becomes positive for small x.

The principal causes of the trouble are the very slow neutrons. These can be preferentially removed by covering the detector with a $1/v$ absorber. This introduces a factor $\exp(-\Sigma_0 d/x)$ into $E(x)$ where d is the absorber thickness and Σ_0 is the macroscopic capture cross section at v_0. If $\Sigma_0 d > L/v_0\tau$ the integral in Eq. 1 will approach a constant value and τ' will approach τ_0.

This material and its experimental verification have been reported in Ref. 1.

Reference

1. J. W. Meadows, *The Reduction of Time-of-Flight Errors in Pulsed Neurton Measurements*, Nucl. Instr. Methods **75**, 163 (1969).

III-4. Time Resolution of a Ge(Li) Detector in $(n,n'\gamma)$ Experiments

W. P. Poenitz

Measurements of γ-rays associated with the inelastic neutron scattering process is a technique in use for some time. The relatively recent application of lithium-drifted germanium detectors in such measurements has led to a tremendous improvement of the energy-resolution. One of the major problems in such γ-ray experiments is a sufficient separation between the prompt γ-rays emitted from the sample material and the effects due to primary and scattered fast neutrons. This problem is usually solved by employing the time-of-flight method. The time resolution and an on-line computer rise-time correction have been tested in the application of a 7 cm^3 planar Ge(Li) detector in $(n,n'\gamma)$ experiments.

The experimental setup for the determination of the time resolution of the Ge(Li) detector is shown schematically in Fig. III-4-1. The preamplifier and the tunnel diode discriminators used for the Ge(Li) detector have been designed at Argonne National Laboratory.[1] The time resolution is a function of the γ-energy and it has been measured by selecting by means of the computer storage program photo peaks of several radioactive samples. The results from these measurements using Co-60, Na-22, Np-239 (fed by Am-243), and Ba-133 samples are shown in Fig. III-4-2. In the lower energy range some contributions to the time resolution is due to the plastic detector; for Co-60 this contribution has been experimentally determined (1.4 nsec at 1.3 MeV) and corrected. The values obtained compare well with recently reported results.[2-5]

A digital correction has been applied to the incoming time information in order to correct for the time shifts due to differences in the rise-time. The effect of this correction is demonstrated by the spectra shown in Figs. III-4-3 and III-4-4 which have been obtained

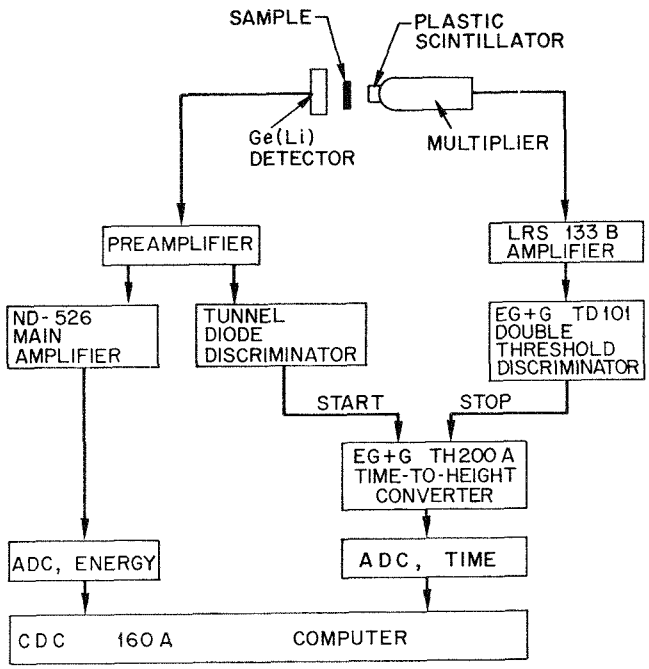

FIG. III-4-1. Experimental Test Setup. *ANL Neg. No. 116-517.*

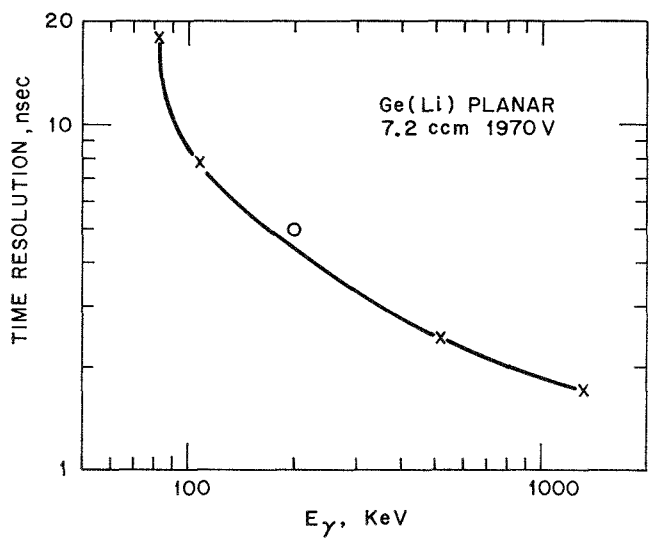

FIG. III-4-2. Time Resolution as a Function of Gamma Energy. *ANL Neg. No. 116-519.*

with the setup as shown in Fig. III-4-1, using Co-60 and Np-239 samples. All pulses have been stored, though the main contributions were from the 1.33 MeV and 1.17 MeV photo peaks of the Co-60 sample and the ~100 keV photopeaks of the Np-239 sample. Fig. III-4-3 shows the resolution curve without the on-line rise-time correction and Fig. III-4-4 shows this curve with the on-line rise-time correction.

The measurements showed that a sufficient separation between the prompt γ-rays and the fast neutrons can be obtained with a flight path of about 40–50 cm and neutron energies <2 MeV. However, care has to be taken for the reduced "dynamical" efficiency of the detector in such applications for lower γ-energies.

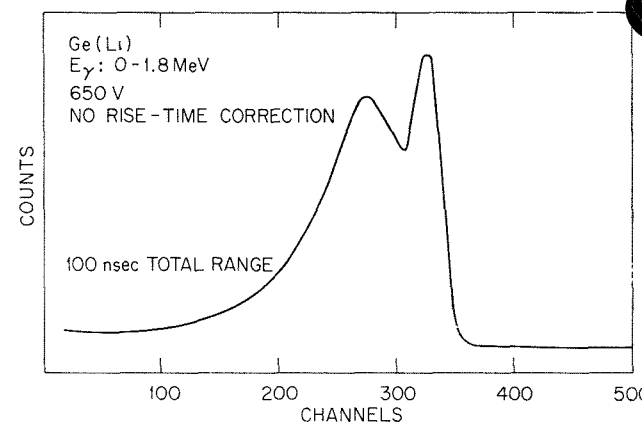

FIG. III-4-3. Time Resolution for a Co-60 and Np-239 Sample. (No Rise-Time Correction). *ANL Neg. No. 116-516.*

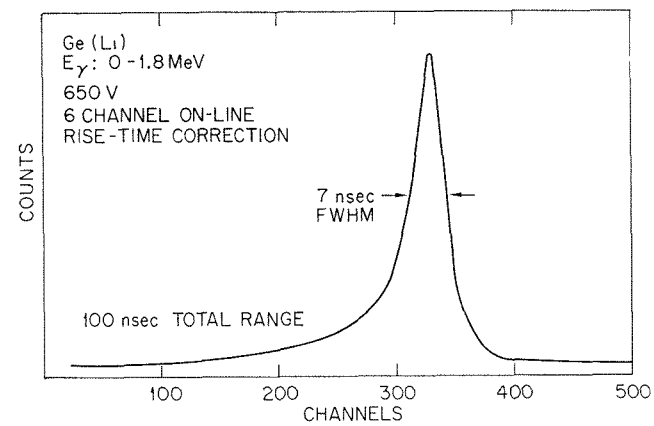

FIG. III-4-4. Time Resolution for a Co-60 and Np-239 Sample (with On-Line Rise-Time Correction). *ANL Neg. No. 116-518.*

REFERENCES

1. R. N. Larsen, Argonne National Laboratory (private communication).
2. W. Michaelis, *Timing Unit for Semiconductor Spectrometers*, Nucl. Instr. Methods **61,** 109 (1968).
3. J. M. Ya Slevic, F. M. Barnthal, J. O. Radeloff and D. A. Landis, *A Pulse-Height Compensation System for Ge(Li) Timing*, Nucl. Instr. Methods **69,** 109 (1969).
4. G. T. Ewan, R. L. Graham and I. K. MacKenzie, *Use of Ge(Li) Detectors in γ-γ Coincidence Experiments*, IEEE Transactions, Nucl. Sci. **13,** 297 (1966).
5. J. Pignetet, Y. J. Samueli and A. Sarazin, *Theoretical and Experimental Results on the Resolving Time of P.I.N. tectors in γ-γ Coincidence Experiments*, IEEE Tran tions, Nucl. Sci. **13**(3), 306 (1966).

III-5. Variation of Efficiency of a Ge(Li) Detector as a Function of Source Distance

D. L. Smith

The variation of detector efficiency with radiation source distance is an important consideration for many experiments. Whenever the distance from the source to the detector is of the same order of magnitude as the dimensions of the detector, the simple inverse square rule is no longer valid. This problem is almost always encountered when Ge(Li) detectors are utilized because these devices have relatively low efficiency and must be placed close to radiation sources in order to obtain satisfactory real-event count rates in the presence of background.

Measurements and calculations of the variation in full-energy peak detection efficiency with source distance have been made for a planar Ge(Li) detector in conjunction with point gamma-ray sources. The results of this investigation will be reported here.

Figure III-5-1 is a schematic diagram of the geometry involved. Several simplifying assumptions are made at the outset to keep the problem reasonably tractable:

1) Multiple scattering is neglected.

2) Edge effects in the detector are neglected.

3) The detector is assumed to be a right circular cylinder with no dead region intervening between the source and the active volume.

4) The fraction, f, of events appearing in the full-energy peak is assumed to be independent of geometry.

An intrinsic efficiency function $I(r)$ is defined by the equation

$$Y = fS\frac{(A/r^2)}{4\pi}(1 - e^{-\mu\tau})\, I(r), \tag{1}$$

where Y is the detector count-rate, S is the source strength, A is the front-face area (πa^2) of the detector, r is the normal distance from the source (on-axis) to the front face of the detector, τ is the thickness of the detector, and μ is the inverse attenuation length for germanium (see Ref. 1 for values of μ).

The effective center of the detector varies with the gamma-ray energy and is assumed to be at a depth z from the front face, where

$$z = \frac{1}{\mu}\ln\frac{2}{1 + e^{-\mu\tau}}. \tag{2}$$

This is the depth at which half of the incident radiation has been absorbed or scattered.

There are three domains of interest, based upon the energy of the gamma radiation:

1) Low-Energy Gamma Rays, ($\mu\tau \gg 1$, $z \approx 0$):

In this limit,

$$Y = \frac{1}{2}fS\,\{1 - \cos[\tan^{-1}(a/r)]\} \tag{3}$$

$$I_L(r) = \frac{2r^2}{a^2}\,\{1 - \cos[\tan^{-1}(a/r)]\}. \tag{4}$$

2) High-Energy Gamma Rays, ($\mu\tau \ll 1$, $z \approx \frac{1}{2}\tau$): In this limit,

$$Y = \frac{1}{2}fS\,\mu\tau\ln\left\{\sec\left[\tan^{-1}\left(\frac{a}{r + \frac{1}{2}\tau}\right)\right]\right\} \tag{5}$$

$$I_H(r) = \frac{2r^2}{a^2}\ln\left\{\sec\left[\tan^{-1}\left(\frac{a}{r + \frac{1}{2}\tau}\right)\right]\right\}. \tag{6}$$

3) Intermediate-Energy Gamma Rays, [$\mu\tau \approx 1$, z is given by Eq. (2)]:

$$I(r) = \frac{2r^2}{a^2}(1 - e^{-\mu\tau})^{-1}\left\{1 - \cos\theta_{max} - \int_0^{\theta_{max}} \sin\theta\, e^{-\mu\tau\sec\theta}\, d\theta\right\} \tag{7}$$

$$\theta_{max} = \tan^{-1}\left(\frac{a}{r + z}\right) \tag{8}$$

and Y is given by Eq. (1).

The predictions of these formulas were compared with experimental measurements made with various

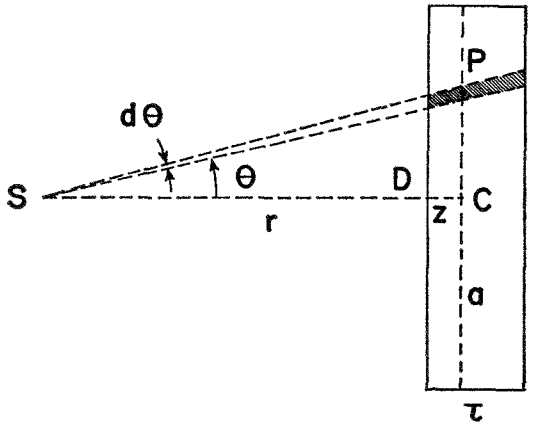

Fig. III-5-1. Side-View Schematic Drawing of a Planar Cylindrical Ge(Li) Detector and a Point Radiation Source Located at S on the Detector Axis. Radiation Emitted Between θ and $\theta + d\theta$ is Assumed to be Detected Within the Shaded Region at an Average Position Identified by the Point P. *ANL Neg. No. 116-144.*

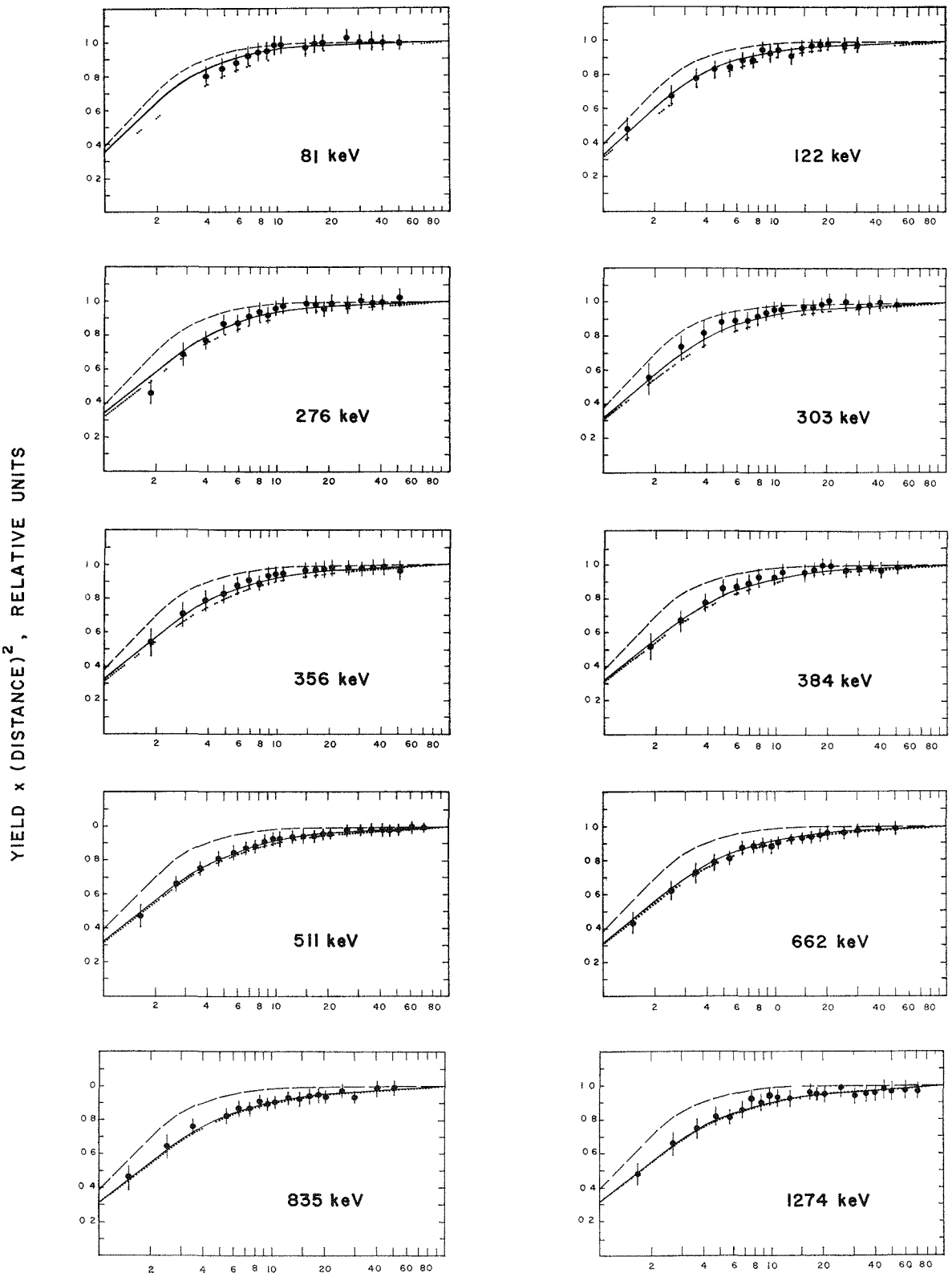

FIG III 5 2 Theoretical and Experimental Results for the Relative Intrinsic Efficiency of a 3 1 cm diam by 0 95 cm Thick Cylindrical Planar Ge(Li) Detector (7 2 cm³ Volume) The Dotted Curve is the High-Energy Limit, $I_H(r)$ of Eq (6), the Dashed Curve is the Low Energy Limit, $I_L(r)$ of Eq (4), and the Solid Curve is the General Formula, $I(r)$ of Eq (7) *ANL Neg No 116-143*

gamma-ray calibration sources and a 7.2 cm³ planar Ge(Li) detector. Corrections were made for analyzer counting deadtime and sum coincidence effects.[2] Uncertainties due to statistics and source distance were taken into consideration. The results of this investigation are shown in Fig. III-5-2. The agreement of the appropriate formulas with the data is quite good within the limits of experimental accuracy. Inaccuracies in measurement of the source distance contribute predominantly to the overall experimental error at close distances. The effect of finite source extent on the efficiency function is currently under investigation.

REFERENCES

1. R. Avida, U. Atzmony and I. Unna, *Finite Solid Angle Corrections to Angular Correlations for Square Ge(Li) Gamma Detectors*, Nucl. Instr. Meth. **46**, 350 (1967).
2. Nuclear Data Sheets, Vol. 6, K. Way, Ed., Nuclear Data Group, Oak Ridge National Laboratory, June 1965.

III-6. On-Line and Interactive Computer System

J. WHALEN, P. GUENTHER and W. POENITZ

The integration of the new SEL 840 M.P. computer subsystems into the experimental program of the FNG group will involve a great deal of design and modification in both hardware and software. Some components which will provide a basic working system have been completed and tested.

The primary hardware addition consists of a dual analog-to-digital converter subsystem and computer controlled scaler subsystem both with appropriate interface circuitry for compatibility with the 840 M.P. Both of these subsystems were modified versions of identical units used with the 160-A on-line computer. These were built and modified by the Electronics Division, ANL, using a more efficient method of electronic packaging.

The new interface for analog-to-digital converters takes advantage of the longer computer word length of the 840 M.P. and permits the strobing of both ADCs (24 bits) into the computer on a single input instruction. This results in less programming space and the saving of a great deal of time, especially considering the increased speed of the computer (factor of four). An additional improvement is gained with this new ADC system in the utilization of the extensive external interrupt network available on the 840 M.P. Modifications were made to the 840 M.P. so that the levels of priority for all external interrupts can be arbitrarily arranged by the individual experimenter on a patch board. The ADCs trigger one of these interrupt levels when an event is available for processing, thus permitting foreground-background operations with no loss of time. The interface is designed to accommodate two additional sets of ADCs which will be added to the system. Any set will be selectable by the program. An additional patch board is available for reading routing signals along with ADC information.

The computer controlled scaler subsystem occupies the second data terminal of the 840 M.P. There are six individually addressable scalers, two of which are of the pre-set variety. Any scaler can be individually started, stopped, cleared, or read by the computer. The recognition pulse from the pre-set scaler can be used to trigger an interrupt level in the 840 M.P. and start, stop, or clear any other scaler. The inputs to the scalers can be switched from external sources to a continuous internal clock or a gated internal clock.

The software efforts required for system integration can be divided into two categories: a) modifications to software delivered with the system, b) modification of software written for the CDC 160-A computer to allow it to run properly on the 840 M.P., c) creation of new software. Although considerable effort was expended on the first two categories, the net result was a debugged software operating system containing an executive program, a Fortran compiler, a mnemonic assembler, and a number of utility routines for specific stand-alone purposes. The largest part of this software will be used for off-line data processing.

The third category included one major effort to create an on-line operating system specifically structured for the FNG group to standardize as much as possible on-line data accumulation and processing. It was felt that standardization, especially in the area of "operator-computer" interactions, would greatly minimize the possibility of man-made errors when the experiment is serviced by less experienced personnel. This on-line operating system known as "CONSP" provides a variety of control options, all initiated from the typewriter which maintains the highest priority interrupt at all times. It is possible at any time to interrupt any process from the typewriter in order to perform such operations as start, stop, hold, continue, display,

insert, add, store on disk, store on paper tape, etc. Although the format for initiating these options will remain fixed, the individual experimenter can tailor the actual data accumulation and processing to fit his specific needs and in this way off-hour personnel left in charge of an experiment need only be familiar with one set of instructions. "CONSP" will be expanded as the specific needs develop.

III-7. Critical Reactivity Measurement Techniques at the Zero Power Plutonium Reactor (ZPPR)

R. W. Goin and C. L. Beck

Reactivity sample worth measurements are performed at ZPPR using two techniques. Both methods require that data be recorded using the ZPPR on-line computer[1] (see Paper III-8) and ZPPR standard data acquisition program.

The first reactivity worth determination technique is based upon the inverse kinetics solution for the power history recorded while the sample is being driven along a traverse path. The power level and sample position are recorded for input to the inverse kinetics program. The inverse kinetics solution provides the reactivity worth as a function of sample position.

The second method for determining reactivity sample worths involves the autorod. Sample position and autorod position are recorded at specified points along the sample traverse path. The autorod calibration (reactivity as a function of position) is used to convert the autorod position to a reactivity worth for the various sample positions. A description of the basic components of the data acquisition and evaluation programs for the reactivity worth determinations is presented below. These basic components apply equally well regardless of the origin of the reactivity change.

ZPPR On-Line Computer Data Acquisition Program

A general purpose computer program has been written for the ZPPR on-line computer to acquire, store, and process data from the ZPPR reactor. The hardware interfacing between the reactor and the computer is described in Paper III-8. The available data include directly addressable scalers and multiplexed digital information.

The multiplexed information includes a shift time, manual data, and twelve shaft encoder readouts. The time is a five digit number expressing the relative time within an eight-hour shift in terms of hours, minutes and seconds. The manual data entry is a five digit number which is entered by an experimenter from a control panel in the control room. The encoder readouts give the positions of the various control rods and shim rods as well as the position of the autorod and sample changer or Doppler drive. The scan time of the multiplexer is 6.4 msec. The maximum sampling rate is usually chosen to be 100 scans per second. The computer resets the multiplexer scan and enables the appropriate interrupt so that each multiplexer channel is input as it becomes available from the multiplexer.

The scalers are input independently of the multiplexer, thus allowing a different sampling rate for the scalers and the multiplexer. Recording of the data is based on the sampling rate of the scalers. The multiplexer readouts may be sampled at the same rate as the scalers or at a faster rate and averaged over the recording time interval.

The data acquisition program allows up to eight different inputs to be sampled for each scan. The data are accumulated into 100 scan blocks for output to magnetic tape. While data are being written on magnetic tape, a second block of data is assembled in a second 100 scan buffer. A software "switch" keeps the input buffer and the output buffer separated for the computer operations. Since the time required to write a data record on magnetic tape is small compared with the time required to accumulate the next data record, some computer processing time is available for on-line data processing. Because of various interleaving timing restrictions, the processing of data point-by-point as it is input is inadvisable. Background processing is allowed to begin only after a 100 scan block has been filled and the output to magnetic tape has begun.

The data acquisition program provides the control room teletype as an experimenter communications device. The experimenter can type in the command "test" together with a time interval specification, and the program will sample and edit all available scalers and multiplexer channels. The values are displayed on the control room cathode ray tube (CRT) as well as the

computer room line printer. Thus a check is provided to ensure that the experimental equipment is functioning correctly.

The initialization of the data acquisition program involves teletype communication from the experimenter to specify the date, run number, assembly number and power level, and a title explaining the experiment to be performed. The program then allows up to eight different inputs to be selected from the counters and multiplexer channels. Data channels from the multiplexer may be selected for averaging at this time. A sampling time for the multiplexer data and a recording time, which also sets the sampling time for the counters, is specified. At this point the program prints a message on the teletype to notify the experimenter that "Data is in Progress". The program also initializes the background program that will provide the on-line calculations. At the end of 100 scans of data the magnetic tape record will be written and the background program will be called.

Reactivity Measurements

To determine the reactivity worth of a sample inserted in the ZPPR reactor we must take the difference of the reactivity worth of the traverse mechanism with and without the sample inserted. For encapsulated samples the difference must be for the traverse mechanism with the sample and with an empty capsule. The problem is to determine the reactivity as a function of position for the traverse mechanism whether with or without a sample. Two methods are available for determining the reactivity. An inverse kinetics solution to a power history determines the reactivity directly while the autorod position converts to reactivity indirectly through the autorod calibration function. Two types of reactivity worth determinations are possible. The sample and dummy may be driven along the traverse path to provide a continuous set of reactivity versus position values, or the sample and dummy may be held stationary at preselected positions along the path to allow for reactivity averaging at these positions. The first method is best suited for large-worth samples while the latter technique lends itself well to small worth samples. A polynomial fit to the continuous traverse reactivity versus position information compensates for drift and provides a convenient method of presenting the results.

To evaluate the reactivity worth of a sample when using the method of assembling data at stationary positions along the traverse path a drift correction must be included. When central worth measurements are made, the sample is stopped at the "out" position and at the "in" position for equal periods of time. The average reactivity is determined for each position and the reactivity change between the "in" and "out" positions is calculated by

$$\Delta k = \tfrac{1}{8}(P_1 - 3P_2 + 4P_3 - 4P_4 + 3P_5 - P_6), \quad (1)$$

where P_1, P_3 and P_5 are the average reactivities at the three "in" positions and P_2, P_4 and P_6 are the average reactivities at the "out" positions. To get the sample reactivity we must subtract off the Δk due to the empty capsule and traverse mechanism.

Equation 1 provides a second order drift correction. The evaluation of Δk can be done on-line for the autorod data since extensive calculations are not required. To extend the drift correction to a higher order, the data may be evaluated off-line using a technique similar to that outlined below. However, the second order drift correction calculation outlined above provides teletype results for experimental monitoring.

The data recorded during a reactivity sample traverse can be expressed in terms of reactivity as a function of sample position (x) and time (t)

$$g(x,t) = f(x) + F(t), \quad (2)$$

where

$g(x,t) \equiv$ the reactivity corresponding to the autorod position (or power level in the case of inverse kinetics)
$f(x) \equiv$ reactivity worth due to sample position
$F(t) \equiv$ reactivity as a function of time and corresponds to temperature drift and other miscellaneous effects.

Now by definition, the sample position is constant from time $t = t_i$ to $t = t_{i+1}$ and therefore $f(x)$ is constant,

$$f(x) = k_i, \qquad t_i \leq t \leq t_{i+1}. \quad (3)$$

The reactivity drift function can be expressed as a polynominal in time,

$$F(t) = \sum_{j=1}^{N} a_j t^{j-1}. \quad (4)$$

For the purposes of this discussion, let $F(t)$ be a third order polynomial,

$$F(t) = at^3 + bt^2 + ct + d. \quad (5)$$

Hence, during the time interval when the sample position is constant, Eq. 2 becomes

$$G(t) = g(x,t) = at^3 + bt^2 + ct + d + k_i, \qquad t_i \leq t \leq t_{i+1}. \quad (6)$$

Now we use the least squares method of curve fitting to provide the best fit of the reactivity data $G(t)$ to a

third order drift curve $F(t)$ plus a reactivity change due to sample positioning k_i.

The sum of the squared deviations is

$$S = \sum_{i=1}^{N} \sum_{j=J_i}^{J_{i+1}} [G(t_j) - at_j^3 - bt_j^2 - ct_j - d - k_i]^2, \quad (7)$$

where

$N \equiv$ number of sample positions

$J_i \equiv$ number of the data point corresponding to t_i.

The above expression gives the sum of the deviations for all sample positions. To minimize the sum of the squares we chose the curve according to

$$\frac{\partial S}{\partial a} = 0 = \sum_{i=1}^{N} \sum_{j=J_i}^{J_{i+1}} t_j^3 [G(t_j) - at_j^3 - bt_j^2 - ct_j - d - k_i] \quad (8)$$

$$\frac{\partial S}{\partial b} = 0 = \sum_{i=1}^{N} \sum_{j=J_i}^{J_{i+1}} t_j^2 [G(t_j) - at_j^3 - bt_j^2 - ct_j - d - k_i] \quad (9)$$

$$\frac{\partial S}{\partial c} = 0 = \sum_{i=1}^{N} \sum_{j=J_i}^{J_{i+1}} t_j [G(t_j) - at_j^3 - bt_j^2 - ct_j - d - k_i] \quad (10)$$

$$\frac{\partial S}{\partial d} = 0 = \sum_{i=1}^{N} \sum_{j=J_i}^{J_{i+1}} [G(t_j) - at_j^3 - bt_j^2 - ct'_j - d - k_i]. \quad (11)$$

The four equations 8 through 11 contain $4 + N$ unknowns. However, a matrix can be formed to give $3 + N$ equations with $3 + N$ unknowns if the following procedure is followed.

Define $k_1 = 0$. Find all other k_i, $i > 1$, values relative to d.

Using Eq. (11) we may form N equations which may be used with Eqs. (8) through (10) to provide $N + 3$ equations to solve for a, b, c, d and k_i $(2 \leq i \leq N)$. (See below for the resulting set of equations.) The standard matrix solution routines on the SEL 480 MP have proven satisfactory for solving this system of equations.

The above derivation could be carried through for any order drift curve by simply using

$$G(t) = a_1 + a_2 t + a_3 t^2 + \cdots + a_n tn - 1 + k_i. \quad (13)$$

Thus, one obtains the time drift behavior of the reactor over the period of interest in addition to the constant relative reactivity at each stationary position of the sample.

$$\sum_i \sum_j t_j^3 G(t_j) = a \sum_i \sum_j t_j^6 + b \sum_i \sum_j t_j^5 + c \sum_i \sum_j t_j^4 + d \sum_i \sum_j t_j^3 + k_2 \sum_{j=J_2}^{J_3} t_j^3 + k_3 \sum_{j=J_3}^{J_4} t_j^3 + \cdots + k_N \sum_{j=J_N}^{J_{N+1}} t_j^3$$

$$\sum_i \sum_j t_j^2 G(t_j) = a \sum_i \sum_j t_j^5 + b \sum_i \sum_j t_j^4 + c \sum_i \sum_j t_j^3 + d \sum_i \sum_j t_j^2 + k_2 \sum_{j=J_2}^{J_3} t_j^2 + k_3 \sum_{j=J_3}^{J_4} t_j^2 + \cdots + k_N \sum_{j=J_N}^{J_{N+1}} t_j^2$$

$$\sum_i \sum_j \iota_j G(t_j) = a \sum_i \sum_j t_j^4 + b \sum_i \sum_j t_j^3 + c \sum_i \sum_j t_j^2 + d \sum_i \sum_j t_j + k_2 \sum_{j=J_2}^{J_3} t_j + k_3 \sum_{j=J_3}^{J_4} t_j + \cdots + k_N \sum_{j=A_N}^{J_{N+1}} t_j$$

$$\sum_{j=J_1}^{J_2} G(t_j) = a \sum_{j=J_1}^{J_2} t_j^3 + b \sum_{j=J_1}^{J_2} t_j^2 + c \sum_{j=J_1}^{J_2} t_j + d \sum_{j=J_1}^{J_2} 1$$

$$\sum_{j=J_2}^{J_3} G(t_j) = a \sum_{j=J_2}^{J_3} t_j^3 + b \sum_{j=J_2}^{J_3} t_j^2 + c \sum_{j=J_2}^{J_3} t_j + d \sum_{j=J_2}^{J_3} 1 + k_2 \sum_{j=J_2}^{J_3} 1$$

$$\sum_{j=J_3}^{J_4} G(\iota_j) = a \sum_{j=J_3}^{J_4} t_j^3 + b \sum_{j=J_3}^{J_4} t_j^2 + c \sum_{j=J_3}^{J_4} t_j + d \sum_{j=J_3}^{J_4} 1 + \cdots + 0 + k_3 \sum_{j=J_3}^{J_4} 1$$

$$\vdots \qquad \vdots \qquad \vdots \qquad \vdots \qquad \vdots \qquad \vdots$$

$$\sum_{j=J_N}^{J_{N+1}} G(t_j) = a \sum_{j=J_N}^{J_{N+1}} t_j^3 + b \sum_{j=J_N}^{J_{N+1}} t_j^2 + c \sum_{j=J_N}^{J_{N+1}} t_j + d \sum_{j=J_N}^{J_{N+1}} 1 + 0 + 0 \cdots + k_N \sum_{j=J_N}^{J_{N+1}} 1$$

References

1 R W Goin, C. L Beck, J E Hutton and A L Hess, *On-Line Computer System for the Zero Power Plutonium Reactor*, Reactor Physics Division Annual Report, July 1, 1968 to June 30, 1969, ANL-7610, p. 371

III-8. Zero Power Plutonium Reactor (ZPPR) Computer Interfaces

J. E. Hutton, R. J. Forrester and D. L. Hall

Introduction

Collections and on-line analysis of much of the experimental data at the ZPPR facility is accomplished through a general purpose data collection system composed of an 840 MP computer and a remote I/O system. This paper describes the changes and additions made to the I/O system since it was first reported,[1] the experimental setups in which it has been used to the present time, and setups which are planned for the near future. The paper also reviews the system for consistency with the initial design concepts, discusses improvements which can be made, and suggests concepts which will be helpful in designing similar systems in the future.

Description of I/O System

The following is a summary of the I/O system as reported in Ref. 1.

General

The remote I/O system collects experimental data from various locations in the ZPPR facility and transmits them to the central SEL 840 MP computer. Where required, results of the analysis can be returned to the appropriate remote terminal for display and control.

This system is flexible, allowing development of new experiments, while at the same time configuration control can be maintained when it is desired to set up and run previously developed collection systems.

To achieve flexibility modular construction and standard interfaces have been used throughout the system, thus insuring interchangeability of experiments and equipment between stations. Computer channels, control lines, and interrupts are routed to remote stations as needed. The control logic is tailored to specific jobs by removable patch panels which, for established tasks, are permanently wired or provided with a cover.

To assist experimental personnel in the setup and checkout of new techniques, data are transmitted on data busses to minimize the number of individual connections required for setup. Standard interface and timing logic is prewired to eliminate race and other control logic problems. In addition, manual controls are synchronized to the system clock and sync circuits are provided for external signals to avoid async-to-sync problems. Local displays and controls operate independently from the computer for checkout of new systems and problem isolation.

The data buss structure and computer channels do not normally change between jobs; therefore, many routine jobs require only changing of the experimental inputs, patch panel, and computer programs.

The system can be separated into three types of subsystems, the SEL digital I/O unit, data link selector unit, and the remote I/O terminal.

SEL digital I/O unit

This unit provides an interface between the SEL 840 MP I/O buss and the data link selector, the necessary synchronizing signals for I/O operations, and the signal conditioning for the interrupt lines. This unit also provides 24-bit output channels, 24-bit input channels, twenty-four control lines, two 16-bit status channels and ten interrupt lines for use by the experimenter.

Data link selector (DLS)

This unit routes control signals, timing pulses, and data to and from the remote I/O terminals.

All signals are transmitted through identical 25 pair connectors; therefore, the configuration of the busses can be adjusted to meet the requirements of particular experiments by moving connectors in the DLS.

Remote I/O terminal

One remote I/O terminal located at each experimental station provides operator controls and displays in addition to data collection and timing equipment. Each terminal is modular in construction, containing three types of units: control, display, and experimental equipment housing.

The control unit contains the signal conditioning and control circuits required for transmission of data to and from the computer. Manual controls, indicators, timing pulses, computer interrupt and control lines, and logic units are also provided on a removable patch panel for control and interface with experimental equipment.

The display unit provides a display of computer generated data or the experimental equipment output at the remote station.

Standard nuclear instrument module (NIM) bins are used for the experimental equipment built for the system. These bins will also accept many commercial

counters, A/D converters, discriminators, amplifiers, and high voltage power supplies.

New System Descriptions

The following additions and modifications have been made to the original system: (1) An External Block Transfer Control (EXT BTC) capability has been added to the SEL 840 MP Computer. (2) The SEL 840 MP Computer which is located in the computer room has been interfaced with the SEL 810 A Computer, some 125 feet distant in the counting room. (3) Several interface modules have been built including an Up-Down Counter, Shift Register, ADC Interface, Relay Control, Manual Data Entry, and a Printed Circuit Card Test Module.

EXT BTC

The external BTC feature of the computer provides a means for entering data directly to core without interrupting the program being executed by the Central Processing Unit. Both the data and the memory location where it is to be stored are supplied from outside the computer. To take advantage of this feature, the necessary priority logic, address counters, and channel selection logic to set up several independent data buffers in core are included in the Data Link Selector.

SEL 840 MP TO SEL 810 A INTERFACE

The SEL 840 MP Computer System and the SEL 810 A Computer System have been equipped with an ANL designed I/O which enables data transfer to/from each other, much like a peripheral device.

The SEL 810 A is interfaced to the SEL 840 MP for high speed 16 bit parallel operation, with cable terminators, cable drivers, and control and sync logic to insure uniform timing and data communication.

Data may be transferred from the SEL 810 A to the SEL 840 MP or from the SEL 840 MP to the SEL 810 A. The SEL 810 A can also transfer data to the SEL 840 MP by way of Block Transfer Control (BTC).

ZPPR UP-DOWN COUNTER

This module provides two 24-bit counter registers with the capability of parallel setting and up/down counting. They can also be separated into two 20-bit counters and two 4-bit counters. Counting is performed through two clock lines, one controlling the count in the up direction and the other in the down direction.

Pulse rate and other frequency information up to 2 MHz can be collected through two BNC connectors on the front or through two connectors on the back of the NIM bin which holds the unit. All controls plus the clock inputs appear on the remote I/O patch panel. The counter outputs are normally gated to the I/O terminal output buss for display or transmission to the SEL 840 MP computer.

A decade select switch and indicator lights are also provided to indicate the pulse rate which the unit is receiving.

SHIFT REGISTER

The shift register module includes several special logic features which enhance its usefulness in applications with experimental work.

It has two 24-bit serial-to-parallel converters. The output from this unit can be gated to the remote I/O terminal output buss for display or transmission to the SEL 840 MP computer.

The input is through two BNC connectors on the front or from the remote I/O patch panel. The controls on the patch panel include Master Reset, Clock, Read, Parallel Enable, and Bit 24 output for indication that the register is full and ready to read. With a small amount of logic on the patch panel, one can collect and transfer data to the computer at a high rate by loading one register while reading the other register to the computer.

MANUAL DATA ENTRY UNIT

This new unit replaces an old system which used a thumbwheel switch. The new system uses a keyboard with numbers from 0 through 9 plus a set and a repeat button. Four other buttons and four switches are used to control logic functions on the remote I/O patch panel. The four switches will send a high or low level to the remote I/O patch panel.

The keyboard is used by the operator to enter a five-digit number in a shift register for setting time and counters, or for transmission to the computer.

A cryptogram feature has also been incorporated which utilizes the four buttons and four switches for logic control functions on the remote I/O patch panel.

RELAY CONTROL

This module contains four relays, each having two normally open contacts. These mercury-wetted relays are controlled by DTL logic with a 5.1 V zener diode used for conditioning input signals of 5 to 10 V.

Signals to control each relay come through four separate BNCs on the front of the unit or from the remote I/O patch panel through a connector on the back of the unit. Signals may also be sent from two other BI to the patch panel through this unit for controlling logic on the patch panel.

ADC INTERFACE

The ADC interface module gates data from a Northern Scientific NS 624 100MHz, 8192 Analog-to-Digital Converter to the Remote I/O Terminal output buss.

PRINTED CIRCUIT CARD TEST MODULE INTERFACE

This unit enables one to set up and check out logic functions of newly designed or malfunctioning printed circuit cards utilizing the various logic functions available on the remote I/O patch panel or bit patterns from the computer.

Current Experimental Setups

At present, two basic configurations are used to collect data from the majority of measurements taken at ZPPR. These two configurations and their related experiments are described below.

POSITION AND COUNTER INPUTS

A large group of ZPPR experiments presently being run require encoder inputs from the ZPPR data collection system, counter inputs, and time information. A standard remote I/O patch panel and a master data acquisition program are available for these experiments (see Paper III-7).

This configuration performs two independent functions: (1) reading and resetting four up-down counters controlled by the remote I/O terminal, (2) requesting and reading encoder position and other information from the data collection system. The counters are gated, read, and when required, reset under computer control. The program-controlled counter gates are synchronized to the 10 kHz pulse in the data link selector to prevent variation in counting time caused by cycle stealing and other variations in the computer program.

Each counter is assigned a position on the cycling address counter so that it can be read by the computer or displayed on the local display. Reset pulses are generated on the remote I/O patch panel each time the computer reads a counter. The control logic for the system is shown in Fig. III-8-1.

Encoder position and other information from the Data Collection System (DCS) is multiplexed by a counter in the encoder control and display (EC&D) unit. The computer received DCS information by requesting an EC&D cycle. The counter is reset and interrupts are generated when the requested data are ready to be transferred to the computer. The DCS output is assigned one position on the cycling counter. After each interrupt the computer addresses this position causing the multiplexed data to be gated to the computer I/O buss.

Using the master data acquisition program, the experimenter inputs the channels to be sampled and the sample rates on the teletype unit located in the reactor control room. Subprograms are attached to the main data acquisition program in accordance with the requirements of the experiment. The data acquisition requirements and descriptions of individual experiments which have been run are summarized below.

Rod Worth and Subcritical Reactivity Measurements

Inverse kinetics has been used almost exclusively for determination of rod worths in ZPPR[2] (see Paper III-7). The reactor power level is followed from a few seconds before to a few minutes after a rod movement, with a high sensitivity ion chamber. An electrometer and voltage-to-frequency (V/f) converter are used to convert this current to a frequency. The output of the V/f converter is routed to a discriminator for conversion to logic form and is scaled in a computer controlled counter which is part of the I/O system. The counter information is sampled and reset at a rate selected by the experimenter. Typical rates are 1 sample/sec for differential worth measurements on motor-driven control rods (reactivity insertion rate approximately 30 Ih/min) and 10 samples per second for total worth measurements on scrammed rods (approximately 150 Ih reactivity change in 90 msec). The sampled counter outputs are stored in two data blocks of 100 words each in the computer memory. While one data block is being stored on magnetic tape, the other is collecting new data. In differential worth measurements, the encoder on the rod is also sampled and stored at the selected time intervals. Subsequent inverse kinetics analysis results in excess reactivity-time or excess reactivity-position curves which can be displayed on the CRT in the control room, plotted on paper, and/or printed on a line printer.

Rod Scram Times

To satisfy a ZPPR operational requirement, the scram times of 20% of the safety rods are measured each week. A significant reduction in the time required for these measurements has been possible by use of inverse kinetics analysis of the power level variations following the scramming of several rods in sequence.[2] The system described in the preceding subsection, "Rod Worth and Subcritical Reactivity Measurements" is used to collect the power level information by periodic sampling and resetting of a counter in the remote I/O system. However, because of the increased time resolution requirement, the counter is sampled at a rate of 100 samples/sec. The rapid accumulation of

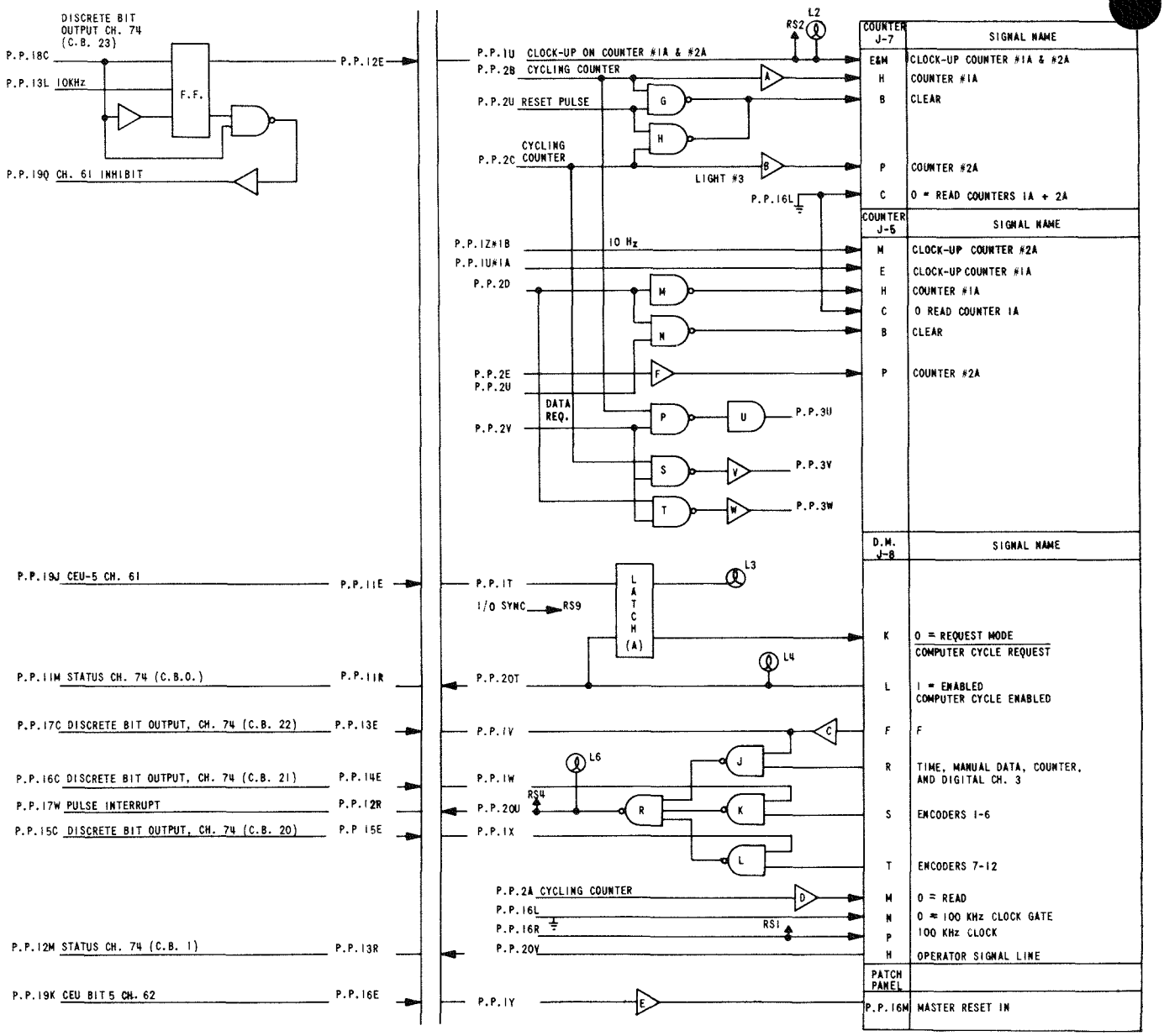

FIG. III-8-1. Data Acquisition Control Logic. *ANL-ID-103-A11576.*

data precludes a data-taking interval sufficiently long to evaluate the source in the kinetics equation (from spontaneous Pu-240 fission). Therefore, the source is derived from previous measurements at lower sample rates. By examination of the reactivity-time curve from an inverse kinetics analysis the drop time of each rod in the sequence is determined.

Central Reactivity Measurements

The measurement of small sample reactivities is a routine ZPPR measurement. During oscillation of the sample in and out of the reactor, the power level is held constant by a tantalum blade autorod. A typical sample oscillation consists of 60 sec of travel time in each direction plus 120 sec constant position time at the "in" and "out" positions. The position encoder of the reactivity sample is sampled continuously, and whenever constant, the autorod encoder is sampled 100 times per second, averaged over 1 sec intervals, and stored on magnetic tape. As soon as the sample is moved, the data points from the last position are averaged to give an autorod position. Upon completion of a specified number of cycles, the worth of the sample is calculated from the difference between the autorod position with the sample in the reactor and the average of the two adjacent "out" positions (and vice versa) for all constant position points, except end points, of the measurement. The computer performs this calcula-

tion using the coefficients of the autorod calibration curve, averages over all differences, and prints the sample reactivity on the teletype near the experimenter. The method of taking differences cancels out first and second order drifts in the reactivity occurring during the measurement.

Reactivity Traverses

In small sample reactivity traverses the sample is moved from "out of reactor" to "in reactor" in stepwise fashion, stopping at intermediate points for a set (constant) time period. After reaching the "in" position and waiting for the set time period, the sample is moved outward, reproducing the time periods and constant position points exactly. The autorod holds the reactor power constant during the sample oscillation. The autorod position encoder and sample position encoder are sampled continuously at a rate of 100 samples/sec, and are stored as data blocks in the computer core. The data blocks are averaged on line and stored on magnetic tape at a rate of 1/sec.

The long time involved in a single oscillation requires that the drift be separated from the sample reactivity at each point. This is accomplished by minimizing the deviations between the observed reactivity and as assumed reactivity (see Paper III-7). The assumed reactivity consists of a drift curve of third order in time, plus a constant sample reactivity at each stationary sample point. In this manner the coefficients of the third order drift and the sample reactivity at each stationary point are obtained.

This measurement is also performed without the autorod by inverse kinetics analysis of power level variations. When this technique is used, the power level variations are recorded by use of a computer controlled counter in the I/O system.

Reaction Rate Traverses

The reaction rate traverse (i.e., by fission chamber or BF_3 counter) is another routine experiment that has, in the past, utilized the on-line capabilities of the ZPPR computer. The position encoder of the fission chamber was sampled and stored along with the contents of a computer-controlled counter which was reset after each sampling. These samplings took place whenever the fission chamber encoder was stationary, and upon movement of the chamber all counter samples at the last stationary position were summed and divided by the total time at that spatial point to give the count rate. This count rate was then normalized to the count rate at the first position measured after initialization of the program (which was chosen to be at the center of the reactor). In this manner, a normalized (normalized to 1.0 at the reactor center) reaction rate traverse was obtained. After each stationary sample point the above normalization was performed and the point was plotted on the CRT in the control room. This allowed the experimenter to check for bad data points as the traverse progressed.

POLARITY CORRELATION

The second remote I/O configuration which has been utilized is described below. The polarity cross correlation function of a ZPPR configuration was calculated from simultaneous samplings of the sign of the analog signal from each of two detectors.[3] The detector (plastic scintillator-phototube) outputs were fed to two level detectors which sensed the sign (positive or negative) of the AC components of the chamber signals. The logic output of each level detector was then fed to a separate computer-controlled 24-bit shift register module at a 50 kHz rate. After 24 samples of the level detector outputs the first shift register contents were transferred to the core of the computer. The returning "data accepted" signal was used to gate the second shift register to the computer. The "data accepted" pulse was also used to set the first shift register with "0" in the first bit and a "1" in remaining bits so that 24 clock pulses later the zero was shifted out into a flip-flop which restarted the read cycle.

The elements and control lines used in this experiment were an integral part of the remote I/O system. Calibration signals and clock pulses for gating data into the shift registers were also derived from the I/O system.

A subsequent data analysis gave an accurate value of β/ℓ for the reactor.

Future Experimental Setups

Experiments contemplated for the near future which will utilize the computer and remote I/O system are listed below. Future plans also call for collection of "position and counter inputs" through permanent logic using the external Block Transfer Control.

DOPPLER EXPERIMENT

The Doppler experiment consists of a measurement of the reactivity associated with oscillating a heated sample in and out of the reactor.[4] This reactivity can be related to autorod position variations while holding the power level constant. The sample oscillations will most likely have a trapezoidal form with periods of constant positions at the "in reactor" and "out of reactor" spatial points. The oscillation will initially be driven by a timer-controlled-indexer stepping-motor combination.

A description of the most probable method of data taking is given below. The autorod encoder reading

will be sampled and stored at rates of 100/sec and averages will be recorded on magnetic tape at a rate of 1/sec. A master data acquisition program and a reactivity measurement subprogram, similar to that described above, under "Central Reactivity Measurements," will be used to collect data on line. The program will provide up-to-date information on autorod positions and fluctuations at each limit of sample travel, and the average sample reactivity after a requested number of cycles. A special feature of the subprogram will be to adjust the data-taking interval in accordance with the time spent at each limit. The signals controlling the data-taking interval will be fed through a remote I/O terminal from the timer which controls the motor indexer. A counter will also be sampled during the data taking interval, and power information will be printed out with reactivity values.

ABSOLUTE FISSION RATE MEASUREMENTS

Measurement of absolute fission rates requires accurate determination of the pulse-height distribution from a fission chamber. In the lower energy portion of the spectrum the fission pulses must be separated from the noise and alpha pulses present. This could be accomplished on line by analog-to-digital conversion using the remote I/O terminals and an external ADC. By storage of these numbers in core, and, with parallel sort and curve fit programs, the pulse height distribution could be constructed along with an extrapolation of the low energy tail. The experimenter would be able to obtain an updated display of the spectra on the CRT and the absolute number of fissions at any time by pressing a button on the remote I/O panel.

The system could be adapted, as time progresses, to measurements with multiple fission chambers so that fission ratios could be measured and evaluated on line with multiple chambers.

ON-LINE REACTIVITY METERS

The evaluation and display of reactivity is a projected future use of the I/O system. The inverse kinetics technique or the polarity cross correlation technique may be used to determine the reactivity in real time.

COMPUTER CONTROL OF EXPERIMENTS

Subject to the appropriate safety approvals, many of the experiments in progress presently may be adapted to computer control. New experimental equipment is now being designed so that computer control of functions such as selecting samples and positioning components can be added by changing a printed circuit board or making other minor changes.

Comparison with the Design Study

After one year of operation it is appropriate to compare the initial concepts of the justification and design study[5] with the actual system, both in general layout and in the areas of equipment and usage.

GENERAL

The design study in a general sense called for a building block or multiple-use approach where a limited number of I/O devices could be adapted to a variety of experiments. To accomplish this, I/O stations were required in several areas. Each station contained control panels plus equipment for communication with the computer and interfacing with experimental equipment. Standard computer peripherals were planned for the reactor control room and the loading room. With the exception of peripherals in the loading room, this general concept has been implemented.

EQUIPMENT

The following differences exist between the equipment as described in the design study and as built.

The design study suggested the capability of handling data in 8-bit bytes. In practice, the capability of dividing the computer word into two 12-bit sectors was provided. However, in almost all cases full 24-bit words are transmitted to the computer.

The general purpose analog data collection equipment, suggested in the design study, has not been constructed. This is due primarily to a shift to digital encoders for position measurements and to requirements for special devices when analog measurements were necessary.

Although the UP/DOWN counters meet the specification of the buffer scaler registers in the design study, the data rates and the design of the experimental equipment have made it unnecessary to buffer data in the remote I/O stations.

SYSTEM UTILIZATION

The differences between actual system utilization and that envisioned in the design study are summarized below.

The design study envisioned a greater extent of preprocessing of data—that is, averaging data points, storing changes only, packing data, etc.,—with magnetic tapes used for slow speed storage only. In practice a large portion of the raw data has been stored directly on magnetic tape. Had this been anticipated, higher speed tape systems would have been specified. The test and calibrate mode of operation has been implemented in a segmented fashion, rather than an

overall system basis, as was envisioned in the design study.

At present the majority of the setup work is being done by the system designers. Increased efficiency in system utilization is contemplated by increasing experimenter participation in system setup. This will probably take the form of seminars on system logic, improving reference material on the system, and investigating changes to the levels of flexibility in the system.

Planned Improvements to the System

Although the overall system is performing satisfactorily, there are several areas in which improvements are planned:

(1) In many instances, BCD data have been generated to provide direct readout of position indicators and counters for the convenience of the experimenters. However, for even the simplest computer operations on these data (averaging, scaling, etc.) the BCD data must be converted to binary form. This is relatively time consuming; therefore, future plans call for BCD to binary hardware conversion. In planning a system, it would be wise to consider alternates to this approach, such as generating all data in binary and feeding back decimal readout data from the computer, properly scaled and converted to engineering units.

(2) In principle, it is possible for two systems to time share data generating equipment, or for two data collection setups at separate remote stations to share the same peripherals. In practice we have found that this requires software checks and housekeeping programs which are undesirably complicated. Therefore, future setups will minimize equipment interdependence.

(3) There are several data collection tasks which have become standard. Permanent logic to perform these tasks can now be added to the system. In addition to releasing the flexible portion of the system for new tasks, this should also reduce operator confusion and, consequently, operator error.

Conclusion

The ZPPR computer and remote I/O system was intended to maximize the quantity and quality of experimental results from the reactor. Systems of this type normally evolve through the steps of data logging, logging and quick-look analysis, and finally feedback control. The ZPPR system is presently in the quick-look analysis phase of development.

While the remote I/O hardware has proven to have sufficient flexibility for all the data collection requirements up to the present, it is anticipated that the system will not cover all future requirements. However, the modularity built into the system should enable future modifications without costly rebuilding of the system.

References

1. J. E. Hutton, *A Remote Input/Output System for the Zero Power Plutonium Reactor (ZPPR) Computer*, Reactor Physics Division Annual Report, July 1, 1968 to June 30, 1969, ANL-7610, pp. 375–378.
2. R. G. Matlock, P. I. Amundson, R. E Kaiser, J. C. Young, R. O. Vosburgh, J. M. Gasidlo and R. J. Forrester, *ZPPR Startup and Operating Experience*, Trans. Am. Nucl. Soc. **12,** 46 (1969).
3. W. K. Lehto and R. W. Goin, *The Effects of S/N Ratio on the Results of Polarity Correlation Experiments*, Trans. Am. Nucl. Soc. **13,** 271 (1970).
4. J. M. Gasidlo, *Results of Recent Doppler Experiments in ZPR-3*, ANL-7320 (1966).
5. A. L. Hess and J. E. Hutton, *Justification and Design Study for an Automatic Data Processing System for the Zero Power Plutonium Reactor*, Second Rev: March 1968 (unpublished).

III-9. Precision Efficiency Calibration Procedures for Ge(Li) Detectors

D. W. Maddison and L. S. Beller*

Precision efficiency calibration of Ge(Li) detectors to the order of 1% is not an easy or necessarily straightforward task. Several methods have been reported in the literature,[1-9] but most of them do not yield consistent results to better than about 5%, depending on the technique used and the particular detector involved. It is virtually impossible to calculate the efficiency for a Ge(Li) detector except in certain idealized cases.[10]

Several authors[4-9] have used multiple gamma-ray sources, such as Ra-226, Ag-110m, Co-56, etc., to perform efficiency calibrations. Such sources require a knowledge of the relative gamma-ray intensities which are usually determined from some previously cali-

* Atomics International, a Division of North American Rockwell Corporation, Canoga Park, California.

brated Ge(Li) detector. The most serious difficulty with this method is that any errors or assumptions made in the initial determination of the relative gamma-ray intensities are already present in the calibration before one starts, and in most cases there is no estimate of these errors available.

The greatest problem in determining the efficiency of a Ge(Li) detector is the method used to find the area of the photo-peak in question. There are several methods that can be used. The gamma-ray photo-peak of a Ge(Li) spectrometer depends on several factors including the detector resolution, its peak-to-Compton ratio, and the electronic noise of the system components. This generally results in a photo-peak shape that is somewhat different from an ideal Gaussian shape, and it may vary with energy, counting rate, and time. An analysis code must make some assumption on the photo-peak shape, particularly with multi-gamma spectra, and the time needed for analysis is usually directly related to the degree of sophistication of the code being used. Ideally, a set of response functions for the photo-peaks at all energies would be desirable, but this requires extensive coding and computer time as well as large quantities of input data. Further complications are introduced by background subtraction, which may vary quite rapidly in some cases, particularly at a Compton edge.

The problem of calibration sources also exists where absolute calibration is desired, or where several sources are used. Good calibrated sources can be obtained for long half-life isotopes, e.g., Co-60, Mn-54, Cs-137. The availability and cost of calibrated sources covering an extended energy range, however, may be a limiting factor.

Our particular method involves the use of a standard 7.59 × 7.59 cm NaI detector and several sources covering the energy range from 165 to 1836 keV. All sources are either single gamma-ray emitters (Ce-139, Hg-203, Sn-113, Cs-137, Mn-54), or multiple gamma-ray sources with widely spaced energies (Co-60, Bi-207, Y-88). Each of the gamma-ray activities from these sources can be easily and accurately determined with the NaI detector, using the information available from Heath's tables.[11] Comparison of several of our NaI-calibrated sources with N.B.S. standards showed agreement within the quoted errors for the N.B.S. standards. These sources were then used to calibrate the four Ge(Li) detectors in the ZPPR counting room,[12] using an analysis code, RAID, developed previously.[13] The four detectors vary considerably in their characteristics, and least-squares fits of the calibration data has produced consistent results for counting of standards to ±0.5% between the three automated detector systems. This agreement has also been verified with some activated materials.

The technique is to first count each standard source with the standard NaI detector at some distance where the source diameter correction is small (for our particular situation, the source-to-detector distance is 20 cm and the source diameter is 0.475 cm). These sources are then counted on the Ge(Li) detectors. If the time interval between the NaI and the Ge(Li) counting is short, the errors in the standard source half-lives can be neglected. The efficiency of the Ge(Li) detectors can be computed from the Ge(Li) counting data and the NaI-determined source activities. Because the spectra are essentially single line spectra, at least in any particular area, many of the difficulties of defining the peak shape and peak area become insignificant. In addition, any code that is used to analyze these Ge(Li) spectra will perform the analysis in the same manner each time; thus errors from the analytical technique employed will be eliminated, especially with subsequent activity determinations.

Reproducibility of our results is about ±0.5% over the presently investigated time period of eleven months. Specific trial cases have shown that the geometrical error (associated with sample position reproducibility) is about 0.1% and analysis error is about 0.4%. The analysis error appears to be due to a truncation effect resulting from using individual channels as peak and background boundaries. This possibly could be reduced by using a different energy dispersion (keV/channel) for the data collection.

References

1. R. W. Mowatt, *A Semi-empirical Efficiency Cure for a Ge(Li) Detector in the Energy Range 50 to 1400 keV*, Nucl. Instr. Methods **70,** 237 (1969).
2. J. M. Freeman and J. G. Jenkin, *The Accurate Measurement of the Relative Efficiency of Ge(Li) Gamma-ray Detectors in the Energy Range 500 to 1500 keV*, Nucl. Instr. Methods **43,** 269 (1966).
3. D. P. Donnelly and M. L. Wiedenbeck, *The Relative Detection Efficiency Calibration of a Ge(Li) Detector at Low Energies*, Nucl. Instr. Methods **64,** 26 (1968).
4. G. Wallace and G. E. Coote, *Efficiency Calibration of Ge(Li) Detectors Using a Radium Source*, Nucl. Instr. Methods **74,** 353 (1969).
5. W. R. Kane and M. A. Mariscotti, *An Empirical Method for Determining the Relative Efficiency of a Ge(Li) Gamma-ray Detector*, Nucl. Instr. Methods **56,** 189 (1967).
6. G. Walford and C. E. Doust, *A Method for the Rapid Calibration of Germanium Spectrometers*," Nucl. Instr. Methods **62,** 353 (1968).
7. Y. Gurfinkel and A. Notea, *Use of Ba-133 as a Calibrati Standard for Ge(Li) Detectors*, Nucl. Instr. Methods 173 (1967).
8. P. H. Barker and R. D. Connor, *Co-56 as a Calibration Source up to 3.5 MeV for Gamma Ray Detectors*, Nucl. Instr. Methods **57** (1967).

9. R. L. Auble et al., *The Decay Schemes of Co-56 and Mn-56 and Their Use as Calibration Standards*, Nucl. Phys. **A91**, 225 (1967).
10. G. Aubin et al., *Calculated Relative Efficiency for Coaxial and Planar Ge(Li) Detectors*, Nucl. Instr. Methods **76**, 85 (1969).
11. R. L. Heath, *Scintillation Spectrometry Gamma-Ray Spectrum Catalogue*, Second Edition, Vol. 1, IDO-16880-1 (TID-4500), 1964.
12. D. W. Maddison and L. S. Beller, *Characteristics and Capabilities of Automated Counting Facilities for the Zero Power Plutonium Reactor (ZPPR)*, Reactor Physics Division Annual Report, July 1, 1968 to June 30, 1969, ANL-7610, pp. 379–381.
13. L. S. Beller and D. W. Maddison, *Automated Spectrum Analysis Methods for Ge(Li) Detectors*, Reactor Physics Division Annual Report, July 1, 1968 to June 30, 1969, ANL-7610, pp. 416–417.

III-10. Contamination Determination with Lithium-Drifted-Germanium [Ge(Li)] Detectors

L. S. Beller* and D. W. Maddison

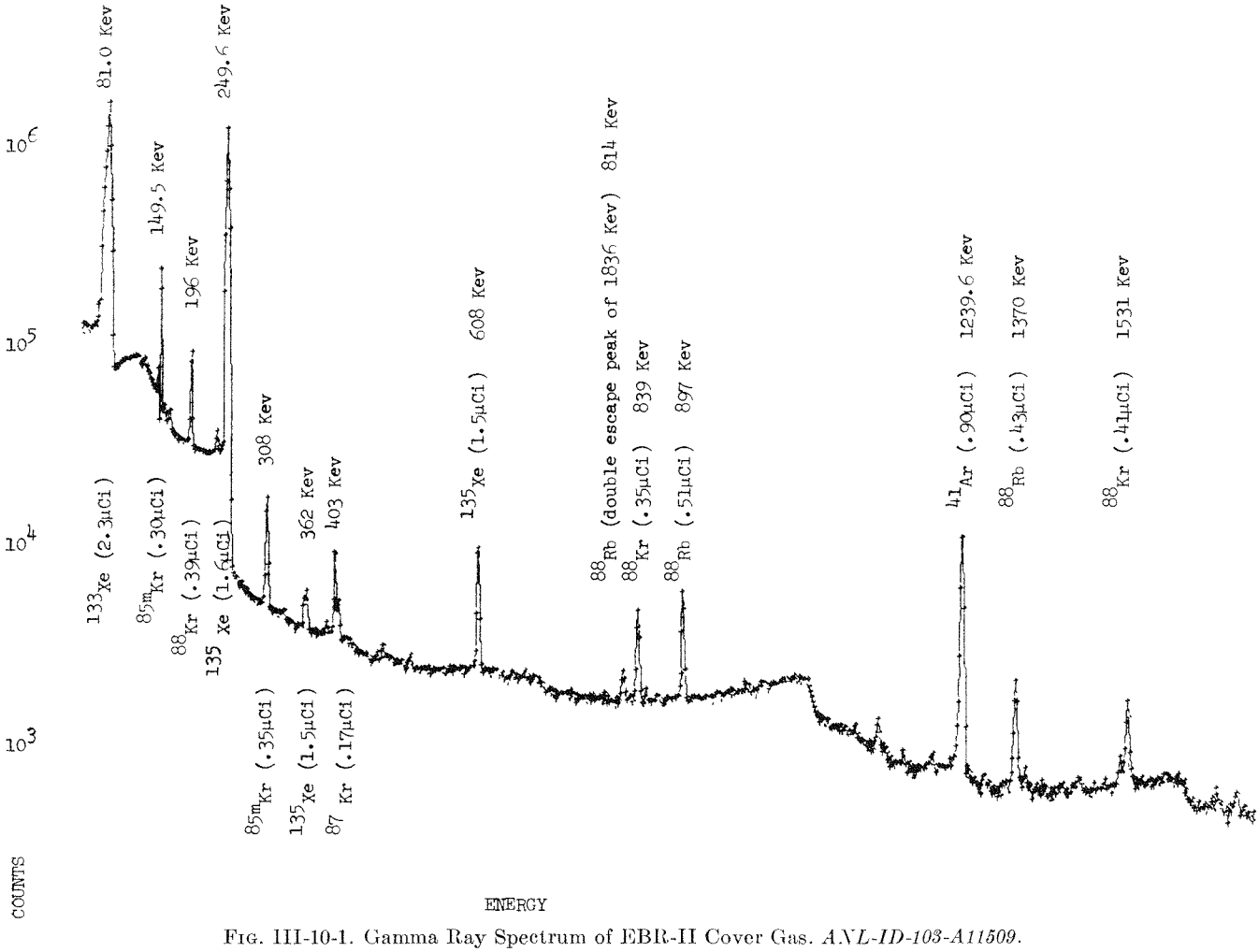

Fig. III-10-1. Gamma Ray Spectrum of EBR-II Cover Gas. *ANL-ID-103-A11509.*

The determination and evaluation of small amounts of radioactive material are often problems of considerable importance. A Ge(Li) detector can be used to solve both of these problems where gamma emitting isotopes are involved. The detection limits of a medium sized Ge(Li) detector are determined primarily

* Atomics International, a Division of North American Rockwell Corporation, Canoga Park, California.

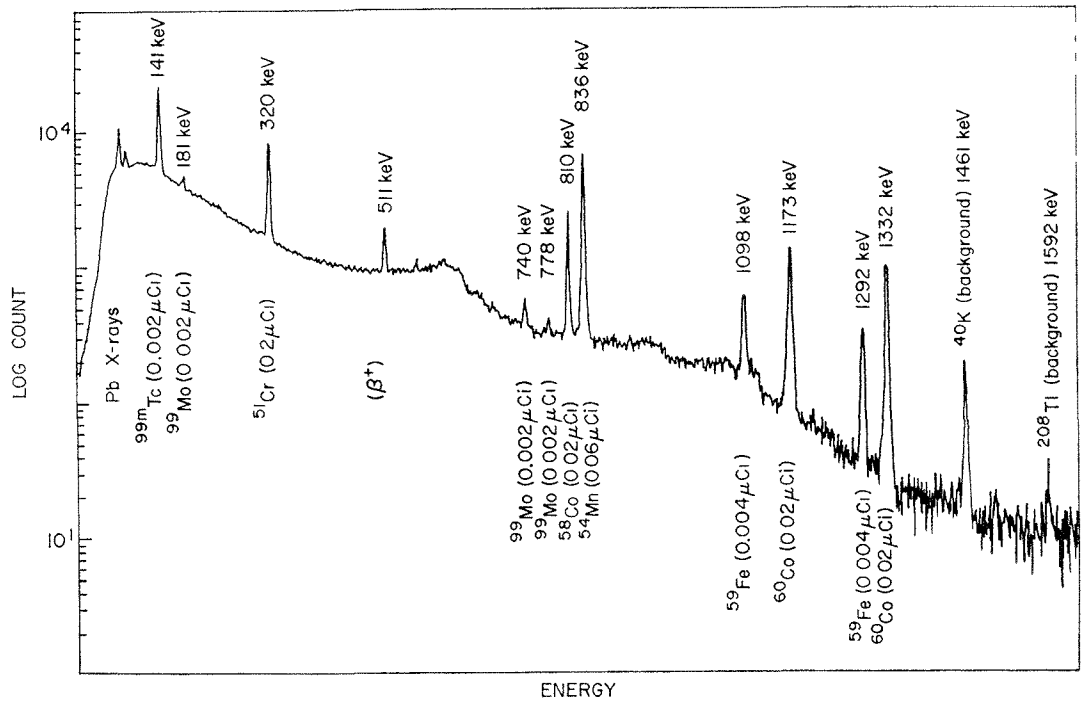

FIG. III-10-2. Gamma Ray Spectrum of Stainless Steel Plate from ZPR-3. *ANL Neg. No. 116-409.*

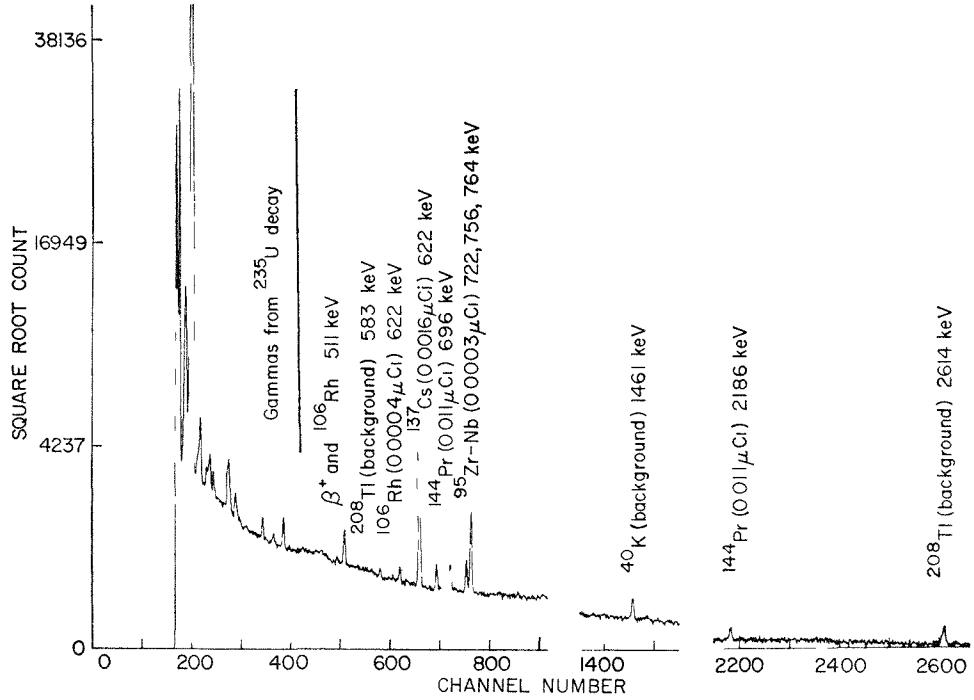

FIG. III-10-3. Gamma Ray Spectrum of Irradiated U-235 Foil, Long Half-Life Fission Products. *ANL-ID-103-A11510 Rev 1.*

by background and not by its small relative efficiency compared with a sodium iodide detector. In most cases, the excellent resolution of a Ge(Li) detector allows a unique identification for each gamma ray line observed in a spectrum, and proper calibration (see Paper III-9) provides accurate determination of the quantity of activity associated with each gamma ray.

Our particular experience has dealt with samples of cover gas from EBR-II, structural materials and contamination smears from ZPR-3, U-235 foils contami-

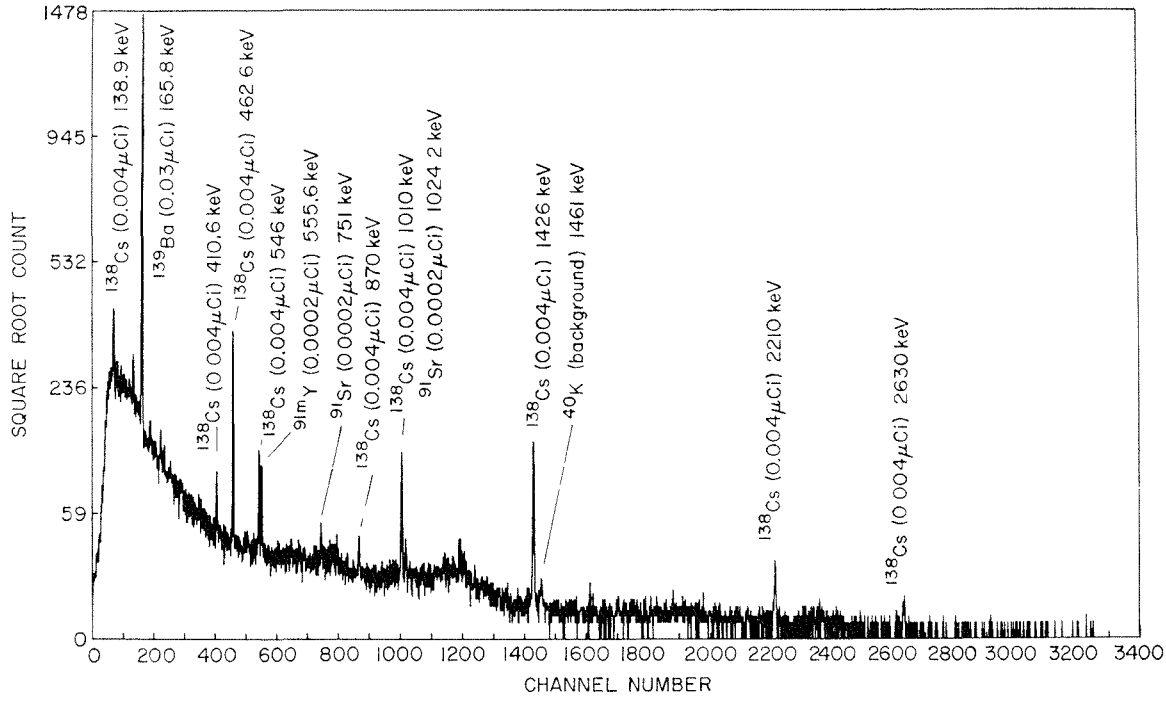

FIG. III-10-4. ZPPR Air Filter, Short Half-Life Components. *ANL Neg. No. 116-408.*

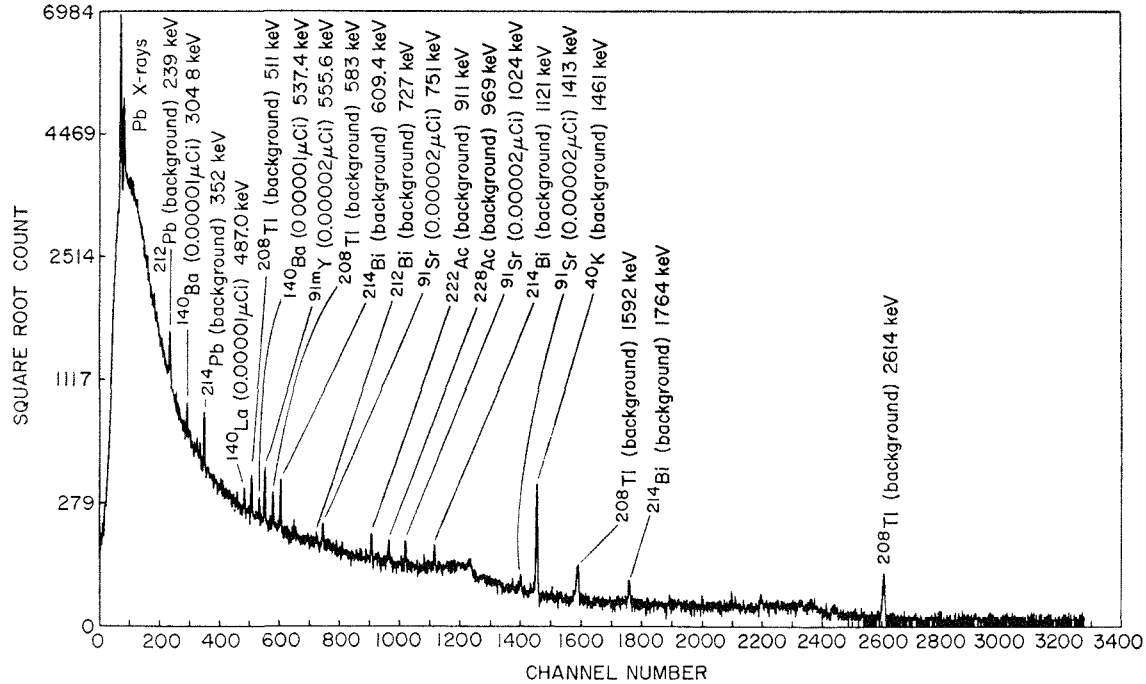

FIG. III-10-5. ZPPR Air Filter, Long Half-Life Components. *ANL Neg. No. 116-407.*

nated with long half-life fission products, and air monitor samples from the Zero Power Plutonium Reactor (ZPPR). In each case the gamma radioactive isotopes and the quantities of such isotopes were determined by the Ge(Li) counting system at ZPPR.[1] The data were analyzed with computer codes developed for this particular system.[2] Figures III-10-1 through III-10-5 are some of the spectra obtained from these investigations. Each spectrum indicates the source of the gamma ray observed and the approximate activity of the isotope.

The sensitivity for any particular isotope depends on its gamma-ray energy and intensity, but generally

most any isotope that emits gamma rays in sufficient quantity to be of interest in contamination considerations can be identified and evaluated with a reasonable Ge(Li) system.

REFERENCES

1. D. W. Maddison and L. S. Beller, *Characteristics and Capabilities of Automated Counting Facilities for the Zero Power Plutonium Reactor (ZPPR)*, Reactor Physics Division Annual Report, July 1, 1968 to June 30, 1969, ANL-7610 pp. 379-381.
2. L. S. Beller and D. W. Maddison, *Automated Spectrum Analysis Methods for Ge(Li) Detectors*, Reactor Physics Division Annual Report, July 1, 1968 to June 30, 1969, ANL-7610, pp. 416-417.

III-11. Detection for $B^{10}(n,\alpha)$-to-Fission Ratio Measurements

L. S. Beller*

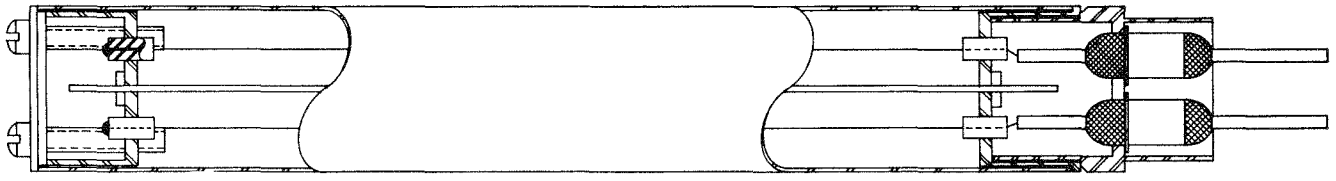

Fig. III-11-1. Overall View of Counter. Active Materials are Coated on Opposite Sides of Central Plate Shown in Side View. The Case and Foil Plate are the Common Cathode. Grid of Three Wires is an Independent Anode (Only One Wire in Each Half is Shown). *ANL-ID-103-A11445.*

A detector has been constructed for measuring reaction rate ratios as a function of position in the Zero Power Plutonium Reactor cores for $B^{10}(n,\alpha)$ and fission reactions. The commonly used gaseous BF_3 counters have been unsatisfactory because of gamma-ray sensitivity, difficulty in obtaining absolute calibrations, and a geometry that is different from the fission counters.

The construction of the new counter is shown in Fig. III-11-1. The arrangement of the anode grid wires minimizes electric field variations and each side of the counter can be used as (1) an ion chamber for counting fissions, (2) a proportional counter for detecting alphas, or (3), by eliminating the coating material, a proportional counter for measurements of the gamma-ray background.

Figure III-11-2 shows a typical pulse-height spectrum with a boron-sensitive counter in a reactor spectrum. The rapidly declining low energy component is due mostly to gamma rays, but probably also includes a contribution from (n,p) events occurring in the walls of the detector. These effects are corrected by using a blank on the other side.

Absolute calibration is possible by using U-235 or another isotope as a standard in a thermal spectrum since the $B^{10}(n,\alpha)$ pulse height distribution in this counter is nearly insensitive to the neutron spectrum and the gamma separation is good.

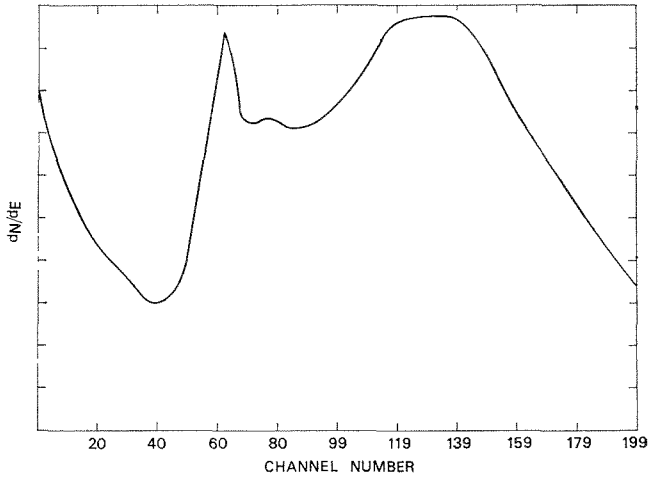

Fig. III-11-2. Pulse-Height Spectrum from Boron-Coated Detector in Presence of Gamma-Ray Field. The Spectrum was Obtained in a Typical Fast Reactor Neutron Energy Spectrum. Relative Intensity of Background Component Varies with Location in Reactor. *ANL-ID-103-A11449.*

* Atomics International, a Division of North American Rockwell Corporation, Canoga Park, California.

III-12. Thermoluminescent Dosimetry Applied to Gamma Ray Dose Measurements in Critical Assemblies

G. G. Simons

Description of Thermoluminescent Dosimeters

Two types of solid extruded 1 × 6 mm thermoluminescent dosimeter (TLD) rods containing approximately 13 mg of lithium fluoride were selected for evaluation of their applicability in gamma-ray dose measurements in a critical facility. One type (TLD-100),* was composed of natural lithium containing nominally 92.5% Li-7 and 7.5% Li-6; the other type (TLD-700)* was enriched to 99.993% in Li-7. Solid rods were selected because they were more convenient to handle than equivalent quantities of TLD powder. Also, the precision over the dose ranges required in this work (1 to 10,000 R) was comparable to powder.

These dosimeters are sensitive to gamma rays, charged particles, and neutrons in varying degrees. Thermal-neutron-induced excitation is considerably less in the enriched TLD-700 rods than in the TLD-100 rods. It was assumed that the dose variations between the TLD-700 and TLD-100 rods were caused by the change in thermal neutron flux in different assembly regions. It was also assumed that fast neutron sensitivity in the TLD-700 rods was negligible. The validity of this latter assumption warrants further study since inconsistencies appear in the literature.[1, 2]

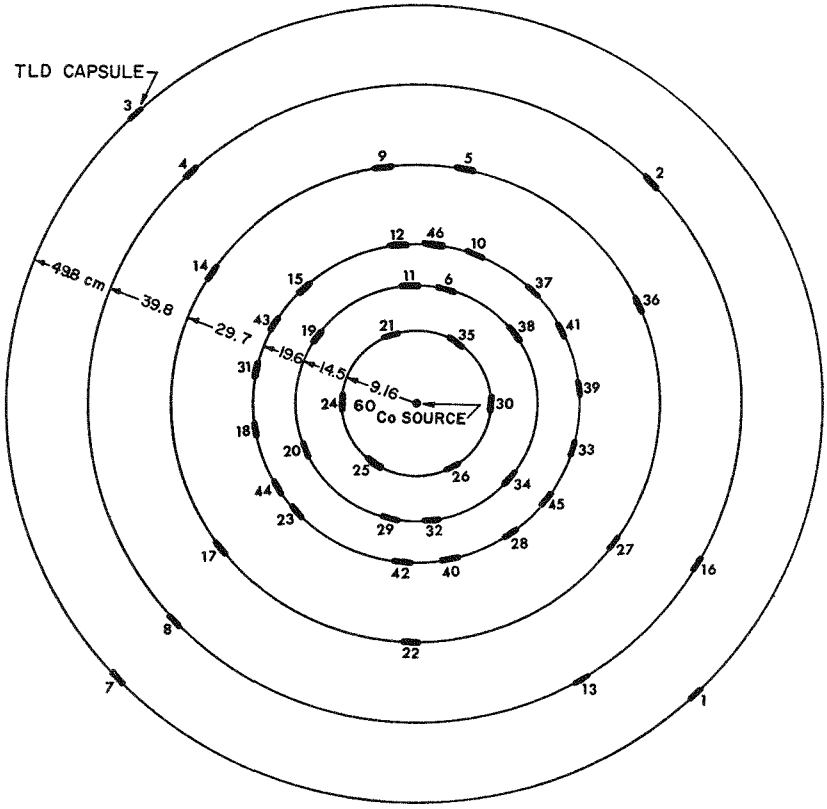

Fig. III-12-1. TLD Calibration Configuration Showing the Stainless Steel Encapsulated TLD's Positioned on the ⅜-in.-Thick Plastic Sheet. The Co-60 Source was Elevated 4 cm above the Sheet; Thus the Source-to-Capule Distances were 10, 15, 20, 30, 40 and 50 cm. *ANL-ID-103-A2056.*

Calibration of Stainless Steel Encapsulated TLD Rods

A calibration procedure for relating TLD readout from a commercial TLD analyzer[3] to gamma ray dose applicable to experiments performed in ZPR-3 Assembly 60 involved using special stainless steel sleeves similar to the sleeves used during TLD exposures in the critical. The TLD encapsulation for calibration purposes consisted of placing a TLD-100 rod

* Nomenclature of Harshaw Chemical Company.

and a TLD-700 rod end to end in a 0.125 in.-diam, 0.035-in.-wall Type 304 stainless steel tube forming a special capsule.

Before the gamma ray exposure, 38 TLD capsules were positioned at various radii on a 0.375-in.-thick plastic sheet (see Fig. III-12-1). This sheet was then suspended in a large hot-cell room and a 1.1-Ci Co-60 source was placed in the center, 4 cm above the plane of the sheet. TLD capsules were removed from the different radii at time intervals such that the absorbed doses ranged from 1 to 7000 R (see Figs. III-12-2 and III-12-3).

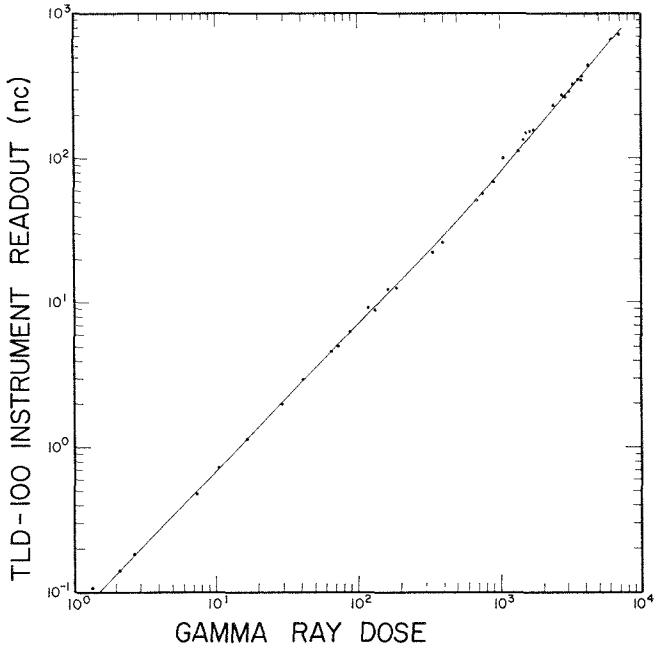

FIG. III-12-2. Response of Solid Extruded TLD-100 Rods Encased in a 35-mil Steel Rod to Co-60. *ANL-ID-103-A2060.*

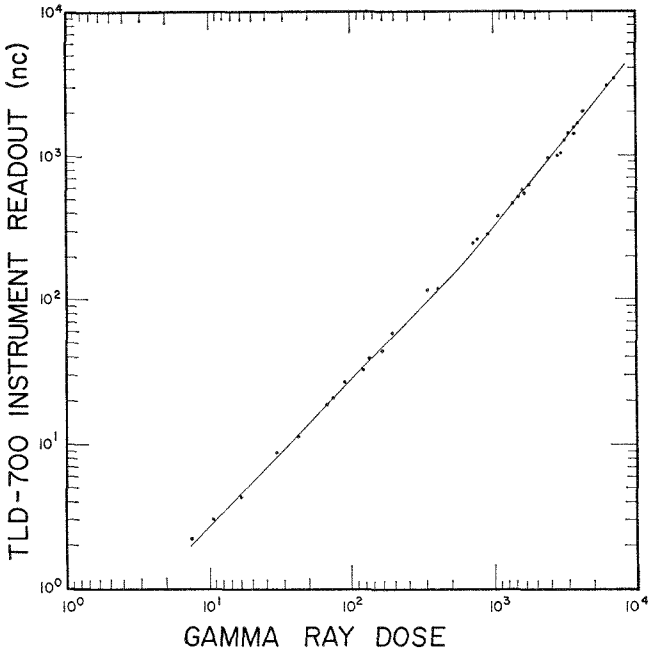

FIG. III-12-3. Response of Solid Extruded TLD-700 Rods Encased in a 35-mil Steel Rod to Co-60. *ANL-ID-103-A2059.*

TABLE III-12-I. TLD-100 AND TLD-700 READOUT VARIATIONS AS A FUNCTION OF ENCASEMENT MATERIALS FOLLOWING A 50-Wh EXPOSURE IN ZPR-3 ASSEMBLY 60 CORE

Drawer Position	TLD Location Across Drawer[a]	Ratio of Instrument Readout: TLD Reading/Reference TLD Encasement Materials[b]		
		0.035-in. Stainless Steel	0.020-in. Stainless Steel	0.035-in. Polyethylene
TLD-100				
1-P-5	a	1.00	0.95	1.17
	c	1.00	1.02	1.24
	e	1.00	1.04	1.21
	g	1.00	1.01	1.11
1-P-14	a	1.00	1.14	1.14
	c	1.00	1.06	1.32
	e	1.00	0.98	1.08
	g	1.00	0.97	1.39
TLD-700				
1-P-5	b	1.00	1.07	1.25
	d	1.00	1.08	1.15
	f	1.00	1.01	1.05
	h	1.00	1.03	1.22
1-P-14	b	1.00	1.02	1.26
	d	1.00	1.02	1.20
	f	1.00	1.03	1.20
	h	1.00	1.10	1.15

[a] Eight TLD rods were inserted into each sleeve starting with a TLD-100 rod and alternating 100, 700, etc. These rod positions across the core cell were labeled a, b, c, d, e, f, g, h.

[b] Reference TLD refers to the TLDs encased in 0.035-in. stainless steel.

TLD ENCAPSULATION STUDY FOR ZPR-3 ASSEMBLY 60

During gamma ray dose mapping studies in ZPR-3 Assembly 60 (see discussion below), TLD rods were loaded into stainless steel sleeves having 0.035 in.-thick walls. The response of TLD rods encased in 0.02-in. stainless steel and 0.035-in. polyethylene sleeves was compared with the 0.035-in. stainless steel enclosure data following a 50-W-h exposure in the ZPR-3 core. Table III-12-I shows that the 0.02-in. steel responses tend to be slightly higher than the 0.035-in. steel responses. However, the 0.02-in. steel responses are not generally significantly higher statistically. Conversely the 0.035-in. polyethylene-clad

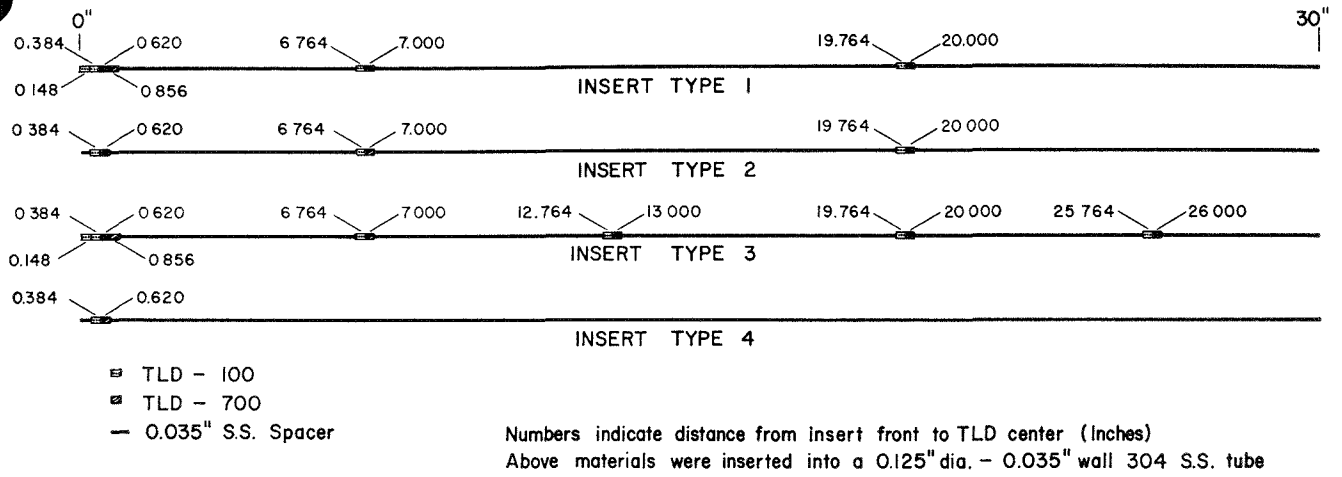

FIG. III-12-4. TLD Loading Configurations for ZPR-3 Assembly 60. *ANL-ID-103-A2058.*

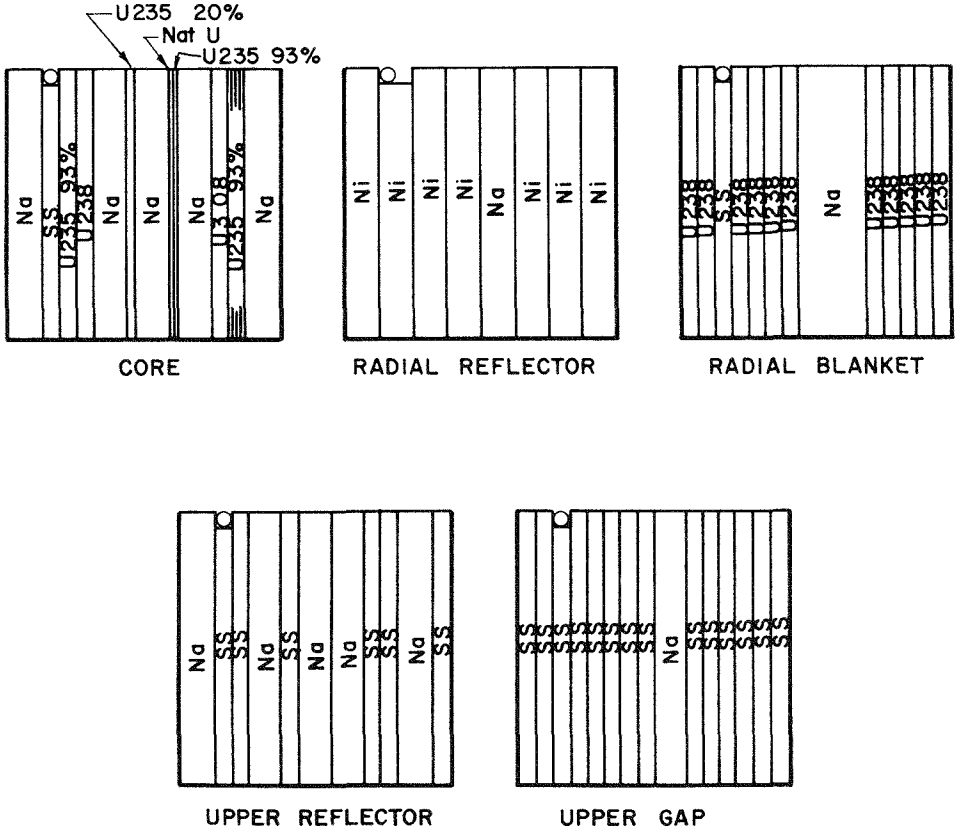

FIG. III-12-5. TLD Drawer Loading for ZPR-3 Assembly 60. *ANL-ID-103-A2121.*

TLD responses are generally higher than the reference 0.035-in. stainless steel responses.

Based on the expression describing the range of electrons given by Evans,[4] the maximum energy electron that could penetrate the 0.035- and 0.02-in. stainless steel and 0.035-in. polyethylene are 1.51, 0.94, and 0.344 MeV, respectively. Therefore increased external electron attenuation in the steel sleeves would cause the total response from these TLD rods to be less than from the polyethylene-covered rods. It is expected that the TLD-700 readouts will allow the determination of gamma ray energy deposition in the stainless steel sleeves. (Neutron excitation was considered constant throughout, independent of the sleeve.)

DOSE TRAVERSE MEASUREMENTS IN ZPR-3 ASSEMBLY 60

A coarse radial and axial dose mapping at 69 discrete locations was completed.

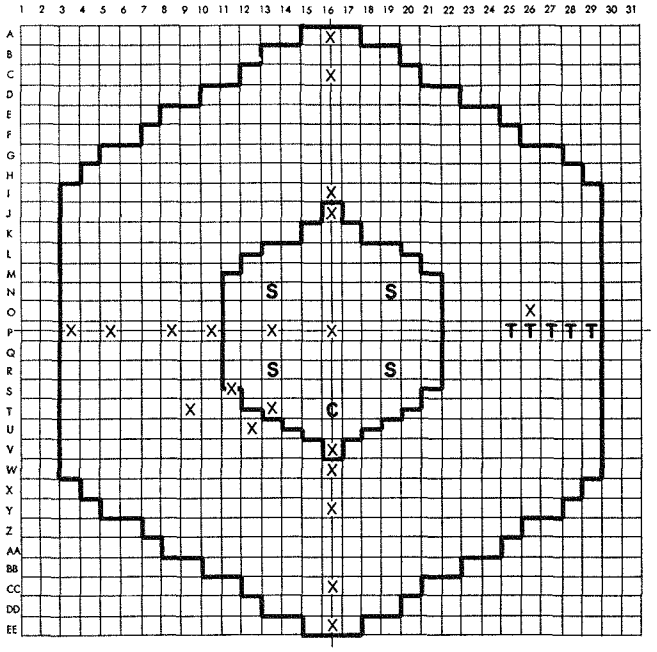

FIG. III-12-6. TLD Radial Positions (*X*) for ZRP-3 Assembly 60. *ANL-ID-103-A2055.*

To minimize residual gamma ray exposure following this mapping irradiation, all the 138 TLD rods were removed immediately after reactor shutdown. This was achieved by preloading groups of TLD rods inside 0.125-in.-diam, 0.035-in.-wall Type 304 stainless steel tubes (see Fig. III-12-4). These steel tubes were rapidly inserted and extracted from the rear of the matrix tubes. The assembly core and blanket drawer loadings were modified to accommodate the steel inserts. These loadings are shown in Fig. III-12-5.

Twenty stainless steel inserts were exposed in the Half 1 at the drawer locations marked by an X in Fig. III-12-6 for 1 h at a nominal 100 W. Surface gamma ray plus beta radiation in the steel tubes was less than 5 mR/h after the exposure. The TLD rods were promptly removed from the inserts and read 48 h later.

Relative dose results obtained from the TLD-700 rods are plotted in Figs. III-12-7 through III-12-9. Note that the lines connecting the data points in these three figures do not describe the dose variations between data points, but are only drawn as a visual aid in distinguishing between data sets.

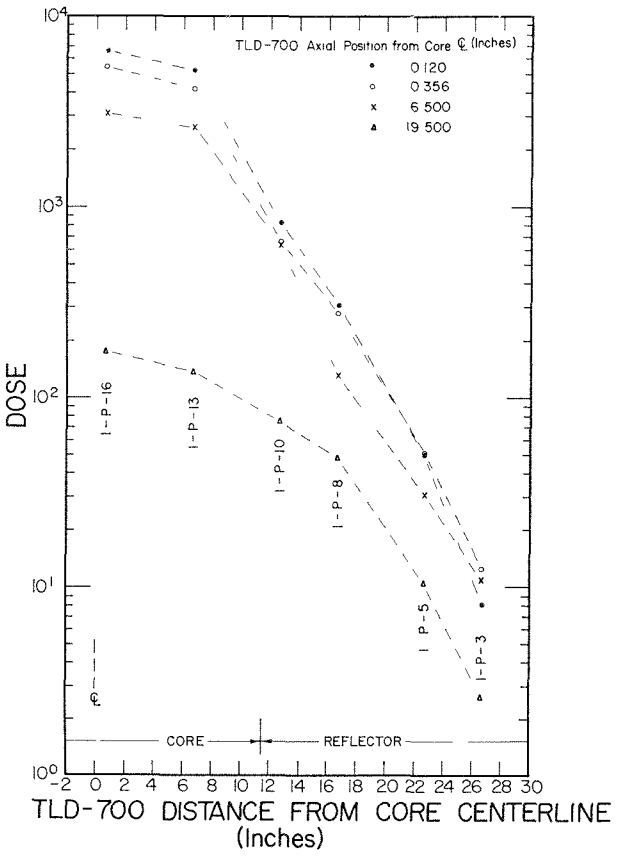

FIG. III-12-7. ZPR-3 Assembly 60 TLD-700 Radial Traverses, P Row, *ANL-ID-103-A11314.*

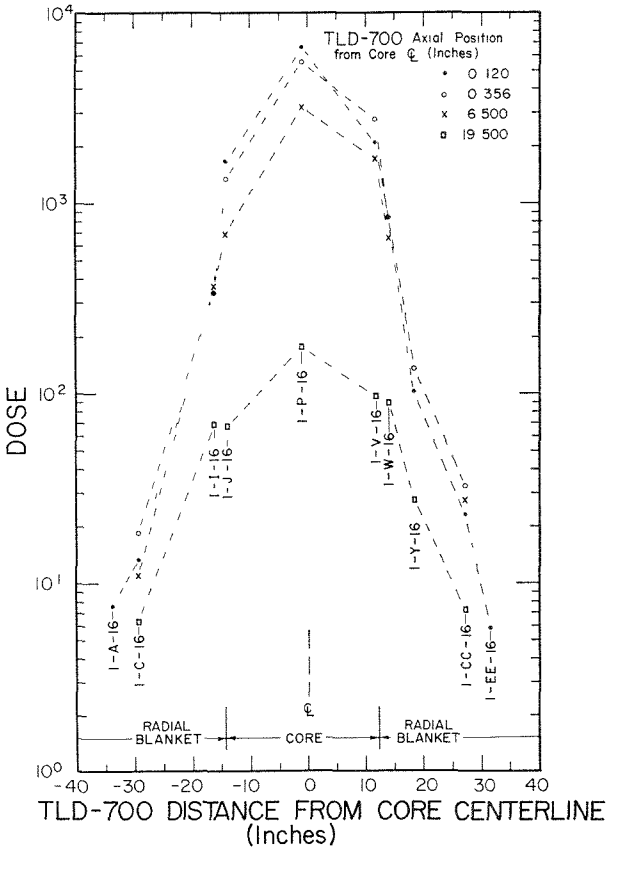

FIG. III-12-8. ZPR-3 Assembly 60, Radial Traverses, 16 Row, *ANL-ID-103-A11313*

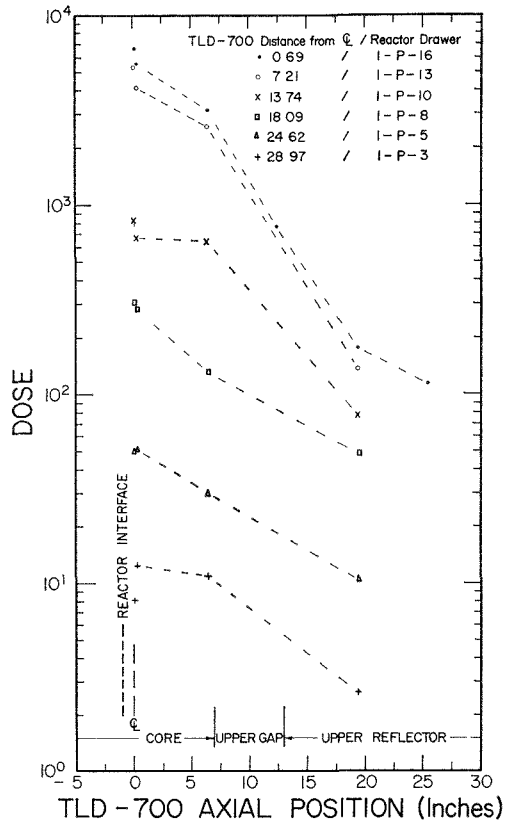

FIG. III-12-9. TLD Axial Traverses for ZPR-3 Assembly 60. *ANL-ID-103-A11315.*

SINGLE-CELL HETEROGENEITY STUDIES

Dose variations across the central core drawer (1-P-16) and a blanket drawer (1-P-8) were measured with both TLD-100 and TLD-700 dosimeters. Since all the dose measurements completed as part of the present study involved measuring the dose at systematic core cell and blanket all locations throughout the critical, it was necessary to investigate the variation across these cells relative to the position of the TLD rods used in the traverse study.

The heterogeneity experiment involved loading two sets of 2-in.-long stainless steel tubes with TLD rods. Each set contained a 2-in.-long insert loaded end to end with eight TLD-100 rods and an insert with eight TLD-700 rods. These were then exposed for 1 h at 50 W. Resulting dose variations are shown in Fig. III-12-10. The centerline of the TLD, marked as Reference TLD, was at approximately an equivalent drawer radial position as the steel inserts used in the dose traverse measurements.

These TLD-700 data show that there is no measurable dose variation across the central cell drawer. Also, there is no fine structure evident in the TLD-700 data across the blanket cell. However, the increase in dose with decreasing distance from the Assembly 60 centerline is clearly evident.

ACCURACY OF TLD DATA

Due to unresolved uncertainties associated with LiF TLD data obtained in a fast-reactor environment, several sources of error potentially exist which would contribute to systematic errors. These uncertainties include such factors as the selection of optimum TLD encasement materials, beta and neutron response, gamma-ray energy dependence, dose calibration procedures, pre- and post-annealing effects, response fade, and neutron and gamma ray dose-rate dependence. Several of these factors are discussed in Refs. 1, 2 and 5. Also preliminary results showed that both exposure and annealing histories may be required for TLD-100 and TLD-700 rods. Tests have been made on new TLD rods, new preannealed TLD rods, gamma ray exposed and annealed rods, and neutron plus gamma ray exposed and annealed rods. The precision obtained from each test was approximately constant (3% for TLD-

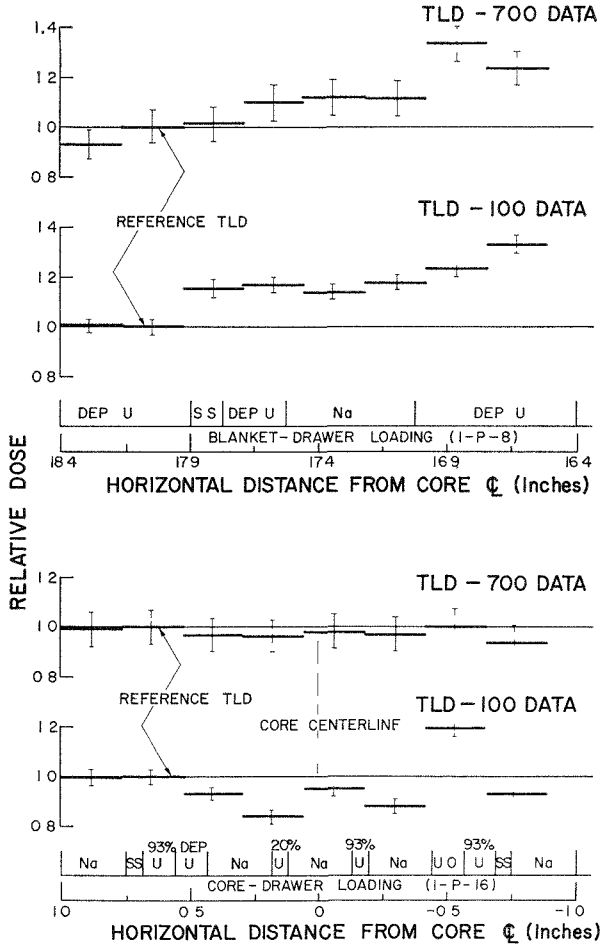

FIG. III-12-10. ZPR-3 Assembly 60, TLD Traverse Across 1-P-16 and 1-P-8. *ANL-ID-103-A2054.*

100 and TLD-700). However, the instrument readout for a single exposure dose with different annealing and irradiation history varied as much as 20%. All of the data reported above were obtained using new preannealed TLD rods from a single batch. Further experimentation is required before meaningful error limits can be attached to these results.

References

1. M. Stuetzer and N. N. Gibson, *Neutron Sensitivities of Various Gamma Dosimeters*, NDL-TM-52 (1968).
2. C. L. Wingate, E. Tochilin and N. Goldstein, *Response of LiF to Neutrons and Charged Particles*, USNRDL-TR-909 (1965).
3. R. W. Carlson and J. B. Rickey, *The Harshaw Model 2000 Thermoluminescence Analyzer*, Conference on Luminescence Dosimetry, U. S. Atomic Energy Commission and Oak Ridge National Laboratory, Gatlinburg, Tennessee, 1968, Conf. No. 680920, pp. 706–719.
4. R. D. Evans, *The Atomic Nucleus*, (McGraw-Hill Book Company, Inc., New York, 1955).
5. F. Morgan Cox, *New Solid Lithium Fluoride Thermoluminescent Dosimeters*, pp. 60–77.

   F. H. Attix, E. J. West and J. A. Pfaff, *Variation of Electron-Induced Radioluminescence in Lithium Fluoride as a Function of Total Dose*, pp. 389–395.

   K. Ayyangar, A. R. Reddy and G. L. Brownell, *Some Studies on Thermoluminescence from Lithium Fluoride and Other Materials Exposed to Neutrons and Other Radiations*, pp. 525–542.

   A. R. Jones, *A Thermoluminescence Dosimetry System Based on Extruded Lithium Fluoride Dosimeters*, pp. 751–772.

   Proc. Second International Conference on Luminescence Dosimetry, U. S. Atomic Energy Commission and Oak Ridge National Laboratory, Gatlinburg, Tennessee, 1968, Conf. No. 680920.

III-13. Non-Perturbing Fission Counter for Use in Plate-Type Critical Assemblies

A. B. Long and E. M. Bohn

Introduction

Fission rate distribution measurements within fast critical assemblies form a fundamental part of any experimental reactor program. The results are easily interpreted and are of importance in reactor design as well as in the evaluation of theoretical calculations. Current techniques employed in these measurements include foil activation, solid-state track recorders, and fission counters. Fission counters provide the only means for real-time accumulation of data and are therefore the only detectors suited for time-dependent applications. However, the volume of these counters often perturb the fission rate being measured. In addition, complex counter geometries make it difficult to compare measured values with calculated quantities. An ultra-thin solid-state fission counter which combines the advantages of a real-time counter with the nonperturbing quality of foils has been constructed and tested. A description of the detector and performance test results are presented below.

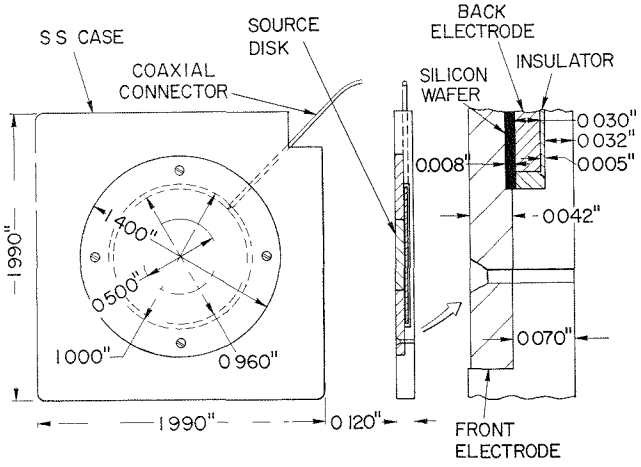

Fig. III-13-1. Diagram of Ultra-Thin Solid-State Fission Counter. *ANL-Neg. No. 116-142.*

Description of the Detector

The solid state fission counter is a 2.0 × 2.0 × 0.12 in. stainless steel clad package shown in Fig. III-13-1. The package consists of a 0.96 in. diam by 8 mil-thick phosphorous diffused 100 Ω-cm, *p*-type silicon diode with SiO_2 edge protection. This diode serves as the active detector and it is held against a stainless back (negative) electrode by the front (positive) electrode. The fissionable material for which the fission rate is to be measured is placed in conjunction with the diffused face of the diode through a hole in the front electrode.

Low resistivity silicon (100 Ω-cm) was chosen to extend the in-core operating life to several months (10^{14} fast neutrons per cm^2).[1, 2] The diffused junction, edge protected diode configuration was chosen because

of its mechanical ruggedness and resistance to surface leakage.[1]

Performance of Detector

The resolution of the detector was evalutated by recording the fission spectrum from a Cf-252 source placed 2 in. from the detector in a vacuum. The spectrum was analyzed by using standard precedures[3] to obtain certain parameters which were found to compare favorably with the recommended values for surface-barrier fission detectors.[4] A typical Cf-252 spectrum is shown in Fig. III-13-2.

When the detector is used in a reactor, the necessity of placing the fission source in close proximity to the face of the detector results in a distribution of fission fragment path lengths through the source, air, and the detector dead layer. As a consequence of the difference in fragment energy loss there is a degradation in the detector resolution. The fission spectrum from a 20 $\mu g/cm^2$ U-235 source recorded by the thin detector in ZPR-9 Assembly 26 is shown in Fig. III-13-3. The energy degradation is evidenced by the increased tail of the spectrum. However, only a few percent of the fission counts fall into the background. A computer program has been developed to determine the absolute

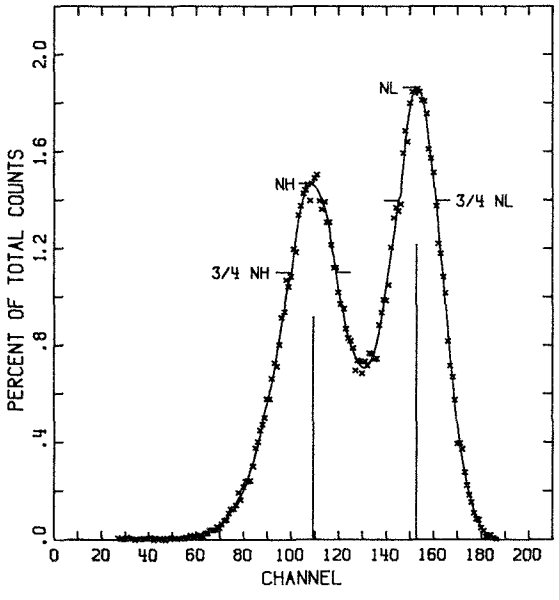

Fig. III-13-2. Cf-252 Spontaneous Fission Pulse-Height Spectrum Recorded by the Thin Detector. The Source and Detector are 2 in. Apart in a Vacuum. *ANL-Neg. No. 116-406.*

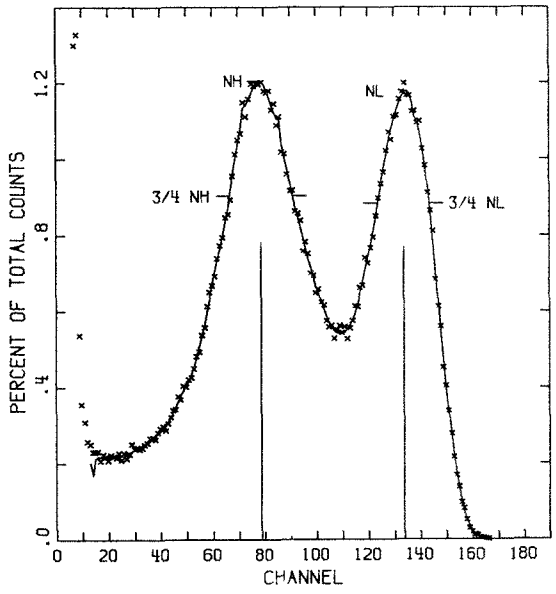

Fig. III-13-3. Pulse Height Spectrum From the Fission of U-235 Recorded by the Thin Detector. The Source is in Contact With the Front Face of the Detector. *ANL-Neg. No. 116-405.*

fission rate from these measured spectra by accounting for fragment energy loss in the source, air, and detector window. (see Paper III-21).

Because the detector is almost identical in shape and composition to the stainless steel plates used in the ZPR facilities, the measured fission rates are unperturbed by the counter. These rates can be compared directly with the reaction rates which are calculated within a stainless steel plate at the same position in the reactor. It is thought that this detector and similar detectors made from different reactor materials can be used to a greater advantage in a real-time evaluation of current heterogeneous calculating techniques.

References

1. G. Dearnaley and D. C. Northrop, *Semiconductor Counters for Nuclear Radiation*, (E. & F. N. Spon Limited, London, 1966).
2. L. M. Epstein and R. R. Ferber, *Radiation Resistant Silicon Diode Neutron Detectors*, Nucl. Appl. **3**, 692 (1967).
3. A. B. Long, B. W. Wehring and M. E. Wyman, *Procedure for Determining the Parameters from a Fission Fragment Energy Spectrum*, Rev. Sci. Instr. **39**, 1566 (1968).
4. L. M. Schmitt and F. Pleasonton, *Evaluation of Semiconductor Detectors for Fission Fragment Energy Measurements*, Nucl. Instr. Methods **40**, 204 (1966).

III-14. Development of an Improved Tritium Counting Facility

A. De Volpi and M. Bretscher

The absolute $Li^6(n,\alpha)H^3$ reaction rate for samples irradiated in fast critical assemblies has been used in the experimental determination of integral alpha (capture-to-fission ratio) values and perturbation denominators for several fast reactors. (See Papers II-11 and II-29). By measuring the tritium activity induced in irradiated samples, the Li-6 absorption rate was determined. Tritium decays entirely by beta emssion with an end-point energy of only 18.6 keV and a half-life of 12.30 yr. An improved counting facility was developed partly for the purpose of detecting these low energy electrons (5.6 keV average) using liquid scintillation counting techniques.

After the irradiation, tritium is removed from the metallic lithium sample (99% Li-6) by an isotopic dilution method[1] using normal hydrogen as the carrier gas. The sample is heated in a hydrogen atmosphere and converted to molten lithium hydride. As the temperature is raised to 900°C, the lithium hydride readily decomposes with the liberation of a mixture of normal hydrogen and tritium. This gas is slowly passed over a hot (750°C) bed of CuO, and the water vapor formed in the process is collected in liquid nitrogen cold traps.

To determine its activity, a portion of the tritiated water sample is dissolved in a dioxane-base liquid scintillator and counted. The scintillator is prepared following the prescription recommended by Moghissi;[2] namely, 7 g PPO, 120 g napthalene, and 1.3 g bis-MSB dissolved in p-dioxane to a volume of 1.00 liter. Samples are prepared for counting by dissolving 5 m liters of the tritiated water in 25 m liters of scintillator solution (i.e., 16.3 w/o H_2O). The counting solution is used to fill two precision vials which are purged with argon prior to sealing to reduce the quenching effect from dissolved O_2. These vials have an effective volume of 12 m liters and can be fitted with either glass or quartz windows. Secondary standards prepared from a calibrated National Bureau of Standards (NBS) tritiated water sample are used to calibrate the counting system.

To achieve relatively high detection efficiencies for liquid scintillators with aqueous solutions, the scintillation counting facility was revamped. Tritium efficiencies doubled from about 20% to about 40% because of these changes.

The original facility[3] was based on two EMI 6255S phototubes operating in coincidence with electronic components of both the vacuum-tube and first generation transistor type. Due in part to the aging and increased difficulty in maintaining the vacuum-tube equipment, a decision had already been made to modernize the electronics. The recent development of high secondary-emission (GaP) dynodes was sufficient reason to change the type of photomultiplier tube as well. The introduction of this type of tube with high-efficiency bialkali photocathode is responsible for most of the improvement in efficiency.

Thus, the new detection facility consists of two RCA 8850 multiplier tubes facing each other in a silicone oil-filled plenum. A liquid scintillation cell of about 12 m liter capacity can be fitted between the two tubes. As in the previous system, coincidence detection of valid tritium-generated electron pulses are required in order to discriminate against natural noise background. The spacing between tubes is adjustable to allow larger cells to be counted.

A small preamplifier directs the anode signals to a fast current amplifier.[4] These augmented pulses are sent to a fast discriminator[4] which imposes a reliable paralysis upon each event. Standardized discriminator output pulses are then routed to the fast coincidence unit which drives a multichannel automatic scaling system.[4] The scaling system produces a written and punched paper tape record which can be used for computer input.

Provisions have been made for further exploratory work with slow side channel pulses to obtain the summed signals and with correlation counting techniques.

At levels which provide tritium efficiencies of 40% with aqueous solutions, the background is about 2–4 counts/sec. Quartz vials tend to give about 0.5 counts/sec lower background than glass.

References

1. M. M. Bretscher, *Li-6 as a Reference Absorber for Capture-to-Fission Ratio Measurements in Zero Power Fast Critical Assemblies*, Reactor Physics Division Annual Report, July 1, 1967 to June 30, 1968, ANL-7410, pp. 178–182.
2. A. A. Moghissi et al., *Low-level Counting by Liquid Scintillation—I. Tritium Measurement in Homogeneous Systems*, Intern. J. Appl. Radiation Isotopes **20**, 145 (1969).
3. A. De Volpi, K. G. A. Porges and R. N. Larsen, *Mn^{56} Coincidence Counting Facility*, ANL-6760 (1963).
4. A. De Volpi, S. Rudnick, R. Daly, J. English and R. Pecina, *Instrumentation for Processing Nuclear Detector Data*, Reactor Physics Division Annual Report, July 1, 1967 to June 30, 1968, ANL-7410, pp. 367–371

III-15. Pulse Selector

J. M. Larson

Proton recoil proportional counting systems of the type first reported by Bennett[1, 2] must often be operated in environments that generate large overloads and high counting rates. This type of operation can lead to spectrum distortion unless appropriate steps are taken to insure the fidelity of the pulses being analyzed. In unipolar pulse shaping systems, a baseline restorer is almost always necessary if base line shifts and their attendant distorting effects are to be avoided. If the counting system is to operate at very high rates, it then also becomes necessary to include circuitry that will inspect the incoming pulses and reject those that are distorted by pileup effects.

This report briefly describes a pulse selector and pileup rejection circuit developed initially for use with the proton recoil spectrometer (see Paper III-17).

This unit was designed to perform the following functions: (1) Reject all pulses whose peak heights do not fall between predetermined upper and lower levels; (2) reject all pulses that occur on the "tail" or trailing edge of a preceding pulse; (3) reject most peak pileup pulses (pulses whose peaks occur within a few tenths of a microsecond of each other); (4) account for dead time of all rejected pulses whose peak heights exceed the lower level discriminators.

Circuitry

The pulse selector described herein is made up almost entirely from commercially available discriminators and DTL/TTL integrated circuit modules.

The overall schematic diagram of the pulse selector is shown in Fig. III-15-1. The unit is comprised of six basic circuit groups as follows:

(1) Upper and lower level discriminators: This group comprises the upper and lower level discriminators and flip-flop memories. These circuits determine whether or not the input pulse has reached a peak height that lies between the upper and lower level discriminator settings, then remembers this information in cross coupled nand gate flip flops (F/F_1 and F/F_2), until the pulse selector makes its decision to keep or reject the pulse. The outputs of this circuit group drives logic gating that participates in the pulse accept-reject decision. The flip-flop memories, (F/F_1 and F/F_2) are reset only after the trailing edge of the measured pulse has returned to the baseline zero reference level.

(2) Threshold discriminator circuit group: This circuit group comprises a threshold discriminator for leading edge discrimination and a "tail" and peak pileup inspection circuit for pileup rejection.

The threshold discriminator level is set just above the noise level of the base line and determines the occurrence of a pulse. When a pulse exceeds the threshold level, a time delay is generated which allows the pulse to reach its peak amplitude before the pulse selector makes an accept-reject decision. At the end of this delay time, the threshold discriminator circuits generate a trigger pulse if it is determined that no "tail" or peak pileup has occurred. The trigger pulse drives the logic gating circuits that make a final decision of pulse acceptability based on the peak height of the pulse and upon whether or not the accompanying multichannel analyzer was busy.

(3) Double differentiator and discriminator: This circuit double differentiates the unipolar input pulse and generates an output pulse whose width is proportional to the time to crossover. The output pulse of this circuit drives the threshold discriminator circuitry where it is used to identify peak pile up events.

(4) Busy flip-flop: The busy flip-flop (F/F_4) is made up from cross coupled nand gates and is set whenever the input pulse exceeds the lower level discriminator. The busy flip-flop remains set until the accompanying multichannel analyzer is "not busy" and the base line has been reestablished at its zero level. The ADC busy discriminator (D_5) senses the busy output signal of the multichannel analyzer.

(5) Logic gating: The logic gating group "ands" the outputs from the upper and lower level discriminators with the output of the busy flip-flop. The resultant signal is used to open a gate to the "pulse accept" single shot that allows this single shot to be triggered by the trigger pulse from the threshold discriminator circuit at the end of the decision delay. The output of the "pulse accept" single shot is used as the coincidence gating signal for the accompanying multichannel analyzer ADC.

(6) Divider: A divider circuit follows the "pulse accept" single shot and divides the output pulse rate from that single shot so that the ADC coincidence gate pulse rate may be reduced by selectable ratios of 1:1, 2:1, 4:1, 8:1, and 16:1. The divider coincidence gate output is useful for high count rate applications where it is sometimes necessary to reduce the input pulse rate to the ADC.

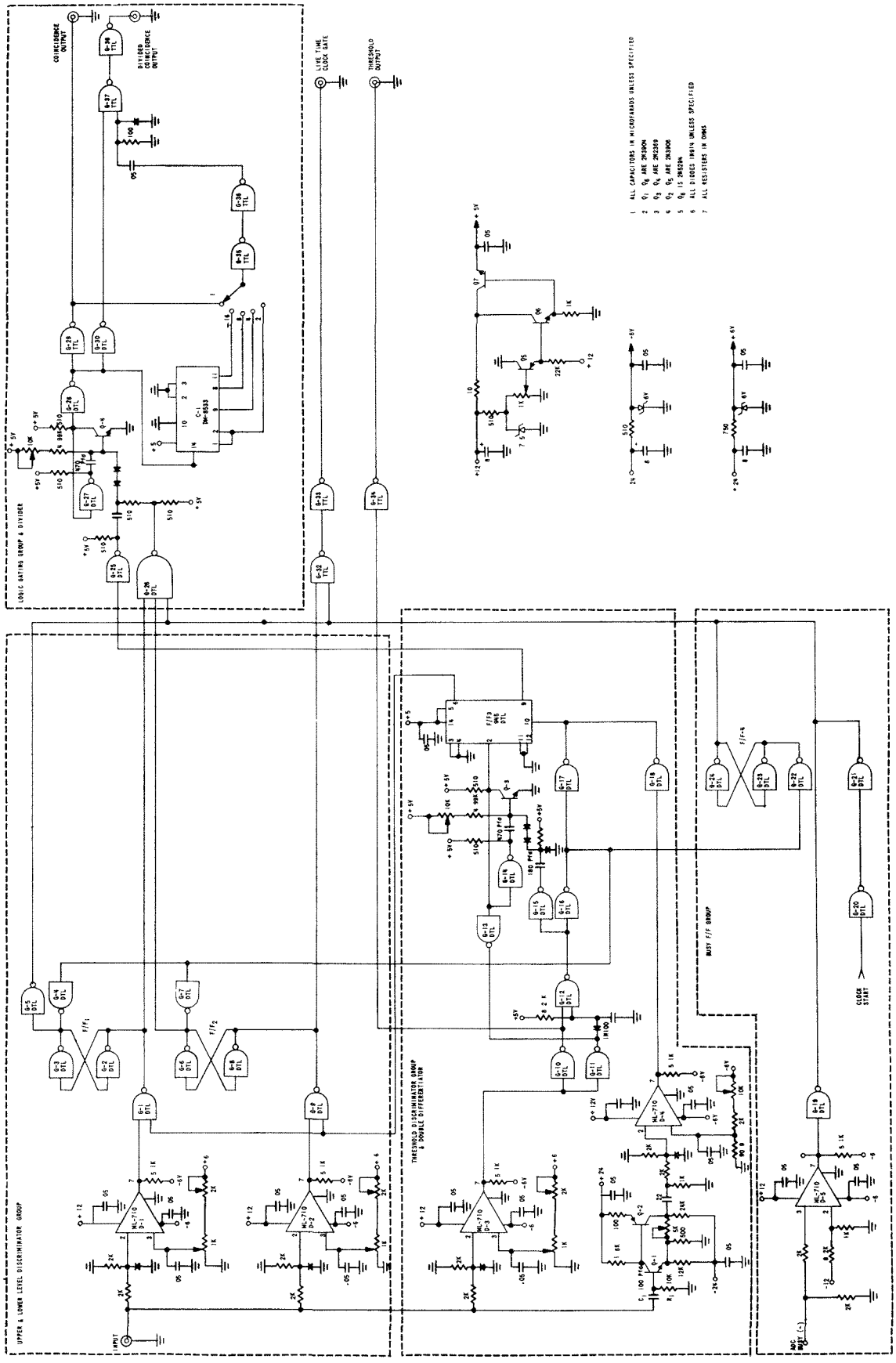

FIG. III-15-1. Pulse Selector Schematic. *ANL Neg. No. None.*

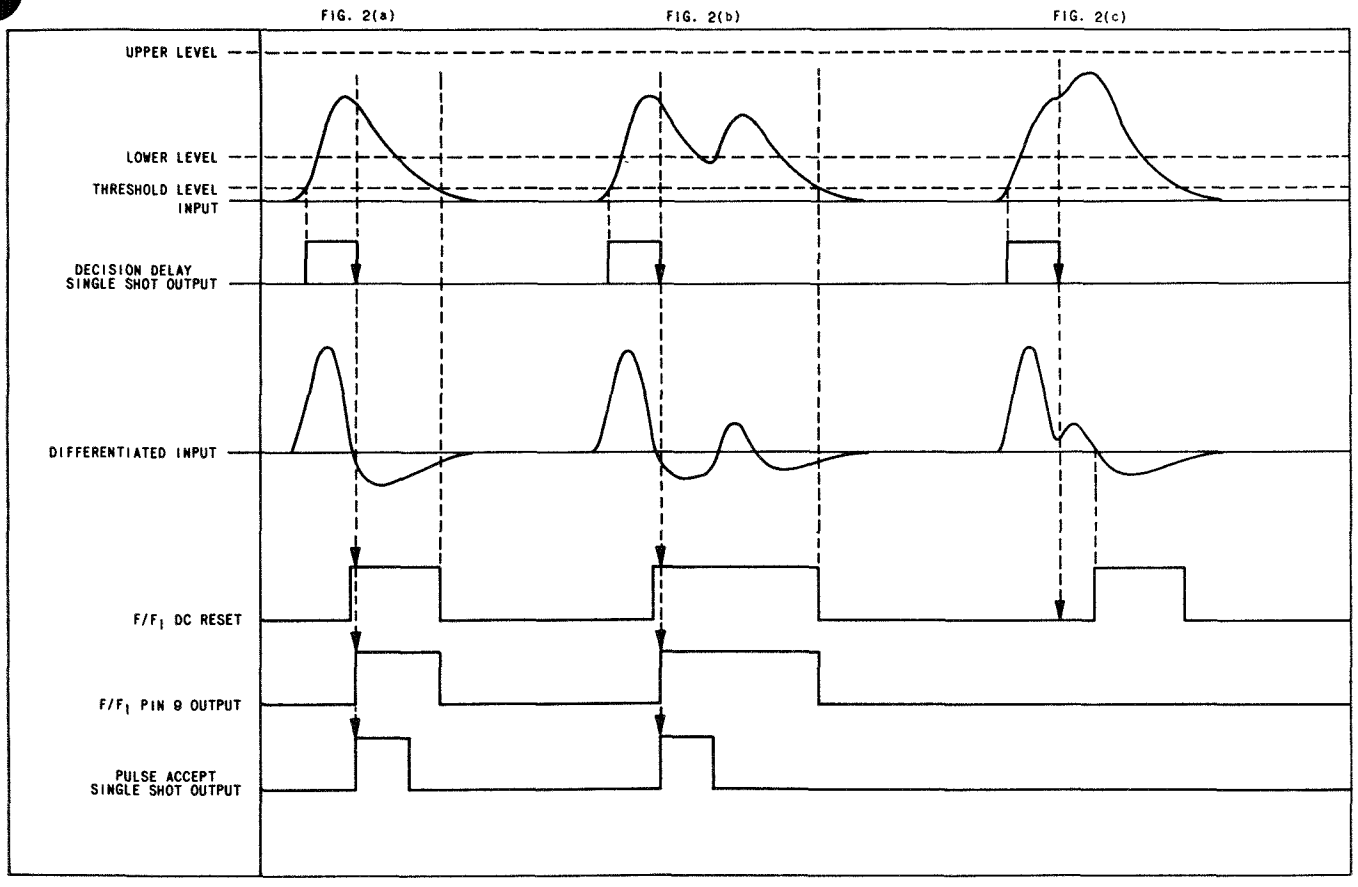

FIG. III-15-2. Pulse Selector Timing Diagram. *ANL-ID-103-A11519.*

OPERATION AND TIMING

Timing diagrams for the pulse selector are shown in Fig. III-15-2. All timing within the unit starts at the instant that the input signal exceeds the threshold level. At this moment the output of discriminator D-3 goes positive, causing the output of gate G-15 to drop to ground. The negative transition of the output of gate G-15 triggers the "decision delay" single shot comprised of Q-3 and G-14. This single shot generates a positive pulse at the collector of Q-3 whose width just exceeds the time required for the input pulse to reach its peak. The negative transition of the trailing edge of the delay pulse triggers flip-flop F/F_3 whose output at pin 9 then goes positive. The output of F/F_3 goes to the logic gating circuit where it is used to trigger the "pulse accept" single shot comprised of Q-4 and G-29.

When a tail pileup event occurs, as in Fig. III-15-2b, the "decision delay" single shot is triggered only for the first pulse. F/F_3 is not retriggered for the second pulse and as a consequence no coincidence gate pulse is generated for the tail pileup event.

Peak pileup events are rejected by holding F/F_3 reset so that it cannot be triggered "on" by the trailing edge of the "decision delay" pulse. The timing for peak pileup events is shown in Fig. III-15-2c. Peak pileup events are detected by first differentiating the input pulse by capacitor C_1, then detecting the crossover of the resulting double differentiated pulse with discriminator D-4.

The time constant of the differentiating network is set so that the crossover point of the double differentiated pulse occurs just before the "decision delay" pulse ends. If a peak pileup event occurs, the crossover point is extended and occurs after the end of the "decision delay" pulse. The output of gate G-18 thus remains at zero volts until after crossover occurs. The zero-volt level of G-18 forces F/F_3 reset so that it cannot respond to the trigger pulse from the "decision delay" single shot. F/F_3 is thus prevented from being triggered "on" and the peak pileup event is rejected.

APPLICATION

The peak pileup detection sensitivity of the pulse selector is limited when the unit is used in systems using proportional counters. This reduction in sensitivity occurs because the crossover time of the differentiated input pulse is also a function of detector collec-

tion time. As a consequence, the peak pileup rejection circuit must be set "loosely" so that the pulse selector does not mistake pulses with long collection times for peak pileup events.

On the other hand, when the selector is used with systems using solid state detectors, the peak pileup circuit also serves to discriminate against pulses having rise time defects, since defective pulses have longer rise times and a correspondingly longer time to cross over when integrated and double differentiated.

References

1. E. F. Bennett, *Fast Neutron Spectroscopy by Proton-Recoil Proportional Counting*, Nucl. Sci. Eng. **27**, 16 (January 1967).
2. E. F. Bennett, *Neutron Spectrum Measurements in a Fast Critical Assembly*, Nucl. Sci. Eng. **27**, 28 (January 1967).

III-16. High Energy Limitation of Proton-Recoil Proportional Counters for Neutron Spectroscopy

T. J. Yule

Introduction

The use of proton-recoil proportional counters for reactor spectrum measurements has received a considerable amount of attention.[1] One of the problems that has been considered is the high energy limitation of proton-recoil proportional counters for neutron spectroscopy.[2, 3] The limitation arises because the track length of recoil protons increases rather rapidly with energy and the probability of distortion arising from the truncation of the tracks by the counter walls or by the extension of tracks into an end region, increases accordingly. The ionization of the proton-recoil is no longer related in a simple way to the proton-recoil energy. Substantial distortion begins at energies less than 1 MeV for proton-recoil counters designed for in-core spectroscopy, i.e., counters meant to measure an isotropic neutron flux having a spectrum of a degraded fission source and whose size is small so as not to perturb the spectrum. The energy region in the neighborhood of a few MeV is especially important in reactor physics studies and radiation damage investigations.[4] Any improvement in accuracy of spectrum measurements in this region is significant. For fertile and fissile isotopes the region between reasonably known discrete excitation cross sections—up to about 1 MeV, and the region at which a clear indication of the statistical distribution becomes apparent—above 3 MeV, is an area of rather large cross section uncertainty. The damage cross section for structural materials peaks at a few MeV.

TABLE III-16-I. Range of Protons in Various Gases

Proton Energy, MeV	Ranges,[a] cm		
	Hydrogen	Methane	Krypton
2	33.8	8.24	5.27
4	118	27.9	15.3
8	417	97.2	47.1

[a] At 760 mm Hg and 15°C (see Ref. 5).

Efforts to increase the high energy capability of proton-recoil counters may be divided into two areas: techniques to increase the containment of proton-recoil tracks and analytical methods to correct measured proton-recoil distributions for track length truncations and for other effects, notably the effect of elastic scattering of neutrons from elements in the gas other than hydrogen. These areas are considered together with examples of the influence of the various corrections on measured spectra.

Techniques for Increased Containment

To reduce the influence of track length truncations, one would like to have a counter with the ratio of proton range at a given energy to the counter diameter as small as possible. This ratio is a function of the type of gas filling, the pressure, and the size of the counter. Table III-16-I lists proton ranges in various counter gases at a few representative energies.[5] The range is approximately proportional to the energy squared. Because of its small stopping power hydrogen is ruled out as a gas for high energy spectroscopy. Of the molecular gases containing hydrogen the most favorable product of stopping power times pressure is obtained for methane. More complex gases, although having a higher stopping power, liquify at rather low pressures. Methane also has a favorable ratio of hydrogen atoms to carbon atoms, which is important for minimizing the interference from carbon recoils. The idea of using a buffer gas such as krypton or xenon to increase the stopping power has been known for

some time. This method has been used in He-3 spectrometers[6] and in proton-recoil spectrometers for use in beam configurations.[7] The possibility of using a buffer gas in spectometers for in-core measurements is being investigated. At the present time a methane filled counter is used to measure the proton-recoil spectrum above 100 keV.

To minimize the influence of track length truncation the counter is filled to as high a pressure as possible as determined by that pressure at which the resolution becomes unacceptable. The resolution is determined by the amount of electron capture by contaminants in the gas—notably oxygen and water vapor. If one assumes that the Townsend energy factor—the ratio of mean agitation energy of the electrons to the mean molecular energy—and the drift velocity are linear functions of the field-to-pressure ratio,[8, 9] and that the cross section for electron capture by the contaminant is independent of energy, then one finds that the probability for capture in a methane filled counter for electrons starting at a distance r from the anode is

$$\text{Capture Prob.} = \frac{1.4 \times 10^7\, Cph}{\dfrac{V}{p \ln b/a}} \cdot \left\{0.5r + 1.75 \frac{V}{p \ln b/a} \sqrt{r^2 + 7.0 \frac{V_r}{p \ln b/a}}\right\}. \quad (1)$$

C is the percentage atom concentration of the contaminants, p is the pressure in mm Hg, h is the probability for capture per collision, V is the anode voltage in volts, and b and a are the radii of the cathode and anode, respectively, in cm. If the gain is held constant, i.e., $V/(p \ln b/a)$ is constant, the resolution is approximately proportional to the product of pressure times counter diameter. Thus, going to very large counters is not the answer to the problem of measuring isotropic spectra at high energy. By using unusually high voltages it is possible to increase the pressure, but the accompanying problems of corona discharges and special cabling and insulators become unwieldy. Using tank methane without any provision for purification a typical pressure is 6 atm for a 1 in. diam counter with a 0.001 in. diam anode. Counters have been built[7] which have a 3.5 in. diam cathode and a 0.001 in. diam anode and which have been filled with 3 atm methane or, using a buffer gas, with 2 atm krypton plus 2 atm methane. It should be possible to improve high energy response by careful purification of optimized gas mixtures.

Corrections for Geometrical Distortions

To make use of as much of the experimentally recorded proton-recoil distribution as possible, i.e. to use that region of the data at which significant geometrical distortion is occurring, it is necessary to correct the measured distribution with the response function for the counter. The response function at a given energy appropriate to a counter in a uniform neutron flux which has cylindrical symmetry about the counter axis is the energy distribution from monoenergetic protons at that energy generated uniformly and isotropically throughout the counter. The response function can be determined[3] from analytic track length probability functions and measured range and stopping power data. Figure III-16-1 illustrates the calculated response function at three energies for a 1 in. diam counter with a 3 in. sensitive length filled with 6 atm methane. For 2 MeV protons a significant number of tracks are not distorted—their distribution is indicated by a dashed-line Gaussian shape, which represents experimental resolution; the solid line represents the distribution from truncated tracks. At 3.5 MeV virtually all tracks are distorted. At 8 MeV the track length is so long that the most energy a track can deposit in the counter is about 2.7 MeV.

For the ⅝ in. diam methane counter with a 1¼ in. sensitive length and filled with 8 atm of methane (the counter used in the most recent spectra measurements; see Paper II-22) the proton-recoil spectrum ends at about 3 MeV. The correction for geometrical effects proceeds in two parts: the first part corrects for proton-recoils arising from neutrons above the cut-off energy; the second part corrects for distortion of proton-recoil tracks arising from neutrons below the cut-off energy. In the first part, it is assumed for an in-core spectrum measurement that the neutron spectrum above 2.5 MeV is that predicted by a fundamental mode calculation (see Paper II-22). To a good approximation the spectrum $N(E)$, as a function of energy, can be represented by

$$N(E) \propto \sqrt{E}\, e^{-E/T}, \quad (2)$$

where T is a coefficient adjusted to fit the calculation. The functional form is the same as that used to describe the fission spectrum. The temperature T is not that for a fission spectrum. The ideal proton-recoil spectrum is generated from the neutron spectrum, and then the response function for the counter is applied to the ideal proton-recoil spectrum to obtain the distorted proton-recoil spectrum arising from neutrons with energies greater than 2.5 MeV. The calculated distorted proton-recoil distribution is normalized to the measured distribution between 2.5 and 3 MeV. The normalized distribution is then subtracted from the measured proton-recoil distribution. Thus, the influence of proton-recoils from neutrons above the measurement limit is eliminated. Figure III-16-2 (curve labeled "downscatter") shows the effect of subtracting out the high

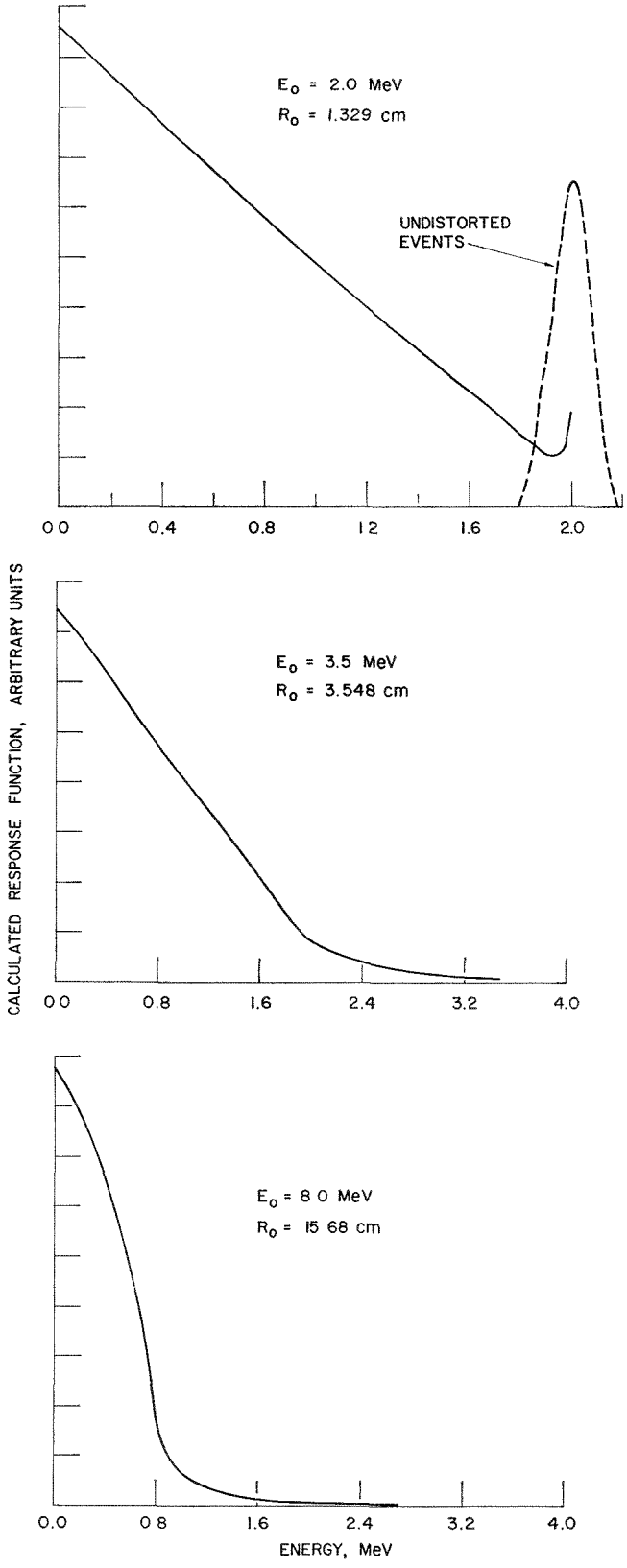

FIG. III-16-1. Calculated Response Function at Various Energies for a 1 in. diam Counter With a Sensitive Length of 3 in. Filled With 6 atm Methane. The Energy, E_0, and Range, R_0, of the Uniformly and Isotropically Generated Monoenergetic Protons are Indicated. *ANL Neg. No. 116-475.*

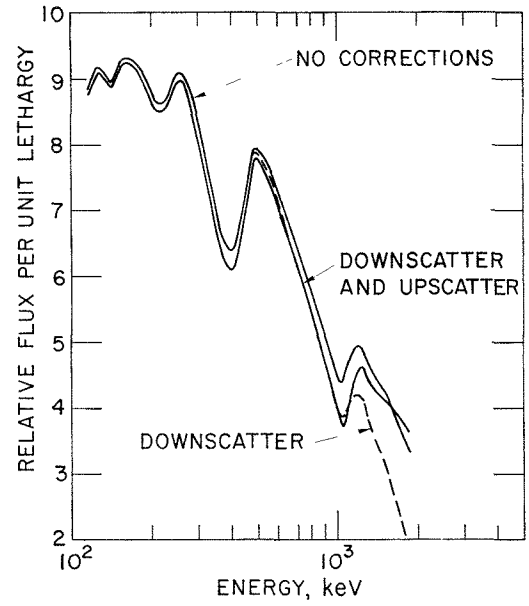

FIG. III-16-2. Measured Neutron Spectra at the Center of ZPR-9 Assembly 26 With a Methane-Filled Counter from a Proton-Recoil Spectrum With No Corrections, One Corrected for Downscatter, and One Corrected for Downscatter and Upscatter. *ANL-Neg. No. 900-301.*

energy neutron contribution on the central neutron spectrum of ZPR-9 Assembly 26 (see Paper II-22). Note that the spectrum is significantly depressed from the spectrum resulting from an uncorrected proton-recoil distribution.

The second part of the correction consists of correcting the already downscattered corrected proton-recoil spectrum for distortion of proton-recoil tracks arising from neutrons below the cut-off energy. In this part of the correction it is not necessary to assume any form for the neutron spectrum. The measured proton-recoil spectrum is simply corrected with the counter response function from high energy to low energy using integral unfolding techniques.[2] Figure III-16-2 (curve labeled "downscatter and upscatter") points out the magnitude of the correction on the neutron spectrum. It is interesting to find that when both the downscatter and upscatter corrections are applied, the neutron spectrum is not much different from one derived from an uncorrected proton-recoil distribution. This situation will usually not apply for neutron spectra with shapes significantly different from those of degraded fission sources.

Elastic Scattering from Heavy Elements

The introduction of hydrocarbons, such as methan or of high-Z noble gases (such as krypton), to decrease

roton range will be accompanied by an undesirable side effect. Elastic scatter from heavy elements in the gas will ionize indistinguishably from proton-recoils and the measured distribution contains a component of this scattering.

The ionization spectrum obtained with a methane counter contains ionization from carbon recoils. This spectrum is corrected for carbon recoils with the assumptions that the center-of-mass system scattering for neutrons by carbon is isotropic, that the total cross section may be represented by

$$\sigma_C(E) = \frac{5520}{E + 1150} \qquad (3)$$

with E in keV and σ in barns, and that the relative ionization created by a carbon fragment is 0.75 that of a proton.[2] Figure III-16-3 shows the magnitude of the correction on the same neutron spectrum considered in Fig. III-16-2.

The addition of krypton to hydrogen gas would be less objectionable than the use of methane, apart from resolution and stopping power considerations. The maximum recoil energy produced by elastic neutron scattering by carbon is about 0.3 of the incident neutron energy but only about 0.05 for krypton.

Figure III-16-4 shows a comparison of neutron spectra for the same in-core measurement. One spectrum is derived from an uncorrected proton-recoil distribution and the other spectrum from a fully corrected distribution, i.e., a distribution which is corrected for downscatter, upscatter and carbon recoil effects. It is seen that if accurate determinations of neutron spectra are to be made, it is necessary to make the above corrections.

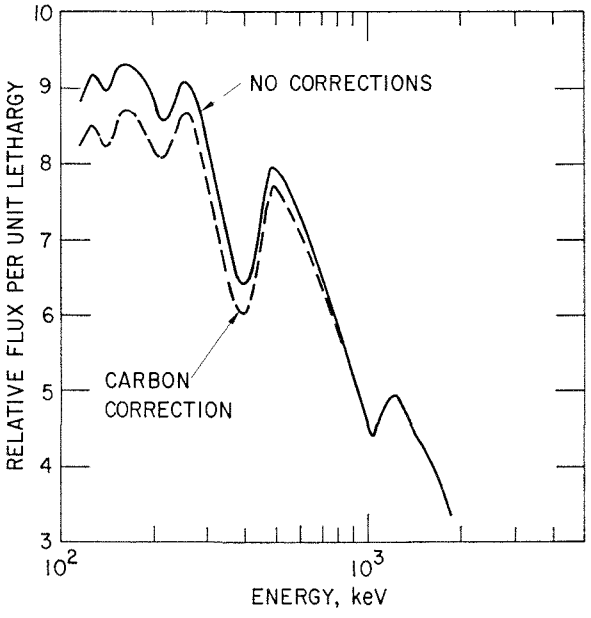

IG. III-16-3. Measured Neutron Spectra at the Center of R-9 Assembly 26 With a Methane-Filled Counter from a Proton-Recoil Spectrum With No Corrections and One Corrected for Carbon Recoils. *ANL-Neg. No. 900-302.*

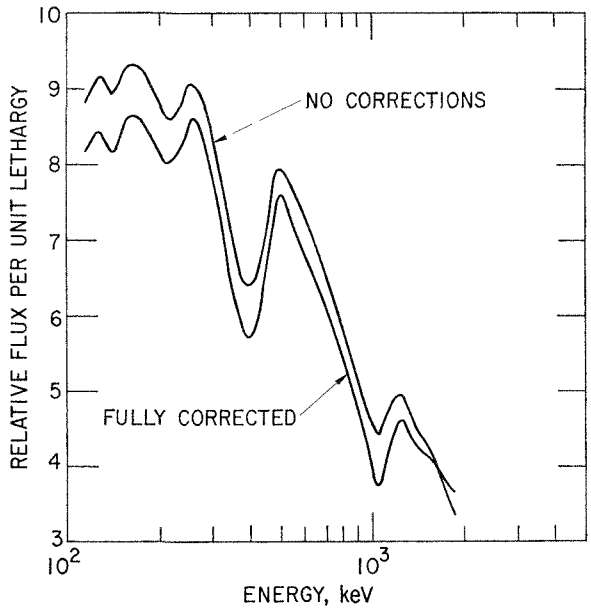

FIG. III-16-4. Measured Neutron Spectra at the Center of ZPR-9 Assembly 26 With a Methane-Filled Counter from a Proton-Recoil Spectrum With No Corrections and One Fully Corrected, i.e. Corrected for Downscatter, Upscatter, and Carbon Recoils. *ANL-Neg. No. 900-306.*

Conclusion

Factors which limit the high energy usefulness of proton-recoil counters for neutron spectroscopy were discussed above. Means of increasing the high energy capability of this method of spectroscopy were considered. Sources of error which in the past have compromised the interpretation of high energy data were investigated, and methods for correcting measured proton-recoil distributions were indicated. With a small nonperturbing methane counter, in-core neutron spectra can be reliably determined to 2 MeV.

References

1. E. F. Bennett, *Fast Neutron Spectroscopy by Proton-Recoil Proportional Counting*, Nucl. Sci. Eng. **27**, 16 (1967).
2. R. Gold and E. F. Bennett, *Effects of Finite Size in 4π-Recoil Proportional Counters*, Nucl. Instr. Methods **63**, 285 (1968).
3. T. J. Yule, *Predictions of Geometrical Distortions in Proton-Recoil Counters and Application to Neutron Spectroscopy*, Reactor Physics Division Annual Report, July 1, 1968 to June 30, 1969, ANL-7610, pp. 404–410.
4. D. Okrent, W. B. Loewenstein, A. D. Rossin, A. B. Smith, B. A. Zolotar and J. M. Kallfelz, *Neutron-Energy Spectra for Fast Reactor Irradiation Effects*, Nuclear Appl. **9**, 454 (1970).

5. W. Whaling, *The Energy Loss of Charged Particles in Matter*, Handbuch der Physik, Vol. IV (1958) pp. 193–217.
6. R. Batchelor and G. C. Morrison, *Helium-3 Neutron Spectrometers*, Fast Neutron Physics, Part I, J. B. Marion and J. L. Fowler, Eds., (Interscience Publishers, Inc., New York, 1960) pp. 413–439.
7. H. Werle, *Spektrumsmessungen Radioactiver Neutronquellen in Energiebereich von 10 keV bis 10 MeV Mit Protonen-ruckstoss-Proportionalzahlrohren*, Institut fur Neutronenphysik und Reaktortechnik INR-4/70-25, Kernforschungszentrum, Karlsruhe, 1970.
8. L. W. Cochran and D. W. Forester, *Diffusion of Slow Electrons in Gases*, Phys. Rev. **126**, 1785 (1962).
9. E. W. McDaniel, *Collision Phenomena in Ionized Gases*, (John Wiley & Sons, Inc., New York, 1964) Chapter 11.

III-17. Electronics for Proton Recoil Systems Using Proportional Counters

J. M. Larson

Introduction

This paper briefly describes the pulse shaping electronics for the proton-recoil proportional counter spectrometer that is presently in use at the ZPPR facility. This spectrometer is an adaptation of the spectrometer previously reported in the 1969 Reactor Physics Division Annual Report[1] and differs from the previously reported spectrometer in that pulse pile-up rejection circuitry has been added.

This spectrometer is now being routinely used for spectrum measurements and allows undistorted proton-recoil spectra to be measured over an energy range spanning 1 keV to 3 MeV. The system will accept counting rates in excess of 20,000 counts/sec and is designed to have high overload capability.

General Description

A block diagram of the system is shown in Fig. III-17-1. In this system, the output of the preamplifier drives two separate channels of pulse shaping amplifiers: (1) a slow channel that determines total ionization or pulse height and (2) a fast channel that determines the rate of ion collection or pulse rise time. The rate-of-rise data from the fast channel is digitized and divided in the accompanying computer by the digitized ionization data from the slow channel to determine specific ionization.

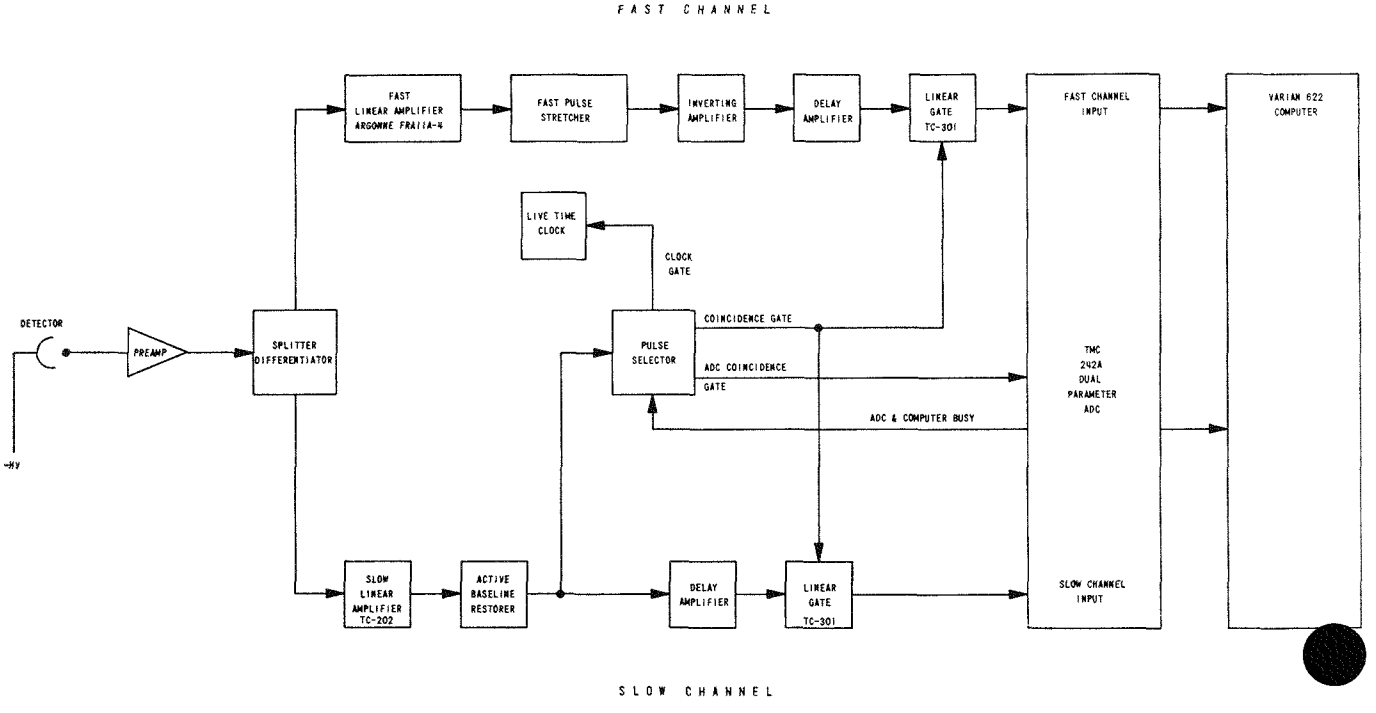

FIG. III-17-1. Block Diagram of Spectrometer. *ANL-ID-103-A11575.*

The fast channel consists of a delay line clipping circuit located in the splitter-differentiator module, a fast rise amplifier, a fast pulse stretcher, an inverter, a delay amplifier and a linear gate. The slow channel is comprised of a TC202 shaping amplifier, an active dc restorer, a delay amplifier and a linear gate. A TMC-242 dual parameter ADC is used.

A pulse selector is used in the system for pulse pile-up and overload pulse rejection. Live time is accounted for by a live time clock that is gated off for the duration that the ADCs and computer are busy and for the time occupied by all rejected pulses. Linear gates are used external to the ADCs to reject overload pulses that might otherwise cause baseline shift within the ADCs.

One of the main problems encountered with proportional counter proton-recoil systems is the large overloads generated when the proportional counter is operated at high multiplication, as when measurements are made in the 1 to 10 keV region.

When spectrum measurements are made in this energy range, protons with higher energies create large overloads in the preamplifier and in the shaping amplifiers. It is thus very important that these amplifiers be designed so that they exhibit graceful baseline recovery following overload events; otherwise, the maximum counting rate capability, without distortion, may be greatly reduced.

Preamplifier

The overload performance of the preamplifier is of primary importance and can be improved by using direct coupling combined with a large output swing capability. In addition, the preamplifier should be designed to have a single dominant decay constant so that pole zero cancellation techniques can be used effectively in the following shaping amplifiers. The preamplifier used in this system was designed expressly for use with proportional counters in proton-recoil systems and is described in Ref. 2. This preamplifier is direct coupled, charge sensitive and has a 20 V peak output swing.

Splitter Differentiator

A schematic of the splitter differentiator is shown in Fig. III-17-2. This circuit provides a termination for the coaxial cable from the preamplifier and inverts and delay-line clips the preamplifier's output signal before it is routed to the fast amplifier channel.

It should be noted that the delay line and inverting [illegible]lifier (comprised of Q_1, Q_2 and Q_3) are direct cou[illegible]. This is essential to prevent bias shift and the possible cutoff of the inverter in the event that the preamplifier saturates.

The output of the delay line drives the pole zero compensation network, comprised of *C-1* and *R-1*, which decreases the decay time of the pedestal following the delay-clipped pulse.

Slow Channel Shaping Amplifier

The slow channel shaping amplifier should utilize pole zero compensation so that graceful overload recovery is obtained. In addition the pole zero compensation network should be placed directly in series with the input of the amplifier, so that differentiation is performed before the input signal is amplified.

The pole zero compensation of the TC-202 amplifier is located at its input, and, in addition, this amplifier features Gaussian shaping which yields shaped pulses having a narrower overall width than is obtained with single *RC* shaping.

Slow Channel DC Restorer

In this system the slow channel pulse shaping amplifier is operated in the unipolar mode, and as a consequence, baseline restoring is required. The baseline restorer should be of the active type because of the high counting rates that occur. In addition, the restorer must be capable of being drived by large amplitude overloads without generating baseline deviations.

The baseline restorer used in this system was specifically designed for use where large overloading pulses are present and is described in Paper III-20.

Slow Channel Delay Amplifier

The slow channel delay amplifier provides appropriate delay so that the input signal and coincidence gate to the slow channel ADC have the proper timing. The delay amplifier follows the dc restorer and drives the slow channel linear gate, and it is therefore important that this amplifier be capable of handling overloads gracefully without generating baseline shift or deviation.

The schematic of the delay amplifier is shown in Fig. III-17-3. The delay amplifier consists of a delay line followed by a low-drift direct-coupled amplifier. The amplifier uses a direct coupled design that eliminates the need for capacitor bypassing across bias networks, thus providing overload immunity.

The fast channel delay amplifier is identical to that in the slow channel except for differences in delay.

Linear gates are used external to the ADCs to prevent large overload pulses from overloading the ADCs' input amplifier stages.

Fast Amplifier, Pulse Stretcher, and Inverter

The fast channel linear amplifier is an adaptation of the Rush circuit[3] and has switchable attenuators for

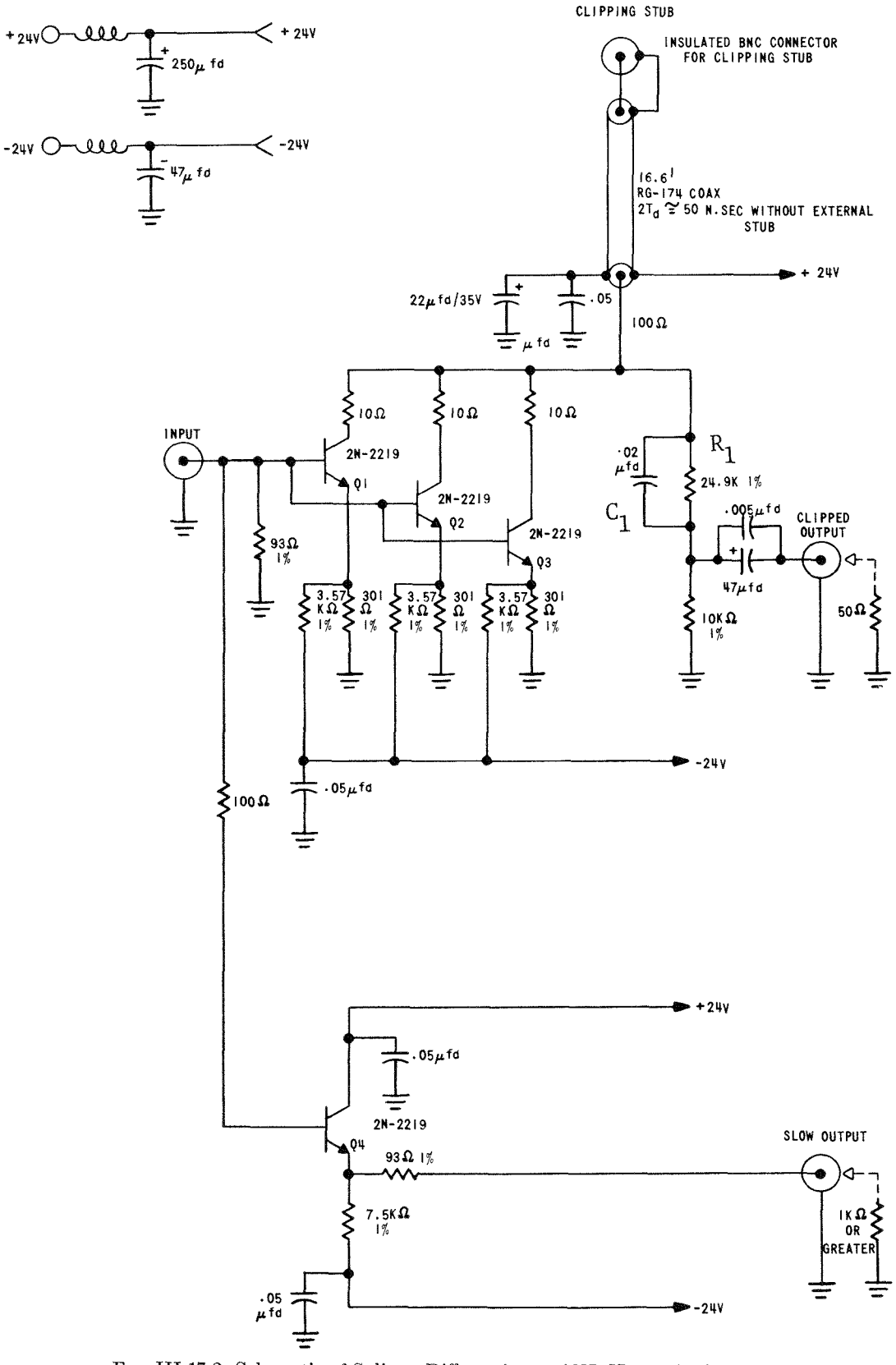

FIG. III-17-2. Schematic of Splitter-Differentiator. *ANL-ID-103-A11499.*

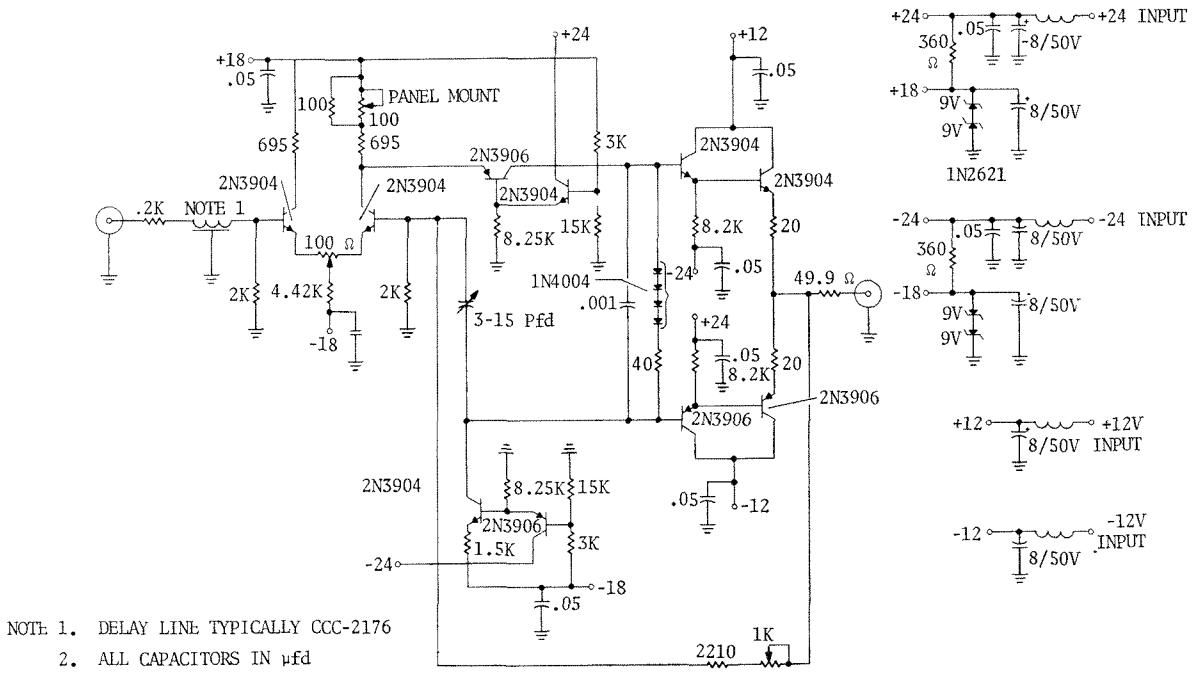

FIG. III-17-3. Schematic of Delay Amplifier. *ANL-ID-103-A11500 Rev. 1.*

gain adjustment. The fast pulse stretcher is the circuit reported by R. N. Larsen.[4]

The fast channel inverter is an operational amplifier connected in the inverting mode. This amplifier inverts the negative output level from the stretcher so that a positive output level is obtained that is compatible with the ADCs.

Pulse Selector

A pulse selector is used to inspect incoming pulses and to reject those that are determined to be overloads or that are distorted by pile-up effects. In addition, the pulse selector operates in conjunction with the ADC busy signal in controlling the live time clock so that the live time clock is gated off for all pulses that exceed a specified lower level. The live time clock remains off until the ADCs are no longer busy and the baseline is restored to its zero reference level. The clock is also gated off for the duration of all rejected pulses. A more detailed description of the pulse selector is given in Paper III-15.

Live Time Clock

The live time clock is comprised of a 10 mc crystal oscillator that drives a series of micro-logic dividers. The unit can be preset to count from 1 to 1000 min. The busy output from the pulse selector controls the time such that the crystal oscillator output is gated off whenever the ADCs are busy or for the duration of a rejected pulse.

Live time is displayed by an octal readout on the front panel of the live time module.

Test and Application

The system described above has been tested in the Argonne Fast Source Reactor by comparing proton-recoil spectra taken at low counting rates with the same spectra taken at very high counting rates. These tests indicate that non-distorted proton-recoil data can be obtained at count rates in excess of 30,000 cps when using methane counters, and 10,000 cps when using hydrogen counters. The maximum possible count rate limit for the system has not been determined but preliminary measurements indicate that counting rates up to 20,000 cps using hydrogen counters should be attainable.

The system has been used for a number of spectrum measurements in ZPPR and ZPR-3. The details of these measurements may be found in Paper II-18.

References

1. J. M. Larson and J. E. Powell, *Electronic System Developments for Proton-Recoil Spectra Measurements in Plutonium Critical Facilities*, Reactor Physics Division Annual Report, July 1, 1968 to June 30, 1969, ANL-7610, pp. 410-414.
2. J. M. Larson, *A Wide Band Charge Sensitive Preamplifier for Proton-Recoil Proportional Counting*, ANL-7517 (1969).
3. C. J. Rush, *New Technique for Designing Fast Rise Transistor Pulse Amplifiers*, Rev. Sci. Instr. **35**(2), (1964).
4. R. N. Larsen, *Nanosecond Pulse Stretcher*, Rev. Sci. Instr. **37**(4), (1966).

III-18. Developments in the Electronic System for Neutron Spectroscopy with Proton-Recoil Proportional Counters

T. J. Yule and E. F. Bennett

Introduction

The measurement of fast neutron spectra in zero power reactors using proton-recoil proportional counters with gamma-ray discrimination has been pursued at Argonne for a number of years.[1-3] During this time numerous improvements in the electronic system have evolved. The electronics of the present spectrometer allows undistorted spectra to be recorded over the full energy range from 1 keV to 3 MeV with count rates exceeding 20,000 counts/sec. A moderately high count rate system is especially desirable for measurements in plutonium cores where the spontaneous neutron source from Pu-240 is rather large.

Electronics System

Amplifier System

One problem that is immediately encountered in measuring neutron spectra with proportional counters is that the electronic system must operate satisfactorily under severe amplifier overloads. When the proton spectra are being recorded in the low keV range with the counter voltage set at high gas multiplication, protons with energies of several MeV create large overloads. These overloads should not be allowed to cause saturation in the preamplifier and should be handled appropriately by the slow ionization amplifier, such that at moderate count rates undistorted spectra can be obtained.

A block diagram of the amplifier system is shown in Fig. III-18-1. The preamplifier, besides not saturating under heavy overloads, must have a moderately fast rise time and low noise. A rise time of less than 15 nsec is adequate, since diffusion of the electron bunch makes meaningless the use of time constants of less than 20 nsec even for a fast gas such as methane. At shorter time constants the separation of proton-recoils and gamma-induced electrons does not improve, while the resolution of the peaks worsens because of increased noise. A charge-sensitive preamplifier specifically designed for proton-recoil proportional counting is used.[4-6] The preamplifier is able to provide an output pulse of 20 V without saturating.

The slow side of the amplifier system, which pro-

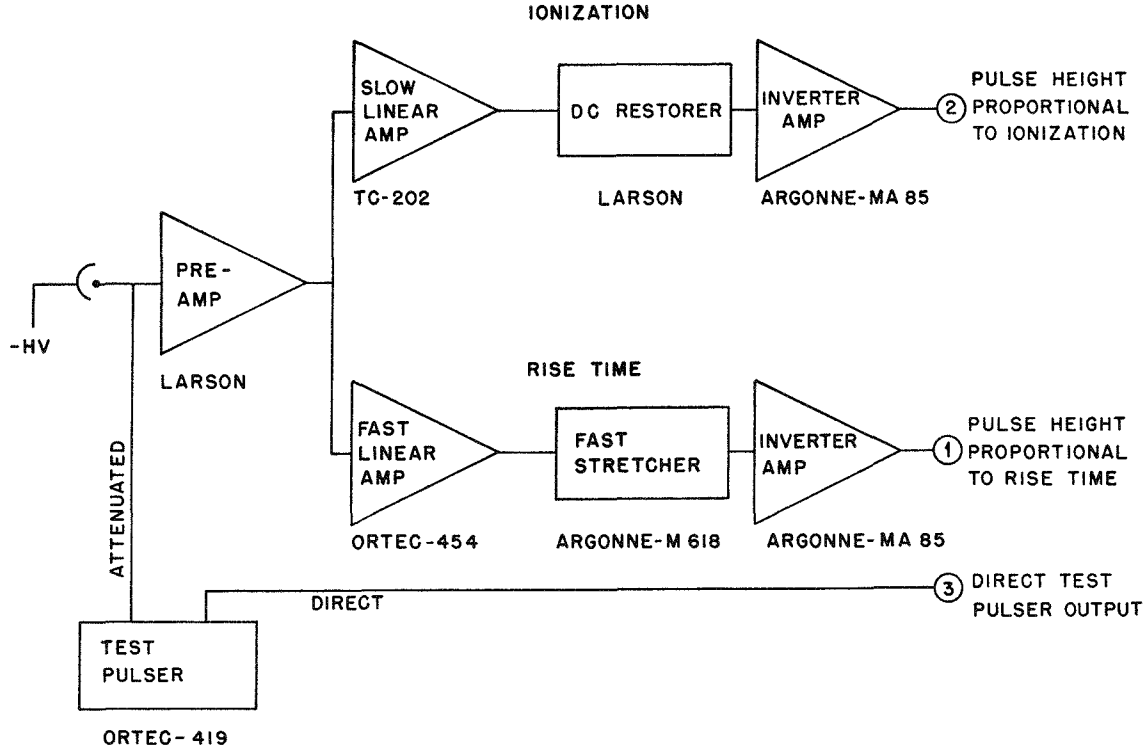

Fig. III-18-1. Block Diagram of the Amplifier System Used for Neutron Spectroscopy With Protron-Recoil Proportional Counters. *ANL Neg. No. 116-316.*

duces a pulse whose height is proportional to the ionization, consists of a pole-zero compensated linear amplifier, baseline restorer, and inverter amplifier. Preamplifier noise dominates the noise in the slow channel; noise from the shaping amplifier is negligible. Because of the shape of the collection profile, it is not obvious whether using unipolar or bipolar pulse shaping is superior in high count rate applications. The shape of the pulse for a point event is given by[7]

$$P(t) = -\frac{e}{C}\ln\left\{\frac{2VKt}{a^2 \ln b/a} + 1\right\}, \qquad (1)$$

until $P = -e/C$ at which time all charge is collected. e is the charge of the electron, C the input capacitance of the counter-preamplifier combination, V the voltage on the counter, K the positive ion mobility, and a and b are the radii of the anode and cathode, respectively. A sketch of the pulse profile is shown in Fig. III-18-2a. The slow component of the pulse persists until positive ion collection-times of the order of milliseconds are usual for hydrogen-filled counters. Using reasonable time constants in the amplifier of a few μsec, a sizeable pedestal results for large overloads with unipolar pulse shaping, as shown in Fig. III-18-2b. It has been suggested that an appropriate way of removing this pedestal, so that reasonable count rate capability can be obtained, is to use the pole-zero correction adjusted such that a slight negative undershoot is observed that just exceeds the amplitude of the pedestal.[5, 6] The pulse is then restored by using a fast restoring baseline restorer. In the bipolar mode the pedestal is strongly attenuated and the dc restorer is not used. Time constants of 2.4 μsec are used for both the unipolar and the bipolar mode. The inverter amplifier inverts the pulse and, for the bipolar pulses, clips the second node to be compatible with the pulse selector and linear gate which is described in the next section.

The fast side of the amplifier system, which produces a pulse whose height is proportional to the rise time of the pulse from the preamplifier, consists of a fast linear amplifier, a fast stretcher and an inverter amplifier. The fast amplifier system must have pulse shaping constants in the 20 to 100 nsec range for proton-recoil spectroscopy. In the past, pulse differentiation was done with a shorted delay line.[1] The pulse was then amplified by a fast amplifier. At the present time a fast amplifier with RC integration and differentiation is being used. The amplifier was designed for timing with Ge(Li) detectors, surface barrier detectors, or photomultipliers. The pulse stretcher and inverter condition the pulse for the linear gate.

LOGIC SYSTEM

A block diagram of the logic system is shown in Fig. III-18-3. The heart of the logic system is the pulse selector,[8,9] which determines whether the slow channel pulse is an acceptable data pulse and if so, allows it along with the corresponding fast pulse to be analyzed by the ADCs. A number of requirements must be met before the pulse is regarded as acceptable. The pulse must be within a window set by an upper level and a lower level discriminator. The ADC-computer combination must not be busy. The pulse must be a data pulse and not a pulser pulse. (Pulser pulses are used for live timing, as explained in the next section.) The timer must be on. The baseline must have been down for a set period of time. This function is performed by a baseline discriminator and paralysis circuit. For a given pulse or combination of overlapping pulses the length of time the baseline discriminator is exceeded is determined, and for our purposes may be referred to as the pulse width. The pulse selector will deem unacceptable any pulse which comes within a present number of pulse widths of a previous pulse. The preset number of dead widths may be 1, 2 or 3. The logic outputs from the pulse selector are: one that indicates that the baseline discriminator has been exceeded—BLD; one that

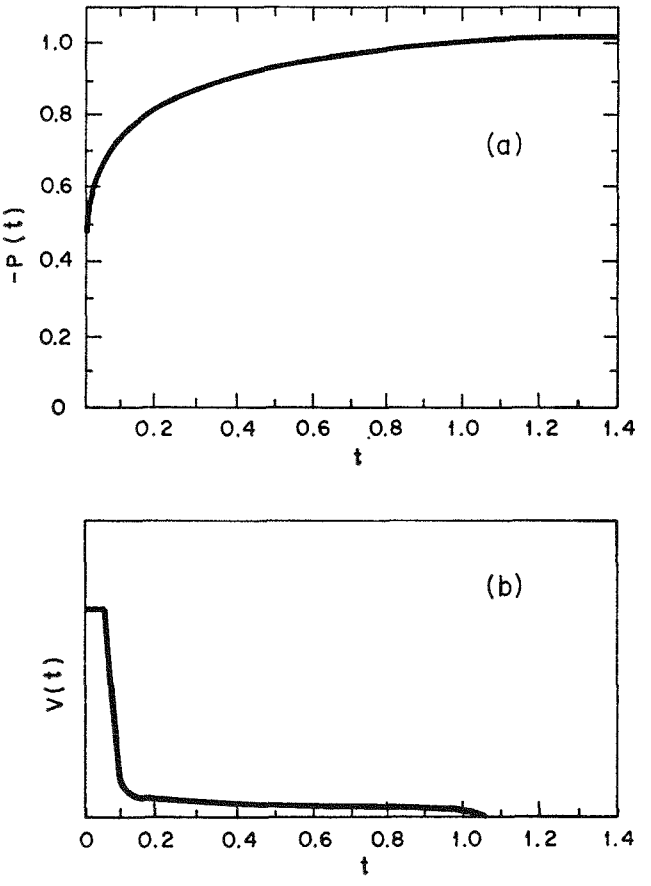

FIG. III-18-2. Pulse Profiles. (a) Pulse Profile at Input of Preamplifier; (b) Overload Profile at Output of Slow Amplifier Without Pole-Zero Correction for Undershoot. *ANL Neg. No. 116-315.*

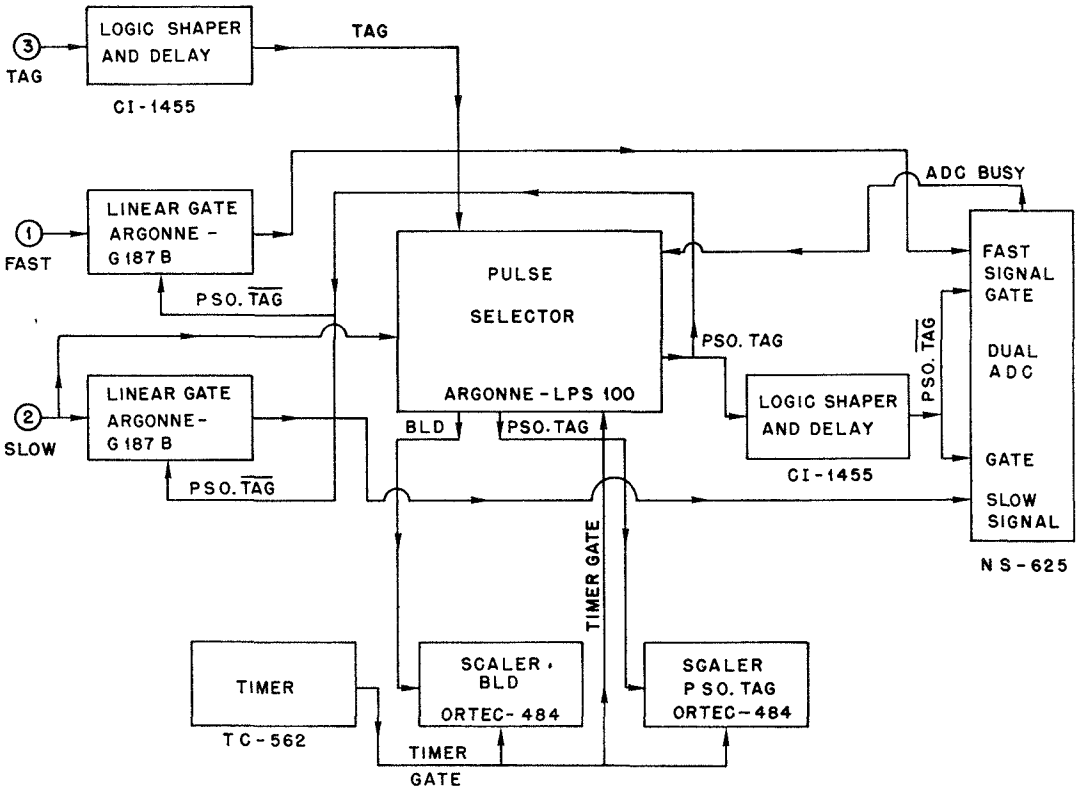

FIG. III-18-3. Block Diagram of Logic System and Data Storage System Used for Neutron Spectroscopy with Protron-Recoil Proportional Counters. *ANL Neg. No. 116-314.*

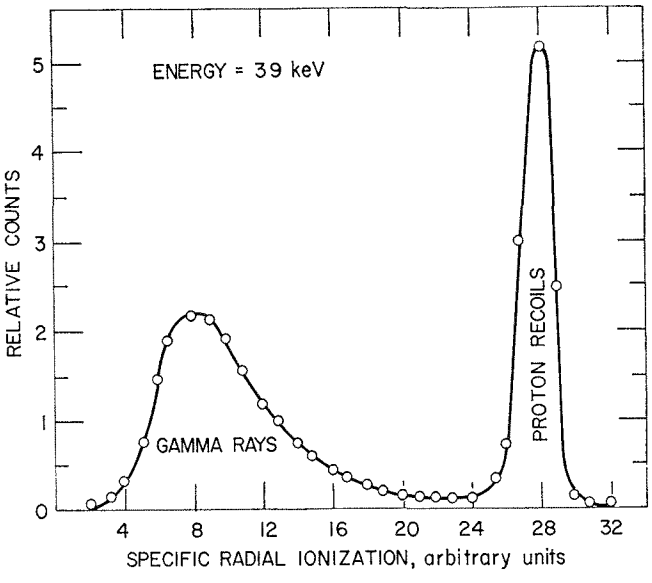

FIG. III-18-4. Typical Specific Ionization Spectrum. *ANL Neg. No. 113-848.*

indicates the pulse is an acceptable data pulse—PSO·$\overline{\text{TAG}}$; and one that indicates that the pulse is an acceptable pulser pulse—PSO·TAG. An acceptable pulser pulse must meet all the requirements that an acceptable data pulse must meet. A test pulser pulse is distinguished from a data pulse at the pulse selector by a coincident tag pulse—TAG.

The pulse selector also contains an option for pile-up rejection. The pile-up rejection circuit differentiates the pulse with a short time constant and checks to see that the zero crossing of the pulse appears at the proper time with respect to the time mark generated by the differentiation. We have chosen not to use the option in two-parameter analysis for two reasons. Firstly, the two-parameter analysis already contains a fast differentiation, whose magnitude is stored with the pulse height. If a proton pulse is distorted because of pile-up, the division of the fast pulse height by the slow pulse height for a given slow pulse height will be such that the event will appear to be a gamma-ray induced event and not be counted as a proton-recoil. Secondly, the large range of rise times for pulses from a hydrogen counter (where electron drift velocities are low) are such that if the pile-up sensor is to be effective for detecting proton event pile-up, some legitimate single gamma-ray induced events will appear to be pile-up events and thus rejected. The shape of the peak of the gamma-ray induced events will depend the count rate. An uncertainty results when one ma a background subtraction using background generated at some different count rate because the backgrounds

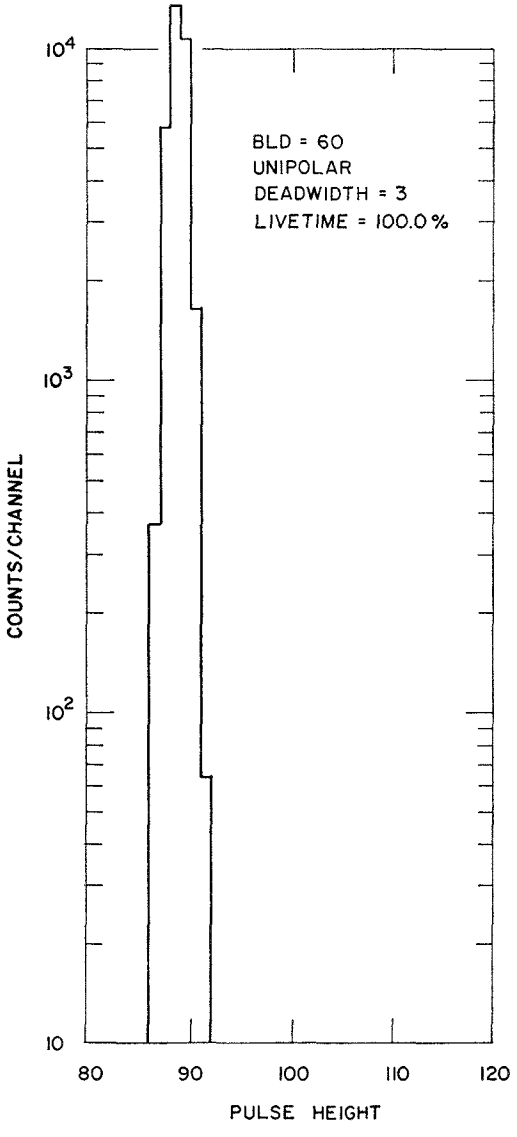

FIG. III-18-5. Pulser Pulse-Height Spectrum Using Unipolar Pulse Shaping and a Preset Dead Width of 3 with Zero Counter Voltage. *ANL Neg. No. 116-310.*

will not match. There are ways around this problem by employing additional circuits, but unless one wants to increase the count rates far in excess of 20,000 counts/sec, such measures are not called for. However, when gamma-ray discrimination is not being employed, pile-up rejection may be effective in limiting distortion. Care must be taken not to set the pile-up rejection for too short a pulse width since even in a fast gas like methane, long track lengths along the diameter have a considerably different rise time than tracks along the axis.

The linear gates delay and stretch the pulses from the slow and fast sides of the system and allow the pulses to be strobed through to the ADCs only if the appropriate PSO·$\overline{\text{TAG}}$ logic pulses are present. Scalers record BLD and PSO·TAG.

COUNTING LOSS DETERMINATION

Because of the presence of the pulse selector, it is not possible to determine counting losses by simply monitoring when the ADC-computer combination is busy.[9] The whole system must be taken into account. Pulses from a test pulser operating at a fixed frequency (60 per sec) are presented to the input of the preamplifier. A tag pulse is also generated to identify pulser pulses. The test pulse must meet all the requirements of an undistorted data pulse and be accompa-

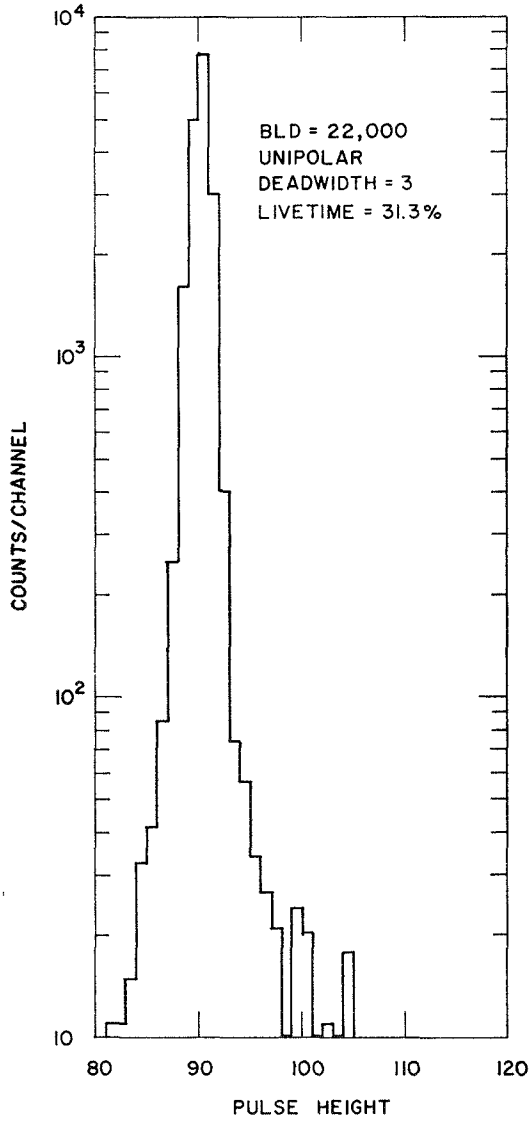

FIG. III-18-6. Pulser Pulse-Height Spectrum Using Unipolar Pulse Shaping and a Preset Dead Width of 3 in the Presence of 22,000 counts/sec from a Hydrogen-Filled Counter. *ANL Neg. No. 116-312.*

nied by a tag to have the pulse selector generate a PSO·TAG pulse. The live time of the system is simply

$$\text{Live Time} = \text{Real Time}\,\frac{\text{PSO}\cdot\text{TAG}}{\text{TAG}}, \qquad (2)$$

where real time is determined from the timer, TAG are the number of test pulses generated during this time, and PSO·TAG are the number of acceptable pulser pulses. Such a live timing system is only suitable for constant count rates.[9]

Such a count loss determination system may be applied as a rapid method of determining distortion as a function of count rate. In this mode one allows only pulser pulses to be analyzed in the presence of counter generated pulses. PSO·TAG is used to strobe the linear gates and ADCs instead of PSO·$\overline{\text{TAG}}$. The resulting distribution of pulser pulses indicates the extent of distortion. Results of such tests are considered in another section.

STORAGE INFORMATION

The ADCs are interfaced to a Varian Data Machines 622 computer. The storage routine[10] and the details of the interface[11] have been described elsewhere. The computer forms the ratio of fast-to-slow pulse height, i.e. the radial specific ionization of the event. This ratio along with the ionization of the event is stored in a two-parameter array. Figure III-18-4 illustrates part of a typical array for a given value of ionization. The region at high values of the specific radial ionization corresponds to proton-recoil events and at low values to fast electrons from interactions of gamma-rays with the walls of the counter.

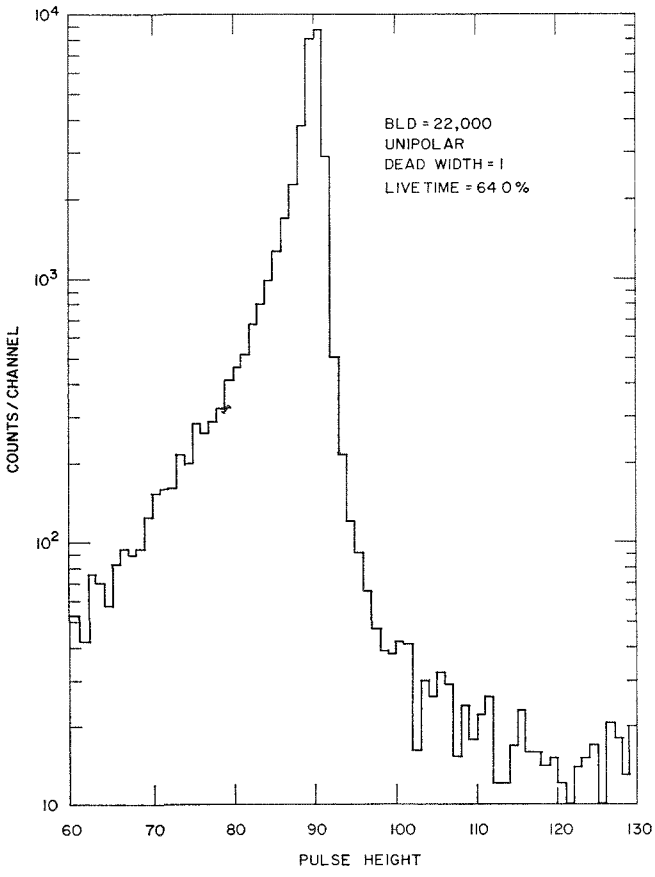

FIG. III-18-7. Pulser Pulse-Height Spectrum Using Unipolar Pulse Shaping and a Preset Dead Width of 1 in the Presence of 22,000 counts/sec from a Hydrogen-Filled Counter. *ANL Neg. No. 116-309.*

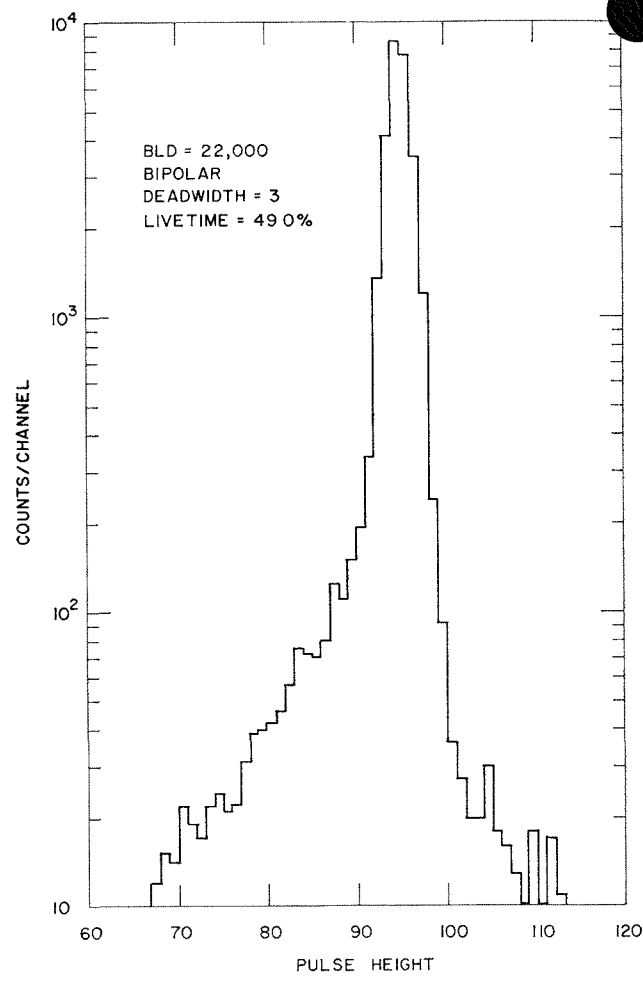

FIG. III-18-8. Pulser Pulse-Height Spectrum Using Bipolar Pulse Shaping and a Preset Dead Width of 3 in the Presence of 22,000 counts/sec from a Hydrogen-Filled Counter. *ANL Neg. No. 116-311.*

TESTING THE ELECTRONIC SYSTEM

DYNAMIC TEST PULSER TEST OF SYSEM

The count rate capability of the system was checked using the test pulser method previously described. A in. diam counter with a 6.5 in. sensitive length fil with predominately hydrogen gas at 80 psi was placed 5 in. from the graphite-uranium interface of the Snell block.[12] The spectrum in this position is quite hard and

long sensitive length of the counter means that proton-recoils of several MeV can be stopped in the counter. The counter was operated at a voltage of 4400 V, which corresponds to a gas gain of about 3300. The electronics were such that full scale ionization would be a few keV. This represents about the most unfavorable condition with respect to severe overloads. The undistorted pulse-height distribution, i.e., no voltage on the counter, is shown in Fig. III-18-5. The effect of various pulse shaping and dead width combinations at a deadtime-corrected, baseline discriminator rate of 22,000 counts/sec are shown in Figs. III-18-6 through III-18-9. Note that the ordinate is a logarithmic scale. The cleanest peak is obtained with unipolar shaping using the baseline restorer and a dead width setting of 3 pulse widths, as shown in Fig. III-18-6. Figure III-18-7 indicates that when the dead width setting is reduced to 1, unacceptable distortion occurs. There is some fast undershoot associated with the large overloads that the baseline restorer is not able to smooth out. Figure III-18-8 indicates the effect of using bipolar pulse shaping and a dead width setting of 3. The pulse width is that associated with only the first node of the bipolar pulse. The amount of distortion is acceptable—only about 3% of the counts fall in channels less than 90 and greater than 100. Figure III-18-9 shows the effect of using unipolar pulse shaping and a dead width setting of 2. When comparing unipolar pulse shaping and bipolar pulse shaping, it is most useful to consider Figs. III-18-8 and III-18-9. The pulse width times the dead width setting is approximately equal for the two cases, when only the width of the first node is taken for the bipolar pulse. It is seen that unipolar shaping produces slightly less of a low energy tail, whereas there is no difference in the high energy tails. For a given live time, the unipolar or bipolar modes are almost equivalent.

The system was also checked for differential linearity in the various modes by using a ramp generator as the voltage reference for the test pulser. The 1 in. diam hydrogen counter at 4400 V was used.

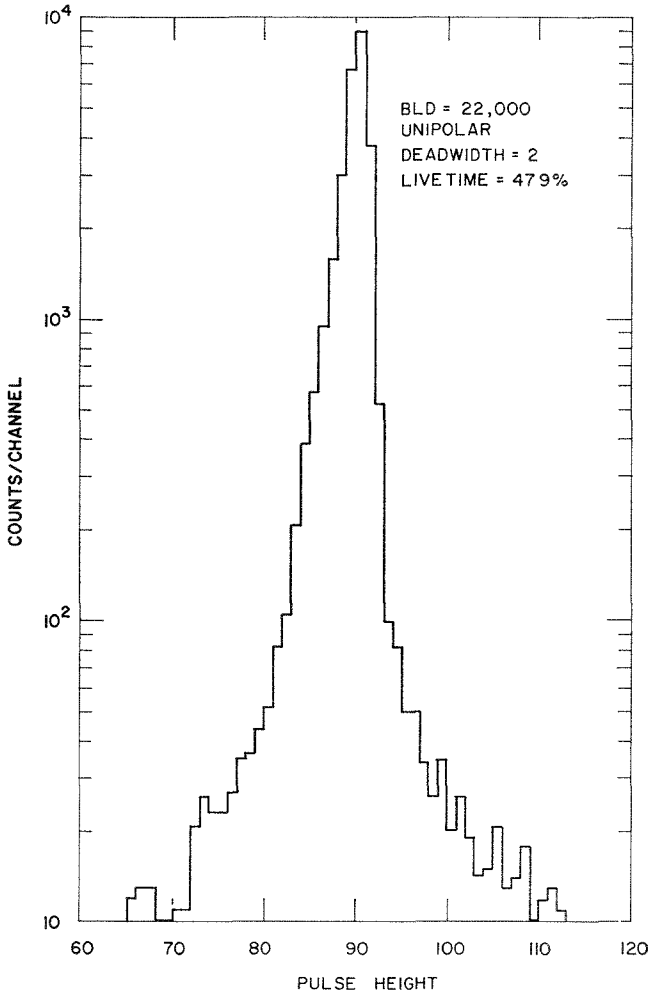

FIG. III-18-9. Pulser Pulse-Height Spectrum Using Unipolar Pulse Shaping and a Preset Dead Width of 2 in the Presence of 22,000 counts/sec from a Hydrogen-Filled Counter. *ANL Neg. No. 116-313.*

GAMMA SPECTRUM TEST OF SYSTEM

Tests were made by looking at the recoil electrons from the wall of the counter when a cesium gamma source was placed near the counter. Various voltage and count rate combinations were investigated. Instead of using a two-parameter analysis, one-parameter was used. The interest was in the recoil-electron distribution and there were no neutrons present. Such tests permit the determination of the quality of overlap of adjacent voltage settings without the uncertainty of background subtraction that is present in a typical proton-recoil measurement, where gamma-ray induced background will always be present. These tests offer some advantage over pulser testing because one is looking at legitimate counter pulses with their variety of profiles. However, these tests are dependent on relative calibration data for the various voltages. Good overlap was realized for the various voltages in the tests, indicating there were probably no systematic errors being overlooked.

It may appear that undue emphasis has been placed in this report in detailing the types and quality of the tests that have been performed. Nevertheless, the tests proved essential in determining the quality of the electronic system. About two years ago a solid-state, voltage sensitive preamplifier passed all the static tests described above, as well as the dynamic tests with the test pulser. However, all data taken with this preamplifier showed differences of a few percent in overlap from voltage to voltage. It was only after making careful tests with the gamma spectrum method that the over-

lap difficulty could be attributed to a small differential non-linearity for proportional counter pulse profiles. The preamplifier was subsequently replaced with the one described above.

References

1. E. F. Bennett, *Proportional Counter Proton-Recoil Spectrometer with Gamma Discrimination*, Rev. Sci. Instr. **33**, 1153 (1962).
2. E. F. Bennett, *Fast Neutron Spectroscopy by Proton-Recoil Proportional Counting*, Nucl. Sci. Eng. **27**, 16 (1967).
3. E. F. Bennett, *Neutron Spectrum Measurement in a Fast Critical Assembly*, Nucl. Sci. Eng. **27**, 28 (1967).
4. J. M. Larson, *A Wide Band Charge Sensitive Preamplifier for Proton-Recoil Proportional Counting*, ANL-7517 (1969).
5. J. M. Larson and J. E. Powell, *Spectrum Distortion from Amplifier Overloads in Proton-Recoil Proportional Counting*, Nucl. Instr. Methods **71**, 157 (1969).
6. J. M. Larson and J. E. Powell, *Electronic System Developments for Proton-Recoil Spectra Measurements in Plutonium Critical Facilities*, Reactor Physics Division Annual Report, July 1, 1968 to June 30, 1969, ANL-7610 pp. 410-414.
7. D. H. Wilkinson, *Ionization Chambers and Counters*, (Cambridge University Press, Cambridge, 1950) p. 91.
8. M. G. Strauss, I. S. Sherman, R. Brenner, S. J. Rudnick, R. N. Larsen and H. M. Mann, *High Resolution Ge (Li) Spectrometer for High Input Rates*, Rev. Sci. Instr. **38**, 725 (1967).
9. H. H. Bolotin, M. G. Strauss and D. A. McClure, *Simple Technique for Precise Determinations of Counting Losses in Nuclear Pulse Processing Systems*, Nucl. Instr. Methods **83**, 1 (1970).
10. T. J. Yule and E. F. Bennett, *Use of a Small Computer for Proton-Recoil Proportional Counting*, Reactor Physics Division Annual Report, July 1, 1967 to June 30, 1968, ANL-7410, pp. 358–360.
11. C. E. Cohn, E. F. Bennett and T. J. Yule, *Hardware and Software for Nuclear Spectroscopy on the Varian Data 622/i Computer*, ANL-7704 (1970).
12. E. F. Bennett and T. J. Yule, *Fast Neutron Spectra in Uranium Metal*, Reactor Physics Division Annual Report, July 1, 1968 to June 30, 1969, ANL-7610, pp. 215–216.

III-19. Comparison of Neutron Spectra from Proton-Recoil Counters Measured with the Idaho and Illinois Configurations

T. J. Yule and G. G. Simons

During the last few years a number of neutron spectrum measurements have been made using proton-recoil proportional counters at Argonne's Idaho and Illinois sites. During this time, some differences have arisen in the experimental configurations and analysis of the data. A considerable effort has taken place at Idaho in improving the count rate capability of the electronics. While the electronics have been continually improved at Illinois, the major effort has been in developing the analysis. It was decided that it would be useful if members from both sites would measure the same spectrum using their existing detector assemblies and pulse shaping electronics. The measurement would enable the two groups to work together at one site and thus insure a consistent approach to measurement techniques and analysis.

Description of the Apparatus

Counters manufactured by Reactor Controls, Inc. were used. Table III-19-I contains the physical dimensions and gas fillings for the counters. The two hydrogen-filled counters and the Illinois methane-filled counter were filled at Illinois. The ratios of sensitive volumes were determined by introducing a known amount of A-37 into the counters and determining the relative count rates. The counters were filled to pressures at which the resolution started to worsen appreciably, i.e., about 10% FWHM. Pressure tests had shown that the small amount of methane, about 1% in the hydrogen-filled counter, was adequate for quenching. The Idaho methane-filled counter was filled by Reactor Controls, Inc. There is some question about

TABLE III-19-I. Physical Dimensions and Gas Fillings for Proportional Counter Chambers

Counter	Inside Diameter, in.	Sensitive Length, in.	Anode Diameter, in.	Relative Volume	Gas Filling, lb/in.² at 0°C		
					Methane	Hydrogen	Nitrogen
Methane—Idaho	0.593	1.25	0.0007	4.33	110.0	—	4.60
Methane—Illinois	0.593	1.25	0.0007	4.19	113.0	—	1.09
Hydrogen—Idaho	0.343	0.75	0.0007	1.00	1.34	135.0	1.38
Hydrogen—Illinois	0.343	0.75	0.0007	1.00	1.34	135.0	1.38

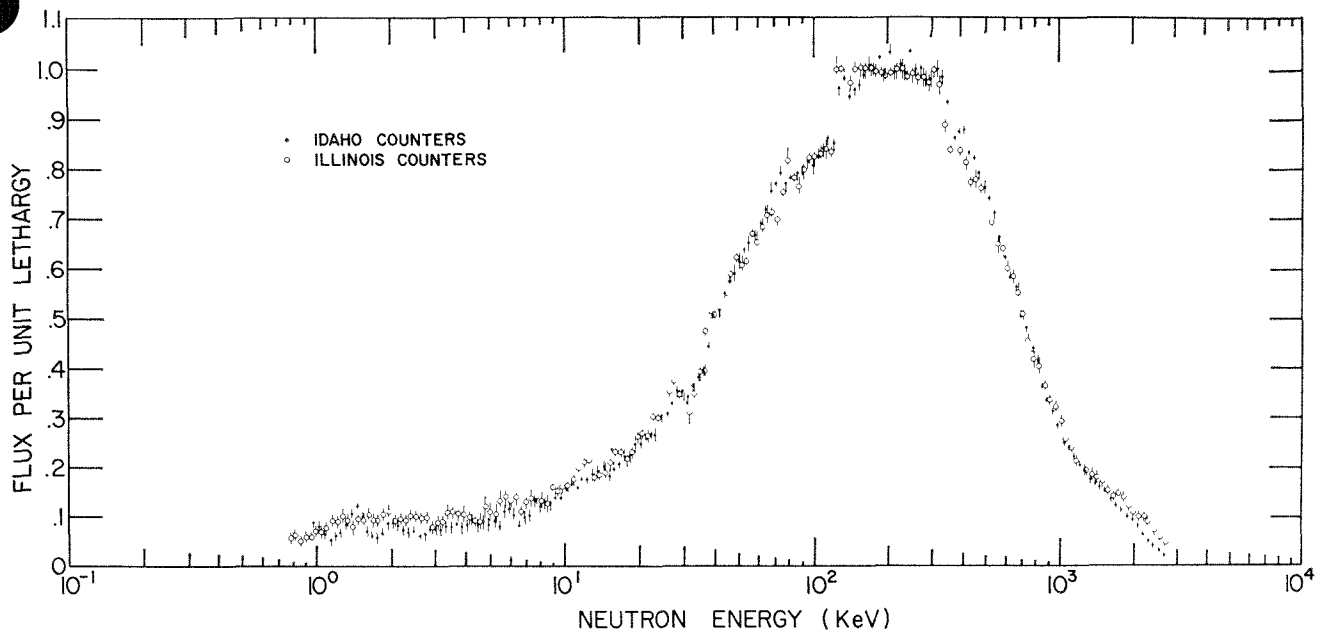

FIG. III-19-1. Comparison of Spectra Measured with Different Idaho and Illinois Detectors and Pulse Shaping Electronics. *ANL-ID-103-A11495.*

the actual filling and the numbers in the table for this counter are tentative.

The pulse shaping compnents for the Idaho and Illinois configurations are described in Papers III-17 and III-18.

DESCRIPTION OF THE MEASUREMENT

The neutron spectrum chosen for the comparison was that found in a large block of uranium metal available at the Argonne Thermal Source Reactor. During the measurements, the count rates were moderate—i.e., less than 10,000 counts/sec above a discriminator set at twice the noise level. Count rate tests had been previously conducted on both systems and this rate was known not to introduce significant distortions.

The methane-filled counter was used to measure recoil protons with energies above a nominal 100 keV. Three voltage runs were required. The two lowest voltage runs were made without gamma ray discrimination.

The hydrogen-filled counter covered energies below a nominal 100 keV. For all five voltages with the hydrogen-filled counter, gamma ray discrimination was used. It is possible to extend the measurements with the hydrogen-filled counter to higher energies, but because of uncertainty in the energy calibration once the track lengths become large, interpretation of the data is difficult.

COMPARISON OF THE TWO MEASUREMENTS

Figure III-19-1 presents the derived neutron spectra. The proton-recoil spectra were corrected for field effects and W, but not for carbon recoils or finite range effects. The upturn in the neutron spectra at the end of the methane region, i.e., at about 100 keV, and structure seen around 1.5 keV in the Idaho data are not real but were traced to errors induced by improper gamma ray background subtraction and not to different fast neutron responses. This particular measurement emphasizes the necessity for care in making background subtractions.

III-20. A Precision dc Baseline Restorer for Proton Recoil Proportional Counting

J. M. Larson

Introduction

This note describes a precision dc restorer that was designed principally for use with the proton recoil spectrometer described in Paper III-17. This spectrometer uses unipolar pulse shaping and, as a consequence, dc restoring is necessary to prevent spectral distortion generated by baseline shifts during overloads and at high counting rates.

A baseline restorer used in this application must have: (1) fast baseline recovery so that high counting rates may be handled without baseline shift, (2) dc baseline stability so that long-term baseline shifts due to temperature or power supply variations remain negligible, and (3) immunity to large amplitude overloads that might otherwise cause the restorer itself to generate baseline deviations.

The restorer described herein achieves fast baseline recovery through the use of an active restoring circuit. Direct current baseline stability with temperature variation is obtained by use of differential pairs and drift compensation using field effect transistors. Overload capability is provided by using a direct coupled design that eliminates the need for capacitor by-passing across bias networks.

Circuit Description

The baseline restorer is shown schematically in Fig. III-20-1 and is comprised of an active restoring circuit (transistors Q_1 through Q_8), and an output driving amplifier (transistors Q_9 through Q_{19}). The restoring circuit is based on the Robinson Circuit[1] in the more elaborate active restorer configuration, similar to that described by Williams.[2]

The simplified Robinson Circuit is shown in Fig. III-20-2, and its output response to a square input pulse is shown in Fig. III-20-3. In this circuit, the current sink draws a current $I_2 = \frac{1}{2} I_1$, and with no input signal the diode currents are of equal magnitude. The individual voltage drops across the diodes are then also equal and cancel so that the output of the circuit is normally maintained very near to zero volts.

When a positive input pulse occurs, diode CR-1 cuts off and CR-2 conducts with a current $I_3 = I_1$. With CR-1 cut off, capacitor C is discharged by the current

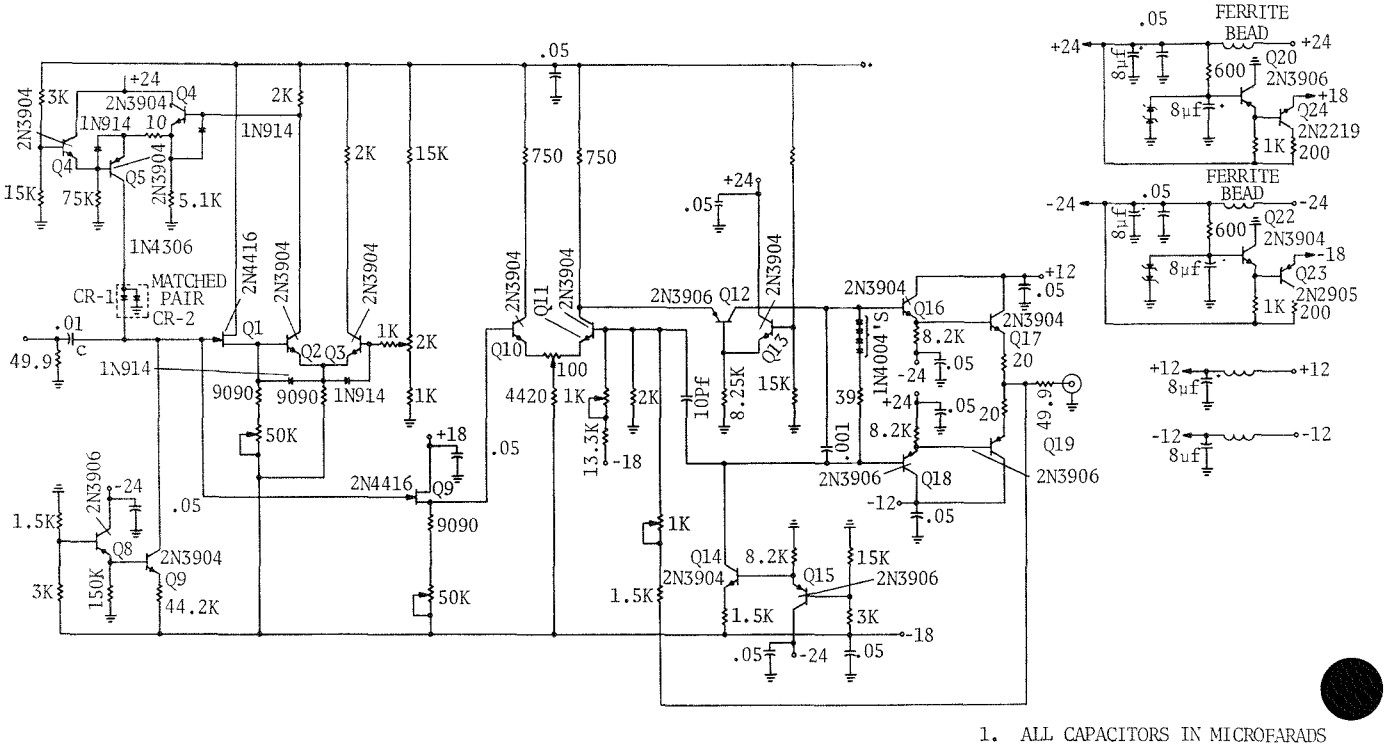

Fig. III-20-1. Baseline Restorer Schematic. *ANL-ID-103-A11490 Rev. 1.*

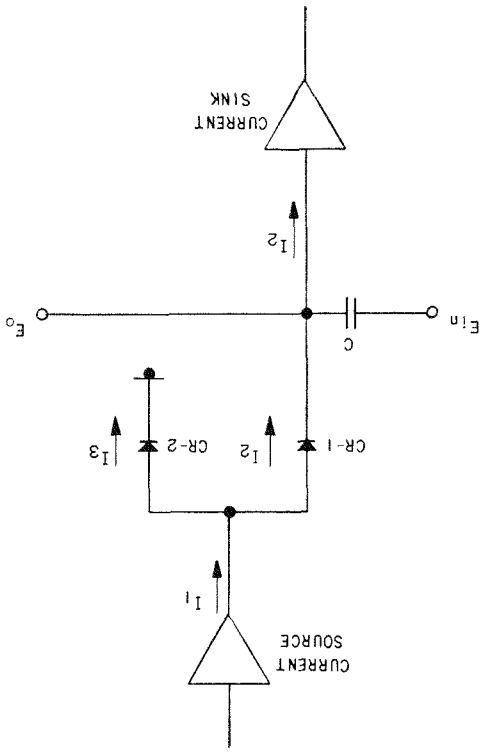

FIG. III.20-2. Basic Robinson Restorer. *ANL-ID-103-A11488.*

I_2, drawn by the current sink, and consequently the output voltage droops by an amount $\Delta V = I_2 \Delta t/C$.

On the trailing transition of the input, the output of the circuit then undershoots by an amount ΔV causing diode CR-1 to conduct, thus cutting off CR-2. Capacitor C is then charged by the current $(I_1 - I_2) = I_1/2 = I_2$, thus restoring the output to the baseline in a time $\Delta t = \Delta VC/I_2$ after the trailing edge of the input pulse.

In actual practice, the time Δt required to restore the output of the circuit to the baseline is generally somewhat longer than indicated by the simplified expressions given above. This effect is due largely to the variation of the dynamic resistance of the diodes as a function of their forward current.

The active restoring circuit described in this paper includes the Robinson Circuit, described above, in an amplifier feedback loop to idealize the diode characteristics and to force large restoring currents to flow whenever the baseline drops below zero volts, thus forcing rapid and precision baseline recovery. This effect is illustrated by the simplified circuit and waveforms of Figs. III-20-4 and III-20-5.

In this circuit I_1 is set equal to $2I_2$ for the condition no input signal and with the output $E_0 = 0$ V. When a positive pulse occurs, CR-1 cuts off, CR-2 conducts, and C is discharged in the same manner as with the basic Robinson circuit described earlier; however, the circuit differs in that when the baseline goes negative and CR-1 conducts, the restoring current I_1 is increased to a value of $I_1 = E_0 A$, where A is the open loop gain of the feedback network. If A is large, I_1 also becomes large when the baseline is negative with the result that baseline recovery can be made extremely rapid. In this particular design, I_1 may take on values as high as 50 mA, yielding typical baseline recovery times of approximately 1 μsec for a 1 V undershoot.

The output voltage from the baseline restorer drives a direct coupled output driving amplifier that provides isolation between the output of the restorer and the external load. This amplifier has an open loop gain in

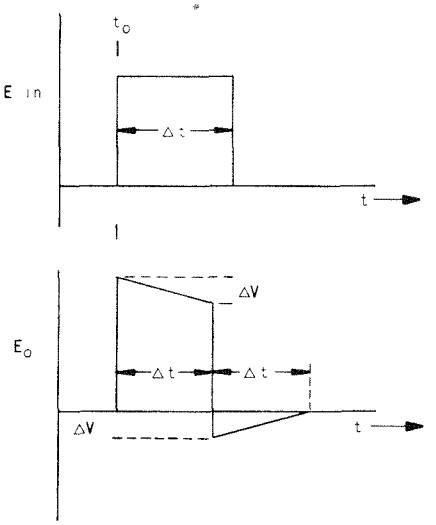

FIG. III-20-3. Pulse Waveforms Using Robinson Restorer. *ANL-ID-103-A11487.*

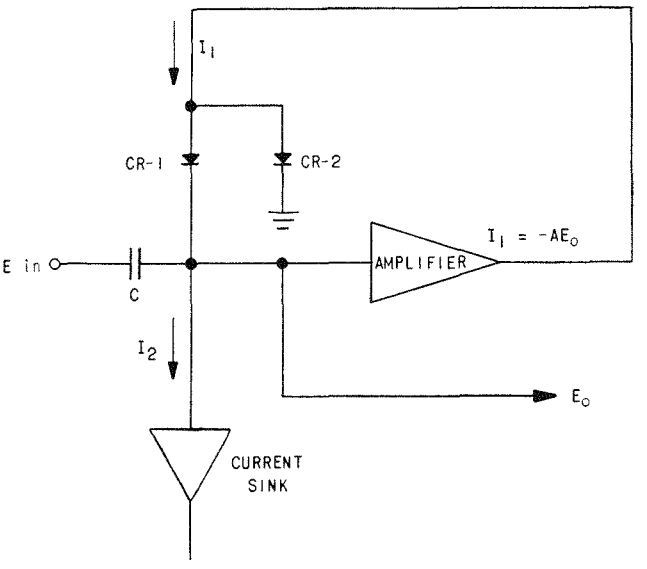

FIG. III-20-4. Active Baseline Restorer. *ANL-ID-103-A114888.*

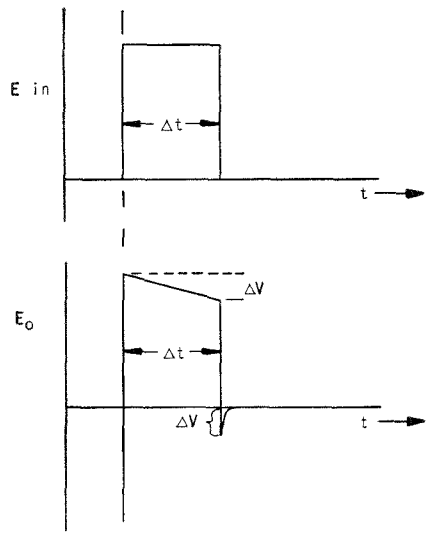

FIG. III-20-5. Pulse Waveforms Using Active Restorer. *ANL-ID-103-A11489.*

excess of 5,000 and a closed loop gain of 2, resulting in excellent linearity and low output impedance.

DRIFT COMPENSATION

Differential transistor pairs are used in the appropriate gain stages of both the restorer and output driving amplifier; however, temperature compensation is achieved primarily by adjusting the temperature drift of the input field effect transistors Q_1 and Q_9. The drift of these transistors is a function of their bias currents, and their drift can be adjusted to compensate for other drifts within the remainder of the circuit.

Initially the bias current of Q_9 is adjusted, with its gate grounded, until the temperature drift of the output driving amplifier is minimized. The gate of Q_9 is then disconnected from ground and the bias current of Q_1 is adjusted until the overall temperature drift of the unit is minimized.

This technique eliminates the necessity of using matched transistor differential pairs and still achieves excellent temperature stability. The baseline of these units typically drifts no more than 2½ mV for a temperature variation from 40 to 130°F.

The restoring circuit and the output driving amplifier are isolated from the ±24 V NIM levels by the internal regulators comprised of Q_{20} through Q_{24}. These regulators essentially remove any ac ripple existing on the supply levels and also maintain a constant 18 V output, thus isolating the internal restorer circuits from any dc variations that might occur on the ±24 V levels due to external power supply loading.

OVERLOAD CAPABILITY

All bias voltages in the circuit are supplied from emitter followers having low output impedances so that capacitor bypassing of the bias networks is eliminated. This arrangement prevents bias network bypass capacitors from charging during overloads, thus preventing unwanted time constants that could degrade or otherwise extend baseline recovery time after the overloading signal has passed.

REFERENCES

1. R. L. Chase and L. R. Poulo, *A High Precision D.C. Restorer,* IEEE Trans. on Nuclear Science, NS-**14,** No. 1, 83 (1967).
2. C. W. Williams, *Reducing Pulse Height Spectral Distortion by Means of DC Restoration and Pile-Up Rejection,* IEEE Trans. on Nuclear Science, NS-**15,** No. 1, 297 (1968).

III-21. Spectrum Analysis for a Silicon Fission-Fragment Detector

E. M. BOHN and A. B. LONG

INTRODUCTION

A thin silicon solid state detector is currently being tested in the ZPR-6 and -9 critical assemblies for the measurement of fission rates.[1] The fission fragment pulse height spectrum obtained with this detector includes extraneous counts due to gamma background in the reactor and electronic noise. This extraneous noise must be separated from the spectrum in order to determine the absolute fission rate. A method based on kinetic energy spectrum analysis for silicon detectors[2] has been developed to aid in the determination of the absolute fission rate.

SPECTRUM ANALYSIS

A typical detector-fission source arrangement is shown in Fig. III-21-1. Fission fragments leaving the source foil and traveling to the detector lose energy in the source deposit, in the layer of air between the source and detector, and in the silicon dead layer of the detector. The measured fission fragment kinetic energy

istribution is distorted and displaced along the energy axis as a result of the energy losses suffered by fission fragments traversing a distribution of paths between source and detector.

The number of fission fragments recorded with kinetic energy T is given by

$$N(T) = \sum_j P_j \sum_i Y(T_{ij})[(1/\sqrt{2\pi\sigma_i^2}) \cdot \exp(-(T - T_{ij})^2/2\sigma_i^2)]. \quad (1)$$

In Eq. (1), P_j is the probability of a fission fragment traversing the source-detector separation along path j, T_{ij} is the most probable kinetic energy for fragment i traversing path j, $Y(T_{ij})$ is the yield of the most probable energy for fragment i traversing path j, and σ_i is the standard deviation of the kinetic energy distribution in fission for fragment i.

The fission fragment energy losses through each material along the source-detector path are computed with the empirical expression[3]

$$\Delta T_i = [2T_i Z M_i/Z_i]^{1/2} \cdot \Delta t_j/0.0685A, \quad (2)$$

where Z and A are the atomic number and mass of the energy absorbing material, T_i is the most probable post-neutron-emission kinetic energy for fragment i, M_i and Z_i are the mass and most probable atomic number of the ith fragment, and Δt is the thickness of the absorbing material. Referring to Fig. III-21-2, for fragment i traveling through material k along path j,

$$\Delta T_{ijk} = [2T_{ij(k-1)} Z M_i/Z_i]^{1/2} \cdot \Delta t_{jk}/0.0685A. \quad (3)$$

The most probable kinetic energy for fragment i traversing a path j from source to detector is then given by

$$T_{ij} = T_i - \sum_{k=1}^{3} \Delta T_{ijk}. \quad (4)$$

In order to compare the calculated spectrum with a measured spectrum, the kinetic energy distribution given by Eq. (1) is converted to a pulse height spectrum using the Schmitt transformation,[4]

$$X_n = (a + bM_i)T_{ij} + c + dM_i, \quad (5)$$

where X_n is the nth pulse height channel and a, b, c, and d are detector constants determined from the experimental pulse height distribution.

Fission Fragment Constants and Detector Parameters

The most probable post-neutron-emission kinetic ergy for each fission fragment from the fission of -235 was computed using the relation[5]

$$T_i = M_i T_i^*/(M_i + \bar{\nu}_i), \quad (6)$$

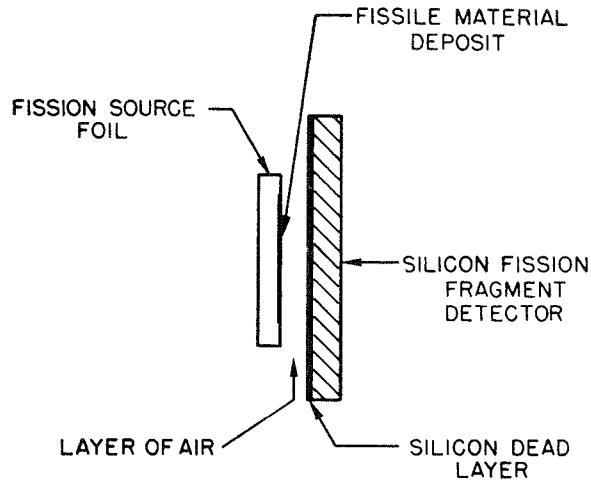

Fig. III-21-1. Detector-Fission Source Configuration. *ANL Neg. No. 116-540.*

where T_i^* is the most probable pre-neutron emission kinetic energy for fragment i[(5)] and $\bar{\nu}_i$ is the average number of prompt neutrons emitted by fragment i after fission.[6] The most probable atomic numbers, Z_i, for U-235 fission fragments were taken from Wahl.[7]

The values of σ_i which are used in Eq. (1) were determined by comparing a calculated distribution with the undistorted (no energy absorbers present) U-235 pulse height spectrum given by Schmitt et al.[9] It was found that values for σ_i of 5.4 for the light mass fragments and 4.4 for the heavy mass fragments reproduced the Schmitt spectrum very well.

Calculated Spectrum

A computer program, utilizing Eqs. (1–5), has been developed to calculate the fission fragment spectrum

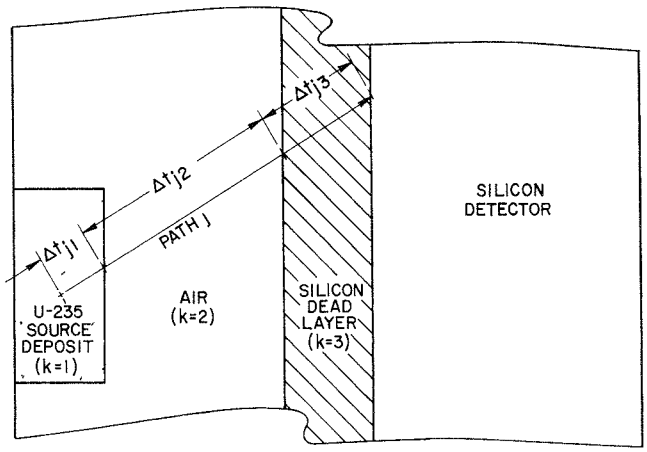

Fig. III-21-2. Detector-Fisson Source Configuration and the Components of Fission Fragment Path j Through the Source Deposit (Material $k = 1$), Through the Air Layer Between Source and Detector (Material $k = 2$), and Through the Silicon Dead Layer of the Detector (Material $k = 3$). *ANL Neg. No. 116-541.*

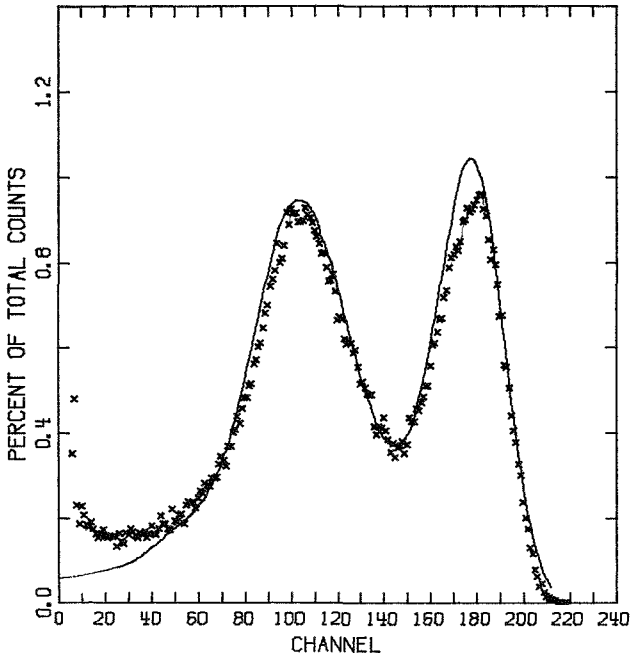

FIG. III-21-3. Observed (xxx) and Calculated (——) Fission Fragment Pulse Height Spectrum for 20 $\mu g/cm^2$ U-235 Source and a Silicon Solid State Detector. *ANL Neg. No. 116-542.*

obtained with a silicon detector and U-235 source foil. Fission fragments are assumed to be emitted isotropically from within the source foil. The source foil is assumed to be small (i.e., a point source) compared with the detector dimensions. The solid angle for detection is divided into a number of discrete solid angles $\Delta\theta_j$ and the probabilities P_j of Eq. (1) are computed as the ratios of these discrete angles to the total solid angle of emission.

The kinetic energy-pulse height distribution obtained with the thin silicon detector described in Ref. 1 and a 20 $\mu g/cm^2$ U-235 source in the thermal column of the Argonne Thermal Source Reactor is shown in Fig. III-21-3. The calculated spectrum, which includes energy losses in the source, the air layer (0.01 in. thick) between the detector and source, a silicon dead layer assumed to be 1.2 μ thick, and a path length distribution including 20 discrete paths, is also shown in Fig. III-21-3.

The measured spectrum contains extraneous counts in the low channels due to electronic noise and gamma background radiation. The total percent counts in the experimental spectrum which are due to fission fragments is determined by comparing the fraction of each spectrum (experimental and computed spectrum) under the high energy, light fragment peak. This portion of the experimental spectrum is uninfluenced by extraneous counts. By summing and comparing the total percent counts under the light fragment peaks (above channel 145) in Fig. III-21-3, it is found that 93.7 % of the counts in the experimental spectrum are due to fissions. Also note in Fig. III-21-3 that the calculated spectrum does not go to zero at channel 0. Some of the fragments leaving the source are completely stopped before reaching the detector. The detector efficiency (fraction of fragments leaving the source that are detected) is computed to be 90.8 %.

SUMMARY

The method presented here for fission fragment spectrum analysis for solid state detectors appears to work well. The pulse height spectrum shape is predicted well, indicating that the fission fragment energy losses through successive layers of absorbing materials (source, air, silicon) are described adequately.

It was found that the thickness of the silicon dead layer of the detector greatly influenced the final spectrum shape. If this method is employed as an aid in the determination of absolute fission rates measured with silicon detectors, a precise knowledge of the silicon dead layer thickness is required.

REFERENCES

1. A. B. Long, E. M. Bohn and W. C. Kaiser, *Non-Perturbing Fission Counter for Use in Plate-Type Critical Assemblies*, Trans. Am. Nucl. Soc. (to be published).
2. L. Bridwell and S. Bucy, *Kinetic Energy Spectra of Foil-Transmitted Fission Fragments of ^{252}Cf*, Nucl. Sci. Eng. **37**, 224–227 (1969).
3. L. B. Bridwell and C. D. Moak, *Stopping Powers and Differential Ranges for ^{79}Br and ^{127}I in UF_4*, Phys. Rev. **156(2)**, 242–243 (1967).
4. H. W. Schmitt, W. E. Kiker and C. W. Williams, *Precision Measurement of Correlated Energies and Velocities of Cf-252 Fission Fragments*, Phys. Rev. **137**, B837–B484 (1965).
5. H. W. Schmitt, J. H. Neiler and F. J. Walter, *Fragment Energy Correlation Measurements for ^{252}Cf Spontaneous Fission and U-235 Thermal-Neutron Fission*, Phys. Rev. **141**, 1146–1160 (1966).
6. J. C. D. Milton and J. S. Fraser, *The Energies, Angular Distributions, and Yields of Prompt Neutrons from Individual Fragments in the Thermal Neutron Fission of U-233 and U-235*, AECL-2163 (March 1965).
7. A. C. Wahl, R. L. Ferguson, D. R. Nethaway, D. E. Troutner and K. Wolfsberg, *Nuclear-Charge Distribution in Low-Energy Fission*, Phys. Rev. **126**, 1112–1127 (1962).
8. H. W. Schmitt and F. Pleasonton, *Evaluation of Semiconductor Detectors for Fission Fragment Energy Measurements*, Nucl. Instr. Methods **40**, 204–208 (1966).

III-22. He-3 Gas Scintillator for Time-of-Flight Neutron Measurements

RAYMOND GOLD and DALE M. SMITH

INTRODUCTION

It is not possible, at present, to measure the entire continuous neutron energy distribution in fast reactors (or fast critical assemblies) with a single detector or method. Present methods of continuous fast neutron spectroscopy possess fundamental energy limitations which lead, in turn, to finite energy regions of applicability. Pulsed critical assembly Time-of-Flight (TOF) measurements afford the possibility of examining the low energy portion of fast reactor spectra—an energy region virtually inaccessible to other methods.

Accurate TOF experiments in this energy region require that the energy dependent efficiency of the detection system be known or determined experimentally. The quality of spectral data obtained in TOF measurements depends crucially upon the accuracy with which this efficiency is known. Additional characteristics of a TOF detection system which bear upon the quality of the spectral measurements are fast response, high neutron sensitivity, and low gamma ray sensitivity.

A detection system using the He-3(n,p)T reaction would satisfy many of these requirements. The cross section of this reaction is 1/v below about 200 keV. Consequently, the energy dependence of such a detection system would be well-known and elaborate calibration experiments would not be required. Furthermore, the He-3(n,p)T reaction becomes dominant (with respect to all other possible neutron reactions) below 10 keV. Hence, a detection system using this reaction would be well suited for measuring the low energy end of fast reactor spectra.

He-3 proportional counters are a conventional and widely used neutron detector. Although these counters are usually of small active volume, they may be stacked to cover a large area. Fast neutron detection efficiency is limited by the maximum He-3 pressure that can be used. In these counters, the typical upper pressure limit is a few hundred psi. However, proportional counters possess slow response time. From the viewpoint of TOF experiments, this characteristic is a serious limitation, since the energy resolution obtained with these detectors would be poor.

An He-3 gas scintillator detection system would possess the advantages described above and at the same time provide good energy resolution. Gas scintillators are very fast. A rise time of a few nanoseconds is not

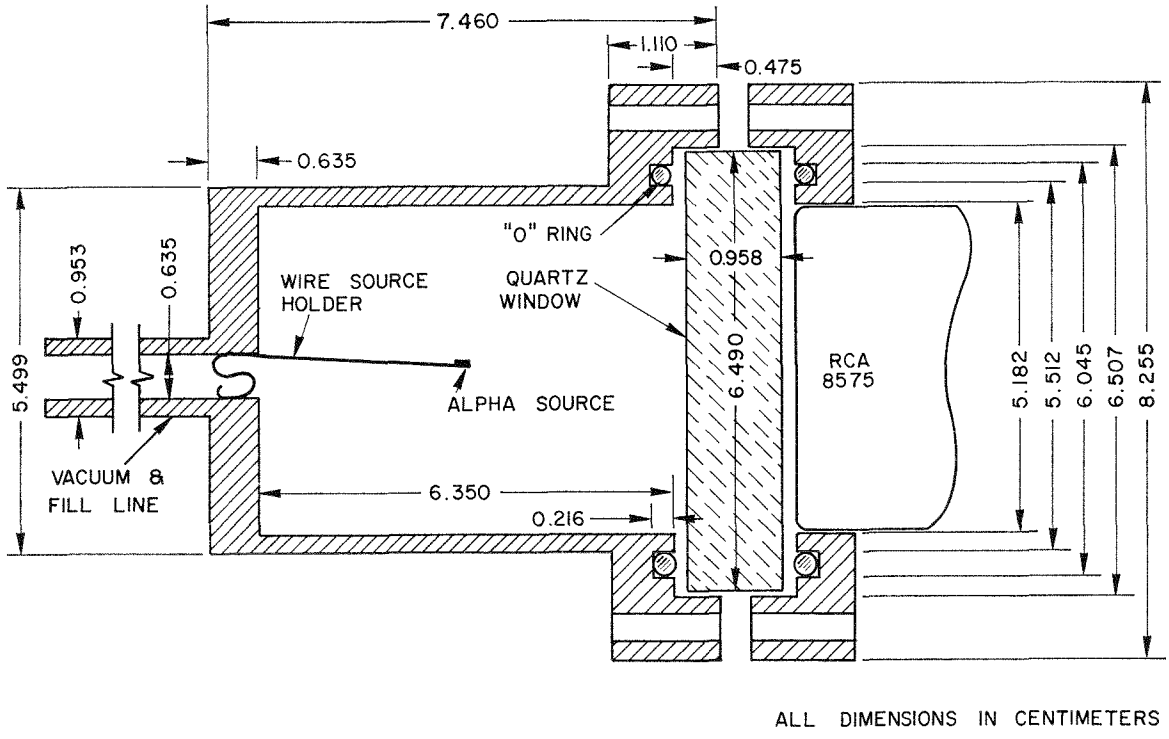

FIG. III-22-1. Gas Scintillator Chamber, Quartz Exit Window and Internal Alpha Particle Source. *ANL Neg. No. 116-468.*

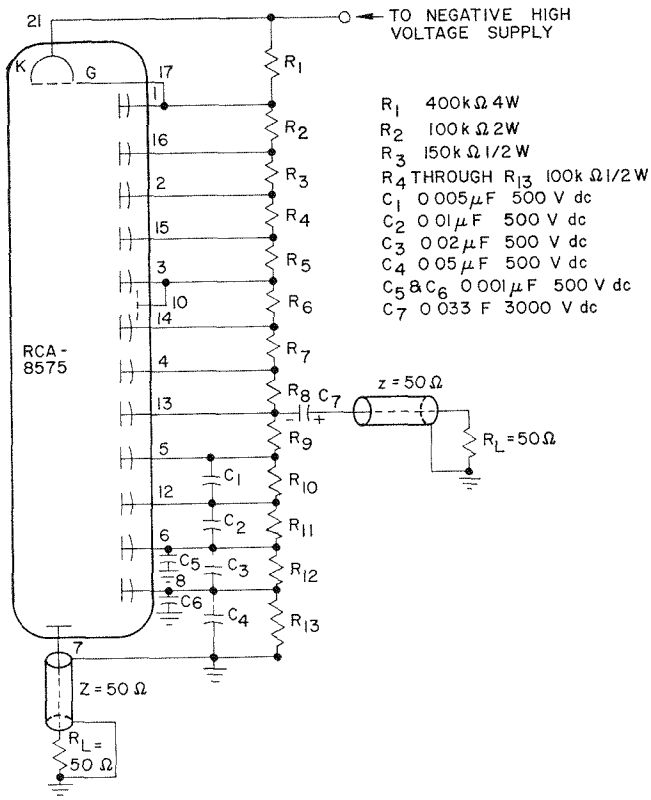

FIG. III-22-2. High Voltage Wiring Diagram for the RCA-8575 Photomultiplier. *ANL Neg. No. 116-465.*

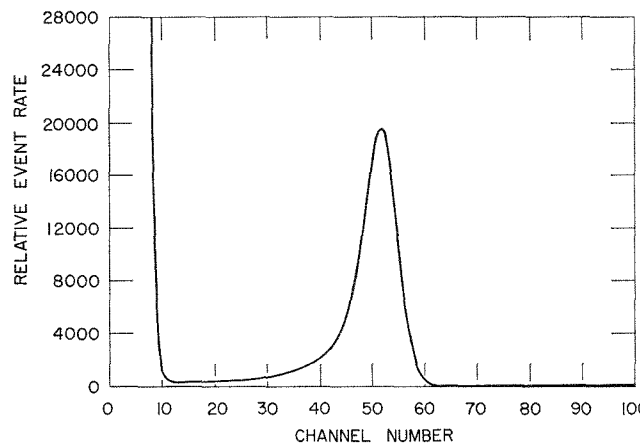

FIG. III-22-3. Gas Scintillator Response to the Cm-244 Alpha Source with a Xenon Filling of Approximately 55 psi. *ANL Neg. No 116 458.*

uncommon for these detectors. Moreover, helium gas scintillators can operate at very high pressures. In fact, it has already been demonstrated that such detectors (with small admixtures of xenon to improve scintillation light output) function properly at pressures above 1000 psi.[1]

GAS SCINTILLATOR DESIGN AND CONSTRUCTION

The general design features of the He-3 gas scintillator can be found in Fig. III-22-1. The gas scintillator chamber body was machined of type 304 stainless steel. The inside surface of the chamber was honed to a smooth mirror-like finish. After fabrication, the chamber was thoroughly cleansed and then baked out at approximately 250°C under vacuum for about 15 hours.

A 0.95 cm thick quartz glass disc serves as the exit window for the gas scintillator. Hydrostatic pressure tests revealed that the counter (with quartz window) was leak tight up to 1100 psi. The quartz exit window is seated to the scintillator body with a Teflon O-ring. Teflon is used to reduce hydrocarbon outgassing that would otherwise severely quench gas scintillation.

An opaque coating of MgO (roughly 1 mm thick) was applied to the interior surface of the chamber to serve as a diffuse white reflector. After the MgO coating was applied, the counter was outgassed by baking at approximately 350°C under vacuum for two weeks. After bakeout, an organic wavelength shifter, diphenylstilbene (DPS), was vacuum deposited over the MgO reflector. A DPS thickness of approximately 300 $\mu g/cm^2$ was deposited.[1]

To view the gas scintillations, an RCA 8575 photomultiplier is directly coupled to the quartz exit window. Negative high voltage is used to obtain a directly coupled fast anode output pulse. The high voltage-dynode schematic is displayed in Fig. III-22-2. A capacity-coupled output pulse is also available from the eighth dynode.

To evaluate detector performance, provision was made for the installation of an internal alpha source. The internal alpha source was located near the cham-

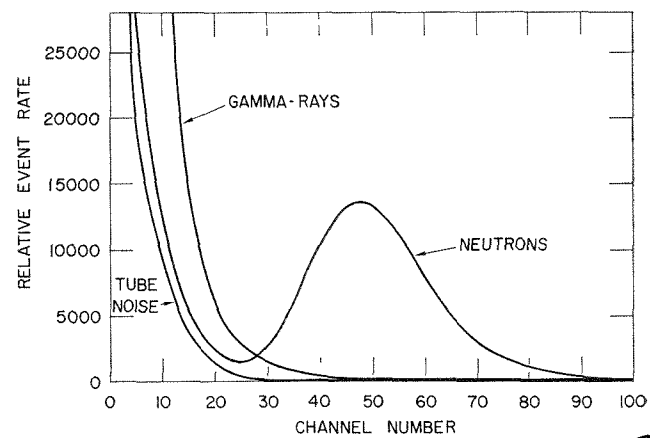

FIG. III-22-4. Gas Scintillator Response to Neutrons a Gamma Rays with a Filling of Approximately 24 psi Xe and 3 psi He-3. *ANL Neg. No. 116-444.*

er center, as shown in Fig. III-22-1, in order to avoid complications that would otherwise arise from wall effects. This internal source was removed for subsequent evaluation of the neutron response of the He-3-gas scintillator.

Preliminary Results

Long term stability of the gas scintillator was tested with an internal Cm-244 alpha source (5.80 MeV) and a xenon gas filling of approximately 55 psi. The scintillator response was followed for a time period of roughly 6 months. Over this interval, the observed alpha particle resolution of the gas scintillator deteriorated quite slowly from an initial value close to 10% (FWHM) to a final value of about 15%. The dynode output response observed with the internal Cm-244 at the end of the stability test period is displayed in Fig. III-22-3.

Preliminary investigations of the neutron response were carried out with a gas mixture of approximately 24 psi xenon and 32 psi He-3. The response of the gas scintillator to neutrons and gamma-rays is compared in Fig. III-22-4. Neutrons were obtained from a moderated americium-beryllium source and gamma-rays from a strong Co-60 source. Note that the gamma response lies in a pulse-height range slightly higher than tube noise (dark current). Consequently, when gamma-ray descrimination is important, better pulse height separation between gammas and neutrons may be possible by selecting low noise photomultipliers. (The particular RCA-8575 photomultiplier chosen for these tests was, at best, an average tube from the viewpoint of dark current.) In any event, Fig. III-22-4 reveals the basic insensitivity of the gas scintillator to gamma radiation, since a gamma-to-neutron flux ratio of roughly 150 was used for these measurements.

A sampling scope was used to analyze the fast anode output directly. The pulse shape response due to neutrons is shown in Fig. III-22-5. It can be seen that the detector rise time is about 3 nsec. Further investigation

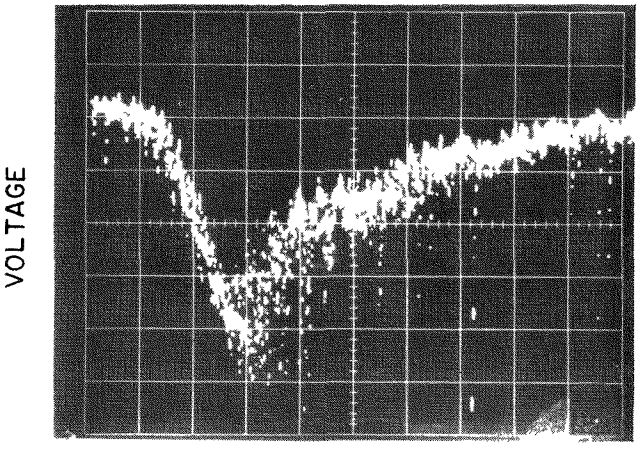

Fig. III-22-5. Sampling Scope Photograph of the Neutron Response of the He-3 Gas Scintillator (Direct Anode Output). *ANL Neg. No. 116-471.*

revealed that noise (dark current) pulses possess virtually the same shape. Consequently, the response time characteristics of the present detector are not limited by the gas scintillator, but can be attributed to the RCA-8575 photomultiplier.

It can be estimated from Fig. III-22-4 that a pulse-height resolution of approximately 50% (FWHM) was obtained in these preliminary neutron measurements at an energy of 780 keV, corresponding to the positive Q of the He-3(n,p)T reaction. Although some improvement in resolution is desirable and may be anticipated, the present detector provides adequate discrimination from the viewpoint of TOF measurements. Satisfactory gamma-ray discrimination has already been demonstrated in Fig. III-22-4. Discrimination against He-3 elastic knock-on events can also be adequately achieved in TOF measurements with the present gas scintillator resolution.

Reference

1. B. D. Walker and R. Gold, *High Pressure Helium-Xenon Gas Scintillator*, UCRL-6878 (1962).

III-23. Statistical Fluctuations and the False Alarm Frequency of Safety Channels

K. G. A. Porges

Continuously operating channels which deliver a warning function or initiate some remedial action (up to and including plant shutdown) whenever their readout exceeds a certain limit have been widely used in various industrial processing plants. In power reactor safety applications, such channels must meet particularly stringent requirements while sensors are at the same time exposed to a hostile and debilitating envi-

ronment. The current development of large LMFBR plants[1] operating at higher temperature and radiation levels, as well as at a considerably higher power density, than conventional water and gas-cooled cores has led to even more difficult requirements—not only as regards radiation and temperature hardness of sensors, but particularly with respect to the required speed or response. In very general terms, the output—usually an analog signal such as a voltage or current—lags behind the direct output at the sensor head due to the finite response speed of the various electronic elements of the channel, beginning with the transmission line. While certain possibilities promising considerable improvements in this response lag have been proposed,[2, 3] existing and well-tested methods of sensing flux level, temperature, flow, etc. all develop an output signal which exhibits a characteristic "rise-time" in response to a step function in the measured parameter input. Earlier warning thus necessarily implies a lower warning or alarm level, which in turn emphasizes the frequency of false alarms due to various fluctuations in the input, translated by the channel into readout fluctuations.

In some types of sensing channels, fluctuations of a special nature appear, e.g. flow measurements of very high sensitivity and wideband frequency response may pick up pump effects as well as "partition noise". Aside from these special effects, however, sensor channels are always subject to certain statistical fluctuations, generated in part by the sensor, and in part by subsequent electronic components. In this paper, we shall specifically emphasize channels employing nuclear detectors which deliver discrete current pulses in response to the absorption of individual neutrons or gamma rays; these current pulses are thereupon processed into an analog voltage or current by direct integration or by using a count rate meter at the output of a wideband amplifier. Either of these apparently dissimilar methods amounts to an electrical filter which may have several time constants or corner frequencies. The fluctuations appearing at the output of this kind of channel in the presence of a steady input rate, i.e. at constant power level, are generated by the quasi-random time distribution of discrete input events, but depend also on the filter constants; a small correlated component in the input time distribution[4] has only negligible effect. These statistical fluctuations would therefore be expected to play an important role in determining such operating parameters of a given sensor channel as the smallest temporary excursions in the local flux which can be detected, or the speed of reaction to a large excursion.

The basic assumption made here is that the level must be set in conformity with a certain maximum false alarm frequency, specified in the instrumentation plan of a projected reactor plant. It should perhaps be stressed that this further implies assured continuous performance of the channel, in contrast to the dominant consideration of finite life on which false alarm frequency estimates of safety channels are usually based. To make such estimates valid, to be sure, the mean time between failures must be known; the further assumption is often made that failure of any one detection channel results in a conditional alarm, such that a false alarm actually occurs when a certain number, perhaps all, of several parallel channels have failed. In temperature sensing channels, where this approach has been traditional, sensors are usually made to read high if the thermocouple (or resistance thermometer) fails by adding a "burnout protection" feature (originally conceived to protect kilns and similar batch-processing equipment). If individual thermocouples (of which there may be a large number) are tested at certain intervals only, a false alarm frequency can be given by estimating the chance that all of a number of parallel sensors fail within the testing interval. However, continuous testing can be provided, for instance, by frequency separation of signal and test currents, hence false alarms due to total channel failure are not unavoidable. Similarly, the operability of nuclear surveillance channels for local flux detection, fuel failure sensing, etc. can be monitored continuously, at least in regard to the electronic components of the system. A remaining possible malfunction leading to a false trip, that is, a breakdown between the electrodes of the counter, can be dealt with by pulse shape discrimination methods, for pulse counting channels and by redundant channels in other applications—the likelihood of simultaneous breakdown in several counters being negligibly small.

These remarks allow the conclusion that statistical fluctuations indeed determine the false alarm frequency in safety channels based on nuclear detection. With that motivation, a study of such fluctuations has been undertaken. The original aim of providing a prescription for the optimum filtering and alarm level settings for a specific installation—the FERD (Fuel Element Rupture Detector) loop of EBR-II[5]—was broadened to a more general investigation when it became apparent that a reliable theoretical framework for false alarm frequency calculations had first to be developed. Preliminary results are reported in Paper III-24.

References

1. USAEF Report, *Liquid Metal Fast Breeder Program Pl 10, Safety*, WASH-1110 (August 1968).
2. T. M. Carpenter and W K. Lehto, *A Gaseous Cherenkov Power-Level Monitor*, Nucl. Appl. **3** (December 1967).
3. K. G. Porges, R. Gold and W. Corwin. *Reactor Power Mon-*

itor Based on Cherenkov Radiation Detection, Trans. IEEE NS-17 #7 (February 1970).
4. E. F. Bennett, *The Rice Formulation of Pile Noise*, Nucl. Sci. Eng. **8**, 53 (1960).
5. K. G. Porges, *Fuel-failure Detection in Sodium-cooled Reactors*, Proc. Conference on Safety, Fuels and Core Design of Large Fast Power Reactors, ANL-7120, October 11–14, 1965, p. 862.

III-24. Fluctuations of Count Rate Meter Signals

K. G. A. Porges and W. Corwin

The practical importance of statistical count rate meter fluctuations in reactor safety monitoring and similar surveillance tasks is discussed in Paper III-23. In this report, we shall summarize some preliminary theoretical and experimental investigations of a descriptive model. The model is ultimately intended to be used for making realistic estimates of the false trip frequency due to fluctuation, hence for optimization of design and adjustment of safety channel information processing equipment.

To provide a useful framework for these calculations, a viable analytic expression of the level distribution $W(V)$ is required. Considering the count rate meter as a device which transduces a randomly distributed input, consisting of discrete events, into an analog voltage V, one can describe the effect of this device in terms of its response $F(t)$ to a single input event. This response is the Fourier transform of the device frequency response $R(\omega)$ and can thus be classified as a filter. In analogy to Carson's theorem, which describes the moments of the filter output in response to a white spectrum, Campbell's theorem,[1] further generalized by Rice,[2] can be used to calculate the *cumulants* λ_k of the voltage level distribution $W(V)$ from the response $F(t)$ in the time domain. Thus equipped with a set of cumulants, one can, in principle, construct the distribution

$$W(V) = (2\pi)^{-1} \int dy \cdot \exp\left[\sum_k \{(iy)^k \lambda_k / k!\} - iyV\right]. \tag{1}$$

However, what is needed here is a practical formulation which can be readily used in further calculations of false alarm rates. For that purpose, it is expedient to provide a fit over a limited range by means of a Gaussian corrected by a polynomial series. This expression is suggested by the fact that any distribution [illegible]nds to approach a Gaussian under certain limiting [illegible]nditions, and within a certain range of parameters. At the same time, it is necessary to make sure that such a series representation converges over the region of actual interest by using a sufficient number of terms; as with all force fitting, divergence outside a certain range becomes more drastic as the fit within the range improves.

We introduce the dimensionless parameter

$$x = (V - \bar{V})/\sigma(\bar{V}), \tag{2}$$

where $\bar{V} \equiv$ first moment or mean of the distribution $W(V)$ and $\sigma^2(\bar{V}) \equiv$ second moment of both $W(V)$ and of the model Gaussian $G(x) = (2\pi)^{-1/2} e^{-x^2/2}$. The "correction" $B(x)$ in our model,

$$W(x) = G(x) + B(x), \tag{3}$$

is expected to be a small but negative fraction of $G(x)$ in the region of the Gaussian peak, $0 \leq x \leq 1$, but to amount to many times the Gaussian for large x, where the actual distribution exceeds the Gaussian. This behavior results from the fact that the higher-order cumulants of the distribution $W(x)$, as predicted by Campbell's general theorem, are necessarily finite whereas all cumulants of third and higher order of the Gaussian vanish, by definition. To be sure, Poisson, Bernoulli and other commonly encountered distributions also have non-zero higher order cumulants, but this can usually be ignored since for purposes of error estimation, only the second moment and the region near the peak are relevant. In the present context, it must be considered that practically tolerable false alarm rates must be exceedingly low, whence alarm level settings are necessarily far from the peak region. Thus, a simple Gaussian model, which is sometimes used in false alarm rate estimates, can easily underestimate the false trip rate by an order of magnitude, and even the more refined model considered here requires a large number of terms.

A series for $B(x)$ is readily found by expressing the dependence on x in an orthogonal polynomial series—specifically, in Hermite functions of the second kind,

$$B(x) = G(x) \sum_{k=1} C_k He_k(x). \tag{4}$$

The Hermite functions oscillate, He_k having k roots for even and an additional root at $x = 0$ for odd k. Thus, termination of the series with a certain order can, at

TABLE III-24-I. Edgeworth Series Terms
$W(x) = G(x)[1 + \sum_k E_k]$; $M_k = \lambda_k/k!\sigma^k$

k	E_k
0	0
1	0
2	0
3	H_3M_3
4	$H_4M_4 + H_6(M_3^2/2)$
5	$H_5M_5 + H_7M_3M_4 + H_9(M_3^3/3!)$
6	$H_6M_6 + H_8[(M_4^2/2) + M_3M_5] + H_{20}(M_3^2/2)M_4 + H_{12}(M_3^4/4!)$
7	$H_7M_7 + H_9[M_3M_6 + M_4M_5] + H_{11}[M_3^2/2)M_5 + (M_4^2/2)M_3] + H_{13}(M_3^3/3!)M_4 + H_{15}(M_3^5/5!)$
8	$H_8M_8 + H_{10}[M_3M_7 + M_4M_6 + (M_5^2/2)] + H_{12}[(M_3^2/2)M_6 + M_3M_4M_5 + (M_4^3/3!)] + H_{14}[(M_3/3!)M_5 + (M_3^2/2)(M_4^2/2) + H_{16}(M_3^4/4!)M_4 + H_{18}(M_3^6/6!)$

best, secure a fit over a range of x extending to the largest root of the term of highest order, and will drastically diverge beyond that range. The constants C_k are readily calculated, making use of the orthogonality of the polynomials, in terms of the moments μ_j of the distribution $W(x)$ (or *central* moments of the distribution $W(V)$):

$$C_j = \sum_{m=0}^{j/2} \frac{(-2)^m \Gamma(m + 1/2)\mu_{j-2m}}{\Gamma(j - 2m + 1)\Gamma(2m + 1)\Gamma(1/2)}. \quad (5)$$

The series thus obtained can be used directly in connection with central moments derived from cumulants calculated by Campbell's theorem. However, the terms of this series turn out to vary in size through the dependence of the cumulants on the input event rate n. As pointed out by Edgeworth,[3] a certain grouping of terms yields successive corrections which decline with increasing negative half-powers of n; this leads to the Edgeworth series representation

$$W(x) = G(x)\left[1 + \sum_{k=3} E_k(x)\right]. \quad (6)$$

A few Edgeworth terms are listed in Table III-24-I; additional terms are readily calculated but become increasingly complex. The higher Hermite polynomials required can be readily developed, for instance by a DESCOMP program using the RESCUE facility. Similarly, the relation between moments μ_j and cumulants λ_j of the voltage distribution $W(V)$ can be worked out to any desired order, using the equations

$$\phi(u) = \int W(V)e^{iuV}dV = 1 + \sum (iu)^j\mu_j/j! \quad (7)$$

and

$$\ln[\phi(u)] = \sum (iu)^k\lambda_k/k!. \quad (8)$$

The cumulants of the voltage distribution,

$$\lambda_k = n\int_0^\infty [F(t)]^k\,dt \quad (9)$$

by Campbell's theorem, must be divided by the kth power of $\sigma = \sqrt{\lambda_2}$ to obtain the cumulants of the distribution in the parameter x, which defines the parameter

$$M_k = \lambda_k/\sigma^k k!$$

used in Table III-24-I.

Equation (6), which completely describes the model distribution, evidently rests on the assumption that Eq. (9), i.e. Campbell's theorem, is valid for any input rate n. Derivations of this theorem, however, get into some difficulty for $N \approx 1$, and a fortiori for $N < 1$, where $N = nT$ and T is the basic time constant of the filter, further discussed below. Because the input rate in practical surveillance monitoring systems may well be quite low, while the system response time, related to T, may be required to correspond to some maximum safe delay of a shutdown or similar remedial action, an experimental test of the model described above was thought to be useful. For that test, a filter with one time constant, $F(t) = \exp(-t/T)$, was used. A count rate meter (CRM) with carefully selected components, strong feedback stabilization, and temperature drift compensating networks was constructed and used in conjunction with a highly stable source of random counts at controllable rates.[4] A series of distributions, using different time constants T, was obtained by sampling the CRM output and digitizing these voltage samples by means of a standard 1024 channel analyzer. To obtain the required statistical precision, each such distribution required many hours of running time. The

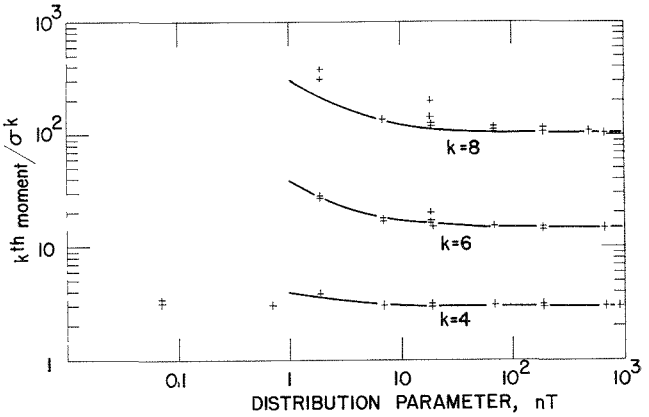

Fig. III-24-1. kth Moment of the Distribution in x (kth Moment of the Observed Voltage Level Distribution Divided by the kth Power of the Second Moment) versus $N = nT$ (n = Input Rate, T = Time Constant of the Filter) for Rand (Poisson Time Distributed) Input and a Single Time Consta CRM. Only Even Moments are Shown. Lines are Derived from Theory. *ANL Neg. No. 116-588.*

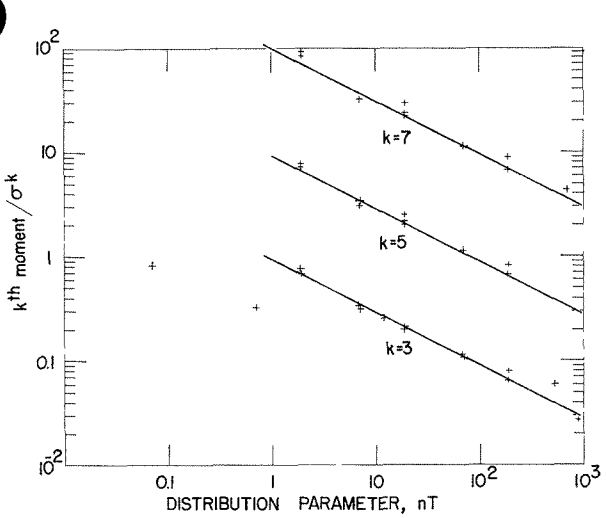

FIG. III-24-2. kth Moment of the Distribution x (kth Moment of the Observed Voltage Level Distribution Divided by the kth Power of the Second Moment) versus $N = nT$ (n = Input Rate, T = Time Constant of the Filter) for Random (Poisson Time Distributed) Input and a Single Time Constant CRM. Only Odd Moments are Shown. Lines are Derived from Theory. *ANL Neg. No. 116-587.*

data were then transferred from the analyzer memory to tape and processed on a DDP-24 computer to find the moments of the distribution in x. Preliminary results[5] indicate very satisfactory agreement with moments calculated from Campbell's theorem down to $N = 1$, but disagreement for smaller values. Some measured points and theoretical curves are shown in Figs. III-24-1 and III-24-2. More careful measurements are now planned to explore the discrepancy near $N = 1$. Tests with two and three time constant filters are also planned. In principle, such filters are capable of improving the practical performance of a surveillance monitor. At the same time, the response of a three-constant filter can be made to resemble the current pulses delivered by standard wideband amplifiers in a typical fission chamber count channel, and thus may lead to certain useful applications of the model distribution in connection with the so-called "Campbelling" technique of power level monitoring during reactor startup.[6]

REFERENCES

1. N. R. Campbell and V. J. Francis, *Random Fluctuations in a Cathode Ray Oscillograph*, Phil. Mag. **37**, 289 (1946).
2. S. O. Rice, *Selected Papers on Noise and Stochastic Processes*, Nelson Wax, Ed. (Dover Publications, New York 1954).
3. F. Y. Edgeworth, *The Law of Errors*, Trans. Cambridge Phil. Soc. **20**, 36 and 113 (1908).
4. K. G. Porges, W. Corwin and R. Daley, *The Fluctuations of Count Rate Meters Used in Reactor Instrumentation Channels*, (to be published).
5. W. Corwin and K. G. Porges, *Level Distribution of Count Rate Meters for Various Circuit Parameters Not Giving Gaussian Distributions*, Trans. Am. Nucl. Soc. **13**, 241 (1970).
6. D. A Gwinn and W. M. Trenholme, *A log N and Period Amplifier Utilizing Statistical Fluctuation Signals from a Neutron Detector*, IEEE Trans. Nucl. Sci. NS-**10**(2), 1 (April 1963).

III-25. Neutron Source Self-Absorption and Cavity-Wall Absorption

A. DE VOLPI

An accurate value of the neutron yield in fission [ν (Cf-252)] was reported last year.[1] In the course of making those measurements, some additional data were generated on various subsidiary correction factors. This is one of two reports on supportive work in the manganese bath neutron detection system.

In this case an investigation was made of neutron losses to capture in the source and in the walls of the cavity which usually surrounds the source. Analysis indicates that our reported value of total neutrons for Cf-252 will have to be increased by 0.1% to the value 3.729 ± 0.015 neutrons/fission. Of great importance for precision measurement, the overall error allowance of 0.4% is further justified in regard to this absorption correction.

Increasing uses are being found for calibrated neutron sources and beams. The most prominent system for accurate determination of the strength of such sources and also for measurement of neutron beam intensity is the manganese bath (and the vanadium bath). Almost all of the correction factors required to relate observed count rates with absolute neutron source rates have been subjected to extensive evaluation. One small correction (ranging from a few tenths of a percent to a few percent), not previously studied in a sufficient number of practical situations, is the compensation factor for neutrons absorbed in the source or surrounding cavity wall.

Usually the calibration of radioactive neutron sources is carried out by placing the source within a

moderating solution of manganese sulfate, generally with a thin-walled cavity separating the source from the solution. In the measurement of neutron beam fluxes, a re-entrant hole into the bath tank is required to introduce the beam to the center of the bath. These materials inevitably absorb thermal neutrons generated from the slowing-down process which follows fast neutron emission. Estimation of the thermal neutron flux returning to the vicinity of the source is difficult because of the hydrogeneous nature of the system, flux depression effects, self-shielding, and sometimes complicated geometry.

The concept of an accurate measurement requires experimental verification of any theoretical formulation of the problem. Thus, transport theory and Monte Carlo calculations are of limited value unless supported by measurements conducted under appropriate conditions.

The work was designed to be direct and to provide a wide range of data for interpolation and extrapolation. In the manganese bath systems used at Argonne, sources were placed in three types of cavities. One cavity is spherical with a radius of 5 cm; another, a cylindrical beam tube running completely through the bath; and the third, a re-entrant half-tube. To obtain an experimental measurement of incident neutron flux, each of these cavities was lined with cadmium sufficiently thick (0.05 cm) to absorb nearly all thermal neutrons. The walls of the stainless steel cylinder are relatively thin (absorption probability 0.63% per thermal neutron passage), while the walls of the steel spherical cavity are thicker (absorption probability 8% per passage). By comparing the activation rates obtained from a variety of neutron sources and at two solution concentrations both with and without the cadmium liners, it has been possible to accumulate a wide-ranging set of data. In addition, one of the simplest of theoretical foundations was adopted for initial fitting of the data, and these calculations—subject to normalization—have been found to be as good or better than more complex formulations.

Several conclusions may be drawn from the measurements and calculations. The calculations, subject to the single normalization factor, provide a reasonable estimate of the source and cavity absorption. Thus, not only may the age-diffusion model be used for interpolation, it may be used within the context of this paper to provide direct estimates of absorption for other sources, cavity radii, geometries and solution concentrations for error function arguments $\lesssim 3$.

The experimental method appears to be sufficiently established by the data and calculations to justify its use for more accurate determination of source and cavity absorption in situations not covered by the present work. In fact, the difficulties arising in comparing these results with other work suggest that deviations from the conditions reported in this paper should be directly evaluated by experiment rather than by extrapolation.

The experimental data generated from the perturbation caused by a cadmium shell, combined with corrections for flux depression and spatial distribution, together establish a simple and accurate basis for evaluation of source and cavity absorption.

For absolute neutron source determinations, a conservative estimate of the error contribution due to source and cavity absorption can be less than 0.1% for most configurations.

Reference

1. A. De Volpi, K. G. Porges and F. Ozer, *The Absolute Yield of Neutrons per Fission for Cf-252*, Reactor Physics Division Annual Report, July 1, 1968 to June 30, 1969, ANL-7610, p. 48.

III-26. Neutron Escape from Water-Moderated Tanks

A. De Volpi

One of the larger (and less certain) corrections for measurements of the neutron yield in fission from Cf-252 with the manganese bath is the correction factor for leakage from the bath. Calculation and experimental data have indicated that a 1 m diam bath should lose between 0.2 to 1.2% of the neutrons from a Cf-252 spontaneous fission spectrum. This uncertainty would be directly reflected in the total yield.

As a result, we embarked upon a program of direct measurement of such leakage making use of the manganese bath itself as the detection medium. We found the appropriate value to range from 0.48 to 0.52% depending upon the concentration. Since these numbers are consistent with earlier estimates, no change is necessary for our reported neutron yield value.[1] Furthermore, the error assignment which takes into account leakage uncertainty is hereby verified to be adequate.

As a result of these measurements it is necessary, however, to recommend modification in reported values for thermal neutrons per absorption (η) meas-

ared at Oak Ridge National Laboratory and Idaho Nuclear Corporation. In both cases calculations appear to underestimate the escape fraction by several tenths of a percent.

The relative number of neutrons which escape through a water-moderated tank surrounding a source of fast neutrons is a quantity of use both in terms of intrinsic studies of the slowing-down process and in terms of applications to quantitative neutron calibration. This report summarizes the integral measurements of escape (for Cf-252 spontaneous fission, Ra(α,n)Be, and Am(α,n)Be sources) fitted to a two-component model which provides an adequate basis for interpolation and extrapolation.

A number of nuclear data determinations have been made with fission neutrons introduced at the center of a sphere or cylinder. Two of these measurements have been for the purpose of accurate assessment of η, the number of neutrons per absorption, and two measurements for $\bar{\nu}$, the average number of neutrons per fission. In addition, certain neutron sources have been used as a standard for comparison throughout the world, although the size of the measuring system chosen by different laboratories has varied widely.

The requirements for accuracy in such experiments are presently in the order of ½%. Yet there have been widely conflicting corrections for neutron escape published, the range of these values exceeding ½%. Furthermore, *ad hoc* measurements with a given source cannot be readily applied to another source spectrum, nor can they be safely extended to different container radii.

Both spheres and cylinders have been used in the above-mentioned experiments. The solution surrounding the source has been either water, or a solution of water and an activating or nonactivating salt. Manganous sulfate, the most prominent activating agent incorporated in the moderating solution, establishes the manganese bath. It is the manganese bath calibration that requires accurate data on neutron escape, and it is with the manganese bath that the integral measurements reported in this paper have been accomplished.

In a number of unrelated experiments it has been convenient to use a relatively small sphere (effective radius 28.2 cm) to obtain high specific activities. A large number of neutron calibrations of sources of different spectra have been done at ANL with a sphere having an effective radius of 48.0 cm. For the present experiment, the small sphere was placed in a cylindrical tank of internal radius 38 cm (effective radius 36.7 cm) and both systems were flooded with a homogeneous aqueous solution of manganous sulfate. The activities produced in the internal sphere and in the cylinder were compared with the previously determined source rates compiled from the 48-cm sphere. An iteration technique was applied to rectify all data under the umbrella of a two-component leakage model (to be discussed later): that is, the relative neutron loss from the small sphere, based on a trial value for the large sphere, was iterated to adjust the trial value to a convergent quantity.

Figure III-26-1 shows the experimental plan. Irradiations were conducted in two steps. First, the source was placed at the center of the sphere for a day and then removed. The two-day pattern of activity generated in the sphere was followed with the on-line counter but only data from the decay phase was utilized. Next, the source was returned to the center of the sphere; this time, solution from the outer cylinder was circulated (in the same two-day pattern) through the on-line counter, the sphere having been bypassed with valves.

Calibrations were conducted by adding known aliquots of manganese sulfate solution and comparing with absolute coincidence calibrations. These calibrations agreed quite closely with the calculated efficiency based on the relative volumes of the 28.2-cm and 48-cm spheres and the 36.7-cm cylinder. Because the calibrations correspond most directly to the "decay" phase of the experiment—which occurs after the activating neutron source has been withdrawn—problems of compensation for solution mixing and fluid transport can be avoided.

As mentioned, sources of three spectra were evaluated: Cf-252 spontaneous fission, Ra(α,n)Be and Am(α,n)Be. In order to determine the influence of solution concentration, all three sources were compared in a dilute manganous sulfate solution (hydrogen/manganese atom ratio of 670) and the first two in a concentrated solution (H/Mn = 30.98). In addition, the first two sources were also tested with an unreflected central sphere by removing the solution from the surrounding cylinder.

A two-component model has been found to appropriately account for the experimental results. Here we select the fractional escape to be

$$\mathfrak{L}' = AB(f_1 e^{-r/L_1} + f_2 e^{-r/L_2}) \qquad (1)$$

with

$$f_1 + f_2 = 1. \qquad (2)$$

We fix A at 1.9, and B is a function of concentration only. The first term $f_1 e^{-r/L_1}$ accounts for neutrons moderated to thermal energy under Fermi Age theory, and the second term $f_2 e^{-r/L_2}$ allows for high-energy neutrons which undergo only a few collisions without much loss of energy. Thus, f_1 is the fraction of neutrons

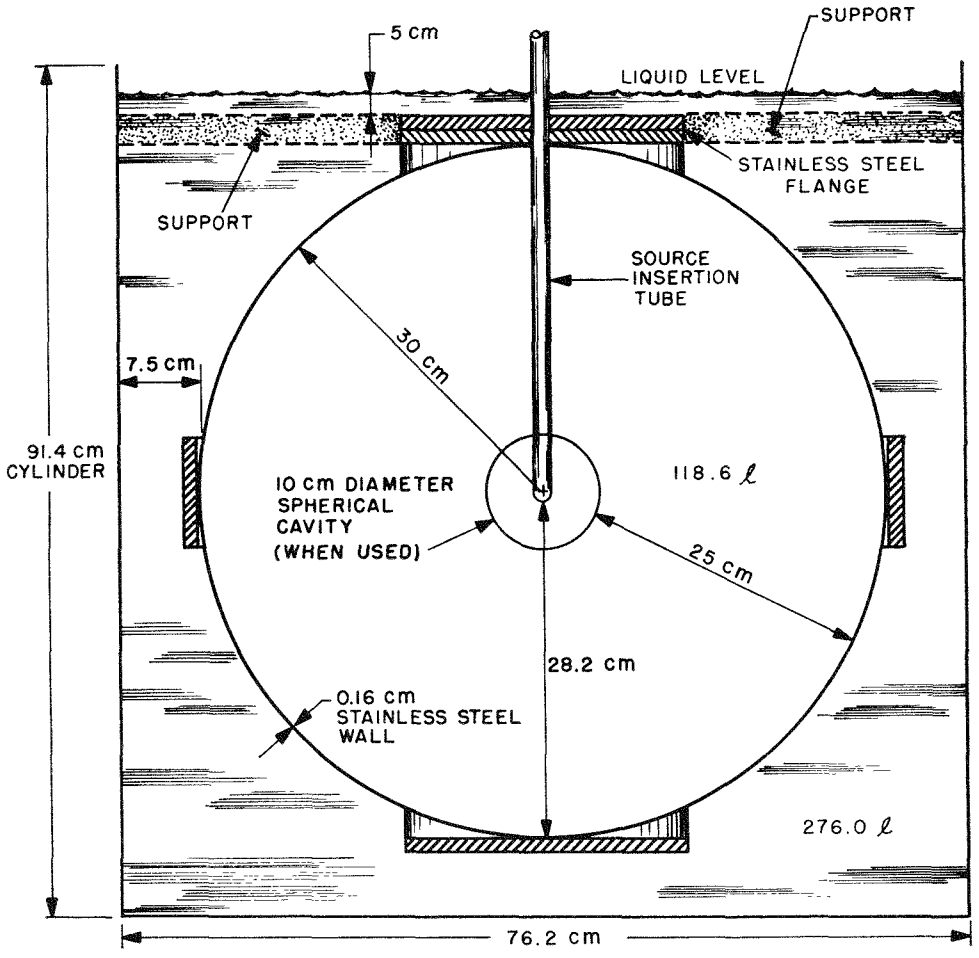

FIG. III-26-1. Experimental Apparatus for Escape Measurements. Not Shown is the Tubing Through Which Activated Liquid is Pumped from Either the Central Sphere of the Surrounding Cylinder to the On-Line Activation Monitor. *ANL Neg. No. 116-42.*

assigned to the first component and f_2 is the fraction attributed to the second component. These two numbers are adjusted from the experimental data.

The relaxation lengths are chosen from tabulated parameters for the relevant neutron sources. L_1 corresponds to the migration length of neutrons in Fermi Age theory:

$$L_1 = (\tau + L_D^2)^{\frac{1}{2}}, \qquad (3)$$

where τ is the Fermi age to thermal and L_D is the diffusion length of thermal neutrons in the medium. These numbers may be found in compilations.

The second relaxation length L_2 is taken from the various measurements of the exponential form measured in aqueous systems as a function of distance from the source. In this application the magnitude of L_2 is adjusted to a best fit with the data.

Data have been obtained for a sphere and a cylinder small with respect to a large sphere used as a reference point in estimating leakage; an iteration process justifies this procedure. It is possible to match the model to experimental data: by choosing the intercept coefficient A on the basis of other published experiments; by determining the reflection factor B from direct experiment and from published estimates; by taking the first exponential relaxation term L_1 as the migration length from Fermi Age theory; and by experimentally fitting with a small degree of arbitrariness the second relaxation length L_2 for the hard component of the neutron spectrum and the fractional coefficient f_2 for the second component.

Leakage from the small sphere is about ten times that of the large sphere. The two-component model appears to provide a useful and accurate basis for extrapolation and interpolation. By applying this model and the associated parameters, several absolute calibration anomalies can be coherently reconciled with the world (and the ANL) averages for neutron source strengths.

Consequently, it is believed that an error in accuracy of about 0.05 % or less can be associated with the escape fraction from spheres of large radius (~50 cm) at

all concentrations of dissolved absorber in aqueous solution. For cylinders an uncertainty of about 0.1% is probable.

For the smaller sphere, which itself has been used for measurements with the vanadium bath, the direct neutron calibration efficiency extrapolated to 30 keV neutrons can be accomplished with an absolute error not exceeding the inaccuracy attributed to the reference sources.

REFERENCE

1. A. De Volpi, K. G. Porges and F. Ozer, *The Absolute Yield of Neutrons per Fission for Cf-252*, Reactor Physics Division Annual Report, July 1, 1968 to June 30, 1969, ANL-7610, p. 48.

III-27. Digital Delay with Substantially Reduced Deadtime

A. DE VOLPI, G. E. CAYA,* C. J. RUSH* AND S. J. RUDNICK*

In the processing of random (or repetitive) events, it is frequently necessary or useful to delay the signals in one circuit path relative to those following another circuit route. Two types of delays are called for: linear and digital. If the signals are "analog" representations, in which pulse amplitude or shape information must be preserved, a linear delay is needed. If only the relative time relationship of the pulses is of interest, such pulses are normally standardized in amplitude and width, thus permitting use of a digital delay.

The transmission of signals along linear delay lines is subject to frequency-dependent attenuation. This limits the length of linear lines to a few microseconds, except where relative amplitude information is sufficient. Many situations arise where delays of some tens or hundreds of microseconds are desirable. If the amplitude-standardizing process can be accepted, then the digital delay circuit reported in this paper accomplishes the required delay function over a widely adjustable range with high accuracy.

A simple monostable can be used as a digital delay generator which would provide similar delay capability. However, its deadtime is equal to the delay interval. Thus a modest random-pulse processing rate of 100/sec delayed 1000 μsec would add about 10% loss due to paralysis during a delay. A circuit recently developed reduces the deadtime considerably so that for this illustration the actual losses would be negligible (less than 10^{-4}).

Restating the example, a 100 c/sec rate subject to an initial processing deadtime of 1 μsec without delay would result in a loss fraction of about 10^{-4}. Imposition of a 1000 μsec delay with this circuit provides essentially no further loss in count.

Figure III-27-1 demonstrates performance data over a wide range.

The suppression of deadtime losses is accomplished by self-distributive routing of random pulses to available standby delay monostables.

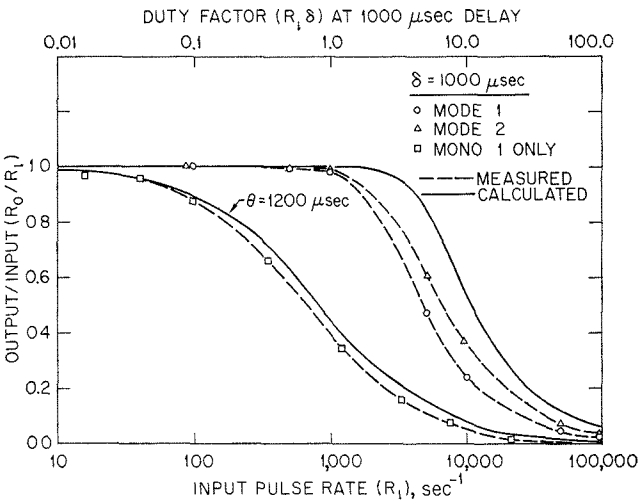

FIG. III-27-1. Calculated and Measured Deadtime Losses for Digital Delay Circuit. *ANL Neg. No 116-380.*

There are three modes of operation. Mode 1 is called the "scaling" mode because of its similarity to the scaling principle used in nuclear counting. Mode 2 is the "sharing" (or distributive) mode. The third mode is for test purposes; the unit may be calibrated in this mode.

The principle of operation of the delay is based on the formation of a delay interval initiated by an input pulse. A monostable produces a pulse of duration equal to the desired delay. At the end of this pulse, an output pulse is formed which has a width adjustable up to 1 μsec.

The deadtime suppression feature for Mode 1 is based on the scaling principle: there are five spare monostables through which signals can be routed when the first monostable is busy. In Mode 2 the inputs are cyclically distributed through all six monostables.

Another major feature of the unit is that it can be

* Electronics Division, Argonne National Laboratory.

accurately and precisely calibrated through a simple random-pulse gating method. For example, a standard deviation of 0.4 μsec was acquired in a 200-sec calibration of a 1000 μsec delay using an available oscillator of frequency 100 kHz. The calibration technique can use any available precision oscillator. Using conventional techniques a 100 MHz oscillator could be used to calibrate any 1000 μsec delay with a digitizing error of only 10 nsec. However, such an oscillator is not always available, and for a 1 μsec delay the digitizing error still corresponds to a 1% effect. The digitizing error in every case can be reduced by the random gating method: a delay interval is initiated by random pulses; during this delay interval the oscillator pulses are fed through the circuit and accumulated in a scaler. Comparison [of (a) the number of pulses fed through with (b) the number of random input pulses] readily yields the delay with reduced digitizing error.

The delay system has five switchable delay ranges with a vernier dial for interpolation, permitting any delay from 0.1 μsec to 10 msec to be chosen. There are a variety of logic provisions, including a capability for automatic deadtime correction. All active elements are integrated circuits and employ standard 5 V positive signal levels. The circuits are enclosed in a standard double-width NIM-module.

III-28. Deadtime Correction in Counting Rapidly Decaying Sources

K. G. A. Porges and A. De Volpi

The correction of counting data for losses due to counting-channel deadtime represents one of the basic requirements in processing such data to determine source strength. A number of authors[1-5] have treated this problem either on the basis of frequency or time interval distributions; while assumptions concerning the deadtime consider both fixed and variable paralysis, all these treatments suppose that the input to the paralyzed channel is precisely Poisson-distributed. With that proviso, and a fixed paralysis of length T, a steady mean input rate n can be shown to result in an expectation value for the count C accumulated over time interval t given by

$$C = nt/(1 + nT) \tag{1}$$

with a variance

$$\sigma^2(C) = nt/(1 + nT)^3. \tag{2}$$

In applying these correction formulae to a counting experiment which demands the best possible precision, one must, of course, make sure that the underlying assumptions of fixed paralysis and Poisson input distribution are indeed closely approximated. Regarding the first assumption, a number of recent circuit designs, as for example those described by Refs. (6) and (7), have paid particular attention to the long-term stability of the paralysis, as well as to the problem of immediate recovery. Equation (1) has been used as the basis of a number of automatic deadtime correction schemes.[8-13] Some of these schemes have been applied to coincidence counting, where a precise formula analogous to Eq. (1) cannot be written down whereas automatic schemes can, in principle, provide an exact correction.[12,13] Regarding the distribution at the input of the channel, some deviation from Poisson distribution cannot be avoided in view of the finite length of pulses delivered by practical detector channels. This results in a certain probability of overlap between different pulses, as well as the possibility of an event occurring just before the end of a paralysis interval generated by an accepted preceding event, such that the pulse generated by the second event is still present when the paralysis ceases and retriggering results. This latter effect can be eliminated with a circuit which provides several paralysis intervals.[7,13] A pulse injection scheme which is capable of removing errors due to both pileup and deadtime to a high degree has been described recently.[14] In that scheme, a fast side-channel is required that registers substantially all input events, or a constant fraction of these events. Counts or multichannel presentations can thus be corrected up to fairly large input rates, whereas at extreme input rates, any correction scheme, whether relying on a formula or on correction circuitry, is apt to fail and empirical correction may have to be resorted to.

There exists, however, another class of counting experiments in which the input deviates from the Poisson law, yet a precise correction can be given: counts during which the source decays appreciably.

To find this correction, we consider a source which yields a pulse rate s_0 at the start of the count. In the presence of a quasi-stable background component of mean rate b, the input $dn(t) = n(t')dt'$ within dt' at time t' after the start of the count then comes to

$$n(t')dt' = (b + s_0 e^{-\lambda t'})\, dt' \tag{3}$$

for the case of a source which decays with a single decay constant λ. Thus, the accumulated count C over an interval t in a channel with fixed paralysis T can be expressed by the integral

$$\begin{aligned} C &= \int_0^t n(t')\, dt'/[1 + n(t')T] \\ &= (1 + bT)^{-1}[bt + (\lambda T)^{-1} \ln \{[(1 + n(0)T]/ \\ &\qquad [1 + n(t)T]\}]. \end{aligned} \tag{4}$$

To secure a more convenient expression, from which a simple correction formula can be readily obtained, we shall introduce the mean signal rate (averaged over the count interval)

$$\bar{s}(t) = s_0(1 - e^{-\lambda t})/\lambda t, \tag{5}$$

and note that the logarithmic term in Eq. (4) can be expanded in a rapidly converging series,

$$\begin{aligned} &\log [(x + 1)/(x - 1)] \\ &\qquad = (2/x)[1 + (\tfrac{1}{3}x^2) + (\tfrac{1}{5}x^4) + \cdots], \end{aligned} \tag{6}$$

by means of the substitution

$$x = \coth (\lambda t/2) + 2(1 + bT)/sT\lambda t. \tag{7}$$

The hyperbolic contangent can be expanded in turn in a rapidly converging series with Bernoulli number (B_{2k}) coefficients:

$$\begin{aligned} \coth (z/2) &= (2/z)f, \\ f &= 1 + z^2/12 - z^4/720 + z^6/30{,}240 \\ &\quad \cdots + z^{2k}B_{2k}/(2k)! + \cdots. \end{aligned} \tag{8}$$

The function f is the ratio between the average defined by Eq. (5) and the linear average s^*,

$$s^* = [s(0) + s(t)]/2 = f\bar{s}. \tag{9}$$

Inserting Eqs. (5) through (8) into Eq. (4), one readily obtains the series

$$\begin{aligned} C/t = c &= [b/(1 + bT)] + [\bar{s}/(1 + n^*T)(1 + bT)] \\ &\quad \{1 + (\lambda t\bar{s}T)^2/12(1 + n^*T)^2 + 0[(\lambda t\bar{s}T)^4/40]\}, \end{aligned} \tag{10}$$

where

$$n^* = s^* + b = (f - 1)\bar{s} + \bar{n}. \tag{11}$$

It thus appears as if the first-order deadtime correction involves the linear average of the signal rates s^*, rather than the correctly averaged mean signal rate $\bar{s}$.

A correction formula which includes terms up to fourth order in $\lambda t\bar{s}T$ is readily obtained by inverting and expanding Eq. (10). If we define the mean signal rate for the limiting case of a quasi-constant source,

$$s' = c/(1 - cT) - b, \tag{12}$$

and approximate

$$(\lambda t)^2/12 = (f - 1)$$

[see Eq. (8)] in the second-order term in Eq. (10), a deadtime correction formula of adequately simple structure but of excellent precision,

$$\bar{s} = s'[1 - (f - 1)s'T(1 - cT)]^{-1}, \tag{13}$$

is obtained. For low background rates, Eq. (12) can be inverted directly:

$$\bar{s} = c/(1 - fcT) - b. \tag{14}$$

The variance or second moment attached to a count involving a decaying source as well as a constant channel deadtime after each accepted input is subject to the same considerations which apply to the mean or first moment of the non-Poisson distribution produced by the combination of paralysis and decay. In analogy to the treatment discussed above, we may therefore obtain the variance by integration over the count interval,

$$\begin{aligned} \sigma^2(C) &= \int_0^t n(t')\, dt'/[1 + n(t')T]^3 \\ &= (\lambda T)^{-1}\{[\tfrac{1}{2}(1 + bT)][(1 + n(t)T)^{-2} \\ &\qquad - (1 + n(0)T)^{-2}] \\ &\qquad - [bT/(1 + bT)^2][(1 + n(t)T)^{-1} \\ &\qquad - (1 + n(0)T)^{-1}] \\ &\qquad - bT \log [1 + n(0)T/[1 + n(t)T]\} \\ &\qquad + bt/(1 + bT)^3. \end{aligned} \tag{15}$$

Expanding and rearranging, as above, this expression can be shown to amount to

$$\begin{aligned} \sigma^2(C) &= [n(0) - n(t)][B^2 - AB(B - 1) \\ &\qquad + (B - 1)AQ^2 - (B - 1)A^2(1 + Q^2) \\ &\qquad \cdot(1 + 3Q^2)^2][\lambda B^3A^3(1 - 3Q^2)^2]^{-1} + bT/B^3, \end{aligned} \tag{16}$$

where

$$A = 1 + [n(0) + n(t)]T/2 = 1 + n^*T,$$

$$B = 1 + bT$$

and

$$Q^2 = [n(0) - n(t)]^2T^2/12A^2.$$

After some more rearrangement, Eq. (16) can be cast into the form

$$\begin{aligned} \sigma^2(C) &= \bar{n}t/(1 + n^*T)^3 \\ &\quad + 3(f - 1)\bar{s}t\bar{b}T/(1 + bT)^3(1 + n^*T)^2 + \cdots. \end{aligned} \tag{17}$$

The principal two reasons for calculating variances are, first, to determine the best counting strategy, i.e.,

ascertain what choices of disposable parameters will minimize the variance; secondly, variances may appear as weighting factors when several independent measurements are eventually combined to obtain the best value of some parameter calculated from the measurements. For either purpose, the second term in Eq. (17) can be safely ignored.

The propagated variance in the signal strength calculated from the measurements is readily found by propagation of error to amount to

$$\sigma^2(\bar{s}_{calc}) = [\bar{n}t/(1 + n^*T)] + [1 + (f - 1)\bar{s}T/(1 + \bar{n}T)]^4\sigma^2(b). \quad (18)$$

The effect of both decay and deadtime on the propagated error attached to the calculated result is seen to be such as to *increase* it, in contrast to the regularizing effect on the observed count C. This is true not only of the first term in Eq. (18), but also of the second term which is due to the uncertainty in mean background level. To be sure, the latter effect is apt to be still very small in precision counting experiments, where it is usually possible to set up the equipment in a low background environment—whence both the expectation value and the second moment $\sigma^2(b)$ of the background rate will contribute very little to the variance expressed in Eq. (18). In other situations, however, a relatively strong and irremovable background may exist; for that case, Eq. (18) suggests that it would pay to go to some trouble to measure this background with considerable precision so as to render $\sigma^2(b)$ small.

References

1. W. Feller, *On Probability Problems in the Theory of Counters*, Courant Anniversary Volume, (Interscience Publishers, Inc., New York, 1948).
2. W. Feller, *An Introduction to Probability Theory and Its Applications*, (John Wiley & Sons, Inc., New York, Third Edition, 1968).
3. L. Takács, *On a Probability Problem in the Theory of Counters*, Ann. Math. Statist. **29**, 1257 (1958); also, *On a Coincidence Problem Concerning Particle Counters*, ibid. **32**, 739 (1961).
4. E. Parzen, *Stochastic Processes*, (Holden-Day, Inc., San Francisco, 1962).
5. W. L. Smith, *On Renewal Theory, Counter Problems and Quasi-Stochastic Processes*, Proc. Cambridge Phil. Soc. **53**, 175 (1957).
6. A De Volpi, J. J. English, A. J. Metz, K. G. Porges and S. J. Rudnick, *A Versatile Discriminator with Adjustable Paralysis*, Rev. Sci. Instr. **37**, 1592 (1966).
7. S. J. Rudnick, J. J. English and R. H. Howard, *Highly Stable High-Rate Discriminator for General Use in Nuclear Counting Applications*, Rev. Sci. Instr. **40**, 9 (1969).
8. T. Emmer, *Multichannel Pulse Height Analyzers*, H. W. Koch and R. W. Johnston, Eds., Acad. Sci., Nat. Res. Council. Publ. **467**, 182 (1957).
9. H. Seufert, *A Device for Automatic Digital Dead-Time Correction of Counting Losses of Single and Coincidence Counting Rates*, Nucl. Instr. Methods **44**, 335 (1966).
10. J. Seda, *A Method for Automatic Compensation of Dead-Time Losses*, Nucl. Instr. Methods **59**, 179 (1968).
11. J. J. Point and A. Blave, *Méthodes Originales de Correction Continue de Pertes de Comptage dues aux temps morts des Détecteurs et de Leur Electronique Associée*, Proc. IAEA Conference on Nucl. Electronics, Vol. 2, p. 345, Belgrade, 1961.
12. A. Gandy, *Mesure Absolue de l'Activité des Radionuclides par la Méthode des Coïncidences β-γ; Etude d'une Méthode de Correction Automatique des Erreurs Instrumentales*, Int. Jour. Appl. Rad. Isotopes **14**, 385 (1963).
13. K. G. Porges and S. J. Rudnick, *Live-Timer Method of Automatic Dead-Time Correction for Precision Counting*, Rev. Sci. Instr. **40**, 1 (1969).
14. H. H. Bolotin, M. G. Strauss and D. A. McClure, *Simple Techniques for Precise Determinations of Counting Losses in Nuclear Pulse Processing Systems*, Nucl. Instr. Methods **83**, 7 (1970).

III-29. Speed Tests on Some Small-to-Medium Computers

Charles Erwin Cohn

Introduction

For the purposes of planning computer applications and selecting equipment, it is helpful to know the time required for certain elementary operations on various computers. This indicates how much real-time computational load may be carried by a given machine.

Some such information has been obtained from speed tests on a limited but representative selection of small-to-medium computers of the class commonly used for process control and data acquisition applications. The tests were done to aid in the selection of computers for on-line data-handling applications and to help evaluate past selections. Tests were run on a total of eight machines including two with 24-bit word length, one with 18-bit, five with 16-bit, and one with 12-bit. These included the machines currently in use in the Applied Physics Division for experimental assistance, as well as some others that were available for testing.

TABLE III-29-I. COMPUTER PARAMETERS

Computer	DDP-24	SEL-840MP		PDP-9	DATA-620	SEL-810A	CDC-1700	IBM-1130	DDP-516	CDC-160A
Bits per word	24	24		18	16	16	16	16	16	12
Memory cycle time, μsec	5 0	1.75		1.0	1.8	1.75	1.1	3.2	0 96	6 4
Memory occupied by timing program and library subroutines:		Non-EAU	With EAU							
Words	953	1129	881	1615	1907	1622	1845	2078	1636	3838
Bits	22872	29496	21144	29070	30512	25952	29520	33248	26176	46056

METHOD

The tests were run with a Fortran program that was specially written to test the speed of various single precision floating-point arithmetic operations and functions. This was adapted from a timing program written many years ago by Dr. John P. Schiffer, Argonne National Laboratory. The use of Fortran was the only means by which it was practical to test a wide range of computers with a reasonable expenditure of effort. However, the applicability of the results is not restricted just to Fortran programs. A floating-point arithmetic or function subroutine can be considered just a particular type of data manipulation in which the bit patterns that we call the "floating-point operands" are operated upon in a prescribed way to yield another bit pattern that we call the "floating-point result". Therefore, the outcome of these tests is a good indication of the relative performance of the tested computers on other data-processing tasks. Moreover, the results do not merely reflect some peculiarity of the compiler-generated code, because most of the time for each operation is spent executing hand-coded library subroutines.

COMPUTERS TESTED

Table III-29-I shows the computers that were tested. The two 24-bit machines were the Honeywell DDP-24 and the Systems SEL-840MP. The latter was tested both with and without its Extended Arithmetic Unit which provides hardware floating-point capabilities. The other machines all had hard-wired fixed-point arithmetic, and used subroutines to perform floating-point arithmetic. The 18-bit machine was the Digital PDP-9, the five 16-bit machines were the Varian Data Machines 620, the Systems SEL-810A, the Control Data CDC-1700, the IBM-1130 and the Honeywell DDP-516, and the 12-bit machine was the CDC-160A. The DDP-24, SEL-840 and DATA-620* belong to the Applied Physics Division while the CDC-160A belongs to the Applied Mathematics Division. The SEL-810A and IBM-1130 were made available through the courtesy of Messrs. T. W. Hardek and N. F. Morehouse, respectively, Argonne National Laboratory, while the PDP-9 and CDC-1700 were made available through the courtesy of Messrs. C. E. Burgart and J. B. Bullock, Oak Ridge National Laboratory. The DDP-516 results were obtained by Dr. J. B. Dragt of Reactor Centrum Nederland, Petten, The Netherlands.

This table also shows the amount of memory occupied by the timing program and the library subroutines that it uses. Practically all of the space is occupied by instructions; only about two or three dozen words are used for data. For the 12, 16 and 18 bit machines the number of words required is enough greater than the number of words required for the 24-bit machines that the total number of bits occupied is comparable. Now, the cost of a core memory is mainly proportional to the number of bits it contains and is not particularly dependent on how those bits are subdivided into words. This suggests that the shorter-word machines would offer no savings in memory cost for a given job, even though a memory containing a given number of words might be cheaper with 16 or 18 bits than with 24 bits.

TEST PROCEDURES

In the timing program the speed of each operation was tested by including it in a DO loop which repeated it a large number of times—500 to 200,000—with different operands. The loop was preceded and followed by a PAUSE. The total running time of each loop was measured in different ways on the different computers. On the PDP-9, CDC-1700, IBM-1130 and CDC-160A the timing was done manually with a stop watch, the elapsed times ranging from 2 to 9 seconds for the first three, much more for the latter. Each loop was measured two or three times and repeatability was within $\frac{2}{10}$ of a second. On all of the other machines except the SEL-840MP and DDP-516, a strip chart recorder was connected to the halt light on the console. The

* Actually, the Applied Physics Division has the optional 18-bit version, designated DATA-622. However, its instruction repertoire and hence its running times are characteristic of the 16-bit basic version, and were treated as such

recorder was run at a speed of 3 in./sec. To eliminate errors due to recorder response time the record was measured from the beginning of the start transition to the beginning of the stop transition. Message typeouts on PAUSE were eliminated by altering instructions in the core.

On the SEL-840MP the timing was done with a binary counter connected to it. The counter received pulses from a time-mark generator. A special halt routine was written to read and reset the counter before and after each loop. The count read in at the end of the loop thus gave the loop duration. The time mark generator was run at a thousand pulses per second for the non-EAU tests and at a million pulses per second for the EAU tests.

On the DDP-516 the timing was done with a 50-Hz real-time clock.

For each loop the gross time per operation was obtained by dividing the total elapsed time by the total number of cycles. To obtain the net time, the time required for a DO cycle was subtracted. In addition the sine, square root, natural logarithm, and exponential operations required subtraction of the time for the add operation used in forming the argument.

Results

Table III-29-II shows the time in microseconds required for each of the operations on the various computers. Factors such as software efficiency or instruction repertoire might be adduced to explain the observed disparities in speed. For example, the very long times on some of the machines for the sine, square root, logarithm, and exponential functions result from the approximation algorithms for these functions being executed in floating-point. Better performance can be had where the approximation algorithms are executed in fixed point with the result being floated upon completion. Furthermore, the SEL-840MP is handicapped in speed by carrying eleven significant figures in its single-precision floating-point arithmetic while the other machines carry just six or seven significant figures. Also, the long time required to complete a DO cycle on the DATA-620 arises from its peculiarity of using a subroutine to increment and test the loop index.

Nevertheless, these disparities in performance would appear to arise primarily from differences in word length. That can be seen from Table III-29-III which shows the same information as before in terms of memory cycles per operation, allowing comparison of how efficiently each computer makes use of its basic speed capability. For the most part, the 12, 16 and 18-bit machines suffer from an evident disadvantage with respect to the 24-bit machines—well over a factor of two.

TABLE III-29-II. Operation Times, μsec

Computer	DDP-24[a]	SEL-840MP		PDP-9	DATA-620[c]	SEL-810A[d]	CDC-1700	IBM-1130[e]	DDP-516[f]	CDC-160A[g]
		Non-EAU	With EAU[b]							
Add	440	308	19	500	518	553	540	850	245	3445
Divide	413	383	37	580	790	2622	720	1130	270	3805
Multiply	369	282	26	500	732	611	550	960	250	3625
Sine	584	4970	365	5235	3396	9862	4540	3600	2375	37460
Square Root	377	824	267	4085	806	13459	8440	5070	535	20710
Exponential	1188	3009	470	6385	1916	N.A.	3340	2833	2105	30960
Logarithm	548	5887	373	4785	4576	11262	5940	5500	2725	32960
If	28	11	11	90	24	85	190	200	36	1723
Fix	130	79	33	160	260	162	330	370	224	3065
Float	105	50	8	160	356	615	760	540	312	2785
Store Subscripted Variable										
1-Dimension	196	77	28	240	53	192	370	640	89	2475
2-Dimension	221	88	39	300	242	213	380	750	124	2465
DO (1 Cycle)	43	18	18	15	266	18	16	52	10	1295

[a] Results also apply to DDP-124 if operation times are multiplied by 0.34 and 40 μsec are added for Add, Divide, Multiply, Sine, Logarithm and Exponential. The memory requirement is increased by 20 words.

[b] EAU ≡ Extended Arithmetic Unit (hardware floating-point).

[c] Results also apply to DATA-620/i.

[d] Results also apply to SEL-810B if operation times are multiplied by 0.45.

[e] Results also apply to IBM-1800 if operation times are multiplied by 0.625 for the 2-μsec memory or 1.25 for the 4-μsec memory. Re-entrant software may run slower.

[f] Results also apply to DDP-116 and H-316 if times are multiplied by 1.82.

[g] With 168 arithmetic unit.

TABLE III-29-III. Memory Cycles per Operation

Computer	DDP-24	SEL-840MP		PDP-9	DATA-62	SEL-810A	CDC-1700	IBM-1130	DDP-516	CDC-160A
		Non-EAU	With EAU							
Add	88	176	11	500	288	316	491	266	255	538
Divide	83	219	21	580	439	1498	655	353	281	595
Multiply	74	161	15	500	407	349	500	300	260	566
Sine	117	2840	208	5235	1887	5635	4127	1125	2474	5853
Square Root	75	471	152	4085	448	7691	7673	1584	557	3236
Exponential	238	3009	269	6385	1064	N A.	3036	885	2192	4838
Log	110	3364	213	4785	2542	6435	5400	1719	2838	5150
If	6	6	6	90	13	49	173	63	38	269
Fix	26	45	33	160	144	93	300	116	233	479
Float	21	29	8	160	198	351	691	169	325	435
Store Subscripted Variable										
1-Dimension	39	44	16	240	29	110	336	200	93	387
2-Dimension	44	50	22	300	134	122	345	234	129	385
DO (1 Cycle)	9	10	10	15	148	10	15	16	10	202

(All of the tested machines have comparably extensive instruction repertoires. In fact, some of the 16-bit machines have a much more extensive list of register-to-register instructions than do the 24-bit machines. Also, with the exception noted above, all of the software systems are of about the same degree of sophistication.)

Discussion

The inefficiency of the short word arises from the inconveniences in memory addressing that it imposes. A single word of 18 bits or less is not large enough to carry both an instruction code and the address of any location in a memory of reasonable size. It is often necessary to circumvent this limitation by the use of indirect addresses or doubleword instructions, both of which consume extra time and space. In addition, multiple precision data handling is more frequently required.

In the light of all this let us reexamine the supposed advantages of the short word, primarily regarded to be cost savings. We have already seen that savings in memory costs are questionable because the lower cost of a memory having a given number of words is offset by the larger number of words required to accommodate a given job. To examine the processor cost situation we may divide the components of a processor into two classes. Class 1 is made up of those components of which there is one for each bit in the word, such as accumulator stages and adder circuits, while Class 2 is made up of those components of which there are a given number per computer regardless of the word length, such as timing and control circuits. Now, a 24-bit computer would contain 50% more Class 1 components than a 16-bit computer of similar architecture but the same number of Class 2 components, so the 24-bit computer should cost at the most 50% more than the 16-bit machine. Furthermore, non-manufacturing costs should be independent of word length since it should cost no more to design, program, and market a 24-bit machine than a 16-bit machine. Therefore, this 50% should be a very extreme upper limit. The results shown here imply that one gains several times 50% in speed by going from 16 to 24 bits, so that the 24-bit word would seem to be much more cost-effective.

Several 16-bit machines are available at present with basic mainframe prices around $10,000. By the reasoning just stated it should be possible to market a 24-bit processor for well under $15,000. However, the 24-bit word has not been employed in computers selling for less than $50,000. One wonders about the reason for this. Is it fashion or is it unawareness of the factors that have been discussed here?

Certainly, the question "what is the most cost-effective word length?" still awaits a definitive answer. All that has been noted here is that 24 bits appears to be closer to the optimum than 18 bits or less. Perhaps 32- or 36-bit machines, which were not tested, would have looked even better. It is the author's belief that the optimum would not be as short as one might think for the smaller computers.

III-30. The Optimum Evaluation of Series of Measurements by Maximum Likelihood, as Applied to Nuclear Source Counting

K. G. A. Porges and A. De Volpi

The last stage of some precision measurements often involves the judicious combination of several independent measurements, carried out under somewhat different conditions and therefore of different reliability. To obtain the "best" value of some quantity or parameter computed from such a series of measurements, it is suggested in elementary texts that "each measurement should be weighted by the reciprocal of its variance".

This prescription is, however, ambiguous unless the type of variance is specified and may become misleading in certain cases where specific corrections must be applied to individual measurements. Several examples given further on point out erroneous applications of inverse variance weighting which are not unknown in the literature. In a complex situation, e.g. a nuclear counting problem which involves separate corrections for deadtime, accidental coincidences, background, source decay, etc., it appears best to derive the weights which are to be assigned to individual determinations directly from the Principle of Maximum Likelihood[1,2] (PML) instead of relying on "inverse variances". Indeed, weights which are inversely proportional to group variances result from the application of this principle in simple cases; similarly, PML provides the rationale for least square fitting and related statistical processing methods. PML-derived data processing has been used in some specific nuclear measurements[3,4] but the general usefulness of the principle, although very thoroughly discussed in a recent test on the statistical treatment of measurements,[2] still appears to be insufficiently appreciated. This note is intended as a partial remedy, with particular emphasis on nuclear measurement processing.

The statistics of nuclear measurements (in contrast perhaps to measurements in some other areas of physics) are predetermined by the fact that the quantity measured is usually itself a "statistic" whose "true" value can never be known exactly. Thus, measurements of cross sections, lifetimes, decay rates, branching ratios, etc., determine either an expectation value or an a priori probability; only energy levels and other stationary nuclear properties have a "true" value in nature, subject only to the uncertainty principle.

In the following brief description of the Principle of Maximum Likelihood, it is not necessary to distinguish between parameters of intrinsically different nature, but only between parameters which are measured and those which remain constant during a given set of measurements. Individual determinations, consisting of sets of values of the former type $(a_1, b_1, \cdots)$, $(a_2, b_2, \cdots)$ etc., may fluctuate because the parameters are in fact statistics or a result of equipment performance; in either case, sets of expectation values $(\underline{a}_1, \underline{b}_1, \cdots)$ etc. can presumably be defined for each measurement. Such expectation values may differ between sets or may be equal, according to whether conditions are varied or not. The other class of parameters, designated here by Greek symbols $\alpha, \beta, \cdots$, are not measurable but their expectation values can be either calculated from some known relation between expectation values of all parameters or may be known beforehand; the evaluation of one of these is evidently the object of the series of measurements.

In addition to this information one also requires some knowledge of the statistics of the measurement process; in particular, the probability w_j of a certain measurement in the series yielding a particular "score", $a_j, b_j, \cdots$, must be explicitly defined in terms of all expectation values,

$$w_j = w(a_j, b_j, \cdots; \underline{a}_j, \underline{b}_j, \cdots; \underline{\alpha}, \underline{\beta}, \cdots). \quad (1)$$

Each such probability w_j may in turn be the product of component probabilities for individual parameter scores when these are mutually statistically independent, or consist of a more complex expression, as the result of either correlation or concatenation between parameters. We shall assume the probabilities w_j for successive measurements to be statistically independent (the more complex case of correlations between such measurements is treated in Ref. 2); hence the overall *likelihood* of the combined score is the product of probabilities w_j,

$$L = \prod w_j. \quad (2)$$

The likelihood L can be shown[1,2] to vary with respect to the choice of expectation values of parameters $\alpha, \beta, \gamma, \cdots$ in such a way that its logarithm is a conditional maximum for the "best" value of those quantities. The set of partial differential equations resulting from this observation,

$$\partial \ln L/\partial \underline{\alpha} = \sum_j \partial \ln w_j/\partial \underline{\alpha} = 0$$

$$(\partial \ln L/\partial \underline{\beta}) = \sum_j \partial \ln w_j/\partial \underline{\beta} = 0$$

. . . . . .

constitutes an operational definition of the Principle

Maximum Likelihood (PML) from which weighting equations are readily obtained by inserting specific probabilities w_j. These equations, to be sure, are not necessarily soluble by straightforward arithmetical means but require, in some cases, iteration or some similar method. That fact may have been persuasive in favor of using simpler but incorrect weights when computers were not widely available, but this should no longer be a deterrent. Incorrect weights will not necessarily result in a very marked difference of the final result, but always amount to, in effect, discarding some valid information. Admittedly, when a large number of individual measurements is available, any weights whatsoever will do. An unweighted mean will yield the same result as a carefully weighted average when the overall statistical uncertainty is eventually reduced to a small value in comparison with suspected systematic errors (which can never be entirely avoided in precision measurements). However, to obtain such a large amount of information that some of it becomes redundant is practical only in experiments which require a major effort in equipment setup and calibration, but is inefficient when running time is a significant part of the overall cost.

The component probabilities w_j defined above frequently (but not necessarily) turn out to amount to concatenated or combined Bernoulli and Poisson distributions. When this is the case, and moreover when the observed scores consist of large numbers, it is permissible to substitute Gaussian functions for actual distribution functions, as treated extensively in textbooks on probability theory. As shown, for instance, in Ref. 5, the error is small in the vicinity of the peak (where differentiations indicated by Eqs. (3) are carried out). In borderline cases, Edgeworth correction series can be used if the exact distribution function w_j is particularly complex, provided its cumulants can be readily calculated.[5-7]

When this substitution is made in Eqs. (3), one obtains a set of weighting equations in which weights are inversely proportional to the second moments of the Gaussians. This amounts to the above mentioned scheme of "inverse variance weighting". The two mistakes most often made in applying this prescription are: (1) use of estimated variances of single measurements instead of distribution variances, (2) application to cases where component probabilities w_j are not effectively represented by Gaussians. This will now be illustrated by some examples.

As a first and trivial case, we consider a series of counts $C_1, C_2, \cdots C_m$ of a radioactive source over a set of different time intervals $t_1, t_2, \cdots t_m$, from which one wishes to infer the best value of the count rate $\underline{c}$. In the absence of deadtime effects, w_j are Poisson distributions

$$w_j = \frac{e^{-\underline{c}t_j}(\underline{c}t_j)^{C_j}}{C_j!} \tag{4}$$

Insertion of Eq. (4) into Eq. (3) and differentiation with respect to $\underline{c}$ leads to the self-evident result

$$\underline{c} = \sum C_i / \sum t_k , \tag{5}$$

which is also obtained by first computing sample count rates $c_i = C_i/t_i$ and weighting these by the reciprocal of the *distribution* variance $\sigma^2(\underline{c}_i) = \underline{c}/t_i$. Note, however that use of the Estimated Single Measurement (ESM) variance $\sigma^2(c_i) = C_i/t_i^2$ yields the wrong result,

$$\underline{c} = \sum t_k / \sum (t_j^2/C_j). \tag{5'}$$

Much the same problem exists for counts which require a deadtime correction. In that case, the correct probability w_j turns out to be rather unwieldy[8,9] but in most cases when deadtime corrections are necessary, observed counts are also large numbers; as discussed above Gaussian distributions can thus be substituted. The expectation value $\epsilon(C_j)$ of count C_j over time t_j is related to the input rate $\underline{n}$, which we wish to determine, through

$$\epsilon(C_j) = \underline{n}t_j/(1 + \underline{n}T), \tag{6}$$

where $T \equiv$ fixed paralysis after each count, and the variance becomes[10-12]

$$\sigma^2(C_j) = \underline{n}t_j/(1 + \underline{n}T)^3, \tag{7}$$

whence

$$-\ln L = \tfrac{1}{2}\sum \ln [2\pi\sigma^2(C_j)] + \sum [C_j - \epsilon(C_j)]^2/2\sigma^2(C_j). \tag{8}$$

Differentiation with respect to the expectation value of the input rate yields the best overall input rate value

$$\underline{n} = \sum C_i / (\sum t_j - T\sum C_i). \tag{9}$$

The use of input rates estimated on the basis of a single measurement,

$$\underline{n}_i = (C_i/t_i)/[1 - (C_iT/t_i)] \tag{10}$$

and/or use of inverse S.M.E. variance weighting,

$$\sigma^2(n_i) = (\partial n_i/\partial C_i)^2\sigma^2(C_i), \tag{11}$$

evidently again produces a spurious result.

A final example illustrating the pitfalls of inverse variance weighting is a count with background subtraction. We suppose, for example, that m counts C_i over various time intervals t_{ci} are made of the same source, interspersed between m background counts B_i over intervals t_{bi}; from this information we wish to extract the best value for the signal rate $\underline{s}$. The likelihood function for this case is elementary and differ-

entiation with respect to $\underline{s}$ and $\underline{b}$ immediately yields the answer

$$\underline{s} = \sum C_i / \sum t_{ic} - \sum B_k / \sum t_{jb}\,, \qquad (12)$$

whereas the attempt to calculate sample signal rates $s_i = C_i/t_{ic} - B_i/t_{ib}$ and combine these with weights $(C_i/t_{ic}^2 + B_i/t_{ib}^2)^{-1}$ leads to a formulation which is both very complex and entirely wrong. A more realistic background subtraction problem is sometimes encountered where background varies: for instance, a preliminary measurement may suggest that an effort be made to reduce the background through shielding, such that a set of measurements is eventually available consisting of the same mean source count rate $\underline{s}$ with different background rates $\underline{b}_i$. For m measurements in the presence of the source and m measurements in the absence of the source, PML yields $m + 1$ equations:

$$\begin{aligned} \sum_i t_{ci} &= \sum_k C_k/(\underline{s} + \underline{b}_k), \\ t_{cj} + t_{bj} &= C_j/(\underline{s} + \underline{b}_j) + B_j/\underline{b}_j\,; \\ & \qquad j = 1, 2, \cdots m, \end{aligned} \qquad (13)$$

an example of a case where a solution for $\underline{s}$ requires iteration or successive approximation. One interesting feature of this set of equations is that the approximation which one would be forced to make for a single measurement, $t_b = B/\underline{b}$, is not valid here, as additional information about the background can be derived from the source counts. Generally speaking, it is the essential function of the PML method to make complete use of all available information contained in the data, for which reason this method would appear to merit more attention than it appears to have received.

References

1. H. Jeffries. *Theory of Probability*, (Oxford University Press, New York, 1961).
2. L. Janossy, *Theory and Practice of the Evaluation of Measurements*, (Oxford University Press, New York, 1965).
3. P. H. R. Orth, W. R. Falk and G. Jones, *Use of the Maximum Likelihood Technique for Fitting Counting Distributions, I*, Nucl. Instr. Methods **65**, 301 (1968).
4. W. R. Falk, P. H. R. Orth and G. Jones, *Use of the Maximum Likelihood Technique for Fitting Counting Distributions, II*, Nucl. Instr. Methods **65**, 307 (1968).
5. F. Y. Edgeworth, *The Law of Error*, Trans. Cambridge Phil. Soc. **20**, 36, 113 (1908).
6. H. Cramer, *Mathematical Methods of Statistics*, (Princeton University Press, 1946).
7. K. G. Porges, *Detection of Transients in Nuclear Surveillance-Counting Channels*, ANL-7470 (1968).
8. I. De Lotto, P. F. Manfredi and P. Principi, *Counting Statistics and Dead-Time Cores*, Energia Nucleare **11**, 557 (1964).
9. F. Carloni, A. Corberi, M. Marseguerra and C. M. Porceddu, *The Asymptotic Method of Deadtime Correction*, Nucl. Instr. Methods **78**, 70 (1970).
10. W. Feller, *On Probability Problems in the Theory of Counters*, Courant Anniversary Volume, (Interscience Publishers, Inc., New York, 1948); W. Feller, *An Introduction to Probability Theory and Its Applications*, (John Wiley & Sons, Inc., New York, Third Edition, 1968).
11. L. Takacs, *On a Probability Problem in the Theory of Counters*, Ann. Math. Statis. **29**, 1257 (1958); L. Takacs, *On a Coincidence Problem Concerning Particle Counters*, Ann. Math. Statis. **32**, 739 (1961).
12. W. L. Smith, *On Renewal Theory, Counter Problems and Quasi-Stochastic Processes*, Proc. Cambridge Phil. Soc. **53**, 175 (1957).

III-31. Estimates of Variance from Measured Quantities of Fluctuating Origin and Inherent Correlation

A. De Volpi

An examination has been made of the origin of variances estimated for quantities calculated from measured numbers. If these measurements are gathered in simultaneous time intervals, they become correlated in a statistical sense. As a result, care must be taken in determining the error to be associated with the calculated quantity.

In carrying this procedure through, a consistent set of derivations has been obtained for common situations in counting random events, without the necessity for introducing *ad hoc* assumptions for each special application. By applying a minimum number of justifiable constraints, it has been possible to avoid leaving the final expressions in incomplete or obscure form.

The initial review establishes that the proper variance to associate with a source rate s measured in the presence of background b is

$$\sigma_s^2 = [(s + b)/t_c] + \sigma_b^2\,, \qquad (1)$$

which indicates isolation of the separately measured background. Of course, for comparative purposes a uniform rate b can be used to estimate the variance for the background measurement. If this is done, then the optimum apportionment of background to sample

unting time becomes

$$t_b/t_c = [b/(s + b)]^{\frac{1}{2}}. \quad (2)$$

In the limit of very low background, we find

$$t_b/t_c = (b/s)^{\frac{1}{2}}, \quad (3)$$

and for relatively high backgrounds,

$$t_b/t_c = 1. \quad (4)$$

A merit ratio F for counting systems has been derived which does not have explicit reference to counting durations. The general expressions reduce to

$$F = (s_2/s_1)^{\frac{1}{2}}, \quad (5)$$

if both signal rates are large with respect to background, and to

$$F = (s_2/s_1)(b_1/b_2)^{\frac{1}{2}}, \quad (6)$$

if both signal rates are greatly exceeded by background.

If there is significant decay (λ) of a radioactive source during the counting interval, a more complex counting time ratio arises:

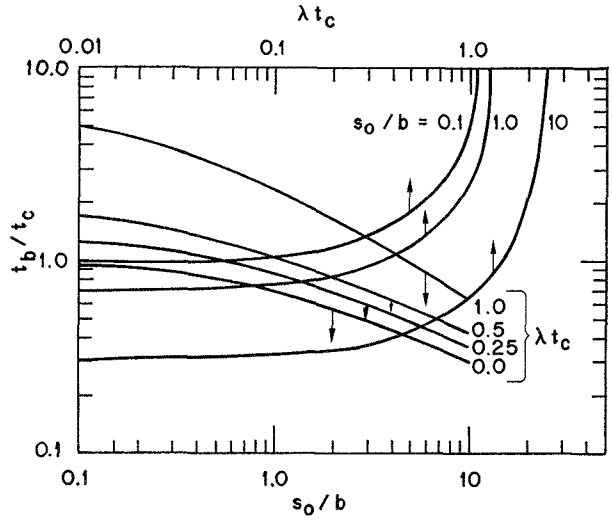

FIG. III-31-1. For Decaying Sources, the Optimum Counting Time Ratio $k = t_c/t_b$ is Plotted as Functions of Initial Signal/Background Ratio S_0/b and Decay Parameter λt_c. *ANL Neg. No. 116-91.*

$$t_b/t_c = \frac{(1 - e^{-\lambda t_c}/f) + \sqrt{(1 - e^{-\lambda t_c}/f)^2 + (s_o e^{-\lambda t_c}/b) + (2e^{-\lambda t_c}/f) - 1}}{(s_o e^{-\lambda t_c}/b) + (2e^{-\lambda t_c}/f) - 1},$$

where

$$f = (1 - e^{-\lambda t_c})/\lambda t_c \quad (8)$$

The counting time ratio is shown in Fig. III-31-1 as a function of signal/background ratio and decay fraction.

The already established relative variance for coincidence counting can also be derived from the present viewpoint. One finds for a disintegration rate N with random components a and b in separate detection channels and correlated component c,

$$\frac{\sigma_N^2}{N^2} = \frac{a}{(a + c)^2} + \frac{b}{(b + c)^2} + \frac{(c^2 - ab)^2}{c(a + c)^2(b + c)^2}. \quad (9)$$

Finally, the results are extended to the high precision calibration of a gate duration or delay period, using random pulses in conjunction with a precision oscillator (pulse separation λ and width τ). An additional step is necessary to bring the calculated variance into agreement with the observed distribution. The formula for the delay is

$$D = (\lambda P/g) - \tau, \quad (10)$$

while the relative variance is computed as

$$(\sigma_D^2/D^2)' = h(\sigma_D^2/D^2), \quad (11)$$

for

$$\sigma_D/D = [a(1 + a/g)]^{\frac{1}{2}}[(p - 1)g + a]^{-1}, \quad (12)$$

where h is a truncated portion of the normal distribution, and

$$a = P - (p - 1)g. \quad (13)$$

P is the number of random pulses passed, g is the number of gating events, and p is the number of oscillator pulses which can be passed during each delay gate.

III-32. Random Numbers from Electronic Noise

CHARLES ERWIN COHN

INTRODUCTION

Recent literature[1] has pointed out serious statistical imperfections in the familiar multiplicative-congruential algorithms used for generating pseudo-random numbers in digital computers. Although methods for partially circumventing these imperfections have been suggested, it is appropriate to bring back the old idea[2, 3] of generating random numbers with the aid of physical sources of noise. This approach is attractive because physical noise arises from atomic processes which have no hidden regularities (to the best of our knowledge).

The problem of random-number generation can be reduced to the problem of random-bit generation. Therefore, this paper is concerned primarily with the use of electronic sources of noise to generate populations of random bits having good statistical properties in spite of the imperfections of practical electronics. Some points on the utilization of these bits will be included.

RANDOM-BIT GENERATION

The simplest approach to random-bit generation is to apply wide-band electrical noise to the input of a polarity detector or amplitude discriminator. The output of this discriminator would be sampled each time a random bit is required. If the noise is above its mean value at the instant of sampling, the derived bit would be a one, while if the noise is below its mean value at the instant of sampling, the derived bit would be a zero. The major drawback of this simple scheme is that the bit population would be biased, that is zeros and ones would not be equiprobable, if the discrimination level of the polarity detector did not coincide exactly with the mean level of the noise. It is not practical to set this level to the required accuracy because of statistical error nor to hold it against circuit drift. Schemes have been proposed[4] to adjust the discrimination level automatically in response to the observed bias, but this would clearly introduce long-term serial correlations.

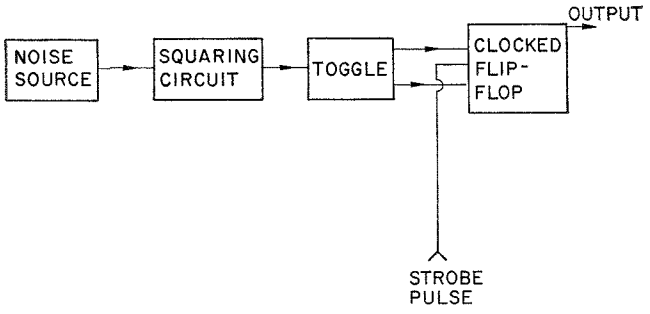

FIG. III-32-1. One Type of Random Generator. *ANL Neg. No. 113-2823 T-1.*

TABLE III-32-I. PROPERTIES OF TWO RANDOM-BIT GENERATORS

Generator	Burr-Brown	Other
No. of bits examined	2,000,060,416	1,916,502,016
Bias (δ)	0.01172 ± 0.00004	0.00193 ± 0.00004
Correlation with previous bit (ϵ)	0.00799 ± 0.00004	0.00312 ± 0.00004

Figure III-32-1 shows an arrangement that has been used to circumvent the above difficulty. As before, a source of wide-band electronic noise feeds an amplitude discriminator which acts as a squaring circuit. The output of the squaring circuit is a square wave with transitions at the discrimination-level crossings of the noise. This square wave is fed to the complementation input of a toggle, which changes state every cycle of the square wave. The operation is largely independent of the discrimination level of the squaring circuit.

The outputs of the toggle go to the steering inputs of a clocked flip-flop. When a random bit is to be read, this flip-flop is strobed. The status of the toggle at that instant is thus sampled and held. In principle, this circuit should show no bias since the toggle should spend equal time in the zero and one state. We shall see to what extent that ideal is realized.

PROPERTIES OF SIMPLE GENERATORS

Tests were made on two random bit generators embodying this arrangement. One was a Burr-Brown Model 4006/25 noise generator module. The other was assembled from a General Radio Model 1390-B noise generator operated at 500-kHz bandwidth, an integrated-circuit amplitude comparator, and two 5-MHz flip-flops in the Honeywell/CCD "S-PAC" series. Table III-32-I shows the measured properties of these generators. Results are shown in terms of probability, that is, the probability of a one bit is $0.5 + \delta$, the conditional probability of a one bit following another one bit is $0.5 + \delta + \epsilon$, the conditional probability of a one bit following a zero bit is $0.5 + \delta - \epsilon$, etc. The limits of standard deviation were estimated from binomial statistics. These data were obtained with the random bit generator connected to the DDP-24 computer.

It can be seen that both generators had significant

s, contrary to our expectations. The explanation for that is believed to lie in the properties of the toggle and the manner in which complementation occurs. As mentioned before, complementation occurs on one transition per cycle of input square wave. The preceding half-cycle must be long enough for the toggle to be primed for the transition. If the half-cycle is too short, complementation will not take place. Now in any actual toggle, the two transistors and their associated components will not be exactly symmetrical so that the time required to prime for a transition in one direction may be slightly longer than that required to prime for the other. Therefore, the shortest half cycle to achieve complementation in one direction may be slightly longer than for the other direction. The input noise will then give a distribution of half cycles such that a certain fraction are sufficient to initiate complementation in one direction but not sufficient for the other direction. Thus, the observed bias will arise. The other generator has a bias almost an order of magnitude better than the Burr-Brown, possibly because the S-PAC flip-flop has a faster response, so that fewer half-cycles fail to initiate complementation.

The bits from each of these generators are not independent but show a significant serial correlation. This can be attributed to two causes, i.e. the finite bandwidth of the noise and the behavior of the clocked flip-flop. Successive noise samplings would be correlated over intervals of the order of the reciprocal of the noise bandwidth. However, in these tests, the interval between bit samplings was much longer (65 μsec) so the observed correlation must have been entirely due to the latter cause. Since the strobe pulses and the toggle transitions are incoherent, there will be a certain number of cases where the time interval between the most recent toggle transition and the fall of the strobe pulse is insufficient to prime the flip-flop so that it will not strobe but will remain at its previous state.

Correlations for these bits were also calculated for lags from 2 to 20 and for 74 selected longer lags with a maximum of 3079 by a method that was previously developed for fast-reactor noise analysis.[5] The correlations were not significantly different from zero to a precision in ϵ from less than 0.00004 at short lags to 0.0004 at the longest lag. Capacitive coupling between the noise source and the squaring circuit eliminates noise components of very low frequency and so prevents serial correlations due to $1/f$ noise.

Bias and Correlation Removal

is evident that the generated bits require further treatment to remove their statistical imperfections. Removing the correlation is relatively easy. For correlations due to limited noise bandwidth, just increase the time interval between samplings. To remove correlation due to flip-flop stickiness, one can strobe the output flip-flops several times for each bit and discard the intermediate samplings.

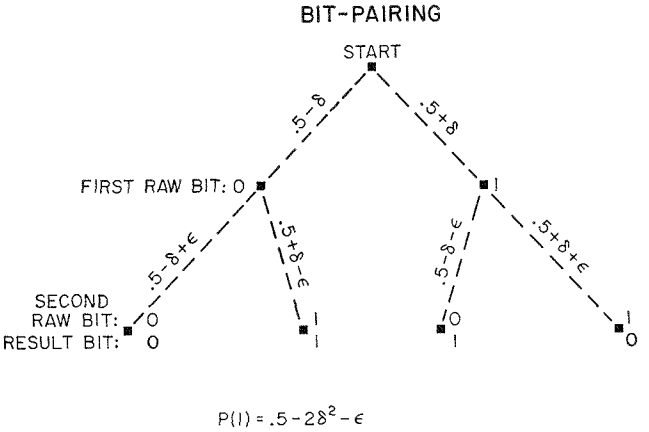

Fig. III-32-2. Flow Diagram of Bias-Removal Scheme. If the Probability of Each Branch is as Shown, the Probability of a Result of 1 is $0.5 - 2\delta^2 - \epsilon$. *ANL Neg. No. 113-2824 T-1 Rev. 1.*

Removal of bias is more difficult but there is an effective procedure that we have developed in which no long-term correlations are introduced. This is merely alternating complementation in which every other bit is changed from a one to a zero or from a zero to a one. It is obvious that such a procedure will yield equal expectations of ones and zeros. However, if the input bits have any great amount of bias significant serial correlations can result. Thus, the alternating complementation is best used as a final processing step, with some other method being used to reduce the bias in preparation for it.

Figure II-32-2 shows a suitable preparatory bias reduction method. Here two raw bits are taken from the generator for every final bit to be produced and the output bit is made equal to the logical difference of the two input bits. In other words, the first input bit is taken, and then the second input bit is used to decide whether or not to complement the first input bit. If the second bit is a one, the first input bit is complemented while if the second input bit is a zero, the first input bit is left unchanged. The probability that the result will be a one is $0.5 - 2\delta^2 - \epsilon$. If the input correlation is sufficiently small, a substantial improvement in bias may be obtained. Note that there is no chance of cancelling off the remaining bias against the correlation because the correlations encountered here are always positive. The output for this process may be used as the input to still another bit pairing step if a further reduction in bias before alternating complementation is required.*

* There is an alternative bit-pairing prescription which might prove advantageous under certain conditions. In this

TABLE III-32-II. BIT PROCESSING TESTS

Generator	Burr-Brown	Other
No. of raw bits taken	1,102,905,344	1,129,709,568
No. of processed bits obtained	551,452,672	564,854,784
Raw bit bias	0.011440 ± 0.000015	0.002084 ± 0.000015
Paired bit bias	−0.000242 ± 0.000021	−0.000447 ± 0.000021
Final bit bias	0.000005 ± 0.000021	0.000018 ± 0.000021
Correlation with previous final bit	0.000025 ± 0.000021	−0.000030 ± 0.000021

These operations would normally be performed by hardware. However, for test purposes they were performed by programming on the DDP-24 computer. Table III-32-II shows the results. Tests were run with both the Burr-Brown and the other random bit generator. One stage of bit pairing proceeded alternating complementation. Each of the generators was strobed three times for each raw bit taken with the two intermediate samplings discarded. Both bias and correlation have been eliminated to within statistics. It is impossible to tell at this level of precision whether the alternating complementation introduced any significant correlation, and hence whether another stage of bit pairing would be desirable.

Correlations at longer lags were checked as previously described and were found to be zero to the precision previously mentioned. In addition, a run test was performed on a sequence of 781,647,873 processed bits from the other generator. The number of runs of consecutive bits of the same value differed from the expected number by 0.150 in standard measure, corresponding to a significance level of 92%.

scheme, input bit pairs with both bits identical, i.e. (0, 0) and (1, 1), are discarded. The pair (1, 0) yields a result of 1 and the pair (0, 1) yields a result of zero (or vice versa). The probability of (1, 0) is $0.25 - \delta^2 - 0.5\epsilon - \delta\epsilon$, while the probability of (0, 1) is $0.25 - \delta^2 - 0.5\epsilon + \delta\epsilon$. Note that these two probabilities differ only in the sign of the last term, so the output bit bias is proportional to $\delta\epsilon$. This scheme, then, although it would require somewhat more elaborate logic than the scheme just described and would reduce the rate of production of bits, offers a smaller output bias whenever $\epsilon < 2\delta$.

USAGE OF RANDOM BITS

These random bits can be either directly sensed by the computer and used as random two-way switches or assembled into words in a word-forming buffer and read into the computer on demand. Most modern computers can read a full word into the accumulator in one to three memory cycles. This is clearly much faster than any algorithmic generator.

There are some situations in which the nonrepeatability of a physical random-number generator is considered a disadvantage. One could use an algorithmic generator for program debugging and checkout and the physical generator for production runs where good statistical properties are most important. For calculation schemes requiring repeated reference to a given sequence of random numbers, the sequence could be recorded on a bulk storage device. With suitable blocking and buffering techniques, no speed need be lost, especially since certain operations, such as conversion to floating point, would not have to be repeated.

REFERENCES

1. G. Marsaglia, *Random Numbers Fall Mainly in the Planes*, Proc. Nat. Acad. Sci. **60**(5), 25 (1968).
2. K. D. Tocher, *The Art of Simulation*, (D. Van Nostrand, Princeton, New Jersey, 1963), Chapter 5.
3. Y. A. Shreider, *Method of Statistical Testing—Monte Carlo Method*, (American Elsevier Publishing Co., New York, 1964), Chapter VI, Section 4.
4. D. R. Koehler, J. T. Grissom and R. G. Polk, *Generator of Mathematically Random Entities*, U. S. Patent 3,445,591 (May 20, 1969).
5. C. E. Cohn, *Reactor-Noise Studies with an On-Line Digital Computer*, Nucl. Appl. **6**, 391 (1969).

III-33. Gamma-Ray Spectral Measurements at JANUS

RAYMOND GOLD and K. E. FREESE

Following modification of the JANUS reactor, gamma-ray spectra were measured in the High Dose Room using Compton recoil gamma-ray spectroscopy.[1] A floor plan of the JANUS High Dose Room is displayed in Fig. III-33-1. A series of gamma spectra measurements was carried out 96 cm above floor level at positions, A, B, C, D, and E.

A second series of measurements was conducted to determine the effects of loading the High Dose Room with a large number of animals. To simulate the mod-

ting effects of mice, one ounce polyethylene bottles were filled with water sufficient to give 3 gm of total hydrogen. (This is approximately the hydrogen content of a 30-gm mouse.) Four hundred fifty-six (456) such "phantom mice" samples were distributed in a uniform array across the High Dose Room from floor to ceiling. The location of this array is depicted in Fig. III-33-1. Measurements were repeated at positions A, B, and E with this phantom configuration.

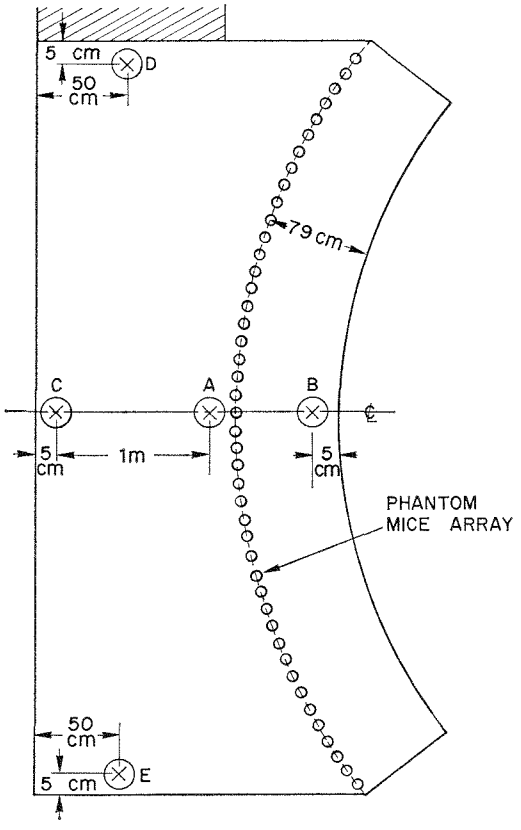

FIG. III-33-1. Layout of the High Dose Room at JANUS. Gamma Spectra were Measured at Positions A–E. All Measurements were Carried Out at a Height of 96 cm from Floor Level. For the Phantom Configuration, the Depicted Array of Phantom Mice Extended from Floor to Within 37 cm of the Ceiling with a 10 cm Vertical Separation Distance Between Phantoms. *ANL Neg. No. 116-460.*

TABLE III-33-I. GAMMA DOSE RATE AT JANUS

Position	Energy Interval, MeV	Dose per Watt of Reactor Power, mR/hr
A	0.28–2.2	0.15
B	0.29–2.2	0.26
C	0.26–2.2	0.084
D	0.26–2.2	0.075
E	0.29–2.2	0.046
Phantom Experiment		
A	0.26–2.2	0.18
B	0.26–2.2	0.30
E	0.26–2.2	0.066

Experimental results are shown in Figs. III-33-2 through III-33-6, where the absolute gamma spectra (photons/cm^2-sec-MeV) per watt of reactor power are displayed for positions A through E, respectively. The dominant peaks arising in these spectra can be attributed, in the main, to gamma emission from either fast neutron inelastic scattering in lead or direct neutron activated gamma-rays from lead. (The external surface of the modified High Dose Room consists of a 4-in. thick lead layer.)

Gamma dose rate is also available from these data.[2] Table III-33-I. summarizes the dose rate (mR/hr) per watt of reactor power in the designated gamma-ray energy regions for positions A–E.

REFERENCES

1. R. Gold, *Compton Recoil Gamma-Ray Spectroscopy*, Nucl. Instr. Meth. **84**, 173–194 (1970).
2. R. Gold and I. K. Olson, *The Analysis of Compton Continuum Measurements*, ANL-7611 (1970).

(FIGS. III-33-2–33-6 on pp. 346–349)

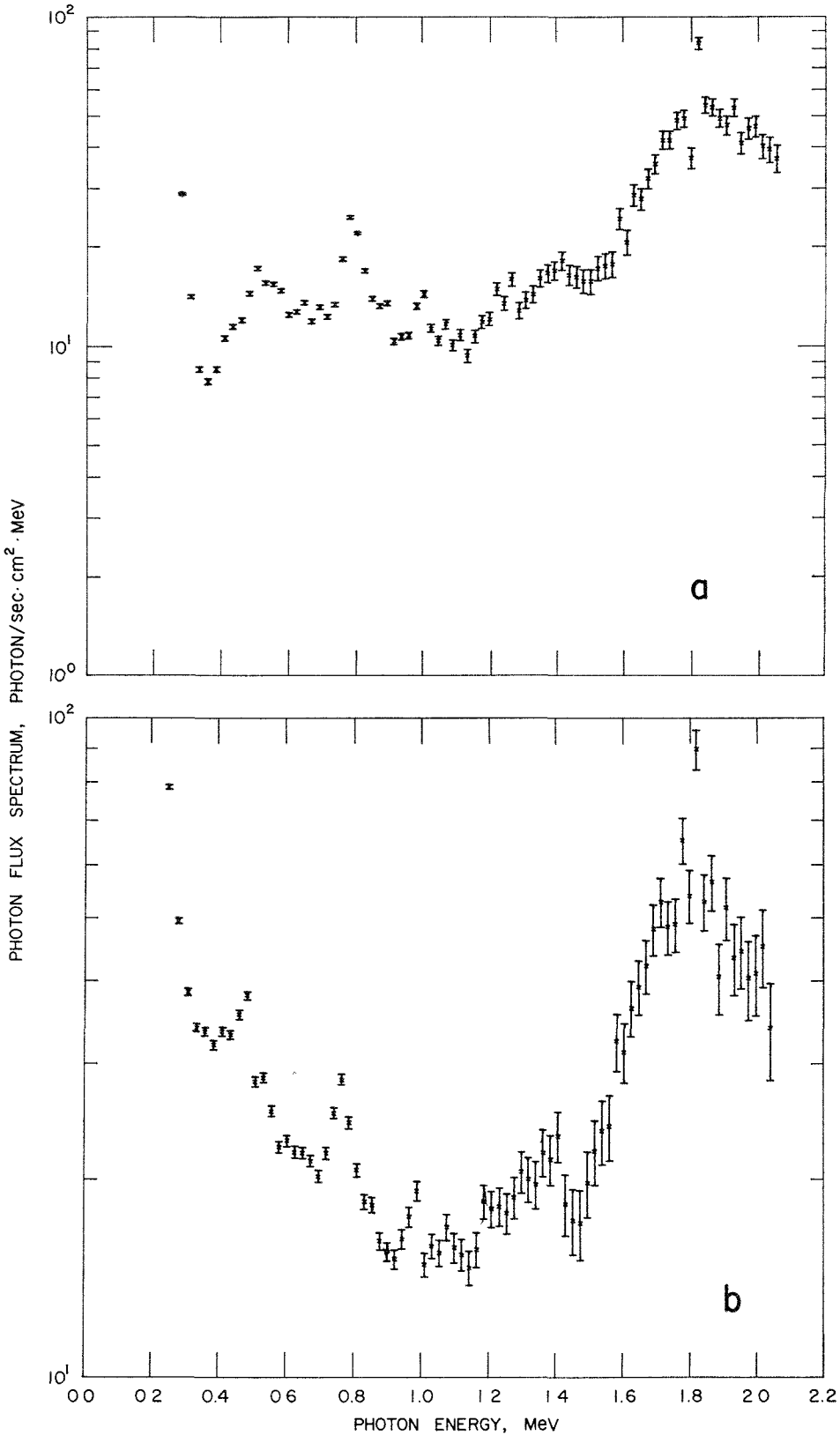

FIG. II-33-2. Absolute Gamma Spectrum per Watt of Reactor Power at Position A: (a) Normal Configuration; (b) Phantom Configuration. *ANL Neg. No. 116-452.*

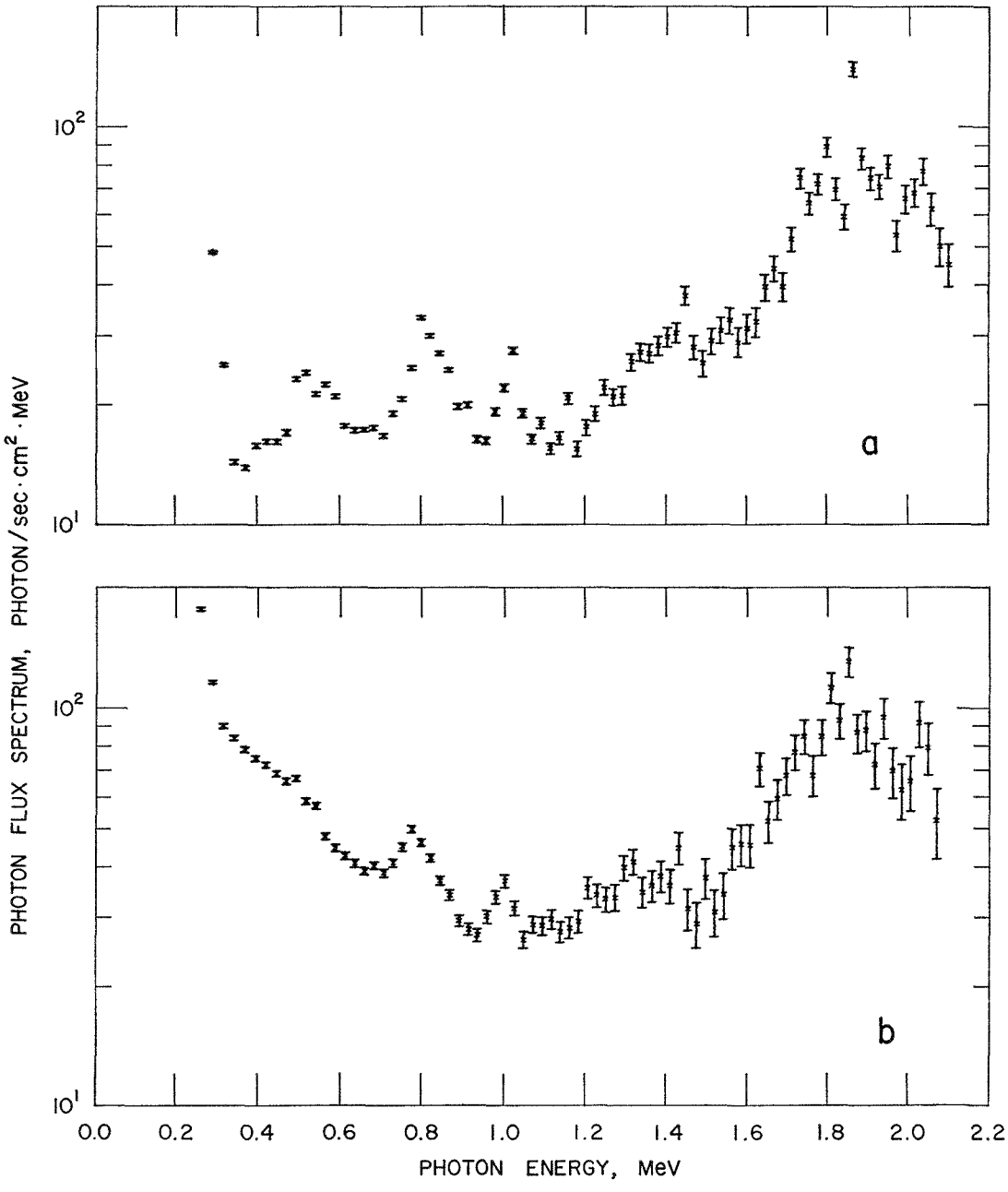

FIG. III-33-3. Absolute Gamma Ray Spectrum per Watt of Reactor Power at Position B: (a) Normal Configuration; (b) Phantom Configuration. *ANL Neg. No. 116-445.*

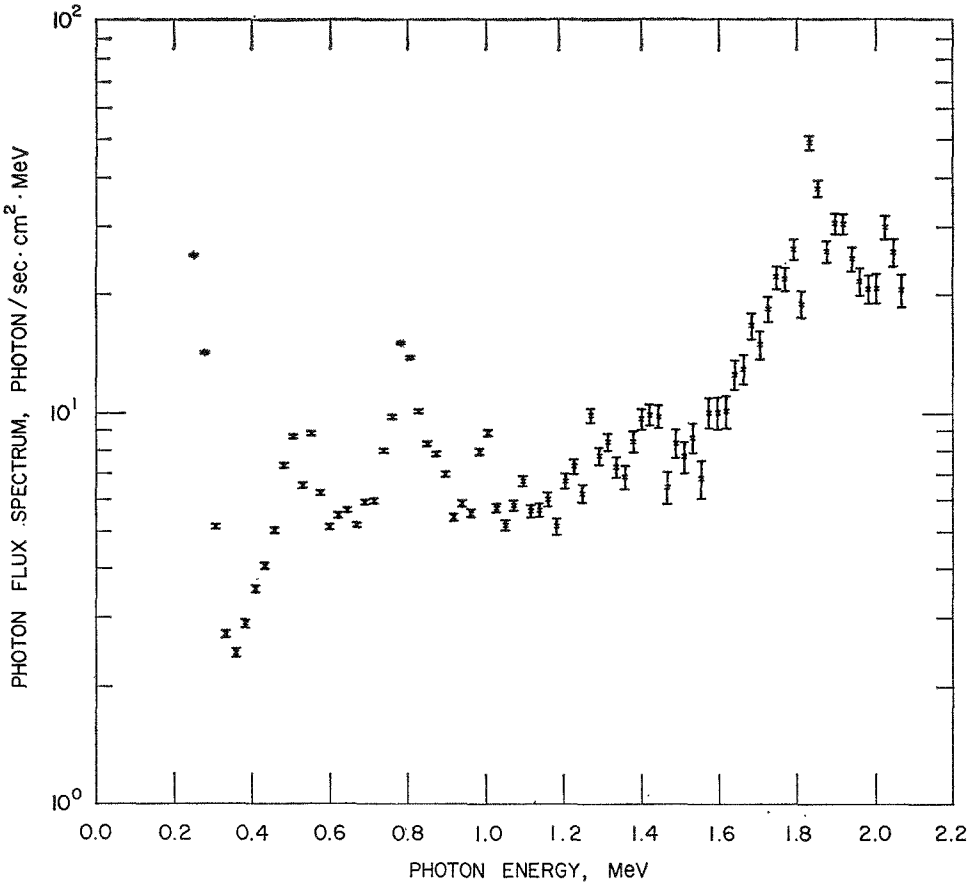

FIG. III-33-4. Absolute Gamma Spectrum per Watt of Reactor Power at Position C. *ANL Neg. No. 116-446.*

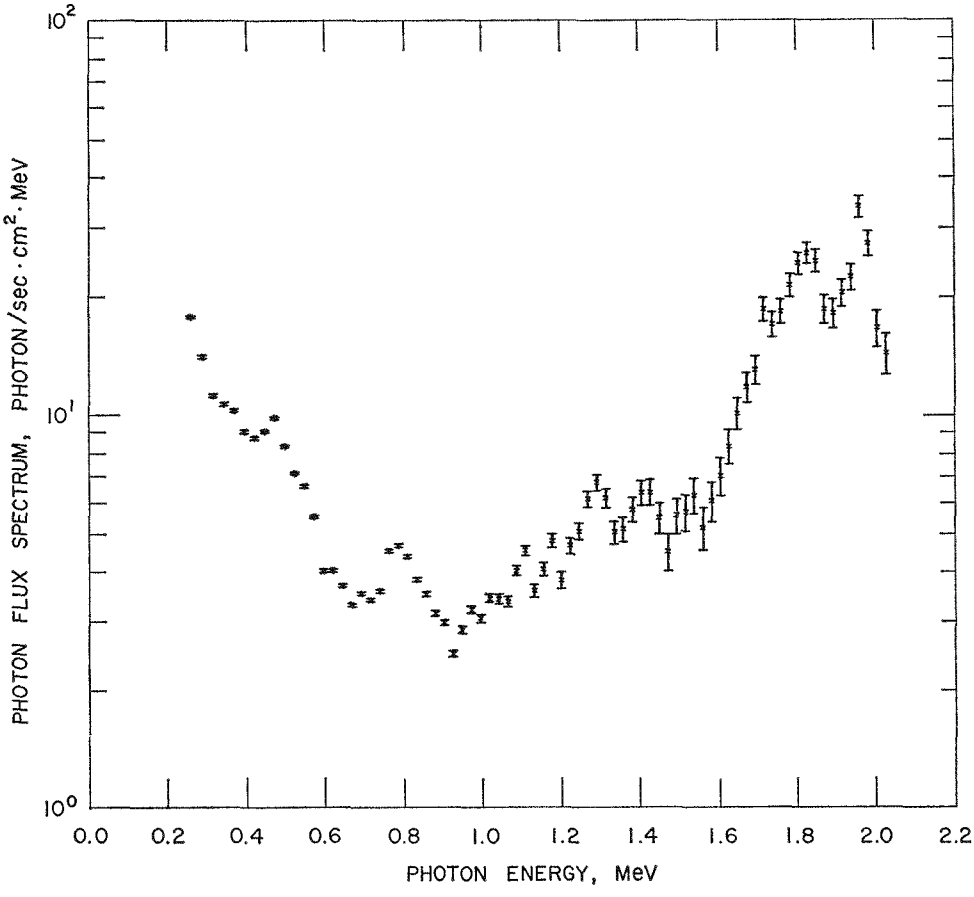

FIG. III-33-5. Absolute Gamma Spectrum per Watt of Reactor Power at Position D. *ANL Neg. No. 116-463.*

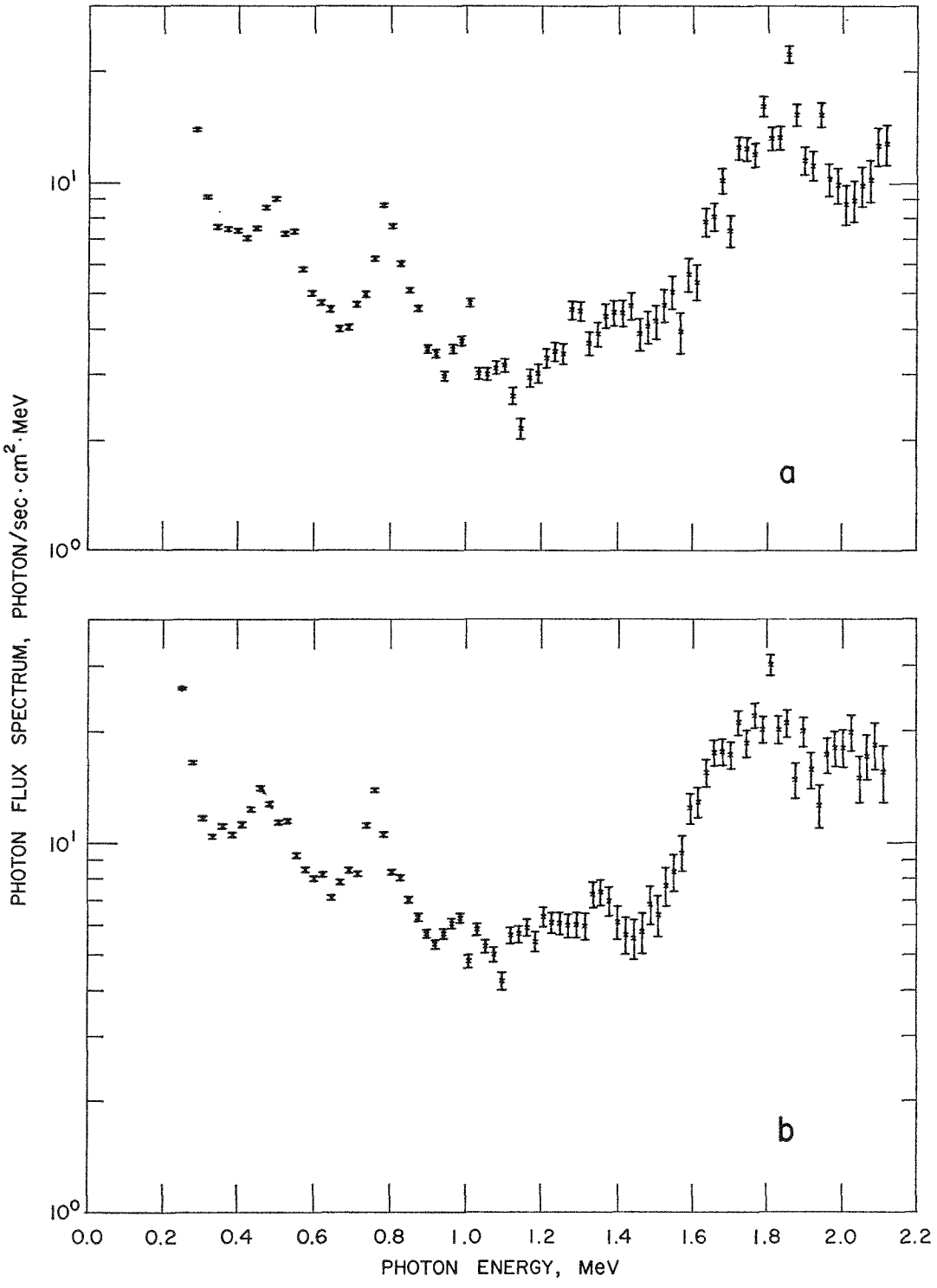

FIG. III-33-6. Absolute Gamma Spectrum per Watt of Reactor Power at Position E: (a) Normal Configuration; (b) Phantom Configuration. *ANL Neg. No. 116-462.*

III-34. A Neutron Spectrum Map of the JANUS Irradiation Facility Using Proton-Recoil Proportional Counters

E. F. Bennett and T. J. Yule

Introduction

Measurements of fast neutron energy spectra in experimental reactors have been carried out at Argonne National Laboratory since 1965.[1] The technique, using proton-recoil proportional counters with gamma discrimination, is applicable to the determination of low intensity degraded fission neutron spectra in the energy range from 1 keV to a few MeV.

Although the developmental effort has been directed towards critical assembly experimentation, the method may be applied to the study of neutron spectra in any environment containing modest (order of 10^4 n/cm^2-sec) fast neutron fluxes. The application of this method to shielding measurements, to the determination of neutron spectra from standard sources, and to neutron flux mapping in biologically interesting environments is certainly feasible.[2] Since biological effects of radiation are not related in a simple way to an integral quantity, such as the kerma, it is desirable to have a differential measurement of neutron spectrum.

The original High Flux Irradiation Room of JANUS[3] had design problems which limited the usefulness for biological research. The neutron energy spectrum contained relatively more slow neutrons than were desired and the neutron-to-gamma ratio was unnecessarily low. High residual gamma-ray radiation from surfaces of the room and neutron leakage around and through the shutter interfered with personnel access for rapid specimen placement or removal. These various deficiencies were deemed sufficiently serious to justify a significant redesign effort on the high flux cell.

The JANUS facility, in its present form,[4] provides a copious flux of fast neutrons (with few thermals) over a large and readily accessible irradiation area. Analyses of the expected neutron flux spectrum were made[5,6] and experiments other than the one reported here have been done in which both neutron spectra[7] and gamma spectra[8] were investigated. Mappings of neutron and gamma doses were also performed.[9] In this paper we describe the technique of neutron spectroscopy with proton-recoil counters as it was used in the JANUS measurements and present the results of a limited spatial mapping of the spectrum over the irradiation room. We also compare a measured spectrum with a calculated spectrum[6] based upon a considerable oversimplification of the geometrical complexities of the cell. A more sophisticated (Monte Carlo) study of the neutron spectrum is in progress[7] and will be reported elsewhere.

Design of the Janus Facility

Figure III-34-1 is a vertical section of the cell and illustrates the combination of lead and borated hardboard used along walls and floors to minimize the gamma dose during neutron irradiation, as well as to shield personnel from wall-activation gammas upon entering the room after a power run. The lead liner also has the effect of reducing the low energy component of the neutron spectrum over that which would exist in the absence of lead by allowing fast neutrons to be returned to the room with little energy loss. The location of the U-235 converter plate and the shutter, which is used to isolate the cell for personnel access, is also shown. Thermal neutrons from a graphite pedestal coupled to the JANUS reactor convert to fast neutrons in the U-235 plate and these fill the irradiation cell. Lead, interposed between the converter and cell, serves to reduce gamma fluxes which occur during neutron irradiation of the converter, as well as gamma fluxes present when the thermal-neutron-absorbing shutter is in place. The solid circles in Fig. III-34-1 indicate detector locations.

Figure III-34-2 is a horizontal section of the cell. The solid rectangles, which represent detector placements, also indicate the orientation of the cylindrical probes. The area indicated by "specimen line" is approximately where most of the intended biological irradiations are to be made. Spectrum measurements were made over the whole cell, however, in order to ascertain the sensitivity of spectral shape and amplitude to cell position.

It should be noted (see Fig. III-34-2) that all the surfaces have a lead inside liner with borated hardboard or boro-bauxite concrete behind the liner, except for the door.

Experimental Method

Detector

Figure III-34-3 is a photograph of the proportional counter probe used. The detector and a preamplifier were mounted in a 2 × 2 in. box or stainless steel $\frac{1}{32}$

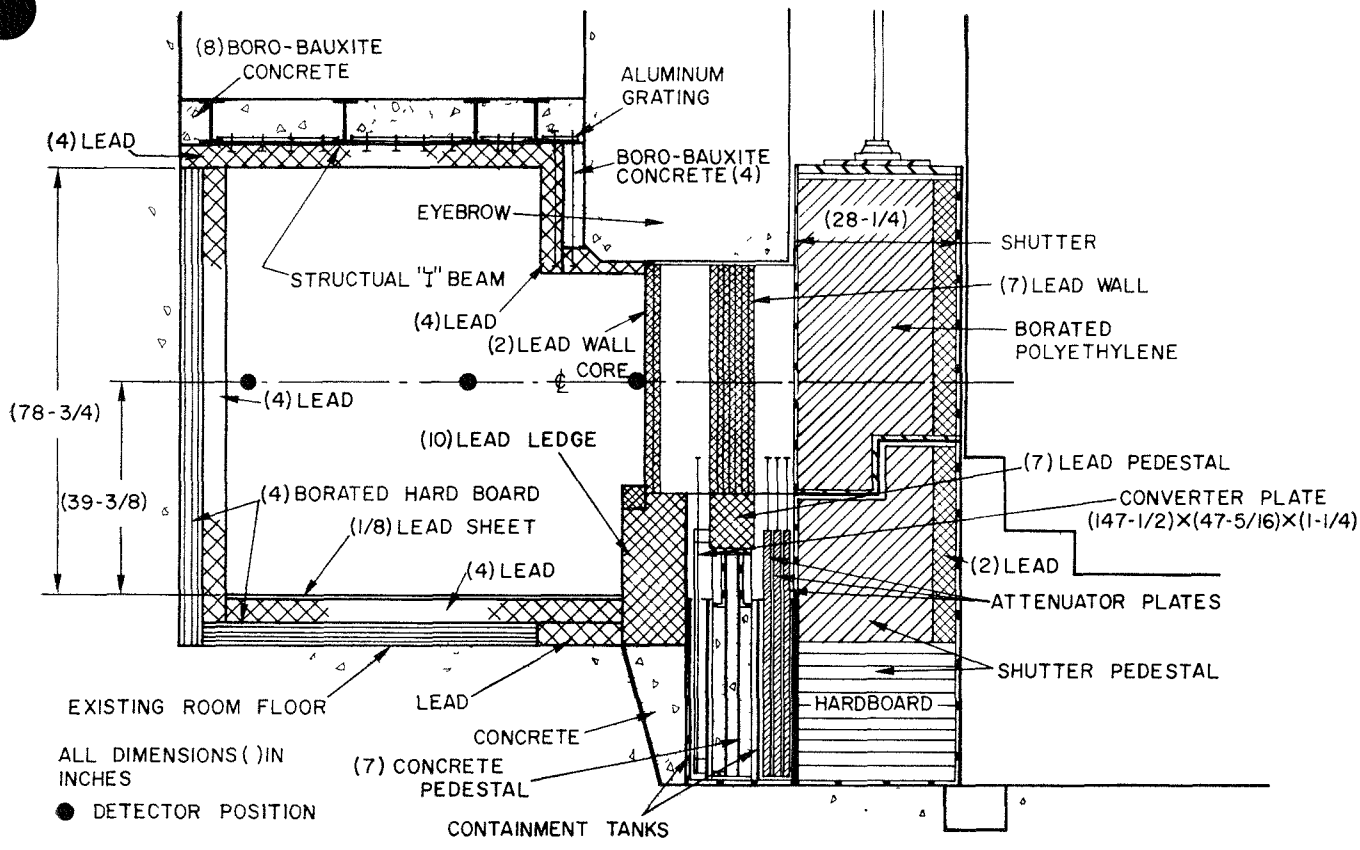

FIG. III-34-1. Vertical Section of the JANUS High Flux Irradiation Cell. The Solid Circles Indicate Detector Locations. *ANL Neg. No. 116-332.*

in. thick, which was held in position by a light aluminum holder.

The cylindrical counting tubes (stainless steel) had an inside diameter of 1 in. and an effective length of 3 in. The wall thickness was 16 mils and the anode (1 mil stainless steel wire) was positioned by a 10 mil diam brass field definition tube.

Two identical detectors were used for each spectrum measurement. One contained predominantly hydrogen gas filled to a pressure of about 80 psia. The spectrum below about 100 keV was measured with the hydrogen filling. The other detector contained about 90 psia of methane and was used for the higher energy portion of the spectrum up to about 3 MeV. The methane filling with increased stopping power to protons was less subject to wall- and end-effect events at the higher energies. It is possible to extend measurements somewhat further in energy than was done here and this would have been desirable since a significant amount of the dose is contributed by neutrons above a few MeV.[10] Counters with greater stopping power, needed for measurements at higher energies, were not available. The detectors used were intended for work in softer spectra. Hydrogen gas is preferable for measurements at the lower energies. Only a slight variation in W (keV per ion pair) exists for protons in hydrogen and there is no contribution to the measured pulse height spectrum due to neutrons scattering from carbon, as occurs to some extent with methane gas fillings.

The detectors were calibrated by the addition of a small amount of nitrogen gas and by observing protons from the reaction $N^{14}(n, p)C^{14}$ when the counters were exposed to thermal neutrons. In this way an absolute relationship between pulse height and proton energy was established for each chamber.

DATA REDUCTION

After accumulation of a complete spectrum of recoil protons several corrections were made for various effects discussed below.[11]

The Variation of W

The desired spectrum of recoil protons per unit energy is obtained from measurements (which produce a spectrum per unit ionization) by dividing by the keV per ion pair W. This is a slowly varying quantity, even at quite low energy, but does require consideration.

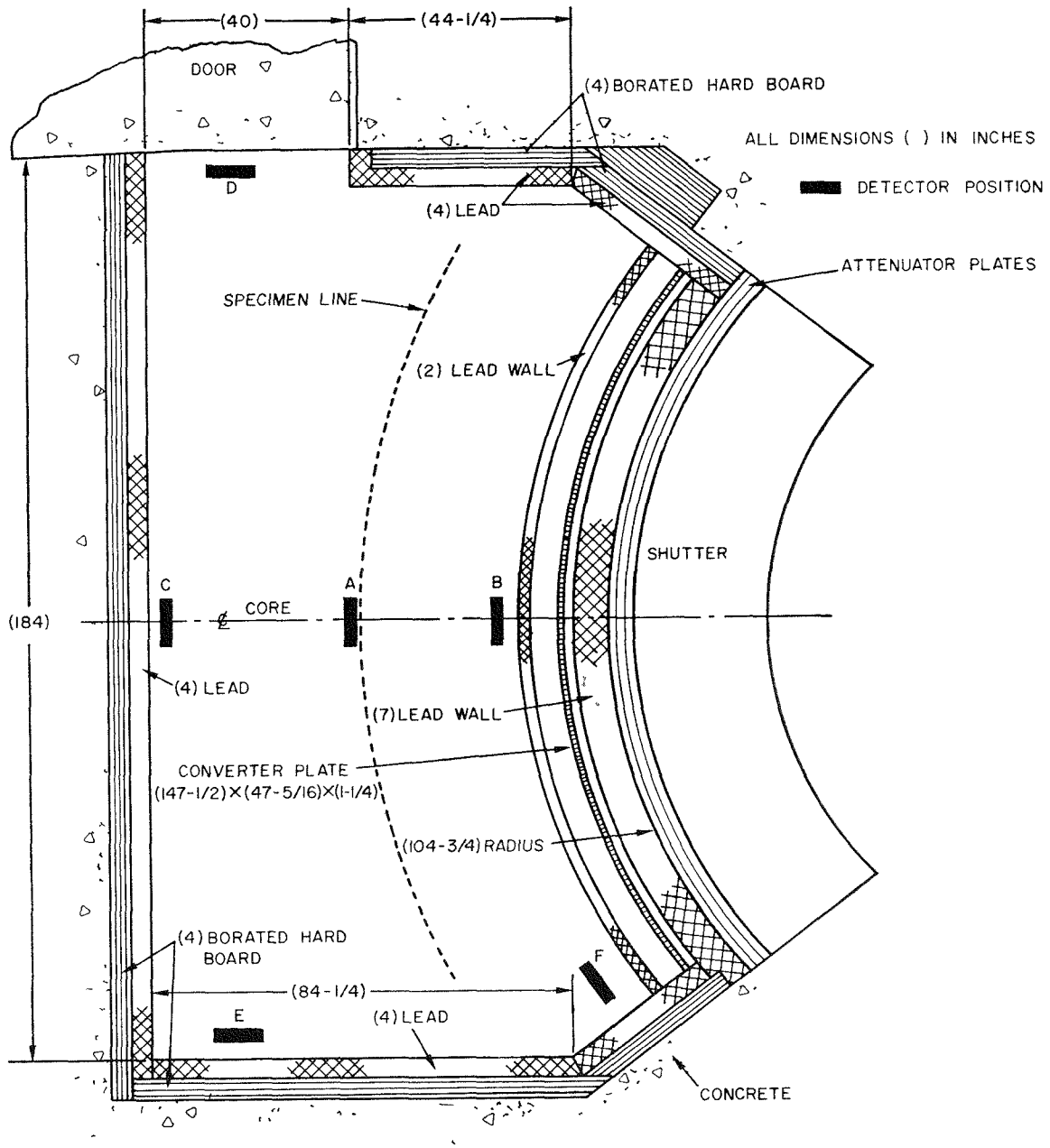

FIG. III-34 2. Horizontal Section of the JANUS Cell The Solid Rectangles which Represent Detector Placements also Indicate the Orientation of the Cylindrical Probes *ANL Neg No 116-333*

Wall and End Effects

The track length of recoil protons will increase (and rather rapidly) with energy until there exists a high probability for truncation where the entire track is not contained in the effective detector. A procedure has been worked out to evaluate truncation and to estimate its significance for measured data. The effect of this correction upon the measured JANUS neutron spectra over the energy region up to a maximum of about 2 MeV, was ascertained as of little consequence and the correction was not applied in any of the reported results.

Carbon-Recoil

The carbon component in methane-filled counters will undergo scattering by fast neutrons and the ionization produced cannot be distinguished from that produced by recoil protons. This effect, which is usually small, does require that a correction be made.

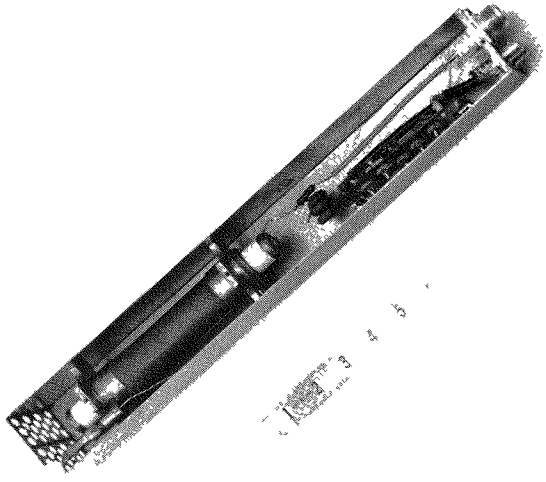

FIG. III-34-3. Photograph of the Detector Probe and Preamplifier Used for JANUS Neutron Spectroscopy. *ANL Neg. No. 900-405.*

Electric Field Distortion

The simple approach used to desensitize counters near the end by thickening the anode (an increase from 1 to 10 mils) is not completely satisfactory since a distortion of internal field lines occurs. The electrical volume of the detectors is not exactly identical with the mechanical volume and the response departs from ideal. The effect may be calculated, however, and with a detailed understanding of the internal field organization a correction for the effect can be made.

After the various corrections for systematic effects mentioned above were made, proton recoil distributions $D(E)$ (per unit energy) were converted into neutron spectra $\phi(E)$ (per unit lethargy) by differentiation according to the well known prescription

$$\phi(E) = -\frac{1}{NT}\frac{E^2}{\sigma(E)}\frac{dD(E)}{dE}, \qquad (1)$$

where NT is the product of the hydrogen atom number in the effective counter volume by the time duration of the measurement, and $\sigma(E)$ is the neutron-proton cross section which is well known experimentally. The experimental derivative is determined by a least squares line fit to segments of the proton spectrum, and the statistical error in the neutron spectrum is that associated with counting statistics in the line fit.

The statistical accuracy obtained in the measured spectrum is generally about ± 3%. The energy resolution varies from something in the vicinity of 12% at the higher energy upward to almost 30% in the vicinity of 1 keV where statistics in ionization become poor and affect resolution accordingly.

A maximum detector counting rate of about 10,000 counts/sec was maintained at each of the positions measured by varying reactor power. A B-10 counter was placed in the cell and used to monitor power independently during a measurement.

RESULTS

The top view of the irradiation cell shown in Fig. III-34-2 indicates the various locations at which measurements were made. Table III-34-I contains the distances of the counter center from various cell surfaces. The spectrum at position A was measured after water-filled containers (simulating mice) were suspended as a semi-uniform vertical sheet from the ceiling along the line indicated. The average surface density was 0.020 gm/cm² of hydrogen, 0.046 gm/cm² of carbon, and 0.10 gm/cm² of oxygen.

Figures III-34-4 through III-34-10 contain the spectrum measured at each position; Fig. III-34-5 is the result at position A with the simulated mice in place. The absolute ordinate scale (flux per unit lethargy) is included at each position; all measurements are referred to a reactor power of 1 W. Some variation in flux intensity and spectrum occurred, depending upon location of the detector in the cell. However, most specimen irradiations would be done over a region where little spectral change was observed. The "A-mice" measurement provides evidence of the flux perturbation introduced by samples undergoing irradiation. There is an observable, although slight, softening of the spectrum which is consistent with some degradation of neutron energy by scattering on the sample material. There is also a noticeable softening of the spectrum as one moves away from positions near the converter to positions near the back of the cell.

One prominent feature which varies systematically with location is the resonance dip seen at about 400 keV. This is probably due to neutrons which are re-

TABLE III-34-I. COUNTER CENTER DISTANCES FROM SPECIFIED CELL SURFACES

Position	Distance[a]
A	On the center line; 30⅜ in. from back wall
B	On the center line; 6¾ in. from curved (2) lead wall
C	On the center line; 2 in. from back wall
D	19⅝ in. from back wall; 2 in. from door
E	19⅝ in. from back wall; 2 in. from side wall
F	9⅞ in. from curved (2) lead wall; 9⅞ in. from short side wall

[a] All measurements were made at the center of the core, 39⅜ in. above the floor.

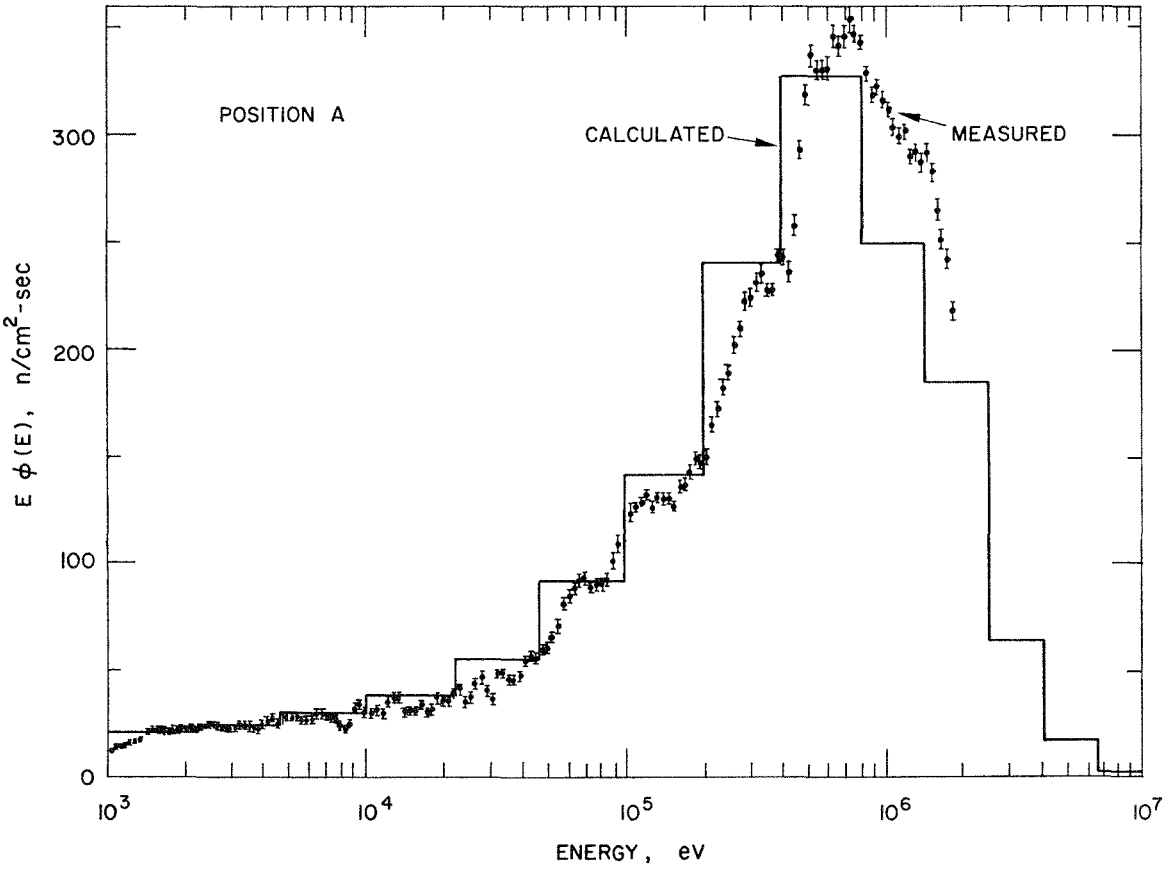

FIG. III-34-4. Position A Neutron Spectrum. The Points are the Measured Values and the Histogram is a Calculated Spectrum. Spectra are Area-Normalized to Each Other from 1 keV to 2 MeV. *ANL Neg. No. 116-326.*

turned through the lead wall liner from underlying concrete. A large scattering resonance in oxygen exists at about 400 keV and the neutron flux returned by the ceiling and door will be displaced at this energy. Essentially no evidence of this return exists at position B (close to the face). Since position B is nearest to the fission converter source relatively fewer neutrons associated with concrete return are present. Position D, on the other hand, is adjacent to the unshielded concrete door and the effect of the oxygen scattering resonance here is quite pronounced.

Some other structure appears to exist in the spectrum; this may involve scattering resonances in the lead room liner and also resonances in steel in the detector and in the container used to hold the detector in place (see Fig. III-34-3).

Figure III-34-4 also contains a histogram, obtained from Ref. 6, representing a calculation of the spectrum. The calculation was performed using a one-dimensional discrete ordinate transport theory code and a multi-energy group cross section set. The one-dimensional approximation is not expected to be especially appropriate to the actual JANUS cell; a relevant three-dimensional calculation with good energy resolution is not feasible. Monte Carlo methods are capable of treating the configuration exactly and are being investigated at present.[7] However, the shape of the energy spectrum is probably more strongly influenced by the materials in the environment than by the precise geometrical arrangement of these materials. The reasonably good agreement as to spectrum shape between theory and calculation in Fig. III-34-4 is presumably evidence of this. Normalization of the calculated histogram to the measurement in Fig. III-34-4 was made by forcing integral fluxes from 1 keV to 2 MeV to agree. Since the one-dimensional calculation predicts the same flux throughout the cell and since measurements indicate systematic changes in both shape and intensity it must be admitted that the comparison of position A results in Fig. III-34-4 leaves much to be desired. The essential qualitative features of the JANUS spectrum, even allowing for this objection, are quite reasonably predicted by the simple calculation of Ref. 6.

CONCLUSIONS

The results of proton recoil measurements of neutron flux in the irradiation cell of JANUS have generally

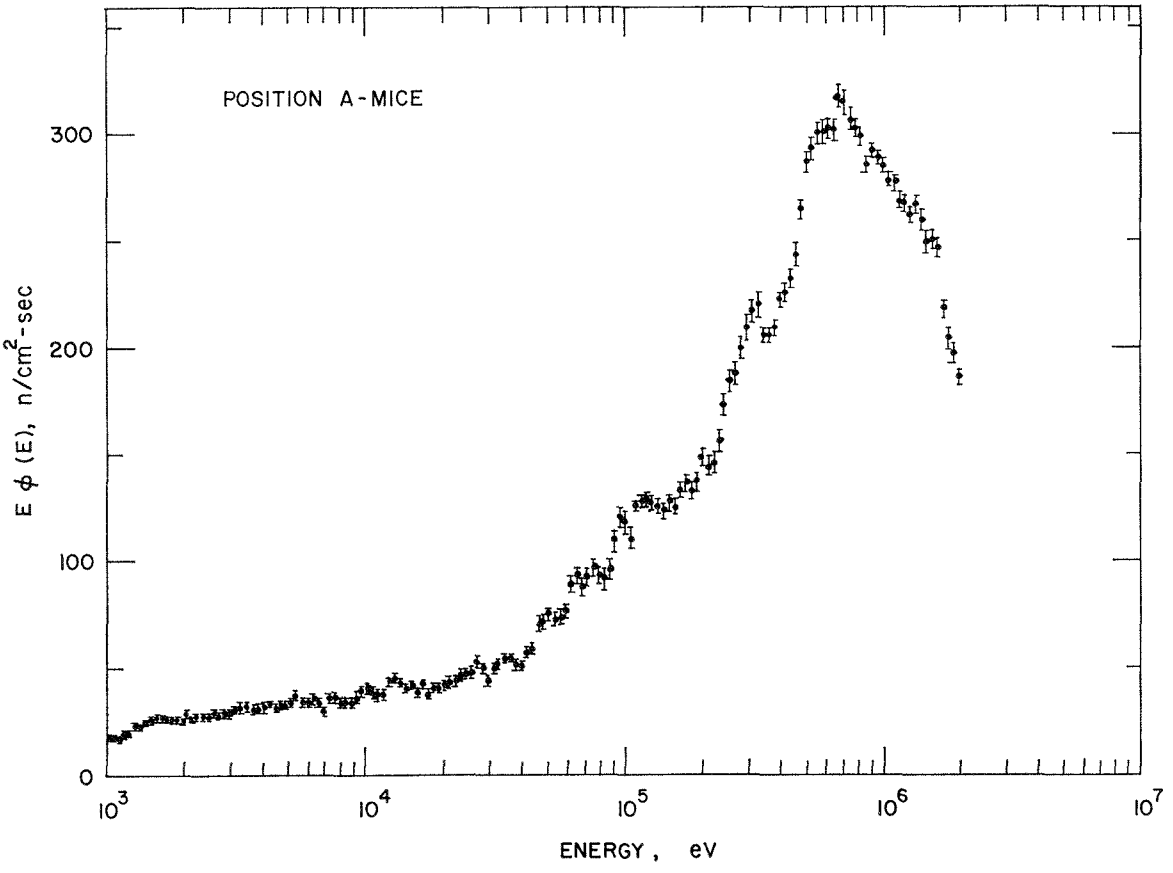

FIG. III-34-5. Position A with Simulated Specimen Loading. The Ordinate is the Same as for Unperturbed Position A Measurement. *ANL Neg. No. 116-327.*

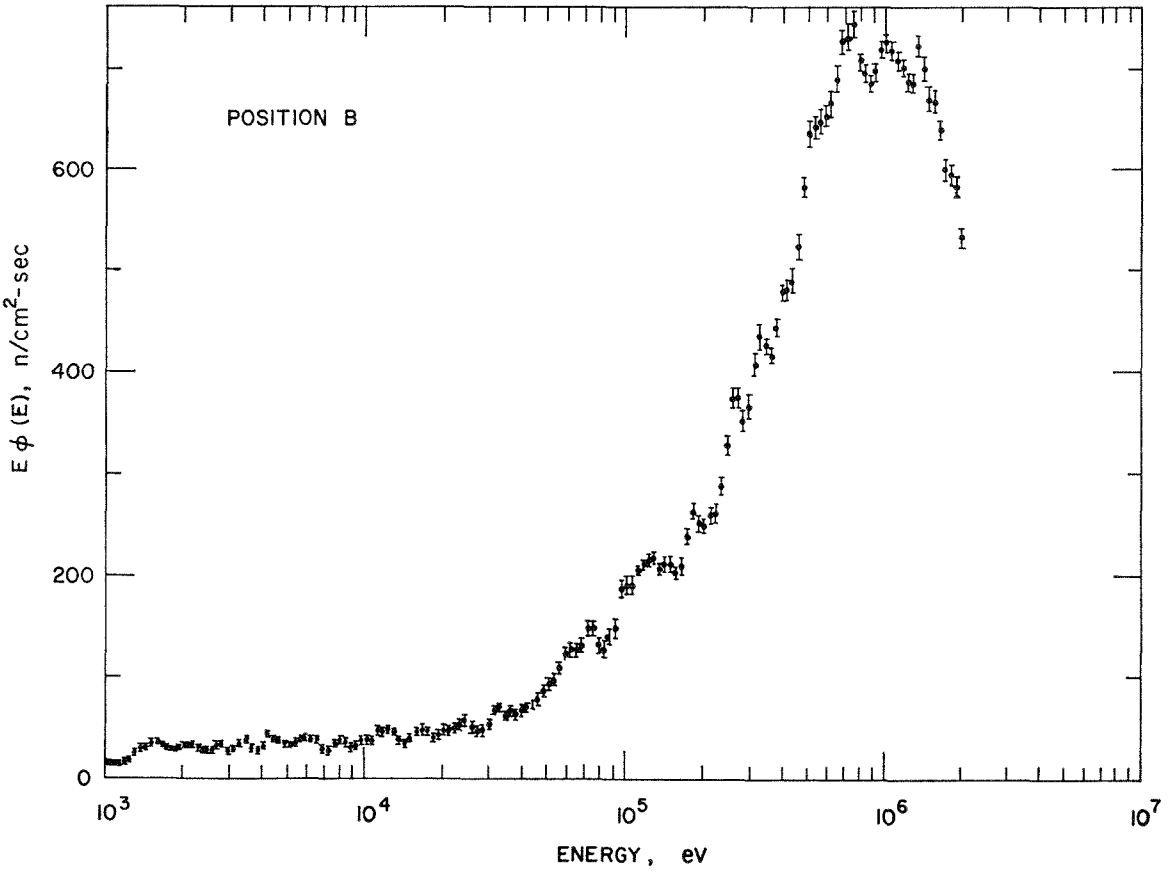

FIG. III-34-6. Position B Measured Neutron Spectrum. *ANL Neg. No. 116-328.*

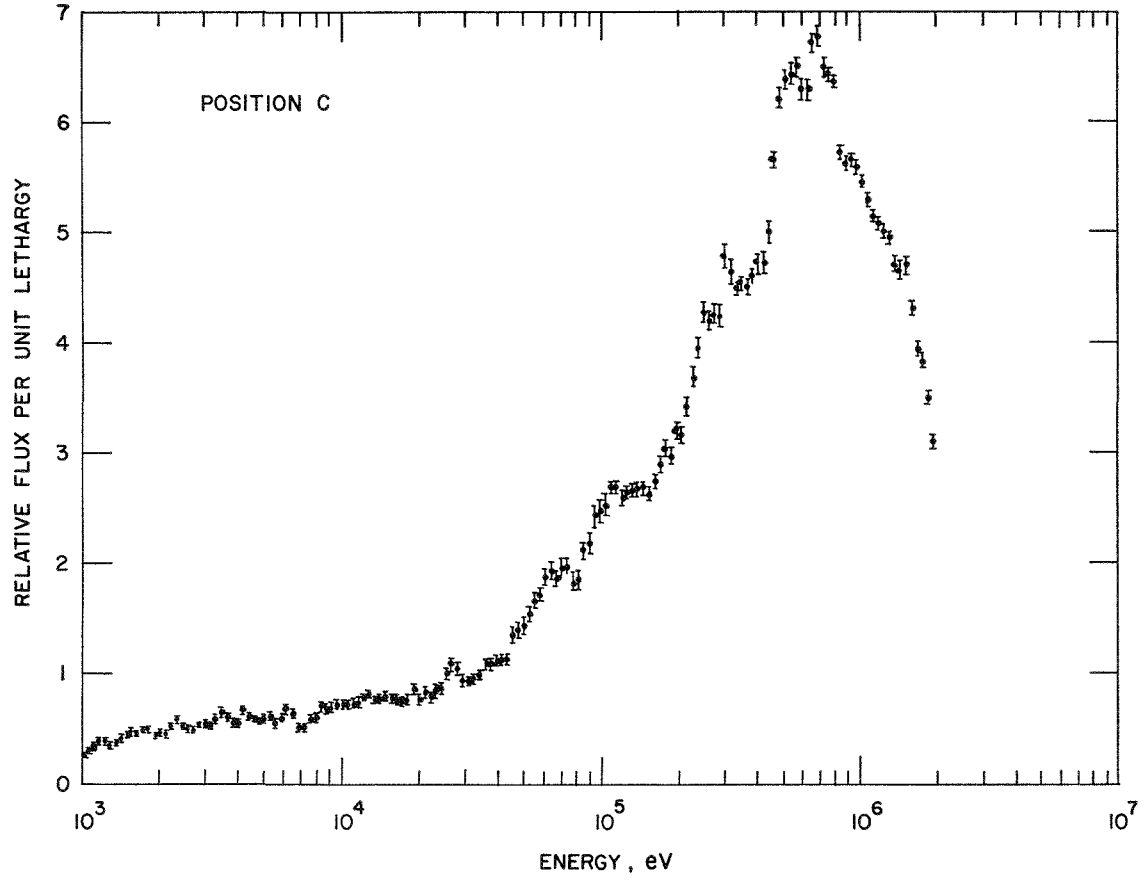

FIG. III-34-7. Position C Measured Neutron Spectrum. *ANL Neg. No. 116-318.*

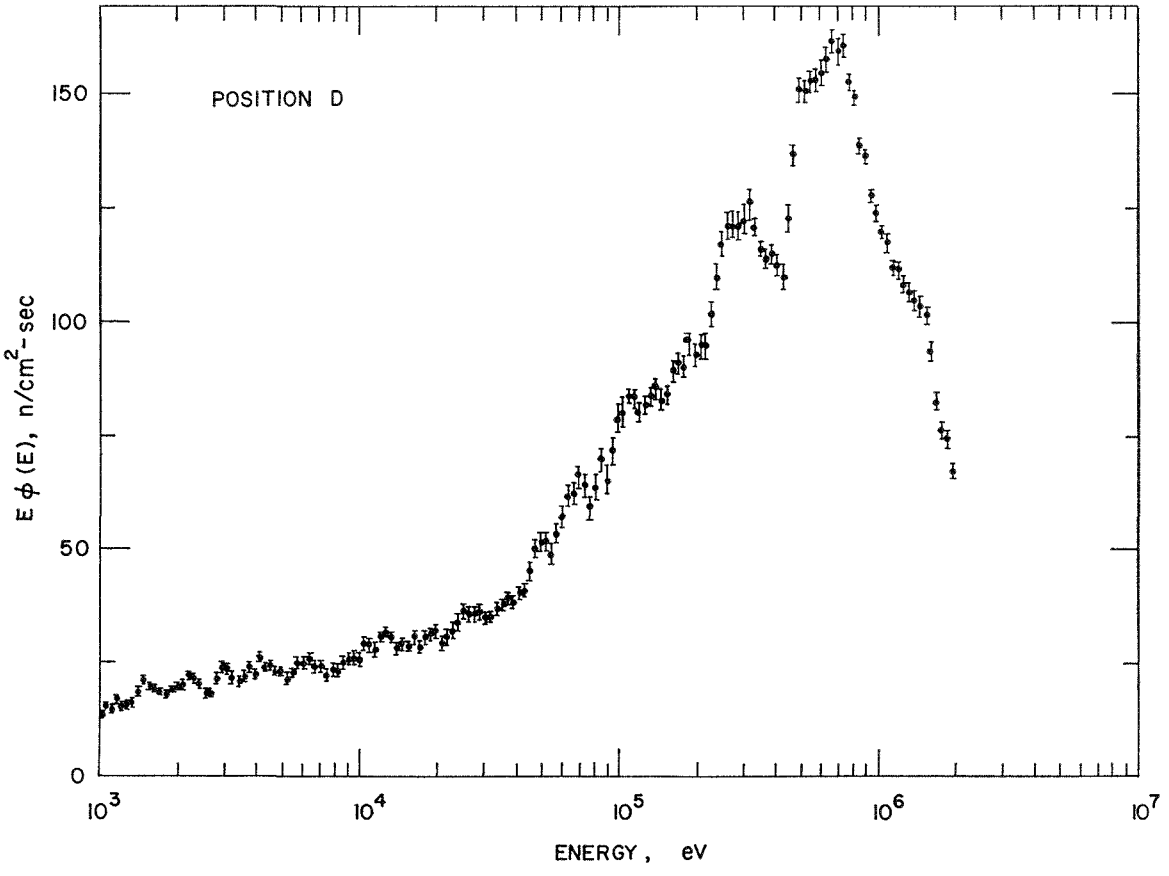

FIG. III-34-8. Position D Measured Neutron Spectrum. *ANL Neg. No. 116-329.*

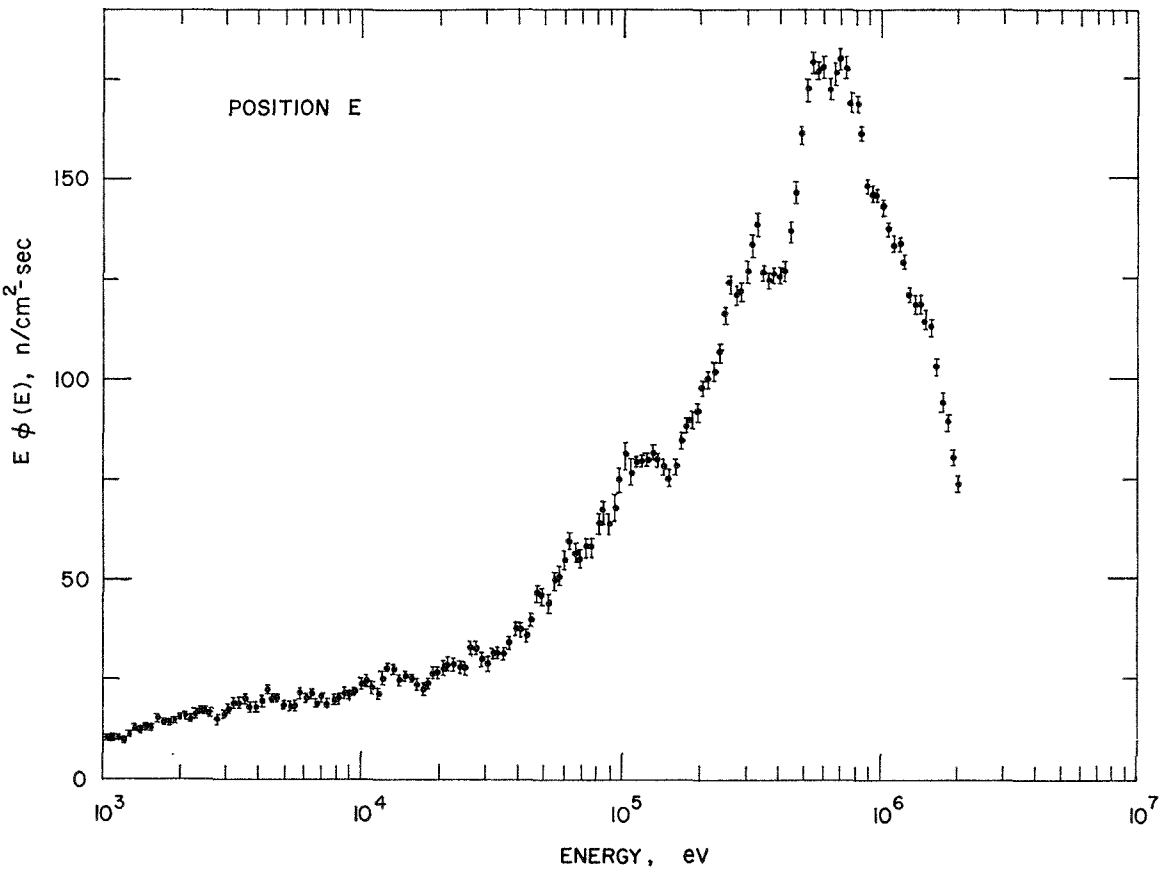

FIG. III-34-9. Position E Measured Neutron Spectrum. *ANL Neg. No. 116-330.*

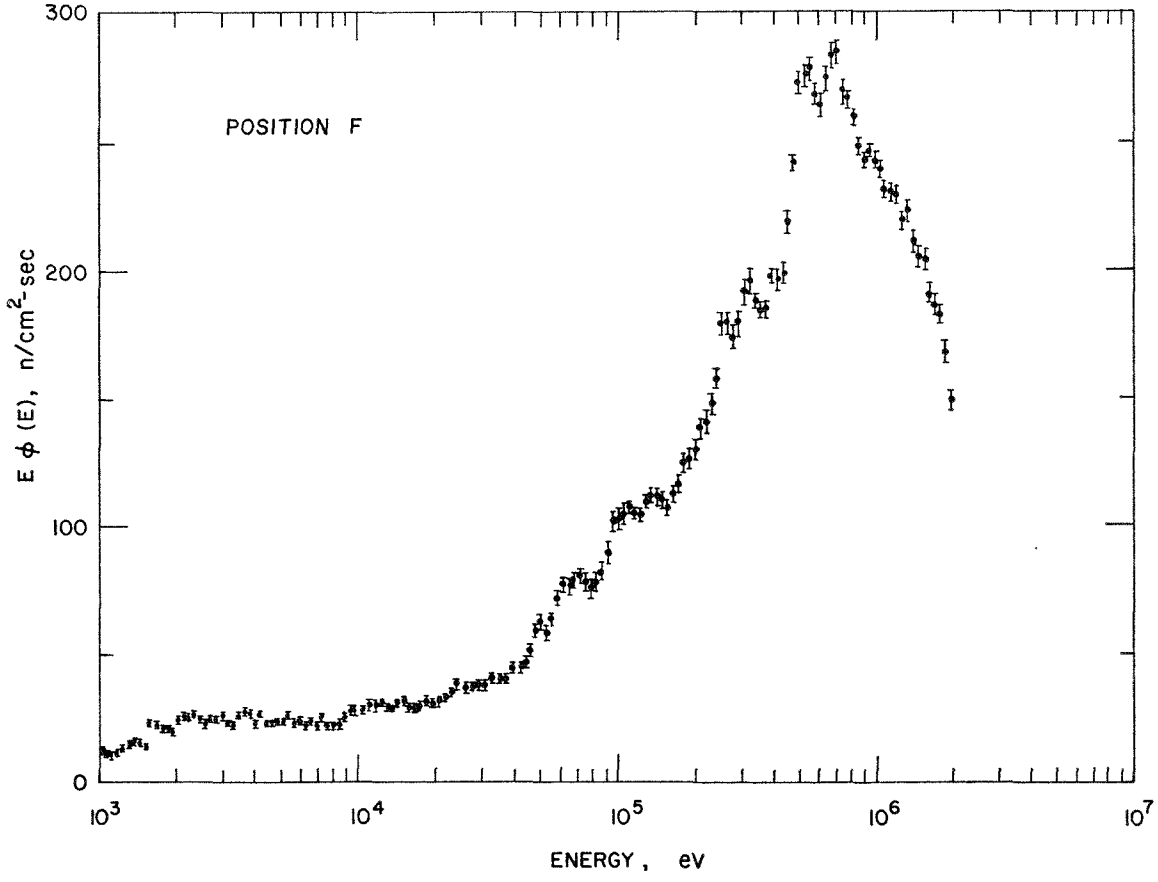

FIG. III-34-10. Position F Measured Neutron Spectrum. *ANL Neg. No. 116-331.*

confirmed the design predictions as to spectral shape above about 1 keV. The effect upon the spectrum of specimens undergoing irradiation has been observed and the dependence of spectrum upon position in the room has been recorded. The results of these (and other related) measurements will provide an excellent description of the radiation environment in JANUS. The energy resolution, response range, and accuracy of the proton recoil results are in general satisfactory for investigations of biological environments; an improved response at high energies would be very useful for dosimetry.

Proton recoil spectroscopy with gamma discrimination does require a considerable amount of electronics and detailed analyses if one is to achieve the full inherent accuracy and energy response. The measurements reported here are typical of what can be achieved in low flux environments and serves to illustrate the method very well.

References

1. E. F. Bennett, *Neutron Spectroscopy by Proton Recoil Proportional Counting*, Nucl. Sci. Eng. **27**, 16 (1967).
2. J. A. G. Davids, A. P. J. Mos, and A. De Oude, *Fast Neutron Facility for Biological Exposures in an Argonaut Reactor: Design Tissue Dosimetry and Neutron Spectrometry*, Phys. Med. Biol. **14**, 573 (1969).
3. W. H. McCorkle, H. W. Pierce and D. C. Thompson, *The Biological Irradiation Facility ('JANUS Reactor') Design Manual*, ANL-6745 (1963).
4. F. S. Williamson, *JANUS, A Status Report*, Argonne National Laboratory, Division of Biological and Medical Research, Annual Report, 1968, ANL-7535, p. 130.
5. A. E. McArthy and D. H. Shaftman, *Shielding Design and Analysis for Modifications of JANUS*, Reactor Physics Division Annual Report, July 1, 1968 to June 30, 1969, ANL-7610, pp. 447–459.
6. D. H. Shaftman, *Reactor Physics Analyses for Modifications to JANUS*, Reactor Physics Division Annual Report, July 1, 1968 to June 30, 1969, ANL-7610, pp. 459–464.
7. N. A. Frigerio, Argonne National Laboratory (private communication).
8. R. Gold, Argonne National Laboratory (private communication).
9. F. Williamson, Argonne National Laboratory (private communication).
10. H. Werle, *Spektrumsmessungen radioaktiver Neutronenquellen im Energiebereich von 10 keV bis 10 MeV mit Protonenrücksstoss-Proportionalzahlrohren*, Diplomarbeit, T. H. Karlsruhe, INR-4/70-25 (February 1970).
11. E. F. Bennett and T. J. Yule, *Techniques and Analyses for Fast Reactor Neutron Spectroscopy with Proton Recoil Proportional Counters*, (to be published).

III-35. A Code for Calculating the Temperatures of Effluent Air from the ZPR-6 and -9 Sand Filters

G. K. Rusch

A potential problem during and subsequent to a postulated Design Basis Accident (DBA) in the ZPR-6 or -9 reactor cell, is the generation of relatively high pressures due to rapidly burning sodium vapor. The pressurized air must be vented in a manner which is compatible with the pressure rating of the reactor cell and such that the release of radioactive material is minimized.

One of the safety features of the ZPR-6 and -9 reactor facilities[1] is the emergency-exhaust-system (EES) which is designed to rapidly release air from the reactor cell and also to minimize the release of radioactive contaminants after a DBA type accident. The EES is comprised of a reactor cell capable of containing internal pressures up to 35 psig, and valves, ductwork, and sand filters compatible with this cell containment capability. The sand filters are designed to remove the major portion of radioactive particulate material flowing out of the cell after a DBA, and as a large heat sink ($\sim 3 \times 10^7$ cal/°C) to absorb heat generated during the accident. Air can flow from the reactor cell through the sand filters and subsequently through a double set of HEPA filters at a rate of about 3000 cfm per psi of pressure head. The effluent air is therefore highly filtered provided the air is sufficiently cooled in the sand filters to protect the integrity of the HEPA filters. A code has been written to calculate the temperature of the effluent air following a postulated DBA in the ZPR-6 or -9 reactor cell.

The details of the code are contained in Ref. 2. Briefly, however, heat is assumed to be generated[3] from burning sodium vapor and liquid metals in accord with the DBA postulated in the Final Safety Analysis Report.[1] This heat is assumed to be transferred immediately to the air in the reactor cell. Numerical approximations to the appropriate differential equations are used to calculate the parameters of interest. Heat is transferred by conduction to the reactor cell walls,

or, and ceiling is calculated. Air pressure within the reactor cell is calculated using temperature and density information. Air flow through the sand filters is determined by use of cell air-pressure information.

The sand filters which absorb heat from the air flowing through them, are assumed to be divided into a number of discrete zones. The divisions are defined by planes perpendicular to the axis of the sand filters. Each zone is assumed to contain spherical particles of a given size; the individual particles are assumed to be divided into spherical shells for the purpose of heat transfer calculations. All of the air within a given zone is assumed to be at the same temperature, as are all corresponding spherical shells within the individual particles. The temperature of the air flowing from a given zone is determined as a function of the quantity and temperature of the inlet air, the quantity and temperature of the air within the zone, and the quantity of heat transferred from the air to the particles within a zone. Heat transfer between particles of the various zones is assumed negligible compared with that transported by air flow.

For the case of the ZPR-6 and -9 DBA, the effluent air from the sand filters was found to be essentially at room temperature (25°C). This low temperature is a consequence of the very large heat capacity of the sand and gravel within the filters and the very large effective surface area for heat transfer to the sand and gravel.

References

1. W. Y. Kato et al., *Final Safety Analysis Report on the Use of Plutonium in ZPR-6 and -9*, ANL-7442 (1970).
2. G. K. Rusch, *A Code for Calculating Effluent Air Temperatures from a Sand Filter*, ANL-7687 (to be published).
3. G. K. Rusch and J. M. van Doorninck. *The Subroutine Used to Calculate Design Basis Accidents For the ZPR-6 and -9 Plutonium Safety Analysis Report*, ANL-7508 (1968).

III-36. A Sodium-Vapor Monitor

J. F. Meyer, T. W. Johnson and J. E. Sustman*

Introduction

A 360 liter heated zone (the VTRZ), capable of operation at temperatures up to 550°C, is to be installed in the ZPR-6 Fast Critical Assembly as part of a study of heterogeneity and temperature effects in LMFBR critical experiments. The sodium in this heated zone will operate in the molten state and safety considerations have led to a double-containment scheme. The primary sodium containment will be sealed individual stainless steel cans (calandria cans), nominally 2 × 2 × 12 in. and containing approximately 300 g sodium; the secondary containment is a sealed outer shell enclosing the entire heated zone (a total of about 400 cans). A circulating argon gas blanket is maintained within the outer shell. The sodium-vapor monitor described in this report is intended to detect a breach of the primary sodium containment cans by detecting the presence of sodium vapor in the circulation argon cover gas.

An initial survey of sodium leak detection methods, undertaken at the beginning of the development of a sodium vapor monitor for this application, indicated that leak detection by the "atomic absorption" of sodium light by sodium vapor was the most practical of the available approaches to the problem.† This report discusses the electronic and mechanical design of the sodium-vapor monitor and the proof-of-performance and sensitivity tests of the prototype model of the instrument.

Monitor Operation

The monitor is to be located immediately outside the heated zone assembly, as shown in Fig. III-36-1, where it will monitor the argon cover gas as it exits from the heated zone. The argon gas will sweep any sodium can leak, no matter how small or remote, picking up sodium vapor and transporting a portion of the vapor through the heated zone to the detector.

The physical configuration of the sodium-vapor monitor is shown in Fig. III-36-2. The sodium-light source produces an essentially monodirectional light beam made up of the emission lines of sodium. The

* Student, Wisconsin State University, Oshkosh, Wisconsin.

† Among the other methods considered were the detection of liquid sodium by electrical-shorting or by chemical reactions; the detection of vaporized sodium by flame or R-F excitation photometry, by gamma detection of Na-24, or by chemical cells; and the detection of sodium combustion or reaction products by such means as sensing sodium smoke.

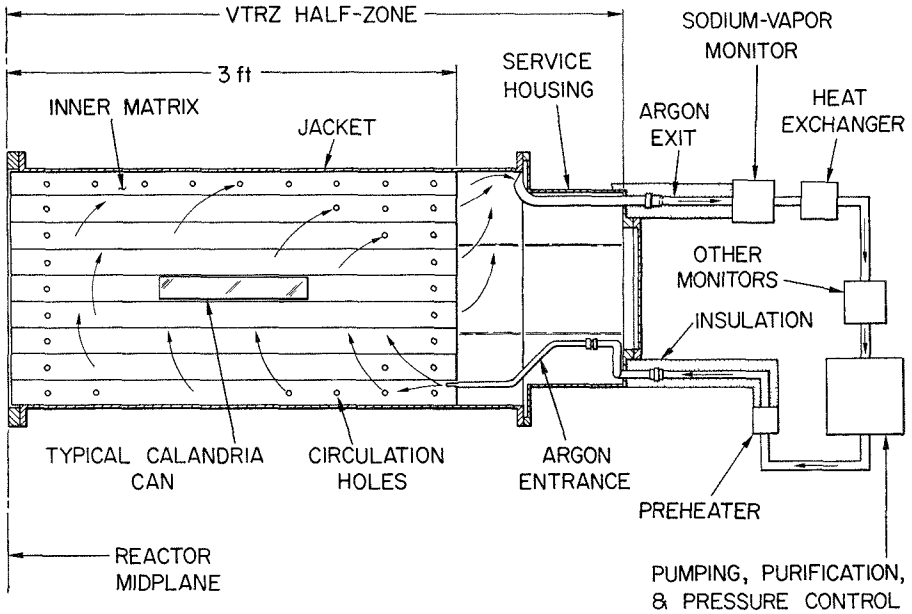

FIG. III-36-1. Relation of Sodium-Vapor Monitor to VTRZ Inner Matrix Assembly. *ANL Neg. No. 116-383.*

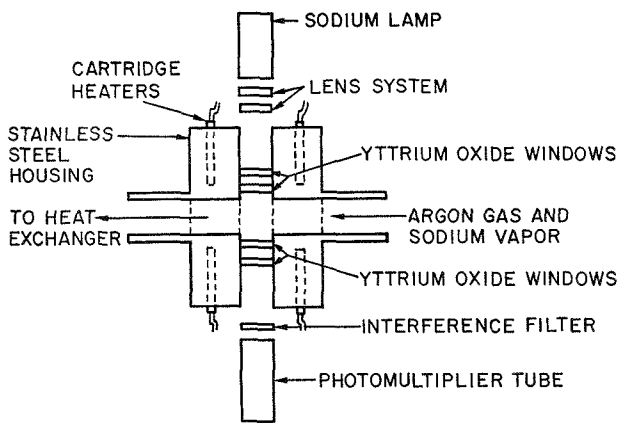

FIG. III-36-2. Block Diagram—Sodium Vapor Monitor. *ANL Neg. No. 900-305.*

sodium light source is made up of a sodium lamp with its associated power supply, a lens system, and two yttrium oxide windows as shown in the figure. The lamp is a high-spectra-output hollow-cathode tube which emits the emission lines of sodium, the strongest of which are at 5890 Å and 5896 Å. The lens system collimates and concentrates this sodium light, directing it through the yttrium oxide windows and through the gas space. Except for some minor dispersion, these windows are transparent to the essentially monodirectional light beam.

Ideally, the sodium-light sensor should be sensitive only to the emission lines of sodium generated by the lamp. It should discriminate against other wavelengths and against sodium light scattered in the monitor housing. The sodium-light sensor used in this monitor is made up of a set of yttrium oxide windows, an interference filter, and a photomultiplier tube with an associated electrometer. Considerable departure from the ideal sensor can be tolerated here because the monitor is essentially light-tight.* Thus the photomultiplier tube will only sense light produced by the lamp. The interference filter will discriminate against scattered sodium light (i.e., sodium light which is not incident normal to the face of the filter) and against light outside the band width of 50 Å (with a peak wavelength of 5895.9 Å).

The emission of sodium light photons in the 5890 and 5896 Å peaks and the absorption of this light by sodium atoms is a resonance phenomenon which is described exactly as in neutron absorption. Involved in this phenomenon then are line widths (natural and doppler), peak values, and resonance line shapes described in terms of Voight profiles. The absorption of photons of frequency ν by sodium atoms is governed by

$$I(x) = I_0 e^{-\sigma(\nu)Nx},$$

where

$I_0 \equiv$ initial intensity
$x \equiv$ distance traveled by the photons through the absorbing medium
$N \equiv$ absorber atom density
$\sigma(\nu) \equiv$ absorption cross section and is described by Voight line shapes.

For example, assuming a sodium-vapor density

* With the sodium lamp turned off the electrometer current drops more than two orders of magnitude.

.002 ppm in argon (this is 3.55×10^{10} atoms/cm^3 and is the density of sodium vapor in equilibrium with a pool of liquid sodium at 130°C), a 100 Å bandwidth (about the 5896 Å peak), and a distance traveled by the photons through the absorbing medium of 3.4 cm, the attenuation, given by

$$A = 1 - \frac{I(x)}{I_0},$$

is approximately 50%. This calculation serves to illustrate the potential sensitivity of the sodium-vapor monitor. At the maximum operating temperature of the heated zone, 550°C, the equilibrium sodium density is about 14,000 ppm (1.22×10^{17} atom/cm^3). Thus, at heated zone operating temperatures the sensitivity of the monitor would be expected to be adequate even if sodium vapor equilibrium were not attained. The dynamic test, described later in this report, demonstrates that the monitor has adequate sensitivity in a flowing argon gas system.

There is a decrease in the monitor efficiency from the theoretical value calculated above due to the re-emission of the absorbed photons from the sodium vapor. The absorbed sodium light is isotropically re-emitted (with a 10 nsec half-life) in a broadened and shifted line shape. The monitor is designed to discriminate against this re-radiation of sodium light in two different ways. First, the monitor light source and light sensor are designed to produce and detect respectively a monodirectional light beam. Second, the monitor filter has been chosen to discriminate against the re-emitted photons whose line shape is broadened and whose line peak is shifted relative to the light source line shape.

Yttrium oxide windows were chosen because of their optical, thermal expansion, and strength properties, and their resistance to chemical reaction with sodium. Although the windows in the present design have never failed, the design incorporates two windows on both the lamp-side and the photomultiplier-side of the housing. The spaces between the two windows are evacuated and monitored for vacuum failure and thereby window failure.

When connected to metal-packed high-temperature unions, the entire stainless-steel housing is leak-tight over many 20°C → 550°C → 20°C cycles. Cartridge heaters maintain the housing at any desired uniform temperature up to 600°C* while refractory-type insulation localizes the heated area to the housing. The outer portion of the monitor containing the lamp, lenses, photomultiplier tube, and filter is light tight and so signed that the lamp and photomultiplier tube faces not rise above 30°C.

* It is not desirable to have cold spots in the housing or upstream piping because of resulting vapor condensation.

The A-C electronics system is stable and virtually noise free. After an initial normalization adjustment to achieve 100% transmission and after a zero check accomplished by turning off the lamp, the monitor will operate for more than 100 hr (with continuous thermal cycling) with less than 5% drift. There are no moving parts, bridge circuits, or reference cells in the design. The unit is essentially fail-safe in that the "on" condition is in the normal (no sodium-vapor present) condition. Most lamp and photomultiplier failures (e.g., a lamp power supply failure) will cause the transmission meter to go down scale. Also, as noted in the description of the tests given later in this report, the monitor response levels off (saturates) at about 80% attenuation (20% transmission). Thus not only are most failures fail-safe but immediately distinguishable from actual indications of sodium-vapor. Adjustable alarm set points are incorporated into the readout meter design and can be wired to trip interlocks and/or alarm display panels.

Static Calibration Tests

The purpose of the calibration tests was to determine monitor attenuation as a function of the sodium-vapor density present in the housing. A small bead of sodium was inserted into an evacuated quartz tube which was then backfilled with a high-purity argon gas to about 8 psia. The tube was then sealed and inserted into the monitor housing. With care taken to avoid temperature gradients inside the tube, the housing was electrically heated and the monitor attenuation noted as a function of the housing temperature. Since the relation between sodium temperature and vapor pressure is well known, it was straight-forward to determine the calibration curve, i.e., the monitor attenuation as a function of sodium vapor density. A typical calibration result is shown in Fig. III-36-3. The quartz tube internal pressure rises during the test to nominally atmospheric pressure, thus mocking-up the static environment to which the housing will be exposed when used in conjunction with the heated zone. Gas flow, of course, was not mocked-up; however this should in no way affect the calibration of the monitor.

Dynamic Tests

Dynamic tests have been performed to determine whether or not the monitor would sense the vapor evaporating from a small pool of liquid sodium remote from the monitor and at temperature comparable to the heated zone operating temperature. The test set-up was basically that of Fig. III-36-1 with a small sodium oven replacing the heated zone. The sodium oven was an electrically heated tee-section attached to the argon

loop piping. The argon gas flowed through the horizontal section of the tee while the vertical section of the tee was blanked-off and contained a glass ampule containing sodium. The oven and the tubing between the oven and the monitor were thermally insulated. After a high-purity atmosphere was achieved in the argon loop (≈ 15 ppm oxygen gas and ≈1 ppm water-vapor) the gas, insulated tubing, and monitor were heated to approximately 300°C and a 1 cu ft/min (STP) argon gas flowrate was established. The gas pressure in the housing was nominally atmospheric. These conditions are typical of heated zone operating conditions. After the sodium ampule (containing 5 g of sodium) was crushed, the sodium oven was turned on, and the liquid sodium pool temperature increased. The typical response of the monitor as a function of pool temperature is shown in Fig. III-36-4. This test demonstrates that the monitor can sense remote sodium leaks at temperatures as low as 250°C.

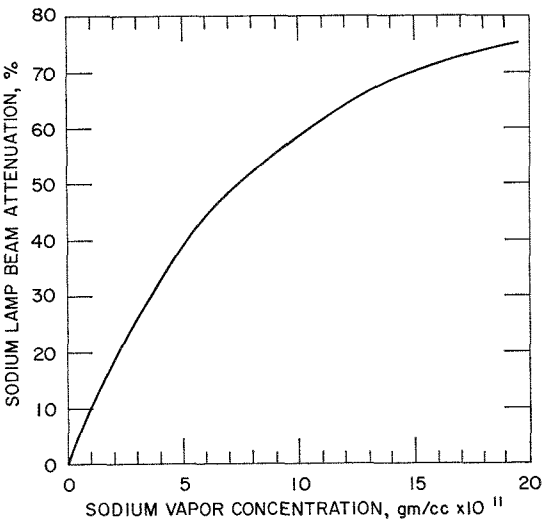

FIG. III-36-3. Sodium-Vapor Monitor Calibration Curve. *ANL Neg. No. 900-304 Rev. 1.*

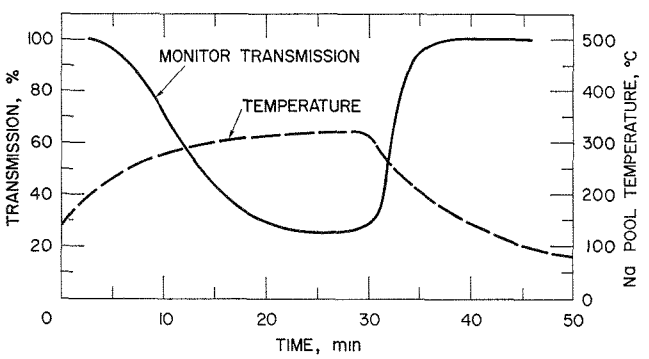

FIG. III-36-4. Sodium-Vapor Monitor Dynamic Test. *ANL Neg. No. 116-384.*

CONCLUSION

A sodium-vapor monitor based upon the atomic absorption of sodium light has been developed. It is capable of detecting as little as 0.03 ppm sodium vapor in argon gas (about 2.5×10^{-11} gm/cm^3). The monitor has been fully tested and is to be incorporated into the instrumentation of the ZPR-6 heated zone experiments to detect leaks in the primary sodium containment cans remote from the detector position.

REFERENCES

1. R. A. Lewis, K. Dance, E. F. Groh, F. H. Martens, J. F. Meyer and T. W. Johnson, *The Argonne Variable-Temperature Rodded-Zone Facility*, Trans. Am. Nucl. Soc. **12**, 696 (1969).
2. R. A. Lewis, K. D. Dance, J. F. Meyer and T. W. Johnson, *The Variable Temperature Rodded Zone (VTRZ) Program*, Reactor Physics Division Annual Report, July 1, 1968 to June 30, 1969, ANL-7610, p. 137.

III-37. Fast Neutron Hodoscope Progress

A. DE VOLPI

Work carried out during the past year on the fast neutron hodoscope will be described in two sections: the first dealing with instrumentation, tests and transients run at TREAT; the second with analysis and data output obtained at the Illinois site. Development of the hodoscope for the Reactor Analysis and Safety (RAS) Division continues to be a responsibility of the Applied Physics Division where the project originated.

ACTIVITIES AT TREAT

Two instrumental improvements have been installed at TREAT. We have introduced noise suppression and automatic deadtime compensation into the steady state scanning instruments. Prior to each transient it is necessary to "focus" the hodoscope so that the central channel coincides with the fuel pin. This also provides preliminary information on the signal/background

tio and on some operational features of the hodoscope. In addition, this procedure is sometimes carried out immediately after a transient in order to obtain an early indication of pin failure or non-failure in cases where other instrumentation is not definitive.

When the reactor is operating at a low power (50 kW) steady-state level, there are a large number of noise sources (mostly control rod relays) which insert millisecond bursts of noise into the counting channels. We have found that the most successful method of suppression has been to introduce a deadtime of about 10 msec after each initial count; in this manner, no more than one count is caused by a noise event rather than a burst of hundreds of counts. Thus out of a few thousand counts collected, only a small fraction are of spurious origin.

Such a large deadtime, though, complicates the process of measuring count rates typically running from 5–20 cps, which means deadtime losses of 5–20%. Thus we have also introduced compensation techniques which automatically correct for the deadtime losses. A dual-scaler with precision oscillator-timer has been installed, along with a count-rate meter also automatically corrected for paralysis. No arithmetical manipulations are needed; the displayed rates are accurate measures of the true input rate.

A second series of instrumental improvements is in the area of camera utilization. Typical time resolution experienced so far in TREAT transients has run from 1.2 to 7 msec. To accommodate this range, it is necessary to adjust the synchronization between the camera shutter and the firing of the lamp array. An improved method of synchronization has been installed.

The new apparatus consists of a neon lamp enclosed in a light-tight box, a flexible light guide which can be attached to the front lens of the camera, and a photomultiplier tube. The neon lamp is fired from a pickoff point at the lamp array; thus it is triggered by the synchronization signals from the camera. The flexible light guide carries the light flash to the camera lens, which then passes the light through the moving shutter to the photomultiplier coupled to the focusing eyepiece. The phototube is powered from the previously existing linear test panel, and signals generated in the tube are amplified at the test panel and forwarded to the test rack oscilloscope. Thus the shape and amplitude of the signal observable on the oscilloscope (triggered externally by the sync signal) are dependent upon the proper timing of the camera shutter with respect to lamp flashing. With an adjustable delay circuit, the correct synchronization can be conveniently established.

A second useful feature of the neon lamp source is to provide an occasional test of lens transmission. Previous experience with an optical head of the camera led to a slow, nearly imperceptible rate of deterioration in light transmission. By comparing the through-the-lens transmission with the direct light output of the lamp, it is possible to obtain a relative measure of optical quality. The flexible light guide accomplishes this by having a connection which can be made to another compartment of the light box where the photo-

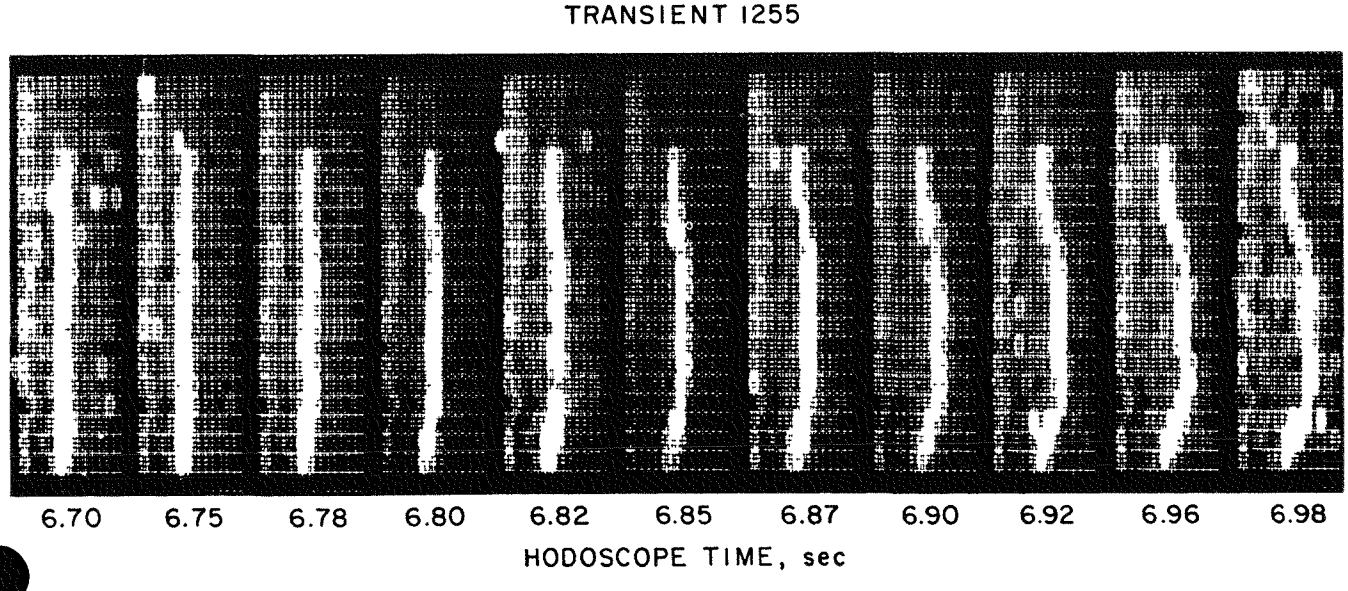

FIG. III-37-1. Meltdown Sequence for Single Bare Pin as Observed by the Fast Neutron Hodoscope at TREAT. *ANL Neg. No. 116-114A.*

multiplier can be directly attached for the light intensity standardization.

We have also established an extended test procedure for the logic system of the hodoscope. This, in association with a logic troubleshooting chart and diagram, is expected to simplify corrective procedures for the very complex electronic system with thousands of integrated circuits. Essentially all diagnostics can be carried out by visually observing improper lamp indication under specified test conditions prior to a transient.

The number of inadvertent system failures resulting in non-availability of the hodoscope at transient time has been greatly reduced, so that it has been possible to have the hodoscope ready for almost every transient. Through the fiscal year 1970 nearly a dozen experiments have been carried out in conjunction with the fast neutron hodoscope.

Analytical Support in Illinois

Shutdown of the CHLOE scanning apparatus curtailed analysis of hodoscope film data. However, a replacement scanning system, ALICE, is now under construction.

Final results from the first meltdown transient conducted with the full-scale hodoscope are shown in Fig. III-37-1. This is for a "clean" condition, namely a bare pin in a gas-filled transparent capsule.

Information gleaned from Transient 1255 and from two Mark II sodium loop transients which have not been fully analyzed to date provide some interesting favorable features of the hodoscope which were not previously appreciated.

First, the signal/background ratio during a transient is about two or three times better than indicated by the preceding steady-state scan. For example, at the peak of the transient 1255 the signal/background ratio was about 20/1 rather than 7/1. For sodium loops about 7/1 instead of 2.5/1 appears to be the case. This bonus arises because of the residual gamma ray sensitivity of the hodoscope. During steady-state reactor conditions, the hodoscope measures equilibrium delayed gamma rays as well as prompt gamma rays. But during a transient, the delayed gammas are stored up and not issued for about a second.

There is a second bonus related to the same phenomenon. The hodoscope was originally designed to have adequate sensitivity when the power level of the transient dropped to 10% of the peak. However, we have found even after full scramming of the reactor that delayed gammas (and neutrons) provided adequate signal intensity to observe the fuel condition for as much as a second or two. This feature greatly extends the utility of the hodoscope in terms of post-transient effects.

At one time it had been feared that the hodoscope instrumentation suffered from a non-linear transient-response condition. Subsequent tests have not supported this concern; instead we have found that some transients which exceed the original design limitation of the hodoscope (5000 MW) have apparently caused an overflow condition in the scalers. We are attempting to correct data where this has occurred. In the meantime some temporary limitations on efficiency have been established for transients which exceed several thousand megawatts peak power.

In addition to preparing for introduction of the new scanning system ALICE, efforts are underway to develop a display and analysis station which will provide a moving rendition of the transient data and which will allow expedited data adjustment.

Section IV

Reactor Computation Methods and Theory

To a large degree, the quality of reactor design and performance depends upon the quality of the conceptual models and their portrayal in accurate mathematical representation, and upon the quality and efficiency of computational methods. A priori, the continuous development and refinement of theory and computational methods leads to the design of more dependable, safer, and better performing reactors. It is with this intent that the studies described in this section were undertaken.

IV-1. MC² Capability in the Argonne Reactor Computation (ARC) System

C. G. Stenberg and H. Henryson, II

Multigroup calculations in the ARC system make use of the four modules CSI001 (Epithermal Cross Section Specifications), CSC001 (Resonance Cross Sections), CSC002 (Non-Resonant Cross Sections and Fundamental Mode Spectrum), and CSC003 (Broad Group Cross Sections and Fundamental Mode Spectrum). These modules represent revised versions of the coding which previously provided the MC² computational capability in the ARC system.[1] The multigroup capability is based on the MC² algorithms[2], and modifications have been made with the intention of providing greater flexibility and accuracy in certain areas with a minimal increase in computing time.

The most significant change in capability has resulted by variably dimensioning the four modules. As in most of the ARC system computational modules, the dynamic allocation routine BPØINTER[3] was used in providing this capability. Prior to modifying the code, users were limited to 20 materials, 4 isotopes per material, 70 broad energy groups, 70 fine energy groups, 2100 ultrafine groups and 2000 resolved resonances. With the variably dimensioned modules, finite computer core size is the only real limitation. Since BPØINTER makes use of large core storage (IBM 2361) as a logical extension of the fast core, variably dimensioning the modules has in effect tripled the core available for running problems on Argonne's IBM 360/75. Using the present capability problems have been run using 350 fine groups and collapsing to 130 broad groups. Extensive testing of the new capability has been performed to ensure its reliability and to compare execution times with the earlier fixed dimension capability.

Timing considerations for the fixed and the variably dimensioned modules are given in Table IV-1-I. The time in seconds is listed for each area in the module. The total time listed for each module includes the time for each area in the module plus any overhead, e.g., subroutine linkage time, printout time, etc. The number in parentheses is the percentage of the problem run-time spent in the module. The sum of the time spent in each of the four modules equals the total charge time for the calculation, i.e., central processing time plus wait time. The times listed are for a calculation using three different options: (i) an all-fine group P_1 fundamental mode problem, (ii) an ultra fine group P_1 problem, and (iii) an ultra fine group consistent P_1 problem. All three problems contained eighteen materials, 27 broad energy groups, and an energy range from 10 MeV to 22.6 eV. The fine group problem consisted of 52 fine groups, the ultra fine problems of 1560 ultra fine groups. For the ultra fine group calculation eight materials were treated as Legendre materials.

Execution of the ARC system standard path STP005 which invokes the modules CSI001, CSC001, CSC002 and CSC003 has been considerably simplified by writing a catalogued procedure which has been added to the procedure library of the Applied Mathematics Division, ANL. Consequently it is possible to invoke the MC² capability in the same manner as all other ARC system standard paths.[4]

In addition to variably dimensioning the four MC² modules in the ARC system, a number of minor changes have been made in the computational algorithms. Some of these changes, (ii) and (iii) below, were made to permit MC² to use the version 2 data of ENDF/B. The other changes were felt to be necessary to remove various inconsistencies and/or provide greater accuracy. The changes are summarized below.

(i) The subroutine QUICKW[2] which calculates the complex function $W(z)$ for use in obtaining the Doppler broadened line shapes, was not sufficiently accurate for obtaining the Pu-239 Doppler effect. The area in question was for $12.0 \leq |z| < 100$. In this range QUICKW used the first term of the continued fraction expression for $W(z)$.[5] The new version makes use of a two-term fraction in the range of interest:

$$W(Z) = \frac{2}{\sqrt{\pi}} iz \left(\frac{1}{2z^2 - 1 - \dfrac{2}{2z^2 - 5}} \right), \qquad 12 \leq |z| < 100.$$

(ii) In the unresolved resonance calculation, level spacings and all widths are permitted to be energy dependent. Previously, the code would accept only energy-dependent fission and neutron widths.

(iii) Unresolved parameters for d-wave scattering are permitted. The d-wave penetration factor[2] is calculated as

$$V_2 = \frac{n^4}{9 + 3n^2 + n^4}, \qquad n = \frac{R}{\lambda\!\!\!^{-}},$$

where R is the nuclear radius and $\lambda\!\!\!^{-}$ is the reduced wavelength.

TABLE IV-1-I. Timing Considerations for the Fixed and Variably Dimensioned MC² Capability in the ARC System

Module	Area	Time in Area, sec					
		P_1 Fine-Group Problem		P_1 Ultrafine-Group Problem		Consistent P_1 Ultrafine-Group Problem	
		Fixed Dimsn MC² Capbl	Varbl Dimsn MC² Capbl	Fixed Dimsn MC² Capbl	Varbl Dimsn MC² Capbl	Fixed Dimsn MC² Capbl	Varbl Dimsn MC² Capbl
Input (CSI001)	Read input, adjust broad group structure, and make consistency check of all input data	2	3	2	3	2	3
	Total time in modules CSI001	2(<1%)	3(<1%)	2(<1%)	3(<1%)	2(<1%)	3(<1%)
Calculate unresolved and resolved resonance cross sections (CSC001)	Reading unresolved and resolved data and W table from ENDF/B library	10	12	10	12	10	12
	Subroutine finds the maximum number of isotopes for the materials in problem, maximum number of energy points in unresolved calculation for materials in problem and maximum number of resolved resonances in problem	—	2	—	2	—	2
	Unresolved calculation	80	92	80	94	80	94
	Resolved calculation[a]	631	714	708	800	708	800
	Total time in module CSC001	721 (87%)	820 (84%)	798 (47%)	908 (61%)	798 (44%)	908 (56%)
Calculate non-resonant cross sections, calculate fundamental mode fluxes, and iterate on buckling to critical (CSC002)	Subroutine finds the maximum number of energy-sigma pairs for use in FIGERØ	—	6	—	6	—	6
	(Subroutine FIGERØ) calculates fine-group effective cross sections for non-resonant quantities	44	44	49	48	49	48
	Subroutine finds the maximum number of energy-sigma pairs for any energy and for any material in INSCAT	—	12	—	12	—	12
	(Subroutine INSCAT) calculates inelastic and $N,2N$ cross sections	12	11	12	11	12	12
	(Subroutine SØURCE) calculates fine and ultrafine-group fission spectrum	<1	<1	3	3	3	3
	Input/output operations	3	4	15	19	15	16
	Buffer Legendre data from ENDF/B library	—	—	69	64	69	63
	Calculation in subroutine ALRAGØ[b] for 1st iteration	—	—	519	125	586	201
	Calculation in subroutine PØNE for 1st iteration	—	—	2	2	2	2
	Time spent in subroutine ALRAGØ[a] for 2nd through 4th iterations	—	—	24	30	37	50
	Time spent in subroutine PØNE for 2nd through 4th iterations	—	—	6	6	6	6
	Total time in module CSC002	60(7%)	78(8%)	699 (41%)	326 (22%)	779 (43%)	419 (26%)

Calculate broad group average macroscopic and microscopic cross sections, calculate broad group fundamental mode fluxes (CSC003)	(Subroutine AVER) collapse the ultrafine- and fine-group cross sections	<1	1	11	13	19	24
	(Subroutine AVER1) compute[a] individual material microscopic cross sections	42	64	188	222	201	240
	(Subroutine BGPØNE) generate homogenized macroscopic broad-group cross sections	<1	2	1	2	1	2
	Variable dimension, input/output	—	2	—	4	—	4
	Total time in module CSC003	44 (5%)	69 (7%)	200 (11%)	241 (16%)	221 (12%)	270 (17%)
	Total running time for problems, sec	827	970	1699	1478	1800	1600

[a] A longer running time was required for the variably dimensioned capability in this area. This is because the variables are passed through the subroutine argument list as opposed to the fixed dimensioned subroutine where these quantities are passed through CØMMØN blocks. For a variably dimensioned subroutine, the compiler does not optimize as effectively as with a fixed dimensioned subroutine. The effect of the less efficient compilation occurring in loops which are repeated a large number of times results in a longer run-time.

[b] The data sets, which are being written, containing the microscopic elastic transfer cross sections for each Legendre material were changed from direct access data sets in the fixed dimensioned capability to sequential data sets in the variably dimensioned capability. Also for the variably dimensioned capability the buffer areas were made large so as to increase the efficiency of data transfer.

TABLE IV-1-II. VALUES OF x_i USED FOR INTEGRATION OF NEUTRON-WIDTH AND FISSION-WIDTH DISTRIBUTIONS

Index, i	Degrees of Freedom, n			
	1	2	3	4
1	5.252368E-3	5.175533E-2	1.129252E-1	1.691497E-1
2	3.717239E-2	1.630945E-1	2.656011E-1	3.407788E-1
3	1.031280E-1	2.884221E-1	4.043878E-1	4.805762E-1
4	2.078431E-1	4.317743E-1	5.477280E-1	6.178288E-1
5	3.598629E-1	5.992178E-1	7.040519E-1	7.623864E-1
6	5.743027E-1	8.005730E-1	8.824531E-1	9.229037E-1
7	8.793660E-1	1.053244	1.096850	1.111406
8	1.334857	1.393041	1.374396	1.350306
9	2.105354	1.916293	1.786401	1.697549
10	4.392862	3.302585	2.825206	2.547115

(iv) The J-integrals in the unresolved resonance calculation are evaluated using a method suggested by Nicholson and Grasseschi.[6] The infinite interval is broken into two finite intervals plus a remainder term. In particular the code assumes

$$\int_0^\infty \frac{\psi(x,\xi)}{\beta+\psi(x,\xi)}\,dx = \int_0^{x_i} \frac{\psi(x,\xi)}{\beta+\psi(x,\xi)}\,dx + \int_{\xi/200}^{1/x_i} \frac{\psi(1/x,\xi)}{\beta+\psi(1/x,\xi)}\,dx + R,$$

where

$\psi(x,\xi)$ is the Doppler broadened shape function[2]

$$R = \frac{1}{\sqrt{\beta(1+\beta)}}\left\{\frac{\pi}{2} - \tan^{-1}\left(\frac{200}{\xi}\sqrt{\frac{1}{1+\beta}}\right)\right\}$$

$$x_i = \text{Max}\begin{cases}[(\beta+1)(1-c)/\beta c]^{\frac{1}{2}} \\ \dfrac{2}{\xi}\ln\left[\dfrac{(1+0.89\,\xi(1-c)/\beta)}{c}\right]^{\frac{1}{2}}\end{cases}$$

$c = 0.15.$

The two integrals are evaluated using an eight-point Gaussian integration. If $\beta \geq 50$, J is calculated using the asymptotic formula

$$J(\xi,\beta) = \frac{\pi}{2\beta}\left[1 - \frac{1}{2\beta}\psi(0,\sqrt{2\xi})\right].$$

(v) The integrations over the chi-squared distributions required in the unresolved resonance calculation have been modified to use a ten point integration over the fission width distribution as well as the neutron width distribution for the four degrees of freedom. The code assumes[2]

$$\int_0^\infty f(x)P_n(x)dx = \frac{1}{10}\sum_{i=1}^{10} f(x_i)$$

where

$P_n \equiv$ chi-squared distribution of order n,

$$x_{i+1} = 10\int_{z_i}^{z_{i+1}} x\,P_n(x)\,dx,$$

and the $N-1$ points z_i are given by

$$\int_{z_i}^{z_{i+1}} P_n(x)\,dx = \tfrac{1}{10}, \qquad z_0 = 0, \qquad z_{10} = \infty.$$

Values of x_i for the four degrees of freedom $n = 1, 2, 3, 4$ are given in Table IV-1-II. These values differ slightly from those reported in Ref. 2 as the latter were calculated numerically whereas those reported in Table IV-1-II are based on analytical integrations of the defining equations.

(vi) The elastic self-scattering cross section for the thermal broad energy group, $\sigma_{el_{j\to j}}$, has been modified from a value of zero to the value

$$\sigma_{el_{j\to j}} = \sigma_{tr_j} - \sigma_{c_j} - \sigma_{f_j} - \sigma_{n\alpha_j} - \sigma_{np_j}.$$

If the user does not input thermal group transport, capture, fission, (n,α) and (n,p) cross sections, the values assigned to the thermal group are the same as those calculated for the lowest energy epi-thermal broad group.

(vii) In problems run with the consistent P_1 or consistent B_1 option, the anisotropic self scattering cross section, σ_{aniso}, for materials not given a Legendre elastic scattering treatment has been modified from a value of zero to the value corresponding to the transport corrected elastic self scattering cross section. This correction was required to ensure the proper total cross section for anisotropic neutronics calculations.

The four variably dimensioned modules representing the MC² capability in the ARC system with the algorithm changes noted above have been incorporated into a stand-alone overlayed code, and this code package is available for distribution. The code was developed for the de facto Computer Code Coordination Committee. The Committee desired a stand-alone MC² code capability written in standard FORTRAN IV which executes in $45K$ ($K = 1000$) 64 bit words and produces the standard interface data set, MULTIGRP, which contains the microscopic group cross sections. The ARC system modules SNIFF[7] and BPØINTER[3] have been modified so that they could be integrated into this stand-alone MC² code package. Both of these modules taken out of the ARC system environment and modified in this way have lost some of their flexibility and usefulness.

REFERENCES

1. C. G. Stenberg and A. L. Rago, *Capabilities of MC² in the ARC System*, Reactor Physics Division Annual Report, July 1, 1968 to June 30, 1969, ANL-7610, p. 469.

B. J. Toppel, A. L. Rago and D. M. O'Shea, *MC²*, *A Code to Calculate Multigroup Cross Sections*, ANL-7318 (1967).
3. A. S. Kennedy, *PØINTR, A Dynamic Storage Allocation Program*, ANL-7408 (1968); also, H. Henryson, II and B. J. Toppel, Argonne National Laboratory (private communication).
4. B. J. Toppel and L. Just, *Status and Developments in the Argonne Reactor Computation System*, Reactor Physics Division Annual Report, July 1, 1968 to June 30, 1969, ANL-7610, p. 467.
5. D. M. O'Shea and H. C. Thacher, *Computation of Resonance Line Shape Functions*, Trans. Am. Nucl. Soc. **6**, 36 (1963).
6. R. B. Nicholson and G. Grasseschi, *A Fast Accurate Technique for Calculation of the Resonance J-Function*, Reactor Physics Division Annual Report, July 1, 1968 to June 30, 1969, ANL-7610, p. 499.
7. B. J. Toppel and L. C. Just, *The Argonne Reactor Computation (ARC) System*, Reactor Physics Division Annual Report, July 1, 1967 to June 30, 1968, ANL-7410, p. 389.

IV-2. Plans for the New MC² Code, MC²-2

B. J. Toppel

Multigroup cross sections are currently being routinely generated through the use of the MC² algorithms[1] in the Argonne Reactor Computation (ARC) system,[2] with the primary data base being the ENDF/B.[3]

The MC² algorithms in the ARC system are encompassed in the standard path module STP005 and the computational modules CSI001 (Epithermal Cross-section Specifications), CSC001 (Resonance Cross-sections), CSC002 (Nonresonant Cross Sections and Fundamental-Mode Spectrum), and CSC003 (Broad Group Cross Sections and Fundamental-mode Spectrum). These modules provide the same basic algorithms originally developed in the CDC-3600 code MC² with, however, added problem size capacity, decreased running time afforded by the IBM 360 50/75, and greatly increased flexibility due to variable dimensioning and due to the modular approach used in the ARC system (see Paper IV-1).

Although use of the MC² algorithms has generally met with approval both at ANL and at various other Liquid Metal Fast Breeder Reactor (LMFBR) contractor laboratories, a number of recognized limitations and inconsistencies in the code have made clear the need for an improved cross section preparation capability which can serve as a standard for the industry.

The arrangement of the data stored in the ENDF/B, although convenient and logical for that compilation, is not appropriate for use as a library in a processing code such as MC². In particular, the ENDF/B data are stored such that all information is given for each material (resonance parameters, tabulated data, Legendre coefficients for elastic scattering, inelastic scattering data, etc.) followed sequentially by all such data for the next material, etc. The use of MC² requires that all data of a given type, such as inelastic scattering data or resonance parameters, be given for all materials, followed by a different type of data, again for all of the materials. This latter arrangement follows from the structure of MC² which is logically arranged into sections each concerned with a particular type of cross section.

Because of the different format requirements of the ENDF/B and the MC² algorithms, processing codes[4, 5] are required to convert the structure of the data. The use of these codes is quite time consuming and they are not well suited for incorporating frequent modifications to the library data. Although these limitations have not so far caused significant problems, it is clear that a more flexible processing package would be desirable to facilitate future experimentation with the basic data as well as to expedite routine library preparations.

In addition to improving the problem of data management, it would be desirable also to incorporate various algorithmic modifications to improve the rigor of the calculation and to extend the current capability into areas not now encompassed, such as shielding applications and the special needs of the critical experiments program.

A major and persistent objection to MC², particularly by the outside contractors, has been with regard to the long running time of the code. Some improvement should be realizable by selectively applying improved programming techniques. However, reduced running time may not be consistent with improved rigor and extension of the algorithms for a new code.

The broadness of the scope of a major new cross section generating capability along with its widespread interest and importance to the LMFBR community require that such an undertaking have the advantage

of recommendations from, and consultations with, an extensive group of prospective users having diverse interests and ranges of expertise. At the same time, the timely accomplishment of such an undertaking demands that a relatively small and knowledgeable group have the primary responsibility for decision making and coordination.

A project was formally initiated at the beginning of 1970 aimed at accomplishing the task of providing a generally acceptable and improved multigroup cross section capability for use by the LMFBR community. Development of such a capability would make use of the IBM System 360 models 50/75 computers at ANL, would anticipate acquisition of increased computer capability by the Laboratory, and would conform to the conventions of the ARC system. General standards of good programming practices and code documentation would be adhered to and the needs of the LMFBR community with regard to standardized coding interfaces would be provided for. It has been assumed that approximately one calendar year will be devoted to this activity.

The planning, decisions, and coordination of the effort are performed by a Steering Committee made up of Applied Physics (AP) Division staff personnel. The project director acts as Chairman of the Steering Committee.

One of the initial actions by the Committee was the active solicitation of recommendations for various algorithms to be included in the coding. These solicitations were directed to LMFBR contractor Laboratories, other interested outside organizations, and to eight ad hoc Algorithm Advisory Subcommittees composed of AP staff personnel having an interest in the particular algorithm in question.

The eight Subcommittees were convened to prepare written recommendations in the following areas:

i) Resolved and unresolved resonance algorithms
ii) ENDF/B data management
iii) Continuous slowing down algorithms
iv) Legendre coefficient elastic scattering algorithms
v) Inelastic scattering algorithms
vi) Higher order transport algorithms
vii) Heterogeneity algorithms
viii) Broad group collapsing algorithms.

The Subcommittees have no specific implementation responsibility and fulfilled their initial obligation upon submission to the Committee of their memorandums of recommendations.

The programming, debugging, and documentation of the new code is the responsibility of the Implementation Group, also consisting of AP staff personnel.

The overall program can be viewed as proceeding through five sequential phases: scheduling and organization, initial algorithm specification, algorithm coding, algorithm verification, and documentation. Algorithm coding is now under way.

The current planning, which resulted from consideration of the recommendations received, both from outside laboratories and from our Advisory Subcommittees, calls for the preparation of a code which in no sense is to compromise rigor. The fast reactor community has expressed the desire to have the new code provide a standard which as far as possible does not contain limiting approximations. In addition it is desired that a wide range of applications are also accommodated by the new code, including critical experiments analysis, core calculations, and shielding applications.

The implementation now underway will have the following features:

1. A multigroup treatment will be used down to the resolved resonance region utilizing an extended transport approximation and optionally using P_1, B_1, consistent P_1, or consistent B_1 approximations. Reconstituting the ϕ_2, ϕ_3 $\cdots$ etc. for use in producing $\ell = 2, 3, \cdots$ broad group scattering matrices is also provided (see Paper IV-5). The elastic scattering matrices will be generated using an improved algorithm as compared with MC^2 in that the variation across the source group will be explicitly accounted for. In addition, a heavy mass approximation is expected to improve calculational time (see Paper IV-8). Inelastic and $(n,2n)$ scattering are to be included at an ultrafine group level (see Paper IV-4). The present fine group-ultra fine group concept will be dropped in favor of everything being evaluated for ultra fine groups.

2. In the resolved resonance energy region, the code will go over to a continuous slowing down (CSD) approach for the spectrum calculation (see Paper IV-10). Although source terms are not relevant in this energy region, the coding will permit sources in anticipation of later utilizing the CSD approach over all energies. The influence of resolved resonances will be superimposed on the CSD spectrum using an integral-attenuation factor treatment (see Papers IV-6 and IV-11). For the case of heterogeneous plate configurations, the integral-attenuation factor formalism will be applied for each unique self-shielded material, (see Paper IV-3) and heterogeneous cross sections will be developed for spatial weighting as the last step in the cross section preparation (see Paper IV-7).

3. It is planned to provide for a RABBLE[6] capability in regard to treatment of heterogeneity and those cases when a narrow resonance approximation is inadequate.

4. A capability for accommodating private modifications to the ENDF/B data will be provided.

References

1. B. J. Toppel, A. L. Rago and D. M. O'Shea, *MC²*, *A Code to Calculate Multigroup Cross Sections*, ANL-7318 (1967).
2. B. J. Toppel, Ed., *The Argonne Reactor Computation (ARC) System*, ANL-7332 (1967).
3. *ENDF-102 ENDF/B Specifications for an Evaluated Nuclear Data File for Reactor Applications*, BNL-50066 (T-467) (1967).
4. *ENDF-110 Description of the ENDF/B Processing Codes CHECKER, CRECT, DAMMET, PLØTFB, and Retrieval Subroutines*, BNL-13582 (1969).
5. E. M. Pennington, J. C. Gajniak, A. B. Cohen and W. Bohl, *Service Routines for the Multigroup Cross Section Code MC²*, ANL-7654 (1970).
6. P. H. Kier and A. A. Robba, *RABBLE, A Program for Computation of Resonance Absorption in Multiregion Reactor Cells*, ANL-7326 (1967).

IV-3. Heterogeneous Formulation of the Resolved Resonance Broad-Group Reaction Cross Section

W. M. Stacey, Jr. and B. A. Zolotar

In the improved fundamental-mode spectrum code MC²-2 it has been recommended

1. That continuous slowing-down theory be used in the resolved resonance range (see Paper No. IV-10).
2. That J functions, corrected for overlap (J^*), be used in the resolved resonance range (see Paper No. IV-11).
3. That, for the heterogeneous case, equivalence theory be used to find plate cross sections and the broad-group weighting be based on the normal homogeneous case (see Paper No. IV-7).

The purpose of this work was to combine these recommendations and show the form which the resolved resonance group reaction cross section should take.

Under the assumption that the source in each plate is the same in the heterogeneous and homogeneous cases, we can approximate the flux in a plate:

$$\phi_{pl}(u) = \frac{q_{as}(u)Q_r\Sigma_h(u)}{M(u)\left[\Sigma^*_{pl}(u) + \sum_{i'r'} {}_{pl}N_{i'}\sigma^{i'}_{tr'}(u)\right]}, \quad (1)$$

where

$\phi_{pl}(u) \equiv$ the heterogeneous flux in each plate
$q_{as}(u) \equiv$ the "asymptotic" † slowing-down density for the homogenized problem
${}_{pl}N_i \equiv$ the number density of isotope i in the plate
$M(u)$ is defined in terms of the non-narrow resonance scattering and absorption properties of the homogenized mixture
$\Sigma_h(u) \equiv$ the total nonresonance cross section for the homogenized system.
$\Sigma^*_{pl}(u) \equiv$ the effective heterogeneous, nonresonance cross section in the plate as found from equivalence theory
$Q_r \equiv$ the homogeneous resonance attenuation down to resonance r, or

$$Q_r = \prod_{\substack{i \\ u_{r'}<u_r}} \prod_{r'} \left(1 - \sum_x p^i_{xr'}\right), \quad (2)$$

where

$$p^i_{xr} = (\Gamma^i_{xr}/E_r)J^*(\beta^i_r, \theta^i_r)[\Sigma_h(u_r)/M(u_r)] \quad (3)$$

for each resonance r, isotope i, and reaction x (fission or capture). The specification that the broad-group weighting be based on the normal homogeneous case requires the use of the J^* corresponding to the homogeneous case for computing Q_r. Then

$$\beta^i_r = \Sigma_h(u_r)/N_i\sigma^0_{ri} \quad (4)$$

$$\theta^i_r = \Gamma^i_r/\sqrt{4kTE_r/M_i}, \quad (5)$$

where

$N_i \equiv$ the homogenized number density of isotope i.
$k \equiv$ Boltzmann constant
$T \equiv$ temperature
$E \equiv$ energy
$M \equiv$ nuclear mass.

A heterogeneous, broad-group-averaged,‡ microscopic cross section of isotope i, for reaction x, in plate pl, is defined by

$$({}_{pl}\sigma^i_x) = \frac{\int_{BG} du\, \sigma^i_x(u)\phi_{pl}(u)}{\int_{BG} du\, \phi_{pl}(u)}. \quad (6)$$

† In the absence of narrow resonance absorption.

‡ The symbol BG is used to denote the lethargy interval corresponding to a broad group.

Using Eq. (1), Eq. (6) becomes†

$$({}_{pl}\sigma_x^i)_{BG} = \frac{\left(\frac{1}{{}_{pl}N_i}\right)\sum_{r\epsilon BG} q_{as}(u_r)Q_r\ {}_{pl}p_{x,r}^i}{\int_{BG}\frac{\Sigma^h(u)}{\Sigma_{pl}^*(u)}\frac{q(u)}{M(u)}\,du - \sum_{x'}\sum_{i'}\sum_{r'\epsilon BG}\frac{q_{as}(u_{r'})Q_{r'}}{\Sigma_{pl}^*(u_{r'})}\cdot\frac{\Gamma_{r'}^{i'}}{\Gamma_{c}^{i'}{}_{,r'}+\Gamma_{f}^{i'}{}_{,r'}}\cdot{}_{pl}p_{x',r'}^{i'}} \tag{7}$$

$$q(u) = q_{as}(u)\prod_{\substack{i\\ u_r<u}}\prod_{r}\left(1-\sum_x p_{x,r}^i\right), \tag{8}$$

and

$${}_{pl}p_{x,r}^i = (\Gamma_{x,r}^i/E_r)J^*({}_{pl}\beta_r^i,\theta_r^i)[\Sigma^h(u_r)/M(u_r)], \tag{9}$$

where

$${}_{pl}\beta_r^i = \Sigma_{pl}^*/{}_{pl}N_i\sigma_{ri}^0\,. \tag{10}$$

A homogeneous, broad-group-averaged, microscopic cross section for isotope i, for reaction x, is defined by

$$(\sigma_x^i)_{BG} = \frac{\frac{1}{N_i}\sum_{r\epsilon BG} q_{as}(u_r)Q_r p_{x,r}^i}{\int_{BG}\frac{q(u)}{M(u)}\,du - \sum_{x'}\sum_{i'}\sum_{r'\epsilon BG}\frac{q_{as}(u_{r'})Q_{r'}}{\Sigma_h(u_{r'})}\cdot\frac{\Gamma_{r'}^{i'}}{\Gamma_{c}^{i'}{}_{,r'}+\Gamma_{f}^{i'}{}_{,r'}}\cdot p_{x',r'}^{i'}} \tag{11}$$

† Note that Σ^*_{pl} may be defined differently for each resonance isotope in a plate, which means that the effective fluxes may differ.

IV-4. Inelastic Matrices in Multigroup Calculations

M. Segev

The evaluation of the in-scattering group source in the present version of the MC^2 code[1] suffers from several defects. For example, the $(n,2n)$ reaction is treated as if a single neutron temperature describes the evaporation of the two emerging neutrons; another example is the neglect of energy-angle correlation in inelastic scattering to single levels; and still another example is the assumption that an in-scattering inelastic source to a fine group is divided up among the ultrafine groups in proportion to the energy widths of the latter.

The purpose of this study is to provide a simple, yet reasonably accurate, basis for an algorithm for the evaluation of the inelastic transfer matrix. In particular, the above-mentioned defects, as well as other defects, are eliminated.

Let k and j denote groups, and let x denote a certain mode of scattering. S_j, the scattering source into group j, breaks up into partial sources,

$$S_j = \sum_{k\le j}\left[\sum_x (\Delta S)_x^{k\to j}\right] \tag{1}$$

On the lowest level of the multigroup calculation the group cross sections and the group fluxes are constants. Therefore, the partial source $(\Delta S)_x^{k\to j}$ is given by

$$(\Delta S)_x^{k\to j} = \phi_k\Sigma_{x,k}P_x(k\to j), \tag{2}$$

where ϕ_k and $\Sigma_{x,k}$ are, respectively, the flux and the x-mode scattering cross section in group k. $P_x(k\to j)$, the x-mode group-to-group scattering probability, is

$$P_x(k\to j) \equiv \left(\frac{1}{E_k - E_{k+1}}\right)\int_{group\ k} dE'\int_{group\ j} dE\ P_x(E',E),$$

where E_k and E_{k+1} are, respectively, the high and low limits of group k, and where $P_x(E',E)$ is the probability that a neutron will emerge from the scattering with energy E, if it approaches the target with energy E' and is scattered by mode x.

In order to evaluate $P_x(k \rightarrow j)$, then, the elementary laws $P_x(E',E)$ need be established, as well as the actual integration limits, briefly denoted above by "group k" and "group j".

Given any group k, the inelastic source element $(\Delta S)_{in}^{k \rightarrow j}$ can be divided as follows:

$$(\Delta S)_{in}^{k \rightarrow j} = \phi_k \left[\sum_{\lambda=1}^{\Lambda_k} \Sigma_{\lambda,k} P_\lambda(k \rightarrow j) + \Sigma_{1n,k} P_{1n}(k \rightarrow j) + \Sigma_{2n,k} P_{2n}(k \rightarrow j) \right]. \tag{4}$$

The breakup is based on the compound-nucleus picture of inelastic scattering, as well as on practical considerations. The collision between a neutron and a nucleus (A) creates the compound nucleus $(A + n)$. $\Sigma_{\lambda,k}$ is the group-averaged cross section for the decay of $(A + n)$ to the λth level of the residual (A); the probabilities $P_\lambda(k \rightarrow j)$ are determined from the threshold energy E_λ in the next section. The quantities $\Sigma_{\lambda,k}$, E_λ, and $\Lambda_k(\lambda = 1, 2, \cdots, \Lambda_k$; $E_1 < E_2 < \cdots < E_{\Lambda_k})$ are assumed to be data, or obtainable from data, in ENDF/B files. $\Sigma_{1n,k}$ is the cross section for the decay of $(A + n)$ to the levels $\lambda > \Lambda_k$ of (A); $P_{1n}(k \rightarrow j)$ is a group transfer probability for this decay. It is assumed that a further decay of (A) is by emission of a secondary neutron,[2] if neutron emission is energetically possible. $\Sigma_{2n,k}$ is the cross section for the emission of the second neutron; $P_{2n}(k \rightarrow j)$ is a group transfer probability for this emission. The quantities $\Sigma_{1n,k}$, $\Sigma_{2n,k}$, $P_{1n}(k \rightarrow j)$, and $P_{2n}(k \rightarrow j)$ are determined in the last section of this paper.

Inelastic Scattering to Single Levels

The PRISM routine, by O'Reilly and Lewis,[3] accounts for energy-angle correlation in single-level scattering in the evaluation of group inelastic matrices. However, the report presents a complex piece of logic. The complexity is the result of two factors: one, an unfortunate choice of variables with which to work; two, an unnecessary pursuit of completeness.

The following is a simple, yet fairly accurate, account of energy-angle correlation in single-level scattering and in the ensuing group inelastic matrices.

A neutron approaches a target of mass number A with the laboratory energy E' and is scattered into the laboratory energy E and by the center-of-mass angle $\cos^{-1} \mu$. The scattering is an excitation of an inelastic level and the $-Q$ value of the reaction is Q_λ in the laboratory coordinates. Energy conservation and momentum conservation yield (for example, see Ref. 4)

$$E = \frac{1 + A^2}{(1 + A)^2} E' - \frac{A}{1 + A} Q_\lambda + \frac{2A}{1 + A} \mu E' \sqrt{1 - \frac{A + 1}{A} (Q_\lambda / E')}. \tag{5}$$

Define

$$E_\lambda \equiv \frac{A + 1}{A} Q_\lambda \tag{6}$$

$$\tau \equiv \sqrt{1 - (E_\lambda / E')} \tag{7}$$

$$\rho \equiv (1 + A)^2 E / E_\lambda. \tag{8}$$

Then Eq. (5) takes the following form:

$$\rho = \frac{1 + 2A\mu\tau + A^2\tau^2}{1 - \tau^2}. \tag{9}$$

The single-valuedness and the monotonic property of Eq. (5) (as well as other properties) need be explored before it is applied to the evaluation of group transfer probabilities. Instead, Eq. (9) is easier to examine and the results will apply to Eq. (5), because $\tau(E')$ and $\rho(E)$ are monotonically increasing functions. The term "energy-angle correlation" will refer to Eq. (9) [rather than to Eq. (5)] which describes the "scattering" $\tau \rightarrow \rho$ (rather than the scattering $E' \rightarrow E$).

E_λ, Eq. (6), is the threshold energy for the scattering, as evident from Eq. (7) and the appearance of the first power of τ in Eq. (9). On the τ-scale the threshold is at $\tau = 0$, and $\tau \rightarrow 1$ as $E' \rightarrow \infty$.

Monotonic properies of $\rho(\tau,\mu)$ can be obtained by partial differentiation of Eq. (9). The results are summarized visually in Fig. IV-4-1. In particular, $\rho(\tau)$ for a given negative μ goes through a minimum; therefore, in solving Eq. (9) for τ, the solution branches:

$$\left.\begin{matrix} \tau^{(R)}(\rho,\mu) \\ \tau^{(L)}(\rho,\mu) \end{matrix}\right\} = \frac{A}{A + \rho^2} [-\mu \pm \sqrt{\mu^2 + (\rho - 1)(1 + \rho/A^2)}]. \tag{10}$$

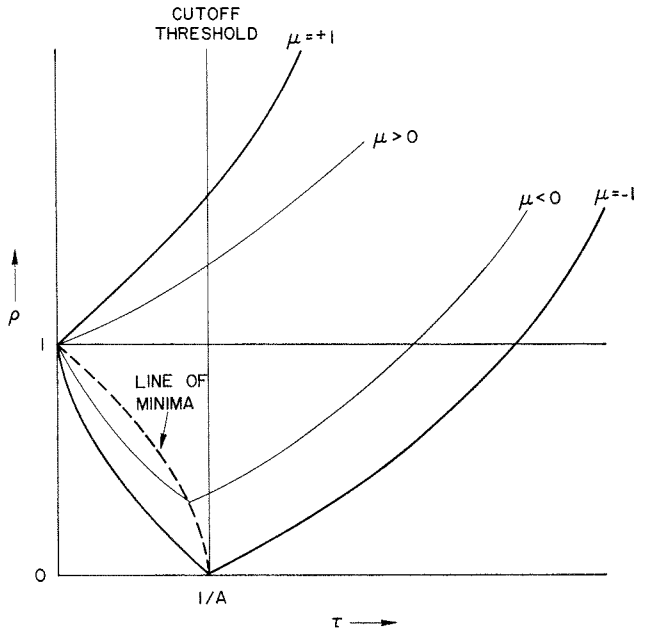

FIG. IV-4-1. Energy-Angle Correlation in Inelastic Scattering. *ANL Neg. No. 116-457.*

The ranges of applicability of $\tau^{(R)}$ and $\tau^{(L)}$ are, respectively, to the right and to the left of the "line of minima" in Fig. IV-4-1.

The logic of group transfer evaluation may become complex because of the branching of $\tau(\rho,\mu)$. However, the complexity can be circumvented with little cost in accuracy. Define a cutoff threshold T_λ,

$$T_\lambda \equiv \frac{A^2}{A^2-1} E_\lambda, \tag{11}$$

(see Fig. IV-4-1) and assume that no scattering occurs below the cutoff threshold. Except for very light elements, the range $[E_\lambda, T_\lambda]$ is very small and the excitation cross section in a very small range above E_λ is practically negligible; therefore, the assumption will introduce virtually no error in the calculation. Also, the exclusion of very light elements sets no real limitation on most fast-reactor computations. On the τ-scale, T_λ corresponds to $\tau = 1/A$ (see Fig. IV-4-1). The simplification in the ensuing logic is now the result of the fact that, for any given prescattering "energy" τ above $1/A$, the neutrons emerge only with "energies" ρ to the right of the "line of minima", thus rendering $\tau(\rho,\mu) = \tau^{(R)}(\rho,\mu)$, a single-valued monotonic inversion of Eq. (9).

Given a prescattering energy E', $P_\lambda(E',E) \neq 0$ if the energies E are within the region $[E_{L,\lambda}(E'), E_{H,\lambda}(E')]$ which is denoted by the "downrange of E'". $E_{L,\lambda}(E')$ and $E_{H,\lambda}(E')$ are found from Eqs. (7) through (9), and from the monotonic character of $\rho(\mu)$ for a given τ:

$$\left.\begin{matrix} E_{H,\lambda}(E') \\ E_{L,\lambda}(E') \end{matrix}\right\} = \left(\frac{1 \pm A\sqrt{1 - E_\lambda/E'}}{1+A}\right)^2 E'. \tag{12}$$

Given a post-scattering energy E, $P_\lambda(E',E) \neq 0$ if the energies E' are within the region $[E'_{L,\lambda}(E), E'_{H,\lambda}(E)]$, which is denoted by the "uprange of E". Since $\tau^{(R)}(\mu)$, for a given ρ, is monotonic, the easiest way to find $E'_{L,\lambda}(E)$ and $E'_{H,\lambda}(E)$ is by a direct inversion of Eq. (12). Overridden by the cutoff threshold, the result is

$$\left.\begin{aligned} E'_{H,\lambda}(E) &= \left(\frac{1 + A\sqrt{1 + \frac{A-1}{A+1}\frac{E_\lambda}{E}}}{1-A}\right)^2 E \\ E'_{L,\lambda}(E) &= \max\left[\left(\frac{1 - A\sqrt{1 + \frac{A-1}{A+1}\frac{E_\lambda}{E}}}{1-A}\right)^2 E, T_\lambda\right] \end{aligned}\right\}. \tag{13}$$

If $P_\lambda(E',E) \neq 0$, then it can be related to $P_\lambda(E',\mu)$, the angular distribution at E', through Eq. (5):

$$P_\lambda(E',E) = \frac{(A+1)^2}{2A}\frac{1}{\sqrt{1-(E_\lambda/E')}}P_\lambda(E',\mu). \tag{14}$$

$P_\lambda(k \to j)$, defined in Eq. (3), can be split up as follows:

$$P_\lambda(k \to j) = \left(\frac{1}{E_k - E_{k+1}}\right)\int_{E^*_{k+1}}^{E^*_k} dE' P_\lambda(E',j), \tag{15}$$

where

$$P_\lambda(E',j) \equiv \int_{E^*_{j+1}}^{E^*_j} dE\, P_\lambda(E',E) \tag{16}$$

is the probability of scattering from energy E' into group j.

The first step is the determination of the range $[E^*_{j+1}, E^*_j]$. If no part of group j is within the downrange of E', then $P_\lambda(E',j) = 0$. Otherwise there are four possibilities, to be referred to as the four categories:

$$\begin{aligned}
&\text{Category 1: } E_{L,\lambda}(E') \le E_{j+1} \le E_j \le E_{H,\lambda}(E')\\
&\text{Category 2: } E_{j+1} \le E_{L,\lambda}(E') \le E_j \le E_{H,\lambda}(E')\\
&\text{Category 3: } E_{L,\lambda}(E') \le E_{j+1} \le E_{H,\lambda}(E') \le E_j\\
&\text{Category 4: } E_{j+1} \le E_{L,\lambda}(E') \le E_{H,\lambda}(E') \le E_j\,.
\end{aligned} \tag{17}$$

The integration range $[E^*_{j+1}, E^*_j]$ is, accordingly,

$$[E^*_{j+1}, E^*_j] = \begin{Bmatrix} [E_{j+1}, E_j] & \text{for Category 1}\\ [E_{L,\lambda}(E'), E_j] & \text{for Category 2}\\ [E_{j+1}, E_{H,\lambda}(E')] & \text{for Category 3}\\ [E_{I,\lambda}(E'), E_{H,\lambda}(E')] & \text{for Category 4}\end{Bmatrix}. \tag{18}$$

The second step is the determination of the range $[E^*_{k+1}, E^*_k]$. For each category one is looking for the broadest group of energies E' consistent with the inequalities in Eq. (17) which define the category. Here the monotonic nature of the functions involved is a helpful feature because E' decreases or increases as either $E_{L,\lambda}(E')$ or $E_{H,\lambda}(E')$ respectively decreases or increases. The range $[E^*_{k+1}, E^*_k]$ is then the broadest group of E' consistent with the category, except that E_{k+1} or E_k will override the limits of this group if they extend, respectively, below E_{k+1} or above E_k. The net result is as follows:

$$\left.\begin{aligned}
&[E^*_{k+1}, E^*_k] =\\
&\quad\text{Category 1: } \{\max[E_{k+1}, E'_{L,\lambda}(E_j)], \min[E_k, E'_{H,\lambda}(E_{j+1})]\};\\
&\quad\text{Category 2: } \{\max(E_{k+1}, E^*), \min[E_k, E'_{H,\lambda}(E_j)]\}\\
&\qquad\text{where}\\
&\qquad E^* \equiv \begin{Bmatrix} E'_{L,\lambda}(E_j) & \text{if} \quad E_{L,\lambda}[E'_{L,\lambda}(E_j)] \ge E_{j+1}\\ E'_{H,\lambda}(E_{j+1}) & \qquad\qquad\quad < E_{j+1}\end{Bmatrix};\\
&\quad\text{Category 3: } \{\max[E_{k+1}, E'_{L,\lambda}(E_{j+1})], \min(E_k, E^*)\}\\
&\qquad\text{where}\\
&\qquad E^* \equiv \begin{Bmatrix} E'_{H,\lambda}(E_{j+1}) & \text{if} \quad E_{H,\lambda}[E'_{H,\lambda}(E_{j+1})] \le E_j\\ E'_{L,\lambda}(E_j) & \qquad\qquad\quad > E_j\end{Bmatrix};\\
&\quad\text{Category 4: } \{\max[E_{k+1}, E'_{H,\lambda}(E_{j+1})], \min\,[E_k, E'_{L,\lambda}(E_j)]\}.
\end{aligned}\right\} \tag{19}$$

If, for any category, the group of contributing E' is an empty group, then Eq. (19) will yield $E^*_k < E^*_{k+1}$. Such an inequality is, therefore, an indication that there is no contribution to the particular $P_\lambda(k \to j)$ coming from the particular category.

The integration in Eq. (16) can be performed numerically if Eq. (14) is substituted for $P_\lambda(E',E)$ and if $P_\lambda(E',\mu)$ is expanded in Legendre polynomials. In practice it means that a library of Legendre coefficients is available for every inelastic level. But this is not the case. Also, such a library is not foreseen in the near future, one reason being perhaps that there is little anisotropy in inelastic scattering. This reason suggests that the evaluation of the integrals in Eqs. (15) and (16) be simplified by the assumption of isotropy, namely, $P_\lambda(E',\mu) = \frac{1}{2}$. The integration in Eqs. (15) and (16) can then be performed analytically. The results may be summarized by the following set of formulas:

$$\left.\begin{aligned} \tau_t^{(i)} &\equiv \sqrt{1 - E_\lambda/E_t^*} \\ &\text{where } E_t^* \text{ is from Category } i \end{aligned}\right\} \tag{20}$$

$$L(\tau) \equiv \ln \frac{1+\tau}{1-\tau} \tag{21}$$

$$\left.\begin{matrix} S_p(\tau) \\ S_m(\tau) \end{matrix}\right\} \equiv \left\{\frac{(1+A^2)\tau \pm 2A}{1-\tau^2}\right. \tag{22}$$

$$\left.\begin{aligned} I_1 &= \begin{cases} \dfrac{(A+1)^2}{4A}(E_j - E_{j+1})[L(\tau_k^{(1)}) - L(\tau_{k+1}^{(1)})] \\ 0 \end{cases} \quad \text{if, in Category 1,} \begin{cases} E_k^* > E_{k+1}^* \\ E_k^* \le E_{k+1}^* \end{cases} \\ I_2 &= \begin{cases} \left[\dfrac{(A+1)^2}{4A}E_j - \dfrac{1-A^2}{8A}E_\lambda\right][L(\tau_k^{(2)}) - L(\tau_{k+1}^{(2)})] - \dfrac{E_\lambda}{4A}[S_m(\tau_k^{(2)}) - S_m(\tau_{k+1}^{(2)})] \\ 0 \end{cases} \\ &\qquad\qquad \text{if, in Category 2,} \begin{cases} E_k^* > E_{k+1}^* \\ E_k^* \le E_{k+1}^* \end{cases} \\ I_3 &= \begin{cases} \left[\dfrac{1-A^2}{8A}E_\lambda - \dfrac{(A+1)^2}{4A}E_{j+1}\right][L(\tau_k^{(3)}) - L(\tau_{k+1}^{(3)})] + \dfrac{E_\lambda}{4A}[S_p(\tau_k^{(3)}) - S_p(\tau_{k+1}^{(3)})] \\ 0 \end{cases} \\ &\qquad\qquad \text{if, in Category 3,} \begin{cases} E_k^* > E_{k+1}^* \\ E_k^* \le E_{k+1}^* \end{cases} \\ I_4 &= \begin{cases} E_k^* - E_{k+1}^* \\ 0 \end{cases} \text{ if, in Category 4,} \begin{cases} E_k^* > E_{k+1}^* \\ E_k^* \le E_{k+1}^* \end{cases} \end{aligned}\right\} \tag{23}$$

$$P_\lambda(k \to j) = \left(\frac{1}{E_k - E_{k+1}}\right)(I_1 + I_2 + I_3 + I_4). \tag{24}$$

Inelastic Scattering to Dense Levels

Measurements provide data on $\sigma_{(n,in),k}$, the cross section for the emission of exactly i neutrons. But if $\sigma_{(n,in),k}$ can be neglected for $i > 2$, then $\sigma_{(n,2n)}$ is also the cross section for the emission of the second neutron,

$$\Sigma_{2n,k} = \Sigma_{(n,2n),k}. \tag{25}$$

$\Sigma_{1n,k}$ is the cross section for emitting the first neutron by other than the decay of $(A+n)$ to the first Λ_k levels of (A). Hence,

$$\Sigma_{1n,k} = \Sigma_{(n,n),k} + \Sigma_{(n,2n),k} - \sum_{\lambda=1}^{\Lambda_k} \Sigma_{\lambda,k}. \tag{26}$$

Thus, $\Sigma_{in,k}$ and $\Sigma_{2n,k}$ are determined by data directly obtainable from ENDF/B files, namely excitation cross sections $\Sigma_{\lambda,k}(\lambda = 1, 2, \cdots, \Lambda_k)$, the total inelastic cross section $\Sigma_{(n,n),k}$, and the $(n,2n)$ cross section $\Sigma_{(n,2n),k}$.

Turning now to the determination of $P_{1n}(k \to j)$, it is noted that the first neutron will scatter either with probabilities of the $P_\lambda(k \to j)$ type, or with the probability $P_{1n}(k \to j)$. However, by the breakup of Eq. (4),

$$\left.\begin{aligned} &P_{1n}(k \to j) \neq 0 \leftrightarrow j \ge J, \\ &\text{where } J \text{ is implicitly defined by } (E_{j+1} \le E_{k+1} - E_{\Lambda_k} < E_j). \end{aligned}\right\} \tag{27}$$

If $P_{1n}(k \to j) \neq 0$, then

$$P_{1n}(k \to j) \equiv \left(\frac{1}{E_k - E_{k+1}}\right)\int_{E_{k+1}}^{E_k} dE' \int_{E_{j+1}}^{E_j} dE\, P_{ev}(E', E).$$

$P_{ev}(E',E)$ is the probability that the inelastic scattering at E' results in the transfer $E' \to E$. The subscript "ev"

abbreviates "evaporation", in anticipation of a later result. If j is k, then Eq. (28) has incorrect integration limits for E'. With small groups, however, little error is introduced by assuming that neutrons within group k can scatter over all the group.

The statistical model of the nucleus[2,5] yields $P_{st}(E',E)$ ("st" implies "statistical") as

$$P_{st}(E',E) \propto E\sigma_{(A+n)}(E)\rho(E' - E), \tag{29}$$

where $\sigma_{(A+n)}(E)$ is the "inverse" cross section for the formation of the compound $(A + n)$ by neutrons of energy E, and where $\rho(E' - E)$ is the level density of the residual (A) at the excitation energy $E' - E$. The notion of "level density" may be improper for low-lying spaced levels but its use may, nevertheless, lead to correct average results.[5]

The "nuclear temperature" T is introduced by the definition

$$\frac{1}{T(U)} \equiv \frac{d}{dU} \ln \rho(U) \tag{30}$$

Integrating Eq. (30), and substituting the result into Eq. (29),

$$P_{st}(E', E) \propto E\sigma_{(A+n)}(E)\rho(E') \exp\left[- \int_{E'-E}^{E'} \frac{dU}{T(U)} \right]. \tag{31}$$

The "evaporation approximation" introduces simplifications into Eq. (31). First, the inverse cross section is assumed to be constant: $\sigma_{(A+n)}(E) \approx$ const.[5] A second simplification concerns the temperature $T(U)$. Ericson[5] assumes $T(U) =$ const. The current evaluations of nuclear temperatures for ENDF/B, however, seem to be oriented toward Weisskopf's assumption that most of the scattered neutrons emerge with low energies,[2] namely that

$$E \ll E'. \tag{32}$$

Based on relation (32), $T(U)$ in Eq. (31) can be replaced by $T(E')$, yielding the "evaporation formula"

$$P_{ev}(E', E) \propto E \exp\left[- \frac{E}{T(E')} \right]. \tag{33}$$

Inspection of ENDF/B data shows T to be smoothly and slowly changing with energy. It is convenient, therefore to introduce the average "group-temperature"

$$T_k \equiv \int_{E_{k+1}}^{E_k} dE' T(E')/(E_k - E_{k+1}), \tag{34}$$

reducing relation (33) to

$$P_{ev}(E', E) \propto E \exp\left[- \frac{E}{T_k} \right] \quad \text{for} \quad E_{k+1} < E' < E_k. \tag{35}$$

Substitution of the unnormalized $P_{ev}(E',E)$ into Eq. (28) yields

$$P_{1n}(k \to j) \propto D_k(E_{j+1}) - D_k(E_j), \tag{36}$$

where

$$D_k(E_m) \equiv \left(1 + \frac{E_m}{T_k}\right) \exp\left(- \frac{E_m}{T_k} \right). \tag{37}$$

$\sum_j P_{1n}(k \to j)$ must sum to unity between $j = J$ and $j = N$, where N is the index of the (lowest energy) group. Since $E_{N+1} = 0$, the result is

$$P_{1n}(k \to j) = \frac{D_k(E_{j+1}) - D_k(E_j)}{1 - D_k(E_J)}, \quad \text{for} \quad j \geq J. \tag{38}$$

In determining $P_{2n}(k \to i)$, the probability that, following an inelastic scattering in group k, a second neutron is emitted in group i, let the probability be written $P_{2n}^{(A-n)}(k \to i)$ to explicitly express the fact that the emission of the second neutron has $(A - n)$ as residual. To simplify the evaluation of $P_{2n}^{(A-n)}(k \to i)$, the first emission neutrons involved in a transfer of $k \to j$ will be assumed to have made the transfer $\hat{E}_k \to \hat{E}_j$, where $\hat{E}_m$ denotes the average energy in group m. Therefore, by Table IV-4-I.

TABLE IV-4-I. ENERGY DIAGRAM FOR COMPOUND NUCLEUS SCATTERING

$\hat{E}_k - \hat{E}_j$ ——		—— $\hat{E}_k - \hat{E}_j - B - \hat{E}_i$
	↑	- - - ground
$(E_{\lambda k}$ — —)	B	
ground - - -	↓	
Excitation of residual (A) following the emission of the first neutron with energy $\hat{E}_j$.		Excitation of the residual $(A - n)$ following the emission of the second neutron with energy $\hat{E}_i$.

$$\left\{\begin{array}{l}\text{Following the emission of the first neutron into group } j\text{, a second neutron will be emitted into group } i \\ \text{only if } i \geq I\text{, where } I \text{ is implicitly defined by } E_{I+1} < \hat{E}_k - \hat{E}_j - B < E_I\text{, and where } \hat{E}_k - \hat{E}_j - \\ B > 0.\end{array}\right\} \quad (39)$$

B is the binding energy of an extra neutron to $(A - n)$; therefore B is the threshold energy for the $(n,2n)$ reaction, an ENDF/B datum.

Given the first-emission neutron in group j, the probability that the second neutron energy will be in group i is the probability that the compound nucleus $(A)(\hat{E}_k - \hat{E}_j)$ [i.e., compound (A) at an excitation energy $\hat{E}_k - \hat{E}_j$] decays to the residual $(A - n)(\hat{E}_k - \hat{E}_j - B - \hat{E}_i)$ (see Table IV-4-I). But in the framework of compound-nucleus physics the decay of a compound does not depend on the mode by which the compound nucleus came into being. Hence, in particular, the latter probability is also the probability that a neutron with energy $\hat{E}_k - \hat{E}_j - B$, scattered inelastically from the target $(A - n)$, is emitted with energy $\hat{E}_i$. Excitation cross section data are generally not available in the present ENDF/B files for targets $(A - n)$; therefore no part of this "inelastic scattering" by the "target" $(A - n)$ can be treated by single-level modes, unless detailed assumptions are made on the excitation cross sections of $(A - n)$. Refraining from such assumptions, the latter probability has to be of the P_{1n} type, namely, $P_{1n}^{(A-n)}(I \to i)$:

$$P[(A)(\hat{E}_k - \hat{E}_j) \to (A - n)(\hat{E}_k - \hat{E}_j - B - \hat{E}_i)] = P_{1n}^{(A-n)}(I \to i). \quad (40)$$

Given k, the total probability for a secondary emission $k \to i$ is a weighted sum over $P_{1n}^{(A-n)}(I \to i)$ for all possible j's. The possible j's are readily determined from Eq. (39):

$$\{\text{Given a first neutron scattering } k \to j\text{, a secondary emission will follow if } j \geq K\text{, where } K \text{ is } I(j = N).\} \quad (41)$$

The weighting factors are the probabilities for the $k \to j$ transfers of the first neutron. In general, $E_{\lambda k} < B$; therefore, $\hat{E}_k - B$, the highest of the first-emission neutron energies to be followed by a second emission, is less than $E_{k+1} - E_{\lambda k}$, the highest of the first-emission neutron energies to be treated by the P_{1n} type probability. In this case $J \leq K$ and the weighting factors are all of the P_{1n} type,

$$P_{2n}^{(A-n)}(k \to i) = \frac{\sum_{j \geq K} P_{1n}^{(A)}(k \to j) P_{1n}^{(A-n)}(I \to i)}{\sum_{j \geq K} P_{1n}^{(A)}(k \to j)}, \quad \text{if} \quad J \leq K. \quad (42)$$

If $J > K$, then,

$$P_{2n}^{(A-n)}(k \to i) = \frac{\sum_{\lambda=1}^{\lambda_k} \sum_{j=K}^{J} P_{\lambda}^{(A)}(k \to j) P_{1n}^{(A-n)}(I \to i) + \sum_{j \geq J} P_{1n}^{(A)}(k \to j) P_{1n}^{(A-n)}(I \to i)}{\sum_{\lambda=1}^{\lambda_k} \sum_{j=K}^{J} P_{\lambda}^{(A)}(k \to j) + \sum_{j \geq J} P_{1n}^{(A)}(k \to j)}, \quad \text{if} \quad J > K. \quad (42')$$

The evaluation of $P_{2n}^{(A-n)}(k \to i)$ via Eqs. (42) calls for the use of neutron temperatures for $(A - n)$, but these are not provided by ENDF/B files. Instead, $T_{(A-n)}$ can be related to $T_{(A)}$. The relation is given, in terms of ρ, by Ericson[5] as $\rho_{(A-n)}(U) = \rho_{(A)}(U + \delta)$, where $\delta(A,Z)$ is the "pairing energy". It is suggested, however, that at this stage of the art the pairing shift be neglected, assuming instead that $\rho_{(A-n)}(U) \approx \rho_{(A)}(U)$; thereupon, by Eq. (29), $P_{1n}^{(A-n)}(I \to i)$ of Eqs. (42) will be replaced by $P_{1n}^{(A)}(I \to i)$:

$$P_{1n}^{(A-n)}(I \to i) \approx P_{1n}^{(A)}(I \to i). \quad (43)$$

The neglect of the pairing shift cannot be serious, because many of the secondary emissions leave the residual $(A - n)$ at low excitation energies where the application of the continuous $\rho(U)$, hence of $T(U)$, is at best a crude first

proximation. At the practical end of the problem, $T(U)$ for low-valued U are not supplied by ENDF/B and long-range extrapolation of $T(U)$ is called for. But where the temperatures are based on extrapolation in the first place, little is to be gained by introducing the pairing shift.

In Eqs. (42), the probabilities $P_{1n}(I \to i)$ must sum to unity for $i \geq I$. Hence, by Eqs. (36), (37), and (43),

$$P_{2n}^{(A-n)}(k \to i) = \sum_{j \geq K} \left[\frac{D_k(E_{j+1}) - D_k(E_j)}{1 - D_k(E_K)}\right]\left[\frac{D_I(E_{i+1}) - D_I(E_i)}{1 - D_I(E_I)}\right], \quad \text{for} \quad i \geq I, \quad \text{if} \quad J \leq K; \tag{44}$$

$$P_{2n}^{(A-n)}(k \to i) = \left\{\sum_{j=K}^{J} \sum_{\lambda=1}^{\Lambda_k} P_\lambda(k \to j)\left[\frac{D_I(E_{i+1}) - D_I(E_i)}{i - D_I(E_I)}\right]\right.$$
$$\left. + \sum_{j \geq J}\left[\frac{D_k(E_{j+1}) - D_k(E_j)}{1 - D_k(E_J)}\right]\left[\frac{D_I(E_{i+1}) - D_I(E_i)}{1 - D_I(E_I)}\right]\right\} \Big/ \left[\sum_{j=K}^{J} \sum_{\lambda=1}^{\Lambda_k} P_\lambda(k \to j) + 1\right] \quad \text{for} \quad i \geq I, \text{if } J \geq K. \tag{44'}$$

Finally, if U^* is the lowest energy for which ENDF/B files provide a value of T, then the extrapolation $T(U) = T(U^*)$ for $U < U^*$ can be employed. This is in accord with modern views on the nucleus at low excitations.[6]

References

1. B. J. Toppel, A. L. Rago and D. M. O'Shea, *MC²*, *A Code to Calculate Multigroup Cross Sections*, ANL-7318 (1967).
2. J. M. Blatt and V. F. Weisskopf, *Theoretical Nuclear Physics*, (John Wiley and Sons, Inc., New York, 1952).
3. B. D. O'Reilly and R. C. Lewis, *The Calculation of Slowing Down Transfer Matrices in the Spherical Harmonics Representation*, NAA-SR-11530 (1966).
4. J. Nelson et al., *Charged Particle Cross Sections*, LA-2014 (1957).
5. T. Ericson, *The Statistical Model and Nuclear Level Densities*, Advances in Physics **9**, 425 (1960).
6. T. Ericson, *A Statistical Analysis of Excited Nuclear States*, Nucl. Phys **11**, 481 (1959).

IV-5. Higher-Order Transport Approximations for MC²-2

C. N. Kelber, H. Henryson, II, E. M. Pennington and W. M. Stacey, Jr.

The objective of the subcommittee on higher-order transport approximations was to recommend algorithms and methods for incorporating higher-order anisotropy in the revised code MC²-2.

The subcommittee recommended that the extended transport approximation be employed with the $P_1(B_1)$ and consistent $P_1(B_1)$ equations so that the formal appearance of the equations solved by MC²-2 is little changed from MC². The one external change is the inclusion of a term $A(K,N)$ in the equation for ϕ_1 instead of the total cross section: K and N are new input parameters. This approximation can also be used with continuous slowing-down theory.

The extended transport approximation consists of treating scattering sources for orders of anisotropy higher than 1 in the transport approximation. Thus, the Fourier transformed P_ℓ equations have the generic form

$$\frac{\ell+1}{2\ell+1}\eta\phi_{\ell+1}(B,u) + \frac{\ell}{2\ell+1}\eta\phi_{\ell-1}(B,u) + \Sigma(u)\phi_\ell(B,u) = S_\ell(B,u)$$
$$+ \sum_i \int_{u-\ln(1/\alpha_i)}^{u} du'\Sigma_{Si}^{\ell}(u' \to u)\phi_\ell(B,u'), \qquad \ell = 0, 1 \cdots \infty, \tag{1}$$

where

$B \equiv$ transform variable
$\eta \equiv iB$, where i is the imaginary unit
$i \equiv$ isotopic index
$u \equiv$ lethargy
$\ell \equiv$ angular momentum component index
$\ln(1/\alpha_i) \equiv$ maximum logarithmic decrement of energy upon scattering
$S_\ell \equiv$ external source of ℓth order angular momentum
$\Sigma \equiv$ total cross section.

Consistent $P_{1,N}$ Approximation

The consistent $P_{1,N}$ approximation is obtained by retaining Eq. (1) for $\ell = 0, 1 \cdots, N$, ignoring the ϕ_{N+1} term in the $\ell = N$ equation, and making a "transport" approximation of the elastic scattering integral

$$\int_{u-\ln(1/\alpha_i)}^{u} du'\, \Sigma_{Si}^{\ell}(u' \to u)\, \phi_\ell(B,u') \cong \Sigma_{Si}^{\ell}(u)\phi_\ell(B,u), \qquad \ell \geq 2. \tag{2}$$

Equations (1) for $\ell = 2, \cdots, N$ are then algebraic and can be solved for ϕ_2 in terms of ϕ_1, which expression can then be substituted into the $\ell = 1$ equation, thus reducing the $N + 1$ equations to

$$\eta\phi_1(B,u) + \Sigma(u)\phi_0(B,u) = S_0(B,u) + \sum_i \int_{u-\ln(1/\alpha_i)}^{u} du'\, \Sigma_{Si}^{0}(u' \to u)\, \phi_0(B,u'), \tag{3}$$

$$\tfrac{1}{3}\eta\phi_0 + A_{1,N}(B,u)\phi_1(B,u) = S_1(B,u) + \sum_i \int_{u-\ln(1/\alpha_i)}^{u} du'\, \Sigma_{Si}^{1}(u' \to u)\phi_1(B,u'). \tag{4}$$

The higher-order angular flux components are constructed recursively from

$$\phi_\ell(B,u) = -\frac{\ell/(2\ell+1)\eta\phi_{\ell-1}(B,u)}{A_{\ell,N}(B,u)}. \tag{5}$$

The quantities $A_{\ell,N}$ are given by a continued fraction expansion

$$A_{\ell,N} = b_{\ell-1} + \cfrac{a_\ell}{b_\ell + \cfrac{a_{\ell+1}}{b_{\ell+1} + \cfrac{a_{\ell+2}}{b_{\ell+2} + \cdots}}} \tag{6}$$

where (for $S_\ell = 0, \ell \geq 2$)

$$\begin{aligned} b_0 &= \Sigma(u) \\ b_\ell &= \Sigma(u) - \Sigma_S^{\ell+1}(u), \qquad 1 \leq \ell \leq N-1 \\ a_\ell &= -\frac{\ell+1}{2\ell+1} \cdot \frac{\ell+1}{2(\ell+1)+1} \cdot \eta^2, \qquad 1 \leq \ell \leq N-1. \end{aligned} \tag{7}$$

When the elastic scattering integrals are treated by continuous slowing-down theory, by defining elastic slowing-down densities as

$$q_\ell(B,u) \equiv \sum_i \int_{u-\ln(1/\alpha_i)}^{u} du' \int_{u}^{u'+\ln(1/\alpha_i)} du''\, \Sigma_{Si}^{\ell}(u' \to u'')\phi_\ell(B,u'), \qquad \ell = 0, 1, \tag{8}$$

and by assuming the variation in the total collision density over the interval $u > u' > u - \ln(1/\alpha_i)$ to be represented by a two-term Taylor's series, Eqs. (3) and (4) can be reduced to

$$\begin{aligned} &\left[\frac{(\Sigma - \Sigma_S^0)\left(A_{1,N} - \Sigma_S^1 + \frac{e_1}{a_1}\hat{\xi}_1\Sigma\right) - \frac{1}{3}\eta^2}{\left(A_{1,N} - \Sigma_S^1 + \frac{e_1}{a_1}\hat{\xi}_1\Sigma\right)\left(\Sigma - \Sigma_S^0 + \frac{e_0}{a_0}\hat{\xi}_0\Sigma\right) - \frac{1}{3}\eta^2}\right]\left[\frac{e_0}{a_0}q_0 + S_0\right] \\ &\quad + \eta\left[\frac{\frac{e_0}{a_0}\hat{\xi}_0\Sigma}{\left(A_{1,N} - \Sigma_S^1 + \frac{e_1}{a_1}\hat{\xi}_1\Sigma\right)\left(\Sigma - \Sigma_S^0 + \frac{e_0}{a_0}\hat{\xi}_0\Sigma\right) - \frac{1}{3}\eta^2}\right]\left[\frac{e_1}{a_1}q_1 + S_1\right] + \frac{dq_0}{du} = S_0, \end{aligned} \tag{9}$$

$$\begin{aligned} &\frac{\eta}{3}\left[\frac{\frac{e_1}{a_1}\hat{\xi}_0\Sigma}{\left(A_{1,N} - \Sigma_S^1 + \frac{e_1}{a_1}\hat{\xi}_1\Sigma\right)\left(\Sigma - \Sigma_S^0 + \frac{e_0}{a_0}\hat{\xi}_0\Sigma\right) - \frac{1}{3}\eta^2}\right]\left[\frac{e_0}{a_0}q_0 + S_0\right] \\ &\quad + \left[\frac{(A_{1,N} - \Sigma_S^1)\left(\Sigma - \Sigma_S^0 + \frac{e_0}{a_0}\hat{\xi}_0\Sigma\right) - \frac{1}{3}\eta^2}{\left(A_{1,N} - \Sigma_S^1 + \frac{e_1}{a_1}\hat{\xi}_1\Sigma\right)\left(\Sigma - \Sigma_S^0 + \frac{e_0}{a_0}\hat{\xi}_0\Sigma\right) - \frac{1}{3}\eta^2}\right]\left[\frac{e_1}{a_1}q_1 + S_1\right] + \frac{dq_1}{du} = S_1, \end{aligned} \tag{10}$$

where Σ_S has replaced Σ_{Si}.

The fluxes are related to the slowing-down densities by

$$\phi_0 = \frac{\left(A_{1,N} - \Sigma_S^1 + \frac{e_1}{a_1}\hat{\xi}_1\Sigma\right)\left(\frac{e_0}{a_0}q_0 + S_0\right) - \eta\left(\frac{e_1}{a_1}q_1 + S_1\right)}{\left(A_{1,N} - \Sigma_S^1 + \frac{e_1}{a_1}\hat{\xi}_1\Sigma\right)\left(\Sigma - \Sigma_S^0 + \frac{e_0}{a_0}\hat{\xi}_0\Sigma\right) - \frac{1}{3}\eta^2} \tag{11}$$

$$\phi_1 = \frac{\left(\Sigma - \Sigma_S^0 + \frac{e_0}{a_0}\hat{\xi}_0\Sigma\right)\left(\frac{e_1}{a_1}q_1 + S_1\right) - \frac{1}{3}\eta\left(\frac{e_0}{a_0}q_0 + S_0\right)}{\left(A_{1,N} - \Sigma_S^1 + \frac{e_1}{a_1}\hat{\xi}_1\Sigma\right)\left(\Sigma - \Sigma_S^0 + \frac{e_0}{a_0}\hat{\xi}_0\Sigma\right) - \frac{1}{3}\eta^2} \tag{12}$$

The new parameters introduced in Eqs. (9) through (12) are defined by

$$\hat{\xi}_\ell(u) \equiv \xi_\ell(u) + \frac{a_\ell(u)c_\ell(u)}{e_\ell(u)}, \tag{13}$$

$$\xi_\ell(u) \equiv \sum_i \int_{u-\ln(1/\alpha_i)}^{u} du' \frac{\Sigma_{Si}(u')}{\Sigma(u')} g_i^\ell(u,u'), \tag{14}$$

$$a_\ell(u) \equiv \sum_i \int_{u-\ln(1/\alpha_i)}^{u} du' \frac{\Sigma_{Si}(u')}{\Sigma(u')} (u'-u) g_i^\ell(u,u'), \tag{15}$$

$$c_\ell(u) \equiv \sum_i \left[\frac{\Sigma_{Si}(u)}{\Sigma(u)} g_i^\ell(u,u) - \int_{u-\ln(1/\alpha_i)}^{u} du' \frac{\Sigma_{Si}(u')}{\Sigma(u')} f_i(u' \to u) P_\ell(\mu_L^*)\right], \tag{16}$$

$$e_\ell(u) \equiv \sum_i \int_{u-\ln(1/\alpha_i)}^{u} du' \frac{\Sigma_{Si}(u')}{\Sigma(u')} (u'-u) f_i(u' \to u) P_\ell(\mu_L^*), \tag{17}$$

where

$$\Sigma_{Si}^\ell(u \to u') = \Sigma_{Si}(u) f_i(u \to u') P_\ell[\mu_L^*(u',u)] \tag{18}$$

with

$$\mu_L^*(u \to u') \equiv \frac{(M_i+1)e^{(u-u')/2} - (M_i-1)e^{(u'-u)/2}}{2} \tag{19}$$

and

$$g_i^\ell(u,u') \equiv \int_u^{u+\ln(1/\alpha_i)} du'' f_i(u' \to u'') P_\ell[\mu_L^*(u',u)]. \tag{20}$$

$P_{1,N}$ Approximation

The $P_{1,N}$ approximation is obtained by retaining Eqs. (1) for $\ell = 0, 1, \cdots, N$, ignoring the ϕ_{N+1} term in the $\ell = N$ equation, and making the "transport" approximation of Eq. (2) for $\ell \geq 1$. The $P_{1,N}$ approximation differs from the consistent $P_{1,N}$ approximation in that the "transport" approximation is also made for the $\ell = 1$ elastic scattering integral in the former.

Equations for $\ell = 1, \cdots, N$ can be solved for ϕ_1 in terms of ϕ_0, which expression can be used in the $\ell = 0$ equation to obtain (when $S_1 = \cdots S_N = 0$)

$$\left[\Sigma(u) - \frac{\eta^2}{3\bar{A}_{1,N}(B,u)}\right]\phi_0(B,u) = S_0(B,u) + \sum_i \int_{u-\ln(1/\alpha_i)}^{u} du' \Sigma_{Si}^0(u' \to u)\phi_0(B,u'). \tag{21}$$

Higher-order angular fluxes are constructed recursively from Eq. (5) with $\bar{A}_{\ell,N}$ replacing $A_{\ell,N}$. The quantity $\bar{A}_{\ell,N}$ differs from $A_{\ell,N}$ of Eq. (6) only in that $b_0 = \Sigma - \Sigma_S^1$ for the former.

The continuous slowing-down approximation in this case is

$$\frac{dq_0}{du}(B,u) = -\frac{\Sigma_{ne}(B,u)q_0(B,u) + \hat{\xi}_0(u)\Sigma(u)S_0(u)}{\hat{\xi}_0(u)\Sigma(u) + [a_0(u)/e_0(u)]\Sigma_{ne}(B,u)}, \tag{22}$$

$$\phi_0(B,u) = \frac{q_0(B,u) + [a_0(u)/e_0(u)]S_0(u)}{\hat{\xi}(u)\Sigma(u) + [a_0(u)/e_0(u)]\Sigma_{ne}(B,u)}, \tag{23}$$

with

$$\Sigma_{ne}(B, u) \equiv \Sigma(u) - \Sigma_S^0(n) - \frac{\eta^2}{3\tilde{A}_{1,N}(B, u)}. \tag{24}$$

Numerical Considerations

The consistent $P_{1,N}$ equations [Eqs. (3) and (4)] are formally identical to the consistent P_1 equations solved by MC^2, the difference being that in the $\ell = 1$ equation $A_{1,N}$ appears instead of Σ. Similarly the $P_{1,N}$ equation [Eq. (21)] differs from the P_1 equations solved by MC^2 only in that $\tilde{A}_{1,N}$ appears in the former where Σ_{tr} appears in the latter. Thus, the solution algorithms in MC^2 would not have to be altered to accommodate the $P_{1,N}$ and consistent $P_{1,N}$ approximations.

The additional numerical work which would be required for the $P_{1,N}$ and consistent $P_{1,N}$ equations is associated with evaluating the higher-order angular moments ($\ell \geq 2$) of the elastic scattering cross section. These moments are required to construct the higher-order angular fluxes which are used in group collapsing to obtain higher-order angular scattering cross sections for broad groups. The primary difficulty in this respect is associated with storing and manipulating ultra-fine group elastic scattering matrices for the higher-order angular scattering.

The continuous slowing-down approximation eliminates the need for the elastic scattering matrices, but requires that the moderating parameters of Eqs. (13) through (17) be evaluated. However, recursive relations can be used to minimize the computational effort associated with this latter requirement.

The recommended set of algorithms is summarized in Table IV-5-I.

The use of a second input buckling, K^2, allows the user the option of selecting the infinite medium approximation for the higher-order terms, $K^2 = 0$. There is no *a priori* justification for $K \neq B$ where B is the MC^2 buckling. It is expected, however, that B is only weakly dependent on K. For large values of K it may not be possible to get a positive diffusion coefficient. This problem, characteristic of any consistent P_N approximation in which the elastic source term is treated with the transport approximation, deserves further study to determine optimal resolution. It may be possible to define criteria which indicate when S_nP_N theory is preferred; or it may be possible to define a "diffusion coefficient" which is always positive, but not as good an approximation at high B^2 as at low B^2.

The computation of the $Q_n(x)$ is complicated by the singularity at $x = 1$. The recommended procedure for $x > 1$ is to compute $Q_N(x)$ first (from, e.g., hypergeometric functions) and use the recursion formula. For arbitrary N this could pose real problems. If this problem cannot be satisfactorily resolved for arbitrary N, setting $N \leq 9$ would be satisfactory. Most S_nP_N shielding calculations use $N = 5$ or 7, with $N = 9$ for a check case. In this event the Q_N might be stored as algebraic functions (plus the singular "arctangent" terms).

The fluxes corresponding to angular order ℓ can be reconstituted from

$$\phi_{\ell,g} = \frac{\dfrac{\ell}{2\ell + 1} K\phi_{\ell-1,g}}{A_{\ell,g}(\kappa, N)}, \qquad \ell = 2, \cdots N. \tag{25}$$

[Equation (25) constitutes Algorithm Set II.]

The complete set of ultra-fine group fluxes, ϕ_0, ϕ_1, and the ϕ_ℓ found from Eq. (25) can then be used as weighting functions to compute higher-order scattering matrices on a fine-group scale.

The elastic scattering cross section σ_S in ETØE (the code which reads the ENDF/B tape and forms the basic data for the ultra-fine group MC^2-2 calculation) is the sum of resolved resonance, unresolved resonance, and smooth (tabulated) contributions in the general case. It is tabulated on a variable mesh since more points are needed near peaks of resonances than in regions where σ_S is nearly constant, and since the smooth contribution is already on a variable mesh in the ENDF/B data. ETØE calculates the resolved and unresolved cross sections from the resonance parameters and adds these to the smooth cross sections to get the total elastic cross section.

In preparing the Legendre data for MC^2, ETØE reads the $\sigma_S - E$ array from a scratch unit, and finds the average σ_S over lethargy increments of $\frac{1}{120}$ centered about the energies in the MC^2 Legendre structure. In some cases it is necessary for ETØE to fit coefficients to tabulated $p(\mu)$ versus μ distributions in the center-of-mass system. $p(\mu)$ is the angular scattering distribution and μ is the cosine of the scattering angle. Presumably the f_ℓ (Legendre coefficients of the fit to the angular scattering distribution) are not averaged because they vary more slowly than σ_S. Finally the σ_S and f_ℓ are multiplied according to

$$B_\ell = (\sigma_S/4\pi)(2\ell + 1)f_\ell \tag{26}$$

to give the B_ℓ coefficients written on the MC^2 library tape for $\ell = 0, 1, \cdots 19$.

TABLE IV-5-I. ALGORITHM SET I

Consistent P_N

$$\eta\phi_{1,g} + \Sigma_g\phi_{0,g} = S_{0,g} + \Sigma_{S,g}^{0,g'}\phi_{0,g'}$$

$$\tfrac{1}{3}\eta\phi_{0,g} + A_{1,g}(\kappa,N)\phi_{1,g} = S_{1,g} + \Sigma_{S,g}^{1,g'}\phi_{1,g'}$$

$$A_\ell(\kappa,N) = (b_{\ell-1} + a_\ell/(b_\ell + a_{\ell+1}/(b_{\ell+1} + a_{\ell+2}\cdots)\cdots), \qquad \text{(terminates at } \ell = N-1)$$

$$S_\ell = 0, \qquad \ell \geq 2$$

$b_0 = \Sigma_g$ = total cross section

$$b_\ell = \Sigma_g - \Sigma_{S,g}^{\ell+1}, \qquad 1 \leq \ell \leq N-1$$

$$a_\ell = -\frac{\ell+1}{2\ell+1}\frac{\ell+1}{2(\ell+1)+1}\kappa^2, \qquad 1 \leq \ell \leq N-1$$

$\Sigma_{S,g}^{\ell+1}$: see Algorithm Set IV, below

$\eta = iB$, B input

$\kappa = iK$, K input

$g = 1, 2, \cdots, G$ = No. of groups, input

$\ell = 2, \cdots, N = P_N$ order, input

Ordinary P_N

As above except:

$$b_0 = \Sigma_0 - \Sigma_{S,g}^1$$

Consistent B_N

$$b_\ell = \Sigma_g - \Sigma_{S,g}^{\ell+1} + \Sigma_g\frac{N+1}{2N+1}\frac{\kappa}{\Sigma_g}\frac{Q_{N+1}(-\Sigma_g/\kappa)}{Q_N(-\Sigma_g/\kappa)}\delta_\ell^{N-1}, \qquad 1 \leq \ell \leq N-1$$

$$b_0 = \Sigma_g, \qquad N \neq 1$$

$$b_0 = \left[1 + \frac{2}{3}\frac{\kappa}{\Sigma_g}\frac{Q_2(-\Sigma_g/\kappa)}{Q(-\Sigma_g/\kappa)}\right]\Sigma_g = \frac{B\tan^{-1}\dfrac{B}{\Sigma_g}}{3\left(1 - \Sigma_g/B\tan^{-1}\dfrac{B}{\Sigma_g}\right)}, \qquad N = 1$$

Ordinary B_N

$$b_\ell = \Sigma_g - \Sigma_{S,g}^{\ell+1} + \Sigma_g\frac{N+1}{2N+1}\frac{\kappa}{\Sigma_g}\frac{Q_{N+1}(-\Sigma_g/\kappa)}{Q_N(-\Sigma_g/\kappa)}\delta_\ell^{N-1}, \qquad 0 \leq \ell \leq N-1$$

Explicitly,

$$b_0 = \Sigma_g - \Sigma_g^1, \qquad N \neq 1$$

$$b_0 = \frac{B\tan^{-1}B/\Sigma}{3(1 - \Sigma_g/B\tan^{-1}B/\Sigma_g)} - \Sigma_g^1, \qquad N = 1$$

$Q_N(x) \equiv$ Legendre functions of the second kind.

In the present version of MC^2, the P_0 and P_1 elastic scattering transfer matrices are obtained from the B_ℓ coefficients and constants stored by DATA statements in the ALRAGO subroutine of MC^2.[1] The method used assumed integration over the receiving ultra-fine group, but a linear average over the ends of the source ultra-fine group. This method is poor for two reasons. Since heavy material can only downscatter to two ultra-fine groups, the linear average over the ends of the source group is inaccurate. Also the numerics of the situation are such that great near-cancellation of terms occurs, and the constants in the DATA statement must therefore be correct to many figures. In the new version of MC^2, it is proposed that the P_0 and P_1 scattering matrices at the ultra-fine group level be computed in ETØE from the $\sigma_S - E$ array and the f_ℓ coefficients, and stored on the library tape to be used by MC^2

directly. This involves the evaluation of double integrals over the energies of the source and receiving groups to give $\Sigma^{\ell}_{g,g'}$ for $\ell = 0$ and 1 as, for example, in Eq. (26) of the SUPERTØG manual, ORNL-TM-2679.[2] There an analytic flux, such as $1/E$ flux, is assumed for the source group. Work must be done to ensure that the method used for calculating the ultra-fine group transfer matrices is sufficiently accurate and fast. Thus, various choices of integration variables (energy, lethargy, angle, etc.) and mesh spacings should be investigated.

In computing $\sigma^{\ell}_{g,g'}$, for $\ell \geq 2$, it was recommended that Eq. (26) of Ref. 2 be used, except that the flux $\phi(E') = 1/E'$ be replaced by the ultra-fine group fluxes obtained by solving the extended P_1 transport equation. In Eq. (26) of Ref. 2 the γ and δ are the boundaries of the source ultra-fine groups so that $\sigma_S(E')(2\ell + 1)\, f_\ell(E')$ might be replaced by $4\pi B_\ell$. However, one is left with the factors $P_\ell(\mu)$ and $P_\ell(\eta)$, where μ and η are the cosines of the scattering angles in the laboratory and center-of-mass systems, respectively. They are given by

$$\mu = \frac{1}{2}(A + 1)\left(\frac{E}{E'}\right)^{1/2} - \frac{1}{2}(A - 1)\left(\frac{E'}{E}\right)^{1/2}$$

and

$$\eta = 1 - \frac{(A + 1)^2}{2A}\left[1 - \frac{E}{E'}\right].$$

Thus, they depend only on A, E, and E'. One might be able to evaluate the integral in Eq. (26) of Ref. 2 by using some sort of average of μ and η for the various γ and δ. This procedure is questionable, because a similar type of averaging causes inaccuracies for heavy materials in the P_0 and P_1 matrices in the present MC^2 code. Apparently the mesh intervals in SUPERTØG are of the same order of magnitude as the MC^2 ultra-fine groups, so that the procedure might be adequate. The only obviously better method would be to compute the ultrafine group transfer matrices for $\ell \geq 2$, which has been rejected because of lack of storage space.

The recommended algorithms are:

*Algorithm Sets III and IV**

The subcommittee recommended that elastic scattering matrices and vectors be calculated using a SUPERTØG[1]-like treatment from the formula

$$\Sigma^{\ell}_s(g' \to g) = \frac{2\ell + 1}{1 - \alpha} \frac{\int_\beta^\lambda du \int_\delta^\gamma du'\, e^{-(u-u')}\, \phi_\ell(u')\Sigma_s(u')P_\ell(\mu) \sum_{j=0}^{J} (2j + 1)\, f_j(u')P_j(\mu_c)}{\int_{g'} \phi_\ell(u')\, du'}. \tag{27}$$

Noting that

$$\begin{aligned} \Sigma^{\ell}_s(u') &= \frac{2\ell + 1}{1 - \alpha} \sum_{j=0} (2j + 1)\, f_j(u')\Sigma_s(u') \int_{u'}^{u' + \ln 1/\alpha} du\, e^{-(u-u')}\, P_\ell(\mu)P_j(\mu_c) \\ &= (2\ell + 1)\, \Sigma_s(u')\, T^{\ell j}\, f_j(u'), \end{aligned} \tag{28a}$$

then:

$$\Sigma^{\ell}_s(g') = \frac{\int_{g'} du'\, (2\ell + 1)\, \Sigma_s(u')\phi_\ell(u')\, T^{\ell j}\, f_j(u')}{\int_{g'} du'\, \phi_\ell(u')}, \tag{28b}$$

where

α, β, λ, δ, and γ are defined in Ref. 1.

$f_j(u') \equiv$ Legendre expansion coefficients in center-of-mass (the B's given in MC^2 are related to f through

$$B_j(E') = \frac{(2j + 1)\, \Sigma_S(E')f_j(E')}{4\pi};$$

finally,

* The summation convention is used: matching lower and upper indices imply a sum. Superfluous indices and sums over materials or isotopes are omitted.

$$\Sigma^{\ell}_{s,g'} = 4\pi T^{\ell j} \frac{2\ell + 1}{2j + 1} B_{j,g'} \tag{29}$$

and

$$\begin{aligned} T^{\ell j} &= \frac{2j + 1}{2} \int_{-1}^{1} P_\ell(\mu) P_j(\mu_c)\, du_c \\ &= -\frac{2j + 1}{2} \int_{0}^{\ln 1/\alpha} P_\ell(\mu) P_j(\mu_c) \frac{du_c}{dU}\, dU \end{aligned} \tag{30}$$

are elements of the transformation matrix from the center-of-mass to the laboratory system as defined by Zweifel and Hurwitz.[3] The $T^{\ell j}$ can be calculated by a routine in ETØE. The angles μ and μ_c are defined as follows:

$$\begin{aligned} \mu &\equiv \text{cosine of scattering angle in the laboratory system} \\ &\equiv \tfrac{1}{2}[(A + 1)e^{(u'-u)/2} - (A - 1)e^{(u-u')/2}] \\ &= \tfrac{1}{2}[(A + 1)e^{U/2} - (A - 1)e^{U/2}] \end{aligned} \tag{31}$$

$$\mu_c \equiv \text{cosine of scattering angle in the center-of-mass system}$$

$$\equiv \frac{(A + 1)^2 e^{u'-u} - (A^2 + 1)}{2A} = \frac{1}{2A}[(A + 1)^2 e^{-U} - (A^2 + 1)]. \tag{32}$$

References

1. B. J. Toppel, A. L. Rago and D. M. O'Shea, *MC²*, *A Code to Calculate Multigroup Cross Sections*, ANL-7318 (1967).
2. R. Q. Wright, J. L. Lucius, N. M. Greene, et al., *SUPERTØG*, ORNL-TM-2679 (September 1969).
3. P. F. Zweifel and H. Hurwitz, Jr., *Transformation of Scattering Cross Sections*, J. Appl. Phys. **25**, 1241 (1954).

IV-6. Preliminary Investigations of the Resolved Resonance Algorithms for the New MC² Code

R. N. Hwang

Investigations have been made on the resolved resonance algorithms for the new MC² code (MC²-2). It has been known for some time that the computer time required for the resolved resonance energy region in the existing MC² code varies from 40 to 60% of the total time. It is by far the most time consuming part in MC².

Perhaps the best way to begin is to investigate the deficiencies of the existing MC² algorithm itself.[1]

Deficiencies of the Existing Algorithm on the Resolved Resonances

Under the assumption of the NR-approximation the self-shielded cross section to be considered is

$$\tilde{\sigma}_x = \frac{\sum_i \int_{E_1}^{E_2} \frac{\sigma_{xi}\, dE}{\Sigma_t}}{\int_{E_1}^{E_2} \frac{dE}{\Sigma_t}}, \tag{1}$$

where σ_{xi} is the cross section of the process x due to the ith resonance, and Σ_t is the total macroscopic cross section.

In the existing MC² algorithm, E_1 and E_2 are the fixed group boundaries of the fine or the ultrafine groups and all resonances within E_1 are included in Σ_t. Both integrals in Eq. (1) are evaluated using the Romberg quadrature whereby the total mesh points are 2^N and N is the Nth iteration that satisfies a relative error criterion of 0.0005 specified by the program.

Three major drawbacks of the existing MC² algorithm will be discussed as follows.

TABLE IV-6-I. Variations of N in Various Energy Regions for a Typical MC² Fine Group Problem

Energy Range, keV	N
4.3–3.35	12
3.35–2.61	12
2.61–2.03	12
2.03–1.58	11
1.58–1.23	11
1.23–0.961	11
0.961–0.749	11
0.749–0.583	10
0.583–0.454	10
0.454–0.354	10
0.354–0.275	9
0.275–0.214	9
0.214–0.167	8
0.167–0.130	8
0.130–0.101	9
0.101–	<9

TREATMENT OF OVERLAPPING RESONANCES

The magnitude of N, to a great extent, depends on how much the integrand fluctuates. The fluctuations in the integrand, in turn, depend strongly on how many overlapping resonances are included between E_1 and E_2. Since each overlapping resonance will give rise to a "dip" in the integrand, it is not difficult to realize that the more "dips" there are, the larger N must be to meet the given convergence criterion. Any relaxation of the given congence criterion is not possible without sacrificing the accuracy of the Doppler effect estimations. Table IV-6-I gives the approximate values of N for each resonance integral in various energy regions taken from a typical MC² fine group problem with U-238 and Pu-239.

The listed values of N and their implication on the computing time required in various energy regions are self-explanatory. The larger N required for each resonance integral in the high energy regions is clearly due to the inclusion of a large number of overlapping levels. For heavy isotopes, in general, the contribution of the overlapping resonances beyond the next nearest neighbors is believed to be insignificant as far as the Doppler effect is concerned.

DEFICIENCY OF ROMBERG QUADRATURE FOR FIXED ENERGY BOUNDARIES

The limits of integration in the existing MC² algorithm are fixed by the ultra fine or fine group structures. In the high energy region, the limits are generally much wider than the extent of a resonance, especially when the fine group calculations are considered. As a result, the mesh points in Romberg quadratures are so widely spaced that a high order of N is required to meet the specified convergence criterion. The problem may be resolved by using an adaptive integration scheme whereby the mesh points are chosen according to the fluctuations of the integrand.

EVALUATION OF THE FLUX CORRECTION FACTOR

The existing MC² algorithm evaluates the numerator and denominator of Eq. (1) separately. It has been pointed out in Ref. 2 that the denominator is related to the numerator in the following way:

$$\int_{E_1}^{E_2} \frac{1}{\Sigma_t}\, dE = \frac{E_2 - E_1}{\Sigma_p}\left\{1 - \frac{1}{E_2 - E_1}\sum_i \frac{\Gamma_i}{\Gamma_{xi}}\int_{E_1}^{E_2} \frac{\Sigma_{xi}\, dE}{\Sigma_t}\right\}. \tag{2}$$

The extra integration is absolutely unnecessary.

Recommendations for the Resolved Region

In view of the deficiencies of the existing algorithm in MC² a semianalytic method is proposed to speed up the computing time while preserving the rigor of the present version. The method is again based on the assumptions of the Breit-Wigner equation and the NR-approximation. The feasibility of extending beyond these assumptions will be briefly discussed in the next section. This method is believed to be particularly effective in conjunction with the application of the continuous slowing down method. The group reaction cross section can be written as[2]

$$\tilde{\sigma}_x^{(j)} = \frac{1/N^{(j)} \sum_{i=1}^{M} F_i \Gamma_{xi} J_i^*/E_i}{\int_{\Delta u} \frac{F(u)\, du}{\Sigma_b} - \sum_{\substack{\text{all} \\ \text{resonances}}} F_\ell \Gamma_\ell J_\ell^*/E_\ell \Sigma_b}, \tag{3}$$

where F_ℓ is the attenuated collision density near the resonance ℓ excluding the Placzek oscillations introduced by the heavy isotopes, Σ_b is total background cross section excluding the resonance cross section of heavy isotopes, and the characteristic integral is defined as

$$J_i^* = J_i - \frac{1}{2} \int_{-\infty}^{\infty} \frac{\psi_i \sum_{k \neq i} A_k \psi_k \, dx_i}{(\beta_i + \psi_i)(\beta_i + \psi_i + \sum_k A_k \psi_k)} \tag{4}$$

where

$$J_i = \frac{1}{2} \int_{-\infty}^{\infty} \frac{\psi_i}{\beta_i + \psi_i} \tag{5}$$

$\sigma_{0i} = 4\pi\lambda^2 g_J \, \Gamma_{ni}/\Gamma_i$
$N_i \equiv$ atoms/cm^3
$A_k \equiv$ ratio of the macroscopic peak cross section of kth and ith resonances
$\theta_i = \Gamma_i/\Delta$
$\Delta \equiv$ Doppler width
$\beta_i = \Sigma_b/N_i\sigma_{0i}$ or $\Sigma_b^{(eq)}/N_i\sigma_{0i}$ (Note that the leakage correction can also be included in Σ_b.)
$\Sigma_b^{(eq)} \equiv$ the equivalent potential scattering cross section.

Here the interference scattering cross section is intentionally left out for simplicity in the preliminary testing of the recommended techniques. The interference scattering may be included by a simple extension of the arguments presented. The advantages of separating J_i^* into two integrals are twofold. With the overlapping contribution separated out, the J integral can be evaluated much more rapidly. On the other hand, the overlapping integral, which is a second order quantity as far as J_i^* is concerned, can be evaluated with a much looser convergence criterion without suffering any significant error in J_i^*. Hence, the computing time can be drastically reduced. Furthermore, the separation makes possible the option for the user to decide whether the overlap effect need be included. For U-238 resonances between 4 keV and the initial energy of the resolved energy region of the second heavy isotope, the inclusion of the overlap effect is clearly unnecessary. It is believed that, for survey calculations, an improvement of the computer time by a factor of 100 can be achieved if the overlap effect is ignored. In addition, Eq. (3) is particularly amenable to the application of the continuous slowing down method. For heterogeneity effect studies, Eq. (3) also requires little change if the equivalence relations are used.

EVALUATION OF THE J-INTEGRAL

Judging from the accuracy and speed requirement, we recommend the use of the optimized scheme using a 4-point Gauss-Legendre quadrature as described by Nicholson and Grasseschi.[3] In this method, the J-integral is broken into two pieces,

$$J = \int_0^{\infty} I(x)\, dx = \int_0^{x_1} I(x)\, dx + \int_0^{1/x_1} \frac{I(1/x)}{x^2}\, dx, \tag{6}$$

where the transformation is made to the second integral and the break point x_1 is to be optimized to give the minimum errors in the integration. The calculated J-integrals using this method are accurate up to the third significant number for practically all ranges of β and θ of interest. While this accuracy in the J-integral is believed to be sufficient in the resolved region where the self-shielding effect is sizable, it is not sufficient in the unresolved region, especially when the Doppler effect of a fissile isotope is considered. For this reason, a trivial modification of the original routine has been made so that for large β or small self-shielding effect, the J-integral can be evaluated analytically:

$$J = \frac{\pi}{2[\beta + \psi(0, \theta)]} + \frac{\psi(0, \theta)\, \frac{\pi}{2} - \frac{\pi}{4} \psi(0, \sqrt{2}\theta)}{[\beta + \psi(0, \theta)]^2}. \tag{7}$$

MATHEMATICAL JUSTIFICATION OF THE PROPOSED METHOD

In spite of the exceedingly favorable results, mathematical justifications of the proposed method are needed. Two questions may arise: (1) why is the integrand in Eq. (6) extremely favorable for Gaussian quadrature and (2) what is the precise mathematical meaning of the break point x_1. In addition to the discussion already given in Ref 3, further investigations have been made.

For the generalized Gaussian quadrature formula[4] utilizing any orthogonal polynomial, it is generally true that the integration is exact for a given number of mesh points N if the integrand is of the form $\sum_k A_k x^k$ where $k \leq 2N - 1$. Clearly, the most favorable integrand for the Gaussian quadrature formulas is the one which can be approximated by the polynomial $\sum_k A_k x^k$ with the value of k as small as possible. For the Gauss-Legendre quadrature in particular, an integral can be expressed as

$$\int_a^b I(x)\,dx = \frac{b-a}{2}\left[\sum_{i=1}^{N} w_i(y_i)I(y_i) + R_N\right], \tag{8}$$

where

$$R_N = B_N \frac{\partial^{2N}}{\partial \xi^{2N}}[I(\xi)], \qquad a < \xi < b \tag{9}$$

$$B_N = \frac{(b-a)^{2N}(N!)^4 2^{2N+2}}{(2N+1)![(2N)!]^3}$$

$$y_i = \left(\frac{b-a}{2}\right)x_i + \left(\frac{b+a}{2}\right)$$

$x_i \equiv i$th zero of the Legendre polynomial $P_N(x)$

$$w_i = 2/(1-x_i)^2[P_N'(x_i)]^2.$$

The qualitative behavior of the integrand under consideration is characterized by the broadened line shape function ψ (and χ if the interference scattering term is included). The broadened line shape functions are directly related to the real and imaginary part of the complex probability integral $W(z)$. Extensive studies by O'Shea and Thacher[5] have shown that $W(z)$ can be represented by a Taylor series

$$W(z) = e^{-z^2} + \frac{2iz}{\sqrt{\pi}} \sum_{n=0}^{\infty} \frac{(-1)^n n! 2^n (2z^2)^n}{(2n+1)!} \tag{10}$$

and an asymptotic series

$$W(z) = \frac{i}{\pi} \sum_{n=0}^{\infty} \frac{\Gamma\left(n+\frac{1}{2}\right)}{z^{2n+1}} \tag{11}$$

for small and large z, respectively. They have also examined the convergence of these series. Equation (10) clearly implies that the integrand $I(x)$ of the J-integral can be represented in the form $\sum_k A_k x^k$ and is particularly suitable for the Gaussian quadrature if the upper limit of integration is not too far from the origin. On the other hand, when x becomes large, Eq. (11) implies that the Guassian quadrature becomes inefficient because the integrand $I(x)$ will no longer assume the form $\sum_k A_k x^k$. Hence, the transformation of the second integrand in Eq. (6) of the Nicholson-Grasseschi method[3] amounts to transforming $I(x)$ back into the form expressible in terms of a Maclaurin series. The theoretical break point should have been the point where the orders of the two Maclaurin series were lowest. The precise theoretical break point is obviously difficult to find. Simple illustrations will be given to show that the Nicholson-Grasseschi method is mathematically sound.

Again, like Ref. 3, two asymptotic cases for small and large θ will be considered. For large θ, $I(x)$ and $I(1/x)/x^2$ become

$$I(x) = \frac{1}{\beta(1+x^2)+1} \approx \left[1 - \frac{\beta}{\beta+1}x^2 + \frac{\beta^2}{(\beta+1)^2}x^4 - \cdots\right] \Big/ (\beta+1) \tag{12}$$

and

$$I(1/x)/x^2 = \frac{1}{\beta(1+x^2)+x^2} \approx \left[1 - \frac{\beta+1}{\beta}x^2 + \frac{(\beta+1)^2}{\beta^2}x^4 - \cdots\right]\Big/\beta, \tag{13}$$

respectively. It is obvious that the choice of x_1 should be

$$x_1 = \left[\frac{\beta+1}{\beta}\right]^{1/2} \tag{14}$$

so that both series are convergent between 0 and the upper limits x_1^- and $1/x_1^+$. Incidentally, for this particular case, x_1 is also equal to $\sqrt{3}\,d$, where d is the point of inflection of the integrand $I(x)$. Both series will converge rapidly except for x near the upper limit. Thus, x_1 is identical with that given in Ref. 3 based on somewhat different arguments. Similarly, for the extreme broadening case with small θ, the integral becomes

$$\begin{aligned}\int_0^{x_1} I(x)\,dx &= \sqrt{\pi}\int_0^{x_1\theta/2} \frac{dy}{\beta e^{y^2} + \frac{\sqrt{\pi}}{2}\theta} \approx \frac{\sqrt{\pi}}{\beta+\frac{\sqrt{\pi}}{2}\theta}\int_0^{x_1\theta/2} \frac{dy}{1+\frac{\beta y^2}{\beta+\frac{\sqrt{\pi}}{2}\theta}\left[1+\frac{y^2}{2!}+\frac{y^4}{3!}+\cdots\right]} \\ &\approx \frac{\sqrt{\pi}}{\beta+\frac{\sqrt{\pi}}{2}}\int_0^{x_1\theta/2} dy\left\{1 - \frac{\beta y^2}{\beta+\frac{\sqrt{\pi}}{2}\theta} + \frac{\beta y^4}{\beta+\frac{\sqrt{\pi}}{2}\theta}\left[\frac{\beta-\frac{\sqrt{\pi}}{2}}{2\beta+\sqrt{\pi}\theta}\right]\cdots\right\}\end{aligned} \tag{15}$$

and the integrand of the second integral is less obvious. It is expected to have the same behavior as Eq. (13) if the choice of x_1 is sufficiently large. In view of the fact that the Taylor's expansion for the exponential function generally converges faster than the series of Eq. (13) and Eq. (14), it is obvious that the choice of x_1 is less restrictive. The first conservative guess based on the ratio of the first two terms is clearly

$$x_1 = \frac{2}{\theta}\left[1 + \frac{\sqrt{\pi}}{2}\frac{\theta}{\beta}\right]^{1/2} \tag{16}$$

so that the series will converge rapidly. A less conservative guess may be based on the ratio of the second and the third order terms so that

$$x_1 = \frac{2}{\theta}\left[\frac{2\beta+\sqrt{\pi}\,\theta}{\beta-\frac{\sqrt{\pi}}{2}\theta}\right]^{1/2}. \tag{17}$$

It is interesting to note that x_1 given by Nicholson and Grasseschi[3] is close to those defined by Eqs. (16) and (17). For small θ/β, x_1 of Ref. 3 is close to that in Eq. (17), whereas for large θ/β, it becomes smaller than that defined in Eq. (16). Hence, the use of x_1 of Ref. 3 will generally ensure a reasonably rapid convergence of the series in Eq. (15), and thus the efficiency of the Gaussian quadrature of small order.

It is also interesting to note the general behavior of the remainder R_n of Eq. (9) upon which the error of Gaussian integration depends. For ξ not too close to the upper limit,

$$I(\xi) \approx e^{-\xi^2/x_1}, \tag{18}$$

which is true for both Eqs. (12) and (15), especially for the latter case; for the second integral

$$I(\xi)/\xi^2 \approx e^{-x_1\xi^2}.$$

Thus, the remainders are approximately

$$R_n = C_N e^{-\xi^2/x_1} H_{2N}(\xi/x_1) \tag{19}$$

for the first integral and

$$R_N = C_N e^{-\xi^2 x_1} H_{2N}(x_1\xi) \tag{20}$$

he second integral, respectively, where $H_{2N}(y)$ is the Hermite polynomial of the order $2N$, and

$$C_N = \frac{(N!)^4 2^{2N+2}}{(2N+1)![(2N)!]^3}. \tag{21}$$

It should be noted that the qualitative behavior of $e^{-y^2}H_{2N}(y)$ explains the fluctuations of the error curves given in Ref. 3. From the remainder R_N, the optimal N, in principle, can be determined. The amplitude C_N decreases rapidly as N increases. For example,

$$C_2 = 6.173 \times 10^{-4}$$

$$C_4 = 1.178 \times 10^{-9}.$$

From the foregoing discussion, it can be concluded that the proposed method is not only efficient from a numerical point of view but also is mathematically justifiable. Whether the proposed 4-point Gaussian quadrature is equally efficient for the case with the interference scattering term included will be further investigated.

EVALUATION OF OVERLAPPING INTEGRAL

One time saving feature is to reduce the total number of overlapping resonances in the calculation. From a practical point of view, the inclusion of up to the next nearest neighbors is sufficient. Preliminary calculations have been carried out using the Romberg integration scheme. It was found that the relative error in the integration of the overlap integral required to give the same accuracy in J^* using the direct procedure of MC^2, is approximately 50 to 100 times larger. The total computing time can be improved by a factor of 3. In view of the fact that the Romberg integration scheme is rather ineffective for integrands with rapid fluctuations, the use of the Romberg quadrature is not recommended. One obvious alternative to the Romberg quadrature is the adaptive integration scheme whereby the mesh points are concentrated according to the fluctuations of the integrand. Such an adaptive method is available.[6] It is believed that the use of this method will further improve the computing speed.

Validity of the Theoretical Models

The existing MC^2 and the discussion in the previous section are based on the validity of two approximations, namely the Breit-Wigner equation and the *NR*-approximation. For the heterogeneous studies, Eq. (3) also implies the validity of the equivalence relations and the rational approximation.

It has been shown[7,8] that the direct use of the multilevel formalism is not only feasible but also practical if the cross sections are expressed in the Adler-Adler form. In view of the increasing number of multilevel parameters now available for the resolved resonances of the principal fissile isotopes, an option using the multilevel formalism is desirable at least for the resolved region. For U-235, for instance, it was found[8] that the use of the existing single level parameters in the ENDF/B file will introduce significant error not only in the Doppler effect but also in the magnitude of the self-shielded cross sections. From a practical point of view, the inclusion of a multilevel option in Adler-Adler form is recommended. The use of this formalism will not cause any difficulty in the programming itself as already demonstrated in Ref. 8.

As for the improvement of the NR-approximation, the problem becomes less straightforward. Some detailed discussions on this subject have been given in Ref. 9. For any future improvement of the NR-approximation, three considerations must be given:

1. For most fast reactor calculations, there exists more than one resonance absorber. The detailed overlap effect is difficult to assess using the well known analytical approximations.
2. A highly accurate temperature effect is required.
3. An optimum that treats heterogeneity effects accurately is highly desirable.

The three requirements are simultaneously satisfied if the RABBLE code[10] is included. The inclusion of the RABBLE code will undoubtedly eliminate the complaints on the NR-approximation once and for all. These three considerations will obviously require a large number of energy mesh points. It is rather doubtful that any other existing numerical techniques can achieve the same degree of sophistication with much less computing time. One possible improvement of the existing RABBLE code is to reduce the total number of resonances for the heavy isotopes in the evaluation of the cross sections for each mesh point. It is quite obvious that only few nearest neighbors need be considered for practical purposes.

References

1. B. J. Toppel, A. L. Rago and D. M. O'Shea, *MC^2, A Code to Calculate Multigroup Cross Sections*, ANL-7318 (1967).
2. R. N. Hwang, *Doppler Effect Calculations with Interference Corrections*, Nucl. Sci. Eng. **21**, 523 (1965).
3. R. B. Nicholson and G. Grasseschi, *A Fast Accurate Technique for Calculations of the Resonance J-Function*, Applied Physics Division Annual Report, July 1, 1969 to June 30, 1970, ANL-7610, p. 499.
4. A. H. Stroud and D. Secrest, *Gaussian Quadrature Formulas*, (Prentice-Hall, Inc., New York, 1966).

5. D. M. O'Shea and H. Thacher, *Computations of Resonance Line Shape Functions*, Trans. Am. Nucl. Soc. **6**, 36 (1963).
6. J. N. Lynn, *Structure in Sub-Threshold Fission Modes*, AERE-R5891 (1968).
7. R. N. Hwang, *Application of Statistical Theory and Multilevel Formalism to Doppler Effect Studies*—II, Nucl. Sci. Eng. **36**, 82 (1970).
8. R. N. Hwang, *Doppler Effect Studies Using Multilevel Formalism*, Nucl. Sci. Eng. **39**, 32 (1970).
9. R. N. Hwang, *Effect of the Fluctuations in Collision Density on Fast-Reactor Doppler Coefficient Calculations*, Proc. Conference on Safety, Fuels, and Core Design in Large Fast Power Reactors, October 11–14, 1965, ANL-7120, pp. 449–461.
10. P. H. Kier and A. H. Robba, *RABBLE, A Program for Computation of Resonance Absorption in Multiregion Reactor Cell*, ANL-7326 (1967).

IV-7. Heterogeneity Algorithms for MC²-2

R. G. Palmer and B. A. Zolotar

Introduction

In order to provide a convenient and reliable method for obtaining a set of group cross sections for use in the analysis of ZPR lattices, a set of heterogeneity algorithms has been formulated. These algorithms will be used in the development of the new MC²-2 code (see Paper IV-2).

In the resonance region the plate absorption cross sections in many ZPR cells can be calculated adequately by equivalence relations. However, certain expertise and judgment are required in the application of two-region equivalence formulae to the complex situations encountered in ZPR cells. The resonance calculation module will be designed to allow the user to perform many different resonance self-shielding calculations in one MC²-2 run to cover each of the absorber plate conditions.

For cases in which it would be deemed desirable to perform more accurate calculations for the resonance region, the RABBLE[1] technique will be included as an optional module. The results of the RABBLE calculations can overwrite the resonance-influenced broad group cross sections produced by the equivalence path. The user will have the results of both available to gain experience in determining the circumstances under which the more accurate approach should be used.

In order to avoid the complexities associated with the use of statistical ladders, the RABBLE calculations will be limited to the resolved resonances. In ZPR cells the most difficult plates to describe by two-region equivalence theory are the U-238-bearing plates because of their variety of compositions—U_3O_8, U, Pu-U and UO_2. However, the group absorption cross sections in the unresolved resonance energy range are not as sensitive to errors in the equivalent σ_p as they are at lower energies.

In ZPR interpretive studies cell-averaged cross sections are frequently required. Two methods for calculating the necessary spatial group flux distributions across the cell, the discrete ordinate transport method and the Storrer-Khairallah integral[2] transport perturbation method, will be available.

Resonance Heterogeneity Treatment using Equivalence Relations

The slowing down calculations and the buckling iterations will be based on the normal homogeneous case in MC²-2. Calculations of the resonance attenuation will involve J-functions in both the resolved and unresolved resonance range. For the heterogeneous case a J-function will be defined and calculated for each of the unique self-shielding conditions as described by the geometrical input, at each selected discrete energy computation point (E^*) in the unresolved range and for each resonance in the resolved range,

The form of the equivalence relations to be used for two-region pin geometry will be the same as that currently used in MC².[(3)] In the multi-plate slab case the Dancoff factor will be based on the two-sided E_3 formulation of D. Meneghetti,[4]

$$1 - C = 1 - E_3(\Sigma_L\chi_L) - E_3(\Sigma_R\chi_R) \qquad (1)$$

where Σ is the total cross section at E_r (or E^*) and χ_L and χ_R are the thicknesses of the diluent regions to the left and the right of the resonance plate. The Dancoff factor will be treated as constant across the resonance.

For each isotope self-shelding condition, $J(\theta_I, \beta_I)$ will be calculated for each resonance in the resolved range and at each E^* in the unresolved range, where

$$\theta_I = \left(\frac{M_I\Gamma^2}{4kTE_r}\right)^{\frac{1}{2}} \qquad (2a)$$

and

$$\beta_I = \frac{\Sigma_i^*}{N_I \sigma_I^0}; \tag{2b}$$

σ_I^0 is the resonance peak cross section and $\Sigma_I^* = \Sigma_I + \Sigma_{eI}^*$, where Σ_I is the total cross section of the region containing the resonance isotope and

$$\Sigma_{eI}^* = \frac{S_I}{4V_I} \cdot \frac{a_1[1 - C_I]}{1 + (a_2 - 1)C_I}. \tag{3}$$

S_I is the surface of the region, V_I is the volume of the region, and a_1 and a_2 are empirical constants which may be user input but which will also have default values of $a_1 = a_2 = 1.35$ for the cylindrical cell and $a_1 = a_2 = 1.09$ for slab cells.

The use of these J-functions in generating in-plate broad group cross sections is discussed in Paper IV-3.

Rabble Module

To provide MC²-2 with the capability to perform precise resonance absorption calculations in the resolved resonance region, a module containing the algorithms found in RABBLE will be included. The RABBLE calculation is appropriate for the lower energy broad groups in which the Narrow Resonance approximation is questionable, overlapping effects between resonances of different nuclides are significant, and where heterogeneity effects are generally most important.

In RABBLE, a broad group is divided into many very narrow intervals of equal lethargy width. For each isotope, region-dependent reaction rates are obtained. These are accumulated over the broad group and then divided by the accumulated regional fluxes to yield spectrum-averaged effective broad-group cross sections. In obtaining the reaction rates, region and lethargy-dependent slowing down sources are used. Regional collision rates are obtained from the regional slowing down sources by means of an approximate algorithm involving the first-flight escape and transmission probabilities, and interface currents. RABBLE can treat circularized cells and plate cells which can have either periodic or zero-current boundary conditions.

RABBLE can be utilized in the MC²-2 code as follows:

1) RABBLE may be optionally involved after completion of the normal MC²-2 run to generate broad-group, in-plate, cross sections for fission and capture.

2) The broad groups for which the RABBLE calculation is involved should be at energy sufficiently low that it can be assumed that no neutrons appear in these groups from fission sources, inelastic scattering sources, and elastic scattering sources that are anisotropic in the center-of-mass system.

3) RABBLE will generate an extra XS.ISØ data set in which the isotopic broad-group cross sections computed by the module replace those computed earlier by MC²-2.

Final Cell Homogenization

Using the in-plate broad-group cross sections it is necessary to calculate the spatial flux distribution through the cell in order to obtain cell-averaged cross sections. Two alternatives will be available to the user. The first will use the standard ARC 1-D transport[5] modules to obtain fluxes within the unit cell. A high-order modified single Gaussian angular quadrature will be available. To simulate the overall leakage from the core a $D_g B^2$ can be added to the total cross section in each region, where D_g is the cell homogeneous diffusion coefficient for group g, and B^2 is the final iteration on buckling from MC²-2.

The second alternative will be to use a modified version of CALHET.[6] This code is based on the use of collision probabilities in the integral transport equations developed by Storrer et al. The homogeneous medium and heterogeneous medium equations (for the same average composition) can be shown to be the same except for differences in the collision probabilities, so that the heterogeneous core can be considered as just a perturbation of the homogeneous core.

Two geometries will be treated, the multi-plate slab case and the multi-region cylindrical geometry. In the latter case two options will be available. For a two-region cylindrical problem the collision probabilities can be calculated from the Hummel et al.[7] modification to the Bell approximation,

$$P_{12} = 1 + \frac{\bar{\ell}\,\Sigma_1}{a} + \frac{\Sigma_1 C}{\bar{\ell}\,(1 - C)}, \tag{4}$$

where

$\Sigma_1 \equiv$ total cross section in region 1 (pin)
$\bar{\ell} \equiv$ mean chord length of the pin
$a \equiv$ Levine-type empirical correction factor; user input, but with a suggested default value of 1.35.

and

$$(1 - C) = \gamma_B + \gamma_B^4(1 - \gamma_B), \tag{5a}$$

where

$$\frac{1}{\gamma_B} = 1 + \frac{2\Sigma_2}{r_1}(r_2^2 - r_1^2) \tag{5b}$$

$\Sigma_2 \equiv$ total cross section in the diluent
$r_1 \equiv$ radius of the pin
$r_2 \equiv$ equivalent radius of the diluent.

Using reciprocity relations,

$$P_{11} + P_{12} = 1 \quad (6a)$$

$$\mu_{t2}P_{21} = \mu_{t1}P_{12} \quad (6b)$$

$$P_{21} + P_{22} = 1. \quad (6c)$$

A more exact option based on RABBLE collision probabilities will also be available. For the multiplate cell the collision probabilities will be calculated by a numerical technique[8] using exponential integral functions.

Two optional forms to allow for the finiteness of the reactor in the cell calculations will be included:

1) Adding D_gB^2 to the total cross section σ_g in each region as for the discrete ordinate method above

2) Reducing the collision probabilities by a non-leakage factor

$$P^1_{ij} = P_{ij}\frac{\Sigma_{t\ hom}}{\Sigma_{t\ hom} + D_gB^2}, \quad (7)$$

where

$\Sigma_{t\ hom} \equiv$ cell homogeneous total cross section.

Having calculated the heterogeneous fluxes across the cell (flat across each plate unless the plate is subdivided into subregions) the code will next perform a normal flux-weighting procedure across the cell to obtain the cell homogenized cross sections

$$\Sigma^m = \sum_{j=1}^{n} \sigma^m N_j^m \phi_j V_j / \sum_{j=1}^{n} \phi_j V_j,$$

where

$V_j \equiv$ volume of region j

$N_j^m \equiv$ the number of atoms/cm^3 of isotope m in region j.

The cell-perturbation module would be limited to using the isotropic problem while the discrete ordinates method can treat anisotropy up to P_1 scattering.

References

1. P. H. Kier and A. A. Robba, *RABBLE, A Program for Computation of Resonance Absorption in Multiregion Reactor Cells*, ANL-7326 (1967).
2. F. Storrer et al., *Heterogeneity Calculations for Fast Reactors by a Perturbation Method*, Nucl. Sci. Eng. **24**, 153 (1966).
3. B. J. Toppel, A. L. Rago and D. M. O'Shea, *MC²*, *A Code to Calculate Multigroup Cross Sections*, ANL-7318 (1967).
4. D. Meneghetti, *Calculational Studies of Sodium-Void Reactivity Variations Due to Thin Slab Heterogeneities in Fast Critical Assemblies*, Proc. International Conference on Fast Critical Assemblies and Their Analysis, October 10–13, 1966, ANL-7320, pp. 377–386.
5. B. J. Toppel, Ed., *The Argonne Reactor Computation (ARC) System*, ANL-7332 (1967).
6. F. L. Fillmore, *The CALHET-2 Heterogeneous Perturbation Theory Code and Application to ZPR-3-48*, AI-69-13 (1969).
7. H. H. Hummel et al, *Recent Investigations of Fast Reactor Reactivity Coefficients*, ANL-7120, 413 (1965).
8. A. P. Olson, Argonne National Laboratory (private communication).

IV-8. Calculation of Elastic Scattering Matrices

H. Henryson, II, C. G. Stenberg and B. J. Toppel

Introduction

In the MC² code,[1] ultrafine group ($\Delta u = 1/120$) elastic scattering matrices are generated for materials whose elastic scattering angular dependence has been represented by a Legendre polynomial expansion. In particular let the elastic scattering angular dependence for the material m at a neutron energy E_J be represented in the center of mass system as

$$\sigma_s^m(\omega', E_J) = \sum_\ell B^m_{\ell J} P_\ell(\mu'), \quad (1)$$

where

$\sigma_s^m(\omega', E_J) \equiv$ the material m cross section for scattering into the solid angle $d\omega'$ in the center of mass

$\mu' \equiv$ the cosine of the scattering angle in the center of mass

and

$P_\ell \equiv$ the ℓth Legendre polynomial.

The $B^m_{\ell J}$ are related to the customarily reported Legendre expansion coefficients $f^m_{\ell J}$ of the angular distribution of scattering in the center of mass by the expression

$$4\pi B^m_{\ell J} = (2\ell + 1)\sigma^m_{sJ} f^m_{\ell J}. \quad (2)$$

If we relate the initial and final energies in the laboratory system, E_J and E, respectively, to the center-of-mass scattering angle, and integrate over the azimuth angle, we obtain

$$\sigma_s^m(E_J \rightarrow E)\, dE = \frac{4\pi}{\alpha^m E_J}\, dE \sum_\ell B_{\ell J}^m P_\ell(\mu'), \tag{3}$$

where α^m, for the mass A^m of nucleus m, is given by

$$\alpha^m = \frac{4A^m}{(A^m + 1)^2} \tag{4}$$

and relates the minimum energy, E_{min}^m, to the initial energy by

$$E_{min}^m = (1 - \alpha^m)E_J\,. \tag{5}$$

The P_0 elastic transfer cross section from initial energy E_J into group K, $\sigma_s^{0m}(E_J \rightarrow K)$, may be obtained by relating μ' with E_J, E, and A^m, and then integrating Eq. (3) over final energy E ranging from E_K to E_{K-1}, the lower and upper energy limits respectively of group K.

The P_0 elastic transfer from group J to group K is obtained by averaging the corresponding $\sigma_s^{0m}(E \rightarrow K)$ with E at each end of group J. Thus

$$\sigma_{el_{J\rightarrow K}}^{0m} = \frac{\sigma_s^{0m}(E_J \rightarrow K) + \sigma_s^{0m}(E_{J-1} \rightarrow K)}{2}\,. \tag{6}$$

The use of Eq. (6) tacitly assumes that $\sigma_s^{0m}(E \rightarrow K)$ varies linearly across the source group J. This assumption is clearly not correct for all receptor groups K and for all degrees of anisotorpy.

The P_1 elastic scattering transfer cross section in MC^2 is defined as

$$\sigma_{el_{J\rightarrow K}}^{1m} = \frac{3}{2}\left(\frac{\bar{E}_K}{\bar{E}_J}\right)^{\frac{1}{2}}\left[(A^m + 1) - \left(\frac{\bar{E}_K}{\bar{E}_J}\right)(A^m - 1)\right]\sigma_{el_{J\rightarrow K}}^{0m}, \tag{7}$$

where $\bar{E}_K$ and $\bar{E}_J$ are the lower energies of group K and J respectively and $\sigma_{el_{J\rightarrow K}}^{0m}$ is given by Eq. (6). Equation (7) is based on the approximation

$$\sigma_{el_{J\rightarrow K}}^{1m} \approx \bar{\mu}_{J\rightarrow K}\sigma_{el_{J\rightarrow K}}^{0m}, \tag{8}$$

where $\bar{\mu}_{J\rightarrow K}$ is the effective cosine of the scattering angle corresponding to a group J to group K energy transfer.

In order to provide a more rigorous treatment for the new code MC^2-2 (see Paper IV-2), a study was made of the problem of the calculation of elastic scattering matrices with particular emphasis on improving the simple approach given in Eqs. (6) and (7) while at the same time minimizing computer running time.

Numerical Studies

The general approach outlined above was followed but the $\sigma_s^{0m}(E_J \rightarrow K)$ were evaluated at hyperfine group (*hfg*) intervals within the ultrafine group (*ufg*) J and then $\sigma_{el_{J\rightarrow K}}^{0m}$ and $\sigma_{el_{J\rightarrow K}}^{1m}$ were obtained by a trazpezoidal integration over the hyperfine groups contained within the source *ufg* J. Figure IV-8-1 schematically indicates the method used. Let N_0 be the number of *hfg* per *ufg* and $\sigma_s^{0m}(E_i \rightarrow k)$ the P_0 scattering from energy E_i at the top of *hfg* i within *ufg* J into *hfg* k within *ufg* K. E_1 corresponds to the energy at the top of the *ufg* J, and E_{N_0+1} corresponds to the energy at the bottom of *ufg* J. Accumulating the P_0 scattering over the receptor group K from the energy E_i gives

$$\sigma_s^{0m}(E_i \rightarrow K) = \sum_{k=1}^{k=N_0} \sigma_s^{0m}(E_i \rightarrow k). \tag{9}$$

The P_0 elastic scattering cross section from *ufg* J to *ufg* K based on a trapezoidal integration over the *hfg*'s within the source *ufg* J is then

$$\sigma_{el_{J\rightarrow K}}^{0m} = \frac{\sigma_s^{0m}(E_1 \rightarrow K) + \sigma_s^{0m}(E_{N_0+1} \rightarrow K) + 2\sum_{i=2}^{N_0} \sigma_s^{0m}(E_i \rightarrow K)}{2N_0}\,. \tag{10}$$

For scattering into the last *ufg* receptor group K, Eq. (10) may be modified in order to correctly account for the partial contribution of the scattering from the highest energetically possible *hfg* ℓ in the *ufg* source group J. The P_0 elastic transfer for scattering into the last *ufg* receptor group K is then given by

$$\sigma_{el_{J\rightarrow K}}^{0m} = \frac{\sigma_s^{0m}(E_{N_0+1} \rightarrow K) + 2\sum_{i=\ell+1}^{N_0} \sigma_s^{0m}(E_i \rightarrow K) - \left[1 - \ln\frac{1}{1-\alpha^m} + \ln\frac{E_{\ell+1}}{E_{K-1}}\right]\sigma_s^{0m}(E_{\ell+1} \rightarrow K)}{2N_0}\,,$$

where E_{K-1} is the energy at the top of *ufg* K.

The P_1 elastic transfer cross section was evaluated in a similar manner. If energies $\bar{E}_i$ and $\bar{E}_k$ are the midpoint energies of the *hfg* intervals in the source and receptor group respectively then

$$\sigma_s^{1m}(E_i \rightarrow k) = \frac{3}{2}\left(\frac{\bar{E}_k}{\bar{E}_i}\right)^{\frac{1}{2}}\left[(A^m + 1) - \frac{\bar{E}_i}{\bar{E}_k}(A^m - 1)\right]\sigma_s^{0m}(E_i \rightarrow k) \tag{12}$$

was taken as the P_1 scattering from energy E_i at the top of *hfg* i within *ufg* J into *hfg* k within *ufg* K. The P_1 scattering is accumulated over the receptor group in a manner similar to the P_0 scattering given in Eq. (9). The P_1 elastic transfer integration over the *ufg* source group J is similar to that given in Eqs. (10) and (11).

Results of the P_0 and P_1 elastic scattering using this method were obtained for various masses and at various energies to display the influences of anisotropy and mass on the kinematics of the scattering. The main parameter of interest is the number of *hfg* per *ufg*. In the original MC[2] code there is one *hfg* per *ufg*. The ETØG code[2] was used for a reference calculation. ETØG uses a very fine mesh Simpson's rule integration over the source and receptor groups and may be considered exact.

By way of demonstrating the variation of the scattering probability across the source group, Figs. IV-8-2 through IV-8-7 show P_0 scattering from the top of various *hfg*'s i within a given *ufg*, to various *ufg*'s $J + N$. The top of *hfg* 1 corresponds to the upper energy boundary of the *ufg*. Two source groups J have been selected for sodium, iron, and Pu-239 to indicate the effect of anisotropy. The straight dashed lines indicate the assumed shape using Eq. (6). The existing MC[2] algorithm becomes progressively worse as the mass number increases and as the scattering exhibits more anisotropy at the higher energies. In all cases, scattering to the lowest *ufg* exhibits the most radical errors, since not all portions of the source groups can scatter to the lowest *ufg*. The error in the present MC[2] algorithm is represented by the difference in the area under the solid and dashed lines for a given group, assuming the solid line results involving 20 *hfg* per *ufg* represent the correct answer. 20 *hfg* per *ufg* were chosen as a base because good agreement was obtained for all materials when compared with the ETØG code.

When integrating the scattering probability across the source *ufg* J to obtain $\sigma_{el_{J\rightarrow J+N}}^{0m}$ and $\sigma_{el_{J\rightarrow J+N}}^{1m}$ for all possible receptor groups, one would like to minimize the number of *hfg* per *ufg* in the integration in order to minimize computer time while at the same time accepting a certain magnitude of error.

In Table IV-8-I, the percentage errors in the calculation of the elastic transfer cross sections as a function of *hfg* per *ufg* are displayed relative to 20 *hfg* per *ufg*. The energy of the source *ufg* J was chosen to be 6.11 MeV in order to illustrate an extreme case (high degree of anisotropy). The percentage error shown in each case is the largest error encountered for all possible *ufg* receptor groups. For B-10, the scattering probability for the next to the last receptor group when integrated across the *ufg* source group produced converging oscillatory values as the number of *hfg* per *ufg* increased. This occurrence was due to the particular shape of the scattering probability across the source group. For the light elements (e.g., beryllium, boron, carbon, oxygen, and sodium) the maximum error in the elastic transfer cross sections always occurred with the scattering into the next to the last receptor group. The next largest error resulted from the in-group scattering, $N = 0$. All other receptor groups for these light elements (even for 1 *hfg* per *ufg*) had errors of less than 1%.

Table IV-8-I also displays a measure of the weighted error in the P_0 and P_1 transfer cross sections in scattering from the source *ufg*. The error for each receptor group was weighted by the fraction of its contribution (relative to 20 *hfg* per *ufg*) to the total scattering from the ultrafine source group. The error displayed was obtained by summing the weighted error for each ultrafine receptor group. Note that in the footnote of Table IV-8-I, the total number of *hfg* scattered for material m when there is 1 *hfg* per *ufg* is denoted by N_{max}^m. The weighted error gives a measure of the overall accuracy of the calculation. For example, the light materials have a large error in the next to last receptor group but the weighted error for these materials is small because the contribution of the next to last receptor group is small.

For all materials at energies where the scattering is isotropic in the center of mass system, the calculation of the P_0 and P_1 elastic transfer cross sections, using 1 *hfg* per *ufg*, resulted in errors of less than 1% for almost all *ufg* receptor groups. The weighted error in scattering from the source *ufg* was always less than 1.5%.

For the new MC[2]-2 code, the probable requirement for the number of *hfg* per *ufg* for the calculation of the P_0 and P_1 elastic transfer cross sections for an accurate and comparably fast computer running time are: 1 *hfg* per *ufg* for all materials of mass less than 161 AMU when scattering is isotropic in the center of mass system; 1 *hfg* per *ufg* for materials lighter than and including sodium when scattering is anisotropic; 2–4 *hfg* per *ufg* for materials heavier than sodium but lighter than mass 161 AMU when scattering is anisotropic; for masses greater than 161 AMU use the heavy mass approximation described below for all scattering.

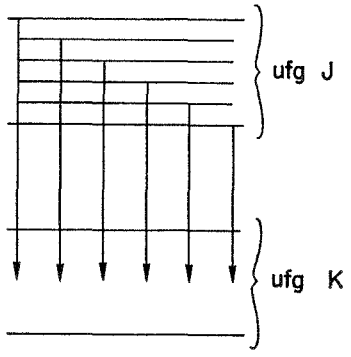

FIG. IV-8-1. Scattering from Hyperfine Groups within Ultrafine Group J into Ultrafine Group K. *ANL Neg. No. 116-461.*

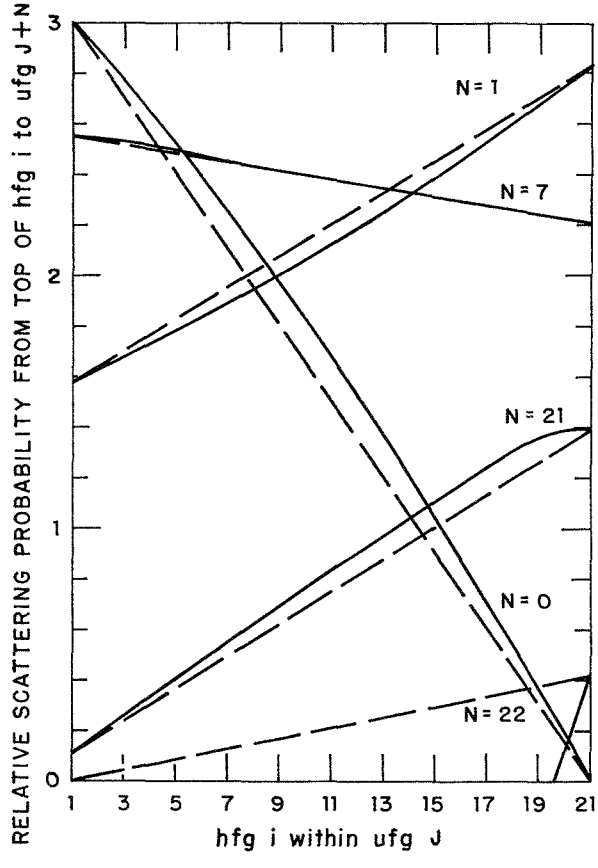

FIG. IV-8-2. Sodium: Source (*ufg J*) Energy Limits of 6.116–6.065 MeV (Maximum of *ufg*'s Scattered). *ANL Neg. No. 116-470.*

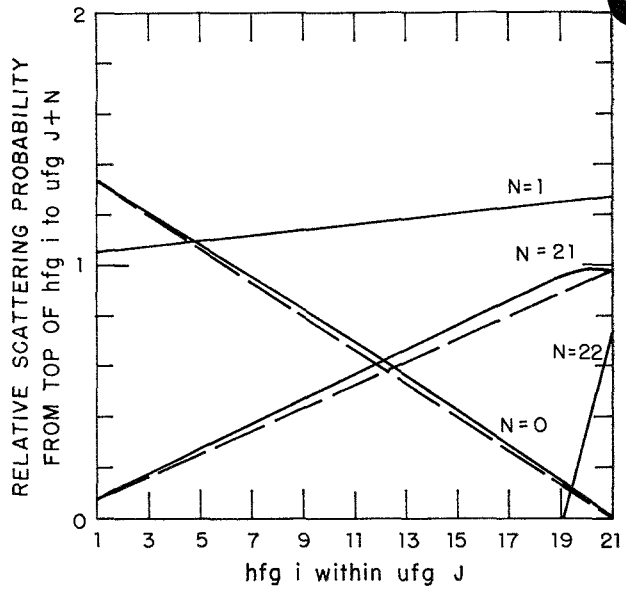

FIG. IV-8-3. Sodium: Source (*ufg J*) Energy Limits of 0.502–0.498 MeV (Maximum of 22 *ufg*'s Scattered). *ANL Beg. No. 116-459.*

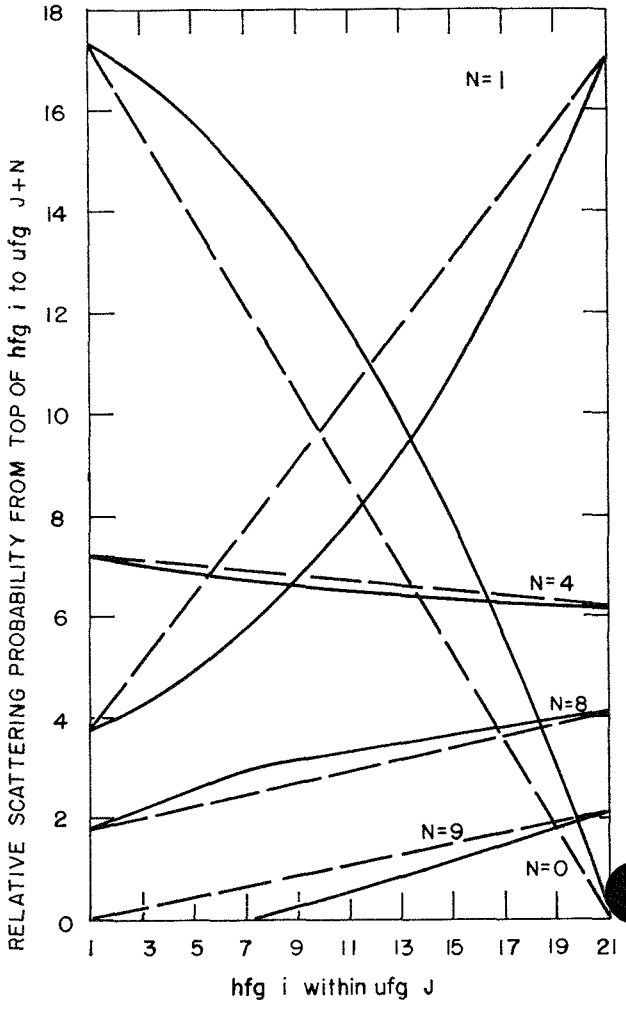

FIG. IV-8-4. Iron: Source (*ufg J*) Energy Limits of 6.116–6.065 MeV (Maximum of 9 *ufg*'s Scattered). *ANL Neg. No. 116-443.*

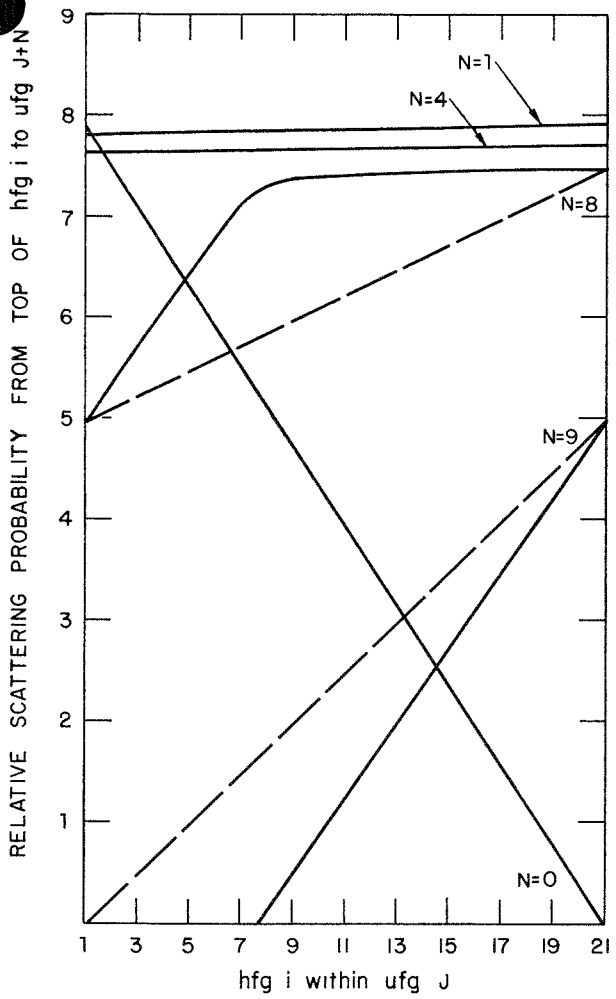

FIG. IV-8-5. Iron: Source (*ufg J*) Energy Limits of 50.33–49.92 keV (Maximum of 9 *ufg*'s Scattered). *ANL Neg. No. 116-449.*

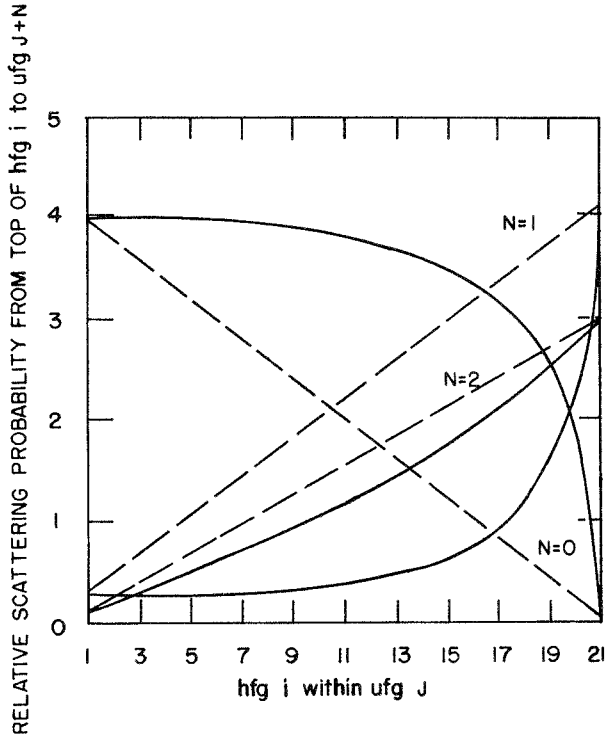

FIG. IV-8-6. Pu-239: Source (*ufg J*) Energy Limits of 6.116–6.065 MeV (Maximum of 3 *ufg*'s Scattered). *ANL Neg. No. 116-450.*

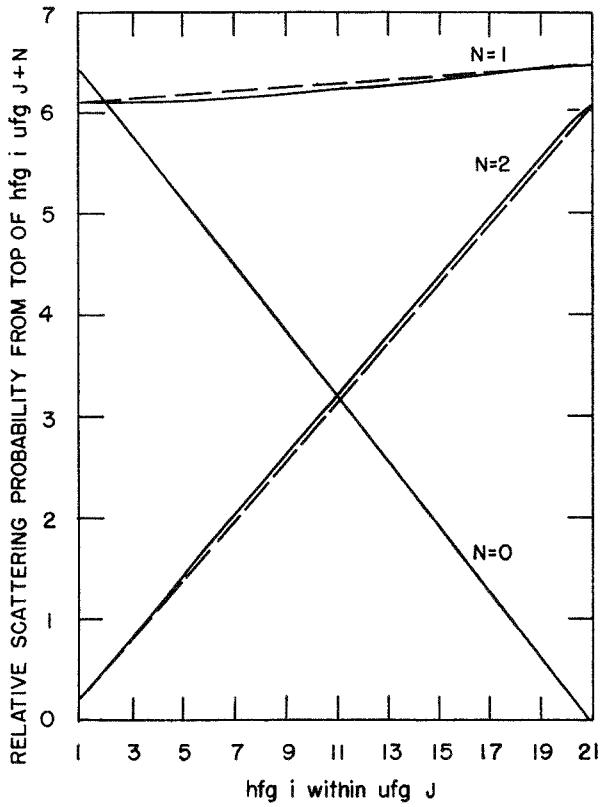

FIG. IV-8-7. Pu-239: Source (*ufg J*) Energy Limits of 2.052–2.035 keV (Maximum of 3 *ufg*'s Scattered). *ANL Neg. No. 116-451.*

TABLE IV-8-I. ERRORS IN ELASTIC SCATTERING TRANSFER CROSS SECTIONS (E_J = 6.11 MeV)

Material m	Percentage Error in σ_{el}^{0m}	Percentage Error in σ_{el}^{1m}	Total Number of *hfg* Scattered	Number of *hfg*/*ufg*	Weighted Error for P_0 Scattering[a]	Weighted Error for P_1 Scattering[b]
Be-9	2.5	3.1	54	1	0.35	0.52
	1.1	1.2	108	2	0.090	0.13
	0.72	0.75	162	3	0.041	0.061
B-10	15.	15.	49	1	0.53	0.84
	0.50	0.56	98	2	0.090	0.15
	1.6	1.6	146	3	0.057	0.092
C-12	16.	16.	41	1	0.58	0.95
	2.5	2.6	81	2	0.13	0.20
	1.2	1.3	122	3	0.057	0.093
O-16	18.	19.	31	1	2.2	3.7
	5.0	5.3	61	2	0.57	0.96
	1.1	1.5	91	3	0.20	0.34
NA-23	8.5	10.	22	1	3.0	4.5
	3.4	3.8	43	2	0.76	1.1
	1.9	2.1	64	3	0.34	0.51
Fe-56	20.	25.	9	1	17.	22.
	5.0	6.4	18	2	4.4	5.8
	2.2	2.8	27	3	1.9	2.6
	1.2	1.6	35	4	1.1	1.4
Cu-63	22.	27.	8	1	23.	28.
	9.2	10.	16	2	5.1	6.4
	4.7	5.5	23	3	2.2	2.8
	2.4	3.0	31	4	1.3	1.6
Mo-96	98.	100.	6	1	45.	54.
	13.	16.	16	3	5.8	8.2
	7.2	9.2	21	4	3.2	4.6
	3.0	3.9	31	6	1.4	2.0
Pu-239	200.	280.	3	1	68.	82.
	4.5	12.	21	10	1.5	2.6
	0.85	2.3	33	16	0.28	0.50
	0.35	0.94	37	18	0.12	0.21

[a] The weighted error in the P_0 scattering from source *ufg* J is

$$\frac{\sum_{N=0}^{N=N_{max}^{m}} \left| \left(\begin{matrix} \% \text{ error in } ufg\ N \\ \text{for } P_0 \text{ scattering} \end{matrix} \right) \sigma_{el_{J\to J+N}}^{0m} \right|}{\sum_{N=0}^{N=N_{max}^{m}} \sigma_{el_{J\to J+N}}^{0m}}.$$

[b] The weighted error in the P_1 scattering from source *ufg* J is

$$\frac{\sum_{N=0}^{N=N_{max}^{m}} \left| \left(\begin{matrix} \% \text{ error in } ufg\ N \\ \text{for } P_1 \text{ scattering} \end{matrix} \right) \sigma_{el_{J\to J+N}}^{1m} \right|}{\sum_{N=0}^{N=N_{max}^{m}} \left| \sigma_{el_{J\to J+N}}^{1m} \right|}.$$

In the final analysis, the number of *hfg* per *ufg* to be used for the different materials in the calculation of the elastic transfer matrices will be dependent on the testing of the new MC²-2 code. The effect of the number of *hfg* per *ufg* on the values of the broad group cross sections and reactivity will determine how small this number can be without compromising the accuracy of the new code.

Heavy Mass Approximation

The numerical studies summarized above indicate that the number of *hfg* per *ufg* required to obtain an accurate value of the transfer matrix depend on both the anisotropy of scattering and the mass of the scatterer. Since heavy nuclei can scatter a neutron only a few ultrafine groups, it is possible to derive semi-analytic expressions which may be used in place of Eqs. (10)–(12) to obtain accurate transfer matrices for all orders of anisotropy with a minimum of computational time.

The ℓth Legendre component of the elastic transfer from group J to group K is defined as

$$\sigma_{el_{J\to K}}^{\ell m} = \frac{\dfrac{2\ell+1}{\alpha^m}\displaystyle\int_J du \int_K du' P_\ell(\mu)\phi_\ell(u)e^{-(\mu'-u)}\sum_n 4\pi B_{nJ}^m P_n(\mu')}{\displaystyle\int_J du\ \phi_\ell(u)}, \tag{13}$$

where

$\phi_\ell(u)$ ≡ ℓth Legendre component of the flux

μ ≡ cosine of scattering angle in the laboratory system

$$= \frac{(A^m+1)e^{\frac{u-u'}{2}} - (A^m-1)e^{\frac{u'-u}{2}}}{2}$$

μ' ≡ cosine of scattering angle in the center of mass system

$$= \frac{(A^m+1)^2 e^{u-u'} - (A^{m^2}+1)}{2A^m}$$

and all other variables have been defined previously. The integration limits of the source (J) and sink (K) groups, which depend on the group lethargy width and the mass of the scatterer, have been given by several authors.[2] If the notation $\langle\ \rangle$ is chosen to designate a suitable average over the source group, Eq. (13) may be written

$$\sigma_{el_{J\to K}}^{\ell m} = \frac{4\pi\sum_n \langle B_{nJ}^m \phi_{\ell J}\rangle A_{nJ\to K}^{\ell m}}{\Delta u\langle\phi_{\ell J}\rangle} \tag{14}$$

$$A_{nJ\to K}^{\ell m} \equiv (2\ell+1)\frac{(2n+1)}{\alpha^m}\int_J du \int_K du'\ P_\ell(\mu)P_n(\mu')e^{-(u'-u)}, \tag{15}$$

where

Δu ≡ group lethargy width.

The ℓth Legendre component of the total scattering cross section for group J may be obtained by integrating Eq. (15) over all sink groups. Let q be defined as the maximum lethargy gain per collision:

$$q^m \equiv \ln\frac{1}{1-\alpha^m}. \tag{16}$$

Integration of Eq. (15) over all sink groups gives

$$A_{nJ}^{\ell m} = (2\ell+1)\Delta u T_{\ell n}^0(\alpha^m), \tag{17}$$

where

$$T_{\ell n}^r(\alpha^m) \equiv \frac{(-)^r}{r!}\frac{(2n+1)}{2}\int_0^{q^m} dU\ U^r P_\ell[\mu(U)]P_n[\mu'(U)]\left(-\frac{d\mu'}{dU}\right) \tag{18}$$

$$U \equiv u' - u.$$

Equation (18) is simply the T function which has been investigated by Amster.[3] Noting that $T_{0n}^0 = \delta_n^0$, substitution of Eq. (17) into Eq. (14) for the $\ell = 0$ component gives the identity

$$\sigma_{el_J}^{0^m} = 4\pi \frac{\langle B_{0_J}^m \phi_{0_J} \rangle}{\langle \phi_{0_J} \rangle}. \tag{19}$$

The general matrix element $A_{n_{J\to K}}^{\ell m}$ depends through the integration limits in Eq. (15) on the ratio $\Delta u/q^m$ which gives the number of groups scattered by material m. These general matrix elements may be expressed in terms of a function similar to the T function of Eq. (18). As an example of the derivation, consider the element $A_{n_{J\to J+3}}^{\ell m}$ if the group lethargy width and maximum lethargy gain per collision are such that a neutron may be scattered through a maximum of three groups:

$$\tfrac{1}{3}q^m \leq \Delta u < \tfrac{1}{2}q^m. \tag{20}$$

In this case Eq. (15) has the form

$$A_{n_{J\to J+3}}^{\ell m} = (2\ell+1)\frac{(2n+1)}{2}\int_{u_{J+2}-q^m}^{u_J} du \int_{u_{J+2}}^{u+q^m} du'\, P_\ell(\mu)P_n(\mu')\frac{2e^{-(u'-u)}}{\alpha^m},$$

where u_J corresponds to the lethargy at the bottom of ultrafine group J. Changing variables to $U = u' - u$ and reversing the order to integration we have

$$\begin{aligned} A_{n_{J\to J+3}}^{\ell m} &= (2\ell+1)\frac{(2n+1)}{2}\int_{u_{J+2}-q^m}^{u_J} du \int_{u_{J+2}-u}^{q^m} dU\, P_\ell(\mu)P_n(\mu')\left(-\frac{d\mu'}{dU}\right) \\ &= (2\ell+1)\frac{(2n+1)}{2}\int_{2\Delta u}^{q^m} dU \int_{u_{J+2}-U}^{u_J} du\, P_\ell(\mu)P_n(\mu')\left(-\frac{d\mu'}{dU}\right) \end{aligned}$$

and performing the inner integral

$$A_{n_{J\to J+3}}^{\ell m} = (2\ell+1)\{2\Delta u[\bar{T}_{\ell n}^0(\alpha^m, 2\Delta u) - \bar{T}_{\ell n}^0(\alpha^m, q^m)] + [\bar{T}_{\ell n}^1(\alpha^m, 2\Delta u) - \bar{T}_{\ell n}^1(\alpha^m, q^m)]\},$$

where

$$\bar{T}_{\ell n}^r(\alpha^m, \beta) = \frac{(-)^r}{r!}\frac{(2n+1)}{2}\int_0^\beta dU\, U^r P_\ell(\mu)P_n(\mu')\left(-\frac{d\mu'}{dU}\right). \tag{21}$$

It is obvious from Eqs. (18) and (19) that

$$\bar{T}_{\ell n}^r(\alpha^m, q^m) = T_{\ell n}^r(\alpha^m).$$

In Table IV-8-II expressions are presented for the matrix elements $A_{n_{J\to K}}^{\ell m}$ for several $q^m/\Delta u$ ratios. Note that Eq (20) is applicable to all materials of mass $240 \geq A^m \geq 161$ for the MC^2 group width $\Delta u = 1/120$.

Although the function $\bar{T}_{\ell n}^r$ does not in general satisfy a heavy mass expansion, since it need be calculated only once for a given A^m and Δu, it may be calculated directly from a high order quadrature of Eq. (21). In Table IV-8-III

TABLE IV-8-II. HEAVY MASS MATRIX ELEMENTS $A_n^\ell(J \to K)$

K	Group Width / Mass	$\frac{1}{2\ell+1}A_n^\ell(J\to K)$
	$\frac{1}{3}q \leq \Delta u < \frac{1}{2}q$	
J		$\Delta u\bar{T}_{\ell n}^0(\alpha,\Delta u) + \bar{T}_{\ell n}^1(\alpha,\Delta u)$
$J+1$		$2\Delta u[\bar{T}_{\ell n}^0(\alpha,2\Delta u) - \bar{T}_{\ell n}^0(\alpha,\Delta u)] + \bar{T}_{\ell n}^1(\alpha,2\Delta u) - 2\bar{T}_{\ell n}^1(\alpha,\Delta u)$
$J+2$		$3\Delta u T_{\ell n}^0(\alpha) + T_{\ell n}^1(\alpha) - 2\bar{T}_{\ell n}^1(\alpha,2\Delta u) + \bar{T}_{\ell n}^1(\alpha,\Delta u)$ $- \Delta u[4\bar{T}_{\ell n}^0(\alpha,2\Delta u) - \bar{T}_{\ell n}^0(\alpha,\Delta u)]$
$J+3$		$-2\Delta u T_{\ell n}^0(\alpha) - T_{\ell n}^1(\alpha) + 2\Delta u\bar{T}_{\ell n}^0(\alpha,2\Delta u) + \bar{T}_{\ell n}^1(\alpha,2\Delta u)$
	$\frac{1}{2}q \leq \Delta u < q$	
J		$\Delta u\bar{T}_{\ell n}^0(\alpha,\Delta u) + \bar{T}_{\ell n}^1(\alpha,\Delta u)$
$J+1$		$2\Delta u T_{\ell n}^0(\alpha) + T_{\ell n}^1(\alpha) - 2\Delta u\bar{T}_{\ell n}^0(\alpha,\Delta u) - 2\bar{T}_{\ell n}^1(\alpha,\Delta u)$
$J+2$		$-T_{\ell n}^1(\alpha) - \Delta u T_{\ell n}^0(\alpha) + \Delta u\bar{T}_{\ell n}^0(\alpha,\Delta u) + \bar{T}_{\ell n}^1(\alpha,\Delta u)$
	$\Delta u \geq q$	
J		$\Delta u T_{\ell n}^0(\alpha) + T_{\ell n}^1(\alpha)$
$J+1$		$-T_{\ell n}^1(\alpha)$

TABLE IV-8-III. Pu-239 ELASTIC SCATTERING MATRIX ELEMENTS, $(\sigma^0_{el}/\sigma^1_{el})_{J\to K}$
($\Delta u = 1/120$)
($E_J = 6.116$ MeV)

Method	K			
	J	$J+1$	$J+2$	$J+3$
ETØG	3.49/9.64	0.724/0.750	0.126/−0.240	0.499×10^{-4}/-0.134×10^{-3}
Heavy Mass Approx.	3.52/9.72	0.714/0.733	0.127/−0.239	0.624×10^{-4}/-0.179×10^{-3}
[a]	3.50/9.65	0.725/0.766	0.127/−0.239	0.601×10^{-4}/-0.177×10^{-3}

[a] This calculation used 20 *hfg* per *ufg* using the method described in this paper.

the results of calculations using Eq. (14) and the matrix elements of Table IV-8-II are compared with ETØG results and the previously discussed numerical algorithm using 20 *hfg* per *ufg*. Once the matrix elements $A^{lm}_{n_{J\to K}}$ have been calculated, the calculation using Eq. (14) is of course significantly faster than a numerical integration of Eq. (13).

References

1. B. J. Toppel, A. L. Rago and D. M. O'Shea, *MC²*, *A Code to Calculate Multigroup Cross Sections*, ANL-7318, (1967).
2. D. E. Kusner, R. A. Dannels and S. Kellman, *ETØG-1*, *A Fortran IV Program to Process Data from the ENDF/B File to the MUFT GAM and ANISN Formats*, WCAP3845-1 (ENDF 114) (December 1969).
3. H. Amster, *Heavy Moderator Approximations in Neutron Transport Theory*, J. Appl. Phys. **29**, (4), 623–627 (April 1958)

IV-9. Calculation of Heterogeneous Fluxes and Reactivity Worths

W. M. Stacey, Jr.

An iterative perturbation method for calculating the change in eigenvalue between a heterogeneous and a homogeneous model of a reactor cell, and for obtaining the spatial flux and importance distribution in the heterogeneous cell, was proposed several years ago by Storrer, et al.[1] This method is based on collision probability theory, and incorporates the assumption that only the collision probabilities (not cross sections or compositions) change between the homogeneous and heterogeneous models. In a later paper,[2] Khairallah and Storrer proposed a first-order perturbation estimate of the eigenvalue in a cell model which differs from a reference model in cross sections and compositions as well as collision probabilities. This estimate is based on the flux and importance solutions for the reference model. No method for calculating the heterogeneous flux and importance or obtaining higher-order estimates of the eigenvalue were given for this latter case.

Methods such as these are useful for calculating reactivity worths associated with heterogeneities, composition changes, and temperature (Doppler and thermal expansion) changes in the central regions of large reactors. The methods could also be used to compute spatially averaged group constants, accounting for heterogeneities, to be used in a gross-region-homogenized reactor calculation. The CALHET code,[3] which is used in the analysis of heterogeneities in the ANL critical assemblies, utilizes these methods.

A similar, but more general, iterative solution technique has been derived in a variational theory context. In this new theory, which reduces to the previous theory when the assumptions of the latter are invoked, the heterogeneous flux and eigenvalue may be obtained when the cross sections and/or compositions, as well as the collision probabilities, vary between the homogeneous and heterogeneous models. This generalization extends the applicability of the theory to several cases of interest (e.g. when the narrow resonance absorption is treated with equivalence theory in the homogeneous model).

The results of this work have been published in the technical literature.[4]

References

1. F. Storrer, A. Khairallah, M. Cadilhac and P. Benoist, *Heterogeneity Calculation for Fast Reactors by a Perturbation Method*, Nucl. Sci. Eng. **24**, 153 (1966).
2. A. Khairallah and F. Storrer, *Calculation of the Sodium-*

Void and Doppler Reactivity Coefficients in Fast Reactors and Critical Assemblies, with Heterogeneity Taken Into Account, Proc. Intern. Conference on Fast Critical Experiments and Their Analysis, ANL-7320, 394 (1966).

3. F. L. Fillmore, *The CALHET-2 Heterogeneous Perturbation Theory Code and Application to ZPR-3-48*, AI-69-13 (1969).
4. W. M. Stacey, Jr., *Calculation of Heterogeneous Fluxes and Reactivity Worths*, Nucl. Sci. Eng. **42**, 233 (1970).

IV-10. Continuous Slowing-Down Theory for the Elastic Moderation of Neutrons

W. M. Stacey, Jr.

It is rather curious that continuous slowing-down (CSD) theory, the basic assumptions of which make it appropriate for mixtures of heavy and intermediate atomic mass nuclei, has not been developed more fully for the treatment of elastic moderation of neutrons in a fast-reactor assembly. Driscoll[1] used the CSD formalism with parameters which could be fit to other results to characterize fast-reactor spectra. Dunn[2] extended this work, using composite moderating parameters which can be evaluated directly from the nuclear data. In both cases, inelastic as well as elastic scattering properties were included in the definition of the moderating parameters.

In this paper, new prescriptions for the composite moderating parameters of the Goertzel-Greuling theory[3] are derived from first principles. These new parameters are demonstrated to lead to accurate flux solutions, even in the presence of strong, wide, and intermediate scattering resonances where the original Goertzel-Greuling theory is inappropriate.

For a homogeneous medium, with isotropic elastic scattering, the neutron balance equation may be written

$$\Sigma(u)\phi(u) = S(u) + \sum_i \int_{u-\ln(1/\alpha_i)}^{u} du'\, \Sigma_{si}(u')\phi(u')\, \frac{e^{u'-u}}{1-\alpha_i}, \tag{1}$$

where S is the source due to fission, inelastic scattering, etc., and the summation is over the different type nuclei present. Σ_{si} is the macroscopic elastic scattering cross section of isotope i The elastic slowing-down density is defined as

$$q(u) \equiv \sum_i \int_{u-\ln(1/\alpha_i)}^{u} \Sigma_{si}(u')\phi(u') \left[\frac{e^{u'-u}-\alpha_i}{1-\alpha_i}\right]. \tag{2}$$

The Goertzel-Greuling approximation may be obtained by an approximation in Eq. (2):

$$\Sigma_{si}(u')\phi(u') \approx \Sigma_{si}(u)\phi(u) + (u'-u)\frac{d}{du}[\Sigma_{si}(u)\phi(u)], \qquad u \geq u' \geq u - \ln(1/\alpha_i) \tag{3}$$

for each nuclear species. This leads to the result

$$\frac{dq(u)}{du} = -\frac{[\Sigma(u)-\Sigma_s(u)]}{M(u)}\, q(u) + \frac{\xi(u)\eta(u)\Sigma_s(u)}{M(u)}\, S(u), \tag{4}$$

$$\phi(u) = \frac{q(u)+\gamma(u)S(u)}{M(u)}, \tag{5}$$

with

$$M(u) \equiv \xi(u)\eta(u)\Sigma_s(u) + \gamma(u)[\Sigma(u)-\Sigma_s(u)], \tag{6}$$

where ξ and γ are the composite parameters of the Goertzel-Greuling theory, and $\eta = 1 - d\gamma/du$. In most past applications, $\eta \equiv 1$, and this formalism will be denoted GG. Use of $\eta(u) \neq 1$ can lead to improved results under certain conditions, as shown by Segev,[4] and this formalism will be referred to as EGG.

If, instead of Eq. (3), the better approximation

$$\Sigma(u')\phi(u') \approx \Sigma(u)\phi(u) + (u'-u)\frac{d}{du}[\Sigma(u)\phi(u)], \qquad u \geq u' \geq u - \ln(1/\alpha_i)$$

is made in each integral of Eq. (2), then Eqs. (4) through (6) are again obtained, but with

$$M(u) \equiv \hat{\xi}(u)\Sigma_s(u) + \hat{\gamma}(u)[\Sigma(u) - \Sigma_s(u)], \tag{8}$$

where

$$\hat{\xi}(u) \equiv \bar{\xi}(u) + \frac{\bar{a}(u)\bar{c}(u)}{\bar{e}(u)}, \qquad \hat{\gamma}(u) = \bar{\xi}(u) + \frac{\bar{a}(u)}{\bar{e}(u)}[1 + \bar{c}(u)] \tag{9}$$

with

$$\bar{\xi}(u) \equiv \sum_i \int_{u-ln(1/\alpha_i)}^{u} du' \frac{\Sigma_{si}(u')}{\Sigma(u')}\left[\frac{e^{u'-u} - \alpha_i}{1 - \alpha_i}\right] \tag{10}$$

$$\bar{a}(u) \equiv \sum_i \int_{u-ln(1/\alpha_i)}^{u} du' \frac{\Sigma_{si}(u')}{\Sigma(u')}(u' - u)\left[\frac{e^{u'-u} - \alpha_i}{1 - \alpha_i}\right], \tag{11}$$

$$\bar{e}(u) \equiv \sum_i \int_{u-ln(1/\alpha_i)}^{u} du' \frac{\Sigma_{si}(u')}{\Sigma(u')}(u' - u)\frac{e^{u'-u}}{1 - \alpha_i}, \tag{12}$$

$$\bar{c}(u) \equiv \sum_i \left[\frac{\Sigma_{si}(u)}{\Sigma(u)} - \int_{u-ln(1/\alpha_i)}^{u} du' \frac{\Sigma_{si}(u')}{\Sigma(u')}\frac{e^{u'-u}}{1 - \alpha_i}\right], \tag{13}$$

with γ in the numerator of Eq. (5) replaced by $\bar{a}/\bar{e}$, and with $\xi\eta\Sigma_s$ in Eq. (4) replaced by $\hat{\xi}\Sigma$. This formalism is referred to as IGG.

The flux spectra in typical fast-reactor mixtures were calculated with the three presciptions for moderating parameters and compared with a direct numerical solution of Eq. (1) obtained with RABBLE.[5] The new prescriptions (IGG) yielded an accurate solution which was superior to that obtained with either the GG or EGG formulations. The flux solution in the vicinity of the 27.9-keV resonance is shown in Fig. IV-10-1.

The Greuling-Goertzel (GG) approximation has been extended to include anisotropic center-of-mass scattering (CM) for a mixture of isotopes, with the moderating parameters expressed in terms of the moments of the scattering transference function $T^n_{\ell\ell'}$ discussed by Hurwitz and Zweifel.[6,7] This approximation reduces to the results obtained in a different manner by Amster[8] for the case of a single isotope. The improved GG approximation (IGG) has also been extended to include anisotropic CM scattering.

The zeroth (ξ^i) and first (a^i) moments of the slowing-down kernel for isotope i, which define the moderating parameters of the GG approximation, are found to be

$$\xi^i = -\sum_{\ell'=0} \frac{\sigma_i^{\ell'}}{\sigma_i^0} T^1_{0\ell',i}, \qquad a^i = \sum_{\ell'=0} \frac{\sigma_i^{\ell'}}{\sigma_i^0} T^2_{0\ell',i}, \tag{14}$$

where σ_i^ℓ is the ℓth Legendre moment of the CM scattering cross section of isotope i. The GG moderating parameters for a mixture are constructed from

$$\xi = \sum_i \Sigma_{si}\xi^i / \sum_i \Sigma_{si}, \qquad \gamma = \sum_i \Sigma_{si}a^i / \sum_i \Sigma_{si}\xi^i. \tag{15}$$

When anisotropic scattering is accounted for, the moderating parameters of the IGG theory, Eqs. (10) through (13), become

$$\bar{\xi}(u) \equiv \sum_i \int_{u-ln(1/\alpha_i)}^{u} du' \frac{\Sigma_{si}(u')}{\Sigma(u')} \int_u^{u+ln(1/\alpha_i)} du'' \sum_{\ell=0}^{L} \frac{2\ell+1}{2} \frac{\sigma_i^\ell(u')}{\sigma_i^0(u')} P_\ell(\mu_c) \frac{2e^{u'-u''}}{1 - \alpha_i}, \tag{16}$$

$$\bar{a}(u) \equiv \sum_i \int_{u-ln(1/\alpha_i)}^{u} du' \frac{\Sigma_{si}(u')}{\Sigma(u')}(u' - u) \int_u^{u+ln(1/\alpha_i)} du'' \sum_{\ell=0}^{L} \frac{2\ell+1}{2} \frac{\sigma_i^\ell(u')}{\sigma_i^0(u')} P_\ell(\mu_c) \frac{2e^{u'-u''}}{1 - \alpha_i}, \tag{17}$$

$$\begin{aligned}\bar{c}(u) \equiv \sum_i \Bigg[&\frac{\Sigma_{si}(u)}{\Sigma(u)} \int_{u-ln(1/\alpha_i)}^{u} du' \sum_{\ell=0}^{L} \frac{2\ell+1}{2} \frac{\sigma_i^\ell(u)}{\sigma_i^0(u)} P_\ell(\mu_c) \frac{2e^{u'-u}}{1 - \alpha_i} \\ &- \int_{u-ln(1/\alpha_i)}^{u} du' \frac{\Sigma_{si}(u')}{\Sigma(u')} \sum_{\ell=0}^{L} \frac{2\ell+1}{2} \frac{\sigma_i^\ell(u')}{\sigma_i^0(u')} P_\ell(\mu_c) \frac{2e^{u'-u}}{1 - \alpha_i}\Bigg],\end{aligned} \tag{18}$$

$$\bar{e}(u) \equiv \sum_i \int_{u-ln(1/\alpha_i)}^{u} du' \frac{\Sigma_{si}(u')}{\Sigma(u')}(u' - u) \sum_{\ell=0}^{L} \frac{2\ell+1}{2} \frac{\sigma_i^\ell(u')}{\sigma_i^0(u')} P_\ell(\mu_c) \frac{2e^{u'-u}}{1 - \alpha_i}, \tag{19}$$

where $P_\ell(\mu_c)$ is the $\ell' th$ Legendre polynomial of argument $\mu_c \equiv$ cosine of the scattering angle in CM.

Making use of the heavy mass expansion for the $T^n_{\ell\ell'}$ given by Amster,[8] the isotopic parameters of Eqs. (14) may be written

$$\xi^i = A_1^i\left(\frac{\sigma_i^1}{\sigma_i^0}\right)(1-\alpha_i) + A_2^i\left(\frac{\sigma_i^1}{\sigma_i^0},\frac{\sigma_i^2}{\sigma_i^0}\right)(1-\alpha_i)^2 + \cdots + A_n^i\left(\frac{\sigma_i^1}{\sigma_i^0},\cdots,\frac{\sigma_i^n}{\sigma_i^0}\right)(1-\alpha_i)^n + \cdots, \quad (20)$$

$$a^i = B_2^i\left(\frac{\sigma_i^1}{\sigma_i^0},\frac{\sigma_i^2}{\sigma_i^0}\right)(1-\alpha_i)^2 + \cdots + B_n^i\left(\frac{\sigma_i^1}{\sigma_i^0},\cdots,\frac{\sigma_i^n}{\sigma_i^0}\right)(1-\alpha_i)^n + \cdots, \quad (21)$$

where A_n^i and B_n^i are functions of the indicated arguments and

$$\alpha_i = \left(\frac{M_i - 1}{M_i + 1}\right)^2.$$

The moderating parameters of the improved GG approximation can be shown to have the same functional dependence upon the atomic mass and scattering moments.

Because $(1 - \alpha_i) \approx 0.01$ for heavy elements and ≈ 0.1 for light and intermediate elements, the moderating parameters ξ and γ depend primarily upon the $\ell = 0, 1$ and $\ell = 0, 1, 2$ scattering moments, respectively. Thus, retention of the first few scattering moments suffices in evaluating the moderating parameters. This is in sharp contrast to the multigroup treatment of elastic moderation wherein many higher-order scattering moments must be retained to evaluate ultra-fine group scattering matrices.

A series of calculations has been performed for mixtures typical of fast breeder reactors, using ENDF/B angular scattering data. Isotopic and mixture-composite moderating parameters have been examined as a function of energy and the number of scattering moments retained. The moderating parameters ξ and γ differ considerably from the parameters for isotropic scattering and vary dramatically with energy. Anisotropy is predominantly forward, which reduces the moderating parameters relative to their isotropic values, but at some energies it is predominantly backwards, which increases the moderating parameters. This is illustrated in Fig. IV-10-2 by ξ and γ for oxygen, which vary considerably about their isotropic values of 0.1194 and 0.0816, respectively.

An advantage of a continuous slowing-down treatment of elastic moderation, relative to the group scattering matrix treatment, is that it is not necessary to compute scattering matrices or have available the flux in many higher energy groups to evaluate the elastic scattering source. Also, only the first few Legendre moments of the angular scattering distribution are needed in the former treatment, while many moments are required in the latter treatment. The IGG method will be provided as an option to treat elastic moderation in the improved fundamental mode spectrum code MC^2-2 being developed at Argonne.

More extensive expositions of this work, which describe numerical algorithms used in the computation of moderating parameters and which give additional examples, have been published in Refs. 9–11.

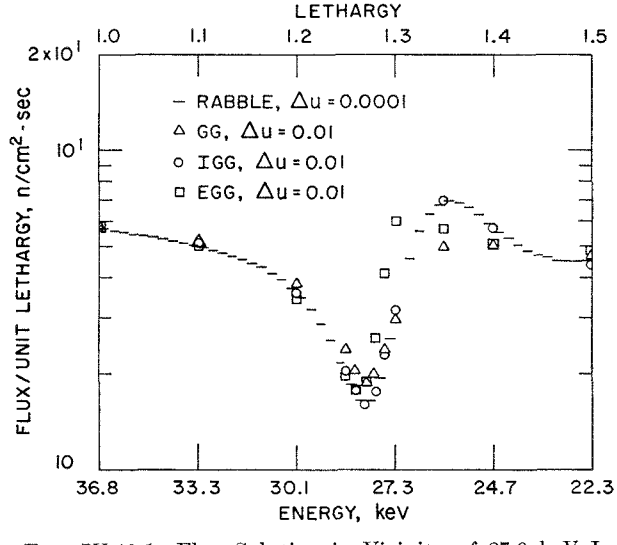

FIG. IV-10-1. Flux Solution in Vicinity of 27.9 keV Iron Resonance for Typical Fast-Reactor Mixture. *ANL Neg. No. 113-2987.*

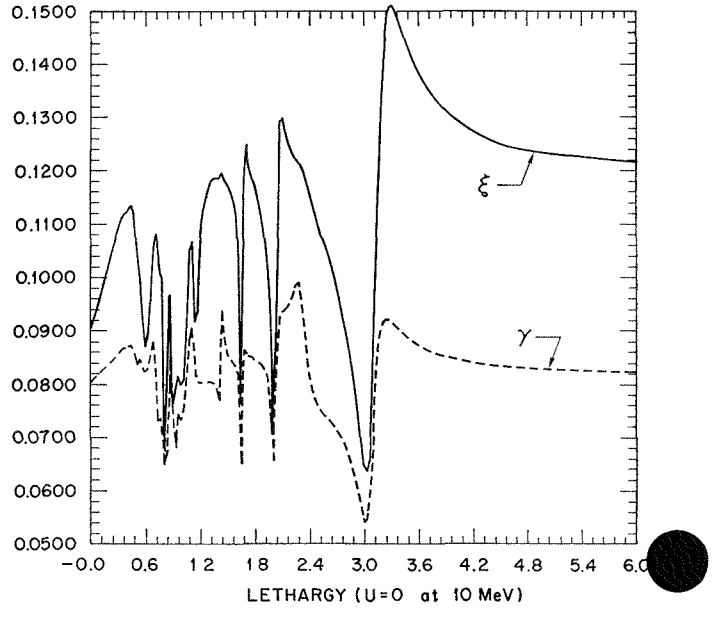

FIG. IV-10-2. Moderating Parameters for O-16. *ANL Neg. No. 116-130.*

REFERENCES

1. M. Driscoll, *Characterization of Neutron Spectra in Fast Reactors*, Sc.D. Thesis, Massachusetts Institute of Technology, Cambridge, Massachusetts (1965).
2. F. E. Dunn, *Analytic Studies of Fast Reactor Flux and Importance Spectra*, Ph.D. Thesis, Rensselaer Polytechnic Institute, Troy, New York (1969).
3. G. Goertzel and E. Greuling, *An Approximate Method for Treating Neutron Slowing Down*, Nucl. Sci. Eng. **7**, 69 (1960).
4. M. Segev, *Resonance Moderation of Neutrons in Weakly Absorbing Mixtures*, Nucl. Sci. Eng. **36**, 59 (1969).
5. P. H. Kier and A. A. Robba, *RABBLE, A Program for Computation of Resonance Absorption in Multiregion Reactor Cells*, ANL-7326 (1967).
6. P. F. Zweifel and H. Hurwitz, Jr., *Transformation of Scattering Cross Sections*, J. Appl. Phys. **25**, 1241 (1954).
7. H. Hurwitz, Jr., and P. F. Zweifel, *Slowing Down of Neutrons by Hydrogeneous Moderators*, J. Appl. Phys. **26**, 923 (1955).
8. H. J. Amster, *Heavy Moderator Approximations in Neutron Transport Theory*, J. Appl. Phys. **29**, 623 (1958).
9. W. M. Stacey, Jr., *Continuous Slowing Down Theory Applied to Fast-Reactor Assemblies*, Nucl. Sci. Eng. **41**, 381 (1970).
10. W. M. Stacey, Jr,. *Continuous Slowing Down Theory for Anisotropic Elastic Neutron Moderation in the P_N and B_N Representations*, Nucl. Sci. Eng. **41**, 457 (1970).
11. W. M. Stacey, Jr., *The Effect of Anisotropic Scattering Upon the Elastic Moderation of Fast Neutrons*, Nucl. Sci. Eng. (submitted for publication).

IV-11. An Integral-Attenuation Factor Treatment of Resolved Narrow Resonance Absorption

W. M. STACEY, JR.

An approximate method for treating neutron reaction rates and moderation in the presence of narrow resonances was developed and shown to yield accurate results for typical fast reactor mixtures. The method is applicable to the resolved resonance region, or to the entire resonance region when the unresolved resonances are represented by a statistical ladder of resolved resonances.

The basic idea is to solve first for the "asymptotic" neutron slowing-down density, ignoring the presence of the resonances. Then the resonance absorption rate is computed for each resonance, starting with the highest energy resonance, using the narrow resonance approximation (with resonance interference corrections) and the flux obtained from the "asymptotic" slowing-down density and attenuated by absorption in higher energy resonances. (It is not necessary to compute the slowing-down density at each resonance, because it is a slowly varying quantity and can be accurately interpolated.) The resonance absorption is then used to attenuate the "asymptotic" slowing-down density.

Continuous slowing-down theory provides an accurate representation of the spectrum in fast reactor mixtures (see Paper IV-10), and yields a relation between the "asymptotic" slowing-down density $q_{as}(u)$ and the "asymptotic" flux $\phi_{as}(u)$ of the form

$$q_{as}(u) = M(u)\phi_{as}(u), \tag{1}$$

where $M(u)$ is defined in terms of scattering and absorption properties of the mixture, exclusive of the narrow resonances.

The NRA-type expression* for the detailed flux in the vicinity of resonance r is

$$\phi(u) = \frac{\Sigma(u_r)}{\Sigma(u_r) + N_r\sigma_r(u) + \sum_{r' \neq r} N_{r'}\sigma_{r'}(u)} \phi_{as}(u_r) Q_r, \tag{2}$$

where Q_r is an attenuation factor to account for the effect of absorption in lower lethargy (higher energy) resonances. Σ is the total cross section exclusive of the narrow resonances, and N_r and σ_r are the concentration and total cross section of resonance species r. Using Eqs. (1) and (2), the absorption rate in resonance r is approximated by

$$\begin{aligned} A_r &\equiv \int_{\Delta u} du\, N_r\sigma_{ar}(u)\phi(u) \\ &\approx \frac{\Gamma_{f,r} + \Gamma_{c,r}}{E_r} J^*(\beta_r, \theta_r)\Sigma(u_r) \frac{q_{as}(u_r)}{M(u_r)} Q_r, \end{aligned} \tag{3}$$

with

$$J^* = J + H,$$

where J is the conventional Doppler J-function[1] and H is an interference correction term[2] which, in this study, includes contributions from nearest neighbors in each sequence.

* This differs from the conventional NRA expression, in which $\phi_{as}Q_r$ is assumed to be unity.

The attenuation of the slowing-down density across a resonance is

$$q(u_r + \Delta u) = q(u_r - \Delta u) - A_r = q_{as}(u_r)Q_r(1 - p_r), \quad (5)$$

where

$$p_r \equiv \frac{A_r}{q_{as}(u_r)Q_r} = \frac{\Gamma_{f,r} + \Gamma_{c,r}}{E_r} J^*(\beta_r, \theta_r) \frac{\Sigma(u_r)}{M(u_r)}. \quad (6)$$

The factor Q_r is

$$Q_r = \prod_{\substack{r' \\ u_{r'} < u_r}} (1 - p_{r'}), \quad (7)$$

and the attenuated slowing-down density is related to the "asymptotic" slowing-down density by

$$q(u) = q_{as}(u) \prod_{\substack{r \\ u_r < u}} (1 - p_r), \quad (8)$$

which is reminiscent of the resonance escape formalism of thermal reactor physics.

Resonance capture and fission rates and the attenuation of the slowing-down density by resonance absorption, and the temperature dependence of these quantities, have been computed for typical fast reactor mixtures using the continuous slowing-down theory and the above procedure. In most cases, ENDF/B parameters were used for U-238 and parameters for Pu-239 were generated from the appropriate statistical distributions. Agreement with a direct numerical solution,[3] in which detail of the resonance cross sections and the flux were treated explicitly, was generally as good or better than was obtained by an MC^2 calculation.[4] An example is given in Table IV-11-I in which the resonance parameters were constructed from Schmidt's tabulation.[5] More extensive comparisons have been published elsewhere.[6]

TABLE IV-11-I. Capture-to-Fission Ratios at 300°K and 1000°K

E_{max}/E_{min}, keV	C/F $\vert_{300°K}$			Δ(C/F) $\vert_{300°K}^{1000°K}$		
	RABBLE[a]	CSD[b]	MC^2[c]	RABBLE	CSD	MC^2
1.525/1.035	2.202	2.189	2.215	0.406	0.400	0.394
0.510/0.347	1.095	1.066	1.047	0.145	0.146	0.149

[a] Direct numerical solution.
[b] Method discussed in this paper.
[c] Current MC^2 code.

In addition to being accurate and fast computationally, the method is quite flexible, and lends itself well to the generation of multigroup resonance cross sections. Because the "asymptotic" solution is independent of the narrow resonances, the effects of temperature and self-shielding variations can be studied by recomputing J^*, hence p_r, without needing to recompute q_{as}. The standard definition of a broad group cross section can readily be evaluated in terms of the J^*, as discussed in Paper IV-6.

This method will be employed to compute resolved resonance effects in the improved fundamental mode MC^2-2 code.

References

1. L. Dresner, *Resonance Absorption in Nuclear Reactors*, (Pergamon Press, New York, 1960).
2. R. N. Hwang, *Doppler Effect Calculations with Interference Corrections*, Nucl. Sci. Eng. **21**, 523 (1965).
3. P. H. Kier and A. A. Robba, *RABBLE, A Program for Computation of Resonance Absorption in Multiregion Reactor Cells*, ANL-7326 (1967).
4. B. J. Toppel, A. L. Rago and D. M. O'Shea, *MC^2, A Code to Calculate Multigroup Cross Sections*, ANL-7318 (1967).
5. J. J. Schmidt, *Resonance Properties of the Main Fertile and Fissionable Nuclei;* A. Goodjohn and G. Pomraning, Eds., *Reactor Physics in Resonance and Thermal Regions*, (MIT Press, Cambridge, Massachusetts, 1966), Vol. II
6. W. M. Stacey, Jr., *Resolved Narrow Resonance Reaction Rates in Fast-Reactor Mixtures*, Nucl. Sci. Eng. **41**, 455 (1970).

IV-12. General Multigroup and Spectral Synthesis Equations

W. M. Stacey, Jr.

Since their introduction, the multigroup neutron diffusion equations[1] have been applied to a wide variety of problems in reactor physics. Definition of appropriate group-averaged nuclear constants has been identified as a crucial aspect of the calculation, particularly in problems for which the neutron energy spectrum is known to be spatially or time dependent. Numerous prescriptions for these group-averaged nuclear constants have evolved, all of which are based upon some type of weighted average of the energy-dependent nuclear data over the energy interval of the group. Various choices of the weighting functions have been proposed (e.g., "flux" weighting which weights with an estimate of the energy-dependent flux).

Although the use (implicit, if not explicit) of different weighting functions in different spatial regions is common practice, and the use of time-varying weighting functions can be motivated by physical considerations, the use of spatially and time-dependent weighting functions for defining group-averaged nuclear constants has not been systematically investigated. (The variational derivation of multigroup equations by Henry,[2] using different spectral trial functions in different spatial regions suggests that some additional terms may turn up, although Buslik's work[3] suggests that such terms might be eliminated by appropriate choice of trial functions and variational functional.)

The primary purposes of this work were to systematically derive multigroup equations with spatially and time-dependent weighting functions used in defining group-averaged nuclear constants and to investigate the mathematical properties of these generalized equations. Because the algorithms used for numerical computation are based on discrete approximations for the spatial and time dependence, the derivation and investigation of mathematical properties were carried through the hierarchy of discretizations leading from the lethargy-dependent P_1 equations to the finite-difference (in space and time) multigroup diffusion equations.

In the derivations, straightforward "weight-and-integrate" procedures were employed, rather than the equivalent, but more elegant, variational methods. The advantage of the former relative to the latter is a greater clarity as to the physical significance of the various approximations.

The spectral synthesis* approximation,[4] an alternative to the multigroup approximation, was also derived using spatially and time-dependent expansion modes and weighting functions. This derivation, and concurrent investigation of mathematical properties, parallels the formally similar development for the multigroup equations.

New terms are introduced by the space- and time-dependence of the weighting spectra. The new terms do not alter the usual positivity properties associated with the discrete multigroup kinetics equations, provided that certain conditions are satisfied. Conditions were also established which are sufficient to insure that the discrete representation is adjoint consistent; i.e. the discrete representation of the adjoint equation is mathematically adjoint to the discrete representation of the direct equation.

Conditions were also established for the adjoint consistency of the discrete representation of the spectral synthesis approximation. The type of positivity argument made for the multigroup equations was shown to be invalid for the spectral synthesis equations.

The results of this work have been published.[5]

* The approximation referred to above as spectral-synthesis is sometimes referred to as the overlapping-group method. This latter is something of a misnomer.

References

1. R. Ehrlich and H. Hurwitz, *Multigroup Methods for Neutron Diffusion Problems*, Nucleonics **12**, 23 (1954).
2. A. F. Henry, *Few-Group Approximations Based on a Variational Principle*, Nucl. Sci. Eng. **27**, 493 (1967).
3. A. J. Buslik, *Interface Conditions for Few-Group Neutron Diffusion Equations with Flux-Adjoint Weighted Constants*, Nucl. Sci. Eng. **32**, 233 (1968).
4. W. M. Stacey, Jr., *Modal Approximations: Theory and an Application to Reactor Physics*, (MIT Press, Cambridge, Massachusetts, 1967); also *Fast-Reactor Calculational Models*, Nucl. Sci. Eng **28**, 443 (1967).
5. W. M. Stacey, Jr., *General Multigroup and Spectral Synthesis Equations*, Nucl. Sci. Eng. **40**, 73 (1970).

IV-13. Applications of Spectral Synthesis to Fast-Reactor Dynamics

W. M. Stacey, Jr.

Calculation of detailed neutron flux spectra by synthesizing precomputed trial spectra was first suggested by Calame and Federighi[1] for the computation of spatially-dependent thermal spectra. This method was applied to compute spatially dependent static neutron spectra in fast reactors initially by Murley,[2] Stacey,[3] and Storrer and Chaumont.[4] Recent refinements, extensions, and studies of the method for static calculations have been reported by Murley and Williamson,[5] Vaughn, Rose and Hausknecht,[6] Neuhold and Ott,[7] and Lancefield.[8] These studies indicate that the method has considerable promise, but that the lack of positivity properties can sometimes lead to difficulty in obtaining the proper solution with conventional numerical techniques.

Potentially, the most promising application of the method is to fast-reactor dynamics, where spectral shift effects associated with composition and tempera-

ture changes play an important role. It appears that a relatively large number of groups* may be necessary to adequately represent these effects in a standard multigroup calculation, which implies that, all else being equal, dynamics calculations will be considerably more costly for fast reactors than for thermal reactors. This would seem particularly true for space-dependent dynamics calculations. However, if the neutron spectrum could be accurately synthesized from two or three trial spectra, then fast-reactor dynamics calculations would involve approximately the same amount of computational effort as is presently required in thermal-reactor dynamics calculations.

The mathematical formulation of the spectral synthesis method, in which the lethargy dependence of the neutron flux and current are expanded in known functions of lethargy which may vary in space and time, was developed for the P_1 representation of the reactor dynamics equations. Results of simulated sodium-voiding transients, with and without Doppler feedback, indicate that the spectral synthesis method may be significantly more accurate than few-group methods of comparable computational complexity for fast-reactor dynamics calculations. The theoretical development and the numerical results have been published in the technical literature.[9-11]

* Compared to the two or three groups used in thermal-reactor dynamics calculations.

REFERENCES

1. G. P. Calame and F. D. Federighi, *A Variational Procedure for Determining Spatially Dependent Thermal Spectra*, Nucl. Sci. Eng. **10**, 190 (1961).
2. T. E. Murley, *A Calculational Model for Fast Reactors*, Ph.D. Thesis, Massachusetts Institute of Technology, Cambridge, Massachusetts (1965).
3. W. M. Stacey, Jr., *Modal Approximations: Theory and an Application to Reactor Physics* (MIT Press, Cambridge, Massachusetts, 1967); see also *Fast Reactor Calculational Models*, Nucl. Sci. Eng. **28**, 443 (1967).
4. F. Storrer and J. M. Chaumont, *The Application of Space-Energy Synthesis to the Interpretation of Fast Multizone Critical Experiments*, Proc. Intern. Conference on Fast Critical Experiments and Their Analysis, ANL-7320, 439–447 (1967).
5. T. E. Murley and J. W. Williamson, *Space-Energy Synthesis Techniques for Fast Reactor Calculations*, Trans. Am. Nucl. Soc. **11**, 174 (1968).
6. E. U. Vaughn, P. F. Rose and D. F. Hausknecht, *Spectrum Synthesis in Fast Reactor Analysis*, AI-AEC-12820 (1969).
7. R. J. Neuhold and K. Ott, *Improvements in Fast-Reactor Space-Energy Synthesis*, Nucl. Sci. Eng. **39**, 14 (1970).
8. M. J. Lancefield, *Space-Energy Flux Synthesis in Neutron Transport*, Nucl. Sci. Eng. **37**, 423 (1969).
9. W. M. Stacey, Jr., *General Multigroup and Spectral Synthesis Equations*, Nucl. Sci. Eng. **40**, 73 (1970).
10. W. M. Stacey, Jr., *Spectral Synthesis Methods in Fast-Reactor Dynamics*, Proc. Symposium on Dynamics of Nuclear Systems, Tucson, Arizona, 1970 (to be published).
11. W. M. Stacey, Jr., *Spectral Synthesis Applied to Fast-Reactor Dynamics*, Nucl. Sci. Eng. **41**, 249 (1970).

IV-14. Some Variational Models for Flux Synthesis in Space-Time

W. L. WOODRUFF and V. LUCO

INTRODUCTION

In order to develop an approximate method which accounts for the spatial changes during a transient and which can be used economically, much attention has focused on the use of discontinuous variational models.[1,2] The discontinuous models, which have been proposed for space and space-time synthesis, are not without certain difficulties.[3,4]

Here a model is proposed which reflects a consistent application of the semidirect method of the calculus of variations and various suggested improvements. The spatial interface difficulties are eliminated in the manner suggested by Luco and Woodruff[5] and the temporal interface difficulties noted by Becker[4] are similarly resolved. Other versions of the basic model are also presented.

PROPOSED FUNCTIONALS

The basic functional has the form

$$J_1[u^*, u, C_\mu^*, C_\mu] = \sum_k \int_{R_k} dR \sum_t \int_{\tau_t} dt \left\{ \left[u^* V^{-1} \frac{\partial u}{\partial t} + \nabla u^* \cdot D \nabla u + u^* [A - (1-\beta)\chi F] u - \sum_{\mu=1}^{M} u^* \lambda_\mu \chi_\mu C_\mu \right] \right.$$
$$\left. + \sum_{\mu=1}^{M} \left[C_\mu^* \frac{\partial C_\mu}{\partial t} + C_\mu^* \lambda_\mu C_\mu - C_\mu^* \beta_\mu F u \right] \right\} + \sum_t \int_{\tau_t} dt \left[\int_{S_{int.}} dS \hat{n} \cdot \left\{ [\gamma_1 \nabla u_+^* D_+ \right. \right.$$

$$+ (1-\gamma_1)\nabla u_-^* D_-](u_+ - u_-) + (u_+^* - u_-^*)[\gamma_1 D_+\nabla u_+ + (1-\gamma_1)D_-\nabla u_-]$$
$$+ \gamma_3 \int_{S_\Gamma} dS \{\gamma_2 u^*\gamma u - (1-\gamma_2)[u^* D\nabla u + (\nabla u^* D)u]\}\Big] \tag{1}$$
$$+ \sum_k \int_{R_k} dR \Big\{u^*(+)V^{-1}[u(+) - u(-)]_{t=t_\ell} + [u^* V^{-1}(u-f)]_{t=t_0} - [f^* V^{-1} u]_{t=t_f}$$
$$+ \sum_{\mu=1}^{M} [C_\mu^*(+)[C_\mu(+) - C_\mu(-)]_{t=t_\ell} + [C_\mu^*(C_\mu - g_\mu)]_{t=t_0} - [g_\mu^* C_\mu]_{t=t_f}]\Big\}$$

Here the reactor volume has been sectioned into regions R_k with internal interfaces denoted as $S_{int.}$, and the time interval has been divided into subintervals τ_ℓ at the points t_ℓ. The admissible functions u^* and u may be discontinuous in both space and time, and C_μ^* and C_μ may be discontinuous in time. The functions are, however, continuous and differentiable over R_k and τ_ℓ. The subscripts $\pm$ denote limiting values of the functions at the internal interfaces $S_{int.}$, and the arguments $(\pm)$ represent limiting values at the time interfaces t_ℓ. S_Γ represents the external boundary of the reactor.

The choice of admissible functions which render the functional stationary will be denoted as $\phi^*, \phi, \bar{C}_\mu^*$ and $\bar{C}_\mu$. Thus, the Euler-Lagrange equations for this functional consist of the following system of equations:

$$V^{-1}\frac{\partial\phi}{\partial t} = \nabla\cdot D\nabla\phi - [A - (1-\beta)\chi F]\phi + \sum_{\mu=1}^{M}\lambda_\mu\chi_\mu\bar{C}_\mu$$

and

$$\frac{\partial\bar{C}_\mu}{\partial t} = -\lambda_\mu\bar{C}_\mu + \beta_\mu F\phi, \qquad \mu = 1, 2, \cdots, M,$$

in each volume R_k and time interval τ_ℓ.

and

$$\left.\begin{aligned}\phi_+ &= \phi_-\\ D_+\nabla\phi_+\cdot\hat{n} &= D_-\nabla\phi_-\cdot\hat{n}\end{aligned}\right\}\gamma_1 = 0, 1,$$

at each internal spatial interface.

$$\left.\begin{aligned}\phi(+) &= \phi(-)\\ \bar{C}_\mu(+) &= \bar{C}_\mu(-), \qquad \mu = 1, 2, \cdots, M,\end{aligned}\right\} \tag{2}$$

at each temporal interface $t = t_\ell$.
The initial conditions are

$$\phi = f$$

and

$$\bar{C}_\mu = g_\mu, \qquad \mu = 1, 2, \cdots, M.$$

The external boundary conditions are:

for $\gamma_3 = 0$

$$D\nabla\phi\cdot\hat{n}\,|_\Gamma = 0;$$

for $\gamma_3 = 1$

$$\left.\begin{aligned}\phi\,|_\Gamma &= 0, \qquad \gamma_2 = 0,\\ [D\nabla\phi\cdot\hat{n} + \gamma\phi]_\Gamma &= 0, \qquad \gamma_2 = 1;\end{aligned}\right\}$$

and a similar set of equations for the adjoint problem.

Thus, this variational formulation of space-dependent neutron kinetics theory is well posed. The first two equations in Eqs. (2) are just the neutron diffusion equation and the corresponding precursor equation, where the notation and symbols here are those used in multigroup diffusion theory.[6] The next four equations are the appropriate con-

tinuity conditions. The multiplier γ_1 is a numerical parameter which is assigned only values of 0 or 1 at the spatial interfaces. The functions f and g_μ represent the initial flux and the μth precursor distributions respectively. The functions f^* and g_μ^* would represent the corresponding final value distribution for the adjoint problem. The last three equations illustrate the various choices of external boundary conditions allowed based on the values assigned to the numerical parameters γ_2 and γ_3 (0 or 1), where the factor γ fixes the linear extrapolation distance in the last equation. Thus, the functional of Eq. (1) also variationally imposes boundary value and initial-final value conditions; that is, the class of admissible functions need not satisfy fixed end point conditions in either space or time.

Various alternate formulations can also be proposed. Two such examples will now be presented as J_2 and J_3 :

$$\begin{aligned} J_2[u^*,u,\mathbf{v}^*,\mathbf{v}] = &\sum_k \int_{R_k} dR \sum_\ell \int_{\tau\ell} dt \left[u^* V^{-1} \frac{\partial u}{\partial t} - \mathbf{v}^* \cdot D^{-1}\mathbf{v} - \mathbf{v}^* \cdot \nabla u - \nabla u^* \cdot \mathbf{v} + u^*(A - \chi F)u \right] \\ &- \sum_\ell \int_{\tau\ell} dt \int_{S_{int}} dS\, \hat{n} \cdot \{ [\gamma_1 \mathbf{v}_+^* + (1-\gamma_1)\mathbf{v}_-^*](u_+ - u_-) + (u_+^* - u_-^*)[\gamma_1 \mathbf{v}_+ \\ &+ (1-\gamma)\mathbf{v}_-] \} + \sum_k \int_{R_k} dR \, \{ u^*(+) V^{-1} [u(+) - u(-)] \}_{t=t\ell} \end{aligned} \tag{3}$$

$$\begin{aligned} J_3[u^*,u,\alpha,\beta] = &\sum_k \int_{R_k} dR \sum_\ell \int_{\tau\ell} dt \left[u^* V^{-1} \frac{\partial u}{\partial t} + \nabla u^* \cdot D \nabla u + u^*(A - \chi F)u \right] \\ &+ \sum_\ell \int_{\tau\ell} dt \int_{S_{int.}} dS \, [\alpha(u_+ - u_-) + (u_+^* - u_-^*)\beta] \\ &+ \sum_k \int_{R_k} dR \, \{ u^*(+) V^{-1} [u(+) - u(-)] \}_{t=t\ell}, \end{aligned} \tag{4}$$

where for simplicity delayed neutron, boundary, and initial-final value terms have been neglected. The functional J_2 is a first order form in the sense that the stationarity conditions include the first order form of the prompt neutron diffusion equations. This functional is similar in form to a time dependent version of the original Selengut-Wachspress (S-W) functional,[7] but here a $\gamma_1 = \frac{1}{2}$ choice is not an allowed value for γ_1 . The functional J_3 is exactly a time dependent form of the functional proposed by Buslik,[3] where α and β are undetermined Lagrange multipliers.

The three functionals presented here, while quite similar in some respects, differ in the number and choice of functions required and in the treatment of the spatial interface contributions. The functional J_1 for prompt neutrons only, requires admissible functions in only u^* and u, while J_2 requires admissible vector functions $\mathbf{v}^*$ and $\mathbf{v}$ as well and J_3 requires a choice for the Lagrange multipliers α and β. In the treatment of the spatial interface contributions, the vector functions $\mathbf{v}_\pm$ and $\mathbf{v}_\pm^*$ of J_2 are replaced by $D_\pm \nabla u_\pm$ and $\nabla u_\pm^* D_\pm$ in the functional J_1 . This identification is consistent with the diffusion theory approximation $\mathbf{j} = -D\nabla\phi$. The multipliers α and β of J_3 are also variationally related to the neutron current and its adjoint at the interfaces. The same temporal interface treatment is used in each of the three functionals.

Synthesis Applications

In this section we will illustrate the application of the functionals J_1 , J_2 and J_3 to combined space-time flux synthesis, where the admissible functions in the direct and adjoint quantities may be simultaneously discontinuous at spatial and temporal interfaces without producing problems of overdetermination in the number of interface conditions specified. The choice of temporal interface weighting will also reflect the proper initial and final value nature of the direct and adjoint problems.

For the functional J_1 , the synthesis expansions for u and u^* in each k, ℓth synthesis "region" can be chosen as

$$\left.\begin{aligned} u_\ell^k(x,y,z,t) &= \sum_{i=1}^{N_{k\ell}} H_{\ell i}^k(x,y)\, Z_{\ell i}^k(z,t) \\ u_\ell^{k*}(x,y,z,t) &= \sum_{i=1}^{N_{k\ell}} Z_{\ell i}^{k*}(z,t)\, H_{\ell i}^{k*}(x,y) \end{aligned}\right\}. \tag{5}$$

Here the functions $H_{\ell i}^{k*}(x,y)$ and $H_{\ell i}^k(x,y)$ are known sets of trial functions, and $Z_{\ell i}^{k*}(z,t)$ and $Z_{\ell i}^k(z,t)$ are undetermined mixing functions in the synthesis variables z and t. The functions C_μ and C_μ^* are expanded in terms of the same sets of trial functions as

$$\left.\begin{aligned} C^{\mu}_{k\ell}(r,t) &= \sum_{i=1}^{N_{k\ell}} F\, H^{k}_{\ell i}(x,y)\, \xi^{k}_{\mu\ell i}(z,t) \\ C^{\mu *}_{k\ell}(r,t) &= \sum_{i=1}^{N_{k\ell}} \xi^{k*}_{\mu\ell i}(z,t)\, H^{k*}_{\ell i}(x,y)\chi_{\mu} \end{aligned}\right\}. \tag{6}$$

where $\xi^{k}_{\mu\ell i}(z,t)$ and $\xi^{k*}_{\mu\ell i}(z,t)$ are undetermined mixing functions.

For this model, the resulting Euler-Lagrange equations for the direct problem are

$$\Lambda^{k}_{\ell\ell}\frac{\partial Z^{k}_{\ell}(z,t)}{\partial t} = \frac{\partial}{\partial z}\left(D^{k}_{\ell}\frac{\partial Z^{k}_{\ell}}{\partial z}\right) + (\rho'^{k}_{\ell} - \bar{\beta}^{k}_{\ell\ell})Z^{k}_{\ell} + \sum_{\mu}\frac{\lambda_{\mu}}{\beta_{\mu}}\bar{\beta}^{k}_{\mu,\ell\ell}\,\xi^{k}_{\mu\ell} \tag{7}$$

$$\frac{1}{\beta_{\mu}}\bar{\beta}^{k}_{\mu,\ell\ell}\left[\frac{\partial \xi^{k}_{\mu\ell}}{\partial t} + \lambda_{\mu}\xi^{k}_{\mu\ell}\right] = \bar{\beta}^{k}_{\mu,\ell\ell}Z^{k}_{\ell}, \qquad \mu = 1, 2, \cdots, M, \tag{8}$$

for each volume R_k and interval τ_ℓ.

At the spatial interface $z = z_k$

$$\left.\begin{aligned} D^{k+1}_{\ell}Z^{k+1}_{\ell} &= X^{k+1,k}_{\ell}(+)Z^{k}_{\ell} \\ X^{k,k+1}_{\ell}(+)\frac{\partial Z^{k+1}_{\ell}}{\partial z} &= D^{k}_{\ell}\frac{\partial Z^{k}_{\ell}}{\partial z} \end{aligned}\right\}, \qquad \gamma_1 = 1, \tag{9}$$

or

$$\left.\begin{aligned} X^{k,k+1}_{\ell}(-)Z^{k+1}_{\ell} &= D^{k}_{\ell}Z^{k}_{\ell} \\ D^{k+1}_{\ell}\frac{\partial Z^{k+1}_{\ell}}{\partial z}\, X^{k+1,k}_{\ell}(-)\,\frac{\partial Z^{k}_{\ell}}{\partial z} \end{aligned}\right\}, \qquad \gamma_1 = 0; \tag{10}$$

at the temporal interface $t = t_\ell$

$$\Lambda^{k}_{\ell+1,\ell+1}\,Z^{k}_{\ell+1} = \Lambda^{k}_{\ell+1,\ell}\,Z^{k}_{\ell} \tag{11}$$

$$\bar{\beta}^{k}_{\mu,\ell+1,\ell+1}\,\xi^{k}_{\mu,\ell+1} = \bar{\beta}^{k}_{\mu,\ell+1,\ell}\,\xi^{k}_{\mu\ell}\,, \qquad \mu = 1, 2, \cdots, M. \tag{12}$$

The initial conditions at $t = t_0$ are

$$\Lambda^{k}_{11}Z^{k}_{1} = \tilde{F}^{k}_{1} \tag{13}$$

$$\frac{1}{\beta_{\mu}}\bar{\beta}^{k}_{\mu,11}\xi^{k}_{\mu,1} = \tilde{G}^{k}_{\mu,1}, \qquad \mu = 1, 2, \cdots, M, \tag{14}$$

and boundary condition options for $k = 1$ and/or $k = K$ are

$$\left.\begin{aligned} \frac{\partial Z^{k}_{\ell}}{\partial z} &= 0, \qquad \gamma_3 = 0, \\ Z^{k}_{\ell} &= 0, \qquad \gamma_2 = 0 \quad \text{and} \quad \gamma_3 = 1, \\ D^{k}_{\ell}\frac{\partial Z^{k}_{\ell}}{\partial z} + \gamma\, Q^{k}_{\ell}Z^{k}_{\ell} &= 0, \qquad \gamma_2 = 1 \quad \text{and} \quad \gamma_3 = 1 \end{aligned}\right\}. \tag{15}$$

Z^{k}_{ℓ} is a column vector with $N_{k\ell}$ elements $[Z^{k}_{\ell}]_i$.

D^{k}_{ℓ} and ρ'^{k}_{ℓ} are $N_{k\ell} \times N_{k\ell}$ matrices with elements

$$[D^{k}_{\ell}]_{ij} = \int_{A} dA\; H^{k*}_{\ell i}\, D_{k\ell}H^{k}_{\ell j} \tag{16}$$

$$[\rho'^{k}_{\ell}]_{ij} = \int_{A} dA\left\{H^{k*}_{\ell i}\left[\nabla\cdot D_{k\ell}\,\nabla - A_{k\ell} + (1-\beta)\chi F_{k\ell} + \sum_{\mu=1}^{M}\beta_{\mu}\chi_{\mu}F_{k\ell}\right]H^{k}_{\ell j}\right\}. \tag{17}$$

$\tilde{F}^{k}_{1}$ and $\tilde{G}^{k}_{\mu,1}$ are $N_{k,1}$ element column vectors with elements

$$\left.\begin{aligned} [\tilde{F}^{k}_{1}]_i &= \int_{A} dA\; H^{k*}_{\ell i}\; V^{-1}_{k,1}\, f \\ [\tilde{G}^{k}_{\mu,1}]_i &= \int_{A} dA\; H^{k*}_{\ell i}\; \chi_{\mu}g_{\mu}\,, \qquad \mu = 1, 2, \cdots, M. \end{aligned}\right\} \tag{18}$$

Q_ℓ^k is an $N_{k\ell} \times N_{k\ell}$ matrix with elements

$$[Q_\ell^k]_{ij} = \int_A dA\ H_{\ell i}^{k*}\ H_{\ell j}^k . \tag{19}$$

$\bar{\beta}_{\mu,rs}^k$ is an $N_{kr} \times N_{ks}$ matrix with elements

$$[\bar{\beta}_{\mu,rs}^k]_{ij} = \beta_\mu \int_A dA\ H_{ri}^{k*}\ \chi_\mu\ F_{ks} H_{sj}^k , \qquad r, s = \ell, \ell + 1, \tag{20}$$

where β has the usual definition

$$\beta = \sum_{\mu=1}^{M} \beta_\mu \quad \text{and} \quad \bar{\beta}_{rs}^k = \sum_{\mu=1}^{M} \bar{\beta}_{\mu,rs}^k .$$

$\underset{\ell}{X}^{p,q}(+)$ and $\underset{\ell}{X}^{p,q}(-)$ are $N_{p\ell} \times N_{q\ell}$ matrices with elements

$$[X_\ell^{p,q}(+)]_{ij} = \int_A dA\ H_{\ell i}^{p*}\ D_{k+1,\ell}\ H_{\ell j}^q \tag{21}$$

$$[X_\ell^{p,q}(-)]_{ij} = \int_A dA\ H_\ell^{p*}\ D_{k\ell}\ H_{\ell j}^q , \tag{22}$$

where $p,q = k,k+1 (p \neq q)$.
$\Lambda_{r,s}^k$ is an $N_{kr} \times N_{ks}$ matrix with elements

$$[\Lambda_{r,s}^k]_{ij} = \int_A dA\ H_{ri}^{k*}\ V_{ks}^{-1}\ H_{sj}^k , \tag{23}$$

where $r,s = \ell,\ell+1$.
A similar set of equations in Z_ℓ^{k*} can be obtained, but will not be considered here.

The system of equations in Z_ℓ^k and $\xi_{\mu\ell}^k$ with appropriate initial and boundary conditions can now be solved for the undetermined mixing functions. The approximate synthesis flux is then given by [the first equation in Eqs. (5)]

$$\phi_\ell^k(\underline{r},t) \approx \sum_{i=1}^{N_{k\ell}} H_{\ell i}^k\ (x,y) \bar{Z}_{\ell i}^k(z,t) , \tag{24}$$

where $Z_{\ell i}^k = \bar{Z}_{\ell i}^k$ represent the solution of the system of equations for a stationary functional.

The system of Eqs. (7)–(15) reflect entirely proper choices of interface conditions in number and kind at both the spatial and temporal interfaces. Equation (11) gives the proper choice of weighting of $u^*(+)$ (or $H_{\ell+1,i}^{k*}$) for an initial-value problem. The expression provides $N_{k,\ell+1}$ values for the $N_{k,\ell+1}$ unknowns $Z_{\ell+1}^k$ at $t = t_\ell^+$ in terms of the $N_{k\ell}$ known functions Z_ℓ^k at $t = t_\ell^-$ (the $\pm$ superscripts indicate limiting values at the interface). This condition thus provides the "initial" conditions $Z_{\ell+1}^k(z,t_\ell^+)$ for the solution over the $\ell + 1st$ subinterval in terms of the known values of $Z_\ell^k(z,t_\ell^-)$ from the ℓth subinterval. A choice of weighting of $u^*(-)$ (or $H_{\ell i}^{k*}$), while possible, would restrict the problem to cases where $N_{k,\ell+1} \equiv N_{k,\ell}$, i.e., the same number of trial functions would be required in each subinterval. A choice of $u^*(-)$ weighting, however, would be proper for the final-value adjoint problem and is in fact the choice produced by the use of the functionals proposed. Equation (12) exhibits the same choice of weighting and the initial-final value nature of the precursor-like problem.

Equations (9) and (10) are each proper choices of spatial interface conditions for the choices of $\gamma_1 = 1$ and $\gamma_1 = 0$, respectively. For a given problem, only one choice of γ_1 (either 0 or 1) can be made at each interface. It is important to note at this point that all other choices of γ_1 will yield an overdetermined problem. For example, the choice of $\gamma_1 = \frac{1}{2}$ would give both of the sets of conditions specified in Eqs. (9) and (10) and exactly the problem noted by Buslik.[3]

Clearly, Eqs. (9) and (10) represent two different sets of conditions in terms of the choice of weighting functions used at the interfaces. The continuity of flux-type expression of Eqs. (9) is weighted by the adjoint function ∇u^*D from the negative side of the interface, while the continuity of current-type expression is weighted by u^* from t plus side of the interface. Equations (10) represent the opposite choice of weighting. In both cases, there is a "mixed" weighting in the two conditions; however there exists no clear choice of "mixed" weighting which is preferred in analogy to the time treatment. At this point it is important to note that a complete asymmetric weighting has not

been considered. It can be shown that for synthesis applications these choices restrict one to the use of the same number of trial functions in each spatial region, while the "mixed" choices of weighting do not make this restriction.

For the functional J_2, the additional expansions required for $\mathbf{v}$ and $\mathbf{v}^*$ can, in theory, utilize a completely independent set of trial functions. However, in practice[1,8] use is made of the same set as used in Eqs. (5), and can have the form

$$\left.\begin{aligned} v_{x\ell}^k(\underline{r},t) &= \sum_{i=1}^{N_{k\ell}} D_{k\ell} \frac{\partial H_{\ell i}^k}{\partial x} \epsilon_{\ell i}^k(z,t) \\ v_{y\ell}^k(\underline{r},t) &= \sum_{i=1}^{N_{k\ell}} D_{k\ell} \frac{\partial H_{\ell i}^k}{\partial y} \eta_{\ell i}^k(z,t) \\ v_{z\ell}^k(\underline{r},t) &= \sum_{i=1}^{N_{k\ell}} D_{k\ell} H_{\ell i}^k \zeta_{\ell i}^k(z,t) \end{aligned}\right\} \tag{25}$$

with corresponding expressions for the adjoints. With such a choice, one can show that the Euler-Lagrange equations obtained are identical to those obtained for J_1, and the following identities are established:

$$\left.\begin{aligned} \epsilon_\ell^k(z,t) &= -Z_\ell^k(z,t) \\ \eta_\ell^k(z,t) &= -Z_\ell^k(z,t) \end{aligned}\right\} \tag{26}$$

and

$$\zeta_\ell^k(z,t) = -\frac{\partial Z_\ell^k}{\partial z}.$$

Thus, the same approximate synthesis flux is obtained [Eq. (24)] for this model.

In the synthesis application of the functional J_3, additional expansions are required in the Lagrange multipliers, and the expansions at the point $z = z_k$ can be expressed as

$$\left.\begin{aligned} \alpha(x,y,t) &= \sum_{i=1}^{N_{k\ell}} a_{\ell i}^{k*}(t) G_{\ell i}^{k*}(x,y) \\ \beta(x,y,t) &= \sum_{i=1}^{N_{k\ell}} G_{\ell i}^k(x,y) b_{\ell i}^k(t), \end{aligned}\right\} \tag{27}$$

where the trial functions $G_{\ell i}^{k*}$ and $G_{\ell i}^k$ are in general unrelated to the trial functions $H_{\ell i}^{k*}$ and $H_{\ell i}^k$. Here, α and β are expanded in terms of $N_{k\ell}$ functions consistent with Eqs. (5) for the kth region; however, one could equally well choose $N_{k+1,\ell}$ expansions consistent with the $k+1$st region.

The Lagrange multipliers are initially arbitrary but are, in fact related variationally to the normal component of the currents at each interface $z = z_k$. Thus, it seems reasonable to choose expansion functions for these multipliers which are related to those used in Eqs. (5). This also reduces the variety of trial functions required. With such a choice, identities for the undetermined functions $a_{\ell i}^{k*}$ and $b_{\ell i}^k$ can be found which are similar to those of Eqs. (26).

It has been established[9] that the choice of expansions

$$\left.\begin{aligned} \alpha(x,y,t) &= \sum_{i=1}^{N_{k\ell}} \frac{\partial Z_{\ell i}^{k*}}{\partial z} H_{\ell i}^{k*} D_{k\ell} \\ \beta(x,y,t) &= \sum_{i=1}^{N_{k\ell}} D_{k\ell} H_{\ell i}^k \frac{\partial Z_{\ell i}^k}{\partial z} \end{aligned}\right\} \tag{28}$$

gives the same interface conditions as those for $\gamma_1 = 0$ [Eqs. (10)]. While the choice

$$\left.\begin{aligned} \alpha(x,y,t) &= \sum_{i=1}^{N_{k+1,\ell}} \frac{\partial Z_{\ell i}^{k+1*}}{\partial z} H_{\ell i}^{k+1*} D_{k+1,\ell} \\ \beta(x,y,t) &= \sum_{i=1}^{N_{k+1,\ell}} D_{k+1,\ell} H_{\ell i}^{k+1} \frac{\partial Z_{\ell i}^{k+1}}{\partial z} \end{aligned}\right\} \tag{29}$$

gives the same interface conditions for $\gamma_1 = 1$ [Eqs. (9)]. The Euler-Lagrange equations for these choices are then again identical to those for J_1, and the same synthesis flux results.

Conclusions and Observations

Although the equivalence of the three proposed functionals can be demonstrated for a given set of trial functions in a synthesis application, it is important to note that this equivalence is not general. In theory, in the functionals J_2 [Eq. (3)] and J_3 [Eq. (4)] one is free to make arbitrary choices for the admissible functions v^* and v and the multipliers α and β which are independent of the choices for u^* and u. In this sense the functional J_1 [Eq. (1)] is more restrictive, since it allows only a choice in the functions u^* and u. However, v^* and v, as well as α and β are physically related to the functions u^* and u.

In each of these expansion choices for J_2 and J_3, the relation between the current- and flux-type expressions satisfies the Fick's law form, $\mathbf{J} = -D\nabla\phi$. While other choices may be made, these choices are most consistent with the diffusion theory model for which the functionals were proposed. The choices reflect not only the physical nature of these quantities but impose, a priori, those conditions which are only variationally imposed in general.

The form, J_1, implicitly removes this ambiguity in the choice of trial functions for the current by forcing the choice to be that defined by Fick's law. Since the quality of the approximate flux is strongly dependent on the choice of good trial functions, the choosing of trial functions in a manner consistent with the diffusion theory model is a preferred choice. Such a choice is assured by the use of the form J_1, and the problem of choosing good trial functions is reduced to one of choosing trial functions only in the functions u^* and u.

Some general observations can also be made concerning a comparison of these proposed functionals with those currently in use. The usual forms[1,2,8] each utilize expansions which yield a finite difference form of Euler-Lagrange equations. In these models the numerical algorithm is fixed by the form of expansions chosen. Each of the proposed new functions, however, can give Euler-Lagrange equations in an analytic form. The partial differential equations can then be solved in a variety of ways completely independent of the form of the expansion used. Since these equations differ from the multi-group neutron diffusion equations, the same numerical methods may not be the most suitable.

A simple test code, SYNTEST, has been developed based on a finite difference representation of the system of Eqs. (7)–(24). The numerical model generates a 2D-time dependent synthesis solution for the direct flux in two energy groups using expansions [Eqs. (5) and (6)] with trial-weight functions in the radial (or x) dimension. The trial function library and the initial flux are computed with the use of the 1D and 2D diffusion capabilities of the ARC system respectively,[10] and the synthesis results are compared with the full numerical solution supplied by TWIGL.[11]

While the analytical development of the proposed functional and synthesis model is complete and general the scope of the numerical model used for testing is somewhat limited. The results obtained necessarily reflect these limitations, but the results are generally quite favorable. The algorithm and results are detailed in Ref. 9 and will not be presented here.

The full combined space-time discontinuous capability of the model has been tested. The perturbed region may be described by one set of trial functions, while the unperturbed region is described by another set, and these trial function sets may be changed over different time intervals. Testing has also been carried out of both the $\gamma_1 = 0$ and $\gamma_1 = 1$ choices of spatial interface weighting and the fixed forward weighting of the temporal interfaces. For cases in which spatial interface is chosen near the interface for the perturbed and unperturbed regions, the choice of γ_1 is very important. The best results are obtained for a choice of γ_1 such that the weighting functions in the integral $X_\ell^{p,q}(+)$ for the first conditions in either Eqs. (9) or Eqs. (10) are those typical of the unperturbed region. The switching of trial functions at some temporal interface presents no particular problem.

The general validity of choosing the trial functions to bracket the shape change expected during a transient is demonstrated. The savings in computing time over the full numerical solution is slightly greater than a factor of three. This comparison, however, includes the computing time required to generate the trial function library which is then available for subsequent problems.

In general, little numerical work has been reported on practical applications of combined space-time variational synthesis methods and its value as a computational tool is yet to be realized. Its greatest potential probably rests in the synthesis of full 3D-time dependent fluxes, where a full numerical solution is impractical for each case of interest. Some experimental data or full numerical solutions would still be needed as benchmarks to establish the quality of the trial function library to be used. Thus, synthesis can become a powerful tool for routine, systematic detailed investigations for reactor design, but confidence in these methods must be gained through a large amount of experience.

REFERENCES

1. Y. B. Yasinski, *Combined Space-Time Synthesis with Axially Discontinuous Trial Functions*, WAPD-TM-736 (1967).
2. W. M. Stacey, *Variational Functional for Space-Time Neutronics*, Nucl. Sci. Eng. **30**, 448–463 (1967).
3. A. J. Buslik, *A Variational Principle for the Neutron Diffusion Equation Using Discontinuous Trial Functions*, WAPD-TM-610 (1966).
4. M. Becker, *Asymmetric Discontinuities in Synthesis Techniques for Initial-Value Problems*, Nucl. Sci. Eng. **34**, 343–344 (1968).
5. V. Luco and W. L. Woodruff, *Solutions to the Problem of Interface Overdetermination in Spatial Flux Synthesis*, Reactor Physics Division Annual Report, July 1, 1968 to June 30, 1969, ANL-7610, pp. 521–525.
6. S. Kaplan, *Synthesis Methods in Reactor Analysis*, Advances in Nuclear Science and Technology, (Academic Press, New York 1965) Vol. III.
7. E. L. Wachspress and M. Becker, *Variational Synthesis with Discontinuous Trial Functions*, Proc. Conference on Applications of Computing Methods to Reactor Problems, ANL-7050 (1965).
8. W. M. Stacey, *A Variational Multichannel Space-Time Synthesis Method for Non-Separable Reactor Transients*, Nucl. Sci. Eng. **34**, 45–56 (1968).
9. W. L. Woodruff, *Some Improvements in Variational Flux Synthesis Methods*, ANL-7696 (1970).
10. B. J. Toppel, Ed., *The Argonne Reactor Computation (ARC) System*, ANL-7332 (1967).
11. J. B. Yasinsky, M. Natelson and L. A. Hageman, *TWIGL—A Program to Solve the Two-Dimensional, Two-Group, Space-Time Neutron Diffusion Equations with Temperature Feedback*, WAPD-TM-743 (1968).

IV-15. Formulations of Space-Energy-Time-Iterative Synthesis

E. L. FULLER

INTRODUCTION

The time-dependent diffusion equation can be written[1]

$$(-M + F_p)\phi(\mathbf{r},E,t) + S_D[\phi(\mathbf{r},E,t')] = v^{-1}(E)\,\frac{\partial}{\partial t}\phi(\mathbf{r},E,t), \tag{1}$$

where $(-M + F_p)$ is the diffusion operator, such that M accounts for removal and scattering, and F_p is the prompt fission operator. The delayed neutron source, $S_D[\phi(\mathbf{r},E,t')]$, has the form of a convolution integral over the flux history. Equation (1) can be thought of either as a continuous-energy scalar equation or a matrix equation in which ϕ is a column vector of the group fluxes in multigroup diffusion theory. In either case, one can attempt to solve Eq. (1) approximately by invoking the method of undetermined functions. For the continuous-energy model, the approximate solution can take the form

$$\phi_I(\mathbf{r},E,t) = \sum_{i=1}^{I} \psi_i(\mathbf{r},E)N_i(t), \tag{2}$$

where the $\psi_i(\mathbf{r},E,t)$ are trial functions, and $N_i(t)$ are the undetermined amplitude functions. For multigroup diffusion theory, the approximate solution is

$$\phi_I(\mathbf{r},t) = \sum_{i=1}^{I} \psi_i(\mathbf{r})N_i(t) \tag{3}$$

where the $\psi_i(\mathbf{r})$ could be $G \times G$ diagonal matrices of trial functions and the $N_i(t)$ could be G-dimensional column vectors.

The use of the method of undetermined functions in conjunction with Eq. (3) to solve the multigroup diffusion equations is well known.[2] Solutions of the continuous-energy model of the form of Eq. (2) have not appeared, however, primarily because much spectral detail is required in the trial functions if accurate solutions are to be expected. Recently, however, some progress has been made in synthesizing space-energy solutions for stationary systems.[3-5] In addition, Stacey[6] has gotten some encouraging results with an energy-time synthesis scheme, in which only a few energy modes are required to achieve an accurate solution. It therefore seems appropriate to seek an approximation technique that could utilize this newly-gleaned knowledge to obtain an accurate solution to the continuous-energy

model. At the same time, the method should also be capable of solving the multigroup diffusion system, which is, of course, only an approximation to the continuous-energy model. Such a technique, which combines iteration with the method of undetermined functions, has been developed and will now be described. It will then be applied to the continuous-energy model and to multigroup theory.

The idea of using iterative schemes along with approximate methods is an old one in reactor physics. Selengut[7] advocated such an idea and illustrated it by an application to the one-group diffusion equation in x-y geometry. Shortly thereafter, Lewins[8] formulated a variational principle for time-dependent group-diffusion theory, which he used to derive Euler equations for either spatial or temporal integration. He used only a one-mode expansion, however, which was in effect equivalent to a point reactor model. He pointed out that iteration between the two sets of equations was possible; this iteration would presumably find the best possible shape for use in the point reactor model.

We shall now present a general outline of the method to show that it can handle systems of many independent variables. The development is similar to that given by Kerr.[9] We begin by writing our system of (possibly non-linear) partial differential equations as[10]

$$H\phi(\underline{x}) = f(\underline{x}) \tag{4}$$

$$B_n\phi(\underline{x}) = g_n(\underline{x}), \qquad n = 1, \cdots, N, \tag{5}$$

where H is a nonlinear differential operator, $\underline{x}$ is a vector of independent variables, $\phi(\underline{x})$ is the vector of dependent variables, $f(\underline{x})$ and $g_n(\underline{x})$ are vectors containing functions of the independent variables, and the B_n are operators representing the N boundary conditions. An approximate solution is now sought in the form

$$\phi_I(\underline{x}) = \psi_0 + \sum_{i=1}^{I} A_i\psi_i, \tag{6}$$

where the functions ψ_0 and ψ_i are trial solutions, chosen beforehand. These functions must be linearly independent, and should also satisfy the boundary conditions, preferably by choosing ψ_0 and ψ_i such that

$$B_n(\psi_0) = g_n, \qquad n = 1, \cdots, N \tag{7}$$

$$B_n(\psi_i) = 0, \qquad i = 1, \cdots, I. \tag{8}$$

When Eq. (6) is substituted into Eq. (4) the following residual is formed:

$$R(A,\psi) = f - H\phi_I = f - H(\psi_0 + \sum_{i=1}^{I} A_i\psi_i). \tag{9}$$

The residual is a measure of the extent to which ϕ_I satisfies Eq. (4). It cannot be calculated, of course, until the A_i are found in some manner. One would hope that any method used to find the A_i would yield a smaller residual as more trial functions are used (i.e., as I increases). Moreover, the method used should be such that it makes the residual "small" in some sense. Since the method of weighted residuals provides this alternative, it is used here. That is, I weighted averages of the residual are set equal to zero:

$$\int_D W_r R dD = 0, \qquad r = 1, \cdots, I. \tag{10}$$

The independent variables in D include all the independent variables upon which the A_i do not depend. If the A are undetermined parameters, then the integration is over all of the independent variables; I algebraic equations remain. This technique is often called the method of undetermined parameters.[11] When the A_i are undetermined functions, I differential equations result. The method of undetermined parameters is often called the direct method; the method of undetermined functions is also known as the semidirect method, or the Kantorovich method. The remainder of the development is concerned only with the method of undetermined functions.

The General Iterative Scheme

When the trial solution given by Eq. (6) is postulated, assume that the A_i are functions of only one independent variable, say x_1. The trial functions ψ_i can be functions of all the independent variables, but we shall choose them to be functions of the remaining members of $\underline{x}$; that is,

$$\psi_i = \psi_i(x_2, \cdots, x_s) \equiv \psi_{i1}^1(x_2, \cdots, x_s) \tag{11}$$

then $\underline{x} = (x_i, \cdots, x_s)$. A weighted-residual criterion will then produce a set of ordinary differential equations to be solved for the $A_i(x_i)$. Limited by the initial choice of the ψ_i's, the approximation nevertheless yields a solution that is tending toward the true solution along the x_1 direction. It is obvious that any improvement along the directions of the remaining independent variables would be welcome. This is the motivation for adopting the following iterative scheme.

After having determined the $A_i(x_1)$, relabel them as $A^1_{i1}(x_1)$ and let

$$\psi^1_{i1}(x_2, \cdots, x_s) = A^1_{i2}(x_2)\, \psi^1_{i2}(x_3, \cdots, x_s), \tag{12}$$

where the ψ^1_{i2} are also chosen beforehand. When Eq. (12) is substituted into Eq. (6), the result is (neglecting ψ_0)

$$\phi_I(\underline{x}) = \sum_{i=1}^{I} A^1_{i1}(x_1)\, A^1_{i2}(x_2)\, \psi^1_{i2}(x_3, \cdots, x_s). \tag{13}$$

The $A^1_{i2}(x_2)$ are determined by using a weighted-residual criterion with respect to $(x_1, x_3, x_4, \cdots, x_s)$. Then, let

$$\psi^1_{i2}(x_3, \cdots, x_s) = A^1_{i3}(x_3)\, \psi^1_{i3}(x_4, \cdots, x_s). \tag{14}$$

Again, substitute Eq. (14) into Eq. (6), and use a weighted-residual criterion with respect to $(x_1, x_2, x_4, \cdots, x_s)$ to determine the $A^1_{i3}(x_3)$.

This process is continued until all the functions $A^1_{i1}(x_1), \cdots, A^1_{is}(x_s)$ have been determined, so that the approximate solution is given by

$$\phi^1_I(\underline{x}) = \sum_{i=1}^{I} \prod_{k=1}^{s} A^1_{ik}(x_k). \tag{15}$$

At this stage a second iteration is begun; the improved expressions for $A_{i1}(x_1)$, now labeled $A^2_{i1}(x_1)$, can be found by using the I products $\prod_{k=2}^{s} A_{ik}(x_k)$ as "trial functions", and so on, until the second iteration has been completed. At this point the approximate solution is

$$\phi^2_I(\underline{x}) = \sum_{i=1}^{I} \prod_{k=1}^{s} A^2_{ik}(x_k). \tag{16}$$

Kerr[9] has found in one particular example that a converged solution can be obtained with very few iterations. More importantly, he also found that the final form of the solution is independent of the initial choice of the ψ_i's. The accuracy of the solution depends only upon the choices of weighting functions and on the number of trial functions chosen.

It should be noted that the A_{ik} need not be functions of only the variable x_k; indeed each A_{ik} could be a function of s-1 variables. By making the A_{ik} multidimensional, however, it becomes necessary to solve systems of partial differential equations to determine them. (Another alternative is to assign a simple functional dependence upon the excess (>1) independent variables. This is the technique used in the "improved quasistatic approximation"[1] of space-time kinetics for the time dependence of the shape function.)

Applications to the Neutron Diffusion Equations

Lancefield[4] and Toivanen[3] have recently used versions of the iterative scheme described above in space-energy synthesis solutions of the steady-state one-dimensional transport equation. Each had only limited success, but Lancefield has pointed out ways of improving estimates of the flux distribution (for example, using discontinuous trial functions). Our attention is focused here on obtaining formulations within the realm of diffusion theory. We shall show how the method can be used to obtain solutions to both the time-dependent continuous-energy diffusion theory model and the time-dependent multigroup diffusion theory model. Possible ways of using spatially and temporally discontinuous trial functions will also be discussed.

Continuous energy model

For the continuous energy model, Eq. (1) becomes (using common notation)

$$\frac{1}{2mE}\frac{\partial \phi}{\partial t}(\mathbf{r},E,t) = \nabla\cdot D(\mathbf{r},E,t)\nabla\phi(\mathbf{r},E,t) - \Sigma_T(\mathbf{r},E,t)\phi(\mathbf{r},E,t) + \int_0^\infty \Sigma_{TR}(\mathbf{r},E'\to E,t)\phi(\mathbf{r},E',t)\, dE' + \chi(E)\int_0^\infty \nu\Sigma_f(\mathbf{r},E'',t)\phi(\mathbf{r},E'',t)\, dE'' + S_D[\phi(r,E,t)]. \tag{17}$$

Now, let each ψ_i in Eq. (2) be given by

$$\psi_i(\mathbf{r},E) = H_i(\mathbf{r})G_i(E). \tag{18}$$

Then Eq. (2) can be put into three equivalent matrix forms as follows:

$$\begin{aligned}\phi_I(\mathbf{r},E,t) &= \sum_{i=1}^{I} H_i(\mathbf{r})G_i(E)N_i(t) = H_R(\mathbf{r})G_D(E)N_C(t) \\ &= G_R(E)N_D(t)H_C(\mathbf{r}) = N_R(t)H_D(\mathbf{r})G_C(E),\end{aligned} \tag{19}$$

where R, D, and C stand, respectively, for I-dimensional row, diagonal, and column matrices. The elements of the column matrix are those that are to be determined, given a knowledge of the elements in the R and D matrices.*

Calculation of the Steady State

Before looking at the transient behavior it is necessary to calculate the steady state. That is, we must find the $H_{i0}(\mathbf{r})$ and the initial values of $G_{i0}(E)$. We can begin by guessing at $G_{R0}(E)$ to calculate $H_{C0}(\mathbf{r})$. Consider, then, the matrix of weighting functions $F_C(E) = \text{col}[F_1(E) \cdots F_I(E)]$. We can use these to form the following weighted-residual criterion for determining the $H_{i0}(\mathbf{r})$:

$$0 = \nabla\cdot P(\mathbf{r},0)\ \nabla H_{C0}(\mathbf{r}) - R_T(\mathbf{r},0)H_{C0}(\mathbf{r}) + R_{TR}(\mathbf{r},0)H_{C0}(\mathbf{r}) + \frac{1}{k_0} R_F(\mathbf{r},0)H_{C0}(\mathbf{r}), \tag{20}$$

where the $I \times I$ matrices P, R_T, R_{TR}, and R_F are given by

$$P(\mathbf{r},0) = \int_0^\infty F_C(E)D(\mathbf{r},E,0)G_{R0}(E)\ dE \tag{21}$$

$$R_T(\mathbf{r},0) = \int_0^\infty F_C(E)\Sigma_T(\mathbf{r},E,0)G_{R0}(E)\ dE \tag{22}$$

$$R_{TR}(\mathbf{r},0) = \int_0^\infty F_C(E) \int_0^\infty \Sigma_{TR}(\mathbf{r},E' \to E,0)G_{R0}(E)\ dE'dE \tag{23}$$

$$R_F(\mathbf{r},0) = \int_0^\infty F_C(E)\chi(E) \int_0^\infty \nu\Sigma_f(\mathbf{r},E'',0)G_{R0}(E'')\ dE''dE. \tag{24}$$

The eigenvalue k_0 is introduced because the steady-state equations are homogeneous (external sources are neglected). Once the spatial distribution of the modes has been found the spectral distributions can be improved. This is done by introducing the matrix of weighting functions

$$W_C(\mathbf{r}) = \text{col}[W_1(\mathbf{r}) \cdots W_I(\mathbf{r})]$$

and using the following weighted residual criterion:

$$\begin{aligned}0 = Q(E,0)G_{C0}(E) - S_T(E,0)G_{C0}(E) + \int_0^\infty S_{TR}(E' \to E,0)G_{C0}(E')\ dE' \\ + \frac{1}{k_0}\chi(E) \int_0^\infty S_F(E'',0)G_{C0}(E'')dE'',\end{aligned} \tag{25}$$

where the $I \times I$ matrices Q, S_T, S_{TR}, and S_F are given by

$$Q(E,0) = \int_V W_C(\mathbf{r})\nabla\cdot D(\mathbf{r},E,0)\nabla H_{R0}(\mathbf{r})dV \tag{26}$$

$$S_T(E,0) = \int_V W_C(\mathbf{r})\Sigma_T(\mathbf{r},E,0)H_{R0}(\mathbf{r})dV \tag{27}$$

$$S_{TR}(E' \to E,0) = \int_V W_C(\mathbf{r})\Sigma_{TR}(\mathbf{r},E' \to E,0)H_{R0}(\mathbf{r})dV \tag{28}$$

* Note that the symbol $\mathbf{r}$ may stand for three independent variables; for instance, x, y, and z. In this case, H_R would actually be $X_R(x)Y_D(y)Z_D(z)$, and $H_D = X_D(x)Y_D(y)Z_D(z)$. If one were to solve for the elements $Y_i(y)$, then $H_C = X_D(x)Z_D(z)Y_C(y)$.

$$S_F(E'',0) = \int_V W_C(\mathbf{r})\nu\Sigma_f(\mathbf{r},E'',0)H_{R0}(\mathbf{r})dV. \tag{29}$$

At this point, the new values of the $G_i(E)$ can be reinserted into Eqs. (20) through (24) to recalculate the $H_{i0}(\mathbf{r})$. Iteration continues until convergence is achieved. Such convergence should be on the eigenvalue and on the flux distribution.

A good steady state distribution could be obtained by starting with $I = 1$ and then iterating to convergence. Then do the same for $I = 2$, and compare the results with those for $I = 1$. If they are arbitrarily close, use a two-mode scheme for the time integration. If they are not close enough, carry out a three-mode steady-state solution and compare it with the two-mode solution, etc., until an acceptable steady-state solution is obtained. At this point, the time integration may begin.

Transient Behavior: Time-Independent Shape Functions

It is obvious that, when the steady-state flux is calculated as described above, the first-guess values of $N_i(0)$ are all unity. So, let us now look at the transient behavior by deriving the differential equations for the $N_i(t)$. We shall first assume that the H_i are time-independent, and then show how time-dependent shape functions can be handled via temporally discontinuous trial function methods.

Let us begin by explicitly writing down the expression for the delayed neutron source in Eq. (17):

$$S_D[\phi(\mathbf{r},E,t)] = \sum_{j=1}^{J} \lambda_j\chi_j(E)\eta_j(\mathbf{r},E,0)\exp[-\lambda_j t] + \beta_j \int_0^t \int_0^\infty \nu\Sigma_f(\mathbf{r},E'',t')\phi(\mathbf{r},E'',t')\exp[-\lambda_j(t-t')]\,dE''dt', \tag{30}$$

where $\chi_j(E)$ is the spectrum for the jth delayed neutron group, β_j is the jth delayed neutron fraction, and $\eta_j(\mathbf{r},E,0)$ is the initial distribution of the precursor of the jth delayed neutron group. Next, we use the method of weighted residuals to obtain the multimode kinetics equations:

$$\Lambda \frac{dN_C}{dt} = [\rho(t) - \bar{\beta}(t)]N_C(t) + \sum_{j=1}^{J} \lambda_j C_j(t), \tag{31}$$

where the $I \times I$ matrices Λ, ρ, and $\bar{\beta}$ are given by

$$\Lambda = \int_V \int_0^\infty W_D(\mathbf{r})F_C(E)\frac{1}{\sqrt{2mE}}H_R(\mathbf{r})G_D(E)\,dE\,dV \tag{32}$$

$$\begin{aligned}\rho(t) = \int_V \int_0^\infty W_D(\mathbf{r})F_C(E)\Bigg(&[\nabla\cdot D(\mathbf{r},E,t)\nabla H_R(\mathbf{r}) - \Sigma_T(\mathbf{r},E,t)H_R(\mathbf{r})]G_D(E) + \Bigg\{\int_0^\infty \Sigma_{TR}(\mathbf{r},E'\to E,t)G_R(E')\,dE' \\ &+ \frac{1}{k_0}\left[(1-\beta)\chi(E) + \sum_{j=1}^{J}\beta_j\chi_j(E)\right]\int_0^\infty \nu\Sigma_f(\mathbf{r},E'',t)G_R(E'')\,dE''\Bigg\}H_D(\mathbf{r})\Bigg)dE\,dV\end{aligned} \tag{33}$$

$$\left(\beta = \sum_{j=1}^{J}\beta_j\text{, the total delayed neutron fraction}\right),$$

$$\bar{\beta}(t) = \sum_{j=1}^{J}\bar{\beta}_j(t) = \sum_{j=1}^{J}\beta_j\int_V\int_0^\infty W_D(\mathbf{r})F_C(E)\chi_j(E)\int_0^\infty \nu\Sigma_f(\mathbf{r},E'',t)G_R(E'')\,dE''\,H_D(\mathbf{r})\,dE\,dV. \tag{34}$$

Furthermore, the I-dimensional column matrices $C_j(t)$ are defined by

$$\sum_{j=1}^{J}\lambda_j C_j(t) = \int_V\int_0^\infty W_D(\mathbf{r})F_C(E)S_D[\phi_I(\mathbf{r},E,t)]dE\,dV, \tag{35}$$

so that the delayed neutron source for Eq. (31) can be found as well.

Note that $N_C(t)$ in Eq. (31) is subject to initial conditions derived as follows from forming an initial residual:

$$\int_V\int_0^\infty \frac{W_D(\mathbf{r})F_C(E)}{\sqrt{2mE}}[H_{R0}(\mathbf{r},0)G_{D0}(E,0) - H_R(\mathbf{r})G_D(E)N_C(0)]\,dE\,dV$$

so that

$$N_C(0) = \Lambda^{-1}\Lambda_0 C_1, \tag{36}$$

where Λ_0 is the generation time matrix at steady state, Λ is the generation time matrix found using the current shape and spectral functions, and C_1 is a column vector whose entries are all unity.

Once the $N_i(t)$ are found they can be used to improve either the $H_i(\mathbf{r})$ or the $G_i(E)$ by means of the iterat scheme. To find new functions for $H_i(\mathbf{r})$, for example, the following scheme is used:

$$0 = \nabla\cdot P(\mathbf{r})\nabla H_C(\mathbf{r}) - R_T(\mathbf{r})H_C(\mathbf{r}) + R_{TR}(\mathbf{r})H_C(\mathbf{r}) + \frac{1}{k_0} R_F(\mathbf{r})H_C(\mathbf{r}) - U_R(\mathbf{r})H_C(\mathbf{r}) + S_R[H_C(\mathbf{r})], \quad (37)$$

where the $I \times I$ matrices P, R_T, R_{TR}, R_F, and U, and the I-dimensional column vector S_R are given by

$$P(\mathbf{r}) = \int_0^\infty \int_0^t F_D(E)T_C(t)D(\mathbf{r},E,t)G_R(E)N_D(t)dt\,dE \quad (38)$$

$$R_T(\mathbf{r}) = \int_0^\infty \int_0^t F_D(E)T_C(t)\Sigma_T(\mathbf{r},E,t)G_R(E)N_D(t)dt\,dE \quad (39)$$

$$R_{TR}(\mathbf{r}) = \int_0^\infty \int_0^t F_D(E)T_C(t)\left[\int_0^\infty \Sigma_{TR}(\mathbf{r},E' \to E,t)G_R(E')dE'\right] N_D(t)dt\,dE \quad (40)$$

$$R_F(\mathbf{r}) = \int_0^\infty \int_0^t F_D(E)T_C(t)\chi(E)\left[\int_0^\infty \nu\Sigma_f(\mathbf{r},E'',t)G_R(E'')dE''\right] N_D(t)dt\,dE \quad (41)$$

$$U_R(\mathbf{r}) = \int_0^\infty \int_0^t F_D(E)T_C(t)\frac{1}{\sqrt{2mE}} G_R(E)\frac{dN_D}{dt}\,dt\,dE \quad (42)$$

$$S_R[H_C(\mathbf{r})] = \int_0^\infty \int_0^t F_D(E)T_C(t)S_D[\phi_I(\mathbf{r},E,t)]dt\,dE, \quad (43)$$

where $T_C(t) = \text{col}[T_1(t) \cdots T_I(t)]$ is a column vector of weighting functions. The elements of S_R contain both homogeneous and inhomogeneous terms. The eigenvalue is retained; however, it now really has the value of unity. It has been found that retention of the eigenvalue is useful in obtaining rapid convergence when the system is almost homogeneous. That is, in the numerical solution, iterations occur until λ is arbitrarily close to unity.

The next logical step is to improve the $G_i(E)$ by utilizing the latest values of $H_i(\mathbf{r})$ and $N_i(t)$. This is done by means of the following weighted residual method:

$$0 = Q(E)G_C(E) - S_T(E)G_C(E) + \int_0^\infty S_{TR}(E' \to E)G_C(E')dE' + \frac{1}{k_0}\chi(E)\int_0^\infty S_F(E'')G_C(E'')dE'' - U_E(E)G_C(E) + S_E[G_C(E)], \quad (44)$$

where

$$Q(E) = \int_0^t \int_V T_D(t)W_C(\mathbf{r})\nabla\cdot D(\mathbf{r},E,t)\nabla H_R(\mathbf{r})N_D(t)dV\,dt \quad (45)$$

$$S_T(E) = \int_0^t \int_V T_D(t)W_C(\mathbf{r})\Sigma_T(\mathbf{r},E,t)H_R(\mathbf{r})N_D(t)dV\,dt \quad (46)$$

$$S_{TR}(E' \to E) = \int_0^t \int_V T_D(t)W_C(\mathbf{r})\Sigma_{TR}(\mathbf{r},E' \to E,t)H_R(\mathbf{r})N_D(t)dV\,dt \quad (47)$$

$$S_F(E'') = \int_0^t \int_V T_D(t)W_C(\mathbf{r})\nu\Sigma_f(\mathbf{r},E'',t)H_R(\mathbf{r})N_D(t)dV\,dt \quad (48)$$

$$U_E(E) = \int_0^t \int_V T_D(t)W_C(\mathbf{r})\frac{1}{\sqrt{2mE}} H_R(\mathbf{r})\frac{dN_D}{dt}\,dV\,dt \quad (49)$$

$$S_E[G_C(E)] = \int_0^t \int_V T_D(t)W_C(\mathbf{r})S_D[\phi_I(\mathbf{r},E,t)]dV\,dt. \quad (50)$$

The sequence of events, then, is an iterative solution of Eqs. (31), (37), and (44), in order to obtain updated tions of $\phi_I(\mathbf{r},E,t)$ by inserting the freshly calculated modes into Eq. (19). The iteration continues until the flux values agree arbitrarily closely for successive iterates.

Transient Behavior: Temporally Discontinous Shape and Spectral Functions

The iterative method as just outlined assumes that the same spatial modes, once they are calculated properly, are to be used throughout the transient. Much more flexibility is required in practice, particularly if the transient is nonlinear. This can be done either by introducing temporally discontinuous shape functions or by using the "improved quasistatic approximation".[1] In both cases the objective is the same: to allow the analysis to proceed with fewer modes than are otherwise needed, and still not impair accuracy. We shall here consider only the discontinuous shape function approach.

Suppose that the shape and spectral functions are to be changed at $t = t_1$. Then, the approximate solution for the flux can be written as

$$\phi_{I1}(\mathbf{r},E,t) = \sum_{i=1}^{I_1} H_{i1}(\mathbf{r})G_{i1}(E)N_{i1}(t) \quad \text{for} \quad 0 \leq t \leq t_1, \tag{51}$$

and as

$$\phi_{I2}(\mathbf{r},E,t) = \sum_{i=1}^{I_2} H_{i2}(\mathbf{r})G_{i2}(E)N_{i2}(t) \quad \text{for} \quad t \geq t_1. \tag{52}$$

Note that I_1 and I_2 do not have to be equal. Now, the true flux must be continuous at $t = t_1$; that is,

$$\phi_1(\mathbf{r},E,t_1) = \phi_2(\mathbf{r},E,t_1). \tag{53}$$

The approximate solutions, however, probably will not match at $t = t_1$. Hence, a residual must be formed and the method of weighted residuals employed to evaluate the initial conditions $N_{i2}(t_1)$ for the use of ϕ_{I2}. The residual is

$$R_{I2}(\mathbf{r},E,t_1) = \phi_{I2}(\mathbf{r},E,t_1) - \phi_{I1}(\mathbf{r},E,t_1). \tag{54}$$

It can be shown [12-13] that the most logical choices for the weighting functions are $W_{D2}(\mathbf{r})R_{C2}(E)$, that is, those to be used throughout the second time interval. The weighted residual criterion for the new initial conditions is thus

$$0 = \int_V \int_0^\infty W_{D2}(\mathbf{r})F_{C2}(E) \frac{1}{\sqrt{2mE}} [H_{R2}(\mathbf{r})G_{D2}(E)N_{C2}(t_1) - H_{R1}(\mathbf{r})G_{D1}(E)N_{C1}(t_1)]dE\, dV. \tag{55}$$

Note that, for the first iterate, $H_{R2}(\mathbf{r})$ and $G_{D2}(E)$ are trial functions (perhaps elements of H_{R1} and G_{D1}). If we define the following $I_2 \times I_1$ matrix

$$L_{21} = \int_V \int_0^\infty W_{D2}(\mathbf{r})F_{C2}(E) \frac{1}{\sqrt{2mE}} H_{R1}(\mathbf{r})G_{D1}(E)dE\, dV, \tag{56}$$

then the initial conditions for the second interval are found by

$$N_{C2}(t_1) = \Lambda_2^{-1}L_{21}N_1(t_1). \tag{57}$$

The solution now proceeds as it did over the first time interval, either until it is again time to change the shape and spectral functions or until the end of the transient is reached.

Spatially Discontinuous Shape and Spectral Functions

If Eq. (17) were written for several regions in the reactor and approximations like Eq. (19) were used for each, then more flexibility is introduced toward obtaining an accurate solution. Hopefully, the number of modes per region is quite a bit less than would be required if partitioning were not used. Such methods have been successful in the past for doing synthesis calculations, particularly when good sets of trial functions were chosen in such a manner as to minimize the discontinuities. They will now be extended for incorporation into the iterative scheme.

In addition to a set of diffusion equations there must be interface conditions for maintaining continuity of flux and current between adjacent regions. For discontinuities in one space-dimension, for example, the interface conditions could be (for a two-dimensional reactor)

$$\phi^{(k)}(x_k,y,E,t) = \phi^{(k+1)}(x_k,y,E,t), \qquad k = 1, \cdots, K-1$$

and

$$D_k(x_k,y,E,t) \left.\frac{\partial\phi^{(k)}}{\partial x}\right|_{x=x_k} = D_{k+1}(x_k,y,E,t) \left.\frac{\partial\phi^{(k+1)}}{\partial x}\right|_{x=x_k}, \qquad k = 1, \cdots, K-1. \tag{59}$$

Now, the approximate solutions can be inserted into Eqs. (58) and (59) to form the following residuals:

$$R_{I_k}(x_k,y,E,t) = \alpha_1[\phi_I^{(k+1)}(x_k,y,E,t) - \phi_I^{(k)}(x_k,y,E,t)], \qquad k = 1, \cdots, K-1, \tag{60}$$

$$R_{J_k}(x_k,y,E,t) = \alpha_2\left[D_{k+1}(x_k,y,E,t)\left.\frac{\partial\phi_I^{(k+1)}}{\partial x}\right|_{x=x_k} - D_k(x_k,y,E,t)\left.\frac{\partial\phi_I^{(k)}}{\partial x}\right|_{x=x_k}\right], \qquad k = 1, \cdots, K-1, \tag{61}$$

where α_1 and α_2 are weighting parameters. It is also convenient to form equivalent interface residuals by adding and subtracting as follows:

$$R_{S_k}(x_k,y,E,t) = R_{I_k}(x_k,y,E,t) + R_{J_k}(x_k,y,E,t), \qquad k = 1, \cdots, K-1 \tag{62}$$

$$R_{D_k}(x_k,y,E,t) = R_{I_k}(x_k,y,E,t) - R_{J_k}(x_k,y,E,t), \qquad k = 1, \cdots, K-1. \tag{63}$$

The next steps are to choose weighting functions, formulate weighted residual criteria, and incorporate them into the weighted residual scheme. The interface residuals are treated in two different ways, depending upon which set of functions is being calculated. If the functions $X_i(x)$ are to be found for each region k, then the weighting functions are just the $W_{Y,D}(y)F_D(E)T_G(t)$ for each region k. These are combined in an appropriate manner to obtain a set of equations analogous to Eq. (37), plus equations for the interface conditions. These are solved in the same manner as are the usual multiregion diffusion equations.

If, on the other hand, one of the other sets of functions is to be found, then the interface weighted residuals must be added in an appropriate way to those formed in constructing Eq. (37), and the result is then allowed to vanish. Interaction between one region and another is then expressed by means of coupling coefficients. The details are very similar to those given in Ref. 13.

Discontinuous Energy Model—The Multigroup Diffusion Equations

The iterative scheme can also be carried out if the energy variable is discretized, for instance if multigroup diffusion theory is used. The group diffusion equations are

$$V^{-1}\frac{\partial\phi}{\partial t} = \nabla\cdot D(\mathbf{r},t)\nabla\phi(\mathbf{r},t) - A(\mathbf{r},t)\phi(\mathbf{r},t) + (1-\beta)\chi_P F^T(\mathbf{r},t)\phi(\mathbf{r},t) + S_D[\phi(\mathbf{r},t)], \tag{64}$$

where

$$\phi(\mathbf{r},t) = \mathrm{col}[\phi^{(1)} \cdots \phi^{(G)}] \tag{65}$$

$$V^{-1} = \mathrm{diag}[1/v_1 \cdots 1/v_G] \tag{66}$$

$$D(\mathbf{r},t) = \mathrm{diag}[D_1 \cdots D_G] \tag{67}$$

$$F^T(\mathbf{r},t) = \mathrm{row}[\nu\Sigma_{f1} \cdots \nu\Sigma_{fG}] \tag{68}$$

$$A(\mathbf{r},t) = \mathrm{diag}[\Sigma_{1T} \cdots \Sigma_{GT}] - [\Sigma_{g,g'}] \tag{69}$$

$$\chi_p = \mathrm{col}[\chi_{p1} \cdots \chi_{pG}]. \tag{70}$$

This time, the trial solution is given by Eq. (3).

Each product $\psi_i N_i$ is a G-dimensional column vector that can be formed in either of two ways:

$$\psi_i(\mathbf{r})N_i(t) = \psi_{iD}(\mathbf{r})N_{iC}(t) = N_{iD}(t)\psi_{iC}(\mathbf{r}). \tag{71}$$

Thus, there are $G \times I$ undetermined functions to evaluate at each sequence of the iteration.

Let us introduce the matrix of weighting functions

$$W_{iD}(\mathbf{r}) = \mathrm{diag}[W_i^{(1)} \cdots W_i^{(G)}].$$

We can now use the following weighted residual criterion to determine the $N_i(t)$:

$$\sum_{i'=1}^{I}\Lambda_{ii'}\frac{dN_{i'C}}{dt} = \sum_{i'=1}^{I}[\rho_{ii'} - \bar{\beta}_{ii'}]N_{i'C}(t) + \sum_{j=1}^{J}\lambda_j C_{ij}(t), \qquad i = 1, \cdots, I, \tag{72}$$

where $\Lambda_{ii'}$, $\rho_{ii'}$, and $\bar{\beta}_{ii'}$ are all $G \times G$ matrices defined by

$$\Lambda_{ii'} = \int_V W_{iD}(\mathbf{r})\, V^{-1}\psi_{i'D}(\mathbf{r})dV \tag{73}$$

$$\rho_{ii'}(t) = \int_V W_{iD}(\mathbf{r}) \left[\nabla \cdot D(\mathbf{r},t)\nabla - A(\mathbf{r},t) + (1-\beta)\chi_p F^T(\mathbf{r},t) + \sum_{j=1}^{J} \beta_j \chi_j F^T(\mathbf{r},t) \right] \psi_{i'D}(\mathbf{r}) dV \tag{74}$$

$$\bar{\beta}_{ii'}(t) = \beta \int_V W_{iD}(\mathbf{r}) \chi_j F^T(\mathbf{r},t) \psi_{i'D}(\mathbf{r}) dV, \tag{75}$$

and the C_{ij} are G-dimensional column vectors given by

$$\lambda_j C_{ij}(t) = \int_V W_{iD}(\mathbf{r}) S_D(\mathbf{r},t) dV. \tag{76}$$

Equations (72) are thus a set of $(G \times I)$ by $(G \times I)$ equations to solve for the $(G \times I)$ undetermined functions $N_i^{(g)}(t)$.

After the amplitude functions are found the shape functions can be recalculated. Consider the matrix of weighting functions

$$T_{iD}(t) = \text{diag}[T_i^{(1)}(t), \cdots, T_i^{(G)}(t)].$$

Then we can use the method of weighted residuals to obtain

$$0 = \sum_{i'=1}^{I} \nabla \cdot P_{ii'}(\mathbf{r}) \nabla \psi_{i'C}(\mathbf{r}) - \sum_{i'=1}^{I} M_{ii'}(\mathbf{r}) \psi_{i'C}(\mathbf{r}) + \sum_{i'=1}^{I} E_i \left[\sum_{i'=1}^{I} \psi_{i'C}(\mathbf{r}) \right], \qquad i = 1, \cdots, I, \tag{77}$$

where $P_{ii'}$ and $M_{ii'}$ are $G \times G$ matrices, defined as

$$P_{ii'}(\mathbf{r}) = \int_0^t T_{iD}(t) D(\mathbf{r},t) N_{i'D}(t) dt \tag{78}$$

$$M_{ii'}(\mathbf{r}) = \int_0^t T_{iD}(t) [(1-\beta)\chi_p F^T(\mathbf{r},t) - A(\mathbf{r},t)] N_{i'D}(t) dt, \tag{79}$$

and E_i is a G-dimensional column vector given by

$$E_i \left[\sum_{i'=1}^{I} \psi_{i'C}(\mathbf{r}) \right] = \int_0^t T_{iD}(t) S_D[\phi(\mathbf{r},t)] dV. \tag{80}$$

After the $(G \times I)$ undetermined functions $\psi_i^{(g)}(\mathbf{r})$ are found from Eqs. (77), they can be used in Eqs. (73)–(76) to recalculate the $N_i^{(g)}(t)$, etc., until a converged solution is obtained. Finally, the method can be extended to include spatially and temporally discontinuous trial functions as was outlined for the continuous-energy model.

Discussion

Nothing has been said to this point on how weighting functions are chosen. In theory the choice is completely arbitrary; in practice, it has been found that Galerkin weighting works quite well, especially when the trial functions are well-chosen. Other alternatives that should work well are least-squares weighting[14] and reaction-rate weighting.[5] In theory, adjoint weighting could be used, but this would be completely impractical because the adjoint equations would also have to be formulated and solved by a similar iterative procedure in which the trial functions for the real system would be the weighting functions for the adjoint system.

Another aspect of the method that has not been discussed is the method of solving the various systems of one-dimensional equations for the various undetermined functions. Let us discuss these one at a time. Firstly, at least one method exists[18] for the solution of the multimode kinetics equations. Solving for the shape functions requires modification of existing one-dimensional diffusion theory codes. The coefficients of the equations, however, are such that the favorable mathematical properties exhibited by the multigroup diffusion equations may not exist. Thus, more work needs to be done in this area. Finally, the spectral equations should be solvable numerically in a straightforward manner since they are integral equations that are, in effect, a coupled set of slowing down equations. The method could be time consuming, however, especially if much spectral detail in cross sections is required.

Finally, the question of rate of convergence has not been raised. The few applications of the iterative scheme that have been made[3,4,9] have indicated that only a few iterations are needed to obtain convergence. One other aspect of the convergence question appears in solving eigenvalue problems; namely, how does one know that the solution has selected the proper eigenvalue? These and other (as yet unformulated) questions must be answered if the method is to be successfully used. Experience is expected to provide all of the answers.

References

1. K. O. Ott and D. A. Meneley, *Accuracy of the Quasistatic Treatment of Spatial Reactor Kinetics*, Nucl. Sci. Eng. **36**, 402 (1969).
2. S. Kaplan, A. F. Henry, S. G. Margolis and J. J. Taylor, *Space-Time Reactor Dynamics*, Proc. 1964 Geneva Conference, **3**, 41 (1964).
3. T. Toivanen, *On the Variational and Bubnov-Galerkin Synthesis of the Epithermal, Spatially Dependent Neutron Energy Spectra*, J. Nucl. Energy **22**, 283 (1968).
4. M. J. Lancefield, *Space-Energy Flux Synthesis in Transport Theory*, Nucl. Sci. Eng. **37**, 423 (1969).
5. R. J. Neuhold and K. O. Ott, *Improvements in Fast Reactor Space-Energy Synthesis*, Nucl. Sci. Eng. **39**, 14 (1970).
6. W. M. Stacey, Jr., *Spectral Synthesis Applied to Fast-Reactor Dynamics*, Nucl. Sci. Eng. **41**, 249 (1970).
7. D. L. Selengut, *Variational Analysis of Multi-Dimensional Systems*, HW-59126, 89 (1958).
8. J. Lewins, *The Approximate Separation of Kinetics Problems Into Time and Space Functions by a Variational Principle*, J. Nucl. Energy, Part A: Reactor Science **12**, 108 (1960).
9. A. D. Kerr, *An Extension of the Kantorovich Method*, Quarterly of Applied Math, XXVI, 219 (1968).
10. W. F. Ames, *Nonlinear Partial Differential Equations in Engineering*, (Academic Press, Inc., New York, 1965).
11. S. H. Crandall, *Engineering Analysis*, (McGraw-Hill Book Company, New York, 1956).
12. M. Becker, *Asymmetric Discontinuities in Synthesis Techniques for Initial Value Problems*, Nucl. Sci. Eng. **34**, 343 (1968).
13. E. L. Fuller, *Weighted Residual Methods in Space-Dependent Reactor Dynamics*, ANL-7565 (1969).
14. M. Becker, *The Principles and Applications of Variational Methods*, (M.I.T. Press, Cambridge, Massachusetts, 1964).

IV-16. Further Studies on the Use of the Method of Undetermined Parameters to Integrate the Multimode Kinetics Equations

E. L. Fuller

Introduction

A description of how the method of undetermined parameters can be used to integrate the multimode kinetics equations was presented in Ref. 1. The solution method was described, the method of time step selection was outlined, and some numerical results were presented in order to indicate the utility of the method. These results showed how the run time varied as a function of the number of spatial modes used. It was also seen that, if good spatial trial functions were used, one could obtain a very accurate solution with a fairly loose convergence criterion ($\epsilon_1 = 0.01$) and with piecewise quadratic trial functions. Since then, studies have been done with various convergence criteria and with piecewise polynomials of varying degree, in an attempt to establish limits within which the method is stable. The results of this rather limited study will now be reported.

The multimode kinetics equations can be written as

$$\Lambda(t)\frac{dN}{dt} = [\rho(t) - \beta(t)]N(t) + \sum_{j=1}^{J}\lambda_j C_j(t) \quad (1)$$

$$\frac{dC_j}{dt} = \beta_j(t)N(t) - \lambda_j C_j(t) \quad (2)$$

$$\beta(t) = \sum_{j=1}^{J}\beta_j(t), \quad (3)$$

where $\Lambda(t)$, $\rho(t)$, $\beta(t)$, and $\beta_j(t)$ are $I \times I$ matrices ($I \equiv$ number of spatial modes) called, respectively, the generation time matrix, the reactivity matrix, and the delayed neutron fraction matrices. The manner in which their matrix elements are formed from the multigroup diffusion equations is shown in Ref. 2. Equations (1) and (2) can be solved by assuming the following trial solution over the interval $t_i \leq t \leq t_{i+1}$:

$$N_K(t) = \sum_{k=0}^{K} A_k(t - t_i)^k \quad (4)$$

$$\frac{dN_K}{dt} = \sum_{k=1}^{K} kA_k(t - t_i)^{k-1}. \quad (5)$$

The parameters A_k are evaluated by inserting Eqs. (4) and (5) into the multimode kinetics equations, and then performing the method of weighted residuals (see Ref. 1 for details). This results in a set of algebraic equations that can be solved for the parameters A_k to be used over the ith time step. The results to be reported below are for subdomain weighting only. Comparisons are made for $K = 1, 2, 3$, and 4.

Results and Conclusions

The reactor to be analyzed is a 240 cm slab reactor which, for convenience, is treated in a symmetric manner by imposing a zero-current boundary condition at the origin and by making the perturbations symmetric about the origin. For simplicity, one-group diffusion theory is used. The parameters for criticality listed in

able IV-16-I lead to the initial shape shown in Fig. IV-16-1. The final shape is that calculated by the WIGLE code[3] as the result of a ramp increase in $\nu\Sigma_f$ in Region 1 to 0.0202962 cm^{-1} at 0.1 sec, after which no further changes occur. The transient is then terminated at $t = 1$ sec; the shape function at this time is the final shape shown in Fig. IV-16-1.

All of the results reported below are for two spatial modes. These are the initial shape and the final shape. Since they bracket the true solution at all times, the true solution should be closely approached if the average time step size is small enough. This indeed happens, as can be seen in Fig. IV-16-2 and Table IV-16-II. Figure IV-16-2 shows the values of the amplitude function at the end of the ramp ($t = 0.1$ sec) as a function of average time step size. It may be seen that WIGLE solutions are the first to diverge. This is because the finite difference time integration technique in WIGLE essentially uses piecewise constant functions over a time interval. Piecewise linear functions, as expected, allow larger time steps to be taken. Correspondingly larger time intervals are allowed as the degree of the piecewise polynomials becomes larger. Note that a single quartic function over the 0.1 sec interval gives a very good approximation.

Some results at the end of the transient are shown in Table IV-16-II. The parameter ϵ_1 is a measure of degree of convergence in the procedure for time step selection (for details, see Ref. 1). The smaller the value of ϵ_1, the more time steps taken and hence the more accurate the solution. It is evident from Table IV-16-II that, as the degree of the piecewise polynomial increases, the larger ϵ_1 may be. These can be pitfalls, however, if too large a value of ϵ_1 is used. Unexpectedly large inaccuracies can occur, as may be seen for $\epsilon_1 = 1.0$ and 0.1 with piecewise quadratic trial functions. In these cases, too few time steps were taken to obtain an accurate solution. Once the value of ϵ_1 became small enough (0.01), a proper number of time steps were taken, and a fairly accurate value for the amplitude function was obtained.

Another anomaly was seen when piecewise quartic trial functions were used: too many time steps were taken for any choice of ϵ_1. Note, however, that accurate results were obtained. It is not known for certain what caused the anomaly. One explanation might be that the effects of roundoff error differ for different degrees of polynomials, and the automatic time step

TABLE IV-16-I. Parameters for Criticality

Parameter	Region 1, 0–15 cm	Region 2, 15–60 cm	Region 3, 60–120 cm
D, cm	1.69531	1.69531	1.69531
$\nu\Sigma_f$, cm^{-1}	0.0194962	0.0194962	0.0194962
Σ_a, cm^{-1}	0.0194962	0.0194962	0.0183343
v, cm/sec	10^6	10^6	10^6

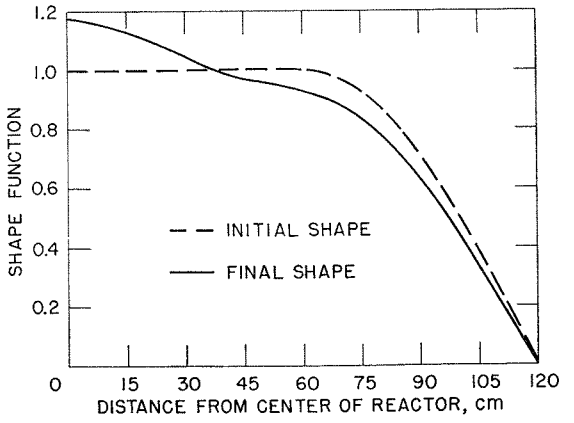

Fig. IV-16-1. Shape Functions Used in Analysis of Transient. *ANL Neg. No. 113-2690.*

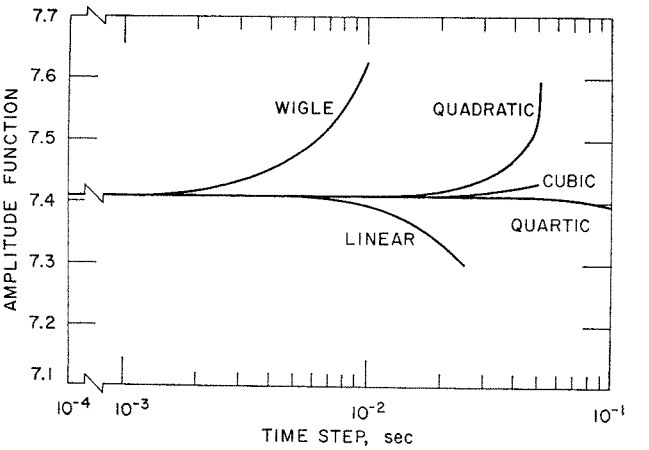

Fig. IV-16-2. Amplitude Functions at $t = 0.1$ sec versus Average Time-Step Size. *ANL Neg. No. 116-299.*

Table IV-16-II. Results at $t = 1$ sec for Two Modes

ϵ_1	Linear	Quadratic	Cubic	Quartic
		Amplitude Function		
1.0	4.20×10^{15}	1.13×10^{11}	6.37×10^{12}	4.22×10^{12}
0.1	5.34×10^{12}	1.11×10^{11}	4.06×10^{12}	3.94×10^{12}
0.01	4.22×10^{12}	3.93×10^{12}	3.94×10^{12}	3.94×10^{12}
0.001	3.95×10^{12}	3.94×10^{12}	3.94×10^{12}	3.94×10^{12}
		Time Steps		
1.0	21	11	11	25
0.1	78	14	30	131
0.01	180	90	54	137
0.001	727	183	98	159

selector tried to minimize these also. Another cause could be the fact that, as the degree of the polynomials increases, more and more weight is given to the times near t_i at the expense of accuracy near t_{i+1}. This could cause rather serious errors in extrapolation if the degree of the polynomials is relatively high.

A few conclusions can be reached from this limited study. The most obvious one is that one needs fewer time steps to obtain accurate solutions as the degree of trial polynomials is increased. This does not mean, however, that savings in computation time automatically result. More time is required to calculate the solution over a time step using quartic functions than using cubic functions, etc. When two spatial modes are used, cubic and quadratic solutions require about the same amount of computer time, for a given ϵ_1. Linear and quartic solutions require quite a bit more time. An optimum degree exists for the polynomial because, although fewer time steps might be required for higher degree polynomials, more time is taken by the matrix inversion routine. For the cases considered here, the optimum appears to be cubic, but only marginally over quadratic.

The most important conclusion is that the use of piecewise quadratic or piecewise cubic functions in an undetermined parameter method is a far more efficient method of integrating the multimode kinetics equations than is the use of traditional finite difference techniques, such as that employed in WIGLE. This conclusion could have important ramifications in other applications as well. Higher order differencing methods can be used to integrate over the spatial and energy variables of the diffusion (or transport) equation. The results of this study indicate that such approaches could very possibly allow practical three-dimensional diffusion theory calculations. This possibility deserves further investigation.

References

1. E. L. Fuller, *Integration of the Multimode Kinetics Equations by the Method of Undetermined Parameters*, Reactor Physics Division Annual Report, July 1, 1968 to June 30, 1969, ANL-7610, pp. 528–532.
2. E. L. Fuller, D. A. Meneley and D. L. Hetrick, *Weighted-Residual Methods in Space-Dependent Reactor Dynamics*, Nucl. Sci. Eng. **40**, 206 (1970).
3. W. R. Cadwell, A. F. Henry and A. J. Vigilotti, *WIGLE—A Program for the Solution of the Two-Group Space-Time Diffusion Equations in Slab Geometry*, WAPD-TM-406 (1964).

IV-17. Spurious Eigenvalues in Flux Synthesis

V. Luco and W. Woodruff

Introduction

The multigroup synthesis equations do not share in general the mathematical properties of the multigroup diffusion equations that guarantee the existence of a unique positive solution corresponding to a unique maximum positive eigenvalue.[1]

Recently Froelich[2] was able to present examples of synthesis equations not having a largest positive eigenvalue with the exception of the case of downscattering only with no group-collapsing.

Adams, Rydin and Stacey[3] have shown group-collapsed situations with Galerkin weighting in which the eigenvalues of the synthesis equations can take real or imaginary values and in which, in some cases, the maximum positive eigenvalue obtained did not correspond to the fundamental mode eigenvalue of the diffusion problem, and in which the synthesis flux had mixed positive and negative values.

Yasinsky and Kaplan[4] encountered group-collapsed synthesis calculations with adjoint weighting in which a poor eigenvalue approximation was associated with fluxes exhibiting mixed negative and positive values.

There are no anomalies on record for the case of down-scattering only without group-collapsing. In the present paper we investigate analytically the behavior of the eigenvalues and fluxes for a two-group slab-geometry version of the downscattering only, noncollapsed, synthesis calculation. Our results to the present have shown a unique maximum positive eigenvalue, but in many of the cases analyzed its value does not correspond to the fundamental mode eigenvalue of the diffusion problem, and the fluxes exhibit a mixed positive-negative behavior similar to that found by some of the other authors mentioned.[3,4]

The Analysis

The problem we have treated is a simple one, in order to make the rather long and involved manipulations tractable. We consider a uniform slab reactor and use a two-energy-group model with fission in the low-energy group and

wnscattering only. The equations for the diffusion model are

$$D_1 \frac{d^2\phi_1}{dx^2} - \Sigma_1 \phi_1 + \lambda \nu \Sigma_f \phi_2 = 0 \tag{1}$$

$$D_2 \frac{d^2\phi_2}{dx^2} - \Sigma_2 \phi_2 + \Sigma_{12} \phi_1 = 0, \tag{2}$$

where the symbols have the usual meaning. The exact solution is easily obtained:

$$\phi_1(x) = \cos \frac{\pi}{2} x \tag{3}$$

$$\phi_2(x) = a \cos \frac{\pi}{2} x = a\phi_1(x), \tag{4}$$

where a is the spectrum factor defined by

$$a = \frac{\Sigma_{12}}{D_2(\pi^2/4) + \Sigma_2}. \tag{5}$$

The system adjoint to Eqs. (1) and (2) is defined in the customary way, and its solution is (with obvious normalizations)

$$\phi_1^*(x) = \cos \frac{\pi}{2} x = \phi_1(x) \tag{6}$$

$$\phi_2^*(x) = a^* \cos \frac{\pi}{2} x = a^* \phi_1(x), \tag{7}$$

with

$$a^* = \frac{D_1(\pi^2/4) + \Sigma_1}{\Sigma_{12}}. \tag{8}$$

The eigenvalue (inverse k_{eff}) for the problem is

$$\lambda_e = \frac{[D_1(\pi^2/4) + \Sigma_1][D_2(\pi^2/4) + \Sigma_2]}{\nu \Sigma_f \Sigma_{12}}. \tag{9}$$

In the usual manner we will synthesize the solution for the problem by expressing the fluxes as linear combinations of known trial functions and determining the combination coefficients, which in this case will be numbers, by making stationary a conveniently chosen functional. The functional chosen is

$$J[u_1, u_2, u_1^*, u_2^*] = \int_{-1}^{+1} dx \left[\frac{du_1^*}{dx} D_1 \frac{du_1}{dx} + \frac{du_2^*}{dx} D_2 \frac{du_2}{dx} + u_1^*(\Sigma_1 u_1 - \lambda \nu \Sigma_f u_2) + u_2^*(\Sigma_2 u_2 - \Sigma_{12} u_1) \right], \tag{10}$$

where u_1, u_2, u_1^*, and u_2^* are the admissible functions, the variables of the variational problem. The set of admissible functions will be functions continuous and differentiable in the interval $-1 \leq x \leq 1$, and which take zero values at both ends of the interval. The Euler-Lagrange stationarity conditions for this problem are Eqs. (1) and (2) and their adjoints.

For the synthesis calculation we have to define a reduced space of admissible functions and its corresponding reduced functional and Euler equations. We expand u_1 and u_2 as follows:

$$u_1(x) = c_1 \phi_1(x) + c_{12} \psi_{12}(x) \tag{11}$$

$$u_2(x) = c_2 a \phi_1(x) + c_{22} \psi_{22}(x), \tag{12}$$

and similarly for the adjoint fluxes:

$$u_1^*(x) = c_1^* \phi_1(x) + c_{12}^* \psi_{12}^*(x) \tag{13}$$

$$u_2^*(x) = c_2^* a^* \phi_1(x) + c_{22}^* \psi_{22}^*(x). \tag{14}$$

We are using a two-trial-function expansion for both groups, and we are using the exact solution to the problem

as one of the trial functions. The synthesis calculation should in this case reproduce the exact solution. In other words there should be a synthesis solution with an eigenvalue equal to Eq. (9) and

$$\frac{c_{12}}{c_1} = 0, \qquad \frac{c_{22}}{c_2} = 0.$$

The other expansion functions are selected from a two-parameter family of functions formed by adding perturbations to the exact spatial solution:

$$\psi_{12}(x) = \cos\frac{\pi}{2}x + \Delta_1\left(\cos\frac{\pi}{2}\alpha_1 x - \cos\frac{\pi}{2}\alpha_1\right) \tag{15}$$

$$\psi_{22}(x) = \cos\frac{\pi}{2}x + \Delta_2\left(\cos\frac{\pi}{2}\alpha_2 x - \cos\frac{\pi}{2}\alpha_2\right) \tag{16}$$

$$\psi^*_{12}(x) = \cos\frac{\pi}{2}x + \Delta^*_1\left(\cos\frac{\pi}{2}\alpha^*_1 x - \cos\frac{\pi}{2}\alpha^*_1\right) \tag{17}$$

$$\psi^*_{22}(x) = \cos\frac{\pi}{2}x + \Delta^*_2\left(\cos\frac{\pi}{2}\alpha^*_2 x - \cos\frac{\pi}{2}\alpha^*_2\right), \tag{18}$$

where the Δ's and α's are numerical parameters which take real values. All of these functions satisfy the zero-flux boundary condition at $x = \pm 1$ identically.

Introducing Eqs. (11)–(14) into the functional we obtain the reduced functional,

$$\begin{aligned} J'[c_1, c_{12}, c_2, c_{22}, c^*_1, c^*_{12}, c^*_2, c^*_{22}] &= c^*_1\left[c_1\left(D_1\frac{\pi^2}{4} + \Sigma_1\right) + c_{12}\left(D_1\frac{\pi^2}{4} + \Sigma_1\right)A_{12} - c_2\lambda\nu\Sigma_f a - c_{22}\lambda\nu\Sigma_f A_{22}\right] \\ &+ c^*_{12}\left[c_1\left(D_1\frac{\pi^2}{4} + \Sigma_1\right)A^*_{12} + c_{12}(D_1 D_{12} + \Sigma_1 B_{12}) - c_2\lambda\nu\Sigma_f A^*_{12} a - c_{22}\lambda\nu\Sigma_f B_{22}\right] \\ &+ c^*_2 a^*\left[c_2 a\left(D_2\frac{\pi^2}{4} + \Sigma_2\right) + c_{22}\left(D_2\frac{\pi^2}{4} + \Sigma_2\right)A_{22} - c_1\Sigma_{12} - c_{12}\Sigma_{12}A_{12}\right] \\ &+ c^*_{22}\left[c_2 a\left(D_2\frac{\pi^2}{4} + \Sigma_2\right)A^*_{22} + c_{22}(D_2 D_{22} + \Sigma_2 E_{22}) - c_{12}\Sigma_{12}A^*_{22} - c_{12}\Sigma_{12}E_{12}\right], \end{aligned} \tag{19}$$

where

$$A_{12} = \int_{-1}^{+1} \psi_{12}(x)\phi_1(x)\,dx \tag{20}$$

$$A^*_{12} = \int_{-1}^{+1} \psi^*_{12}(x)\phi_1(x)\,dx \tag{21}$$

$$A_{22} = \int_{-1}^{+1} \psi_{22}(x)\phi_1(x)\,dx \tag{22}$$

$$A^*_{22} = \int_{-1}^{+1} \psi^*_{22}(x)\phi_1(x)\,dx \tag{23}$$

$$B_{12} = \int_{-1}^{+1} \psi^*_{12}(x)\psi_{12}(x)\,dx \tag{24}$$

$$B_{22} = \int_{-1}^{+1} \psi^*_{12}(x)\psi_{22}(x)\,dx \tag{25}$$

$$E_{12} = \int_{-1}^{+1} \psi^*_{22}(x)\psi_{12}(x)\,dx \tag{26}$$

$$E_{22} = \int_{-1}^{+1} \psi^*_{22}(x)\psi_{22}(x)\,dx \tag{27}$$

$$D_{12} = \int_{-1}^{+1} \psi^{*\prime}_{12}(x)\psi'_{12}(x)\,dx \tag{28}$$

$$D_{22} = \int_{-1}^{+1} \psi_{22}^{*\prime}(x)\psi_{22}'(x)\,dx. \tag{29}$$

The stationary point for J' is obtained by solving the set of necessary conditions

$$\frac{\partial J'}{\partial c_1^*} = \frac{\partial J'}{\partial c_{12}^*} = \frac{\partial J'}{\partial c_2^*} = \frac{\partial J'}{\partial c_{22}^*} = 0, \tag{30}$$

for the values c_1, c_{12}, c_2, and c_{22}.

The conditions (30) in detail are

$$c_1\left(D_1\frac{\pi^2}{4} + \Sigma_1\right) + c_{12}\left(D_1\frac{\pi^2}{4} + \Sigma_1\right)A_{12} - c_2\lambda\nu\Sigma_f a - c_{22}\lambda\nu\Sigma_f A_{22} = 0 \tag{31}$$

$$c_1\left(D_1\frac{\pi^2}{4} + \Sigma_1\right)A_{12}^* + c_{12}(D_1 D_{12} + \Sigma_1 B_{12}) - c_2\lambda\nu\Sigma_f A_{12}^* a - c_{22}\lambda\nu\Sigma_f B_{22} = 0 \tag{32}$$

$$-c_1\Sigma_{12} - c_{12}\Sigma_{12}A_{12} + c_2\left(D_2\frac{\pi^2}{4} + \Sigma_2\right)a + c_{22}\left(D_2\frac{\pi^2}{4} + \Sigma_2\right)A_{22} = 0 \tag{33}$$

$$-c_1\Sigma_{12}A_{22}^* - c_{12}\Sigma_{12}E_{12} + c_2\left(D_2\frac{\pi^2}{4} + \Sigma_2\right)A_{22}^* a + c_{22}(D_2 D_{22} + \Sigma_2 E_{22}) = 0. \tag{34}$$

This homogeneous system of algebraic equations has a solution for those values of λ satisfying the equation

$$\begin{vmatrix} \left(D_1\frac{\pi^2}{4} + \Sigma_1\right) & A_{12}\left(D_1\frac{\pi^2}{4} + \Sigma_1\right) & -\lambda\nu\Sigma_f & -\lambda\nu\Sigma_f A_{22} \\ A_{12}^*\left(D_1\frac{\pi^2}{4} + \Sigma_1\right) & (D_1 D_{12} + \Sigma_1 B_{12}) & -\lambda\nu\Sigma_f A_{12}^* & -\lambda\nu\Sigma_f B_{22} \\ -\Sigma_{12} & -A_{12}\Sigma_{12} & \left(D_2\frac{\pi^2}{4} + \Sigma_2\right) & \left(D_2\frac{\pi^2}{4} + \Sigma_2\right)A_{22} \\ -A_{22}^*\Sigma_{12} & -E_{12}\Sigma_{12} & \left(D_2\frac{\pi^2}{4} + \Sigma_2\right)A_{22}^* & (D_2 D_{22} + \Sigma_2 E_{22}) \end{vmatrix} = 0. \tag{35}$$

This is a quadratic equation in λ. Its two roots are real and distinct. Their values are

$$\lambda_1 = \lambda_e = \frac{[D_1(\pi^2/4) + \Sigma_1][D_2(\pi^2/4) + \Sigma_2]}{\nu\Sigma_f\Sigma_{12}} \tag{36}$$

$$\lambda_2 = \lambda_s = \frac{\{A_{22}A_{22}^*[D_2(\pi^2/4) + \Sigma_2] - (D_2 D_{22} + \Sigma_2 E_{22})\}\{(D_1 D_{12} + \Sigma_1 B_{12}) - A_{12}A_{12}^*[D_1(\pi^2/4) + \Sigma_1]\}}{\nu\Sigma_f\Sigma_{12}(E_{12} - A_{22}^* A_{12})(A_{22}A_{12}^* - B_{22})}. \tag{37}$$

As expected one of the roots is the exact solution to the problem, reflecting the fact that the set of trial functions contains the exact solution. The other one, which we call λ_s for "lambda spurious" is the nondiffusion eigenvalue introduced by the synthesis manipulations.

The values of the ratios c_{12}/c_1 and c_{22}/c_2 are

$$\frac{c_{12}}{c_1} = \frac{1}{F_1}\left\{\nu\Sigma_f\Sigma_{12}(\lambda_e - \lambda)A_{12}^*\left[\left(D_2\frac{\pi^2}{4} + \Sigma_2\right)A_{22}A_{22}^* - (D_2 D_{22} + \Sigma_2 E_{22})\right]\right\} \tag{38}$$

and

$$\frac{c_{22}}{c_2} = \frac{1}{F_2}\left\{a\nu\Sigma_f\Sigma_{12}(\lambda_e - \lambda)A_{12}^*(E_{12} - A_{12}A_{22}^*)\right\}, \tag{39}$$

where

$$F_1 = (D_1 D_{12} + \Sigma_1 B_{12})\left(D_2\frac{\pi^2}{4} + \Sigma_2\right)\left[\left(D_2\frac{\pi^2}{4} + \Sigma_2\right)A_{22}A_{22}^* - (D_2 D_{22} + \Sigma_2 E_{22})\right]$$
$$+ \lambda\nu\Sigma_f\Sigma_{12}\left\{A_{12}^*\left[\left(D_2\frac{\pi^2}{4} + \Sigma_2\right)A_{22}E_{12} - (D_2 D_{22} + \Sigma_2 E_{22})A_{12}\right]\right.$$

$$+ B_{22}\left(D_2\frac{\pi^2}{4}+\Sigma_2\right)(A_{12}A_{22}^*-E_{12})\Big\}$$

and

$$F_2=\lambda\nu\Sigma_f\Sigma_{12}B_{22}(E_{12}-A_{12}A_{22}^*)-(D_1D_{12}+\Sigma_1B_{12})\left[\left(D_2\frac{\pi^2}{4}+\Sigma_2\right)A_{22}A_{22}^*-(D_2D_{22}+\Sigma_2E_{22})\right]$$
$$-A_{12}^*\left(D_1\frac{\pi^2}{4}+\Sigma_1\right)\left[\left(D_2\frac{\pi^2}{4}+\Sigma_2\right)A_{22}E_{12}-(D_2D_{22}+\Sigma_2E_{22})A_{12}\right].$$

For $\lambda=\lambda_e$ we get, as expected,

$$\frac{c_{12}}{c_1}=0$$
$$\frac{c_{22}}{c_2}=0, \tag{40}$$

yielding the exact solution for the flux. When $\lambda=\lambda_s$, we get flux solutions different from those of the exact solution

Having obtained analytical expressions for the eigenvalues and fluxes, we have to use them now to answer the questions: Is the value of λ_e always the smaller of the two synthesis eigenvalues obtained, and what are the characteristics of the fluxes corresponding to λ_s?

The magnitudes λ_s, (c_{12}/c_1), (c_{22}/c_2) can be expressed as functions of the α and Δ parameters using the results just obtained: e.g. Eqs. (37) through (39) together with the definitions in Eqs. (15) through (18) and Eqs. (20) through (29). The very complex functions of the parameters resulting are unmanageable for hand calculations, especially for the survey type needed here. A computer code called SPURIOUS has been written to calculate the values of λ_s, (c_{12}/c_1), and (c_{12}/c_2) and of the reconstructed flux as functions of α_1, α_1^*, α_2, α_2^*, and Δ_1, Δ_2, Δ_1^*, Δ_2^*. The reactor chosen for this numerical survey is the 60-cm slab reactor of Yasinsky and Henry[5] with $\lambda\Sigma_{f_1}$ neglected. The numerical results obtained to the present are the following:

(1) The synthesis flux for $\lambda=\lambda_s$ is in general unrealistic, having large regions of negative magnitude.

(2) There are numerous choices of parameters α and Δ that yield values of λ_s smaller than λ_e. In numerous cases the values of λ_s are even negative.

The following are just a few typical results among the many similar ones obtained so far:

Case 1:

$$\alpha_1=3.00; \qquad \alpha_1^*=5.002$$
$$\alpha_2=0.90; \qquad \alpha_2^*=1.003$$
$$\lambda_e=1.0218; \qquad k_e=0.9786$$
$$\lambda_s=0.0233; \qquad k_s=42.9056.$$

In this case the value of λ_s is much smaller (and of course the value of k_{eff} much larger) than the corresponding exact values. Both energy groups exhibit large areas of negative values.

Case 2:

$$\alpha_1=1.010; \qquad \alpha_1^*=4.502$$
$$\alpha_2=1.500; \qquad \alpha_2^*=5.003$$
$$\lambda_e=1.0218; \qquad k_e=0.9786$$
$$\lambda_s=1.0085; \qquad k_s=0.9916.$$

Exact and spurious eigenvalues are in this case close to each other but the corresponding fluxes are quite different. The spurious fluxes exhibit large areas of negative values.

Case 3:

$$\alpha_1=4.500; \qquad \alpha_1^*=3.000$$
$$\alpha_2=2.000; \qquad \alpha_2^*=5.000$$

$$\lambda_e = 1.0218; \qquad k_e = 0.9786$$

$$\lambda_s = -0.2394; \qquad k_s = -4.1764.$$

The spurious k is negative in this case and larger in magnitude than the true one. Once more the fluxes have negative values. Multiple areas of negative values for Group 1 are observed in this instance.

The parameters Δ have no influence on the eigenvalue and their effect on the flux has not been investigated yet. Their values throughout were taken as follows: $\Delta_1 = 1.0$; $\Delta_2 = 1.0$; $\Delta_1^* = 1.0$; and $\Delta_2^* = 1.0$.

Summary of Results and Conclusions

We have been able to show that anomalies of the type previously reported for collapsed group flux synthesis occur also for non-collapsed synthesis calculations.

The values found for the spurious eigenvalues cover a wide range from very large positive to very large negative values. The accompanying fluxes are quite unrealistic. The situation is one with a great deal of potential trouble for synthesis calculations performed by a machine code using a power iteration routine to search for the eigenvalues. The code would always converge to the largest k_{eff} and consequently would produce totally wrong results.

The true solution could be present, as is the case in our calculation, but masqued completely "behind" the spurious one. The situation clearly deserves attention, and we intend to devote some time to it: by making a more detailed and systematic study of the behavior of λ_s as a function of the parameters; by using the two-dimensional Argonne synthesis capability (the ARC system module SYN2D) to calculate the cases presented here by iterative methods; and by extending the theory to more complex cases.

References

1. E. L. Wachspress, *Some Mathematical Properties of the Multichannel Variational Synthesis Equations and Two-Dimensional Synthesis Numerical Studies*, KAPL-M-6588 (December 12, 1966).
2. R. Froelich, *Anomalies in Variational Flux Synthesis*, Trans. Am. Nucl. Soc. **12**, 150 (1969).
3. C. H. Adams, R. A. Rydin and W. M. Stacey, Jr., *A Numerical Study of Single-Channel Flux Synthesis*, Trans. Am. Nucl. Soc. **11**, 169 (1968).
4. Y. B. Yasinsky and S. Kaplan, *Anomalies Arising from the Use of Adjoint Weighting in a Collapsed Group-Space Synthesis Model*, Nucl. Sci. Eng. **31**, 354 (1968).
5. Y. B. Yasinsky and A. F. Henry, *Some Numerical Experiments Concerning Space-Time Reactor Kinetics Behavior*, Nucl. Sci. Eng. **22**, 171 (1965).

IV-18. Modification of the Multiregion Resonance Absorption Code RABBLE

P. H. Kier

A method of computing regional slowing down sources has been developed which eliminates the instabilities[1] that appeared previously. In RABBLE,[2] the energy region of interest is divided into broad groups for which effective cross sections are edited. These broad groups are divided into very narrow fine groups of equal lethargy width. For each fine group an integral transport formulation uses regional slowing down sources to compute regional collision densities.

The regional slowing down source for a fine group of width Δu is the rate at which neutrons are scattered into Δu. If the group extends from u to $u + \Delta u$, the regional slowing down source is taken to be $S(u)\Delta u$:

$$S(u) = \sum_{n=1}^{N} \frac{1}{1 - \alpha_n} \int_{u-\epsilon_n}^{u} F_{s_n}(u')e^{-(u-u')}\, du', \quad (1)$$

where $F_s(u')$ is the rate at which neutrons are scattered at lethargy u' by nuclide n, ϵ_n is the maximum lethargy gain per collision (or scattering interval) for nuclide n, and $\alpha = \ln(1/\epsilon_n)$. The method of evaluating $S(u)$ must be extremely fast because it is computed tens of thousands of times in typical problems. Obviously, straightforward numerical integration is too slow. The methods that had been tried were based on recursion formulations in which Eq. (1) is essentially differentiated:

$$\frac{dS(u)}{du} + S(u) = F_s(u) - \alpha F_s(u - \epsilon), \quad (2)$$

where, for simplicity of notation, the nuclide index has been suppressed. From Eq. (2) it can be seen that in a fast reactor in which the flux can be attenuated greatly

over a scattering interval, it is possible for negative slowing down sources to be computed.

In the method of calculating the slowing down source that has eliminated these instabilities, the lethargy range of interest is divided into sections, each a scattering interval wide. Thus lethargy $u = n\epsilon + \delta$ is in the $(n + 1)th$ section. The source is expressed as the sum of two components: one which consists of neutrons that are scattered from the same scattering interval section and another component which consists of neutrons that are scattered from the preceding section.

For the first component, which will be denoted by $S_1(u)$, neutrons are scattered from the interval $n\epsilon$ to $n\epsilon + \delta$. Therefore $S_1(u)$ is given by

$$S_1(u) = \frac{1}{1-\alpha}\int_{n\epsilon}^{n\epsilon+\delta} du' F_s(u') e^{-(u-u')}. \quad (3)$$

With the objective of relating $S_1(u)$ to $S_1(u - \Delta u)$ let us rewrite Eq. (3) in the following form:

$$S_1(u) = \frac{1}{1-\alpha}\int_{u-\Delta u}^{u} du' F_s(u') e^{-(u-u')} + \frac{e^{-\Delta u}}{1-\alpha}\int_{n\epsilon}^{n\epsilon+\delta-\Delta u} du' F_s(u') e^{-(u-u')}. \quad (4)$$

The second term on the right hand side of Eq. (4) is just $e^{-\Delta u} S_1(u - \Delta u)$; hence Eq. 4 becomes:

$$S_{1,k} = P_1 F_{s,k-1} + e^{-\Delta u} S_{1,k-1}, \quad (5)$$

where k is the group index and P_1 is the probability that a neutron is scattered down one group. It should be noted that Eq. (5) can be evaluated rapidly, that it does not require much memory and that it yields an inherently positive $S_{1,k}$.

To insure that the slowing down be positive, a somewhat different procedure is used to compute the contribution to the slowing down source from the preceding scattering interval section, $S_{2,k}$. The scattering rate distribution in the preceding interval is assumed to have an approximate form, $\tilde{F}(x)$, where $x = u - (n-1)\epsilon$. Then $S_{2,k}$ is found by substituting $\tilde{F}(x)$ in Eq. (3) and integrating over the appropriate limits:

$$S_{2,k} = \frac{1}{1-\alpha}\int_{\delta}^{\epsilon} e^{-(\epsilon+\delta-x)} \tilde{F}_s(x)\, dx. \quad (6)$$

A form for $\tilde{F}_s(x)$ that has been quite satisfactory is

$$\tilde{F}_s(x) = e^{-x}(a_1 + a_2 x + s_3 x^2). \quad (7)$$

The lethargy moments of the scattering rate distribution,

$$M_n = \int_0^{\epsilon} x^n F_s(x)\, dx, \quad (8)$$

are computed. Then the coefficients a_n are obtained by substituting Eq. (7) into Eq. (8), for $n = 0, 1, 2$, and by inverting the resulting matrix. The use of Eqs. (6) and (7) to compute $S_{2,k}$ has several favorable characteristics: $S_{2,k}$ is computed rapidly, it is positive, and it requires relatively little storage, in contrast to earlier formulations which required the storage of tens of thousands of scattering rates.

Several other changes have been made in RABBLE to reduce its running time and to increase its utility. A major reduction in running time has been achieved by permitting the user to specify the number of closest resonances of a particular sequence that contribute to the cross section at a given energy. The utility of the program has been increased by permitting it to compute elastic scattering matrices, by allowing for a transverse buckling, and by permitting group cross sections to be averaged over specified regions.

References

1. P. H. Kier, *Modification of the Multiregion Resonance Absorption Code RABBLE* Reactor Physics Division Annual Report, July 1, 1968 to June 30, 1969, ANL-7610, pp. 486–488.
2. P. H. Kier and A. A. Robba, *RABBLE, A Program for Computation of Resonance Absorption in Multiregion Reactor Cells*, ANL-7326 (1967).

IV-19. Further Developments in Integral Transport Methods for Resonance Region Calculations in Plate-Type Lattices Using the RABID Code

Arne P. Olson

The theory used by the RABID code to solve the one-dimensional slab geometry integral transport equation for neutrons slowing down in the resonance energy region has been reported in Ref. 1. In that work, the integral transport equation was written as

$$\vec{CR} = \underline{P}[\vec{S_0} + \underline{R}\,\vec{CR}], \quad (1)$$

where $\vec{CR}$ and $\vec{S_0}$ are collision rate and source vectors, $\underline{P}$ is a collision probability matrix, and $\underline{R}$ is a diagonal matrix representing the probability of scattering within a group.

Solving Eq. (1),

$$\vec{CR} = [\underline{P}^{-1} - \underline{R}]^{-1}\vec{S}_0 . \qquad (2)$$

Formerly, the RABID code solved Eq. (1) by an approximate method which had the property of reducing to the exact solution for the homogeneous case. Since that time it has been found possible to solve Eq. (2) exactly for heterogeneous problems without incurring more than a few percent increase in computation time.

The basic fault of the approximate method was the build-up of errors in fluxes which came about as a result of errors in the spatial transfer of ingroup scattered neutrons. In the rather extreme example of a binary cell consisting of a heavy-atom absorber plate and a light-atom moderator plate, the flux in the absorber plate was overestimated by about 1% when it was optically thin. Physically, most of the ingroup scattered neutrons were produced by collisions in the absorber plate, and should have suffered their next collision in the optically thick moderator plate. However, it was found that in the approximation method, the ingroup scattered neutrons tended to remain in the absorber plate, giving too high a flux there.

The matrix inversions of Eq. (2) can be eliminated by introducing the assumption that ingroup scattering does not occur. In order to conserve neutrons, the down-scatter probability, P_ℓ (as defined in Eq. (10) of Ref. 1), must be slightly altered. The sum of the down-scatter probabilities must remain unity. Noting that

$$\sum_{\ell=1}^{L} P_\ell = 1 - e^{-\Delta u} \neq 1 \qquad (3)$$

it is apparent that dividing P_ℓ by $1 - e^{-\Delta u}$ will conserve neutrons when ingroup scattering has zero probability ($P_s = 0$). In that case,

$$P'_\ell \Delta u \equiv P_\ell \Delta u/(1 - e^{-\Delta u}) = \frac{1 - e^{-\Delta u}}{1 - \alpha} e^{-(\ell-1)\Delta u}, \qquad \ell = 1, 2, \cdots L. \qquad (4)$$

The user can decide whether or not to include ingroup scattering. An exhaustive study has not been made to establish how important this choice is. Certainly in many typical problems where $L \gtrsim 100$, one can safely ignore ingroup scattering. Problems for which $L < 100$ should be examined using both options before arbitrarily ignoring ingroup scattering.

In order to represent neutron losses by leakage from a finite-sized system with buckling B^2, one need only scale the collision probability matrix $\underline{P}$ by a nonleakage probability, PNL. A reasonable definition of PNL is obtained as follows:

$$\mathrm{PNL}_k = \frac{\langle \Sigma_t \rangle_k}{\langle \Sigma_t \rangle_k + \langle D \rangle_k B^2}, \qquad (5)$$

where

k is the fine-group index,

$\langle \Sigma_t \rangle_k$ is the flux-volume-weighted total macroscopic cross section for the unit cell,

$$\langle \Sigma_t \rangle_k = \sum_{i=1}^{\mathrm{KREG}} (\Sigma_{tk}\phi_k A)_i / \sum_{i=1}^{\mathrm{KREG}} (\phi_k A)_i \qquad (6)$$

$$\approx \sum_{i=1}^{\mathrm{KREG}} (\Sigma_{tk}\phi_{k-1} A)_i / \sum_{i=1}^{\mathrm{KREG}} (\phi_{k-1} A)_i , \qquad (7)$$

A_i is the thickness of region i,

KREG is the number of regions, and

$$\langle D \rangle_k = \left[\frac{3 \sum_{m=1}^{\mathrm{KCOMP}} A_m \sum_{j=1}^{\mathrm{KMAT}} N_{jm}\, \sigma_{tj} \left(\frac{\sigma_{aj}}{\sigma_{sj}} + 1 - \bar{\mu}_{0j} \right)}{\sum_{m=1}^{\mathrm{KCOMP}} A_m} \right]^{-1} . \qquad (8)$$

KCOMP and KMAT are the number of compositions and materials, respectively, and $\bar{\mu}_{0j}$ is the average cosine of the scattering angle for material j. Hopefully, a better recipe for $\langle D \rangle$ can be found, for example, by using a transport-theory code which will account for leakage parallel and perpendicular to the plates in slab geometry. In the meantime, it should be noted that PNL is rather insensitive to errors in $\langle D \rangle$ for large systems. Also, group-averaged cross sections will in general be quite insensitive to $\langle D \rangle$. Provision has been made to use broad-group-dependent bucklings in finite systems.

To illustrate the use of RABID in studying in-cell reaction rates, some results will be given for comparison with experiments[2] on U-238 capture rates in ZPR-3 Assemblies 53 and 54. In the experiments, depleted uranium foils were irradiated in the cell locations as shown in Fig. IV-19-1.

Heterogeneously self-shielded, 23-epithermal-group neutron cross sections generated by MC^2 were used by the TESS[3] transport code in a one-dimensional, double S_{12} cell calculation. The amplitude variation exhibited by this calculation was clearly too small, because the self-shielding of each foil was inadequately accounted for.

More accurate calculations of the reaction rates in each foil were obtained from RABID. U-238 capture cross sections in the energy range from 24.8 keV to 3.35 keV (a span of 8 MC^2 fine groups, each 0.25 lethargy units wide) were obtained from statistically generated resolved resonance sequences for (ℓ,J) states of (1/2,0), (1/2,1), and (3/2,1). The Schmidt[4] tabulation was used for both the unresolved and the resolved resonance parameters. The resonance sequences were centered on each MC^2 fine group. Resolved U-238 resonances were used from 3.35 keV down to 13.7 eV. Resolved resonances for aluminum, iron, chromium,

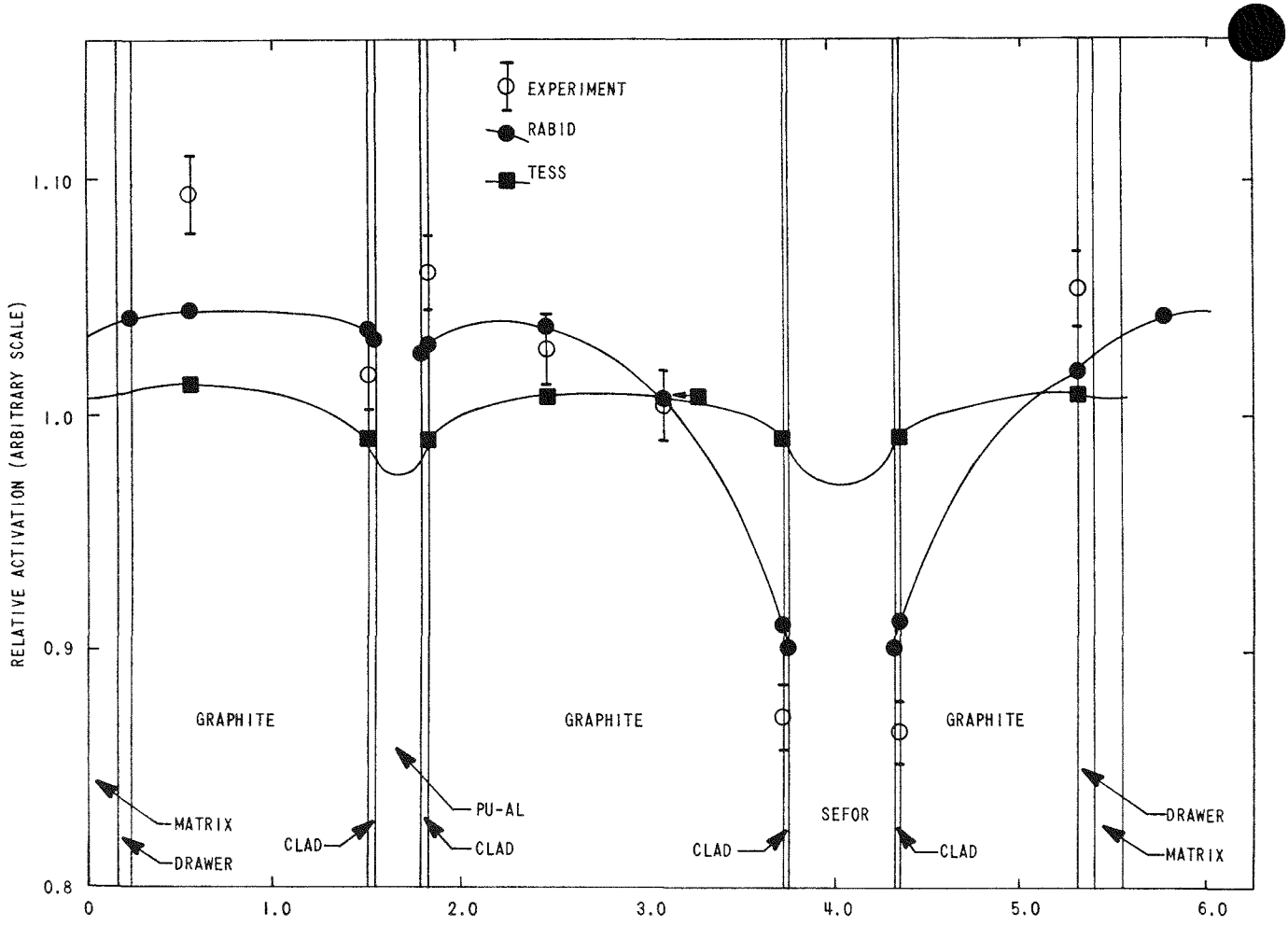

FIG. IV-19-1. U-238 In-Cell Capture Rates in ZPR-3 Assemblies 53 and 54. *ANL-ID-103-A11290.*

and nickel were used from 24.8 keV to 13.7 eV. Smooth cross sections for Pu-239 were used down to 275 eV, below which resolved resonance parameters were used. Similarly, Pu-240 was accounted for by smooth cross sections above 130 eV and resolved resonances below 130 eV. Fine group fluxes from an ultra-fine group homogeneous MC^2 calculation were used to weight the RABID foil reaction rates. Above 24.8 keV the spatial flux was very flat, the self-shielding of each foil became uniform, and the contribution to the total capture rate was about 28%. The RABID calculations are the same (to within 0.3%) whether a spatially flat flux is assumed above 24.8 keV, or if TESS spatial fluxes are used to weight the foil activations. Also, the contribution by neutrons below 13.7 eV is negligible. The amplitude variation shown by this calculation would be expected to increase slightly if resonance sequences were used above 24.8 keV, but not enough to display the experimental variation.

It is concluded that broad-group transport calculations of U-238 capture rates in foils are rather inadequate, and that "exact" RABID calculations agree fairly well with experiment. Uncertainties in U-238 resonance parameters may explain those differences remaining between theory and experiment. Also, "scatter" in the experimental data indicates that the errors assigned to them may be too small.

REFERENCES

1. A. P. Olson, *Developments in Integral Transport Methods for Resonance Region Studies in Plate-Type Lattices*, Reactor Physics Division Annual Report, July 1, 1968 to June 30, 1969, ANL-7610, pp. 501–504.
2. D. W. Maddison and L. S. Beller, Reactor Development Program Progress Report, ANL-7669, 13 (February 1970).
3. R. W. Goin and J. P. Plummer, *TESS—A One-Dimensional S_n Transport Theory Code for the CDC-3600*, ANL-7406 (to be published).
4. J. J. Schmidt, *Neutron Cross Sections for Fast Reactor Materials. Part I: Evaluation.* KFK 120 (EANDC-E-35 U) (February 1966).

IV-20. Testing of the Perturbation Modules in the Argonne Reactor Computation (ARC) System

P. H. Kier

Testing of the 1D-perturbation module and the 2D-perturbation module in the ARC system[1] and their associated paths, which was begun during the preceding fiscal year, was completed successfully during this period. The types of perturbations considered were: changes in chi fission vectors and matrices, changes in isotopic cross sections, and region-dependent buckling changes. Also the capability of computing the effective delayed neutron fraction was tested. An error in the modules that appeared with a change in transverse leakage was uncovered and corrected. This error accounted for the discrepancies between the results of perturbation and of diffusion calculations that were reported earlier.[2]

TABLE IV-20-I. Configuration for Composition Chi Matrix Perturbations

Region	r_{outer}, cm	Composition	Material	Volume Fraction
1	10	1	B1	1.0
			B2	1.0
2	60	2	C1	1.0
			C2	1.0
3	80	3	B1	0.7
			B2	0.7
			C1	0.3
			C2	0.3
4	110	4	R1	1.0

Chi Matrix and Vector Perturbations

Problems were run with both the 1D- and the 2D-perturbation standard paths in which an isotopic cross section set, ARC.JM31F, was used which has fissionable isotopes with different chi vectors. Isotopes subscripted with "B" have one chi vector while isotopes subscripted with "C" have the standard data set chi vector. The problems were run for a parallelepiped reactor described in Table IV-20-I and IV-20-II. Because Composition 3 is composed of isotopes with different chi vectors it has a chi matrix. A 1D criticality search resulted in a critical half-height of 92.02078 cm (the extrapolation distance was taken to be 16 cm) in the two transverse directions. In the 2D computations, the half-height of the reactor in the y-direction was taken as 92.03078 cm and a logarithmic boundary condition was imposed so that a cosine flux distribution would vanish at 108.03078 cm.

The description of the problems and the comparison of the results of 1D-perturbation, 2D-perturbation and 1D-diffusion calculations are given in Table IV-20-III. For these calculations and others to be described the diffusion calculations were run with very tight convergence criteria so that k was computed with eight figure accuracy. In these problems, the chi vector for certain isotopes was perturbed by multiplying it by a factor for specified groups to yield reactivities between 10^{-4} and 10^{-3}. As can be seen from Table IV-20-III the agreement between the three types of calculations is excellent.

Problems were also run to test the 1D-perturbation

TABLE IV-20-II. Isotopic Concentrations of Materials for Compositions used in Chi Matrix Perturbations, 10^{24} atoms/cm^3

Material	Isotope	Conc.	Isotope	Conc.	Isotope	Conc.
B1	Fe B	0.03	Ni B	0.003	Cr B	0.006
	Na B	0.006				
B2	U-235 B	0.000025	U-238 B	0 01		
C1	Fe C	0.03	Ni C	0 003	Cr C	0 006
	Na C	0.008				
C2	U-235 C	0.00004	U-238 C	0 008	Pu-239 C	0.0013
R1	Fe R	0.04	Ni R	0 004	Cr R	0.008
	Na R	0.01				

TABLE IV-20-III. Comparison of 1D-Diffusion and 2D-Perturbation Calculations for Chi Vector Changes

Isotope	Factor	Group		$\Delta k/k^2$, 10^{-4}		
		From	To	1D-Diff.	1D-Pert.	2D-Pert.
U-235 B	20	5	7	8.100	8.034	8.033
U-235 B	1.1	1	22	2.029	2.028	2.028
SETCHI	1 0004	1	22	3.943	3.943	3.942
SETCHI	1.01	5	5	1 684	1.684	1.684
SETCHI	1.004	5	7	2.824	2.824	2.824

TABLE IV-20-IV. Description of Critical Spherical Reactor for Isotopic Chi Matrix Perturbations

Region	Radius, cm	Composition	Isotope	Concentration, 10^{24} atoms/cm^3
1	22.594	1	U-235	0.006727
			U-238	0.007576
			Al	0.019019
			Ni	0.000839
			Cr	0.001918
			Fe	0.007712
2	55.094	2	U-235	0.000089
			U-238	0.040026
			Al	0.001359
			Ni	0.000049
			Cr	0.001129
			Fe	0.004539

module with respect to perturbations in the neutron source induced by changes in isotopic chi matrices. For these problems the 26-group, Bonderenko, isotopic cross section set, XS233.D1R was used. The reactor was chosen to be a two-region sphere with compositions shown in Table IV-20-IV. The outer radii for criticality were obtained from a search within which the mesh was changed.

The description of the problems and the comparison between the results of 1D-perturbation and 1D-diffusion calculations are given in Table IV-20-V. The cross section set has an energy structure such that neutrons are born in Groups 1–11 and a neutron can induce fission of U-238 only in Groups 1–5. In the first four problems selected elements of the chi matrix for U-235 were multiplied by the factor f. In the fifth problem, elements of the chi matrix for U-238 for source neutrons appearing in Groups 12–18 were made non-zero. In the last problem, neutron-induced fission reactions for U-238 were added in Groups 6–10 and the chi matrix was changed so that source neutrons appear in all groups. For all six problems the agreement between perturbation and diffusion calculations is excellent, the discrepancies being less than 0.1%.

Isotopic Cross Section Perturbations

Problems were run to test the perturbation modules with respect to changes in cross sections for specified reactions and groups for specified isotopes. The configuration considered and the cross section set used were the same as in the chi vector perturbation problems described earlier. The cross sections, σ_f, σ_c, $\nu\sigma_f$ and σ_{tr} were perturbed by multiplying them by a factor for specified groups. The description of the problems and the final comparison of 1D-diffusion, 1D-perturbation, and 2D-perturbation calculations are given in Table IV-20-VI. It can be seen that the agreement is excellent.

When these problems were first run there were large discrepancies between the diffusion calculations and the perturbation calculations when the transport cross section was changed. It was found that the limits of integration in transverse directions were being taken as the physical heights of the reactor. However this was inconsistent with diffusion theory in which the only relevant transverse dimension is the extrapolated height. The basic equation for $\Delta k/k^2$ used by the perturbation modules is

$$\delta(1/k) = \frac{\langle [\delta M - (1/k)\delta F]\phi, \phi^* \rangle}{\langle F\Phi, \Phi^* \rangle}, \qquad (1)$$

where F is the fission operator, M is the operator that contains the Laplacian, absorption and scattering terms, ϕ is the real flux, and ϕ^* is the adjoint flux. The brackets represent the inner product integrated over the volume of the reactor. The use of incorrect limits of integration in Eq. (1) causes errors only when there is a change in transverse leakage so that discrepancies arose when the transport cross section was perturbed.

The perturbation modules were modified such that the limits of transverse integration in the denominator of Eq. (1) were fixed at the extrapolated height of the

TABLE IV-20-V. Comparison of the Results of Perturbation and Diffusion Computations for Isotopic Chi Matrix Changes in a Two-Region Spherical Reactor

Isotope	Matrix Perturbed for Groups:		f	χ_{ij}	$\Delta k/k^2$, 10^{-4}	
	Absorption	Source			Diffusion	Perturbation
U-235	1–26	1–11	1.0005		1.707	1.708
U-235	1–26	3–6	1.0006		1.332	1.332
U-235	3–6	1–11	1.001		1.505	1.505
U-235	3–6	3–6	1.002		1.466	1.466
U-238	1–5	12–18		0.005	1.701	1.702
U-238	6–10	1–26		0.00025[a]	1.531	1.532

[a] $\nu\Sigma_f = 0.1$ was added in groups 6–10.

TABLE IV-20-VI. Comparison of 1D-Diffusion, 1D-Perturbation, and 2D-Perturbation Calculations for Changes in Isotopic Cross Sections

Isotope		σ_x	Groups		Factor	$\Delta k/k^2$, 10^{-4}		
			From	To		1D-Diff.	1D-Pert.	2D-Pert.
U-235	B	σ_f	1	22	1.15	−1.295	−1.296	−1.296
U-235	B	σ_f	22	22	1.75	−1.790	−1.796	−1.796
U-238	B	σ_c	1	22	1.003	−1.496	−1.498	−1.497
U-238	B	σ_c	22	22	1.0075	−1.462	−1.465	−1.463
Pu-239	C	$\nu\Sigma_f$	1	22	1.0002	1.739	1.739	1.739
Pu-239	C	$\nu\Sigma_f$	5	5	1.1	1.304	1.304	1.304
Na	C	σ_{tr}	1	22	1.04	6.311	6.315	
Na	C	σ_{tr}	1	22	1.01	1.581	1.579	
Na	C	σ_{tr}	1	22	1.004	0.633	0.632	
Na	C	σ_{tr}	1	22	1.01		1.317[a]	1.316[b]

[a] Perturbation extended over extrapolated height in z-direction and over physical height in y-direction.
[b] Perturbation extended over extrapolated height in z-direction; boundary condition imposed at physical height.

TABLE IV-20-VII. Reactor Configuration for 2D Region-Dependent Buckling Perturbations

Region	Comp.	X-Dimensions, cm	Mesh Points
1	C1	0–9.2	4
2	C2	9.2–54.0	12
3	C3	54.0–94.0	12
4	C4	94.0–148.0	8

reactor, while the limits of integration in the numerator are specified by the user. The latter permits the reactor to be perturbed over only a part of the transverse distance and gives the perturbation modules the same versatility as the MACH-1[3] package.

The validity of perturbing only part of the reactor in the transverse direction was confirmed as follows. A 1D-perturbation calculation was run in which the perturbation extended over the extrapolated half-height, 108 cm, in the z-direction and over the physical half-height, 92 cm, in the y-direction, etc. This system was mocked up in a 2D-perturbation problem by having the perturbation extend over the extrapolated half-height in the z-direction and by imposing a logarithmic boundary condition at the physicial half-height. From Table IV-20-VI we saw that the agreement between the 1D- and the 2D-perturbation calculations was excellent.

Region-Dependent Buckling Perturbations

Problems were run to test the 2D-perturbation module with respect to region-dependent buckling changes for finite x-y geometry. The reactor was composed of the four compositions that are described in Tables V-5-1 and V-5-2 of Ref. 2. In the y-direction, the reactor was taken to be uniform with a physical half-height of 102 cm. A logarithmic boundary condition was imposed to correspond to an extrapolation distance

TABLE IV-20-VIII. Comparison of Perturbation and Diffusion Calculations for 2D Region-Dependent Buckling Perturbations

Problem	Region	Half Height, cm	Extrap. Distance, cm	$\Delta k/k$, 10^{-4}	
				Diffusion	Pert.
1	1	102.5	16.0	1.006	1.0053
2	2	100.882	15.75	−1.203	−1.2024
3	3	96.0	16.0	−1.093	−1.095

of 14 cm. A buckling search was made to attain the critical system; it converged to an extrapolated half-height of 116.882 cm for the transverse z-direction.

The configuration is described in Table IV-20-VII and the comparison of results of perturbation with diffusion calculations is given in Table IV-20-VIII. From Table IV-20-VIII, we see excellent agreement between the results of diffusion and perturbation calculations, the discrepancies being less than 0.1%.

Effective Delayed Neutron Fraction

During the fiscal year, data on delayed neutron parameters have been incorporated into the ARC system and the perturbation modules and their associated standard paths have been modified to use these data together with the real and adjoint fluxes to compute the effective delayed neutron fraction β_{eff}.

For the same reactor configuration as was used in the testing for region-dependent buckling perturbations, the 1D- and 2D-perturbation modules were tested for the calculation of β_{eff}. The computed β_{eff} differed by only 0.1% between the two modules when using identical basic ENDF delayed neutron data. The β_{eff} computed by the ARC modules differed from that computed by the BAILEFF portion of the MACH-1

package by approximately 1%. Much of this discrepancy can be attributed to approximate neutron emission spectra in the MACH-1 library.

REFERENCES

1 B J Toppel, Ed , *The Argonne Reactor Computation (ARC) System*, ANL-7332 (1967).

2. P. H. Kier, *Testing of the Diffusion Perturbation Modules in the Argonne Reactor Computation (ARC) System*, Reactor Physics Division Annual Report, July 1, 1968 to June 30, 1969, ANL-7610, pp. 482–485.

3 D A Meneley, L. C. Kvitek and D. M. O'Shea, *MACH1, A One Dimensional, Diffusion Theory Package*, ANL-7223 (1966)

IV-21. Modifications to the Integral Transport Heterogeneity Code CALHET-2

ARNE P. OLSON and P. H. KIER

A method for calculating heterogeneity effects on flux, adjoint flux, and eigenvalue in fast reactors was developed by Storrer et al.[1] It consisted of considering the difference between the true heterogeneous structure of a reactor and the homogeneous equivalent as a perturbation. This integral transport perturbation method is the basis for the CALHET-2 code.[2]

CALHET-3 is the Argonne version of CALHET-2. Extensive modifications have been made in order to increase its speed, accuracy, and scope. For example, interaction with the ARC system[3] without cross section format conversion problems is now achieved through the ability to read input cross sections in XS.ISØ (ARC) format.

A new output edit option is available in which neutron cross sections are cell-averaged using real flux weighting, and placed in an XS.ISØ data set. The method of cross section weighting is as follows:

$$\langle \sigma^g \rangle = \sigma^g \int_{cell} \phi(x) N(x) dx \Big/ \left[N_h \int_{cell} \phi(x)\, dx \right] \quad (1)$$

$$\langle \sigma^g \rangle \approx \sigma^g \sum_j \phi_j^g V_j N_j / [N_h \sum_j \phi_j^g V_j]. \quad (2)$$

where ϕ_j^g is the real flux in group g and in plate j; N_j is the atom density of a given material in plate j; and V_j is the volume of plate j, respectively. The homogeneous atom density of the given material is

$$N_h = \sum_j N_j V_j / \sum_j V_j . \quad (3)$$

The same weighting factor is applied to σ^g for all reaction processes: σ_{tr} , σ_e , σ_f , and $\sigma_{g \to i}$ [elastic, inelastic, or $(n,2n)$ scattering].

Collision probabilities are obtained using the methods which were developed for RABID.[4] That is, the collision probabilities are calculated from analytical expressions or by numerical integration using a special 4-point Gaussian quadrature. The original collision probability calculation performed by CALHET used a 50-point Simpson's Rule numerical integration. It was found that collision probabilities were obtained by the methods used in RABID in about 20% of the time required by the Simpson's Rule approach. The accuracy of the latter method was also inferior, especially for optically thin plates.

Neutron leakage originally was accounted for by introducing a group-dependent $D_g B_g^2$ term as a fictitious absorption cross section. Another treatment now optional consists of reducing the collision probabilities by a group-dependent non-leakage probability:

$$\mathrm{PNL}^g = \frac{\langle \Sigma_{tr}^g \rangle}{\langle \Sigma_{tr}^g \rangle + D_g B_g^2}, \quad (4)$$

where $\langle \Sigma_{tr}^g \rangle$ is the homogenized macroscopic transport cross section in group g. An additional feature now available is provision for using different $D_g B_g^2$ terms in calculating the homogeneous collision probabilities than those used in calculating the heterogeneous collision probabilities. In this manner, the effects of streaming introduced by neutron leakage parallel to the plates can be included if an appropriate recipe for the $D_g B_g^2$ were available.

The capability of treating a cylindrical cell which consists of a rod surrounded by concentric annuli has been incorporated into the code. The collision probabilities for this configuration are obtained from an adaptation of the method used to obtain regional collision densities from regional slowing-down sources in RABBLE.[5,6] In RABBLE, the regional collision densities are obtained from the regional source distribution by an integral transport procedure which utilizes the first-flight escape probabilities for a spatially flat volume source in an annular region and the first-flight transmission probabilities for neutrons impinging on one of the surfaces of an annular region. If in the RABBLE formulation the source distribution is taken as unity in region i and zero elsewhere, the resulting collision density in

gion j is identically the collision probability that is needed by CALHET-3.

A subroutine has been incorporated into CALHET-3 which solves the RABBLE algorithm for regional source distributions that are Kronecker delta functions. For each energy group, the algorithm is solved NØR times, where NØR is the number of regions.

References

1. F. Storrer et al., *Heterogeneity Calculation for Fast Reactors by a Perturbation Method*, Nucl. Sci. Eng. **24**, 153 (1966).
2. F. L. Fillmore, *The CALHET-2 Heterogeneous Perturbation Theory Code and Application to ZPR-3-48*, AI-69-13 (1969).
3. B. J. Toppel, Ed., *The Argonne Reactor Computation (ARC) System*, ANL-7332 (1968).
4. A. P. Olson, *RABID, An Integral Transport-theory Code for Neutron Slowing Down in Slab Cells*, ANL-7645 (1970).
5. P. H. Kier and A. A. Robba, *RABBLE, A Program for Computation of Resonance Absorption in Multiregion Reactor Cells*, ANL-7326 (1967).
6. P. H. Kier, *RABBLE and RABZPR, Two Codes to Compute Resonance Absorption in Multi-Composition Reactor Cells*, Reactor Physics Division Annual Report, July 1, 1966 to June 30, 1967, ANL-7310, pp. 445–449.

IV-22. The Improved Spatial Cross Section Homogenization Capability of the Double *Sn* Transport Theory Code TESS

J. P. Plummer and R. W. Goin

Introduction

TESS is a one-dimensional code which solves the transport equation in slab or spherical geometry and has been operational on the CDC-3600 computer since early 1968. The code is based on a direct method of solution (i.e., one requiring no "inner iterations") of the double S_n formulation in slab geometry, developed by G. E. Putnam and programmed as the MIST Code.[1] TESS allows up to 26 groups, 150 mesh points, 40 regions and 20 angular intervals. The number of downscatter groups is limited to 12 with the option of one-group P_1 anisotropic downscatter. TESS has certain user conveniences, like change case capability and flux or bilinear (flux and adjoint) cross section homogenization over both space and energy. Currently TESS operates on a CDC 3600.

TESS was written to perform heterogeneity analysis on the plate-type Argonne fast critical facilities. The cross section homogenization routine is thus a major feature of the program, and this has been completely revised and expanded recently. The theory upon which all the weighting prescriptions now programmed in TESS are based is due to R. B. Nicholson.[2] This theory indicates that the proper normalization of the cross section weighting expressions depends on whether the entire system of repeating cells is to be represented as a slab or an equivalent sphere in a later calculation in which the homogenized cross sections would be used as the re composition data. Furthermore, a system with leakage predominantly parallel to the plates, rather than perpendicular, is better treated by a third normalization.

The Changes to the Program

The various weighting options differ in the way in which the quantity—called η in Ref. 2—which divides every weighted cross section is calculated. Following are the three different expressions for η:

$$\eta_G^{(1)} = \frac{1}{4\pi V} \sum_{g \epsilon G} \int\int N_g^c(x,\Omega) N_g^{c*}(x,\Omega)\, dV\, d\Omega \tag{1}$$

$$\eta_G^{(2)} = \frac{1}{2\pi V} \sum_{g \epsilon G} \int\int N_g^c(x,\Omega) |\mu| N_g^{c*}(x,\Omega)\, dV\, d\Omega \tag{2}$$

$$\eta_G^{(3)} = \frac{1}{\pi^2 V} \sum_{g \epsilon G} \int\int N_g^c(x,\Omega) \cdot \sqrt{1-\mu^2} N_g^{c*}(x,\Omega)\, dV\, d\Omega. \tag{3}$$

$N_g^c(x,\Omega)$ and $N_g^{c*}(x,\Omega)$ are the angular flux and adjoint, respectively, and are functions of position and angle; V is the volume of the repeating cell; g is an energy group within homogenized energy group G (if one is doing group collapse); Ω is the direction vector of the neutron, with μ being the direction cosine with respect to a designated direction (in TESS, the $\mu = 0$ direction is perpendicular to the direction of the one-dimensional calculation; hence the two values of $\mu = 0$ in slab geometry properly treat discontinuities in the angular flux at slab interfaces and allow higher accuracy at lower angular order than single S_n codes.); finally, the superscript "c" on the angular flux and adjoint denotes that these quantities are solutions to the cell problem with appropriate leakages and boundary conditions input to the code.

Let us assume that the structure of an individual cell in the repeating lattice is in slab geometry. However, if the entire system is to be represented in the ensuing

TABLE IV-22-I. Revised Output Options in TESS

NOT	Weighting	η
5	Bilinear	1
6	Flux	1
7	Flux	2
8	Bilinear	2
9	Flux	3
10	Bilinear	3

calculation by an equivalent sphere, the proper η to use is $\eta^{(1)}$. If the entire system is a slab, $\eta^{(2)}$ is preferable. If it is a cylinder, one must decide whether its height-to-diameter ratio makes it closer to a sphere or a slab. The third expression defines $\eta^{(3)}$, and use of $\eta^{(3)}$ is indicated in the special case in which the leakage from the system is predominantly parallel to the plates. Table IV-22-I shows which values of the output parameter NOT correspond to which cross section homogenization schemes. For NOT = NOT + 6, the weighting option is unchanged, but the code expects fluxes (and adjoints if bilinear weighting is to be performed) already stored in memory from a preceding problem. For values of NOT < 5, TESS does not do cross section homogenization. It should be pointed out that the only option for cell weighting of cross sections which works in spherical geometry is NOT = 6.

The options NOT = 7 and 8 have been thoroughly tested and compared in the GEDANKEN studies, the results of which have been reported in Ref. 3. The options NOT = 5 and 6 did not apply since the GEDANKEN systems are semi-infinite slabs but occasional use of NOT = 6 gave a heterogeneity factor typically about 15% too high. The results for NOT = 7 and 8 were invariably quite good, to the extent that a choice between the two would be difficult to make.

It is of interest to repeat here the expressions for the various cell averaged quantities just as they are defined in Ref. 2, because this is exactly what TESS calculates:

$$\Sigma_G = \frac{1}{4\pi V \eta_G} \sum_{g\epsilon G} \int\int d\Omega\, dV \cdot \left[N_g^{c*}(x,\Omega)\Sigma_g(x) N_g^c(x,\Omega) + N_g^{c*}(x,\Omega) \frac{\mu\, dN_g^c(x,\Omega)}{dx} \right] \tag{4}$$

$$\langle \chi^p \Sigma_f \rangle_{JG} = \frac{1}{16\pi^2 V \eta_G} \sum_{g\epsilon G} \sum_{j\epsilon J} \int\int\int dV\, d\Omega\, d\Omega' \cdot N_g^{c*}(x,\Omega)\chi_g \nu_j \Sigma_{fj}(x) N_j^c(x,\Omega') \tag{5}$$

$$\Sigma_{JG}^{is} \equiv \frac{1}{16\pi^2 V \eta_G} \sum_{g\epsilon G} \sum_{j\epsilon J} \int\int\int dV\, d\Omega\, d\Omega' \cdot N_g^{c*}(x,\Omega)\Sigma_{jg}^{is}(x) N_j^c(x,\Omega') \tag{6}$$

$$\Sigma_{JG}^{(1)} \equiv \frac{3}{16\pi^2 V \eta_G} \sum_{g\epsilon G} \sum_{j\epsilon J} \int dV \Sigma_{jg}^{(1)}(x) \cdot \int d\Omega\, |\mu|\, N_g^{c*}(x,\Omega) \int d\Omega'\, |\mu'|\, N_g^c(x,\Omega'). \tag{7}$$

Expressions (4) through (7) define, respectively, the homogenized total cross section, fission cross section (multiplied by the fission spectrum fraction in homogenized group G and the number of neutrons produced per fission of a neutron with energy in homogenized group J), isotropic scattering cross section, and first-order anisotropic scattering cross section.

We shall briefly indicate how the code performs the numerical integration of products of functions depending on both position and angle. Take, for example, $\eta_G^{(3)}$ as defined in expression (3). Both flux and adjoint are expanded to the following order in a two-variable, finite difference Taylor series:

$$f(r,\mu) = f(r_i,\mu_j) + \left[\frac{f(r_{i+1},\mu_j) - f(r_i,\mu_j)}{(r_{i+1} - r_i)}\right](r - r_i) + \left[\frac{f(r_i,\mu_{j+1}) - f(r_i,\mu_j)}{(\mu_{j+1} - \mu_j)}\right](\mu - \mu_j) + \left[\frac{f(r_{i+1},\mu_{j+1}) - f(r_{i+1},\mu_j) - f(r_i,\mu_{j+1}) + f(r_i,\mu_j)}{(r_{i+1} - r_i)(\mu_{j+1} - \mu_j)}\right](r - r_i)(\mu - \mu_j) \tag{8}$$

This expansion applies to the ranges $r_i \le r \le r_{i+1}$ and $\mu_j \le \mu \le \mu_{j+1}$. The product of an expansion like this for the flux and a similar one for the adjoint is formed. Each term is multiplied by $\sqrt{1-\mu^2}$. The resulting lengthy expression is then integrated analytically from μ_j to μ_{j+1} and from r_i to r_{i+1}. This expression is then summed over all i in the cell and all j such that μ_j runs from -1 to 1.

There has been one more significant addition to TESS, and that is in the area of leakage treatment. As mentioned previously, TESS accepts buckling input in any of four forms: 1) a single value of B^2; 2) a different value of B^2 for each material; 3) a different value of B^2 for each group, independent of material; and 4) a different value of B^2 for each group and each material. The choice is determined by setting input parameter IBUK equal to 1, 2, 3, or 4, respectively. The code calculates D for each group and material as $1/(3\Sigma_t)$ and calculates DB^2 for each group and material which it then adds to Σ_t as a pseudo-absorption cross section. After the flux iterations have converged, the DB^2 additions are subtracted from the Σ_t values so that any ensuing cross section homogenization is done correctly. The new addition to TESS involves an entirely different method of handling leakages, developed by A. P. Olson*

* Applied Physics Division, Argonne National Laboratory.

the CALHET-2 code. It consists of multiplying the source term for each group by a non-leakage probability for that group which is simply $\Sigma_t/(\Sigma_t + DB^2)$. The cross sections are unaltered, and in this case the user inputs as many DB^2 (not B^2) values to the code as there are energy groups in the calculation. The option is chosen by setting IBUK = 5. Comparisons of the effectiveness of this option, compared to IBUK = 4, are also made in Ref. 3. Both gave quite good results.

Work Still in Progress

The options NOT = 9 and 10 are still being tested to determine how useful they are. Due to the reduction in the number of tapes available to the CDC 3600, the reaction rate option in TESS is currently not available. This calculation will probably be converted to employ a disk. The manual for TESS is now near completion and will be released as ANL-7406[4].

References

1. G. E. Putnam and D. M. Shapiro, *MIST (Multigroup Internuclear Slab Transport)*, IDO-16856 (1963).
2. R. B. Nicholson, *Cross Section Averaging Schemes for Group Collapsing and Cell Homogenization in Neutron Transport Calculations for Critical Assemblies*, Reactor Physics Division Annual Report, July 1, 1968 to June 30, 1969, ANL-7610, pp. 488–498.
3. R. G. Palmer and J. P. Plummer, *GEDANKEN Studies*, Argonne National Laboratory Reactor Development Progress Reports: ANL-7705, pp. 9–12 (June 1970); ANL-7669, pp. 14–15 (February 1970); and ANL-7606, pp. 8–10 (August 1969).
4. R. W. Goin and J. P. Plummer, *TESS—A One-Dimensional S_n Transport Theory Code for the CDC 3600*, ANL-7406 (to be published).

IV-23. Self Shielding of Annular and Solid Cylinders

R. B. Nicholson

There are in the available literature[1] tabulations and graphical presentations of neutron self-shielding factors for monoenergetic neutrons and pure absorbers (negligible scattering). It has been found convenient in the analysis of central reactivity worth samples in the fast critical assemblies to develop some analytical approximations for the self-shielding factors and related functions for use on the computer. Also it was useful to derive a simple correction factor for finite-length thin-walled annular cylinders. Usually in the experiments the mean chord length in the sample is less—and often much less—than a neutron mean free path. One can therefore employ series expansions.

In this paper the self-shielding factor is the ratio of the average flux in the sample to the incident surface flux. The latter is assumed to be monoenergetic, isotropic, and unperturbed by the presence of the sample. The monoenergetic limitation can of course be removed by averaging the self-shielding factor f over the incident energy spectrum.

Infinite Solid Cylinders

The self-shielding factor for an infinite solid cylinder can be expressed as an integral over the Ki_3 function[1]:

$$f = \frac{1 - \frac{4}{\pi}\int_0^{\pi/2} \cos\theta Ki_3(2\xi\cos\theta)\,d\theta}{2\xi},$$

where

$$\xi = R\Sigma, \qquad Ki_3(x) = \int_1^\infty \frac{e^{-xt}(t^2-1)^{-1/2}\,dt}{t^3},$$

R is the radius of the cylinder, and Σ is the macroscopic cross section (pure absorber).

An infinite series expression for f in the expansion parameter ξ is obtained by integrating the expansion for Ki_3. The Ki_3 expansion is obtained by a threefold integral of the expansion for the K_0 Bessel function. The result is

$$f = 1 - \frac{4\xi}{3} + \sum_{n=0}^{\infty} b_n \xi^{2n+2}(a_n - \ln\xi),$$

where*

$$a_n = \ln 2 + \left(1 + \frac{1}{2} + \cdots + \frac{1}{n}\right) - \gamma + \frac{12n^2 + 24n + 11}{(2n+1)(2n+2)(2n+3)} - \sum_{m=0}^{n+1} \frac{1}{(2m+1)(2m+2)}$$

$$b_n = \frac{4(2n-1)!!}{(n+1)(n!)^2(2n+4)!!}$$

$$\gamma = 0.5772156649015.$$

The first three coefficients are given in Table IV-23-I.

* $m!! \equiv \begin{cases} m(m-2)(m-4)\cdots(1) & m \text{ odd} \\ m(m-2)(m-4)\cdots(2) & m \text{ even.} \end{cases}$

Because of the rapid convergence of the coefficients of the series, it is a practical calculational formula for values of $\xi < 2.0$. Asymptotic formulae are available[1] for larger values.

Infinite Hollow Cylinders

The situation is more complex for the hollow cylinders and the most economical approach appears to be solution of the final integral by a computer. The self-shielding factor is[1]

$$f = \left[1 - \frac{4}{\pi}\left\{\int_{\theta_1}^{\pi/2} \cos\theta Ki_3(m\cos\theta)\,d\theta + \int_0^{\theta_1} \cos\theta Ki_3[m(\cos\theta - \sqrt{\cos^2\theta - \cos^2\theta_1})]\,d\theta\right\}\right] \Big/ m\cos^2\theta_1,$$

where

$$m = 2R_0\Sigma$$

$$\theta_1 = \sin^{-1}(R_i/R_0)$$

and R_0 and R_i are the outside and inside radii of the hollow cylinder, respectively.

We have found power series and asymptotic expansions for Ki_3 suitable for small and large values of the argument respectively. However, many terms are required to obtain good accuracy at intermediate values. A more useful approximation for use on the computer is given in terms of a ratio of polynomials[2] and is valid for the complete range of arguments. Table IV-23-II gives the results for f for the range of radii and cross sections of interest in the critical assembly measurements.

TABLE IV-23-I. Coefficients for Series Expansion of f for Infinite Solid Cylinders

n	a_n	b_n
0	$\ln 2 - \gamma + \frac{5}{4}$	$\frac{1}{2}$
1	$\ln 2 - \gamma + \frac{7}{6}$	$\frac{1}{24}$
2	$\ln 2 - \gamma + \frac{77}{56}$	$\frac{1}{384}$

Thin-Walled Finite Hollow Cylinders

The reactivity samples for the critical assembly measurements do not have a high enough length-to-diameter ratio to treat them as infinite cylinders with no end correction. The correction can be made to an acceptable approximation by considering the ratio of self-

TABLE IV-23-III. Self-Shielding Factor for Finite Thin-Walled Hollow Cylinders

ξ	L/D						
	0.25	0.5	1.0	2.5	5.0	10.0	25.0
0.01	0.979	0.978	0.976	0.975	0.974	0.973	0.973
0.02	0.963	0.961	0.958	0.956	0.954	0.953	0.952
0.05	0.927	0.922	0.917	0.910	0.907	0.904	0.903
0.10	0.880	0.872	0.863	0.852	0.846	0.842	0.839
0.20	0.809	0.796	0.781	0.763	0.753	0.747	0.743
0.50	0.665	0.645	0.621	0.591	0.575	0.566	0.561
1.0	0.519	0.495	0.464	0.428	0.410	0.400	0.394
2.0	0.356	0.333	0.303	0.268	0.252	0.244	0.238
5.0	0.173	0.158	0.139	0.118	0.109	0.105	0.102

TABLE IV-23-IV. Ratio of Self-Shielding Factors for Finite and Infinite Thin-Walled Hollow Cylinders

ξ	L/D						
	0.25	0.5	1.0	2.5	5.0	10.0	25.0
0.01	1.007	1.005	1.004	1.002	1.001	1.000	1.000
0.02	1.012	1.010	1.007	1.004	1.003	1.001	1.001
0.05	1.028	1.023	1.017	1.010	1.006	1.003	1.001
0.10	1.052	1.042	1.031	1.017	1.010	1.006	1.002
0.20	1.093	1.075	1.055	1.030	1.017	1.009	1.004
0.50	1.196	1.159	1.115	1.061	1.033	1.017	1.007
1.0	1.330	1.268	1.190	1.096	1.051	1.026	1.010
2.0	1.518	1.417	1.290	1.140	1.073	1.037	1.015
5.0	1.734	1.584	1.394	1.185	1.095	1.048	1.019

TABLE IV-23-II. Self-Shielding Factor for Infinite Hollow Cylinders

$R_0\Sigma$	R_i/R_0									
	0.95	0.90	0.85	0.80	0.75	0.70	0.65	0.60	0.55	0.50
0.10	0.984	0.972	0.962	0.953	0.944	0.937	0.930	0.923	0.918	0.912
0.20	0.969	0.946	0.927	0.910	0.895	0.882	0.869	0.858	0.848	0.839
0.50	0.928	0.878	0.838	0.804	0.774	0.748	0.725	0.705	0.686	0.670
1.0	0.868	0.785	0.721	0.670	0.627	0.591	0.560	0.533	0.510	0.4
2.0	0.770	0.646	0.559	0.495	0.444	0.404	0.371	0.345	0.323	0.3
5.0	0.577	0.414	0.320	0.261	0.220	0.192	0.170	0.154	0.142	0.132
10.0	0.402	0.248	0.176	0.138	0.114	0.098	0.086	0.078	0.072	0.067

elding factors for finite and infinite hollow cylinders calculated in the thin-walled limit. The parameter of thinness in this case is the ratio of thickness-to-diameter. It is not necessary for the thickness to be small compared to a mean-free path, although this is usually also true in the fast critical experiments.

In the thin-walled limit we find

$$f = \frac{2}{\pi\xi}\int_0^{\pi/2} d\theta \int_0^1 dx \int_0^{\tan^{-1}(xL/\cos\theta)} \cos\theta\cos^2\Phi \cdot\left[1 - \exp\left(\frac{-\xi}{\cos\theta\cos\phi}\right)\right] d\Phi + \frac{4}{\pi\xi}\int_0^{\pi/2} d\theta \int_0^1 dx \int_{\tan^{-1}(xL/\cos\theta)}^{\pi/2} \cos\theta\cos^2\Phi \cdot\left[1 - \exp\left(\frac{-\xi}{2\cos\theta\cos\Phi}\right)\right] d\Phi,$$

where

$\xi \equiv 2t\Sigma$

$t \equiv$ wall thickness

$L \equiv$ ratio of length to diameter.

In the same limit the self-shielding factor for an infinite cylinder is

$$f_\infty = \frac{2}{\pi\xi}\int_0^{\pi/2} d\theta \int_0^1 dx \int_0^{\pi/2} d\Phi \cos\theta\cos^2\Phi \cdot\left[1 - \exp\left(\frac{-\xi}{\cos\theta\cos\Phi}\right)\right] d\Phi.$$

Table IV-23-III gives f as a function of ξ and L for the thin-walled finite cylinder. Table IV-23-IV is the ratio of f to f_∞.

References

1. J. Dwork, P. L. Hofmann, H. Hurwitz, Jr. and E. F. Claneg, *Self-Shielding Factors for Infinitely Long, Hollow Cylinders*, KAPL-1262 (1955).
2. I. Gargantini and T. Pomentale, *Rational Chebyshev Approximation to the Bessel Function Integrals $Ki_s(x)$*, Comm. ACM **7**, 727–730 (1964).

IV-24. An Extended Equivalance Relation

C. N. Kelber

Despite advances in computing hardware and methods, the computation of resonance capture still represents a serious problem. In an effort to reduce computing time, recourse is frequently made to the equivalence relation[1] as modified by Levine[2] and Bell.[3] Such a method represents the escape probability from the lump by Wigner's rational approximation. The approximation is modified by dividing the mean chord length in the lump by a material-dependent factor, A.

Otter[4] pointed out that if the factor A were adjusted to vary from resonance to resonance, more accurate results could be obtained. In his paper Otter[4] presented methods for calculating the variation of A. In a subsequent paper[5] we showed how Otter's procedure could be modified to yield more accurate estimates with no change in computational method.

In a recent paper[6] this problem was again taken up in an effort to present a formula for A that includes the significant dependence of A on resonance parameters but does not materially increase computing time. The technique was straightforward: Otter's[4] relationship was d for the detailed dependence on line shape, and the ighting procedure developed earlier[5] was used to calculate an effective value for A for a wide range of resonance parameters. Then, after cross plotting to get approximate parametric forms, the effective values were fitted by a least-squares procedure to get the best values of the parametric representation. This process was applied to cylindrical geometry only.

TABLE IV-24-I. Values of Fitted Parameters for $\bar{A} = C_0 + (C_1 + C_6\Sigma_p + C_7\ell)/\Sigma_0 + C_2\Sigma_p + C_3\Sigma_p^2 + C_4\ell + C_5\Sigma_p\ell$

Parameter	4-Parameter Fit		8-Parameter Fit	
	Value	Standard Deviation	Value	Standard Deviation
C_0	1.	0 016	1.	0.011
C_1	1.305	0.042	1.302	0.028
C_2	—	—	−0.0021	0.003
C_3	—	—	−0.0000019	0.00000002
C_4	—	—	0.171	0.004
C_5	—	—	−0.00254	0.000089
C_6	−0.042	0.0025	−0.0367	0.0018
C_7	−0.547	0.05	−0.922	0.04
χ^2	0.0199		0.0086	

The representation studied was:

$$\bar{A} = C_0 + (C_1 + C_6\Sigma_p + C_7\ell)/\Sigma_0 + C_2\Sigma_p + C_3\Sigma_p^2 + C_4\ell + C_5\Sigma_p\ell,$$

where

$\ell \equiv$ rod radius, cm

$\Sigma_0 \equiv$ peak resonance cross section, cm^{-1}

$\Sigma_p \equiv$ potential scattering cross section, cm^{-1}.

The results of this procedure are given in Table IV-24-I. The average residual of the eight-parameter fit, 0.093, is high; by excluding the range of values $\Sigma_0 < 20$, $\ell < 0.3$, the average residual is decreased by a factor of about two. Inasmuch as the constant value of $\bar{A} = 1.35$, which is commonly used, is in error by 0.17 to 0.35 over the entire range, use of the fitted form should yield a better representation of capture on a fine energy cale and, hence, of differential effects such as Doppler coefficient without causing serious discrepancies in c culation of resonance capture.

References

1. J. Chernik and R. Vernon, *Some Refinements in the Calculation of Resonance Integrals*, Nucl. Sci. Eng. **4**, 649 (1958).
2. M. M. Levine, *Resonance Integral Calculations for U-238 Lattices*, Nucl. Sci. Eng. **16**, 271 (1963).
3. G. I. Bell, *Theory of Effective Cross Sections*, LA-2327, (1959).
4. J. M. Otter, *Escape Probability Approximations in Lumped Absorbers*, NAA-SR-9744 (August 1, 1964); see also Trans. Am. Nucl. Soc. **7**, 275 (1964).
5. C. N. Kelber, *Improved Rational Escape Probability in Lumped Absorbers*, Nucl. Sci. Eng. **22**, 244 (1965).
6. C. N. Kelber, *An Extended Equivalence Relation*, Nucl. Sci. Eng. **42**, 257–259 (December 1970).

IV-25. A Fast Exponential Subroutine for Calculating Collision Probabilities on the IBM/360

Arne P. Olson

A method of calculating collision probabilities in slab geometry has been previously described.[1,2] The numerical technique involves integration via special Gaussian quadratures of the form

$$\sum_{k=0}^{\infty} E_n(z + kh) = \int_1^{\infty} \frac{e^{-zt}\,dt}{(1 - e^{-ht})t^n} \approx \sum_{i=1}^{m} w_i \exp(-zt_i). \tag{1}$$

The m-point quadrature weights and nodes are w_i and t_i, respectively, and $E_n(x)$ is the exponential integral function of order n.

The use of this method in the RABID code[3] results in about half of the central processor time being devoted to evaluating e^{-x} for $0 \leq x \leq 18$. Hence a 50% cut in time involved in calculating e^{-x} would provide a gain in speed of about 25% for RABID—a significant improvement for any code.

Such large gains in speed have been obtained at the expense of accuracy and core requirements. The method by which Eq. (1) is evaluated uses linear interpolation to approximate e^{-x} by a continuous sequence of line segments. The usual method of linear interpolation would approximate e^{-x} as follows:

$$e^{-x} = y \approx y_i' + a_i'(x - x_i'). \tag{2}$$

This method retains numerical precision by keeping the linear increment, $a_i'(x - x_i')$, relatively small. However, the x_i are redundant subject to this accuracy restriction. The most compact linear interpolation scheme,

$$e^{-x} = y \approx y_i - m_i x, \qquad 0 \leq i < 1022 \tag{3}$$

does result in a loss of precision due to round-off, but it is much less than the error inherent in the linear approximation. The tabular intercepts y_i and slopes m_i are

$$y_0^* = \frac{2}{\Delta}\frac{1 - e^{-\Delta}}{1 + e^{-\Delta}} \tag{4}$$

$$y_i^* = e^{-\Delta} y_{i-1}^*, \qquad 0 < i \leq 1022 \tag{5}$$

$$m_i = \frac{y_i^* - y_{i+1}^*}{\Delta}, \qquad 0 \leq i \leq 1022 \tag{6}$$

$$y_i = y_i^* + i\Delta m_i, \qquad 0 \leq i \leq 1022. \tag{7}$$

The tabular interval is $\Delta = 18.0/1022$. With these definitions, the average error in Eq. (3) is zero for $0 \leq x \leq 18$.

A function subroutine, SXP, has been coded in Assembler Language for the IBM/360-75. Logical extractions and bit-shifting are used to generate the table addresses of the y_i and m_i. Arithmetic operations f the same result would be much slower. The tables initiated by a single prior call to a companion subroutine, SXPTBL, which is coded in FORTRAN-IV.

The maximum relative error found by testing with 10,000 random number generated arguments was 3.5×10^{-5}, the average relative error was 1.0×10^{-5}, and the computation time was 0.0366 milliseconds per functional value—53% of the time used by the standard EXP Library Subprogram. Typical gains in speed of the RABID code of 21–23% have since been obtained using this method. The errors introduced by the reduced accuracy of SXP compared with EXP were found to be insignificant.

REFERENCES

1. A. P. Olson, *Developments in Integral Transport Methods for Resonance Region Studies in Plate-Type Lattices*, Reactor Physics Division Annual Report, July 1, 1968 to June 30, 1969, ANL-7610, pp. 501–504.
2. A. P. Olson, *Summing Exponential Integral Functions with Application to the Calculation of Collision Probabilities*, Reactor Physics Division Annual Report, July 1, 1968 to June 30, 1969, ANL-7610, pp. 499–501.
3. Arne P. Olson, *RABID: An Integral Transport-theory Code for Neutron Slowing Down in Slab Cells*, ANL-7645 (1970).

IV-26. Improved Subroutine Efficiency Through Calling-Sequence Modification[1]

CHARLES ERWIN COHN and MARK H. ELFIELD*

In present programming practice, the calling sequence for subroutines has become standardized. With minor variations, it consists of a save-place-and-branch instruction pointing to the subroutine entry, followed by a series of words containing the argument addresses. We have found some efficiency gains possible if the words in the calling sequence are replaced by instructions which do all or part of the subroutine's job. This replacement is done by the subroutine the first time it is called from a given location.

Our implementations of this concept have been done on computers whose word length is sufficient to carry any operation code in association with the address of any location in memory (i.e. the 24-bit-word DDP-24 and SEL-840). Some of the ideas may not be applicable to shorter-word machines that do not have this capability.

A simple example is a FORTRAN-callable two-argument integer function subroutine whose result is the bit-by-bit logical product of the arguments. Before execution, the calling sequence for this function contains the following three words:

1. Save-place-and-branch to the subroutine
2. Address of first argument
3. Address of second argument.

On entry, the subroutine replaces the above with the following:

1. Load-accumulator instruction addressed to first argument
2. No-operation instruction
3. And-to-accumulator instruction addressed to second argument.

In the process, any index tags and/or indirect flags associated with the argument addresses are carried over to the respective instructions. This takes care of cases where the arguments are subscripted variables, dummy variables, or arithmetic expressions. The no-operation instruction is included just to fill up space.

After performing these substitutions, the subroutine transfers control to the first instruction in the sequence. On subsequent passes, the sequence is executed in-line with no further reference to the subroutine. Such execution saves six memory cycles out of eleven over the tightest possible conventional subroutine coding on the DDP-24. Similar routines have been written for logical-sum and exclusive-or operations.

The concept is particularly well suited to intrinsic functions in FORTRAN. Sophisticated compilers often implement such functions with in-line coding. However, compilers for smaller computers usually resort to subroutine calls because of memory size limitations at compile time.

An example is IABS, integer absolute value. Its calling sequence has the form

1. Save-place-and-branch to IABS
2. Address of argument.

For machines with sign-magnitude arithmetic, the above may be replaced by

1. Load-accumulator instruction addressed to argument
2. Masking instruction to drop sign bit.

On the DDP-24, this takes 4 memory cycles for each execution after the first, compared to 10 for optimal conventional coding, and 17 for the existing library subroutine. For a machine with a suitable instruction set, still another memory cycle may be saved by the sequence

1. Clear-accumulator instruction

* Ohio State University, Columbus, Ohio

2. Add-magnitude instruction addressed to argument.

The limitation on the use of this technique is the calling sequence not being long enough for all the instructions needed to do the subroutine's job. This is true of the IABS function for machines with two's complement arithmetic, where the accumulator is negated if it is negative but left unchanged if it is positive. Here, the work can be partitioned between an instruction in the calling sequence to retrieve the argument and a special closed subroutine that operates on the accumulator. That subroutine is coded as part of IABS. The calling sequence would thus be altered to contain a load-accumulator instruction addressed to the argument, followed by a save-place-and-branch to the subroutine. This saves 1–2 memory cycles over optimum conventional coding on the SEL-840. The saving arises from the improved efficiency of argument retrieval.

Another example in this area is the FORTRAN library function FLOAT. In many systems the FLOAT subroutine retrieves the argument and then calls a conversion routine that operates on the accumulator. (This conversion routine is the same one for which the compiler generates a call when an integer-to-real mode shift occurs across an equal sign.) It is then logical to replace the two-word calling sequence with a load-accumulator instruction addressed to the argument, followed by a save-place-and-branch to the conversion subroutine. Again, the increased efficiency of argument retrieval as well as the elimination of one save-place-and-branch plus return yields a saving of 6 cycles over optimal conventional coding and 13 cycles over an existing library subroutine on the DDP-24.

In one of our implementations of the method, i.e. a pair of FORTRAN-callable subroutines for performing shift operations, the need for an auxiliary subroutine is dependent on the nature of the argument. These subroutines have two integer arguments, with a calling sequence as follows:

1. Save-place-and-branch to subroutine
2. Address of word to be shifted
3. Address of shift count.

The results are left in the accumulator.

If the address of the shift count is direct, the above may be replaced by

1. Load-accumulator instruction addressed to word to be shifted
2. No-operation instruction
3. Shift instruction indirect-addressed to shift count.

If the address of the shift count is indirect, the above would not work, because the direct address of the shift count would be misinterpreted as the shift count itself. (In most computers, the effective address of a shift instruction indicates the shift count itself rather than its memory location.) There, the following is required:

1. Load-accumulator-extension instruction addressed to word to be shifted
2. Load-accumulator instruction indirect-addressed to shift count
3. Save-place-and-branch to a shift subroutine which takes its operands from the above registers.

Again, the simplification of argument retrieval improves efficiency.

A final application to be discussed allows the FORTRAN programmer to make use of the increment-memory instruction that is available on many modern computers. This is done through a subprogram that may be referenced either as a function or subroutine to perform the work of the statement I = I + 1. That statement as normally compiled requires a load, an add, and a store instruction taking a total of three locations and six cycles. It is replaced by the statement CALL INCRMT(I) which is compiled into a two-word calling sequence. The subroutine INCRMT replaces the calling sequence with

1. Increment-memory instruction addressed to argument
2. No-operation instruction,

taking a total of four cycles. For the subprogram to be used as a function, the no-operation instruction must be replaced with a load-accumulator instruction addressed to the argument if the increment-memory instruction does not leave its result in the accumulator. That way, the pair of statements

```
I = I + 1
IF(I - N)3, 3, 4
```

may be replaced by the single statement

```
IF(INCRMT(I) - N)3, 3, 4.
```

The time savings yielded by these techniques come at a slight cost in memory space, since a subroutine that substitutes instructions takes a few more words than an optimally-coded subroutine for directly performing the given task. (For INCRMT, that penalty is offset by a saving of at least one word in the calling program for each reference.)

Finally, in contrast to most contemporary programming practice, these techniques take advantage of the original Von Neumann concept of a computer capable of modifying its own instructions.

Reference

1. M. H. Elfield and C. E. Cohn, *Improved Subroutine Efficiency Through Calling-Sequence Modification*, Software Age 4, No. 2, 5–6 (February 1970).

IV-27. Software Methods of Data Acquisition on a Small Computer

D. W. Maddison and C. L. Beck

The modern small computer has a great potential for application to data acquisition tasks. Its application to such tasks can vary widely. Because it is programmable with software, it can be adapted to several jobs simultaneously. The software is easily altered to accommodate completely new and different problems. As data acquisition requirements change, the appropriate changes in the computer can be rapidly and easily accomplished in most cases.

As pointed out by Cohn,[1] many of these small computers are relatively slow in executing certain operations, particularly floating point arithmetic. Most data, however, is in integer form or can be considered as integer, and the small computer is capable of executing integer operations very rapidly. Most data acquisition applications are strongly time dependent, and any data storage module must not introduce significant time delay with respect to other equipment. Most small computers have sufficient instructions that this problem is not appreciable. The use of medium sized or large computers for data acquisition cannot be justified in most cases in terms of cost and time required to service external devices. A small computer, however, often can operate as efficiently as a larger computer when acquiring data. The extensive data reduction usually required to produce meaningful results can be done with a larger machine by using some intermediate storage media, such as magnetic tape. Extensive data reduction can be accomplished even with a small computer if sufficient time is available.

The first apparent drawback of a small computer is the limited storage available. Relatively simple software techniques, however, can solve most, if not all, of these limitations. A 16 bit computer, for instance, could store a maximum unsigned number of 65,535. By using double precision storage, this can be extended to 32 bits, or a maximum unsigned number of about 4×10^9. The major drawback to using a double precision technique is that the effective storage array is halved. If only a few entries are expected to exceed 65,535, then an "overflow table" is a more economical method to use. Another fact, often overlooked, is that much of the data acquired is of little or no use. A computer can easily and rapidly make a decision as to whether any particular datum should be stored, discarded, or put into a common storage. This decision making is easily programmed and can be readily controlled by external devices or by the operator as desired.

Our particular experience has been with multichannel gamma-ray spectra. The system has been described before,[2] but basically it consists of one small, 16-bit, 4096-word computer which controls three independent gamma-ray spectrometers, including three sample changers, three live timers, three analog-to-digital converters, a real time clock, and a visual display unit. The real time clock is actually done with software within the computer. The major output device is a magnetic tape unit, but here again the control is accomplished with software. The primary restrictions are on the time required to service three 8192-channel analog-to-digital converters. Since our particular data analysis method involves, among other things, a determination of the half-life of the decaying radioactive material, the data acquisition must be limited by the analog-to-digital converter and not by the computer. In addition, the 4096-word computer must store data from three 8192-channel converters, and some of this space is required for program. Even with complicated, unseparated fission-product spectra, we have found that about 10 percent of an 8192-channel spectrum is all that we require for routine analysis. In the few cases where either much more data storage is required or the counting rate is extremely high, we use another program that services only one analog-to-digital converter.

A high counting rate requires a maximum computer data acquisition time of about 20 μsec and one might reasonably expect that several "channels" could exceed a count of 65,535. The particular instructions listed are some, but not all, of those available on our SEL 810A computer. Most small computers have equivalent or similar instructions. The input program looks like this:

1) AIP	Input data from converter to A register.
2) TAB	Transfer the number in the A register to the index register.
3) IMS R,1	Add one to the memory location specified by the sum of the index register and R, where R would be the memory location for "channel O," and skip the next instruction if the result is zero (overflowed).
4) BRU 1	Go to instruction 1.
5) LBA OF	Load the index register with the content of overflow counter.
6) STA S,1	Store the A register (the channel

number) in the appropriate place in the overflow table.

7) IMS OF — Add one to the contents of OF (the overflow counter) and skip the next instruction of the result if zero.
8) BRU 1 — Go to instruction 1.
9) BRU STOP — Go to data termination loop.

The main part of this data input loop involves steps 1, 2, 3, and 4, with a total execution time of 14 μsec. If a particular channel overflows (exceeds 65,535), steps 5, 6, 7, and 8 are executed. Typically, the overflow table will contain 100 locations, so 100 overflows can be accommodated. If more than 100 overflows occur, the program goes to an exit loop which terminates data collection. If this occurs, usually more than enough data have been accumulated and the system can then go on to count the next sample.

While the data collection loop is operating, a real time clock sequence also is functioning. A fixed frequency pulser is connected to a high priority interrupt on the computer, and each time a pulse occurs the following loop is executed:

1) IMS X — Add one to memory location X and skip the next instruction if the result is zero (overflow).
2) BRU P — Return to the previous operation before the interrupt occurred.
3) IMS X + 1 — Same as step 1, except for location X + 1.
4) BRU P — Same as step 2.

This loop keeps track of the real time since the program was initialized. Typically we use a 10 Hz pulser; thus the 32-bit double precision register, consisting locations X and X + 1, would be capable of counting clock time for about 12 years.

The program that collects data from all three converters uses the same clock loop and three input loops, each containing an additional check to see if the data should be stored or not. Each input loop takes about 36 μsec to execute (without overflows) and provides considerable freedom in data handling.

The data for any channel can easily be reconstructed to its full value by searching the overflow table and then the data storage array. Our technique is to essentially make a core dump to magnetic tape of the spectrum, or all three spectra as the case may be, and then reform the data on a larger computer that performs a lengthy data analysis.[3] There is not sufficient core available on our small computer to execute this analysis program, but simplified parts of it have been used at various times. A manually controlled analysis program that gives modified visual data displays and printed output is operational on our small computer.

References

1. C. E. Cohn, *Speed Tests on Some Control Computers*, Trans. Am. Nucl. Soc. **13**, 177 (1970).
2. D. W. Maddison and L. S. Beller, *Characteristics and Capabilities of Automated Counting Facilities for the Zero Power Plutonium Reactor (ZPPR)*, Reactor Physics Division Annual Report, July 1, 1968 to June 30, 1969, ANL-7610, pp. 379–381.
3. L. S. Beller and D. W. Maddison, *Automated Spectrum Analysis Methods for Ge(Li) Detectors*, Reactor Physics Division Annual Report, July 1, 1968 to June 30, 1969, ANL-7610, pp. 416–417.

IV-28. New Features in the NURF Foil-Data Program

G. S. Stanford

Some changes and additions have been made to the NURF code,[1] to provide increased flexibility and to incorporate some data corrections that hitherto had to be done by hand. Among the new features are: a means for making gamma-ray self-absorption corrections; a method for making weight-dependent background corrections; provision for applying special background corrections to specified foils; and automatic rejection of seriously deviant datum points.

The subroutine that has been added to NURF to make gamma-ray self-absorption corrections currently applies only to 100-keV gamma rays—that is, to coincidence counting for determining radiative captures in U-238. It makes the correction by modifying the input foil weight. Because the absolute magnitude of the gamma-ray self-absorption in uranium foils at 100 keV is not well known at present, the subroutine applies only a compensation for thickness differences, not a reduction to zero thickness. The reference thickness used is 0.268 g/cm^2, corresponding to ~5.58 mils. The correction is based on an assumed absolute attenuation factor G of ~0.73 for foils of the reference thickness.

Occasionally one might want to count U-238 captures in enriched uranium foils that were irradiated in

thermal flux, requiring a correction for self-shielding as well as for self-absorption. This correction also is made, if the foil is properly designated in the input, on the assumption that an enriched foil of the reference thickness has a self-shielding factor of 0.593. Taking into account the non-linearity of the self shielding as a function of thickness, the composite attenuation factor G for such foils was calculated to be ~0.52. (A very large cadmium ratio is assumed.)

The adjusted foil weight w' is defined to be the weight which, when divided into the observed activity of the foil, yields the specific activity that would be observed for a foil of the reference thickness. The adjusted weight is calculated according to the formula

$$w' = \frac{w}{G}\left[1 - \frac{w}{w_0}(1 - G)\right], \qquad (1)$$

where w_0 is the weight of a foil of the reference thickness, and w is the actual weight of the foil.

The reference weight w_0 is proportional to the area of the uranium foil, and several sizes of depleted uranium foils are used in the Zero Power Reactor activation measurements. The self-absorption routine assigns reference weights on the basis of the foil weight. Occasionally the weight of a foil will fall outside the assigned limits for its type. Such cases require special handling.

The new weight-dependent background-correction facility permits subtracting from the counting data a background component B_w that is proportional to the weight of the foil, along with subtraction of the empty-planchet background. To allow for decay of the component B_w, or for other purposes, B_w can be multiplied by a constant multiplier.

It sometimes happens that foils that are counted together do not all have the same specific background activity, because of different irradiation histories or because they are different materials—e.g., enriched and depleted uranium. Hitherto in NURF it has been necessary to collate the cards in order to make such specified-foil background corrections. A new feature eliminates this requirement, permitting special (weight-dependent, as above) background rates to be specified for individual foils.

Occasionally, some malfunction in the counting equipment (e.g., a burst of noise) leads to a bad datum point, which should not be included when repeated counts of the same foil are averaged. For automatic rejection of the more flagrant of such points, NURF now uses a new subroutine, DOCTOR, in two places: to reject bad points from the least-squares decay-curve determination, and to do the same for the final averaging of the repeated counts for each foil. DOCTOR computes χ^2 for each set of points to be averaged, and rejects points on the basis of criteria involving χ^2, the deviation of the point from the (weighted) average, the statistical accuracy of the point, and the number of points to be averaged.

References

1. G. S. Stanford, *The Codes NURF, COMBO, and TWOSORCE for Processing Foil Counting Data*, ANL-7356 (1967).
2. R. J. Armani, Argonne National Laboratory (private communication).

IV-29. The Effects of S/N Ratio on the Results of Polarity Correlation Experiments

W. K. Lehto and R. W. Goin

Polarity correlation involves the coarse quantization of an analog signal into two bits, representing the positive and negative states, and calculation of the correlation functions from the resulting time series. It has been shown that accurate correlation measurements can be made using the two-bit quantization.[1-3] It has also been shown that reducing the level of quantization also reduces the available dynamic range,[4,5] with the limit being one decade in a two-bit quantization scheme. This work covers the less well-known effects of varying signal-to-noise ratio on the results of polarity-correlation experiments.

This experimental study was undertaken to determine the practical limit of the S/N ratio. The experiment was performed using a polarity correlator (see Paper II-17) coupled to the on-line computer at the Zero Power Plutonium Reactor. Prior work[6] has established the limit as 0.1 in a full amplitude cross power spectral density measurement.

Analog data from a detector (phototube and plastic scintillator) driven by a neutron source was low pass filtered (to simulate fast reactor data) and passed into each channel of the polarity cross correlator; these data represented the correlated part of the total signal. The noise for each channel was derived from separate detectors and superimposed on the correlated signal

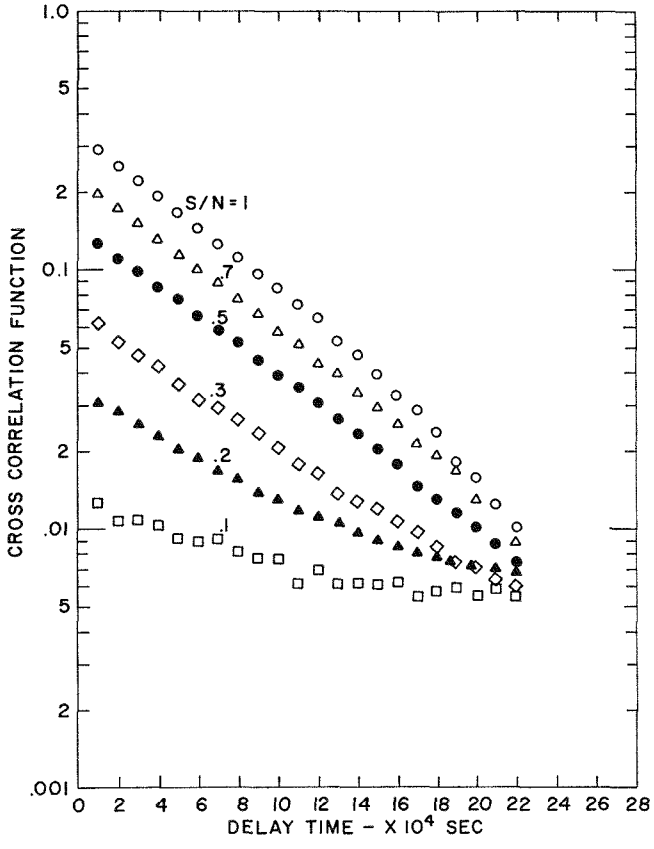

FIG. IV-29-1. Correlation Functions for Varying S/N Ratios. *ANL-ID-103-A11388.*

TABLE IV-29-I. LEAST SQUARES FITTED PARAMETERS
$C_{12}(\tau) = A_1 + A_2 e^{-\alpha\tau}$

S/N	Slope-α sec^{-1}	% Error	A_1	A_2
1.0	1323	2.0	−0.0080	0.343
0.8	1287	1.2	−0.0075	0.271
0.7	1321	1.8	−0.0025	0.228
0.6	1268	2.4	−0.0021	0.194
0.5	1283	1.2	−0.0011	0.147
0.3	1305	0.5	0.0022	0.067
0.2	1357	4.1	0.0052	0.030
0.1	1457	12.0	0.0048	0.014

through an isolation network to avoid cross-talk. The polarity-cross-correlation function was then calculated for systematically varying ratios of signal-to-noise. The record lengths were varied to keep the estimated errors constant for each run.

Some of the results are shown in Fig. IV-29-1. The amplitude of the correlation function decreases systematically with decreasing signal-to-noise ratio. The quality of the data deteriorates rapidly below S/N 0.2. The decay constants obtained from a least-squares fit of the data vary from $\approx$1.2 to 12% (S/N = 0.1) from the true value of 1300 sec^{-1}, as shown in Table IV-29-I.

At the longer delay times, the data with the higher S/N ratios exhibit a larger than expected falloff and show a downward curvature which resulted in negative backgrounds from the least-squares fit. This effect is thought to be due to quantizer saturation,[7] since only the high amplitude low frequency data contribute to the correlation function at these long delays. Under these conditions the correlation function is no longer amplitude dependent and has essentially a linear behavior with time, indicative of the downward curvature. As the S/N ratio is decreased by addition of Gaussian white noise, saturation for long times at low frequencies is reduced and the data follow the expected behavior as evidenced in the results for $S/N < 0.5$. Similar saturation effects have been observed in the measured polarity correlation functions of high efficiency thermal reactor data.

These results indicate that polarity correlation measurements with this particular equipment require signal-to-noise ratios at least two times greater than those required for the full amplitude cross correlation experiments. This limit is expected to apply to similar type equipment and is reasonable in view of the reduced precision of the coarse quantization in polarity sampling.

REFERENCES

1. J. B. Dragt, *Analysis of Reactor Noise Measured in a Zero Power Reactor and Calculations on Its Accuracy*, Proc. Symposium on Neutron Noise, Waves and Pulse Propagation, University of Florida, Gainesville, Florida, CONF-660206 (1966).
2. C. E. Cohn, *Reactor Noise Studies With an On-Line Digital Computer*, Nucl. Appl. **6**, 391 (April 1969).
3. W. Seifritz, *The Polarity Correlation of Reactor Noise in the Frequency Domain*, Nucl. Appl. and Tech. **7**, 513 (1969).
4. P. D. Welch, *The Dynamics of a Subharmonic Oscillator with Linear Dissipation*, IBM Journal of Research and Development **5**, 141–156 (April 1961).
5. R. C. Kryter, Oak Ridge National Laboratory (private communication).
6. W. Seifritz, D. Stegeman and W. Vath, *Two-Detector Correlation Experiments in the Fast-Thermal Reactor STARK*, Proc. Symposium on Neutron Noise, Waves and Pulse Propagation, University of Florida, Gainesville, Florida, CONF-660206 (1966).
7. G. C. Anderson and M. A. Perry, *A Calibrated Real Time Correlator/Averager/Probability Analyzer*, Hewlitt-Packard Journal **21**, 9 (November 1969).

IV-30. MATDIAG, A Program for Computing Multilevel S-Matrix Resonance Parameters[1]

P. A. Moldauer, R. N. Hwang and B. S. Garbow*

Introduction

The purpose of the computer program MATDIAG is to compute cross section resonance parameters from Wigner's R-matrix.[2,3]

The R-matrix parameters (energy levels E_μ and channel amplitudes $\gamma_{\mu c}$) may either be specified individually in the input, or they may be generated statistically according to appropriate distribution laws.

The computed cross section resonance parameters are the poles and residues of the collision matrix,[4] which are useful for a variety of purposes. They can be employed for the direct calculation of Doppler-broadened multilevel cross sections by means of the Adler-Adler cross section code,[5-8] or for multilevel cross-section and neutron-flux calculations using the improved RABBLE program or other similar programs.[9] Of particular interest to the fast-reactor research program is the Doppler effect of the fissile isotopes in the low keV region, which has been studied by Hwang with the help of the MATDIAG program.[9-11]

The statistical analysis of the S-matrix resonance parameters that is performed in the MATDIAG program is needed for the precise specification of average cross sections where resonances overlap and is also useful for the interpretation of cross-section fluctuations.[12] Moldauer[13,14] has used the program for the study of resonance-parameter statistics and for the clarification of the averaging process.

Two considerations necessitate the computation of S-matrix parameters in terms of R-matrix parameters in the region of overlapping resonances.

The first step required to insure the unitary character of the collision matrix, which imposes severe and generally complicated restrictions on the resonance parameters, particularly when the number of competing open channels is small.[15] Second, there exists no satisfactory theory that gives the statistical properties of the S-matrix parameters directly, but there is a very extensive and well-developed statistical theory of R-matrix parameters.[15]

The program generates resonance parameters by inversion of the level matrix and therefore requires the diagonalization of a complex symmetric matrix whose dimension is equal to the number of resonances included in the calculation. The version of the program used in earlier applications[10-16] was written for the CDC-3600 computer and used in complex eigenvalue and eigenvector routines of Ehrlich[17] with a restriction to a maximum of 50 resonances. The program described in this report has been significantly improved in the following ways: (1) The program has been converted to run on the faster IBM system 360-75; (2) the complex eigenvalue and eigenvector routines† written by Garbow[18] were used in place of Ehrlich's routine (this change reduced considerably the computer time required); (3) the modified version is capable of treating a maximum of 120 poles; and (4) options are available to punch cards with Adler-Adler parameters[5-8] for the Doppler-broadened cross sections in the modified RABBLE[9] format for the calculation of self-shielded reaction cross sections.

* Applied Mathematics Division, Argonne National Laboratory.

Theory

The theory of multilevel and statistical cross-section calculations has been discussed in great detail in Ref. 12 and was further summarized in Ref. 19. We give here only an outline containing the definitions required for an understanding of the MATDIAG code.

The collision matrix elements can be written in the form

$$S_{cc'} = \exp\left[i(\phi_c + \phi_{c'})\right] \cdot \left[W_{cc'} - i\sum_\mu \frac{g_{\mu c} g_{\mu c'}}{E - \epsilon_\mu + \frac{1}{2} i \Gamma_\mu}\right], \tag{1}$$

where all parameters are assumed to be energy-independent constants and the multilevel cross section is given by

$$\sigma_{cc'} = \pi^2 \mid \delta_{cc'} - S_{cc'} \mid^2, \tag{2}$$

whose energy dependence is directly determined by the resonance energies ϵ_μ, the widths Γ_μ, and the residue amplitudes $g_{\mu c}$, where the subscript c refers to a particular channel. The program calculates these parameters from the eigenvalues and eigenvectors of the matrix $B_{\mu\nu}$, which is specified in terms of R-matrix parameters E_μ and $\gamma_{\mu c}$ as follows:

$$B_{\mu\nu} = E_\mu \delta_{\mu\nu} - \frac{D}{4\pi} \sum_c (\sigma_c + i\tau_c) \hat{\gamma}_{\mu c} \hat{\gamma}_{\mu c'} \tag{3}$$

† The complex eigenvector routine is unpublished

where, in the absence of a background R-matrix,*

$$\sigma_c + i\tau_c = 4\pi(S_c^0 + iP_c)\langle\gamma_{\mu c}^2\rangle/D \tag{4}$$

and

$$\hat{\gamma}_{\mu c} = \gamma_{\mu c}/\langle\gamma_{\mu c}^2\rangle^{1/2}, \tag{5}$$

where S_c^0 is the shift function with the R-matrix boundary condition subtracted. This parameter can often be selected to be zero. P_c is the penetrability function, and D is the mean spacing of resonances; $\langle\gamma_{\mu c}^2\rangle$ is the value of $\gamma_{\mu c}^2$ averaged over all resonances μ. These parameters are determined by the optical-model transmission coefficient T_c in each channel c, which has the value

$$T_c = \frac{\tau_c}{(1 + \frac{1}{4}\tau_c)^2 + (\frac{1}{4}\sigma_c)^2}. \tag{6}$$

For a fission channel, T_c should be associated with the penetration probability of Hill and Wheeler.[20]

The resonance energies ϵ_μ and the widths Γ_μ are the real and imaginary parts of the eigenvalues of $B_{\mu\nu}$:

$$B_{\mu\nu}Z_\nu^{(\lambda)} = (\epsilon_\lambda - \tfrac{1}{2}i\Gamma_\lambda)Z_\mu^{(\lambda)}, \tag{7}$$

where $Z_\nu^{(\lambda)}$ is the νth component of the λth eigenvector of $B_{\mu\nu}$.

The residue amplitudes are given by

$$g_{\mu c} = \sqrt{\frac{D\tau_c}{2\pi}}\,\frac{\tau_c - i\sigma_c}{(\tau_c^2 + \sigma_c^2)^{\frac{1}{2}}}\sum_\nu Z_\nu^{(\mu)}\hat{\gamma}_{\nu c}. \tag{8}$$

The eigenvectors are normalized so that

$$\sum_\nu Z_\nu^{(\lambda)2} = 1, \tag{9}$$

and the normalization factor

$$\sum_\nu |\, Z_\nu^{(\lambda)}\,|^2 = N_\lambda \geq 1 \tag{10}$$

is computed to obtain the definition of partial widths

$$\Gamma_{\mu c} = |\, g_{\mu c}\,|^2/N_\mu \tag{11}$$

which add up to the total width

$$\Gamma_\mu = \sum_c \Gamma_{\mu c}. \tag{12}$$

For statistical analysis, the program also calculates the real and imaginary parts of

$$\theta_{\mu c} = \sum_\nu Z_\nu^{(\mu)}\gamma_{\mu c} \tag{13}$$

as well as their absolute values and phase angles. Also it calculates the generalized transmission coefficients.[12]

$$\theta_{\mu c} = 2\pi N_\mu^2\Gamma_{\mu c}/D \tag{14}$$

and

$$\theta_\mu = \sum_c \theta_{\mu c}, \tag{15}$$

as well as the statistical parameters[12,14]

$$B_c = |\,\langle g_{\mu c}^2\rangle/\langle g_{\mu c}\rangle^2\,|^2 \tag{16}$$

and

$$B = \langle B_c\rangle_c. \tag{17}$$

Option is also available to print and punch cards with the Adler-Adler amplitudes for the Doppler-broadened cross sections in the format of the modified RABBLE[9] so that the self-shielded cross sections can be readily calculated. The Adler-Adler amplitudes for the Doppler-broadened cross sections are related to the fundamental S-matrix parameters in the following way:[5-10]

$$G_\mu^{(x)} = \sum_{c'} Im\zeta_\mu, \tag{18}$$

$$H_\mu^{(x)} = \sum_{c'} Re\zeta_\mu, \tag{19}$$

$$G_\mu^{(T)} = Re[g_{\mu c}^2 \times \exp(-i2R/\lambda)] \tag{20}$$

and

$$H_\mu^{(T)} = Im[g_{\mu c}^2 \times \exp(-i2R/\lambda)], \tag{21}$$

where the complex reaction amplitude ζ_μ is defined as

$$\zeta_\mu = g_{\mu c}g_{\mu c'}\sum_{\mu'}\frac{g_{\mu' c}^* g_{\mu' c'}^*}{\epsilon_\mu - \epsilon_{\mu'} - \frac{i}{2}(\Gamma_\mu + \Gamma_{\mu'})}. \tag{22}$$

Another option available in connection with the Doppler-effect studies is to punch out cards with the initially generated R-matrix parameters in the RABBLE format. Such information is useful in examining the validity of the Breit-Wigner equation, because these studies are often made on the basis of an *ad hoc* assumption that the single-level parameters and R-matrix parameters are identical.[9] This assumption is correct if resonances are widely spaced.

Description of Input

Input parameters include the number of resonances NN, the number of channels NR, and the R-matrix parameters σ_c, τ_c, E_μ, and $\hat{\gamma}_{\mu c}$.

The E_μ can be specified in three ways:

(1) They may be specified to have unit spacing with an average value $\langle E_\mu\rangle$ of zero (picket fence).
(2) They may be read in individually.
(3) They may be specified statistically so that the lowest E_μ and the mean spacing D are specified and the individual spacings $\Delta_\mu = E_{\mu+1} -$ are generated randomly to follow the Wigner distribution

* The meaning of σ_c and τ_c in more general circumstances is explained in Ref. 14.

$$W(\Delta_\mu/D) = \frac{1}{2}\pi(\Delta_\mu/D)\exp\left[-\frac{\pi}{4}\Delta_\mu^2/D^2\right].$$

The $\hat{\gamma}_{\mu c}$ may be specified in two ways:

(1) They may be generated randomly to have a normal distribution with unit standard deviation. This means that the $\gamma_{\mu c}^2$ have a Porter-Thomas distribution.

(2) They may be read in individually.

Description of Output

The various collision-matrix resonance parameters are given in the output. In addition, certain statistical properties of these parameters are calculated, such as their averages, their dispersions, and their correlations, which are defined as follows:

$$\text{X AV} = \langle X_\mu\rangle \sum_\mu X_\mu/NN,$$

$$\text{X MSQ} = (\langle X_\mu^2\rangle - \langle X_\mu\rangle^2)/\langle X_\mu\rangle^2,$$

and

$$\text{X CORR} = (\langle X_{\mu+1}X_\mu\rangle - \langle X_\mu\rangle^2)/\langle X_\mu\rangle^2.$$

When channels with large transmission coefficients ($T_c > 0.5$) are present, the distributions of collision-matrix resonance parameters are apt to be distorted near the edges of the set of resonances.[14] For this reason, provision is made to exclude from the above averages a number NKK of resonances at each edge.

The MATDIAG Code

The MATDIAG code consists of several subroutines, which are listed in Ref. 1. The function of the main program is to read input information, set up the matrix B, and then print and punch out the quantities of interest as obtained by other subroutines. To set up the matrix B, random sequences of $\gamma_{\mu c}$ and E_μ are generated by subroutines RANN and ESUB, respectively, using the random numbers obtained in the subroutine RANF.[21] Where the elements of $B_{\mu\nu}$ are exceedingly large, the matrix can be scaled down by a factor of SF specified by the users in order to avoid the possible overflow in the computation of the eigenvalues and the eigenvectors.

The most important routines required are clearly those that compute the complex eigenvalues and their corresponding complex eigenvectors. Because the dimensions of matrices of interest are generally very large, these routines must be fast and efficient to be of any practical interest. Two such programs available at Argonne National Laboratory are MATSUB[17] and FRANCC[18] with VCTR (unpublished). MATSUB, originally written for the CDC-3600 computer,[17] has been converted to the IBM 360/75. It was found, however, that FRANCC[18] is faster by as much as a factor of three, compared with MATSUB. Furthermore, it avoids the direct evaluation of the determinant, which, for large matrices of interest, causes overflow in MATSUB. Hence, FRANCC is recommended. Recently, another program that treats the complex symmetric matrices of interest became available. This program, written by Seaton,[22] is based on a modified Jacobi method. Preliminary tests have shown that Seaton's program is comparable to FRANCC in speed and is perhaps more efficient when the diagonal elements of the matrix B predominate or when only moderate accuracy is required. These programs will be compared further.

Once the complex eigenvalues and eigenvectors are obtained, the main program computes and prints out the S-matrix resonance parameters. Subroutines ORDER and ORDER1 order the quantities $|\epsilon_\mu - \epsilon_\nu|\,\Gamma_\mu/2$ and N_μ in increasing order so that the statistical behavior of these quantities can be examined more readily. Subroutine AVERAGE computes average quantities required in the determination of the averaged cross sections. The detailed description and the FORTRAN listing of this code is given in Ref. 21.

References

1. P. A. Moldauer, R. N. Hwang and B. S. Garbow, *MATDIAG, A Program for Computing Multilevel S-Matrix Resonance Parameters*, ANL-7590 (1969).
2. E. P. Wigner and L. Eisenbud, *Higher Angular Moments and Long-Range Interaction in Resonance Reactions*, Phys. Rev. **72**, 29 (1947).
3. H. B. Willard, L. C. Biedenharn, P. Humber and E. Baumgartner, *Fast Neutron Physics*, Part II, p. 1217, J. B. Marion and J. Fowler, Eds. (Interscience Publishers, Inc., New York, 1963).
4. J. Humblet and L. Rosenfeld, *Theory of Nuclear Reactions*, Nucl. Phys. **26**, 529 (1961).
5. D. B. Adler and F. T. Adler, *Neutron Cross Sections in Fissile Elements*, Proc. Conference on Breeding, Economics, and Safety in Large Power Reactors, October 7–10, 1963, ANL-6792, pp. 695–709.
6. F. T. Adler and D. B. Adler, *Neutron Cross Sections in Fissile Elements*, Proc. National Topical Meeting on Reactor Physics in the Resonance and Thermal Regions (MIT Press, Cambridge, 1966), p. 47.
7. F. T. Adler and D. B. Adler, *Interpretation of Neutron Cross Sections of the Fissionable Materials for the Resolved Resonance Region*, Proc. Neutron Cross Section Technology Conference, CONF-660303, Book 2 (1966), p. 873.
8. D. B. Adler and F. T. Adler, *Cross Section for Fissile Elements: A Simple Approach to the Multilevel Formalism*, Trans. Am. Nucl. Soc. **5**(1), 53 (1962).
9. R. N. Hwang, *Doppler Effect Studies Using Multilevel Formalism*, Nucl. Sci. Eng. **39**, 32–49 (1970).
10. R. N. Hwang, *Application of Statistical Theory and Multi-Level Formalism to Doppler Effect Analysis—I*, Nucl. Sci. Eng. **39**, 32–49 (1970).
11. R. N. Hwang, *Application of Statistical Theory and Multi-*

Level Formalism to Doppler Effect Analysis—II, Nucl. Sci. Eng. **36**, 67 (1969).
12. P. A. Moldauer, *Statistical Theory of Nuclear Collision Cross Sections*, Phys. Rev. **135**, B642 (1964).
13. P. A. Moldauer, *Statistical Theory of Nuclear Collision Cross Sections. II. Distributions of the Poles and Residues of the Collision Matrix*, Phys. Rev. **136**, B947 (1964).
14. P. A. Moldauer, *Resonance Widths and Spacings: Their Averages and Distributions*, Phys. Rev. **171**, 1164 (1968).
15. P. A. Moldauer, *Interfering Resonances*, ANL-7467 (1968).
16. P. A. Moldauer, *Statistical Theory of Intermediate Resonances*, Phys. Rev. Letters **18**, 249 (1967).
17. L. W. Ehrlich, *MATSUB, Eigenvalues and Eigenvectors of Complex Nonhermitian Matrices*, (University of Texas Computation Center, Austin, Texas, 1961).
18. B. S. Garbow, *FRANCC, Eigenvalues of Complex Matrices*, Applied Mathematics Division, Argonne National Laboratory, ANL-F251S (1968).
19. P. A. Moldauer, *Average Compound Nucleus Cross Sections*, Rev. Mod. Phys. **36**, 1079 (1964).
20. D. L. Hill and J. A. Wheeler, *Nuclear Constitution and Interpretation of Fission Phenomena*, Phys. Rev. **89**, 1102 (1953).
21. N. W. Clark, *RANF, OS/360 FORTRAN IV Routine to Produce a Series of Random Numbers*, Applied Mathematics Division, Argonne National Laboratory, ANL-G552S (1967).
22. M. J. Seaton, *Diagonalization of Complex Symmetric Matrices*, Computer J. **12**, No. 2, 156 (1969).

IV-31. Shielding Study for the University of Chicago Experiment in Pioneer F/G

C. N. Kelber and A. E. McArthy

Introduction

During a six-week period, starting in April 1970, Argonne National Laboratory assisted the University of Chicago in assessing the possibilities of shielding an experiment planned for Pioneer Mission F/G. This report is a summary of the assistance given the University of Chicago personnel.

The experiment objectives included the measurement of electron fluxes in outer space and in the Jovian radiation belts. For that part of the mission in interplanetary space, the electron flux was to be determined by a type of counter telescope involving a number of solid-state detectors and anticoincidence circuits. It was considered desirable to measure the flux of electrons as a function of energy down to energies of the order of 150 keV.

Because of the direction and duration of its flight, Pioneer F/G is to be powered by radioisotope thermoelectric generators (RTG's) and chemical propellants within the space craft, as well as by nozzles for the small rocket motors which are to be heated by radioisotopic heating units (RHU's). These radioisotope sources are to contain Pu-238 as the major source of decay heat. Pu-238 decays largely through alpha emission which is accompanied by some neutron emission, both from spontaneous fission and more importantly from (α,n) reactions in light nuclei. The alpha particle decay is easily shielded by structural material encapsulating the Pu-238. There is, however, isotopic contamination present, principally in the form of Pu-236. The latter isotope has a typical alpha particle decay chain ending in Tl-208 with a characteristic 2.6 MeV gamma emission.

Calculations and early crude measurements on simulated RTG's performed at Thompson Ramo-Wooldridge Company predicted a radiation level of the order of 50–100 photons/cm^2-sec in the neighborhood of the experiment, and a fission neutron flux of the order of 50 neutrons/cm^2-sec at the same location. The photon flux, and to a lesser extent the neutron flux, induce secondary reactions within the electron detector. In particular, there will be Compton electrons induced by the principal gamma-ray emissions at 2.6 and 0.8 MeV. The Compton electrons have energies in the range of interest. There is no way to distinguish these Compton electrons from electrons incident from outer space. The target of our work was to determine if, within the limitations imposed by the conditions of the outer space mission, the background of Compton electrons induced by radiation from the RTG's and RHU's could be reduced by a minimum factor of 20 and hopefully by a factor of 100.

The limitations on the solutions were essentially those of weight and placement. The weight limitation was strict: no more than four pounds of material was allowed. The space limitation was less strict, provided the space in question was in the vicinity of the experiment site itself. However, volumes of more than a few cubic inches were probably out of the question.

There were three types of solutions considered: one was shielding at the radiation source. Such shield would be constrained not to degrade the thermal effi-

ncy of the source and had to be accommodated within the space limitations of the existing design, there being no time for redesign of the space craft. Moreover, the weight distribution in the space craft could not be adversely affected. The second method of solution was shielding at the experiment site and it was this method which received our greatest attention. The third solution was to provide a source with a much lower level of contamination and, hence, radiation escaping from the source itself. While it does not seem possible to provide such a solution for the Pioneer F/G Mission, it may be possible to provide such a solution for the so-called "Grand Tour" Mission for late in this decade.

In concluding the Introduction, we must record that the experiment to measure the low energy electron flux was abandoned, although it did seem that a marginally effective shield could be constructed, provided back-scattering from the space-craft auxiliary fuel tank was not too effective. The emphasis therefore in this report is on the analysis of what was done, as a guide to future long-range plans—especially for the Grand Tour Mission.

Selection of Materials

The primary interaction process with which we are concerned is the process of Compton scattering. When a photon is scattered inelastically and an atomic electron recoils out of an atom, Compton scattering has taken place. The energy taken up by the electron depends primarily on its recoil momentum. The Compton effect is predominant for the 1–5 MeV gamma rays in high Z materials. It is predominant over a much wider range of photon energies in low Z materials. The photo-electric effect is predominant for the low-energy photons and is the second process with which we are chiefly concerned. In general, the photo-electric effect is proportional to the proton number Z to the fifth power and decreases roughly as $1/E$ where E is the photon energy. In general, the Compton effect increases with Z and decreases slowly with E, with a value typically between 1 and 0.1 b/electron. From the foregoing we see that the major criteria for shielding of photons in the energy range from 2.6 MeV downwards is the product ZN, where Z is the number of electrons, or equivalently the proton number of the element, and N is the number of atoms of the element per b-cm. The product is the number of electrons per b-cm and since the Compton cross section is somewhere between 1 and 0.1 b/electron, this product is an indicator of the magnitude of the macroscopic Compton cross section in the material. Table IV-I lists the product ZN for a selection of materials. Of the materials listed in Table IV-31-I, four were investigated further: lead, tungsten, depleted uranium

TABLE IV-31-I. ZN for Various Materials
(Z = *proton number*; N = *atoms/b-cm*)

Element	ZN	Element	ZN
Fe	2.2	Pt	5.1
Cu	2.5	Au	4.7
W[a]	4.7	Pb	2.7
Os	5.4	U	4.4
Ir	5.4		

[a] At full density.

(U-238), and platinum. Lead was selected because of its ready availability and easy machinability even though its product ZN is low. It is, of course, a familiar shielding material. Tungsten, depleted uranium, and platinum are very similar in their shielding properties. The reason for the choice of depleted uranium instead of natural uranium is, of course, the presence of the neutron flux which, through fission of the U-235 isotope in natural uranium, would induce high energy secondary gamma rays. Even so, there is a small fraction of U-235 in the depleted uranium and this might cause some additional trouble. None of these three dense materials is particularly easy to machine, although methods exist for working with all three. In particular, there are various alloys of tungsten, primarily with nickel and copper which are only slightly less dense than the tungsten itself; these alloys are more readily machined. One such is called "heavimet". Depleted uranium is readily available and can be machined without special equipment, provided the scrap and fine metal particles are collected, while platinum requires provisions to recover the scrap because of its high intrinsic worth. Osmium, which is an obvious contender on the basis of the product ZN was not investigated because of serious questions about its availability and workability. Moreover, it is only marginally better than platinum. Both lead and gold suffer from the deficiency of being too soft. That is, under the severe accelerations to which the space-craft is subject, there is the possibility that the lead and gold might plastically deform and not only work ineffectively as shields but interfere with the experiment itself. In the case of uranium, provision would have to be made to encapsulate the uranium so that chips would not break off and possibly contaminate other experiments. This comes about because of the natural emission of the uranium itself and its daughter products.

Method of Evaluation and Results

In the short time permitted for this preliminary investigation, it was felt that highly sophisticated calculational methods would not be justified. Instead,

TABLE IV-31-II. GAMMA-RAY ATTENUATION FACTORS (INCLUDING BUILDUP) OF SLAB SHIELDS 5-CM THICK
(*calculated by hand*)

Photon Energy, MeV	Uranium	Tungsten	Lead
0.8	3.3×10^{-4}	2.0×10^{-3}	0.020
2	2.6×10^{-2}	4.1×10^{-2}	0.15
2.6	5.1×10^{-2}	4.8×10^{-2}	0.16
8	2.0×10^{-2}	2.6×10^{-2}	0.10

transport theory in slab geometry was used to calculate the transmission of photons through slabs of material. These calculations were checked by hand calculations of the gamma-ray attenuation factors including buildup. Attenuation factors were calculated by hand for shields of fixed thickness and isotopic point source. The attenuation factors were determined for source photon energies of 0.8, 2.6 and 8.0 MeV. The transport calculations were based on the use of photon cross sections originally computed by the use of the code GAMLEG in which the Klein-Nishina formula for the scattering of photons by electrons is averaged over an assumed photon energy spectrum and the scattering cross sections expanded in spherical harmonics. The cross section set used here, known as CK234, contains only the spherical harmonics of orders 0 and 1, corresponding to the capability of the neutron transport theory codes commonly in use at Argonne National Laboratory. The capability exists at ANL of generating new cross sections of higher spherical harmonic order and using them in transport theory codes, but it was felt that time did not permit nor did the needs of the preliminary investigation require such precision. Nevertheless, retention of only the zero and first-order harmonics is not a recommended procedure. In the transport problems a plane isotropic source was assumed at the origin of a slab of material 5 cm thick and infinite in the two transverse directions. The photon fluxes were calculated at centimeter intervals throughout the 5-cm thick slabs and a vacuum boundary condition was assumed at the right-hand side. The gamma flux attenuation factors calculated by hand methods are tabulated in Table IV-31-II. The gamma fluxes from the transport calculations are in Table IV-31-III.

The response of the detector to the gamma flux is expected to be proportional to the Compton cross section since the Compton electron production rate is equal to the gamma flux times the Compton cross section. The response will also be proportional to the efficiency for the detection of electrons, and this is assumed flat over the range 0.1 to 10 MeV. Then using the results given by Goldstein and Wilkins[1] the Compton response (actually the cross sections in Thomps units) is listed in Table IV-31-IV. This response function when multiplied by the gamma flux found in Table IV-31-III is the relative response for any given material. As an example, the expected response in platinum is tabulated in Table IV-31-V. The response in uranium is essentially the same as that in platinum with the exception that the uranium is somewhat more effective at lower gamma energies and slightly less effective at the higher energies. Tungsten is less effective at all energies than either uranium or platinum. By examining the ratio of the relative response at various depths of penetration through the platinum, one can arrive at an average attenuation factor per centimeter for the platinum of 3.66 for a 2 MeV source. Using this factor, we estimate that the attenuation of a 3 cm thickness of platinum will be approximately a factor of 50, which will meet most of the experiment objectives.

The recommended solution is to use a shadow shield covering approximately 50% of the detector body other than the face of the detector itself, with about 3 cm of either platinum or depleted uranium. The reason for the shadow shield is that otherwise the weight limit would be exceeded by a factor of two. Detailed mockup experiments are required to determine if backscattering from the space-ship components and other experimental equipment is sufficient to require shielding over a more extensive portion of the surface of the instrument. The instrument itself is in a housing that is similar in shape to a truncated cone. The broad base of the cone contains the sensitive element and is not shielded. There are disadvantages to either form of solution. The platinum is estimated to cost, with machining, approximately $10,000. This represents an expensive component which is essentially nonproductive of data. The depleted uranium represents a radiation source which was shown to be negligible, provided the uranium is encapsulated in a layer of heavy material. Not only is the natural uranium emission itself a source of radiation to other experiments but the other products of the uranium also contribute. This was noticed in some of the mockup experiments carried out.

EXPERIMENTAL RESULTS

Crude mockup experiments were conducted at ANL by University of Chicago personnel with ANL assistance. The experiments were conducted in an experimental cell in Building 316. Backscatter was undoubtedly present from the nearby concrete walls and a large steel tank. Low-intensity sources were used, so counting statistics were poor. The summary of results gi here was prepared at the University of Chicago:

"To investigate the extent to which given thick-

TABLE IV-31-III. Gamma Fluxes Transmitted through 5-cm Slabs from Plane Sources
(*Calculated by P_1 transport theory*)

Photon-energy Range, MeV	Material					
	Lead			U-238		
	Source Energy, Mev					
	8	2	0.8	8	2	0.8
8–6	3.44 (−3)[a]			3.44 (−3)		
–5	3.7 (−3)			6.37 (−4)		
–4	2.26 (−3)			4.21 (−4)		
–3	2.8 (−3)			5.4 (−4)		
–2.5	3.7 (−3)			7.53 (−4)		
–2.0	2.4 (−3)			4.99 (−4)		
–1.75	3.0 (−3)	4.75 (−2)		6.26 (−4)	5.48 (−3)	
–1.5	1.8 (−3)	7.96 (−3)		3.7 (−4)	1.33 (−3)	
–1.25	2.1 (−3)	8.45 (−3)		4.13 (−4)	1.38 (−3)	
–1.0	2.3 (−3)	8.77 (−3)		4.26 (−4)	1.33 (−3)	
–0.8	2.6 (−3)	9.1 (−3)		4.29 (−4)	1.24 (−3)	
–0.6	2.3 (−3)	7.6 (−3)	7.35 (−3)	3.38 (−4)	9.29 (−4)	3.55 (−5)
–0.5	2.3 (−3)	7.3 (−3)	3.3 (−3)	3.07 (−4)	8.2 (−4)	1.92 (−5)
–0.4	1.05 (−3)	3.4 (−3)	1.24 (−3)	1.42 (−4)	3.8 (−4)	7.36 (−6)
–0.3	9.04 (−4)	2.8 (−3)	9.13 (−4)	1.23 (−4)	3.28 (−4)	5.36 (−6)
–0.2	7.07 (−4)	2.2 (−3)	6.4 (−4)	0.932 (−4)	2.36 (−4)	3.0 (−6)
–0.15	3.83 (−4)	1.3 (−3)	3.4 (−4)	0.453 (−4)	1.21 (−4)	1.38 (−6)
–0.10	4.0 (−5)	1.3 (−4)	4.4 (−5)	0.04 (−6)	0.1 (−4)	1.68 (−7)
–0.0	3.83 (−6)	1.25 (−5)	3.6 (−6)	0.009 (−7)	0.02 (−4)	3.21 (−8)
	Tungsten			Platinum		
8–6	5.2 (−3)			2.6 (−3)		
–5	9.93 (−4)			5.5 (−4)		
–4	6.5 (−4)			3.7 (−4)		
–3	8.4 (−4)			4.9 (−4)		
–2.5	1.2 (−3)			7.1 (−4)		
–2.0	8.07 (−4)			4.9 (−4)		
–1.75	1.03 (−3)	8.37 (−3)		6.4 (−4)	4.5 (−3)	
–1.5	6.3 (−4)	2.2 (−3)		3.9 (−4)	1.3 (−3)	
–1.25	7.2 (−4)	2.4 (−3)		4.4 (−4)	1.4 (−3)	
–1.0	8.1 (−4)	2.55 (−3)		4.8 (−4)	1.4 (−3)	
–0.8	9.1 (−4)	2.7 (−3)		5.3 (−4)	1.5 (−3)	
–0.6	8.1 (−4)	2.3 (−3)	3.9 (−4)	4.5 (−4)	1.2 (−3)	6.9 (−5)
–0.5	8.44 (−4)	2.3 (−3)	2.5 (−4)	4.5 (−4)	1.2 (−3)	4.8 (−5)
–0.4	4.2 (−4)	1.13 (−3)	1.17 (−4)	2.2 (−4)	6.0 (−4)	2.3 (−4)
–0.3	3.76 (−4)	1.02 (−3)	1.05 (−4)	2.0 (−4)	5.0 (−4)	1.8 (−5)
–0.2	3.1 (−4)	8.4 (−4)	6.8 (−5)	1.6 (−4)	4.0 (−4)	1.1 (−5)
–0.15	1.8 (−4)	4.9 (−4)	3.4 (−5)	8.8 (−5)	2.3 (−4)	5.4 (−6)
–0.10	2.3 (−5)	6.3 (−5)	5.68 (−6)	1.0 (−5)	2.7 (−4)	9.0 (−7)
–0.0	2.4 (−6)	6.5 (−6)	5.1 (−7)	1.0 (−6)	2.7 (−5)	7.0 (−8)

[a] $x.xx(-y)$ is read as $x.xx \times 10^{-y}$.

nesses of heavy metal absorbers would shield semiconductor detectors from the radiations emitted by the RTG units to be aboard the Pioneer space-craft, experimental studies were carried out at Argonne National Laboratory using gamma-ray and neutron sources and detectors typical of the type to be used in the Pioneer experiment. The sources were supplied by the ANL people and were nominally 1 mCi of Co-60 (gamma-ray energies of 1.17 and 1.33 MeV), 1 mCi of Na-24 (gamma-ray energy of 2.76 MeV), and an americium-beryllium neutron source with an activity of 2×10^7 neutrons/sec. Studies were carried out primarily with a "windowless" lithium-drifted detector, called D-1, with a total thickness of 414 μ, a sensitive

TABLE IV-31-IV. Compton Response Function

Photon Energy Range, MeV	Response Function
8–6	0.09
–5	0.10
–4	0.12
–3	0.14
–2.5	0.18
–2.0	0.19
–1.75	0.22
–1.5	0 25
–1.25	0.26
–1.0	0.28
–0.8	0.31
–0.6	0.35
–0.5	0.40
–0.4	0.45
–0.3	0.47
–0.2	0.53
–0.15	0.60
–0.10	0.67
–0.	0.74

TABLE IV-31-V. Expected Platinum Response

Platinum Thickness, cm	Relative Response
3.0	56.
4.0	13.
5.0	4.3

TABLE IV-31-VI. Attenuation Factors, A, for Various Sources and Shields

Material	Absorber Thickness, in.		Co-60 (1.17; 1.33 MeV)	Na-24 (2.76 MeV)
	Top	Sides		
Tungsten	1½	2	A(W) = 27[a]	A(W) = 16[b]
Uranium	1½	2	A(U) = 30	
Tungsten	1¼	None	A(W) = 18	A(W) = 11
Platinum	1¼	None	A(Pt) = 28	A(Pt) = 16
Mallory-2000	1	None		A(Mall) = 6.7
Tungsten	1	None		A(W) = 6.7
Platinum	¼	None	A(Pt) = 3	

[a] See Figs. IV-31-2 and IV-31-3.
[b] See Figs. IV-31-4 and IV-3-15.

depth of 359 μ, and a sensitive area of 1.6 cm^2. This detector, hereafter referred to as D-1, was operated at 20 V bias. The shielding materials studied were tungsten, "depleted" uranium, Mallory 2000, and platinum.

"For a given source-detector geometry, the measurements consisted of taking energy loss spectra in D-1 and observing the count rate from D-1 above a given discriminator level, under conditions of no shielding and shielding. The gross features of the experimental gamma-ray findings are summarized in Table IV-31-VI, and the corresponding geometry is given in Fig. IV-31-1. The discriminator level is 155 keV for all measurements. The attenuation factor A is defined here as

$$A \equiv \frac{\text{count rate from D-1 with no shielding}}{\text{count rate from D-1 with shielding}}.$$

The quantity A is then a function of the gamma-ray energy from the source, the material used for the absorber, and the thickness of the absorber. Figures IV-31-2 through IV-31-5 give the energy loss spectra in D-1 corresponding to the entrees in the first row of Table IV-31-VI. The uranium used in these studies was found to give counts from D-1 in the absence of any gamma source. Attempts were made to correct the data taken with uranium for the direct "emissions" from the uranium. Thus, the data for the uranium is to be considered less reliable than the remaining data.

"From Table IV-31-VI, one sees that for given absorber thickness, platinum is superior to tungsten attenuation (for 1¼ in. absorber thickness) by approximately 1.5 for both Co-60 and Na-24 gamma rays. Also, for a given absorber of fixed thickness, the shielding is less effective (smaller A) for the 2.76-MeV gamma ray than for the ~1 MeV gamma rays. Figure IV-31-6 gives the attenuation A for tungsten as a function of thickness for Na-24 gamma rays. Experimental points were taken for three thicknesses only but the curve illustrates the general dependence to be expected.

"For a qualitative measure of the effects of "backscatter", the arrangement of Fig. IV-31-7 was used. The change in count rate observed when the tungsten

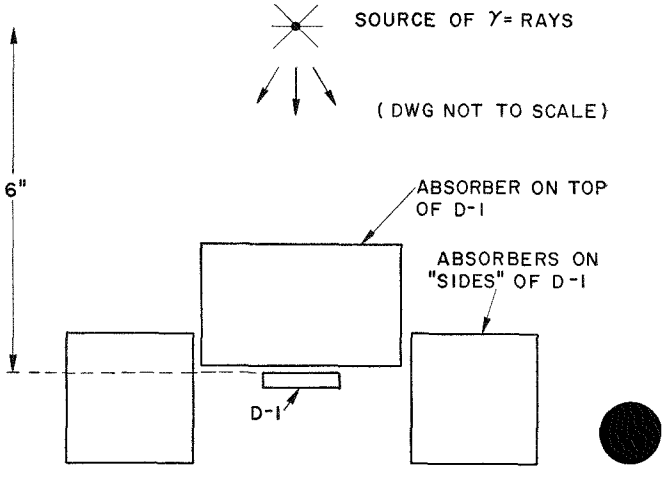

Fig. IV-31-1. Experiment Set-Up. *ANL Neg. No. 116-137.*

as substituted for the paper indicates a backscatter effect of approximately 20%. A similar measurement using platinum in place of tungsten also showed an approximate 30% effect. Crude attempts at shadow-

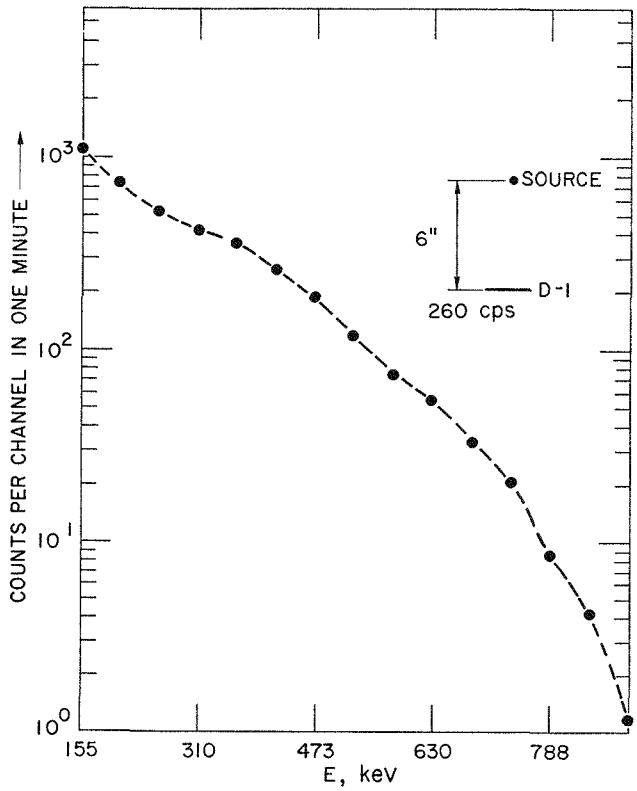

FIG. IV-31-2. Energy Loss Spectrum from CO-60 Source. *ANL Neg. No. 116-135.*

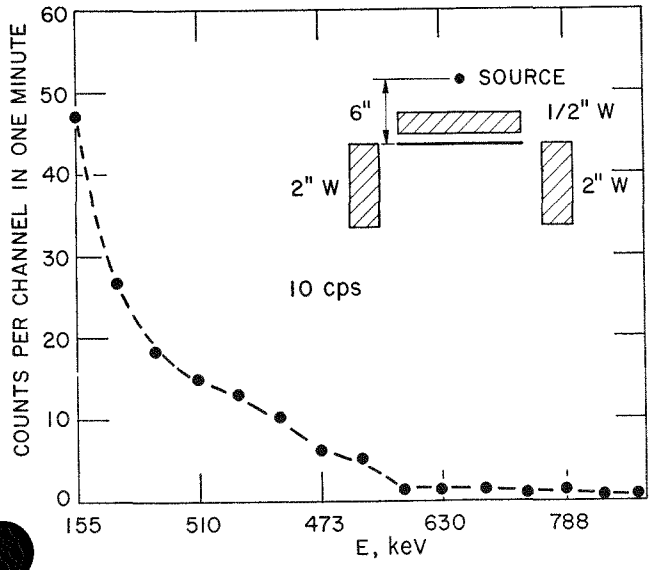

FIG. IV-31-3. D-1 Energy Loss Spectrum from Co-60 Source with W on All Four Sides. *ANL Neg. No. 116-134.*

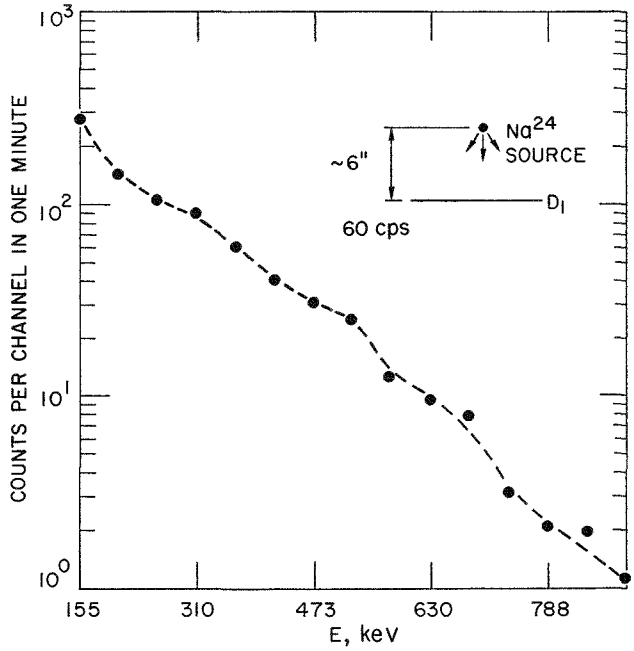

FIG. IV-31-4. D-1 Energy Loss Spectrum from Na-24. *ANL Neg. No. 116-138.*

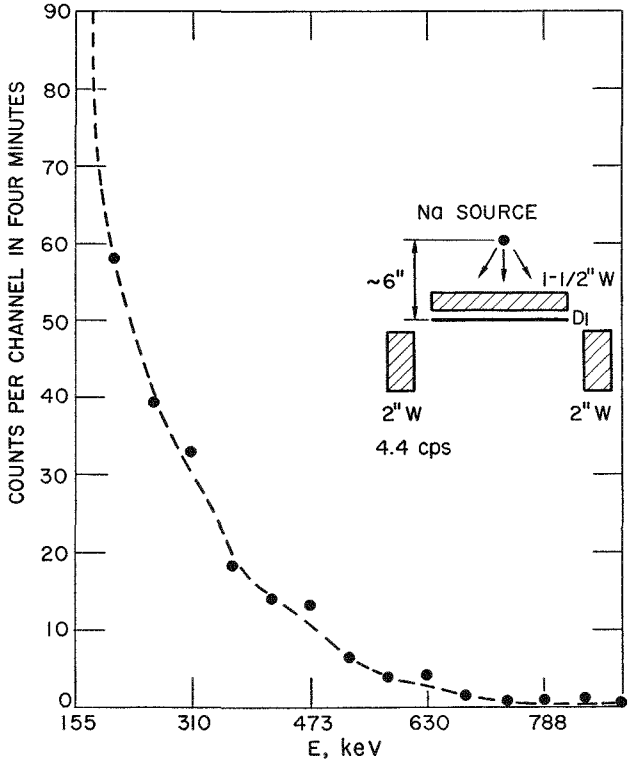

FIG. IV-31-5. D-1 Energy Loss Spectrum from Na-24 with W on All Four Sides. *ANL Neg. No. 116-133.*

shielding suggested that shadow-shielding could be successfully employed.

"The neutron source was placed at a distance of 6

in. from D-1 so that approximately 10^4 neutrons/sec were incident on D-1. The count rate from D-1 was 35 counts/sec above 155 keV. A 2-in. thickness of lithium hydride between the source and detector appeared to have no effect on the count rate from D-1."

The attenuation factor observed for 1.25 in. of platinum (~3 cm) is only 16 to 28 compared to the estimated value of approximately 50. This error arises from three sources:

(1) Backscatter in the experiment
(2) Lack of conservatism in the calculations
(3) Poor statistics.

Nevertheless, the experiments and calculations are in good agreement on the relative worth of the various materials. An estimate of the backscatter effect may be obtained by comparing the first and second entries for tungsten in Table IV-31-VI. If we estimate a constant attenuation factor per unit thickness between 1.25 and 1.5 in., then we estimate that about 25% of the counts in the 1¼ in. tungsten experiment entered through the sides—that is, from back scattering. Eliminating these counts would increase A by a factor of 1.33. For platinum this would yield $A = 37$. The other factors mentioned above should account for the remainder of the discrepancy.

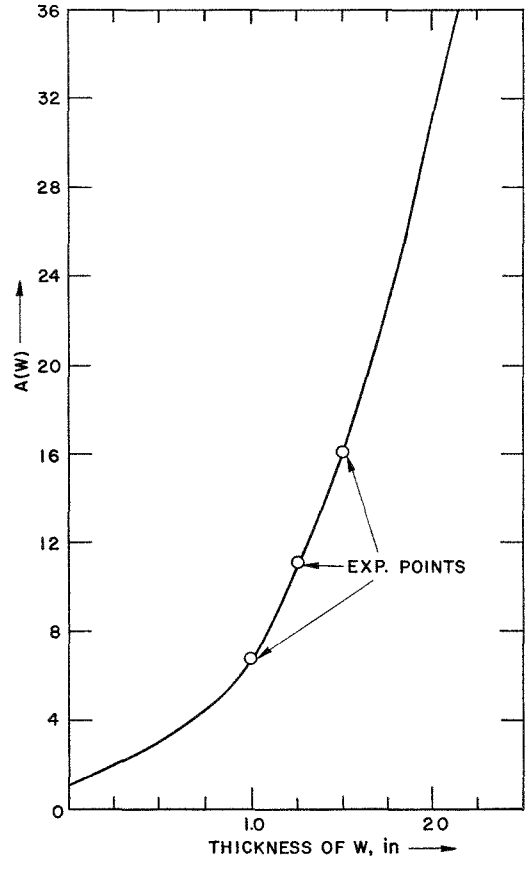

FIG. IV-31-6. Attenuation Factor for W and Na-24 γ-Rays versus W Thickness. *ANL Neg. No. 116-139.*

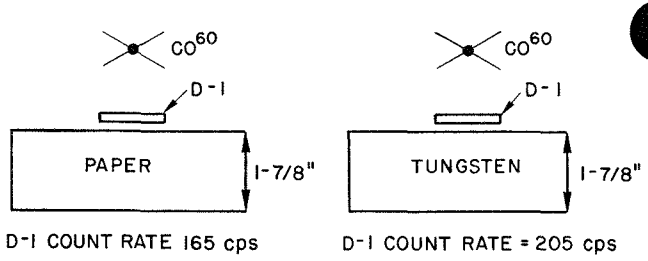

FIG. IV-31-7. Backscatter Experiment *ANL-Neg. No. 116-136.*

RECOMMENDATIONS FOR FUTURE WORK

As can be seen from both the calculations and crude mockup of experiments, it is within reason to expect that a heavy metal shield of platinum, tungsten, or depleted uranium would be satisfactory in a space craft experiment. If it is desired to measure the low-energy electron fluxes in the Grand Tour Experiment, such shielding will be necessary unless the irradiation from the sources, that is, the RTG's and RHU's, can be reduced. We therefore propose that future work, beginning in the very near future, should concentrate on two lines.

First, an effort should be made to ascertain if sources of low radiation level can be procured for the Grand Tour. Some of the ways in which such low radiation level sources can be procured are:

1. Produce low Pu-236 contamination by irradiating Np-237 in a highly thermal flux with a clad material that does not yield energetic capture gammas. This reduces Pu-236 production via $(n,2n)$ and (γ,n) processes.
2. Electromagnetic separation.
3. Chemical separation of Pu-236 daughter products following aging to allow the Pu-236 (3 year half-life) to decay.
4. Prepare Pu-238 from the irradiation of Am-241 to Am-242 which decays to Cm-242. The Cm-242 then decays to Pu-238.[2]

Because of the time limitations and the necessary long lead time for the establishment of the design parameters for deep space probes, this survey cannot take very long.

The second line of endeavor would be to optimize the shielding requirements for the space craft. The emphasis should be on optimizing the shielding requirements for all the experiments in the space craft considered as a system since the procedure of optimizing shielding for each individual experiment does not necessarily lead to the minimum shield weight. The shielding limitation, for example, of four pounds for the Uni-

versity of Chicago experiment was based on the necessarily rough estimate of probable needs prepared at a very early date without adequate knowledge of the flux distribution at the experiment site, nor of the detector sensitivity.

Argonne National Laboratory has exceptional skills in the measurement of low energy neutron and gamma fluxes and of the operation of particle detectors in gamma and neutron fields. It would appear reasonable for the Laboratory to take on the task of optimizing the space craft shield requirements with the space craft regarded as a complete system. This means involvement in the design of the Grand Tour space craft and experiment program at a very early stage.

References

1. H. Goldstein and J. E. Wilkins, Jr., *Calculation of the Penetration of Gamma Rays*, NYO-3075 (June 30, 1954).
2. D. C. Stewart, R. W. Anderson and J. Milsted, *The Production of Curium by Neutron Irradiation of* ^{241}Am, ANL-6933 (1964).

Section V

Publications

July 1, 1969 to June 30, 1970

Open Literature

1. Agrawal, A. K. and Yip, S., *Rotational Correlation Functions and Neutron Scattering by Symmetric Molecules*, Phys. Rev. **A1**(3), 970–974 (1970).
2. Agrawal, A. K. and Yip, S., *Slow-Neutron Scattering by Molecular Liquids*, Nucl. Sci. Eng. **37**, 368–379 (1969).
3. Avery, R., *Fast Reactor Physics*, Proc. ASEE-AEC Conference on Fast Reactors and the University, Rensselaer Polytechnic Institute, August 28–30, 1968, Ed., M. Becker, BI-1, pp. 1–14.
4. Bretscher, M. M. and Redman, W. C., *Low-Flux Measurements of ^{239}Pu and ^{235}U Capture-to-Fission Ratios in a Fast Reactor Spectrum*, Nucl. Sci. Eng. **39**, 368–378 (1970).
5. Cohn, C. E., Karam, R. A., Marshall, J. E. and van Doorninck, J. M., *Computer-Aided Calibration of a Fine Autorod*, Nucl. Appl. **7**, 342–345 (1969).
6. Cohn, C. E., *Digital-Computer Processing of Sampling-Oscilloscope Data*, Nucl. Instr. Methods **71**, 349 (1969).
7. Cohn, C. E., *Reading ASCII Tape on a BCD Computer*, Software Age **3**, 20–21 (1969).
8. Cohn, C. E., *Reactor-Noise Studies with an On-Line Digital Computer*, Preprints of Japan-United States Seminar on Nuclear Reactor Noise Analysis, Tokyo, September 2–7, 1968, pp. 141–160.
9. Dance, K. D., *Resonance Neutron Absorption in a Foil in a Plate-Type Lattice*, Nucl. Sci. Eng. **37**(2), 300-304 (1969) Note.
10. Davey, W. G., *An Analysis of the Neutron Capture Cross Section of U^{238} between 1 keV and 15 MeV*, Nucl. Sci. Eng. **39**, 337–360 (1970).
11. DeVolpi, A. and Porges, K. G., *Absolute Calibration of Neutron Sources Having a Wide Range of Emission Spectra*, Metrologia **5**(4), 128–141 (1969).
12. DeVolpi, A. and Porges, K. G., *^{252}Cf Half-Life by Neutron Counting: Revision*, Inorg. Nucl. Chem. Letters **5**, 699 (1969).
13. DeVolpi, A. and Porges, K. G., *Neutron Yield of ^{252}Cf Based on Absolute Measurements of Neutron Rate and Fission Rate*, Phys. Rev. **C1**(2), 683–694 (1970).
14. Fuller, E. L., Meneley, D. A. and Hetrick, D. L., *Weighted-Residual Methods in Space-Dependent Reactor Dynamics*, Nucl. Sci. Eng. **40**, 206–223 (1970).
15. Gold, R., *Cosmic Radiation and Evolution: A Lunar Experimental Test*, Radiation Effects **1**(3), 173–175 (1969).
16. Gold, R., *Cosmic-Ray Neutrons and Carbon-14 Production*, Extra-Terrestrial Matter, Ed., C. E. Randall, (Northwestern Illinois University Press, DeKalb, Illinois, 1969), pp. 275–287.
17. Gold, R., Armani, R. J. and Roberts, J. H., *Spontaneous-Fission Decay Constant of ^{241}Am*, Phys. Rev. **C1**(2), 738–740 (1970).
18. Graham, W. W., Harmer, D. S. and Cohn, C. E., *Accurate Delayed-Neutron Parameter Measurements in a Heavy-Water Reactor*, Nucl. Sci. Eng. **38**, 33–41 (1969).
19. Henryson, H. and Selengut, D. S., *Solution of the One-Velocity Transport Equation in Terms of Synthetic Kernels*, Nucl. Sci. Eng. **37**, 1–18 (1969).
20. Hwang, R. N., *Doppler Effect Studies Using Multilevel Formalism*, Nucl. Sci. Eng. **39**, 32–49 (1970).
21. Karam, R. A., *Measurements of the Normalization Integral and Spatial Distribution of the Importance of Fission Neutrons*, Nucl. Sci. Eng. **37**, 192–197 (1969).
22. Karam, R. A., Dance, K. D., Nakamura, T. and Marshall, J. E., *Analysis of Central Reactivity Worths in Fast Critical Assemblies*, Nucl. Sci. Eng. **40**, 414–423 (1970).
23. Kastner, J., Oltman, B. G., Feige, Y., Gold, R. and Congel, F., *Nuclear Radiation Detection for the Natural Environment*, IEEE Trans. Nucl. Sci. **NS-17**, 144–150 (1970).
24. Lambropoulos, P., *Multilevel Parameters for the ^{239}Pu Fission Cross Section from 40 to 100 eV*, Nucl. Sci. Eng. **40**, 342–346 (1970) Note.
25. Larsen, J. M. and Powell, J. E., *Spectrum Distortion from Amplifier Overloads in Proton-Recoil Proportional Counting*, Nucl. Instr. Methods **71**, 157 (1969).
26. Lehto, W. K., *Fission Cross-Section Ratio Measurements of ^{239}Pu and ^{233}U to ^{235}U from 0.24 to 24 keV*, Nucl. Sci. Eng. **39**, 361–367 (1970).
27. Lister, D. B. and Smith, A. B., *Fast-Neutron Scattering from Germanium*, Phys. Rev. **183**, 954–963 (1969).
28. McCarthy, P. B. and Lawroski, H., *The Design and Mechanical Performance Characteristics of the Zero Power Plutonium Reactor*, J. Eng. Power **92**, 166–181 (1970).
29. Meadows, J. W., *The Reduction of Time-of-Flight Errors in Pulsed Neutron Measurements*, Nucl. Instr. Methods **75**, 163 (1969).
30. Meadows, J. W. and Whalen, J. F., *The Thermal-Neutron-Absorption Cross Sections of ^{6}Li and ^{10}B*, Nucl. Sci. Eng. **40**, 12–16 (1970).
31. Moldauer, P. A., *Analog Fine Structure and Asymmetry*, Nuclear Isospin, Proc. 2nd Conference, Pacific Grove, California, March 13–15, 1969, Ed. J. D. Anderson, S. D. Bloom, J. Cerny, and W. W. True, (Academic Press, Inc., New York, 1969) pp. 415–419; also Bull. Am. Phys. Soc. **14**, 961 (1969).
32. Moldauer, P. A., *Averaging Methods in Nuclear Reactor Theory*, Phys. Rev. Letters **23**, 708–711 (1969).
33. Moldauer, P. A., *ERRATUM—Unitary Models of Nuclear Resonance Reactions [Phys. Rev. 157, 907 (1967)]*, Phys. Rev. **182**, 1360 (1967).
34. Pacilio, N., *Reactor-Noise Analysis in the Time Domain*, AEC Critical Review Series. USAEC, Washington, D. C. (1969).

35. Poenitz, W. P., *Experimental Determination of the Efficiency of the Grey Neutron Detector*, Nucl. Instr. Methods **72**(1), 120–122 (1969) Letter.
36. Poenitz, W. P., *Measurement of the Ratios of Capture and Fission Neutron Cross Sections of ^{235}U, ^{238}U, and ^{239}Pu at 130 to 1400 keV*, Nucl. Sci. Eng. **40**, 383–388 (1970).
37. Porges, K. G., *Note on the S^2/B Criterion of Quality for Counting Equipment [Int. J. Appl. Radiat. Isotopes **19**, 711 (1968)]*, Int. J. Appl. Radiat. Isotopes **21**, 181–182 (1970).
38. Porges, K. G., Gold, R. and Corwin, W. C., *Reactor Power Monitor Based on Cherenkov Radiation Detection*, IEEE Trans. Nucl. Sci. **NS-17**, 501–505 (1970).
39. Porges, K. G., Rush, C. J. and Caya, G. E., *Reduction of Processing Losses in On-Line or Off-Line Acquisition of Random Counts at High Rates*, Nucl. Instr. Methods **78**(1), 115–119 (1970).
40. Porges, K. G., Corwin, W. C., Burkel, L. P. and Lewandowski, E., *Signal Transmission Line with Low Attenuation and Wide Frequency Passband*, Rev. Sci. Instr. **41**, 138–139 (1970) Note.
41. Rudnick, S. J., Michaud, P. L. and Porges, K. G., *Continuous Digital Ratemeter*, Nucl. Instr. Methods **71**(2), 196–200 (1969).
42. Sanathanan, C. K., Sandberg, A. A., Carter, J. C. and Bryant, L. T., *Advances in the Hybrid Simulation of Nuclear Reactor Transients*, Proc. Intern. Symposium on Analogue and Hybrid Computation Applied to Nuclear Energy, Versailles, September 16–18, 1968 (Presses Academiques Europeennes, Brussels, 1969), pp. 111–120.
43. Segev, M., *An Approximate Solution to the Asymptotic Slowing Down Equations of Fast Neutrons*, Nucl. Sci. Eng. **40**, 424–437 (1970).
44. Sherwood, G. L., Smith, A. B. and Whalen, J. F., *Fast Neutron Cross Sections of Hafnium, Gadolinium, and Samarium*, Nucl. Sci. Eng. **39**, 67–80 (1970).
45. Smith, A. B., Whalen, J. F., Barnard, E., DeVilliers, J. A. M. and Reitmann, D., *Fast-Neutron Total and Scattering Cross Sections of Bismuth*, Nucl. Sci. Eng. **41**, 63–69 (1970)
46. Smith, A. B., Whalen, J. F. and Takeuchi, K., *Fast Neutrons Incident on Vanadium*, Phys. Rev. **C1**(2), 581–593 (1970).
47. Smith, R. R., Cushman, R. A., Hyndman, R. W., Kirn, F. S., Long, J. K., Loewenstein, W. B., Madell, J. T., Bump, T. R. and Persiani, P. J., *Recent Operating Experience with EBR-II*, Proc. British Nuclear Energy Soc. Meeting on the Physics of Fast Reactor Operation and Design, London, June 24–26, 1969, pp. 354–361.
48. Stacey, W. M., *Space Time Nuclear Reactor Kinetics*, (Academic Press, New York, 1969).
49. Stacey, W. M., *General Multigroup and Spectral Synthesis Equations*, Nucl. Sci. Eng. **40**, 73–90 (1970).
50. Till, C. E., Gasidlo, J. M., Groh, E. F., LeSage, L. G., Robinson, W. R. and Stanford, G. S., *Null-Reactivity Measurements of Capture/Fission Ratio in ^{235}U and ^{239}Pu*, Nucl. Sci. Eng. **40**, 132–136 (1970).
51. Till, C. E., Davey, W. G., Lewis, R. A. and Palmer, R. G., *Argonne National Laboratory Critical Experiment Program*, Proc. British Nuclear Energy Soc. Meeting on Physics of Fast Reactor Operation and Design, London, June 24–26, 1969, Paper 1.3, pp. 40–49.
52. Whalen, J. F., *A Fast Neutron Automated Data Acquisition System*, Proc. Skytop Conference on Computer Systems in Experimental Nuclear Physics. U. S. Atomic Energy Commission Report, CONF-690301 (1969), pp. 77–89.

Reports

1. Fuller, E. L., *Weighted-Residual Methods in Space-Dependent Reactor Dynamics*, ANL-7565 (1969).
2. Lambropoulos, P. P. and Luco, V., *Functionals for Flux Synthesis with Discontinuous Trial Functions*, ANL-7627 (1969).
3. Moldauer, P. A., Hwang, R. N. and Garbow, B. S., *MATDIAG, A Program for Computing Multilevel S-Matrix Resonance Parameters*, ANL-7590 (1969).
4. Plumlee, K. E., Daughtry, J. W., Johnson, T. W., Robinson, W. R., Schultz, R. A. and Stanford, G. S., *Argonne Advanced Research Reactor Critical Experiments*, ANL-7483 (1969).
5. Robinson, L. E. and Purviance, R. T., *Pressure Transducers for TREAT Sodium Loops*, ANL-7107 (1969).
6. Sherwood, G. L., Smith, A. B. and Whalen, J. F., *Fast-Neutron Cross Sections of Hafnium, Gadolinium, and Samarium*, ANL-7567 (1969).
7. Smith, A. B., Whalen, J. F., Barnard, E., DeVilliers, J. A. M. and Reitmann, D., *Fast-Neutron Total and Scattering Cross Sections of Bismuth*, ANL-7636 (1969).
8. Smith, A. B., Whalen, J. F. and Takeuchi, K., *Fast Neutrons Incident on Vanadium*, ANL-7564 (1969).
9. Smith, R. R., Bump, T. R., Cushman, R. A., Hyndman, R. W., Kirn, F. S., Loewenstein, W. B., Long, J. K., Madell, J. T., Persiani, P. J. and Wallin, W. R., *The Effects of an Over-Cooled Stainless Steel Reflector on the EBR-II Power Coefficient*, ANL-7544 (1969).
10. Stanford, G. S. and Seckinger, J. H., *Thickness Corrections for Neutron Activated Gold Foils*, ANL-7545 (1969).
11. Stewart, R. R., Dickerman, C. E., Robinson, L. E. and Doe, W. B., *Studies of Fast Reactor Fuel Element Behavior under Transient Heating to Failure. III. In-Pile Experiments on Irradiated UO_2 Fuel Pins in the Absence of Coolant*, ANL-7552 (1969).
12. Stewart, R. R., Dickerman, C. E., Stalica, N. R. and Doe, W. B., *A Study of the Physical Properties of Nominal 0.7, 3, and 6 a/o Burnup UO_2 Fast-Reactor Fuel Pins Preparatory to Transient TREAT Exposure*, ANL-7571 (1969).
13. Swanson, C. D. and Bohn, E. M., *GASOUT—The Code Used to Calculate Gaseous Fission Product Release for a ZPR-6 and -9 Design Basis Accident*, ANL-7534 (1970).
14. *Reactor Physics Division Annual Report, July 1, 1968 to June 30, 1969*, ANL-7610.

Abstracts

1. Agrawal, A. K., *On the Analyses of the Fuel Meltdown Studies with TREAT*, Trans. Am. Nucl. Soc. **12**(2), 865 (November 1969).
2. Armani, R. J., Gold, R., Larsen, R. P. and Roberts, J. H., *Measured Fission Yields of ^{99}Mo and ^{140}Ba in Fast-Neutron-Induced Fission of ^{239}Pu*, Trans. Am. Nucl. Soc. **13**(1), 90 (June 1970).
3. Armani, R. J., Gold, R. and Roberts, J. H., *Fission Process Phenomena Observed with Solid-State Track Recorders*, Abstracts of Papers Presented at the 158th American Chemical Society Meeting, New York, September 8–12, 1969, NUCL-41.
4. Bennett, E. F., *Low-Energy Limitations on Proton-Recoil Spectroscopy through the Energy Dependence of W*, Trans. Am. Nucl. Soc. **13**(1), 269 (June 1970).
5. Bretscher, M. M., Gasidlo, J. M. and Redman, W. C., *Comparison of Measured and Calculated Capture-to-Fis-*

sion Ratios in a Soft Spectrum Fast Critical Assembly, Trans. Am. Nucl. Soc. **13**(1), 89 (June 1970).
6. Carpenter, S. G., Gasidlo, J. M. and Stevenson, J. M., β_{eff} *Measurements in Two Fast Reactor Critical Assemblies*, Trans. Am. Nucl. Soc. **13**(1), 92 (June 1970).
7. Carpenter, S. G. and Ramchandran, S. β_{eff} *Ratio Measurements*, Trans. Am. Nucl. Soc. **12**(2), 650 (November 1969).
8. Cohn, C. E., *A Physical Random-Number Generator*, Trans. Am. Nucl. Soc. **12**(2), 725 (November 1969).
9. Cohn, C. E., *Speed Tests on Some Control Computers*, Trans. Am. Nucl. Soc. **13**(1), 177 (June 1970).
10. Congel, F. J., Roberts, J. H., Armani, R. J., Casson, H., Gold, R., Kastner, J. and Oltman, B. G., *Measurements of Absolute Thermal Neutron Densities with Mica Fission Track Recorders*, Bull. Am. Phys. Soc. **15**, 86 (January 1970).
11. Corwin, W. C., Porges, K. G. and Daly, R. T., *Level Distribution of Count Rate Meters for Various Circuit Parameters Not Giving Gaussian Distributions*, Trans. Am. Nucl. Soc. **13**(1), 241 (June 1970).
12. Dance, K. D., Karam, R. A., Marshall, J. E. and Pond, R. B., *Central Reactivity Worth Measurements and Calculations*, Trans. Am. Nucl. Soc. **12**(2), 647 (November 1969).
13. Daughtry, J. W. and Lewis, R. A., *Uranium Doppler Measurements in Oxide Core Critical Assemblies*, Trans. Am. Nucl. Soc. **12**(2), 720 (November 1969).
14. Davey, W. G. and Hess, A. L., *Validity of Fast-Critical Experiments as Integral Test of ENDF/B*, Trans. Am. Nucl. Soc. **12**(2), 717 (November 1969).
15. DeVolpi, A. and Porges, K. G., *An Absolute Measurement of* ν^{252} *(Cf) and Its Relationship to the Neutron Yield for Fissionable Materials*, Trans. Am. Nucl. Soc. **12**(2), 759 (November 1969).
16. DeVolpi, A., Dickerman, C. E. and Boland, J. F., *Preliminary Performance Data from Fast Neutron Hodoscope at TREAT*, Trans. Am. Nucl. Soc. **12**(2), 868 (November 1969).
17. Dickerman, C. E., Robinson, L. E., Agrawal, A. K. and Boland, J. F., *First TREAT Loop Experiments on Oxide Fuel Meltdown*, Trans. Am. Nucl. Soc. **12**(2), 867 (November 1969).
18. Fuller, E. L., Meneley, D. A. and Hetrick, D. L., *Integration of the Multimode Kinetics Equations by the Method of Undetermined Parameters*, Trans. Am. Nucl. Soc. **12**(2), 710 (November 1969).
19. Gold, R., *Compton Recoil Measurement of Continuous Gamma-Ray Spectra*, Trans. Am. Nucl. Soc. **13**(1), 421 (June 1970).
20. Gold, R. and Porges, K., *Detection System for Super-Heavy Cosmic Rays*, Bull. Am. Phys. Soc. **14**, 1210 (December 1969).
21. Hess, A. L., Palmer, R. G. and Stevenson, J. M., *A Post-analytical Study of Eight ZPR-3 Benchmark Criticals Using ENDF/B Data*, Trans. Am. Nucl. Soc. **13**(1), 288 (June 1970).
22. Hoover, L. J. and Meneley, D. A., *The Influence of Neutron Energy Group Structure on Fuel Cycle Analysis of Fast Breeder Reactors*, Trans. Am. Nucl. Soc. **12**(2), 441 (November 1969).
23. Karam, R. A. and Marshall, J. E., *Analysis of Sodium-Void Coefficients*, Trans. Am. Nucl. Soc. **13**(1), 254 (June 1970).
24. Karam, R. A. and Marshall, J. E., *Critical Mass Sensitivity to the Treatment of Heterogeneity Effects in a Large UC Fast Core. Assembly 5 of ZPR-6*, Trans. Am. Nucl. Soc. **12**(2), 718 (November 1969).
24a. Kastner, J., Oltman, B. G., Feige, Y. and Gold, R., *Safety Considerations for Plutonium Fuel Operation for ZPR-6 and -9*, Trans. Am. Nucl. Soc. **12**, (Suppl.), 27 (October 1969).
25. Kato, W. Y., Armani, R. J., Larsen, R. P., Moreland, P. E., Mountford, L. A., Gasidlo, J. M., Popek, R. J. and Swanson, C. D., *An Integral Measurement of* ^{239}Pu *Alpha*, Trans. Am. Nucl. Soc. **13**(1), 88 (June 1970).
26. Kato, W. Y., Dates, L. R., Rusch, G. K. and Plumlee, K. E., *Safety Considerations for Plutonium Fuel Operation for ZPR-6 and -9*, Trans. Am. Nucl. Soc. **12**(Suppl.), 27 (October 1969).
27. Kikuchi, Y., *The Intermediate Structure of the Fission Width of* ^{239}Pu, Trans. Am. Nucl. Soc. **13**(1), 312 (June 1970).
28. Lambropoulos, P. P. and Luco, V., *On the Evaluation of Functionals with Discontinuous Trial Functions*, Trans. Am. Nucl. Soc. **13**(1), 178 (June 1970).
29. Lehto, W. K. and Goin, R. W., *The Effects of S/N Ratio on the Results of Polarity Correlation Experiments*, Trans. Am. Nucl. Soc. **13**(1), 271 (June 1970).
30. LeSage, L. G., Till, C. E. and Stanford, G. S., *Comparison of Measured and Calculated Null Compositions, Central Reaction Ratios and Reactivity Worths in ZPR-9 Assemblies 24 and 25 and ZPR-3 Assembly 55*, Trans. Am. Nucl. Soc. **13**(1), 93 (June 1970).
31. Lewis, R. A., Dance, K. D., Groh, E. F., Martens, F. H., Meyer, J. F. and Johnson, T. W., *The Argonne Variable-Temperature Rodded-Zone Facility*, Trans. Am. Nucl. Soc. **12**(2), 696 (November 1969).
32. Matlock, R. G., Amundson, P. I., Kaiser, R. E., Young, J. C., Vosburgh, R. O., Gasidlo, J. M. and Forrester, R. J., *ZPPR Start-Up and Operating Experience*, Trans. Am. Nucl. Soc. **12**(Suppl.), 46 (October 1969).
33. Matlock, R. G., Kaiser, R. E. and Gasidlo, J. M., *Reactivity Effects in Critical Facilities Due to Fissile Isotope Decay*, Trans. Am. Nucl. Soc. **12**(2), 652 (November 1969).
34. McElroy, W. N., Armani, R. J., and Tochilin, E., *Comparison of Multiple Foil and Time-of-Flight Neutron Flux Spectra in a Bare* ^{235}U *Assembly*, Trans. Am. Nucl. Soc. **12**(2), 757 (November 1969).
35. Meneley, D. A. and Ott, K. O., *Spectral Effects in Liquid Metal Fast Breeder Reactor Transients*, Trans. Am. Nucl. Soc. **12**(2), 706 (November 1969).
36. Meyer, W. and Simons, G. G., *Measured Fast-Neutron Spectra after Reflection of Fission Source Neutrons from a Six-Inch-Thick Steel Slab*, Trans. Am. Nucl. Soc. **12**(2), 960 (November 1969).
37. Moldauer, P. A., *Theory of Neutron Cross Sections for Shielding*, Trans. Am. Nucl. Soc. **12**(2), 921 (November (1969).
38. Moldauer, P. A., *Theory of Fast Reactor Cross Sections*, Abstracts of Papers Presented at the 158th American Chemical Society Meeting, New York, September 8–12, 1969, NUCL-37.
39. Nicholson, R. B., *Bilinear Weighting of Cross Sections for Group Collapsing and Cell Homogenization in Transport Calculations*, Trans. Am. Nucl. Soc. **12**(2), 731 (November 1969).
40. Okrent, D., Kallfelz, J. M., Loewenstein, W. B., Rossin, A. D., Smith, A. B. and Zolotar, B. A., *Neutron Energy Spectra for Fast Reactor Irradiation Effects*, Trans. Am. Nucl. Soc. **12**(2), 701 (November 1969).

41. Olson, A. P. and Stevenson, J. M., *Calculation of Heterogeneity Effects in ZPR-Type Reactors*, Trans. Am. Nucl. Soc. **12**(2), 625 (November 1969).
42. Ott, K. O., *An Improved Definition of the Breeding Ratio for Fast Reactors*, Trans. Am. Nucl. Soc. **12**(2), 719 (November 1969).
43. Palmer, R. G., Plummer, J. P. and Nicholson, R. B., *Testing of Heterogeneity Methods Used in Fast Reactor Critical Analyses by Comparison with Theoretical (GEDANKEN) Experiments*, Trans. Am. Nucl. Soc. **13**(1), 253 (June 1970).
44. Plummer, J. P. and Palmer, R. G., *Extended Equivalence between Homogeneous and Heterogeneous Resonance Integrals in Slabs*, Trans. Am. Nucl. Soc. **12**(2), 625 (November 1969).
45. Poenitz, W. P., *The Fission Cross Section Ratio of ^{239}Pu and ^{235}U in the Neutron Energy Range 150 to 1400 keV*, Trans. Am. Nucl. Soc. **12**(2), 742 (November 1969).
46. Powell, J. E., *Comparison of Proton-Recoil Proportional Counter and Time-of-Flight Neutron Spectrum Measurements in a ^{235}U-Fueled Fast Reactor*, Trans. Am. Nucl. Soc. **12**(2), 712 (November 1969).
47. Ramchandran, S. and Palmer, R. G., *Analysis of Graphite Density Reactivity Measurements in ZPR-3, Assembly 53*, Trans. Am. Nucl. Soc. **12**(2), 691 (November 1969).
48. Roberts, J. H., Congel, F. J., Armani, R. J., Gold, R., Kastner, J. and Oltman, B. G., *Environmental Neutron Measurements with Solid-State Track Recorders*, Trans. Am. Nucl. Soc. **13**(1), 419 (June 1970).
49. Rogers, V. A., *^{239}Pu Doppler Analysis for a Proposed ZPR-3 Assembly*, Trans. Am. Nucl. Soc. **13**(1), 320 (June 1970).
50. Rothman, A. B., Renken, C. J., Stewart, R. R., Dewey, G. G., Hutchinson, D. R. and Dickerman, C. E., *Transient Behavior of Pre-Irradiated "High-Swelling" EBR-II Driver Fuel in TREAT*, Trans. Am. Nucl. Soc. **12**(2), 867 (November 1969).
51. Segev, M., *A Simple Analytic Representation of Fast Reactor Spectra*, Trans. Am. Nucl. Soc. **12**(2), 640 (November 1969).
52. Segev, M., *Single-Level Inelastic Scattering in a Simple Approximate Way*, Trans. Am. Nucl. Soc. **13**(1), 295 (June 1970).
53. Sha, W. T. and Waltar, A. E., *Fast Reactor Disassembly Calculation Utilizing a Temperature-Density-Dependent Equation of State*, Trans. Am. Nucl. Soc. **12**(2), 8[illegible] (November 1969).
54. Seigmann, E. R., *A Compressible Model for Transient Sodium Boiling*, Trans. Am. Nucl. Soc. **12**(2), 904 (November 1969).
55. Simons, G. G. and Larson, J. M., *Liquid Organic Fast-Neutron Detector Assembly*, Trans. Am. Nucl. Soc. **13**(1), 429 (June 1970).
56. Smith, A. B. and Whalen, J. F., *Fast Neutrons Incident on Holmium*, Bull. Am. Phys. Soc. **15**, 86 (January 1970).
57. Smith, D. L., *Investigation of Low-Excitation States in ^{75}As by the $^{75}As(n,n'\gamma)$ Reaction*, Bull. Am. Phys. Soc. **15**, 86 (January 1970).
58. Stacey, W. M., *A New Definition of Composite Moderating Parameters for the Goertzel-Greuling Continuous Slowing Down Theory*, Trans. Am. Nucl. Soc. **13**(1), 199 (June 1970).
59. Stacey, W. M., *Resolved Resonance Reaction Rates in Fast Reactors*, Trans. Am. Nucl. Soc. **13**(1), 295 (June 1970).
60. Stanford, G. S., Till, C. E. and Robinson, W. R., *Measuring Reaction Rates in Heterogeneous Fast-Reactor Cells*, Trans. Am. Nucl. Soc. **12**(2), 715 (November 1969).
61. Takeuchi, K. and Moldauer, P. A., *R-Matrix Shell Model Calculations of Scattering and Reaction Cross Sections*, Bull. Am. Phys. Soc. **15**, 503 (April 1970).
62. Till, C. E. and Davey, W. G., *The Demonstration Reactor Benchmark Critical Assemblies Program*, Trans. Am. Nucl. Soc. **13**(1), 293 (June 1970).
63. Travelli, A., *A Formulation of High-Order Perturbation Theory for Critical Systems*, Trans. Am. Nucl. Soc. **13**(1), 186 (June 1970).
64. Travelli, A., Ulrich, A. J. and Beitel, J. C., *Analysis of Reactivity Changes Associated with Large Perturbations in ZPPR/FTR-2*, Trans. Am. Nucl. Soc. **13**(1), 321 (June 1970).
65. Yule, T. J., *High-Energy Limitations in Neutron Spectrometry with Proton-Recoil Proportional Counters*, Trans. Am. Nucl. Soc. **13**(1), 269 (June 1970).
66. Yule, T. J. and Bennett, E. F., *Prediction of Wall and End Effects in Proton-Recoil Spectrometers*, Trans. Am. Nucl. Soc. **12**(2), 517 (November 1969).
67. Zolotar, B. A., Sehgal, B. R. and Kallfelz, J. M., *Fast Reactor Integral Studies of Modifications to ENDF/B ^{238}U Inelastic Scattering*, Trans. Am. Nucl. Soc. **12**(2), 743 (November 1969).